GSI Scientific Report 2013

GSI Report 2014-1
<http://www.gsi.de/library/GSI-Report-2014-1/>
DOI:10.15120/GR-2014-1

ISSN: 0174-0814
and GSI Report 2014-1

Publisher: GSI Helmholtzzentrum für Schwerionenforschung GmbH,
Planckstr. 1, 64291 Darmstadt, Germany, <http://www.gsi.de>
GSI is a member of the Helmholtz association of national research centres <http://www.helmholtz.de>.
E-only-edition: <http://www.gsi.de/library/GSI-Report-2014-1/>
DOI:10.15120/GR-2014-1

Editor: Katrin Große,
Contact: gsilibrary@gsi.de, phone: +496159 712610, fax: +496159 713049.
Cover design: B. Schausten.
Publication date: October 2014

Copyright © 2014 by GSI Darmstadt, all rights reserved.

For the production of this report templates and scripts of the JACoW collaboration (Joint Accelerator Conferences on Web <http://www.jacow.org>) were used.

Foreword

The year 2013 has been exceptional - in two extreme ways.

On one hand, we witnessed important progress in the technological developments for the accelerator and detector components for FAIR, the Facility for Antiproton and Ion Research, the future project of GSI and the international science community in the fields of hadron and nuclear sciences as well as for many applications in atomic and biophysics and material research. Several Technical Design reports have been concluded in 2013 (i.e. CBM Silicon Tracking Stations). From the Manne-Siegbahn-Laboratory in Stockholm the CRYRING storage ring has been delivered to the future FAIR accelerator facility. This storage ring will be assembled first at the existing GSI facility to conduct experiments and machine tests. Elaborate alterations of GSI's large ring accelerator SIS18 have been concluded end of 2013 after one year of work which included in particular the installation of a new accelerator cavity.

On the other hand, the necessary focussing of GSI on the FAIR project came with a price: no beam time at GSI and financial support in the research department at the bare minimum. Despite these less than optimal conditions, my colleagues in the research department have reached many scientific firsts, based on experiments performed in earlier years or outside of GSI and very often supported by collaborations with the Helmholtz Institutes in Jena and Mainz or within the HIC4FAIR excellence initiative and the Helmholtz Alliance 'Cosmic Matter in the Laboratory'. This report summarizes the achieved scientific highlights and the path taken by the research department towards FAIR.

I am grateful to my colleagues for not having lost the motivation accepting the severe cuts in the ongoing research activities and maintaining their drive for our joint goal in 2020: to open up an unprecedented science program at the international FAIR facility in Darmstadt.

Karlheinz Langanke

Contents

Foreword . . . iii
Contents . . . v

Division CBM / NQM (Nuclear and Quark Gluon Matter) **1**
Department HADES . . . 1
NQM-HADES-01 – Investigations on two-particle correlations in $p + ^{93}Nb$ collisions at E_{kin} = 3.5 GeV . . . 1
NQM-HADES-02 – Kaon in-medium potential probed in proton-nucleus reactions . . . 2
NQM-HADES-03 – Search for a "ppK^-" bound state in p+p collisions . . . 3
NQM-HADES-04 – A new upper limit on the rare decay $\eta \to e^+e^-$ . . . 4
NQM-HADES-05 – Searching a Dark Photon with HADES . . . 5
NQM-HADES-06 – Hunting for K^{*+} in pp and pNb reactions . . . 6
NQM-HADES-07 – Electron identification in Au+Au collisions at 1.23 GeV/u in HADES using multivariate analysis . . . 7
NQM-HADES-08 – π^0 reconstruction via conversion method in Au+Au at 1.23AGeV with HADES 8
NQM-HADES-09 – The HADES alignment strategy . . . 9
NQM-HADES-10 – Integration of the Pion-Beam Tracker into the HADES DAQ . . . 10
NQM-HADES-11 – Diamond detector preparation for high intensity beam monitoring and high precision T0 determination . . . 11
NQM-HADES-12 – Test of the HADES Electromagnetic Calorimeter modules on photon beam . 12
NQM-HADES-13 – A Precise Multi-Channel QDC FEE utilizing FPGAs as Discriminators and Delay Elements Based on the TRB3 as TDC and Readout Platform . . . 13
Department CBM . . . 15
NQM-CBM-01 – Status of the Compressed Baryonic Matter (CBM) experiment at FAIR . . . 15
NQM-CBM-02 – Quench calculation for the CBM Dipole magnet . . . 17
NQM-CBM-03 – Quench detection and protection system for the CBM dipole magnet . . . 18
NQM-CBM-04 – Quality assessment of ultra-thin CMOS sensors for the Micro Vertex Detector of the CBM experiment at FAIR . . . 19
NQM-CBM-05 – The next generation of CBM MVD read-out electronics . . . 20
NQM-CBM-06 – The layout of the CBM Silicon Tracking System . . . 21
NQM-CBM-07 – Silicon strip sensor layout for the CBM Silicon Tracking System . . . 22
NQM-CBM-08 – Performance of neutron irradiated prototype sensors for the CBM Silicon Tracking System . . . 23
NQM-CBM-09 – Measurement of coupling and interstrip capacitances in silicon microstrip sensors for the CBM experiment at FAIR . . . 24
NQM-CBM-10 – In-beam test of prototype modules for the CBM Silicon Tracking System . . . 25
NQM-CBM-11 – Full-size prototype microstrip sensors for the CBM Silicon Tracking System . . 26
NQM-CBM-12 – First mock-up of the CBM STS module based on a new assembly concept . . . 27
NQM-CBM-13 – Low and high voltage power supply for STS detector electronics . . . 28
NQM-CBM-14 – Calibration of a laser scanning system for quality assurance of CBM prototype silicon microstrip sensors . . . 29
NQM-CBM-15 – Automized quality assurance of sensors for the CBM Silicon Tracking System . 30
NQM-CBM-16 – Application of the CBM Silicon Tracking System CAD model for integration studies . . . 31
NQM-CBM-17 – An improved detector response simulation for the Silicon Tracking System . . . 33

NQM-CBM-18 – A front-end electronics board to test the assembly procedure of modules for the CBM Silicon Tracking System . . . 34
NQM-CBM-19 – A mechanical model of an STS station for the study of cable routing . . . 35
NQM-CBM-20 – A setup for adjustment of process parameters for CBM module production . . 36
NQM-CBM-21 – Development of a CO_2 cooling prototype for the CBM Silicon Tracking System 37
NQM-CBM-22 – Cherenkov photon detection with WLS coated MAPMTs . . . 38
NQM-CBM-23 – Ronchi test for measurements for the mirror surface of the CBM-RICH detector 39
NQM-CBM-24 – Characterization of the GET4 v1.0 TDC ASIC with detector signals . . . 40
NQM-CBM-25 – Event based unpacker and digitizer for the CBM TOF in CBMROOT . . . 41
NQM-CBM-26 – High counting rate test of the basic structure for the inner zone of the CBM RPC-TOF . . . 42
NQM-CBM-27 – 100 Ohm transmision line multi-strip multi-gap high counting rate RPC prototype 43
NQM-CBM-28 – RPC prototype test with cosmic irradiation . . . 44
NQM-CBM-29 – CBM TRD radiator simulation in CbmRoot . . . 45
NQM-CBM-30 – Construction and first performance studies of a CBM TRD prototype with alternating wires developed in Frankfurt . . . 46
NQM-CBM-31 – Development of an online feature extraction pre-processing stage for TRD based on SPADIC 1.0 . . . 47
NQM-CBM-32 – e/π Discrimination and position resolution of a real size CBM-TRD prototype . 48
NQM-CBM-33 – Design of new SPADIC front-end boards for TRD readout . . . 49
NQM-CBM-34 – Commissioning of the SPADIC 1.0 Amplifier / Digitizer Chip . . . 50
NQM-CBM-35 – Testing of $31cm \times 31cm$ GEM Chamber at COSY . . . 51
NQM-CBM-36 – CBM First-level Event Selector Data Management Developments . . . 52
NQM-CBM-37 – Status of the CBMnet based FEE DAQ readout . . . 53
NQM-CBM-38 – A Monte Carlo feasibility study of the CBM event reconstruction at high interaction rates based on time information . . . 54
NQM-CBM-39 – Employing the CBM Micro Vertex Detector for Background Rejection in Dilepton Analyses . . . 55
NQM-CBM-40 – Production of hyperons at FAIR energies . . . 56
NQM-CBM-41 – Reaction plane reconstruction in the CBM experiment . . . 57
NQM-CBM-42 – The di-muon measurements with CBM at SIS100 . . . 58
Department FOPI . . . 59
NQM-FOPI-01 – Constraining the nuclear matter equation of state around twice saturation density 59
NQM-FOPI-02 – Differences in population of the phase space for $K^{\pm}$-mesons produced in π-induced reactions with heavy and light targets . . . 60
NQM-FOPI-03 – Status of the $pk\Lambda$ Analysis in pp Collisions with the FOPI Spectrometer . . . 61
NQM-FOPI-04 – Cluster Error of the FOPI TPC . . . 62
NQM-FOPI-05 – Discharge probability studies with GEM detectors . . . 63
NQM-FOPI-06 – Ion backflow studies with a triple GEM detector . . . 64
Department ALICE . . . 65
NQM-ALICE-01 – Performance of the ALICE Experiment during the LHC Run 1 . . . 65
NQM-ALICE-02 – Multiplicity dependence of the average transverse momentum in pp, p-Pb, and Pb-Pb collisions at the LHC . . . 66
NQM-ALICE-03 – Nuclear Modification Factor and Centrality Determination in p-Pb Collisions at ALICE . . . 67
NQM-ALICE-04 – Measurement of charged jets in p-Pb collisions with ALICE . . . 68
NQM-ALICE-05 – Measurement of electrons from charm and beauty-hadron decays in p-Pb collisions at $\sqrt{s_{NN}}$ = 5.02,TeV with ALICE at the LHC . . . 69
NQM-ALICE-06 – J/ψ production in p-Pb collisions measured with ALICE at the LHC . . . 70
NQM-ALICE-07 – J/ψ production in Pb-Pb collisions measured with ALICE . . . 71
NQM-ALICE-08 – Azimuthal correlation measurements with ALICE at the LHC . . . 72
NQM-ALICE-09 – Deuteron production in Pb-Pb collisions measured with ALICE at the LHC . 73
NQM-ALICE-10 – Validation of Bayesian PID in ALICE, for the channel $D^0 \rightarrow K^-\pi^+$ in pp at $\sqrt{s}$ = 7 TeV . . . 74
NQM-ALICE-11 – Study of Higher Order Net-Particle Fluctuations at LHC Energies . . . 75

Division PANDA / HSD (Hadron Structure and Dynamics) **77**
Departments Hadron Physis I and Hadron Physics II . . . 77
HSD-01 – Collaboration report PANDA progress in 2013 . . . 77
HSD-02 – Invariant mass reconstruction of ${}^{3}_{\Lambda}H$ and ${}^{4}_{\Lambda}H$ . . . 78
HSD-03 – Breakthrough in the Lifetime of Microchannel Plate PMTs . . . 79
HSD-04 – In-Beam Tests of Double-Sided Silicon Microstrip Sensors Employing Flex-PCB Readout for the $\overline{P}$ANDA MVD . . . 80
HSD-05 – Quality assurance for large-scale GEM-foils . . . 81
HSD-06 – The PANDA GEM-Tracker Prototype 'GEM2D', Simulations and Pad-Plane design . . . 82
HSD-07 – Time-based reconstruction in the GEM Tracker . . . 83
HSD-08 – Comparison of Radiation Damage Effects in PWO Under Proton Irradiation at 150 MeV and 24 GeV Energy . . . 84
HSD-09 – Quality of $PbWO_4$ Crystals Manufactured at SICCAS . . . 86
HSD-10 – Dark count measurements of SiPM detectors . . . 88
HSD-11 – Further Development of Lattice-FPGA based TDC and Its Implementation on different Platforms . . . 89
HSD-12 – Study of PANDA Barrel DIRC design options . . . 90
HSD-13 – Study of a PANDA Barrel DIRC design based on radiator plates . . . 91
HSD-14 – Study of the timing resolution of a PANDA Barrel DIRC prototype . . . 93

Division NuSTAR / ENNA (Nuclear Structue, Astrophysics and Reactions) **95**
Department FRS / SFRS . . . 95
NUSTAR-FRS-01 – Collaboration report NUSTAR progress in 2013 . . . 95
NUSTAR-FRS-02 – Progress on the Super-FRS Experimental Program . . . 98
NUSTAR-FRS-03 – Spectroscopy of η'-mesic nuclei at FRS and Super-FRS . . . 100
NUSTAR-FRS-04 – Experimental Setup for hypernuclear study at the Super-FRS . . . 101
NUSTAR-FRS-05 – Measurement of β-delayed neutrons around the third r-process peak . . . 102
NUSTAR-FRS-06 – A Cherenkov detector as a possible TOF detector for the Super-FRS . . . 103
NUSTAR-FRS-07 – Performance of the Prototype Cryogenic Stopping Cell for the Low-Energy Branch of the Super-FRS . . . 104
NUSTAR-FRS-08 – Recent Technical Improvements for the Multiple-Reflection A Laser Ablation Carbon Cluster Ion Source and an RFQ-based Switchyard for the FRS Ion Catcher . . . 105
NUSTAR-FRS-09 – Conceptual Design of A Next-Generation Cryogenic Stopping Cell for the Low-Energy Branch of the Super-FRS . . . 106
NUSTAR-FRS-10 – Recent Technical Improvements for the Multiple-Reflection Time-of-Flight Mass Spectrometer at the FRS Ion Catcher . . . 107
NUSTAR-FRS-11 – Experimental Investigations and Technical Design for The Time-OF-Flight Detectors in the CR at FAIR . . . 108
NUSTAR-FRS-12 – Efficiency calibration of the neutron detector BELEN-48 with (p,n) and (α,n) reactions at the PTB Braunschweig . . . 109
NUSTAR-FRS-13 – Tests of scintillation Fibers for the compact neutron Detector NeuRad . . . 110
NUSTAR-FRS-14 – Atomic Mass Compilations . . . 111
Department Gamma Spectroscopy . . . 113
NUSTAR-GS-01 – Status of PreSPEC Commissionning Data Analysis . . . 113
NUSTAR-GS-02 – Automatic Self-consistent Gain-Matching of DSSSD Detector Channels . . . 115
NUSTAR-GS-03 – Development and test of a segmented Time-of-Flight plastic detector . . . 117
NUSTAR-GS-04 – In-beam γ-ray spectroscopy with AGATA@PreSPEC: Development of new experimental tools for HISPEC@FAIR . . . 119
NUSTAR-GS-05 – Simulations for DEGAS detectors at FAIR . . . 121
NUSTAR-GS-06 – Simulations for position-sensitive tracking of γ rays in scintillators Approach for source reconstruction . . . 123
Departements SHE Physics and SHE Chemistry . . . 125
NUSTAR-SHE-01 – Study of the ^{48}Ca+^{249}Bk fusion reaction leading to element Z = 117: long-lived α-decaying ^{270}Db and discovery of ^{266}Lr . . . 125
NUSTAR-SHE-02 – Element 115 studied with TASISpec . . . 126
NUSTAR-SHE-03 – Neutron Shell Strengths at N = 152 and towards N = 162 . . . 127
NUSTAR-SHE-04 – Decay of $^{201-203}Ra$ . . . 128

NUSTAR-SHE-05 – Decay of $^{200,201}Fr$ . . . 129
NUSTAR-SHE-06 – Compound nucleus spin distribution for ^{64}Ni +^{100} Mo . . . 130
NUSTAR-SHE-07 – Diamond dE-E-ToF-telescope for heavy ion reactions at the Coulomb barrier 131
NUSTAR-SHE-08 – Electronic Structure, Properties and Volatility of Chlorides and Oxychlorides of Group-4 Elements Zr, Hf, and Element 104, Rf . . . 132
NUSTAR-SHE-09 – Relativistic coupled cluster study of the MAu and M_2 dimers of Hg, Cn, and Fl 133
Department Nuclear Reaktions . . . 135
NUSTAR-KR-01 – Measurement of the Dipole Polarizability of ^{68}Ni . . . 135
NUSTAR-KR-02 – Observation of Unbound States in ^{16}Ne/^{15}Ne via 1n- / 2n-Knockout on ^{17}Ne . . . 136
NUSTAR-KR-03 – Study of the ^{14}Be Continuum . . . 137
NUSTAR-KR-04 – Coulomb Dissociation of ^{17}Ne . . . 138
NUSTAR-KR-05 – Coulomb Dissociation of ^{27}P . . . 139
NUSTAR-KR-06 – Fewbody theoretical studies of Quasi Free Scattering reactions . . . 140
NUSTAR-KR-07 – Total Fission Cross Sections for Proton-Induced Fission of ^{208}Pb . . . 142
NUSTAR-KR-08 – Identification and Reconstruction of Fission Fragments for Proton-Induced Fission of ^{208}Pb at 500 MeV in Inverse Kinematics . . . 143
NUSTAR-KR-09 – Progress report of the CALIFA/R^3B calorimeter . . . 144
NUSTAR-KR-10 – Heavy-ion tracking detectors for the R^3B setup . . . 147
NUSTAR-KR-11 – Tests of timing silicon photomultipliers for NeuLAND . . . 150
NUSTAR-KR-12 – Application of Calorimetric Low Temperature Detectors (CLTD's) for Precise Stopping Power Measurements of Heavy Ions in Matter . . . 151
NUSTAR-KR-13 – Efficiency calibration of the neutron detector BELEN-48 with (p,n) and (α,n) reactions at the PTB Braunschweig . . . 152
NUSTAR-KR-14 – SOFIARoot: Simulation of the SOFIA/ANDES Setup . . . 153
NUSTAR-KR-15 – GGLAND - command line simulations . . . 154

Division APPA / PNI (Atomic, Plasma Physics and Applications) **155**
Department Atomic Physics . . . 155
PNI-AP-01 – FOCAL - precision x-ray spectroscopy for extreme fields in high-z ions . . . 155
PNI-AP-02 – Forward-angle electron spectroscopy in ion-atom collisions studied at the ESR . . . 157
PNI-AP-03 – The Effect of the Breit-Interaction Studied for the Emission Characteristics of $1s2s^22p_{1/2}$ Decay in Be-like Uranium . . . 158
PNI-AP-04 – Innovative Concepts for Collision Studies at GSI's and FAIR's Storage Rings . . . 160
PNI-AP-05 – High-resolution measurement of the time-modulated orbital electron-capture and of the β^+ decay of hydrogen-like $^{142}Pm^{60+}$ ions . . . 161
PNI-AP-06 – Further insight into Bayesian and Akaike information criteria of the EC-decay rate oscillations . . . 163
PNI-AP-07 – Increased lifetime of hydrogen-like ^{192m}Os observed in the ESR . . . 164
PNI-AP-08 – Odd-Even Staggering in Fragment Yields from ^{78}Kr + Be Reactions . . . 165
PNI-AP-09 – A study of Coulomb displacement energies for nuclides with A around 67 . . . 166
PNI-AP-10 – Angular differential measurement of linear polarization of elastically scattered hard x-rays . . . 167
PNI-AP-11 – Demonstrator: Electronic Readout for a Si(Li) - Compton - Polarimeter . . . 168
PNI-AP-12 – Dominant secondary nuclear photoexcitation with the XFEL . . . 169
PNI-AP-13 – The HILITE Penning trap and first tests at the HILITE setup . . . 170
PNI-AP-14 – Highly charged ions at SpecTrap . . . 171
PNI-AP-15 – In-trap production of highly charged ions at ARTEMIS . . . 172
PNI-AP-16 – New approach for the induced charge calculation for cylindrical electrodes . . . 173
PNI-AP-17 – Polarization transfer in elastic Rayleigh scattering . . . 174
PNI-AP-18 – Development of the HITRAP experimental facility . . . 175
PNI-AP-19 – SPARC at Storage Rings of FAIR . . . 176
Department Materials Research . . . 177
PNI-MF-01 – Swift heavy ion induced radiation damage in $EuPO_4$ . . . 177
PNI-MF-02 – New approach to investigate irradiated calcite crystals - UV Raman and Photoluminiscence with UV excitation . . . 178
PNI-MF-03 – Spectroscopic study on ion irradiated calcites and gypsum . . . 179

PNI-MF-04 – High Aspect Ratio Nanotubes fabricated by Ion-Track Technology and Atomic Layer Deposition . . . 180
Department Plasma Physics / PHELIX . . . 181
PNI-PP-01 – Generation of Physical Conditions Similar to Interior of Superearth Extrasolar Planets by Imploding Solid Iron in LAPLAS Experiments at FAIR . . . 181
PNI-PP-02 – Operation and Improvements of PHELIX . . . 182
PNI-PP-03 – Upgrade of the PHELIX Target Area . . . 184
PNI-PP-04 – Preplasma characterization at PHELIX . . . 185
PNI-PP-05 – Energy loss measurements of heavy ions in dense weakly coupled plasma generated by volumetric heating with hohlraum generated x-rays . . . 186
PNI-PP-06 – Theoretical investigation of the charge transfer processes of heavy ions at intermediate energies interacting with a plasma . . . 187
PNI-PP-07 – Radiation-hydrodynamic simulations of foils heated by hohlraum radiation . . . 188
PNI-PP-08 – Ion energy loss at maximum stopping power in a laser-generated plasma . . . 189
PNI-PP-09 – A laser-driven proton beamline at GSI . . . 190
PNI-PP-10 – Laser-driven ion acceleration with a hollow beam at PHELIX . . . 191
PNI-PP-11 – Laser-driven Ion Acceleration with Cryogenic Hydrogen Targets . . . 192
PNI-PP-12 – Coloration quenching of radiochromic films irradiated with proton energies close to maximum energy loss . . . 193
PNI-PP-13 – Electron beam based space charge measurement of intense ion beams . . . 194
PNI-PP-14 – Target development for Warm Dense Matter research . . . 195
PNI-PP-15 – Simulations of a conical target for Warm Dense Matter-experiments . . . 196
PNI-PP-16 – Experimental Studies and Theoretical Interpretation of Hydrodynamic Tunneling of SPS Protons in Solid Targets . . . 197
PNI-PP-17 – Numerical Simulations of Hydrodynamic Tunneling Experiments Performed at HiRadMat Facility Using SPS Proton Beam . . . 198
PNI-PP-18 – Laser acceleration of small projectiles for hypervelocity impact experiments . . . 199
PNI-PP-19 – Radiation protection related x-ray spectrometry at PHELIX . . . 200

Division Biophysics **201**
BIOPHYSICS-01 – Report of the biophysics department . . . 201
BIOPHYSICS-02 – Species conserved response at heterochromatic DNA damage . . . 204
BIOPHYSICS-03 – Visualization of DNA double-strand breaks induced by high LET particles and X-rays in murine bones and soft tissues . . . 205
BIOPHYSICS-04 – Formation of 5hmC following exposure to Ionizing Radiation . . . 206
BIOPHYSICS-05 – A discontinuous detection of phospho-histone H2AX in endothelial cells following low-dose irradiation is mediated by reactive oxygen species (ROS) . . . 207
BIOPHYSICS-06 – X-rays advance osteoblast differentiation probably involving the cholinergic system in vitro . . . 208
BIOPHYSICS-07 – The radiation-induced G2 cell cycle delay is comparable in human hematopoietic stem- and progenitor cells and mature lymphocytes . . . 209
BIOPHYSICS-08 – Response of bone marrow progenitor cells to ionizing irradiation . . . 210
BIOPHYSICS-09 – Purified cultures of mouse embryonic stem cell-derived cardiomyocytes for electrophysiological studies with ionising radiation . . . 211
BIOPHYSICS-10 – Interaction of endothelial cells and lymphocytes after X-ray exposure . . . 212
BIOPHYSICS-11 – Inflammatory cytokine release by vascular cells after X-irradiation . . . 213
BIOPHYSICS-12 – Inflammation-related response to irradiation in different human skin culture systems . . . 214
BIOPHYSICS-13 – Immune system activation through Carbon ion irradiation (Ab-scopal effect) 215
BIOPHYSICS-14 – Image segmentation of alveolar macrophages reveals chronic inflammation in carbon ion irradiated rat lungs . . . 216
BIOPHYSICS-15 – Human embryonic stem cells: an ideal model for the risk assessment of ionizing radiation during early embryo development . . . 217
BIOPHYSICS-16 – Electrophysiological Effects of Ionising Radiation on Cortical Rat Neurons in vitro . . . 218
BIOPHYSICS-17 – Effects of X-rays and titanium ions on cardiomyocyte cultures . . . 219

BIOPHYSICS-18 – Effects of X-rays and carbon ions on pluripotency maintenance and differentiation capacity of mouse embryonic stem cells . . . 220
BIOPHYSICS-19 – Effect of hypoxia on the growth of glioma-initiating cells . . . 221
BIOPHYSICS-20 – Cellular radiation response of mouse embryonic stem cell derived cardiomyocytes . . . 222
BIOPHYSICS-21 – Carbon ion induced vascular damage in the rat lung . . . 223
BIOPHYSICS-22 – Time course of radiation induced chromosome aberrations in mouse bone marrow cells . . . 224
BIOPHYSICS-23 – Radioresistant subpopulation in a culture of glioma-initiating cells . . . 225
BIOPHYSICS-24 – Preparatory experiments to investigate the radiosensitivity of human embryonic stem cells . . . 226
BIOPHYSICS-25 – Adaptive cell killing for ion beam treatment planning of hypoxic tumors . . . 227
BIOPHYSICS-26 – An in silico Trial of X-rays vs Carbon Ions in Lung Cancer Radiosurgery . . . 228
BIOPHYSICS-27 – Auger electrons emitted from metallic nanoparticles under proton irradiation 229
BIOPHYSICS-28 – Application of a LEM based DNA DSB kinetic rejoining model to the analysis of dose dependence after photon irradiation . . . 230
BIOPHYSICS-29 – Comparison between different dose calculation algorithms available in TRiP98 and between the beam model of HIT and GSI . . . 231
BIOPHYSICS-30 – Comparison of the beam mixing models proposed by Lam and Zaider & Rossi and a derived Dt extension for the Zaider & Rossi model . . . 232
BIOPHYSICS-31 – Fast 4D dose calculation with TRiP4D . . . 233
BIOPHYSICS-32 – Influence of the distal fall-off on the biological effective proton range . . . 234
BIOPHYSICS-33 – Oxygen enhancement ratio of heavy ions in partial hypoxic conditions . . . 235
BIOPHYSICS-34 – Irradiation with α-particles causes rapid activation of K^+ channels in A549 cells 236
BIOPHYSICS-35 – Purified cultures of mouse embryonic stem cell-derived cardiomyocytes for A sensitivity analysis of the Giant LOop Binary LEsion model . . . 237
BIOPHYSICS-36 – Robust 4D-optimized treatment plans in scanned carbon ion beam therapy for intrafractionally moving lung cancer . . . 238
BIOPHYSICS-37 – Studying inter- and intrafraction motion mitigation with sequential 4DCTs of NSCLC patients . . . 239
BIOPHYSICS-38 – Towards helium ions for radiotherapy . . . 240
BIOPHYSICS-39 – TLD Efficiency calculation for heavy ions: a new approach . . . 241
BIOPHYSICS-40 – Construction of a X-Ray Cabinet for Live Cell Experiments . . . 242
BIOPHYSICS-41 – Construction of an alpha-irradiation-setup for cells . . . 243
BIOPHYSICS-42 – Detector setup for Heavy Ion Computed Tomography . . . 244
BIOPHYSICS-43 – Development of an automatic counting system for cell spheroids in suspension 245
BIOPHYSICS-44 – Prototype of a rasterscan control system for BIOMAT@FAIR . . . 246
BIOPHYSICS-45 – Radon exposure setup for cells and small animals . . . 247
BIOPHYSICS-46 – The ROSSINI project at GSI . . . 248
BIOPHYSICS-47 – Heart beat modelling in a water and anthropomorphic phantom . . . 249
BIOPHYSICS-48 – Heavy Ion Beam Irradiation of a Langendorff Heart . . . 250
BIOPHYSICS-49 – Influence of cardiac motion on porcine AV node for the non-invasive treatment of atrial fibrillation with a scanned carbon ion beam . . . 251
BIOPHYSICS-50 – Online Bragg Peak monitoring for radiotherapy with ions using pixel sensors 252

Department Theory **253**
THEORY-01 – A phase-space representation of nucleon-nucleon potentials . . . 253
THEORY-02 – The ^{12}C continuum in a microscopic coupled channel calculation . . . 254
THEORY-03 – Theory of Nuclear Excitation and their Astrophysical Relevance . . . 255
THEORY-04 – Charged-current interactions for muon neutrinos in supernova . . . 256
THEORY-05 – Finite temperature pasta matter with the TDHF approximation . . . 257
THEORY-06 – Symmetry energy of nuclear matter with liquid-gas phase transition and cluster formation . . . 258
THEORY-07 – The chiral condensate in neutron matter . . . 259
THEORY-08 – A low-energy effective model for quantum chromodynamics . . . 260
THEORY-09 – Probing deconfinement with Polyakov loop susceptibilities . . . 261
THEORY-10 – QCD phase structure and conserved charge fluctuations in a chiral effective model 262

THEORY-11 – The role of fluctuations in the phase diagram of two color QCD . . . 263
THEORY-12 – Higher order quark-mesonic scattering processes and the phase structure of QCD 264
THEORY-13 – Inhomogeneous condensation in nuclear matter . . . 265
THEORY-14 – Pions in a strong magnetic background . . . 266
THEORY-15 – Investigating the Transition Between Hydrodynamics and Transport . . . 267
THEORY-16 – Collision Energy Evolution of Elliptic and Triangular Flow in a Hybrid Model . . 268
THEORY-17 – Initial conditions, hadronization and transport coefficients in heavy-ion collisions 269
THEORY-18 – On- and off-shell heavy quark transport properties in the quark-gluon plasma . . 270
THEORY-19 – Studies of jet quenching within a partonic transport model . . . 271
THEORY-20 – Strange and heavy mesons in hot and dense nuclear matter: hadronic models and transport simulations for a road to FAIR . . . 272
THEORY-21 – Heavy Quarks in Strongly Coupled Plasmas with Chemical Potential . . . 273
THEORY-22 – Off-equilibrium photon production in heavy-ion collisions . . . 274
THEORY-23 – On finite volume effects in the chiral extrapolation of baryon masses . . . 275
THEORY-24 – The salar-isovector sector in the extended Linear Sigma Model . . . 276
THEORY-25 – In-Medium strangeness dynamics at PANDA . . . 277
THEORY-26 – Charmonium production in $\bar{p}$A reactions at threshold . . . 278

Departments High Performance Computing, Experiment Systems and Base IT **279**
IT-01 – Lustre in WAN Environment and Development . . . 279
IT-02 – Improving the logging infrastructure of HPC and Linux services . . . 280
IT-03 – Status of the FairRoot framework . . . 281
IT-04 – ALFA: A new Framework for ALICE and FAIR experiments . . . 282
IT-05 – Streaming data processing with FairMQ . . . 283
IT-06 – DDS: A new Dynamic Distribution System . . . 284
IT-07 – Event building in FairRoot . . . 285
IT-08 – New software for the R^3B calorimeter CALIFA within FairRoot . . . 286
IT-09 – Remote Event Client Implementation in FairRoot Framework . . . 287
IT-10 – FairDB: The FairRoot Virtual Database . . . 288
IT-11 – Time Based Version Management with FairDB . . . 289
IT-12 – FairDB SQL Persistency Scheme . . . 290
IT-13 – E-Science Activities at GSI . . . 291
IT-14 – High-Level Data Flow Description of FPGA Firmware Components for Online Data Preprocessing . . . 292
IT-15 – gStore - the GSI Archive Storage for Experiment Data . . . 293

Division FAIR@GSI **295**
General . . . 295
FG-GENERAL-01 – FAIR@GSI progress in 2013 . . . 295
Machine UNILAC . . . 297
FG-UNILAC-01 – UNILAC Status Report . . . 297
FG-UNILAC-02 – Status of the Compact LEBT Project . . . 298
FG-UNILAC-03 – Investigation of the Compact LEBT Design Prerequisites . . . 299
FG-UNILAC-04 – Investigation of beam brilliance of high current Ta-beam on HOSTI in the frame of compact-LEBT project . . . 300
FG-UNILAC-05 – Collimation and decoupling of ECR source beams for brilliance optimization . 301
FG-UNILAC-06 – Research and Development on ECR Ion Sources . . . 302
FG-UNILAC-07 – Status of the EMittance Transfer EXperiment EMTEX . . . 303
FG-UNILAC-08 – Upgrade preparation for the 1.4 MeV/u gas stripper system for FAIR . . . 304
FG-UNILAC-09 – Thermal Simulations of Thin Solid Carbon Foils for Charge Stripping of High Current Uranium Ion Beams at New GSI Heavy-Ion Linac . . . 305
FG-UNILAC-10 – The Status of the High-Energy Linac Project at GSI . . . 306
FG-UNILAC-11 – CUPID: New System for Scintillating Screen based Diagnostics . . . 307
FG-UNILAC-12 – REMBRANDT - The REMote Beam instRumentation And Network Diagnosis Tool . . . 308
FG-UNILAC-13 – Retrofitting of a non-invasive Bunch Shape Monitor for GSI LINACs . . . 309
FG-UNILAC-14 – Direct measurement of mechanical vibrations of the 4-rod RFQ at the HLI . . 310

FG-UNILAC-15 – Calculation of the quadrupole moment $\sigma_x^2 - \sigma_y^2$ for an asymmetrical Pick-up . 311
FG-UNILAC-16 – Progress of the 325 MHz sc CH Cavity . . . 312
Machine SIS18 . . . 313
FG-SIS18-01 – Controlled beam loss experiment at SIS18 . . . 313
FG-SIS18-02 – Beam Phase Feedback for Dual-Harmonic Operation of RF Cavity Systems . . . 314
FG-SIS18-03 – Measurement of the magnetic properties of the Ferroxcube 8C12m material . . . 315
FG-SIS18-04 – Status and Results of the TFS for SIS18/SIS100 . . . 316
FG-SIS18-05 – Observation and simulation of transverse BTFs of high energy bunched beams . . 317
Machine P-LINAC . . . 319
FG-P-LINAC-01 – Ion source and 4-grid analyzer for the proton injector for FAIR . . . 319
FG-P-LINAC-02 – Mechanical Design for the p-LINAC BPMs Inter-tank Section . . . 320
Machine HEBT . . . 321
FG-HEBT-01 – FAIR HEBT System - Status Report . . . 321
FG-HEBT-02 – Interdisciplinary development of a support structure for components in building H0705A - A challenge for systematic requirements engineering . . . 322
Machine SIS100 . . . 323
FG-SIS100-01 – Status of the Superconducting Magnets for FAIR . . . 323
FG-SIS100-02 – Cryogenics for SIS100 Accelerator . . . 325
FG-SIS100-03 – Cryogenic Tests of Ceramic Feedthroughs for SIS100 BPM . . . 326
FG-SIS100-04 – Design of a Mutual Inductance Based Quench Detector for the Corrector Magnets of the SIS100 . . . 327
FG-SIS100-05 – Estimation of beam induced heat load in SIS100 kicker magnets . . . 328
FG-SIS100-06 – Halo collimation of fully-stripped light and heavy ions in the SIS100 . . . 329
FG-SIS100-07 – Measurement of the behaviour of residual gas particles on cryogenic surfaces to improve the simulation of dynamic vacuum effects . . . 330
FG-SIS100-08 – FPGA Based Tunable Digital Filtering for Closed Loop RF Control in Synchrotrons 331
Machine Super-FRS . . . 333
FG-S-FRS-01 – Development of a tool for CBM STS module assembly . . . 333
FG-S-FRS-02 – Setup for adjustment of process parameters for CBM module production . . . 334
FG-S-FRS-03 – Silicon strip sensor layout for CBM STS . . . 335
FG-S-FRS-04 – A new Time-of-flight wall for R^3B . . . 336
FG-S-FRS-05 – High precision multi-hit time-of-flight measurements at R^3B . . . 338
FG-S-FRS-06 – New time-of-flight system for the R^3B set-up . . . 340
FG-S-FRS-07 – Development of Heteroepitaxial DoI Plates for Diamond Detectors . . . 342
FG-S-FRS-08 – Laser Lithography for Production of Diamond Detectors . . . 343
FG-S-FRS-09 – Optimizing the manufacturing method of detector parts . . . 344
FG-S-FRS-10 – Characterizing the SOFIA/ANDES TwinMUSIC . . . 345
FG-S-FRS-11 – NeuLAND - from prototypes to double-planes . . . 346
FG-S-FRS-12 – Simulations of the GEM-TPC response . . . 351
FG-S-FRS-13 – Threshold calibration of the n-XYTER readout ASIC . . . 352
FG-S-FRS-14 – Time and trigger distribution for NUSTAR DAQ systems . . . 353
FG-S-FRS-15 – TRLO II - friendly FPGA trigger control . . . 354
Machine P-BAR . . . 355
FG-P-BAR-01 – A 400 kA Pulsed Power Supply for Magnetic Horn at the pbar Separator . . . 355
Machine ESR . . . 357
FG-ESR-01 – Ion Optics of the High Energy Storage Ring for Operation With Heavy Ions . . . 357
Machine CR . . . 359
FG-CR-01 – Progress report on the Collector Ring (CR) . . . 359
FG-CR-02 – Developments for the CR Stochastic Cooling System . . . 362
FG-CR-03 – Software development for stochastic cooling study in the time domain . . . 363
FG-CR-04 – Progress in development of resonant Schottky pickups with transverse sensitivity for the CR . . . 364
FG-CR-05 – The status of the CRYRING@ESR project . . . 365
Machine CRYRING . . . 367
FG-CRYRING-01 – Beam Instrumentation for CRYRING@ESR . . . 367
Machine CW-LINAC . . . 369
Common Systems CS . . . 369

FG-CW-LINAC-01 – Status of the sc cw-linac demonstrator installation . . . 369
FG-CS-01 – Accelerator Shutdown Report . . . 371
FG-CS-02 – Development of a FPGA based PCI-express to optical link interface card, KINPEX . 372
FG-CS-03 – Features of the new MBS Production Version 6.2 . . . 373
FG-CS-04 – FPGA Hit Finder and Energy Filter for the FEBEX Pipelining ADC . . . 374
FG-CS-05 – Status of the software development for the FAIR accelerator control system . . . 375
FG-CS-06 – Project status of the new setting generation system for GSI and FAIR . . . 376
FG-CS-07 – SCU system goes productive . . . 377
FG-CS-08 – Paving the Way for the FAIR General Machine Timing System . . . 378
FG-CS-09 – White Rabbit Applications for FAIR Experiments . . . 380
FG-CS-10 – The credit-card sized, general purpose controls platform: HadCon2 . . . 381
FG-CS-11 – The GSI Event Driven TDC ASIC GET4 V1.23 . . . 382
FG-CS-12 – Web interface in DABC . . . 383
FG-CS-13 – POLAND - Low Current Profile Measurement Readout System . . . 385
FG-CS-14 – Status of the Coating Activities at the Magnetron Sputtering Facility . . . 386
FG-CS-15 – Status of the SuperFRS Cryogenics . . . 387

Annex **389**
ANNEX-01 – JCR publications to the programme physics of hadrons and nuclei published in 2013 389
ANNEX-02 – Further publications to the programme physics of hadrons and nuclei published in 2013 . . . 413
ANNEX-03 – JCR publications to the programme large-scale facilities for research with photons, neutrons and ions published in 2013 . . . 415
ANNEX-04 – Further publications to the programme large-scale facilities for research with photons, neutrons and ions published in 2013 . . . 427
ANNEX-05 – JCR publications to the programme health published in 2013 . . . 431
ANNEX-06 – Further publications to the programme health published in 2013 . . . 435
ANNEX-07 – Doctoral theses 2013 supported by GSI . . . 436
ANNEX-08 – Organigram . . . 438

List of Authors **439**

Investigation of two-particle correlations in p+^{93}Nb collisions at $E_{kin} = 3.5$ GeV*

O. Arnold[1,2], *L. Fabbietti*[1,2] *for the HADES collaboration*

[1]Physik Department E12, Technische Universität München, James-Franck-Str. 1, 85748 Garching, Germany;
[2]Excellence Cluster 'Origin and Structure of the Universe', Boltzmannstr. 2, 85748 Garching, Germany

With the HADES setup the reaction p+^{93}Nb was measured in September 2008, where the proton had a kinetic energy of 3.5 GeV ($\sqrt{s}_{\mathrm{NN}} = 3.18$ GeV). This rather moderate energy gives us the possibility to study the production and interaction of particles at small excess energies.

Studying two-particle correlation functions at small relative momenta provide information about the spatio-temporal extent of the particle emitting source. Originally, the formalism of intensity interferometry was developed for astrophysical investigations to measure the angular size of stars [1]. Nowadays, the technique is mainly applied in the field of heavy-ion physics to gain information about the highly excited matter state and its properties created during the collision of the two nuclei.

The basic idea of femtoscopy is to deduce effects of final state interactions (FSI) from phase-space correlations of emitted particles. In low energy p+A systems we expect no contributions from collective effects to the particle emission like flow or energetic jets. Because of this reason, we are in the position to study only FSI of different particle species and do not have to consider effects from physical non-femtoscopic sources.

FSI can be studied with correlation functions, which are defined as the ratio of the two-particle probability divided by the uncorrelated probabilities:

$$C(\mathbf{p}_1, \mathbf{p}_2) = \frac{P(\mathbf{p}_1, \mathbf{p}_2)}{P(\mathbf{p}_1)P(\mathbf{p}_2)}, \qquad (1)$$

where $\mathbf{p}_i$ is the single-particle momentum of the particle i. Whenever this ratio deviates from unity one measures particle correlations.

We started to study the correlation function between identical particles to have a benchmark for more complex correlation functions like p-Λ [2]. This would enable a study of the YN interaction in terms of scattering lengths. For protons, three correlation classes enter in Eq. (1): quantum statistics, Coulomb and strong interaction. The Pauli exclusion principle and Coulomb interaction both act repulsively between protons which shows up in the correlation function as a suppression of the correlation signal at very low relative momenta ($k < 10$ MeV/c). The attractive strong interaction acts mainly via the s-wave channel and leads to an enhancement of the correlation signal at around $k \approx 20$ MeV/c. The height of the correlation peak ($C(k = 20\,\mathrm{MeV/c})$) is inversely proportional to the length of homogeneity R_G (often called source size) which will be deduced in future work. Fig. 1 displays the preliminary result of proton-proton correlations measured in the p+Nb system, which shows the characteristic functional shape as discussed above.

For identical negative pions one expects a positive correlation signal at small relative momenta due to Bose-Einstein statistics, which leads to an attraction as is seen in Fig. 1 where the correlation function shows an increase at low k and stays positive. However, this signal is still distorted by the repulsive Coulomb interaction. For pions, one can correct this effect by folding the Coulomb wave function with a source parametrization. This correction will be part of our future work.

To summarize, we have reconstructed the correlation function for protons and negative pions. In the next step, we have to correct this functions for certain detector deficiencies and will then compare them to theoretical models. For the p-Λ correlation function we determined the number of Λs which can be used for the correlation study to about 5×10^5 with a signal-to-background ratio of 1.23.

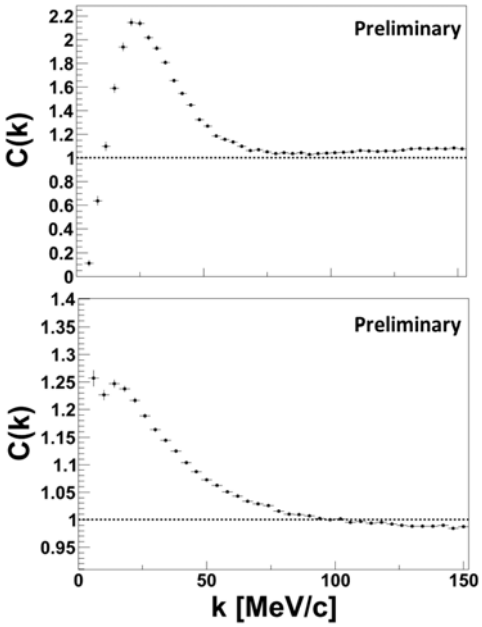

Figure 1: Proton-proton (upper) and $\pi^-\pi^-$ (lower) correlation function.

References

[1] R. Hanbury Brown and R. Q. Twiss, Nature 178, 1046 (1956).
[2] F. Wang and S. Pratt, Phys. Rev. Lett. 83, 3138 (1999).

*Work supported by Helmholtz funds VH-NG-330 and Excellence Cluster 'Universe'

Kaon in-medium potential probed in proton-nucleus reactions*

J.-C. Berger-Chen[1,2], L. Fabbietti[1,2], K. Lapidus[†1,2] for the HADES collaboration

[1]Physik Department E12, TU München, James-Franck-Str. 1, 85748 Garching, Germany; [2]Excellence Cluster "Universe", TU München, Boltzmannstr. 2, 85748 Garching, Germany

Insight into the fundamental properties of the strong interaction in the low energy domain — confinement and broken chiral symmetry — might be gained with measurements of hadron in-medium properties. Of particular interest in this context are light vector mesons (ρ, ω, ϕ) and (anti)kaons. Modifications of the kaon (K^+, K^0) spectral function in a baryonic environment do not show substantial broadening and are characterized by a positive and density dependent mass shift reaching 25-35 MeV at nuclear ground state density [1].

A number of experiments recently addressed this issue and deduced a repulsive potential of 25 to 40 MeV based on a comparison of data to microscopic transport model calculations [2, 3]. Thus, the magnitude of the kaon potential remains unsettled in spite of relative simplicity of the underlying kaon-nucleon interaction.

The HADES collaboration addressed the issue of the momentum-dependent kaon potential with the high-statistics data on neutral kaon production (reconstructed via the short-lived component K^0_S) collected in proton-niobium collisions at a beam energy of 3.5 GeV. As a reference measurement data obtained in proton-proton reactions at the same beam energy have been used.

Kinematical distributions of kaons were measured in a broad region of the phase space. Figure 1 shows the (efficiency corrected and normalized) transverse momentum spectrum in a selected rapidity bin (the complete rapidity span amounts to $y_{CM} \in (-0.85, 0.35)$).

The effect of the kaon potential as follows from ChPT was studied by comparing the data to results obtained with the GiBUU transport model [4], parameters of which (kaon production cross sections) were tuned to reproduce the reference proton-proton measurement. Two sets of calculations (with and without the kaon potential) are shown in Fig. 1. The strength of the ChPT potential at normal nuclear density for the kaon at rest is ≈ 35 MeV.

The comparison was done in all rapidity bins and the agreement of the experimental data with the transport model simulations was quantified by means of a χ^2-analysis. Simulations including the ChPT potential deliver a significantly lower χ^2 value as compared to calculations without potential. Moreover, and this is a distinct feature of the present study, variations of the uncertain parameters of the model (such as, for example, kaon yield in neutron-proton reactions) have been performed. For each set of physical parameters, calculations that include the potential consistently result in lower χ^2-values.

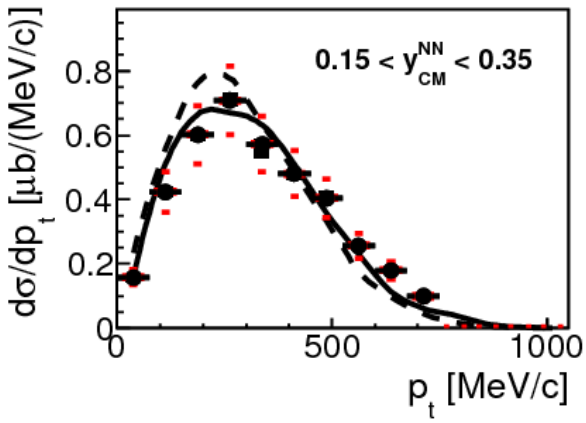

Figure 1: K^0 transverse momentum spectrum reconstructed in proton-niobium collisions in a selected rapidity bin. Experimental data are shown with black markers. GiBUU calculations without and with the kaon ChPT potential are shown by dashed and solid curve, respectively.

To summarize, the K^0 kinematical distributions reconstructed in proton-niobium collisions favour the GiBUU transport model calculations that incorporates the ChPT prediction for the potential.

References

[1] C. L. Korpa and M. F. M. Lutz, Acta Phys. Hung. A **22**, 21 (2005) [nucl-th/0404088].

[2] M. L. Benabderrahmane *et al.* [FOPI Collaboration], Phys. Rev. Lett. **102** (2009) 182501 [arXiv:0807.3361 [nucl-ex]].

[3] G. Agakishiev *et al.* [HADES Collaboration], Phys. Rev. C **82**, 044907 (2010) [arXiv:1004.3881 [nucl-ex]].

[4] O. Buss, T. Gaitanos, K. Gallmeister, H. van Hees, M. Kaskulov, O. Lalakulich, A. B. Larionov, T. Leitner, J. Weil and U. Mosel, Phys. Rept. **512**, 1 (2012) [arXiv:1106.1344 [hep-ph]].

* Work supported by BMBF and the Excellence Cluster "Universe".

† kirill.lapidus@ph.tum.de

 doi:10.15120/GR-2014-1-NQM-HADES-02

Search for a "ppK$^-$" bound state in p+p collisions*

E. Epple[1,2]*, L. Fabbietti*[1,2]*, and the HADES collaboration*[1]

[1]Excellence Cluster 'Universe', München, Germany; [2]Physik Department E12, Technische Universität München

We report, here, on the progress in our analysis of data taken with the HADES detector. As described in last year's GSI Scientific report [1], we have reconstructed ∼20.000 $pK^+\Lambda$ events that were produced in p+p reactions at a beam kinetic energy of 3.5 GeV. To describe the measured observables we have employed a PWA analysis [2]. In this analysis several transition amplitudes, including the production of the $pK^+\Lambda$ final state via the decay of various N* resonances, were fitted to the events. A good description of the data was obtained and presented in [1]. We have now performed a more refined statistical analysis of the experimental event yield.

The main motivation for the presented analysis is the possibility of a kaonic nuclear bound state production via:

$$p + p \rightarrow K^+ + "ppK^-" \rightarrow p + K^+ + \Lambda \qquad (1)$$

If the kaonic cluster would be abundantly produced and fairly narrow the $p\Lambda$ invariant mass distribution could show a signal of the latter. Due to the intense debate if the state is deeply or shallow bound and whether it is narrow or broad, experimental data are needed to clarify the theoretical situation. In the following the methods and results of the analysis procedure are presented.

No new signal but an upper limit

A signal in the data would manifest itself as a deviation of the data from a model which does not contain such a signal. This type of model is called a null hypothesis H_0 and is, in our case, constructed by the PWA solutions that were obtained by a fit to the experimental data. The H_0 hypothesis is illustrated in the upper panel of Figure 1 as gray band overlaid to the experimental data points. The solution includes the systematic variation of the transition waves included in the PWA fit. The lower panel of Figure 1 illustrates the local p-value as a function of the $p\Lambda$ invariant mass. The p-value was calculated from a Pearson χ^2-variable and expresses the agreement between data and model. This agreement can be translated into an equivalent significance (nσ). The equivalent significance also presented in the lower figure shows that the data are in agreement with the model within a range of 3σ. There is no significant deviation from the H_0 hypothesis and, thus, an additional signal is not required to describe the data. The mass point at M=2600 MeV/c^2 shows a deviation larger than 3σ. This is, however, a downward fluctuation of the data in respect to the model.

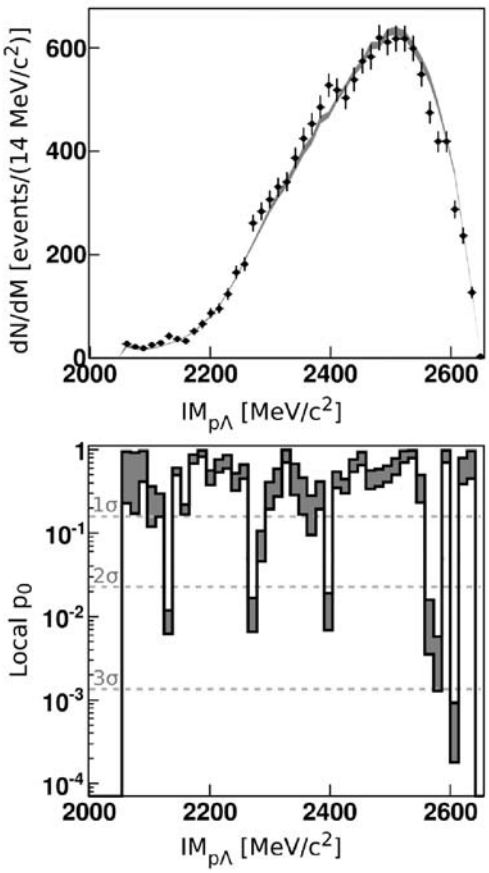

Figure 1: Upper panel: subset of the data shown together with the PWA solution including systematic uncertainties. Lower panel: local p_0-value of the H_0 hypothesis.

The last step in the data analysis is to include an additional signal to the PWA solution to obtain a new hypothesis H_1. This was done for several masses, widths, transition properties and production strengths of the kaonic cluster. The new hypothesis H_1 was compared to the data and only those values of H_1 were accepted that lie within a certain confidence limit. The values of production strength rejected by this test build the upper limit of the production strength of a "ppK^-" in p+p collisions at 3.5 GeV. The results will be presented in an upcoming publication.

References

[1] E. Epple and L. Fabbietti, GSI Report 2012 (2013), p. 13.

[2] A.V. Anisovich et al., Eur.Phys.J. A34, (2007), p. 129.

*This research was supported by VH-NG-330 and the DFG cluster of excellence 'Origin and Structure of the Universe'

A new upper limit on the rare decay $\eta \rightarrow e^+e^-$ *

M. Gumberidze[1], *and R. Holzmann*[2] *for the HADES collaboration*
[1]TU Darmstadt, Germany; [2]GSI, Germany

Introduction

Experimental measurements of neutral pseudoscalar meson decays into lepton pairs ($P \rightarrow l^+l^-$) and their comparison with theoretical predictions offer an interesting way to study long-distance dynamics and to probe new physics interactions.

The direct decay of the π^0 and η mesons into a lepton pair (e^+e^- or $\mu^+\mu^-$) proceeds in leading order through a 2-photon intermediate state. As the e^+e^- decay is furthermore strongly suppressed by helicity conservation, it is very hard to observe. So far only the $\pi^0 \rightarrow e^+e^-$ decay has been observed by the KTeV collaboration [1], whereas for the η only an upper limit of the branching is given.

The latest value on the eta branching has been set to $< 5.6 \times 10^{-6}$ at CL = 90 % by the HADES collaboration [2,3]. This is still four orders of magnitude above calculations based on chiral perturbation theory and quark models which put this branch at $BR^{QCD}_{\eta \rightarrow e^+e^-} \simeq 5 \times 10^{-9}$ [4,5].

HADES search for a direct η decay

Using inclusive dilepton data measured in 3.5 GeV p+Nb collisions [6] we have derived a new upper limit for the branching ratio of the direct η decay. Fig. [1] shows the invariant mass distribution of e^+e^- pairs (within the HADES acceptance) in the η mass range. The data points were fitted with a model function consisting of a 5^{th}-order polynomial and a Gauss peak of fixed position M_{ee} and fixed width $\sigma(M) = fwhm/2.35$. Here M_{ee} is the nominal mass of the η (548 MeV) and σ is the known mass resolution of the HADES detector. Already from the fits it is apparent that no significant peak is present in our data. Consequently, a statistical likelihood-based test was used to determine at a given Confidence Level (CL) an upper limit (UL) for a possible η signal [7,8].

The present analysis of our p+Nb data allows to set an improved limit (CL = 90%) at 2.5×10^{-6}. Combining the p+p [2] and p+Nb [6] results, a final limit of 2.3×10^{-6} can be given, i.e. about a factor 2.5 lower than the actual PDG value, but still a far way above theoretical predictions [4,5]

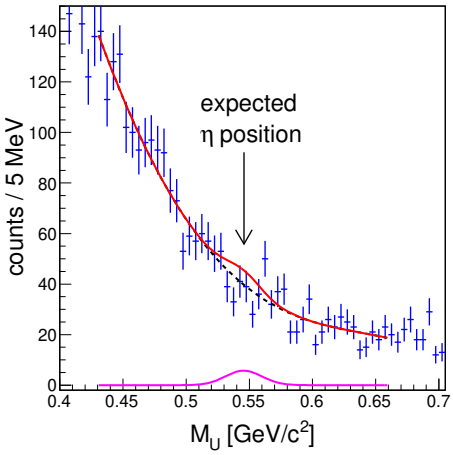

Figure 1: Zoom into the η peak region of the invariant-mass distribution of e^+e^- pairs reconstructed in the p(3.5GeV) + Nb reaction. The data is fitted with a polynomial (dashed black curve) onto which a gaussian signal of strength S set equal to the found upper limit (CL=90%) of $BR_{\eta \rightarrow e^+e^-} < 2.5 \times 10^{-6}$ is superimposed (solid red and pink curves).

References

[8] E. Abouzaid et al., Phys. Rev. D 75 (2007) 012004.

[8] G. Agakishiev et al., Eur. Phys. J. A 48 (2012) 64.

[8] J. Behringer et al. (PDG), Phys. Rev. D 86 (2012) 010001.

[8] M. Savage et al., Phys. Lett. B 291 (1992) 481.

[8] A.E. Dorokhov et al., Phys. Rev. D 75 (2007) 114007.

[8] G. Agakishiev et al., Phys. Lett. B 715 (2012) 304.

[8] G. Cowan et al., Eur. Phys. J. C 71 (2011) 1554.

[8] W.A. Rolke et al., Nucl. Inst. Meth. A 551 (2005) 493.

* Work supported by VH-NG-823, EMMI

 doi:10.15120/GR-2014-1-NQM-HADES-04

Searching a Dark Photon with HADES *

R. Holzmann†[1], *M.Gumberidze*[2] *for the HADES collaboration*
[1]GSI, Darmstadt, Germany; [2]TU Darmstadt, Germany

Introduction

The unexpected excess observed at high momenta in the cosmic e^+/e^- flux [1] can not easily be reconciled with known astrophysical sources. Alternative explanations have been proposed, in particular scenarios in which the excess radiation stems from the annihilation of weakly interacting dark matter particles [2]. There is indeed compelling evidence from various astronomical and cosmological observations [3] that non-baryonic matter of some sort, so-called dark matter (DM), is responsible for 20-25% of the total energy density in the Universe. To accommodate DM in elementary particle theory and to allow it to interact with visible matter, the Standard Model (SM) must be extended, e.g. with an additional sector characterized by another $U(1)'$ gauge symmetry [4]. The corresponding vector gauge boson — called U boson or *dark photon* — could thereby mediate the annihilation of DM particles into charged lepton pairs. The mixing parameter ϵ relating the respective coupling strengths α‘ and α of the dark and SM photons to visible matter ($\epsilon^2 = \alpha'/\alpha$) is expected to be of order $10^{-2} - 10^{-8}$ [5]. A number of experimental searches have been conducted looking at e^+e^- pair distributions produced either in electron scattering [6, 7] or in the electromagnetic decays of light mesons [8,9]. Finally, from the very precisely measured values of the anomalous gyromagnetic factor $(g-2)$ of the muon and electron [10], additional constraints can be put on the allowed range of the mixing parameter ϵ and the mass M_U [11].

The HADES dark photon search

We present results of a search for a narrow $U \rightarrow e^-e^+$ decay signal in dielectron spectra obtained with HADES in 3.5 GeV p+p and p+Nb reactions, as well as in the 1.756 GeV/u Ar+KCl reaction. In contrast to previous experiments [8,9] focussing on a specific decay channel, our analysis is based on the inclusive measurement of all e^+e^- pairs produced in a given mass range, i.e. from Dalitz decays of the π^0, η, and Δ mostly. Using the method proposed in [12] we have extracted an upper limit (UL) at a confidence level CL = 90%. Details of the procedure are published in [13]. With known detector efficiencies and decay branching fractions, this UL has then been transformed into an UL on the mixing parameter ϵ^2 as shown in Fig. 1 together with limits from the searches conducted by BaBar [14], KLOE-2 [9], APEX [7], WASA at COSY [8], and A1 at MAMI [6]. At low masses ($M_U < 0.1$ GeV/c^2) we improve on the recent result obtained by WASA [8], excluding now to a large degree the parameter range allowed by the muon $g-2$ anomaly. At higher masses, the sensitivity of our search is compatible with, albeit somewhat lower than the KLOE-2 analysis of ϕ decays.

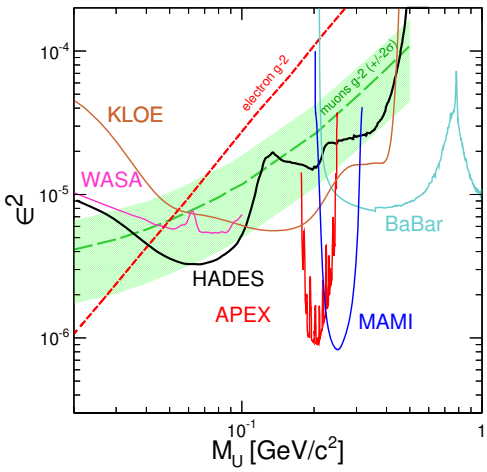

Figure 1: The 90% CL upper limit on ϵ^2 versus the U-boson mass obtained from the combined analysis of HADES data (solid black curve).

References

[1] M. Aguilar *et al.*, Phys. Rev. Lett. 110 (2013) 141102 and referances therein

[2] I. Cholis *et al.*, Phys. Rev. D 80 (2009) 123518.

[3] G. Bertone *et al.* Phys. Rept. 405 (2005) 279.

[4] M. Pospelov *et al.* Phys. Lett. B 662 (2008) 53.

[5] N. Arkani-Hamed *et al.*, Phys. Rev. D 79 (2009) 015014.

[6] H. Merkel *et al.* Phys. Rev. Lett. 106 (2011) 251802.

[7] S. Abrahamyan *et al.* Phys. Rev. Lett. 107 (2011) 191804.

[8] P. Adlarson *et al.* Phys. Lett. B 726 (2013) 187.

[9] D. Babuski *et al.* Phys. Lett. B 720 (2013) 111.

[10] G.W. Bennett *et al.* Phys. Rev. D 73 (2006) 072003.

[11] M. Endo *et al.* Phys. Rev. D 86 (2012) 095029.

[12] W.A. Rolke *et al.* Nucl. Inst. Meth. A 551 (2005) 493.

[13] G. Agakishiev *et al.* Phys. Lett. B 731 (2014).

[14] B. Aubert *et al.* arXiv:0902.2176.

* Work supported by VH-NG-823, EMMI
† r.holzmann@gsi.de

Hunting for K^{*+} in pp and pNb reactions*

D. Mihaylov† [1,2], *L. Fabbietti*[1,2], *K. Lapidus*[1,2], *and the HADES collaboration*

[1]Physik Department E12, TU München, James-Franck-Str. 1, 85748 Garching, Germany; [2]Excellence Cluster "Universe", TU München, Boltzmannstr. 2, 85748 Garching, Germany

In a recent study performed by the HADES collaboration for $p+p$ and $p+Nb$ collisions at 3.5 GeV, the production of neutral kaons was investigated [1]. The high statistics available for this analysis suggests that the exited states of the kaons can be investigated as well. One excited state that is decaying into a neutral kaon is the $K^{*+}(892)$ (Fig. 1). Information about the production of this particle at the energy of 3.5 GeV is of great interest, since no $K^{*+}(892)$ measurements at such low energy are available [2, 3].

The study of the $K^{*+}(892)$ resonance can be divided into two main steps. In the first step the total and differential cross sections for $K^{*+}(892)$ production in $p+p$ reactions are reconstructed. The second step is to use this result as a reference for a further investigation of $K^{*+}(892)$ production in $p+Nb$ reactions. The latter is interesting, because one can study the contribution by $p+n$ reactions to the total yield, scattering processes inside the nucleus, secondary production processes (e.g. $\pi+N\rightarrow K^*+\Lambda$) and eventual in-medium modifications of the $K^{*+}(892)$. The most efficient way to reconstruct $K^{*+}(892)$ using HADES data is by the decay scheme shown in Fig. 1.

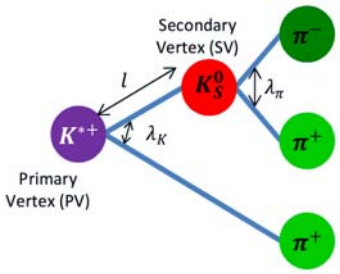

Figure 1: The short-lived K^{*+} decays at the primary vertex into a K^0_S and a π^+. The K^0_S decays into a pair of charged pions after a short time.

By selecting triplets of charged pions in each event and applying geometrical cuts to constrain the decay topology one can reconstruct the invariant mass spectrum of $K^0_S\pi^+$-pairs, showing the signal of $K^{*+}(892)$ (Fig. 2).

For $p+p$ reactions we find more than 1000 reconstructed $K^{*+}(892)$. This statistics is sufficient to perform a differential analysis. In order to correct the data for acceptance and efficiency a model capable of reproducing the experimental data was needed. For this reason, as well as to test the efficiency of the implemented reconstruction procedure, simulations of the $K^{*+}(892)$ production in $p+p$ collisions were performed. The two production channels,

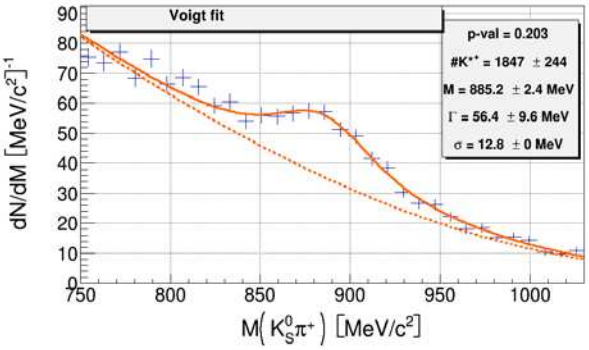

Figure 2: The invariant mass spectrum of the selected $K^{*+}(892)$ candidates. The measured values are in a fair agreement with the properties listed in PDG, which are $M=891.66$ MeV/c^2 and $\Gamma=50.8$ MeV/c^2.

that are expected to be dominant, $p+p\rightarrow p+K^{*+}+\Lambda^0$ and $p+p\rightarrow p+K^{*+}+\Sigma^0$, were simulated and the data is to be modeled by determining the relative contribution of each channel, that allows to reproduce the experimental data. In the simulations a uniform phase space population was assumed. There are, however, few effects that complicate the analysis. One is the detector resolution, which was estimated from simulations to be around 12 MeV/c^2. This effect can be accounted for by fitting the signal using a Voigt function, which is a convolution of a Breit-Wigner function, which represents the resonance, and a Gaussian function, which models the resolution. A second issue is the phase-space limitation for the production of $K^{*+}(892)$. The threshold energies for the two main production channels (see above) are 2.95 and 3.02 GeV, respectively. This means that the available center of mass energy of 3.18 GeV is just a bit above those values. Hence, the phase space limitations will be substantial, especially for particles with high transverse momentum. Thus, the fitting function must be further modified in order to account for the shape of the signal.

After the analysis of $p+p$ data is completed, it will be extended to $p+Nb$ data in order to study the nuclear effects in the production of $K^{*+}(892)$.

References

[1] Berger-Chen *et al.*, Hyperfine Int., 210(1-3), 111 (2013).

[2] Baldini *et al.*, "Numerical Data and Functional Relationships in Science and Technology", Springer, Volume 12b (1988).

[3] Bockmann *et al.*, Nucl. Phys. B 166, 284 (1980).

* Work supported by BMBF and the Excellence Cluster "Universe".

† dimitar.mihaylov@mytum.de

 doi:10.15120/GR-2014-1-NQM-HADES-06

Electron identification in Au+Au collisions at 1.23 GeV/u in HADES using multivariate analysis*

S. Harabasz[1,2], P. Salabura[2], T. Galatyuk[1], M. Gumberidze[1] for the HADES Collaboration
[1]Technische Universität Darmstadt, Darmstadt, Germany; [2]Jagiellonian University, Krakow, Poland

HADES [1] has measured Au+Au collisions at a beam kinetic energy of 1.23 GeV/u in 2012. In the data analysis, e^+ and e^- are identified by applying appropriate selection cuts to RICH ring observables, time-of-flight, PreShower and energy loss signals. Particle momenta were obtained by tracking the charged particles through the HADES magnetic field.

To achieve high purity in the reconstruction of the rarely produced electrons(positrons) a series of conditions on the PID-detector signals are usually applied consecutively. Although correlations of signals can be taken into account if graphical conditions are applied to two-dimensional spectra (correlation plots) yet a truely simultaneous assessment of all detector signals is not possible in this way.

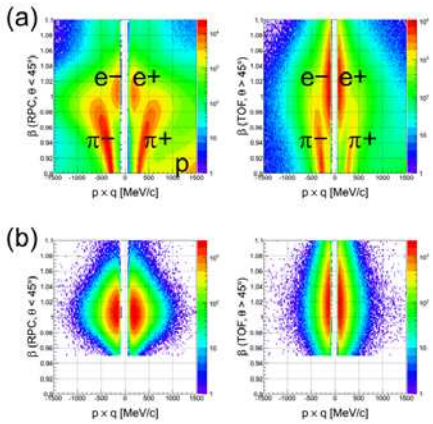

Figure 1: Particle's velocity versus momentum for (a) all particles and particles with MLP $>$ 0.6 (b) for particles falling into different time-of-flight detectors.

A way out is to use a multivariate analysis, which allows to create a multidimensional decision boundary optimizing it in all dimensions simultaneously. In the current work the MultiLayer Perceptron (MLP) model (implemented in the ROOT framework, TMVA [2]) was used (for details see [3]).

There are two challenges in training the neural network in order to give the correct response: one is the selection of pure signal and background training samples. The other one is choosing variables with the highest separation power between hadron and lepton tracks.

The neural network output can be understood as a probability that the subjected particle belongs to signal. Finding a boundary discriminating between signal and background is a matter of compromise between purity and efficiency of the identification. A comparison of velocity-momentum correlations before and after requiring MLP to be larger than 0.6 is presented in Fig.1. It can be seen that most of the hadrons have been removed and a significant statistics of electrons has been kept.

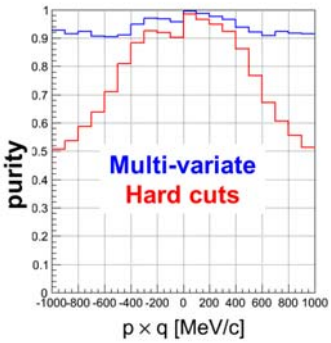

Figure 2: Lepton purity as a function of momentum, using MLP or hard cuts for PID.

The purity of the remaining lepton candidates can be estimated by extracting accidental coincidences of hadron tracks with RICH rings. The amount of such fake matches is obtained by matching way tracks reconstructed in one sector with rings from the neighboring sector.

Figure 2 shows the obtained purity of identified leptons for both PID methods as a function of momentum. Integrated values are 0.94 and 0.85 for MLP and hard cuts, respectively. It demonstrates the superior performance of the MLP method over the hard cut method for larger momenta.

References

[1] G. Agakishiev et al. (HADES Collaboration), Eur. Phys. J. A 41, 243 (2009).

[2] A. Hoecker et al., "TMVA: Toolkit for Multivariate Data Analysis," PoS A CAT 040 (2007).

[3] S. Harabasz, Fairness 2013 proceedings to appear in J. Phys. Conf. Ser. (2014).

*Work supported by VH-NG-823, BMBF (06FY9100I and 06FY7114), HIC for FAIR, EMMI, GSI, HGS-HIRe and H-QM.

π^0 reconstruction via conversion method in Au+Au at 1.23AGeV with HADES*

C. Behnke[1], J. Stroth[2], T. Galatyuk[3], M. Gumberidze[3] for the Hades Collaboration
[1]Goethe-Universität, Frankfurt; [2]GSI; [3]TU, Darmstadt

Lepton pairs emerging from decays of virtual photons are excellent probes of dense hadronic matter. The interpretation of the corresponding experimental results calls for a detailed understanding of conventional sources. Comprehensive information on meson production is therefore an important prerequisite. In this context, the neutral pion and eta mesons are of particular interest as they contribute largely to the dilepton spectrum via their Dalitz decays $\pi^0/\eta \rightarrow \gamma e^+e^-$. HADES [1] measured the collision system Au+Au at the highest (achievable at SIS18) beam energies of E_{kin} = 1.23 GeV/u in April/May 2012. In total 7.3×10^9 events, corresponding to 140 TByte of data, have been collected. Data taking was triggered for events with apparent hit multiplicity in the outer time-of-flight detector system $ToF_{Mult} \leq 20$ (PT3) translating to the 50% most central collisions.

Since HADES has no photon detector yet, the measurement of the electromagnetic decays of π^0 is only possible via external pair conversion of photons in detector material. The average conversion probability for π^0 decay photons was obtained from simulations and amounts to approximately 1,6% (taking into account the Au target, the target holder, the beam pipe and the radiator).

To study the π^0 reconstruction performance we selected leptons through their characteristic correlation between their velocity (β) and their momentum (the black box in Fig 1).

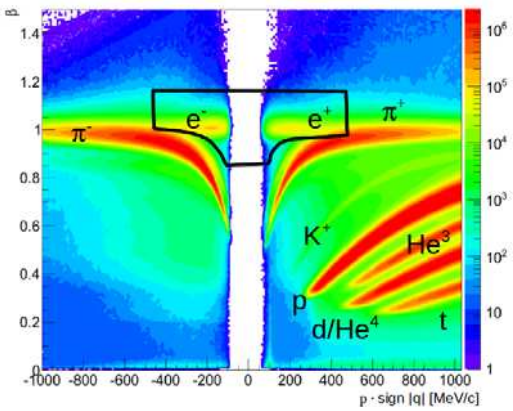

Figure 1: Velocity versus momentum · sign$|q|$ in the RPC region of the HADES spectrometer.

In the next step of the analysis, topological selection criteria on opening angle between the leptons of a given pair were used to identify conversion pairs (α <2.5°) and Dalitz pairs (α <20°) at the same time (for details see [2,3]).

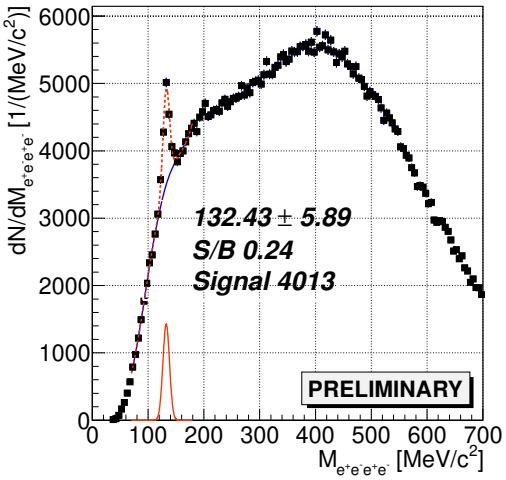

Figure 2: 4 lepton invariant mass spectrum after the topological cuts.

Such identified leptons have then been combined into opposite-sign e^+e^- pairs and further into $e^+e^-e^+e^-$ multiplets. In addition, a condition was applied on the relative angle between the two dileptons in a multiplet, namely $\theta_{\gamma^*\gamma^*} > 5°$, to suppress spurious counts at low invariant mass. Figure 1 shows a preliminary invariant mass spectrum of $e^+e^-e^+e^-$ multiplets (within the HADES acceptance, uncorrected for efficiency and acceptance). A clear signal peak is visible at the nominal mass of the π^0 (135 MeV). The data points were fitted with a model function consisting of a 4^{th}-order polynomial and a gaussian distribution. We extract 4000 counts from the π^0 peak. This result demonstrates that the π^0 can in principle be reconstructed in Au+Au collisions via the conversion method. In the next step, the uncertainties of the efficiency and acceptance corrections will be investigated.

References

[3] G. Agakishiev *et al.*, Eur. Phys. J. A **41**, 243 (2009).

[3] G. Agakishiev *et al.*, Phys. Rev. C 88, 024904 (2013).

[3] C. Behnke, Fairness 2013 proceedings to appear in J. Phys. Conf. Ser. (2014).

* Work supported by BMBF (06 FY 9100 I), HIC for FAIR, VH-NG-823 and EMMI

 doi:10.15120/GR-2014-1-NQM-HADES-08

The HADES alignment strategy*

V. Pechenov,[1] *O. Pechenova*[2] *and J. Markert*[2] *for the HADES collaboration*
[1]GSI, Darmstadt, Germany; [2]Goethe Universität, Frankfurt, Germany

To achieve the required momentum resolution of the HADES [1] spectrometer a precise alignment of the detectors is necessary. A set of global alignment parameters of detectors and intrinsic alignment parameters describing detector specific intrinsic geometry are obtained by several procedures:

1) photogrammetric alignment of the MDC [2] plane II with respect to the magnet by means of the Photomodeler software [3]. 2) alignment with reconstructed particle tracks (tracker alignment). Global and intrinsic geometric parameters with respect to the MDC plane II by MillepedeII [4] software. 3) tracker alignment for the RPC, TOF, Shower detectors.

A common problem of tracker alignment algorithms is that the total track χ^2 without constraints is mostly insensitive to so-called "scaling" and "shearing" (fig. 1) of the detectors. To overcome this effect in unconstrained modes [5] we focus on the following prescriptions: (i) take into account the measurements for MDC modules from technical drawings, (ii) define space position for MDC plane II with high accuracy (few hundred micrometers) by photogrammetric alignment, (iii) use MDC plane II as strong constraint, (iv) use simultaneous beam and cosmic tracks.

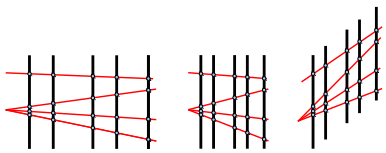

Figure 1: Unconstrained tracker alignment is insensitive to "scaling" and "shearing". Black: detector planes, red lines: reconstructed tracks.

The Photomodeler [3] photogrammetry software provides image-based modeling and accurate measurement to survey objects in 3D. Dedicated markers are positioned on the detector such that they can be resolved with high accuracy in the taken photos for the MDC plane from various views. After processing the space position of the markers including errors are extracted and the planes of the detector frames fitted by a software procedure. Translation and rotation matrices of the MDC module relative to the magnet are obtained and constrain the position of MDC II. These parameters are fixed for the following tracker alignment.

The set of parameters can be classified into alignment and local parameters. Local parameters characterize tracks of charged particles traversing the detector. The main goal of the alignment is to find the optimum values of the alignment parameters. The software package Millepede solves the linear least squares problem by a simultaneous fit of alignment and local track parameters using the last iteration [4] of the track fit only. The alignment procedure adjusts around 500 parameters simultaneously.

The sector to sector alignment is performed using arround 200000 tracks of each cosmic ray and beam data. A straight-line-track model is used for the fit. For the last iteration of the track fit Millepede requieres the partial derivatives provided by the tracking procedures. Due to nonlinearities of the alignment parameters the procedure converges after around 10 iterations to the optimum parameters for translation and rotation of the MDC modules, the orientation of the wires, the layer coordinates and the distance between two layer parts. In simulations the procedure reconstructed an arteficially introduced misalignment by a precision of 25 μm.

The tracker alignment for TOF and RPC detector determines the global alignment and calibration parameters simultaneously using an iterative procedure.

The resulting intrinsic parameters of the tracking detector were found in the range of 100-550 μm for the clearance between two parts of the layer, 0.00-1.03 mrad for the wire orientation in the layer and 50-700 μm for the wire number corresponding to physical center of layer.

A significant improvement has been observed in the track reconstruction compared to an alignment procedure using global parameters for the detectors only. The number of fitted MDC track segments and the number of accepted drift cells per fitted segment were increased at a better value of χ^2/ndf for the fitted segment. As physics observable the peak width of the invariant mass of the direct decays of ω-mesons [7] decreased by a factor of two.

References

[1] G. Agakishiev *et al*. The High-Acceptance Dielectron Spectrometer HADES. Eur. Phys. J. A41 (2009)

[2] C. Müntz *et al*. Nucl. Instr. Meth. A535 (2004) 242.

[3] http://www.photomodeler.com/

[4] V. Blobel. Software alignment for tracking detectors. Nucl. Instr. Meth. A566 (2006) 5-13.

[5] J. Amoraal. Application of vertex and mass constraints in track-based alignment. Nucl. Instr. Meth. A712 (2013) 48-55.

[6] http://seal.web.cern.ch/seal/work-packages/mathlibs/minuit/

[7] G. Agakishiev *et al*. Eur.Phys.J. A48 (2012) 64

* supported by GSI, BMBF (06FY9100I), Helmholtz Alliance EMMI, HIC for FAIR

Integration of the Pion-Beam Tracker into the HADES DAQ*

L. Fabbietti[1,2], R. Lalik[1,2], P. Louis[1,2], L. Maier[2], J. Michel[4], J. Pietraszko[3], T. Schmitt[1,2], M. Traxler[3], J. Wirth[1,2] for the HADES collaboration

[1]Excellence Cluster "Universe", Garching, Germany; [2]TU München, Garching, Germany; [3]GSI, Darmstadt, Germany; [4]Goethe-University, Frankfurt, Germany

In the 2014 HADES campaign with secondary pion beams, tracking detectors will be mounted into the chicane following the production target. They will provide the pion momentum with a resolution of 0.3 %, i.e. a factor 2 better than the momentum spread of the secondary beam, enabling exclusive analyses of reaction channels. To guarantee fast tracking, silicon sensors read out with the n-XYTER chip are employed. Due to its self-triggering architecture and local storage capability, the n-XYTER chip enables on-line tracking of each individual pion . The readout of the tracker data is realized with the TRB3 board [1].

The tracking capability of CERBEROS[1] and its integration into the HADES data acquisition system has been tested with proton beams at COSY in Juelich. A diamond-based device has been used as start detector acting as trigger for data taking, like it is planned for the campaign with pion beams. As the start detector is located several meters behind the first silicon detector causing a trigger delay of around 800 ns, the self-triggering architecture of the n-XYTER is crucial. All hits registered by the n-XYTER are buffered inside the TRB3 and only the hits correlated in time with the Start detector trigger signal are sent to the DAQ system. Additionally, the 2 GeV proton beam provided by COSY opened up the possibility to study the stability of the whole system under beam condition.

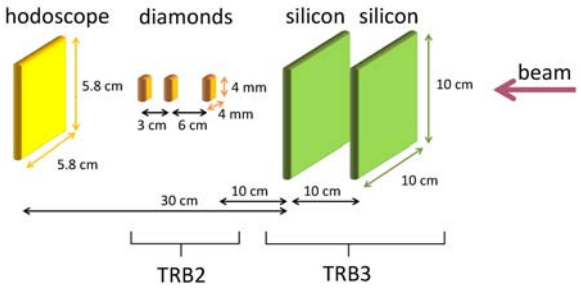

Figure 1: Experimental setup for the beam tests at COSY.

Figure 1 presents the experimental setup consisting of two double-sided silicon detectors of 10×10 cm^2 dimension and 128 strips on each side. The trigger was provided either by the hodoscope or by one of the three diamond detectors placed behind the silicon sensors.

The system was tested with beam rates varying from 2 – 550 KHz measured at the hodoscope, and trigger rates from 2 – 100 kHz as accepted by the CTS. In the beam spot of 16×16 mm^2 (Fig. 2) hit rates of up to

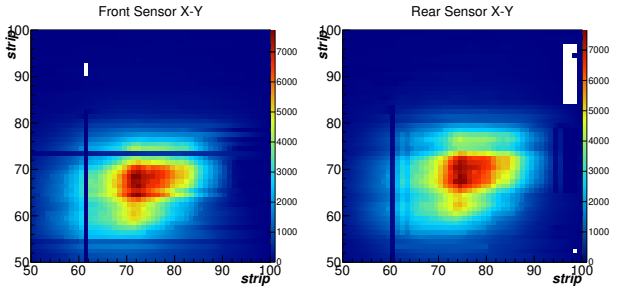

Figure 2: Beam profile as recorded by both silicon sensors using the hodoscope as a trigger.

2e5/s/cm^2 were achieved. Assuming such hit rates for the full sensor surface when operated in the pion beam experiment the detector will deliver 400 Mbit/s. The registered energy-deposition spectrum of the minimum ionizing protons shows good agreement with the expected energy-loss in 300 μm of silicon and the time resolution of the full trigger chain was found to be 30 ns.

In the pion experiments the detector is located in a vacuum chamber (Fig. 3) attached to the accelerator beam pipe. The first chamber close to the pion production target has been already assembled in the NE5 area, and successfully tested. The second chamber is under construction and will be located in the HADES cave.

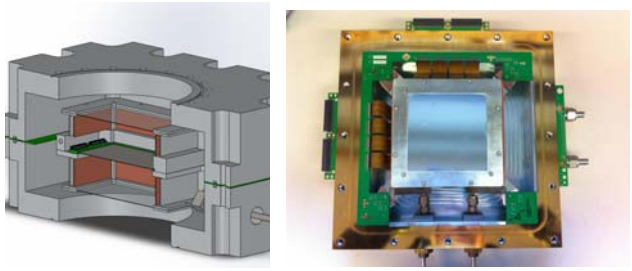

Figure 3: Left: Cross section of the chamber. It consists of two pieces made out of aluminium and with a feed-through PCB sandwiched in between. The Si sensors are located in the middle, covered by mylar foil. Right: One half of the vacuum chamber with a Si sensor covered by its mylar window.

References

[1] M. Traxler *et al.*, *J. Instrum.*, 6(12), C12004 (2011).

* Supported by VH-Ng-330, TMFABI1012 and BmBf 05P12WOGHH

[1]Central Beam Tracker for Pions

 doi:10.15120/GR-2014-1-NQM-HADES-10

Diamond detector preparation for high intensity beam monitoring and high precision T0 determination.*

J. Pietraszko[†1], *W. Koenig*[1], *M. Träger*[1], *T. Galatyuk*[2], *A. Rost*[2], *J. Klett*[2], *J. Kaiser*[2], *F. Hug*[2], *and the HADES Collaboration*[1]

[1]GSI, Darmstadt, Germany; [2]Technische Universität Darmstadt, Germany

CVD diamond material has been extensively used for particle detection [1, 2]. This radiation hard material for detector application is of great importance for existing as well as for newly planned high intensity experiments. Besides radiation hardness there are other properties like: wide-band-gap, high breakdown voltage, high thermal conductivity, small dielectric constant, which are very attractive for detector applications. To take advantage of these properties, there is a need for reliable contacts between the diamond material and metal electrodes. As it was widely investigated, depending on applied preparation procedure, the metal-diamond interface can show either rectifying Schottky or low resistant ohmic characteristic (see for example [3]). For detector applications it is essential to obtain a homogeneous low resistance ohmic interface between diamond and metal. Failing this the charge created in the diamond material by ionizing particles can not be transported freely and gets blocked at the metal-diamond contact surface causing significant reduction of the effective electric field in the detector.

For the detectors discussed in this report scCVD diamond sensors with thickness of 300μm and size of 4.7 mm x 4.7 mm were used. The sensors were metallized with 50nm Cr layer followed by a 150 nm Au layer. It has been shown that the onset of the transition from a rectifying to an ohmic contact for Cr-diamond occurs between 580-620^{o}C when a first carbide phase is formed (Cr_2C) [4]. Following this measurement the typical annealing process for Cr-diamond ohmic contact should be conducted at temperatures above 650^{o}C for a period longer than 20 min. To avoid surface contamination during the high temperature annealing the procedure has to be conducted in the UHV chamber. The annealing of the metallized samples was performed at the DAISY-Fun facility (DArmstädter Integriertes SYstem für FUNdamentale Untersuchungen) at Technical University of Darmstadt. The metallized samples, after cleaning in ultrasonic bath, were installed in the vacuum chamber. At a vacuum of about 10^{-8} mbar the heater was started. The temperature was slowly increased, about 1^{o}C per 10 sec, keeping the vacuum better than 10^{-7} mbar. The sample was finally annealed at 780^{0}C for 20 minutes.

The annealed samples were investigated by means of a high intensity electron beam from S-DALINAC (Der supraleitende Darmstädter Elektronenbeschleuniger) at Technical University of Darmstadt. During the experiment a high quality electron beam, with energy of 70 MeV was delivered to the experimental area where the annealed diamond detectors were installed. The detectors were readout by a fast scope with histograming capability. In Figure 1 the ADC spectra are shown for very low intensity (2 kHz) and high intensity (10 MHz). The ADC spectra showed stable response of the detector independent of the beam intensity indicating a perfect ohmic character of the contact between Cr and diamond material. The tail in the bottom figure at large amplitude is due to particle pileup at such high rates.

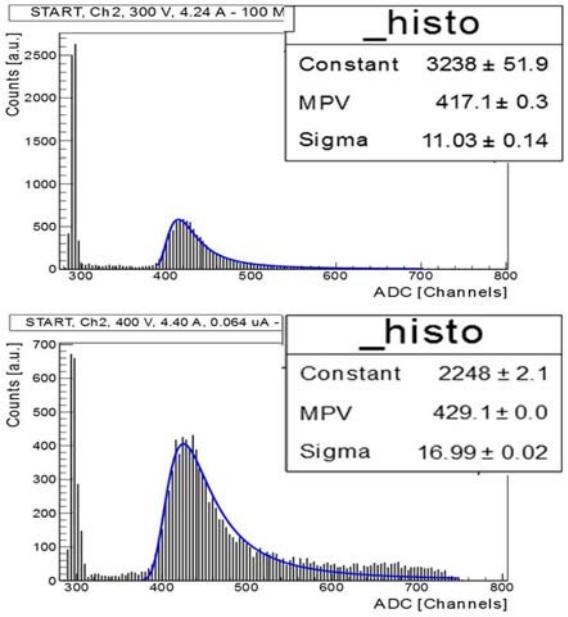

Figure 1: ADC spectrum measured at low electron beam intensity, about 2 kHz, - top picture and spectrum measured at high beam intensity, about 10 MHz, - bottom picture. The MPV values for both measurements stay at the same position indicating very stable detector operation.

References

[1] G. Agakishiev et al., Eur.Phys.J. A41 (2009) 243-277

[2] J. Pietraszko et al., NIMA 618 (2010) 121-123

[3] D A Evans et al., J. Phys.: Condens. Matter 21 (2009) 364223

[4] W.P. Leroy at al., J. Appl. Phys. 101, 1 (2007)

*This work has been supported by BMBF (05P12RFGHJ), Helmholtz Alliance EMMI, HIC for FAIR, HGS-HIRe, VH-NG-823

†j.pietraszko@gsi.de

Test of the HADES Electromagnetic Calorimeter modules on photon beam*

O. Svoboda† [1], *T. Galatyuk*[2], *B. Kardan*[3], *G. Korcyl*[4], *W. König*[5], *A. Neiser*[6], *S. Linev*[5], *P. Ott*[6], *P. Otte*[6], *O. Petukhov*[7], *J. Pietraszko*[5], *P. Ramos*[1], *A. Rost*[2], *A. Thomas*[6], *P. Tlustý*[1], *and M. Traxler*[5]

[1]Nuclear Physics Institute of ASCR, Rez; [2]TU Darmstadt, Darmstadt; [3]Goethe-Universität, Frankfurt; [4]Smoluchowski Institute of Physics, Jagiellonian University of Kraków, Poland; [5]GSI, Darmstadt; [6]Institut für Kernphysik, Johannes Gutenberg-Universität Mainz, Germany; [7]Institute for Nuclear Research, Moscow, Russia

Development of the electromagnetic calorimeter (ECAL) for the HADES experiment is coming to its final stage. A dedicated measurement using secondary gamma beam from MAMI facility at Johannes Gutenberg Universität Mainz was employed to verify the selected technical solutions.

The ECAL will allow the HADES experiment to measure data on neutral meson production in heavy ion collisions in the energy range of 2-10 AGeV with the beam of the future accelerator SIS100@FAIR. The detector is a lead glass calorimeter read out by photomultipliers connected to a novel electronic. A detailed description of the ECAL can be found in [1, 2].

Beam tests of single ECAL modules were performed to measure energy resolution, test the two new front-end boards ("Cracow" and PaDiWa AMPS) and measure detector response on beam inclined with respect to the module axis.

The tagger detector from MAMI was used to select eight different gamma energies ranging from 81 up to 1399 MeV (eight different triggers were used). Modules were exposed to collimated gamma beam of approx. 6 mm diameter at a 5 kHz load. The CAEN DT5742 and GSI made MA8000 shaper was used as a referential read out system to be able to compare with the two tested front-end boards. Stored pulse shapes were compared with the pulses measured using cosmic muons and LED monitoring system, see figure 1. Results measured with PaDiWa AMPS front-end board can be found in [3].

Energy resolution was studied to be able to decide which size of photomultiplier is the most suitable in terms of in terms of the price-performance ratio. Resolution of modules with a photomultiplier with 1" diameter seems to be significantly worse than that one with 1.5" and 3" diameter, see figure 2. These measurements are in a good agreement with the measurements done with the two new front-end boards.

Measurements with inclined modules confirmed the results of our simulations, namely that we are able with a good precission to detect particles hitting more than one module or placed close to module border.

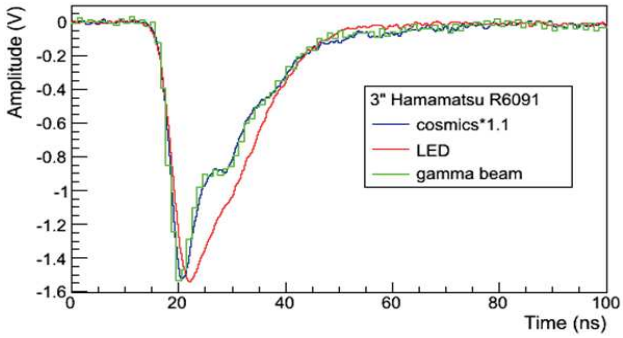

Figure 1: Pulse shapes induced by photons with energy of 1399 MeV, cosmic muons passing the full module length and by light from a LED diode.

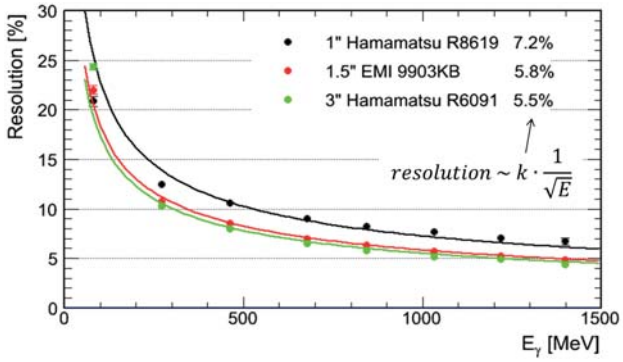

Figure 2: Energy resolution of ECAL modules with different PMTs. Numbers behind the PMT type show energy resolution at 1 GeV.

Acknowledgements

Authors are grateful to the staff of the MAMI facility in Mainz for providing excellent beam conditions.

References

[1] A. Kugler et al., "Electromagnetic calorimeter for HADES experiment", Proceedings of the 14th ICATPP Conference, vol. 8 (2013)

[2] P. Tlusty et al., "Development of the HADES Electromagnetic Calorimeter", GSI Scientific Report 2012 (2013) 37

[3] M. Traxler et al., "A Precise Multi-Channel QDC FEE utilizing FPGAs as Discriminators and Delay Elements Based on the TRB3 as TDC and Readout Platform", GSI Scientific Report 2013

* Work supported by GSI, HIC for FAIR, EMMI and Czech MSMT LG 120007, GACR 13-067595 and AS CR M100481202 grants

† svoboda@ujf.cas.cz

 doi:10.15120/GR-2014-1-NQM-HADES-12

A Precise Multi-Channel QDC FEE utilizing FPGAs as Discriminators and Delay Elements Based on the TRB3 as TDC and Readout Platform *

M. Traxler[1], *T. Galatyuk*[3], *J. Michel*[2], *B. Kardan*[2], *W. Koenig*[1], *S. Linev*[1], *A. Neiser*[4], *P. Ott*[4], *P. Otte*[4], *A. Rost*[3], *P. Skott*[1], *A. Thomas*[4], *and C. Ugur*[1]

[1]GSI, Darmstadt, Germany; [2]Institut für Kernphysik, Goethe-Universität Frankfurt, Germany; [3]Institut für Kernphysik, Technische Universität Darmstadt, Germany; [4]Institut für Kernphysik, Johannes Gutenberg-Universität Mainz, Germany

A very compact 8 channel Front-End-Electronics for precise TDC and QDC measurements was developed with the focus on the readout of the HADES-Electromagnetic-Calorimeter PMTs. The measurement principle of the FEE is to convert the charges of the PMT signals into pulses, where the charges are encoded as the width of the pulses. The high precision is achieved by implementing a modified Wilkinson-ADC method, so actively discharging the integrated signal resulting in a fast crossing of the threshold. The lengths of the pulses are measured by the well established TRB3 platform [1], [2]. The circuitry of the FEE is based on the Come&Kiss principle, where analog electronics is used only for the amplification stage and integration, while the other tasks, e.g. discrimination, threshold settings, delay generation for discharging and the LVDS drivers, are implemented in an FPGA (see figure 1).

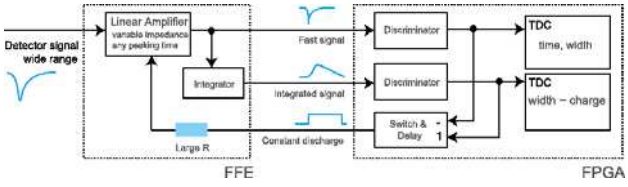

Figure 1: Schematic overview of the Come&Kiss TDC and QDC Front-End-Electronics.

This results in conceptionally simple electronics, hiding complex operations inside the FPGA. The developed FEE is very compact and the finished module is shown in figure 2, which can be directly attached to the TRB3 platform. The charge measurement precision (resolution of the system defined as $RMS/mean$ of the distribution) as a function of the measured charge has been determined with a pulser input signal and the uncorrected raw data is shown in figure 3. In beam measurements (with photons at MAMI in Mainz) with the FEE connected to lead glass ECAL modules show a comparable result in the determined energy resolution of the complete system as measured with an oscilloscope. The measurements are shown in figure 4.

References

[1] C. Ugur et.al, GSI Scientific Report 2013

[2] C. Ugur et.al, NoMe TDC Workshop - Perugia/Italy, 2013, `http://trb.gsi.de`

*The authors are grateful to the staff of the MAMI facility in Mainz for providing excellent beam conditions.

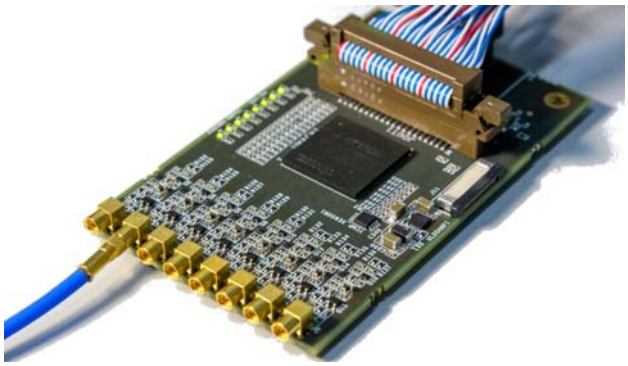

Figure 2: The Padiwa-Amps1 FEE module implementing 8 channels of fast discriminators and precise charge to width conversion.

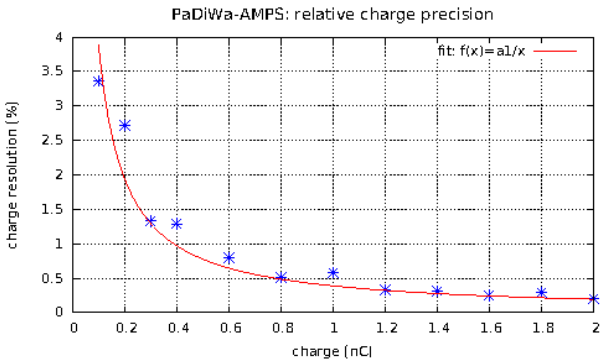

Figure 3: Relative charge measurement precision ($RMS/mean$) determined with a pulser.

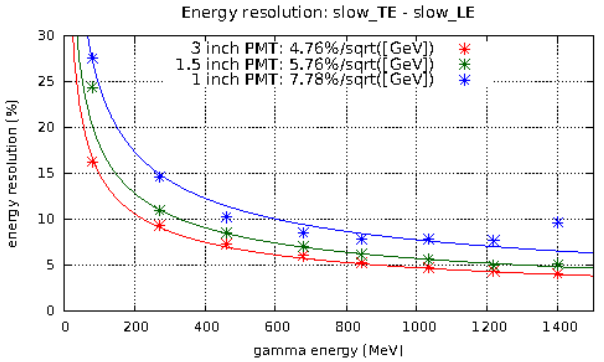

Figure 4: Energy resolution of a system with lead glass ECAL modules, different PMTs, Padiwa Amps as discriminator and QDC and a TRB3 as digitizer.

 doi:10.15120/GR-2014-1-NQM-HADES-13

Status of the Compressed Baryonic Matter (CBM) experiment at FAIR*

P. Senger and the CBM collaboration
GSI, Darmstadt, Germany

The Compressed Baryonic Matter (CBM) experiment will be one of the major scientific pillars of the future Facility for Antiproton and Ion Research (FAIR) in Darmstadt. The goal of the CBM research program is to explore the QCD phase diagram in the region of high net-baryon densities using high-energy nucleus-nucleus collisions. A sketch of the QCD phase diagram is shown in figure 1, highlighting the expected structures at large baryon chemical potentials: a first order-phase transition separating the hadronic phase from quarkyonic matter [2], followed towards larger baryon-chemical potentials by the quark-gluon plasma at high temperatures, and by exotic phases at low temperatures. At small baryon-chemical potentials, theory predicts a smooth crossover between hadronic and partonic matter. According to transport calculations, baryonic densities of about 6 times saturation density can be reached in central collisions between gold nuclei at 10 A GeV, an energy which will be provided by the future SIS100 machine. At these densities, quarkyonic matter is expected to be created. A similar state of matter, a mixture of strange baryons and free quarks, is predicted to exist in the core of neutron stars at densities beyond 4 times saturation density [3].

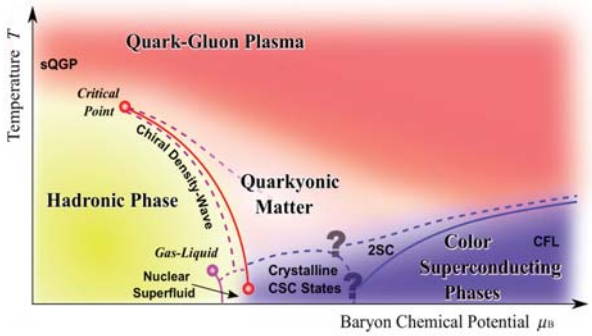

Figure 1: Sketch of the QCD phase diagram [1].

The CBM research program includes the study of the equation-of-state of nuclear matter at neutron star core densities, the search for the chiral phase transition, and for new forms of strongly interacting matter. The CBM detector is designed to measure rare diagnostic probes such as multi-strange hyperons, charmed particles and vector mesons decaying into lepton pairs with unprecedented precision and statistics. In the following, the results of the technical developments in 2013 will be briefly reviewed.

*Work upported by the Hessian LOEWE initiative through the Helmholtz International Center for FAIR (HIC for FAIR), and by EU/FP7 Hadronphysics3

The superconducting dipole magnet

The design of the CBM SC dipole magnet has been optimized. It has a large aperture (gap height 140 cm, gap width 260 cm) in order to host the Silicon Tracking System. The field integral is 1 Tm. Detailed quench calculations have been performed, and the quench protection system has been designed. The Technical Design Report has been approved in January 2014.

The Micro-Vertex Detector

A refined geometry of the CBM-MVD based on 4 detector stations has been developed. Together with IPHC Strasbourg the 0.18 μm CMOS process has been investigated with respect to radiation hardness and noise. The 2^{nd} generation of MAPS read-out and TRBv3-based data acquisition has been developed. The Analysis of the CERN-SPS test beam data has been concluded, reproducing the intrinsic features of the MAPS chips mounted in the prototype and validating the general concept of the MVD integration.

The Silicon Tracking System

For the CBM Silicon Tracking System (STS) double-sided micro-strip sensors in all required dimensions (6.2 $\times$ 6.2 cm^2, 6.2 $\times$ 4.2 cm^2, 6.2 $\times$ 2.2 cm^2) have been produced in cooperation with CiS, Erfurt, Germany and Hamamatsu, Japan. The front side strips are inclined by 7.5°. In order to interconnect short strips in the sensor corners to a strip in the opposite corner the sensors are equipped either with a second metallization layer, or with pads for an additional micro-cable. The performance of both options will be investigated. Each sensor (2048 strips) will read out via 16 low-mass micro cables (128 wires each) by 16 free-streaming ASICs 125 channels each). A mockup of such a module has been produced, and the tab-bonding of the cables has been successfully tested. Several of these modules consisting of a sensor, the cables and the front-end board carrying 8 ASICs will be mounted on a light-weight carbon ladder. Up to 16 of these ladders will be integrated into a detector station. A mechanical mockup of a half station has been built. A prototype CO_2 cooling system has been designed. Several prototype modules comprising single and daisy-chained sensors, read-out cables and a free-streaming read-out-system has been successfully tested in December 2013 with a proton beam at COSY/Research Center Jülich. The STS Technical Design Report submitted to FAIR in December 2012 has been approved in August 2013.

The Ring Imaging Cherenkov (RICH) detector

The analysis of beam time data from the test campaign in 2012 has been finalized. Important results have been obtained on the performance of the different photon sensors, on the optimal wavelength-shifter coverage, and on the requirements for mirror alignment and gas purity. In the lab new testing devices for single photon scans of photon sensors and the mirror surface have been set up. A larger prototype of the mirror wall is being constructed to perform tests of its stability while minimizing the material budget. The RICH Technical Design Report has been submitted in June 2013, and was approved in January 2014.

The Transition Radiation Detector

The analysis of the test beam established that all full size prototypes (by the groups from Bukarest, Frankfurt and Münster) perform according to the specification in terms of electron-pion separation. Several promising foam-type radiator materials have been identified. The SPADIC 1.0 readout chip has been finalized and tested and can now be commissioned for the upcoming test beams. Also, feature extraction algorithms have been implemented and are ready for tests with real data. The writing of the Technical Design Report is in progress.

The Muon Detection System

The layout of the Muon Chamber system (MuCh) and its performance have been optimized by replacing the first 20 cm thick iron absorber by a 60 cm thick carbon absorber. The mechanical structures supporting the detectors and the absorbers have been designed. A large area (31×31 cm^2) triple-GEM chamber made from single-mask foils has been built by the group in VECC Kolkata and successfully tested in December 2013 with a proton beam at COSY/FZ Jülich. Various prototype hybrid detector systems based on GEM and micromegas technologies have been built and tested at PNPI Gatchina. A full-size prototype Straw-chamber has been built at JINR Dubna. The development of a read-out ASIC has been started at MEPhI in Moscow. The MuCh Technical Design Report has been submitted in December 2013.

The time-of-flight system

The CBM - TOF - wall will mostly be composed of differential impedance matched strip MRPCs that are adjusted to the strongly polar angle dependent particle fluxes by implementing different strip lengths and employing low resistance electrodes where necessary. The low resistance electrodes can be constructed by ceramic, low resistivity glass or for more moderate rate requirements by thin standard glasses. Supermodule designs based on pad - MRPCs for the small polar angles are made available and might offer some advantage in terms of cost and rate capability.The exact layout of the wall is being optimized with the help of a newly created generic geometry description in the CBM simulation framework that also includes a proper description of the passive materials. For the first time a free streaming data processing chain based an the PADI and GET4 ASICs was realized with prototype detectors signals demonstrating the feasibility to achieve system timing resolutions in the order of 80 ps without any noticable dead time. First step are undertaken towards a common software framework capable of handling test beam data and simulations in a consistent way. The TOF Technical Design Report has been submitted in December 2013.

The Projectile Spectator Detector

The layout of the Projectile-Spectator detector (PSD), its distance from the target, and the settings of the magnetic field have been optimized in order to improve the performance in determining the reaction plane and the collision centrality over the full SIS100/300 beam energy range. The PSD Technical Design Report has been submitted in April 2013.

DAQ and First Online Event Selection (FLES)

In order to achieve the required precision, the measurements will be performed at very high reaction rates of 1 to 10 MHz. This requires a novel data read-out and analysis concept based on free streaming front-end electronics and a high-performance computing cluster for online event reconstruction and selection. The development of the full read-out and analysis chain based on detector hits with time stamps is in progress. The FLES system consists of a scalable supercomputer with custom FPGA-based input interface cards and a fast event-building network. It will be largely constructed from standard components, and will be located in the new FAIR data center. The submission of the DAQ/FLES Technical Design Report is planned for 2014.

Status of the Technical Design Reports

Subsystem	Status TDR
Superconducting Dipole Magnet	approved
Micro-Vertex Detector	submission 2014
Silicon Tracking System	approved
Ring Imaging Cherenkov Detector	approved
Time-of-Flight wall	in evaluation
Transition Radiation Detector	submission 2014
Muon Tracking Chambers	in evaluation
Projectile Spectator Detector	in evaluation
Electromagnetic Calorimeter	submission 2014
DAQ/First Level Event Selection	submission 2014

References

[1] K. Fukushima, T. Hatsuda, Rept.Prog.Phys.74(2011)014001

[2] L. McLerran, R. D. Pisarski, Nucl. Phys. A 796(2007)83

[3] M. Orsaria et al, arXiv:1308.1657

 doi:10.15120/GR-2014-1-NQM-CBM-01

Quench calculation for the CBM Dipole magnet

P. Kurilkin[*1], *P. Szwangruber*[2], *E. Floch*[2], *F. Toral*[3], *A. Malakhow*[1], *and V. Ladygin*[1]
[1]LHEP-JINR, Dubna, Russian Federation; [2]GSI, Darmstadt, Germany; [3]CIEMAT, Madrid, Spain

The CBM dipole magnet will store about 5.15 MJ at its nominal current of 686 A. When designing the quench protection scheme for the CBM magnet it is important to estimate the overall characteristics of the quench process in the coil.

Three types of the quench calculation were performed for the CBM dipole magnet: "first approximation", instantaneous quench and 3D calculation using GSI[1] and CIEMAT[2] quench programs.

The "first approximation" is a simplified calculation which can be used to obtain the good order of magnitude of average coil temperature (T_{av}) and maximum quench voltage (V_{qm}) for self-protecting magnets. T_{av} can be derived out of following equation:

$$\frac{E}{Vc} = \int_{4.5K}^{T_{av}} C_v(T)dT \quad (1)$$

where E is the magnet energy, Vc is the coil volume and C_v is the volumetric specific heat. In our case Tav is 90 K.

Having T_{av} one can estimate V_{qm} using an empiric formulation[**?**]:

$$V_{qm} = 0.403 * R_{pole}(T_{av}) * I_n \quad (2)$$

where I_n is the nominal current and $R_{pole}(T_{av}) = \rho_{Cu}(T_{av}) * 1749 * 5/A_{Cu}$. In this case $R_{pole}(T_{av}) = 4.7\Omega$ and $V_{qm} = 1307V$.

The instantaneous quench means that the whole coil is heated up instantaneously above the critical temperature. It is assumed that one coil has one uniform temperature (T_{av}) and field (B_{av}) distributions. At the start of the quench T_{av} is equal to 10 K and $B_{av} = B_{max}(I_n)/2$, where I_n is the nominal current.

For a short-circuited magnet electrical equation[3] gives the following current decrease:

$$dI = -\frac{R_q(T_{av}) * I}{L_d(I)} * dt \quad (3)$$

where L_d, R_q is the differential inductance and resistance of the coil, respectively. dt is the time which corresponds to the current increase[3] dI. From the heat equation written for one pole one can get the following temperature increase:

$$dT_{av} = \frac{R_q(T_{av}) * I^2}{Vc * Cp_{av}(T_{av})} * dt \quad (4)$$

where Vc is the coil volume, Cp_{av} is the average specific heat. The instantaneous quench calculation takes into account the inductance function $L_d(I)$ and the $B_{max}(I)$. It gives the average temperature of about of 90 K. The resistance of quenched pole is equal to 4.7 Ohm and the maximum quench voltage is equal to 1230 V.

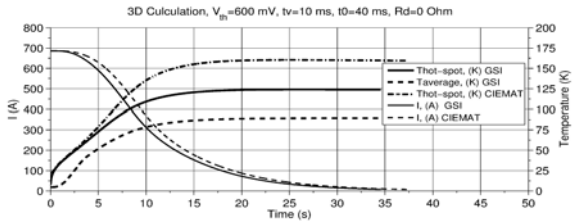

Figure 1: 3D quench calculation of the CBM dipole – the magnet current, hot-spot temperature and the average coil temperature.

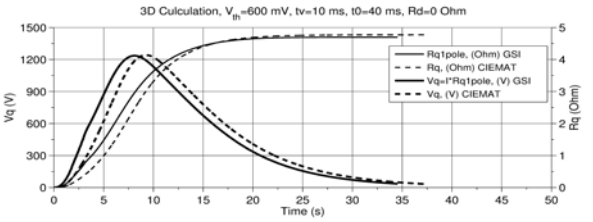

Figure 2: 3D quench calculation of the CBM dipole – the quench voltage and the quench resistance.

The 3D quench analysis has been performed using GSI[1] and CIEMAT[2] programs. The results of calculations when no dump resistor was used are presented in Fig.1 and Fig.2. The difference between the results calculated with the GSI and CIEMAT models is related to the different field map distribution in the coil, and also to different material data bases used in those programs. The maximum hot-spot temperature and quench voltage equals to 160 K and 1240 V, respectively.

The presented results show that the CBM dipole magnet is a self-protecting.

References

[1] P. Szwangruber et al., "Three-Dimensional Quench Calculations for the FAIR Super-FRS Main Dipole", IEEE Transactions on Applied Superconductivity, **23** No.3 (2013) 4701704

[2] F. Toral, "Design and Calculation Procedure for Particle Accelerator Superconducting Magnets: Application to an LHC Superconducting Quadrupole", Ph. D. Thesis, Madrid, 2001

[3] E.Floch, "Magnet inductances and quench computations", MT-INT-ErF-2009-010.

* pkurilkin@jinr.ru

Quench detection and protection system for the CBM dipole magnet.

P. Kurilkin[*1], *P. Szwangruber*[2], *H. Ramakers*[2], *E. Floch*[2], *and F. Toral*[3]
[1]LHEP-JINR, Dubna, Russian Federation; [2]GSI, Darmstadt, Germany; [3]CIEMAT, Madrid, Spain

The CBM dipole magnet has very large dimensions and stores about 5.15 MJ. An adequate protection of the superconducting CBM dipole magnet means minimizing of the coil peak temperature and of the resistive-inductive voltage imbalances, which can generate large voltages to the ground.

The quench protection of the CBM dipole magnet will be based on the extraction of the stored magnetic energy in an external dump resistor to avoid vaporization of helium. Fig.1 and Fig.2 present the results of 3D quench calculation using GSI[1] and CIEMAT[2] code. The detailed information about the data used in the calculation can be found in Ref.[3]. Both models predict a maximum hot-spot temperature on the level of 70 K. The maximum quench voltage equals to 249 (190) V, for GSI[1] and CIEMAT[2] computations, respectively. The maximum voltage across the magnet (1441 V) occurs when the dump resistor turns on. The difference between the calculated results is related to the different field map distribution in the coil and to the different material data bases used in GSI[1] and CIEMAT[2] programs. Fig.3 shows the power supply (PS) scheme, the

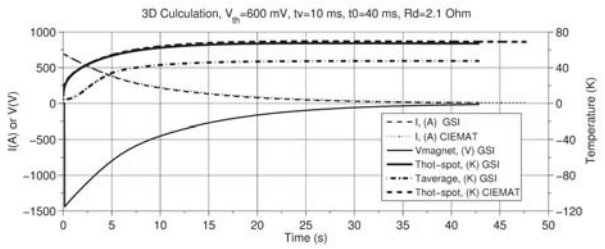

Figure 1: 3D quench calculation of the CBM dipole – magnet current, magnet voltage and the maximum (hot spot) coil temperature.

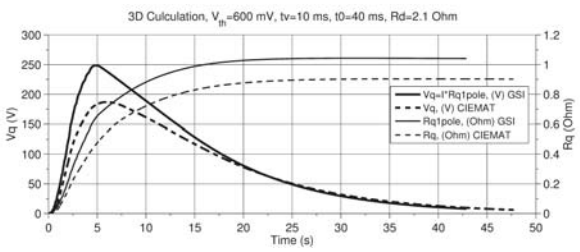

Figure 2: 3D quench calculation of the CBM dipole – the quench voltage and the quench resistance.

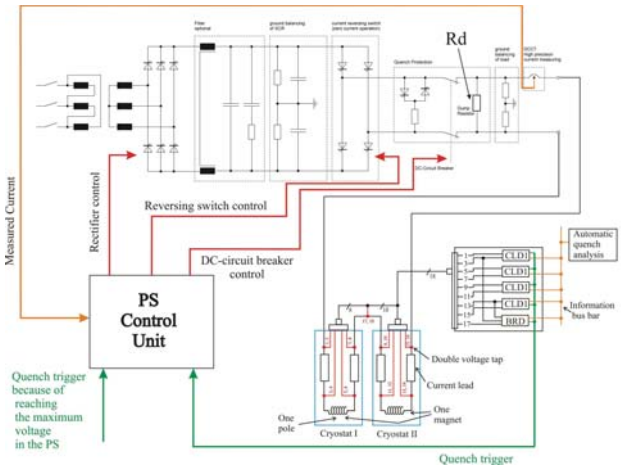

Figure 3: Quench detection and protection scheme (including power supply and voltage taps).

simplified PS control unit scheme the magnet, the dump resistor (for quench protection) and the quench detection system. Each magnet pole has a separate cryostat. The current is brought from the room temperature to the cryostat (4.5 K) by current leads (CL). There are 4 current leads (two per one pole). The quench detection system consists of:

- 4 voltage detectors (CLD1) used for current leads
- 1 classical bridge detector (BRD) used for the magnet
- Voltage threshold in the power supply unit (safety trigger).

During the normal operation the DC-circuit breaker is closed. When a quench occurs a quench trigger is given by detection system.

After the quench trigger, the DC-circuit breaker disconnects the PS and the magnet current is dumped via the dump resistor. The use of a dump resistor of 2.1 Ω provides the evacuation of about 85% energy stored in the magnet.

References

[1] P. Szwangruber et al., "Three-Dimensional Quench Calculations for the FAIR Super-FRS Main Dipole", IEEE Transactions on Applied Superconductivity, **23** No.3 (2013) 4701704

[2] F. Toral, "Design and Calculation Procedure for Particle Accelerator Superconducting Magnets: Application to an LHC Superconducting Quadrupole", Ph. D. Thesis, Madrid, 2001

[3] The CBM collaboration, Technical Design Report: "Superconducting Dipole Magnet for CBM", 2014

* pkurilkin@jinr.ru

 doi:10.15120/GR-2014-1-NQM-CBM-03

Quality assessment of ultra-thin CMOS sensors for the Micro Vertex Detector of the CBM experiment at FAIR.*

M. Koziel† [1], *N. Bialas*[1], *M. Deveaux*[1], *B. Milanovic*[1], *J.Stroth*[1], *and the CBM-MVD collaboration*[1]
[1]Goethe-University Frankfurt, IKF

The future Compressed Baryonic Matter experiment (CBM) will be equipped with a high-precision micro-vertex detector (MVD) aiming at an outstanding primary and secondary vertex resolution. Highly granular and ultra-light, so-called Monolithic Active Pixel Sensors (MAPS), which are manufactured with standard CMOS processes, will be employed. Imperfections in the CMOS production as well as the subsequent dicing and thinning procedures may limit the production yield of the sensors to about 60-70%. Probe testing the sensors prior to integrating them to the MVD is a mandatory step of the quality assurance related to the mass production of this detector. This is as it allows to recognize and reject sensors with insufficient performance.

The feasibility of probe testing the only 50 µm thick sensors was studied with the MIMOSA-26 prototype, which is considered as a realistic precursor of the final sensor of the MVD. Moreover, the existing readout system of the MVD-prototype [1] could be used for the test.

The probe-tests were carried in the IKF technology lab. As shown in Figure 1, the probe tester was equipped with a probe-card hosting 65 tungsten needles with a minimum pitch of 120 µm. The MIMOSA-26 sensors were held by a chuck adapter with micro-vacuum channels, contacted with the needles and their signals were routed through the probe-card to a so-called adapter-card. The latter was introduced as building it came out to be easier and cheaper than adapting the probe-card itself to our readout system. In addition, a test board hosting a wire-bonded working MIMOSA-26 sensor was manufactured. It is to test the readout chain including the probe-card independently of the delicate issue of contacting of sensors with needles.

After commissioning the system, first tests with 300 µm thick MIMOSA-26 sensors were carried out. The response of the sensors to JTAG programming and to various threshold settings matched our expectations. Next, the 50 µm sensors were probe-tested. The distance between the probe-card and the sensor, which is needed to establish a save contact between sensors and needles, was found smaller than expected from the tests with thicker sensors. This is attributed to the fact that the 50 µm sensors become soft enough to follow the imperfections of the surface of their support. Nevertheless, we succeeded to probe-test the thinned sensors.

In a next step, we are working on implementing a full test protocol, which is suited for testing the sizable number of sensors foreseen in the future mass production. To do so, we intend to update the software of our readout system and to migrate this system from the current TRBv2 to a TRBv3 platform [4].

Concluding, a 50 µm-thin precursor of a final CBM-MVD sensors was successfully tested with a probe-card. This activity and the related know-how found meanwhile some interest of a larger community, which is employing thinned MIMOSA-26 sensors into various experimental setups. This includes the PLUME project and the vertex detector project of the NA-61 experiment at CERN.

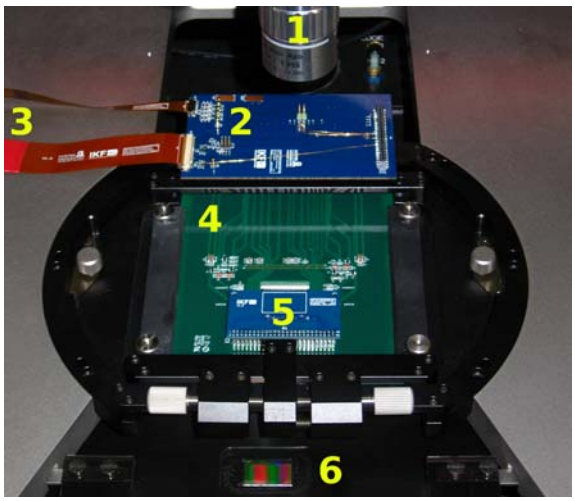

Figure 1: Probe-station setup: (1) microscope lens, (2) adapter-card, (3) connectivity to DAQ, (4) probe-card, (5) test-board hosting the reference sensor and (6) chuck-adapter with one Mimosa-26 sensor.

References

[1] M. Koziel et al., Nuclear Instruments and Methods in Physics Research A 732 (2013) 515–518C

[2] A.Nomerotski et al., "PLUME collaboration : Ultra-light ladders for linear collider vertex detector", Nuclear Instruments and Methods in Physics Research A650 (2011) 208-212.

[3] N.Abgrall for NA61/SHINE Collaboration, "Report from the NA61/SHINE experiment at the CERN SPS", CERN-SPSC-2013-028 ; SPSC-SR-124, October 2013, page 57.

[4] J.Michel at al., this report.

*Work supported by HIC for FAIR, GSI , BMBF (05P12RFFC7), EU-FP7 HadronPhysics3.

† m.koziel@gsi.de

The next generation of CBM MVD read-out electronics*

J. Michel[1], *M. Wiebusch*[1], *and the CBM-MVD collaboration*[1]
[1]Goethe-Universität Frankfurt

The on-going development of the support electronics of the CBM Micro-Vertex-Detector (MVD) focuses on two major aspects: First, the integration in a new DAQ system (based on the TRB3 system developed by HADES) and, second, the design of an integrated control and monitoring interface for systems consisting of several sensors.

New Electronics

The major goal of front-end electronics development was to migrate the read-out to a new, more powerful read-out platform, TRB3. Even though the central parts of software and FPGA designs need not to be changed, the read-out chain between digital electronics and sensors was re-designed to gain better performance and additional monitoring features. Here, also the principal structure of the chain was simplified by dropping the separated connection for control signals and merging all supply and data lines for a sensor on one common cable.

Special care was taken for the most sensitive supply voltage, a biasing voltage for the pixel matrices of the sensors. Several generation and distribution schemes were implemented to investigate which setup results in the best noise performance. Furthermore, all relevant voltages and currents can be monitored remotely to further study the behavior of sensors and, subsequently, to design a matching powering scheme for the final detector setup.

In the current connection scheme, the new FPGA platform can support up to 16 sensors in parallel. Note that this value is mostly limited by the number of I/O connections for the huge number of control and monitoring signals in the current design version and is likely to increase in future iterations. The resources of the FPGA also allow for further data sparsification algorithms like cluster detection as described in [1].

New Control Interface

The MVD user software serves three main purposes: Editing the sensor and electronics settings, coordination of data taking, and continuous monitoring of sensor parameters (power consumption, temperature, etc). In order to make the functionality accessible to non-hardware-experts, the development of an elaborate graphical user interface has been initiated.

The user software consists of two parts: a back end software suite implemented in Perl and a web interface front end written in HTML/CSS/Javascript. Though this approach appears intricate, the strict separation of front end and back end has substantial advantages: The DAQ is inherently remotely accessible to multiple users on different machines, while the design flexibility of HTML and CSS helps providing a clear structure and a good overview of the functionality. Furthermore the back end scripts can be also used from the command line or shell scripts to automate complex configure and/or measurement tasks.

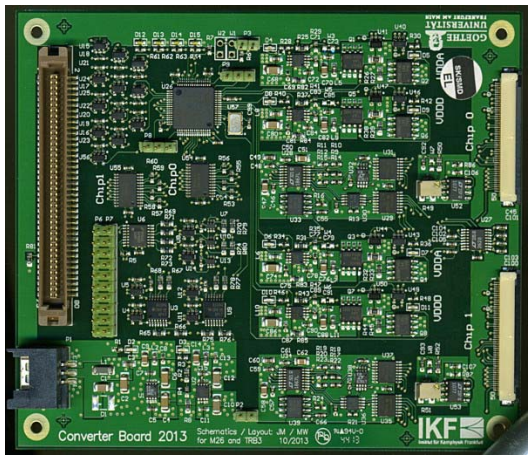

Figure 1: The new Converter Board with power supply, control and monitoring for two sensors.

All configuration files are stored in the strictly hierarchical but human readable XML format in order to keep the system transparent to the developer. The user interface does not only include access to all vital configuration options of each individual sensor, but also allows to monitor all information gathered on the converter board, i.e. voltages and currents as mentioned above.

These developments are a further steps towards the final read-out electronics, although it is evident that further steps will be taken this year. The plans foresee to adapt the read-out to a new sensor generation (Mistral) with higher data band-width and to develop cabling schemes for the geometry of the complete MVD detector setup.

References

[1] Qiyan Li, FPGA-based Cluster Finding, this issue.

* Work supported by BMBF (05P12RFFC7), HIC for FAIR and GSI

 doi:10.15120/GR-2014-1-NQM-CBM-05

The layout of the CBM Silicon Tracking System*

T. Balog[1] *and J. Heuser*[1]
[1]GSI, Darmstadt, Germany

As the central detector in the Compressed Baryonic Matter experiment, the Silicon Tracking System (STS) is required to perform efficient charged-particle tracking with high momentum resolution. With feedback from the engineering activities, the detector's layout has been further optimized, in particular to minimize the number of modules, the component with most complex assembly and associated production risks and costs.

Detector structure

The STS will be located in the gap of the 1 T dipole magnet and will comprise 8 tracking stations between 30 and 100 cm distance downstream of the target. Its polar aperture, where minimal material budget is achieved, is 2.5-25°. The STS stations are built from detector ladders that are populated with detector modules. A detector modules is the functional unit of a single silicon microstrip sensor (or a pair of daisy-chained sensors), read out by two front-end electronics boards, and read-out cables between the sensoric part and the electronics. Eight or ten modules mounted onto a carbon fiber support structure form a ladder; the electronics is arranged at the top and bottom end of the ladder, reaching already out of the physics aperture. The ladders themselves are arranged on further support frames to form the stations of the STS. As an active material double-sided silicon sensors of 300 μm thickness and readout strip pitch of 58 μm will be used. The angle between front and back side is 7.5^o where only the strips of the p-side are tilted and n-side strips are vertically oriented. Different strip lengths are used for the different regions of the STS (short in inner region and long in outer areas). Such way the maximum occupancies are kept all over the tracker below few per cent. Sensors and read-out electronics will be interconnected via low-mass micro-cables.The total material budget in a station ranges from 0.3% X_0 (inner regions) to 1.2% X_0 (outer parts).

Minimizing STS modules

The recent optimization to the detector layout were made due to a paradigm change with respect to the component with most complex assembly. As this was previously the detector ladder, where the mechanical assembly had to be made with highest accuracy and involved costly machinery and survey time, the recent progress in the module development now revealed that the modules themselves present as the most work intensive objects. The ladders turned out to need less absolute mechanical precision, but stability and compatibility with mechanical survey for later alignment procedures with straight particle tracks and suitable software. An optimization of the population of STS ladders with modules of different strip length was possible since there was a reserve of unnecessarily high segmentation near the horizontal coordinate, a consequence of multiply deployed ladders of the same design.

New STS layout

The new layout of the STS stations reduces now significantly the absolute number of modules. The variety of modules increases, though, but only involving differently long read-out cables that can be accommodated in the assembly fixtures and leave the mechanical complexity unchanged. The stations were commuted into doublets, where four (almost) identical pairs of stations were introduced, increasing the number of identically populated ladders.

The STS breaks down into 106 ladders to be produced in 17 variations, i.e. that many different module combinations are to be arranged on carbon fiber supports. They realize a symmetrical granularity within the stations decreasing from their center to the outer edge. The total number of modules in the STS amounts to 896. The modules come in 18 varieties having differently long sensors and read-out cables in certain combinations. In the optimized layout requirements such as full acceptance coverage (including the innermost areas around the beam-pipe) have been considered. The layout of one pair of stations is shown in Fig. 1. The performance of the re-arranged detector system has been verified in simulation studies. The tracking efficiency of 97% for fast primary tracks and 90% for secondary tracks together with a momentum resolution of 1.3% were confirmed.

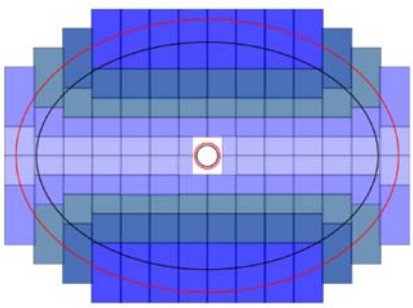

Figure 1: Layout of the second doublet of STS tracking stations. Black and red lines indicate the acceptance for stations number 3 and 4, respectively, including the horizontal enlargement for low-momentum tracks.

* Work supported by HIC4FAIR

Silicon strip sensor layout for the CBM Silicon Tracking System

D. Soyk[1], *I. Tymchuk*[2], *J. Heuser*[1], *and C.J. Schmidt*[1]
[1]GSI, Darmstadt, Germany; [2]LTU, Kharkov, Ukraine

The CBM Silicon Tracking System will be equipped with double-sided Silicon micros-strip sensors, where the strips on the p-side are inclined by 7.5° with respect to the n-side strips as well as the sensor edge. The final and homogeneous layouts for the 3 different sensor lengths, namely 22mm, 42mm and 62mm, has been elaborated. Longer sensors may be realized as a daisy-chain of two 62mm sensors. The sensors will be produced by two vendors to avoid the stop of module production in case of problems with any one single vendor.

The stereo angle of 7,5° effects a correlation between the x and y coordinate of a bond pad on a strip. The x distance between to strips on the sensor is 58 μm, equivalent to the pitch of the straight n-side strips. Therefore the second row of bond pads must have a y distance of at least once the multiple of 58 μm/tan(7,5°). On the sensor a pad pattern with x distance of 58 μm and y distance of $\sim$ 440,554 μm is possible, but the minimum producible pitch for the long analog microcables is in x direction 116 μm. In order to contact all strips, a double layered cable needs to be employed und thus a doubly staggered bond pattern is needed.

This leads to a checker-board-pattern where every second pattern-point is alternatingly reserved for a bond pad. The pitch of the bond pads is in x 116 μm and in y $\sim$ 881.108 μm (the center of the pads in the second row is shifted in x direction by 58 μm relative to the center of the first row of pads). Figure 1 shows an exemple of the such pattern.

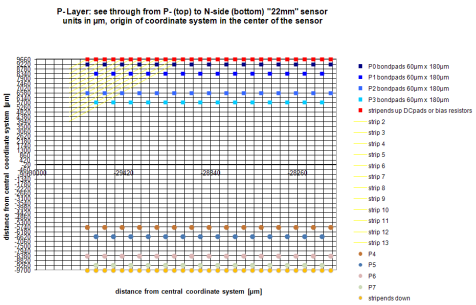

Figure 1: Schematic view on the bond pad and DC pad pattern.

As there are different lengths of sensors and as the pad rows should be located on the same x-position on the top edge as on the bottom edge it proved most adequate to allocate the origin of the coordinate system in the center of the sensor. Further, the distance from the coordinate center to the innermost pad row was fixed to be a multiple of the y-pitch of two staggered pad rows, namely 881.108 μm. Consequently the distance from the outermost pad row to the edge of the sensor is a variable of the sensor length, as the pre-chosen lengths are none multiples of this pitch.

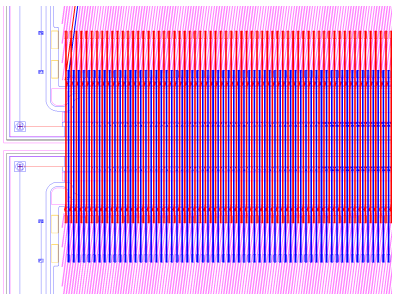

Figure 2: Schematic view of a sensor to sensor daisy chain. The red and blue lines are the leads of the short 58 μm-pitch cable that serves to daisy chain two sensors.

These definitions together with the respective symmetry allow daisy-chaining of sensors of the same as well as different lengths to each other. Figure 2 shows two daisy-chained sensors with a microcable of a constant lead length.

Consequently, also one FEB-design may serve all sensor configurations as well as either sensor side. In Fig. 3 a scheme of a microcable connection between the foreseen CBM STSxyter chip and the STS sensor is shown.

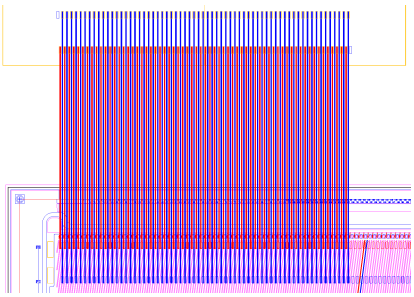

Figure 3: Schematic view of a sensor to chip connection. The red and blue lines are the leads of the microcable on two different layers with a pitch of 116 μm.

All participating vendors will employ this layout of the bond pads even though they may vary the sensor design according to their proprietory design and production preferences.

doi:10.15120/GR-2014-1-NQM-CBM-07

Performance of neutron irradiated prototype sensors for the CBM Silicon Tracking System *

J. Heuser[1], *U. Frankenfeld*[1], *S. Chatterji*[1], *O. Bertini*[1], *P. Larionov*[2,1], *M. Singla*[2,1], *and I. Sorokin*[2,1,3]
[1]GSI, Darmstadt, Germany; [2]Goethe University, Frankfurt, Germany; [3]KINR, Kiev, Ukraine

We report on the performance of prototype microstrip sensors for the CBM Silicon Tracking System (STS) after their exposure to neutron equivalent fluences as they are expected for the running scenario in the CBM experiment.

CBM radiation environment

The neutron fluence at the STS detector is expected to reach about 2×10^{13} $n_{eq}cm^{-2}$ per year, depending on the detailed physics programme performed and accumulating over several years of running. The maximum integrated fluence in some areas of the tracker will amount to 10^{14} $n_{eq}cm^{-2}$ beyond wich the affected detector modules will be replaced [1]. During the CBM experimental runs, periods of two or three months per year, the sensors will be operated at -5°C to limit radiation-induced leakage currents and to prevent from thermal runaway. During the periods of shutdown, the STS detector system may have to be warmed up to allow for maintenance of its components. The radiation damaged sensors will undergo annealing processes, with properties like leakage current, full depletion voltage (V_{fd}) and breakdown voltages changing with temperature and time.

Irradiation of prototype sensors

We have irradiated small test sensors from the most recent production of CBM05 prototypes, produced by CiS, Erfurt, Germany. The exposure to neutrons was performed at Institute Jozef Stefan, Ljubljana, Slovenia, within the EU-FP7 project AIDA. The sensors were irradiated in sets of four to the fluences 1×10^{13}, 5×10^{13} and 1×10^{14} $n_{eq}cm^{-2}$. During transport and storage after irradiation, a log of temperature and humidity was kept.

Full depletion voltage, charge collection

The sensors were installed in printed circuit boards allowing to apply bias voltage and to read out a number of strips with fast self-triggering front-end electronics. The sensors were operated in a nitrogen conditioned freezer at -5°C. Through the bias cable, scans of the bulk current and capacitance were made as a function of the applied reverse voltage. The determined depletion voltages as a function of the neutron equivalent fluence are summarized in Table 1. Applying significantly higher bias, the sensors' charge collection performance was determined with reading out signals induced with a ^{241}Am source and its 59 keV and lower energy gamma lines. Spectra of collected charge are shown in Fig. 1, applying a simple clustering algorithm to combine charge simultaneously seen on neighbouring strips. The results are reported in the table, assuming gain calibration factors of 117±3 (p) and 113±3 (n) ADC units for the full signal to yield the charge collection efficiencies.

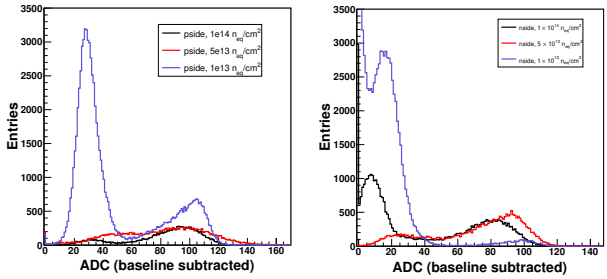

Figure 1: Charge distributions from the sensors' p (left) and n (right) sides as a function of neutron equivalent fluence.

Table 1: Charge collection performance of the sensors.

fluence ($n_{eq}cm^{-2}$)	V_{fd} (V)	V_{bias} (V)	peak ADC p ±3	peak ADC n	eff. (%) p ±4	eff. (%) n
0	80±2	160±1	117	102	100	90
1×10^{13}	35±5	130±1	105	100	90	88
5×10^{13}	45±5	180±1	95	95	81	84
1×10^{14}	110±2	300±1	95	81	81	71

Annealing studies

The leakage currents increase linearly with neutron fluence. The value of the damage constant, α, is initially at around 4.0×10^{-17} Acm^{-1}. After annealing at different temperatures, α can be used to yield the evolution of dark currents and V_{fd}. According to [2], radiation damage in silicon has several contibutions: a constant, a "beneficial annealing" and a "reverse annealing" component. Their determination is in progress.

References

[1] J. Heuser et al., Technical Design Report for the CBM Silicon Tracking System, GSI Report 2013-4, http://repository.gsi.de/record/54798

[2] M. Moll et al., *Nucl. Instrum. Methods. A* 439 (2000) 282.

* supported by EU-FP7 AIDA

Measurement of coupling and interstrip capacitances in silicon microstrip sensors for the CBM experiment at FAIR*

I. Sorokin[1,2], *P. Larionov*[1], *and J. Heuser*[1]

[1]Uni Frankfurt, Frankfurt am Main, Germany; [2]Kiev Institute for Nuclear Research, Kiev, Ukraine

The main component of the future CBM experiment [1] at FAIR (Darmstadt, Germany) [2] is the Silicon Tracking System [3]. It is going to be based on double-sided silicon strip sensors. Among the important characteristics of silicon strip sensors are the coupling (C_c) and the interstrip capacitances (C_{iImp}, C_{iStrip}), because they affect the signal amplitude [4, 5]. Measurement of these capacitances is therefore important both in the stage of detector prototyping and in the stage of series production for their quality assurance.

The coupling capacitance (C_c), is the capacitance between a metal strip ("Metalisation" in Fig. 1) and the implant underneath. C_{iImp} — is the total capacitance of an implant to the neighboring metal strips, and C_{iStrip} — is the total capacitance of a metal strip to the neighboring metal strips. The capacitances were measured with a QuadTech 7600 precision LCR meter. To determine the coupling capacitance the test voltage (0.5 V) was applied to the selected implant, and the current, induced on the metal strip above, was measured. To measure C_{iImp}, the test voltage was applied to an implant, the metal strip above the implant was grounded, and the current was picked from the neigboring metal strips (three on each side). For C_{iStrip} measurement the test voltage was applied to a metal strip, and the current was picked up from the neighboring metal strips (three on each side).

In the measurements of C_c and C_{iImp} the observed values decrease at high frequencies (example in Fig. 2) because the resistance of the implant (which is on the order of 100 kΩ/cm) becomes comparable to, or larger than the impedance of the measured capacitance, thus the test signal does not propagate along the whole implant length [5, 6]. Correct values for C_c and C_{iImp} are obtained only at low frequencies.

The obtained values (shown in the table below) were applied to estimate the expected signal amplitude [5]. The developed measurement techniques will be used for further characterization and quality assurance of the sensors.

Sensor, side	C_c, pF/cm	C_{iImp}, pF/cm	C_{iStrip}, pF/cm
CBM02, n	37.8 ± 0.5	1.0 ± 0.5	1.4 ± 0.5
CBM02, p	34.7 ± 0.5	1.4 ± 0.5	2.2 ± 0.5
CBM03′, p	17.2 ± 0.5	1.0 ± 0.5	1.5 ± 0.5

*Work supported by HIC4FAIR, HGS-HIRe, and H-QM Helmholtz research school

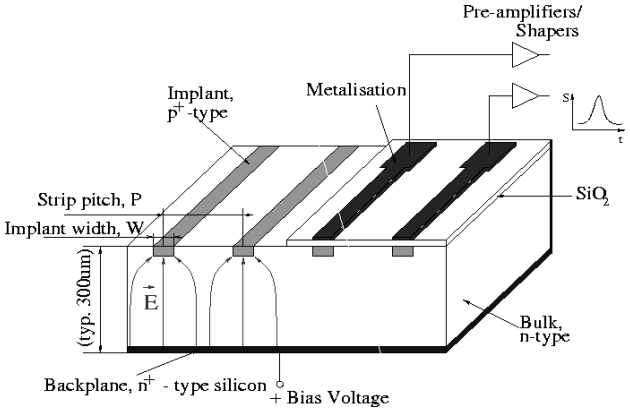

Figure 1: Schematic view of one side of a silicon microstrip sensor.

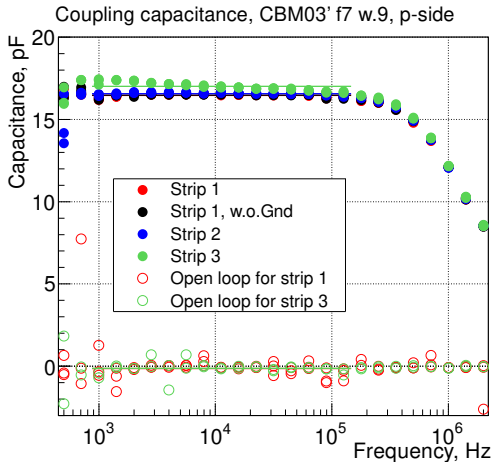

Figure 2: Coupling capacitance as a function of frequency in the CBM03' sensor.

References

[1] http://www.fair-center.eu/for-users/experiments/ cbm.html

[2] http://www.fair-center.eu/

[3] Technical Design Report for the CBM Silicon Tracking System (STS), GSI, Darmstadt (2013)

[4] C. Bozzi, Signal-to-Noise Evaluations for the CMS Silicon Microstrip Detectors, CMS Note 1997/ 026, 1997

[5] I. Sorokin, Characterization of silicon micro-strip sensors, front-end electronics, and prototype tracking detectors for the CBM experiment at FAIR, submitted as dissertation thesis, Frankfurt am Main.

[6] E. Barberis, Nucl. Instr. Meth. A342 90-95 (1994)

 doi:10.15120/GR-2014-1-NQM-CBM-09

In-beam test of prototype modules for the CBM Silicon Tracking System*

T. Balog[1,2], O. Bertini[1], J. Eschke[3], V. Friese[1], P. Ghosh[4,1], T. Heinz[1], J. Heuser[1], V. Khomyakov[5], P. Larionov[4,1], W. Niebur[1], C. Pauly[6], F. Uhlig[1], M. Singla[4,1], I. Sorokin[4,1,7], C. Sturm[1], A. Wolf[1], and P. Zumbruch[1]

[1]GSI, Darmstadt, Germany; [2]Comenius University, Bratislava, Slovakia; [3]FAIR, Darmstadt, Germany; [4]Goethe University, Frankfurt, Germany; [5]ITEP, Moscow, Russia; [6]Bergische Universität Wuppertal, Germany; [7]KINR, Kiev, Ukraine

In December 2013 three groups of the CBM and HADES collaborations tested recently developed prototype detectors in the 2.8 GeV high-intensity proton of COSY, Research Center Jülich, Germany. The beam was provided within a week long shift block dedicated to FAIR detector tests. On the test bench in the JESSICA cave were several prototype modules of the CBM Silicon Tracking System, several prototypes of GEM detectors for the CBM muon detection system developed by the CBM groups at VECC, Kolkata, India, and GSI, and diamond detectors for the T0 determination in CBM and HADES developed by GSI and the Technical University Munich. The beam definition was made with the already approved scintillating fiber hodoscopes built at Wuppertal University.

Prototype STS modules

The modules were to demonstrate the charge collection properties of the recent full-size CBM prototype microstrip sensors CBM05, and the signal transmission to the front-end electronics with optimized micro cables. They were designed at GSI and assembled at SE SRTIIE (team now with LTU) in Kharkov, Ukraine. The read-out was performed with the established front-end boards based on the n-XYTER ASIC. This limited the number of read-out channels to 128 per side, one eighth of all sensor channels. Therefore, the modules were produced in four versions to probe different sensor regions. Two modules used a single CBM05 sensor, one attaching to the central long strips on either side, and another reading out strips of the sensor corners. Two further modules realized, for the first time, also the operation and read-out of daisy-chained sensors, as they will be deployed in the outer regions of STS stations where the track densities allow minimizing the number of read-out channels by using particularly long strips.
The STS set-up on the beam table is shown in the left panel of Fig. 1. Two reference stations (STS 0, STS 1) defined the particle trajectories for impact on station STS 2 comprising a module under test. Such a module, here with daisy-chained sensors and the 25 cm long read-out cable, is shown in the right panel of the figure.

Measurement programme

The beam profile was adjusted to a diameter of about one centimeter. As the CBM05 microstrip sensors provide an active area of 6.2 cm by 6.2 cm, the middle station could be adjusted to probe certain sensor regions with beam. In addition to adjusting the horizontal and vertical position, also the impact angle of the beam was changed by rotating the station around the vertical axis. Several tens of runs with large statistics were taken for every module to study the charge collection properties as a function of various parameters, including bias voltage, strip length, signal path length, and beam incidence angle. Detailed analyses are being performed.

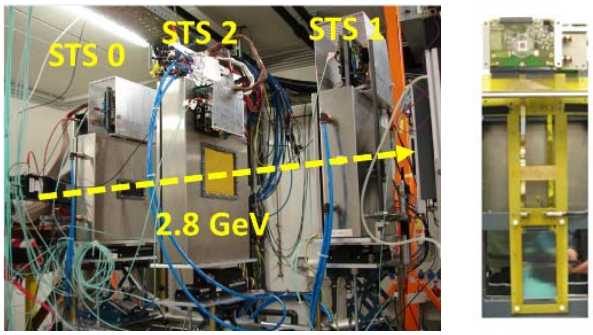

Figure 1: Prototype silicon tracking system in the JESSICA cave at COSY. Station STS 2 comprised the modules under test; one is shown in the right panel.

First results

The performance of the modules shall be illustrated with charge spectra, here from a module with two daisy-chained CBM05 sensors operated in self-triggered read-out mode. The distributions show, for both the n and p sides of the sensor, the charge collected on all of the 128 channels, after transmission through the read-out cables. The small peak is residual noise, the large peak charge from transient protons.

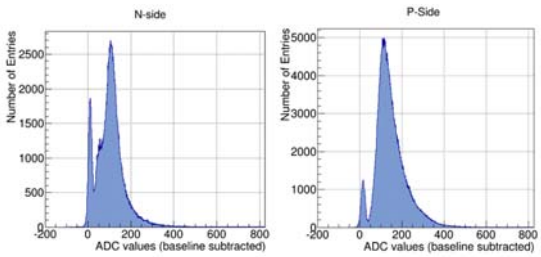

Figure 2: Charge spectra from both sides of a module.

* supported by EU-FP7 HadronPhysics3

Full-size prototype microstrip sensors for the CBM Silicon Tracking System

J. Heuser[1], *D. Soyk*[1], *C.J. Schmidt*[1], *Y. Murin*[2], *V.M. Borshchov*[3], *I. Tymchuk*[3], *and M. Protsenko*[3]
[1]GSI, Darmstadt, Germany; [2]JINR, Dubna, Russia; [3]LTU, Kharkov, Ukraine

The CBM Silicon Tracking System will comprise double-sided microstrip sensors of three basic geometries. Those differ in the lengths of their strip-shaped sensing elements, chosen to match the hit densities in their location of deployment in the tracking stations. Strip lengths of about 2 cm, 4 cm and 6 cm have been found adequate to achieve a sufficiently limited hit occupancy even under the harshest running conditions of the CBM experiment [1].

Sensor layout

The sensors have in common the number of 1024 strips per side at a read-out pitch of 58 μm, arranged parallel to the sensor edge (n-side) and under a tilt angle of 7.5 ° on the p-side. This will allow reconstructing space points within a sensor, with the required spatial resolution and at limited combinatorics resulting from the projective geometry. The strips are read out from one edge only, as to integrate the sensors into detector modules with the read-out electronics located at one end. On the stereo side, the strips in one corner of the sensor are not reached directly. They require further electrical connections to their partner strips in the other corner which are attached to the read-out electronics. Two technical solutions are being evaluated, one with metal lines integrated on a second aluminum layer on the sensor, another utilizing an extra thin cable layer bonded onto the sensor. The overall dimensions of the sensors are 6.2 cm width and 2.2 cm, 4.2 cm and 6.2 cm height. A depiction of their layouts can be seen in [2]. This allows producing them with 4" wafer technology, a pre-requisite for a sufficiently large circle of vendors. Also the on-sensor cable as an alternative to the routing lines on a second metal layer are shown there.

Prototypes CBM05

In 2013 the production of prototype sensors in all three sizes has been achieved. All sensors of this CBM05 series have a compatible layout of their bonding pads which was worked out within the CBM collaboration and its technology partners. The prototypes were produced in cooperation with the CiS Research Institute for Micro Sensorics and Photovoltaics, Germany, and Hamamatsu Photonics, Japan. The large prototype sensor with double-metal interconnections came from CiS on a GSI bill. The mid-sized sensor has been realized with Hamamatsu with support to GSI from BMBF. The small sensor was ordered at Hamamatsu through JINR. All sensors but the small one are double-sided. The small sensor was made as simple as possible, therefore single-sided, with the specific aim to verify the viability of the on-sensor cable concept. Some of the large sensors were employed in new prototype modules and tested extensively in lab and beam. Such sensor with its integrated double-metal lines is shown in Fig. 1.

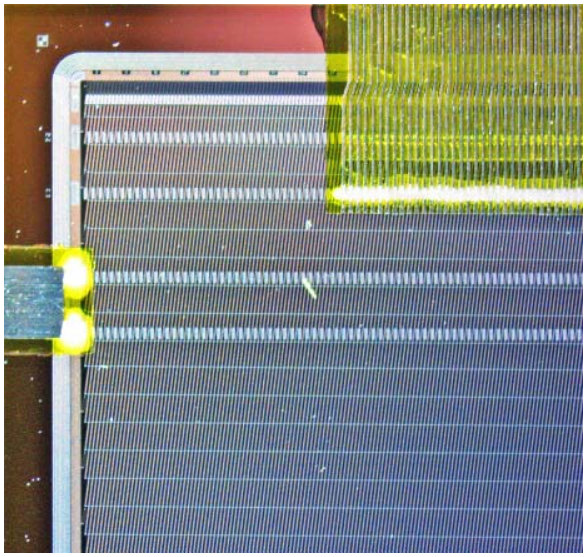

Figure 1: Corner region of a CBM05 sensor produced at CiS. The sensor has been fitted with a bias cable (left) and has a micro read-out cable tab bonded to it (top).

Prototypes CBM06

A further series of prototype sensors, CBM06, has been designed and launched for production with CiS and Hamamatsu to be available in 2014. They will serve extended effort with the development of prototype detector modules. In view of the preparation of tooling for the technical integration of their components, larger amounts of dummy sensors and dummy ASICs have been produced in 2013, providing no active functionality but the the same contact patters on the same metallic surfaces as the full sensors.

References

[1] J. Heuser et al., Technical Design Report for the CBM Silicon Tracking System, GSI Report 2013-4, http://repository.gsi.de/record/54798

[2] J. Heuser et al., GSI Scientific Report 2012, GSI Report 2013-1, PHN-NQM-EXP-16, http://repository.gsi.de/record/51950

 doi:10.15120/GR-2014-1-NQM-CBM-11

First mock-up of the CBM STS module based on a new assembly concept

V.M. Borshchov[1], *C.J. Schmidt*[2], *Y.A. Murin*[3], *I.T. Tymchuk*[1], *M.A. Protsenko*[1], *J.M. Heuser*[2], *R.A. Kushniruk*[1], *L.V. Klimova*[1], *and N.F. Chernikova*[1]

[1]LED Technologies of Ukraine (LTU) Ltd, Kharkov, Ukraine; [2]GSI, Darmstadt, Germany; [3]JINR, Dubna, Russia

The first mock-up of the CBM STS detector module based on a modified design and new assembly concept has been developed and manufactured by the Kharkov team at the newly created assembly site of LTU Ltd.

Composition of the detector module mock-up

The initial module concept [1, 2] foresaw multi-layered cables comprising 512 traces at each signal layer. Based on the experience obtained in the prototyping stage and taking into account risk minimization and yield increase with the manufacture and assembly of components a new design and assembly concept was suggested [3]. The module mock-up was developed for verification of this concept. It includes the following components, similar as in real full-scale modules:

- dummy microstrip double sided sensor (1024 strips on each side at 58 um pitch, 7.5° stereo angle of strips);
- prototypes of multilayered connection microcables (1024 lines for one side of sensor);
- dummy chips with 128 input pads;
- dummy FEBs with 8 seats for chips.

A microcable consists of the following layers:

- eight multilayered microcables (128 lines for chip to sensor connection). Each multilayered cable includes two connecting layer (FDI-A-24, 64 traces at 113 μm pitch) and meshed spacers (Kapton 50 μm thick, fill factor about 40%).
- overall meshed spacer for all 8 multilayered microcables (Kapton 100 μm thick or two spacers 50 μm thick, fill factor about 40%).
- overall shielding layer for all 8 multilayered microcables (FDI-A-24) with glued meshed spacer (Kapton 50 μm thick, fill factor about 40%).

Assembly sequence of mock-up

For the first detector module mock-up the following technological sequence has been developed:

1. Assembly (gluing) of multilayered components (connecting and shielding layers with spacers).
2. SpTAB bonding bottom connecting cables to chips, bond joints protecting.
3. SpTAB bonding top connecting cables to chips, bond joints protecting.
4. Aligning of sensor sides of the top and bottom cables and cables gluing (fixing precise aligned position one to each other).
5. Aligning of sensor sides of 8 assembled multilayered connecting cables to sensor.
6. Gluing of overall meshed spacer or shielding layer (depending on modules side).
7. Mounting (gluing, wire bonding, encapsulating) of assembled multilayered cable with chips to the FEB (first 4 chips than second 4 chips),
8. Multilayered cables (mounted on the FEB) SpTAB bonding to the sensor (bottom cables, then top cables), bond joints protecting,
9. Flipping the assembled half-module upside down,
10. Repetition of operations 7 and 8 for second side.

Module mock-up manufacturing

For the first module mock-up were developed and produced more than 10 types of component requiring more than 20 photomasks. As a result of abovementioned works the first half-module (only one sensor side connected, without wire bonding chip-to-FEB) was assembled (Fig. 1).

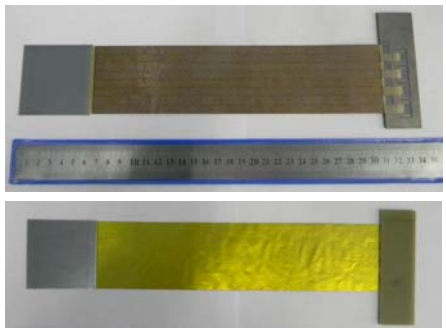

a)

b)

Figure 1: First mock-up of the CBM STS detector half-module a) top view, b) bottom view.

During the assembly of the first module mock-up only visual inspection were performed but for real detector modules after each bonding of connecting layers to sensors or chips need to be done electrical QA testing.
Results of development and assembling of the first mock-up of the CBM STS half-module confirm practical feasibility of suggested concept on detector modules creation.

References

[1] V.M. Borshchov et al., CBM Progress Report 2009, p 17

[2] Yu.A.Murin et al., CBM Progress Report 2011, p 19

[3] C.J. Schmidt et al., CBM Progress Report 2012, p 18

Low and high voltage power supply for STS detector electronics

P. Koczoń[1], *B. Ernst*[1], *and C.J. Schmidt*[1]
[1]GSI, Darmstadt, Germany

Environmental conditions for STS at CBM

The silicon tracking detector STS for the CBM experiment at FAIR will work inside a magnetic field of 1 T and will have to stand a radiation load of up to 10^{14} n_{eq}/cm^2 in the regions close to the beam pipe. It consists of more than 1200 double sided silicon sensors arranged in 8 planes covering a cone of the opening angle of ± 25 degrees, illustrated in Fig. 1 [1].

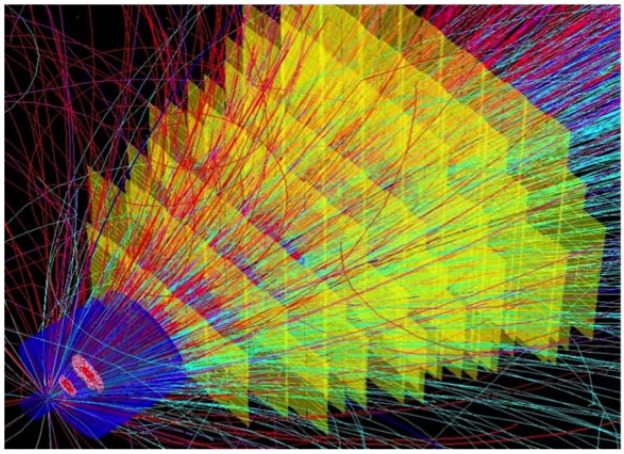

Figure 1: Silicon Tracking System with simulated tracks.

The readout electronics should work floating what means that each side of every sensor has to be operated on electric potential of up to ± 250 V (sensor bias up to 500 V) and read out independently of each other.

High voltage supply system

Each side of each silicon sensor will be supplied with a half of the nominal biasing voltage to achieve full depletion and floating operation mode. Low leakage currents in the sensors allow sufficiently compact feed-through construction and off-the-shelf system for full control of the depletion voltages from outside of the STS thermal enclosure.

Low voltage power supply system

The electrical supply needs are a power of about 45 W per detector module at several voltages (1.2, 1.5, 3.3 V). These voltages have to be delivered for each side of every sensor separately. The sheer number of feed-throughs with pin cross sections allowing for currents of 1 - 3 A would exceed the available mounting surface. Cable power losses would require additional sensing wires and would heat-up the surrounding volume. Instead, DC/DC conversion inside the temperature controlled STS-container is proposed.

DC/DC converter

Several DC/DC converter ICs have been evaluated, both isolated discrete systems (like VICORS P048T048T24AL and B048F012T30) and non-isolated systems (Linear Technology LT3605, LT3610, LTM4619, Texas Instruments LM2596 or Yutaka Electric YSD812). All investigated buck (step-down) systems are equipped with an inductance driven by a pair of high-power transistors. An air-coil type inductivity can work in a magnetic field in contrary to ferrite coils which saturate and cause system malfunction.

Both isolated DC/DC converters appeared to break down already at 50 mT due to the failure of the built-in ferrite inductivity. Measurements of converters based on other chips proved that some of them can work in a magnetic field of up to 0.7 T (field strength at the STS periphery) with efficiency of 80 - 90 % (Fig. 2). Since the evaluation boards in test have been equipped with metal oxide coils there is still a room for efficiency improvement by using air coils.

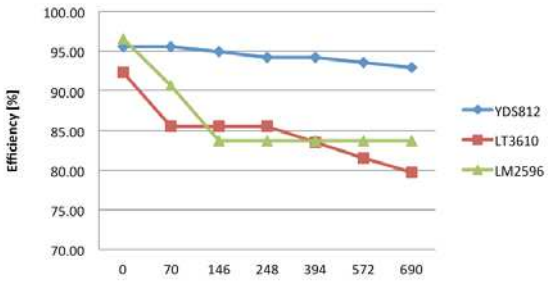

Figure 2: Converter efficiency as function of the magnetic field [mT].

Selected DC/DC converter chips have been tested for radiation hardness and results of these measurements are reported in [2] together with other electronic parts.

References

[1] STS Technical Design Report, 2013.

[2] S. Löchner, GSI Annual Report 2013

 doi:10.15120/GR-2014-1-NQM-CBM-13

Calibration of a laser scanning system for quality assurance of CBM prototype silicon microstrip sensors *

P. Ghosh[1,2], J. Eschke[2,3], W. Niebur[2,3], H. Malygina[1,2], P. Zumbruch[2], and B. Kolb[2]

[1]Goethe Universität, Frankfurt am Main, Germany; [2]GSI, Darmstadt, Germany; [3]FAIR, Darmstadt, Germany

For the characterization and Quality Assurance (QA) of prototype sensors produced for the Silicon Tracking System (STS) at the Compressed Baryonic Matter Experiment (CBM), a infrared pulsed Laser Testing System (LTS) has been developed. The main aim for the LTS is to scan and characterize the prototype sensors. These QA scans are intended to understand charge sharing in the interstrip region and investigate uniformity of sensor performance in the active area of prototype sensors. The prototype sensor CBM02 which has 256 strips with a pitch of 50 μm on each side has been investigated in the LTS [1]. The strips on the sensors are wire bonded to connectors on a board and readout via self-triggering n-XYTER prototype electronics.

The goal for the LTS is to have automatized quality assurance tests in a controlled manner at several thousands positions across the sensor with focused infra-red laser light ($\sigma_{spotsize} \approx 15$ μm). The duration ($\sim$10 ns) and power (few mW) of the laser pulses are selected such that the absorption of the laser light in the 300 μm thick silicon sensors produces about 24 000 electrons,which is similar to the charge created by minimum ionizing particles (MIP) there.The wavelength of the laser was chosen to be 1060 nm because the absorption depth of infra-red light with this wavelength is of the order of the thickness of the silicon sensors [2¹

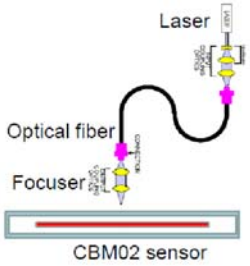

Figure 1: Schematic representation of the laser setup.

A schematic view of the measurement setup is shown in Figure 1. The laser light is transmitted through a 6 μm thick optical fiber to a two-lens focusing system, which focuses the light to a spot of about 15 μm diameter and the working distance is about 10 mm. Figure 2 shows a dependence of the distanceto the sensor surface as a function of the number of strips fired with a signal just above threshold. With this measurement the proper focus distance has been achieved. Figure 3 shows the charge sharing function between neighboring strips represented in the form of fraction of amplitudes collected by the individual strip.

* Work supported by HIC4FAIR, HGS-HIRe and H-QM

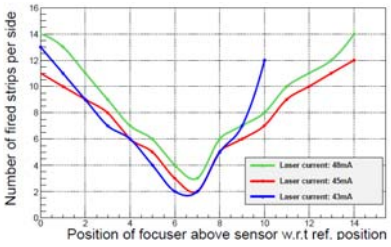

Figure 2: Dependence of distance to focuser from the sensor surface as a function of strips fired.

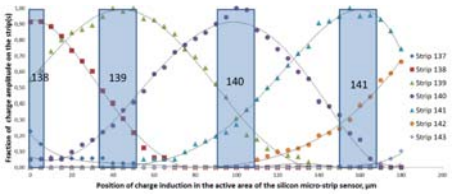

Figure 3: Charge division (fraction of amplitude) in the interstrip region as a function of position of laser spot.

The LTS has recently been upgraded with motor controls using EPICS [3] and programs have been written to step over the active area make several measurements automatically. Figure 4 shows an operator interface of the running system using EPICS tools. The next step is to integrate the data acquisition software DABC [4] plugin for the EPICS position information for data taking, logging and further analysis using the Go4 analysis software.

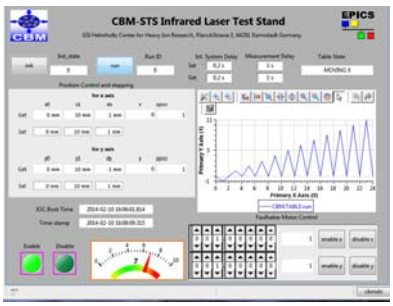

Figure 4: Run time operator interface for the LTS.

References

[1] J.M. Heuser et al., CBM Progress Report 2011

[2] P.O'Connor et al., Proc. of SPIE Vol. 6276 62761W-1, p.2

[3] EPICS: http://www.aps.anl.gov/epics

[4] DABC: http://dabc.gsi.de

Automized quality assurance of sensors for the CBM Silicon Tracking System*

P. Larionov[1] *and U. Frankenfeld*[2]

[1]Goethe Universität, Frankfurt am Main, Germany; [2]GSI, Darmstadt, Germany

The Silicon Tracking System is the main tracking detector of the Compressed Baryonic Matter (CBM) experiment. It will comprise 8 stations that will be built out of around 1200 double-sided silicon microstrip sensors. The sensors will be AC-coupled and have 7.5 degree stereo angle between p- and n-side strips. The latest sensor prototypes, CBM05, manufactured by CiS, are currently being evaluated for their parameters before the series production will take place [1].

To achieve the required tracking efficiency of the whole tracking system, each sensor has to be evaluated in a number of quality assurance procedures. Some of those allow checking the overall sensor health, as it has already been done with earlier sensor prototypes [2]. This report emphasizes on the procedure that has been developed for an advanced quality assurance tests applying to the sensors that have been accepted after the basic check.

The procedure itself comprises automization with LabView software and involves the use of the following equipment: a wafer prober Süss PA300PS with a mechanical accuracy of 2 μm, picoampere meters Keithley 6487 and 2410, and a LCR meter Quad Tech 7600. The following advanced quality tests of silicon sensor can be realized: (a) number of pinholes, (b) leakage current of each strip, (c) number of shorted strips, (d) number of ragged strips. The measurements are being performed in a clean room with temperature and humidity control.

The software includes two communicating programs developed on a master and slave principle, installed on two personal computers. The master program communicates with the measuring devices and generates the commands for the slave program which in turn manages the wafer prober perfomance.

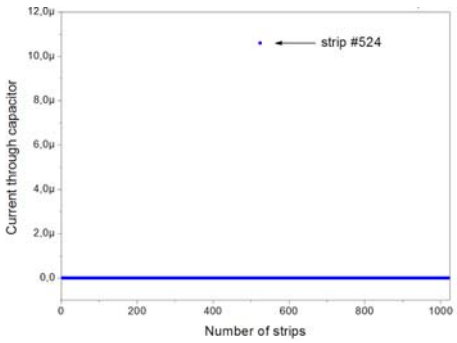

Figure 1: Result of strip current test for CBM03' sensors.

The pinhole measurement provides information about defected strips with disrupted capacitive coupling and which cannot be used for charge collection. Figure 1 indicates the result of the pinhole test of CBM05 sensor prototype detecting one broken capacitor on the p-side of the sensor. Table 1 summarizes results of pinhole measurements for different prototype sensor.

Table 1: Results of the pihole tests for CBM03' and CBM05 sesnor prototypes

Sensor Prototype	Sensor Size	Wafer Number	Number of pinholes *p-side*	*n-side*
CBM03'	Full size	7	0	-
CBM03'	Full size	10	5	-
CBM03'	Full size	13	0	-
CBM05	Full size	4	0	4
CBM05	Full size	6	0	0

Measurement of the leakage current of individual strip helps us to identify the number of strips having relatively high leakage current which have to be masked in the read-out electronics. Figure 2 shows the distribution of strip leakage currents of one prototype sensor. If the number of defective strips is below a certain quality acceptance threshold, the sensor can be used for module assembly and only the bad strips should not be connected to the read-out electronics. Otherwise, the sensor should be discarded.

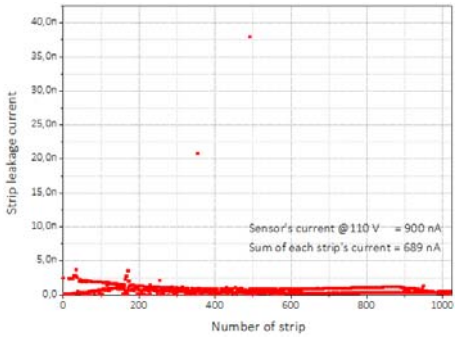

Figure 2: Result of strip current test for CBM03' sensor prototype.

References

[1] J. M. Heuser *et al.*, CBM Progress Report 2012, Darmstadt 2012, p.8

[2] P. Larionov and P. Ghosh, CBM Progress Report 2012, Darmstadt 2012, p.11

* Supported by HIC4FAIR, HQM, HGS-HIRe.

 doi:10.15120/GR-2014-1-NQM-CBM-15

Application of the CBM Silicon Tracking System CAD model for integration studies

S. Belogurov[*2]*, A. Kolosova*[2]*, and J. Kunkel*[1]
[1]GSI, Darmstadt, Germany; [2]ITEP, Moscow, Russia

Motivation

The high density of equipment inside the gap of the CBM dipole magnet requires special attention to the integration effort and, more generally speaking, to the system engineering of the set-up. In this report we discuss the current status of the system integration effort, the tasks to be solved and the methods in use.

CAD (Computer Aided Design) software is one of the major tools in complex system development. It is used to create a virtual model of the product in development. For the CBM STS detector system a virtual model of the whole system is created with CATIA, a software package for product development that covers the whole process from first sketches to final drawings for the manufacturing of components.

Status and tasks of the system integration

The STS detector system is designed in functional parts, such as main detector parts, mounting structures, enclosures and supply lines. The virtual model in the CAD software is set up in the same way. Since parts and assemblies are stored in separate files, collaborative work on different parts of the detector at the same time is possible.

One important integration task is to reserve space for various functional nodes. Currently we develop to arrange in space of the following items: Sensors, sectors, modules, ladders, data cables, C-shaped supporting frame for ladders, fixation for the ladders and for the cables, front-end-boards (FEB), FEB fixation and cooling boxes, cooling plates common for a unit (i.e. two neighbouring half stations belonging to the two consequent stations), CO_2 cooling connections, power supply lines for FEBs, data transport lines from FEBs to data aggregation boards, voltage conditioners for the FEBs, optical links and cooling boxes for voltage conditioners, data aggregation boards and optical links. An overall view of the STS and a detailed view of one quarter of the 8th station are shown in Figs. 1 and 2, respectively. Generally, the design of the STS follows an onion logic from the innermost parts to the outer ones.

Space analysis allows to see the critical elements in the system. E.g. it has been demonstrated that the availability of single-channel radiation hard SFP optical links only causes a limitation on the total number of channels in the system. Any development towards higher granularity would require new radiation hard multichannel optical links.

Another task for the system integration is to study and to balance contradictory requirements of various origin. E.g. front-end electronics developers tend to insist on the shortest possible cables in any particular case, however the reasoning of the C-Shaped frame rigidity and cooling plate beauty forces us to use sometimes the cables a bit longer than absolute minimum. A further issue under investigation is the checking for all the possible dependencies, e.g. the thickness of cooling plates has influence on the space available for bending of cables, and the pad pattern on different sensors, staggering of the sensors in a ladder and spacing between the FEBs in the working position are connected to the reduction of the number of different types of cables.

Methods in use

For the integration studies a deeply parametrized model has been created using the CATIA VBA code called "STS creator". The tool arranges correctly in space all the components based on parametrized templates. The composition of the ladders can be modified later and all the parts like CF ladder support frames, C-shape unit frames and cooling plated will be adjusted automatically. The entire model can be checked for interferences, margins and free space. Using such a tool allows saving a lot of manpower and time since, for the CBM STS, the active detector part consists of several hundreds of parts.

For making design information available for further analysis each functional node has an *HTML* description accessible from CATIA. Cross links to descriptions of mother and daughter products are generated automatically. A data base for design solutions, options, versions, open questions and mutual dependencies is under development. Data retrieval from this base can be made available from the above mentioned *HTML* documentation.

Next steps

We plan to establish a CAD data exchange platform for efficient collaborative work on the project. Dedicated programs like Git and Subversion are available for software developers. Although CATIA files are binary such a tool could satisfy our needs for sharing data and revision control. Special programs for CAD data handling are under investigation, too. The design solution database mentioned above should be transferred from prototype to development status. The outer layers of the system, like connecting unit to the outside world, thermal enclosure and the mechanical super structure should be developed rather soon.

* Work supported by FAIR Russia Reseach Center

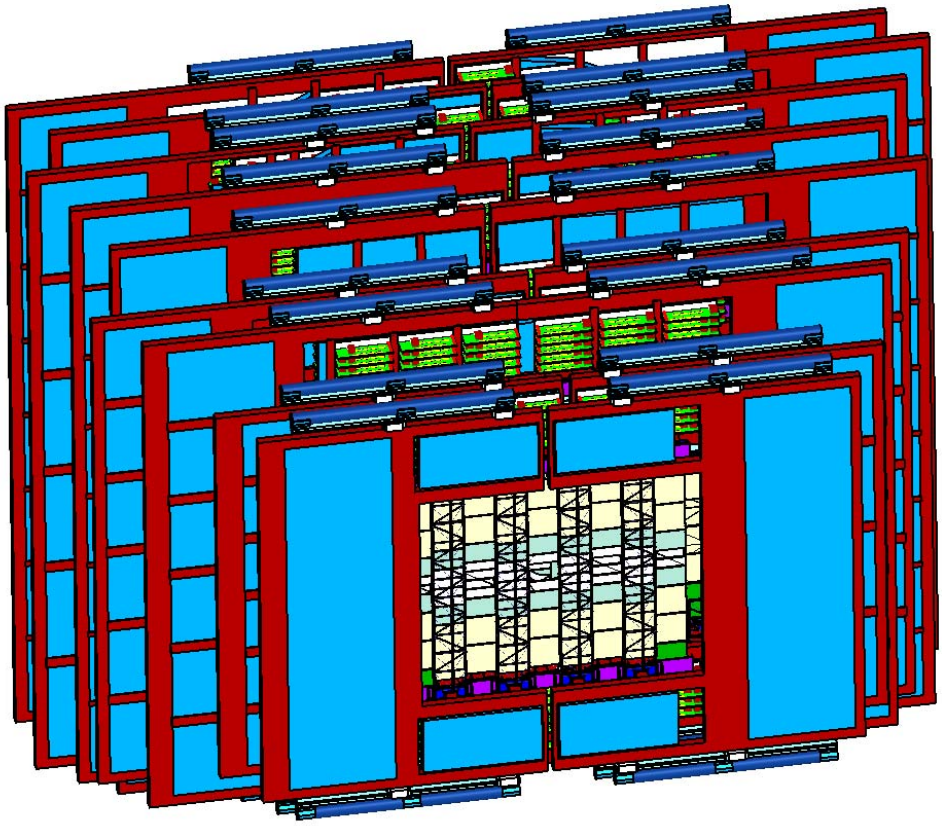

Figure 1: Overall view of all 8 STS stations.

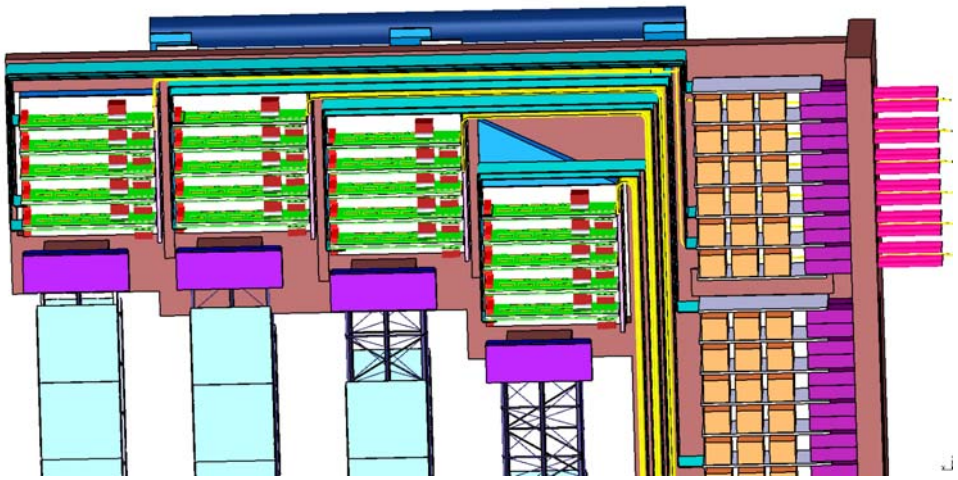

Figure 2: One quarter of station 8 including readout and data transfer electronics, power supply and cooling equipment.

 doi:10.15120/GR-2014-1-NQM-CBM-16

An improved detector response simulation for the Silicon Tracking System*

V. Friese[1], *J. Heuser*[1], *and H. Malygina*[2,3]

[1]GSI, Darmstadt, Germany; [2]Goethe University, Frankfurt, Germany; [3]KINR, Kyiv, Ukraine

To achieve realistic simulations the response of the silicon strip sensors should be precisely included in the digitizer, which simulates a complete chain of physical processes caused by a charged particle traversing the detector, from charge creation in silicon to a digital output signal. In the CbmRoot software, the current version of the STS digitizer [1] doesn't include all the processes needed to obtain results with sufficient accuracy. It assumes a uniform energy loss distribution along the incident particle track and accounts for the Lorentz shift and effects of the read-out electronics, as threshold, random noise, charge collection inefficiency, channel dead time. We considered the following improvements to the digitizer: non-uniform energy loss distribution, thermal diffusion, and charge re-distribution over the read-out channels due to interstrip capacitances (the so-called "cross-talk"). There are several possibilities to model each process with a different level of detailing. We suggest the following procedure:

- to divide the incident particle trajectory into thin layers ($3\mu m$); to calculate the deposited energy in each layer according to the Urban method [2];
- to estimate the charge broadening due to thermal diffusion according to the Gaussian low for the charge in each layer [3];
- for each fired strip to calculate the charge sharing due to the cross-talk, to add random noise distributed according to the Gaussian low with $\sigma = ENC$ (Equivalent Noise Charge);
- to convert the charge in each strip from number of electrons to ADC-value; to apply a threshold and other effects of electronics.

We verify the new procedure by choosing tracks with random impact and inclination from -45° to 45° (see [4] for more details) and utilizing the Center-Of-Gravity algorithm [5] to reconstruct clusters. From the obtained results we conclude that the most significant effect is the non-uniform energy loss along the incident particle track. Figure 1 shows a comparison between experimental data from the LHCb and our simulation. The experimental data agrees better with the new procedure. The current digitizer predicts most probable amplitude loss for perpendicular tracks to be 0%, whereas the improved version yields 10%. The measured value is yet higher, verifying the advance in development of the digitizer.

Several STS prototype modules based on CBM05 prototype sensors were operated during an in-beam experiment at COSY. Figure 2 shows a comparison between the

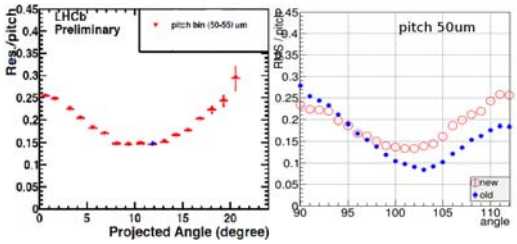

Figure 1: The RMS of the hit position residuals distribution VS track inclination: left panel – the LHCb Vertex Locator (0° – perpendicular tracks) [6]; right panel – our simulation (red circles – the new Digitizer, blue dots – the current version, 90° – perpendicular tracks).

simulated data and the data obtained during the experiment, in the external triggering mode at different track inclinations. For perpendicular tracks we adopt a threshold of 9375 electrons and for 20° tracks 6250 electrons. As our simulation does not produce noise separately, but only adds random noise to the signal, a slight underestimation of small clusters is acceptable. We can see it for inclined tracks. However we reproduce a general behaviour of the measured cluster size distributions. Eventually, we found several points, where the improved Digitizer agrees better with experiment.

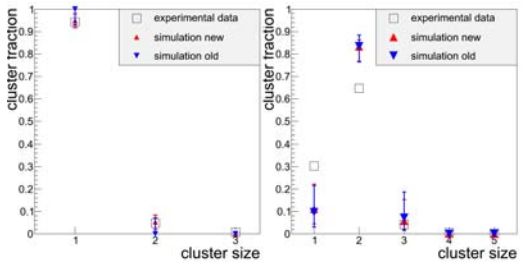

Figure 2: Cluster size distribution for perpendicular tracks (left) and for 20° tracks (right). The experimental data – empty squares, the new procedure – red triangles, the current – blue triangles. Error bars show the uncertainty in angle determination.

References

[1] A.Kotynia and J.M.Heuser, CBM Progress Report 2011 p. 14

[2] K.Lassila-Petini and L.Urban, Nucl. Instr. Meth. A362 (1995), 416-422

[3] M.Brigida et al., Nucl. Instr. Meth. A533 (2004), 322-343

[4] V.Friese and H.Malygina, STS-Note-07-2013

[5] R.Turchetta, Nucl. Instr. Meth. A335 (1993), 44-58

[6] E.Rodrigues, Presentation at Vertex2013

* Work supported by HIC4FAIR, HGS-HIRe and H-QM.

A front-end electronics board to test the assembly procedure of modules for the CBM Silicon Tracking System*

V. Kleipa[1], *C.J. Schmidt*[1], *C. Simon*[1], *and D. Soyk*[1]
[1]GSI, Darmstadt, Germany

The STS front-end electronics board

For the Silicon Tracking System (STS) of the CBM experiment, about 2000 read out electronic boards (FEBs) have to be produced. They comprise eight readout ASICs of 128 amplifier channels each which will read the 1024 sensor channels on either side of a STS detector module [1]. So there is a need to prepare tools and assembly instructions for their serial production. In order to develop and verify the assembly procedures, a test board has been designed.

Module assembly chain

The assembly chain will start with the tab-bonding of the read-out micro-cables on the ASICs. Then the ASICs must be glued in spares of the FEB's printed circuit board. In a next step the ASICs will be connected to the supply, control and read-out lines with wire bond. The challenge is how to adjust the ASICs with the sensitive tab-bonded sensor-cables on the PCB and how to connect the ASÌCs further with bond wires to the main PCB.

In all these cases the hight of additional components on the PCB have to be respected. I.e. SMD capacitors and resistors or the globtop - which is protecting the bond-wires, cause barriers for the second row of ASIC chips. It needs also to be verified, if embedded passive devices are required to be reduced in height.

Two ASIC footprints are prepared on the PCB for the different test purposes. One footprint needs to be generated with laser cavity technology. Here the bond wires can be connected directly to the inner layers of the PCB. The other footprint consists only of bond pads on the top layer. Some additional routing space will be required here too. Additional thermal cycling tests are planned to proof the safety of the tab and wire bond connetions.

Test board and assembled object

The front-end board designed to test the assembly procedure and the functionality of the pairs of ASICs and tab-bonded micro cables is shown in Figures 1 to 3:

- Figure 1 depicts the FEB layout for the assembly test.
- Figure 2 is a 3D rendering of a possible FEB PCB.
- Figure 3 depicts an assemby with FEB, ASICs and micro cables.

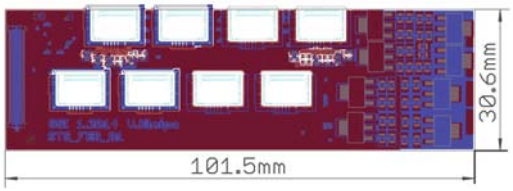

Figure 1: STS FEB8 test layout.

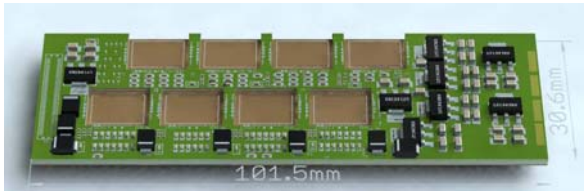

Figure 2: 3D View of equipped STS FEB Board.

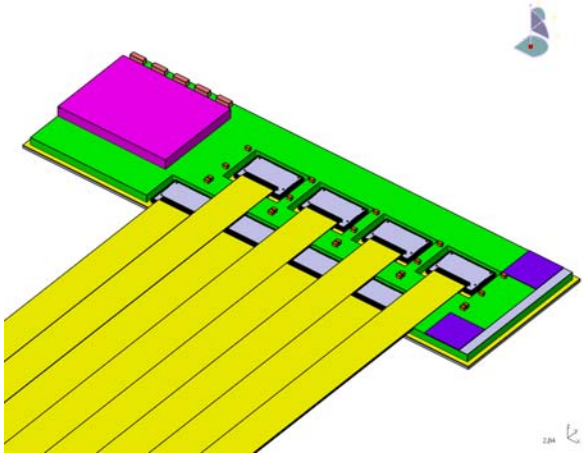

Figure 3: Assembly of sensor cables and FEB.

References

[1] J. Heuser et al., Technical Design Report for the CBM Silicon Tracking System, GSI Report 2013-4, Chapter 5.3 Modules, p. 79-83, http://repository.gsi.de/record/54798

* supported by EU-FP7 HadronPhysics3

doi:10.15120/GR-2014-1-NQM-CBM-18

A mechanical model of an STS station for the study of cable routing

P. Koczoń[1], *J. Kunkel*[1], *D. Soyk*[1], *and C.J. Schmidt*[1]
[1]GSI, Darmstadt, Germany

Mechanical aspects of STS construction

The silicon tracking detector STS for the CBM experiment at FAIR poses an engineering challenge due to its compactness and requirements concerning signal density, signal-to-noise ratio, and efficiency. The restricted height of the magnet yoke opening together with the number of readout channels and requirement to geometrical acceptance, operating temperature and mass budget [1] leave very little room for the readout and data transfer electronics and needed power conversion electronics inside of the STS container (Fig. 1).

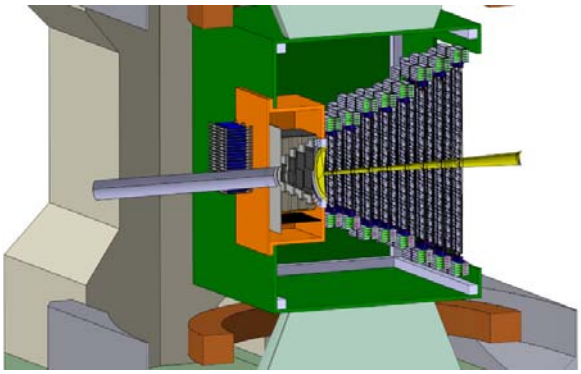

Figure 1: STS in the yoke of the dipole magnet.

Under such restrictive conditions it is very critical to find proper mechanical, electronic and electrical solutions/components like very compact circuits of highest efficiency, fine-pitch flexible cables for analog and digital signals, corresponding connectors or bonding methods as well as thin and flexible cables of adequate lead cross section for power supply. Last but not least the positioning of the components and shape of the cooling bodies together with the topology of cable routing paths have to be defined.

Real-size model of the STS

In order to verify many of the posed questions and corresponding tentative answers a three-dimensional model of one STS station has been constructed. Axial symmetry of the STS allows to concentrate on one quarter of the most crowded station 7 of the STS (Fig. 2). The model has been constructed according to mechanical design drawings and fulfills requirements like parts' dimensions, cable thickness and flexibility. This mechanical mockup allows confirming methods elaborated for the handling of STS stations and its subsystems as well.

Figure 2: Mechanical model of one STS station.

References

[1] J. Heuser et al., Technical Design Report for the CBM Silicon Tracking System, GSI Report 2013-4, http://repository.gsi.de/record/54798

doi:10.15120/GR-2014-1-NQM-CBM-19

A setup for adjustment of process parameters for CBM module production

D. Soyk[1], C. Simons[1], C. Schmidt[1], I. Tymchuk[2], M. Protsenko[2], and V.M. Borshchov[2]
[1]GSI, Darmstadt, Germany; [2]LTU, Kharkov, Ukraine

The sensor modules for the CBM STS comprise an STS microstrip sensor, 16 CBM STS-XYTER readout chips and 32 microcables of 64 leads each. The double-sided STS sensor has 1024 strips on each side. Consequently 2048 channels per module must be connected by means of 4096 bonds. It is obvious that the quality assurance of theses tab-bonds is a major ingredient to the yield of module production and reliability of the detector as a whole. Especially the large number (around 1000) of modules needed for the entire CBM STS requires to have a detailed look at the tab-bond process and its parameters, as potentially required repair actions on defective modules will be time consuming and adds the risk of additional inadvertent damage to the module. Therefore it is the best solution to improve and bring the tab-bond process to perfection before starting the serial production of modules for the CBM STS.

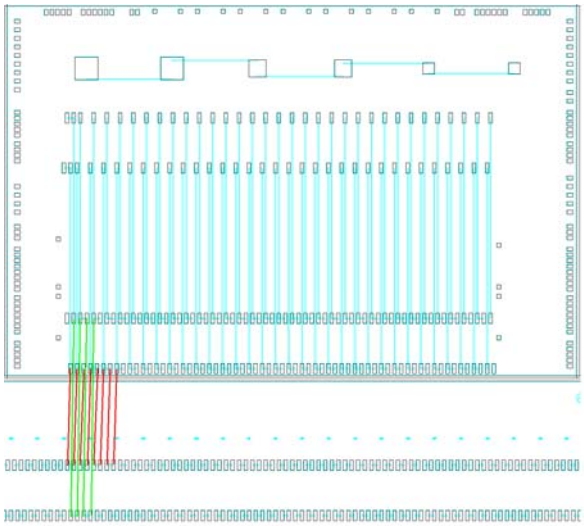

Figure 1: Dummy CBM STS-XYTER chip (up) and a partial plan of a CBM sensor dummy (down). The red lines are the connections via the microcable for the first row of bond pads. The green lines are the connections via a second microcable for the second row of the pads. In the upper part of the Dummy CBM STS-XYTER are the contact pads for the test equipment directly connected to the tab-bond pads in the lower part of the chip.

It is clear that for such process optimization no original full functional STS sensor and CBM STS-XYTER chip will be used or needed. The first reason is the costs of the original components and second reason is the missing of fast and easy ways to check the quality of the tab-bonds. For this reason, dedicated dummy-sensors as well as dummy-chips have been designed and manufactured. To check the quality of bonding two tests are necessary. One is the pull test to check mechanical adhesion of the aluminum lead of the microcable to the bond pad. The second is the electrical connectivity of the bond.

In order to make this test conclusive for the real module the microcable must the original, the surface and the material of the bond pads for dummy-sensors and chips must be identical to the material on the original sensors and chips. Also, the Silicone wafer material and thickness should be identical. If these requirements to the microcables, dummy sensors and chips are fulfilled, it is possible to transfer the process data to the serial production process.

To improve the test routines for the electrical contacts, additional pads for test needles and connections between the pads were added to the dummy-sensors and -chips. (These additional features will not be part of the layout of the final devices.) In Fig. 1 the scheme of electrical connections is shown with the layout of the dummy chip and sensor. On the dummy chip, each second pad of each row is electrically connected to a pad far away from the tab-bond area. (The first pad of a row is like the second also electrically connected to a shifted pad.) The non duplicated pad is electrically connected to its left neighbor. On the dummy sensor two neighboring pads of a row are electrically connected together.

The idea behind this set-up is to make an electrical connection between the pad of the test needle via the tab-bond on the chip, the microcable, the tab-bond on the sensor and back to the second test pad for each row. With this simple serial routing it is possible to check 4 tab-bond connections and two leads of the microcable with one single measurement. If the connection is good the first needle is kept on its starting position whereas the second needle is shifted to the next pad of the row. This daisy chaining now allows to check 8 tab-bonds and 4 leads of the microcable in one go. While continuing this daisy chaining it is possible to check numerous tab-bonds and microcable leads. If a broken lead or damaged tab-bond is found the first needle of the test set-up must be moved to the unconnected pad and the second needle can step further. With this test strategy we can reduce the number of single tests, because only broken leads or tab-bonds will cause a restart of the test procedure. Additionally the test procedure could be done automatically on a wafer prober.

At the moment the dummy chips and sensors have been delivered. We are now waiting for a sufficient number of sample microcables to start process optimization.

 doi:10.15120/GR-2014-1-NQM-CBM-20

Development of a CO_2 cooling prototype for the CBM Silicon Tracking System*

J. Sánchez[1], *J. M. Heuser*[1], *W. Niebur*[1], *C. Sturm*[1], *H. R. Schmidt*[2], *A. Lymanets*[2], *P. Petagna*[3], *B. Verlaat*[3], *and L. Zwalinski*[3]

[1]GSI, Darmstadt, Germany; [2]Eberhard Karls University, Tübingen, Germany; [3]CERN, Geneva, Switzerland

Nowadays the high energy physics detectors require ever more powerful cooling plants as well as a non-invasive piping. This means that the mass budget has to be as small as possible in order to not decrease the efficiency of the detector effective surface. We report on the development of a bi-phase CO_2 test cooling system, called TRACI-XL, that is based on the "2 phase accumulator controlled loop (2PACL)" concept and is carried out at GSI within the EU-FP7 project CRISP in cooperation with experts of the DT group at CERN, and the CBM group at Eberhard Karls University, Tübingen. TRACI-XL is the 1 kW prototype that will be used as a pre-plant design for the cooling of electronics in the CBM Silicon Tracking System STS. A design study of the system is depicted in Fig. 1.

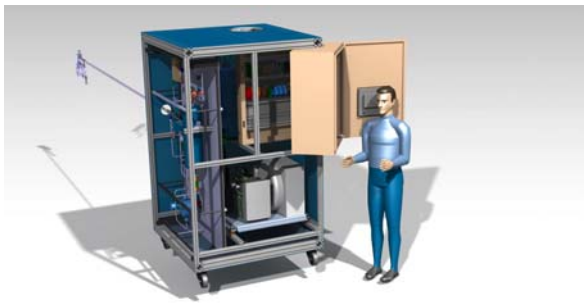

Figure 1: A CATIA model of TRACI-XL.

Concept definition stage

Several fields of engineering have been addressed for the realization of this phase of the prototype design. Different areas as thermodynamics and its study of nucleate boiling, had to be carefully considered. Due to the complexity of this type of evaporative process only the experimental findings can provide more information for the design of the final plant to be installed in the CBM experiment.

Technical documentation like PID diagrams have been developed to be as clear as possible and being similar to some of the screens that were subsequently used in the HMI (Human Machine Interface) thus making TRACI-XL a user-friendly prototype in which a malfunction can quickly be detected. Considering it as one of the most important parts of the system, the secondary CO_2 line has been designed as rigorously as possible, taking into account the possibility of future upgrades to the plant, providing extra flexibility to implement in the future other functionality such as electrical valves to be fully controlled by PLCs. All this is achieved through the choice of high performance Swagelok VCR fittings with high life cycle where subsequently modules may include new parts.

Development of control electronics

The STS cooling system has to provide necessary cooling power for the front-end electronics at a given thermal load. For this reason, process variables have to be monitored and maintained at their desired values by communicating to the devices in the cooling plant, e.g., heaters, pumps, indicators, etc. The task is automated using Siemens modular programmable logic controllers (PLC). The PLC functionality includes sensor monitoring, device control, data logging and archiving. The system is controlled via a touch panel Human-Machine Interface (HMI). The software framework STEP 7 v11 (TIA Portal) communicates to the PLCs via PROFINET protocol, thus providing a compact automated solution for the TRACI-XL project. Figure 2 shows a test system including the PLC controller with sensor-specific modules (resistance temperature detector, thermocouple, analog input for pressure transmitter readout, etc.) Analog values and digital indicators are displayed on the touch panel.

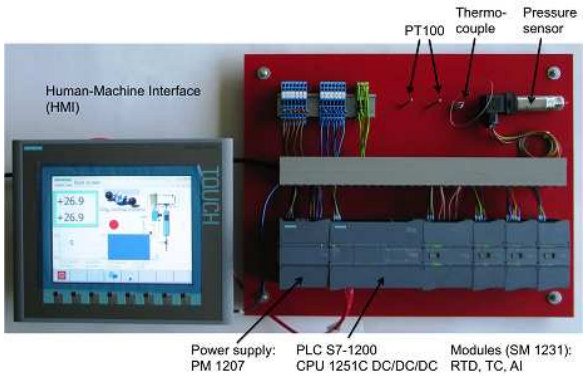

Figure 2: PLC-based test system with analog sensors and touch panel control.

References

[1] Verlaat, B., International Conference of Refrigeration 2007, Beijing, China, ICR07-B2-1565

[2] Proposed correlation data for isothermal two-phase two-component flow in pipes. R. W. Lockhart, R. C. Martinelli, Chem. Eng. Progr., Vol. 45 (1949), pg 39-45.

* Supported by EU-FP7 CRISP.

Cherenkov photon detection with WLS coated MAPMTs

J. Kopfer[1], *C. Deveaux*[2], *M. Dürr*[2], *J. Eom*[3], *C. Höhne*[2], *K.-H. Kampert*[1], *L. Kochenda*[4], *P. Kravtsov*[4], *S. Lebedev*[2], *E. Lebedeva*[2], *T. Mahmoud*[2], *Y. Nam*[3], *C. Pauly*[1], *S. Reinecke*[1], *Y. Riabov*[4], *J. Song*[3], *J. Yi*[3], *and I.-K. Yoo*[3]

[1]Bergische Universität, Wuppertal, Germany; [2]Justus-Liebig-Universität, Gießen, Germany; [3]Pusan National University, Pusan, Korea; [4]Petersburg Nuclear Physics Institute, St. Petersburg, Russia

The performance of wavelength shifting (WLS) films on the front windows of MAPMTs installed in the CBM RICH prototype camera was studied during the beam test campaign in 2012 [1]. Three types of MAPMTs were coated with WLS films of approximately 200 nm thickness, which has been shown to be the optimium thickness for the respective MAPMTs with UV-extended front window [2].

The WLS films were evaluated by first measuring Cherenkov rings on an array of two by two MAPMTs with WLS films, then cleaning these MAPMTs, and measuring a second time on the same MAPMTs without WLS coverage. A correction for variations of the refractive index due to temperature and pressure changes during the cleaning process was done by using the data recorded by the gas system [3].

The analysis shows an increased hit multiplicity, i.e. photoelectrons per electron ring after ring finding and ring fitting [4], for WLS coated MAPMTs. Figure 1 depicts the hit multiplicity distribution for coated and uncoated MAPMTs of the H8500D-03 type. When comparing different MAPMT types, the following result is obtained (see Table 1): The gain with WLS films is 21.2 % for H10966A-103 (size 2", SBA photocathode, UV-extended window), 18.2 % for H8500D-03 (size 2", BA photocathode, UV-extended window), and 18.0 % for R11265-103-M16 (size 1", SBA photocathode, UV-extended window). This hierarchy is also seen in full Monte Carlo simulations using the measured wavelength dependent quantum efficiency (*QE*) for the different MAPMT types. The larger gain in hit multiplicity of the H10966A-103 compared to the H8500D-03 type can be understood when considering that, in the case of SBA photocathodes, the UV photons are shifted to a wavelength range with higher *QE* when compared to BA photocathodes. The comparison between both SBA MAPMT types, H10966A-103 and R11265-103-M16, reveals that the thinner front glass of the 1" R11265-103-M16 is more UV transparent than the thicker glass of the 2" H10966A-103 and thus makes the use of WLS films less effective.

When using WLS films on the MAPMTs, in principle two effects can lead to a decrease of the ring sharpness. First, due to the isotropic fluorescence of WLS films, the majority of wavelength shifted photons pass the MAPMT front window under a more inclined angle than without WLS film. Since the window has a certain thickness, the photon will thus enter the photocathode at a different position compared to the point of incidence on the window surface and the ring sharpness is therefore expected to decrease. Second, since chromatic dispersion is more pronounced in the UV range, the enhanced UV sensitivity with WLS coating may lead to a decrease in ring sharpness. Here, the ring sharpness is quantified by the parameter *dR*, which is defined as RMS of the distribution of the distance between each hit and the circular ring fit.

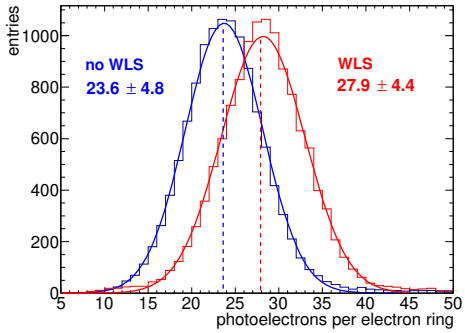

Figure 1: Number of photoelectrons per electron ring on H8500D-03 MAPMTs with WLS film in comparison to the same MAPMTs after film removal. Numbers show mean and sigma of gaussian fits to the distributions.

Table 1: Hit multiplicity gain due to WLS films on different MAPMT types in data and simulation.

MAPMT type	hit multiplicity gain data	hit multiplicity gain MC
H10966A-103	(21.2 ± 1.4) %	(23.1 ± 4.8) %
H8500D-03	(18.2 ± 1.5) %	(18.3 ± 4.7) %
R11265-103-M16	(18.0 ± 1.4) %	(14.8 ± 3.9) %

For H8500D-03 MAPMTs, the parameter *dR* has a value of 2.73 mm with WLS films and 2.42 mm without. The difference of $\approx$ 0.3 mm is small compared to the absolute value of *dR*. Given the pixel size of 6.125 mm and the resulting spatial resolution of the MAPMTs under test of $(6.125/\sqrt{12})$ mm $= 1.8$ mm, the effect on the ring sharpness is not significant.

References

[1] S. Reinecke et al., CBM Progress Report 2012, p. 30

[2] T. Schweizer et al., CBM Progress Report 2012, p. 34

[3] L. Kochenda et al., CBM Progress Report 2012, p. 36

[4] S. Lebedev and C. Höhne, CBM Progress Report 2012, p. 37

doi:10.15120/GR-2014-1-NQM-CBM-22

Ronchi test for measurements for the mirror surface of the CBM-RICH detector*

E. Lebedeva[1], *T. Mahmoud*[1], *and C. Höhne*[1]
[1]JLU Gießen University, Gießen, Germany

The CBM RICH detector will be operated with CO_2 radiator gas, MAPMTs (Multi-Anode Photo Multiplier) as photodetector and spherical glass mirrors as focusing element. Surface homogeneity is one of the important properties required for the single mirror tiles. The global homogeneity has been tested with the $D0$ measurement as reported earlier [1]. Local deformations e.g. by the mirror holding structure can be investigated with the Ronchi test method from which first results are discussed in this contribution.

The principle of the Ronchi test is quite simple. A grating, called Ronchi ruling, consisting of fine, opaque, equally spaced lines ruled onto a transparent substrate is projected onto the whole mirror surface. The shadows of these lines then appear on the face of the mirror under test and will be reflected back onto a camera. The shape and position of these bands is examined and interpreted to give information about the shape of the mirror's surface. Contrary to the $D0$ measurement the Ronchi test thus allows to get information on local mirror deformations which is of particular interest considering e.g. inhomogeneities which may be caused by the mirror mounts.

The Ronchi test is inherently qualitative and needs detailed comparison to a computer model in order to assess possible distortions more quantitatively. The band shapes observed in the Ronchi test can be caused by many different mirror types, i.e. surface profiles. Therefore the pattern seen in the Ronchi test has to be compared with a virtual, perfect mirror copy of the mirror under test. However, the qualitative picture quickly achieved and presented in this contribution already reveals a lot of useful information about the mirror at a glance. It later may also be used for a fast semi-qualitative test which allows to quickly check the local mirror homogeneity in particular after gluing the mirror mounts.

Figure 1 shows the sketch of the experimental setup for the $D0$ measurement, which was used for the Ronchi test as well. The only difference is the usage of the Ronchi grating in front of the CCD camera (c) and the laser point source (b). The Source-Camera (SC) unit is located exactly at the mirror radius R. The active area of SC is located in the same plane orthogonal to the optical axis of the mirror. A mirror prototype with a curvature radius of 3 m from SLO Olomouc was tested. The mirror is flashed with light from the point source. If the mirror would have an ideal spherical shape the fringes seen on the camera would appear straight. Deviations from the spherical surface cause deformations of the fringes, but the measurement is only sensitive to changes of the curvature radius perpendicular to the grating direction. In order to get a complete picture of a given mirror, several different grating orientations should be measured.

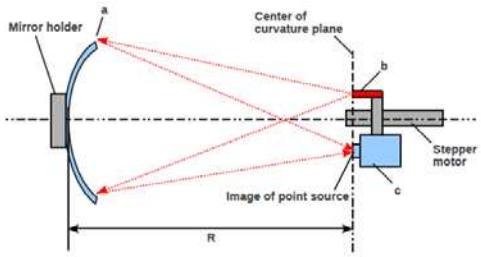

Figure 1: Experimental setup.

Figure 2 shows the image of a reflected light on the camera chip. The left Ronchigram was obtained at the distance of 3 m (nominal curvature), the right plot was obtained at 3.01 m. A possible interpretation of the deformed fringes in the center can be a depressed center of the mirror. The three dark sports correspond to local deformations due to the mount system [2]. Cutting the squared mirror tiles from the produced circular shapes in the manufacturing process can be the reason for the modification of fringes seen at the mirror edges. For further detailed understanding of the mirror surface the comparison with a computer model is under way.

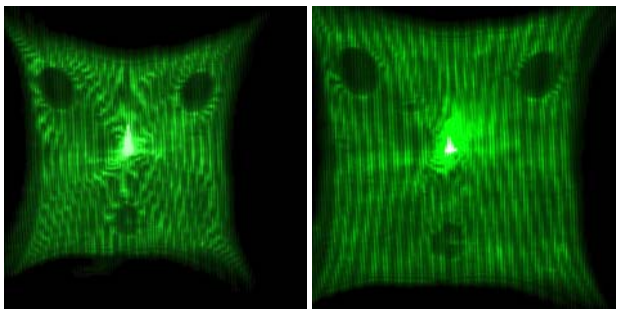

Figure 2: CCD camera view. Left: for R = 3 m. Right: for R = 3.01 m

References

[1] E. Lebedeva, CBM Progress report 2011, p.37

[2] V. Dobyrn et al, CBM Progress report 2011, p.39.

*Supported by the Hessian LOEWE initiative through the Helmholtz International Center for FAIR (HIC for FAIR), and by the BMBF (05P12RGGHM, 05P12RGFCG)

Characterization of the GET4 v1.0 TDC ASIC with detector signals *

P.-A. Loizeau[1], N. Herrmann[1], I. Deppner[1], C. Simon[1], C. Xiang[1,2], M. Ciobanu[3], H. Deppe[3], H. Flemming[3], J. Frühauf[3], M. Kiš[3], K. Koch[3], S. Linev[3], S. Manz[4], and the CBM ToF working group

[1]Physikalisches Institut, Universität Heidelberg, Germany; [2]Institute of Particle Physics, Central China Normal University, China; [3]GSI, Darmstadt, Germany; [4]IRI Goethe Universität, Frankfurt, Germany

A free-streaming readout chain is planned for the CBM Time-of-Flight (TOF) wall. The first element in this readout chain with a difference to usual triggered systems is the Time to Digital Converter (TDC). The GET4 ASIC is a free-streaming TDC developed for the CBM TOF wall. After tests with a first version called GET4 *Proto*, the GET4 v1.0 became available at the end of 2012 [1]. It was tested with pulser first alone [3] and then in conjunction with the PADI-6 pre-amplifier and discriminator ASIC [2].

Another interesting option for the TDC in the CBM TOF readout chain is the development of FPGA-TDCs. A first prototype for those is the VFTX board. A cosmic irradiation test campaign was performed throughout 2013 in Heidelberg using our last MRPC prototype, PADI-6 cards and VFTX boards to validate the detector design and this TDC option. Two plastics scintillators readout on both ends by photo-multipliers provide the efficiency and time reference. Results of the VFTX readout chain are presented in [5]. In the current VFTX readout chain, splitter boards are used between the PADI output and the VFTX input to ensure proper LVDS levels of the signals. As pictured in Fig. 1, the GET4 readout chain was connected in parallel for some of the data taking periods using the second output of the splitters. The GET4 readout chain is composed of 8 GET4 v1.0 chips, a Syscore v2 Readout Controller and an ABB PCI-E board for the optical readout. The analysis chain in software is the same as in the VFTX case.

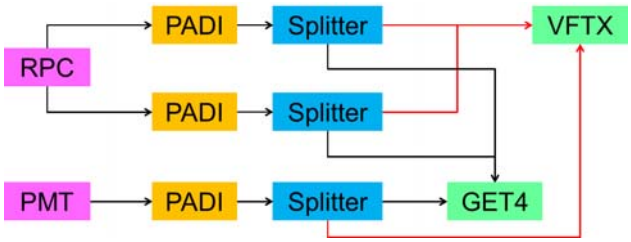

Figure 1: Connection scheme of the setup used for the cosmic rays test of GET4 v1.0.

A measurement was done with the systems running in parallel at an RPC High Voltage of 11.5 kV. At this high voltage, the RPC efficiency relative to coincidences of the plastic scintillators reaches 97.5 % in the GET4 system. The system time resolution obtained after all calibrations is 82 ps. This can, however, be separated into two classes of events: those with multiple TDC hits on at least one RPC channel, for which the resolution is 90 ps, and those with only single TDC hits, for which the resolution is 76 ps. This stresses the importance of a proper matching between the components in a free-streaming TOF system to reduce fake data from reflexions, noise and cross-talk. When taking only single hit events, a time resolution of 49 ps can be extracted for the RPC and its electronics, by subtracting the contribution of the reference system. Similar results were obtained both when using a synchronization signal from the triggered system and in free-streaming mode.

In parallel to the trigger on coincidences of the two plastics, triggers on the OR of the PMTs and on the OR of the RPC strips were used to prevent buffer overflows in the VFTX system. This provides the opportunity to extract the time resolution of the GET4 system in real conditions with quite good statistics. As the time resolution of the VFTX systems and of the splitter boards are known, this can be done by comparing the time measured in the VFTX system to the one measured in the GET4 system. As the time frames of the two systems are independent, one actually needs to compare the value of time differences measured in both the VFTX and GET4 systems (Eq. 1).

$$\Delta t = (t_A - t_B)_{GET4} - (t_A - t_B)_{VFTX} \qquad (1)$$

Assuming the jitters of the VFTX, GET4 and splitter are independent and Gaussian, the GET4 resolution can be extracted for each pair (A,B) of signals (Eq. 2). This procedure was done for the left-right time differences of both plastics and of the equipped RPC strips. The counts for each left-right pairs are used to obtain a mean time resolution. The values of time resolution for the other elements are $\sigma_{VFTX} = 12$ ps [4] and $\sigma_{Splitter} = 10$ ps. The mean time resolution for GET4 v1.0 channels on different daughter boards and with RPC signals is then $\sigma_{GET4} = 24$ ps.

$$\sigma_{GET4\ channel} = \sqrt{\frac{1}{2}\sigma^2_{\Delta t} - \sigma^2_{VFTX} - \sigma^2_{Splitter}} \qquad (2)$$

These value are within the CBM TOF specifications, but need to be tested with higher particle fluxes.

References

[1] H. Flemming et al., CBM Progress Report 2012, Darmstadt 2013, p. 70

[2] P.-A. Loizeau et al., CBM Progress Report 2012, Darmstadt 2013, p. 66

[3] J. Frühauf et al., CBM Progress Report 2012, Darmstadt 2013, p. 67

[4] J. Frühauf et al., CBM Progress Report 2012, Darmstadt 2013, p. 71

[5] C. Simon et al., "RPC prototype test with cosmic irradiation", this report

* Work supported by EU/FP7-Hadron Physics 3/WP19, BMBF 05PRVHFC7 and DFG GRK 1039

 doi:10.15120/GR-2014-1-NQM-CBM-24

Event based unpacker and digitizer for the CBM TOF in CBMROOT *

P.-A. Loizeau[1], N. Herrmann[1], D. Kresan[2], F. Uhlig[2], and the CBM ToF working group

[1]Physikalisches Institut, Universität Heidelberg, Germany; [2]GSI, Darmstadt, Germany

In CBM the Time-of-Flight (TOF) method will be used to provide charged hadron identification. The measurement will be done with a wall built from Resistive Plate Chambers (RPC). The electronics and the reconstruction software for the TOF wall will follow the CBM data acquisition concept called free-streaming.

Figure 1 presents a summary of the previous status of the CBM TOF software. The software chains for real test data (top) and the one for simulated data (bottom) are fully separated. Until 2013 the unpacking, monitoring and analysis software for the TOF test setups was based on the *GO4* framework [1]. A CBM dedicated library containing standard *GO4* analysis sub-steps and sub-events for the CBM test hardware was developed to re-use existing software parts in the analysis of the data from various beamtimes [2]. In parallel, the tools used for the simulation of the TOF wall and the evaluation of its physics performance in the CBM setup were developed within the *CBMROOT* framework. These tools were mainly a direct hit producer, which converts directly the Monte-Carlo points at the TOF wall position into TOF hits with a position and time. This method, however, ignores the effect of charge sharing between channels, that in real data causes the formation of clusters (correlated hits).

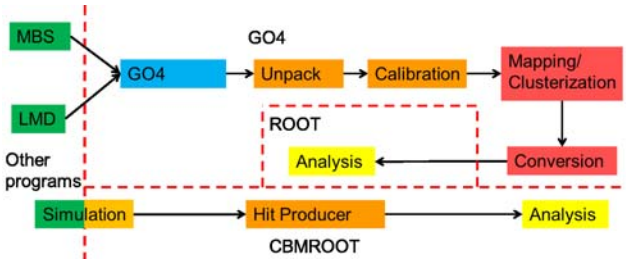

Figure 1: Status of the ToF wall analysis softwares before the integration of the unpackers in CBMROOT.

In order to speed up the development of the TOF reconstruction tasks, it is necessary to have compatible unpacking and simulation chains implemented in the same framework and feeding the same reconstruction algorithm. Reconstruction tasks are e.g. the channels alignment, the clusters building or the mapping between an electronics oriented address scheme and a detector/physics oriented geometric position. The free-streaming data acquisition concept also pushes toward this software unification as the difference between the offline physics analysis software and the online event selection software needs to be minimal in order to ensure a good quality of the archived data. The final software also needs to be compatible with a time-based data organization.

The first steps toward a final time-based common software are the conversion of the existing *GO4* unpacker to *CBMROOT*, the development of an event-based realistic digitization chain for the simulation and the development of common output objects for the unpacker and the digitization chain.

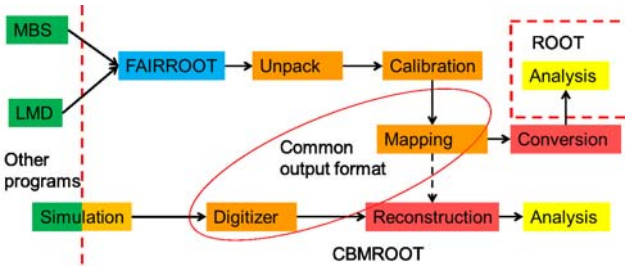

Figure 2: Currently available ToF wall analysis softwares organization using only CBMROOT and ROOT macros.

These three tasks were realized. Figure 2 presents the current status of the TOF software in *CBMROOT*. The unpacker supports the two main TDC system used in last TOF test setups, the GET4 v1.0 [1] and the VFTX [3]. A calibration tool for the TDC data is included in the data processing chain. A conversion tool was developed in addition to keep the compatibility with the existing analysis in *ROOT* macros. A new TOF digitizer gives the possibility to use as input for the simulation detector parameters measured during test beamtimes, e.g. cluster size, efficiency or time resolution. It also provides a choice between various methods to obtain the signal charge and the cluster size. Both branches of the TOF software are filling objects of the CbmTofDigi class, which is the input format of a newly developed TOF clusterizer. The clusterizer delivers the same TofHit format as the direct hit producer. For testing the unpacker, its output was compared to the one of the original *GO4* unpacker. No significant differences were found. The digitizer+clusterizer branch was tested in comparison to the direct hit producer. While the new implementation reproduces the results of the direct hit producer when the cluster size is minimized, it now allows for the study of a more realistic detector response

References

[1] P.-A. Loizeau et al., CBM Progress Report 2012, Darmstadt 2013, p. 66

[2] J. Adamczewski-Musch and S. Linev, CBM Progress Report 2011, Darmstadt 2012, p. 68

[3] J. Frühauf et al., CBM Progress Report 2012, Darmstadt 2013, p. 71

* Work supported by EU/FP7-Hadron Physics 3/WP19, BMBF 05PRVHFC7 and DFG GRK 1039

High counting rate test of the basic structure for the inner zone of the CBM RPC-TOF *

A. Bălăceanu[1], V. Aprodu[1], D. Bartoş[1], G. Caragheorgheopol[1], F. Constantin[1], I. Deppner[2], V. Duţă[1], N. Herrmann[2], P. Loizeau[2], M. Petriş[1], M. Petrovici[1], L. Prodan[1], A. Radu[1], L. Rădulescu[1], V. Simion[1], and C. Simon[2]

[1]NIPNE, Bucharest, Romania; [2]Physikalisches Institut der Universität Heidelberg, Germany

A basic structure for the inner zone of the CBM-TOF wall using multi-strip multi-gap low resistivity glass RPCs was designed, built and successfully tested in terms of time resolution and efficiency [1]. The performance as a function of counting rate was tested exposing the counter in high intensity proton beam of 2.5 GeV/c at COSY-Jülich on a rather limited surface corresponding to the size of the beam spot [2]. In the present contribution we report for the first time results obtained exposing the whole detector surface at counting rates up to 10^4 particles/(cm^2·s).

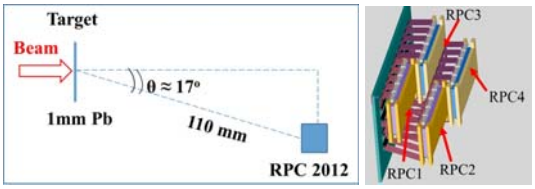

Figure 1: Left side - experimental geometry. Right side - the architecture based on four RPC cells

The in-beam test was performed at the SIS18 accelerator of GSI-Darmstadt. The RPC prototype was exposed to charged particles produced by colliding 1.7 A·GeV Ni ions with a 1 mm thick Pb - target at the highest intensity per spill delivered by SIS18. Fig. 1 shows the geometry of the experiment (left side) and the staggered structure of the 4 RPC cells (right side). The spill length was varied between 5 s and 2.5 s. The analysis is based on ROOT [3] and Go4 [4]. The detector was operated in a standard gas mixture of 85% $C_2F_4H_2$+10% SF_6+5% iso C_4H_{10} and at an electric field strength of 157 kV/cm. Signals of 16 strips of each cell were processed by NINO fast amplifiers [5], their differential outputs being converted by FPGA TDCs [6]. The

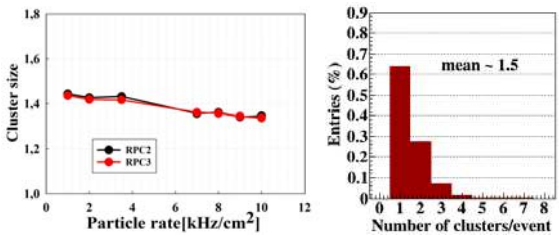

Figure 2: Left side - cluster size as a function of counting rate. Right side - number of clusters per event for a counting rate of 8x10^3 part/(cm^2·s) .

number of simultaneously recorded signals (calles cluster size) is shown in Fig.2 left side as function of the counting rate. A decrease of about 7% is observed. On the right side of Fig.2 the number of clusters per event is represented for one of the RPC cells.

The time resolution was obtained using the time difference between two RPC cells overlapped along the strips, i.e. RPC2-RPC1 or between two RPCs overlapped across the strips, i.e. RPC1-RPC3. For the first case, where the overlap is at the edge of the strip, some influence of edge effects is not excluded. After walk correction, a time resolution of ≈70 ps was obtained, including electronic resolution and considering an equal contribution of the two RPC cells. For the overlap across the strips a time resolution of ≈60 ps was obtained. The corresponding time difference spectrum for a flux of 10^4 part/(cm^2·s) is presented in Fig.3 left side. The non-Gaussian tails are at the level of 1-2%. The time resolution as a function of counting rate is shown in Fig.3 right side. A slight deterioration of the time resolution of about 5% is observed up to 3·10^3 particles/(cm^2·s) counting rate followed by a levelling off, within the error bars, up to 10^4 particles/(cm^2·s), the highest counting rate accessed in the experiment

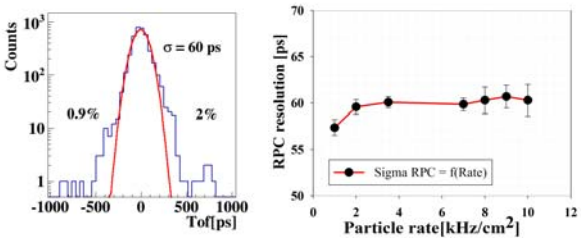

Figure 3: Left side -time difference between two overlapped strips of RPC1 and RPC3 cells. Right side - time resolution as a function of particle rate.

These results together with the previous reported ones [1],[2] show that such RPC architecture, based on low resistivity glass electrodes conserves their excellence performance in counting rates up to 10^4 particles/(cm^2·s) on the whole area of the detector. Such tests will continue at even higher rates and longer exposure periods in order to confirm that these type of RPCs can be used even for the most forward regions of the CBM-TOF wall with negligible ageing effects.

References

[1] M. Petris et al.,CBM Progress Report 2012, p. 68
[2] M. Petrovici et al., JINST 7 (2012) P11003
[3] R. Brun and F. Rademakers Linux Journal 1998 July Issue 51
[4] J. Adamczewski et al, IEEE TNS 51(2004)565
[5] F. Anghinolfi et al., Nucl.Instr.and Meth. A533(2004)183
[6] J. Frühauf et al., CBM Progress Report 2012, p. 71

* Work supported by EU-FP7/HP3 Grant No 283286, NASR/CAPACITATI-Modul III contract nr. 179EU and NASR/NUCLEU Project PN09370103

 doi:10.15120/GR-2014-1-NQM-CBM-26

100 Ohm transmision line multi-strip multi-gap high counting rate RPC prototype *

V. Aprodu[1], *D. Bartoş*[1], *A. Bălăceanu*[1], *G. Caragheorgheopol*[1], *F. Constantin*[1], *V. Duţă*[1], *M. Petriş*[1], *M. Petrovici*[1], *L. Prodan*[1], *A. Radu*[1], *L. Rădulescu*[1], *and V. Simion*[1]

[1]NIPNE, Bucharest, Romania

A basic structure for the inner zone of the CBM-TOF wall using multi-strip, multi-gap low resistivity glass RPCs showed excellent performance in terms of time resolution and efficiency [1] up to local counting rates of 10^5 particles/(cm^2·s) [2] and up to 10^4 particles/(cm^2·s) all over the counter surface [3]. The differential read-out of the RPC cells had 50 Ohm impedance and therefore using fast NINO amplifiers [4] of 100 Ohm input impedance, an impedance matching was required at the level of mother-boards. In order to circumvent this aspect and at the same time to have a solution for the higher granularity required for the most inner zones of the CBM-TOF, a new RPC prototype was designed and built. The strip structure of the readout and high voltage electrodes was decided based on APLAC simulations such to obtain a differential readout impedance as close as possible to 100 Ohm. The measured value of the glass permitivity was used in the simulation. The central read-out electrode was considered as a single layer strip structure sandwiched between two thin layers of FR4. For the standard structure of the RPC cells developed by us, [1], in order to obtain a 100 Ohm impedance for the transmission line, a pitch of 4.19 mm (2.16 mm strip width and 2.03 mm gap) is required.

The simulated signals on the anode and cathode electrodes read-out on 50 Ohm load resistors and the differential one can be seen in Fig. 1. They were obtained with APLAC injecting in the transmission line pulses of ± 1 V with a 100 ps rise time and 600 ps fall time through a 50 Ohm resistor.

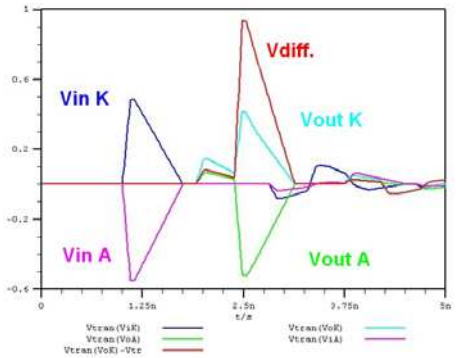

Figure 1: The signals on the anode and cathode electrodes and the differential one obtained with APLAC.

The active area of the new prototype is 283 x 200 mm^2. A photo of the assembled RPC structure on the back flange and closing box is presented in Fig.2 left. The PCB with the structure of the read-out electrodes can be seen on the right side of Fig. 2. The prototype based on such strip characteristics was built and the results in terms of the differential and the anode and cathode signals, respectively, obtained directly from the RPC with a ^{60}Co source can be followed in Fig. 3.

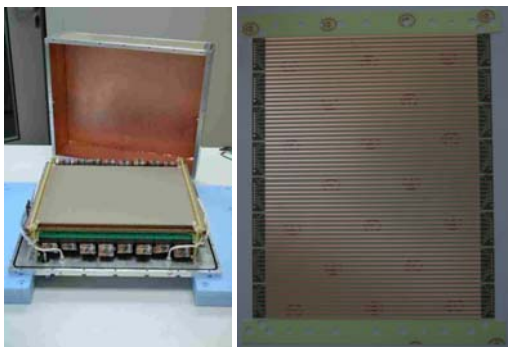

Figure 2: Left side: A photo of the assembled RPC structure on the back flange and closing box. Right side: the PCB with the structure of the read-out electrodes.

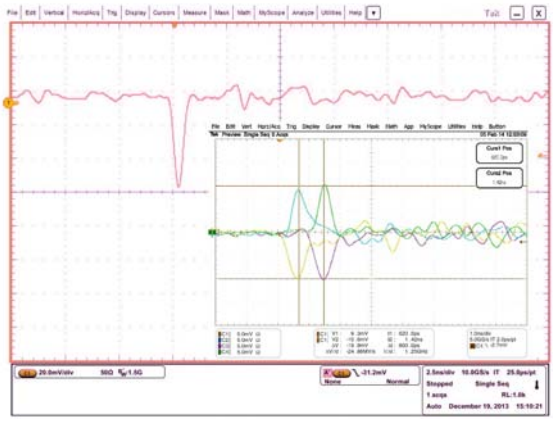

Figure 3: The differential and the anode and cathode signals at the two ends of a strip.

As can be seen, the APLAC predictions are rather well confirmed by the real signals delivered by the RPC.

Detailed cosmic ray tests are in progress and in-beam tests are foreseen in the near future.

References

[1] M. Petriş et al.,CBM Progress Report 2012, p. 68

[2] M. Petrovici et al., JINST 7 (2012) P11003

[3] A. Bălăceanu et al., this Progress Report

[4] F. Anghinolfi et al., Nucl.Instr.and Meth. A533(2004)183

*Work supported by EU-FP7/HP3 Grant No 283286 and Romanian NASR/CAPACITATI-Modul III contract nr. 179EU and NASR/NUCLEU Project PN09370103

RPC prototype test with cosmic irradiation*

C. Simon[1], I. Deppner[1], N. Herrmann[1], P.-A. Loizeau[1], J. Frühauf[2], C. Xiang[1,3], and the CBM-TOF working group

[1]Ruprecht-Karls-Universität Heidelberg, Heidelberg, Germany; [2]GSI, Darmstadt, Germany; [3]Central China Normal University, Wuhan, China

Following the proposal to construct the outer ToF wall based on fully differential multi-strip MRPCs [1] the response of a new prototype RPC designed in Heidelberg to cosmic irradiation was measured throughout the year 2013. In particular, a focus was put on compatibility with the read-out electronics, i.e. PADI-6 preamplifier cards [2] and VFTX FPGA-TDC modules [3], and on refinement of the existing calibration and correction algorithms [4].

The RPC prototype implements an 8-gap single-stack configuration with a gap width of $220\,\mu\mathrm{m}$. It features 56 read-out electrodes of length $53\,\mathrm{cm}$ and pitch $9.4\,\mathrm{mm}$ that add up to an active area of about $2800\,\mathrm{cm}^2$. As RPCs in the outer wall region do not have to stand incident particle fluxes larger than $1\,\mathrm{kHz}$, the prototype is equipped with float glass of resistivity $10^{12}\,\Omega\mathrm{cm}$. The working voltage of the counter amounts to $\pm 11\,\mathrm{kV}$. The preamplifier cards are placed inside the gas volume (cf. Fig. 1, right) and connected directly to the read-out electrodes.

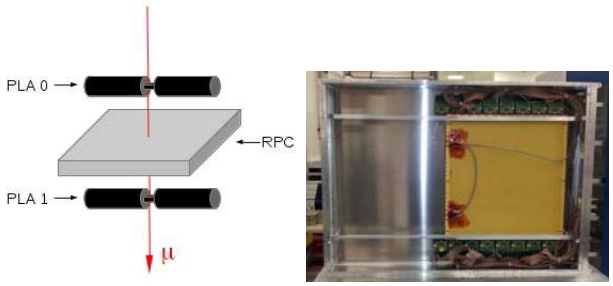

Figure 1: Sketched arrangement (left) of two plastic scintillators with respect to the RPC prototype (right) to measure its response to cosmic irradiation.

The test setup in the lab comprises—besides the RPC prototype—two plastic scintillators (PLA) of dimensions $8 \times 2 \times 1$ and $11 \times 4 \times 2\ \mathrm{cm}^3$ which are each read out on two sides by photomultipliers. One PLA counter is placed above, the other one below the RPC (cf. Fig. 1, left). From the coincidence of signals in both scintillators a trigger is built that is used to read out the RPC.

To evaluate the characteristic RPC parameters time resolution and detection efficiency of the prototype a calibration algorithm needs to process the TDC raw data. In this way, fixed time offsets due to different runtimes of the signals inside the TDCs and the cables connecting the RPC and the PLA counters with the TDCs can be accounted for. Also, systematic effects varying from event to event are corrected for, like charge walk, the velocity spectrum of the incident cosmic muons, and their angular distribution in the test arrangement. After applying all corrections to the raw data the algorithm proceeds with clustering RPC signals on neighboring read-out electrodes that show correlations in time and space. Here, the idea is that an avalanche triggered by a single charged particle traversing the RPC prototype can induce mirror charges on more than one read-out electrode. A typical cluster size for the prototype is 1.3 strips.

In the cosmic muon setup, i.e. for the section of the counter surface affected by the PLA coincidence (cf. Fig. 2, right), a detection efficiency of $98.5\,\%$ and a system time resolution of $67\,\mathrm{ps}$ were found. The term system time resolution refers to the Gaussian standard deviation σ of the time difference spectrum between the RPC and the PLA counters (cf. Fig. 2, left). With a resolution of $55\,\mathrm{ps}$ for the plastic reference system, this allows for an estimate of the counter time resolution—still including the electronics resolution—of about $40\,\mathrm{ps}$. An in-beam test of the prototype in April 2014 at GSI/SIS-18 will demonstrate if these very promising results also hold under heavy-ion load.

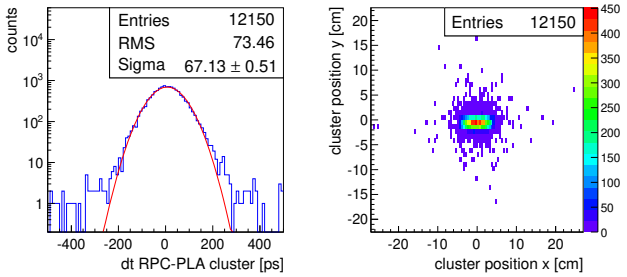

Figure 2: Time resolution of the PLA-RPC system (left) obtained in the trigger spot on the counter surface (right) requiring coincidence of the plastic scintillators.

References

[1] I. Deppner *et al.*, CBM Progress Report 2012, Darmstadt 2013, p. 64

[2] M. Ciobanu *et al.*, CBM Progress Report 2012, Darmstadt 2013, p. 72

[3] J. Frühauf *et al.*, CBM Progress Report 2012, Darmstadt 2013, p. 71

[4] C. Simon *et al.*, CBM Progress Report 2012, Darmstadt 2013, p. 65

*Work supported by EU/FP7-HadronPhysics3/WP19 and BMBF 05PRVHFC7.

 doi:10.15120/GR-2014-1-NQM-CBM-28

CBM TRD radiator simulation in CbmRoot*

C. Bergmann[1], *N. Heine*[1], *W. Verhoeven*[1], *D. Emschermann*[1], *A. Andronic*[1,2], *and J.P. Wessels*[1]
[1]Institut für Kernphysik, Münster, Germany; [2]GSI, Darmstadt, Germany

The transition radiation photon yield of a periodic radiator with N_f layers of thickness l_1 and spacing l_2 can be effectively described by

$$\frac{dN}{d\omega} = \frac{4\alpha}{\omega(\kappa+1)} \frac{(1-\exp(-N\sigma))}{(1-\exp(-\sigma))} \sum_n \Theta_n \left(\frac{1}{\varrho_1+\Theta_n} - \frac{1}{\varrho_2+\Theta_n} \right)^2 [1-\cos(\varrho_1+\Theta_n)] \quad (1)$$

according to [1] with σ being the total photon absorption cross section σ ($\sigma = \mu_1 \cdot l_1 + \mu_2 \cdot l_2$) for one foil and gas layer. This equation includes coherent and incoherent effects as well as the self-absorption of gap and foil material. Therefore it was used to calculate the total transition radiation (TR) yield per keV in CbmRoot. The variables are defined as

$$\varrho_i = \frac{\omega l_1}{2c} \left(\gamma^{-2} + \left(\frac{\omega_{P,i}}{\omega} \right)^2 \right), \quad (2)$$

and

$$\kappa = \frac{l_2}{l_1} \quad (3)$$

$$\Theta_n = \frac{2\pi n - (\varrho_1 + \kappa\varrho_2)}{1+\kappa} > 0. \quad (4)$$

The resulting TR photon yield spectrum is folded with the detector absorption spectrum (presented in Figure 1) to obtain the effective energy deposition spectrum in the active gas volume of the detector. Systematic deviations between measurements and theoretical predictions arising from the material budget between radiator and MWPC and radiator material and irregularity can be compensated by adding an attenuation factor a [0,1], with:

$$\left(\frac{dN}{d\omega}\right)_{measurement} = a \cdot \left(\frac{dN}{d\omega}\right)_{simulation}. \quad (5)$$

The parameters N_f, l_1 and l_2 have been measured for regular radiator or approximated for irregular radiators for each radiator prototype. The attenuation factors a have been evaluated by comparing in beam measurements and simulation as presented in Figure 2. For most radiators simulations and measurements are found to be in agreement within errors. Radiators B++, K++ and H have been implemented in CbmRoot. B++ is a classical foil Radiator made from POKALON (N_f=350, l_1=24 μm, l_2=700 μm and a=0.65), K++ is a micro-structured self-supporting foil radiator with the same parameters like B++. The best irregular radiator prototype is H made from 125×2 mm thick Polyethylene foam foils with an average bubble diameter of 900 μm, an average l_1 of 12 μm and a=0.78.

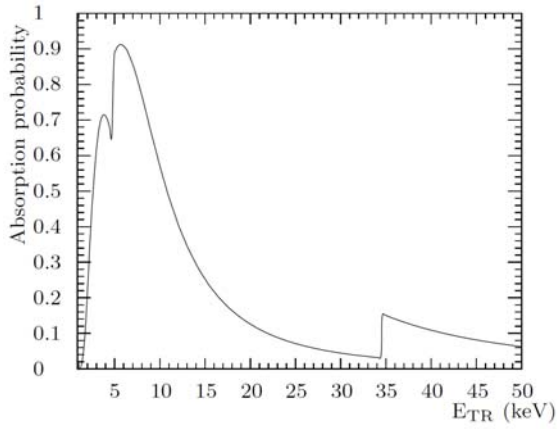

Figure 1: Approximate photon absorption probability of the 2012 MS prototypes using $XeCO_2$ (80/20).

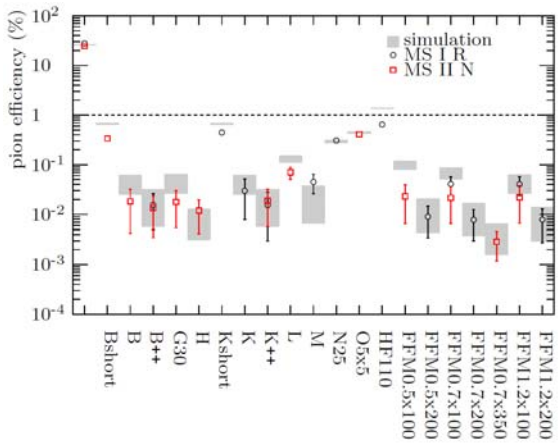

Figure 2: Comparison of different radiators showing the pion efficiency at 90% electron efficiency with 10 detector hits. The design goal for CBM TRD consisting of 10 detecor layers is indicated by the dashed line.

References

[1] M. N. Mazziotta, "A Monte Carlo code for full simulation of a transition radiation detector", arXiv:physics/9912042 [physics.comp-ph], 2000

* Work supported by BMBF and the HadronPhysics3 project financed by EU-FP7.

Construction and first performance studies of a CBM TRD prototype with alternating wires developed in Frankfurt*

S. Gläßel, W. Amend, A. Arend, C. Blume, P. Dillenseger, and F. Roether
Institut für Kernphysik, Goethe-Universität, Frankfurt am Main, Germany

Introduction

The Transition-Radiation Detector (TRD) for the Compressed Baryonic Matter (CBM) experiment at the Facility for Antiproton and Ion Research (FAIR) has to deliver electron identification and tracking performance in a high particle-density environment. To deliver the required fast detector response for the expected high signal rates, a thin Multi-Wire Proportional Chamber (MWPC) without drift region has been developed [1].

One key challenge of this setup is the sensitivity of the field geometry to deformations of the cathode planes. With a thin foil as front cathode, even minor internal pressure variations can affect the gas gain [2]. In order to minimize this effect, the robust field geometry of an alternating wire structure, as proposed for the ALICE VHMPID [3], has been explored. Field wires are introduced between the sense wires to generate field lines from the field to the sense wires that are independent of the front cathode. Consequently, the electrical field in the sensitive area near the entrance window becomes significantly lower.

Construction and experimental set-up

To study the effects of an alternating wire set up on the gas gain, a small aluminium prototype with dimensions of 21,8 x 21,8 cm^2 has been built. Thin sense wires (gold-plated tungsten, 20 μm) and thicker field wires (copper, 79 μm) are arranged on the anode plane with a pitch of 2.5 mm. A thin aluminized Mylar-foil (19 μm) serves as front cathode and entrance window at the same time. A padplane with 15 read-out pads is used as rear cathode. Both, front and rear cathode, have a distance of 4 mm to the anode plane, leading to a total gas gap of 8 mm (see Fig. 1).

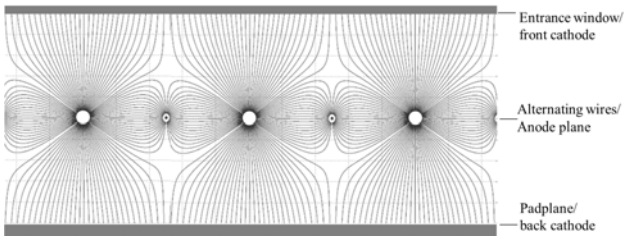

Figure 1: Schematic profile with field lines of the new prototype with alternating wires.

First measurements in a laboratory environment were performed with an ^{55}Fe source. The sense wire current was measured for different positions at various differential pressures. Field wires were on ground potential. A standard prototype without field wires and with similar dimensions was employed for reference measurements.

Results

The first tests give a clear indication for a superior performance in terms of gas gain stability for the new prototype. The effect that the gas gain shows variations up to 60 % in the case of internal overpressure, as seen for the standard set up, is drastically reduced for the setup with alternating wires (variations are below 10 %, as shown in Fig. 2).

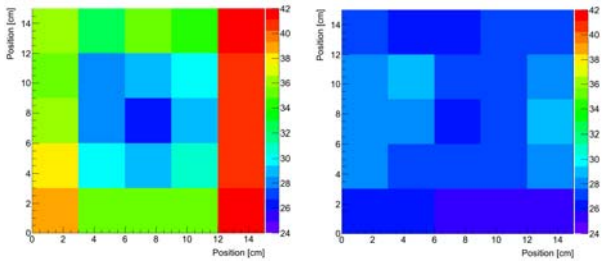

Figure 2: Gas gain as function of position at 0.5 mbar overpressure for standard (left) and new prototype (right).

Outlook

The superior performance of the new prototype will be further investigated to confirm it on a quantitative level. Measurements with different field wire potentials and of the energy resolution will be performed.

A second prototype with alternating wires and an asymmetric structure, i.e. the wire plane is moved towards the readout cathode, has been built and will be tested as well.

References

[1] P. Dillenseger et al., "In-beam performance studies of the first full-size CBM-TRD prototypes developed in Frankfurt ", GSI Scientific Report 2012 (2013) 66.

[2] E. Hellbär et al., "Construction and simulations of full-size CBM-TRD prototypes without drift region", GSI Scientific Report 2012 (2013) 60.

[3] D. Varga et al., "Close cathode chamber: Low material budget MWPC", Nuclear Instruments and Methods in Physics Research, 2013, p. 11-18.

* Work supported by BMBF and HIC for FAIR.

 doi:10.15120/GR-2014-1-NQM-CBM-30

Development of an online feature extraction pre-processing stage for TRD based on SPADIC 1.0 *

C. Garcia[1] *and U. Kebschull*[1]

[1]Infrastructure and Computer Systems for Data Processing (IRI), Frankfurt University, Frankfurt/Main, Germany

One of the main challenges for the data acquisition of the Transition Radiation Detector (TRD) of the Compressed Baryonic Matter experiment (CBM) is to efficiently process the high data rate produced by the front-end electronics operating in a free streaming data acquisition mode. In this scenario, the TRD detector is read-out by the front-end mixed-signal SPADIC 1.0 chip [1]. The SPADIC 1.0 delivers 32 autonomous read-out channels with a large set of meta-information attached to the generated messages. In order to fulfill the processing requirements for the TRD, a feature extraction online pre-processing stage has been proposed [2]. The aim of the feature extraction is to do an online pre-processing of the front-end electronics data, in order to reduce it by means of parameter extraction and clustering. The Feature Extraction pre-processing stage would be integrated within the functionality of the Data Processing Board (DPB) [3].

As seen in Figure 1, the internal processing logic of the Feature Extraction firmware would allow to instantiate multiple "link processors" in parallel in order to handle the data from different data-input optical links. However, the maximum number of link processors would be constrained by the FPGA resources available.

The internal architecture of the feature extraction core is based on the following processing stages: first, a message interpreter module decodes the incoming SPADIC 1.0 event words wrapped around the CBMnet 2.0 headers and delivers the full timebin RAW data, as well as useful metadata attached to the hit message (e.g. timestamp, channel id, group id, hit type, etc). This decoded data is then handled by the double-hit detection logic. The double-hit logic works in two configurable modes: first, in conjunction to the double-hit detection logic implemented in the SPADIC 1.0 chip and second, as a stand-alone detection logic. In the first case, the double-hit logic compares the hit-message flags set by the SPADIC 1.0 that tell whether a double-hit was detected or not. In the second case, as a stand-alone detection mode, the logic compares the signal charge with different virtual thresholds at different timebin positions. A parallel running module finds the peaks and valleys in the signal evolution. These information is used by a later logic that splits the message between two maxima, when a valley has been found.

The second processing stage consists mostly of two parallel processes, a total charge integrator (Qtot) and a temporal center of gravity calculator (COG). The Qtot module delivers an amplitude vs. time integration from a region of interest or from all the timebins included in the event. On the other hand, the COG calculates the center of gravity of the signal in time direction. In order to save FPGA resources, the feature extraction can be configured to use only one of the before mentioned cores. Further beamtest analysis will show which processing module gives better results for the event reconstruction. A final processing stage is called cluster finder and processor. This module finds clusters from events that share similar characteristics, e.g. contiguous fired pads, events with a timestamp that falls within a certain threshold and also by comparing the neighbor trigger matrix flags generated by the SPADIC 1.0. Finally, after a cluster has been completed, the data from each event that belongs to the found cluster is processed by a Center of Gravity (COG) algorithm that provides a temporal resolution of the hit position within the found cluster. In the end, the event building logic wraps the hit-message into CBMnet2.0 containers in order to be shipped to later DPB processing stages.

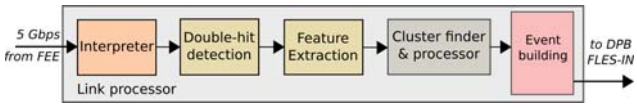

Figure 1: Block diagram of the internal architecture of the feature extraction core.

Currently, most functionality of the Feature Extraction firmware has been developed and is under continuous testing in a laboratory setup. In 2014, a TRD beamtest will be performed in order to test and provide consistent results about performance and FPGA resource consumption.

References

[1] T. Armbruster et al., "SPADIC 1.0 a self-triggered amplifier/digitizer ASIC for the CBM-TRD",CBM Progress Report 2012

[2] C. Garcia et al., "Beam test results of the CBM-TRD feature extraction using SPADIC v1.0",CBM Progress Report 2012

[3] J. Gebelein et al., "SysCore3 A universal Read-Out Controller and Data Processing Board",CBM Progress Report 2012

* Work supported by BMBF No. 05P12RFFCM.

e/π Discrimination and position resolution of a real size CBM-TRD prototype *

M. Târzilă[1], J. Adamczewsky-Musch[2], V. Aprodu[1], D. Bartoş[1], A. Bercuci[1], G. Caragheorgheopol[1], V. Cătănescu[1], F. Constantin[1], S. Linev[2], M. Petriş[1], M. Petrovici[1], L. Prodan[1], A. Radu[1], and V. Simion[1]

[1]NIPNE, Bucharest, Romania; [2]GSI, Darmstadt, Germany

A high-granularity real size TRD prototype, designed to fulfil the requirements of the innermost zone of the first CBM-TRD station of 1 cm^2 readout cell area, combines a multi-wire proportional chamber with a 2×4 mm amplification region and a drift zone of 4 mm. Architecture details of this type of TRD prototype were described in [1]. The e/π discrimination obtained with other types of radiators than those whose performances were already reported in [1] and the position resolution will be the focus of the present contribution.

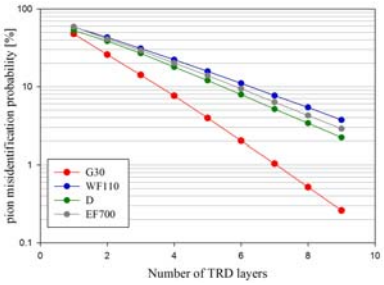

Figure 1: Pion misidentification as a function of the number of TRD layers for different types of radiators.

The chamber was tested with a mixed beam of electrons and pions of 2 - 8 GeV/c particle momenta at the T9 beam line of the CERN-PS. A 80%Xe+20%CO_2 gas mixture was flushed through the chamber, operated at 2000 V anode and 800 V drift voltages. Several types of radiators were tested. The signals from three consecutive rows of 16 triangular pads each were processed by FASP V0.1 front-end electronics [2, 3].

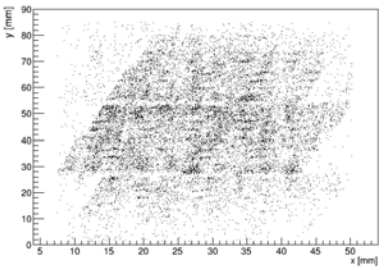

Figure 2: Two dimensional hit position reconstruction.

The pion misidentification probability for 90% electron efficiency as a function of the number of TRD layers was obtained with a Monte Carlo simulation using the likelihood method based on the measured pulse height spectra of electrons and pions. The particles were identified and selected based on the information delivered by a Cherenkov detector and a lead-glass calorimeter positioned in front and at the end of the beam line, respectively. A pion misidentification probability of ∼1% was obtained with a regular foil radiator (20 μm foil thickness, 250 μm gap, 220 foils) [1]. Fig.1 presents the performance of the chamber with other types of radiators: G30 (fiber radiator made from 16 mats of pure LRP 375 BK polypropylene fibers), D (5 PE foam plates thermally glued to a block), WF110 (30 mm Rohacell plate) and EF700 (50 mm PE foam plate).

The hit position across and along the pads is represented in Fig.2. The position reconstruction is based on the charge sharing among consecutive rectangular and tilted pads obtained by the corresponding pairing of the triangular pads of the three operated rows. It was determined from the standard deviation of a Gauss function fitted to the difference between the positions reconstructed with two identical chambers (Fig.3). A position resolution of 385±0.02 μm across the pads and of 1.6±0.2 mm along the pads was achieved considering equal contributions of the two identical chambers.

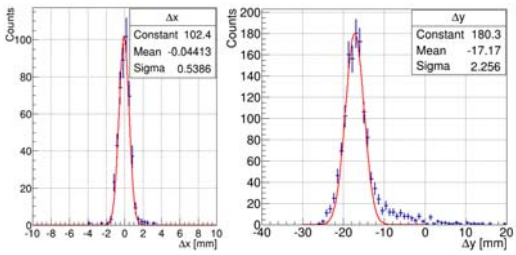

Figure 3: Difference between the hit position across the pads (left) and along the pads (right) reconstructed with two identical detectors, both fitted with a Gauss function.

The support of the drift electrode of this prototype was made from a 9 mm honeycomb plate sandwiched between 2 Rohacell HF71 plates of 3 mm thickness. The measured transmission of such a structure for 5.9 keV X rays of ^{55}Fe is ∼43.77%. This could be improved by ∼10% if the Rohacell plates are replaced by aluminized carbon foil of ∼300 μm. A future TRD prototype will be built using this new drift electrode structure. These very good results in terms of e/π discrimination and position resolution will be further improved using a new version of FASP where the signals delivered by triangular pads will be paired inside the chip, so that the effect of the large dynamical range caused by triangular pads will be drastically reduced.

References

[1] M. Târzilă *et al.*, CBM Prog. Rep. 2012, p. 60

[2] V. Cătănescu *et al.*, CBM Prog. Rep. 2009, p. 47

[3] A. Caragheorgheopol *et al.*, CBM Prog. Rep. 2010, p. 46

* Work supported by EU-FP7/HP3 Grant No 283286, NASR/CAPACITATI-Modul III contract nr. 179EU and NASR/NUCLEU Project PN09370103

 doi:10.15120/GR-2014-1-NQM-CBM-32

Design of new SPADIC front-end boards for TRD readout

M. Krieger[*1]
[1]ZITI, University of Heidelberg, Germany

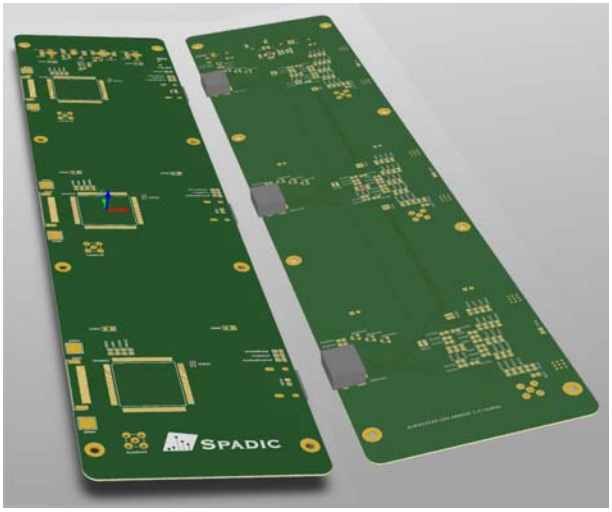

Figure 1: Rendered view (front and back side) of the new FEB for 3 packaged SPADIC 1.0 chips.

The design of the TRD subsystem foresees the use of different types of modules and front-end boards (FEBs). In order to keep the hit rates per channel within controlled limits across the detector, the modules and FEBs cover a range of different channel densities.

This means that between 4 and 10, or even more, SPADIC chips must be assembled on one FEB of approximately 50 cm length. For testing the type of FEB with the lowest SPADIC density, for 2014 a prototype FEB is designed that connects one SPADIC every 114 mm.

As the first prototype of such a multi-chip FEB, a new PCB holding 3 SPADIC chips with this pitch has been designed (Figure 1). It contains voltage regulators and power-on sequencing logic shared by all SPADICs, and for each SPADIC individually a TRD input connector, decoupling capacitors, charge injection, and an HDMI connector for CBMnet data links. Neighboring SPADICs are connected to allow exchange of trigger signals. Additionally, a smaller version of the FEB containing only one SPADIC has been designed (Figure 2b).

For the evaluation of integration options and a simplified FEB assembly, most of the remaining SPADIC 1.0 chips have been cased into ceramic quad-flat packages with 176 pins (QFP176, Figure 2a) and 23 mm×23 mm in size. This allows saving space by placing the decoupling capacitors on the opposite size of the PCB directly beneath the package, as shown in Figure 3.

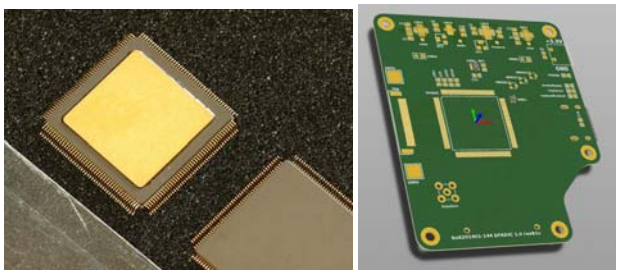

Figure 2: (a) SPADIC 1.0 chip assembled in QFP176 package. (b) The smaller version of the new FEB for only one SPADIC 1.0 chip allows easier testing.

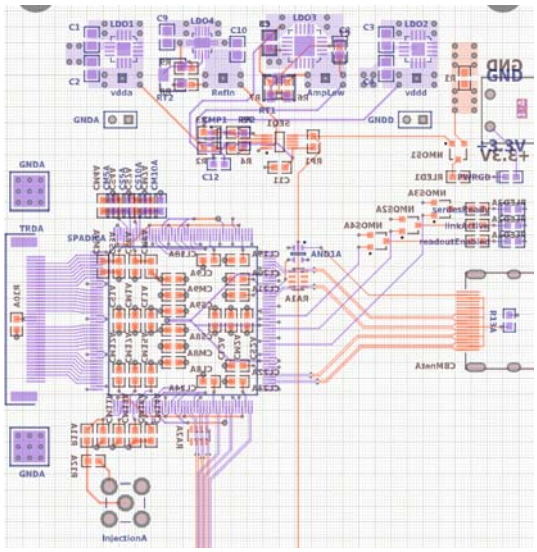

Figure 3: Layout of the top third of the new PCB, containing the voltage regulators and one of three SPADIC chips.

This new 3-SPADIC FEB has a size of 83 mm×339 mm and requires 4 layers. Using the same layout, the SPADIC pitch could be reduced to approximately 60 mm.

References

[1] M. Krieger, P. Fischer, “Commissioning of the SPADIC 1.0 Amplifier/Digitizer Chip”, this report.

[2] D. Emschermann, “Development of the Münster CBM TRD prototypes and update of the TRD geometry to version v13a”, CBM Progress Report 2013, p. 53

[3] F. Lemke et al., “Status of the CBMnet based FEE DAQ readout”, this report.

* michael.krieger@ziti.uni-heidelberg.de

Commissioning of the SPADIC 1.0 Amplifier / Digitizer Chip*

M. Krieger[†1] *and P. Fischer*[‡1]
[1]ZITI, University of Heidelberg, Germany

The SPADIC chip has been developed for the readout of the CBM TRD. The latest version SPADIC 1.0 has 32 channels on an area of $5 \times 5\,\mathrm{mm}^2$. The chip is fully functional and has been extensively tested in 2013.

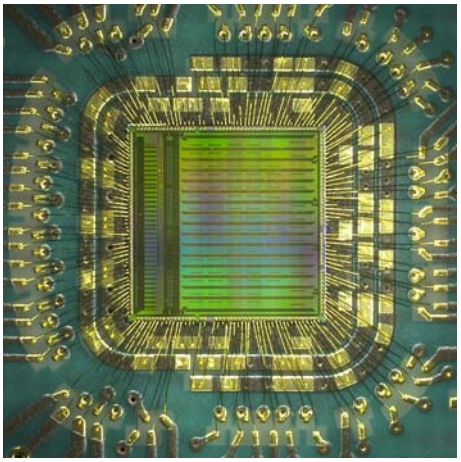

Figure 1: SPADIC1.0 chip bonded to readout PCB.

Chip Description

SPADIC 1.0 contains 32 identical channels on a die of $5 \times 5\,\mathrm{mm}^2$ size. It is fabricated in the 180 nm technology from UMC. The digital part uses custom made mixed mode standard cells and 44 SRAM blocks for data buffering. Each channel contains

- A charge amplifier / first order shaper ($\tau = 80\,\mathrm{ns}$) for positive input pulses with a noise of $\approx 800\,\mathrm{e}$ at $C_{in} = 30\,\mathrm{pF}$. This part consumes $\approx 5\,\mathrm{mW}$. In addition an experimental frontend for negative pulses is available.
- A $25\,\mathrm{MHz}$, $4.8\,\mathrm{mW}$ pipeline ADC with 9 bit output and an ENOB of > 8 Bit.
- A fully programmable digital IIR filter with 4 first order stages (16 bit processing, 6 bit coefficients).
- A sophisticated hit detection logic with differential threshold option for double hit detection and forced 'neighbor' trigger from channels on the same chip or even from different chips.
- A unit to pick an arbitrary set of amplitude samples from each pulse.
- A time ordered derandomization FIFO.
- Various error detection and recovery features (mainly for full buffers).

The data link backend implements for the first time the CBMNet protocol on an ASIC. It sends out the agglomerated hit data in a compact data format over two serial LVDS links running at up to 500 Mbps. In order to simplify system design as much as possible, SPADIC 1.0 contains all further required infrastructure (current reference, bias DACs, monitoring busses, test pulse injectors) required to operate the chips with a minimum of external components and signals. For simplified assembly of detector readout modules, some chips have been packaged in QFP176 carriers of $26 \times 26\,\mathrm{mm}^2$ size.

Test Environment

The chip is bonded to an adapter board (Fig. 1) which is connected to a custom FPGA board holding a CBM net receiver firmware. The FPGA is accessed through USB2.0 using multi threaded Linux applications allowing for configuration of all chip settings, injections and data readout.

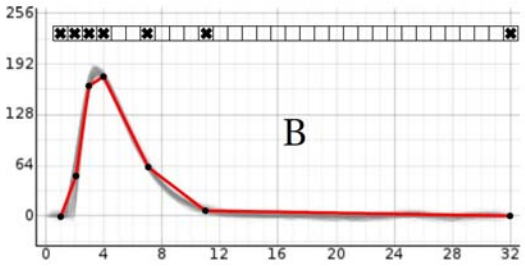

Figure 2: Samples sent out for a pulse using selection mask.

Results

All features of the chip have been operated successfully. Only few minor bugs have been identified which do not prevent chip operation on detectors. As just one example, Fig. 2 shows how interesting samples in one pulse can be picked using a freely programmable mask.

References

[1] M. Krieger, "Self-triggered charge pulse processing ASIC", Conference Proceedings of the TWEPP-13, Perugia, Italy, September 2013

[2] T. Armbruster, P. Fischer, M. Krieger and I. Peric, "Multi-Channel Charge Pulse Amplification, Digitization and Processing ASIC for Detector Applications", 2012 NSS Conference Record (IEEE), Anaheim, USA, October 2012

[3] http://spadic.uni-hd.de/

* Work supported by BMBF under grant number 05P12VHFCF.
† michael.krieger@ziti.uni-heidelberg.de
‡ peter.fischer@ziti.uni-heidelberg.de

 doi:10.15120/GR-2014-1-NQM-CBM-34

Testing of $31cm \times 31cm$ GEM Chamber at COSY

R. P. Adak[1], A. K. Dubey[2], J. Saini[2], V. Jain[2], S. Chattopadhyay[2], S. Das[1], U.Frankefeld[3], J.Henner[3], W. Niebur[3], I. Sorokin[3], T. Blog[3], F. uhlig[3], V. Friese[3], P. Ghosh[3], and J. Heuser[3]

[1]Bose Institute, Centre for Astroparticle Physics And Space Sciences, Kolkata-91, INDIA

[2]Variable Energy Cyclotron Centre, Kolkata-64, INDIA

[3]GSI Helmholtzzentrum für Schwerionenforschung GmbH (GSI), Darmstadt, Germany

Introduction

Operation of CBM-MUCH at high interaction rate requires a detector with large acceptance, high granularity and high rate capability. In this direction, we have conducted a beam test of triple GEM detectors at COSY using 2.36 GeV/c proton beams. Our goal was to study the response of the detector with high intensity beam using nXYTER based self-triggered readout electronics and also to test for the first time the performance of a large size triple GEM detector. In this study, we compare the results at different peak intensities in a typical spill in a run. The highest intensity as calculated from spill structure is $\sim$565kHz$/cm^2$ which is close to the peak intensity expected by the 1st MUCH detector station. Here we report preliminary results of the beam test.

Experimental Setup

The schematic layout of the test setup is shown in Fig.1. Out of the three GEM detectors tested, first two detectors (GEM1 & GEM2) are of $10cm \times 10cm$ size having square readout pads of sizes $3mm \times 3mm$ and $6mm \times 6mm$ respectively. The drift, transfer and induction gap of GEM1 are $3mm, 1mm, 1.5mm$ and the corresponding values for GEM2 are $3mm, 2mm, 2mm$. Third detector (GEM3) is made out of large GEM foils of $31cm \times 31cm$ in size with trapezoidal readout pads of radially increasing size [1]. The drift, transfer and induction gap of the chamber are $3mm, 1mm, 1.5mm$. A premixed gas mixture of Ar and CO_2 mixed in the ratio of 70:30 by mass was used for all the GEMs. Data were acquired by DABC based DAQ sysytem. GEM1 and GEM2 were read out using 2 nXYTER and one ROC while GEM3 was read out using 8 nXYTERs and 4 ROCs. In this test beam, the feedback parameter $v_b f_b$ of nXYTER was set as per high frequency requirement as reported in [2]. All the hits above a predefined threshold and time-correlated with the trigger window are used for analysis.

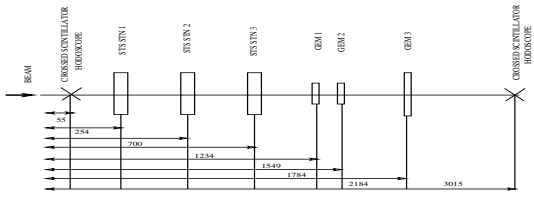

Figure 1: Experimental Setup at COSY

Results

The beamspots of GEM2 and GEM3 are shown in Fig.2. We do not observe any structure inside the beamspot as was the case in the earlier beam tests at higher intensities. The ADCs are obtained by assuming a baseline value of 2000 ADC for all the nXYTER channels. The pulse height distributions for GEM2 and GEM3 for both low and high intensity cases fitted to a Landau distribution have been shown in Fig.3 corresponding to the pad with highest ADC taken event by event.

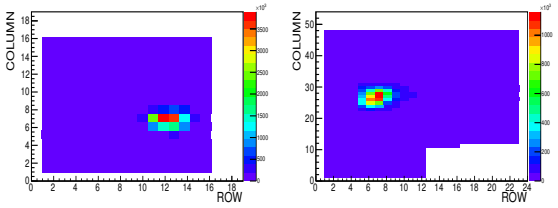

Figure 2: Beam spot of GEM2 (left) and GEM3 (right) at high intensity

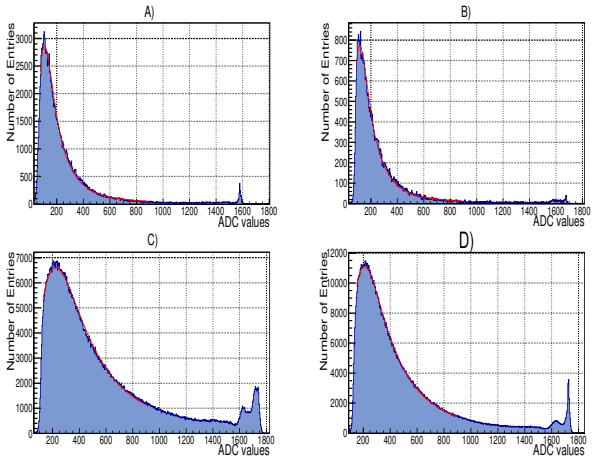

Figure 3: Pulse height spectra for GEM2 (A,B) and GEM3 (C,D) respectively for ΔV_{GEM}= 359.06V. The peak intensities corresponding to (A), (B), (C), (D) are 30 kHz, 253kHz, 25.23 kHz and 357kHz respectively.

The MPV of the ADC spectra at low and high intensities are 124.85 and 122.53 for GEM2 and 240.0 and 227.0 for GEM3 respectively for given sets of high voltage of GEM2 and GEM3. The MPV values of GEM2 differ from GEM3 due to different configurations of the detectors mentioned earlier. We observed that the MPV remains nearly same for both high and low intensity cases for the two detectors. Preamplifier saturation effects as observed in earlier beam tests is no longer present owing to the choice of appropriate $v_b f_b$ values. Further analysis of the data is under process.

References

[1] A.K.Dubey et al., Building and Testing a Large Size Triple GEM Detector, this proceedings.

[2] J.Saini et al., CBM Progress Report 2012, P.N.47.

CBM First-level Event Selector Data Management Developments*

J. de Cuveland[1], *D. Hutter*[1], *and V. Lindenstruth*[1]

[1]FIAS Frankfurt Institute for Advanced Studies, Goethe-Universität Frankfurt am Main, Germany

The First-level Event Selector (FLES) is the central event selection system in the CBM experiment. Its task is to select data for storage based on online analyses including a complete event reconstruction. To do so, the FLES timeslice building has to combine data from all input links to time intervals and distribute them via a high-performance network to the compute nodes. Data rates at this point are expected to exceed 1 TByte/s.

The FLES system consists of a scalable supercomputer with custom FPGA-based input interface cards and a fast event-building network (Fig. 1). Constructed largely from standard components, it will be situated at the new FAIR data center.

Timeslice Building

A *timeslice* is the fundamental data structure that manages access to all detector raw data of a given time interval. It provides random access to *microslices*, each containing data from a small amount of time and a single input detector link (Fig. 2). By duplicating a small number of microslices at the border of a timeslice (*overlap region*), differences in detector readout timing performance can be accomodated, and it is ensured that every timeslice can be processed independently.

These data structures and a timeslice-based API for the following online data processing have been developed and optimized such that computer memory access (e. g., required by additional copy operations) can be minimized.

For data transfer between the FLES nodes, it has proven practical to use an InfiniBand network. A prototype software for efficient timeslice building based on InfiniBand Verbs has been developed, especially addressing questions regarding data structures and buffer management. It implements the full data structures as intended for the final setup. The feasibility of employing a more high-level interface to the network hardware, like MPI, is currently under investigation.

Efficient Timeslice building over a state-of-the-art InfiniBand FDR network has been successfully demonstrated on a small scale on the Micro-FLES cluster installed at GSI.

FLES Interface Board (FLIB)

The CBM detector data enters the FLES system through custom add-on cards in the FLES PCs. These FLES Interface Boards (FLIBs) require high-speed optical inputs to receive the data from the CBM readout electronics, a high-performance interface to the host PC, and a large buffer memory. A specially developed FPGA-based card with a

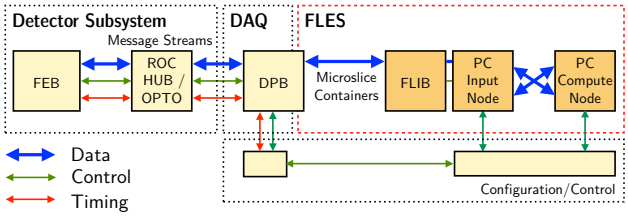

Figure 1: The First-level event selector (FLES) in the CBM read-out data path.

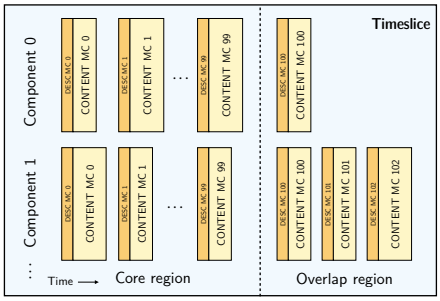

Figure 2: The FLES timeslice data structure provides indexed access to detector raw data packaged in microslices.

PCIe interface at the maximum achievable rate will be employed here.

The FPGA design implements the DAQ protocol for receiving the data, manages the buffer memory, and controls the PCIe transfer. In contrast to the final system, early prototype setups lack the DPB layer (cf. Fig. 1) and do not support the creation of microslices. The current prototype firmware therefore includes a mockup of the foreseen DPB design and is capable of directly receiving CBM-Net messages as delivered by the CBM front-end electronics.

The FPGA design has been ported to the Xilinx Kintex-7 family of FPGAs, as the current standard readout chain for CBM detector development employs a prototype board with this device. The prototype firmware, implemented in a total of 9700 lines of VHDL code, has been completed and successfully tested in a readout setup. In the future, further optimization of the DMA architecture including the software device driver will have to be performed to minimize memory access operations on the host PC.

Both aspects, input interface and timeslice building over Infiniband, have been intergrated in a common data management software project. This allowed to set up and successfully demonstrate the FLES data chain from data generating boards connected to the FLIB optical inputs to substitute analysis code on a FLES compute node after complete timeslice building.

* Work supported by BMBF (05P12RFFCP) and HIC for FAIR

doi:10.15120/GR-2014-1-NQM-CBM-36

Status of the CBMnet based FEE DAQ readout*

F. Lemke[1], *S. Schatral*[1,2], *and U. Bruening*[1]
[1]University of Heidelberg, Mannheim, Germany; [2]GSI, Darmstadt, Germany

Front-end read-out status

In the past year, the CBM read-out data acquisition (DAQ) network capabilities based on the CBMnet protocol [1] have been extended. Currently, there are two FEE ASIC implementations which include the CBMnet module blocks. The first is the SPADIC V 1.0 [2] with functioning communication, which is currently in the process of commissioning. The second ASIC is the STS-XYTER [3] which provides twice the data bandwidth in backend direction compared to the SPADIC. Therefore, the CBMnet has been extended to a four-lane core and a lot of improvements were implemented. The functional verification of the digital part has been done with two Spartan6 FPGAs in a long term test running more than 7 days. Hence, the FEE LVDS interconnect [4] has been proven as stable under laboratory conditions. To get more information about the status and error behaviour of the LVDS link in the STS-XYTER, a CBMnet diagnostics core has been developed. With that, it is possible to get information about the link quality, read the status of the link initialization and collect statistics about bit-error rates and retransmissions of the active interconnect. The test setup of the STS-XYTER connected to a SysCore3 with HDMI cables is shown in figure 1. The Syscore3 firmware has been extended and now provides a full deterministic optical link.

Figure 1: STSXYTER read-out setup

HUB ASIC prototype design

Further research has been done concerning the HUB ASIC to provide a hierachical synchronized DAQ network [5]. In addition to controlling the FEEs, the focus was to achieve a high density and enable early multilayered data aggregation capability. Thus, flexible build-up scenarions are possible, which are required due to varying amounts of data for different detector parts. The HUB will support up to 40 FEE links (500 Mb/s) and up to 4 back-end links (5 Gb/s). Besides high density, special difficulties include handling and deadlock avoidance for the traffic, radiation tolerance, and the design of a serializer/deserializer (SERDES) capable of 5Gb/s. A collaboration with the Indian Institue of Technology Kharagpur (IITKGP) was initiated to build this SERDES in partly full-custom design. A SERDES structure diagram is presented in figure 2. It depicts handling of the receive and transmit streams, including features such as clock data recovery (CDR) and eye measurement. Currently, a prototype ASIC is being designed with the focus on testing the SERDES and critical HUB functionality. Therefore, a miniASIC submission will be prepared in 2014 with the TSMC 65nm Europractice process.

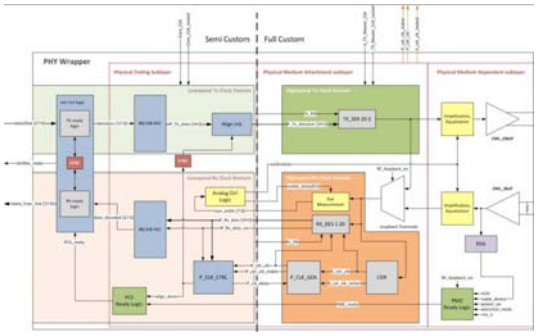

Figure 2: SERDES blockdiagram for HUB ASIC

References

[1] F. Lemke, S. Schatral, “Design concepts and measurements of the CBM DAQ network”, Deutsche Physikalische Gesellschaft EV (DPG13), Frühjahrstagung, March 4-8, Dresden, Germany, 2013.

[2] M. Krieger, P. Fischer, “Commissioning of the SPADIC 1.0 Amplifier / Digitizer Chip”, CBM Progress Report 2013.

[3] K. Kasinski, R. Szczygiel, “Status of the STS-XYTER, a prototype silicon strip detector readout chip”, CBM Progress Report 2013.

[4] S. Schatral, F. Lemke, U. Bruening, “Design of a deterministic link initialization mechanism for serial LVDS interconnects”, TWEPP 2013 - Topical Workshop on Electronics for Particle Physics, Sept. 23-27, Perugia, Italy, 2013.

[5] F. Lemke, U. Bruening, “A Hierarchical Synchronized Data Acquisition Network for CBM”, IEEE Transactions on Nuclear Science (TNS), Journal Paper, VOL. 60, No. 5, Part II, Oct. 2013.

* Work supported by GSI, BMBF FAIR-CBM 05P12VHFCE

A Monte Carlo feasibility study of the CBM event reconstruction at high interaction rates based on time information. *

A. Senger[†1]*, the CBM collaboration*[1]*, and the FAIR@GSI division*[1]
[1]GSI, Darmstadt, Germany

A Monte-Carlo simulation was performed in order to study the feasibility of event reconstruction at high interaction rates based on the timing information provided by the Silicon Tracking System (STS). A parameter which could be used for event separation is the reconstructed interaction time T_0. In our study, the resolution of the reconstructed T_0 is determined mostly by the time resolution of the STS which is in the order of 5 ns. We will study the separation of events in time-base simulations using a cut in ΔT_0 for a reaction rate of $10^7/s$. We have to take into account two different situations: if ΔT_0 of two different interactions is smaller than the ΔT_0 cut value, there is the possibility to combine reconstructed tracks of particles from two different interactions in one event; If the T_0 reconstruction resolution is greater than ΔT_0 cut value, there is the possibility to divide the reconstructed tracks of particles from the same interaction in two different events. In Figure 1 the relative numbers of combined and divided events are presented as function of the ΔT_0 cut value, the assumed T_0 resolution is 5 ns. It can be seen that with a ΔT_0 cut value of 5 ns for example the number of divided events (red squares) is about 15%, and the number of combined events (black circles) is about 6%. With increasing ΔT_0 cut value the number of divided events decreases dramatically, but the number of combined events increases up to 20% for a ΔT_0 cut value of 20 ns. It is clear, that for event separation at interaction rates as high as $10^7/s$ an additional cut variable is needed.

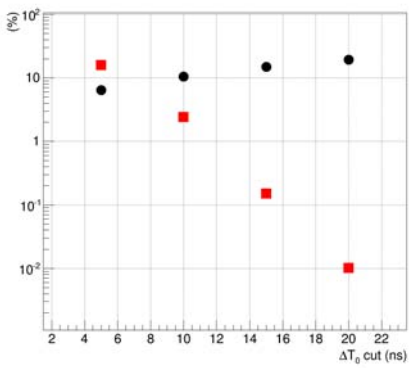

Figure 1: Number of combined (black circles) and divided (red squares) events as a function of the ΔT_0 cut value for a resolution of the reconstructed interaction time of 5 ns.

The separation of different events can be improved by using the information on the different positions of the primary vertices in addition to the reconstructed T_0 values. For the simulation we assume a Gaussian distribution of the beam particles at the target (i.e. of the primary vertices) with a FWHM of 1cm. In figure 2 the distribution of the primary vertices in horizontal (upper plot) and vertical position (lower plot) is shown as function of time. The height and the length of the symbols correspond to a vertex resolution of 100μm and a reconstruction resolution of 20 ns, respectively. It can be seen that the events are clearly separated in space and time for an interaction rate of $10^7/s$. Taking into account the position information of the primary vertex it is possible to reduce the number of combined events by up to 2 orders of magnitude.

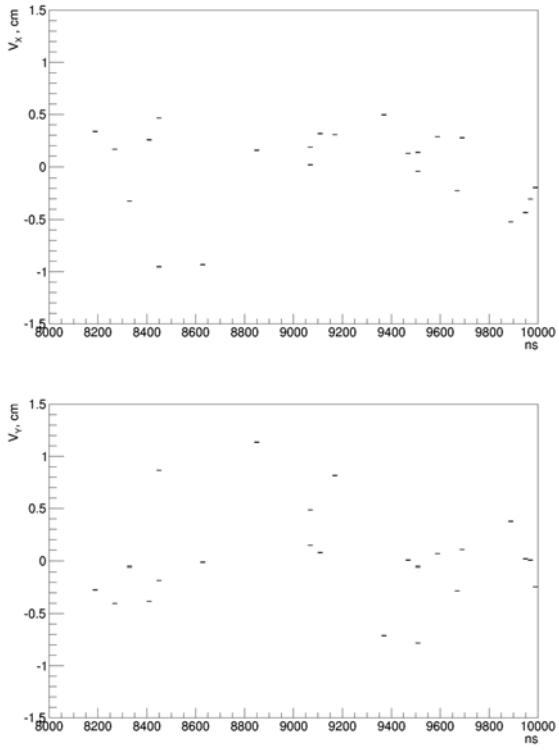

Figure 2: Primary vertex distribution in horizontal (upper plot) and vertical (lower plot) direction for a Gaussian distribution of the beam particles with FWHM = 1 cm for an interaction rate of $10^7/s$ as function of time. The symbol size corresponds to a vertex resolution of 100μm, and a resolution of the interaction time of 20 ns.

* Work supported by GSI.
† a.senger@gsi.de

 doi:10.15120/GR-2014-1-NQM-CBM-38

Employing the CBM Micro Vertex Detector for Background Rejection in Dilepton Analyses *

E. Krebs[1], T. Galatyuk[2], J. Markert[1], and J. Stroth[1,3] for the CBM collaboration

[1]Goethe-Universität, Frankfurt, Germany; [2]Technische Universität Darmstadt, Germany; [3]GSI Darmstadt, Germany

Low mass electron (muon) pairs are considered to be excellent probes of the processes taking place in the interior of extreme states of matter formed in the collision zone of heavy-ions. However, the reconstructed distribution of of electron pairs contains in addition contributions from mesons decaying after freeze-out and from combinatorial pairs. Single electron or positron tracks from incompletely detected γ-conversions and Dalitz decays of π^0-mesons are the most abundant source contributing to the significant combinatorial background. The excellent position resolution of the Micro-Vertex Detector (MVD) of the CBM experiment and its proximity to the target offers a chance to reject efficiently the close pairs. This holds in particular for the abundant case, in which the magnetic field of CBM bends the low momentum partner out of the CBM acceptance while the high momentum partner contributes to the combinatorial background of the invariant mass spectrum. We tried to improve the reconstruction the low momentum partner by including points from the MVD into the track reconstruction and to reject the pair based on the reconstructed opening angle.

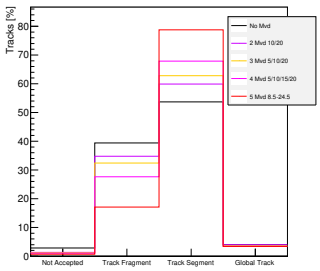

Figure 1: Track topology of dielectrons from π^0-Dalitz decays assuming different configurations of the MVD, i.e. no MVD or a MVD featuring different amount of sensor planes, see text.

Emission from a thermal source was assumed to simulate electron pairs from meson decays for Au+Au reactions at SIS-100 and SIS-300 energies. The simulation parameters were chosen such that the meson spectra are consistent with p_T and rapidity distributions measured by NA49 [1]. The pairs simulated with the Pluto[4] event generator are embedded into hadronic final states calculated with UrQMD. Two versions of the hadronic cocktail were used: one cocktail simulates vector meson decay in vacuum, the second one assumes an in-medium modification of the ρ_0.

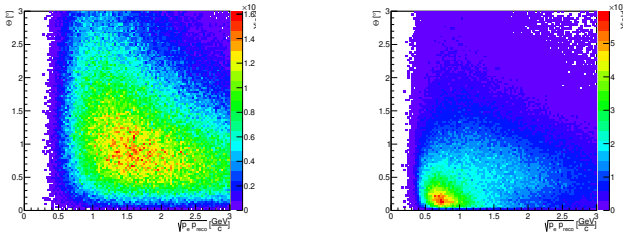

(a) ρ^0 (b) π^0-Dalitz

Figure 2: Opening angle vs. momentum of an identified electron and its nearest reconstructed track for pairs from (a) ρ^0 decays and (b) π^0-Dalitz decays.

Figure 1 shows the track type of the low momentum partner of an e^+/e^--pair from a π^0-Dalitz decay, where the high momentum partner was reconstructed and identified in the RICH. We distinguish track fragments (only individual hits are seen), track segments (also charge and momentum were reconstructed) and global tracks (also particle ID was reconstructed). The number of reconstructed track segments was found to increases substantially with the amount of MVD stations. This comes with draw backs in terms of increasing computing time. In Figure 2, the opening angle between an identified electron and its nearest track segment is correlated to the product of the momenta of these two tracks. A wedge cut can be applied to reduce the background [2] [3]. The additional number of reconstructed low-momentum electrons increases the number of background pairs, which is rejected by this cut. This suggests that the MVD might help to reduce the related background and that this capability is getting more pronounced with an increasing number of MVD-stations.

Further studies are needed to conclude on the optimal number and positions of MVD stations and the optimal magnetic field configuration. The impact of the numerous δ-electrons emitted from the target remains to be taken into account. Finally, the rejection strategy for γ-conversions occurring in the additional MVD stations has to be optimized.

References

[1] C. Alt et al. (NA49 Collaboration), Phys. Rev. C 78, 044907 (2008)

[2] T. Galatyuk, PhD Thesis, Goethe-Universität, Frankfurt am Main, (2009)

[3] E. Lebedeva, GSI-SR2012-PHN-NQM-EXP-54, (2012)

[4] I. Froehlich et al., arXiv:0708.2382

* This work is supported by BMBF (05P12RFFC7), HIC for FAIR, H-QM and GSI.

Production of hyperons at FAIR energies

H. Jahan[*1], *S. Chattopadhyay*[2], *P. Senger*[3], *N. Ahmad*[1], *and M. Irfan*[1]
[1]AMU, Aligarh, India; [2]VECC, Kolkata, India; [3]GSI, Darmstadt, Germany

One of the main aims of studying relativistic heavy-ion collisions is to investigate the characteristics of nuclear matter under extreme conditions of temperature and energy density. Under high temperature and/or baryon density, nuclear matter is expected to undergo a transition to a state of free quarks and gluons, known as quark-gluon plasma (QGP)[1]. The determination of yields of strange particles is one of the key parameters to study the properties of the matter created in high energy heavy-ion collisions. The relative enhancement of strange and multi-strange baryons as well as their ratios in central heavy ion collisions in comparison to those for proton induced interactions have also been suggested as a possible signature for the formation of QGP [2]. In the present work, A Multi-Phase Transport (AMPT) model [3] is employed to study production of strange particles in cental Au+Au collisions at FAIR energies (i.e. E_{Lab} = 5 to 40 AGeV). In order to see whether the hyperon production is sensitive to the degrees-of-freedom in the collision volume, both the string melting (partonic matter) and the default mode (hadronic matter) of the AMPT model have been used for calculating the particle yields.

The results of the calculations are shown as excitation functions of Λ^0 and $\bar{\Lambda}^0$ hyperons, Ξ^- and $\bar{\Xi}^+$ hyperons, and Ω^- and $\bar{\Omega}^+$ hyperons in the upper, center, and lower panel of Fig. 1, respectively. The yields have been calculated in the FAIR energy range for both modes of AMPT, i.e., string melting (partonic) and default (hadronic). In the case of $\bar{\Lambda}^0$ hyperons, the yield for hadronic production is one order of magnitude higher than the yield for partonic production at top SIS100 energies (11 A GeV), an effect which is clearly measurable. A similar effect, although smaller in magnitude, is found for $\bar{\Xi}^+$ hyperons. In contrast, the yields of Ξ^- and Ω^- hyperons for partonic production are well above the yield for hadronic production in the beam SIS100 energy range. The yield of $\bar{\Omega}^+$ hyperons seems not to be sensitive to the production mechanism. However, this result should be checked by a calculation with much better statistics. In conclusion, according to the AMPD code the yields of hyperons and anti-hyperons produced in central Au+Au collisions at FAIR energies exhibit a measurable sensitivity to the degrees-of-freedom in the fireball.

References

[1] S. A. Bass, M. Gyulassy, H. Stöcker and W. Greiner, J. Phys. G 25, R1 (1999) [arXiv:hep-ph/9810281]

[2] J. Rafelski and B. Müller, Phys. Rev. Lett. 48, 1066(1982); J. Rafelski, Phys. Rep. 88, 331 (1982);P. Koch, B. Müller and J. Rafelski, Phys. Rep. 142,167 (1986)

[3] B. Zhang C. M. Ko, B. A. Li and Z. W.Lin, Phys. Rev. C 61, 067901 (2000); Z. W. Lin,S. Pal, C. M. Ko, B. A. Li, and B. Zhang, Phys.Rev. C [arXiv:nucl-th/0011059]

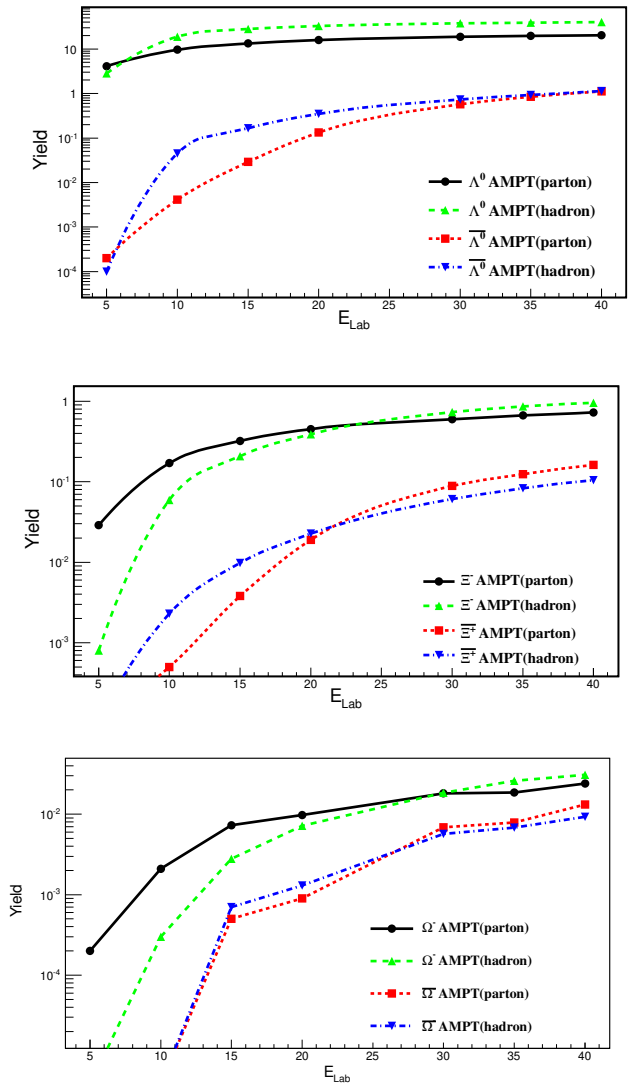

Figure 1: Yield of hyperons in central Au+Au collisions as function of beam energy calculated with the AMPT code with string melting (partonic) and without (hadronic). Upper panel: Λ^0 and $\bar{\Lambda}^0$ hyperons. Center panel: Ξ^- and $\bar{\Xi}^+$ hyperons. Lower panel: Ω^- and $\bar{\Omega}^+$ hyperons.

*hushnud.jahan@gmail.com

 doi:10.15120/GR-2014-1-NQM-CBM-40

Reaction plane reconstruction in the CBM experiment*

S. Seddiki[1] *and M. Golubeva*[2]
[1]GSI, Darmstadt, Germany; [2]INR, Russian Academy of Sciences

The determination of the reaction plane in nucleus-nucleus collisions is crucial for several measurements, including anisotropic collective flow. In CBM, the reaction plane can be measured by the forward hadronic calorimeter, referred to as the Projectile Spectator Detector (PSD). The Silicon Tracking System (STS) of the experiment, designed to cover a large fraction of the particle phase space, can also provide a complementary measurement. In this work, we investigated the capabilities of these two detectors for reconstructing the reaction plane at FAIR energies.

The simulations were carried for Au+Au collisions in the CBMROOT framework, using the event generator SHIELD, the simulation package GEANT4 and the physics list FTFP BERT. The detector model includes a 250 μm thick Au target, a STS consisting of 8 stations (located between 30 cm and 1 m from the target) embedded inside a dipole magnet and a PSD constituted transversally of 45 modules of 20 $\times$ 20 cm^2. Each module is composed longitudinally of 60 layers with combined Lead absorber and scintillator material. The central one features a cylindrical beam hole (to let beam ions pass) with a diameter of 6 cm.

The azimuthal orientation of the reaction plane has been determined using the event plane method [1]. The flow of emitted particles (used in the method) is exploited directly by measuring the momentum of charged particles in the STS, while the flow of projectile spectators is reflected in the azimuthal distribution of the energy measured in PSD modules. In this study, Monte Carlo tracks with at least 4 hits in STS stations have been used. As the elliptic flow of charged particles is relatively weak at FAIR energies, the results are given using the directed flow of emitted particles (a selection of forward rapidity particles measured by the STS is performed). The reaction plane resolution is defined as the Gaussian width ($\sigma(\Psi_1-\Psi_{MC})$) of the distribution of the measured 1^{st} harmonic event plane angle (Ψ_1) around the true reaction plane angle (Ψ_{MC}).

At SIS100 energies, the PSD reaction plane resolution is optimal ($\sigma(\Psi_1 - \Psi_{MC}) \leq 40°$ for collision impact parameters below 11 fm) when the detector is located at 8 m from the target (see Fig.1), accordingly at 15 m at SIS300 due to higher Lorentz boosts of spectators.

The integrated magnetic dipole field is of about 1 Tm in the target region at $E_{beam} \geq 10$ AGeV, while it is scaled down with beam momentum at lower energies to reduce the induced bias in the PSD event plane calculation. However, a minimal field is required (of about 0.6 Tm) to keep the tracking performance on an acceptable level. A significant degradation of the PSD resolution was only seen for

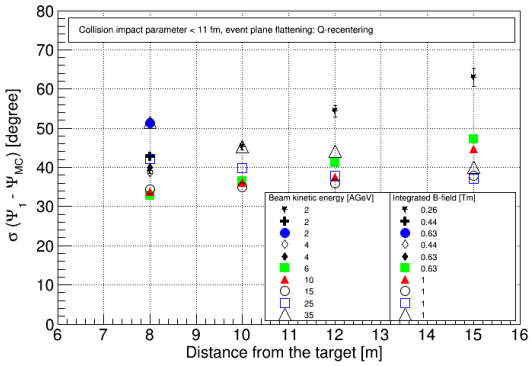

Figure 1: PSD reaction plane resolution (1^{st} harmonic event plane) at several distances from the target in Au+Au collisions (impact parameters below 11 fm) at FAIR energies. The Gaussian fits were performed in the range [-80, 80] degrees. The effect of the magnetic dipole field is also shown for $E_{beam} \leq 4$ AGeV and a PSD distance of 8 m.

$E_{beam} < 4$ AGeV e.g. at E_{beam} = 2 AGeV, $\sigma(\Psi_1 - \Psi_{MC})$ increases from 39° to 51° while enhancing the field from 0.26 Tm to 0.63 Tm.

The resolutions obtained with the PSD and the STS can be compared in Fig.2. At FAIR energies, both detectors provide good and complementary performance: $\sigma(\Psi_1 - \Psi_{MC})$ between 30° and 40°.

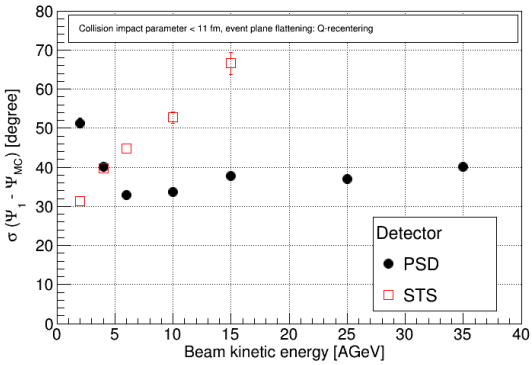

Figure 2: Reaction plane resolution (1^{st} harmonic event plane) as a function of beam energy. The PSD is located at 8 (15) m from the target at SIS100 (SIS300) energies. The integrated magnetic dipole field is of 0.63 Tm at E_{beam} = 2, 4 and 6 AGeV and 1 Tm at higher energies.

References

[1] A. M. Poskanzer et al., Phys. Rev. **C 58** (1998) 1671-1678

* Work supported by EU-FP7:283286-HP3

The di-muon measurements with CBM at SIS100.*

A. Senger† [1], *the CBM collaboration*[1], *and the FAIR@GSI division*[1]
[1]GSI, Darmstadt, Germany

The CBM muon detection system is designed to measure muon pairs from the decay of vector mesons ($\rho, \omega, \phi, J/\psi$) produced in heavy-ion collisions. At FAIR energies the muon momenta can be rather low, therefore, we developed a muon detection concept whith a variable definition of absorber thickness according to the muon momentum. The full design of the muon detector system consists of 6 hadron absorber layers (carbon block of thickness 60 cm with lead shielding around the beam pipe and iron plates of thickness 20, 20, 30, 35, 100 cm). The 18 gaseous tracking chambers are located in triplets behind each hadron absorber. The start version of the muon system consists of 4 hadron absorbers and 4 tracking stations. It will be used for measurements of low mass vector mesons at SIS100 energies. In the following we present results of simulations for central Au+Au collisions at a beam energy of 8 A GeV . It turned out that additional information from the time-of-flight system helps to further suppress protons and kaons. This is illustrated in figure 1. which depicts the mass squared of the particles seen by the muon detector as reconstructed from their time-of-flight as function of momentum measured in the Silicon Tracking System. Muons from ω meson decays and background particles are shown in the left and in the right panel, respectively.

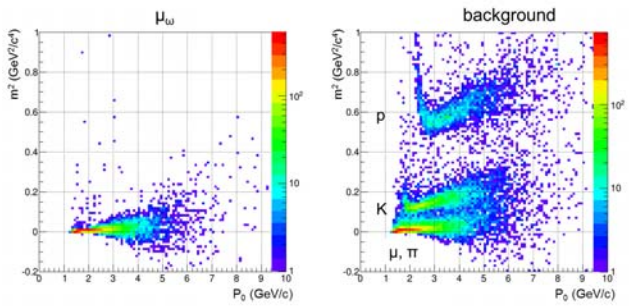

Figure 1: Mass squared of particles in the muon detector as reconstructed by their time-of-flight as function of momentum measured in the Silicon Tracking System. Left panel: muons from ω decays. Right panel: background particles.

The final invariant mass distributions of the remaining background and of low-mass vector mesons is shown in the left panel of figure 2, whereas the resulting signal-to-background ratio is shown in the right panel. The reconstruction efficiencies for mesons are 0.75% for ρ, 0.78% for ω, and 1.1% for ϕ.

* Work supported by GSI.
† a.senger@gsi.de

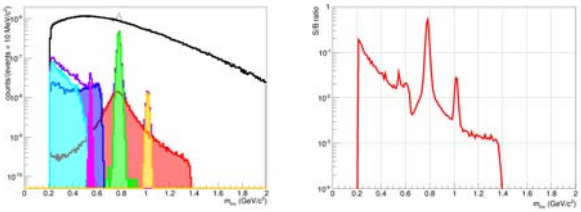

Figure 2: Left picture: Invariant mass spectrum of low mass vector mesons for 8 AGeV central Au+Au collisions. Black line - combinatorial background, red - ρ, green - ω, yellow - ϕ, magenta - η, blue - ω Dalitz, light blue - η Dalitz. Right picture: Signal-to-background ratio.

The measurement of J/ψ mesons at 10 A GeV will be an exciting experiment at SIS100 because it will provide information on the process of charm production at energies close to the threshold, in this case even below threshold. According to the HSD transport code [1], in central $Au + Au$ collisions at 10 A GeV the dilepton yield per event is 1.04×10^{-8} for J/ψ mesons. We performed J/ψ simulations in central $Au + Au$ collisions at 10 AGeV using full muon system. The invariant mass distribution of background and signal is shown in Figure 3. The signal-to-background ratio is 0.13, and the J/ψ reconstruction efficiency is 0.2%.

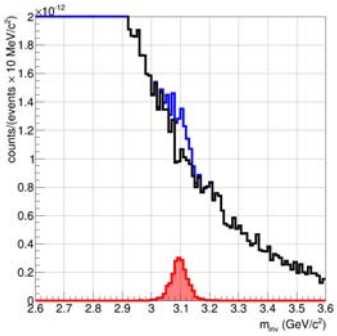

Figure 3: Reconstructed invariant mass distribution of muon pairs for central Au+Au collisions at 10 A GeV. Red histogram: J/ψ meson, black histigram: combinatorial background, blue histogram: background + J/ψ meson.

References

[1] O. Linnyk et al., Nucl. Phys. A 786 (2007) 18

 doi:10.15120/GR-2014-1-NQM-CBM-42

Constraining the nuclear matter equation of state around twice saturation density *

A. Le Fèvre †[1], *Y. Leifels*[1], *W. Reisdorf*[1], *J. Aichelin*[2], *Ch. Hartnack*[2], *and N. Herrmann*[3]

[1]GSI Helmholtzzentrum für Schwerionenforschung GmbH, Darmstadt, Germany; [2]SUBATECH, Université de Nantes, IN2P3/CNRS; [3]Physikalisches Institut der Universität Heidelberg, Heidelberg, Germany

Heavy ion collisions at intermediate energies as a tool to constrain the properties of the nuclear equation of state EOS is object of intense experimental and theoretical efforts since several decades [3]. During a heavy ion reaction the colliding system reaches densities larger than the nuclear saturation density. The nuclear EOS determines the densities reached during the collisions as well as the forces which are driving the colliding matter apart.

The FOPI Collaboration has measured the excitation function of 'elliptic flow' between 0.09 to 1.5 A.GeV [1]. Elliptic flow, denoted by $v_2(p_t, y) =< cos(2\Phi) >$, where Φ is the azimuthal angle with respect to the reaction plane, is shown in the left panel of Fig. 1. The data is compared to predictions of the IQMD transport model [2] using various phenomenological EOS's: HM ('stiff momentum dependent'), SM ('soft momentum dependent'), with compression moduli at ground state density $K_0 = 380$ MeV and $K_0 = 200$ MeV. The data is best described by using a 'soft' EOS. In order, to account for the complete shape of $v_2(y_0)$ a new observable is introduced $v_{2n} = |v_{20}| + |v_{22}|$, v_{20} and v_{22} result from a fit to $v_2(y_0)$ using the function $v_2(y_0) = v_{20} + v_{22}y_0^2$. Model predictions for the quantity $v_{2n}(E_{beam})$ for different EOS are shown together with FOPI data in the right panel of Fig. 1. The predictions vary by a factor ≈1.6 which is far above the measured uncertainty (≈1.1), the comparison clearly favors a 'soft' EOS. This is valid not only for protons but for all light charged particles (A $\leq$ 4).

In order to characterize which 'typical' densities where probed during the collisions we have determined within the same transport model at which times in the course of the collision and which conditions influence the most the development of the proton elliptic flow. The model predicts elliptic flow develops its final shape quite early, just after projectile and target have passed, and that its strength and shape – i.e. v_2 as function of the rapidity – are mostly influenced by the force of the mean field. Therefore, in this scope, the 'typical' density of the 'measured' EOS can be built from the mean value weighted by this force up to the passing time. It is depicted in Fig. 2 as a function of the bombarding energy in the Au+Au system at b=3 fm. It shows that the density range, relevant to the EOS evidenced by the FOPI Collaboration, spans in the range $\rho = (1.25 - 2.0)\rho_0$.

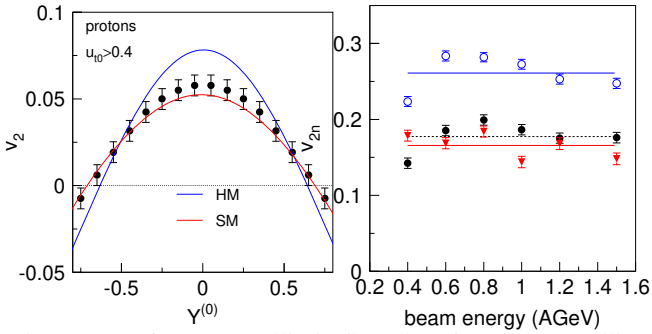

Figure 1: Left: Proton elliptic flow data for Au+Au collisions at 1.2A GeV as a function of the rapidity $-v_2(y_0)$, and IQMD-SM/HM simulations. See [1] for further explanations. Right: Experimental data of the shape parameter v_{2n} for protons as a function of beam energy for semi-central Au+Au collisions.

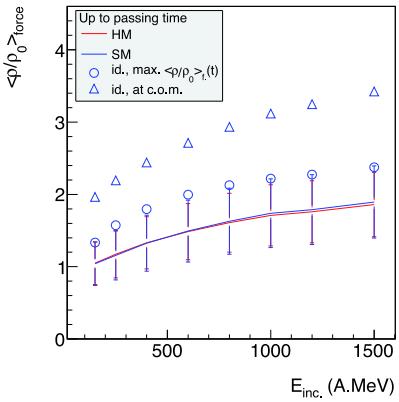

Figure 2: Mean value of the reduced density, computed up to the passing time, weighted by the force of the mean field seen by the participant protons, as a function of the incident energy as predicted by IQMD in Au+Au collisions at b=3 fm, for various EOS's. The error bars are the standard deviations. The blue symbols refer to the SM EOS: the circles depict the instantaneous maximum value of the force-weighted density reached over all times. The triangle is the same, restricted to the central compression zone.

References

[1] W. Reisdorf, et al. (FOPI Collaboration), Nucl. Phys. A 876 (2012) 1.

[2] J. Aichelin, Phys. Rep. 202 (1991) 233. and C. Hartnack, et al., Eur. Phys. J. A 1 (1998) 151.

[3] P. Danielewicz, R. Lacey, W. G. Lynch, Science 298 (2002) 1592.

* Supported by the IN2P3-GSI agreement contract number 13-70.

† a.lefevre@gsi.de

Differences in population of the phase space for $K^{\pm}$-mesons produced in π-induced reactions with heavy and light targets. *

V. Zinyuk[†1], *N. Herrmann*[1,2], *and the FOPI Collaboration*[1]

[1]Physikalisches Institut, Universität Heidelberg, Germany; [2]GSI, Darmstadt, Germany

In hot and dense baryonic matter, several non-trivial in-medium effects such as partial restoration of chiral symmetry, the modification of baryon-meson couplings, and the nuclear potentials are expected. As a result the properties of hadrons (e.g. mass, width, dispersion relation) may change. For K-mesons these changes are parametrized as a density dependent mean field $KN(\bar{K}N)$-potential, repelling(attracting) the kaons(anti-kaons) toward nucleons [1]. In pion-induced reactions these potentials can be studied at normal nuclear matter density.

The FOPI Collaboration in cooperation with the GEM-TPC Collaboration has recorded about 4M $\pi^- + {}^{208}Pb$ collisions and 3M $\pi^- + {}^{12}C$ collisions in the S339 experiment. After background subtraction about 16000 K^+- and about 450 K^--candidates produced in C target, 19000 K^+- and about 230 K^--candidates in Pb target could be identified. Both K^+- and K^--mesons could be measured down to $p_K = 0.1 GeV/c$ disclosing the most sensitive phase space region for $KN(\bar{K}N)$-potential investigation.

To see a possible influence from nuclear potentials we evaluate the momentum distributions of K-mesons. The momentum distribution of K^+-mesons produced in Pb-target ($(dN/dp)_{Pb}$) should be shifted to higher momenta with respect to the one of K^+-mesons from the C-target($(dN/dp)_C$) due the stronger repulsion felt by the K^+-mesons emitted from the heavier nucleus.. The 'momentum ratio' $R((d\sigma/dp)_{Pb}/(d\sigma/dp)_C)$ (normalized to the geometrical cross section) is expected to undergo a maximum. Fig.1 (upper panel) shows the result for K^+-mesons from the recent data sample. This measurement is in qualitative agreement with the previous results by the FOPI Collaboration (K^0_S measurement [2]) and ANKE collaborations (K^+ measurement [3]) showing a maximum around $p_{K^+} = 0.25 GeV/c$ and confirming the expected behavior for the repulsion scenario. However we do not observe the strong decrease, as seen bei ANKE, at smaller momenta, possibly due to different intermediate states.

Since K^- are attracted to nucleons, the 'momentum ratio' would have the largest value at smallest momentum and decrease with increasing momenta. Fig. 1 (lower panel) reveals that K^--mesons show a nearly constant ratio, which might be due to the strong absorption in nuclear matter. The observed K^--mesons are emitted from the surface of the target nuclei, do not feel the $\bar{K}N$-potential within the nucleus, and therefore have the same phase space distribution in both targets. The beam momentum of 1.7 GeV/c allows the direct production of K^+K^--pairs and hence also the production of intermediate ϕ-mesons decaying to K^+K^- (48.9 % BR). Currently it is not clear to which extent the observed K^--mesons originate from ϕ-meson decays.

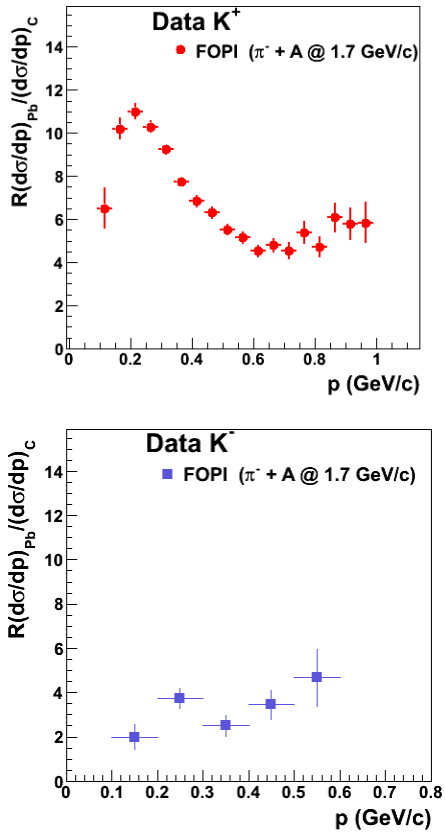

Figure 1: The 'momentum ratio' of K^+(upper panel) and K^- (lower panel). See text for details.

To obtain a consistent description of strangeness, especially K^-, in nuclear matter we intend to evaluate further particles connected to K-mesons by production/absorption. In the further analysis steps phase space distributions of particles like K^0 - mesons, ϕ-mesons and Λ-baryons produced in light and heavy systems will be evaluated.

References

[1] C. Fuchs, Prog. Part. Nuclear Phys. **56**, 1 (2006).

[2] M. L. Benabderrahmane *et al.*, Phys. Rev. Lett. **102**, (2009) 182501.

[3] M. Bueschner *et al.*, Eur. Phys. J. A **22**, 301 (2004).

* Work supported by BMBF 05P12VHFC7.

† v.zinyuk@gsi.de

 doi:10.15120/GR-2014-1-NQM-FOPI-02

Status of the pkΛ Analysis in pp Collisions with the FOPI Spectrometer*

R. Münzer[1], *L. Fabbietti*[1], *and M. Berger*[1] *for the FOPI Collaboration*

[1]Excellence Cluster 'Origin and Structure of the Universe' , Physik Department E12, Technische Universität München, 85748 Garching

The investigation of the kaon-nucleon interaction has been intensified in the last years due to new results on Λ(1405) and indications on the existence of the ppK^- bound state [1]. The possible creation of the ppK^- state has been investigated with the FOPI spectrometer at GSI in proton-proton-collisions at 3.1 GeV beam energy. According to theoretical predictions, this reaction and beam energy favor the formation of the ppK^-[2].

A silicon detector system was placed close to the target in the FOPI setup. It was constructed and employed to improve the vertex determination, and it is used as an on-line trigger for the selection of Λ hyperons. This trigger system allows an enhancement of events containing a Λ-hyperon of a factor $14.1 \pm 7.9(stat)^{+4.3}_{-0.5}$ with respect to the standard multiplicity trigger (LVL1)[3]. About $70 \cdot 10^6$ events have been collected with the second level trigger selection.

The exclusive events p+p→p $K^+\Lambda$ are extracted in several selection steps. First kaon and Λ candidates are selected. Then follows the major step of the event selection which is to require energy and momentum conservation. It consists in the application of a kinematic refit based on energy and momentum conservation constraints. The remaining background due to misidentified kaons is subtracted by applying a sideband analysis technique. Finally a sample of ≈ 900 exclusive events of the reaction p+p → p K^+ Λ were extracted. The background originating from the reaction p+p → p K^+ $\Sigma(\rightarrow \gamma + \Lambda)$ is determined to be 1/14 of the total yield. [4]

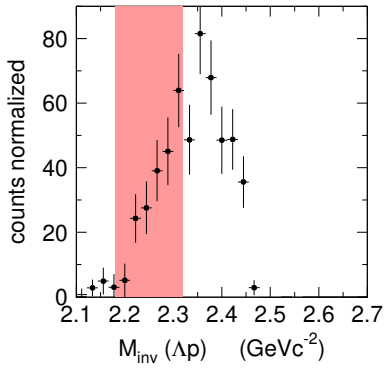

Figure 1: Spectrum of the invariant mass p,Λ.

In Fig. 1 the invariant mass spectrum of p,Λ is shown after the background subtraction. The red marked area covers the mass region in which a signal for the ppK$^-$ is be expected.
Since no clear signal is visible only a determination of an upper limit for the ppK$^-$ state possible. For this determination an adequate description of the background is needed. The best description was obtained using the Bonn Gatchina Partial Wave Analysis framework. In this fitting procedure different contributions are considered, like the direct production of p K^+ Λ and the production via an intermediate $N^{*,+}$ resonance, including the interference between different transition waves with the same quantum numbers.

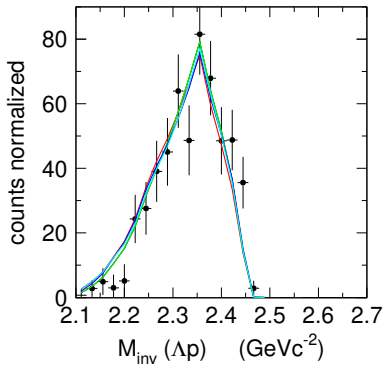

Figure 2: Spectrum of the invariant mass p,Λ. The different colored line show the 5 best fitting solution of the BG-PWA.

A systematic study was performed using this BG-PWA package. In this study different combinations of $N^{*,+}$ were included. In figure 2 the invariant mass of p and Λ is shown (black dots). The colored lines show the distribution of the five solutions which fit best to the experimental data. From these results a clear trend for the contributing processes was obtained. The production has a dominant contribution of channels with an intermediate $N^{*,+}$ resonance. Especially, the $N^{*,+}(1710)$ contributes with 40-50%. Also the $N^{*,+}(1900)$ adds 10% to the production within all five best solutions.

Since the BG-PWA reproduces the experimental data rather well ($\chi^2 \approx 1.2$), an accurate determination of the upper limit for the ppK$^-$ production could be possible. This will be performed in the near future for different mass and width hypothesis of the ppK$^-$.

References

[1] G. Agakishiev et al.,arXiv:1208.0205

[2] T. Yamazaki and A. Akaishi, Phys.Rev.C 76(2007)045201

[3] SiΛViO - A Trigger for Λ-Hyperons - arXiv:1307.7470v1

[4] R.Muenzer - PhD Thesis - TU München 2014

* Work supported by VH-NG-330

Cluster Error of the FOPI TPC*

M. Berger[1] *and the GEM-TPC Collaboration*[1,2,3,4,5]

[1]Physik Department E12, Technische Universität München and Excellence Cluster 'Origin and Structure of the Universe; [2]GSI Helmholtzzentrum für Schwerionenforschung GmbH, Darmstadt, Germany; [3]Helmholtz-Institut für Strahlen- und Kernphysik, Bonn, Germany; [4]Universität Heidelberg, Heidelberg, Germany; [5]Stefan Meyer Institut für Subatomare Physik, Wien, Austria

In past experiments, Time Projection Chambers (TPCs) have been equipped with a gating structure to prevent the migration of avalanche ions created during gas amplification – traditionally realized with Multi Wire Proportional Chambers (MWPCs) – in order to maintain drift field homogeneity. This, however, limited the application of TPCs to experiments with trigger rates smaller than $\mathcal{O}(10^3\,\mathrm{Hz})$. To overcome this limitation a TPC with GEM (Gas Electron Multiplier) foils [1] exploiting their intrinsic ion backflow suppression, has been built [2]. This GEM-TPC has a drift length of 728 mm, an inner radius of 50 mm and an outer radius of 155 mm. For the readout a padplane with hexagonal shaped pads with 1.5 mm radius was used.

For tests with cosmic tracks and different heavy ion beams as well as for a physics experiment with an pion beam the GEM-TPC was employed inside the FOPI spectrometer [3].

To reduce the data rate and to introduce the possibility of an early noise suppression, pad hits are collected in entities called clusters which are defined by an amplitude, a position and a corresponding error. This is done by a full 3D local minima search which is independent of the pad shape or pad plane geometry. The clusters are then passed to the pattern recognition algorithm performing track finding employing a conformal mapping method [4]. Finally, a track can be fitted to these clusters. For this the Kalman Filter implementation provided by the GENFIT [5] framework is used.

For track fitting it is mandatory to have a precise knowledge of the error on the cluster position. By calculating the error for the three spacial directions without taking correlations between them into account one introduces strong dependencies of the track topology. This dependency can be seen in Fig. 1 where the RMS of the cluster error distribution in X direction is plotted for tracks with different azimuth angles but fixed polar angles as a function of the drift length. In this case the error is calculated by:
$Var_i = \frac{1}{A_{\mathrm{Cl}}} \cdot \Sigma A_{\mathrm{Padhit}} \cdot (\mathbf{X}_{\mathrm{Padhit},i} - \mathbf{X}_{\mathrm{Cluster},i})^2$,
and $\sigma_i = \sqrt{\frac{Var_i}{A_{\mathrm{Cl}}}}$.

To eliminate these dependencies a different way to calculate the cluster position errors was introduced. The errors are calculated by first creating the shape matrix:
$\mathbf{M} = \frac{1}{A_{\mathrm{Cluster}}} \Sigma A_{\mathrm{Padhit}} \cdot (\mathbf{X}_{\mathrm{Padhit}} - \mathbf{X}_{\mathrm{Cluster}}) \otimes (\mathbf{X}_{\mathrm{Padhit}} - \mathbf{X}_{\mathrm{Cluster}})$.

* Work supported by BMBF

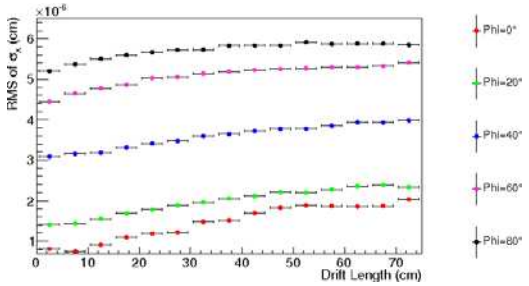

Figure 1: RMS of the standard cluster error distribution for different track topologies (see text) as a function of the drift length.

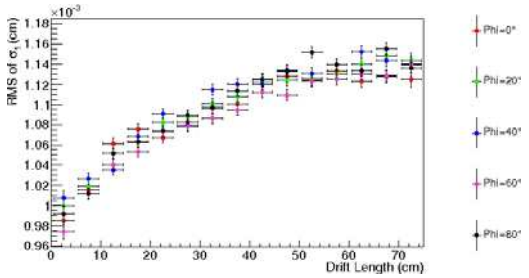

Figure 2: RMS of the matrix cluster error distribution for different track topologies (see text) as a function of the drift length.

This matrix can be seen as an ellipsoid with its three main axes representing the cluster position error. The eigenvectors of the shape matrix describe the direction of the error and the eigenvalues the magnitude. This way, the correlations between the three spacial coordinates can be taken into account. Figure 2 shows the RMS of the magnitude distribution of the first eigenvalue. One can see that the influence of the track topology can now be completely neglected.

References

[1] F. Sauli, NIM A, 386 (1997), 531

[2] L. Fabbietti et al., NIM A, 628 (2011), 204-208

[3] K. Hildenbrand, GSI Nachr. 91-02, 6 (1992)

[4] J. Rauch, Journal of Physics: Conference Series 396 (2012) 022042.

[5] C. Höppner et al., NIM A 620 (2010) 518.

 doi:10.15120/GR-2014-1-NQM-FOPI-04

Discharge probability studies with GEM detectors *

P. Gasik[†1,2], *M. Ball*[1,3], *L. Fabbietti*[1,2], *B. Ketzer*[1,3‡], *J. Margutti*[1,2], *A. Mathis*[1,2], *and S. Weber*[1,2]

[1]TU München, Excellence Cluster 'Origin and Structure of the Universe', Boltzmannstr. 2, 85748 Garching, Germany; [2]TU München, Physik Department E12, James-Franck-Str. 1, 85748 Garching, Germany; [3]TU München, Physik Department E18, James-Franck-Str. 1, 85748 Garching, Germany

GEM (Gas Electron Multiplier) [1] foils are commonly known structures used as proportional counters, which permits to obtain high gains at very high radiation rates. However, highly ionizing particles, which may be produced during heavy ion collisions, may trigger an electrical breakdown which may result in damage of the foils or readout electronics. The key parameter for a long-term operation of the GEM-based detectors for high-intensity beams is the stability against electrical discharges. We have successfully started a dedicated discharge probability studies with multi GEM structures in various gas mixtures to find operational conditions for these type of detectors.

The scheme of experimental setup used for discharge probability studies is shown in Fig. 1. The detector housing contains a GEM stack positioned between a drift cathode and a read-out anode. It is equipped with HV feedthroughs for up to 4 GEM foils. The cathode is made out of a PCB covered with copper layer on one side, where the high potential is applied. Charged particles traversing active area of the detector are ionising gas creating electron-ion pairs. Electrons from the primary ionisation are drifting towards the GEM stack, where the charge amplification occurs. High voltage is applied to the GEM stack via a resistor chain which specifies potential differences across each GEM foil and the values of transfer (E_{T1}, E_{T2}) and induction (E_{IND}) fields. After the amplification process a signal is induced on a single-pad anode plate and then can be processed in different ways, indicated by different readout branches in Fig. 1. Branch a) is for energy spectra and rate measurements. The information about the rate of the primary ionisation together with measurement of the current induced at the anode (branch b) is used to calculate the effective gain of the detector. Branch c) processes raw signals induced on the readout anode and is used to determine number of discharges which occur during the detector operation. The principle of operation is based on fact that signals induced by sparks are by orders of magnitude higher than signals induced by the primary ionisation.

The discharge probability is defined as a ratio of number of detected discharges over the total number of particles irradiating the detector. For our studies the detector is irradiated with highly ionising, 5.59 MeV α particles emitted with a rate of $\sim$0.5 Hz from gaseous ^{222}Rn source randomly distributed within active area of the detector.

So far, the only comprehensive discharge studies in the

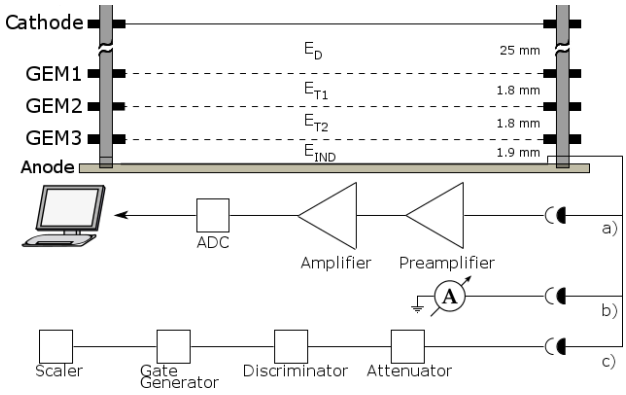

Figure 1: Experimental setup.

Gas Electron Multiplier were reported in [2] and concerns mainly Ar-based gas mixtures. With our setup we performed a set of measurements in a quencher-rich mixture Ar-CO_2 (70-30). Preliminary results are shown in Fig. 2 for a triple GEM irradiated, at high gains of $\mathcal{O}(10^4$-$10^5)$, and compared with data from [2] obtained with the same gas mixture under similar conditions. Our results are in good agreement with the published data.

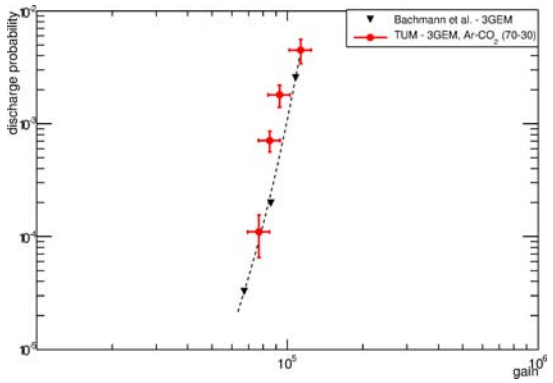

Figure 2: Discharge probability in Ar-CO_2 (70-30).

After the successful commissioning of the setup we are planning a long campaign of discharge probability studies involving measurements in various gas mixtures, employing multi-GEM structures (triple, quadruple), using standard as well as exotic GEM geometries.

References

[1] F. Sauli, NIM **A386** (1997) 531

[2] S. Bachmann et *al.*, NIM **A479** (2002) 294

* Work supported by BMBF

† p.gasik@tum.de

‡ Present affiliation: HISKP, Nussallee 14-16, 53115 Bonn, Germany

Ion backflow studies with a triple GEM detector*

M. Ball† [1,3], *J. Bloemer*[1,3], *K. Eckstein*[1,3], *L. Fabbietti*[1,2], *P. Gasik*[1,2], *D. Heuchel*[1,3], *A. Hoenle*[1,3], *B. Ketzer*‡ [1,3], *J. Margutti*[1,2], *and A. Mathis*[1,2]

[1]Technische Universität München, Germany; [1]TU München, Excellence Cluster 'Origin and Structure of the Universe', Boltzmannstr. 2, 85748 Garching, Germany; [2]TU München, Physik Department E12, James-Franck-Str. 1, 85748 Garching, Germany; [3]TU München, Physik Department E18, James-Franck-Str. 1, 85748 Garching, Germany

Time Projection Chambers (TPCs) are usually equipped with a gating structure to prevent the migration of avalanche ions created during gas amplification – traditionally realized with Multi Wire Proportional Chambers (MWPCs) – in order to maintain drift field homogeneity. This, however, limits the application of TPCs to experiments with trigger rates smaller than $\mathcal{O}(10^3\,\mathrm{Hz})$. To overcome this important limitation introduced by gating techniques, one has to find other means of ion suppression. One promising alternative is to employ a TPC with Gas Electron Multiplier (GEM) [1] instead of MWPC. A first GEM TPC prototype [2, 3] has been succesfully built and operated in FOPI at the GSI, Darmstadt.

For a GEM-TPC in a high rate environment it is mandatory to minimize the ion backflow (IB) as a prerequisite for minimal space charge distortions that allows the maintainance of the excellent TPC performance. The GEM technology has been established in the last decade as a robust and well proven amplification technique for gaseous detectors with an excellent detector performance. The usage of GEM detectors in a high rate TPC, however, is new with regard to several aspects. Many conflicting requirements such as a low ion backflow, good point and energy resolution, low discharge probability as well as stable long term behavior have to be optimized. The challenge is not to find an optimal working point for only one of these parameters, but to define a working point that satifies all requirements within an acceptable limit. In the following only results on ion backflow will be shown. For studies concerning the discharge probability I refer to [4].

Our setup consists of a triple GEM setup. We are using 10×10 cm^2 GEM foils with a pitch of 140 μm, an outer hole diameter of 70 μm, and an inner hole diameter of 50 μm. The effective gain of the system has been kept at 2000 for all measurement. As gas we were using Ne-CO_2-N_2 in the ratio 90-10-5. Neon is advantageous over argon as it has an ion mobility that is 2.5 times higher. As the space charge density is anti-proportional to the ion drift velocity, the higher ion mobility results in a lower space charge density. Figure 1 shows the ion backflow as a function of the first transfer field E_{T1} for several values of the second transfer field E_{T2}. A clear decrease of the ion backflow as a function of E_{T1} is visible due to the higher extraction of electrons out of GEM1 and higher ion blocking efficiency of GEM1 top and bottom electrode. The minimal IB value achieved is about 3 % for an E_{T1} of 5.5 kV/cm and an E_{T2} of 0.2 kV/cm. For a gain of about 2000 this results in a number of back-drifting electrons coming from the amplification system (ε) of about 60 per incoming ion. Present high rate experiments require a much smaller number that is in the order of $\varepsilon \sim 20$.

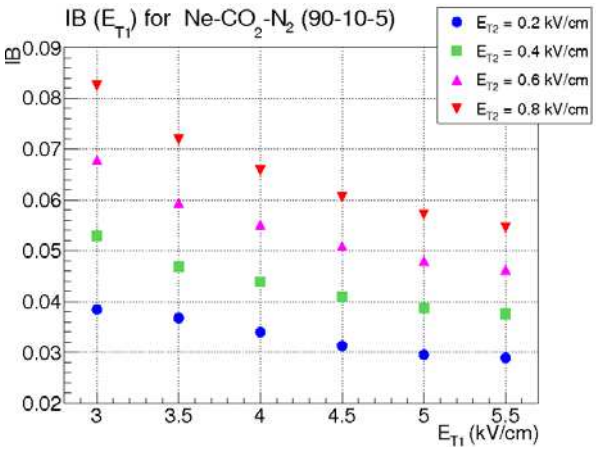

Figure 1: Ion backflow in a triple GEM detector as a function of E_{T1} for several values of E_{T2}.

Future R&D activities will investigate quadruple GEM systems, which is a very promising solution including alternative GEM geometries such as large and small pitch foils. Furthermore Cobra GEMs or a combination of two GEMs and a Micromega might be an interesting options.

References

[1] F. Sauli, *"GEM: A new concept for electron amplification in gas detectors"*, Nucl. Instr. and Meth. A, 386 (1997), p. 531

[2] L. Fabbietti et al., *"The PANDA GEM-based TPC prototype"*, Nucl. Instr. and Meth. A, 628 (2011), pp. 204-208

[3] M. Ball et al., *"Technical Design Study for the PANDA Time Projection Chamber"*, arXiv:1207.0013 (2012)

[4] P. Gasik et al., *"Discharge probability studies with GEM dtectors"*, GSI Scientific Report (2014)

* Work supported by BMBF, EU

† markus.ball@tum.de

‡ Present affiliation HISKP, Bonn, Germany

 doi:10.15120/GR-2014-1-NQM-FOPI-06

Performance of the ALICE Experiment during the LHC Run 1

D. Miśkowiec[1] *for the ALICE Collaboration*
[1]Research Division and EMMI, GSI Darmstadt, Germany

ALICE (A Large Ion Collider Experiment) is a major experiment at the CERN Large Hadron Collider (LHC), built for studies of QCD matter created in high-energy collisions between lead nuclei. ALICE took data for all the collision systems and energies offered by the LHC in its Run 1 (2009-2013) (Table 1) and published ∼70 physics articles [1]. The ongoing LHC shutdown provides an opportunity to assess the performance of the experiment [2].

Table 1: Data sets recorded by ALICE in 2009–2013. The quoted statistics is that of minimum-bias and centrality-triggered events before the quality cuts.

system	$\sqrt{s_{\rm NN}}$	recorded statistics
pp	0.9 TeV	9×10^6 events
pp	2.76 TeV	100×10^6 events
pp	7-8 TeV	1.4×10^9 events
Pb–Pb	2.76 TeV	100×10^6 events
p–Pb	5.02 TeV	140×10^6 events

The ALICE group at GSI is strongly involved in two major detectors of the central barrel, the Time Projection Chamber (TPC) and the Transition Radiation Detector (TRD). These two large-volume gas-drift detectors require care during data taking and a sophisticated calibration. The tracking performance of the TPC was as expected; the particle identification power even exceeded the expectations. Figure 1 illustrates the latter by showing the identification of anti-alpha particles, first such measurement at the LHC and contemporaneous with the analogous RHIC result.

The response of the TRD detector is shown in Fig. 2. Measurements performed in ALICE with electrons, pions,

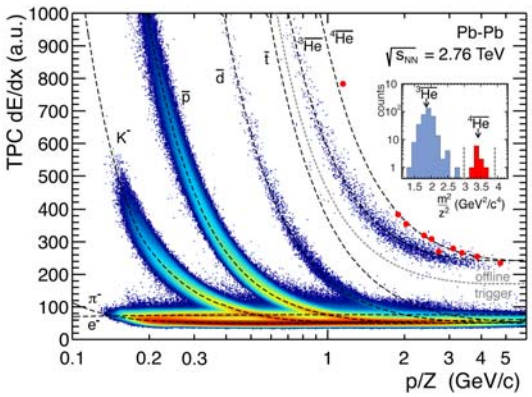

Figure 1: Particle identification in the TPC. The inset plot shows the additional separation between $^3\overline{\rm He}$ and $^4\overline{\rm He}$ for tracks with p/Z>2.3 GeV/c provided by TOF.

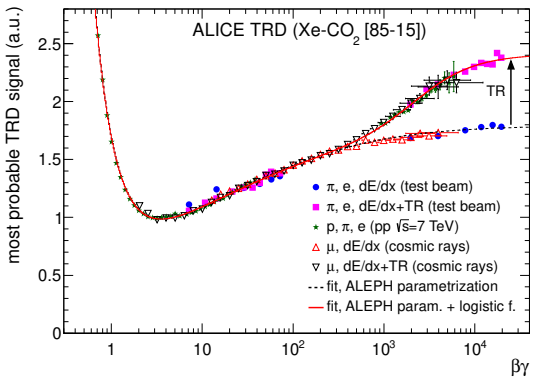

Figure 2: The TRD signal as a function of $\beta\gamma$.

and protons from pp collisions, as well as with cosmic muons, agree with the results from the chamber tests done with electron and pion beams. The lower branch represents the chamber signal without the contribution of the transition radiation, measured during the chamber tests by removing the radiator and in the ALICE setup by selecting those cosmic muons that entered the detector from outside.

Table 2 compares the observed performance with the expectations. An extensive performance report is in Ref. [2].

Table 2: The expected [3] and achieved [2] performance of the ALICE detectors for selected observables.

parameter	expected	achieved
event vertex resolution with ITS–TPC tracks		
trans. vertex resol. at $\mathrm{d}N_{\rm ch}/\mathrm{d}\eta = 5$	85 μm	97 μm
trans. vertex resol. at $\mathrm{d}N_{\rm ch}/\mathrm{d}\eta = 25$	35 μm	32 μm
DCA resolution of ITS–TPC tracks in central Pb–Pb coll.		
trans. DCA resol. at $p_{\rm T} = 0.3$ GeV/c	200 μm	200 μm
trans. DCA resol. at $p_{\rm T} = 20$ GeV/c	15 μm	15 μm
barrel $p_{\rm T}$ resolution		
$\Delta p_{\rm T}/p_{\rm T}$ ITS–TPC $p_{\rm T} = 10$ GeV/c	1–2%	1.5%
$\Delta p_{\rm T}/p_{\rm T}$ ITS–TPC $p_{\rm T} = 30$ GeV/c	2–3%	2.5%
barrel particle identification		
TPC $\mathrm{d}E/\mathrm{d}x$ resol. in pp	5.4%	5.2%
TPC $\mathrm{d}E/\mathrm{d}x$ resol. in central Pb–Pb	6.8%	6.5%
TOF resolution	80 ps	80 ps

References

[1] `http://aliceinfo.cern.ch/ArtSubmission/publications`
[2] ALICE Collaboration, arXiv:1402.4476 [nucl-ex]
[3] ALICE Collaboration, J. Phys. **G 32**, 1295 (2006)

Multiplicity dependence of the average transverse momentum in pp, p–Pb, and Pb-Pb collisions at the LHC*

A. Andronic[1], *J. Gronefeld*[1,2], *M.L. Knichel*[1], *P. Lüttig*[3], *M. Marquard*[3], *D. Miśkowiec*[1], *J. Otwinowski*[1], *K. Schweda*[1] *for the ALICE Collaboration*

[1]EMMI & GSI Darmstadt; [2]Technische Universität Darmstadt; [3]Universität Frankfurt

One of the key ways of investigating particle production in high-energy hadron collisions is to measure the relationship between the number, or multiplicity, of particles produced and their momentum transverse to the direction of the colliding beams. The results cast light on processes ranging from the interactions of individual partons (quarks and gluons) to the collective motion of hot, dense matter containing hundreds of partons. We have investigated, using data collected with ALICE in proton-proton (pp), proton-lead (p–Pb) and lead-lead collisions (Pb–Pb) at the LHC, the first moment, $\langle p_{\rm T} \rangle$, of the charged-particle transverse momentum spectrum and its correlation with the charged-particle multiplicity $N_{\rm ch}$ [1].

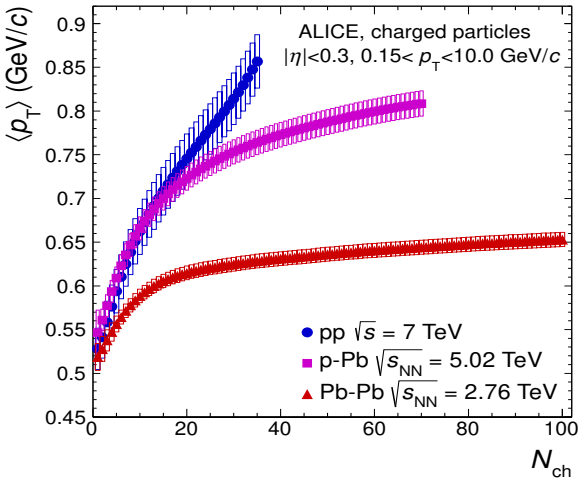

Figure 1: Average transverse momentum $\langle p_{\rm T} \rangle$ versus charged-particle multiplicity $N_{\rm ch}$ in pp, p–Pb, and Pb–Pb collisions for $|\eta| < 0.3$. The boxes represent the systematic uncertainties on $\langle p_{\rm T} \rangle$. The statistical errors are negligible.

Figure 1 shows the average transverse momentum $\langle p_{\rm T} \rangle$ of charged particles versus the charged-particle multiplicity $N_{\rm ch}$ measured in pp collisions at $\sqrt{s}$ = 7 TeV, in p–Pb collisions at $\sqrt{s_{\rm NN}}$ = 5.02 TeV, and in Pb–Pb collisions at $\sqrt{s_{\rm NN}}$ = 2.76 TeV. We note that the same $N_{\rm ch}$ value corresponds to a very different collision regime in the three systems. The p–Pb data exhibit features of both pp and Pb–Pb collisions, at low and high multiplicities, respectively. The saturation trend of $\langle p_{\rm T} \rangle$ versus $N_{\rm ch}$ is less pronounced in p–Pb than in Pb–Pb collisions and leads to a much higher value of $\langle p_{\rm T} \rangle$ at high multiplicities than in Pb–Pb.

* Work supported by GSI, BMBF, Helmholtz Alliance HA216/EMMI, H-QM, and HGS-HIRe

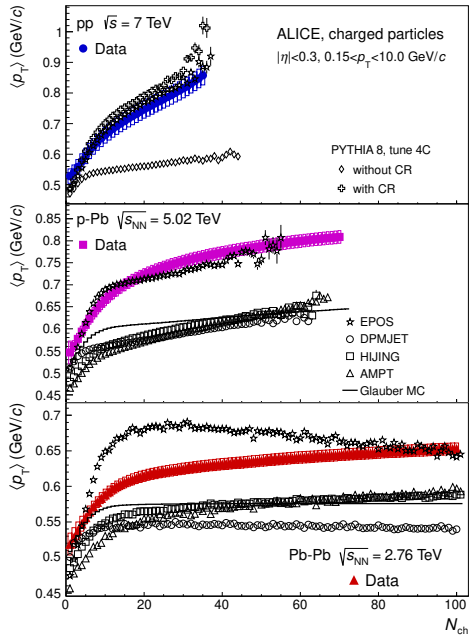

Figure 2: Average transverse momentum $\langle p_{\rm T} \rangle$ as a function of charged-particle multiplicity $N_{\rm ch}$ measured in pp (upper panel), p–Pb (middle panel), and Pb–Pb (lower panel) collisions in comparison to model calculations.

Figure 2 shows a comparison of the data to model predictions (see references in [1]). The strong correlation of $\langle p_{\rm T} \rangle$ with $N_{\rm ch}$ is reproduced in the PYTHIA event generator with the mechanism of color reconnections between hadronizing strings. This can be interpreted as a collective final-state effect, in which strings from independent parton interactions do not independently produce hadrons, but fuse prior to hadronization. This leads to fewer, but more energetic, hadrons. The EPOS model, which implements collective behavior in pp collisions, also describes the pp data. Remarkably, also p–Pb collisions are well described, while for Pb–Pb collisions there is a significant discrepancy between model and data. A Glauber Monte Carlo model for p–Pb and Pb-Pb collisions, with inputs from pp data, fails to describe the data. These data are an essential input to improve our understanding of particle production as well as the role of initial and final state effects in these systems.

References

[1] ALICE Collaboration, B. B. Abelev *et al.*, Phys. Lett. **B727**, 371 (2013).

 doi:10.15120/GR-2014-1-NQM-ALICE-02

Nuclear Modification Factor and Centrality Determination in p-Pb Collisions at ALICE *

A. Andronic[1], *J. Gronefeld*[1,2], *M.L. Knichel*[1], *P. Lüttig*[3], *J. Otwinowski*[1] *for the ALICE Collaboration*
[1]EMMI & GSI Darmstadt; [2]Technische Universität Darmstadt; [3]Universität Frankfurt

In the ALICE detector at the LHC the physics of the Quark-Gluon-Plasma is investigated, in collisions of lead nuclei. In those collisions not only the created medium but also cold nuclear matter could play a role. The influence of this is investigated by using proton-lead (p–Pb) collisions and calculating the nuclear modification factor R_{pPb}, which is defined as:

$$R_{\mathrm{pPb}}(p_{\mathrm{T}}) = \frac{1}{\langle T_{\mathrm{pPb}} \rangle} \frac{d^2 N_{ch}^{pPb}/d\eta dp_{\mathrm{T}}}{d^2 \sigma_{ch}^{pp}/d\eta dp_{\mathrm{T}}} \qquad (1)$$

In this formula N_{ch}^{pPb} represents the multiplicity of charged particles in pPb collisions while σ_{ch}^{pp} describes the cross section in proton-proton (pp) collisions. T_{pPb} is the nuclear overlap function calculated with Glauber Monte Carlo. In case of minimum bias (MB) collisions, the nuclear overlap function is $T_{\mathrm{pPb}} = 0.0983 \pm 0.0035\,\mathrm{mb}^{-1}$.
In Fig. 1 the measurement of R_{pPb} at $|\eta_{\mathrm{cms}}| < 0.3$ is compared to shadowing calculations [2] and to predictions in a framework combining leading order (LO) pQCD and cold nuclear matter effects [3]. The predictions for shadowing, performed at NLO with the EPS09s Parton Distribution Functions and DSS fragmentation functions, describe the data very well (the calculations are for π^0), while the LO pQCD model exhibits a trend of decreasing R_{pPb}, which is not supported by the data.

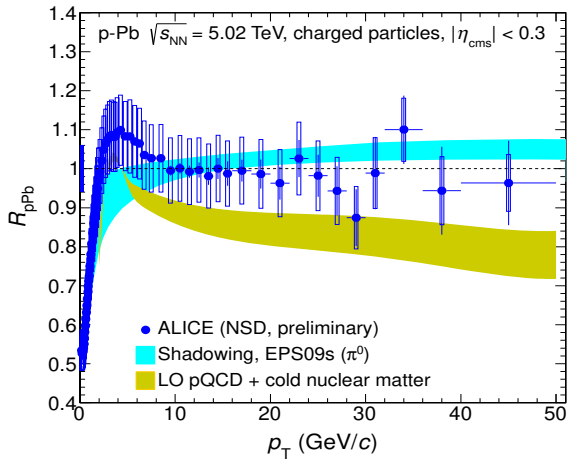

Figure 1: The measured R_{pPb} compared to model calculations.

While in Pb–Pb collisions centrality determination is straightforward, it remains more difficult in p–Pb collisions. Centrality is determined by measuring the multiplicity of particles with different detector systems within the ALICE apparatus [4]. Figure 2 shows the biased nuclear modification factor Q_{pPb} for two different estimators. ZNA relies on the forward neutron calorimeter located 114 m away from the interaction point, while V0A relies on a forward detector much closer to the interaction point.

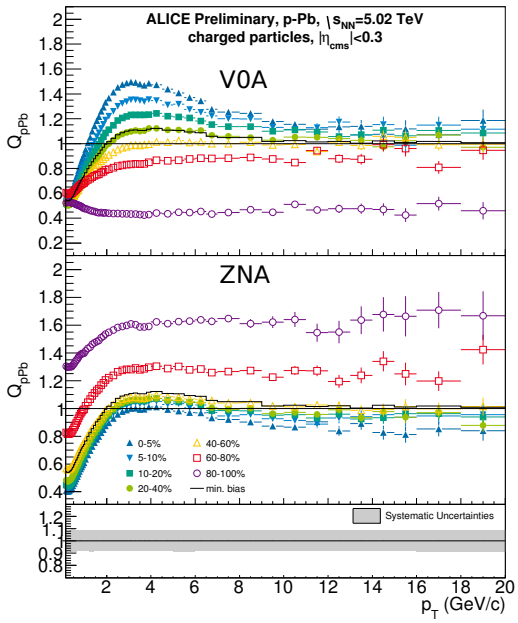

Figure 2: The transverse momentum dependence and the dependence on centrality of the biased nuclear modification factor Q_{pPb} for two different centrality estimators ZNA (upper panel) and V0A (middle panel).

The large difference between the estimators shows, that different events are selected in the different centrality classes. This shows that the geometrical correspondence of experimental centrality selection remains a challenge.

References

[1] ALICE Collaboration, B. B. Abelev *et al.*, Phys. Rev. Lett. **110**, 082302 (2013).

[2] I. Helenius et al., JHEP **1207**, 073 (2012).

[3] Z.-B. Kang et al., Phys. Lett. **B718**, 482 (2012).

[4] A. Morsch, arXiv: 1309.5525

* Work supported by GSI, BMBF, Helmholtz Alliance HA216/EMMI, H-QM, and HGS-HIRe

Measurement of charged jets in p-Pb collisions with ALICE

R. Haake[*1], *J. Anielski*[1], *B. Bathen*[1], *L. Feldkamp*[1], *M. Heide*[1], *P. Kähler*[1], *C. Klein-Bösing*[1,2], *M. Kohn*[1], *D. Mühlheim*[1], *A. Passfeld*[1], *H. Poppenborg*[1], *J. P. Wessels*[1], *U. Westerhoff*[1], *and M. Wilde*[1]

[1]Institut für Kernphysik, University of Münster, Germany; [2]ExtreMe Matter Institute EMMI, GSI Darmstadt, Germany

Highly energetic jets are sensitive probes for the kinematics and the topology of high energy collisions. Jets originate from high-momentum partons that are produced early in the collision and subsequently fragment into collimated sprays of hadrons.

The measurement of jet production in p-Pb collisions provides an ideal tool to study the effects of cold nuclear matter on hadronization and provides constraints for the nuclear parton density functions. In addition, the measurements of jet properties in p-Pb collisions can also serve as an important reference for Pb-Pb collisions. [1]

Our analysis focuses on charged jets in p-Pb collisions. The analyzed data – roughly 100 million minimum bias events – was taken in the beginning of 2013 with the ALICE detector at $\sqrt{s_{\mathrm{NN}}} = 5.02$ TeV. The charged constituents of the jets are reconstructed mainly using the Time Projection Chamber (TPC) and the Inner Tracking System (ITS). Tracks with $p_{\mathrm{T}} > 0.150$ GeV/c and within a pseudorapidity interval $|\eta| < 0.9$ were used. The minimum bias events are selected by demanding at least one hit in both of the scintillator trigger detectors (V0A and V0C).

For our analyses, the FastJet [2] package is used in conjunction with the anti-k_{T} algorithm to clusterize the tracks into jets using a jet resolution parameter of $R = 0.4$. Those jets have to be corrected for the background momentum density, the fluctuation of those, and for detector effects. The background density is estimated event-by-event using a similar ansatz as in reference [3]. The within-event background fluctuations are determined using a random cone approach. Detector effects, e.g. including the tracking efficiency, are corrected via unfolding with a response matrix from a full detector simulation with PYTHIA and GEANT3. The *Singular Value Decomposition* unfolding technique is applied by using the RooUnfold package.

The two basic observables of our analysis are given by the nuclear modification factor R_{pPb} and the jet shape ratio. The latter is just the ratio of the spectra using $R = 0.2$ and $R = 0.4$ and is a measure for the collimation of jets in p-Pb collisions. R_{pPb} is defined by

$$R_{\mathrm{pPb}} = \frac{\text{pPb yield}}{\text{pp x-section}} \cdot \frac{1}{T_{\mathrm{pPb}}}, \qquad (1)$$

and relates to pp collisions. T_{pPb} accounts for the increased "parton luminosity" in p-Pb and is calculated using the Glauber model.

Since pp data at 5 TeV is not available, the necessary pp cross section is created by scaling of 7 TeV pp data. The scaling is done using PYTHIA at the two energies.

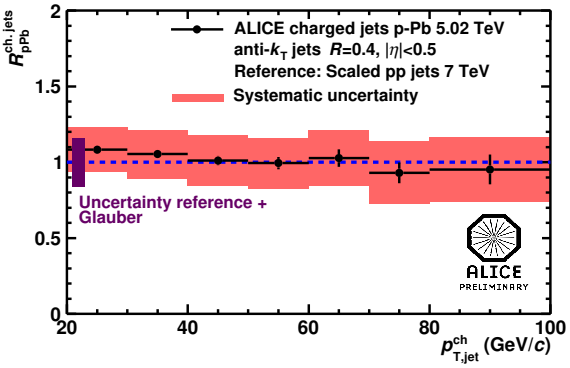

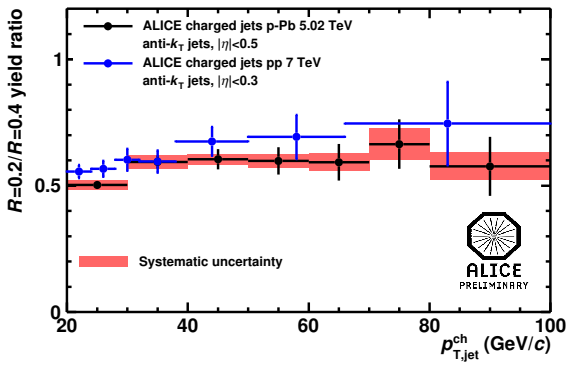

The nuclear modification factor R_{pPb} is shown up to $p^{\mathrm{ch}}_{\mathrm{T,jet}} = 100$ GeV/c and no strong nuclear effects on the jet spectra are visible – it is compatible with no effect. The jet shape ratio $R = 0.2/0.4$ is compatible with 7 TeV pp data and it can be shown that it is also compatible with the predictions from PYTHIA Perugia 2011 at the same energy. There is no indication for a nuclear modification of the jet structure in p-Pb reactions between $R = 0.2$ and 0.4.

References

[1] The ALICE Collaboration: [nucl-ex/1311.0633].

[2] M. Cacciari / G.P. Salam: [hep-ph/0512210].

[3] The CMS Collaboration: [hep-ex/1207.2392].

*ruediger.haake@uni-muenster.de

 doi:10.15120/GR-2014-1-NQM-ALICE-04

Measurement of electrons from charm and beauty-hadron decays in p-Pb collisions at $\sqrt{s_{\rm NN}}$ = 5.02 TeV with ALICE at the LHC *

R. Averbeck[1], M. Fasel[2,3], S. Masciocchi[1], Y. Pachmayer[2], J. Wagner[1] for the ALICE Collaboration

[1]Research Division and ExtreMe Matter Institute, GSI Helmholtzzentrum für Schwerionenforschung GmbH, Darmstadt, Germany; [2]Physikalisches Institut, Ruprecht-Karls Universität Heidelberg, Germany; [3]Frankfurt Institute for Advanced Studies, Frankfurt, Germany

The characterisation of the Quark-Gluon Plasma (QGP), the deconfined state of strongly-interacting matter produced in high-energy heavy-ion collisions, is the main purpose of ALICE at the LHC. Because of their large masses, charm and beauty quarks are mostly produced in initial hard partonic interactions and thus can be used to probe the medium created in such collisions. The $p_{\rm T}$ differential heavy-flavour yield is sensitive to the energy loss of heavy quarks in the hot and dense medium. Also, the presence of cold nuclear matter in the initial state may affect the production of heavy-flavour hadrons. With a measurement of the nuclear modification factor $\rm R_{pPb}$ in p–Pb collisions, the initial-state effects can be quantified. Because of large branching ratios to semi-leptonic decay channels, heavy-flavour production can be studied via an inclusive electron measurement.

The electron identification strategy involves a combination of the Time Projection Chamber (TPC) and the Time-of-Flight detector (TOF). In the TPC charged particles are identified via their specific energy loss $\mathrm{d}E/\mathrm{d}x$ in the drift gas. Due to overlapping $\mathrm{d}E/\mathrm{d}x$ bands from kaons, protons and deuterons, a large hadron contamination is persistent. At low momentum ($p < 2\,\mathrm{GeV}/c$), TOF is used to separate nearly massless electrons from kaons and protons by their time of flight to the detector. In Fig. 1 the $\mathrm{d}E/\mathrm{d}x$ in the TPC, relative to the expected $\mathrm{d}E/\mathrm{d}x$ for electrons, is shown. The kaon and proton bands, visible in the top left of the plot, are suppressed due to the use of the TOF information.

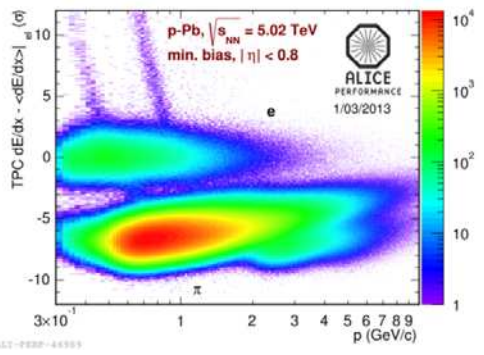

Figure 1: TPC $\mathrm{d}E/\mathrm{d}x$ as deviation from the expected energy loss of electrons, normalized by the $\mathrm{d}E/\mathrm{d}x$ resolution, after TOF selection of charged particle tracks.

Electrons from background sources have to be subtracted from the inclusive electron spectrum to obtain the heavy-flavour electron spectrum. The main sources of these background electrons are Dalitz decays of π^0 and η mesons or conversions of photons in the detector material. This background can be calculated based on the measured pion spectrum or measured by reconstructing electrons from photonic sources (γ conversions, π^0, η) using the invariant mass of $\mathrm{e^+e^-}$ pairs. Corrections for detector efficiency and acceptance are estimated with a full detector simulation.

In order to obtain a pp reference the cross section measured at $\sqrt{s_{\rm NN}}$ = 7 TeV [1] was scaled to 5.02 TeV based on a FONLL perturbative QCD calculation [2]. Fig. 2 shows the $\rm R_{pPb}$ measured with ALICE for electrons from heavy-flavour hadron decays together with predictions from pQCD calculations including shadowing effects from cold nuclear matter, calculated on the base of the EPS09 parametrization [3]. The ALICE result is consistent with this calculation and with unity within the current substantial uncertainties of the measurement, indicating that cold nuclear matter effects are small.

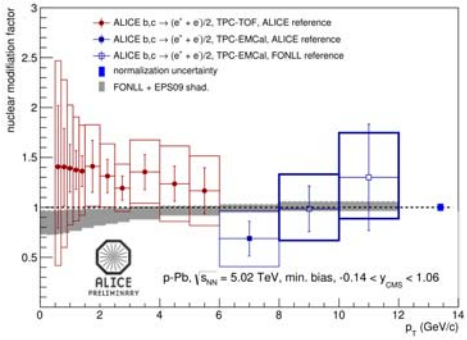

Figure 2: $\rm R_{pPb}$ of electrons from heavy-flavour decays with shadowing predictions calculated on the base of the EPS09 parametrization [3].

References

[1] B. Abelev et al. (ALICE Collaboration) *Phys. Rev. D*, 86:112007, Dec 2012.

[2] R. Averbeck et al. arXiv:1107.3243 [hep-ph], Jul 2011

[3] K.J. Eskola et al., *JHEP*, 0904:065, 2009.

* Work supported by GSI, BMBF, Helmholtz Alliance HA216/EMMI, HQM, and HGS-HIRe

J/ψ production in p-Pb collisions measured with ALICE at the LHC*

M. Winn[1], A. Andronic[2], I. Arsene[2,6], C. Blume[3], J. Book[3], P. Braun-Munzinger[2,4], A. Maire[1,7], J. Stachel[1], S. Weber[2], J. Wiechula[5] for the ALICE Collaboration

[1]Universität Heidelberg; [2]EMMI & GSI Darmstadt; [3]Universität Frankfurt; [4]Technische Universität Darmstadt; [5]Universität Tübingen; [6]University of Oslo; [7]Université de Strasbourg

Charmonium production in proton-nucleus (pA) collisions is a crucial ingredient for the interpretation of J/ψ production in nucleus-nucleus (AA) collisions, where it is a prominent probe of deconfinement. The measurement of modifications of the J/ψ yield in pA collisions with respect to proton-proton (pp) collisions give access to nuclear effects, which are commonly not attributed to the presence of a deconfined medium.

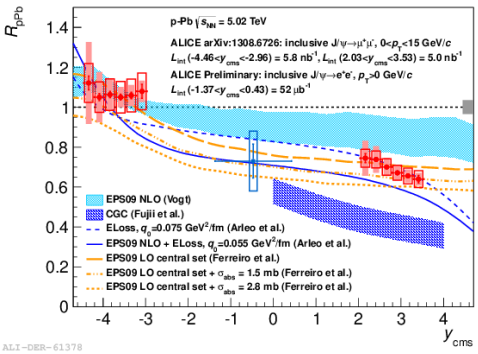

Figure 1: Nuclear modification factor for J/ψ production in p-Pb collisions measured by ALICE compared to theoretical models. The error bars represent the statistical uncertainty, the boxes the uncorrelated systematic uncertainties and the filled areas the partially correlated systematic uncertainties.

ALICE is unique among the detectors at LHC, since it accesses charmonium production down to transverse momentum $p_{\rm T}$=0 at mid-rapidity ($|y_{\rm lab}| < 0.9$) in the dielectron decay channel.

Preliminary results of inclusive $p_{\rm T}$-integrated and $p_{\rm T}$-differential cross sections and nuclear modification factors at mid-rapidity were released based on the proton-lead (p-Pb) collisions recorded at $\sqrt{s_{\rm NN}} = 5.02$ TeV with a minimum bias collision trigger in early 2013. They complement the measurements carried out in Pb-Pb [1] and pp [2–5] collisions.

Figure 1 compares the experimental data with theory predictions. The result at mid-rapidity is shown together with the result in the dimuon decay channel at forward and backward rapidity [6]. The measurements are consistent with predictions based on parametrisations of nuclear Parton Distribution Functions (nPDF) including moderate gluon shadowing [7,8] and on coherent energy loss [9]. The color class condensate model is disfavoured by data [10].

The $p_{\rm T}$-differential $R_{\rm pA}$ is depicted in Fig. 2. The result is consistent with theoretical models based on shadowing [7].

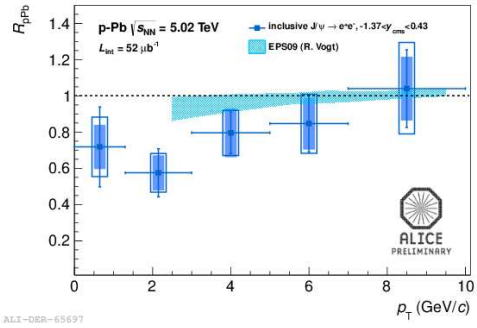

Figure 2: The nuclear modification factor as a function of transverse momentum compared with calculations by R.Vogt. The uncertainty denotations are analogous to Fig. 1.

Further analyses on J/ψ production are ongoing in the p-Pb collision system. The fraction $f_{\rm B}$ of J/ψ at mid-rapidity from decays of hadrons carrying bottom quarks and the dependence of J/ψ production on the charged hadron multiplicity will be measured. The acquired data sample with TRD triggers in p-Pb collisions at mid-rapidity will increase the available statistics for transverse momenta of J/ψ larger than 1 GeV/c [11].

References

[1] B. Abelev *et al.* [ALICE Collaboration], arXiv:1311.0214, see also I. Arsene *et al.*, this Report.

[2] K. Aamodt *et al.* [ALICE Collab.], Phys. Lett. B **704** (2011) 442 [Erratum-ibid. B **718** (2012) 692]

[3] B. Abelev *et al.* [ALICE Collab.], JHEP **1211** (2012) 065

[4] B. Abelev *et al.* [ALICE Collab.], Phys. Lett. B **718** (2012) 295

[5] B. Abelev *et al.* [ALICE Collab.], Phys. Lett. B **712** (2012) 165

[6] B. Abelev *et al.* [ALICE Collab.], arXiv:1308.6726, accepted for publication in JHEP

[7] J.L. Albacete *et al.*, Int. J. Mod. Phys. **E22** (2013) 1330007 and private communication with R. Vogt

[8] E. G. Ferreiro *et al.*, Phys. Rev. C **88** (2013) 047901

[9] F. Arleo and S. Peigné, JHEP **1303** (2013) 122

[10] H. Fujii and K. Watanabe, Nucl. Phys. A **915** (2013) 1

[11] J. Klein for the ALICE Collaboration, arXiv:1112.5110

* Work supported by GSI, BMBF, Helmholtz Alliance HA216/EMMI, HQM, HGSFP, HGS-HIRe and the Studienstiftung des deutschen Volkes

 doi:10.15120/GR-2014-1-NQM-ALICE-06

J/ψ production in Pb-Pb collisions measured with ALICE*

I.C. Arsene[1,6], A. Andronic[1], C. Blume[2], J. Book[2], P. Braun-Munzinger[1,3], A. Maire[4,7], J. Stachel[4], S. Weber[1], J. Wiechula[5], M. Winn[4] for the ALICE Collaboration

[1]EMMI & GSI Darmstadt; [2]Universität Frankfurt; [3]Technische Universität Darmstadt; [4]Universität Heidelberg; [5]Universität Tübingen; [6]University of Oslo; [7]Université de Strasbourg

Heavy quarkonium production is a prime probe for the investigation of the deconfined nuclear medium created during ultra-relativistic nuclear collisions, also dubbed quark-gluon plasma. Early predictions assumed that, depending on their binding energy, some of the quarkonium states melt in such a hot and dense medium due to colour screening [1]. At the LHC energies, and to a smaller extent at the RHIC top energy, the large number of charm quark pairs produced in the initial partonic interactions open the possibility for creating charmonium by combining $c\bar{c}$ pairs during the lifetime of the fireball [2] or at its phase boundary (chemical freeze-out) [3].

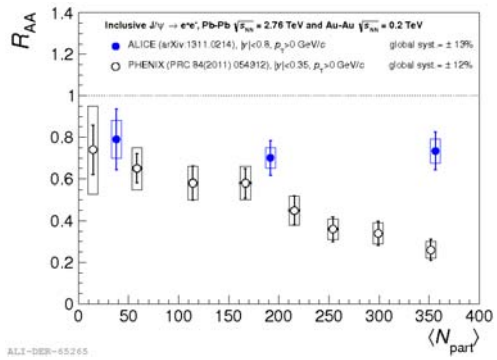

Figure 1: Centrality dependence of the R_{AA} for inclusive J/ψ measured by ALICE and PHENIX.

ALICE is a very well suited detector to measure J/ψ mesons via their di-leptonic decay channels [4] in a wide range of rapidity and down to zero transverse momentum. The nuclear effects on the J/ψ production are quantified using the nuclear modification factor, R_{AA}, which is the ratio between the yields obtained in nuclear collisions and the yield in pp collisions scaled by the number of binary nucleon-nucleon collisions corresponding to a given collision centrality.

Figure 1 shows the inclusive J/ψ R_{AA} at mid-rapidity as a function of the number of nucleons participating in the collision. The ALICE results [5] are obtained for Pb-Pb collisions at $\sqrt{s_{NN}} = 2.76$ TeV while the PHENIX [6] ones come from Au-Au collisions at $\sqrt{s_{NN}} = 0.2$ TeV. The lower energy data shows an increasing suppression of the J/ψ yield with increasing the collision centrality, being very suggestive of the colour screening effect predicted in [1]. The ALICE results indicate a much smaller suppression for larger system sizes and, within the uncertainties, no centrality dependence. The striking difference in R_{AA} in central collisions indicates that a new mechanism, namely charm quarks (re)combination, is at play at LHC energies.

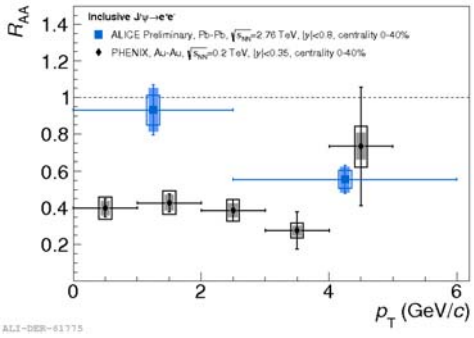

Figure 2: Transverse momentum dependence of the R_{AA} for inclusive J/ψ measured by ALICE and PHENIX.

In figure 2, we show the p_T dependence of the J/ψ R_{AA} for the 40% most central collisions from both ALICE and PHENIX. Our data is compatible with no suppression in the low p_T region ($p_T < 2.5$ GeV/c), opposite to the strong suppression seen at the RHIC top energy. At higher p_T, the J/ψ R_{AA} obtained by ALICE drops to ≈ 0.5 and is compatible with the one observed by PHENIX. If J/ψ mesons would be formed via the coalescence or statistical hadronisation of charm quarks, it is expected from phase space considerations that these mechanisms contribute especially in the low p_T region, as observed in our data.

These results, together with the ones obtained at forward rapidity in the di-muon channel [5], provide important evidence for deconfinement and for a new mechanism of charmonium creation. Further studies on understanding the cold nuclear matter effects using p-Pb collisions are currently ongoing [7].

References

[1] T. Matsui and H. Satz, Phys. Lett. B **178** (1986) 416

[2] R. L. Thews, M. Schroedter and J. Rafelski, Phys. Rev. C **63** (2001) 054905

[3] P. Braun-Munzinger and J. Stachel, Phys. Lett. B **490** (2000) 196

[4] ALICE Collaboration, arXiv:1402.4476

[5] ALICE Collaboration, arXiv:1311.0214

[6] PHENIX Collaboration, Phys. Rev. C **84** (2011) 054912

[7] M. Winn *et al.*, this Report

* Work supported by GSI, BMBF, Helmholtz Alliance HA216/EMMI, HQM, HGSFP, HGS-HIRe and the Studienstiftung des deutschen Volkes

Azimuthal correlation measurements with ALICE at the LHC *

M. Krzewicki[1,2], J. Onderwaater[1,2], and I. Selyuzhenkov[1,2] for the ALICE Collaboration

[1]ExtreMe Matter Institute EMMI and GSI Helmhotzzentrum für Schwerionenforschung, Darmstadt; [2]Frankfurt Institute for Advanced Studies (FIAS), Germany

Anisotropic flow in heavy-ion collisions is a key observable related to the early time evolution of the nucleus-nucleus interaction. We report on recent results of the ALICE Collaboration at the LHC on the directed flow of charged particles relative to the spectator plane in Pb-Pb collisions at $\sqrt{s_{\rm NN}} = 2.76$ TeV. Also recent findings from the search for effects of local parity violation in the strong interaction are presented.

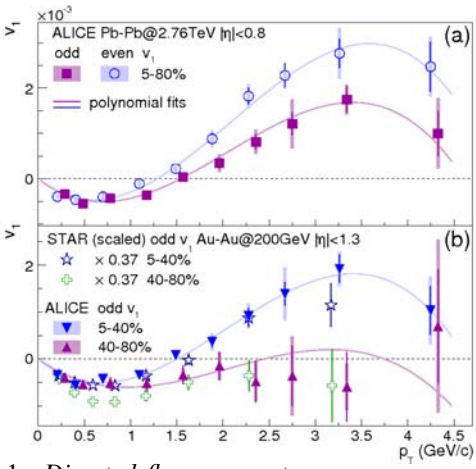

Figure 1: *Directed flow versus transverse momentum in Pb–Pb collisions at $\sqrt{s_{\rm NN}} = 2.76$ TeV. (a) v_1 for 5-80% centrality range. (b) $v_1^{\rm odd}$ in Pb-Pb collisions compared to Au-Au collisions at RHIC at $\sqrt{s_{\rm NN}} = 200$ GeV downscaled with a factor 0.37.*

Directed flow, v_1, is a probe of the spatial orientation and fluctuations of the shape of the fireball created in a heavy-ion collision. The observed negative slope [1] of the rapidity-odd v_1 component is about three times smaller than observed at the highest RHIC energy, suggesting a smaller longitudinal tilt of the initial system and disfavours the picture of strong fireball rotation predicted at the LHC energies. Measured for the first time with respect to the spectator nucleons, the rapidity-even v_1 component is found to be independent of pseudorapidity and changes sign at transverse momenta around $1.2 - 1.7$ GeV/c (figure 1). This is expected for dipole-like energy fluctuations when momentum of the low $p_{\rm T}$ particles is balanced by that of the high $p_{\rm T}$ particles. The magnitude of the rapidity-even v_1 w.r.t. the participant plane has a similar shape, but is a factor of forty larger, which indicates that fluctuating participant and spectator planes are weakly correlated. Compared to the measurements at the highest RHIC energy, in figure 1(b), $v_1^{\rm odd}$ shows a similar trend including the sign change around $p_{\rm T} \sim 1.5$ GeV/c in central collisions and negative value at all $p_{\rm T}$ for peripheral collisions.

*Supported by GSI, BMBF, HGS-HIRe, and Helmholtz Alliance HA216/EMMI

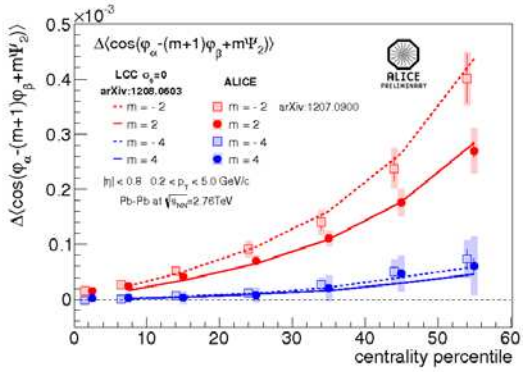

Figure 2: *Centrality dependence of the correlation $\Delta\langle\cos[\varphi_\alpha - (m+1)\varphi_\beta + m\Psi_2]\rangle$ in comparison with the Blast Wave model incorporating effects of local charge conservation. Δ denotes the difference between same and opposite charge correlations.*

The parity symmetry violation in strong interactions remains one of the open fundamental questions about QCD. It is argued that parity symmetry can be locally violated in a heavy-ion collision which will result in an experimentally observable separation of charges along the extreme magnetic field generated by the moving ions, the so called chiral magnetic effect (CME). An experimental probe of CME are the azimuthal correlations with respect to the collision reaction plane which is perpendicular to that magnetic field.

ALICE observed a clear charge dependence of the two-particle correlation with respect to the reaction plane [2]. This can be due to a number of other charge-dependent effects which preserve parity, such as local charge conservation (LCC). Higher order charge-dependent correlations help to disentangle parity conserving contributions from CME. Recent ALICE results, in figure 2 , show that models which combine LCC and the radial expansion of the medium, while failing to describe the correlation $\Delta\langle\cos n(\phi_\alpha - \phi_\beta)\rangle$ in figure 3 [3]), give a good description of the correlations shown in figure 2 up to higher orders. This suggests that a significant fraction of the observed two-particle correlation may be due to LCC. A study of charge-dependent correlations with identified particles was also recently started to further disentangle the CME and LCC contributions.

References

[1] B. Abelev *et al.* [ALICE Collaboration], Phys. Rev. Lett. **111** (2013) 232302

[2] B. Abelev *et al.* [ALICE Collaboration], Phys.Rev.Lett. **110** (2013) 012301

[3] Y. Hori [ALICE Collaboration], Nucl. Phys. A904-905 **2013** (2013) 475c

 doi:10.15120/GR-2014-1-NQM-ALICE-08

Deuteron production in Pb–Pb collisions measured with ALICE at the LHC*

B. Dönigus[†1], *A. Kalweit*[2], *N. Martin*[3,4] *for the ALICE Collaboration*

[1]Institut für Kernphysik, Goethe-Universität Frankfurt, Frankfurt, Germany; [2]European Organization for Nuclear Research (CERN), Geneva, Switzerland; [3]ExtreMe Matter Institute EMMI and Research Division, GSI Helmhotzzentrum für Schwerionenforschung, Darmstadt, Germany; [4]Institut für Kernphysik, Technische Universität Darmstadt, Darmstadt, Germany

Heavy-ion collisions at the LHC give the opportunity to measure all known particles in higher abundances than it was possible before, like for example light nuclei. These heavy particles are rarely produced, because the production probability decreases with increasing mass. But the energy regime reached at the LHC leads to large production probabilities even for these particles, as described for example by thermal models [1, 2]. The excellent performance of the Time-Projection Chamber (TPC) [3] and the Time-Of-Flight detector (TOF) [4] allows for the clear identification of charged stable particles over a range of 0.15 to 5 GeV/c in rigidity $R = p/z$, where p is the track momentum and z is the charge number. The measurement of deuterons is affected by a large background, as for all nuclei, coming from knockout from material. Rejection of this background is possible by restricting the distance-of-closest-approach (dca) of the track to the primary vertex in z-direction dca_z and then fitting the dca_{xy} distribution to extract the signal in the transverse momentum (p_{T}) window between 0.6 and 1.9 GeV/c (technique is described in more detail in [6]). The deuterons are identified using only the specific energy loss (dE/dx) measurement in the TPC for $p_{\mathrm{T}} < 1.5$ GeV and combining the TPC and TOF information for higher p_{T}. A sample of deuteron selected within a 3σ cut around the expected dE/dx value is initially used to build the $m^2 - m_{\mathrm{d}}^2$-distribution, where m_{d} is the deuteron mass and m is the mass measured with TOF using $m^2 = p^2/(\gamma^2 - 1)$. Then, this distribution is fitted in p_{T} intervals. The extracted yields are then efficiency and acceptance corrected and the final spectra are shown in Figure 1 for five different collision centralities. The spectra show a characteristic hardening with increasing centrality, qualitatively similar to proton spectra. To extract p_{T} integrated yields the spectra in the different centrality bins are fitted by individual blast-wave distributions. The ratios of these yields with those of protons are shown in Figure 2 for five different centralities. The measured ratio agrees well with the mean of the d/p and the $\bar{\mathrm{d}}/\bar{\mathrm{p}}$ from PHENIX [7], which is a fair comparison since the baryo-chemical potential μ_B at the LHC is getting close to 0 MeV [2].

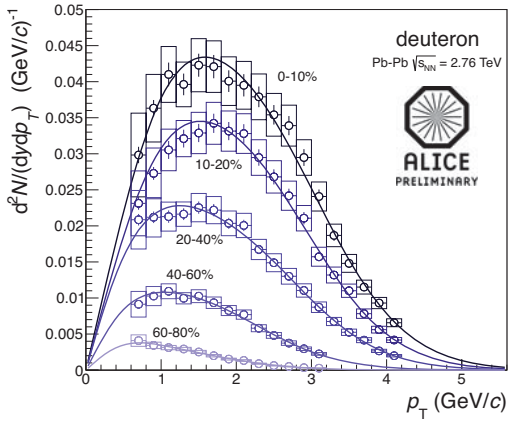

Figure 1: Measured deuteron spectra at $\sqrt{s_{\mathrm{NN}}} = 2.76$ TeV for five different centralities. The lines through the measured points are individual blast-wave fits.

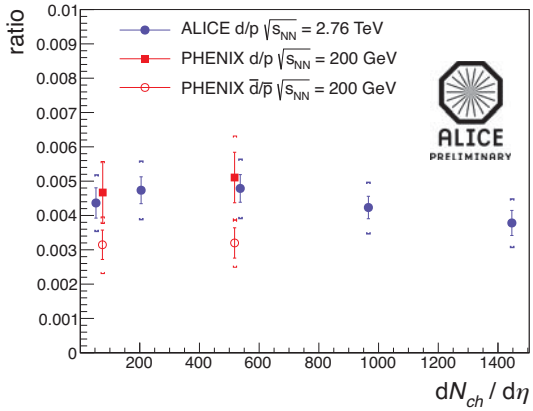

Figure 2: Deuteron-to-proton ratio over centrality compared with the PHENIX measurement [7] of deuteron-to-proton ratio and the anti-deuteron-to-anti-proton ratio at $\sqrt{s_{\mathrm{NN}}} = 200$ GeV.

References

[1] A. Andronic *et al.*, *Phys. Lett.* B **697** (2011) 203

[2] J. Cleymans *et al.*, *Phys. Rev.* C **84** (2011) 054916

[3] J. Alme *et al.* (ALICE TPC Collaboration), *Nucl. Instr. Meas.* A **622** (2010) 316

[4] K. Aamodt *et al.* (ALICE Collaboration), *JINST* **3** (2008) S08002

[5] B. Dönigus (for the ALICE Collaboration), *Nucl. Phys.* A **904-905** (2013) 457c

[6] B. Abelev *et al.* (ALICE Collaboration), CERN-PH-EP-2013-019, (2013) arXiv:1303.0737v2 [hep-ex]

[7] S. S. Adler, *Phys. Rev. Lett.* **94** (2005) 122302

* Work supported by GSI, BMBF, Helmholtz Alliance HA216/EMMI, H-QM, and HGS-HIRe.

† b.doenigus@gsi.de

Validation of Bayesian PID in ALICE, for the channel $D^0 \rightarrow K^-\pi^+$ in pp at $\sqrt{s} = 7$ TeV*

J. Wilkinson[1] *and K. Schweda*[2]

[1]Physikalisches Institut, Ruprecht-Karls-Universität Heidelberg, Germany; [2]Research Division and ExtreMe Matter Institute EMMI, GSI Helmholtzzentrum fur Schwerionenforschung, Darmstadt, Germany

In order to make measurements of open heavy-flavour production, ALICE makes use of its excellent tracking and vertexing capabilities, as well as particle identification (PID) provided by dE/dx measurements in the Time Projection Chamber (TPC) and time-of-flight information from the Time-Of-Flight (TOF) detector. The standard PID method uses an nσ approach, meaning that a cut is made based on a number of standard deviations from the expected responses for a given species at a given momentum. The alternative Bayesian PID method instead has a probabilistic approach, basing its cuts on knowledge of the detector responses combined with additional information on the relative abundances of different particle species (π, K, p, etc.). These abundances are obtained using an iterative Bayesian procedure on data and used as *a priori* probabilities in Bayes' theorem, which is applied as follows:

$$\mathrm{P(species|response)} = \frac{\mathrm{P(species)} \cdot \mathrm{P(response|species)}}{\sum_{\mathrm{species}} \mathrm{P(response|species)}}, \quad (1)$$

where P(species|response) is the probability of the particle belonging to a given species; P(species) is the prior probability discussed above; and P(response|species) is based on the expected detector response for each species. Cuts can then be made on this probability, for example by accepting only the most likely species as the identity (hereafter referred to as the "maximum-probability" method); selecting candidates only if they pass some predetermined probability threshold, with a higher threshold signifying a stricter cut ("threshold"); or applying a weight to all candidates in the invariant mass spectra, based on the product of the species probabilities of the decay daughters ("weighted").

In order to ensure that the choice between Bayesian and nσ PID does not cause a bias in the corrected yield, the method was tested in a variety of channels and compared directly to nσ results. Among these channels was $D^0 \rightarrow K^-\pi^+$ in pp collisions at $\sqrt{s} = 7$ TeV, for which all of the aforementioned Bayesian selection strategies were studied. The topological selections used were the same as those used for the D^0 analysis published in [1].

First, a standard invariant mass analysis was performed in order to extract the raw yields for each method by fitting the spectra with a Gaussian function for the signal and an exponential function for the background. A comparison of the invariant mass spectra for analysis without PID, with nσ PID and with maximum-probability Bayesian PID is shown for $1 < p_{\mathrm{T}} < 4$ GeV/c in Figure 1. From this it

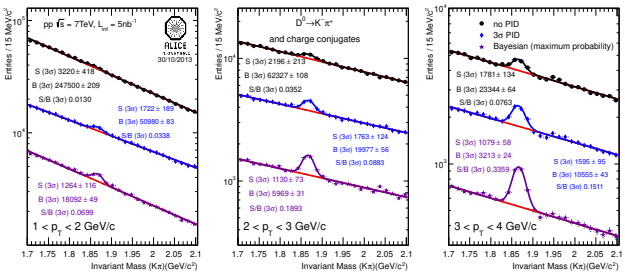

Figure 1: Invariant mass plots for $D^0 \rightarrow K^-\pi^+$ in three p_{T} bins for (top) no PID, (middle) nσ PID, and (lower) maximum-probability Bayesian PID.

can clearly be seen that in this p_{T} region, there is a sharp increase in the significance and signal-to-background ratio when applying 3σ PID compared to no PID, which is further improved when applying Bayesian PID. A similar trend was seen in the other PID methods, with an increase in signal-to-background ratio for all PID strategies over nσ at all p_{T}. In addition, apart from when applying especially strict probability threshold cuts of 70 or 80%, the significance was found to be generally higher than for nσ at low p_{T}, and remained similar to nσ at higher p_{T}.

Once the raw yields were corrected for their respective efficiencies, the yields for each method were compared to the result for 3σ PID. Despite large differences in the efficiencies between these methods, it was found that there was little significant deviation between the 3σ method and the various Bayesian PID strategies. On average, the deviations for the weighted and maximum-probability PID methods were on the order of 5%, and various probability thresholds varying between 40% and 80% gave an agreement within approximately 8%. This can be attributed to systematics in determining the PID response. A further check, scaling the kaon abundances up and down by 10%, showed that there was also no significant dependence of the yield on the choice of priors.

We can therefore conclude that the Bayesian PID strategy does not bias our results, and so is valid for use in other analyses. In particular, it will allow us to extend our analysis of D^0 mesons to ultra-low p_{T}, and enable new measurements such as $\Lambda_{\mathrm{c}} \rightarrow \mathrm{pK}\pi$, which is currently being studied in pp, Pb–Pb and p–Pb collisions using this method.

References

[1] B. Abelev et al. (ALICE Collaboration), JHEP 01 (2012) 128

* Work supported by HGS-HIRe, BMBF and HA216/EMMI

 doi:10.15120/GR-2014-1-NQM-ALICE-10

Study of Higher Order Net-Particle Fluctuations at LHC Energies*

J. Thäder† [1]

[1]Institut für Kernphysik, Technische Universität Darmstadt, Darmstadt, Germany

Higher moments of net-particle fluctuations are used to study the QCD phase structure of matter which is created in high-energy heavy-ion collisions. Theoretically, the fluctuations of net-charge, net-baryon, and net-strangeness distributions allow to explore the QCD phase diagram, including the search for a critical point and the cross-over transition. Experimentally, they are accessible via higher order moments of those distributions, expressed in cumulants c_{k} and their ratios of net-charge, net-proton, and net-kaon fluctuations, eg. the 4th order moment $\kappa = c_4/c_2^2$, see [1]. At LHC energies, these measurements allow to test Lattice QCD calculations at zero chemical potential ($\mu_{\mathrm{B}} = 0$) [2].

Experimental measurements are influenced by detector effects, such as limited detector acceptance, reconstruction and particle identification inefficiencies, as well as contamination from miss-identified particles. Typically inefficiencies are fluctuating due to detector inhomogeneities and can not be corrected on an event-by-event basis, but rather on average. Recent developments take these effects into account by calculating factorial moments for the so-called K-cumulants [3]. The typical available statistics of recorded heavy-ion collisions at LHC experiments impose limitations on the observables, which are possible to calculate.

A Toy Monte-Carlo simulation was developed, assuming Poisson statistics for particle and anti-particle distributions, mimicking a Hadron Resonance Gas (HRG) distribution and a finite reconstruction and identification efficiency. The difference of two Poissonian distributions is described by a Skellam distribution, the net-particle distribution. The mean of the particle and anti-particle distributions, as well as the efficiencies are variable input parameters for this simulation. The reconstruction efficiency is assumed independent of the transverse momentum p_{T}. In general the efficiencies are dependent on p_{T}. These dependences are taken into account in [4] and will be studied further within the context of this work.

To study the influence on the observables of the number of simulated events, several independent samples with varying number of events have been produced in steps from 10^5 to 10^9 events. Furthermore, the efficiencies have been varied in 10% steps in the range of 20-100%.

The results of these simulations with different efficiencies for cumulants and efficiency corrected K-cumulants have been compared to the expected values from the generated particles as well as analytical calculations.

It can be seen in Figure 1, that the 4th order moment κ obtained from cumulants of reconstructed particles agrees with the analytical value after the efficiency corrections for K-cumulants are applied. It was found that for a mean number of particles/anti-particles ($M = 40$) a minimum of $5 \cdot 10^7$ events are required in order to estimate the 4th order moment.

The above describe procedure will be applied to LHC data, in particular to the experimental data of the upcoming high-statistics RUN 2.

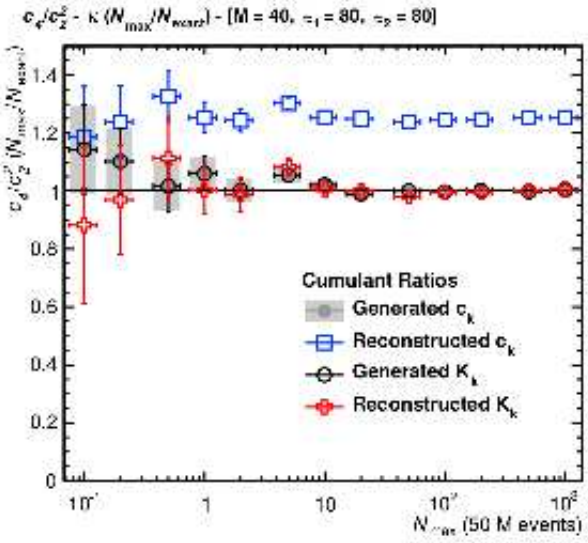

Figure 1: Ratio of the calculated κ to the exact value obtained from the Skellam distribution for a reconstruction efficiency $\epsilon_{1,2} = 80\%$ of each particle and anti-particle type and a mean of 40 (anti-)particles per event. The open and closed circles show κ for generated particles, while the boxes (crosses) show κ for the reconstructed cumulants (K-cumulants) with different number of simulated events N_{max}.

References

[1] P. Braun-Munzinger, B. Friman, F. Karsch, K. Redlich, and V. Skokov, *Phys. Rev. C* **84** (2011) 064911

[2] F. Karsch arXiv:1202.4173 [hep-lat] (2012)

[3] A. Bzdak and V. Koch, *Phys. Rev. C* **86** (2012) 044904

[4] A. Bzdak and V. Koch, arXiv:1312.4574 [nucl-th] (2013)

* Work supported by GSI, BMBF, Helmholtz Alliance HA216/EMMI.

† jochen@thaeder.de

 doi:10.15120/GR-2014-1-NQM-ALICE-11

Collaboration report PANDA progress in 2013

K. Peters[1]

[1]GSI, Darmstadt, Germany

The PANDA Experiment (antiProton-Annihilation at Darmstadt) is a dedicated hadron physics experiment with a focus on the structure and dynamics of hadrons with explicit scientific programs in

- charm spectroscopy and the search for exotic hadronic matter,
- hadron dynamics of baryons and mesons,
- hadron structure and proton formfactors,
- hypernuclei (single and double strange), and
- hadrons (in particular J/psi) in nuclear media.

These goals will be achieved by utilizing a 1.5-15 GeV/c antiproton beam which annihilates off a proton or a nuclear target. The PANDA experiment comprises an onion-like detector structure enabling tracking, calorimetry and particle identification for a variety of particle species over a wide momentum and rapidity range.

The phase of development and construction of PANDA is progressing very well at GSI and it's partners and is in line with the FAIR construction schedules. A great success is that three more TDRs of PANDA were approved by FAIR: Straw Tube Tracker (STT) in January 2013, Micro Vertex Detector (MVD) in February 2013 and the Cluster Target in August 2013. Apart from development and construction of several detectors and parts, the GSI group is also responsible for the technical coordination and the infrastructure for the PANDA experiment.

For the construction of the PANDA solenoid is well under way and a cooperation with the ATLAS magnet group was initiated. The mechanical design of the yoke and support platform were studied with FEM calculations and a construction contract is envisaged for 2014. The architectural design of the PANDA Experimental Hall reached the next level of detail and was checked and improved and at the same time the routing of services and installation planning were expedited. Another important step is that new crystals have been produced by SICCAS in Shanghai (China) for the PANDA calorimeter and were characterized at Gießen.

GSI is involved in the research, development and the construction of the DIRC (Detector for Internally reflected Cherenkov Light), the EMC (Electromagnetic Calorimeter) and the GEM-Discs (Gas Electron Multiplier).

The DIRC is an assembly of either narrow slabs or bars of artificially fused silica, where Cherenkov light of traversing particles is internally reflected to one end, where the individual photons are registered and time tagged with photon detectors. In simulations the layout of radiators and focusing elements of the barrel DIRC was optimized with respect to resolution, granularity and expected production cost. The GSI partners in Erlangen characterized micro-channel plate photomultipliers that have an enhanced lifetime achieving now for the first time the limits necessary for a long-term operation in the PANDA experiment. Both are important steps towards the completion and the start of construction of this particular device.

The EMC consists of several lead-tungstate crystal arrangements in a backward, a barrel and a forward section. The light collected by the crystals from electromagnetic showers is detected with LAAPDs (Large Area Avalanche Photodiodes) with a large collection area (1 square cm) and a high gain. The final version of the LAAPD for the PANDA EMC was established and a pre-production batch was ordered by RU Bochum to be characterized at GSI. For maximum throughput and quality assurance the construction of the APD screening lab was started at a new dedicated location and will be finished in 2014.

The GEM Tracker consists of a series of circular planes to cover mainly particles from the forward-peaked event topologies. In 2013 the layout of the readout pad plane was simulated to find an optimal value for occupancy, resolution and number of channels. In addition the quality assurance for large-scale GEM foils was successfully developed. Finally for the reconstruction of realistic tracks in the GEM Tracker a time-based approach was implemented.

In addition the GSI groups are involved in electronics, software and data acquisition. Details can be found throughout the report.Since several decades, the year 2013 was the first year without beamtimes at GSI. Various NUSTAR detectors and sub-systems for FAIR are already in operation and the collaboration looks forward to their implementation and use at FAIR. The lack of beamtime induced a serious change of the daily scientific work and hampered the beam-related preparations of FAIR experiments, component tests and R&D-work, including pilot experiments for FAIR.

doi:10.15120/GR-2014-1-HSD-01

Invariant mass reconstruction of ${}^{3}_{\Lambda}$H and ${}^{4}_{\Lambda}$H

O.Bertini[1]
[1]GSI, Darmstadt, Germany

One of the main goal of hypernuclear physics is to improve our understanding of baryon-baryon interactions under flavored $SU(3)$ symmetry. Standard nuclear reaction experiments provide information only about the nucleon-nucleon interaction while, experiments focusing to hypernuclear physics provide information to the hyperon-nucleon and hyperon-hyperon interaction.

The first HypHI [1] experiment was designed to study the mesonic weak decay (MWD) of light hypernuclei produced by the coalescence of a projectile fragment with a Λ-hyperon at the projectile rapidity. The experiment, was performed at GSI Helmholzzentrum für Schwerionenforschung GmbH in Darmstadt. The hypernculei are produced by the collision of a primary ^{6}Li beam at 2.0 A GeV with intensity of 3×10^{6} particles per second impinging into a 4 cm thick ^{12}C target.

The HypHI Phase 0 experiment focuses on producing and identifying mainly: ${}^{3}_{\Lambda}$H, ${}^{4}_{\Lambda}$H, and ${}^{5}_{\Lambda}$He by their mesonic weak two or three body decay channels ${}^{3}_{\Lambda}\mathrm{H} \rightarrow \pi^{-}+{}^{3}\mathrm{He}$, ${}^{4}_{\Lambda}\mathrm{H} \rightarrow \pi^{-}+{}^{4}\mathrm{He}$, ${}^{5}_{\Lambda}\mathrm{He} \rightarrow \pi^{-}+{}^{4}\mathrm{He}+p$.

In the previous analysis [2] the invariant mass reconstruction was done without performing a vertex fit, but using only the geometrical criteria. In the current analysis the secondary vertices are obtained with a vertex fitting procedure which improved the significance of the signal by providing a selection criteria deduced from the vertex fit.

A dedicated track fitting algorithm based on the Kalman Filter technique was implemented for the track reconstruction [3]. In order to improve the performance of the method, a precise calculation of the physical effects, mainly the energy loss and multiple scattering effects affecting the track parameters and its errors, have been included at each iteration of the Kalman filter algorithm. In order to optimize the removal of fake tracks, the canonical Kalman filter has been modified and supplemented by a smoothing algorithm. Average achieved relative momentum resolution is about 8% for the ^{4}He, 6% for ^{3}He and around 4% for protons and π^{-}.

The independent secondary-vertex fitting algorithm, a global χ^{2} fit, was developed in order to perform secondary vertex reconstruction with a statistical selection criterion. It had shown that addition of the vertex fitting improve significantly the final invariant mass resolution. Achieved position resolution in both methods for secondary vertex is 0.08 cm in X and Y (transversal) and 0.83 cm in Z (longitudinal) direction.

The black point in Figure 1 shows the obtained invariant mass distribution for the ^{3}He + π^{-} and ^{4}He + π^{-} respectively. The blue points correspond to the distributions obtained from the mixed event analysis.

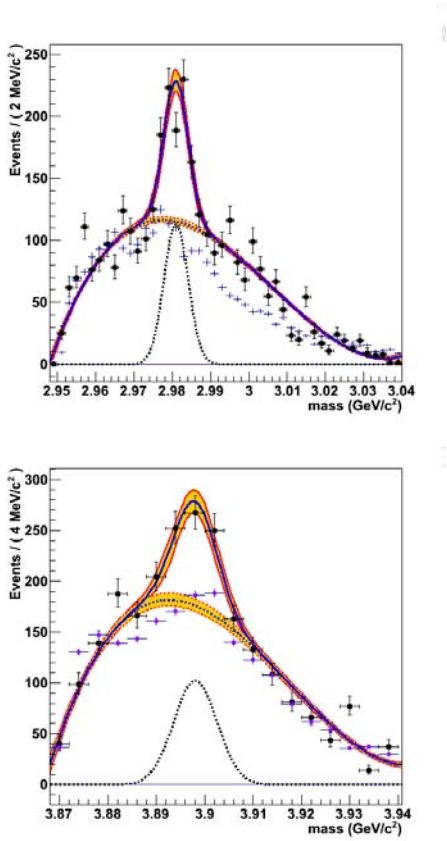

Figure 1: *Invariant mass distribution (black dots) fitted with the signal+ background distribution for ${}^{3}_{\Lambda}H$ (top) and ${}^{4}_{\Lambda}H$ (bottom). The blue lines represent the most probable solution returned by the fit, the red lines and yellow area show the 1σ uncertainty band. The light purple markers correspond to the scaled mixed event invariant mass distribution*

References

[1] T. Fukuda and T. Saito "The study of hypernuclei with heavy ion beams at GSI", Nucl. Phys. A, 790(14), 2007, p. 161

[2] C. Rappold et al.C "Hypernuclear spectroscopy of products from ^{6}Li projectiles on a carbon target at 2 A GeV", Nucl. Phys. A, 913(0), 2013, p.170

[3] O. Bertini "Study of ${}^{3}_{\Lambda}$H and ${}^{4}_{\Lambda}$H in the reaction of ^{6}Li+^{12}C at 2 A GeV" , PhD thesis Mainz 2013, http://ubm.opus.hbz-nrw.de/volltexte/2013/3421/pdf/doc.pdf

 doi:10.15120/GR-2014-1-HSD-02

Breakthrough in the Lifetime of Microchannel Plate PMTs*

A. Britting[1], *W. Eyrich*[1], *A. Lehmann*[†1], *F. Uhlig*[1], *and PANDA Cherenkov subgroup*
[1]Physikalisches Institut IV, Universität Erlangen-Nürnberg, Erwin-Rommel-Str. 1, D-91058 Erlangen

The charged particle identification in the PANDA experiment will be done with DIRC detectors. Since their focal planes will be placed inside the magnetic field of up to 2 Tesla microchannel-plate (MCP) PMTs are the favored photon sensors. These devices show very promising properties except that aging was a serious issue until very recently. Due to ion backflow the photo cathode (PC) gets damaged and the quantum efficiency (QE) drops rapidly. Just 3 years ago the best MCP-PMTs were unusable after $<$200 mC/cm^2 integrated anode charge [1], while for the PANDA DIRCs at least 5 C/cm^2 are needed.

With novel techniques the manufacturers recently succeeded in significantly increasing the lifetime of MCP-PMTs. This was accomplished by reducing the ion backflow either with a protection film (Hamamatsu R10754X) between the two MCPs or by applying an atomic layer deposition (ALD) technique to coat the micro pores and reduce the outgassing of the MCP glass (PHOTONIS XP85112, and now also Hamamatsu), but also by using a modified PC (BINP).

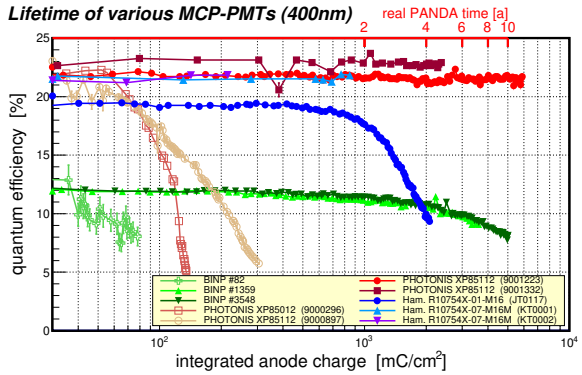

Figure 1: QE at 400 nm for old (open) and latest (solid dots) MCP-PMTs versus the integrated anode charge.

Our group is doing a long-term comparative measurement of the lifetime of the most recent MCP-PMTs by permanently illuminating the sensors with a single photon rate comparable to that expected at PANDA [2]. Gain, dark rate and QE (spectral and as a function of the PC surface) are measured in irregular intervals as a function of the integrated anode charge. A compilation of the QE of all tubes investigated are displayed in Fig. 1. While the QE of older models (open dots) drop to less than half the original value after $<$200 mC/cm^2 the situation for the most recent models (solid dots) is very different. Especially the ALD coated PHOTONIS XP85112 has meanwhile accumulated an anode charge of 5.9 C/cm^2 with only minor QE degradations. This corresponds to over 10 years of PANDA running.

We have also measured the spatial distribution of the QE at the PC surface for all MCP-PMTs. For the Hamamatsu R10754X (with protection film) and the BINP MCP-PMTs we observe that the QE starts degrading from the corners and the rims of the PC [3] and proceeds to the inner regions afterwards. In Fig. 2 a QE chart of the ALD coated PHOTONIS XP85112 is shown. For this tube we observe only moderate QE degradations of 1-2% up to 5.1 C/cm^2. Beyond this charge the sensor shows more QE damage, but still at a tolerable level. At 5.9 C/cm^2 a clear step emerges around x = 0 mm. This stems from the fact that the right half of the PC (x $>$ 0 mm) was covered during the illumination process.

These new results can be considered as a breakthrough in the lifetime of MCP-PMTs and will have implications also on other experiments.

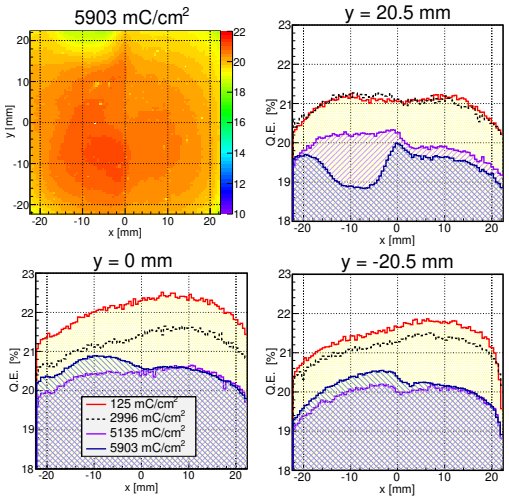

Figure 2: QE at 372 nm as a function of the PC surface for the PHOTONIS XP85112 (9001223) MCP-PMT. Upper left: 2-dim. QE chart (in % [color level]); other plots: QE x-projections at different y-positions and anode charges.

References

[1] A. Lehmann et al., GSI Scientific Report 2010, p. 106
[2] A. Lehmann et al., Nucl. Instr. and Meth. A 718 (2013) 535
[3] A. Lehmann et al., J. Instr. 9 (2014) C02009

* Work supported by GSI contract No. EREYRI1012 and BMBF
† Albert.Lehmann@physik.uni-erlangen.de

In-Beam Tests of Double-Sided Silicon Microstrip Sensors Employing Flex-PCB Readout for the $\overline{\text{P}}$ANDA MVD*

R. Schnell† [1], *K.-Th. Brinkmann*[1], *T. Quagli*[1], *and H.-G. Zaunick*[1]

[1]II. Physikalisches Institut, Justus-Liebig-Universität Gießen, Heinrich-Buff-Ring 16, 35392 Gießen, Germany

Introduction

Detectors close to the interaction point, such as the $\overline{\text{P}}$ANDA Micro-Vertex-Detector (MVD), should feature a low material budget. Hence, the amount of passive material needs to be kept small and materials with high radiation lengths should be used. In terms of detector readout electronics, the utilization of thin flexible PCB technology is favored. Detector modules based on standard rigid-PCB applying flex-PCB pitch-adapters to interconnect between the silicon microstrip detector and the front-end chip, as reported in [1], were succesfully tested. Together with the high-density flex-PCB pitch-adapters, designs for flex-PCB were developed to test the transition from rigid to thin and flexible readout boards [2]. Several beam tests were performed using detector modules based on these designs in beams of electrons at the CERN SPS in Sept. 2012 as well as protons at COSY in Dec. 2013 and Jan. 2014.

Flex-PCB Detector Module

The front-end board is based on a ThinFlex-A® double-sided electrodeposited copper clad polyimide film with a dielectric thickness of 50 µm and 12 µm copper. The total thickness is approximately 100 µm. Figure 1 shows a photograph of the detector module to read out a double-sided silicon microstrip sensor using the APV25 front-end chip [3]. The flexible PCB is glued to a glass-fiber reinforced plastic frame that supports the flex-PCB and the sensor in a way that both sensor sides are accessible for wire bonding. A pitch-adapter fan-out structure is integrated in the 2-layer board to read out every third strip of a double-sided silicon detector with a strip pitch of 50 µm. The front-end board is connected to a transition card by a flex-PCB cable based on the same board specifications.

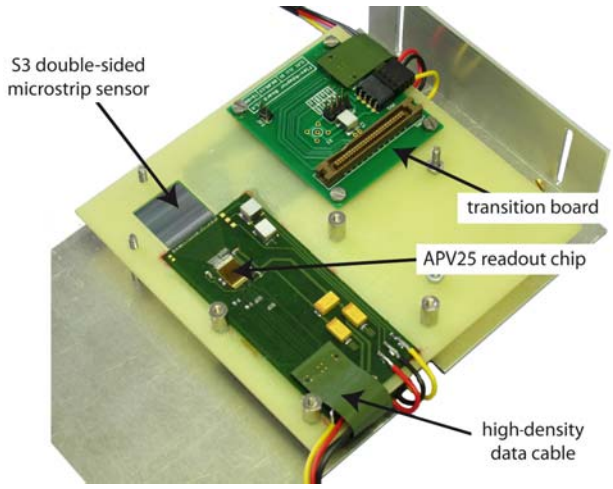

Figure 1: Photo of the detector module based on flex-PCB.

Results

The aforementioned module was used in beam tests with proton beams of 2.95 GeV/c and 0.8 GeV/c momentum. A hitmap from a measurement with 0.8 GeV/c protons can be seen in figure 2. The signal-to-noise ratio that was obtained from this measurement was (54.5 ± 16.2) for the p-side and (15.2 ± 5.1) for the n-side, respectively. The excellent performance proved the concept of this flex-PCB technology for future application in the $\overline{\text{P}}$ANDA MVD.

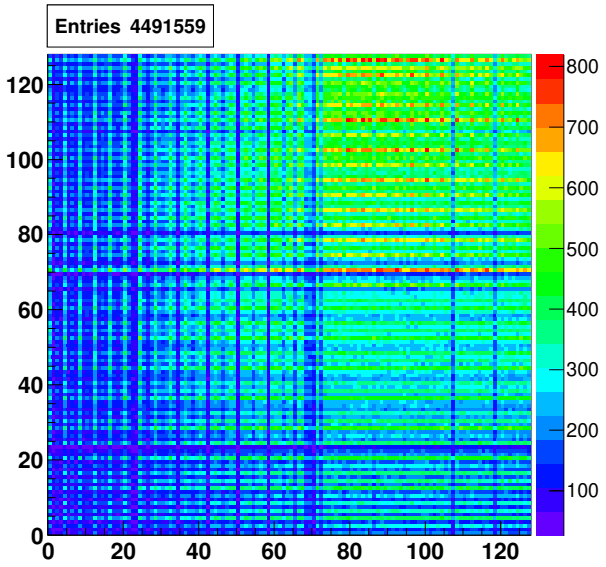

Figure 2: Raw hitmap from test beam with protons at COSY (unordered channel mapping).

References

[1] R. Schnell et al., GSI-SR2012-PHN-HSD-EXP-10, (2013).

[2] GS Swiss PCB AG

[3] L. Jones, "APV25-S1: User guide version 2.2", RAL Microelectronics Design Group, (2001).

* This work was supported by BMBF (grant no. 05P12RGFP6), JCHP-FEE and HIC for FAIR.

† Robert.Schnell@exp2.physik.uni-giessen.de

 doi:10.15120/GR-2014-1-HSD-04

Quality assurance for large-scale GEM-foils*

N. Saito[1,2], *A. Ehret*[1,3], *T.R. Saito*[1,2], *and B. Voss*[1]

[1]GSI, Darmstadt, Germany; [2]HI Mainz, Mainz, Germany; [3]Hochschule Darmstadt, Darmstadt, Germany

A large scale GEM-based tracker has been designed [1] as a forward particle-track detector for the PANDA experiments. The detector system consists of three GEM-Discs, each working as a large-area planar GEM detector. The size of GEM-foils is three orders of magnitudes larger than the 'standard' one (10x10cm^2), therefore a fast and automated quality assurance method has to be established.

A 2D-scanning system has been designed to optically inspect the quality of GEM foils and micro-patterned readout structures to be exploited with a prototype GEM-tracker (active area of 30x30cm^2). The current system is capable to scan a maximum area of 40x40cm^2 at a time by moving a sample with a high-precision 2D-stage (ALS36240 Aerotech). The system is designed to use various devices for detector inspection and tests [2]. For an optical inspection of GEM-foils, a digital microscope can be mounted on the scanning system.

A control software of the 2D-scanning system has been made using LabVIEW to perform an automated image taking. Figure 1 demonstrates the scan results for a scale. The scanning reproducibility has been measured using a microscope (VHX-600 KEYENCE) by comparing images of the same scan position for different runs using an pattern matching algorithm. In order to inspect micro scale structure of GEM foils (fig.2 top), an analysis program has been developed detecting pre-definable objects e.g. contours of GEM holes (fig.2 bottom). The diameters which have been fitted with circles and resulting in parameters such as location of the respective centers and deviation from the ideal circle are plotted and stored in a file.

The scanning reproducibility has been deduced to be (1.7±1.1)μm for the test performed on a stone table in the clean room of the GSI detector laboratory. The 2D-stage and microscope head will be mounted on a dedicated supporting structure in spring 2014 to be constructed as the complete scanning system. Similar reproducibility tests are foreseen after the assembly.

Image analysis has been performed for 5 samples of standard GEM-foils with various optical settings to find an optimum setting for an appropriate image analysis. Currently, the analysis process is sensitive to the image quality and time consuming. Appropriate algorithms to speed up the whole processing as well as improvements on the hardware are under investigation.

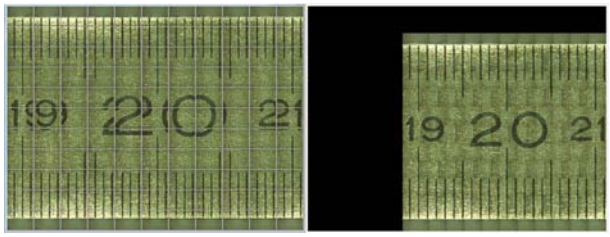

Figure 1: An example of an automated scan showing 121 consecutive images of a scale with 2mm pitch, unstitched (left) and successfully joined (right).

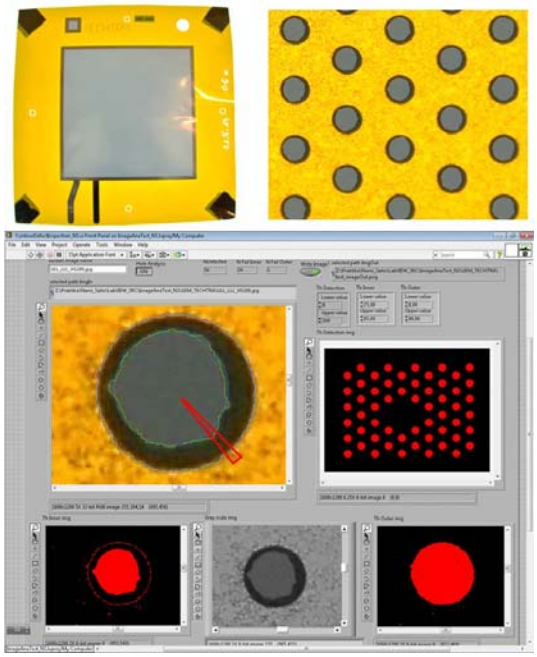

Figure 2: A sample GEM foil (top left) and a zoomed view (top right). GUI of the image analysis program (bottom). An example of analyzed contours and circular fit of an inner hole in the base material and an outer rim in the copper cladding of a GEM hole are shown. A large deviation from the ideal circle is detected and marked by a triangle.

References

[1] B. Voss et. al., GSI scientific rep. 2011, p123 (2012)

[2] A. Ehret et.al., contribution to this report

* Work supported by GSI(RBDL) / HI Mainz / BMBF FKZ 05E12CD2 / HIP Helsinki, Finland / Universidad Antonio Nariño, Bogotá, Colombia / RD51 collaboration (CERN) / EU-FP7:283286-HP3-WP24-JointGEM

The PANDA GEM-Tracker Prototype 'GEM2D', Simulations and Pad-Plane design

A. Gromliuk[1,2]*, J. Kunkel*[1]*, and B. Voss*[1]
[1]GSI, Darmstadt, Germany; [2]HGS-HIRe for FAIR

In the PANDA experiment particles emitted at angle in the range 5°-22° will be tracked with a set of three large-area planar gaseous micro-pattern detectors based on Gaseous-Electron-Multiplier (GEM) foils as amplification stages [1]. According to simulations [2] of the particle flux of up to 140 kHz/cm^2 the granularity of the read-out structures, the so called 'pad planes', is purely driven by the required resolution of 150μm, not by particle occupancy.

Simulations of a triple-GEM system have been performed using the Garfield++ toolkit. The ANSYS model of the single conical GEM cell with a top diameter of 70 μm and a bottom diameter of 50 μm was used as an input. According to these simulations the expected gain, which is the number of electrons produced per number of initial electrons is 4000, which reproduces the COMPASS triple GEM detector data within a factor of 2. The endpoints of electrons at the pad plane exhibit a 2-dimensional Gaussian distribution with σ=270 μm, which is in agreement with the simple estimation $\sigma = \sqrt{L} \times D$ =240μm, where L is a 1cm drift gap and D is the transverse diffusion coefficient extracted from the Magboltz program. If the size of an electron cloud could be neglected with respect to the strip/pad size, the resolution would be simply $Pitch/\sqrt{12}$. For a pitch of 400μm it would be 115μm and would be significantly improved in case of a weighted mean calculation (best achievable ∼30μm, see Fig. 1).

In order to verify the feasibility of the targeted spatial resolution of 150μm, a ∼200μm thin pad plane was designed realizing two-dimensional readout structures on both faces. The structure of the *top* projection (see Fig. 2 left) consists of vertical stripes with 75μm width to provide information on the *x* coordinate and interconnected pads with the sizes 100×100μm to provide information on the *y* coordinate. In such a configuration the pitch in *x* and *y* coordinates is the same and equals 400μm. The structure of the *bottom* projection (see Fig. 2 right) is almost the same as on top, but rotated by 45°, which increased the pitch by factor of $\sqrt{2}$ (400×$\sqrt{2}$=566μm), which additionally allows us to test different strip capacitances. The active area of the 'GEM2D' GEM-Tracker prototype exploiting this design is 310×310mm^2 and exhibits 3072 readout channels in total (see Fig. 3. which are routed to high-density connectors. The readout is done exploiting 12 nXYTER-based GEMEX front-end boards[3].

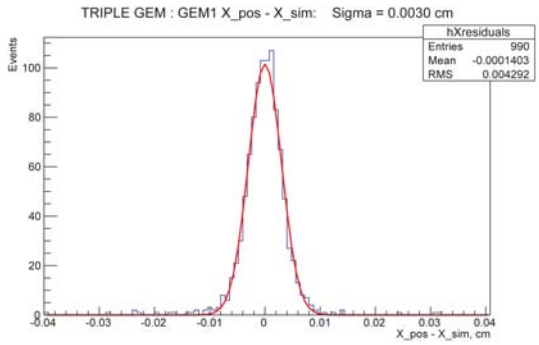

Figure 1: Distribution of the residuals between the generated and the reconstructed track X-positions.

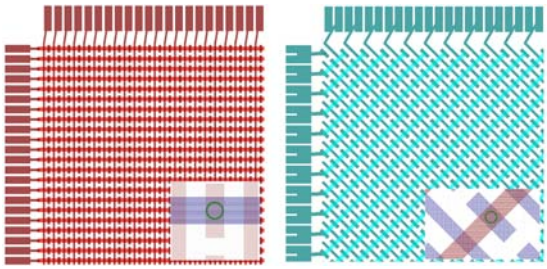

Figure 2: Top (left) and Bottom (right) projection patterns. The insets visualize details of the structures.

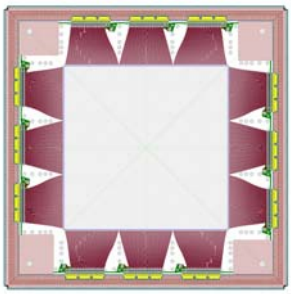

Figure 3: Outer part of the GEM2D PadPlane. The blanked inner part is patterned with structures shown in fig.2

References

[1] Voss B. et al., GSI Scientific Report 2008, GSI Report 2009-1, p.242.

[2] Voss B. et al., GSI Scientific Report 2009, GSI Report 2010-1, p.338.

[3] Voss B. et al., GSI Scientific Report 2011, GSI Report 2012-1, p.247.

 doi:10.15120/GR-2014-1-HSD-06

Time-based reconstruction in the GEM Tracker

R. Karabowicz[1]
[1]GSI, Darmstadt, Germany

Introduction

The GEM Tracker, a set of three planar Gaseous Electron Multiplier detectors, is a forward part of the central barrel of the PANDA experimental setup. Covering polar angles from 5 to 20 degrees it is responsible for track reconstruction. The charged particles are crossing two drift volumes (front and back) per each station and ionize the gas.The signal is detected on the double sided pad plane located in the centre of each station. Each side is equipped with sensitive pads that are connected into strips in two directions per pad plane. This results in recording particle trajectory position on each station in 4 different views. The paper presents the reconstruction chain of the time-based digitized data from the GEM Tracker, that was introduced in [1].

Implementation

The time-stamped digitized data from the GEM Tracker is stored in the time ordered buffer assuming PANDA goal event rate of 2×10^7 events per second. The reconstruction tasks request data from these filled buffers and obtain time slices of data, as presented in Figure 1. The time slices are defined by gaps in the data stream and thus are independent of the simulated events structure, often consisting of several events or spreading event data between different slices.

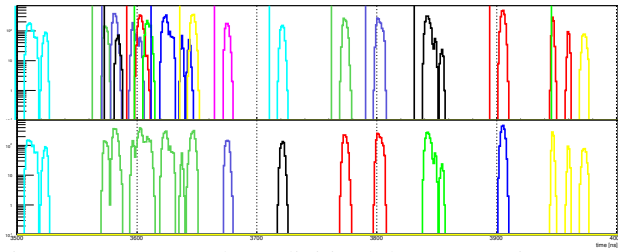

Figure 1: GEM Tracker's digitized data versus time. Top panel shows different simulated events in different colors (vertical line indicates the beginning of a corresponding event), in the bottom panel different colors represent different time slices.

The reconstruction chain include finding of clusters, hits and eventually tracks. The original idea was to operate on the data from individual time slices with the help of the previously developed algorithms that worked on events. However obtained results, specifically the low track finding efficiency of about 57% for the primary tracks from the DPM event generator, forced searching for new solutions. The first change was to use the time information when combining data, that was originally combined only geometrically. That increased the efficiency by few percent, but still well below the acceptable levels.

In many cases events are inseparably close in time, resulting in higher combinatorics and thus lowering track finding efficiency. The other sources of the tracking inefficiencies are the high occupancy in the GEM Tracker and relatively large strip dead time of 100 ns, resulting in up to 7% chance of any strip being hit again while being inactive. The original hit finding algorithm identified hits from intersections of strips on front (radial and concentric) or back (horizontal and vertical) readout planes. In case of the time-based reconstruction that resulted in hit finding inefficiencies of 10% with about 70% of the found hits being fake hits, stemming from combining signals from different particle trajectories.

In order to cope with these problems it was necessary to amend for the possible influence of previous events. To achieve this, for each reconstructed hit on front (or back) pad plane a confirmation in the form of fired strips on the back (or front) is required. The confirmation may come from the currently analyzed time slice, or from previous time slices. This information is stored in newly developed GEM Tracker Monitor, that gathers information about last activation of each strip.

This method reduced drastically the number of combinatorial fake hits, cutting only small number of real hits, and resulted in improving track finding efficiency to 87% for primary tracks with momentum larger than $1\ GeV/c$.

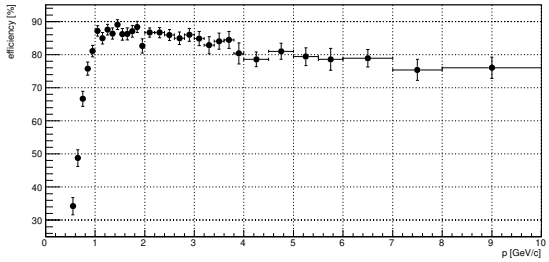

Figure 2: Track finding efficiency in the GEM Tracker as a function of momentum magnitude.

Summary

The current efforts in the PANDA computing community focus on the reconstruction of constant data stream from various detectors. In this report it has been shown that the data from the GEM Tracker can be analyzed with satisfactory results. Further improvements are still necessary to increase the tracking efficiency and reduce reconstruction time, which amounts today to about $50\ ms$ per simulated event.

References

[1] R. Karabowicz, "Panda GEM Tracker software status", GSI Scientific Report 2012 (2013) 301

Comparison of Radiation Damage Effects in PWO Under Proton Irradiation at 150 MeV and 24 GeV Energy*

V. Dormenev†, T. Kuske, R.W. Novotny, R. Schubert, and for the $\overline{\mathrm{P}}$ANDA collaboration
II. Physikalisches Institut, Justus-Liebig-Universität Gießen, Heinrich-Buff-Ring 16, 35392 Gießen, Germany

The electromagnetic target calorimeter [1]. of the future PANDA detector is based on PbWO4 scintillation crystals of improved, so called PWO-II quality. To reach sufficient resolution down to a few tens of MeV, the calorimeter has to be operated in addition at a low temperature of $T = -25°$C. As a consequence, high radiation resistivity of the crystals is required since thermo-activated recovery processes are drastically slowed down. One can overcome or at least significantly compensate the damage by stimulated recovery [2] using external infrared light of ~ 1000 nm wavelength. The mechanism has been applied even at low temperatures but leading to longer recovery times. However, it turns out that the recovery technique is limited to damage originating from interactions of electromagnetic probes. Recent investigations of radiation damage of lead tungstate under hadron beams with high fluence show a similar behavior of the degradation of optical transmittance like under γ-irradiation. Moreover, an additional shift of the fundamental absorption edge in the wave-length range below 400 nm is observed after irradiation at a total fluence above 1012 particles/cm^2 as illustrated in Fig. 1.

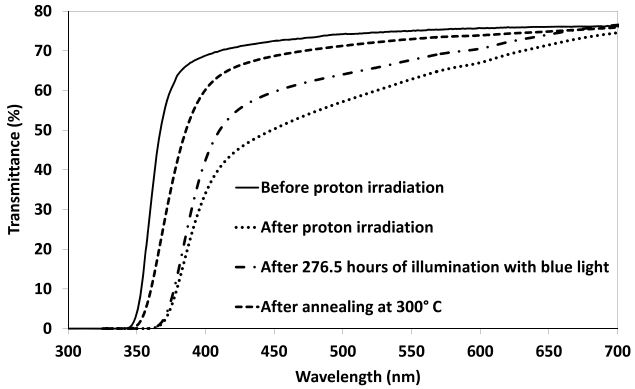

Figure 1: Longitudinal optical transmittance of 22 cm CMS type PWO crystal before irradiation, three month later after irradiation with 24 GeV/c protons (integral fluence = 1013 protons/cm^2), after illumination with blue LED light (max = 464 nm) for 276.5 hours and after annealing at 300 °C for 3 hours

Only additional thermal annealing at 300 °C can reverse the observed shift of the transmission curve and recover the collectable light output. The effect is addressed to local macro defects leading to Rayleigh scattering or the formation of clusters of so called Frenkel defects. The severe damage might be caused by highly ionizing fission and fragmentation products initiated by interactions of protons in the crystal matrix. In that respect, similar effects should appear using protons at significantly lower energies as long as fission processes become possible. In close

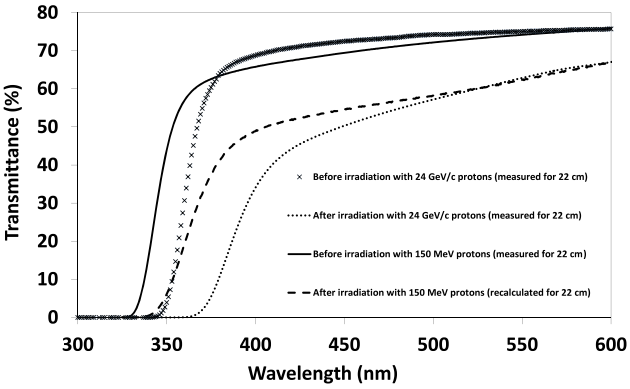

Figure 2: Comparison of the experimental data for the irradiation damage due to 24 GeV/c and 150 MeV protons. The results at lower energy have been rescaled to a crystal length of 22 cm using the experimental absorption coefficient dk(λ) obtained for the 5 cm sample

collaboration with the group at KVI (Groningen) we have performed an investigation using 4 samples of PWO crystals produced by Czochralski method (BTCP) and 4 samples produced by modified Bridgman method (SICCAS), respectively. Each sample was cut from a full size (20 cm) crystal to rectangular dimensions of 2 cm · 2 cm · 5 cm. The irradiation was performed with 150 MeV proton beam provided by the AGOR Facility. Four samples (2 BTCP + 2 SICCAS) were irradiated with an integral fluence of 1012 protons/cm^2 (low), the remaining four with 1.8 1013 protons/cm^2 (high). After irradiation the samples were placed in a freezer at a tem-perature well below 0°C to decelerate spontaneous recovery processes of the radiation damage. Finally, all measurements were started four months later. At the high fluence a similar shift of the fundamental absorption edge and the typical damage in the range above 400 nm are observed. The deterioration above 400 nm can be recovered with illumination of red light (780 nm). However, the onset of the shift of the fundamental edge can be only compensated after 10 hours annealing at 200°C. Rescaling the damage effect to an crystal length of 22 cm shows a similar picture as illustrated in Fig. 2. This provides the opportunity to use low energy

*This work was supported by BMBF (grant no. 05P12R6FP7) and HIC for FAIR.

† Valery.Dormenev@exp2.physik.uni-giessen.de

 doi:10.15120/GR-2014-1-HSD-08

protons for systematic studies of the mechanisms and perform tests searching for alternative new materials for future calorimetry focusing components with lower Z-values.

References

[1] "Technical Design Report for: PANDA Electromagnetic Calorimeter (EMC)", arXiv:0810.1216v1, (2008).

[2] V. Dormenev et al., Nucl. Instr. and Meth. in Phys. Res. A 623 (2010) 1082-1085.

[3] V. Dormenev et al., IEEE Trans. on Nucl. Sci. Vol. 61 (2014) 501-506.

Quality of $PbWO_4$ Crystals Manufactured at SICCAS*

V. Dormenev† [1], *T. Eissner*[1], *R. W. Novotny*[1], *R. Schubert*[1], *I. Tarasov*[1,2], *and for the* $\overline{P}$*ANDA collaboration*[1]

[1]II. Physikalisches Institut, Justus-Liebig-Universität Gießen, Germany; [2]GSI, Darmstadt, Germany

The electromagnetic target calorimeter of the future $\overline{P}$ANDA detector is based on $PbWO_4$ scintillator crystals of improved, so called PWO-II quality. These crystals provide a nearly doubled luminescence output and a superior radiation hardness comparad to PWO-I quality. These improvements are mandatory for the challenging aim to detect high energy photons from 15 GeV down to a few tens of MeV. To reach this goal, the calorimeter has to be operated at a low temperature of T = -25 °C. The extremely high radiation hardness of the crystals is required since thermally activated recovery processes are drastically suppressed. Therefore, the maximum loss of light output due to the deterioration of the optical transparency is primarily determined by the concentration of intrinsic defects created during the growing process. One can overcome or at least significantly compensate the damage by the recently discovered new effect of stimulated recovery [1].

Before completing the production of the total number of ≈11,000 PWO crystals for the barrel part of the calorimeter the former manufacturer BTCP (Bogoroditsk Technical Chemical Plant) in Russia went out of business due to lack of funding for the missing 8,350 crystals. The barrel section comprises 11 different geometries in two symmetric versions. Presently, the company SICCAS at Shanghai is the only active manufacturer of PWO crystals. Therefore, an R&D project has been restarted to inspect and further improve the quality of crystals to meet the $\overline{P}$ANDA-EMC requirements. Tab. 1 summarizes the relevant parameters of the quality specifications.

Parameter	Unit	Limit
Light yield LY measured at T = +18°C, polished crystal	phe/MeV	≥16.0
LY(100 ns)/LY(1 μs) light yield integrated over 100 ns and 1 μs		> 0.9
Induced absorption coefficient Δk measured at RT, integral dose: 30 Gy	m^{-1}	≤ 1.1

Table 1: Some relevant quality specifications.

Within this project 25 full size crystals of geometry type 11L have been produced and completely tested at the facilities at Giessen and CERN. In the latter case, the semi-automatic testing machine ACCOS has been used to determine the geometrical dimensions, the optical performance, luminescence parameters like the relative light yield and decay kinetics. At the detector laboratory and radiation facility at Giessen, the absolute light yield at different operating temperatures as well as the radiation hardness were tested with gamma rays originating from a set of ^{60}Co sources.

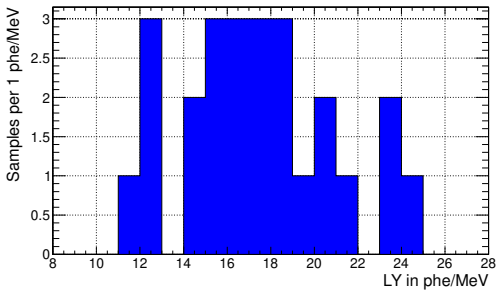

Figure 1: Distribution of absolute light yield measured at T = +18°C for all 25 PWO crystals.

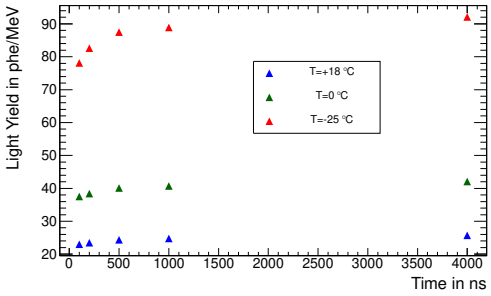

Figure 2: Light yield of one PWO sample (#120904) as function of and integration time for selected temperatures.

Figs. 1 and 2 illustrate the determined light yield at +18°C and the increase at lower temperatures as a function of integration time. Most of the crystals reach the limits and show no dominant slow scintillation components. The optical performance delivers sufficient transmittance over the relevant wavelength region. However, the required radiation hardness, expressed by the change of absorption coefficient at 420 nm due to an integral radiation dose of 30 Gy need further improvement of the used raw material or the growing technology. Fig. 3 shows the distribution of the obtained Δk values.

References

[1] V. Dormenev et al., Nucl. Instr. and Meth. in Phys. Res. A 623 (2010) 1082-1085.

*This work was supported by BMBF (grant no. 05P12RGFP7), and HIC for FAIR.

† valery.dormenev@physik.uni-giessen.de

 doi:10.15120/GR-2014-1-HSD-09

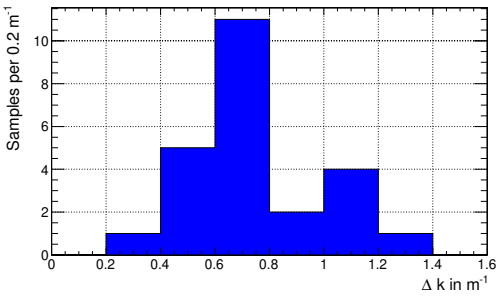

Figure 3: Distribution of the measured Δk values at 420 nm.

Dark count measurements of SiPM detectors*

A. M. Ketchieumen Tchitnga[1], *H. Orth*[2], *C. Sahin*[†3], *A. Sanchez*[3], *and C. Schwarz*[2]

[1]Justus-Liebig-University, Giessen, Germany; [2]GSI Helmholtzzentrum GmbH, Darmstadt, Germany; [3]Johannes Gutenberg University, Mainz, Germany

The advantages of SiPMs as compared to conventional photomultipliers are high photon detection efficiency, moderate bias voltages, magnetic insensibility, and small size. Limitations for their usage in experiments come from dark count rate and after pulsing. These properties are a function of temperature and were measured here for two sensors. The temperature of the sensors was controlled by placing them in a Peltier-cooled light-tight aluminum box.

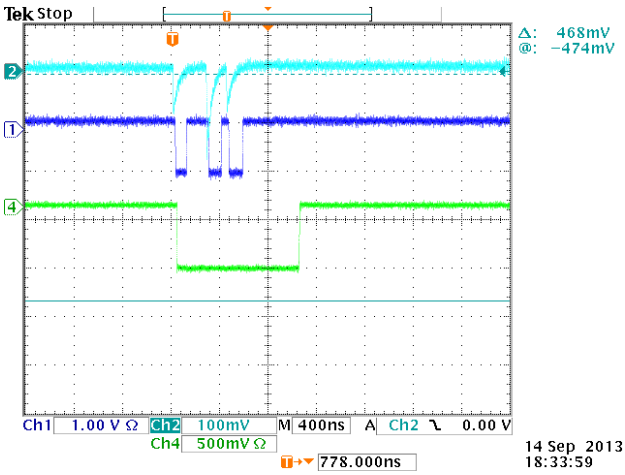

Figure 1: Oscilloscope example for dark count signals from a SiPM S10362-11-100P [1] at room temperature. The top trace shows a dark count with two after pulses. The middle one shows a gate from a discriminator which counts all signals, the bottom gate counts the groups, excluding the after pulses.

Electronic sensors (LM35AH) measured the temperature at two positions of the walls. Measurements were done when the temperature difference was below 0.5^{o}C. The dark count signals were followed by after pulsing, an example is shown in Fig. 1, top trace. In order to distinguish between true dark counts and after pulsing, we counted the hits with the help of two electronic gates from a discriminator. The $1\mu s$ long gate (bottom row) counted the dark counts, the short one of 100ns (middle row) includes after pulsing.

The count rate per second and square millimeter is shown in Fig. 2, for two devices. The error bars are within the symbol size. The top curves are for a S10362-11-100P from Hamamatsu [1], the bottom curves for PM3375 with trench technology from Ketek [2]. The closed symbols and

	PM3375	S10362-11-100P
Area	3x3 mm^2	1x1 mm^2
Cell pitch	75 μm	100 μm
Geo. effi.	72%	78.5%

Table 1: Geometric properties of the measured sensors.

open symbols denote the count rate without and with after pulsing, respectively. For each measurement the breakthrough voltage was determined and the device operated at 1 V overvoltage. The decrease of the dark count rate with decreasing temperature is clearly seen. It drops by a factor of two for a temperature decrease of 8.2^{o}C and 9.8^{o}C for the Hamamatsu and Ketek sensor, respectively. These values are close to the expected decrease of a factor 2 every 8^{o}C [3]. For both sensors the amount of after pulses decreases with decresasing temperatures as can also be seen in Fig,2 by the larger rate difference for closed and open symbols at the higher temperatures

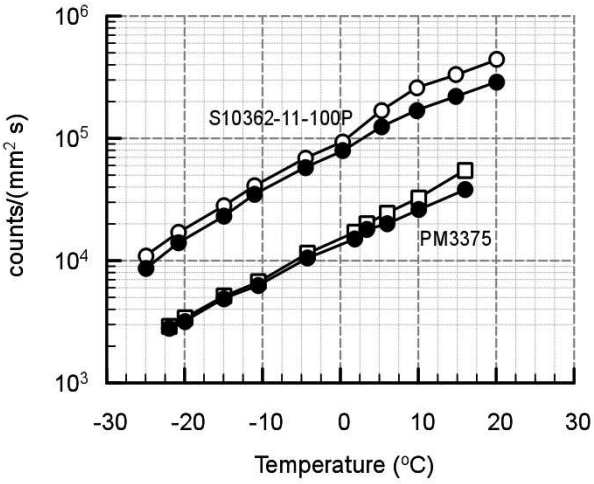

Figure 2: Dark count rates for two SiPMs. The open symbols denote the pulse rate including after pulsing, the closed symbols denote the pulse rate excluding after pulses.

References

[1] http://www.hamamatsu.com

[2] http://www.ketek.net/

[3] NIM A567 (2006) 48, D. Renker

* EU FP7 grant, contract number 227431, HadronPhysics3.

† sahin@kph.uni-mainz.de

 doi:10.15120/GR-2014-1-HSD-10

Further Development of Lattice-FPGA based TDC and Its Implementation on different Platforms

C. Ugur[*1], *J. Frühauf*[1], *J. Hoffmann*[1], *N. Kurz*[1], *T. Schweitzer*[1], *and M. Traxler*[1]
[1]GSI, Darmstadt, Germany

The research on the Lattice ECP3 FPGA based TDC described in [1] was carried out during the year 2013 in order to implement further features (e.g. semi-asynchronous stretcher, calibration trigger) and fix bugs in the design. Moreover, the design was adapted to other readout platforms (e.g. MBS) and implemented on different boards (e.g. FEBEX3, CBMTOF) and several tests were applied to assess the TDC in detail.

Some detectors used in particle physics experiments - e.g. Microchannel Plate (MCP) Detectors used for single photon detection - can generate pulses as short as 1 ns. These short signals cannot be measured by the traditional TDL based TDCs, where the state of the start signal has to be preserved until the rising edge of the stop signal, as the falling edge of the start signal would induce another transition in the delay line. In our case the start signal has to conserve the logic high state until the rising edge of the next clock cycle. Therefore, a semi-asynchronous pulse stretcher is designed to extend the length of the hit signals more than one clock period. The stretcher is shown in Figure 1(a).

The stretcher was tested with a $\sim 500\ ps$ wide pulse. In order to measure the width of the short pulse the rising and falling edges of the pulse were measured on two channels. The difference between these two channels was recorded in a histogram after calibration. In Figure 1(b) it can be seen, that the mean of the peak is at $519\ ps$, which gives the width of the pulse. Also the measured precision not considerably deteriorated ($12\ ps$).

As the delay lines of the TDC channels don't have a constant propagation delay and each of them is unique, they have to be calibrated using random input signals with enough statistics ($\sim 10^5$). However, during the experiments it might not be possible to get enough statistics on every channel. Therefore, the TDC was designed to be prompted with a calibration trigger (if supported by the readout platform) to fire every channel with random pulses generated by the on-chip oscillator of the FPGA. After several tests, no deterioration was observed and this unprecise oscillator ($130\ MHz \pm 15\%$ [2]) proved to be an excellent candidate as a random hit generator.

The performance of the TDC was tested for long time intervals between the hit signals (up to 1 us). The long time intervals were spawned by using a data timing generator (Tektronix DTG5078) and were measured on two TDC channels on different boards (TRB3, FEBEX3, CBMTOF). In the FPGAs, which are powered by DC-DC converters, a periodic change of the precision over the delay time was discovered. The amplitude of this degradation was recorded as $\sim 35\ ps$ (Figure 2(a)). This effect seems to be caused by the noise induced in the supply voltage of the FPGA. In order to test the assumption the DC-DC converters on the board were removed and the test was repeated after the FPGAs were powered with a linear power supply. The peak-to-peak change in the precision over the same delay time was logged as $< 3\ ps$ (Figure 2(b)).

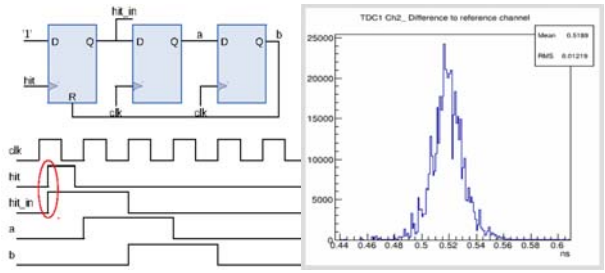

(a) (b)

Figure 1: (a) The falling edge of the input signal is delayed for two clock rising edges. (b) ToT measurement of a $500\ ps$ wide pulse was done on two channels of the TDC with a precision of $12\ ps$.

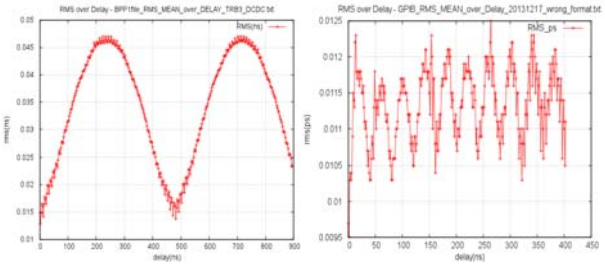

(a) (b)

Figure 2: The precision change of the TDC over long delay measurements in an FPGA powered by (a) DC-DC converters and (b) linear power supply.

During the July 2013 PANDA Barrel-DIRC Detector Prototype beamtime tests at MAMI-Mainz (Mainzer Mikrotron) the TDC design on TRB3 platform was operated successfully.

References

[1] C. Ugur et.al, "GSI Scientific Report 2012", p.299.

[2] Lattice Semiconductors, "LatticeECP3 Family Handbook", July 2013, HB1009 Version 05.2.

*c.ugur@gsi.de

Study of PANDA Barrel DIRC design options*

R. Dzhygadlo[†1], *K. Götzen*[1], *G. Kalicy*[1], *H. Kumawat*[3], *M. Patsyuk*[1,2], *K. Peters*[1,2], *C. Schwarz*[1], *J. Schwiening*[1], *and M. Zühlsdorf*[1,2]

[1]GSI, Darmstadt, Germany; [3]BARC, Mumbai, India; [2]Goethe Universität Frankfurt, Germany

The PANDA Barrel DIRC detector [1] will be an essential component of the PANDA experiment at FAIR. It will perform hadronic particle identification, in particular to separate charged pions and kaons for momenta between 0.5 and 3.5 GeV/c. The physics program of PANDA requires the separation to be better than three standard deviations for polar angles between 22° and 140°.

To achieve this performance a number of design options for the PANDA Barrel DIRC geometry are considered. In the baseline design 16 modules, each comprising 5 narrow fused silica radiator bars (1.7 cm $\times$ 3.2 cm $\times$ 240 cm) surround the beam line at a radial distance of 47.6 cm. A charged particle passing through a bar produces Cherenkov photons, which are guided inside the radiator via total internal reflection to the mirror at the one side and to the expansion volume (EV) at the other. Fused silica or mineral oil are candidate materials for the EV. The photons are detected by an array of micro-channel plate photomultiplier tubes [2] with a pixel size of about 6.5 mm $\times$ 6.5 mm. A doublet lens between bar and EV focuses the hit pattern on the imaging plane.

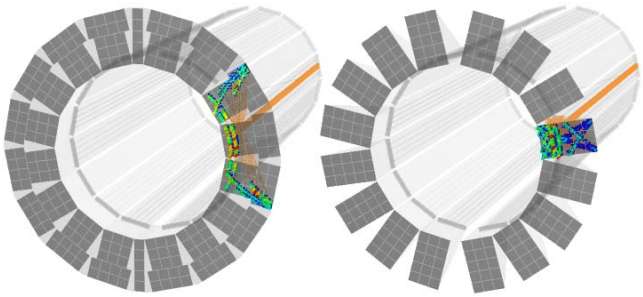

Figure 1: Geant-based simulation of the PANDA Barrel DIRC using narrow bars as radiators in combination with an oil-tank (left) and with compact solid fused silica prisms (right) as expansion volumes. The colored histogram shows the accumulated hit pattern from 20 charged kaons of the same momentum and angle.

In order to optimize the performance and reduce the detector cost, realistic simulations of different design options are performed using Geant [3] within the PandaRoot framework [4]. Fig. 1 shows two example geometries for different EV materials and shapes together with accumulated hit patterns.

The performance of each design is evaluated in terms of the reconstructed single photon resolution (SPR) and the photon yield per particle. The SPR is defined as the difference between the expected and reconstructed Cherenkov angle of each photon. Fig. 2 shows an example of the obtained SPR and photon yield as a function of the kaon polar angle for an oil-tank EV without focusing and with a two-component spherical lens. Of the two geometries only the focusing design, with 12–60 photons per particle and an SPR around 10 mrad, meets the Barrel DIRC requirements for PANDA.

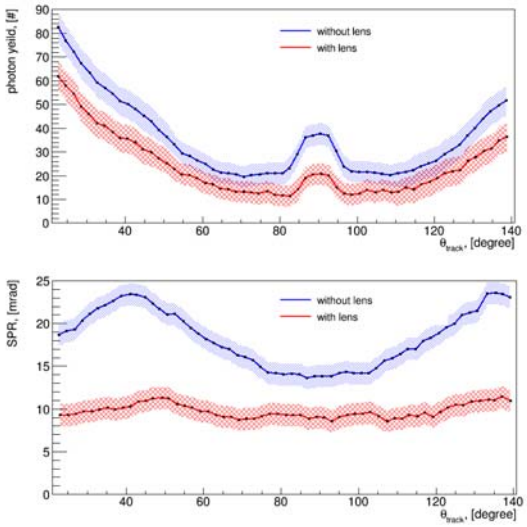

Figure 2: SPR and photon yield for an oil-tank EV with (red line) and without (blue line) a focusing system. The bands correspond to the rms of the distributions in each bin.

The evaluation of others detector design options, in particular the use of wide plates instead of narrow bars, in combination with different cylindrical and spherical lens designs, is ongoing. Several of the most promising designs will be implemented in a prototype and tested with particle beams at GSI in the summer of 2014.

References

[1] J. Schwiening, Nucl. Instr. and Meth. Phys. Res. Sect. A 639 (2011) 315.

[2] A. Lehmann et al., Nucl. Instr. and Meth. Phys. Res. Sect. A 718 (2013) 535.

[3] S. Agostinelly et al., Nucl. Instr. and Meth. Phys. Res. Sect. A 506 (2003) 250; J. Allison et al., Nuclear Science, IEEE Transactions **53** (2006) 270-278.

[4] S. Spataro, J. Phys. Conf. Ser. **119** (2008) 032035; M. Al-Turany and F. Uhlig, Proceedings of Science (ACAT08) 048.

*Work supported by HGS-HIRe, HIC for FAIR, EU FP6 grant #515873, and EU FP7 grant #227431.

† R.Dzhygadlo@gsi.de

 doi:10.15120/GR-2014-1-HSD-12

Study of a PANDA Barrel DIRC design based on radiator plates*

R. Dzhygadlo[1], *K. Götzen*[1], *G. Kalicy*[1,2], *H. Kumawat*[1,3], *M. Patsyuk*[1,2], *K. Peters*[1,2], *C. Schwarz*[1], *J. Schwiening*[1], *and M. Zühlsdorf*[†1,2]

[1]GSI, Darmstadt, Germany; [2]Goethe Universität Frankfurt, Germany; [3]BARC, Mumbai, India

A Cherenkov detector based on the DIRC (**D**etection of **I**nternally **R**eflected **C**herenkov light) principle [1] will be used in the target spectrometer of the PANDA experiment to distinguish between charged pions and kaons for momenta between 0.5 and 3.5 GeV/c. It is centered around the target point, in the shape of a barrel to cover polar track angles between 22 and 140°. The design of the PANDA Barrel DIRC is based on the BABAR DIRC [2] (the first successful DIRC counter) with some important improvements, such as fast photon timing, focusing optics, and a compact expansion volume [3].

In the PANDA Barrel DIRC baseline design the barrel of 47.6 cm radius comprises 16 sections with 5 fused silica radiator bars (1.7 cm×3.2 cm×240 cm) each. Cherenkov photons, produced along the charged particle track in the bar, are guided inside the radiator via total internal reflection. A mirror is attached to the forward end of the bar to reflect photons towards the read out end, where they are focused with a lens and projected onto a flat photo detector plane behind the 30 cm-deep oil-filled expansion volume. An array of Micro-Channel Plate Photomultiplier Tubes (MCP-PMTs) is used to detect the photons and measure their arrival time with a precision of about 100 ps.

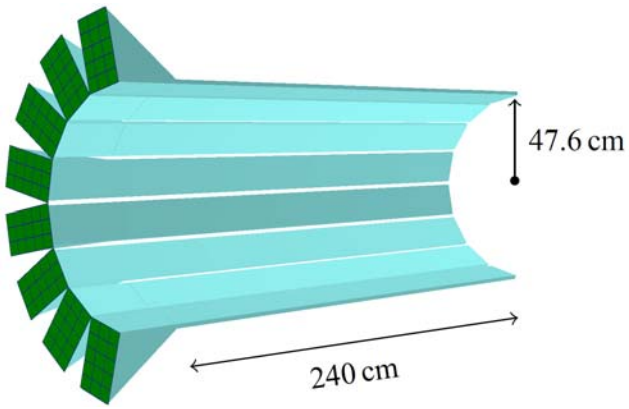

Figure 1: Geant simulation of one half of a barrel DIRC using radiator plates.

In order to meet the PANDA resolution requirement and reduce the detector cost, the influence of different parameters and geometry options on the detector performance are being studied in simulations. The use of one wide plate per bar box significantly reduces the total detector production cost in comparison to the baseline design with narrow bars, as there are fewer pieces to be polished. In addition, a compact fused silica prism can be used as a photon camera in front of each bar box instead of the single volume filled with mineral oil. This option reduces the number of pixels and provides better optical properties, which improves the photon yield. Figure 1 shows a simulation of a DIRC where both options are applied. Figure 2 illustrates the propagation paths of Cherenkov photons inside the plate and prism.

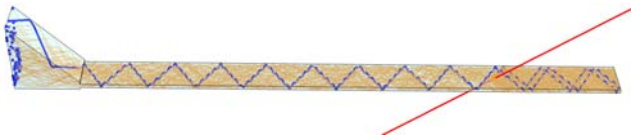

Figure 2: A single DIRC module, comprising a radiator plate, forward mirror, prism, and MCP-PMT array. The kaon track is shown in red, Cherenkov photon trajectories in orange. For clarity, the path of a single photon is highlighted in blue.

In 2013, two reconstruction approaches were developed for these design options and tested with Geant [4] simulations. The first approach, reconstructing the Cherenkov angle with lookup tables and geometrical photon path reconstruction, fails to meet the PANDA requirements due to excessive combinatorial backgrounds created by chromatic dispersion.

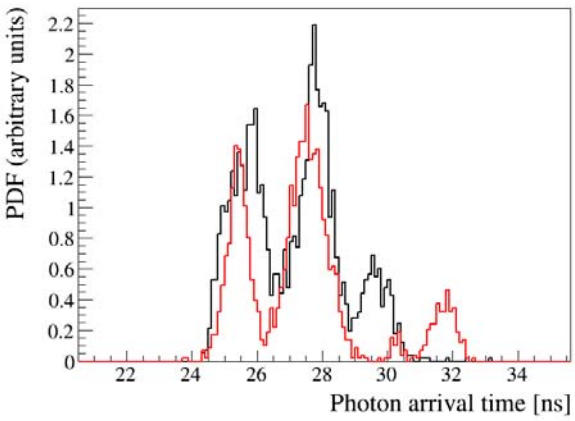

Figure 3: Propability density functions of pion (red) and kaon (black) hypotheses for a selected pixel.

A second approach uses the photon arrival time for each track momentum and direction, pixel by pixel, to produce

*Work supported by HGS-HIRe, HIC for FAIR, EU FP6 grant #515873, and EU FP7 grant #227431.

† m.zuehlsdorf@gsi.de

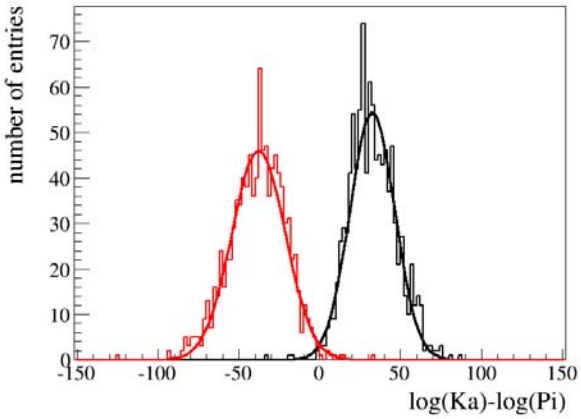

Figure 4: Log-likelihood difference for pion and kaon hypotheses for a sample of pions (red) and kaons (black) at 3.5 GeV/c track momentum and 22° polar track angle.

probability density functions (PDF, see fig. 3), so that for each particle track time-based likelihoods can be assigned to the particle hypotheses. This approach shows promising results with realistic DIRC geometries and PDFs created from simulation, and seems to meet the resolution requirements for PANDA, even without the aid of focusing elements. A critical region in the final state kaon phase space for the barrel DIRC is at 3.5 GeV/c track momentum and 22° polar track angle, as most of the kaons are expected in forward direction at high momenta, and a pion/kaon separation is challenging due to the small Cherenkov angle difference at higher momenta. The separation power, which is defined by the difference of the kaon and pion likelihood-ratio distribution divided by the average standard deviation, is a figure of merit for the PID performance. Figure 4 shows a separation power of 4.7 standard deviations at 3.5 GeV/c track momentum and 22° polar track angle, which is better than the 3 standard deviations set as goal of the PANDA PID. Simulation studies of the performance of the wide plate in combination with a cylindrical lens are ongoing.

The reconstruction approach is currently being applied to experimental data taken with a DIRC prototype at CERN in 2012. Additional data will be taken with an improved prototype setup at GSI in summer 2014.

References

[1] B. N. Ratcliff, SLAC-PUB-5946 (1992), SLAC-PUB-6047 (1993); P. Coyle et al., Nucl. Instr. and Meth. Phys. Res. Sect. A 343 (1994) 292.

[2] I. Adam et al., Nucl. Instr. and Meth. Phys. Res. Sect. A 538 (2005) 281.

[3] J. Schwiening, Nucl. Instr. and Meth. Phys. Res. Sect. A 639 (2011) 315.

[4] S. Agostinelly et al., Nucl. Instr. and Meth. Phys. Res. Sect. A 506 (2003) 250; J. Allison et al., Nuclear Science, IEEE Transactions **53** (2006) 270-278; S. Spataro, J. Phys. Conf. Ser. **119** (2008) 032035; M. Al-Turany and F. Uhlig, Proceedings of Science (ACAT08) 048.

 doi:10.15120/GR-2014-1-HSD-13

Study of the timing resolution of a PANDA Barrel DIRC prototype

M. Krebs[*1,2], *K. Peters*[1,2], *C. Schwarz*[1], *and J. Schwiening*[1]
[1]GSI, Darmstadt, Germany; [2]Goethe Universitaet, Frankfurt, Germany

A prototype of the PANDA Barrel DIRC [1] detector was tested with hadronic beams at the CERN PS in the summer of 2012. The outcome of this test was analysed during the last year and converted into design improvements. A synthetic fused silica bar ($17 \times 35 \times 1225$ mm^3) with a focusing lens attached to one end and a mirror to the other end was placed into a light-tight container. A large synthetic fused silica prism with a depth of 30 cm, located about 2 mm from the lens, served as expansion volume. The hit location and the photon propagation time of photons were measured with an array of nine Micro-Channel Plate Photomultiplier Tubes (MCP-PMTs) coupled with optical grease to the back surface of the prism. The data acquisition for 896 channels was performed using the TRB (version 2) boards [2] in combination with TOF addOns [3], customized for MCP-PMT readout. The primary goal were the determination of the single photon Cherenkov angle resolution and the photon yield for several design options, including different focusing systems and radiator sizes.

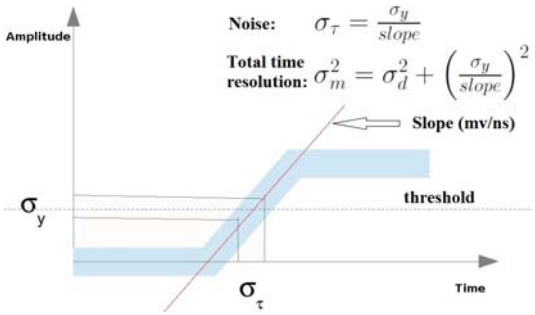

Figure 1: Schematic of signal amplitude vs. time, illustrating the influence of noise on the timing resolution.

The observed timing resolution of $\sigma \approx 150 - 200$ ps was significantly worse than the goal of $\sigma < 100$ ps. Since test bench measurements had previously demonstrated that the intrinsic resolution of the Photonis Planacon MCP-PMT is less than 50 ps [4], the readout system was studied in detail at GSI after the beam time. For this study we used a Tektronix pulse generator (AFG3252) to vary amplitude and rise time of the signal. Any noise on the pure single photon signal, picked up by the MCP-PMT or the cable connecting the sensor to the discriminator, contributes to the measured timing jitter σ_m via the slope of the signal, as shown in Fig. 1, taking the timing jitter of the discriminator σ_d into account. The results of a measurement for one of the addOn boards used during the beam time are shown in Fig. 2 for a range of signal amplitudes. The slopes of the signals were adjusted by changing the rise times for the corresponding signal heights. The timing resolution drops as as a function of the signal slope, independent of the signal amplitude and converges asymptotically to the timing jitter value of the discriminator. The slope of the rise time of a Planacon MCP-PMT is about 5 mV/ns, which corresponds to a contribution of 60 ps from the readout to the single photon timing resolution.

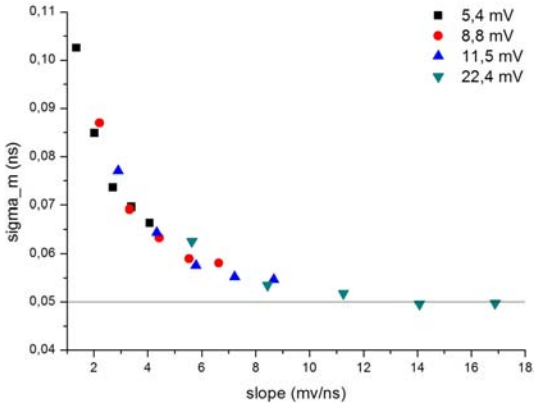

Figure 2: Timing resolution sigma_m vs. slope of the signal for a NINO threshold of 1.65 mV. The symbols represent different signal amplitudes.

The time resolution observed during the CERN test beam experiment would be consistent with a rather high noise level of $\sigma_{noise} = 1.2$ mV. This noise may have been pick-up from the 2 m-long cables between the MCP-PMT array and the addOn boards with the long cables acting as antennas in the busy T9 beam line area.
The next PANDA Barrel DIRC prototype, with an improved readout system based on the TRB version 3 [5] in combination with a new discriminator board (PADIWA), will be tested with particle beams at GSI in the summer of 2014.

References

[1] J. Schwiening, et al., Nucl. Instr. and Meth. Phys. Res. Sect. A 639 (2011) 315.

[2] I. Fröhlich, et al., IEEE Trans. Nucl. Sci. 55 59 (2008).

[3] F. Anghinolfi, et al., Nucl. Instr. and Meth. Phys. Res. Sect. A 533 183 (2004);
J. Christiansen, et al., "HPTDC High Performance Time to Digital Converter," 2004 CERN/EP-MIC.

[4] A. Lehmann, et al., Nucl. Instr. and Meth. Phys. Res. Sect. A 718 (2013) 535-540.

[5] A. Neiser, et al., 2013 JINST 8 C12043.

* M.Krebs@gsi.de

 doi:10.15120/GR-2014-1-HSD-14

Collaboration report NUSTAR progress in 2013

C. Scheidenberger[1]

[1]GSI, Darmstadt, Germany

Since several decades, the year 2013 was the first year without beamtimes at GSI. Various NUSTAR detectors and sub-systems for FAIR are already in operation and the collaboration looks forward to their implementation and use at FAIR. The lack of beamtime induced a serious change of the daily scientific work and hampered the beam-related preparations of FAIR experiments, component tests and R&D-work, including pilot experiments for FAIR.

NUSTAR collaboration

The NUSTAR collaboration is fully operational. All bodies and gremia are established and work continuously since several years.

Like in previous years, NUSTAR has held its two major collaboration meetings: in spring 2013 the NUSTAR Annual Meeting took place as usual at GSI, and in fall the NUSTAR Week, which is traveling to the major NUSTAR partner countries and institutes, took place in Helsinki (Finland). These meetings focus on the scientific achievements, on technical developments and they are important meeting platforms for the various groups and boards of the collaboration; they also give opportunity to present status and progress of the NUSTAR common working groups to the whole collaboration. Besides these meetings, the NUSTAR News Letter appears regularly several times per year and keeps all collaboration members and other people up-to-date on all relevant collaboration activities. For the missing LEB building, a task force was established to firmly promote the realization of the LEB hall. The Super-FRS experimental program was established as comprising part of NUSTAR, and a scientific high-level program has been identified, which is characteristic for the high-energy accelerator capabilities at FAIR. With few, dedicated ancillary detectors, a NUSTAR science program extended in scope and quality, competitive on the world scale, will become possible by the time when FAIR operation will start.

The NUSTAR groups at GSI and FAIR fulfil important integrating activities and play a vital role for the whole scientific collaboration. They are an essential prerequisite for the exploitation of existing instruments at UNILAC and SIS-ESR of GSI and the future facilities of FAIR. They are a melting pot of all relevant scientific activities and provide organizational support and coordination. Together with the scientific-technical infrastructure departments and the collaboration, they perform cross-sectional developments, for instance data acquisition, electronics, data analysis, quality assurance etc., and integrate and coordinate the collaborative efforts for operating, maintaining and upgrading the experimental instruments and laboratories.

Project developments

NUSTAR builds on a continuous transition from GSI towards FAIR. The central device of the NUSTAR collaboration at FAIR will be the superconducting fragment separator (Super-FRS), which is in preparation. The separator itself and its three exit branches will be equipped with complex detectors for forefront experiments. These detector systems are mostly built modularly and allow for a stepwise setup and integration. Already today, all of them have reached the status of a basic “start version” for experiments.

Also the procurement of Super-FRS components is well underway. The collaborative work with FAIR members and in-kind partners is in full swing. Also the fruitful scientific-technical collaboration with KVI continues with work packages like the cryogenic ion catcher for the Low-Energy Branch of the Super-FRS or the slit system for the separator itself. The layout of the energy buncher spectrometer at the Low-Energy Branch of the Super-FRS was finalized. The new layout has many experimental advantages and will solve several technical challenges. It builds mostly on standard Super-FRS components and reduces R&D efforts and costs. Target and material tests, R&D work of detectors, new ion-optical modes and separation schemes are carried out as a concentrated effort of the whole NUSTAR collaboration with a large degree of synergy and cross-fertilization among the various NUSTAR sub-collaborations and the GSI NUSTAR groups.

Scientific achievements

The NUSTAR groups at GSI made several important scientific achievements. The year prompted many publications and conference contributions, and awards for several group members. They are described in this annual report, and the most important ones are briefly mentioned here.

In the theory groups the main focus of last year’s activities was on astrophysical applications of nuclear physics. The inclusion of charged-current interactions for muon neutrinos in supernova calculations showed a significant change in opacities that will have consequences for the neutrino spectra emitted from a proto neutron star. In studies of nuclear matter at low densities the relativistic density functional approach was extended with an explicit treatment of clusters of light nuclei and nucleon-nucleon correlations. These additional degrees of freedom are nec-

essary to obtain a correct low-density limit as provided by the virial equation of state.

Calculations within an extended Hartree-Fock-Bogoljubov (HFB) approach with multiphonon excitations provided an improved description of M1 strength distributions and neutron-capture cross sections at low energies. Microscopic calculations for resonances and continuum states with the fermionic molecular dynamics (FMD) approach were extended with an explicit treatment of coupled channels, and used to investigate the structure of the continuum states in ^{12}C. Realistic nucleon-nucleon interactions have a non-trivial momentum dependence. A phase-space representation was developed to provide a better visualization of interaction properties.

The activities of the superheavy element research groups concentrated on the analysis of previously measured data, technical developments for their experimental setups and FAIR injectors, and participation in experiments elsewhere.

Together with the partners at the University of Mainz, the Helmholtz Institute in Mainz, and several foreign groups, the chemistry group performed two experiments at the RIKEN facility in Japan. The goal was the synthesis and chemical characterization of a compound class, which would be new for superheavy elements: seaborgium hexacarbonyl (element 106). The physics group performed in collaboration with the superheavy element group of RIKEN an experiment at the GARIS separator: in reactions ^{48}Ca + ^{248}Cm → ^{296}116* several decay chains of Z=116 isotopes were observed, whose decay pattern were previously measured at SHIP. This experiment was a starting point for the future experiments with 248Cm targets at RIKEN. Further, the physics group participated in transfer and fusion-fission reaction experiments at JINR in Dubna and contributed a diamond dE-E-TOF telescope as a new asset to the CORSET set-up for studies at the Coulomb barrier. These activities help to maintain the experimental expertise and develop practical skills for working towards the future FAIR facility.

Other main activities included performing the data analyses from the long experiments in 2011/12 on the search for the new elements 119 and 120 as well as the synthesis of element 117, which were partially completed, and the preparations for experiments foreseen for 2014 at GSI, including experimental and theoretical studies of chemical properties of superheavy elements. Analysis of spin distributions for compound nuclei from compound nuclei from Ni-64 + Mo-100 reactions at energies around the Coulomb barrier measured previously at INFN Legnaro was performed, decay properties of neutron deficient Fr- and Ra-isotopes were studied, nuclear shell strengths towards N = 162 was analyzed.

Construction and purchase for the new focal plane detector system for SHIP was sustained, first off-line tests were started. Improved detection for trapped ions using the 'phase imaging ion cyclotron resonance' (gaining more than one order of magnitude higher mass resolution) was successfully applied in off-line measurements. The RADRIS method for laser spectroscopy of superheavy elements was further optimized on the basis of results from test experiment in late 2012 and is now ready for laser spectroscopy experiments on 254No. As a new activity an upgrade program to optimize the operation of the UNILAC gas stripper with respect to the requirements of FAIR was started.

The first determination of radii of proton distributions of $^{12-17}$B nuclides from charge changing cross section (σcc) measurements at the FRS has been reported. The radii are deduced from a finite-range Glauber model analysis of the σcc and show an increase from ^{13}B to ^{17}B. The measurements show the existence of a thick neutron surface with a neutron-proton radius difference of 0.51(0.11) fm in 17B.

The in-flight decay measurement of the short-lived proton-drip-line nuclide ^{31}Ar has been analysed. The experiment setup was similar to the previously successfully measured two-proton emitter ^{19}Mg.

The FRS group worked also intensively on the ion-optical layout of the LEB of the Super-FRS and its experimental performance in different scenarios with the ion-catcher in combination with the Multiple- Reflexion Time-of-Flight Mass Spectrometer (MR-ToF-MS). High-resolution Super-FRS spectrometer experiments can be performed with the dispersion-matched energy buncher combined with the main Separator. The extraction efficiency of the stopping cell has been significantly improved to about 60% by higher gas purity and lower temperatures of 70-100 K. The average extraction time for uranium fragments was 24 ms. Broad band mass spectra have demonstrated the cleanliness of the gas-filled stopping cell. The performance of the MR-ToF-MS has been investigated experimentally at the FRS with isobars of A=211 produced with 1000 MeV/u ^{238}U projectiles in a Be target. The achieved accuracy and resolution of the MR-ToF-MS has not yet reached the off-line results but with the performed technical changes it will be possible. However, the presently achieved online resolving power (R > 2·105) is already sufficient to unambiguously identify the nuclides of hot fusion products in the range of Z>113. This identification was not possible in the past.

The analysis of the data obtained from two different isochronous mass measurements with the correlation matrix has made a lot of progress.

The analysis of data obtained at the R^{3}B-LAND setup yielded several highlights concerning the spectroscopy of nuclear systems beyond the drip lines. On the proton-rich side, the ground state of the unbound nucleus ^{15}Ne could be identified for the first time. Several cases beyond the neutron drip line have been studied, including the neutron-unbound systems ^{25,26}O, which are presently the heaviest nuclei beyond the neutron drip line which can be reached experimentally. The structure of the unbound ^{13}Be nucleus has been investigated in detail on the basis of high-quality data from knockout reactions measured at the R^{3}B-LAND setup in conjunction with results from

 doi:10.15120/GR-2014-1-NUSTAR-FRS-01

previously published data. A consistent description of the ^{13}Be excited states was obtained resolving previous discrepancies in the interpretation. For the nucleus ^{14}Be, the second 2+ excited state was identified and its structure and decay mechanism was investigated for the first time.

The program concerning the investigation of collective dipole excitations, in particular low-lying Pygmy strength in neutron-rich nuclei has been continued. The analysis of the data on electromagnetic excitation of ^{68}Ni has been finalized and published. The dipole polarizability has been measured for the first time for a short-lived nucleus from which a neutron-skin thickness for 68Ni of 0.17(2) fm has been extracted, which provides constraints on the density dependence of the symmetry energy. The Pygmy dipole resonance (PDR) was observed at 9.6 MeV exhausting 2.8(5)% of the energy-weighted sum rule. In addition, a gamma decay branch for the PDR of 7(2)% could be extracted by combining our result with a previous measurement.

The activities of the nuclear spectroscopy group was dominated by the preparations of the PRESPEC experiments using the AGATA-detector. The set-up was further optimized, based on the experience gained in the beamtimes in 2012, and the data analysis of the 2012 runs was continued and data integrity confirmed. A new concept for the DESPEC DEGAS array, backed by simulations, has been worked out. A new segmented scintillator detector (finger detector) for very high beam particle rates has been realized. As spin-off a novel position sensitive gamma-detector for industrial applications has been developed and successfully tested. A conceptually new data analysis software suite has been developed and implemented, allowing to analyse data from FRS, PRESPEC and other detection systems in an easy and versatile manner.

Awards

- Michael Block was awarded the Flerov Preis 2013 of the JINR Dubna
- Timo Dickel received the GENCO Young-Scientist Award 2013 of the GSI Exotic Nuclei Community
- Sophie Heinz has been named by Elsevier for excellence in reviewing as “one of the most valued reviewers of 2013”
- Sigurd Hofmann became member of the “Polish Academy of Arts and Sciences”

Progress on the Super-FRS Experimental Program

J. Äystö[1], K. Gales[2], H. Geissel[3,4], C. Nociforo[3], C. Scheidenberger[3,4], H. Simon[3], I. Tanihata[5,6], H. Weick[3], M. Winkler[3], and for the Super-FRS Collaboration [1]

[1]Helsinki Institute of Physics, FI-00014 University of Helsinki, Finland; [2]IPN Orsay/IN2P3-CNRS and University Paris XI, 91406 Orsay Cedex, France; [3]GSI Helmholtzzentrum für Schwerionenforschung GmbH, 64291 Darmstadt, Germany; [4]Justus-Liebig-Universität Gießen, 35392 Gießen, Germany; [5]Research Center for Nuclear Physics, Osaka University, Osaka 567-0037, Japan; [6]School of Physics and Nuclear Energy Engineering, Beihang University, Beijing, China

The superconducting fragment separator (Super-FRS) will not only provide several thousand different short-lived isotopes to the experimental destinations of its three branches, but, taking advantage of its nature being a high-resolution spectrometer [1], it will enable a variety of unprecedented, unique nuclear physics experiments, too. The key feature common to these "spectrometer experiments" is the high-resolution momentum measurement. The highest possible momentum resolution will be reached with the energy-buncher/spectrometer [2] at the LEB when this is coupled to the main separator in a dispersion-matched ion-optical mode: to first order, this combination will yield a momentum resolving power up to $p/\Delta p \sim 20,000$. Another important trait is the multi-stage operation, where the separator-spectrometer capabilities as such are a comprising and integral part of the measurement. With this intention, the Super-FRS Collaboration has identified experiments, which are complementary to the other NuSTAR experiments and emerge as new physics opportunities with the Super-FRS instrument. The common feature is that these experiments will employ

- individual stages of the Super-FRS (roughly speaking: pre-separator, first and second half of the main separator, spectrometer/energy buncher at the Low-Energy Branch)
- different ion-optical modes of the Super-FRS (achromatic, mono-energetic, dispersive)
- several target and degrader stations at the major focal planes (including secondary or tertiary targets)
- various functions (separation including the suppression of the primary beam or unwanted species, identification, momentum measurement).

This opens up a large variety of experimental conditions, customized for the specific goals of the measurement, including new measurement concepts, not fully explored yet. For most of the experiments, the standard equipment of the Super-FRS can be used, while some experiments will need additional ancillary detector setups, which are currently under development. Scientific contributions to the following main topics can be expected:

Basic studies: this category of Super-FRS experiments goes hand in hand with the performance verification of the separator and its standard detector systems; ion-optical measurements will also include atomic collision experiments of ions penetrating (shaped) matter over the full energy range down to thermalized reaction products (e.g. in the cryogenic gas-filled stopping cell of the Low-Energy Branch [3]). These studies will also aim at the search for new isotopes, production cross section and rate measurements and provide data needed for all other NuSTAR experiments.

Nuclear structure and nuclear matter: the structure of nuclei far off stability is a major topic of modern nuclear physics and a central pillar of all next-generation radioactive beam facilities. The present approach is associated with nuclear reactions at relativistic speed and subsequent high-resolution longitudinal momentum-distribution measurements that give access to nuclear radii and matter distributions of the most exotic nuclei. The discoveries of neutron and proton halos, neutron skins and new "'magic numbers"' originated from such inclusive experiments. The experiments will provide information on the equation-of-state (EOS) of cold asymmetric matter by nuclear density distributions and neutron skin thicknesses, where the saturation density of asymmetric nuclear matter can be extracted from systematic data on interaction cross sections, charge changing cross sections, and proton elastic scattering of neutron rich nuclei. Exotic decay modes, such as 2-proton radioactivity, appear near the drip-lines at the limits of stability. Multiple neutron or proton radioactivity, appearing in extremely short-lived nuclei ($T_{1/2} \sim 10^{-10}s$), can only be studied with the in-flight decay technique, which was pioneered at the FRS [4], and which is based on relativistic exotic nuclei impinging on a secondary target within a fragment separator and subsequent identification. Also beta-delayed ternary fission is so far unobserved, but with the sensitivity of novel detector systems, such as an O-TPC [5], combined with the universal isotope production capabilities, short separation times and the selectivity of Super-FRS, even very weak decay branches can be identified. Finally, the study of tensor forces is an important new direction in nuclear physics [6]. The tensor interaction introduces a high-momentum component in the nucleus through specific proton-neutron correlations, which can be "visual-

 doi:10.15120/GR-2014-1-NUSTAR-FRS-02

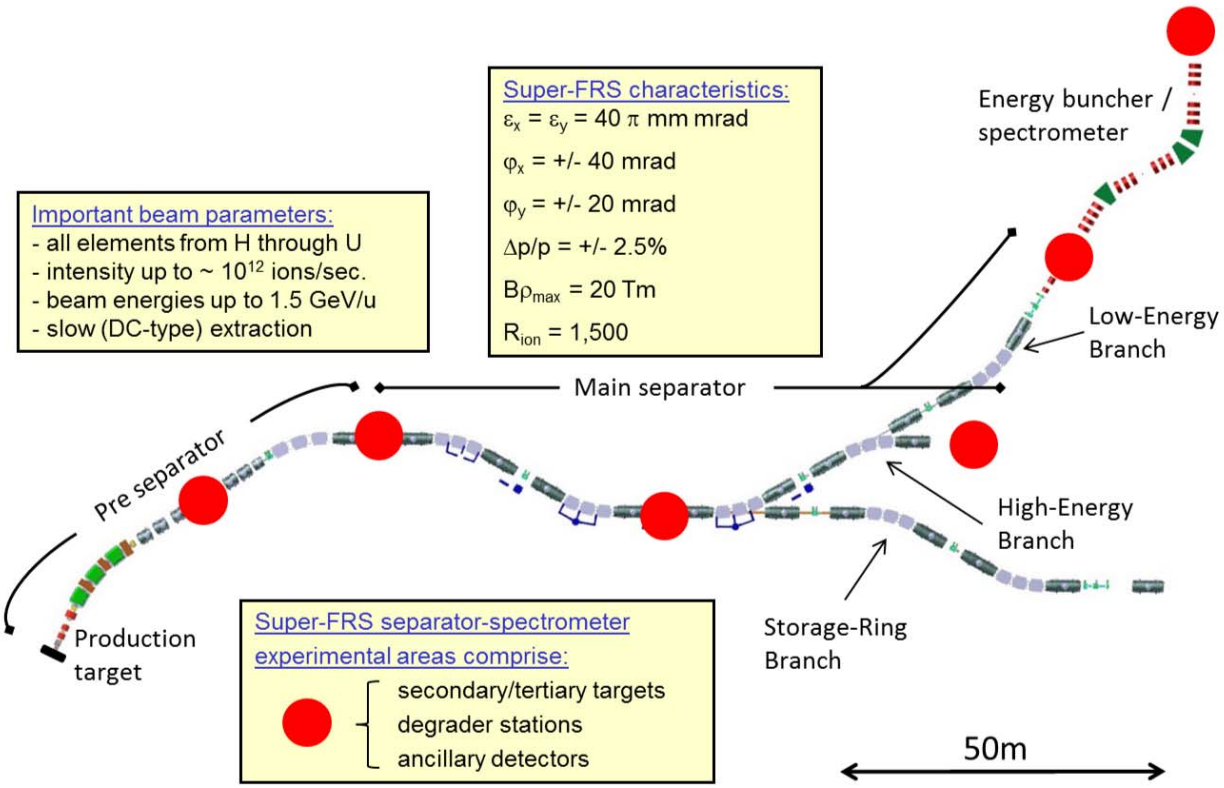

Figure 1: Schematic view and characteristic features of the Super-FRS with its three branches and the LEB energy-buncher/spectrometer system. The different separator stages and the experimental areas, which will be used for high-resolution separator-spectrometer experiments, are indicated.

ized" by high-momentum transfer reactions and subsequent high-resolution momentum analysis of the beam-like reaction product at beam energies above 400 A MeV.

Exotic atoms: at relativistic energies and with sufficiently intense beams (typically in excess of $\sim 10^5$ ions per second), various exotic atoms can be produced, for instance hypernuclei or Δ and N^* excitations in nuclei, or mesic nuclei respectively mesic atoms. Both are of interest to study chiral symmetry breaking via direct measurements of in-medium mass modifications. Also interactions between such exotic particles and nucleons or nuclear matter are subjects of interest. Resonance physics in radioactive nuclei is completely unexplored. A recent pilot experiment [7] with the FRS has demonstrated that new properties of the Δ resonances can be observed in charge-exchange reactions of heavy ions. Also the possibility to produce (multiple) strangeness in nuclei by coalescence in fragmentation reactions, recently demonstrated [8], opens up a completely new and wide field of studies. Production rates for exotic atoms are sufficiently high in the region of $1 \ldots 1.5$ A GeV (cross sections are at the micro-barn level), and the Super-FRS with its capability to serve as zero-degree spectrometer, its momentum resolution down to $\delta p \sim 10^{-4}$ (essential for missing-mass measurements of bound states with a precision of $\sim$ MeV/c2), and its high primary-beam or contaminant suppression will allow unique experiments in this emerging field.

References

[1] H. Geissel et al., Nucl. Instr. Meth. B204 (2003) 71.

[2] H. Geissel et al., Nucl. Instr. Meth. B317 (2013) 277.

[3] W. R. Plaß et al., Nucl. Instr. Meth. B317 (2013) 457.

[4] I. Mukha et al., Phys. Rev. Lett. 99, 182501 (2007).

[5] M. Ćwiok et al, IEEE TNS 52, 2895 (2005), K. Miernik et al., Nucl.Instr.Meth. A581, 194 (2007).

[6] H. J. Ong et al., Phys. Lett. B725, 277(2013).

[7] J. Benlliure et al., publication in preparation.

[8] C. Rappold et al., Nucl. Phys. A 913, 170 (2013).

Spectroscopy of η'-mesic nuclei at FRS and Super-FRS*

H. Fujioka†[1], *K.-T. Brinkmann*[2], *S. Friedrich*[2], *H. Geissel*[3], *E. Gutz*[2], *R.S. Hayano*[4], *Y. Higashi*[5], *S. Hirenzaki*[5], *K. Itahashi*[6], *M. Iwasaki*[6], *D. Jido*[7], *N. Kurz*[3], *V. Metag*[2], *T. Nagae*[1], *H. Nagahiro*[5], *M. Nanova*[2], *T. Nishi*[4], *H. Outa*[6], *A. Prochazka*[3], *K. Suzuki*[8], *T. Suzuki*[4], *Y.K. Tanaka*[4], *H. Weick*[3], *E. Widmann*[8], *and H. Yamakami*[1]

[1]Department of Physics, Kyoto University, Kyoto, Japan; [2]II. Physikalisches Institut, Universität Gießen, Gießen, Germany; [3]GSI, Darmstadt, Germany; [4]Department of Physics, The University of Tokyo, Tokyo, Japan; [5]Department of Physics, Nara Women's University, Nara, Japan; [6]RIKEN Nishina Center, RIKEN, Saitama, Japan; [7]Department of Physics, Tokyo Metropolitan University, Tokyo, Japan; [8]Stefan Meyer Institut für subatomare Physik, Wien, Austria

A meson-nucleus system is a good tool to investigate the properties of mesons at finite density, which may be altered as a consequence of partial restoration of chiral symmetry. A series of pionic atom experiments at FRS has revealed partial restoration of chiral symmetry, by deducing the isovector parameter in the pion-nucleus potential. The $(d,^3\mathrm{He})$ reaction was used to produce deeply-bound pionic states in Sn or Pb atoms.

We will search for and investigate $\eta'(958)$-nucleus bound states by using the (p,d) reaction on $^{12}\mathrm{C}$ target with the incident energy of $2.5\,\mathrm{GeV}$ [1]. The η' meson is expected to have a smaller mass at finite density, due to the suppression of the $\mathrm{U_A}(1)$ anomaly effect. We will make use of the FRS and later of the Super-FRS as a spectrometer for zero-degree deuterons.

S437: First experiment at FRS

The first experiment (S437) will take place in July 2014. The detectors to be used in the experiment are almost ready. We will perform an integrity test for them by using the proton beam at the COSY synchrotron, Forschungszentrum Jülich, in January-Feburary 2014 (Fig. 1).

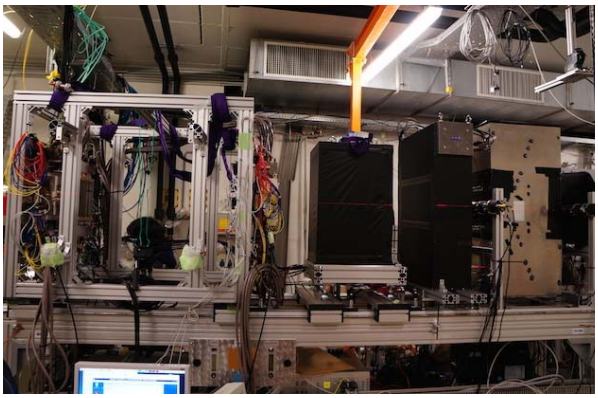

Figure 1: Experimental setup at the COSY-JESSICA site. Two sets of MWDC's, two types of high-refractive-index aerogel Čerenkov counters, and a total-internal-reflection Čerenkov counter are aligned along the beam axis.

Future plans at Super-FRS

The prolonged Super-FRS will enable us to carry out not only an inclusive measurement but also a semi-exclusive measurement. Each measurement has its own advantage, and we will improve the sensitivity of finding the signature of η'-mesic nuclei by the two different ways.

inclusive measurement

Since more intense beam from SIS-100 can be anticipated, we plan to upgrade the current VME-based DAQ system in order to cope with higher trigger rates. We will adopt an all-in-one readout board with Amplifier-Shaper-Discriminator (ASD) chips, Flash-ADC, and FPGA, based on the readout board for the Cylindrical Drift Chamber in the Belle-II experiment [2]. We will develop a new DAQ system for MWDC's with these readout boards.

semi-exclusive measurement

One promising idea for improving the signal-to-noise ratio, which is poor in an inclusive measurement, is to tag fast protons from the target. η' mesons in nuclei will be partly absorbed by two nucleons like $\eta' NN \to NN$, and the kinetic energy of the ejected nucleons will be around $500\,\mathrm{MeV}$, larger than from any other process.

Monte Carlo simulations of a microscopic transport model, JAM [3], is under way to get a better understanding of background processes with proton emission as well as the signal, i.e. the production of η'-mesic nuclei.

References

[1] K. Itahashi *et al.*, "Spectroscopy of η' mesic nuclei with (p,d) reaction — Interplay of $\mathrm{U_A}(1)$ anomaly and chiral restoration in η' mass —", Letter of Intent for GSI-SIS (2011); K. Itahashi, H. Fujioka *et al.*, Feasibility Study of Observing η' Mesic Nuclei with (p,d) Reaction", Prog. Theor. Phys. **128** (2012) 601–613.

[2] N. Taniguchi *et al.*, "All-in-one readout electronics for the Belle-II Central Drift Chamber", Nucl. Instrum. Meth. **A732** (2013) 540–542.

[3] Y. Nara *et al.*, "Relativistic nuclear collisions at 10A GeV energies from p+Be to Au+Au with the hadronic cascade model", Phys. Rev. C **61** (1999) 024901.

*Work supported by Grants-in-Aid for Scientific Research (Nos. 24105705 and 25707018) in Japan and HIC-for-FAIR.

† fujioka@scphys.kyoto-u.ac.jp

 doi:10.15120/GR-2014-1-NUSTAR-FRS-03

Experimental Setup for hypernuclear study at the Super-FRS

C.Rappold[*1,2], *T.R. Saito*[1,3,4], *C. Scheidenberger*[1,2], *and H. Geissel*[1,2]

[1]GSI, Darmstadt, Germany; [2]Justus-Liebig-Universität Giessen, Germany; [3]Johannes Gutenberg-Universität, Mainz, Germany; [4]The Helmholtz Institute Mainz, Mainz, Germany

The first experiment of the HypHI collaboration aimed to demonstrate the feasibility of the hypernuclear spectroscopy by means of heavy ion beam induced reactions. The final results show that the experimental method is viable for the study of hypernuclei [1, 2, 3].

The study of exotic hypernuclei which can not be produced in typical missing mass experiments involved at JPARC or JLab and MamiC is the topic of the future phases of the project[4]. The use of rare-isotope beams is mandatory to the study of exotic hypernuclei toward the proton- and neutron-drip line. The Super-FRS is crucial to the future phases of the HypHI project at FAIR, a feasibility study of the Super-FRS capability toward high energy of several GeV had to be achieved. A dedicated apparatus for exclusive measurement can be set up within the fragment separator Super-FRS, as an alternative to the experimental apparatus devoted to inclusive measurement as it was performed during the first experiments of the HypHI project. A detection apparatus consisting of an additional set magnetic optics could be install in order to separate the π^- meson of the mesonic weak decay of produced hypernuclei, while the second part of the Super-FRS is used as a fragment spectrometer to determine precisely the momentum of the fragment of hypernucleus of interest. Two different strategies have been investigated. The first strategy is to use a couple of dipole magnets in order to deflect the π^- meson from the positively charged particles and fragments with a first dipole magnet. The induced deflection to the fragments is then compensated with the second magnet in order to allow them to enter appropriately the second part of the Super-FRS. The second approach consists of using a solenoid magnet in order to analyze the momentum of the π^- meson while the fragments is to enter the second part of the Super-FRS as in the case of first approach. The detection apparatus is then to be considered to allow the vertex reconstruction of the hypernuclear decay. In the first case, detectors already developed and used in the first experiment of the HypHI project such as the fiber detectors can used in a similar way to track charged particles around the decay volume and in the upstream of the dipole magnets. π^- meson are then detected with a set of a hodoscope wall and drift chambers already available from the first HypHI experiment in order to complete the information needed for the track reconstruction. In solenoid magnet approach, a dedicated detection apparatus has to be developed in order to perform the position and energy-loss measurements within the solenoid magnet and the solenoid end-cap.

In both case, Monte Carlo simulations of the experimental apparatus has been carried out in the case of the study of the d+π^- final state of the ${}^{3}_{\Lambda}$n that was reported to be found by the HypHI collaboration [3]. In those case studies, dedicated detection apparatus as described above was designed. The main purpose of those first Monte Carlo simulations was to estimate the possible improvement that the use of the Super-FRS as spectrometer could provide. The invariant mass distributions of d+π^- final state of the event reconstruction of the simulated data is shown figure 1. On the left panel, the invariant mass was calculated exclusively with the track reconstruction involving the simulated data from the detection apparatus, without including the Super-FRS momentum measurement of the deuteron fragment, while on the right panel, the distribution include the expected momentum measurement of the deuteron with the momentum reconstruction of the π^- within the detection apparatus. An improvement on the mass resolution of a factor 4.5 is expected when the momentum resolution $\delta p/p$ of deuteron is about 10^{-3}. It demonstrates the gain of performing a exclusive measurement of hypernuclear matter with the Super-FRS.

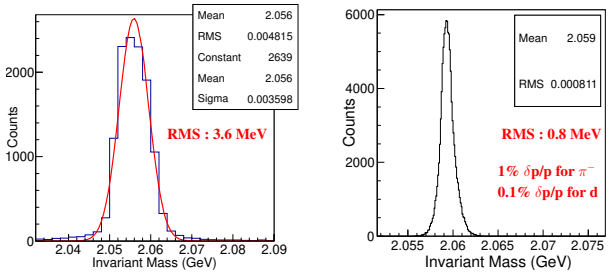

Figure 1: The invariant mass distribution of simulated d+π^- final state of ${}^{3}_{\Lambda}$n, without (left panel) and with (right panel) the expected momentum measurement of the deuteron fragment by Super-FRS as a spectrometer.

References

[1] C. Rappold *et al.*, Nucl. Phys. A **913**, 170 (2013).

[2] C. Rappold *et al.*, Phys. Lett. B **728**, 543 (2014).

[3] C. Rappold *et al.*, Phys. Rev. C **88**, 041001 (2013).

[4] T.R. Saito et al., Letter Of Intent of HypHI project.

* c.rappold@gsi.de

Measurement of β-delayed neutrons around the third *r*-process peak *

R. Caballero-Folch[1], C. Domingo-Pardo[2], J. Agramunt[2], A. Algora[2], F. Ameil[3], Y. Ayyad[4], J. Benlliure[4], M. Bowry[5], F. Calviño[1], D. Cano-Ott[6], G. Cortès[1], T. Davinson[7], I. Dillmann[3,8,9], A. Estrade[3,10], A. Evdokimov[3,8], T. Faestermann[11], F. Farinon[3], D. Galaviz[12], A. García-Rios[6], H. Geissel[3,8], W. Gelletly[5], R. Gernhäuser[11], M.B. Gómez-Hornillos[1], C. Guerrero[13], M. Heil[3], C. Hinke[11], R. Knöbel[3], I. Kojouharov[3], J. Kurcewicz[3], N. Kurz[3], Y. Litvinov[3], L. Maier[11], J. Marganiec[14], M. Marta[3,8], T. Martínez[6], F. Montes[15,16], I. Mukha[3], D.R. Napoli[17], Ch. Nociforo[3], C. Paradela[4], S. Pietri[3], Z. Podolyák[5], A. Prochazka[3], S. Rice[5], A. Riego[1], B. Rubio[2], H. Schaffner[3], Ch. Scheidenberger[3,8], K. Smith[18,19], E. Sokol[20], K. Steiger[11], B. Sun[3], J.L. Taín[2], M. Takechi[3], D. Testov[20,21], H. Weick[3], E. Wilson[5], J.S. Winfield[3], R. Wood[5], P. Woods[7] and A. Yeremin[20]

[1]DFEN-UPC, Barcelona, Spain; [2]IFIC, CSIC-UV, València, Spain; [3]GSI, Darmstadt, Germany; [4]USC, Santiago de Compostela, Spain; [5]Department of Physics, University of Surrey, Guildford, UK; [6]CIEMAT, Madrid, Spain; [7]School of Physics and Astronomy, University of Edinburgh, UK; [8]II. Physikalisches Institut, Justus-Liebig Universität Giessen, Germany; [9]TRIUMF, Vancouver, Canada; [10]St. Mary's University, Halifax, Nova Scotia, Canada; [11]Department of Physics E12, TUM, München, Germany; [12]CFNUL, Lisboa, Portugal; [13]CERN, Geneva, Switzerland; [14]EMMI, GSI, Darmstadt, Germany; [15]NSCL, MSU, East Lansing, Michigan, USA; [16]JINA, MSU, East Lansing, Michigan, USA; [17]INFN, Legnaro, Italy; [18]Department of Physics, University of Notre Dame, South Bend, Indiana, USA; [19]JINA, University of Notre Dame, South Bend, Indiana, USA; [20]Flerov Laboratory, JINR, Dubna, Russia; [21]IPN Orsay, France

This report summarizes the present status of the data analysis of the S410 experiment, which is about to reach final results. The measurements will give new relevant data such as half-lives and β-delayed neutron emission branching ratios of neutron rich nuclei beyond N=126 for isotopes of mercury, thallium and lead. The measurement used a primary beam of ^{238}U at 1 GeV/u impinging on a 1629 mg/cm^2 Be target with a 223 mg/cm^2 Nb stripper behind it. The FRS was operated using degraders at S1 and at S2 and the separation was done with the Bρ-ΔE-Bρ method. Nuclei identification was determined with standard FRS tracking detectors which allowed to identify about 40 isotopes in the range from Platinium (Z=78) to Francium (Z=87), all of them identified previously in [1] and [2].

The detection system consisted of SIMBA (Silicon IMplantation detector and Beta Absorber) [3], based on a double side silicon detectors array.

In order to determine the half-lives for the implanted nuclei, several correlation methods have been studied. As a first approach the numerical method reported by [4] and [5] was applied as described in [6]. Recently we have been able to successfully apply a more conventional analysis method [7], based exclusively on time correlations for each implant, with all β -decay events in the neighboring pixels. Furthermore, it has been possible to determine the half-life of ^{216}Pb via two different approaches: using the information of the alpha line of 6.778 MeV (^{216}Po), in a similar way as it is reported in [8] for ^{215}Pb, and by means of implant-β correlations. The good agreement between both values confirms that the implant-β method gives consistent half-lives for the measured nuclei.

In summary there are at least eight nuclei with enough statistics to determine their half-lives: ^{209,210}Hg, $^{211-213}$Tl, $^{215-217}$Pb. Some of them were measured in previous experiments [5] [8]. The obtained half-lives are in reasonable agreement with those reported in these references.

Neutron emission events in correlation with implant-β have been observed for several of the measured nuclei using the Beta dELayEd Neutron (BELEN) detector [9]. First values of P_n for nuclei beyond N=126 will be given for the first time for several nuclei in the region of interest.

References

[1] H. Alvarez-Pol *et al.*, Phys.Rev. C 82, (2010) 041602(R)

[2] L. Chen *et al.*, Nucl.Phys A 882 (2012) 71-89

[3] C. Hinke, "Spectroscopy of the doubly magic nucleus ^{100}Sn and its decay" (PhD thesis), TU München (Germany) (2010).

[4] T. Kurtukian-Nieto *et al.*, Nucl.Instr. and Meth. A 589 (2008) 472-483

[5] G. Benzoni *et al.*, Phys.Lett. B, 715 (2012) 293.

[6] R. Caballero-Folch *et al.*, Int.Conf.Proc. (ND2013).

[7] M. Bernas *et al.*, Z.Phys.A - Atomic Nuclei 336, 41 (1990)

[8] A.I. Morales *et al.*, Phys.Rev. C 89, (2014) 014324

[9] M.B. Gómez-Hornillos *et al.*, J.Phys.: Conf. Ser. **312** (2011) 052008.

* This work was supported by Spanish Ministry of Enonomy and Competitivity under grants FPA 211-28770-C03-03 and AIC-D-2011-0705 and the Helmholtz association via the Young Investigators Group VH-NG-627.

 doi:10.15120/GR-2014-1-NUSTAR-FRS-05

A Cherenkov detector as a possible TOF detector for the Super-FRS

N. Kuzminchuk-Feuerstein[*1], *N. Ferber*[1,2], *E. Fiks*[3], *and B. Voss*[1] *for the SFRS collaboration*

[1]GSI, Darmstadt, Germany; [2]University of Applied Science, Rüsselsheim, Germany; [3]National Research Tomsk Polytechnic University, Tomsk, Russia

In order to separate and identify fragmentation products with the Super-FRS (SFRS) [1] at FAIR a high resolving power detection system is required for position and Time-of-Flight (TOF) measurements. In order to separate the heaviest ions with masses of 200u and 201u with an energy of ∼1GeV/u at the distance of 52 m from the middle plane FMF2 to the final FMF4 a detection system with σ∼54 ps time resolution is required. Along with a fast timing response the detector has to satisfy requirements of the harsh environmental surroundings of the SFRS. The rate of particles at FMF2 is expected to be up to 10^7 ions/spill (spill=500 ns÷10 s). This requires a highly radiation resistant material.

In many relativistic heavy ion experiments gaseous [2] or solid [3], [4] Cherenkov radiator materials are used for particle identification and energy measurements. The application of gaseous or liquid active materials allows to refresh them by circulation and therefore greatly reduces the degradation of the performance due to aging after exposure to the high ion rates. Typically the refractive index (n) of gases equals to 1.0003 at normal ambient conditions and is pressure depended. Even for the maximum ion energy at the SFRS that does not allow to reach the Cherenkov threshold velocity of photon creation $\beta=\frac{1}{n}$, where $\beta=1/\sqrt{1-\gamma^2/2}$. To measure Cherenkov photons with heavy ions of 400 MeV/u, a radiator material with n≈1.5÷2 is required. In order to achieve this for gases one has to increase significantly its pressure what makes it impossible to easily use them under usual experimental condition. Fig. 1 illustrates the dependency of the refractive index on wavelength for several materials with the corresponding threshold velocity.

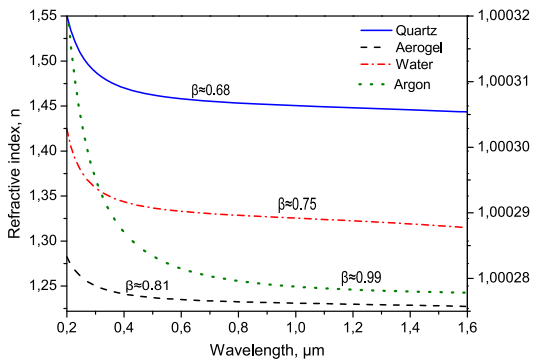

Figure 1: Refractive index as a function of wavelength for materials commonly used as Cherenkov radiators. Left ordinate shows n for argon. The threshold velocity β is indicated for n at 589 nm.

Consequently, for a future TOF detector an Iodine Naphthalene liquid ($C_{10}H_7I$) radiator with n=1.705@589nm is proposed. The liquid is kept in a cuvette made out of float/quartz glass and glued together with an optical glue. The entrance and exit window of the cuvette will be coated with Al to act as a mirror for the Cherenkov photons. To be sure that the $C_{10}H_7I$ does not react with the optical glue several samples from fused silica have been glued and stored for several months in the liquid as well as heated and shaken. The transmission spectra were measured with an UV spectrometer before and after an exposure to light and contact with optical glue (Fig. 2). No change of the transmission has been recorded after contact with the glue.

As an example after pathing of ^{59}Ni ion with an energy of ∼400 MeV/u about $3{\cdot}10^4$ Cherenkov photons are created. The measurement of the efficiency of the liquid radiator was performed with cosmic muons as a reference to 2 plastic scintillators and equals to 24%. The detection efficiency of Cherenkov photons was investigated as well by the GEANT based Monte Carlo simulations. PMTs for photon detection and several concepts of redout system were tested. First test of the prototype detector will be performed early 2014 at the SIS/GSI.

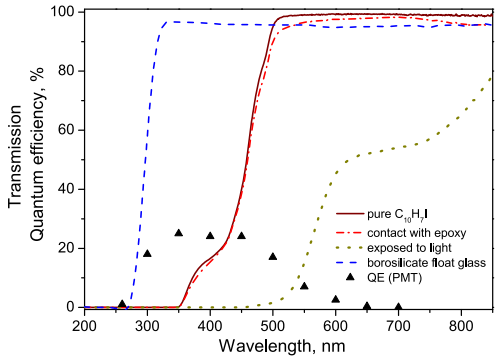

Figure 2: UV transmission spectra of $C_{10}H_7I$ liquid before and after exposure to light and contact with optical glue as well as of borosilicate float glass and quantum efficiency (QE) of the photomultiplier tube (PMT).

References

[1] H. Geissel et. al., NIM B204, (2003) p.71-85
[2] T. Chujo, NIM A383, (1996) p.409-412
[3] J. Ruzicka et. al, NIM A369, (1996) p.23-28
[4] J. Schwiening et. al, NIM A369, (2011) p.315

* n.kuzminchuk@gsi.de

Performance of the Prototype Cryogenic Stopping Cell for the Low-Energy Branch of the Super-FRS*

M.P.Reiter[1], A-K.Rink[1], P.Dendooven[3], T.Dickel[1,2], J.Ebert[1], H.Geissel[1,2], E.Haettner[1,2], C.Jesch[1], W.R.Plaß[1,2], S.Purushothaman[2], M.Ranjan[3], H.Weick[2], F.Amjad[2], S.Ayet[2], M.Diwisch[1], A.Estrade[2], F.Farinon[2], F.Greiner[1], C.Hornung[1], N.Kalantar-Nayestanaki[3], R.Knoebel[1,2], J.Kurcewicz[2], J.Lang[1], I.Moore[4], I.Mukha[2], C.Nociforo[2], M.Petrick[1], M.Pfutzner[2], S.Pietri[2], A.Prochazka[2], S.Rinta-Antila[4], C.Scheidenberger[1,2], M.Takechi[2], Y.Tanaka[2], J.S.Winfield[2], and M.I.Yavor[5]

[1]Justus-Liebig-Universität, Giessen, Germany; [2]GSI, Darmstadt, Germany; [3]KVI-CART, University of Groningen, Netherlands; [4]University of Jyväskylä, Finland; [5]Institute for Analytic Instrumentation, St. Petersburg, Russia

At the Low-Energy Branch [1] of the Super-FRS at FAIR, projectile and fission fragments will be produced at relativistic energies, separated in-flight, range-bunched, and then slowed down and thermalized in a cryogenic stopping cell (CSC) [2] filled with helium gas, extracted and delivered to precision experiments at MATS and LaSpec.
The key goal is to operate the stopping cell at high stopping and extraction efficiencies, requiring a high density and an ultra pure stopping gas. To get access to rare and short-lived exotic nuclei, short extraction times (< 50 ms) are needed. To achieve these goals the prototype of the LEB stopping cell has been designed as a cryogenic stopping cell, using DC and RF electric fields for the extraction of the ions. The CSC is filled with He at 50 to 100 mbar and 70 to 100 K, resulting in an areal density of up to 5 mg/cm^2. The cryogenic operation increases the buffer gas density for the same pressures and drastically enhances the cleanliness of the stopping gas, via the freeze out of contaminants.
The CSC has been commissioned online as part of the FRS Ion Catcher [3] using heavy Uranium fragments produced at 1000 MeV/u during two experiments. The spatial isotopic separation in flight and the momentum compression were performed by the FRS. A total efficiency of up to 15 % and a combined ion survival and extraction efficiency of about 50 % have been achieved [4]. ^{223}Th, ^{221}Ac, ^{220}Fr, ^{213}Fr, ^{211}Fr, ^{219}Rn, ^{218}Rn, ^{213}Rn, ^{211}Rn, ^{211}Po, ^{210}Pb and ^{207}Tl ions have been successfully thermalized, extracted and identified at the FRS Ion Catcher using different detection methods (Si-detector, MR-TOF-MS). No element dependent ion survival and extraction efficiencies have been seen, showing the universality of the CSC. Using an electric field of 22.2 V/cm along the body of the CSC, a mean extraction time of 24 ms for ^{221}Ac ions has been measured, agreeing well with simulations and theory.
Figure 1 shows a broadband spectrum of the ions extracted from the CSC taken by a multiple reflection time-of-flight mass spectrometer (MR-TOF-MS) [5] connected to the CSC. All prominent ions measured result from a ^{218}Rn beam or the ^{223}Ra source installed inside the CSC. The ions are extracted without addition of adducts, demonstrating the excellent cleanliness of the CSC.

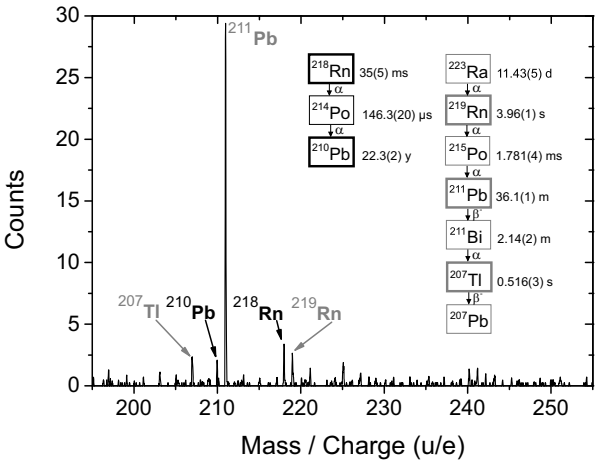

Figure 1: Broadband mass spectrum of a ^{218}Rn beam and a ^{223}Ra source extracted from the CSC. No major contaminants or adducts are formed in the CSC.

For further investigation of the behavior of the CSC, two new ion sources have been implemented. First, a movable ^{223}Ra source, which allows studies of the focussing DC electric fields and the behavior of the RF carpet. Second, a laser ion source with a movable target wheel, allowing the production of reference and calibration ions of different elements and therefore measurments of mass dependencies. Using short laser pulses (~ 10 ns) for the production of the reference ions, the extraction time of the CSC can be measured and monitored during operation.
The intensity limitations of the CSC will be investigated in an upcomming experiment at GSI, and the final version of the LEB stopping cell will be designed.

References

[1] J.S. Winfield et al., NIM A 704 (2013) 76-83.
[2] M. Ranjan et al., Eur. Phys. Lett. 96 (2011) 52001.
[3] W.R. Plass et al., NIM B 317 (2013) 457-462.
[4] S. Purushothaman et al., EPL 104 (2013) 42001.
[5] W.R. Plass et al., NIM B 266 (2008) 4560-4564.

* Work supported within the collaboration agreement between the GSI and KVI, University of Groningen, by the BMBF under contracts no. 06GI185I, 06GI9114I and 05P12RGFN8, by the state of Hesse (LOEWE Center HICforFAIR), by JLU Giessen and GSI under the JLU-GSI strategic Helmholtz partnership agreement, and by EC FP7 - Capacities, contract ENSAR no. 262010

 doi:10.15120/GR-2014-1-NUSTAR-FRS-07

A Laser Ablation Carbon Cluster Ion Source and an RFQ-based Switchyard for the FRS Ion Catcher *

C. Hornung[1], *D. Short*[2], *T. Dickel*[1,3], *J. Ebert*[1], *C. Jesch*[1], *H. Geissel*[1,3], *F. Greiner*[1], *W. R. Plaß*[1,3], *A-K. Rink*[1], *and C. Scheidenberger*[1,3]

[1]Justus-Liebig-Universität, Giessen, Germany; [2]TRIUMF, Vancouver, Canada; [3]GSI, Darmstadt, Germany

At the FRS Ion Catcher [1] projectile and fission fragments can be produced at relativistic energies, separated in-flight, range-bunched, slowed down and thermalized in a cryogenic stopping cell. Afterwards a Multiple-Reflection Time-Of-Flight Mass Spectrometer (MR-TOF-MS) [2, 3] can perform ultra-high accuracy mass measurements of very short-lived exotic nuclei at low yields, which are not accessible by other methods. In Addition, the MR-TOF-MS can be used as isobar separator to deliver an isobarically clean beam to experiments downstream of the device. The FRS Ion Catcher serves as test setup for the Low-Energy Branch of the Super-FRS at FAIR. Additionally the MR-TOF-MS can be used as isobar separator to deliver an isobarically clean ion beam to future downstream precision experiments at MATS and LaSpec.

A long term stable Laser Ablation Carbon Cluster Ion source (LACCI) for the MR-TOF-MS at the FRS Ion Catcher was developed and commissioned [4]. LACCI can provide calibrant ions over a broad mass range with a ^{13}C enriched fullerene target. The use of ^{13}C allows to create isobaric ions to the ions of interest, which are ideal calibrants, because they experience almost the same fields in the MR-TOF-MS. LACCI can be operated at very high repetition rates (100 Hz) and is thus ideally suited for the needs of the MR-TOF-MS (repetition rates $\sim$100 Hz).

In the commissioning, LACCI was successfully operated with glassy carbon (Sigradur®) and ^{13}C enriched fullerene targets. Single positively charged carbon clusters were produced by laser ablation with a frequency-doubled Nd:YAG laser with frequencies up to 100 Hz. C_n^+ cluster with a mass up to 240 u were detected and identified by their flight time along a short drift space in the test chamber (Fig.1). To increase the long term intensity stability of LACCI, an x-y-movable target-table which also provides space for different targets was developed and tested. It is now possible to change the target materials in a short time ($\sim$ s). This x-y-movable table shows high reliability and accuracy during long term operation.

At the FRS Ion Catcher, a very compact, electrically switchable, gas-filled RFQ switchyard will connect the LACCI with the current beam line. An RFQ switchyard is a novel device which acts like six gas-filled RFQs leading away from a central point along three perpendicular axes. A prototype switchyard has been commissioned [5] and initial results are promising. Modes with input or output along multiple axes at once are possible, allowing for beam splitting or combination, and the user may easily switch between input/output configurations during operation. The switchyard is quite compact (it fits inside an 8 cm cube) and it is a gas-filled device, meaning that it may be coupled to other ion optics requiring a buffer gas with no additional differential pumping stages. These features - small size with no additional pumping requirements - allow users to install new ion optical components on existing beam lines even in confined spaces. The RFQ switchyard has already enabled an MR-TOF-MS upgrade to the TITAN experiment at TRIUMF in Vancouver, Canada (scheduled for installation in 2015). Due to tight mechanical constraints on the beamline at TRIUMF, this upgrade would be impossible without the switchyard.

In the future, LACCI will be completed with the x-y-movable table and switchyard and will be installed at the FRS Ion Catcher facility at GSI.

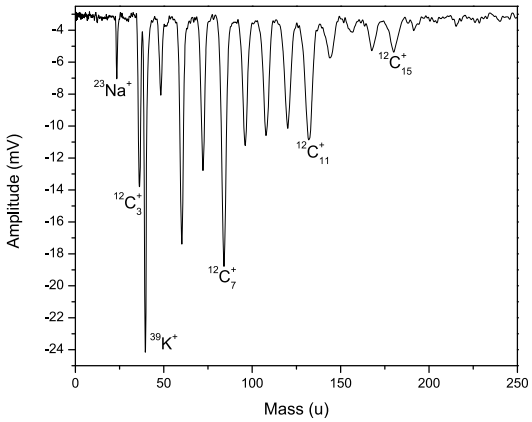

Figure 1: Mass spectrum of C_n^+ clusters produced by laser ablation with a frequency-doubled Nd:YAG laser from a Sigradur target. Carbon clusters up to C_{20}^+ with a mass of 240u were detected and identified by a mass calibration.

References

[1] W.R. Plaß et al., NIM B 317 (2013) 457-462.

[2] W.R. Plaß et al., Int. J. Mass Spectrom. 349 (2013) 134-144.

[3] T. Dickel, PhD thesis, JLU Gießen, 2010.

[4] C. Hornung, Master thesis, JLU Gießen, 2013.

[5] F. Greiner, Bachelor thesis, JLU Gießen, 2013.

* Work supported by the BMBF under contract No. 05P12RGFN8, by the state of Hesse (LOEWE Center HICforFAIR) and by JLU Gießen and GSI under the JLU-GSI strategic Helmholtz partnership agreement.

Conceptual Design of A Next-Generation Cryogenic Stopping Cell for the Low-Energy Branch of the Super-FRS*

T. Dickel[1,2], *W. R. Plaß*[†1,2], *M. P. Reiter*[1], *H. Geissel*[1,2], *and C. Scheidenberger*[1,2]

[1]Justus-Liebig-Universität, Gießen, Germany; [2]GSI Helmholtzzentrum für Schwerionenforschung, Darmstadt, Germany

The conceptual design of a next-generation cryogenic stopping cell (CSC) for the Low-Energy Branch (LEB) [1] of the Super-FRS has been developed. It builds on advanced stopping cell techniques implemented in the first version of the cryogenic stopping cell for the LEB [2, 3], which has recently been commissioned as part of the FRS Ion Catcher [4]. These include in particular (i) a cryogenic operation to ensure a high purity of the stopping gas and (ii) high density operation enabled using an RF carpet with a small electrode structure size.

The new CSC is shown schematically in Fig. 1. It consists of two main vacuum chambers, an outer chamber that provides the insulation vacuum for the inner chamber, which is held at cryogenic temperature ($\sim$ 70 K). The inner chamber is divided into a high-density stopping region and a low-density extraction region and is pumped differentially. The ion beam enters the stopping region horizontally through two windows and is stopped in the buffer gas. Using electric DC fields the ions are transported in the vertical direction to a wall of RF carpets, which focuses the ions onto the intermediate extractions nozzels. There the ions are swept into the low-pressure extraction region by the gas flow, where they are transported to the main exit nozzle from the stopping cell.

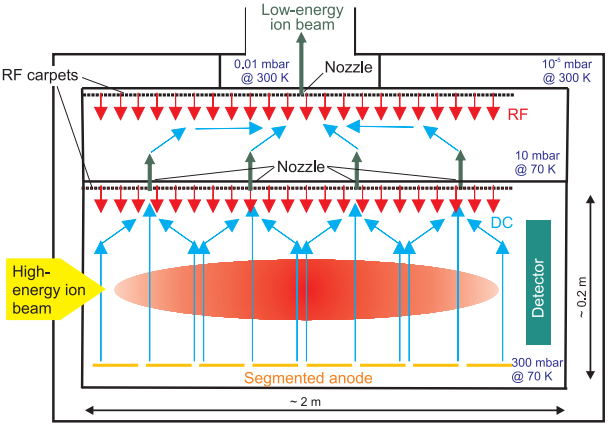

Figure 1: Schematic figure of the next-generation cryogneic stopping cell for the LEB of the Super-FRS.

Compared to conventional stopping cells, the new design features several important advantages: (i) Due to the vertical extraction the extraction path is shortened considerably. (ii) Higher DC field strengths can be applied in the direction of extraction, extending the rate capability of the CSC. (iii) Compared to stopping cells with an RF body the ratio of RF carpet area to stopping volume is reduced significantly, thus minimizing power disspipation, which is crucial for cryo-operation. (iv) The design scales favorably with an increased length of the stopping volume; the length can be increased without increasing extraction times or decreasing ion extraction efficiencies or rate capability. (v) A segmented anode opposite to the RF carpet wall collects the electrons created during the stopping; the electron current indicates the stopping distribution of the ions. (vi) A detector can be mounted on the inner side of the CSC opposite to the entrance windows. Alternatively, two windows can be implemented, through which ions with a longer range leave the cell. These ions can be identified in a detector positioned behind the CSC. (vii) The ion beam does not hit the RF carpet and desorption of atoms and molecules from the RF carpet is avoided. (viii) The dual-density design enables very efficient pumping of the CSC.

In the stopping region, a dual-layer RF carpet with rectangular geometry and electrode lines that overlapp at right angles is used. It has a structure size with up to 6 electrodes / mm. A maximum helium buffer gas pressure of 300 mbar at 70 K will be achieved. The stopping volume has a width of 25 cm, a height of 10 cm and a length of 2 m. The corresponding maximum areal density amounts to 40 mg/cm^2, an increase by a factor of 8 from the areal density of the present CSC. The extraction region is kept at a pressure of 10 mbar at 70 K. Due to the lower pressure, an RF carpet with a larger structure size can be used in this region and fast ion transport is achieved.

In combination with the momentum compression provided by the energy buncher of the Super-FRS [1], stopping efficiencies close to unity are expected for all but light nuclei. Ion survival and extraction effciencies of better than 50% are expected. The extraction time of the ions will be about 5 ms, shorted by a factor of 5 compared to the present CSC. The novel CSC will thus remove the performance bottleneck of present stopping cells and give access to very exotic and short-lived nuclei available at the Super-FRS.

References

[1] J. Winfield et al., Nucl. Instrum. Methods A 704 (2013) 76.

[2] M. Ranjan et al., Eur. Phys. Lett. 96 (2011) 52001.

[3] S. Purushothaman et al., Eur. Phys. Lett. 104 (2013) 42001.

[4] W. R. Plaß et al., Nucl. Instrum. Methods B 317 (2013) 457.

*This work was supported by the BMBF under contract no. 05P12RGFN8 and by JLU Gießen and GSI under the JLU-GSI strategic Helmholtz partnership agreement.

† W.Plass@gsi.de

 doi:10.15120/GR-2014-1-NUSTAR-FRS-09

Recent Technical Improvements for the Multiple-Reflection Time-of-Flight Mass Spectrometer at the FRS Ion Catcher*

S. Ayet[1,2], *J. Ebert*[1], *T. Dickel*[1,2], *W. R. Plaß*[1,2], *J. Bergmann*[1], *H. Geissel*[1,2], *E. Haettner*[2], *C. Hornung*[1], *C. Jesch*[1], *J. Lang*[1], *W. Lippert*[1], *A. R. Pikhtelev*[3], *S. Purushothaman*[2], *M. P. Reiter*[1], *A.-K. Rink*[1], *C. Scheidenberger*[1,2], *and M. I. Yavor*[4]

[1]Justus-Liebig-Universität, Gießen, Germany; [2]GSI, Darmstadt, Germany; [3]Institute of Energy Problems of Chemical Physics of the Russian Academy of Science, Chernogolovka, Russia; [4]Institute for Analytical Instrumentation of the Russian Academy of Sciences, St. Petersburg, Russia

The multiple-reflection time-of-flight mass spectrometer (MR-TOF-MS) [1, 2] is part of the FRS Ion Catcher experiment [3], which serves as a test facility for the Low Energy Branch (LEB) of the Super-FRS at FAIR. At the FRS Ion Catcher, range-bunched nuclides from the FRS are stopped in a novel cryogenic stopping cell (CSC)[4], extracted and transported via an RFQ system to the MR-TOF-MS. At the LEB, the MR-TOF-MS will perform mass measurements, isobar separation and broadband mass spectrometry for ion identification and diagnostics purposes.

A unique feature of the MR-TOF-MS is its capability of shifting the potential of the incoming ions [5]. The potential shift is effected by pulsing the storage potential in the injection trap in front of the time-of-flight analyzer within a few tens of nanoseconds by a high voltage (HV) pulser. Thus the MR-TOF-MS can accept ions at different entrance potetials, which may be required e.g. if the MR-TOF-MS is used at different RIB facilities, without the need of placing the MR-TOF-MS on a high-voltage platform. The amplitude of this potential shift has been increased from 750 V to 1300 V. For an ion entrance potential close to ground, the kinetic energy of the ions in the time-of-flight analyzer therefore also was increased increased to 1.3 keV. This increase in kinetic energy will reduce the turn-around time and the emittance of the ions in the analyzer. Hence the mass resolving power and mass accuracy will be increased, while decreasing the time-of-flight required to achieve a given mass-resolving power [5].

The stability of the voltages of the analyzer electrodes are of primary importance for long-term high-accuracy mass measurements. A new voltage stabalization was developed and commissioned together with new high voltage power supplies for the MR-TOF-MS. Fig. 1 shows the voltage stability achieved with the new electronics. Over a measurement period of 330 minutes, the rms deviation of the time-of-flight now amounts to 0.5 ppm only. This exceptional performance will enable direct mass measurement of rare exotic nuclei at very high mass measurement accuracy.

A new data acquisition software has been developed for the MR-TOF-MS. It supports a variety of data acquisition hardware, including different TDCs and ADCs. The software also allows real-time data processing during the measurement such as mass calibration of the time-of-flight spectra, peak detection, and the online identification of masses.

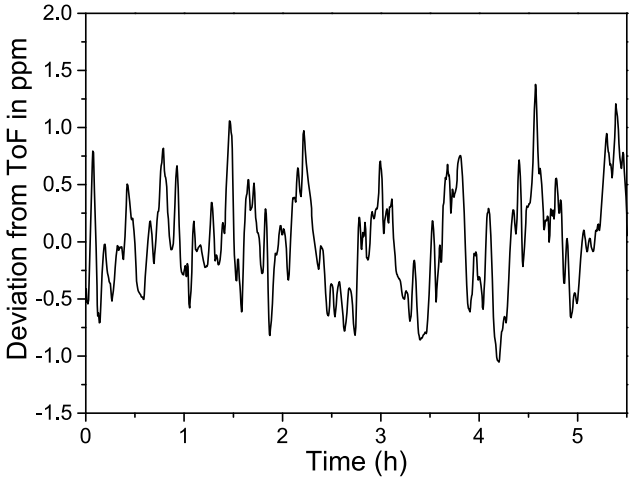

Figure 1: Stability of the mass measurement[6] of ^{133}Cs ions over a time period of 330 minutes. The time-of-flight amounts to 5.843 ms, and a mass resolving power (FWHM) of more than 150,000 is achieved. The rms value of the time-of-flight is about 0.5 ppm.

In an upcoming beam time with the CSC at the FRS Ion Catcher, the MR-TOF-MS will be the key device for the performance characterization of the CSC. In particular, it will be used to identify β-decaying ^{238}U fission fragments extracted from the CSC by their mass values and to perform isobar separation with short-lived nuclei.

References

[1] W. R. Plaß et al., Nucl. Instrum. Methods B 266 (2008) 4560.

[2] T. Dickel, PhD Thesis, 2010, JLU Gießen.

[3] W. R. Plaß et al., Nucl. Instrum. Methods B 317 (2013) 457.

[4] S. Purushothaman et al., Eur. Phys. Lett. 104 (2013) 42001.

[5] W. R. Plaß et al., Int. J. Mass Spectrom. 394 (2013) 134 .

[6] J. Lang, PhD thesis in preparation.

*This work was supported by the BMBF under contracts no. 06GI9114I and 05P12RGFN8, by the state of Hesse (LOEWE Center HICforFAIR) and by JLU Gießen and GSI under the JLU-GSI strategic Helmholtz partnership agreement

Experimental Investigations and Technical Design for The Time-OF-Flight Detectors in the CR at FAIR.*

M. Diwisch[1], J. Bergmann[1], T. Dickel[1,2], H. Geissel[1,2], R. Knöbel[1,2], S. Nazarenko[3], W. R. Plaß[1,2], C. Scheidenberger[1,2], and H. Weick[2]

[1]Justus-Liebig Universität Gießen, Gießen, Germany; [2]GSI, Darmstadt, Germany.; [3]Tomsk Polytechnic University , Tomsk, Russia

Technical design and performance simulations of a larger TOF detector

To perform isochronous mass spectrometry (IMS) [1] in the future CR at FAIR, investigations in instrumentation and designs for a about a factor 2 larger Time-Of-Flight (TOF) detector have been conducted. For future applications of IMS simulations of the CR have been performed and showed, that the currently used 40 mm diameter carbon foil (areal density: $10\mu g/cm^2$) would be too small for the large emittance of the beam in the CR and too many ions would be lost in each turn. This challenge has been met by the the design of an improved and larger TOF detector. The carbon foil size will be increased from 40 mm to 80 mm diameter and will be used for the first time. Simply increasing the size of the detector leads to decreased timing performance of the detector. To compensate for this one can apply higher voltages to the detector to transport the secondary electrons faster from a carbon foil to the MCPs [2]. As part of the improved design of the larger TOF detector the transport efficency is improved to almost 100% and the timing resolution to 40 ps. All this is achieved while keeping the stringent spatial requirments at the CR.

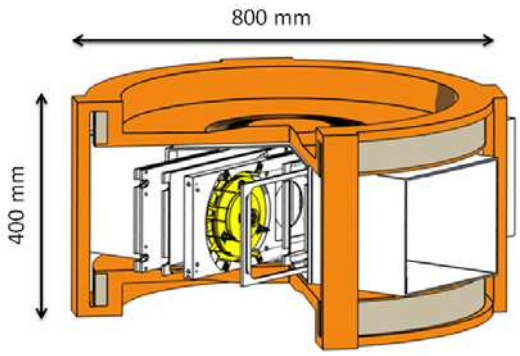

Figure 1: CAD drawing of the new TOF detector surrounded by a Helmholtz magnet for the CR which provides the detector with a homogenious (10^{-3}) magnetic field in the transport area.

Testing of Larger Carbon Foil Properties for a TOF Detector in the CR

In order to investigate the feasibility and the properties of those large carbon foils a test chamber has been built. In this test chamber the possible changes of the physical properties of larger foils compared to the currently used small foils (e.g. flatness of the surface after evacuation of the detector volume) in the timing performance are measured. The test chamber has been operated in a first step with the currently used 40 mm diameter carbon foils. This allows us to see the differences between small and large foils directly. Measurements are performed with an alpha-source from which alpha-particles penetrate the carbon foil in the center of the chamber and emits secondary electrons which are detected by two MCP detectors. Simulations predicted that the secondary electron transport in the setup only contributes with only 2 ps to the timing of the whole measurement. Experimental predictions state, that the measured time uncertainty will therefore be approximately 25 ps and is solely due to effects in the MCPs and flatness of the foil [3].

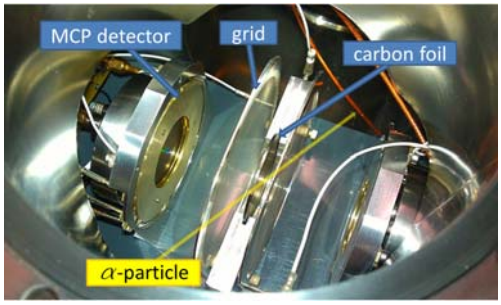

Figure 2: Photography of the assembled test chamber. The carbon foil is placed in the center inbetween two grids. By applying voltages to the grids the secondary electrons are guided to two MCPs on the side. The diameter of the grids is 80 mm and therefore has the same size as the future carbon foils.

As soon as the large foils will be available they will be tested and compared to the small foils.

References

[1] J. Trötscher et al., NIM B 70 (1992) 455-458

[2] M. Diwisch, Master Thesis, JLU Giessen, (2011)

[3] M. Diwisch, PhD Thesis in progress, JLU Giessen, (2014)

*Work supported by the BMBF under contract No.06GI9115I, by the HGF (NAVI) and by GSI (strategic university cooperation GSI-JLU-FAIR)

 doi:10.15120/GR-2014-1-NUSTAR-FRS-11

Efficiency calibration of the neutron detector BELEN-48 with (p,n) and (α,n) reactions at the PTB Braunschweig *

M. Marta[1,2], *J. Agramunt*[3], *R. Caballero-Folch*[4], *G. Cortés*[4], *I. Dillmann*[1,2,5], *M. Erhard*[6], *L.M. Fraile*[7], *U. Giesen*[6], *B. Kindler*[1], *B. Lommel*[1], *R. Nolte*[6], *A. Riego*[4], *S. Röttger*[6], *and J.L. Taín*[3]

[1]GSI Helmholtzzentrum für Schwerionenforschung GmbH, Darmstadt, Germany; [2]II. Physikalisches Institut, Justus-Liebig Universität Giessen, Germany; [3]IFIC-CSIC University of Valencia, Valencia, Spain; [4]INTE-DFEN, Universitat Politecnica de Catalunya, Barcelona, Spain; [5]TRIUMF, Vancouver, Canada; [6]Physikalisch-Technische Bundesanstalt (PTB), Braunschweig, Germany; [7]Universidad Complutense de Madrid, Spain

The BEta-deLayEd Neutron detector BELEN is a highly efficient device designed for the DESPEC project at FAIR. It has already been successfully used during the experiments S323 and S410 at the Fragment Separator to measure β-delayed neutron probabilities and half-lives of neutron-rich nuclei close to the r-process path, for nuclear structure and nuclear astrophysics studies.

In its present version, it consists of 48 ^{3}He proportional counters arranged to form three concentric rings embedded in a polyethylene matrix. Due to the thermalization process, the information about the initial neutron energy is lost but the detection efficiency is strongly increased. Therefore the position and number of counters in the rings are designed in such a way that the efficiency remains constant over a broad range of neutron energy from thermal up to a few MeV. The simulations are performed with an MCNPX code and have to be validated by experiments that make use of known neutron fluxes produced in the center of the detector.

Measurements with a calibrated ^{252}Cf source provide only one efficiency value corresponding to a spectrum-averaged neutron energy of 2.14 MeV. In order to have a more stringent test on the simulated efficiency curve, the calibration has been extended with well-known (p,n) and (α,n) reactions on ^{13}C and ^{51}V targets producing neutrons with limited energy spread, ranging between 0.2 and 5.3 MeV. The list of reactions and energies used is summarized in table 1.

Reaction	E_{proj} [MeV]	E_{n} [MeV] min	max
^{51}V(p,n)^{51}Cr	1.80	0.20	0.25
^{51}V(p,n)^{51}Cr	2.14	0.51	0.59
^{51}V(p,n)^{51}Cr	2.27	0.63	0.73
^{13}C(p,n)^{13}N	4.45	0.77	1.36
^{13}C(α,n)^{16}O	1.05	2.5	3.2
^{13}C(α,n)^{16}O	3.30	3.6	5.3

Table 1: List of reactions used for the calibration. Maximum and minimum neutron energies E_n refer to the smaller (forward) and largest (backward) angle covered by BELEN-48, i.e. from about 16 to 164 degrees.

The experiment was performed at the PTB ion accelerator facility (PIAF) of the Physikalisch-Technische Bundesanstalt (PTB) in Braunschweig/Germany, where a Van de Graaff accelerator and cyclotron provided the α and p beams of desired energy and intensity. The BELEN-48 polyethylene matrix was installed with the air-cooled target holder located at the end of a beam line at the center of the detector. The target chamber was designed as a Faraday cup to measure the beam currents on target with suppression electrodes and collimators. At a second beam line it was possible to produce the same neutron flux as inside BELEN, with very similar target and beam conditions, and to measure reaction yields and angular distributions with the calibrated neutron detectors of PTB at several angles with respect to the beam axis. The reactions on ^{13}C target show large anisotropy in the center-of-mass frame. The angular distributions of ^{51}V(p,n)^{51}Cr are still to be measured.

The measured angular distributions need to be taken into account in the simulation of the efficiency for each reaction and beam energy, since neutrons enter BELEN with different probabilities and energies at different angles. For the moment the preliminary experimental efficiency (Fig. 1) is obtained as the ratio of neutrons *detected* in BELEN-48, and a normalized-to-isotropy value for neutrons *emitted*. The normalization takes into account each measured angular distribution and the detection solid angle, making a comparison of all data and simulation possible.

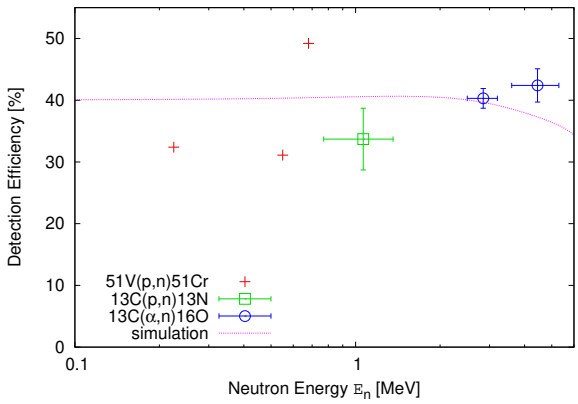

Figure 1: Comparison of the efficiency curve simulated with MCNPX (dotted line) and preliminary experimental values. The Vanadium data is shown without uncertainty due to the missing angular distribution information that prevents its normalization.

* This work was supported by the Helmholtz association via the Young Investigators Group VH-NG-627.

Tests of scintillation Fibers for the compact neutron Detector NeuRad*

I. Mukha [1] *and D. Kulik*[2]

[1]Helmholzzentrum GSI, Darmstadt, Germany; [2]Moscow State Technical University of Radio-engineering, Electronics and Automation, Dubna, Russia

We have constructed three prototypes of the fiber-based scintillation neutron detector and tested their light yield in response to γ-ray sources. The derived energy threshold of detection of protons scattered by incident neutrons in the prototypes is 0.5 MeV.

The theoretical and experimental ways of searches for neutron radioactivity expected for exotic extremely neutron-rich nuclei have been recently proposed [1]. The first indication on this not-observed yet phenomenon has been obtained [3] for ^{26}O whose lifetime is 4 ps. Such a lifetime of ^{26}O should correspond to the very small decay energy of 1 keV [2] which is difficult to measure with the present neutron detectors. The experiment on observation of the neutron radioactivity can be performed at the Super-FRS with a suitable neutron detector. In the proposed tracking experiment, radioactive beam produces short-lived isotopes which decay in flight. The fragments resulted from the neutron radioactivity are detected by tracking detectors which determine the vertex point of the radioactive decay. The neutron detector provides spatial coordinates of neutrons and their angles respective to the heavy residue. Since the expected angles are extremely small, the neutron detector should have a fine spatial resolution.

The neutron detector NeuRad (Neutron Radioactivity) with a high spatial resolution has been proposed for future experiments at the Super-FRS NUSTAR [4]. The detector is based on spaghetti-like scintillation fibers with small cross areas. Neutrons scattered in fibers produce recoil protons causing light flashes which are optically trapped inside the fibers and then are read-out on both fiber ends. We have tested multi-clad fibers BCF12 (produced by Saint Gobain) whose dimensions of $2 \times 2 \times 250$ mm^3 allow for a fine spatial resolution.

We have assembled three samples of the fibers: (i) without additional painting of fibers, (ii) with a white paint on each fiber in order to prevent a light cross-talk between the fibers, and (iii) with a black paint. Each sample consisted of 64 fibers assembled into a 8×8 bundle whose end has been glued by epoxy glue and polished by using a diamond tool. The test setup comprised of the fiber bundle viewed by the PMT Hamamatsu R7600 followed by the fast amplifier, the 5 GHz digital oscilloscope with the spectroscopic functions, and the sources of γ-rays, ^{137}Cs and ^{60}Co. The light flashes cased in fibers by the Compton-scattered γ rays were converted into the electrical signals, amplified and directed into the oscilloscope where the amplitude spectra were accumulated. All spectra had the shapes typical for a Compton effect. The maximum energies of the Compton spectra (i.e., Compton edges) are 1118 keV for ^{60}Co and 477 keV for ^{137}Cs. The respective maximal amplitudes of signals allowed to produce calibration curves for each sample, which is shown in Fig. 1. The values of maximal amplitudes A were obtained by fitting the spectra tails corresponding to the Compton edges.

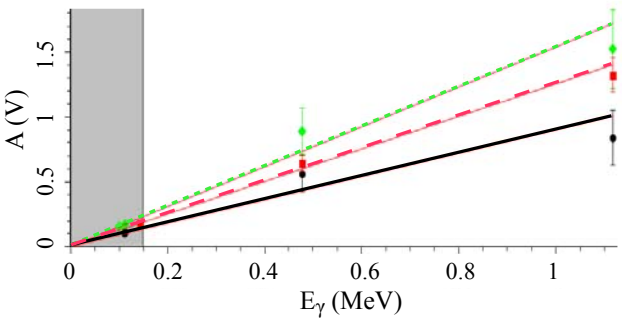

Figure 1: The calibration curves for all prototypes of the fibers scintillation detector NeuRad. The solid, dashed and dotted lines correspond to the black-painted, white-painted and not-painted prototypes, respectively. The grey area shows the threshold of γ-ray detection.

The obtained calibrations allow to find the detection thresholds for each fiber prototype. The amplitude range where the Compton effect disappears in the measured spectrum are shown by the grey area (see Fig. 1) whose highest value corresponds to the concluded threshold energy. The highest threshold is in the black prototype, of 160 keV. The assumed total systematic uncertainty is 20%.

In summary, the measured light yields and the derived detection thresholds of the three prototypes of the scintillating fibers BCF12 have demonstrated detection of γ-rays at least down to 160 keV. Thus the lowest-measured energy of protons scattered by incident neutrons should be 500 keV. This conclusion opens a way for more tests of the NeuRad performance, in particular its spacial and time resolutions.

References

[1] L.V. Grigorenko, I. Mukha, C. Scheidenberger, M.V. Zhukov, Phys. Rev. **C84** (2011) 021303 (R).

[2] L.V. Grigorenko, I. Mukha, M.V. Zhukov, Phys. Rev. Lett., **111** (2013) 0425010.

[3] Z. Kohley *et al.,* Phys. Rev. Lett., **110** (2013) 0152501.

[4] I. Mukha, Acta Phys. Polonica B, **45** (2014) 1001.

*Work supported by the HGS-HIRe Summer Student Programm at GSI in 2013

 doi:10.15120/GR-2014-1-NUSTAR-FRS-13

Atomic Mass Compilations

B. Pfeiffer[1,2]*, K. Venkataramaniah*[3]*, U. Czok*[1]*, and C. Scheidenberger*[2,1]

[1]II. Phys. Inst., Justus-Liebig-Universität, Gießen; [2]GSI Helmholtzzentrum für Schwerionenforschung, Darmstadt, Germany; [3]Sri Sathya Sai Institute of Higher Learning, Prasanthinilayam, India

The "Atomic Mass Compilation 2012" has been prepared in close collaboration of the II. Phys. Inst., Universität Gießen, the GSI and the Sri Sathya Sai Institute of Higher Learning, India, and is now accessible at "Atomic Data and Nuclear Data Tables" [1].
Compilations of (elemental) atomic masses have been established ever since the beginning of the 19^{th} century [2]. One of the most recent ones has been published in the Landoldt-Börnstein New Series [3], but is rarely available in scientific libraries. Therefore we started a new compilation to be published in a peer-reviewed journal accessible in most scientific institutions.

German precursors

From 1921 to 1945, the "Deutsche Atomgewichts-Kommission" (see, e.g. [4]) published annual reviews on recent experiments on atomic masses and compilations of elemental and isotopic masses [5]. Since 1932, these reports were prepared by the "Kaiser-Wilhelm-Institut für Chemie" [6]. Gradually the preponderant experimental methods shifted from chemical to physical techniques. Mass spectroscopy was represented at the Kaiser-Wilhelm-Institut by the team of J. Mattauch. *[One of the post-docs was Heinz Ewald, later the first director of the II. Phys. Inst. in Gießen* [1]*. He was involved in the construction of instruments like LOHENGRIN and OSTIS in Grenoble and SHIP at GSI, installations which yielded many contributions to atomic mass determinations.]*
After WWII, the study of atomic masses was continued at the Max-Planck-Institut für Chemie. The mass compilation published in 1949 [7] included also the recent american results on nuclear properties, which were made available to Mattauch by G.T. Seaborg as preprint of the "Table of Isotopes" [8].
In 1960, the group of Mattauch in collaboration with A.H. Wapstra published the first edition of the "Atomic Mass Evaluation" [9]. After the retirement of Mattauch in 1965, the work was directed first by Wapstra and later on by G. Audi. The last edition [10] had been prepared by an international collaboration including the GSI and the II. Physik. Inst.

[1]Two of the authors, U.C.and B.P., were admitted to the institute by Prof. Ewald.

Follow-up work in preparation

The information contained in the mass tables can be displayed in plots of the binding energy (or mass) versus Z, N or A. Any plots of derivatives of the binding energies (meaning a specified difference between the binding energies of two nearby nuclides) show a smooth behaviour and have in addition the advantage of displaying much smaller variations. In [11], two representative examples for such graphs of double β-decay energies and two-neutron separation energies, respectively, are displayed, clearly showing the trends in the mass surface.
Thus, dependable estimates of unknown , poorly known or questionable masses can be obtained. It is foreseen to use such graphs for more dependable extrapolations of masses toward the drip lines and also to test theoretical models.

References

[1] B. Pfeiffer, K. Venkataramaniah, U. Czok, C. Scheidenberger, Atomic Data Nuclear Data Tables 100 (2014) 403

[2] J. Dalton, Memoirs and Proceedings of the Manchester Literary and Philosophical Society, Manchester, 6 (1805)

[3] Z.N. Soroko and S.I. Sukhoruchkin, Landolt-Börnstein New Series I/22A,B (2009) Nuclear Bindung Energies and Atomic Masses: Nuclei with Z=1 - 54 and Z=55 - 100; ISBN 978-3-540-69944-6 and ISBN 978-3-540-70608-3

[4] O. Hahn, Die Naturwissenschaften 10/43 (1922) 934

[5] "Atomgewichtstabellen für das Jahr 1921", in Ber. d. deutsch. chem. Ges. 54 (1921) A. 181.
All reports can be found on the webpage of the European Journal of Inorganic Chemistry:
http://onlinelibrary.wiley.com/journal/10.1002/(ISSN)1099-0682c

[6] O. Hahn, Berichte d. D. Chem. Gesellschaft 65A (1932) 1

[7] J. Mattauch und A. Flammersfeld, *Isotopenbericht*, Sonderheft der Zeitschrift für Naturforschung, Tübingen (1949)

[8] G.T. Seaborg and I. Perlman, Rev. Mod. Phys. 20 (1948) 585

[9] F. Everling, L.A. König, J.H.E. Mattauch, A.H. Wapstra, Nucl. Phys. 18 (1960) 529

[10] G. Audi et al., Chinese Physics C36 (2012) 1157; G. Audi et al., Chinese Physics C36 (2012) 1287; M. Wang et al., Chinese Physics C36 (2012) 1603

[11] B.Pfeiffer, Shreesha Rao D.S., K. Rajasinha, K. Venkataramaniah, U. Czok and C. Scheidenberger, Proceedings of DAE Symp. on Nucl. Phys. 58 (2013) 174

 doi:10.15120/GR-2014-1-NUSTAR-FRS-14

Status of PreSPEC Commissioning Data Analysis*

M. Reese [1], *C. Domingo-Pardo* [2], *J. Gerl* [3], *N. Pietralla* [1], *and the PreSPEC and AGATA collaborations*

[1]Institut für Kernphysik, Technische Universität Darmstadt, D-64289 Darmstadt, Germany ; [2]IFIC, CSIC-Universitat de Valencia, E-46980 Paterna, Spain ; [3]GSI Helmholtzzentrum für Schwerionenforschung GmbH, D-64291 Darmstadt, Germany

PreSPEC-AGATA is an experiment for in-flight γ-spectroscopy at GSI to investigate the structure of exotic nuclei. Two physics campaigns were done: 2012 and 2014. This report is about the progress in the data analysis of the commissioning runs in August 2012.

Introduction

The goal of the experiment was a measurement of the performance of the PreSPEC-AGATA [1] setup, a unique combination of the GSI Fragment Separator (FRS) [2], the Advanced Gamma Tracking Array (AGATA) [3], Lund-York-Cologne CAlorimeter (LYCCA) [4], and HECTOR for in-beam γ-spectroscopy. Further details about the setup and an earlier status report about the data analysis can be found in [5]. A ^{80}Kr beam with a kinetic energy of about 150 MeV/u at the secondary target position was used to do two types of experiments: Coulomb excitation on a ^{197}Au target, and secondary fragmentation reactions on a Be target. ^{80}Kr was chosen as projectile because of its high Coulomb excitation cross-section of $\sigma_{\mathrm{clx}} \approx 550\mathrm{mb}$ for the 2_1^+ state. The challenge in the analysis of in-flight γ spectroscopic data is the large Doppler shift of emitted γ-rays at velocities of $v/c \approx 0.5$. The data is being analyzed, using a software framework described in [6].

Coulomb Excitation

If ^{197}Au is the target material, the dominating excitation mechanism of the projectile is Coulomb excitation (Coulex), i.e. exchange of virtual photons. At relativistic energies, one-step Coulex is dominating and the first excited 2_1^+ state at 616.6 keV in ^{80}Kr is populated. The observed yield in the γ line of the excited state can be used to determine the B(E2) value. Because of the strong Doppler effect at large projectile velocity, the γ-rays have to be corrected for the Doppler shift in energy before a discrete line in the γ spectrum can be seen. The strength of the Doppler shift depends also on the angle of observation in the laboratory frame, which can be seen in Fig. 1. The spectrum of γ-energy in the laboratory frame shows the emission of the excited target nuclei from the state $7/2_1^+$ at 547.5 keV. Another line is the emission from electron-positron annihilation at 511 keV. Towards lower energies (below 500 keV), the background radiation level rises very quickly because of the abundant atomic radiation emitted during the interaction of the projectile with the target electrons. The emission line of the 2_1^+ state at 616.6 keV in ^{80}Kr can only be seen after Doppler correction (Fig. 1, bottom). Simultaneous observation of emission lines from target and projectile de-excitation allows for a relative measurement of the Coulex cross-sections and thus B(E2) value of the two excited states ^{197}Au and ^{80}Kr.

Final quantitative results for total efficiency and energy resolution will be obtained after taking into account the AGATA detector efficiency at different angles and for different γ-energies. This is difficult, because efficiency is influenced by the combined effects of the Doppler shift: Change in angular distribution and in the energy of the emitted radiation.

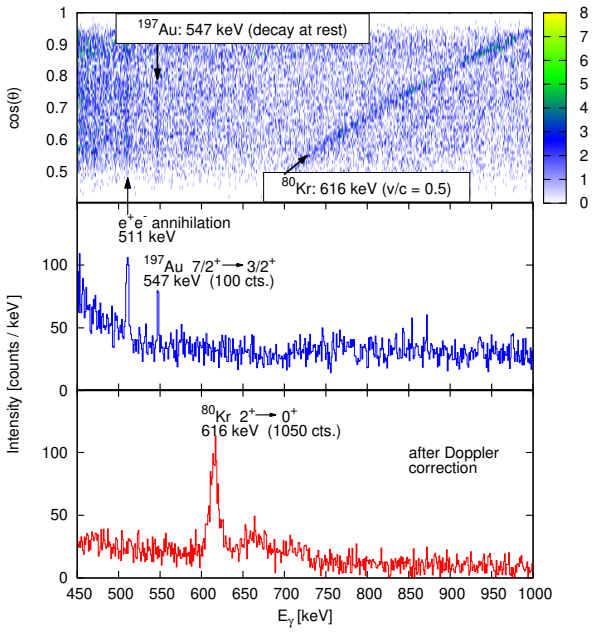

Figure 1: Top: Detected γ energy in the laboratory system as seen from different detection angles. γ-rays emitted in-flight can be seen as curved lines. Middle: The background subtracted spectrum of γ energy in the laboratory system, shows the decay from the excitation of the target material (^{197}Au). Bottom: Background subtracted spectrum of Doppler-corrected γ energy show the decay spectrum of the projectile.

*Work supported by BMBF NuSTAR.DA - TP 6, FKZ: BMBF 05P12RDFN8 (TP 6), HGS-HIRe

Secondary Fragmentation

If the secondary target is Beryllium, the cross-section for fragmentation reactions is large. Such a setup is used to study the decay of excited fragments. In order to assign the observed γ-radiation to specific ion species, full identification of outgoing fragments is needed. This is done with the LYCCA device [4] that performs ΔE-E and precise time-of-flight measurement of the ejectiles. From these quantities, the outgoing isotopes can be identified as shown in Fig. 2. In the mass region around ^{80}Kr, Z-identification is very good while different mass peaks are overlapping. The calibration of the LYCCA DSSSD detectors was partly done using an automatic method described in [7].

After the Doppler correction of observed γ-rays in coincidence with the LYCCA identification, γ-emission spectra of selected excited ejectiles can be obtained. Yrast states of the most abundant even-even isotopes after the target can be seen in Fig. 3. The half-life $T_{1/2}$ of the excited state has an influence on the resolution that can be obtained. If $T_{\rm tar}$ is the time the projectile needs to travel through the target material, most de-excitation processes will happen inside the target if $T_{1/2} < T_{\rm tar}$. In this case, the particle velocity after the target is not equal to the velocity at the moment of γ emission and the Doppler correction will be done with a wrong velocity. This results in a reduced resolution for the states with shorter half-life as can be seen in Fig. 3 where $T_{1/2}$ is given in the label of each peak. On the other hand the observed line shape enables in principle the determination of lifetimes.

Furthermore, data from the ^{80}Kr fragmentation run was used to show the feasibility for new experimental techniques as described in [8].

Outlook

The analysis is ongoing. Since the AGATA detector is a complicated device, exploiting pulse-shape analysis (PSA) an γ-ray tracking, some improvements can be expected from a refined preprocessing of the detected γ-rays. This is possible, because during AGATA experiments, the preamplifier signals of all channels are written to disk. Later improvements in software algorithms for PSA and γ-tracking can be used to increase both, efficiency and energy resolution of the Doppler-corrected peaks.

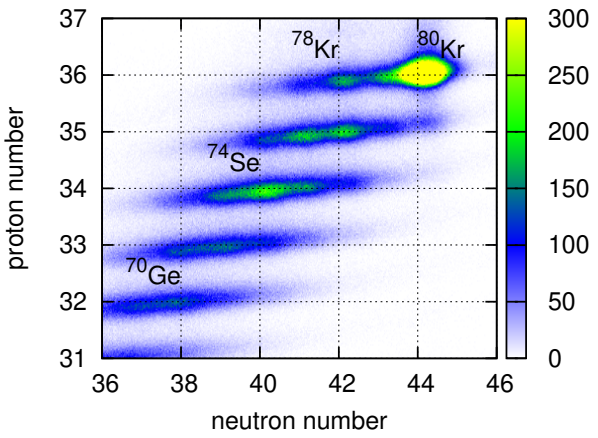

Figure 2: The charge and mass identification plot that is used to produce the gated spectra of Fig. 3. Particle charge is determined, using the E-ΔE method, while the mass is obtained from an additional time-of-flight measurement.

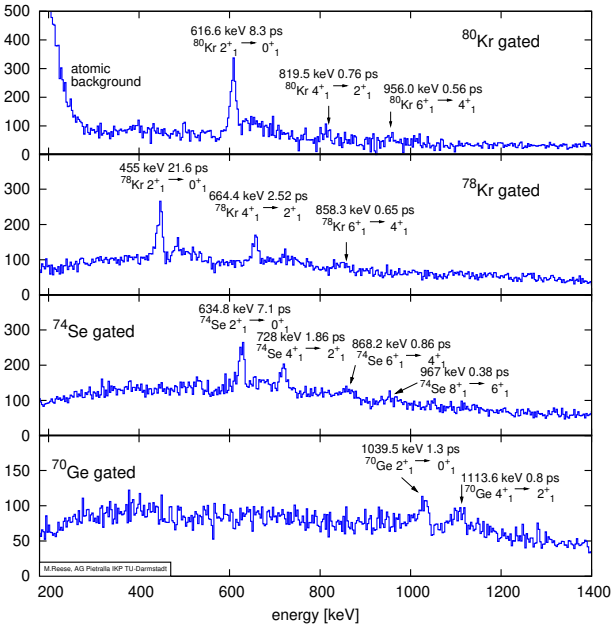

Figure 3: Doppler-corrected γ spectra for the strongest even-even nuclei identified by LYCCA. Decays of the first few Yrast states can be clearly seen. Peak labels indicate the γ-ray energy and the half-life of the initial state.

References

[1] P. Boutachkov et al., GSI Report 2012 (2013) 148.

[2] H. Geissel et al., Nucl. Instr. and Meth. Phys. Res. B 70, 286-297 (1992).

[3] S. Akkoyun et al., Nucl. Instr. and Meth. Phys. Res. A 668, 26-58 (2012).

[4] P. Golubev et al., Nucl. Instr. and Meth. Phys. Res. A 723, 55-66 (2013)

[5] N. Pietralla et. al., EPJ Web of Conferences 66, 02083 (2014).

[6] M. Reese et. al. , GSI Scientific Report 2012 (2013) 48.

[7] M. Reese et. al. , This report.

[8] C. Stahl et. al. , This report.

 doi:10.15120/GR-2014-1-NUSTAR-GS-01

Automatic Self-consistent Gain-Matching of DSSSD Detector Channels*

M. Reese[1], P. Golubev[2], N. Pietralla[1], J. Gerl[3], and the PreSPEC and AGATA collaborations
[1]Technische Universität Darmstadt, Germany; [2]Lund University, Sweden; [3]GSI, Darmstadt, Germany

Double-sided silicon strip detectors (DSSSD) are a widely used type of detector in nuclear and particle physics experiments for position and energy measurements. This report describes an automatic method that allows to gain-match all strips of DSSSD detectors without the need of dedicated in-beam calibration.

Introduction

DSSSD detectors are constructed as large area silicon diodes with electrically segmented p and n-side contacts. Signals are read out on both, p and n-side simultaneously. The segmentation is usually such that there are unique intersection points of opposite side's contacts, the measurement of one p and on n-side signal allows to reconstruct the two dimensional spatial position of an event inside the detector.

Method

In the following, it will be assumed that the deposited energy $E = s \cdot A$, in the detector is proportional to the amplitude, i.e. there are no offsets or nonlinearities in the electronics. A is the measured amplitude of the detected signal and s the slope factor for calibration.

Given a DSSSD detector with N strips on each side, each event that is registered in a given pixel will create a signal with amplitude A_p in the strip number p on the p-side and a signal with amplitude A_n in strip number n on the n-side $(n, p = 1 \ldots N)$. Assuming that both strips measure the same energy E deposited in the active area of the detector, one can write

$$E_p = s_p\, A_p\,, \quad E_n = s_n\, A_n \quad \text{and} \quad E_p = E_n = E\,, \tag{1}$$

with s_p and s_n being the calibration coefficients (slopes) for the p-th p-side strip and n-th n-side strip, respectively.

For each pixel of the detector, the values of A_p and A_n for various values of energy depositions ΔE are assumed to be linearly related. For each pixel, the relation between the amplitudes is

$$A_p = S_{pn}\, A_n\,, \tag{2}$$

with the slope parameter S_{pn} which can be determined from the data (see below). The set of N^2 slope parameters can be used to deduce a set of $2N$ calibration coefficients $\{s_p, s_n\}$ by minimizing the expression

$$\chi^2 = \sum_{p,n} \left(\frac{S_{pn} - \frac{s_n}{s_p}}{\Delta S_{pn}} \right)^2 , \tag{3}$$

that follows directly from Eqs. (1,2).

Implementation

There are two independent steps: First, the determination of the coefficients S_{pn}. Second, finding a set of calibration coefficients $\{s_p, s_n\}$ based on S_{pn}. The former is done using a Bayesian approach, updating the posterior probability distribution of the quantity of interest for each detected event. The latter is done by a nonlinear least squares fit algorithm.

Determination of S_{pn}: The posterior probability distribution of the quantity of interest is in this case $p\,(S_{pn}|\,\{d_{pn}\})$, with $\{d_{pn}\}$ being the set of all measured data points, i.e. the ratio of amplitudes $d_{pn} = A_p/A_n$. Knowing this distribution allows to get the most likely value for each slope parameter S_{pn} and its variance ΔS_{pn}. Starting with an initial guess for this distribution, i.e. uniform within reasonable limits, one can refine it by iterating over the measured data points, each time applying Bayes' theorem [4, 5]

$$p\,(S_{pn}\,|d_{pn}\,) = \frac{p\,(S_{pn})\;p\,(\,d_{pn}|\,S_{pn})}{p\,(d_{pn})}\,, \tag{4}$$

with the commonly used terminology [6]: $p\,(S_{pn}\,|d_{pn}\,)$ is called posterior distribution, $p\,(S_{pn})$ is the prior distribution, $L\,(\,d_{pn}|\,S_{pn})$ the likelihood function and $p\,(d_{pn})$ the evidence of the measured data. After each treated data point the normalized posterior distribution becomes the prior for the next data point.

The likelihood function is chosen to be a Lorentzian-shaped distribution with width w

$$L\,(\,d_{pn}|\,S_{pn}) \propto \frac{1}{w^2 + \left(\log d_{pn} - \log S_{pn}\right)^2}\,. \tag{5}$$

Such a distribution makes the result less sensitive to abundant background events as it would be the case with a Gaussian-shaped likelihood function. It depends on the logarithm of the slope parameter, because the slope is a scale parameter with a possible range inside $[0, \infty[$.

*Work supported by BMBF NuSTAR.DA - TP 6, FKZ: BMBF 05P12RDFN8 (TP 6), HGS-HIRe

While iterating over the data, the posterior distribution is represented as a discrete number N_p of points between the limits $S_{\min}$ and $S_{\max}$. The density of points depends on the desired accuracy of the final result and can be in the order of a few thousands. After all data is processed, the best estimates for all slopes S_{pn} and their uncertainties ΔS_{pn} are determined from the mean and variance of the final posterior probability distribution. For the example data shown here, the set of values was: $N_p = 1000$, $S_{\min} = 0.3$, $S_{\max} = 3$ and $w = 0.1$

Computing a set of calibration coefficients: Minimizing (3) is done using the implementation of a nonlinear least squares fit provided by [2]. The set of fit parameters is $\{s_p, s_n\}$, and the data is the complete set of measured slope parameters $\{S_{pn}\}$. The algorithm performs the minimization of (3). After convergence is reached, the parameter set describes the best calibration coefficients for the data set on a common arbitrary scale.

Results

The described procedure was applied to data from the PreSPEC-AGATA setup [7]. The DSSSD detector was mounted close to the position of the secondary target and had 2×32 strips, read out with two 32-channel ADCs. It is part of the Lund-York-Cologne CAlorimeter (LYCCA) [1] that is tracking and identifying heavy ions.

The result of the procedure is best summarized in a two-dimensional sum histogram of all p-side vs. all n-side amplitudes, without and with calibration coefficients as determined by the described method. In a correctly calibrated detector, each event should have equal calibrated amplitudes for both sides of the detector. That is confirmed by the Fig. 1.

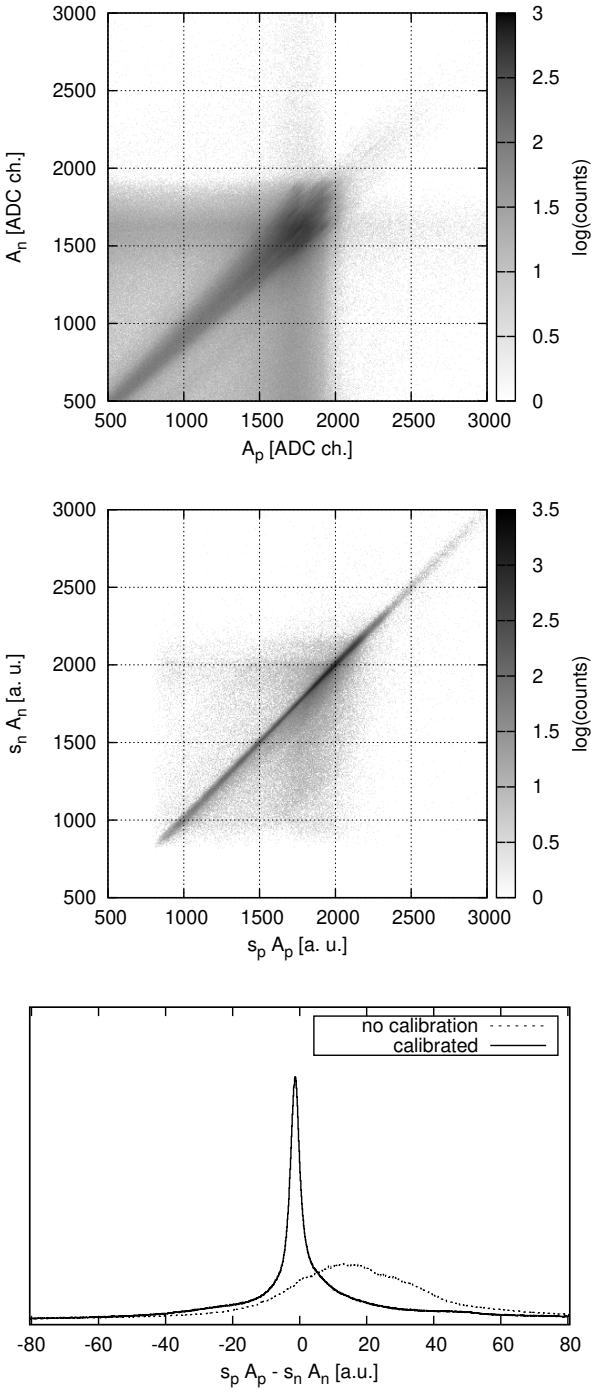

Figure 1: Sum histogram of the p and n-side amplitude distributions before (top) and after (middle) the calibration procedure. The picture on the bottom shows the difference of p and n-side amplitude before and after calibration.

References

[1] P. Golubev, et al., Nucl. Instr. and Meth. A 723, (2013), 55-66.

[2] M. Galassi et al, GNU Scientific Library Reference Manual (3rd Ed.), ISBN 0954612078.

[3] O.B. Tarasov, et al., Nucl. Instr. and Meth. B 266 (2008) 4657-4664.

[4] T. Bayes, Philosophical Transactions of the Royal Society, pp. 370-286.

[5] P.S. Laplace Mémoires de l'Académie royale des sciences, 6, 621-656 (1774).

[6] D.S. Sivia and J. Skilling, Data Analysis, (2006).

[7] P. Boutachkov et al., GSI Report 2012 (2013) 148.

 doi:10.15120/GR-2014-1-NUSTAR-GS-02

Development and test of a segmented Time-of-Flight plastic detector*

M. L. Cortés† [1,2], *H. Schaffner*[2], *I. Kojouharov*[2], *B. Voss*[2], *F. Ameil*[2], *K. Koch*[2], *S. Pietri*[2], *J. Gerl*[2], *N. Pietralla*[1], *P. Bednarczyk*[3], *J. Kotuła*[3], *Z. Sułek*[3], *and the PreSPEC and AGATA collaborations*

[1]TU Darmstadt, Darmstadt, Germany; [2]GSI, Darmstadt, Germany; [3]IFJ PAN, Kraków, Poland

Introduction

Improved SIS primary beam intensities converts directly into higher yields of exotic nuclei. Improvements to the FRS [1] tracking detectors are necessary to allow for higher rates. This concerns in particular the rate at the intermediate focal plane S2 where tracking detectors allowing for rates higher than $10^6 s^{-1}$ are needed.

In September 2010 a first Finger detector made of 15 strips of plastic scintillator, 14 mm wide each, was successfully commissioned and used [2]. As an upgrade from that detector, a new Finger detector was developed consisting of 51 strips, 4.4 mm wide, of BC420 plastic scintillator. This detector is used as a test case for further developments for HISPEC/DESPEC at FAIR.

Setup

Each pair of strips was glued to a bended UV-transparent PMMA light guide using a 2 component silicon glue. The light guides were then optically coupled to Hamamatsu R9880U-01 photo-multiplier tubes (PMTs) using silicon pads. To power up the PMTs, 13 power supplies were used, each one powering up 4 tubes. Independent potentiometers were added to the setup to allow independent adjustment of the voltages. Figure 1 shows the new Finger detector mounted.

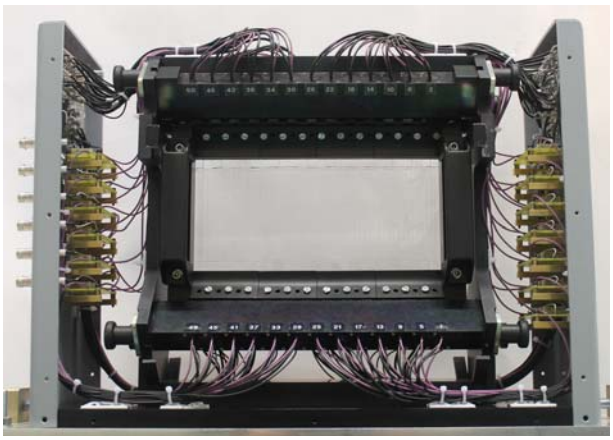

Figure 1: The new Finger detector

The PMTs are read-out using the LANDFEE discriminator. This electronics determines the leading and trailing edges of the incoming PMT pulses as time signals. These two times are then recorded using two CAEN V1290 Multihit TDCs. Using the two times given by the electronics it is possible to obtain, apart from the time of occurrence, the time-over-threshold (ToT) of the signal, which provides a measure of the signal amplitude. TRIPLEX cards [3] are used for the remote control of the thresholds and to obtain an OR signal and an analogue sum of the signals for monitoring. One of the TRIPLEX cards is connected with a network module which makes the system remote controllable via Ethernet by a lab-view program.

In-beam test

The New Finger detector was tested from February to April 2014 as part of the PreSPEC-AGATA setup at GSI [4]. Time and ToT spectra were obtained for Fe and Ni beams with different intensities. The efficiency of the new Finger detector was in average 2% lower than the one of the standard scintillator at S2, mainly because of gaps between the strips. Figure 2 shows a typical ToT spectrum recorded in one of the PMTs. Using these spectra it is possible to decide which strip had the higher charge collection and therefore which was the strip that was hit. Position and timing information from that strip were used for each event and a preliminary analysis was performed. Figure 3 shows the correlation between the strip selected as being hit and the position determined in TPCs. In spite of the clear correlation, background is also present, coming from two different sources: The high rate present as S2, which reduces the performance of the TPCs and the possibility of having

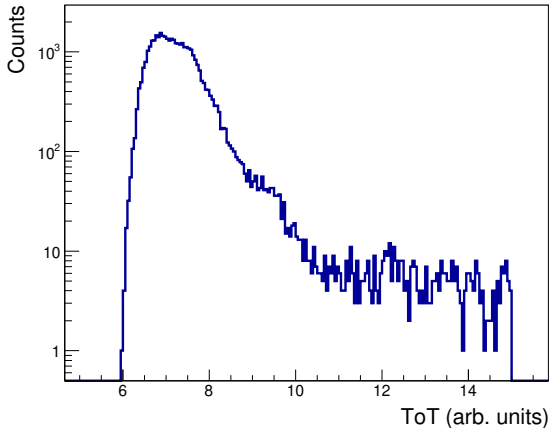

Figure 2: Time-over-threshold spectrum

* Work partially supported by HIC4FAIR
† m.l.cortes@gsi.de

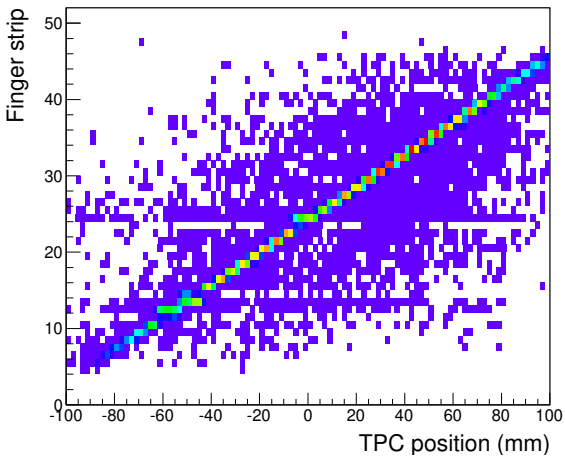

Figure 3: Strip number vs. position projected from TPCs

two particles hitting the Finger detector during the same trigger, which gives the possibility of a wrong strip selection. To study this effect, the number of PMTs fired per event was calculated. When all fired PMTs are consecutive they are considered as coming from a single particle interaction. When they are not consecutive, a second particle could have produced the signals. The number of this sets of consecutive PMTs is called cluster multiplicity. Figure 4 shows the number of clusters recorded versus the number of PMTs fired. We can see that for the case of one particle

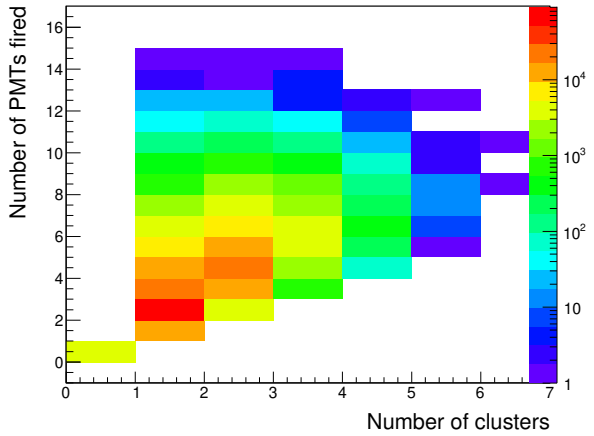

Figure 4: Cluster multiplicity vs. PMT multiplicity

the most likely is to have two PMTs fired, corresponding to one strip. The rest of the events can be properly reconstructed with more detailed analysis.

Using the timing information given by the strip selected, the Time-of-Flight (ToF) between the new Finger detector and the scintillator placed in the last focal point of FRS (S4) was calculated. Figure 5 shows the ToF versus the atomic number of the particles obtained from the MUSIC ionization chambers.

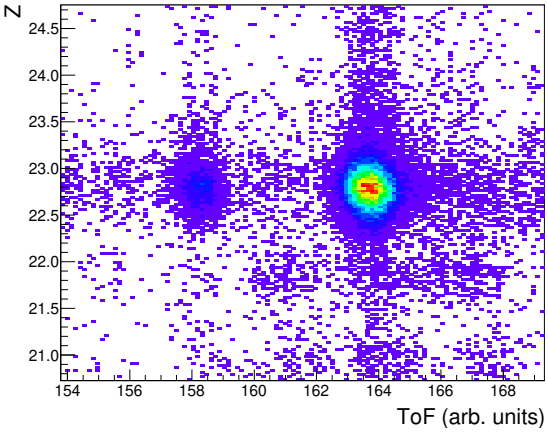

Figure 5: Time of flight vs. atomic number

This plot presents a preliminary identification plot and can be further improved by a more detailed analysis which includes strip selection, considering multiple particles and proper calibrations.

Outlook

A new Finger detector with higher count rate capabilities was developed and tested. ToT technique to select the strip was proved to be feasible. The preliminary analysis of the data obtained during the PreSPEC-AGATA campaign 2014 show a reasonable efficiency and the possibility to characterize multiple particles hitting the detector. The outcome of this study will be used to optimize further developments for a Time-of-Flight detector at the Super FRS.

References

[1] H. Geissel et al. Nucl. Instr. Meth. B70 (1992) 286

[2] F. Ameil et al. “Time of flight with a segmented plastic finger detector at high particle rate”, GSI Scientific Report 2011 (2012) 171

[3] K. Koch et al., “TRIPLEX, an Upgrade for the TACQUILA System”, GSI Scientific Report 2010 (2011) 235

[4] H.J.Wollersheim, “Relativistic Coulomb Excitation: From RISING to PreSPEC”, Acta Phys. Pol. B42 (2011), 705

 doi:10.15120/GR-2014-1-NUSTAR-GS-03

In-beam γ-ray spectroscopy with AGATA@PreSPEC: Development of new experimental tools for HISPEC@FAIR*

C. Stahl† [1], *M. Lettmann*[1], *M. Reese*[1], *N. Pietralla*[1], *and the PreSPEC collaboration*
[1]IKP TU Darmstadt, Darmstadt, Germany

The high γ-ray energy- and position resolution of the AGATA detector system in combination with relativistic ion beams from GSI's SIS/FRS opens up new perspectives for the development of experimental techniques for in-beam γ-ray spectroscopy

Background

The use of beams of exotic nuclei for in-beam γ-ray spectroscopy experiments imposes new challenges to experimentalists due to drastically reduced beam intensities as compared to "standard" stable ion beams, for example. One way to overcome this shortcoming is to increase the efficiency of detector systems and the use of new instrumental approaches and detector technology. The European γ-ray spectrometer AGATA [1] is an example of a next-generation detector system that helps to boost the efficiency of experiments with radioactive ion beams. It is employed in a first phase in GSI's PreSPEC setup at the S4 experimental site for beamtimes in 2012 [2] and 2014 and will be a central part of the HISPEC@FAIR setup. Its ability to extract the interaction points of γ-rays inside the detector material and, hence, the detection position of the γ-rays with a resolution as good as 5 mm FWHM is of paramount benefit for the experiments with relativistic ion beams performed at GSI. However, dedicated experimental techniques have to be developed in order to fully exploit the capabilities of AGATA in combination with GSI's unique relativistic ion beams.

Concepts

The relativistic beam energies of SIS/FRS induce strong Doppler-shifts of the γ-rays emitted at the de-excitation of atomic nuclei in flight. The magnitude of the observed Doppler-shift is a function of both emitter velocity and γ-ray emission direction with respect to the emitter velocity vector. In order to be able to precisely correct for the occurring Doppler-shifts, the measurement of both the ion trajectories and γ-ray detection positions with the best possible resolution is a major task of the PreSPEC in-beam γ-ray spectroscopy setup and also for the future HISPEC@FAIR setup. Convincing performance is achieved by the combination of the FRS detectors, AGATA and the LYCCA [3] detector system. Here, especially the position resolution of AGATA facilitates the study of the distribution of observed Doppler-shifted γ-rays as a function of their detection position in the laboratory system. This gives, inter alia, rise to substantial improvements of Doppler-shift based techniques for the determination of nuclear level lifetimes, such as the Doppler-shift attenuation method (DSAM) for level lifetimes in the (sub-)picosecond range. A further-development of the DSA method taking advantage of AGATA's position resolution has already been developed in our group [4].

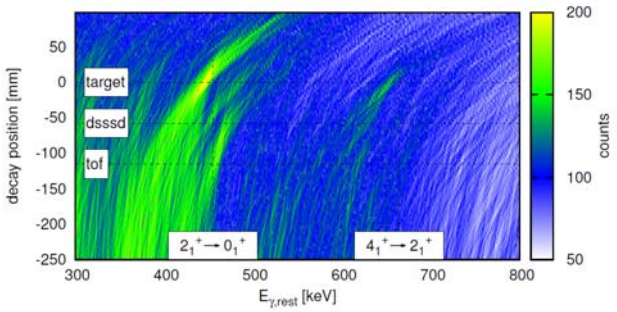

Figure 1: Doppler-corrected γ-rays from the de-excitation of the 455-keV 2_1^+-level of ^{78}Kr as function of the γ-ray emission position along the beam-path. Sharp peak arise if the position of the secondary target, the target DSSD or the LYCCA TOF start detector are assumed as γ-ray emission position along the ion trajectory. The shown data was taken during the performance commissioning phase of the PreSPEC experimental campaign.

However, the emission direction of the γ-rays is pinned down not only by the γ-ray detection position, but also by its vertex. Therefore, precise knowledge of the ion trajectory, the detection position and the observed Doppler-shift allows to draw conclusions on the γ-ray vertex along the ion trajectory. The sensitivity to the longitudinal emission position is shown in fig. 1: The excitation of the short-lived 455-keV 2_1^+-state of ^{78}Kr via two-neutron knock-out of ^{80}Kr can occur in the secondary target as well as in two detectors upstream of the target. De-excitation after a detector or the secondary target can be distinguished by the longitudinal emitter position assumed in the Doppler-correction.

Applications

The sensitivity of the PreSPEC setup to the γ-ray vertices arises from the unique combination of the position-

*This work was supported by the BMBF under grant 05P12RDFN8, HIC for FAIR and HGS-HIRe for FAIR
† stahl@ikp.tu-darmstadt.de

sensitive AGATA-array, high-quality beam-tracking in FRS/LYCCA and relativistic ion beams. It can be used for a novel class of γ-spectroscopic techniques. As described for example in [5, 6], the γ-vertex sensitivity gives rise to lifetime-sensitive effects in the observed Doppler-corrected γ-energy spectra because of the ignorance of the "true" de-excitation point if nuclear level-lifetimes are in the order of a few hundred picoseconds and the ions thus de-excite at significant average distances $\langle z \rangle = \tau\beta$ behind the excitation target (see fig. 2). An analysis method taking advantage of this effect has been developed and implemented into a computer code by our group [7].

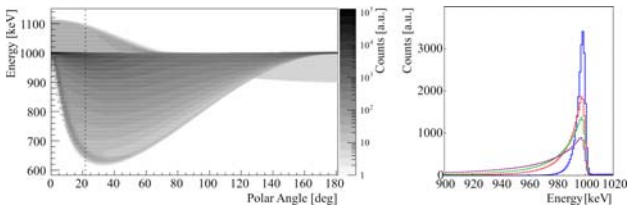

Figure 2: Effect of level-lifetimes on Doppler-corrected γ-ray spectra as function of γ-ray energy and detection polar angle (left). The spectrum shows a calculated "2D-lineshape" for a model-transition with rest energy 1000 keV and lifetime of 200ps, emitted from a 150 AMeV beam of ^{80}Kr excited on a 0.5 g/cm^2 gold target. The tail towards higher energies at small angles stems from de-excitations inside the target, the tail to lower energies from de-excitation well behind the target. The right part of the figure shows the γ-ray spectrum observable under a detection angle of 22° for different level lifetimes (30ps: blue, solid; 80ps: red, dashed; 120ps: green, dotted; 200ps: purple, dash-dotted)

Another new experimental approach using the ability to distinguish γ-rays emitted at different positions along the ion trajectories that aims at determining multipole mixing ratios was recently developed in our group. The "*Coulex-multipolarimetry by active-degrader method*" makes use of the fact that the cross-section for Coulomb-excitation has a different energy-dependence for different radiation characters. For example, the cross-section for M1-excitation is almost independent of ion velocity, whereas the E2 cross-section rapidly drops with increasing velocity. Hence, the ratio of Coulomb-excitation cross-sections at two different beam energies is a measure for the M1/E2 multipole mixing ratio [8]. The measurement of the cross section ratio at two different ion velocities can be performed in one single experiment using two thick targets installed in some distance from each other (see fig. 3). Because the ions are significantly slowed down in the first target, the average ion velocities in the first and second target are different. If the level lifetime is sufficiently short, excitations in the first and second target can be distinguished by the different Doppler-shift of the de-excitation radiation caused by the different vertices of the γ-radiation. This approach is particularly helpful if standard methods for the determination of multipole mixing ratios like the analysis of angular correlations cannot be applied due to too low statistics in rare ion beam experiments or because of the spin of the excited state.

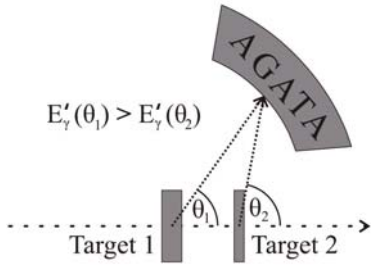

Figure 3: Principle of the "*Coulex-multipolarimetry by active-degrader method*". See text for details.

Conclusion

The extraction of spectroscopic data from in-beam γ-ray spectroscopy experiments faces some complications in the case of rare, relativistic ion beams. Established methods may not be applicable or have to be further developed for efficient use with state-of-the-art experimental setups like PreSPEC or, in the future, HISPEC@FAIR. However, the advent of the next generation of γ-ray detection systems such as AGATA opens up new possibilities for experimental techniques for the exploration of nuclear structure far off stability. For us, the PreSPEC-setup is an important testing ground to observe and understand the experimental phenomena that the powerful combination of AGATA, relativistic ion beams from SIS/FRS and the detection capabilities of LYCCA can reveal. Only performing experiments under these conditions puts us in the position to develop experimental techniques that are required to take full advantage of the possibilities that will arise with the future HISPEC@FAIR setup.

References

[1] S. Akkoyun et al., NIM A 668 (2012) 26–58

[2] N. Pietralla: *On the Road to FAIR: First Operation of AGATA in PreSPEC at GSI*, talk at the INPC 2013, to be published

[3] P. Golubev et al., NIM A 723 (2013) 55–66

[4] C. Stahl, Master Thesis, TU Darmstadt, AG Pietralla (2011)

[5] C. Domingo-Pardo et al., NIM A 694 (2012) 297–312

[6] P. Doornenbal et al., NIM A 613 (2010), 218–225

[7] M. Lettmann, Master Thesis, TU Darmstadt, AG Pietralla (2013)

[8] G. Rainovski et al., Experiment S426, Proposal to the G-PAC (2011)

 doi:10.15120/GR-2014-1-NUSTAR-GS-04

Simulations for DEGAS detectors at FAIR*

C. Louchart-Henning[1], G. Henning[2], J. Gerl[2], N. Pietralla[1], and the DESPEC collaboration
[1]IKP, TU Darmstadt, Germany; [2]GSI, Darmstadt, Germany

DEGAS detector

For the future Low Energy Branch of FAIR facility, experiments using stop beam in the focal plan of the Super FRS aim at studying the decay properties of exotic nuclei. The AIDA [1] active stopper, consisting of a stacks of DSSD (8x8 cm^2), will cover the large focal plan of 24x8 cm^2. The γ rays emitted by the implanted nuclei will be detected by HPGe detectors arranged in a compact geometry around the DSSD. For the γ detection, three steps are forseen [2]. The first is to use standart Ge detectors, like the existing RISING detectors [3]. In a second step, the new generation of Ge detectors, who have the ability to reconstruct the path of the γ rays inside the Ge volume, will be used. Finally, the goal is to use imaging detectors (with planar Ge for instance [4]).

Simulations

In this report we present the results of the efficiency simulated using RISING detectors arranged in seven-detectors per cluster (as used for the previous stop beam campain in GSI [5]) or three-detectors per cluster. The idea is to optimize the space occupation around the large focal plan while having the maximum γ detection efficiency. The simulations have been performed using the Monte Carlo code GEANT4 [6]. Several configurations have been tried for both 3- and 7-fold clusters. First, placing the detectors in a sphere like configuration. Then a very compact configuration with the detectors arrranged as a box around the decay chamber. And finally, a *shell* configuration, intermediate between box and sphere, characterized by a less compact arrangement than the box, but detectors closer to the chamber than for the sphere. The source of γ rays was extended over the surface of the focal plan.
The effect of γ multiplicity, energy, and the presence of a γ *flash* associated with the ion implantation at the focal plan (simulated by a burst of $\simeq$ 30 gamma rays of energy $\leqslant$ 100 keV in addition to the γ of interest) were investigated. A computer rendering of 3-fold clusters in box configuration is presented figure 1.

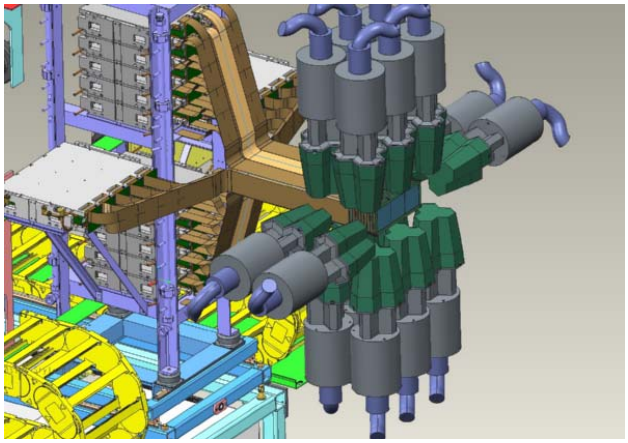

Figure 1: Integration of the Box configuration with the AIDA detectors, including their support and electronics [7].

Results

The simulated efficiency for the shell and box configurations are reported in table 1. The simulations show an advantage for the triple clusters in respect to the 7-fold clusters in both shell and box configurations, but not in the sphere configuration where both 7-fold and 3-fold clusters have similar and low efficiency. The effect of gamma multiplicity has been investigated and we conclude that higher multiplicities of gamma rays ($M_\gamma \geq 4$) decreases the efficiency in the addback mode (sum of the energy over a cluster), without any significant impact on single crystal efficiency. The presence of the γ flash is larger at low energy, and most proeminent in the most compact configuration (box) as the crystals are more exposed to the γ rays from the flash. Overall, the simulations show that, for low γ multiplicity and even with the γ flash, a better detection efficiency is acheived by using a more compact configuration than by increasing the number of detectors. In that respect, 3-fold clusters present less geometric constrains as they are smaller and allow a better compact coverage of the decay chamber.

E (keV)	$\epsilon 3_{Box}$	$\epsilon 7_{Box}$	$\epsilon 3_{Shell}$	$\epsilon 7_{Shell}$
122	29.7%	22.4%	24.4%	18.0%
244	26.0%	20.0%	21.4%	16.1%
511	19.1%	15.6%	15.9%	12.6%
1333	12.8%	11.0%	10.7%	8.7%

Table 1: Efficiency of the Box and Shell configurations for 3- and 7-fold clusters at four energies. An expended source with γ multiplicity of 5 has been considered, without taking into account the γ flash.

To conclude, a compact configuration has high detection

*This work was supported by the BMBF under grant 05P12RDFN8, HIC for FAIR and HGS-HIRe for FAIR

efficiency, in particular with a γ-multiplicity $\leqslant 3$. This preliminary study favors the use of triple clusters arranged in box configuration. It seems that it is more favourable to keep the detectors close to the source than to increase the number of detectors. The integration of this geometry with AIDA is under study and is presented in Fig.1. For using triple cluster in box configuration, electronic cooling should be used. The technic is now investigating in GSI.

References

[1] AIDA TDR (2008); http://www2.ph.ed.ac.uk/∼td/DSSD/Design/tdr_aida.pdf

[2] J. Gerl, TDR in preparation

[3] H.J. Wollersheim et al., NIMA 537, 637 (2005)

[4] A. Algora et al., Simulations of possible Ge arrays for the DESPEC setup at FAIR, GSI scientific report 2005.

[5] P.H. Regan et al. Nuclear Physics A 787 (2007) 491c–498c

[6] S. Agostinelli et al., Nucl. Inst. and Meth. A506 (2003) 250; http://wwwasd.web.cern.ch/wwwasd/geant4/geant4.html

[7] Courtesy of Paul Aden.

 doi:10.15120/GR-2014-1-NUSTAR-GS-05

Simulations for position-sensitive tracking of γ rays in scintillators Approach for source reconstruction

N. Lalovic[*1,2], *J. Gerl*[1], *D. Rudolph*[2], *R. Hoischen*[1], *and P. Golubev*[2]
[1]GSI, Darmstadt, Germany; [2]Lund University, Lund, Sweden

Introduction

There is a growing demand for gamma radiation detectors with imaging capability. This is relevant not only in the basic research sector, but even more in societal and industrial applications, such as medical imaging, environmental and safety investigations. Scintillation materials with position-sensitive read-out are viable candidates for this purpose and have been tested using Geant4 simulation toolkit [1].

Geant4 Simulations

The present simulation code enables easy and quick optimization of different geometries. Detailed simulations were performed with both BC404 and CsI(Na) scintillators. Here we present results with the latter detector elements, providing higher efficiency. Energy response and associated light production of the initial radiation (γ rays) has been investigated, hence including all the underlying physics processes. In addition, optical photons have been treated, with an assumption that the surface was a perfectly polished mirror. So far, $511\,keV$ e^+e^- annihilation radiation has been considered. First geometry simulated comprises nine $18 \cdot 18 \cdot 100\,mm^3$ scintillator bars with Hamamatsu R7600U-2000 PMTs with $2\,mm$ distance between each 2 crystal elements in the 'matrix', as represented in Fig 1. The second geometry included nine times four $\cdot 9 \cdot 9 \cdot 100\,mm^3$ scintillator bars with Hamamatsu R7600U-2000M4 PMTs with $2\,mm$ between 'submatrix' elements and $4\,mm$ between 'matrix' elements.

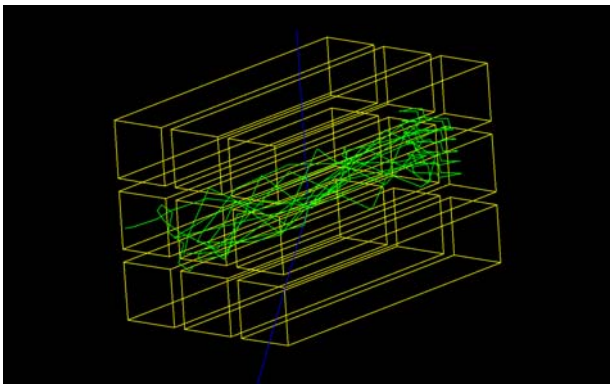

Figure 1: Geometry 1

Analysis and Reconstruction Algorithm

We are interested in multiple Compton scattering [2, 3] in those events causing the incoming γ photon to be scattered from one detector element and then photoabsorbed in the second one. Add-back energy spectra showed Peak-To-Total approximately 50 % and 60 % in case of the first and second geometry, respectively. Compton kinematics and energy conservation law then give the scattering angle (with respect to ΔE-energy deposited in the second detector element and E_i-energy before scattering):

$$\beta = \arccos\left(1 - \frac{m_e c^2 \Delta E}{(E_i)^2 - E_i \Delta E}\right) \qquad (1)$$

For our offline analysis it is essential to find the scattered direction, i.e. vector. Simulation gives the exact coordinates of the interaction points, so the 3D vector $(\rho,\, \theta,\, \phi)$ is easily extracted. The algorithm concentrates on the reference plane (θ, ϕ), where the centre of each circle (θ, ϕ) characterizes the scattered direction. Finally, the scattering angle is seen as a radius of the corresponding circle, as illustrated in Fig 2.

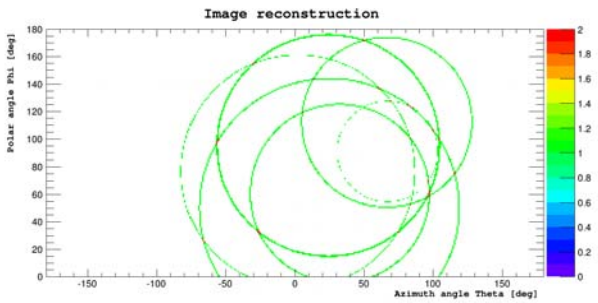

Figure 2: Representation of the reconstructing algorithm

Summary and Outlook

The simulation code has been developed providing the input data for the offline analysis and the flexibility for deploying different materials and/or geometries has been achieved. First version of the algorithm which aims to reconstruct the source position confirmed the idea of possible reconstruction of source position and is currently being tested on the larger set of data, since the preliminary results (see Fig 3.) don't yet provide an unambiguous conclusion. In addition to that, the experimental tests are ongoing and the parameters from the simulations have to be normalized with respect to the response from the realistic setup [4].

* n.lalovic@gsi.de

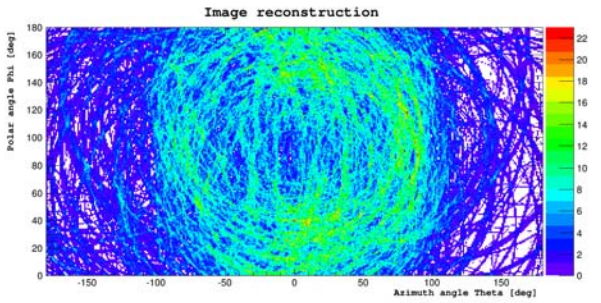

Figure 3: Reconstructing algorithm applied on a small set of data

References

[1] Geant4 - A Simulation Toolkit, Nucl. Instr. Meth. A506, 250 (2003)

[2] N. Dogan, D. K. Wehe, A. Z. Akcasu, IEEE Trans. Nucl. Sci. 39, 1427 (1992)

[3] N. Dogan, D. K. Wehe, G. F. Knoll, Nucl. Instr. Meth. A299, 501 (1990)

[4] P. Golubev, D. Rudolph, private communication

 doi:10.15120/GR-2014-1-NUSTAR-GS-06

Study of the ^{48}Ca + ^{249}Bk fusion reaction leading to element $Z = 117$: long-lived α-decaying ^{270}Db and discovery of ^{266}Lr *

J. Khuyagbaatar †[1,2], *A. Yakushev*[2], *Ch.E. Düllmann*[1,2,3], *D. Ackermann*[2], *L.-L. Andersson*[1], *M. Asai*[4], *M. Block*[2], *R.A. Boll*[5], *H. Brand*[2], *D.M. Cox*[6], *M. Dasgupta*[7], *X. Derkx*[1,3], *A. Di Nitto*[3], *K. Eberhardt*[1,3], *J. Even*[1], *M. Evers*[7], *C. Fahlander*[8], *U. Forsberg*[8], *J.M. Gates*[9], *N. Gharibyan*[10], *P. Golubev*[8], *K.E. Gregorich*[9], *J.H. Hamilton*[11], *W. Hartmann*[2], *R.-D. Herzberg*[6], *F.P. Heßberger*[1,2], *D.J. Hinde*[7], *J. Hoffmann*[2], *R. Hollinger*[2], *A. Hübner*[2], *E. Jäger*[2], *B. Kindler*[2], *J.V. Kratz*[3], *J. Krier*[2], *N. Kurz*[2], *M. Laatiaoui*[2], *S. Lahiri*[12], *R. Lang*[2], *B. Lommel*[2], *M. Maiti*[12], *K. Miernik*[5], *S. Minami*[2], *A. Mistry*[6], *C. Mokry*[1,3], *H. Nitsche*[9], *J.P. Omtvedt*[13], *G.K. Pang*[9], *P. Papadakis*[6], *D. Renisch*[3], *J. Roberto*[5], *D. Rudolph*[8], *J. Runke*[2], *K. Rykaczewski*[5], *L.G. Sarmiento*[8], *M. Schädel*[2,4], *B. Schausten*[2], *A. Semchenkov*[13], *D.A. Shaughnessy*[10], *P. Steinegger*[14], *J. Steiner*[2], *E.E. Tereshatov*[10], *P. Thörle-Pospiech*[1,3], *K. Tinschert*[2], *T. Torres De Heidenreich*[2], *N. Trautmann*[3], *A. Türler*[14,15], *J. Uusitalo*[16], *D.E. Ward*[8], *M. Wegrzecki*[17], *N. Wiehl*[1,3], *S.M. Van Cleve*[5], *and V. Yakusheva*[1]

[1]Helmholtz Institute Mainz, 55099 Mainz, Germany; [2]GSI Helmholtzzentrum für Schwerionenforschung, 64291 Darmstadt, Germany; [3]Johannes Gutenberg-Universität Mainz, 55099 Mainz, Germany; [4]Advanced Science Research Center, Japan Atomic Energy Agency, Tokai, Ibaraki 319-1195, Japan; [5]Oak Ridge National Laboratory, Oak Ridge, TN 37831, USA; [6]University of Liverpool, Liverpool L69 7ZE, United Kingdom; [7]The Australian National University, Canberra, ACT 0200, Australia; [8]Lund University, 22100 Lund, Sweden; [9]Lawrence Berkeley National Laboratory, Berkeley, CA 94720, USA; [10]Lawrence Livermore National Laboratory, Livermore, California 94551, USA; [11]Vanderbilt University, Nashville, TN 37235, USA; [12]Saha Institute of Nuclear Physics, Kolkata 700064, India; [13]University of Oslo, 0315 Oslo, Norway; [14]Paul Scherrer Institute, 5232 Villigen, Switzerland; [15]University of Bern, 3012 Bern, Switzerland; [16]University of Jyväskylä, 40351 Jyväskylä, Finland; [17]The Institute of Electron Technology, 02-668 Warsaw, Poland

The fusion-evaporation reaction ^{48}Ca + ^{249}Bk, was studied at the gas-filled TransActinide Separator and Chemistry Apparatus (TASCA) [1], which was significantly upgraded [2] now being able to register nuclei with half-lives from sub-μs to a few days. We observed four decay chains among them two long ones comprising seven α decays and a spontaneous fission, both chains have similar properties (Fig. 1). Our data is largely consistent with previously reported data [3] on the decay chains assigned to ^{294}117. In addition to data from [3], a hitherto unknown α branch in ^{270}Db, which populated the new isotope ^{266}Lr, was identified.^{270}Db with a half-life of $1.0^{+1.9}_{-0.4}$ h is the most long-lived α-decaying nucleus above No ($Z = 102$). The decay chain members from ^{290}115 to ^{266}Lr all decay with $T_{1/2} \gtrsim 1$ s, which opens prospects for their chemical investigation and off-line studies.

We are grateful to GSI's ECR ion-source and UNILAC staff, and the Experimental Electronics Department for their continuous support of the experiment.

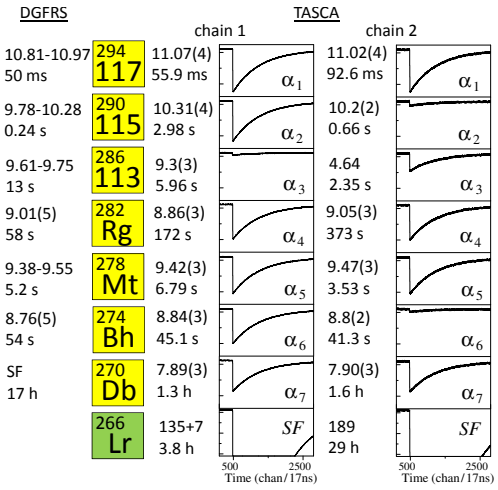

Figure 1: Decay chains assigned to ^{294}117 from this work (together with traces of members) and data from [3].

References

[1] A. Semchenkov et al., NIM. B **266**, 4153 (2008), J.M. Gates et al., PRC **83**, 054618 (2011).

[2] see GSI Scientific Report-2011, pages-206, 212, 217, 218, 251-253 (2012).

[3] Yu.Ts. Oganessian et al., PRL. **104**, 0142502 (2010), PRC. **83**, 054315 (2011), PRL. **109**, 162501 (2012), PRC. **87**, 054621 (2013).

*This work was financially supported in part by the German BMBF (05P12UMFNE), the Swedish Research Council, the U.S. Department of Energy by LLNL (DE-AC52-07NA27344), the Laboratory Directed Research and Development Program at LLNL (11-ERD-011) and the Helmholtz Institute Mainz. This work was co-sponsored by the Office of Science, U.S. Department of Energy, and supported under U.S. DOE grants No. DE-AC05-00OR22725.

† J.Khuyagbaatar@gsi.de

Element 115 studied with TASISpec

D. Rudolph[1], U. Forsberg[1], P. Golubev[1], L.G. Sarmiento[1], A. Yakushev[2], L.-L. Andersson[3], A. Di Nitto[4], Ch.E. Düllmann[2,3,4], J.M. Gates[5], K.E. Gregorich[5], C.J. Gross[6], R.-D. Herzberg[7], F.P. Heßberger[2,3], J. Khuyagbaatar[3], J.V. Kratz[4], K. Rykaczewski[6], M. Schädel[2,8], S. Åberg[1], D. Ackermann[2], M. Block[2], H. Brand[2], B.G. Carlsson[1], D. Cox[7], X. Derkx[3,4], K. Eberhardt[3,4], J. Even[3], C. Fahlander[1], J. Gerl[2], E. Jäger[2], B. Kindler[2], J. Krier[2], I. Kojouharov[2], N. Kurz[2], B. Lommel[2], A. Mistry[7], C. Mokry[3,4], H. Nitsche[5], J.P. Omtvedt[9], P. Papadakis[7], I. Ragnarsson[1], J. Runke[2], H. Schaffner[2], B. Schausten[2], P. Thörle-Pospiech[3,4], T. Torres[2], T. Traut[4], N. Trautmann[4], A. Türler[10], A. Ward[7], D.E. Ward[1], and N. Wiehl[3,4]

[1]Lund University, Lund, Sweden; [2]GSI Helmholtzzentrum für Schwerionenforschung GmbH, Darmstadt, Germany; [3]Helmholtz Institute Mainz, Mainz, Germany; [4]Johannes Gutenberg-Universität Mainz, Mainz, Germany; [5]Lawrence Berkeley National Laboratory, Berkeley, USA; [6]Oak Ridge National Laboratory, Oak Ridge, USA; [7]University of Liverpool, Liverpool, United Kingdom; [8]Advanced Science Research Center, Japan Atomic Energy Agency, Tokai, Japan; [9]University of Oslo, Oslo, Norway; [10]Paul Scherrer Institute and University of Bern, Villigen, Switzerland

An experiment was conducted at GSI to fingerprint the proton number of one or several isotopes along anticipated decay chains of element 115 by means of high-resolution coincidence spectroscopy of α decays and photons. The fusion-evaporation reaction ^{48}Ca+^{243}Am [1] was used. The residues were separated from primary beam and background by TASCA [2-4] and guided into the TASISpec set-up [cf. Fig. 1(a)] [5, 6].

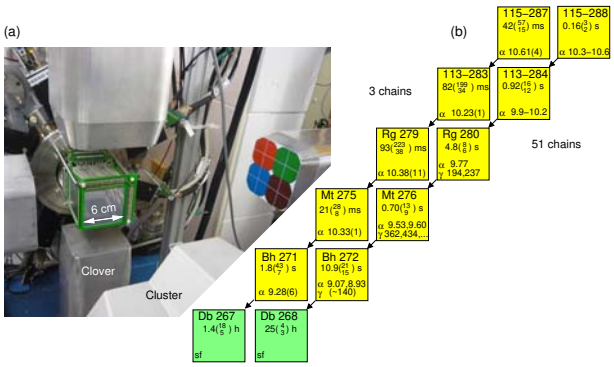

Figure 1: (a) Photograph of the TASISpec α-photon coincidence set-up [5] in the focal plane of the TASCA gas-filled separator at GSI [2]. See text for details. (b) Proposed decay chains of ^{287,288}115 based on the combined data and assignments of Refs. [7-9].

22 and 1 correlated decay chains were found to be consistent with 31 and 2 previously reported chains associated with ^{288}115 and ^{287}115, respectively [cf. Fig. 1(b)] [7, 8]. 16 prompt α-photon coincidences were recorded along the ^{288}115 chain [9-11]. Seven short chains of types recoil-α-(α)-fission deserve specific attention [12].

The conclusion of Ref. [9] notes that "thirty correlated α-decay chains were observed following the reaction ^{48}Ca+^{243}Am. Decay schemes arising from high-resolution spectroscopic coincidence data, in conjunction with comprehensive Monte-Carlo simulations, open the door for direct nuclear structure insights of these heaviest man-made atomic nuclei. Previous assignments linking the majority of the decay chains to the decay of ^{287,288}115 [7, 8] are confirmed. This includes first candidates for Z-fingerprinting the decay of Mt by means of characteristic K-X ray detection. There is clearly potential for direct determination of the atomic number of the descendants of superheavy elements."

Following press releases the topic received significant media attention [13], not least due to precisely element 115 starring in various computer games – and Area 51 [14].

The authors thank the ion-source and accelerator staff at GSI. This work is supported by the European Community FP7 – Capacities ENSAR No. 262010, the Royal Physiographic Society in Lund, the Euroball Owners Committee, the Swedish Research Council, the German BMBF, the Office of Nuclear Physics, U.S. Department of Energy, and the UK Science and Technology Facilities Council.

References

[1] ^{243}Am material provided by ORNL and targets made at JGU.
[2] M. Schädel, Eur. Phys. J. D **45**, 67 (2007).
[3] J.M. Gates *et al.*, Phys. Rev. C **83**, 054618 (2011).
[4] U. Forsberg *et al.*, Acta Phys. Pol. B**43**, 305 (2012).
[5] L.-L. Andersson *et al.*, Nucl. Instr. Meth. **A622**, 164 (2010).
[6] L.G. Sarmiento *et al.*, Nucl. Instr. Meth. **A667**, 26 (2012).
[7] Yu. Ts. Oganessian *et al.*, Phys. Rev. C **69**, 021601(R) (2004).
[8] Yu. Ts. Oganessian *et al.*, Phys. Rev. C **87**, 014302 (2013).
[9] D. Rudolph *et al.*, Phys. Rev. Lett. **111**, 112502 (2013).
[10] U. Forsberg *et al.*, Proceedings *INPC 2013*, Florence, Italy, EPJ Web of Conferences, in press.
[11] D. Rudolph *et al.*, Acta Phys. Pol. B, in press.
[12] U. Forsberg *et al.*, to be published.
[13] http://www.fysik.lu.se/om_institutionen/nyheter/nyheter_2013/element-115-news-feed/ (selection of news articles).
[14] http://www.youtube.com/watch?v=mpmAXO2-gSo
http://www.youtube.com/watch?v=BJYDrugEtxY
http://www.youtube.com/watch?v=q0lSL1yD5qQ
http://www.youtube.com/watch?v=YW4zzo3F2ac

 doi:10.15120/GR-2014-1-NUSTAR-SHE-02

Neutron Shell Strengths at N = 152 and towards N = 162

F.P. Heßberger[1,2] *and D. Ackermann*[1]
[1]GSI, Darmstadt, Germany; [2]HIM, Mainz, Germany

Determination of the shell strengths is an important feature to characterize the properties of superheavy elements and to test the power of theoretical predictions. Recently ground-state masses of several nobelium (Z=102) and lawrencium (Z=103) isotopes have been measured directly with high precision at SHIPTRAP [1, 2]. The results have been used to determine the strength of the N = 152 subshell for Z = 102 and Z = 103 [2]. The experimental data from [2] are compared in fig. 1 with the results from a microscopic - macroscopic approach [3] and a selfconsistent calculation using the SLy4 - force [4]. The latter has been used recently to calculate properties of neutron stars, e.g. the relation between mass and radius (see e.g. [7]). This circumstance demonstrates that properties of the nuclear force (or strong force, respectively) derived from the structure and stability of nuclei can be used to describe astrophysical phenomena or in general, phenomena where the strong force plays an essential role (e.g. quark-gluon plasma). Vice versa, information on the strong force obtained from 'such other' studies will have a feedback on the description of nuclei. Superheavy nuclei are a specific, but of course not the only one, laboratory for such studies, as they exist only due to a delicate balance between the nuclear force and the Coulomb force.

Another source of information on shell strength in the transactinide region are the α - decay chains passing through ^{252,254}No. Based on the measured masses of these isotopes [1] the 2n- binding energies of the N-Z = 50 nuclei could be determined up to ^{266}Hs [5]. The results are compared with predicted values in fig. 2. It is seen that the 2n-binding energies obtained from the microscopic - macroscopic models [3, 6] describe the experimental trend, which shows a maximum value at N = 152, at least qualitatively, while the agreement between experimental and calculated values is somewhat better for [3] than for [6]. The selfconsistent calculation using the SkP force, however, does not show a local maximum at N = 152 and gives too low values for N$\leq$152. Towards higher neutron numbers all calculations show a steeper increase of the 2n - binding energies than measured. This may indicate that the N = 162 neutron shell might be weaker or stronger localized. To check this possibility it is necessary the estimate the 2n - binding energy of ^{270}Ds, which requires the identification of the so far unknown nuclide ^{268}Ds. Based on production cross-sections for ^{269,270,271}Ds measured previously at SHIP it can expected to be produced with $\sigma \approx$ 1-2 pb in the reaction ^{207}Pb(^{62}Ni,n)^{268}Ds.

This finding is in-line with the trend which is indicated by the spontaneous fission half-lives, which show a slower increase towards N = 162 than the values predicted in [8], which are based masses and shell effects from [3].

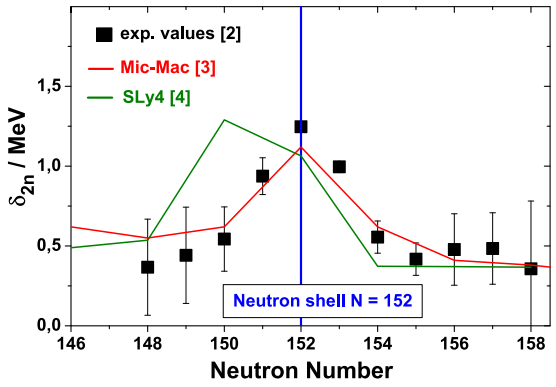

Figure 1: Experimental shell strength parameters of No isotopes in comparison with results from calculations.

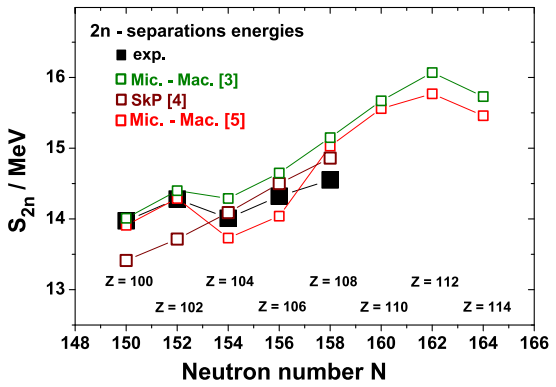

Figure 2: Experimental 2n - separation energies in comparison with results from calculations.

References

[1] M. Dworschak et al., PRC 81, 064312 (2010)
[2] E. Minaya Ramirez et al., Science 337, 1207 (2012)
[3] R. Smolanczuk, A. Sobiczewski, Proc. EPS Conf. 'Low Energy Nucl. Dyn.', St. Petersburg (Russia), 1995
[4] J. Dobaczewski et al., arXiv:nucl-th/0404077vl (2004) (http: fuw.edu.pl/ dobaczew/thodri/thodri.htm)
[5] D. Ackermann et al. GSI-Scientific Report 2011, PHN-NUSTAR-SHE04
[6] P. Möller et al. ADNDT 59, 185 (1995)
[7] M. Hempel, Physik in unserer Zeit 01/2014(45), 12 (2014)
[8] R. Smolanczuk et al., PRC 52, 1871 (1995)

Decay of $^{201-203}$Ra*

Z. Kalaninová†[1], *S. Antalic*[1], *A.N. Andreyev*[2,3], *F.P. Heßberger*[4,5], *D. Ackermann*[4], *B. Andel*[1], *L. Bianco*[6], *S. Hofmann*[4], *M. Huyse*[7], *B. Kindler*[4], *B. Lommel*[4], *R. Mann*[4], *R.D. Page*[6], *P. Sapple*[6], *J. Thomson*[6], *P. Van Duppen*[7], *and M. Venhart*[8,1]

[1]Comenius University, Bratislava, Slovakia; [2]University of York, York, UK; [3]ASRC, JAEA, Ibaraki, Japan; [4]GSI, Darmstadt, Germany; [5]Helmholtz Institut Mainz, Mainz, Germany; [6]University of Liverpool, Liverpool, UK; [7]KU Leuven, Leuven, Belgium; [8]Institute of Physics, SAS, Bratislava, Slovakia

For the most neutron-deficient radium isotopes not much experimental information about decay properties is available up to now and in some cases reported data are not consistent. This was the motivation for our study of $^{201-203}$Ra.

The investigated isotopes were produced in fusion-evaporation reactions ^{56}Fe + ^{147,149}Sm at the velocity filter SHIP at GSI in Darmstadt. After separation from other particles, evaporation residues (ERs) were implanted into a 16-strip position sensitive silicon detector (PSSD) registering their α decays. α particles escaping from the PSSD were recorded by a system of six silicon detectors placed in the backward hemisphere covering 80 % of 2 π. Nuclei were identified based on time and position correlations of ER implantations and their subsequent α decays.

Only two decay chains of ^{202}Ra were reported until now, each one in different measurement [1,2]. Both experiments were performed at the RITU separator at JYFL yielding different values for α-decay energies (7860(60) keV [1] and 7740(20) keV [2]) and half-lives ($0.7^{+3.3}_{-0.3}$ ms [1] and 16^{+30}_{-7} ms [2]). In our study we registered 16 correlation chains attributed to the decay of ^{202}Ra. Nuclei were produced in the reaction ^{56}Fe + ^{149}Sm at several beam energies in the range of (244-275) MeV. Measured α-decay energy and half-life were 7722(7) keV and $3.8^{+1.3}_{-0.8}$ ms. The reduced α-decay width (δ^2_α) for this decay was 210^{+70}_{-50} keV calculated using the Rasmussen formula [3] and assuming $\Delta L = 0$. It confirms the trend of increasing δ^2_α at decreasing neutron number for radium isotopes. This is consistent with the trends for neighboring even-even radon and thorium isotopic chains [4].

Prior to our study, only one decay chain attributed to ^{201}Ra was reported at RITU [2]. Based on daughter and granddaughter decay properties it was assumed to originate from the 13/2$^+$ state. In our measurement we registered one ER-α1-α2-α3 correlation chain in the reaction ^{56}Fe + ^{147}Sm at E_{beam} = 249 MeV with parent α-decay energy of 7842(12) keV and a half-life of 8^{+40}_{-4} ms. Properties of the α2 and α3 decays correspond to known decays of the 3/2$^-$ states in ^{197}Rn and ^{193}Po, respectively. Based on the deduced unhindered character of the observed α1 decay we assume that it originates from the 3/2$^-$ state in ^{201}Ra. We localized the 13/2$^+$ state in this isotope at 260(30) keV, which follows the trend of decreasing energies of the 13/2$^+$ levels at decreasing N for radium isotopes (see Fig. 1). A similar trend is also seen in radon isotopes.

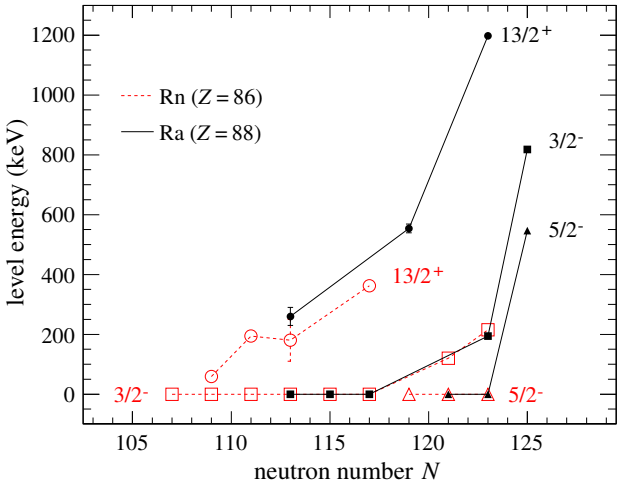

Figure 1: (Color online) Energy level systematics for odd-A radon (dashed lines and open symbols) and radium (solid lines and full symbols) isotopes.

The ^{203}Ra isotope was observed in two studies reporting seven [1] and $\sim$30 decay chains [2] with significantly different decay properties for the 3/2$^-$ state. We detected nine ER-α1-α2 correlation chains in the reaction ^{56}Fe + ^{149}Sm at beam energies from 244 to 275 MeV, which were assigned to ^{203}Ra. Five of them were attributed to the decay of the 3/2$^-$ state and four to the 13/2$^+$ state based on the reference values for parent and daughter decays. However, neither for ^{203}Ra, nor for its α-decay daughters, the order and energy difference between the 3/2$^-$ and 13/2$^+$ states is known. Our values of E_α = 7575(10) keV, $T_{1/2} = 50^{+40}_{-15}$ ms for the 3/2$^-$ state and E_α =7607(8) keV, $T_{1/2} = 37^{+37}_{-12}$ ms for the 13/2$^+$ state agree with values in Ref. [2]. However, the ratio of decays from the 13/2$^+$ and 3/2$^-$ states from our data is 0.8(5), which is in contrast to the previous measurements [1,2], where more decays were observed from the 13/2$^+$ state (with corresponding ratio $\sim$6 [1] and $\sim$3 [2]).

References

[1] M. Leino, *et al.*, *Z. Phys. A* **355**, 157 (1996).

[2] J. Uusitalo, *et al.*, *Phys. Rev. C* **71**, 024306 (2005).

[3] J.O. Rasmussen, *Phys. Rev.* **113**, 1593 (1959).

[4] Z. Kalaninová, *et al.*, *submitted to Phys. Rev. C.*

* Work supported by Slovak Research and Development Agency and Slovak grant agency VEGA.

† Zdenka.Kalaninova@fmph.uniba.sk

 doi:10.15120/GR-2014-1-NUSTAR-SHE-04

Decay of ^{200,201}Fr*

Z. Kalaninová[†1], *S. Antalic*[1], *A.N. Andreyev*[2,3], *F.P. Heßberger*[4,5], *D. Ackermann*[4], *B. Andel*[1], *L. Bianco*[6], *S. Hofmann*[4], *M. Huyse*[7], *B. Kindler*[4], *B. Lommel*[4], *R. Mann*[4], *R.D. Page*[6], *P. Sapple*[6], *J. Thomson*[6], *P. Van Duppen*[7], *and M. Venhart*[8,1]

[1]Comenius University, Bratislava, Slovakia; [2]University of York, York, UK; [3]ASRC, JAEA, Ibaraki, Japan; [4]GSI, Darmstadt, Germany; [5]Helmholtz Institut Mainz, Mainz, Germany; [6]University of Liverpool, Liverpool, UK; [7]KU Leuven, Leuven, Belgium; [8]Institute of Physics, SAS, Bratislava, Slovakia

In the region of neutron-deficient nuclei above lead several interesting nuclear-structure phenomena can be observed, e.g., coexistence of states with different shapes within one nucleus, or β-delayed fission. This motivated us to investigate the neutron-deficient isotopes ^{200,201}Fr.

The studied nuclei were produced at the velocity filter SHIP (GSI, Darmstadt) in fusion-evaporation reactions ^{56}Fe + ^{147,149}Sm at several beam energies from 236 to 275 MeV. Evaporation residues (ERs) were separated from other particles and transported into a focal-plane detector system. ERs were implanted into a 16-strip position-sensitive silicon detector (PSSD) recording also their α decays. Escaping α particles were recorded by a system of six silicon detectors placed upstream the beam covering 80 % of 2π. A germanium clover detector placed closely behind the PSSD registered γ and X-rays.

We measured $E_\alpha = 7470(5)$ keV and $T_{1/2} = 46(4)$ ms for ^{200}Fr confirming known α-decay data for this isotope. For its daughter isotope, ^{196}At, we observed a new weak α line at 6732(8) keV with a relative intensity of 4(2) % besides the main 7045(5)-keV α line. The determined energy of the level in ^{192}Bi populated by the 6732(8)-keV decay is 320(10) keV. Within a 5-μs coincidence time with implanted ERs followed by α decays of ^{200}Fr we observed weak γ lines at 75.5 and 77.1 keV and K_α(Fr) X-rays. They indicate a short-lived γ-decaying state in ^{200}Fr with $T_{1/2} = 0.6^{+0.5}_{-0.2}$ μs. One β-delayed fission (βDF) event attributed to ^{200}Fr was observed. Deduced probability of βDF for the daughter isotope ^{200}Rn is more than 1.4 % .

We identified a short-lived γ-decaying activity with $T_{1/2} = 0.7^{+0.5}_{-0.2}$ μs also in ^{201}Fr based on the registration of γ and K_α X-rays. From the analysis of K-shell internal conversion coefficients (α_K) [1] and estimated single-particle half-lives ($T_{1/2,SP}$) according to Weisskopf [2] we suppose that observed γ and X-rays arise from an internal transition of $M2$ multipolarity. We tentatively assigned the spin and parity of $13/2^+$ to the observed isomeric state in ^{201}Fr. The lower energy limit for this level was determined to be higher than the K-shell atomic-electron binding energy of francium (101.13 keV) because of the detection of K X-rays. The upper energy limit was roughly estimated to be 300 keV from the comparison of experimental and expected α_K and $T_{1/2,SP}$ for $M2$ transitions.

For most of the neutron-deficient francium ($Z = 87$) and astatine ($Z = 85$) isotopes a $9/2^-$ state related to a spherical shape was identified to be a ground state. In astatine isotopes, the $7/2^-$, $1/2^+$, and $13/2^+$ levels, related to oblate shapes, were observed with energies decreasing at decreasing N (see Fig 1). Starting with ^{195}At ($N = 110$), the $1/2^+$ level becomes the ground state in astatine isotopes [3]. The energy interval of the tentative $13/2^+$ level in ^{201}Fr estimated from our data follows the trend of decreasing energies at decreasing N of this level in francium isotopes. A similar trend was also observed for the $1/2^+$ level. In the lightest francium isotopes we can expect a change of spin of the ground state, but it was not definitely identified so far. All of the $13/2^+$, $7/2^-$, $1/2^+$ levels were reported to be detected in ^{199}Fr within 300 keV [4]. However, in recent measurements at SHIP we only observed the $7/2^-$ level, and tentatively also the $1/2^+$ level [5]. Higher statistics are needed to disentangle the level structure in this isotope.

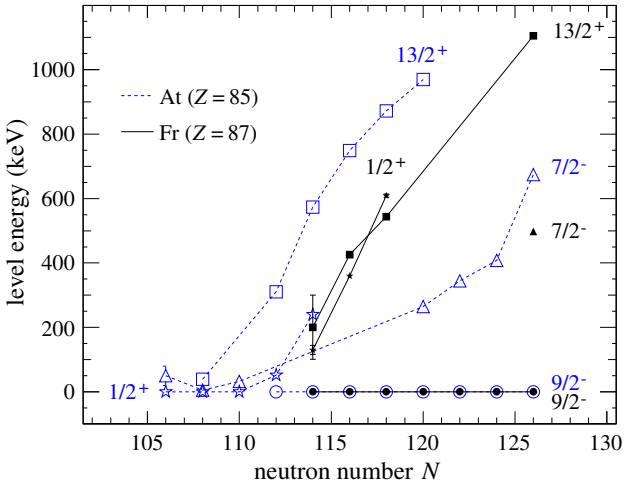

Figure 1: (Color online) Energy level systematics for odd-A astatine (dashed lines and open symbols) and francium (solid lines and full symbols) isotopes.

References

[1] T. Kibédi, *et al.*, *Nucl. Instr. and Meth. A* **589**, 202 (2008).

[2] V.F. Weisskopf, *Phys. Rev.* **83**, 1073 (1951).

[3] H. Kettunen, *et al.*, *Eur. Phys. J. A* **16**, 457 (2003).

[4] J. Uusitalo, *et al.*, *Phys. Rev. C* **87**, 064304 (2013).

[5] Z. Kalaninová, *et al.*, *Phys. Rev. C* **87**, 044335 (2013).

* Work supported by Slovak Research and Development Agency and Slovak grant agency VEGA.

† Zdenka.Kalaninova@fmph.uniba.sk

Compound nucleus spin distribution for ^{64}Ni + ^{100}Mo *

V. Singh[1,2], D. Ackermann[1], S. Antalic[3], M. Axiotis †[4], D. Bazzacco[5], L. Corradi[4], G. De. Angelis[4], E. Farnea[5], A. Gadea‡[4], F.P. Heßberger[1], M.G. Itkis[6], G.N. Kniajeva[6], E.M. Kozulin[6], T. Martinez §[4], N. Marginean¶[4], R. Menegazzo[5], G. Montagnoli[5], D.R. Napoli[4], Yu. Ts. Oganessian[6], M. Ruan[7], R.N. Sagaidak[6], F. Scarlassara[5], A.M. Stefanini[4], S. Szilner[8], and C. Ur‖[4]

[1]GSI Helmholtzzentrum für Schwerionenforschung GmbH, Darmstadt, Germany; [2]Department of Physics, Panjab University, Chandigarh, India; [3]Comenius University in Bratislava, Slovakia; [4]INFN, Laboratori Nazionali di Legnaro, Legnaro (PD); [5]Dipartimento di Fisica and INFN Padova.; [6]JINR Flerov Laboratory of Nuclear Reaction, Dubna, Russia; [7]Institute of Atomic Energy, Beijing, China; [8]RBI, Zagreb, Croatia

In the last decades, a number of measurements have been performed to understand the fusion reaction dynamics and to obtain an experimental representation of the barrier distribution D_b using precisely measured fusion excitation functions [1]. As an alternative approach to this the employment of the compound nucleus (CN) spin distribution σ_ℓ (SD) was proposed [2]:

$$D_b = \frac{dT_{E'}}{dE'} \tag{1}$$

with

$$E' = E - \frac{\ell(\ell+1)}{2\mu R_b^2} \tag{2}$$

and

$$\sigma_\ell(E) = T_\ell(E,\ell)(2\ell+1)\pi\lambda^2, \tag{3}$$

where T is the transmission as a function of the spin ℓ or the energy E' as defined above, μ the reduced mass of the colliding system, λ the de Broglie wave length and R_b the barrier radius.

To explore aspects like the fusion-fission competition, the role of deformation in fusion of a heavy system and the possible effect of the Z=82 shell closure on enhancement of evaporation residue (ER) cross-sections, a series of experiments has been performed to measure the SD for ^{64}Ni, ^{34}S and ^{48}Ca induced reactions using the γ detector array GASP at the Laboratori Nazionali di Legnaro, Legnaro (PD), Italy. The GASP array consisted of 80 BGO detectors (total efficiency $\approx$ 80 % as a multiplicity filter) and 40 HPGe detectors (used for identification of ERs) In the present work, we are reporting on the results for the reaction ^{64}Ni + ^{100}Mo at beam energies ranging from 230 MeV to 260 MeV. The experimentally recorded data is used to obtain the fold distribution of each ER channel by gating the fold spectrum with respective characteristic γ transitions. In an earlier measurement at the Argonne/Notre Dame Crystalball integral ER data had been obtained with some limitations in accuracy for spin and cross section assignment [4]. These fold distributions are converted into multiplicity distributions using the response function of the detector array. Finally the multiplicity distributions are converted to σ_ℓ distributions using eq. 2 in Ref. [3]. The comparison of the SDs at the three measured beam energies is shown in Fig. 1. It is observed that the high spin tail of the SD becomes steeper and steeper with increasing beam energy. With increasing beam energy fission starts competing with ER production and the partial wave with higher spin end up as fission which results in cutting of the SD at the high spin end. The extraction of D_b from those spin distributions is presently being pursued and will be reported soon.

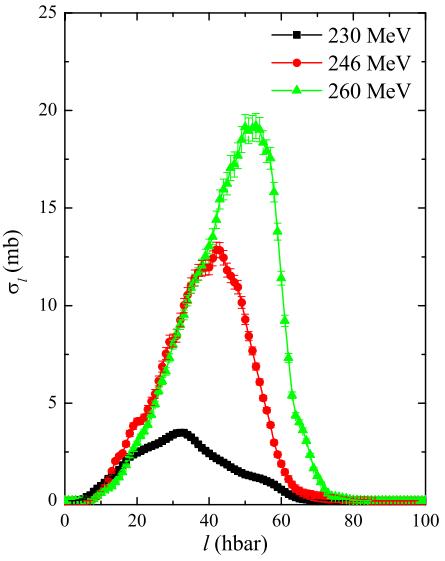

Figure 1: A comparison of the spin distribution at different beam energies.

References

[1] M. Dasgupta *et al.*, Ann. Rev. Nucl. Part. Sci. **48**, 401 (1998).

[2] D. Ackermann *et al.*, Eur. Phys. J. A **20**, 151 (2004); D. Ackermann, Acta Physica Polonica B **26**, 517 (1995).

[3] A.M. Stefanini *et al.*, Nucl. Phys. A **548**, 453 (1992).

[4] D. Ackermann *et al.*, Nucl. Phys. **A** 630, 442c (1998).

* Work supported by DFG Grant to Support Initiation of an International Collaboration

† now INP Demokritos, Athens, Greece

‡ now IFIC, Valencia, Spain

§ now CIEMAT, Madrid, Spain

¶ now IFA, Bucharest, Romania

‖ now IFA, Bucharest, Romania

 doi:10.15120/GR-2014-1-NUSTAR-SHE-06

Diamond dE-E-ToF-telescope for heavy ion reactions at the Coulomb barrier*

O. Beliuskina†[1], *C. Heinz*[2], *S. Heinz*[1], *C. Kozhuharov*[1], *M. Pomorski*[3], *and M. Träger*[1]
[1]GSI, Darmstadt, Germany; [2]JLU, Giessen, Germany; [3]CEA-LIST, Saclay, France

Target of our interest is the study of heavy ion reactions, such as multinucleon transfer, quasi-fission and/or fusion-fission, at energies close to the Coulomb barrier as well as their possible application for the synthesis of new isotopes, especially in the high-Z neutron-rich region.

The conventional time-of-flight technique, combined with the dE-E method, allows us (in general) to identify the mass and the charge of the reaction products and to study the reaction kinematics. Nonetheless, studying heavy particles at low energies needs a special approach. There are some limitations: pulse hight defect, radiation hardness, etc. Moreover, heavy ions at low energy have very short ranges, which means that we have to find a very thin detector capable of measuring energy loss and time simultaneously.

Due to their unique properties (a good energy resolution comparable to silicon detectors, e.g. ΔE=20keV for alphas; time resolution on the order of few ten ps due to very high electron and hole mobilities, high count rate up to 10^9 due to very short rise and fall times (∼20ps) and high radiation hardness[1]) diamonds are good candidates for this application. Very recently, Pomorski et al. succeeded in fabricating ultra-thin diamond membranes with only few micrometers thickness that are able to measure energy loss and produce simultaneously time signals with excellent resolution[2].

Based on these findings we initiated a program to investigate single crystal (sc) diamond detectors for identification of low-energy heavy ion reaction products. For this application we realized the very first dE-E-ToF telescope [3] which consists of 2 sc diamond detectors: "dE/Start" and "E/Stop". First measurements were carried out with a mixed nuclide α-source. The diamond "dE/Start"-detector had a thickness of ∼4 μm and the diamond "E/Stop"-detector ∼50 μm. The distance between the detectors was 14 mm. In Fig. 1a-1c the obtained result is shown. Fig. 1a shows the two-dimensional dE versus residual energy E_r spectrum measured with the mixed nuclide α-source. There are three well separated ridges which correspond to the three α-lines. Fig 1b shows the one-dimensional energy spectrum where line 1 is the energy loss in the membrane detector, line 2 is the residual energy measured in the stop detector and line 3 is the sum of dE and E_r for each event. Fig. 1c shows the time of flight spectrum.

Furthermore, we applied the diamond dE-E-ToF telescope to study reaction products from collisions of

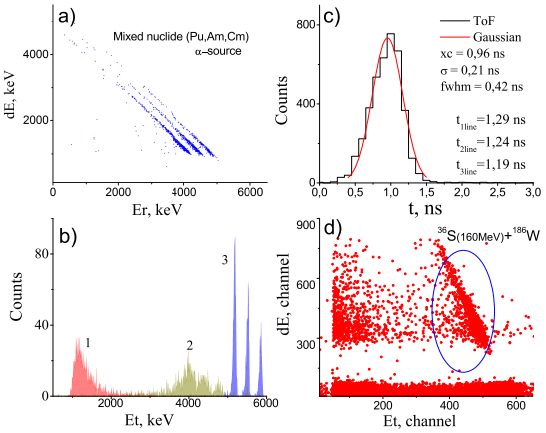

Figure 1: a) dE versus E_r spectrum of α-particles measured with diamond detectors b) Energy spectrum of α particles c) Time of flight spectrum of α-particles d) dE versus E_r spectrum measured in ^{36}S+^{186}W reactions at 160 MeV.

^{36}S+^{186}W at a beam energy of 160 MeV. The experiment was carried out at JINR Dubna where we installed the diamond dE-E-ToF telescope together with the CORSET-setup [4] which will be subject of a different report. Figure 1d shows the two-dimensional dE versus E spectrum of reaction products from S+W measured with the diamond detectors. The most intensive ridge corresponds to elastically scattered sulfur which passes through the membrane and loses about 20 MeV. The intensity of the elastically scattered W is 150 times lower than of S at the chosen detection angle of 20 degrees. Therefore, the W line is not visible in the spectrum.

Our first results are very encouraging and show that we are on the right track by utilizing ultra-thin sc diamond detectors as "dE/Start" combined with sc diamond stop counters for the A and Z identification of reaction products at the Coulomb barrier. Further studies are anticipated aiming at improved time and energy resolutions, radiation hardness, pulse hight defects, etc.

References

[1] E. Berdermann et al., Proc. of the XXXVI Intern. Winter Meeting on Nucl. Physics, Bormio 1998

[2] M. Pomorski et al., Applied physics letters 103, 112106 (2013)

[3] O. Beliuskina, 2nd ADAMAS Workshop, GSI, Darmstadt December, 2013, http://www-adamas.gsi.de

[4] E. M. Kozulin et al., Instruments and Experimental Techniques 51, 44 (2008)

* Work supported by FAIR@GSI PSP code:500457
† o.beliuskina@gsi.de

Electronic Structure, Properties and Volatility of Chlorides and Oxychlorides of Group-4 Elements Zr, Hf, and Element 104, Rf

V. Pershina[1], *A. Borschevsky*[2], *and M. Iliaš*[3]

[1]GSI, Darmstadt, Germany; [2]HIM, Mainz, Germany; [3]Department of Chemistry, Faculty of Natural Sciences, Matej Bel University, Tajovského 40, SK-974 00 Banská Bystrica, Slovakia

Volatility of halides, oxyhalides and oxides of elements at the beginning of the 6d-series, i.e., of Rf through Hs has been studied using gas-phase separation techniques [1]. While the understanding of nature of molecule-surface interactions has been gained in group 6 through 8, such an understanding in group 4 and 5 has never been achieved. Neither have the experimentally observed trends in volatility of the halides, Zr $<$ Hf $>$ Rf and Nb $<$ Ta $>$ Db, been explained.

Recently, we have studied volatility of the group-5 bromides, MBr_5 (M = Nb, Ta, and Db), on the basis of calculated molecular properties and a model of dispersion interaction [2]. We have shown that the properties of these compounds change smoothly in the group, so that the volatility should also change smoothly. In this work, we undertake a similar study for the group-4 chlorides. With this aim in view, we have calculated the electronic structures and properties of MCl_4 (M = Zr, Hf, and Rf).

The calculations were performed with the use of the 2-component relativistic X2C DFT method implemented in the DIRAC12 program package [3]. The uncontracted triple-zeta relativistic basis sets of Dyall were used [4]. The obtained results, for the B88/P86 exchange-correlation potential (Table 1), show an increase in the bond lengths and a decrease in the ionizations potentials in the group, though the polarizabilities show a "zig-zag" behaviour. The latter are much reduced by relativity, with the effect increasing with Z. Using these properties and a model of dispersion interaction [5], adsorption enthalpies, $-\Delta H_{\rm ads}$, of the chlorides on a quartz surface were determined (Table 1).

Table 1: Equilibrium bond lengths, R_e (in Å), dissociation energies, D_e (in eV, from Ref. [6]), ionization potentials, IP (in eV), polarizabilities, α (in a.u.), and adsorption enthalpies, $\Delta H_{\rm ads}$ (in kJ/mol), of MCl_4 (M = Zr, Hf, and Rf) on quartz

	R_e	D_e	IP	α	$\Delta H_{\rm ads}$
$ZrCl_4$	2.336	20.34	11.00	103.6	106.5
$HfCl_4$	2.316	20.80	11.00	99.3	103.0
$RfCl_4$	2.370	19.40	10.96	101.2	102.7

The obtained $-\Delta H_{\rm ads}$ are indicative of the following trend in the adsorption strength: Zr $>$ Hf $>$ Rf. Using a correlation of $-\Delta H_{\rm ads}$ with the sublimation enthalpies, $\Delta H_{\rm sub}$ of 104.2 kJ/mol was predicted for $RfCl_4$. Thus, according to the calculations, $RfCl_4$ should be the most volatile compound in its group, in agreement with previous predictions [7]. The obtained trend is, however, in contradiction with the experimental observations [1].

Table 2: Equilibrium bond lengths, R_e (in Å), dissociation energies, D_e (in eV), ionization potentials, IP (in eV), and dipole moments, μ (in D), of $MOCl_2$ (M = Zr, Hf, and Rf)

	R_e(M-Cl)	R_e(M=O)	D_e	IP	μ
$ZrOCl_2$	2.386	1.741	21.76	10.76	3.67
$HfOCl_2$	2.352	1.753	21.01	10.63	4.33
$RfOCl_2$	2.385	1.822	19.40	10.35	5.20

To check the possible (at the presence of oxygen in the chromatography column) formation of the oxychlorides, as well as their volatility, we have also performed the electronic structure calculations for $MOCl_2$ (M = Zr, Hf, and Rf). The obtained total energy differences between $MOCl_2$ and MCl_4 are indicative of the following trend in the oxychloride formation: Zr $>$ Hf $>$ Rf. This means that the assumed earlier preference of Hf to form the oxychloride should not take place. The other properties of interest are summarized in Table 2. The $MOCl_2$ are shown to be stable as a bent structure, though the difference in the total energy with respect to the flat one is very small. The Rf compound should be less stable than those of Zr and Hf, similarly to MCl_4. The central atom - ligand separation increases from Hf to Rf, which also leads to an increase in the dipole moments. Such an increase in μ should result in a decrease in the volatility of $MOCl_2$ with Z as adsorption on a quartz surface due an increase in the dipole moment - surface charge interactions. Thus, volatility of the oxychlorides should change as Zr $<$ Hf $<$ Rf. This trend is, however, also in disagreement with the experimental observations [1]. Thus, the experimentally determined reversed trend in group 4 cannot find its theoretical explanation; neither can the one in group 5 be interpreted.

References

[1] A. Türler and V. Pershina, Chem. Rev. **113**, 1237 (2013)

[2] V. Pershina and J. Anton, J. Chem. Phys. **136**, 034308 (2012)

[3] DIRAC12 program package (http://diracprogram.org/)

[4] K. G. Dyall, Theor. Chem. Acc. **129**, 603 (2011)

[5] V. Pershina and T. Bastug, Chem. Phys. **311**, 139 (2005)

[6] J. Anton *et al.*, Chem. Phys. Lett. **380**, 95 (2003)

[7] V. Pershina and B. Fricke, In: Heavy Elements and Related New Phenomena, W. Greiner and R. K. Gupta, Eds., World Scientific, Singapore, 1999, Vol. 1, p. 194.

 doi:10.15120/GR-2014-1-NUSTAR-SHE-08

Relativistic coupled cluster study of the MAu and M_2 dimers of Hg, Cn, and Fl

A. Borschevsky[1]*, V. Pershina*[2]*, E. Eliav*[3]*, and U. Kaldor*[3]
[1]HIM, Mainz, Germany; [2]GSI, Darmstadt, Germany; [3]Tel Aviv University, Tel Aviv, Israel

The electronic structure of Cn (Z=112) and Fl (Z=114) experiences strong relativistic effects due to the relativistic stabilization and contraction of their valence orbitals, the $7s$ orbital in case of Cn, and the $7p_{1/2}$ orbital in case of Fl. Thus, their molecular and chemical properties are expected to be determined by relativity.

These two elements are the heaviest atoms studied in chemical experiments. Their relative inertness makes them good candidates for studies of volatility through their adsorption on metal surfaces (such as gold) using the gas-phase thermochromatography technique [1, 2]. By performing calculations of the binding energy of the MAu dimers, the trends in the adsorption enthalpies of the atoms on a gold surface, $-\Delta H^{\rm Au}_{\rm ads}({\rm M})$, can be estimated. Bonding of an element in the solid state in the first approximation can be described by the bonding in its M_2 dimer. Thus, in order to obtain a theoretical insight into the trends in the binding of Hg, Cn, and Fl to a gold surface, and their binding in a solid, *ab initio* study of the molecular properties of their MAu and M_2 dimers was performed.

The calculations were carried out within the infinite-order two-component relativistic Hamiltonian obtained after the Barysz-Sadlej-Snijders (BSS) transformation of the Dirac Hamiltonian in a finite basis set [3]. This method treats scalar and spin-orbit relativistic effects simultaneously, and for valence molecular properties achieves similar accuracy to that of the 4-component Dirac Hamiltonian, while significantly reducing the computational effort. Electron correlation was treated in the framework of the single reference coupled cluster approach with single, double, and perturbative triple excitations (CCSD(T)). Faegri's dual family basis sets [4] were used; the basis sets were extended to convergence of the calculated molecular properties. All the calculations were performed using the DIRAC08 computational program package [5].

Table I contains the calculated bond lengths, R_e, and dissociation energies, D_e, of the MAu and M_2 molecules. Hg_2 is the only system for which experimental parameters are available [6]. The excellent agreement of the calculated binding energy with the experiment in case of Hg_2 lends credence to our predictions for the rest of the systems.

The calculated trend in the bond length of the MAu molecules is R_e(FlAu)>R_e(CnAu)>R_e(HgAu). The increase in R_e from HgAu to CnAu corresponds to the weakening of the bond in CnAu, and the R_e of FlAu is larger than that of CnAu due to the participation of the more diffuse $7p_{1/2}$ and $7p_{3/2}$ orbitals of Fl in the bond [7]. The present calculations predict the HgAu molecule to be the most stable of the three, followed by FlAu, and CnAu as the least stable. Bonding in CnAu is weaker than in HgAu due to the strong relativistic stabilization of the $7s$ orbital in Cn compared to the $6s$ in Hg. FlAu should be stronger bound than CnAu due to the $7p_{1/2}$ orbital in Fl being more accessible than the $7s$ of Cn for the bonding with the $6s$ orbital of gold [7]. Assuming that the trends in the binding energies of the gold containing diatomic molecules are a good indication of the trends in the adsorption enthalpies of the atoms on a gold surface, according to the current calculations Fl should be stronger adsorbed on gold than Cn.

Table 1: Equilibrium bond lengths, R_e (in Å), and dissociation energies, D_e (in eV), of the MAu and M_2 molecules. The values in parenthesis are experimental for Hg_2 [6].

	HgAu	CnAu	FlAu
R_e	2.640	2.720	2.791
D_e	0.563	0.368	0.446
	Hg_2	Cn_2	Fl_2
R_e	3.744 (3.69)	3.461	3.547
D_e	0.050 (0.046)	0.084	0.117

Comparing the results for the three M_2 dimers, we observe that Hg_2 has the longest and Cn_2 the shortest bond. The trend in the dissociation energy is D_e (Fl_2)>D_e(Cn_2)>D_e(Hg_2). Cn_2 and Hg_2 dimers behave as van der Waals systems; thus Cn_2 has a higher dissociation energy of the two, due to the strong relativistic contraction of the $7s$ orbital, which causes a decrease of $R_{\rm vdW}$(Cn) and a subsequent increase in the binding energy of the dimer. Group-14 elements, including Fl, behave like chemically bound systems, where D_e decreases with Z due to the spin-orbit splitting and the relativistic stabilization of the $np_{1/2}$ orbital. Thus, Fl_2 is the least bound dimer in group 14 [7]; however, due to the different type of interaction, it is stronger bound than both Hg_2 and Cn_2.

References

[1] R. Eichler *et al.*, Nature **447**, 72 (2007)

[2] A. Yakushev *et al.*, Inorg. Chem. **53**, 1624 (2014)

[3] M. Iliaš and T. Saue, J. Chem. Phys. **126**, 064102 (2007)

[4] K. Faegri, Theor. Chim. Acta **105**, 252 (2001)

[5] DIRAC08 program package (http://diracprogram.org/)

[6] J. Koperski, J.B. Atkinson, and L. Krause, J. Mol.Spectrosc. **184**, 300 (1997); Can. J. Phys. **72**, 1070 (1994)

[7] V. Pershina *et al.*, J. Chem. Phys. **131**, 084713 (2009)

 doi:10.15120/GR-2014-1-NUSTAR-SHE-09

Measurement of the Dipole Polarizability of ^{68}Ni*

D. M. Rossi[1,2,3], P. Adrich[2], F. Aksouh[4], H. Alvarez-Pol[5], T. Aumann[2,6], J. Benlliure[5], M. Böhmer[7], K. Boretzky[2], E. Casarejos[8], M. Chartier[9], A. Chatillon[10], D. Cortina-Gil[5], U. Datta Pramanik[11], H. Emling[2], O. Ershova[12], B. Fernandez-Dominguez[5,9], H. Geissel[2], M. Gorska[2], M. Heil[2], H. T. Johansson[13], A. Junghans[14], A. Kelic-Heil[2], O. Kiselev[2,3], A. Klimkiewicz[2,15], J. V. Kratz[3], R. Krücken[7], N. Kurz[2], M. Labiche[16,17], T. Le Bleis[2,7], R. Lemmon[17], Yu. A. Litvinov[2], K. Mahata[2,18], P. Maierbeck[7], A. Movsesyan[6], T. Nilsson[13], C. Nociforo[2], R. Palit[19], S. Paschalis[6,9], R. Plag[2,12], R. Reifarth[12], D. Savran[20], H. Scheit[6], H. Simon[2], K. Sümmerer[2], A. Wagner[14], W. Waluś[15], H. Weick[2], and M. Winkler[2]

[1]NSCL/MSU, USA; [2]GSI Darmstadt, Germany; [3]University of Mainz, Germany; [4]King Saud University, Saudi Arabia; [5]University of Santiago de Compostela, Spain; [6]Technische Universität Darmstadt, Germany; [7]Technische Universität München, Germany; [8]University of Vigo, Spain; [9]University of Liverpool, United Kingdom; [10]CEA Bruyères-le-Châtel, France; [11]SINP Kolkata, India; [12]Goethe University Frankfurt, Germany; [13]Chalmers University of Technology, Göteborg, Sweden; [14]Helmholtz-Zentrum Dresden-Rossendorf, Germany; [15]Jagiellonian University of Krakow, Poland; [16]University of the West of Scotland, Paisley, United Kingdom; [17]STFC Daresbury Laboratory, United Kingdom; [18]BARC Mumbai, India; [19]TIFR Mumbai, India; [20]Extreme Matter Institute/GSI Darmstadt, Germany

The Equation of State (EOS) of nuclear matter is at the center of many current research axes in nuclear science, ranging from nuclear structure considerations, over heavy-ion collisions to the physics of neutron stars. When dealing with radioactive nuclei with a large proton-neutron imbalance, one component of the nuclear EOS is of particular importance: the symmetry energy. Especially its density dependence is of interest, since this parameter has been shown to correlate strongly with nuclear properties such as the neutron-skin thickness or the amount of low-lying electric dipole (E1) strength [1]. Previously, measurements of low-lying E1 strength have been used to determine the parameters of the symmetry energy [2]. It has, however, been shown that the measurement of the dipole polarizability α_D is a more robust and less model-dependent observable to extract this information [3].

In an experiment performed at the R^{3}B-LAND setup at GSI, Coulomb excitation of ^{68}Ni was measured in inverse kinematics. By measuring the invariant mass of the ^{68}Ni(γ^*,n)^{67}Ni and ^{68}Ni(γ^*,2n)^{66}Ni decay channels, the excitation energy distribution of this nucleus was reconstructed in an energy window ranging from its 1n threshold and covering the regions of low-lying E1 strength and of the IVGDR. The latter was quantitatively measured at a centroid energy of $E_m = 17.1(2)$ MeV, with a width of $\Gamma = 6.1(5)$ MeV and exhausing 98(7)% of the energy-weighted sum rule (EWSR) [4]. Low-lying E1 strength described by a Gaussian function was also observed at $E_m = 9.55(17)$ MeV, with a width of $\sigma = 0.51(13)$ MeV and 2.8(5)% of the EWSR. Based on this observed E1 strength, a polarizability of $\alpha_D = 3.40(23)$ fm^3 was measured from the 1n threshold to the upper integration limit of 28.4 MeV. Relativistic RPA calculations using the FSUGold parametrization [5] provided the correlation between the observable α_D and the neutron-skin thickness $\Delta R_{n,p}$ of ^{68}Ni, as shown in Fig. 1. The extrapolation to the measured value of α_D provides a neutron-skin thickness of 0.17(2) fm, which is in good agreement with the value obtained from the measurement of low-lying E1 strength [1]. This new method for the extraction of neutron-skin thicknesses will also be applied to more exotic systems, thus constraining the symmetry energy further.

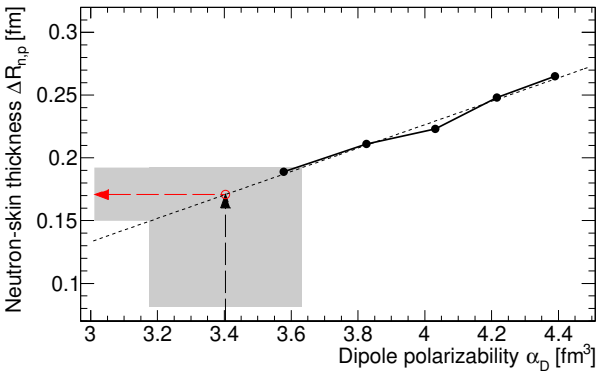

Figure 1: Correlation between the dipole polarizability α_D and the neutron-skin thickness $\Delta R_{n,p}$ of ^{68}Ni [4].

References

[1] A. Carbone, *et al.*, Phys. Rev. C **81**, 041301(R) (2010).

[2] A. Klimkiewicz, *et al.*, Phys. Rev. C **76**, 051603(R) (2007).

[3] P.-G. Reinhard and W. Nazarewicz, Phys. Rev. C **81**, 051303 (2010).

[4] D. M. Rossi, *et al.*, Phys. Rev. Lett. **111**, 242503 (2013).

[5] J. Piekarewicz, Phys. Rev. C **73**, 044325 (2006).

*This work was supported in part by the Helmholtz International Center for FAIR (HIC for FAIR), the Alliance Program of the Helmholtz Association (HA216/EMMI), the GSI-TU Darmstadt cooperation agreement, the Helmholtz-CAS Joint Research Group HCJRG-108, and BMBF Grants No. 06MZ222I, No. 05P12RDFN8, and No. 06MT9156.

Observation of Unbound States in ^{16}Ne / ^{15}Ne via 1n- / 2n-Knockout on ^{17}Ne *

F. Wamers[1,2,3], J. Marganiec[2,3,1], T. Aumann[2,3], L. Chulkov[4,3], M. Heil[3], B. Jonson[5], R. Plag[3,6], H. Simon[3], and the R^{3}B Collaboration

[1]ExtreMe Matter Institute @ GSI; [2]Technische Universität Darmstadt; [3]Nuclear Reactions and Astrophysics @ GSI; [4]NRC Kurchatov Institute, Moscow; [5]Chalmers Tekniska Högskola, Göteborg; [6]Goethe Universität, Frankfurt

In recent years, experiments investigating the driplines have unearthed rich evidence on the peculiarities of the nuclear force, in particular those connected to weak binding and large proton-neutron asymmetry. While for very neutron-rich systems, e.g., various manifestations for 1n and 2n halo systems are found, the existence of the dripline is known only up to $Z = 8$. Quite reversed due to the additional presence of the Coulomb barrier, the proton dripline is sharp and known up to $Z = 91$, whereas halo formation is suppressed and just a few case exist. In the recent past we have investigated proton-knockout reactions studying the borromean 2p-halo nucleus ^{17}Ne [1, 2], and here we have used the dataset from the same experiment as a stepping stone to reach beyond the proton dripline and explore yet unknown regions of the nuclear landscape.

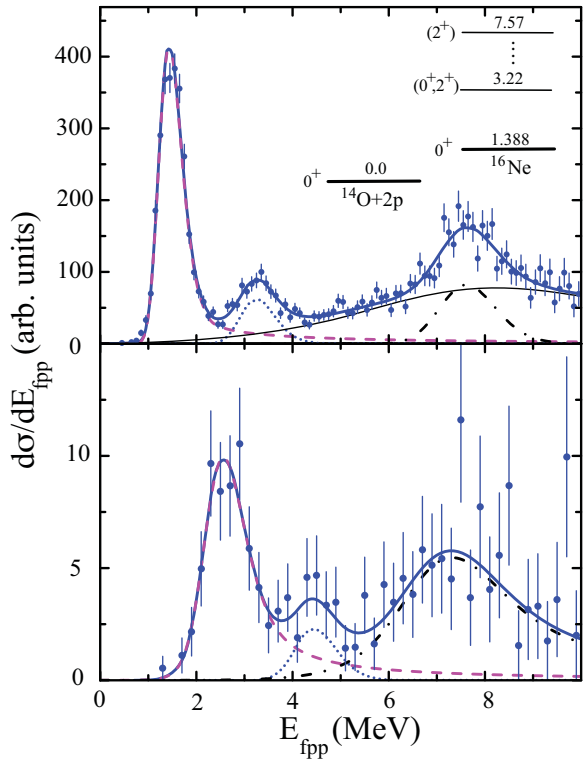

Fig. 1: Relative-energy (E_{fpp}) of ^{16}Ne (top) and ^{15}Ne (bottom), after 1n-/2n-knockout from ^{17}Ne projectiles.

* Work supported by the Spanish research agency CICYT under project FPA2009-07387,by the Helmholtz Alliance EMMI, by HIC for FAIR, by the GSI-TU Darmstadt cooperation agreement, and by the BMBF under contract number 05P12RDFN8. (B. J.) is a Helmholtz International Fellow.

This report presents data of 1n- and 2n- knockout reactions on ^{17}Ne projectiles in light targets (C, CH_2), populating states in the unbound nuclei ^{16}Ne and the yet unobserved ^{15}Ne. In a simple picture, the respective neutrons were removed from the ^{17}Ne core, ^{15}O, thus creating ^{14,13}O fragments coupled to the two remaining s^2/d^2 protons, all travelling under forward angles and being detected in coincidence. The data analysis procedure, via 4-momentum reconstruction and invariant-mass technique, is equivalent to the description in [1]. The excitation spectra, in terms of f-2p relative-energy spectra, of the ^{16}Ne and ^{15}Ne systems are shown in Fig. 1. The shown data (full dots with errorbars) have been corrected for experimental acceptance, and the peaks have been fitted by Coulomb-Breit-Wigner functions (dashed, dotted lines) folded with the experimental resolution, and in the case of ^{16}Ne in addition by a non-resonant background (full line). The experimental acceptance and the E_{rel} calibration and resolution have been obtained from R3BROOT-based simulations [2] in combination with the width and position of the known $5/2^-$ state in the ^{15}O+2p continuum of ^{17}Ne as a reference.

For ^{16}Ne (^{14}O+2p) we have extracted the positions and widths of the ground state and the first two excited states as E_r(g.s.) = 1.388(15) MeV, Γ_r(g.s.) = 0.082(15) MeV; E_r(1.x.) = 3.22(5) MeV, Γ_r(1.x.) $\leq$ 0.05 MeV; E_r(2.x.) = 7.57(6) MeV, Γ_r(2.x.) $\leq$ 0.1 MeV. These values are in good agreement with previous publications on ^{16}Ne, e.g. [4], and confirm the validity of our technique and calibrations.

For the first time, the unbound isotope ^{15}Ne has been observed, as coincidences between ^{13}O and two beam-like protons (see Fig. 1(bottom)). The same type of analysis as for the ^{16}Ne case has been performed for the ^{15}Ne (E_{fpp}) spectrum. We identified the ground state and the first excited state with parameters of E_r(g.s.) = 2.522(66) MeV, Γ_r(g.s) = 0.59(23) MeV; E_r(1.x.) = 4.42(4) MeV, Γ_r(1.x.) $\leq$ 0.1 MeV. The observed position of the ^{15}Ne ground state at S_{2p} = -2.522(66)MeV is in good agreement to a recent model prediction [5].

References

[1] F. Wamers and the R^{3}B collab., GSI Scientific Report 2010

[2] F. Wamers and the R^{3}B collab., GSI Scientific Report 2011

[3] F. Wamers and the R^{3}B collab., GSI Scientific Report 2012

[4] I. Mukha et al., Phys. Rev. C 79, 061301(R) (2009)

[5] H.T. Fortune, Phys. Lett. B 718, 1342 (2013)

 doi:10.15120/GR-2014-1-NUSTAR-KR-02

Study of the ^{14}Be Continuum *

Yu. Aksyutina[1,2], *T. Aumann*[2,3], *L. Chulkov*[3,4], *B. Jonson*[5], *H. Simon*[3], *and the R ^{3}B Collaboration*

[1]Institut für Energie- und Klimaforschung, Jülich; [2]Nuclear Reactions and Astrophysics @ GSI; [3]Technische Universität Darmstadt; [4]NRC Kurchatov Institute, Moscow; [5]Chalmers Tekniska Högskola, Göteborg

The nuclide ^{14}Be has been studied in a radioactive-beam experiment performed at ALADIN-LAND setup. There was till now only scarce information about its detailed structure.

In this report we present new experimental data on inelastic scattering of an energetic (304 MeV/u) ^{14}Be beam in a liquid hydrogen target [1]. The details about the data reduction and treatment are given in Refs. [2]. The

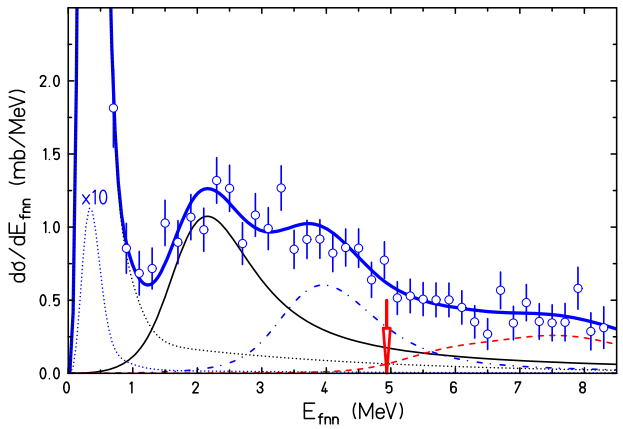

Fig. 1: The distribution of internal energy in the ^{12}Be+n+n system ($d\sigma/dE_{fnn}$). Curves show the decomposition of the spectrum into Breit-Wigner shaped resonances. The arrow indicates the four-neutron decay threshold.

distribution of internal energy in the ^{12}Be+n+n system, $d\sigma/dE_{fnn}$, obtained from the present data is shown in Fig. 1. The spectrum was decomposed into three Breit-Wigner shaped resonances and a contribution from unresolved resonances. The collected statistics made it impossible to perform a least-square fit with all parameters free. By a stepwise analysis this problem could be overcome and the parameters arrived at in the final fit, with χ^2/N=27.9/35, are given in Table 1.

The analysis of distributions on fractional energies, $\epsilon_{nn} = E_{nn}/E_{fnn}$ and $\epsilon_{fn} = E_{fn}/E_{fnn}$, were performed to determine spin and parities on the resonances. The $W(\epsilon_{fn})$ and $W(\epsilon_{nn})$ distributions, derived from events belonging to the energy regions $0.5 < E_{fnn} < 1$ MeV and $2 < E_{fnn} < 3$ MeV, are analyzed with the assumption of a democratic decay. Correlations between the decay products in democratic decays may generally be described as

*Work supported by the Helmholtz International Center for FAIR within the framework of the LOEWE program, by the BMBF (Project No. 05P12RDFN8), by the Helmholtz Alliance EMMI, by Swedish Research Council, and the Spanish Ministry (Grant No. FPA2009-07387).

Table 1: Resonance parameters for excited states in ^{14}Be. The fit results to $\chi^2/N = 27.9/35$.

I^π	E_r MeV	E_{exc} MeV	Γ MeV	σ mb
2_1^+	$0.28^{a,b}$	$1.54(13)^b$	0.025^a	5.07(58)
2_2^+	2.28(9)	3.54(16)	1.5^a	2.57(19)
(3^-)	3.99(14)	5.25(19)	1.0^a	1.35(16)

[a] parameters were fixed
[b] taken from Ref.[3]

superpositions of different partial waves in the binary subsystems. The measured $W(\epsilon_{fn})$ and $W(\epsilon_{nn})$ can contain thus contributions from all possible waves, including cross terms. But at low energy only terms with the lowest possible angular momenta, consistent with selection rules, are needed [4]:

$$W(\epsilon) = \sum_i \frac{\Gamma(3+l_1^i+l_2^i)}{\Gamma(\frac{3}{2}+l_1^i)\Gamma(\frac{3}{2}+l_2^i)} A_i^2 \epsilon^{l_1^i+\frac{1}{2}}(1-\epsilon)^{l_2^i+\frac{1}{2}}.$$

Here $\Gamma(z)$ is the Euler gamma function, l_1 is the angular momentum between two neutrons or between one neutron and the fragment, l_2 is the angular momentum between one neutron or the fragment and the centre-of-mass of the remaining two-body system. A_i is the decay amplitude of a particular configuration i, ($\sum_i A_i^2 = 1$). Different components, A_{02}, A_{20}, A_{11} and A_{22}, were obtained from the fit to $W(\epsilon_{fn})$ and $W(\epsilon_{nn})$ distributions.

The analysis of the energy correlations between decay products shows that the 2_1^+ resonance contains two neutrons mainly in the $(0d_{5/2})^2$ configuration. Also a strict evidence was obtained, that the state at $E_r = 2.28(9)$ MeV is a 2_2^+ state with predominantly $(1s_{1/2}0d_{5/2})$ structure.

Strong similarity exists between the level schemes of N=10 isotones. Thus the first excited state (2_1^+) of ^{14}Be, $E_{exc} = 1.54$ MeV, is a close analogy to the 1.77 MeV state in ^{16}C and to the 1.98 MeV state in ^{18}O. Also excitation energies of the second 2_2^+ states for the members of N=10 isotone chain do not differ much, . The state at $E_r = 3.99(14)$ can be an analog of the 3^- state in ^{18}O and ^{16}C.

References

[1] Yu. Aksyutina *et al.*, Phys.Rev.Lett. **111**, 242501 (2013).
[2] Yu. Aksyutina *et al.*, Phys.Lett. **B 666**, 430 (2008).
[3] T. Sugimoto *et al.*, Phys. Lett. **B 654**, 160 (2007).
[4] L.M. Delves, Nucl. Phys. **20**, 275 (1960).

Coulomb Dissociation of ^{17}Ne*

J. Marganiec[1,2], F. Wamers[2,1,3], T. Aumann[1,3], I. Egorova[5], L. Grigorenko[6,7], M. Heil[3], R. Plag[3,4], and the R^{3}B collaboration

[1]TU Darmstadt, Germany; [2]EMMI, GSI Darmstadt, Germany; [3]GSI Darmstadt, Germany; [4]Goethe-Universität, Frankfurt am Main, Germany; [5]BLTP JINR Dubna, Russia; [6]FLNR JINR Dubna, Russia; [7]RRC KI, Moscow, Russia

Introduction

The ^{17}Ne is a proton-dripline nucleus that causes special interest in nuclear structure and nuclear astrophysics. As a (^{15}O+2p) Borromean 3-body system it represents a promising candidate for a two-proton halo structure [1]. The main uncertainty of the ^{17}Ne ground state is the yet unknown mixture of the d^2 and s^2 configurations of the two protons outside the ^{15}O core. Predictions of the s^2-weight run from 15 to 70% [2, 3, 4, 5, 6, 7, 8]. The solution to this situation is an experimental determination of the s^2/d^2 mixture.

The Coulomb dissociation of ^{17}Ne can provide also an important information about a ^{15}O$(2p,\gamma)^{17}$Ne reaction, which can serve as a bypass of the ^{15}O waiting point in the CNO cycle. At high temperature and density conditions, which occure in X-ray bursts, the CNO cycle and the *rp* process are linked by the α capture reaction on ^{15}O. However, the reaction flow between the CNO cycle and the FeNi-mass region is hampered by the waiting point nuclei like ^{15}O [9]. The two-proton capture reaction can be an alternative way to process the initial CNO material towards heavier nuclei. The ^{15}O$(2p,\gamma)^{17}$Ne cross section is investigated by studying the time-reversed process, using the Coulomb dissociation method.

Experiment and preliminary results

The experiment was performed with the secondary ^{17}Ne ion beam of energy $E = 500$ MeV/nucleon, using the R^{3}B-LAND setup at GSI. To investigate the Coulomb dissociation reaction a Pb target (200 mg/cm^2) was used. All reaction products have been identified and tracked. Their mass and momenta have been determined, and the excitation energy spectrum reconstructed. The required efficiency and acceptance corrections have been estimated. The preliminary differential (Fig. 1) and integral Coulomb dissociation cross sections have been obtained - $\sigma_{tot} = 256 \pm 15\,(stat.) \pm 18\,(syst.)$ mb. The shape of the differential Coulomb dissociation cross section is in agreement with experimental results from Ref. [10] and with the theoretical predictions from Ref. [11]. In the next steps, the photoabsorption and the radiative capture cross sections will be calculated.

By analyzing different types of energy and angular correlations between internal clusters ($[core, p+p]$ or $[core+p, p]$) in Jacobi coordinates, the mixture of the d^2 and s^2 configurations can be obtained [12]. The experimental data is compared to theoretical predictions, provided by Ref. [13], convoluted with simulated experimental response, using the simulation package R3BROOT. The analysis is in progress.

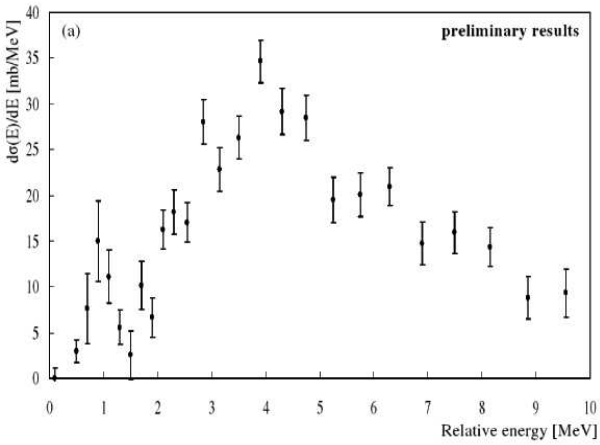

Figure 1: The preliminary differential Coulomb dissociation cross section.

References

[1] R. Kanungo *et al.*, Phys. Lett. B 571 (2003), p. 21

[2] R. Kanungo *et al.*, Eur. Phys. J. A 25 (2005), p. 327

[3] L.V. Grigorenko, I.G. Mukha, M.V. Zhukov, Nucl. Phys. A 713 (2003), p. 372

[4] L.V. Grigorenko, Yu.L. Parfenova, M.V. Zhukov, Phys. Rev. C 71 (2005), p. 051604

[5] W. Geithner *et al.*, Phys. Rev. Lett. 101 (2008), p. 252502

[6] E. Garrido, D.V. Fedorov, A.S. Jensen, Nucl. Phys. A 733 (2004), p. 85

[7] K. Tanaka *et al.*, Phys. Rev. C 82 (2010), p. 044309

[8] T.Oishi, K. Hagino, H. Sagawa Phys. Rev. C 82 (2010), p. 024315

[9] J. Görres *et al.*, Phys. Rev. C 51 (1995), p. 392

[10] M.J. Chromik *et al.*, Phys. Rev. C 66 (2002), p. 024313

[11] L.V. Grigorenko *et al.*, Phys. Lett. B 641 (2006), p. 254

[12] L.V. Grigorenko *et al.*, Phys. Lett. B 677 (2009), p. 30

[13] L.V. Grigorenko, Yu.L. Parfenova, I. Egorova, *private communication.*

* Work supported by NAVI, GSI-TU Darmstadt cooperation, HIC for FAIR, EMMI and BMBF.

 doi:10.15120/GR-2014-1-NUSTAR-KR-04

Coulomb Dissociation of ^{27}P*

J. Marganiec[1,2], S. Beceiro-Novo[3], S. Typel[4], C. Wimmer[5], T. Aumann[1,4], D. Cortina Gil[3], M. Heil[4], K. Sümmerer[4], and the R^{3}B collaboration

[1]TU Darmstadt, Germany; [2]EMMI, GSI Darmstadt, Germany; [3]Universidade de Santiago de Compostela, Santiago de Compostela, Spain; [4]GSI Darmstadt, Germany; [5]Goethe-Universität, Frankfurt am Main, Germany

To model explosive hydrogen burning in nova, X-ray burst or γ-ray burst scenarios, the *rp* process has to be understood in detail. In this process, the light to medium-mass nuclei near the proton-drip line play an important role and their nuclear structures should be well known. The aim of the present experiment is the investigation of the nuclear structure of ^{27}P and the reaction ^{26}Si(p,γ)^{27}P, which can indirectly give rise to the famous 1.8 MeV γ-ray that was observed in the Milky Way galaxy [1, 2]. The radiative-capture reaction on ^{26}Si was studied by the Coulomb dissociation (CD) method. By the detailed balance theorem, the one-proton-removal CD cross section can be converted to the radiative-capture cross section and subsequently to the resonance strength [3].

The experiment was performed at GSI Darmstadt using the R^{3}B-LAND setup. A secondary ^{27}P ion beam, with energy $E = 500$ MeV/nucleon, was produced by fragmentation of a ^{36}Ar primary beam. The incoming ^{27}P beam was identified by means of energy-loss, position, and time-of-flight measurements. In order to investigate the CD reaction the ^{27}P beam was focused onto a secondary ^{nat}Pb target (515 mg/cm^2). To accurately subtract the background and to properly estimate the nuclear contribution, several runs without target and with a ^{12}C target (660 mg/cm^2) were also performed. The reaction products were identified using one Si-microstrip detector placed before a large-gap dipole magnet. After the magnet the heavy fragments were detected with two scintillating-fibre arrays and a two-layer time-of-flight (ToF) wall. For proton identification two drift chambers and a two-layer ToF wall were used.

The outgoing silicon fragment and the proton were tracked and their masses and momenta determined. The excitation-energy spectrum was reconstructed. The preliminary inclusive integral one-proton removal CD cross section up to 5 MeV of relative energy was calculated to be $\sigma_{tot} = 84.7 \pm 6.1$(stat.) mb; the spectrum is shown in Fig. 1.

The CD cross-section spectrum was fitted using four resonances and one direct-capture component. The free parameters for the fit were the heights and locations of the four peaks. The widths of the resonant peaks were fixed to the experimental resolutions, the shape of the direct-capture component was predicted by [4]. The measured relative energies for the first two states ($E_{rel} = 0.27$ and 0.73 MeV) are consistent with the excitation energies of the states obtained previously [5, 6, 7] and the third state

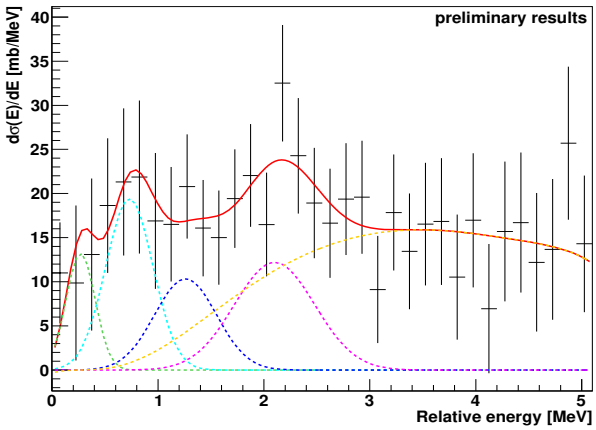

Figure 1: Preliminary inclusive differential one-proton removal CD cross section.

($E_{rel} = 1.26$ MeV) with [5]. Compared to a previous CD study [5], we have carefully subtracted the nuclear contribution, a component not removed in the data of [5]. To explain the structure above the third peak, a fourth resonance corresponding to $E_{rel} = 2.1$ MeV had to be introduced. The nature of this resonance is not clear yet.

The analysis is in progress. As the next step, the CD cross section to the ground state will be determined and converted to the radiative-capture cross section, σ(^{26}Si(p,γ)^{27}P). To study the nuclear structure of ^{27}P, the experimental data are also compared to theoretical predictions by [4] using the simulation package R3BROOT.

References

[1] R. Diehl *et al.*, Astron. Astrophys. Suppl. Ser. 97 (1993), p. 181.

[2] R. Diehl *et al.*, Astron. Astrophys. 298 (1995), p. 445.

[3] G. Baur and C.A. Bertulani, Nuc. Phys. A458 (1986), p. 188.

[4] S. Typel, *private communication*.

[5] Y. Togano *et al.*, Phy. Rev. C 84 (2011), p. 035808.

[6] J.A. Caggiano *et al.*, Phys. Rev. C 64 (2001), p. 025802.

[7] A. Gade *et al.*, Phys. Rev. C 77 (2008), p. 044306.

* Work supported by NAVI, GSI-TU Darmstadt cooperation, HIC for FAIR, EMMI and BMBF.

Fewbody theoretical studies of Quasi Free Scattering reactions

R. Crespo[1,2], A. Deltuva[3], E. Cravo[3,4], the R3B collaboration[1], and the FAIR@GSI division[1]

[1]Departamento de Física, Instituto Superior Técnico, Univ. de Lisboa, Portugal; [2]Centro de Ciências e Tecnologias Nucleares, Univ. de Lisboa, Portugal; [3] Centro de Física Nuclear da Univ. de Lisboa, Portugal; [4]Departamento de Física, Faculdade de Ciências da Univ. de Lisboa, Portugal

Introduction

Proton-induced quasifree scattering nucleon knockout reactions have been recently measured and are planed in future experiments of the R3B collaboration aiming extracting spectroscopy of valence and deeply bound nuclei, and pinning down structure correlation effects. To model and analyze these experiments it is of utmost importance to have a reliable reaction framework in order to extract meaning structure information. Few-body reaction frameworks recently developed are a useful tool to interpret this experiments.

Electron scattering reactions (e,e'p) have been a long-standing tool to obtain information from single-nucleon structure information of nuclei. Systematic studies have shown that for a wide range of magic and near magic nuclei, the single particle occupancies are significantly bellow the values expected from the values predicted by independent-particle shell model calculations (IPSM).

Occupancies have also been extracted using nuclear probes. In particular, single-nucleon (p,2p) and (p,pn) knockout reactions from light target at intermediate have also been used in the past to obtain information on single-particle occupancies.

Proton-induced quasifree scattering nucleon knockout reactions have been performed recently at GSI in inverse kinematics within the R3B program, at around 400 MeV per nucleon. At high incident projectile energies, it is expected the reaction mechanism to be simpler and that one be able to obtain structure information about inner and outer shells. In particular, one aims to obtain information about deviations from single particle occupancies, and correlation effects.

There are several timely issues associated with single nucleon (p,2p) and (p,pn) QFS knockout reactions: (i) A key issue is to disentangle structure correlations from effective dynamical effects. In particular, one needs to get insight to what extent the reduced factors found by comparing the theoretical cross sections with the results extracted from the experimental data can, be traced exclusively to structure correlations or to effective dynamical effects associated with the reaction framework used to interpreted the data. Thus a tight control on the reaction formalism is needed; (ii) Another important aspect is to identify clearly the role of distortion effects to the nucleon-nucleon free scattering; (iii) The recent experiments performed at GSI, have allowed a unique opportunity to perform systematic studies of knockout reactions along the isotope chain at nearly the same incident energy. The study of the behaviour of calculated observables using a well constrained reaction framework, with respect to angular momentum, mass and binding will allow to identify and analyse common features, and identify new physics as experimental deviations to this systematic. (iv)A reliable assessment of possible dynamical core excitation effects and nucleon knockout contributions from inner shells is also mandatory for the interpretation of recent and future experiments at GSI.

Reaction studies

The study of proton-induced quasifree scattering nucleon knockout reactions can be addressed by the three-body Faddeev/AGS [1, 2] reaction formalism, which treats all relevant three-body observables in equal footing [3]. According to this reaction framework, one needs to evaluate the operators $U^{\beta\alpha}$, whose on-shell matrix elements are the transition amplitudes. These operators are obtained by solving the three-body Faddeev/AGS integral equations

$$U^{\beta\alpha} = \bar{\delta}_{\beta\alpha} G_0^{-1} + \sum_\gamma \bar{\delta}_{\beta\gamma} t_\gamma G_0 U^{\gamma\alpha} \ , \qquad (1)$$

with $\alpha, \beta, \gamma = (1, 2, 3)$, ($\beta = 0$ in the final breakup state). In here, $\bar{\delta}_{\beta\alpha} = 1 - \delta_{\beta\alpha}$ and the pair transition operator is

$$t_\gamma = v_\gamma + v_\gamma G_0 t_\gamma \ , \qquad (2)$$

where G_0 is the free resolvent $G_0 = (E + i0 - H_0)^{-1}$, and E is the total energy of the three-particle system in the center of mass (c.m.) frame. For breakup, the solution of the Faddeev/AGS equations can be found by iteration

$$U^{\beta\alpha} = \sum_\gamma \bar{\delta}_{\beta\gamma} t_\gamma \bar{\delta}_{\gamma\alpha} + \sum_\gamma \bar{\delta}_{\beta\gamma} t_\gamma \sum_\xi G_0 \bar{\delta}_{\gamma\xi} t_\xi \bar{\delta}_{\xi\alpha} + \cdots \ .$$

The successive terms of this series can be considered as terms of first order or single scattering, represented diagrammatically in Fig. 1, second order or double scattering, represented diagrammatically in Fig. 2 and so on in the transition operators t_γ.

In order to model and interpret recent proton-induced quasifree scattering nucleon knockout reactions by the R3B collaboration we have evaluated total cross sections and core momentum distributions for several isotopes in inverse kinematics at around 400 MeV making use of the AGS/Faddeev reaction framework:

We have analyzed QFS (p,2p), for the case of valence proton knockout from ^{12}C. In particular, we have studied the role of higher order distortions, valence-nucleon rescattering contributions and the effect of some approximations

 doi:10.15120/GR-2014-1-NUSTAR-KR-06

performed by the standard Distorted Wave Impulse Approximation reaction framework. We found that the multiple scattering expansion of the DWIA might differ from the corresponding Faddeev/AGS result.

We have analyzed the Faddeev/AGS equations in terms of its multiple scattering expansion, and found that at high incident energies that the terms up to second order provide the dominant contribution of the series.

We have analyzed QFS (p,pn), for the case of valence neutron knockout from the halo nuclei ^{11}Be, ^{15}C and along the Oxygen isotope chain ^{17,22,23}O. A detailed analyse of the role of higer terms distortion and its dependence of the binding energy and angular dependence of the valence particle was made.

Most few-body theoretical reaction studies rely on the a model of an inert core and a valence nucleon. However, the internal degrees of freedom might pay an important role as shown in [4], [5]. In order to predict the total cross sections obtained at recent experiments performed at GSI, the effects of dynamical core excitation were estimated. Also the contribution from the knockout of nucleons from the core were evaluated and found to be important.

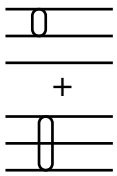

Figure 1: Single scattering diagrams for breakup in the Faddeev scattering framework.

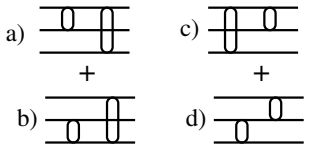

Figure 2: Double scattering diagrams for breakup in the Faddeev scattering framework.

References

[1] L. D. Faddeev, Zh. Eksp. Theor. Fiz. **39**, 1459 (1960) [Sov. Phys. JETP **12**, 1014 (1961)].

[2] E. O. Alt, P. Grassberger, and W. Sandhas, Nucl. Phys. B **2**, 167 (1967).

[3] R. Crespo, A. Deltuva, M. Rodríguez-Gallardo, E. Cravo, and A. C. Fonseca, Phys. Rev. C **79**, 014609 (2009).

[4] A.M. Moro and R. Crespo, Phys. Rev. C **85**, 054613 (2012); R. Crespo, A. Deltuva, A.M. Moro, Phys. Rev. C **83**, 044622 (2011).

[5] A. Deltuva, Phys. Rev. C **88**, 011601 (R) (2013).

Total Fission Cross Sections for Proton-Induced Fission of ^{208}Pb

J.L. Rodríguez-Sánchez[1], J. Benlliure[1], J. Taïeb[2], H. Álvarez-Pol[1], L. Audouin[3], Y. Ayyad[1], G. Bélier[2], G. Boutoux[2], E. Casarejos[4], A. Chatillon[2], D. Cortina-Gil[1], T. Gorbinet[2], A. Heinz[5], A. Kelić-Heil[6], N. Kurz[6], B. Laurent[2], J.-F. Martin[2], C. Paradela[1], E. Pellereau[2], B. Pietras[1], A. Prochazka[6], D. Ramos[1], C. Rodríguez-Tajes[7], D. Rossi[6], H. Simon[6], L. Tassan-Got[3], J. Vargas[1], and B. Voss[6]

[1]University of Santiago de Compostela, Spain; [2]CEA DAM, Arpajon, France; [3]IPN Orsay, Orsay, France; [4]University of Vigo, Spain; [5]University of Chalmers, Sweden; [6]GSI, Darmstadt, Germany; [7]GANIL, Caen, France

Fission reactions may have a significant effect on the performance of the spallation target in accelerator-driven system (ADS), in particular on the production of radioactive and/or chemically hazardous materials. Moreover, different experiments have provided the total fission cross sections for proton on lead reactions with large uncertainties or even with rather discrepant values [1]. In the present work, we report on the first results with a new generation of accurate measurements of total fission cross sections in spallation reaction on ^{208}Pb at different proton energies: 370, 500 and 650A MeV. The measurements were performed in inverse kinematics using a full-acceptance detection system, which measured both fission fragments in time coincidence.

The experiment was performed at the ALADIN-LAND cave at GSI. The number of projectiles was determined from a MUSIC, selecting ^{208}Pb beam which hits a liquid hydrogen target. The fission events were determined by the detection in coincidence of both fission fragments using a double ionization chamber (Twin MUSIC) [2], which also allowed us to reconstruct the reaction vertex based on accurate drift time measurement. In order to obtain the fission cross sections, corrections due to the beam attenuation (less than 4%) and the production of secondary reactions (less than 2.2%) were applied. Losses due to geometrical constraints were also evaluated using Geant4 simulations [3], resulting into a detection efficiency of about 88%.

The results obtained for the total fission cross section (open circles) [4] are shown in Fig.1 compared to previous measurements reported in literature for the reactions p+^{nat}Pb and ^{208}Pb+p. As can be seen in the figure, our data have in general better accuracy than any of the previous ones. Moreover, our measurement at 500 MeV is in perfect agreement with the recent measurement of K.-H. Schmidt [5] using a similar detection setup. However, the cross section obtained by B. Fernández (full square) at the FRS presents a non-negligible deviation with respect to our results and the systematics, which could be due to the limited acceptance of the spectrometer requiring large corrections. Our measurements are also in agreement with the values reported by E. Hagebo (open cross) and R. Brandt (full star) who measured in direct kinematics the reaction p+^{nat}Pb at 600 and 590 MeV, respectively. The present measurements also seem consistent with the measurements between 50 and 200 MeV and with the measurements performed by V.A. Konshin (stars) if one looks at the downward trend and also with the measurement performed by T. Enqvist (full circle) at the FRS if one looks at the upward trend. One can also observe a discrepancy at 1 GeV between the measurements performed by T. Enqvist and M. Gloris (open diamond) but our results are only consistent with Enqvist's measurement. Finally, the measurements performed by A.A. Kotov (full triangles down) also have a deviation, but these were performed in direct kinematics with a proton beam impinging on a ^{nat}Pb target, which could prevent fission fragments to escape from the target reducing the total fission cross section if one does not apply the accurate corrections.

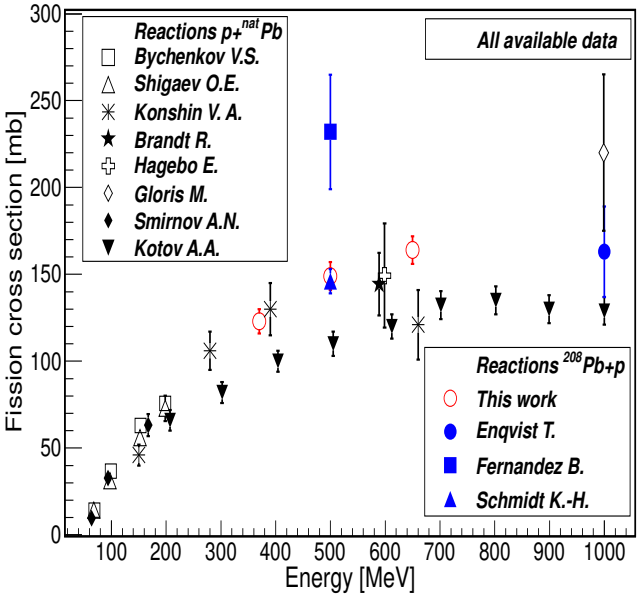

Figure 1: Total fission cross sections for p+^{nat}Pb and ^{208}Pb+p. The red open circles represent our data.

References

[1] A.V. Prokofiev, Nucl. Inst. Meth. A 463 557 (2001).

[2] B. Voss et al., GSI Scientific Report 2011, p.184-186.

[3] J.L. Rodríguez-Sánchez et al., "SOFIARoot: Simulation of the SOFIA/ANDES Setup" in this annual report.

[4] J.L. Rodríguez-Sánchez et al., EPJ Vol. 62 07009 (2013) and references therein.

[5] K.-H. Schmidt et al. Phys. Rev. C 87, 034601 (2013).

 doi:10.15120/GR-2014-1-NUSTAR-KR-07

Identification and Reconstruction of Fission Fragments for Proton-Induced Fission of ^{208}Pb at 500 MeV in Inverse Kinematics

J.L. Rodríguez-Sánchez[1], J. Benlliure[1], J. Taïeb[2], H. Álvarez-Pol[1], L. Audouin[3], Y. Ayyad[1], G. Bélier[2], G. Boutoux[2], E. Casarejos[4], A. Chatillon[2], D. Cortina-Gil[1], T. Gorbinet[2], A. Heinz[5], A. Kelić-Heil[6], N. Kurz[6], B. Laurent[2], J.-F. Martin[2], C. Paradela[1], E. Pellereau[2], B. Pietras[1], A. Prochazka[6], D. Ramos[1], C. Rodríguez-Tajes[7], D. Rossi[6], H. Simon[6], L. Tassan-Got[3], J. Vargas[1], B. Voss[6], and the SOFIA/ANDES collaboration

[1]University of Santiago de Compostela, Spain; [2]CEA DAM, Arpajon, France; [3]IPN Orsay, Orsay, France; [4]University of Vigo, Spain; [5]University of Chalmers, Sweden; [6]GSI, Darmstadt, Germany; [7]GANIL, Caen, France

Spallation reactions have interest for a wide range of applications as neutron sources in material science or nuclear technology (ADS) and also make possible the production of intense Radioactive Nuclear Beams. In astrophysics, these reactions play an important role to interpret the abundances of medium-mass nuclei and actinides in the universe. Moreover, the fission is one of the most complex phenomena that has not a clear theoretical description. In this context, the measurement of the fission fragment distributions in the spallation energy domain makes possible to investigate some fundamental questions connected to the fission dynamics as the dissipation and transient time effects. In this report, we present for the first time the mass (A) and atomic (Z) numbers of both fission fragments measured in inverse kinematics for proton-induced fission of ^{208}Pb at 500 MeV.

The experiment [1] was performed at the ALADIN-LAND cave at GSI. The beam identification was done by an ionization chamber (MUSIC) and its position on the liquid hydrogen target was determined by a time-projection chamber (TPC). Fission events were identified by a high-resolution double ionization chamber (Twin MUSIC) [2], which provided an unambiguous determination of the atomic number of both fission fragments. Moreover, an accurate tracking obtained using Multi-Wire Proportional Counters (MWPC), the Twin MUSIC drift time and the high-resolution Time-of-Flight (ToF) [3] measurement allowed us to determine the fission fragment masses from their bending through the ALADIN dipole.

The reconstruction of the fission fragments was performed with the help of a GEANT4 simulation [4], which reproduce the full detection setup and the dipole magnetic field. In this case, we have used a constant magnetic field around 1.6 T. For the tracking, the atomic number measured by the Twin MUSIC and the polar and azimuthal angles at the entrance of the dipole obtained with the positions measured in the TPC, MWPC and Twin MUSIC are used as an input in the simulation. For each event, we simulate different trajectories covering the expected Bρ range and then we look for the correlation between the simulated Bρ and the horizontal position behind the dipole, which is also checked for the simulated flight path length. Using this method we have found third-order and second-order correlations for the Bρ and flight path length, respectively. These correlations allow to reconstruct the experimental Bρ and the flight path length which, together with the ToF and the Z, give access to the mass number for each fragment.

The reconstruction results are shown in Fig. 1, representing the mass number dependence on the nuclear charge. The calibration in mass and charge was performed by using a previous FRS measurement [5] and maximum charge of the fissioning system (Z_1+Z_2=83). As can be seen in the figure the reconstruction allows a clear identification for all fission fragments. Furthermore, in the inset of the figure we show the mass distribution for the nuclear charge Z=40 where the mass resolution is around 0.63 FWHM.

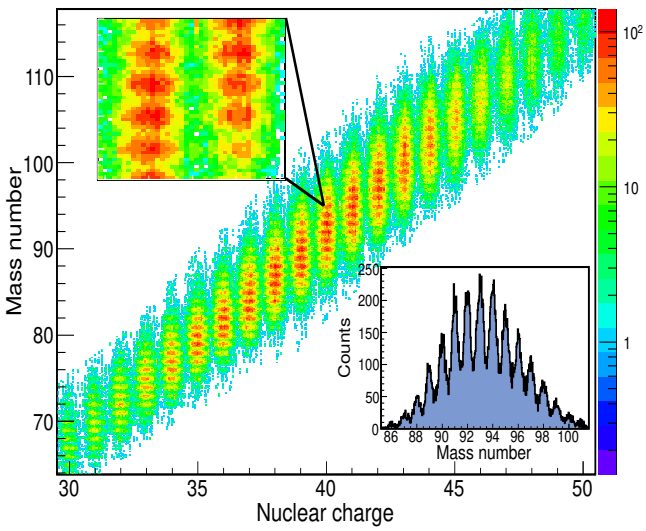

Figure 1: Identification in mass number and nuclear charge for ^{208}Pb (500A MeV)+p. In the inset of the figure we show the mass distribution for nuclear charge Z=40.

References

[1] J.L. Rodríguez-Sánchez et al., EPJ Vol. 62 07009 (2013).

[2] B Voss et al., GSI Scientific Report 2011, p.184-186.

[3] A. Ebran et al., Nucl. Instrum. Methods A 728 (2013) 40.

[4] J.L. Rodríguez-Sánchez et al., "SOFIARoot: Simulation of the SOFIA/ANDES Setup" in this annual report.

[5] B. Fernández-Domínguez et al. Nucl. Phys. A 747, 227 (2005).

Progress report of the CALIFA/R^{3}B calorimeter*

D. Cortina-Gil †[1], *H. Alvarez-Pol*[1], *T. Aumann*[13], *V. Avdeichikov*[4], *M. Bendel*[7], *J. Benlliure*[1], *D. Bertini*[5], *A. Bezbakh*[11], *T. Bloch*[13], *M. Böhmer*[7], *M.J.G. Borge*[2], *J.A. Briz*[2], *P. Cabanelas*[1], *E. Casarejos*[8], *M. Carmona Gallardo*[2], *J. Cederkäll*[4], *L. Chulkov*[12], *M. Dierigl*[7], *D. Di Julio*[4], *I. Durán*[1], *E. Fiori*[10], *A. Fomichev*[11], *D. Galaviz*[9], *M. Gascón*[1], *R. Gernhäuser*[7], *J. Gerl*[5], *P. Golubev*[4], *M. Golovkov*[11], *D. González*[1], *A. Gorshkov*[11], *A. Heinz*[3], *M. Heil*[5], *B. Heiss*[7], *W. Henning*[7], *G. Ickert*[5], *A. Ignatov*[13], *B. Jakobsson*[4], *H.T. Johansson*[3], *M. Kmiecik*[14], *Th. Kröll*[13], *R. Krücken* ‡[7], *S. Krupko*[11], *F. Kurz*[7], *T. Le Bleis*[7], *B. Löher*[10], *A. Maj*[14], *E. Nacher*[2], *T. Nilsson*[3], *A. Perea*[2], *C. Pfeffer*[7], *N. Pietralla*[13], *B. Pietras*[1], *R. Reifarth*[6], *J. Sanchez del Rio*[2], *D. Savran*[10], *S. Sidorchuk*[11], *H. Simon*[5], *L. Schnorrenberger*[13], *O. Tengblad*[2], *P. Teubig*[9], *R. Thies*[3], *J.A. Vilán*[8], *M. von Schmid*[13], *M. Winkel*[7], *S. Winkler*[7], *F. Wamers*[13], *P. Yañez*[8], *and M. Zieblinski*[14]

[1]Universidad de Santiago de Compostela; [2]Instituto Estructura de la Materia, CSIC Madrid; [3]Chalmers University of Technology, Göteborg; [4]Lund University; [5]Helmholtzzentrum für Schwerionenforschung, Darmstadt; [6]Goethe University Frankfurt am Main; [7]Technische Universität München; [8]Universidad de Vigo; [9]Centro de Física Nuclear da Universidade de Lisboa; [10]Extreme Matter Institute and Research Division, GSI; [11]Joint Institute for Nuclear Research, Dubna; [12]Nuclear Reseach Center, Kurchatov Institute Moscow; [13]Technische Universität Darmstadt; [14]Institute of Nuclear Physics PAN, Krakow, Poland

CALIFA, the CALorimeter for In Flight detection of γ rays and light charged pArticles, surrounds the R^{3}B reaction target and is one of the key detectors of the R^{3}B experiment [1]. The CALIFA design is optimised for the requirements given by the ambitious physics program proposed for the R^{3}B facility and combines very stringent calorimetric and spectrometric properties.

The Technical Design Report [2] of the Barrel section, with a polar angular coverage of 43.2-140.3^o, was approved in January 2013 by FAIR, following the recommendation of the Expert Committee Experiments (ECE) [1]. The technical solution adopted for this section, needed to reach the required spectrometric properties, defines a very segmented device with 1952 CsI(Tl) crystals that are readout by Large Area Avalanche Photodiodes (LAAPDs). The crystals are orientated within a compact geometry, with an internal radius of 30 cm, to optimise the calorimetric properties.
The Forward EndCap section (polar angular coverage 7-43.2^o) is in the R&D phase.

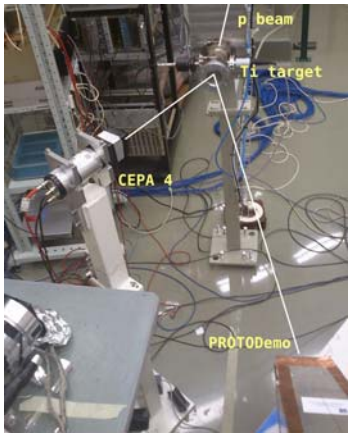

Figure 1: Prototypes detectors surrounding a 50μm Ti target at IFJ PAN, where irradiation with protons 70 - 230 MeV was possible with a beam energy spread better than 1%.

The main activities of the CALIFA Working group over 2013 have concentrated around three lines of work: a) determination of the final technical specifications and the purchase of "Barrel" detector components, b) development of innovative solutions to fulfil the requirements of the "Forward EndCap" and c) realisation of in-beam tests of different small size prototypes.

The performance of single elements of the CALIFA Barrel have been carefully evaluated. Light collection and output signal proportionality over the crystal length are central when long scintillator crystals are used for spectroscopic purposes. These properties can be adjusted by surface treatment, in the CALIFA case by surface lapping. Considering the large number of crystals involved in CALIFA it is also important to investigate if an optimum strategy for surface treatment can be found that could simplify industrial production. For this reason models of the different crystal geometries have been introduced in GEANT4 and testing procedures for the surface lapping have been simulated for a large number of different cases by tracing optical photons through the crystals. This work continues in parallel with laboratory tests on individual crystals, already at this stage clear trends can be identidied between the size and position of lapped areas and the linearity of the response.

* Work performed in the CALIFA/R^{3}B Working group and supported by the Helmholtz International Centre for FAIR
† Convener of the CALIFA Working group
‡ Also affiliated to TRIUMF
[1]decision adopted in the ECE first meeting in November 2012

 doi:10.15120/GR-2014-1-NUSTAR-KR-09

Beam tests were undertaken at the IFJ PAN Kraków cyclotron. This accelerator, designed for medical treatment, provides mono-energetic proton beams over an energy range of 70-230 MeV with a beam energy spread better than 1%. A range of smaller size prototypes, corresponding to different sections of the CALIFA detector, were tested using scattered protons on a 50μm thick Ti target, the setup is shown in Fig. 1.

- A scattered proton beam with energies ranging from 70 to 230 MeV was used to irradiate a 4x8 array (ProtoDemo) of 180 mm long CsI(Tl) crystals with a truncated pyramidal shape corresponding to a crystal geometry used in the Barrel section. The dimensions of the exit face are well matched to the Hamamatsu S12102 double LAAPDs. The signals from the APDs were fed into MPRB-16 preamplifiers. The amplified signals are distributed to FEBEX3 boards, which contain two 8-channel fast-sampling ADCs and one FPGA [3]. To fit the output range of the preamplifier exactly to the input range of the FEBEX boards, a new add-on board was developed for the FEBEX module (FAB for FEBEX Addon Board). It adjusts the baseline of the input signals and implements a Nyquist filter to avoid aliasing effects due to the 50 MHz sampling of the ADCs. The baseline correction is active and the correction is directly controlled by the FPGA. The first FAB prototypes have been implemented and tested during this beam time, validating the principle of the method. In a second revision currently under test, the noise figure and dynamic range of the boards have been further improved.

  In addition to detector response to protons over the full energy range, the prototype was used in various configurations to probe inactive matter effects, which may be extrapolated from using the R3BRoot dedicated simulation framework. The response to protons was complemented by a gamma calibration reaching up to 6.13 MeV. A direct scaling of the gamma - proton linear fits reveals a surprisingly uniform relation, where a common factor of 10.24 (close to the MPRB-16 preamplifier high - low gain factor of 10) applied to the gamma calibration matched well to calibrate over the proton energy range. The importance of extending the gamma calibration energy is evident on examination of the residuals, as seen in Fig. 2.

  The high linearity of the CsI(Tl)+LAAPD combination looks promising to allow simple gamma calibration scaling to be used as a method to calibrate CALIFA at the R^{3}B proton energies.

  A new algorithm for particle identification, adapted to real-time use in logic electronics, has been developed from the observation and concepts reported in [4]. The algorithm showed a clear separation between γ rays and protons. Several papers published in 2013 detail the R&D campaign and report progress in areas such as advancement in event reconstruction algorithms and characterization of a range of CALIFA prototype detectors at a number of international facilities [5, 6, 7]. They are complemented by R3BRoot simulations which allow to extrapolate to the full calorimetric performance of CALIFA.

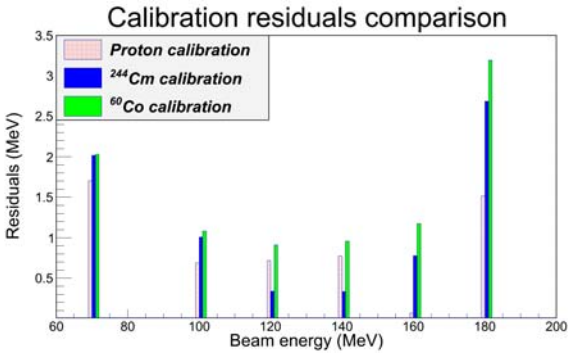

Figure 2: Mean proton energy residuals for a sample of five 180 mm CsI:Tl crystals after scaling a ^{137}Cs, ^{60}Co gamma calibration with, and without, the inclusion of the 6.13 MeV photopeak (^{244}Cm+^{13}C).

- We also tested a new prototype of the Forward End-Cap: CEPA4. This is an array of 4 individual scintillator detectors, each of them consisting of 4 cm of $LaBr_3$(Ce) crystals optically coupled to 6 cm of $LaCl_3$(Ce) in phoswich configuration (see Fig. 3).

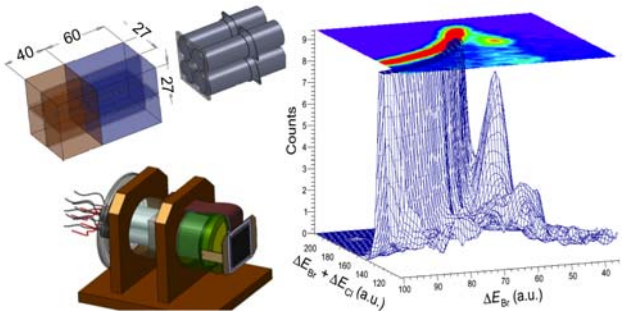

Figure 3: Left: schematic view of CEPA4 with its crystals, casing and photomultiplier tubes. During the experiment it was coupled to a DSSSD allowing the study of proton response at different positions. Right: proton spectrum at 220 MeV. The horizontal axis represent, respectively, the total energy deposited in the phoswich ($LaBr_3$+$LaCl_3$) and the partial energy deposited in the first part of it (the $LaBr_3$). At the top there is a 2-dimensional projection of the plot. The peak corresponding to 220 MeV protons is clearly separated from the rest.

The response of CEPA4 to high-energy protons was measured with the available proton beams. The maximum energy was just enough to test the punch-through of protons in a 10 cm phoswich, which happens at 200 MeV. Fig. 3 right shows a 220 MeV proton spectrum. In this plot the XY-plane represents the energy deposited in the $LaBr_3$(Ce) versus the total energy deposited in the phoswich, and the Z-axis represents the number of events. The method used to disentangle the energy deposited in each of the two crystals is explained in Ref. [8]. In the plot one can clearly see the peak corresponding to the 220 MeV protons that have passed through the two crystals leaving part of their energy in each of them. This is the first time the initial energy of the protons have been reconstructed from the partial deposition of their energy in two different crystals.

- The $LaBr_3$-$LaCl_3$ phoswich concept functions well over the IFJ PAN proton energy range, though simulations highlight potential energy resolution concerns when employed at the R^3B operational energies. Additionally, the encapsulation required due to the material's high hygroscopy introduces inactive matter, which does not aid optimisation of calorimetric performance. Therefore, alternative solutions are also investigated. In particular, the concept of a CsI(Tl)-LYSO phoswich was studied as it contains cheaper material which is less hygroscopic and may reduce the amount of dead material required. It would not require new readout electronics as the time constants (600 ns and 3200 ns for CsI(Tl) and 40 ns for LYSO) allow for a clear signal separation, however the internal radioactivity of LYSO is a subject of concern as when scaled to EndCap proportions the background radiation would be non-negligible. The tested prototype was composed of two crystals of $1 \times 1 \times 1\text{cm}^3$ from each material coupled with optical glue. The electronic pulse allowed a good qualitative identification of the signals from the energy deposited in both crystals. A modified version of the algorithm mentioned above allowed the reconstruction of the energy deposited as shown in Fig. 4. The illustrated example shows a good energy reconstruction for the tested energies, validating this concept for a phoswich. The counts outside the branches are related to the different particle types and arises from surface effects of the small prototype crystals.

The development of CALIFA is now entering a very intense period. The purchase and construction of 20% of the Barrel has started. The full implementation and commissioning of the CALIFA Demonstrator is expected in 2014-2015. In parallel, the submission of the Technical Design Report corresponding to the Forward section is foreseen by the end of 2014. According to our schedule, the complete CALIFA could be installed and operational in the R3B cave by the end of 2016.

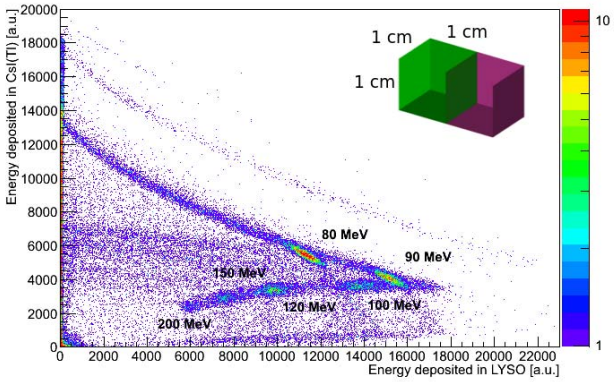

Figure 4: Reconstructed energy deposited in CsI(Tl) as a function of the reconstructed energy deposited in LYSO for protons at various energies. Protons punching through the 1 cm CsI layer show an increasing signal in LYSO while the CsI amplitude is dropping. Protons with energies larger than ∼95 MeV are not stopped any more and appear in the lower branch of the figure.

Acknowledgements

We would like to thank the full crew of the IFJ PAN cyclotron for the support provided during the realization of the experiment. This work has been supported by the following projects MINECO (FPA2012-39404-C02-01, FPA2012-39404-C02-02, FPA2012-32443), Xunta de Galicia (GRC2013-11), Swedish research council (VR 2009-3939, VR 2012-4550, VR 2013-4178), GANAS (Eranet), ENSAR (VII PM), HIC for FAIR, BMBF (05P12WOFNF, 05P12WOFNUE, 05P12RDFN8) and DFG (EXC153).

References

[1] T. Aumann et al., Technical Proposal for the design, construction, commissioning and operation of R^3B, A universal setup for kinematical complete measurements of Reactions with Relativistic Radioactive Beams (2005).

[2] T. Aumann et al., Technical report for the Design, Construction and Commissioning of the CALIFA Barrel: The R^3B CALorimeter for In Flight detection of γ rays and high energy charged particles (2011)

[3] T. Le Bleis et al., Test of Integration of CALIFA into R3B, GSI SCIENTIFIC REPORT 2012

[4] M. Bendel et al., Eur. Phys. J. A. 49 (2013) 69

[5] R. Wirth et al., Nucl. Instr. and Meth. A 717 (2013) 77

[6] B. Pietras et al., Nucl. Instr. and Meth. A 729 (2013) 77

[7] M. Gascon et al., Jour. of Inst. 8 (2013) P10004

[8] O. Tengblad et al., Nucl. Instr. and Meth. A 704 (2013) 19

 doi:10.15120/GR-2014-1-NUSTAR-KR-09

Heavy-ion tracking detectors for the R^{3}B setup*

S. Paschalis[1], T. Aumann[1,2], C. Caesar[1], R. Gernhäuser[3], M. Heil[2], M. Holl[1], J.G. Johansen[1], A. Kelic-Heil[2], O. Kiselev[2], D. Körper[2], Y. Litvinov[2], A. Movsesyan[1], M. Petri[1], R. Plag[1], H. Scheit[1], P. Schrock[1], H. Simon[2], I. Syndikus[1], H. Törnqvist[1], F. Wamers[4,1,2], and the R^{3}B collaboration

[1]TU Darmstadt, Germany; [2]GSI, Darmstadt, Germany; [3]TU, München, Germany; [4]EMMI @ GSI, Darmstadt, Germany

Overview

The high-intensity radioactive ion beams foreseen within the FAIR project will give us access to study the most exotic nuclear systems. In order to fully explore these rare short-lived species the experimental apparatuses are undergoing major upgrades. In this challenging environment the R^{3}B collaboration is working towards the development of a versatile system offering an unprecedented combination of high-efficiency, high-resolution and high-rate-capable kinematically complete measurements.

A pivot point in these developments is the installation of the new superconducting magnet GLAD. This magnet is capable of bending effectively the high-rigidity beams and allows for projectile-like neutrons to be detected at zero degrees and the bent beam to be momentum analysed. A series of charged-particle detectors are placed along the trajectory of the beam in order to measure precisely the position, charge and time of the incoming beam particles and the outgoing beam-like fragments. Although the current technologies of charged-particle detectors offer solutions that could meet our resolution requirements alone, the challenge is to combine this with minimum material budget, high-rate capability, radiation hardness, large active area, large dynamic range, low cost and high flexibility.

Heavy-ion tracking detectors

Along these lines we are focusing our developments on the following detectors: 1) Ultra-thin scintillating fiber detectors. 2) Ultra-thin resistive strip Si detectors. 3) Large area time-of-flight wall. In this report we present the current status of these developments.

Plastic-scintillator fiber detectors

Some of the advantages of using plastic-scintillator material is the low cost, fast response and high-rate capability. Five new fiber detectors are being developed for the needs of precision position measurement. Each detector plane provides precise information in one dimension and, where two-dimensional information is needed two detector planes are packed closely into one detector. All planes are built using a 200 μm square fiber and have varying dimensions ranging from small 5x5 cm^2 active area up to 110x80 cm^2. The total number of fibers needed to cover these areas is almost 3x10^4 and the total length exceeds 60 km of fiber.

The light collection is performed by multi-pixel photon counters (MPPC) and multi-anode photomultiplier tubes. The boards for powering the MPPCs and providing a first stage amplification are designed and built in-house at the electronic workshop of the Institut für Kernphysik at the Technical University of Darmstadt. The electronic readout is performed using a combination of NXYTER, FEBEX and TAMEX depending on the physical location of the detector and the needs for a high multi-hit capability readout. We have currently tested, for example, a fully independent single-fiber readout based on NXYTER [1]. In many cases, however, the large number of fibers makes it impractical and costly to read out all fibers individually. A readout scheme, in which the different fibers are bundled in a unique way in both ends, enables a way of determining the hit fiber with a reduction of the readout channels to $2\sqrt{N_{\text{fiber}}}$ per plane. This reduces the readout of the 3x10^4 fibers to 944 channels, but at the same time compromises the multi-hit capability of the detector. A simple example of the bundling is shown in Fig. 1.

Resistive strip Si detectors

The Si detectors, in general, are one of the most popular tracking devices, since they combine high-resolution position and energy-loss measurements. The Si micro-strip detectors deliver excellent position resolution, but have a large number of readout channels and the total energy-loss reconstruction for heavy-ions is not trivial. For these reasons, without excluding the use of micro-strip technology for certain experiments, we are also working on optimising the concept of resistive charge division. Detectors based on this technology can deliver excellent position and energy resolution when the deposited energy is sufficiently high, as is the case for most heavy-ion experiments at R^{3}B. In addition, the number of readout channels is significantly reduced compared to the micro-strip Si detectors.

However, these detectors suffer from slow charge collection as the charge is defused at the resistive side with a time-constant defined by the detector capacitance and the anode resistance. This limits the rate capability of the detector. Compared to the micro-strip detectors they also have higher noise levels due to the presence of the anode resistance and due to the generally higher capacitance. This noise is, however, not the dominant factor in the energy-loss measurements as discussed in [2].

* Work supported by BMBF (05P12RDFN8) and (05P12WOFNF), by GSI via the GSI-TU Darmstadt cooperation contract and by HIC for FAIR.

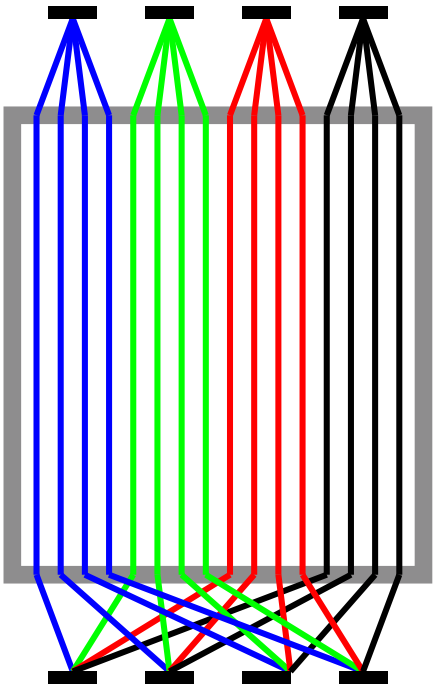

Figure 1: A fiber-bundling scheme that reduces the number of readout channels to $2\sqrt{N_{\text{fiber}}}$ pr. plane.

These limitations of the resistive charge division detectors can be reduced by e.g. segmenting the detectors and reducing the anode resistance, which however increases the number of readout channels and worsens the position resolution, respectively. The aim of this work is to find the optimum trade off between the number of channels, position resolution, thickness, and rate capability, and to take full advantage of the varying pulse shapes in this type of detectors.

We have performed a detailed characterisation and comparison of two types of resistive charge division detectors: a continuous two-dimensional detector and a strip Si detector using an ^{241}Am source. In addition, the read out of these detectors is performed using digital electronics and the waveforms of the pulses are recorded for further offline processing. We have found that both the position resolution and the pulse rise time are significantly improved in the case of the strip detector compared to a continuous two-diminensional detector. Namely, the position resolution obtained for an ^{241}Am alpha source and a 3 KΩ anode resistance has improved threefold to be $\sigma \approx 150$ μm (see Fig. 2 adopted from Ref. [3]) and the signal rise time from the central detector area has become ten times faster t ≈ 350 ns. We plan to verify these results in an in-beam test where the limits of high-rate capability will also be tested. The currently used detectors have a thickness between 100 and 300 μm and typically a 5x5 cm^2 active area. In the future we plan to test also larger detectors with area 7x7 cm^2 and 10x10 cm^2.

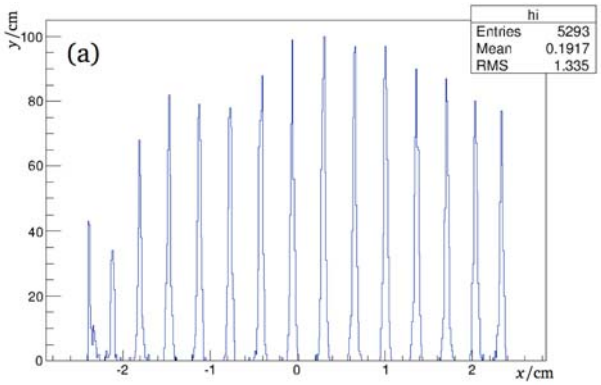

Figure 2: Position resolution obtained with a Si resistive strip 140 μm thick detector and an ^{241}Am source.

Large area time-of-flight wall detector

A large-area plastic-scintillator wall is used in the R^{3}B setup to obtain simultaneously excellent time-of-flight and energy-loss measurement. An optimised wall, with an active area of 110x80 cm^2 (see Fig. 3), is currently being built and will be tested in-beam this year. The optimisation is driven mainly by the requirement for a precise energy-loss measurement at high rate.

Design-wise one can highlight the following differences of this detector compared to older versions: The light guides at the ends of the paddles have been removed and the paddle width and photomultiplier diameter have been chosen to fit well with minimal loss of light collection. The paddles are oriented vertically with respect to the dispersive axis of the dipole magnet. In this way the paddles are mainly hit in their central area minimising the non-uniformity and the "smiley effects" in the total energy reconstruction. Vertically oriented paddles also share the beam rate more evenly. Four such planes with vertical paddles are placed behind each other and are slightly shifted with respect to each other so that there are effectively no dead areas between the paddles.

The paddles are produced with a maximum variation of a few percent in their thickness. The energy-loss measurement is, however, anticipated to be much better than this variation. In order to correct for non-uniformities in the thickness of the paddle and the position dependent response of the scintillator, this detector is packed closely on the same frame with the aforementioned large area fiber detectors that cover the same active area.

On the electronics readout side there have also been major advances. It is found that the energy-loss measurement, when performed with a standard QDC type of electronics, suffers greatly from rate dependencies. The new readout is based on a time-over-threshold technique which effectively

 doi:10.15120/GR-2014-1-NUSTAR-KR-10

cancels any baseline variation and at the same time gives a much higher dynamic range. These electronics are a combination of the in-house TAMEX board and a QTC add-on delivering simultaneously good time and energy measurements.

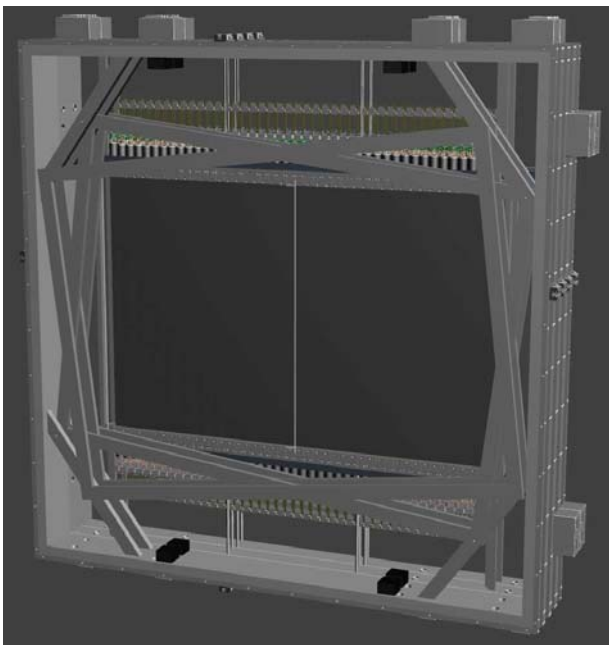

Figure 3: A CAD drawing of the plastic-scintillator wall. In front of the paddles, the tilted frames foreseen to support the large-area fiber planes are also shown.

References

[1] P. Schrock et al., "Development of a Thin Large-Area Fiber Detector for Radioactive-Beam Experiments" GSI-SR2012-PHN-ENNA-EXP-69, GSI Report 2013-1

[2] S. Paschalis et al., "Position-Sensitive Si Detectors for In-Beam Tracking at the R^3B Setup" GSI-SR2012-PHN-ENNA-EXP-68, GSI Report 2013-1

[3] I. Syndikus master thesis, "Testing of Position Sensitive Silicon Detectors for the R^3B-Setup" February 2014.

Tests of timing silicon photomultipliers for NeuLAND*

S. Gohl[1,2], *T. Reinhardt*[2], *D. Bemmerer*[†1], *T.E. Cowan*[1,2], *K. Heidel*[1], *M. Röder*[1,2], *D. Stach*[1], *A. Wagner*[1], *D. Weinberger*[1], *J. Wüstenfeld*[1], *K. Zuber*[2], *and the R*^{3}*B collaboration*[1]

[1]Helmholtz-Zentrum Dresden-Rossendorf (HZDR), Dresden, Germany; [2]TU Dresden, Germany

It is investigated whether NeuLAND may be re-instrumented with semiconductor based photosensors. Tests with an 11 cm long slab of RP-408 plastic scintillator and a PiLas 45 ps laser diode system show time resolutions of σ = 100 ps.

The NeuLAND time-of flight detector for 1 GeV neutrons will consist in its final configuration of 30 double planes of 100 scintillator bars (RP-408) each. Each bar of $270\times5\times5\,\mathrm{cm}^3$ must be read out at each end. Thus altogether 6000 timing photomultipliers of 1" diameter are needed [1]. In order to limit their cost impact, it is being investigated whether parts of NeuLAND may be (re-)instrumented with semiconductor-based photosensors, so-called Silicon Photomultipliers (SiPMs).

Previous experiments using the one-electron-per-bunch mode of the superconducting electron accelerator ELBE have shown that nearly full efficiency can be reached even when instrumenting one NeuLAND bar with just one $3\times3\,\mathrm{mm}^2$ SiPM [2]. However, in those first tests the charge resolution did not allow to separate single photons, and the time resolution did not fulfill the required $\sigma \leq 150$ ps.

Electronics and preamplifier

Subsequently some improvements were made in the electronics circuits. For the timing, both a digital constant-fraction algorithm based on the recorded waveforms in a 12-bit 1 GHz, 2.5 GS/s digital oscilloscope and a constant fraction discriminator developed in house with a threshold of just 7 mV were tested and found to give satisfactory results.

* Supported by NupNET NEDENSAA (BMBF 05 P 09 CRFN5), GSI F&E DR-ZUBE, and by the Helmholtz Association Detector Technology and Systems Platform (DTSP).

† d.bemmerer@hzdr.de

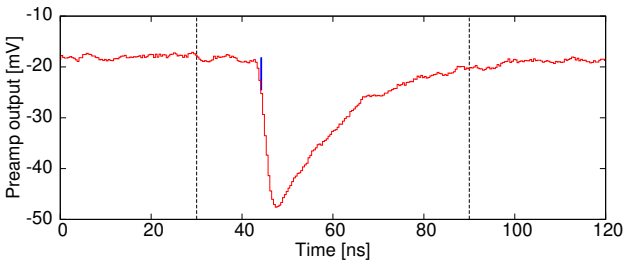

Figure 1: Waveform for a signal generated by a 421 nm 45 ps PiLas laser diode in a $3\times3\,\mathrm{mm}^2$ Hamamatsu MPPC. The 60 ns wide integration window for the QDC is shown.

Due to the scarcity of commercial preamplifiers for SiPMs, a new preamplifier was developed in-house. It is based on a common-emitter circuit with a discrete complementary Darlington transistor with a bandwidth of 2 GHz and an input impedance of 25 Ω. There is no overshoot of the amplified signal as in some other SiPM preamplifiers, enabling to integrate the current pulses with a QDC. The gain of the output signals is 15-25, controlled by varying the supply voltage from 5-12 V. The rise time of the output signals is about 650 ps (fig. 1).

Preliminary results and outlook

The preliminary spectra shown a clean separation between single photons on the charge axis and have a slight time walk (fig. 2). The typical resolution is now σ = 100 ps for the time difference between the detected signal and the PiLas laser reference signal when using the in-house developed electronics and even 60-80 ps when adding a PS 775 fast amplifier. Future tests will show whether the satisfactory timing capability will also be maintained when exciting the scintillator with minimum ionizing electrons from ELBE.

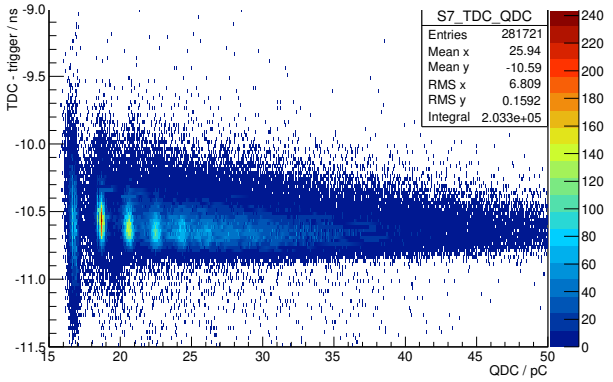

Figure 2: Time versus charge for the PiLas illuminating the RP-408, which is, in turn, read out by the MPPC. The pedestal (17 pC) and peaks for 1-4 photons can be seen.

References

[1] NeuLAND@R3B: A Fully-Active Detector for Time-of-Flight and Calorimetry of Fast Neutrons, NeuLAND Technical Design Report, http://www.fair-center.de/fileadmin/fair/experiments/NUSTAR/Pdf/TDRs/NeuLAND-TDR-Web.pdf

[2] T. Reinhardt *et al.*, GSI Scientific Report 2012, SR2012-PHN-ENNA-EXP-62

 doi:10.15120/GR-2014-1-NUSTAR-KR-11

Application of Calorimetric Low Temperature Detectors (CLTD's) for Precise Stopping Power Measurements of Heavy Ions in Matter

A. Echler[1,2,3], *P. Egelhof*[1,3], *P. Grabitz*[1,3], *H. Kettunen*[4], *S. Kraft-Bermuth*[2], *M. Laitinen*[4], *K. Müller*[2], *M. Rossi*[4], *W.H. Trzaska*[4], *and A. Virtanen*[4]

[1]GSI, Darmstadt, Germany; [2]University of Gießen, Germany; [3]University of Mainz, Germany; [4]University of Jyväskylä, Finland

Precise data on electronic stopping powers, i.e. specific energy loss dE/dx, for heavy ions are of high interest in various fields of research [1]. Unfortunately the accuracy of theoretical ab-initio dE/dx-calculations is nowadays still unsatisfactory. Therefore, predictions of stopping powers are usually calculated by semi-empirical computer codes, which are based on best fits to available experimental data. To improve the reliability of these calculations, precise dE/dx data are needed for various projectile-target combinations and over a wide range of projectile energies, in particular for heavy projectiles at low energies, as measured data are scarce in that region [2]. However, for high ion masses and low energies ionization based energy detectors, that are commonly used in experiments for stopping power determination [3, 4], suffer from incomplete energy detection, resulting in pulse height defect and a relatively poor energy resolution. As CLTD's provide substantially better energy resolution and linearity for heavy ion detection, with the absence of any pulse height defect [5, 6], this type of energy detectors has the potential to increase sensitivity and accuracy for dE/dx measurements and to extend the accessible energy range towards lower energies.

For that purpose a CLTD array, that has been developed at GSI in the past years [5, 6, 7], has been used to replace the Si-detector in an established setup for dE/dx measurements at the K-130 cyclotron at the University of Jyväskylä [3, 8], and to perform measurements with 0.05–1 MeV/u ^{131}Xe-ions in different absorber materials. As an example the measured electronic stopping power of Xe ions in carbon is displayed in fig. 1. A summary of all results for carbon as well as nickel and gold absorbers can be found in [9], where also a more detailed description of the experiment is given. The obtained dE/dx values show in general a good agreement with previously measured data in the higher energy range for all studied absorber materials, what provides a consistency check of the new experimental setup. Moreover the application of CLTD's for the present investigations allowed to considerably reduce calibration errors as compared to previous measurements with Si-detectors [10], and to extend the datasets to lower energies, not accessible before.

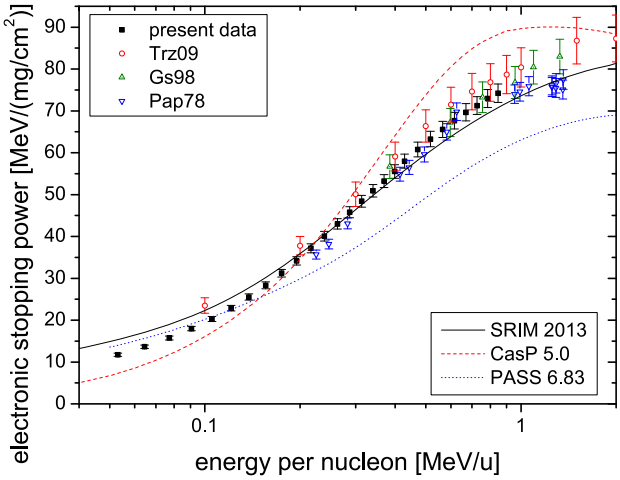

Figure 1: Electronic stopping power of Xe ions in carbon obtained from the present experiment [9] together with literature values that have been taken from the electronic library for stopping powers of H. Paul [2] (Trz09 [10], Gs98 [11], Pap78 [12]). The lines represent theoretical calculations with the semi-empirical computer code SRIM [13] and the ab-initio models CasP [14] and PASS [15].

References

[1] ICRU Report 73, *Journal of the ICRU 5*, No 1 (2005).

[2] H. Paul, web site: www.exphys.jku.at/stopping/

[3] W.H. Trzaska et al., *Nucl. Instr. Meth. B* **195**, 147, (2002).

[4] J. Zhang, *Nucl. Instr. Meth. B* **196**, 1, (2002).

[5] P. Egelhof and S. Kraft-Bermuth, *Topics in Applied Physics* **99**, 469, (2005).

[6] S. Kraft-Bermuth et al., *Rev. Sci. Instrum.* **80**, 103304, (2009).

[7] A. Echler et al., *J. Low Temp. Phys.* **167**, 5-6, 949, (2012).

[8] A. Javanainen et al., *IEEE Trans. Nuc. Sci.* **54**, 4, 1158, (2007).

[9] A. Echler et al., *J. Low Temp. Phys.* DOI 10.1007/s10909-013-1043-y (2014).

[10] W.H. Trzaska et al., *Nucl. Instr. Meth. B* **267**, 3403, (2009).

[11] H. Geissel et al., *various data summarized in electronic library of H. Paul [2].*

[12] H. Pape et al., *Zeitschr. f. Phys. A* **286**, 159, (1978).

[13] J.F. Ziegler, *Nucl. Instr. Meth. B* **268**, 11-12, 1818, (2010), www.srim.org.

[14] G. Schiwietz and P.L. Grande, *Nucl. Instr. Meth. B* **273**, 1, (2012), CasP download: http://www.casp-program.org/

[15] PASS-code based on *Binary theory of electronic stopping*, P. Sigmund and A. Schinner, *Nucl. Instr. Meth. B* **195**, 64, (2002)

Efficiency calibration of the neutron detector BELEN-48 with (p,n) and (α,n) reactions at the PTB Braunschweig *

M. Marta[1,2], *J. Agramunt*[3], *R. Caballero-Folch*[4], *G. Cortés*[4], *I. Dillmann*[1,2,5], *M. Erhard*[6], *L.M. Fraile*[7], *U. Giesen*[6], *B. Kindler*[1], *B. Lommel*[1], *R. Nolte*[6], *A. Riego*[4], *S. Röttger*[6], *and J.L. Taín*[3]

[1]GSI Helmholtzzentrum für Schwerionenforschung GmbH, Darmstadt, Germany; [2]II. Physikalisches Institut, Justus-Liebig Universität Giessen, Germany; [3]IFIC-CSIC University of Valencia, Valencia, Spain; [4]INTE-DFEN, Universitat Politecnica de Catalunya, Barcelona, Spain; [5]TRIUMF, Vancouver, Canada; [6]Physikalisch-Technische Bundesanstalt (PTB), Braunschweig, Germany; [7]Universidad Complutense de Madrid, Spain

The BEta-deLayEd Neutron detector BELEN is a highly efficient device designed for the DESPEC project at FAIR. It has already been successfully used during the experiments S323 and S410 at the Fragment Separator to measure β-delayed neutron probabilities and half-lives of neutron-rich nuclei close to the r-process path, for nuclear structure and nuclear astrophysics studies.

In its present version, it consists of 48 ^{3}He proportional counters arranged to form three concentric rings embedded in a polyethylene matrix. Due to the thermalization process, the information about the initial neutron energy is lost but the detection efficiency is strongly increased. Therefore the position and number of counters in the rings are designed in such a way that the efficiency remains constant over a broad range of neutron energy from thermal up to a few MeV. The simulations are performed with an MCNPX code and have to be validated by experiments that make use of known neutron fluxes produced in the center of the detector.

Measurements with a calibrated ^{252}Cf source provide only one efficiency value corresponding to a spectrum-averaged neutron energy of 2.14 MeV. In order to have a more stringent test on the simulated efficiency curve, the calibration has been extended with well-known (p,n) and (α,n) reactions on ^{13}C and ^{51}V targets producing neutrons with limited energy spread, ranging between 0.2 and 5.3 MeV. The list of reactions and energies used is summarized in table 1.

Reaction	E_{proj} [MeV]	E_{n} [MeV] min	max
^{51}V(p,n)^{51}Cr	1.80	0.20	0.25
^{51}V(p,n)^{51}Cr	2.14	0.51	0.59
^{51}V(p,n)^{51}Cr	2.27	0.63	0.73
^{13}C(p,n)^{13}N	4.45	0.77	1.36
^{13}C(α,n)^{16}O	1.05	2.5	3.2
^{13}C(α,n)^{16}O	3.30	3.6	5.3

Table 1: List of reactions used for the calibration. Maximum and minimum neutron energies E_n refer to the smaller (forward) and largest (backward) angle covered by BELEN-48, i.e. from about 16 to 164 degrees.

The experiment was performed at the PTB ion accelerator facility (PIAF) of the Physikalisch-Technische Bundesanstalt (PTB) in Braunschweig/Germany, where a Van de Graaff accelerator and cyclotron provided the α and p beams of desired energy and intensity. The BELEN-48 polyethylene matrix was installed with the air-cooled target holder located at the end of a beam line at the center of the detector. The target chamber was designed as a Faraday cup to measure the beam currents on target with suppression electrodes and collimators. At a second beam line it was possible to produce the same neutron flux as inside BELEN, with very similar target and beam conditions, and to measure reaction yields and angular distributions with the calibrated neutron detectors of PTB at several angles with respect to the beam axis. The reactions on ^{13}C target show large anisotropy in the center-of-mass frame. The angular distributions of ^{51}V(p,n)^{51}Cr are still to be measured.

The measured angular distributions need to be taken into account in the simulation of the efficiency for each reaction and beam energy, since neutrons enter BELEN with different probabilities and energies at different angles. For the moment the preliminary experimental efficiency (Fig. 1) is obtained as the ratio of neutrons *detected* in BELEN-48, and a normalized-to-isotropy value for neutrons *emitted*. The normalization takes into account each measured angular distribution and the detection solid angle, making a comparison of all data and simulation possible.

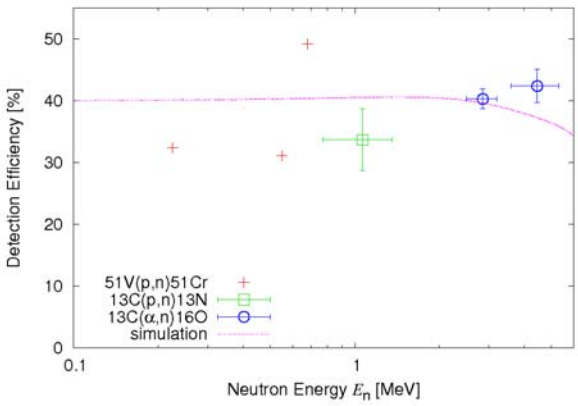

Figure 1: Comparison of the efficiency curve simulated with MCNPX (dotted line) and preliminary experimental values. The Vanadium data is shown without uncertainty due to the missing angular distribution information that prevents its normalization.

* This work was supported by the Helmholtz association via the Young Investigators Group VH-NG-627.

 doi:10.15120/GR-2014-1-NUSTAR-KR-13

SOFIARoot: Simulation of the SOFIA/ANDES Setup

J.L. Rodríguez-Sánchez, H. Álvarez-Pol, Y. Ayyad, J. Benlliure, P. Cabanelas, and C. Paradela for the SOFIA/ANDES collaboration

University of Santiago de Compostela, Spain

SOFIA/ANDES is an innovative experimental programme on nuclear fission developed at GSI-FAIR. These experiments provide for the first time complete isotopic yields (nuclear charge and mass) for both fragments over a broad range of fissioning nuclei from ^{238}Np down to ^{183}Hg. Moreover ANDES experiment provides the light charged particles and neutron multiplicities.

SOFIARoot is the simulation tool for the SOFIA / ANDES setups [1, 2] within the FAIRRoot [3] framework, a Root-based software for the simulation and data analysis developed at GSI for the analysis of the future FAIR experiments.

Part of this framework was also inherited from R3BRoot [4] that delivers base classes which allowed to implement detectors and derive simulation and analysis tasks in a simple way. It also supplies some general functionality like track visualization, database support and event structure as well as the full mathematical, histogramming and advance analysis machinery contained in the ROOT classes.

As a data-analysis tool, SOFIARoot allows an event-by-event based analysis, from the unpacking and basic calibration to the final processing of the combined physics observables, following a set of succesive tasks, ruled by user-friendly macros. As a simulation tool (Fig. 1), SOFIARoot supports Geant3 and Geant4 transport engines, interfacing with their geometry constructors. Furthermore the ALADIN magnet field map is included as an interpolation based on field-map measurements. The simulation also provides a constant magnetic field which is described in the macros. The user can switch between the two fields by a simple setup selection in the configuration macros which allow to do a selection without blending or overlapping fields. The detectors (TPC, MUSIC, Twin MUSIC[5], MWPCs and ToF Walls [6]) used in the experiments were also included while LAND detector was exported from R3BRoot.

Calibration and digitization parameters, geometry elements of detectors and other parameters are stored in a runtime database supporting different input/output methods, including ASCII, ROOT binary format and several available databases using SQL lenguage.

The most important of SOFIARoot is that allows the realization of the analysis and simulation under the same platform. The benefits of this approach include the evaluation of the geometrical efficiencies and other systematical uncertainties under the same platform which have already been used for the analysis of [7, 8].

References

[1] E. Pellereau et al., EPJ Vol. 62 06005 (2013).

[2] J.L. Rodríguez-Sánchez et al., EPJ Vol. 62 07009 (2013).

[3] FAIRRoot, http://fairroot.gsi.de/

[4] R3BRoot, simulation and analysis framework for the R3B experiment at FAIR, D. Bertini, J. Phys.: Conf. Ser. 331 032036 (2011).

[5] B Voss et al., GSI Scientific Report 2011, p.184-186.

[6] A. Ebran et al., Nucl. Instrum. Methods A 728 (2013) 40.

[7] J.L. Rodríguez-Sánchez et al., "Total Fission Cross Sections for Proton-Induced Fission of ^{208}Pb" in this annual report.

[8] J.L. Rodríguez-Sánchez et al., "Identification and Reconstruction of Fission Fragments for Proton-Induced Fission of ^{208}Pb at 500 MeV in Inverse Kinematics" in this annual report.

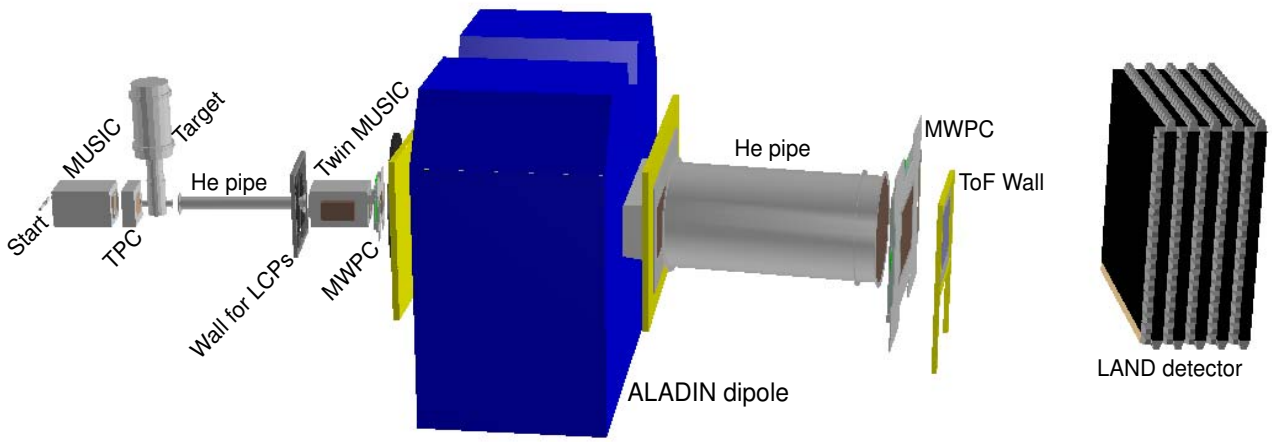

Figure 1: ANDES setup implemented in simulation.

GGLAND — command line simulations

H.T. Johansson[1], *R. Thies*[1], *S. Buller*[1], *A. Heinz*[1], *S. Lindberg*[1], *J. Magnusson*[1], *T. Nilsson*[1], *T. Rathsman*[1], *and the R*^{3}*B collaboration*

[1]Chalmers Univ. of Technology, Göteborg, Sweden

GGLAND is a small wrapper program around the GEANT3 and GEANT4 physics simulation libraries. Its task is to make it easy to perform the simulations needed for physics analysis of LAND/R^{3}B experiments, as well as other smaller nuclear physics setups.

The basic idea behind GGLAND [1] is that the physics knowledge needed for particle transport through matter is handled by the general libraries GEANT3/4 [2]/[3]. To perform a simulation, the user has to write code to interface the libraries, to setup and declare the geometry, generate particles, and retrieve results; often an obstacle for quick tests.

The wrapper program has grown organically out of a need to simulate calibrations of the Crystal Ball detector. But for each new feature, the handling has been generalised to allow use in other cases as well. GGLAND has thus become a rather versatile tool, especially for quick back-of-the-envelope simulations (see Fig. 1), since the user generally does not have to write or modify any code. Operation is controlled by command-line options and output data can be recorded in ROOT-files, with content very much resembling real data that has passed the first steps of analysis.

The program can run simulations in parallel by forking itself as several slave processes after setup. The master process gives the pseudo-random seeds for each event, and automatically merges the output data in original event order, with results independent of actual simulation order.

Geometry definition — detectors

The geometry elements making up the detectors are created on program startup, every time. This avoids bitrot in the creation code, is a very small fraction of the execution time, and gives flexibility in the creation and subsequent hit handling. Each detector type can be maintained in a single source file. The creation function constructs objects according to variables in an associated structure, describing vital measurements and other characteristics of the design. The default values can be overriden on the command line. Several detectors using the same design but with different parameters can be instantiated, as well as exact clones. Magnetic fields are placed using the same mechanism.

Particle gun

For each simulated event, one or more particles need to be generated, and passed to the physics interaction packages of GEANT3/4. The particle gun takes options to control various forms of randomisation of the source location, particle type, direction and energy. Matching the flexibility

```
./land_geant4 --gun=T=1MeV,gamma,z0=-2cm \
  --test=d=1cm,type=Ge,tree=1 \
  --tree=test4.root --events=100000
```

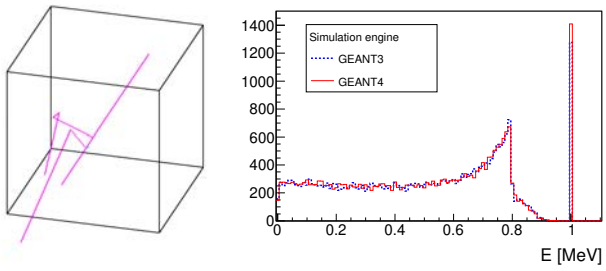

Figure 1: Top: command-line example with a beam of 1 MeV photons directed at a 1 cm^3 cube of Ge, using a flexible test detector. Left: display of 10 events. Right: results, showing full energy detection and the Compton edge.

of physicists in specifying energies, many ways are supported: kinetic, total, momentum, β, and $B\rho$. Particles with correlations can be produced, e.g. for γ decay schemes with level feeding and back-to-back photons. Muons can be drawn from a realistic cosmic distribution [4], as well as particles in phase-space distributions, and boosting (e.g. reaction products from a fixed beam velocity).

To use particles from other reaction generator codes, particles can also be created from an input file.

Digitisation

For selected detector volumes, the discretised energy deposits reported by GEANT3/4 are collected. They are combined by a clusteriser, considering separation in space and time to determine which deposits to join. The resulting hits can be stored in ROOT trees for subsequent analysis. To help understand the processes simulated, the vertices with particles produced can be dumped as structured text, which can be colourised by a special markup program (`ggmark`).

References

[1] H.T. Johansson, "The ggland command-line simulation wrapper" (2013), Göteborg, http://fy.chalmers.se/~f96hajo/ggland/

[2] "GEANT, Detector Description and Simulation Tool, CERN Program Library Long Write-up W5013", CERN Geneva.

[3] S. Agostinelli *et al.*, "Geant4—a simulation toolkit", NIM A 506 (2003), 250–303.

[4] J. Kempa A. Krawczynska, "Low energy muons in the cosmic radiation", Nucl.Phys. B (Proc. Suppl.) 151 (2006) 299-302.

 doi:10.15120/GR-2014-1-NUSTAR-KR-15

FOCAL – PRECISION X-RAY SPECTROSCOPY FOR EXTREME FIELDS IN HIGH-Z IONS *

H.F. Beyer[1], D. Banaś[2], K.-H. Blumenhagen[8], F. Bosch[1], C. Brandau[4], W. Chen[1], Chr. Dimopoulou[1], E. Förster[3,8], T. Gaßner[1,8], A. Gumberidze[4], S. Hagmann[1,5], R. Heß[1], P.-M. Hillenbrand[1], P. Indelicato[6], P. Jagodzinski[2], T. Kämpfer[8], Chr. Kozhuharov[1], M. Lestinsky[1], D. Liesen[1], Yu.A. Litvinov[1], R. Loetzsch[8], B. Manil[7], R. Märtin[8], F. Nolden[1], N. Petridis[4,5], M.S. Sanjari[1,4], K.S. Schulze[8], M. Schwemlein[1], A. Simionovici[10], U. Spillmann[1], M. Steck[1], Th. Stöhlker[1,8], C.I. Szabo[6], M. Trassinelli[10], S. Trotsenko[8], I. Uschmann[3,8], G. Weber[8], O. Wehrhan[3,8], N. Winckler[1], D. Winters[1], N. Winters[1], and E. Ziegler[11]

[1]GSI Helmholtzzentrum, Darmstadt, Germany; [2]Institute of Physics, Swietokrzyska Academy, Kielce, Poland; [3]Inst. für Optik und Quantenelektronik, Friedrich-Schiller-Universität, Jena, Germany; [4]Extreme Matter Institute, EMMI, GSI Helmholtzzentrum, Darmstadt, Germany; [5]Institut für Kernphysik, Goethe-Universität, Frankfurt am Main, Germany; [6]Lab. Kastler Brossel, Université P. et M. Curie, Paris, France; [7]Laboratoire de Physique des Lasers (LPL) UMR 7538 CNRS - Université Paris 13, Villetaneuse, France; [8]Helmholtz-Institut Jena, Jena, Germany; [9]LGIT, Observatoire des Sciences de l'Univers de Grenoble, Grenoble, France; [10]Institut des Nanosciences de Paris, Université Pierre et Marie Curie-Paris 6 and CNRS-UMR 7588, Paris, France; [11]ESRF, Grenoble, France

Introduction and Motivation The extraordinarily strong electric field provided by the nucleus of a very heavy one-electron ion exposed to its inner electrons is the testing ground for bound-state quantum electrodynamics (QED) in a largely unexplored domain. Experimentally the QED contribution to the 1s binding energy is accessible via a direct measurement of the K-shell transitions with sufficient accuracy. The corresponding Lyman transitions in high-Z ions lie in the hard x-ray region. Previously the x-ray energy has been measured with the aid of germanium x-ray detectors of limited resolution [1]. The present experiment marks the leap to wavelength-dispersive spectroscopy of substantially higher spectral resolving power simultaneously coping with the low x-ray intensity.

Experiment Figure 1 schematically shows the twin crystal-spectrometer assembly, Bi-FOCAL, operated in the **FO**cusing **C**ompensated **A**symmetric **L**aue [2] geometry which has been arranged at the ESR gas jet. The spectrometer system [3, 4] equipped with two 2D position-sensitive Ge strip detectors [5, 6], F1 and F2, was used in an experiment with one-electron Au^{78+} ions at a velocity corresponding to $\beta = 0.4711$. The twin spectrometers were deliberately arranged symmetrically around the ion-beam at observation angles of $\pm 90^\circ$ in an angular-sensitive geometry where the usual Doppler broadening and angular Doppler uncertainties are near their maximum. The imaging properties of the FOCAL crystal optics are turned to advantage retaining nearly full spectral resolution also for the fast moving source.

Complementary to the crystal spectrometer an array of low-temperature micro calorimeters were mounted in a velocity-sensitive geometry at an observation angle of 145°, where angular uncertainties are reduced. That experiment, run in parallel, is described in another report [7].

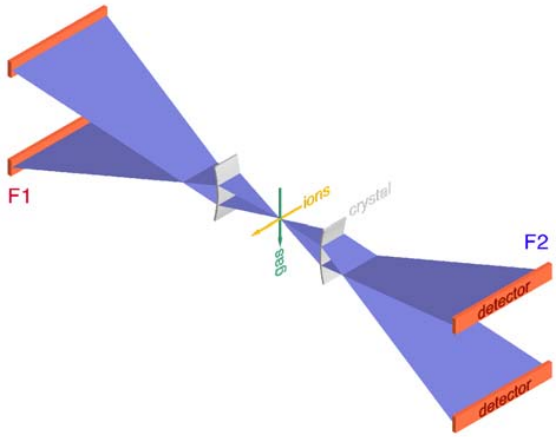

Figure 1: Two crystal-spectrometers, Bi-FOCAL, symmetrically arranged around the ion beam at the ESR gas jet. Wavelength dispersion occurs in the vertical direction and the spectra are recorded by two position-sensitive x-ray detectors F1 and F2 mounted at two of the possible four locations as indicated.

Besides the high background-suppression capabilities of FOCAL figure 2 demonstrates its slanted Lyman-α and -β lines of Au^{78+} in accordance with the underlying x-ray-optical design. Without crystal optics Doppler broadening would blur the whole spectral range displayed. The spectrum shown in figure 3 was obtained by projecting the intensity along the slanted lines. In the experiment the Lyman-α_1 line was Doppler tuned to the position of the 63.1-keV gamma-ray line emitted from a radioactive sample of ^{169}Yb used as a calibration source rendering dispersion uncertainties unimportant.

Systematic Effects At an observation angle of exactly 90° the required transition wavelength λ_{ion} in the emit-

* This work has been supported by the European Community FP7 Capacities, contract ENSAR No. 262010. D. Banas acknowledges the support by the Polish Ministry of Science and Higher Education under Grant No. N N202 46353. P.-M. Hillenbrand acknowledges support by HIC-for-FAIR through HGS-HIRe and the Helmholtz-CAS Joint Research Group HCJRG-108.

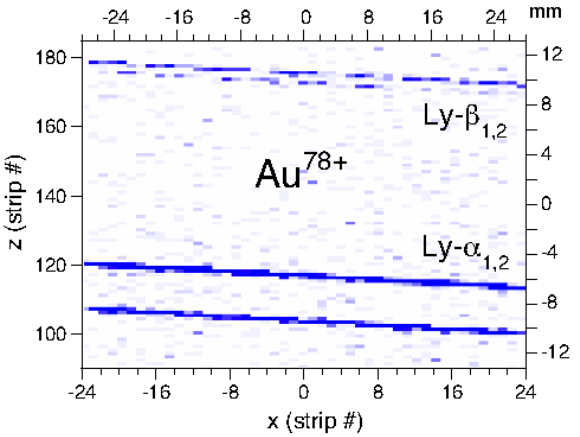

Figure 2: The spectrum of hydrogen-like Au^{78+} revealed as a position spectrum taken by F2. The Lyman-α and -β doublets appear as slanted lines caused by the Doppler effect in counterplay with the crystal optics employed.

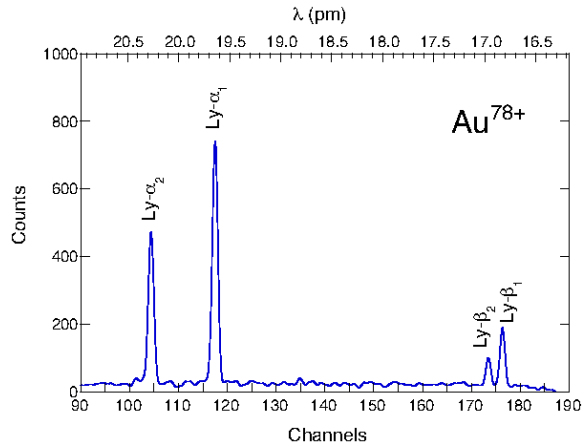

Figure 3: The Lyman-α and -β doublets of Au^{78+} obtained by a projection of the two-dimensional intensity distribution of figure 2.

ter frame is simply related to the laboratory wavelength by $\lambda_{lab} = \gamma\,\lambda_{ion}$ where γ denotes the relativistic Lorentz parameter. The two arms of the spectrometer assembly are mounted accurately inline resulting in observation angles $\lambda_{\rm lab}(\vartheta)$ and $\lambda_{\rm lab}(\pi - \vartheta)$, respectively. However missalignment of the ion beam relative to the spectrometer axis might still persist. This class of uncertainties are well canceled by averaging the two laboratory wavelengths as $\lambda_{\rm ion} = (\lambda_{\rm lab}(\vartheta) + \lambda_{\rm lab}(\pi - \vartheta))/(2\gamma)$.

In addition there are a number of systematic influences on the measured wavelength that do not simply cancel and which need to be carefully identified and analyzed. We are currently in the process of assessing systematic corrections and their corresponding uncertainties referring to the procedures and mathematical algorithms by which the spectral lines are located including long-term drifts plus all the geometrical effects due to the positions and angular orientations of the x-ray source, of the curved silicon crystals and of the x-ray detectors. A particularly important example is the position of the gas-jet target in the horizontal plane

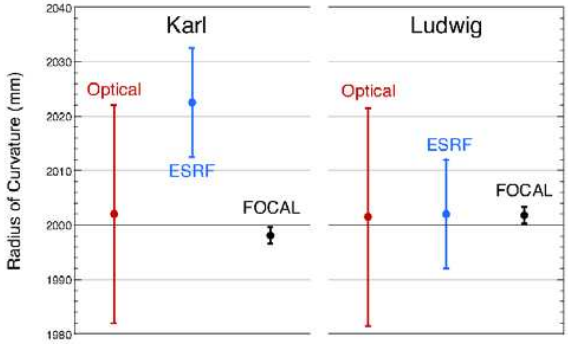

Figure 4: The radius of curvature of the two silicon crystals *K*arl and *L*udwig determined by three different methods: optical reflections on the polished crystal surfaces, mapping with synchrotron radiation at the ESRF and by operating FOCAL as a scanner.

spanned by the ion-beam and the spectrometer axis. This was investigated in a separate experiment by scanning a thin wire across the gas jet [8].

Here we mention two other examples of the crystal optics which need to be understood: *(i)* the radius of curvature of the two crystals named *Karl* and *Ludwig* was measured by three different methods which gave consistent results as summarized in figure 4. *(ii)* the observed slope of the spectral lines along with the calculated prediction is summarized in Table 1. Although the slanting effect is generally confirmed the measured slopes tend to be slightly lower than predicted.

Table 1: Doppler slanting: predicted and observed slopes of the Lyman-$\alpha_{1,2}$ and Lyman-β spectral lines of Au^{78+} at a velocity of $\beta \equiv v/c = 0.4711$.

	Lyman-α_2	Lyman-α_1	Lyman-β
predicted	0.01922	0.01862	0.01597
observed			
FOCAL-1	0.0184(2)	0.0183(2)	
FOCAL-2	0.0188(3)	0.0179(2)	0.0165(4)

We thank K. Eberhard from the Institut für Kernchemie of the Johannes Gutenberg-Universität, Mainz, for the preparation of our calibration sources.

References

[1] A. Gumberidze *et al.*, Phys. Rev. Lett. **94** (2005) 223001.

[2] H. F. Beyer, Nucl. Instrum. Methods. A**400** (1997) 137.

[3] H.F. Beyer *et al.*, Spectrochimica Acta **B 59** (2004) 1535.

[4] H.F. Beyer *et al.*, Spectrochimica Acta **B 64** (2009) 736.

[5] D. Protić *et al.* IEEE Trans. Nucl. Sc. **52** (2005) 3194.

[6] U. Spillmann *et al.*, Rev. Sc. Instr. **79** (2008) 083101.

[7] S. Kraft-Bermuth *et al.*, GSI scientific report 2013.

[8] T. Gaßner *et al.*, GSI scientific report 2013.

 doi:10.15120/GR-2014-1-PNI-AP-01

Forward-angle electron spectroscopy in ion-atom collisions studied at the ESR*

P.-M. Hillenbrand[1,2], S. Hagmann[1,3], D. Banaś[4], C. Brandau[2,5], K.-H. Blumenhagen[6,7], W. Chen[1], R. Dörner[3], E. De Filippo[8], A. Gumberidze[5], D. L. Guo[9], O. Kovtun[10], C. Kozhuharov[1], M. Lestinsky[1], Yu. A. Litvinov[1], A. Müller[2], H. Rothard[11], S. Schippers[2], M. S. Schöffler[3], U. Spillmann[1], S. Trotsenko[1,6], N. Winckler[1], X. L. Yan[9], X. L. Zhu[9], and Th. Stöhlker[1,6,7]

[1]GSI Darmstadt; [2]Univ. Giessen; [3]Univ. Frankfurt; [4]Univ. Kielce, Poland; [5]EMMI Darmstadt; [6]HI Jena; [7]Univ. Jena; [8]INFN Catania, Italy; [9]IMP Lanzhou, China; [10]Univ. Heidelberg; [11]CIMAP-CIRIL-Ganil, Caen, France

The spectroscopy of electrons emitted in low-energy ion-atom collisions, in particular in forward direction parallel to the projectile ion beam, has been in the focus of research in atomic physics for several decades. These electrons populate low-lying continuum states of the projectile and, due to Lorentz transformation, are observed in the laboratory frame as electrons emitted under $\vartheta_e \approx 0°$ with a velocity v_e similar to the projectile velocity $v_e \approx v_p$. Experimentally the spectroscopy of these so-called "cusp-electrons" benefits from enhanced energy resolution due to a reduced Doppler broadening.

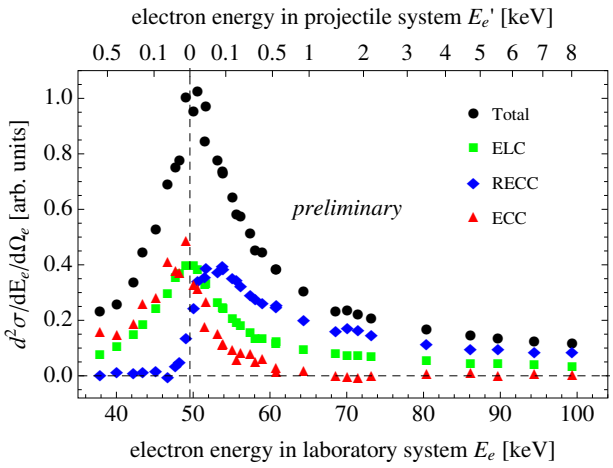

Figure 1: Energy distribution of forward emitted electrons originating from processes (a) – (c).

At GSI this field of research was extended to high-energy heavy-ion atom collisions. For this purpose collisions of beryllium-like U^{88+} projectile ions at 90 MeV/u colliding with a molecular gas-jet target of N_2 were studied at the ESR in a beam time in 2012. The energy distribution of cusp electrons emitted in these collisions was measured with a dedicated magnetic electron spectrometer located downstream the gas-jet target. Additionally five X-ray detectors were positioned around the target, and two particle detectors were used to detect projectile ions which had lost or captured one electron during a collision with the target (or the residual gas). Applying coincidence conditions between the electrons observed in the spectrometer and signals of one of the X-ray or particle detectors three different collision processes could be observed. Each of them resulted in an electron populating a low-lying continuum state of the projectile:

(a) The **electron loss to continuum** (ELC) corresponds to the ionization of a projectile electron into the projectile continuum during the collision with the target:

$$U^{88+} + N_2 \rightarrow U^{89+} + [N_2]^* + e^-.$$

(b) The **electron capture to continuum** (ECC) corresponds to the capture of a target electron into the projectile continuum, while the excess energy is carried away by the recoil of the generated target ion:

$$U^{88+} + N_2 \rightarrow U^{88+} + \left[N_2^+\right]^* + e^-.$$

(c) The **radiative electron capture to continuum** (RECC) corresponds to the capture of a target electron into the projectile continuum, while the excess energy is carried away by a photon:

$$U^{88+} + N_2 \rightarrow U^{88+} + \left[N_2^+\right]^* + e^- + \gamma.$$

Previously the RECC process (c) was for the first time observed unambiguously at GSI and experimentally proven to be equivalent to the high-energy endpoint of electron-nucleus bremsstrahlung studied in inverse kinematics [1]. Succeeding this pioneering experiment a high-resolution measurement of the processes (a) – (c) was performed in 2012, with a significantly improved experimental setup [2]. Whereas for low-energy projectiles used in former studies the cusp electron spectrum was dominated by ECC or ELC, it was proven within this experiment that at 90 MeV/u the cross sections of the three processes are comparably large, while the shapes of the electron energy distributions show significant differences (Fig. 1). Notably the opposite asymmetry of ECC and RECC gives a clear signature of the different underlying collision mechanisms. Comparison of the experimental results with various theoretical calculations is currently under way and soon to be published.

References

[1] M. Nofal *et al.*, Phys. Rev. Lett. **99**, 163201 (2007)

[2] P.-M. Hillenbrand, *Elektronenspektroskopie im Fundamentalprozess der Elektron-Kern-Bremsstrahlung*, Dissertation Universität Giessen (2013)

*Work supported by HIC-for-FAIR through HGS-HIRe and Helmholtz-CAS Joint Research Group HCJRG-108.

The Effect of the Breit-Interaction Studied for the Emission Characteristics of $1s2s^22p_{1/2}$ Decay in Be-like Uranium *

S. Trotsenko[1,2], A. Gumberidze[3,4], Y. Gao[2,5], C. Kozhuharov[2], S. Fritzsche[1,6], A. Surzhykov[1,2,6], N. Petridis[2,7], D. B. Thorn[3,4], H.F. Beyer[2], R.E. Grisenti[2,7], S. Hagmann[2,7], P.-M. Hillenbrand[2], U. Spillmann[2], G. Weber[1], and Th. Stöhlker[1,2,3,6]

[1]Helmholtz-Institut Jena, D-07743 Jena, Germany; [2]GSI Helmholtzzentrum für Schwerionenforschung, D-64291 Darmstadt, Germany; [3]ExtreMe Matter Institute EMMI, D-64291 Darmstadt, Germany; [4]FIAS, Frankfurt a. M., Germany; [5]Institute of Modern Physics, Chinese Academy of Sciences, Lanzhou, China; [6]Friedrich-Schiller-Universität Jena, D-07743 Jena, Germany; [7]Institut für Kernphysik, Universität Frankfurt, Germany

The well-known Breit interaction was first worked out by Gregory Breit in order to calculate the fine-structure of atomic helium [1]. Nowadays, the Breit interaction is described as quantum electrodynamics (QED) effect. It includes magnetic interactions and retardation in the exchange of a single virtual photon between the electrons, and affects not only the energy level structure but also the dynamics of atomic processes. The interaction has aroused great interest in further exploration and analysis of relativistic contributions to the electron-electron interaction, and its importance has already been confirmed for several processes in the collisions between electrons and highly charged ions (HCI) [2, 3, 4, 5, 6, 7, 8, 9].

More often than not the influence of the Breit interaction is small, so it is treated as a minor correction to the Coulomb interaction. However, in certain cases it can even dominate dynamics involving highly charged ions. Nakamura et al. [10] found that the Breit interaction can enhance dielectronic recombination (DR) resonant strengths by almost 100%. Soon afterwards, Fritzsche et al. [11] predicted that the Breit interaction could dominate the Coulomb interaction in the x-ray emission of Li-like heavy ions following dielectronic recombination and could even qualitatively change the angular distribution of x-rays for heavy ions with nuclear charge $Z \geq 73$. Three years later, Hu et al. [12] obtained experimental evidence for the prediction of Fritzsche et al. by measuring the angular distribution of the $[1s2s^22p_{1/2}]_1 \rightarrow [1s^22s^2]_0$ transition in dielectronic recombination of Li-like Au with free electrons in an electron beam ion trap (EBIT).

In this report, we present the experimental results for angular distribution of characteristic x-rays following the resonant transfer and excitation (RTE) in U^{89+} collisions with H_2 target at the experimental storage ring ESR of GSI. The RTE is equivalent to the DR processes, but with the difference that the electron is initially in a bound state of target. The experiment performed by colliding Li-like uranium (U^{89+}) ions with H_2 at the resonance energy (116.15 MeV/u) for the $U^{89+}[1s^22s] \xrightarrow{H_2} U^{88+}[1s2s^22p_{1/2}]_1$ process. The accurate and stable value of the ion beam energy was guaranteed by the electron cooler of the ESR. The layout of the experimental arrangement at the gas-jet target is shown in Fig. 1. We measured the angular distribution of the $[1s2s^22p_{1/2}]_1 \rightarrow [1s^22s^2]_0$ x-ray transition following the resonant transfer and excitation.

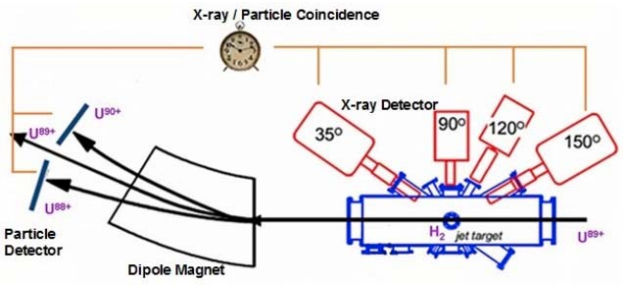

Figure 1: The experimental setup at the internal gas-jet target of the ESR.

The x-ray emission from the collisions was recorded with four high purity intrinsic germanium (HPGe(i)) detectors placed at 35^0, 90^0, 120^0 and 150^0 angles with regard to the direction of the ion beam. Exploiting time coincidences between the x-ray detectors and a particle detector mounted after the ESR dipole magnet, we were able to obtain the x-ray spectra corresponding only to the events of U^{89+} capturing an electron into singly or doubly excited states.

Four x-ray spectra have been obtained in the experiment at 35^0, 90^0, 120^0 and 150^0 observation angles corresponding to one-electron-capture events. As an example, Fig. 2 shows the spectrum recorded at 35^0 angle. In the spectrum, several radiative electron capture (REC) lines are present. They are denoted according to the shell where the target electron is captured into, i.e. L-REC stands for the capture into the L-shell (n=2), M-REC stands for the capture into the M-shell (n=3), etc. In addition, the RTE induced peak ($[1s2s^22p_{1/2}]_1 \rightarrow [1s^22s^2]_0$ transition) very close to the radiative electron capture into the $2s_{j=1/2}$ and $2p_{j=1/2}$ states ($L\text{-}REC_{1/2}$) is found. The REC peaks are significantly broader than the RTE-induced characteristic transition, due to the Compton profile of the target. This allows us to fit the RTE and REC lines separately and obtain the corresponding intensities. This is also possible for x-ray spectrum recorded at 150^0. However, at 90^0 and 120^0, the large Doppler broadening and a poorer energy resolution

* Work supported by HI Jena/EMMI/GSI(ESR)

 doi:10.15120/GR-2014-1-PNI-AP-03

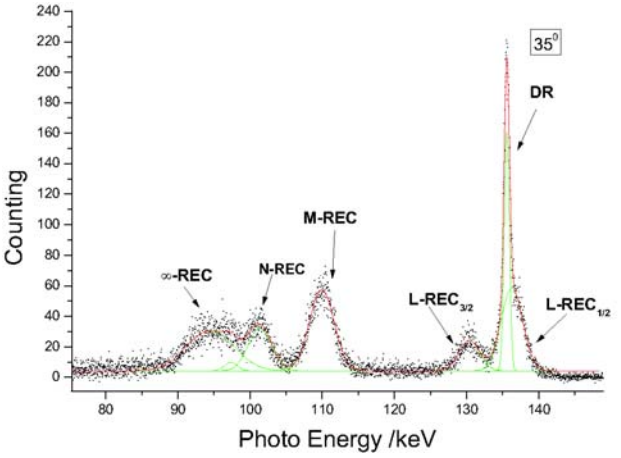

Figure 2: X-ray spectrum obtained at the ESR corresponding to one-electron-capture events in 116.15 MeV/u U^{89+} collisions with the H_2 gas target, obtained at 35^0 observation angle.

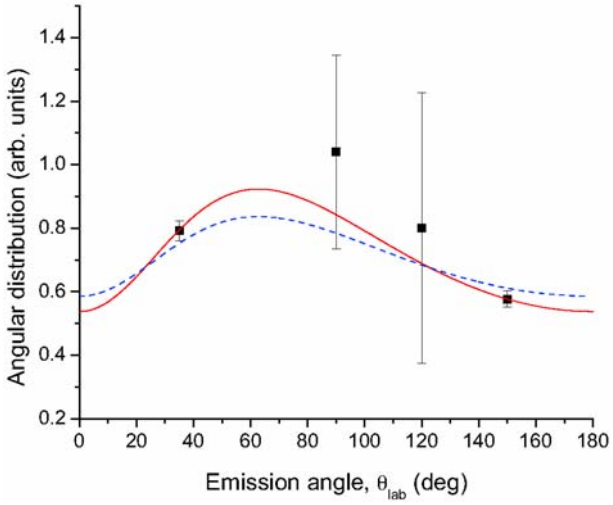

Figure 3: Experimental angular distribution for the $[1s2s^22p_{1/2}]_1 \rightarrow [1s^22s^2]_0$ transition following the RTE into initially Li-like uranium. The dashed line is a theoretical angular distribution from [11], with the alignment parameter A_2= -0.314. The solid line is from fitting the equation of the electric dipole emission [11] to our experimental data, having A_2 as a free fit parameter.

of the corresponding detectors smear out the difference between the RTE and L-$REC_{1/2}$ peaks, making it impossible to fit them separately and obtain directly their intensities. Therefore, we have to rely on the relativistic REC theory which has been extensively tested in many different experiments [13] and is currently known to provide accurate description of the process. Namely, we used the angular differential cross sections for L-$REC_{3/2}$, L-$REC_{1/2}$ and M-REC [14] together with our experimental data for obtaining the intensity of the L-$REC_{1/2}$. As a cross check of theory, we also compared the theoretical values with our experimental results for L-$REC_{1/2}$: L-$REC_{3/2}$ and L-REC : M-REC ratios at 35^0 and 150^0 where we could obtain the experimental values independently from the theory. We found a fair agreement between the theoretical and experimental results, however, in couple of cases a deviation of about 10% has been observed. The reason of this deviation is currently unclear. Therefore, we included the uncertainty of 10% for obtaining the experimental RTE intensity values at 90^0 and 120^0 angles. Furthermore, in order to obtain the angular distribution of the RTE induced $[1s2s^22p_{1/2}]_1 \rightarrow [1s^22s^2]_0$ transition, we normalized its intensity to the one of the closely spaced L-$REC_{3/2}$ peak and used the theoretical angular differential cross-section for the latter. In this way, uncertainties related to different solid angles and efficiencies of the x-ray detectors are almost completely cancelled out.

Our experimental and theoretical angular distributions [11] of the $[1s2s^22p_{1/2}]_1 \rightarrow [1s^22s^2]_0$ transition are shown in Fig. 3. From the figure, a good qualitative agreement between the experiment and theory agreement can be observed. By fitting the equation for angular distribution of the electric dipole emission [11] to the experimental angular distribution, we received the experimental value for alignment parameter $A_2 = -0.46 \pm 0.07$. Our result is definitely closer to the prediction from [11] with Breit interaction included (-0.314) than to the one without the Breit interaction (0.47). This can be considered as a proof for the high importance of the Breit interaction for this case. The reason for the relatively small ($\sim 2\sigma$) quantitative deviation between our experimental and theoretical results for the alignment parameter (A_2) has still to be clarified.

References

[1] G. Breit, *Phys. Rev.* **36**, 383 (1930).

[2] G. Breit, *Phys. Rev.* **39**, 616 (1932).

[3] C. Fontes, D. Sampson, and H. Zhang, *Phys. Rev. A* **59**,1329 (1999).

[4] R. E. Marrs, S. R. Elliott, and D. A. Knapp, *Phys. Rev.* **72**, 4082 (1994).

[5] W. R. Johnson, Springer, New York (2007).

[6] I. P. Grant, Springer, New York (2007).

[7] R. W. Childers, *Phys. Lett. B* **126**, 485-488 (1983), ISSN 0370-2693.

[8] C.-Y. Wong and R. Becker, *Phys. Rev. B* **182**, 251 (1986), ISSN 0370-2693.

[9] I. P. Grant and H. M. Quiney, *Int. J. Quantum Chem.* **182**, 283 (2000).

[10] Nobuyuki Nakamura *et al.*, *Phys. Rev. Lett.* **100**, 073203 (2008).

[11] Stephan Fritzsche *et al.*, *Phys. Rev. Lett.* **103**, 113001 (2009).

[12] Zhimin Hu *et al.*, *Phys. Rev. Lett.* **108**, 073002 (2012).

[13] J. Eichler, Th. Stöhlker, *Physics Reports* **439**, (2007) 1-99.

[14] A. Surzykov, (private communication).

Innovative Concepts for Collision Studies at GSI's and FAIR's Storage Rings*

C. Brandau[1,2,4], J. Glorius[2,3], C. Trageser[1,4], R. Reifarth[3], M. Heil[2], A. Müller[4], A. Gumberidze[1,2], C. Kozhuharov[2], Yu.A. Litvinov[2,6], M. Meister[2], S. Sanjari[1,2], S. Schippers[4], T. Stöhlker[2,7,8], T. Davinson[5], and P. Woods[5]

[1]EMMI/FIAS, Darmstadt; [2]GSI, Darmstadt; [3]Universität Frankfurt; [4]Universität Gießen; [5]University of Edinburgh; [6]MPIK, Heidelberg; [7]Helmholtz-Institut Jena; [8]Universität Jena

Installation of two new detector manipulators in the dipoles of the ESR

Two prototype systems of a new particle detector manipulator ([1], and Fig. 1) are currently being installed in the ESR's first dipole magnets in the south and the north arc, i.e., behind the electron cooler and the gas-target, respectively. The manipulators are equipped with vacuum gate valves and vacuum pumps and can thus be separated completely from the main vacuum system of the storage ring. The present design is especially adapted for the installation of detectors at the last ports of the C-type dipole magnets. The set-up in the south arc behind the electron cooler features a detector pocket with an entrance window of 25 μm thickness and is primarily targeted at recombination studies with a stochastically cooled ion beam using the electron cooler solely as a target for free electrons (cf. e.g. [2]).
In the north arc a special detector mount is installed that allows for the placement of a detector in-vacuum on the inside of the ring. As a consequence of the C-type magnet design, the detector has to be inserted from the outside of the ring prior to beam injection leaving sufficient space for the circulating initially uncooled primary beam.
The main purpose of this set-up is to enable nuclear reaction studies at the internal gas-target at ion energies around the Coulomb barrier or around the Gamov window such as nuclear astrophysics (p,γ) experiments [3]. A new UHV compatible position sensitive ceramic-mounted Si-detector (Micron semiconductors) is delivered, was vacuum tested at GSI and will be mounted in the near future. Commissioning of the manipulators with beam and first (p,γ) data taking runs at the ESR are scheduled for the upcoming beamtimes spring/summer 2014.

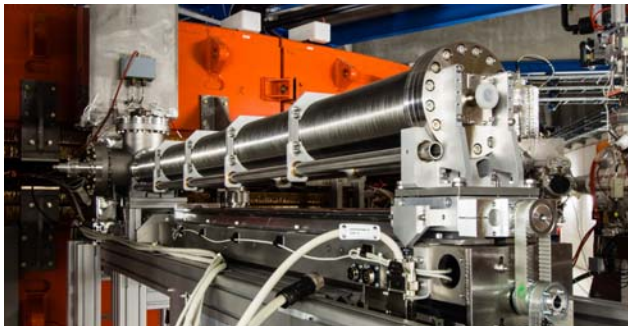

Figure 1: New detector manipulator in the first dipole magnet of the south arc (behind the electron cooler) of the ESR.

A new data acquisition for the integration of Schottky signals in AP experiments

In a collaboration of Giessen University, EMMI and GSI a new data acquisition is presently being set-up that aims at the continuous and broadband recording of RF Schottky signals at the present ESR, and in perspective at FAIR's future storage rings. In addition to the well-established Schottky mass and decay studies (cf. e.g. [4]) it is envisaged to provide a transparent, seamless and non-destructive recording of ion beam parameters ('beam logbook') and supply the data for storage ring experiments. The DAQ system comprises a modular PXIe crate and corresponding modules (National Instrument VSA type NI-5663E and Counter NI-6602, additional digitizer SPDevices ADQ-214) and is capable of uninterrupted high-resolution recording of the full ring momentum acceptance. The DAQ records the Schottky signals of both, the old parallel plate pick-up and the new high-resolution cavity-based pick-up [5] simultaneously. In particular, the single particle sensitivity of the new resonant pick-up features a much improved time-resolution. The combination of both pick-ups with the new highly performant DAQ will also facilitate new experimental schemes for atomic and nuclear collsion studies at storage rings [6].
The system is presently being commisioned offline with test signals: an initial data taking software (using NI Labview) and first data analysis routines have already been implemented. Tests and optimizations with beams are planned for the course of 2014.

References

[1] C. Brandau et al., GSI annual report 2012, p. 327.

[2] D. Bernhardt et al., Phys. Rev. A **783** (2011), 020701.

[3] Q. Zhong, et al., J. Phys: Conf. Ser. **202** (2010), 012011.

[4] Yu.A. Litvinov and F. Bosch, Rep. Prog. Phys. **74** (2011), 016301.

[5] F. Nolden et al., Nucl. Instrum. Meth. A (2011) **659**, 69.

[6] C. Trageser et al., 11th ECAMP, Aarhus, Denmark, 24.-28.6.2013.

*Work is supported by BMBF (contracts 06GI911I and 06GI7127/05P12R6FAN), by the Alliance Program of the Helmholtz Association (HA216/EMMI), by the HGF Young Investigators Project VH-NG-327 and by HIC for FAIR.

 doi:10.15120/GR-2014-1-PNI-AP-04

High-resolution measurement of the time-modulated orbital electron-capture and of the β^+ decay of hydrogen-like $^{142}Pm^{60+}$ ions*

P. Kienle[†1,2], *F. Bosch*[3], *P. Bühler*[2], *T. Faestermann*[1], *Yu.A. Litvinov*[3,4,5], *M.S. Sanjari*[3,6,7], *D.B. Shubina*[4,5], *N. Winckler*[3,4], *D. Atanasov*[4,8], *H. Geissel*[3,9], *V. Ivanova*[3], *X.L. Yan*[3,4,10], *D. Boutin*[3,11], *C. Brandau*[3,7,12], *I. Dillmann*[3,9], *C. Dimopoulou*[3], *R. Hess*[3,7], *P.-M. Hillebrand*[3,12], *I. Izumikawa*[13], *R. Knöbel*[3,9], *J. Kurcewicz*[3,8], *N. Kuzminchuk*[3,9], *M. Lestinsky*[3], *S.A. Litvinov*[3], *X.W. Ma*[10], *L. Maier*[1], *M. Mazzocco*[3,14], *I. Mukha*[3], *C. Nociforo*[3], *F. Nolden*[3], *C. Scheidenberger*[3,9], *U. Spillmann*[3], *M. Steck*[3], *Th. Stöhlker*[3,15,16], *B.H. Sun*[3,9,17], *F. Suzaki*[18], *S.Yu. Torilov*[19], *M. Trassinelli*[3,20], *X.L. Tu*[3,10], *M. Wang*[10], *H. Weick*[3], *D.F.A. Winters*[3], *N. Winters*[3], *P.J. Woods*[21], *T. Yamaguchi*[18], *and G.L. Zhang*[17]

[1]Technische Universität München, 85748 Garching, Germany; [2]Stefan Meyer Institut für subatomare Physik, 1090 Vienna, Austria; [3]GSI Helmholtzzentrum für Schwerionenforschung, 64291 Darmstadt, Germany; [4]Max-Planck-Institut für Kernphysik, 69117 Heidelberg, Germany; [5]Physikalisches Institut, Universität Heidelberg, 69120 Heidelberg, Germany; [6]J.W.-Goethe Universität, 60438 Frankfurt, Germany; [7]ExtreMe Matter Institute EMMI, 64291 Darmstadt, Germany; [8]CERN, 1211 Geneva 23, Switzerland; [9]II Physikalisches Institut, Justus-Liebig-Universität Gießen, 35392 Gießen, Germany; [10]Institute of Modern Physics, Chinese Academy of Sciences, Lanzhou 730000, PR China; [11]Service de physique nucléaire CEA-Saclay, F 91191 Gif-Sur-Yvette Cedex, France; [12]Institut für Atom- und Molekülphysik, Justus-Liebig-Universität Gießen, 35392 Gießen, Germany; [13]Radio Isotope Center, Niigata University, Niigata-951-8510, Japan; [14]Dipartimento di Fisica, INFN, 135131 Padova, Italy; [15]Institute of Physics, Friedrich-Schiller-Universität Jena, 07743 Jena, Germany; [16]Helmholtz-Institut Jena, Fröbelstieg 3, 07743 Jena, Germany; [17]School of Physics and Nuclear Energy Engineering, Beihang University, 100191 Beijing, China; [18]Graduate School of Science and Engineering, Saitama University, Saitama 338-8570, Japan; [19]St. Petersburg State University, 198504 St. Petersburg, Russia; [20]INSP, CNRS and Université Pierre et Marie Curie, UMR 7588, 75005 Paris, France; [21]School of Physics and Astronomy, University of Edinburgh, Edinburgh EH9 3JZ, United Kingdom

We report on the re-investigation of the two-body orbital electron-capture (EC) decay of hydrogen-like $^{142}Pm^{60+}$ ions, stored and cooled in the Experimental Storage Ring ESR of GSI [1]. In a first measurement of this system, a couple of years ago, a modulation superimposed on the exponential decay has been observed with a period of $T = 7.1$ seconds and an amplitude of about $a = 0.2$ [2]. In the present experiment we benefitted from a newly designed Schottky-noise frequency detector [3]. This device, a 245 MHz pillbox-like resonator, exhibits a signal-to-noise ratio improved by about two orders of magnitude with respect to the capacitive pick-up used in the previous experiment. It reveals in an unprecedented manner hitherto hidden details of the EC decay of a single ion and provides the true decay time as well as the time- and frequency-resolved kinematics and the entire cooling process of the recoiling daughter nucleus just from the moment of its generation, as demonstrated in Fig. 1. In particular, the projection of the recoil velocity onto the beam direction is signalled within 32 ms after the decay by a frequency shift Δf with respect to the revolution frequency of the cooled daughter ion (see Fig.1). From the distribution of these frequency shifts, observed for many thousand EC decays, finally the modulus of the recoil velocity could be figured out and, hence, the momentum of the recoiling daughter ion and of the generated electron neutrino which are entangled by momentum- and energy conservation. Furthermore, the clearly visible onset of the cooling trace of the daughter ion provides an unambiguous signature of the decay time, in strict contrast to the previous experiment, where only the appearance of the cooled daughter ion could be observed [2].

The whole of all EC-decays recorded in the present experiment does *not* show significant modulations. However, it could happen that due to technical failures, "old" ions were not removed from the ESR thus leading to washing out the modulation. An uninterrupted series of 7125 consecutive injections of the ions into the ESR was determined and used for the data analysis. This is outlined in detail in [1]. A fit of the data recorded by the 245 MHz resonator yields a modulation with a period of $T = 7.10(11)$ seconds and an amplitude of $a = 0.107(24)$ (see Fig. 2), and for the simultaneously used "old" pick-up detector a period of $T = 7.12(11)$ seconds and an amplitude of $a = 0.134(27)$. Both periods are not only in perfect agreement to each other, but also to the previously reported period of $T = 7.10(25)$ seconds [2]. Both amplitudes are,

* Work supported in part by the DFG cluster of excellence "Origin and Structure of the Universe" of the Technische Universität München, the Helmholtz Association via the Young Investigators Project VH-NG 627, the Helmholtz-CAS Joint Research Group HCJRG-108, the Alliance Program of the Helmholtz Association (HA216/EMMI), the BMBF (contracts 06GI911I70, 06GI7127/05P12R6FAN, and 05E12CD2), the External Cooperation Program of the Chinese Academy of Sciences Grant No. GJHZ1305, the Japanese Ministry of Education, Science, Sport and Culture by Grant-In-Aid for Science Research under Program No. A 19204023, the HIC-for-FAIR through HGS-HIRE, and the Joint Max Planck/CAS Doctoral Promotion Program.

† deceased at January 29, 2013

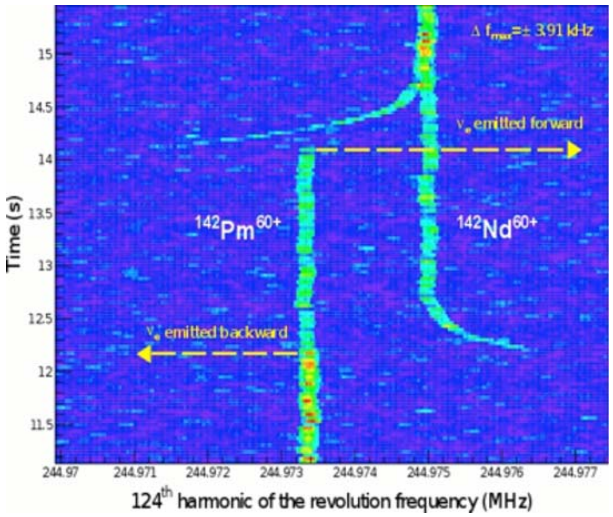

Figure 1: Time traces of two cooled ^{142}Pm^{60+} parent ions, recorded at the 124$^{\text{th}}$ harmonic of the revolution frequency by the 245 MHz resonator vs the the time after injection, with time-and frequency binning of 32 ms and 31.25 Hz, respectively. The arrows indicate the true decay times, as unambiguously identified by the onset of the trace of the recoiling daughter ion. It starts at a revolution frequency shifted by Δf with respect to the frequency of the cooled daughter ion, where Δf reflects the projection of the recoil velocity onto the beam direction immediately after the decay.

however, significantly smaller than the previous value of $a = 0.23(4)$.

In order to assess the significance of these results evidence criteria in favour of a certain model have been used. We compared the reliability of a strictly exponential distribution (model M_0) of the data on the one hand, and of a periodical modulation superimposed on an exponential distribution (model M_1) on the other hand, according to the "Akaike Information Criterion (AIC)" which is based on a maximum likelihood analysis. For the data recorded by the 245 MHz resonator we get a "weight of evidence" of $w_1 = 0.998$ for model M_1 and $w_0 = 0.002$ for model M_0 and of $w_1 = 0.9998$, $w_0 = 1.8 \cdot 10^{-4}$ for the data of the capacitive pick-up. These weights of evidence lead to the conclusion that the reported modulation period of $T = 7.1$ s has been confirmed by the new experiment, although with significantly smaller amplitude.

For the three-body β^+ decays observed in the same data set *no significant modulation* was found, as shown in Fig. 3. This might point to a weak-interaction origin of the modulation which is observed in connection with the (almost) monoenergetic electron-neutrinos from the two-body EC decays, but absent for the continuous neutrino spectrum of the three-body β^+ decay branch. Any conclusive and commonly accepted explanation of the modulation is (still) missing. One of the proposed suggestions, strongly disputed in literature, is that the modulations reflect – like the well-known quantum beats – the interference of two coher-

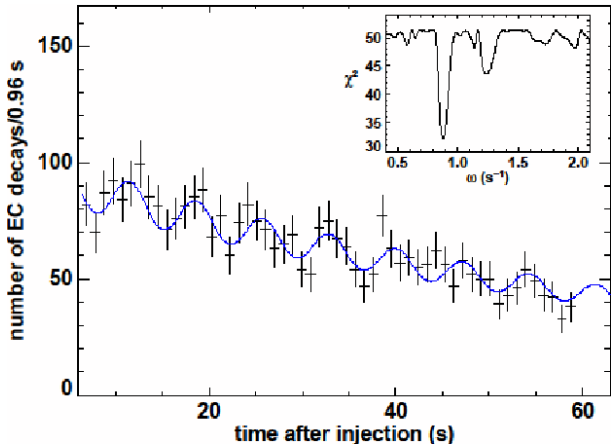

Figure 2: Number of EC decays per 0.96 s of hydrogen-like ^{142}Pm^{60+} ions, recorded by the 245 MHz resonator, vs. the time t after injection of the ions into the storage ring ESR. Displayed is also the modulation fit. The inset shows the χ^2 values vs. the angular frequency ω, for a fixed total decay constant λ and a variation of amplitude a and phase ϕ.

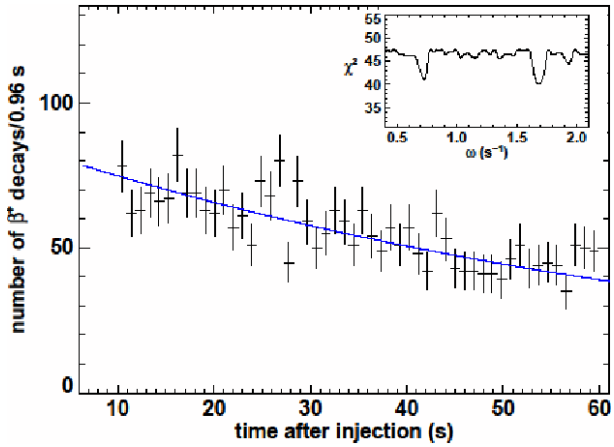

Figure 3: Number of β^+ decays per 0.96 s of hydrogen-like ^{142}Pm^{60+} ions, recorded by the 245 MHz resonator, vs. the time t after injection of the ions into the storage ring ESR. Displayed is also the exponential fit. The inset shows the χ^2 values vs. the angular frequency ω, for a fixed total decay constant λ and a variation of amplitude a and phase ϕ.

ent states, separated in the ion rest frame by an energy difference $\Delta E = h\gamma/T = 8.3 \cdot 10^{-16}$ eV, for $T = 7.11$ s and the Lorentz factor $\gamma = 1.43$ of the stored ions. To be able to confirm or disprove this suggestion, further experiments are mandatory which exploit other systems, different magnetic fields acting on the stored ions and which provide, first of all, significantly higher decay statistics.

References

[1] P. Kienle *et al.*, Phys. Lett. B **726** (2013) 638.

[2] Yu. A. Litvinov *et al.*, Phys. Lett. B **664** (2008) 162.

[3] F. Nolden *et al.*, Nucl. Instr. Meth. A **659** (2011) 69.

 doi:10.15120/GR-2014-1-PNI-AP-05

Further insight into Bayesian and Akaike information criteria of the EC-decay rate oscillations*

N. Winckler[1,2], F. Bosch[1], P. Bühler[3], T. Faestermann[4], P. Kienle†[4], Yu.A. Litvinov[1,2], M.S. Sanjari[1,5], D. Shubina[1,2], and the Two-Body Weak Decay collaboration[1]

[1]GSI, Darmstadt; [2]MPI-K, Heidelberg; [3]SMI, Vienna; [4]TU, Munich; [5]EMMI, Darmstadt

Introduction

We discuss the Akaike and Bayesian information criteria obtained from the model and data set presented in [1]. Both criteria are model-selection methods that consists in penalizing the log-likelihood as a function of the parameters: $\mathrm{IC}_i = -2\log(L(\hat{\theta}_i|\mathrm{data}, M_i)) + A_n K_i$. The Akaike information criterion (AIC) is a measure of the relative goodness of fit of a statistical model. Under appropriate conditions, the model that minimizes the AIC corresponds to the one that minimizes the Kullback-Leibler divergence with respect to the true unknown distribution.

The Bayesian Information Criterion (BIC) stems from Bayesian probabilities. If proper conditions are satisfied, it is twice the negative logarithm of the marginal likelihood, i.e. $-2\log(P(\mathrm{data}|M_i))$. From the BIC difference of model M_i and M_j, i.e. $\Delta\mathrm{BIC}_i$, an approximation of the Bayes' factor : $B_{i,j} \approx \exp(-\Delta\mathrm{BIC}_i/2)$ can be obtained. In this sense, the minimum BIC corresponds to the best model describing the data.

Results

The AIC and BIC values have been obtained from unbinned maximum likelihood method [2] and are thus free from any approximation. The AIC and BIC values as well as their differences and weights are listed in the table. Note that ΔAIC and ΔBIC values in the table are defined with respect to the minimum IC value : $\Delta\mathrm{IC} = \mathrm{IC}_i - \mathrm{IC}_{\mathrm{min}}$. The Bayesian and Akaike weights are both defined for two models M_i, M_j as $w_i = \frac{e^{-\Delta\mathrm{IC}_i/2}}{e^{-\Delta\mathrm{IC}_i/2}+e^{-\Delta\mathrm{IC}_j/2}}$. We observe that the AIC and BIC model selection methods can lead to different conclusion depending on the data.

Discussion: AIC vs BIC

It is *a priori* not trivial to choose between the AIC and BIC as they rely on various assumptions and asymptotic approximations, which in both cases are considered unrealistic [3]. Usually AIC prefers complex models and BIC simpler ones [3]. Although information criteria stem from different paradigms, the decision making of choosing M_1 rather than M_0 is mathematically equivalent to a likelihood ratio test in rejecting the null when:

$$-2\log(L_0/L_1) > A_n(K_1 - K_0) \qquad (1)$$

where the rejection region is given by the right hand term.The likelihood ratio distribution obtained from MC-toys is in very good agreement with a χ^2_4 distribution[1]. Thus, in the case of AIC, rejecting the null translates in the frequentist interpretation to a likelihood ratio test at an α level of $P(\chi^2_4 > 6) = 0.199$. In the case of BIC the α level depends on the sample size (c.f. α_{BIC} in table). Here we observe that AIC would have, in the frequentist interpretation, a Type I error rate of about 20% while for BIC the error rates decrease as the sample size increases and are all below $10^{-2}\%$. On the other hand, the Type II error rates are in general lower for AIC than for BIC [3]. Therefore in situations where Type I error has to be avoided, the BIC is usually prefered. And vice versa, AIC is recommanded against Type II error. In the case of the resonator EC-data M_1 is favoured if AIC is used and M_0 in the case of the BIC. In order to resolve this issue, a proper alternative would be the computation of the Bayes' factor from unbinned likelihood, which would significantly reduce the number of assumptions and approximations made.

	EC data (245 MHz res.)	β^+ data (245 MHz res.)	EC data (cap. pick-up)
N	3616	2912	2989
AIC_0	28683.5	22711.2	23718.4
AIC_1	28674.7	22710.4	23689.4
$\Delta\mathrm{AIC}_0$	8.78	0.8	29
w_0	1.2 %	40.1 %	$5 \times 10^{-5}\%$
w_1	98.8%	59.9%	$100(1-w_0)\%$
BIC_0	28689.67	22717.1	23724.4
BIC_1	28699.26	22734.3	23713.4
$\Delta\mathrm{BIC}_0$	0	0	11
$\Delta\mathrm{BIC}_1$	9.6	17	0
$B_{0,1}$	121.5	4914.7	0.0041
w_0	99.2%	99.98%	0.4%
w_1	0.8%	0.02%	99.6%
α_{AIC}	$\approx 20\%$	$\approx 20\%$	$\approx 20\%$
α_{BIC}	$6.1 \times 10^{-3}\%$	$8.2 \times 10^{-3}\%$	$7.96 \times 10^{-3}\%$

References

[1] P. Kienle et al. PLB 726 (2013) 638

[2] N. Winckler et al. GSI report 2013

[3] J. Dziak *et al.*, Penn. State U.,Tech. Rep. Ser. 12-119 (2012)

*Work supported in part by the DFG cluster of excellence "Origin and Structure of the Universe" of the Technische Universität München, the Helmholtz-CAS Joint Research Group HCJRG-108, the Alliance Program of the Helmholtz Association (HA216/EMMI), and the HIC-for-FAIR through HGS-HIRE

†deceased at January 29, 2013

[1]From the Wilks theorem one expects a χ^2_3 distribution which is not obtained from MC toys. Assuming the Wilks theorem is valid in our case, α_{AIC} reduces to 11.1% and α_{BIC} reduce slightly as well.

Increased lifetime of hydrogen-like ^{192m}Os observed in the ESR*

A. Akber[1], M.W. Reed[1], P.M. Walker[2], I.J. Cullen[2], Yu.A. Litvinov[3,4,5], K. Blaum[3,5], F. Bosch[4], C. Brandau[4,6], J.J. Carroll[7], D.M. Cullen[8], A.Y. Deo[2], B. Detwiler[9], C. Dimopoulou[4], G.D. Dracoulis[1], F. Farinon[4], H. Geissel[4,10], E. Haettner[10], M. Heil[4], R.S. Kempley[2], T. Kibédi[1], R. Knöbel[4,10], C. Kozhuharov[4], J. Kurcewicz[4,11], N. Kuzminchuk[4,10], G.J Lane[1], S. Litvinov[4], Z. Liu[12,13], R. Mao[13], C. Nociforo[4], F. Nolden[4], W.R. Plass[4,10], A. Prochazka[4], C. Scheidenberger[4,10], D. Shubina[3,5], M. Steck[4], Th. Stöhlker[4,14,15], B. Sun[4], T.P.D. Swan[2], G. Trees[9], H. Weick[4], N. Winckler[3,4], M. Winkler[4], P.J. Woods[12], and T. Yamaguchi[16]

[1]Department of Nuclear Physics, R.S.P.E., Australian National University, Canberra ACT 0200, Australia; [2]Department of Physics, University of Surrey, Guildford, Surrey GU2 7XH, United Kingdom; [3]Max-Planck-Institut für Kernphysik, Saupfercheckweg 1, 69117 Heidelberg, Germany; [4]GSI Helmholtzzentrum für Schwerionenforschung, Planckstraße 1, 64291 Darmstadt, Germany; [5]Physikalisches Institut, Universität Heidelberg, 69120 Heidelberg, Germany; [6]ExtreMe Matter Institute EMMI, 64291 Darmstadt, Germany; [7]US Army Research Laboratory, 2800 Powder Mill,Road, Adelphi MD, USA; [8]Schuster Laboratory, University of Manchester, Manchester M13 9PL, United Kingdom; [9]Youngstown State University, One University Plaza, Youngstown, Ohio 44555, USA; [10]II Physikalisches Institut, Justus-Liebig-Universität Gießen, 35392 Gießen, Germany; [11]CERN, 1211 Geneva 23, Switzerland; [12]School of Physics and Astronomy, University of Edinburgh, Edinburgh EH9 3JZ, United Kingdom; [13]Institute of Modern Physics, Chinese Academy of Sciences, Lanzhou 730000, PR China; [14]Institute of Physics, Friedrich-Schiller-Universität Jena, 07743 Jena, Germany; [15]Helmholtz-Institut Jena, Fröbelstieg 3, 07743 Jena, Germany; [16]Graduate School of Science and Engineering, Saitama University, Saitama 338-8570, Japan

Using the Experimental Storage Ring (ESR) it is possible to distinguish between charge states of an isotope with sensitivity down to single ions [1]. Projectile fragmentation of a ^{197}Au beam (478-492 A·MeV) with a ^{9}Be target was performed and the resultant fragments were passed through the FRagment Separator [2] where isotopes of interest were separted before being injected into the ESR. The ions were cooled by electron and stochastic cooling enabling Schottky Mass Spectrometry to be used and nuclear decays within the ESR are inferred from changes in ion revolution frequency [3].

Prior studies of ^{192}Os revealed an isomer with a lifetime of $\tau_{\rm neut} = 8.5(14)$ s at 2015 keV. Three decay branches have been observed with transition energies of 47, 302, and 307 keV [4]. Neutral [5] and hydrogen-like internal conversion coefficients were calculated and indicate a decrease for all transitions (Table 1). For the 47 keV transition internal conversion in the hydrogen-like state is forbidden. An increased lifetime of $\tau_{\rm calc} = 13.0(24)$ s due to the reduction of internal conversion can be expected.

Table 1: Calculated total internal conversion coefficients for transitions from ^{192m}Os [4, 5].

$E_{\rm trans}$	I_γ	$\sigma\lambda$	$\alpha_{t\,(\rm neut)}$	$\alpha_{t\,(\rm H-like)}$
47.4	0.0031(6)	E3	7760	0
302.6	100(6)	E3	0.433	0.084
307.0	13.3(3)	M2	0.975	0.374

*Work supported in part by the Helmholtz-CAS Joint Research Group HCJRG-108, National Natural Science Foundation of China (No. 11105010), the Australian Research Council, UK STFC and AWE plc.

An increased lifetime for ^{192m}Os was measured from observations of 106 single hydrogen-like ions in the ESR (Figure 1). After Lorentz correction ($\gamma = 1.4$) the measured mean lifetime of ^{192m}Os^{75+} was $\tau_{\rm Lorentz} = 14.2(16)$ s. The observed increase in lifetime is attributed to the reduction of internal conversion because of the high charge state.

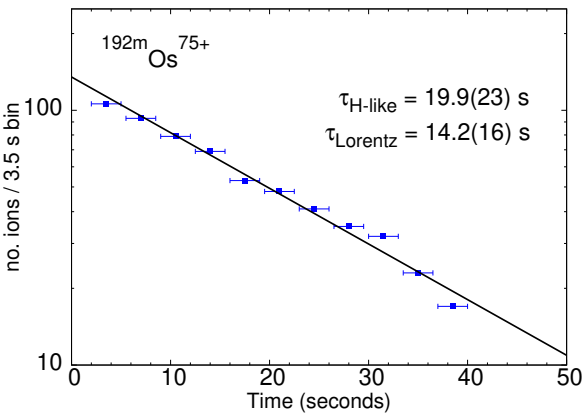

Figure 1: Lifetime curve for ^{192m}Os^{75+} produced by direct observation of highly charged single ions in the ESR.

References

[1] Yu. Litvinov, *et al.*, Nucl. Phys. A **756**, 3 (2005).

[2] H. Geissel *et al.*, Nucl. Inst. Meth. B **70**, 286 (1992).

[3] Yu. Litvinov & F. Bosch, Rep. Prog. Phys. **74**, 016301 (2011).

[4] G.D. Dracoulis *et al.*, Phys. Lett. B **720**, 330 (2013).

[5] T.Kibédi *et al.*, Nucl. Inst. and Meth. A **589**, 202 (2008).

 doi:10.15120/GR-2014-1-PNI-AP-07

Odd-Even Staggering in Fragment Yields from ^{78}Kr+Be Reactions *

B. Mei[1,2,3], *H. S. Xu*[1], *X. L. Tu*[1,2,4], *Y. H. Zhang*[1], *Yu. A. Litvinov*[1,2,4], *K. -H. Schmidt*[2], *M. Wang*[1], *Z. Y. Sun*[1], *X. H. Zhou*[1], *Y. J. Yuan*[1], *M. V. Ricciardi*[2], *A. Kelić-Heil*[2], *R. Reifarth*[3], *K. Blaum*[4], *R. S. Mao*[1], *Z. G. Hu*[1], *P. Shuai*[1,5], *Y. D. Zang*[1], *X. W. Ma*[1], *X. Y. Zhang*[1], *J. W. Xia*[1], *G. Q. Xiao*[1], *Z. Y. Guo*[1], *J. C. Yang*[1], *X. H. Zhang*[1], *X. Xu*[1], *X. L. Yan*[1,4], *W. Zhang*[1], *and W. L. Zhan*[1]

[1]IMP, Lanzhou; [2]GSI, Darmstadt; [3]University of Frankfurt; [4]MPIK, Heidelberg; [5]USTC, Hefei

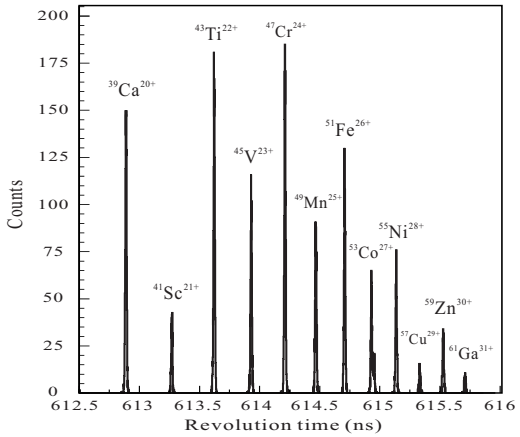

Figure 1: A part of the measured revolution time spectrum of the $T_z = -1/2$ nuclides produced in ^{78}Kr fragmentation reactions on Be target.

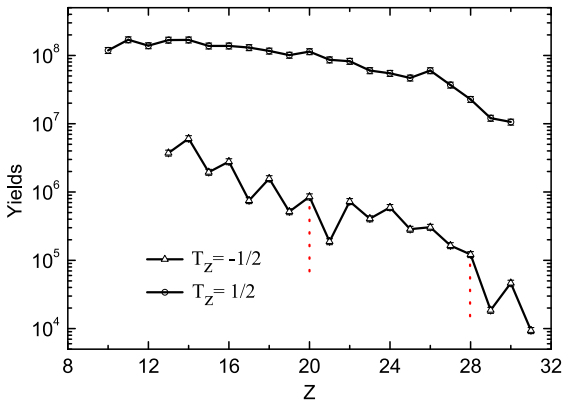

Figure 2: Fragment yields of $T_z = -1/2$ and $T_z = 1/2$ nuclei measured in this experiment. The closed shells $Z = 20$ and 28, where the strongest OES is reached for the $T_z = -1/2$ nuclei, are indicated.

Nuclear fragmentation yields can provide unique information on nuclear structure properties, e.g. pairing, shell effects, and densities of excited levels. Odd-even staggering (OES) in the fragment yields, that is the enhancement in the yields of the even-Z nuclides compared with the neighbouring odd-Z nuclides, has been observed for different fragmentation reactions [1]. But an understanding of the origin of this OES is not yet reached. Our study allowed for the first time to quantitatively understand the origin of this OES.

OES in the fragment yields has been measured in the storage ring CSRe at the HIRFL-CSR facility in Lanzhou [2]. The fragments were produced in the ^{78}Kr+Be reactions at an energy of 482.9 AMeV. The $T_z = -1/2$ and $T_z = 1/2$ nuclides of interest were transmitted through RIBLL2 and injected into CSRe, which was tuned into an isochronous mode [3]. In this mode the revolution times of ions, which were measured using a dedicated time-of-flight detector [4], are used to measure their m/q values. Fig. 1 shows a part of the measured revolution-time spectrum of the $T_z = -1/2$ nuclides.

The momentum distributions and the transmission efficiencies for various fragments were estimated by using the LISE++ program [5]. The transmission efficiency varies almost smoothly with Z along a chain of nuclides with a constant T_z. The yields of $T_z = -1/2$ and $T_z = 1/2$ nuclei are presented in Fig. 2. The OES is very evident for the yields of the $T_z = -1/2$ nuclei, but small for the $T_z = 1/2$ nuclei. For the $T_z = -1/2$ nuclei, a sharp drop of the fragment yields near the closed shells $Z = 20$ and 28, where the strongest OES is shown, is observed for the first time. To our knowledge, no nuclear reaction model can reproduce the above OES over such a wide range of mass numbers, especially for the $T_z = -1/2$ nuclei.

The measured OES in the yields for the $T_z = -1/2$ and $T_z = 1/2$ mirror nuclei enabled us to compare the relative OES in fragment yields and the relative OES in PETE of mirror nuclei [6]. This comparison reveals unambiguously that the origin of the OES of fragment yields is mainly determined by the OES of the particle-emission threshold energies, where the impact of both pairing correlations and evident shell effects are clearly observed.

References

[1] M. V. Ricciardi et al., Nucl. Phys. A733 (2005) 299.

[2] J. W. Xia et al., Nucl. Instr. Meth. A 488 (2002) 11.

[3] B. Franzke et al., Mass Spectrom. Rev. 27 (2008) 428.

[4] B. Mei et al., Nucl. Instr. Meth. A 624 (2010) 109.

[5] O. Tarasov et al., Nucl. Instr. Meth. B 266 (2008) 4657.

[6] B. Mei et al., submitted.

* Work supported in part by the BMBF WTZ grant (No. 01DO12012), by the Helmholtz-CAS Joint Research Group HCJRG-108, by the HGF Young Investigators Projects VH-NG-327, by the ESF through EuroGENESIS program, by the 973 Program of China (No. 2013CB834401), and by the NNSFC grants 10925526, 111035007, 10675147, 10805059, U1232208, 1135005, 11075103, 11205205.

A study of Coulomb displacement energies for nuclides with A around 67*

X. L. Tu[1,2,3], *Y. H. Zhang*[†2], *H. S. Xu*[2], *Y. Sun*[2,4], *K. Kaneko*[5], *M. Wang*[2], *and Yu. A. Litvinov*[‡1,2,3]

[1]GSI, Darmstadt, Germany; [2]IMP, LanZhou, China; [3]MPIK, Heidelberg, Germany; [4]SJTU, China; [5]KSU, Japan

If one assumes that nuclear force is charge symmetric, Coulomb displacement energy (CDE) can be extracted as the binding energy difference of mirror nuclei [1]. CDEs play an important role in nuclear structure, like e.g., can be use to study deformation of nuclei [2]. Recent experiments provided a wealth of new data on nuclear masses of neutron-deficient nuclei, either measured for the first time or with significantly improved uncertainties [3]. With these mass data, experimental CDEs (ΔE_c) for the T=1/2 mirror nuclei up to A=73 in pf-shell can be mapped, as Fig. 1 shows.

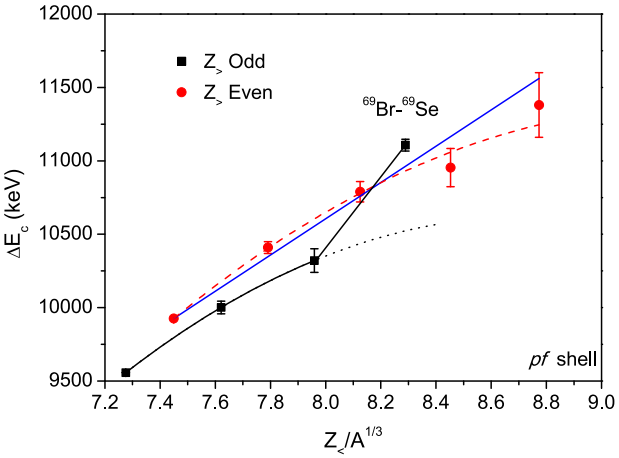

Figure 1: Coulomb displacement energy for the $T = 1/2$ mirror nuclei in the fp-shell as a function of $Z_</A^{1/3}$, labelled differently for odd-$Z_>$ and even-$Z_>$. ΔE_c for even-$Z_>$ were fitted by a linear function (solid line) and second order polynomial function (dashed line) of $Z_</A^{1/3}$, respectively. For odd-$Z_>$, the dotted line shows an expected tendency obtained by second order polynomial fitting.

For a homogeneously charged spherical nucleus, the CDEs can be fitted well by an empirical linear formula. However, it is well known that the deformation can lead to modifications of single-particle states and cause qualitative changes in the structure, and therefore can alter the linear dependence of CDE on $Z_</A^{1/3}$. If one assumes that a deformed nucleus has a quadrupole deformation, β, then the modified CDE, $\Delta E_c(\beta)$, can be estimated by the following expression [2],

$$\triangle E_c(\beta) \simeq \triangle E_c(0)\left[1 - \frac{4}{45}\beta^2\right] \qquad (1)$$

where $\Delta E_c(0)$ is the spherical CDE, which can be fitted by using the known spherical nuclei.

The notable difference from the spherical shells is that the CDE values in the fp-shell can not be fitted by a linear function of $Z_</A^{1/3}$, but show a slowing-down increase as $Z_</A^{1/3}$ increases [4]. The data are better fitted by a second order polynomial function as described by Eq. (1) with non-zero deformation parameters. This implies that spherical shape of nuclei starts to change at $Z_</A^{1/3} \sim 7.96$ (corresponding to $A = 65$ and $Z_> = 33$) and the quadrupole deformation β is developed for larger $Z_</A^{1/3}$ values. This is precisely the region where Hasegawa *et al.* [5] suggested, based on the study of the low-lying energy levels, that a spherical-to-deformed shape phase transition occurs along the $N \approx Z$ line.

Another feature seen in Fig. 1 is the staggering of the CDE values between the groups with odd-Z and even-Z. This so-called odd-even staggering is such that CDE with even-$Z_>$ are larger than the CDE with odd-$Z_>$. The occurrence of the odd-even staggering in CDE was first explained by Feenberg and Goertzel [6] as being due to the fact that the paired protons with antiparallel spins have a space-symmetric wave function in their relative coordinates and therefore repel each other stronger than the pairs with parallel spins. This strong Coulomb repulsion for systems with all protons paired leads to larger CDE values for even-$Z_>$. However, with the new data, as seen in Fig. 1, the data point for the ^{69}Br-^{69}Se mirror pair obviously departures from the staggering rule, and the regular trend of the odd-even staggering is thus destroyed. This is the first observation of this apparent anomaly, which has to be questioned theoretically on possible fundamental reasons as well as experimentally on possible systematic errors of the corresponding measurements [4].

References

[1] B. A. Brown *et al.*, Phys. Rev. C **65**, 045802 (2002).

[2] M. S. Antony and V. B. Ndocko Ndongue, Il Nuovo Cimento **93**, 249 (1986).

[3] M. Wang *et al.*, Chin. Phys. C **36**, 1603 (2012).

[4] X. L. Tu *et al.*, J. Phys. G **41**, 025104 (2014)

[5] M. Hasegawa *et al.*, Phys. Lett. B **656**, 51 (2007).

[6] E. Feenberg and G. Goertzel, Phys. Rev. **70**, 597 (1946).

*Work supported by by NSFC grant no. 11205205, by the BMBF grant in the framework of the Internationale Zusammenarbeit in Bildung und Forschung Projekt-Nr. 01DO12012 and by the Helmholtz–CAS Joint Research Group HCJRG- 108

† YHZhang@impcas.ac.cn

‡ Y. Litvinov@gsi.de

 doi:10.15120/GR-2014-1-PNI-AP-09

Angular differential measurement of linear polarization of elastically scattered hard x-rays.*

M. Schwemlein[1,2,3], K.-H. Blumenhagen[4,5], T. Gassner[4,6], T. Groß[7], A. Gumberidze[1,2], R. Märtin[4,6], N. Schell[8], U. Spillmann[4,6], S. Trotsenko[4,6], G. Weber[4,6], and Th. Stöhlker[4,5,6]

[1]ExtreMe Matter Institute EMMI, Darmstadt, Germany, ; [2]FIAS, Frankfurt a.M., Germany;
[3]PI, Univ. Heidelberg, Germany; [4]HI-Jena, Jena, Germany; [5]IOQ, Univ. Jena, Germany; [6]GSI, Darmstadt, Germany;
[7]IGVP, Univ. Stuttgart, Germany; [8]HZG, Geesthacht, Germany

Elastic scattering of photons from atoms and molecules, also known as Rayleigh scattering, is one of the fundamental processes in the interaction of light with matter. Understanding of this scattering process, in particular in the hard X-ray regime, is important for various applications such as medical imaging, material research and it also provides information about the inner structure of atomic and molecular systems [1,2]. Also from theoretical point of view, there is ongoing interest at present [3,4].

Former experimental studies of this scattering process have used either unpolarized or linearly polarized photon sources to investigate the angular distribution and absolute peak intensities of the scattered radiation. However, the polarization properties of the elastically scattered photons have not been resolved up to now. Due to recent development in coherent light sources on one side and highly-segmented semiconductor based detection systems [5,6] on the other, it became feasible to control both, the polarization of the incident as well as the scattered photons.

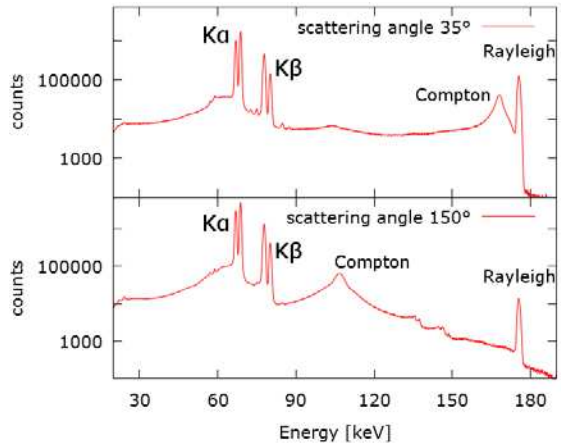

Figure 1: Ge(i) detector response to synchrotron radiation that is scattered at a Au target under 35° and 150°. The characteristic target radiation $K\alpha_2$ (67 keV), $K\alpha_1$ (68.8 keV), $K\beta_1$ (77.9 keV) and $K\beta_2$ (80.1 keV) is clearly visible. The 175 keV line correspond to elastic Rayleigh-scattering. The broader structure, shifting with the scattering angle, correspond to inelastic Compton scattering.

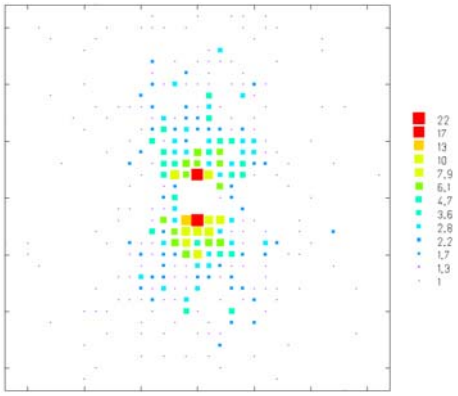

Figure 2: 175 keV X-rays are elastically scattered in the Au target at a scattering angle of 120°. These Rayleigh photons are again Compton-scattered in the Si(Li) detector crystal. The figure shows their position distribution inside the Si(Li) detector with respect to the scattering position.

The present experiment aims to measure the angular distribution and polarization of the initially linearly polarized hard x-rays, scattered off a high-Z target. Therefore, a Si(Li) Compton polarimeter, developed for experiments at the international FAIR facility, as well as standard Ge(i) detectors have been used. The experiment took place at the DESY PETRA III beamline P07-EH3, where nearly 100% linearly polarized photons in the hard X-ray regime can be produced.

Fig. 1 shows the Ge(i) detector response to the radiation, coming from the target. A thin Au foil was used as the target. The synchrotron radiation energy was set to 175 keV. Fig. 2 shows the position distribution of Compton scattered photons (elastically scattered in the target) inside the Si(Li) detector crystal. The anisotropy indicates a high degree of linear polarization of the Rayleigh-scattered photons from the Au target. The data are currently being evaluated.

References

[1] S. C. Roy, Radiat. Phys. Chem. **41**, 725 (1993).

[2] M. Y. Sfeir et al., Science **306**, 1540 (2004).

[3] A. Surzhykov, Phys. Rev. A **88**, 062515 (2013).

[4] L. Safari, Phys. Rev. A **85**, 043406 (2012).

[5] U. Spillmann et al., Rev. Sci. Instr. **79**, 083101 (2008).

[6] G. Weber et al., JINST **5**, C07010 (2010).

* Work supported by HGS-Hire / Helmholtz Alliance EMMI / DESY and HZG support at beamline P07.

Demonstrator: Electronic Readout for a Si(Li) – Compton – Polarimeter

U. Spillmann[1,2], E. Badura[1], K.H. Blumenhagen[2], H. Bräuning[1], J. Hoffmann[1], K. Koch[1], N. Kurz[1], R. Märtin[2], S. Minami[1], W. Ott[1], I. Rusanov[1], Th. Stöhlker[1,2,3], G. Weber[2], and M. Weber[4]

[1]GSI, Darmstadt, Germany; [2]HI Jena, Jena, Germany; [2]IOQ, Friedrich-Schiller-Universität, Jena, Germany; [2]IPE, KIT, Karlsruhe, Germany

Within the portfolio process of the Helmholtz Association Detector Technology and System Platform (DTS) [1] KIT, GSI, and HI Jena collaborate closely bringing together the expertise of the partners in the development of advanced detector readout systems. As one of the first common projects we develop a self-triggering 2-dimensional position-, time-, and energy sensitive Si(Li)-strip detector read out with modern custom designed FPGA-based signal digitizer hardware as a demonstrator system. This project is of great importance for future x-ray spectroscopy and polarimetry experiments of the SPARC collaboration [2] at GSI and FAIR. As detector platform we have chosen an already existing Si(Li)-strip detector [3] that has worked reliable in several beam times at the ESR as well as external places, e.g. TU Darmstadt and DESY, Hamburg, and has produced excellent results [4]. Up to now it was equipped with standard NIM and VME electronic. The outcome of this project using custom designed FPGA-based signal digitizer hardware will serve as a blue print for the next generation of compact and cost efficient readout electronics of thick planar strip detectors within the collaboration. The concept is based on the fast digitizing of the preamplifier signals coming from the detector to acquire the small signals directly. The consecutive employment of pulse shape analysis techniques will show the energy and timing information of an event. For this first demonstrator we profit from recent developments of the Experiment Electronics department of GSI. They provided us with a set of 8 FEBEX2 – ADC boards [5] with 8 input channels each. Sampling the data is performed with a frequency of 65 Ms/s and a resolution of 12 bit at an input range of +/-1V. A 1.6 Gbit fibre link connects the digitizer board with the PLEXOR3-PCIe Interface hosted by a commercial PC that manages the event building and data transport by ethernet. In addition a TRIXOR-PCIe board takes over the trigger handling and the dead time locking. The PC runs a LYNX RT-operating system and as DAQ we employ MBS [6] to take advantage of the GSI data acquisition and storage environment. With this system we studied the electronic response of the strip detector system for offline testing of appropriate pulse shape analysis algorithms. Meanwhile we moved to the next FEBEX generation (version 3a) which is a 16 channel ADC-board with differential inputs. The FEBEX3a boards are mounted in a crate with PCIe backplane together with a fibre link interface to fit into the existing DAQ environment. The digitizer cards host enough on-board FPGA resources to perform online self-triggering, double hit detection and trapezoidal filters for energy and timing applications. To adapt the signal output of the preamplifier to the input of the FEBEX3a board the fast linear amplifier SiLiVer was developed. At a later stage the small form factor of the amplifier boards will allow us to mount them inside the preamplifier housing to avoid losses on the signal cables. The main goal of this first step is to rebuild the functionality of the NIM and VME hardware and to be able to handle photo effect and Compton events. From this point on we can make use out of the system in atomic physics experiments. In collaboration with the KIT we will refine the algorithms for the digital pulse shape analysis with the aim to manage more complex event histories like two or three Compton events for one incident photon. We plan to meet the demand of increased computing power by dedicated hardware solutions designed by KIT.

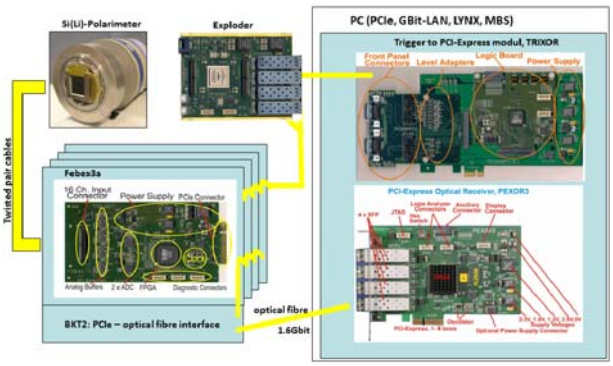

Figure 1: Sketch of the new readout chain of the Si(Li)-Polarimeter Demonstrator

References

[1] http://www.helmholtz-detectors.de

[2] Technical Report of the SPARC collaboration http://www.gsi.de/fair/experiments/sparc/index_e.html

[3] G. Weber et al., "Performance of a position sensitive Si(Li) x-ray detector dedicated to Compton polarimetry of stored and trapped highly-charged ions", JINST 5,C07010 (2010)

[4] Th. Stöhlker et al., "Polarization and angular correlation studies of X-rays emitted in relativistic ion-atom collisions", EPJ-ST 169, 5-14 (2009)

[5] https://www.gsi.de/fileadmin/EE/Module/FEBEX/febex2.pdf

[6] http://www-win.gsi.de/daq/

 doi:10.15120/GR-2014-1-PNI-AP-11

Dominant secondary nuclear photoexcitation with the XFEL

J. Gunst[*1], *Y. A. Litvinov*[†2], *C. H. Keitel*[‡1], *and A. Pálffy*[§1]

[1]Max-Planck-Institut für Kernphysik, Heidelberg, Germany; [2]GSI, Darmstadt, Germany

Photon energies accessible with the new x-ray free-electron laser (XFEL) facilities open the way for the resonant driving of nuclear transitions. In particular, the high brilliance and coherence features of the XFEL light promise an increase in nuclear excitations in comparison to synchrotron radiation experiments. While in the latter experiments the electronic response only acted as background, the unique interaction between high-intensity XFEL pulses and matter can lead to new states, like cold, high-density plasmas [1] where secondary nuclear processes from the coupling to the atomic shell are rendered possible. In this work we show on the example of $^{93\mathrm{m}}$Mo isomer triggering that secondary nuclear excitation by electron capture (NEEC) can even dominate the direct resonant photoexcitation.

The idea of isomer triggering is to connect the metastable isomeric state to an above-lying level in order to release the stored excitation energy on demand [2]. The 6.85 h long-lived $^{93\mathrm{m}}$Mo isomer is particularly attractive for an XFEL-induced activation, since the 2.5 MeV excitation energy can be retrieved by a 4.85 keV triggering transition accessible by todays XFELs. In the subsequent decay cascade an outstandingly high energetic photon of 1 MeV can be used as distinct signature for the nuclear excitation. Moreover, in $^{93}_{41}$Nb(p,n)$^{93\mathrm{m}}_{42}$Mo reactions, the isomers can be produced directly embedded into 1 μm thick niobium foils, providing high-density targets. Using, for instance, the LINAC proton beam at GSI a density of 10^{16} isomers/cm^3 can be achieved.

The direct light-nucleus coupling between the XFEL radiation and the Nb target foils can be described by the density matrix formalism using the semiclassical approach. Although the XFEL pulse is tuned on the 4.85 keV triggering transition, only a small fraction of the laser photons fulfill the nuclear resonance condition due to the large discrepancy between the laser width Γ_{XFEL} ($\sim$10 eV) and the nuclear transition width Γ_{n} ($\sim 10^{-7}$ eV). Taking this effective intensity reduction into account and considering laser parameters for the LCLS at SLAC a signal rate of 5.6×10^{-14} photons/s is obtained [3]. A further analysis shows that the nuclear photoexcitation is strongly suppressed by the poor temporal coherence of current XFEL facilities.

The nuclear excitation induced directly by the laser should be compared to its secondary electronic-processes-induced counterpart. The XFEL-induced plasma formation is governed by inner-shell photoionization and subsequent refilling by either radiative or Auger decay. Due to the fast and uniform heating process the plasma stays almost at solid-state density. After the irradiation of the sample, radiative and collisional processes lead to a fast thermalization among the electrons. In our scenario, we estimate an electron temperature T_e and density of 350 eV and 1.3×10^{24} cm^{-3}, respectively, and consider the plasma conditions to hold for 100 ps.

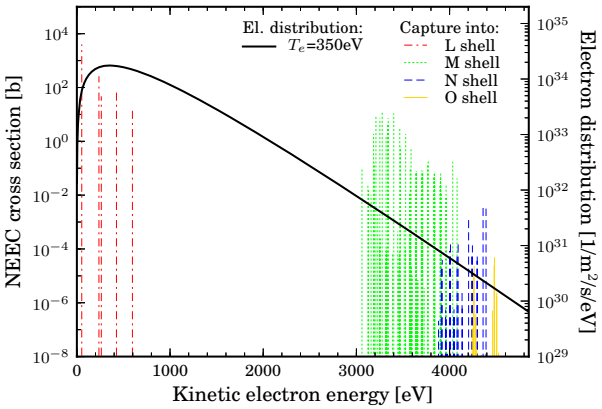

Figure 1: NEEC resonance cross sections (left axis) together with the electronic energy distribution (right axis).

In this environment, NEEC takes place on a longer time scale compared to the laser pulse duration. The total NEEC rate in the plasma relies on the available charge states and electron energies. As shown in Fig. 1, NEEC prefers the capture into deep vacancies. At T_e=350 eV, the L shell seems to provide the pivotal NEEC channels. However, the available charge states are limited to q=18+...30+ prohibiting the capture into the L shell. Nevertheless, a summation over all open resonance channels results in a NEEC-induced signal rate of 1.7×10^{-7} photons/s which is 6 orders of magnitude higher than the direct process [3]. Additionally, NEEC represents the more robust mechanism since it is less sensitive to the match between the photon frequency and the nuclear resonance condition.

References

[1] S. Vinko *et al.*, Nature **482**, 59 (2012).

[2] A. Pálffy *et al.*, Phys. Rev. Lett. **99**, 172502 (2007).

[3] J. Gunst *et al.*, Phys. Rev. Lett. **112**, 082501 (2014).

* Jonas.Gunst@mpi-hd.mpg.de
† Y.Litvinov@gsi.de
‡ Keitel@mpi-hd.mpg.de
§ Palffy@mpi-hd.mpg.de

The HILITE Penning trap and first tests at the HILITE setup

M. Vogel[1,2], *W. Quint*[2,3], *G. Paulus*[4], *and Th. Stöhlker*[2,4,5]

[1]TU Darmstadt; [2]GSI, Darmstadt; [3]Ruprecht Karls-Universität Heidelberg; [4]Universität Jena; [5]Helmholtz-Institut Jena

We have built a dedicated Penning trap for preparation and control of suitable ion targets for irradiation with high-intensity laser light and study of subsequent reactions, depicted in figure 1. Of particular interest is the detailed investigation of multiphoton-ionisation of confined particles by highly intense laser light. One important aspect is control over the confined particles' mass, charge, density, localization and optimized overlap with the laser light by Penning trap techniques like the use of trap electrodes as 'electrostatic tweezers' and by application of a 'rotating wall', respectively [1]. Also, the non-destructive detection of reaction products is a central property. The Penning trap setup is designed in a portable fashion, such that it can be attached to existing laser systems easily, see figure 2.

The interaction of highly intense radiation with matter and the corresponding non-linear effects have been subject of lively research, both theoretical and experimental, especially in the infrared and visible photon energy regimes. Laser systems capable of producing high intensities also at photon energies in the extreme ultra-violet (EUV) and (soft) X-ray regime open access to novel effects like non-linear Compton effects or simultaneous elastic and inelastic photon scattering, and allow multiphoton-ionisation experiments in a new domain. However, experiments have so far not been able to prepare and investigate well-defined particle ensembles and to non-destructively analyse the reaction products with high accuracy, nor were they able to select or prepare products for further studies in a well-defined way.

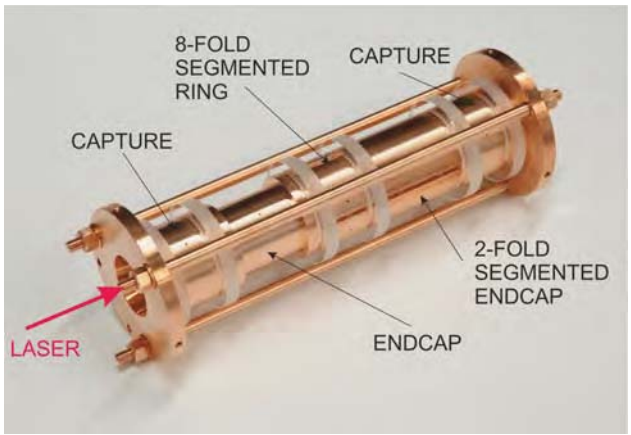

Figure 1: Photography of the HILITE Penning trap. The function of the individual electrodes is indicated, separation between electrodes is achieved by Sapphire rings (milky white).

The particles (atomic or molecular ions) are confined in the Penning trap following in-trap production or capture of externally produced ions. Confined ions can be cooled, compressed, positioned and selected with respect to their mass and charge prior to laser irradiation. The reaction products are analysed by non-destructive methods and hence remain confined for further studies. Such measurements are, for example, able to determine cross sections for multiphoton-ionisation in an energy- and intensity- regime so far not or not sufficiently examined. Additionally, the created electrons may be extracted from the trap and analysed externally. Hence, the reaction energetics may be reconstructed as completely as possible.

Figure 2: Photography of the HILITE superconducting magnet setup. The Penning trap from figure 1 will be installed in the centre of the magnet bore.

By now, we have completed the vacuum system which will host the Penning trap inside the magnet bore and cool it to cryogenic temperatures using a two-stage cryocooler. The magnet has been operated at fields up to 6 T and the vacuum system has successfully been tested to leak rates below the 10^{-10} mbar l/s scale. We will now focus on the operation and detection electronics as well as on connectivity to an external (EBIT) ion source for highly-charged ions.

References

[1] M. Vogel, W. Quint, Th. Stöhlker and G.G. Paulus, Nucl. Inst. Meth. B **285**, 65 (2012).

 doi:10.15120/GR-2014-1-PNI-AP-13

Highly charged ions at SpecTrap*

T. Murböck[1], G. Birkl[1], A. Martin[1], M. Vogel[1], K. König[2], W. Nörtershäuser[2], S. Schmidt[2], S. Scholl[2], Z. Andelkovic[3], V. Hannen[4], J. Vollbrecht[4], C. Weinheimer[4], D. Segal[5], and R. Thompson[5]

[1]IAP, TU Darmstadt; [2]IKP, TU Darmstadt; [3]GSI, Darmstadt; [4]Westfälische Wilhems-Universität, Münster; [5]Imperial College London

The SpecTrap collaboration aims at high precision laser spectroscopy of forbidden transitions in highly charged ions (HCIs). Similar experiments performed to date with ions stored in an EBIT or in a storage ring still suffer from Doppler broadening or the difficulties in wavelength conversion between the laboratory frame and the rest frame [1, 2]. Therefore, the SpecTrap experiment employs a cryogenic Penning trap suitable for trapping externally produced ions and sympathetically cooling them with laser cooled Mg^+ ions [3]. Cooling of HCI to the mK-regime will dramatically reduce the Doppler broadening of the fluorescence signal and allow the measurement of the hyperfine splitting of the HCI with an expected relative accuracy of 10^{-8} for a stringent test of bound state QED.

In 2013, a new beamline was installed at the HITRAP platform to connect a commercial EBIT with the SpecTrap Penning trap [4]. This EBIT can be used to produce argon ions with any desired charge state up to bare Ar. Since Ar^{13+} is a suitable candidate for a laser-accessible, forbidden transition in a HCI, the beamline has been optimised for maximum transmission of this charge state. Several 10^4 Ar^{13+} ions have been transported with a kinetic energy of 4 keV/q to the SpecTrap experiment. Because of the maximum voltage that can be applied to the trap electrodes only low energy ions with kinetic energies of a few hundreds eV/q can be trapped in the SpecTrap-Penning trap whereas much lower transport energies would be desirable. Unfortunately, intra-beam scattering and electron capture sets constraints to the minimum transport energy of the beam and further reduction of the current value of 4 keV/q would lead to much lower transport efficiency from the EBIT to the trap. Therefore, a pulsed drift tube has been installed close to the trap and used to decelerate several 10^4 Ar^{13+} ions in a single bunch to energies as low as 600 eV/q. Ions with this energy can be easily trapped with the Penning trap's electrodes and the number of Ar^{13+} ions even in one single bunch is now sufficient for the designated spectroscopy experiments at SpecTrap.

Prior to the installation of the HITRAP beamline, the experiment had been connected to two different ion sources simultaneously. The first source supplied the experiment with singly charged magnesium, the second one with Ar^+ and Ar^{2+}. With this setup, alternating trapping of Mg^+ and Ar^+ was demonstrated, being the first step for simultaneous storage and sympathetic cooling of HCI. Ar^+ transported with a kinetic energy of 600 eV has been trapped and electronically detected with the resonant circuit attached to the endcaps of the SpecTrap Penning trap. Furthermore, resistive cooling of Ar^+ with the resonant circuit has been demonstrated as well. Different ion species and charge states were identified via their axial and radial oscillation frequencies. To this end, the trap parameters that influence the axial oscillation frequency have been determined with the species Mg^+ and Ar^+. Resonant excitation of different ion species has been performed and detected by changes in the fluorescence signal of $^{24}Mg^+$ (see Fig. 1). This demonstrates the potential for non-destructive detection and identification of arbitrary ion species.

With these tools at hand, the SpecTrap experiment is ready for trapping and detection of HCI like Ar^{13+}. In a first step the storage time, resistive, and sympathetic cooling and the interaction between Ar^{13+} and Mg^+ will be investigated. As soon as a cold and dense ion cloud of Ar^{13+} is available, the forbidden transition of Ar^{13+} will be measured in a high precision laser spectroscopy experiment, followed by experiments with different ion species like Ca^{14+} and Bi^{82+} once HITRAP is fully operational.

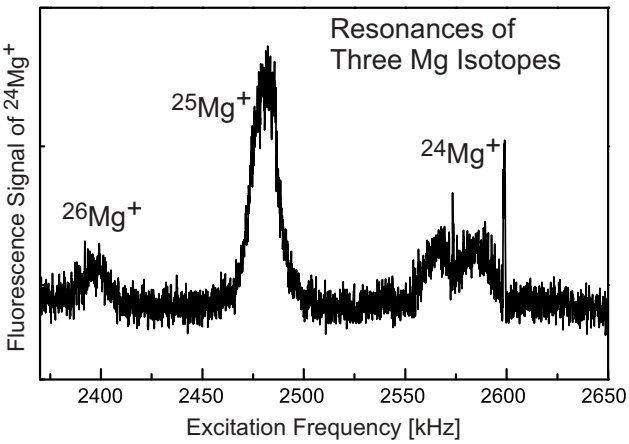

Figure 1: Reduced cyclotron frequencies ν_c of $^{24-26}Mg^+$ isotopes. Excitation of ν_c changes the state of the ion cloud and therefore increases the fluorescence signal received from ^{24}Mg isotopes.

References

[1] Mäckel et al., Phys. Rev. Lett. 107, 143002 (2011)

[2] Lochmann et al., arXiv:1401.8224 (2013)

[3] Murböck et al., Phys. Scr. T156 (2013)

[4] Andelkovic et al., GSI Scientific Report (2013)

*This work has been supported financially by BMBF (05P12RDFA4, 06DA9020I), DFG, EPSRC, GSI, HGS-HiRe and HIC for FAIR.

In-trap production of highly charged ions at ARTEMIS

M. Vogel[1,2], *G. Birkl*[1], *D. von Lindenfels*[2,3], *A. Martin*[1], *W. Quint*[2,3], *and M. Wiesel*[1,2,3]
[1]Institut für Angewandte Physik, TU Darmstadt; [2]GSI, Darmstadt; [3]Ruprecht Karls-Universität Heidelberg

We are currently setting up a laser-microwave double-resonance spectroscopy experiment with highly charged ions in a Penning trap, which combines precise spectroscopy both of optical transitions and microwave Zeeman splittings [1, 2, 3]. The experiment aims at spectroscopic precision measurements of such energy level splittings and magnetic moments of bound electrons on the ppb level of accuracy and better. For first tests, the $^{40}Ar^{13+}$ ion has been chosen. It has a spinless nucleus, such that only a fine structure is present. Similar measurements in hyperfine structures are to be performed with ions of higher charge states such as for example $^{207}Pb^{81+}$ and $^{209}Bi^{82+}$ as available to ARTEMIS within the framework of the HITRAP facility.

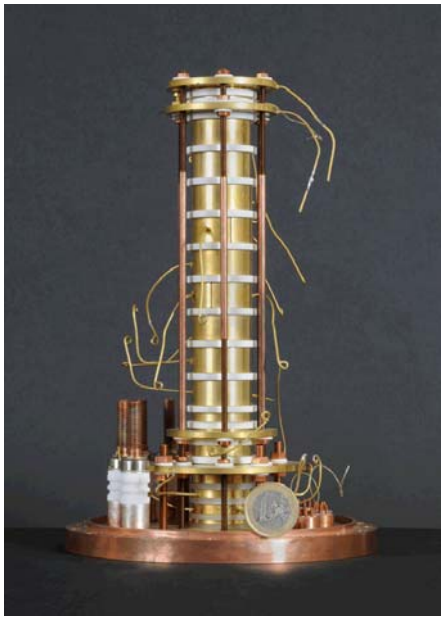

Figure 1: Photography of the ARTEMIS Penning trap, in which the ions are created and confined for spectroscopy.

In an external magnetic field, the Zeeman effect lifts the degeneracy of energies within fine- and hyperfine-structure levels. For highly charged ions in magnetic fields of a few Tesla strength, the Zeeman splitting is well within the microwave domain and thus accessible for precision spectroscopy. In addition, in case of fine- and hyperfine-structure transitions, the strong scaling with Z eventually shifts the corresponding energies into the laser-accessible region and thus makes them available for precision optical spectroscopy [1]. Figure 1 shows the Penning trap of the ARTEMIS experiment, in which the ions of interest are created and confined for spectroscopy. Creation takes place by electron impact ionization in close similarity to the charge breeding processes used in electron beam ion sources (EBIS). We have installed this trap arrangement in the superconducting magnet of the ARTEMIS experiment, and have used an EMCCD-camera to detect photons emitted during the charge breeding process of highly-charged argon ions. Figure 2 shows a false-colour image from this camera looking into the cylindrical trap along its symmetry axis from above. This optical tracking of the ion creation

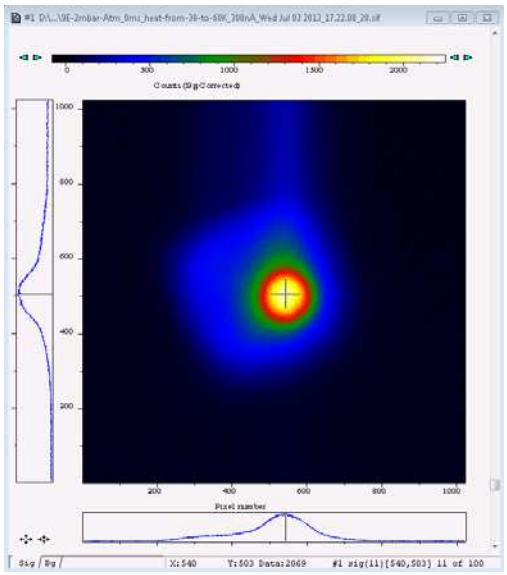

Figure 2: EMCCD-image of photons emitted during creation of highly-charged ions in the trap.

process is a powerful diagnostic tool to control and optimize the charge breeding process in real-time. In a next step, it will be combined with non-destructive electronic detection able to yield mass spectra of produced ion distibutions, thus providing optimal control.

This work has been supported in part by DFG (Grants VO 1707/1-2 and BI 647/4-1), by GSI, HGS-HiRe, and by the IMPRS for Quantum Dynamics Heidelberg.

References

[1] W. Quint, D. Moskovkin, V.M. Shabaev and M. Vogel, Phys. Rev. A **78** (2008) 032517.

[2] D. von Lindenfels, N. Brantjes, G. Birkl, W. Quint, V. Shabaev and M. Vogel, Can. J. Phys. **89**, 79 (2011).

[3] D. von Lindenfels, G. Birkl, D.A. Glazov, A. Martin, G. Plunien, W. Quint, V.M. Shabaev, M.M. Sokolov, M. Vogel, A.V. Volotka, and M. Wiesel, Phys. Rev. A **87** 023412 (2013).

 doi:10.15120/GR-2014-1-PNI-AP-15

New approach for the induced charge calculation for cylindrical electrodes*

J. Steinmann[1,2], *J. Groß*[2], *F. Herfurth*[1], *and G. Zwicknagel*[3]

[1]GSI Helmholtzzentrum, Darmstadt, Germany; [2]University of Applied Sciences, Darmstadt, Germany; [3]University, Erlangen-Nuernberg, Germany

The HITRAP facility is part of the GSI accelerator complex and it is designed to store and cool up to 10^5 bare uranium ions. One of the cooling mechanisms is the resistive cooling where energy is dissipated in an external RLC circuit, which is connected to the so called pick-up electrodes. These electrodes pick up the induced charge and the related current caused by the ion dynamics and give a feedback to the ion dynamics due to an imbalance of the potential on these electrodes. But since there exists no theoretical treatment of resistive cooling which is able to accurately predict cooling time and cooling behavior numerical simulations are necessary. In [1] we presented a model for the simulation of resistive cooling of ion clouds in cylindrical penning traps, which includes the complete ion-ion interaction. To handle the large computational effort this is done on graphic boards using parallel programming techniques [2]. The induced current is the time derivative of the induced charge and can be calculated by a finite element solver. This allows to model precisely the real geometry. But due to the increasing number of necessary elements, the simulation time increases strongly with the required numerical accuracy, and this method gets inefficient for a time discrete integration scheme in which these calculations must be repeated some billion of times. Based on the solution of the Poisson equation, we therefore worked out an analytical formula for the charge Q which is induced on the electrodes by an ion:

$$Q = \frac{q}{\pi}\int_0^\infty \frac{I_0\left(v\cdot\frac{r}{R}\right)}{v\cdot I_0(v)}\cdot\sum_{j=0}^{1}(-1)^j\sin\left(v\cdot\frac{\Delta z_j}{R}\right)dv \qquad (1)$$

Here, I_0 is the modified Bessel function of order zero, R is the trap radius, $\Delta z_j = z - z_j$ with z_0 and z_1 are the left and right axial coordinate of the pick-up electrode and q is the charge of the ion at position $(r,\ z)$. The total charge induced on the pick-up electrode caused by an ion cloud is calculated by superimposing the contributions of all single ions. Since we did not find an analytical solution of (1) some further simplification is needed to ensure a fast evaluation. Approximating now the term $I_0\left(v\cdot\frac{r}{R}\right)/I_0(v)$ in expression (1) leads to an analytical formula which allows fast calculation and provides high accuracy:

$$Q \approx \frac{q}{2}\sum_{k=0}^{k_{max}}\beta_k\sum_{j=0}^{1}(-1)^j\left[\mathrm{erf}\left(\frac{\Delta z_j}{\gamma_k}\right)+\frac{r^2\Delta z_j}{\sqrt{\pi}\,\gamma_k^3}\,\mathrm{e}^{-\left(\frac{\Delta z_j}{\gamma_k}\right)^2}\right]$$

Here erf is the error function, k_{max} the order of approximation, $\gamma_k = 2R\alpha_k$, α_k and β_k are numerical parameters.

* Work supported by FE, Project-Number DAGROS1012.

The calculated charge induced on single electrodes is shown in figure 1. The approximation error depends on

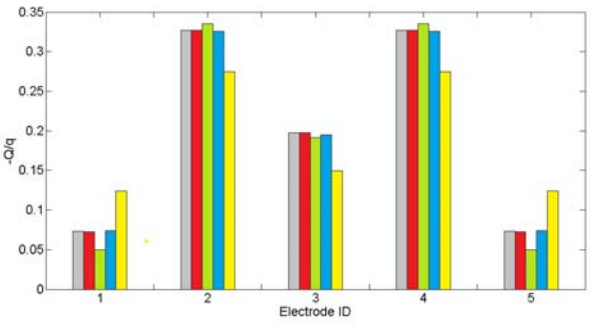

Figure 1: Induced charged at five cylindrical electrodes. The bins from left to right: Analytical solution (gray), approx. $k_{max} = 2$ (red), approx. $k_{max} = 1$ (green), Comsol (blue), calculation scheme of Ref.[3] (yellow). Electrode 2 and 4 are the pick-up electrodes

the choice of k_{max}, see figure 2. Already at $k_{max} = 2$ the results of (1) and the analytical approximation are in good agreement. The resulting absolute error for the pick-up electrodes of less than $5\cdot10^{-3}$ will be sufficiently accurate for our simulations.

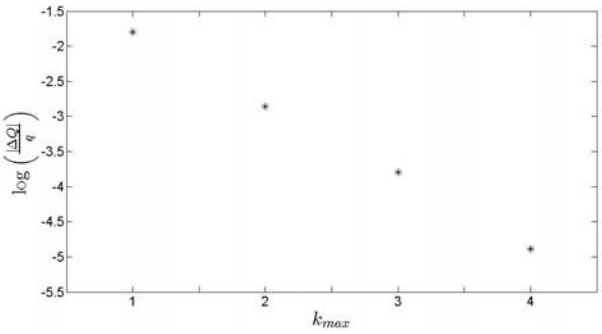

Figure 2: Approximation error per unit charge versus the order of approximation k_{max}

References

[1] J. Steinmann *et. al.*, AIP Conference Proceedings **1521**, 2013, pp. 240-249.

[2] J. Steinmann *et. al.*, "Simulation of Ion Clouds in Penning traps using graphic boards", GSI Scientific Report (2012).

[3] G. Maero *et. al.*, Applied Physics B: Lasers and Optics **107** (2012) 1087.'

Polarization transfer in elastic Rayleigh scattering *

A. Surzhykov[†1], *V. A. Yerokhin*[2], *Th. Jahrsetz*[1,3], *Th. Stöhlker*[1,4,5], *and S. Fritzsche*[1,4]

[1]Helmholtz Institute Jena, Germany; [2]St. Petersburg State Polytechnical University, Russia; [3]University of Heidelberg, Germany; [4]University of Jena, Germany; [5]GSI Helmholtzzentrum, Darmstadt, Germany

Studies on the elastic Rayleigh scattering of photons by bound atomic (or ionic) electrons have a long tradition. Since the mid 1930's, a large number of experimental and theoretical works have dealt with the total as well angle–differential Rayleigh cross sections [1]. More recent investigations were focused, moreover, on the linear polarization of the scattered photons. Of particular interest here is the question of how this polarization is affected if the incident light is itself (linearly) polarized. Owing to recent advances in coherent light sources and efficient detection techniques, a new generation of experiments has currently become feasible, in which such a "polarization transfer" can be explored for heavy atomic targets and the radiation in the x–ray region. Polarization analysis of the Rayleigh scattering in the high–Z—and—high–energy domain may serve as a valuable tool for exploring this second–order quantum electrodynamical (QED) process in very strong electromagnetic fields.

In order to analyze the current and future experiments on the polarization transfer in elastic Rayleigh scattering of x–rays by heavy targets, detailed theoretical study has been performed by us based on the second–order perturbation theory and Dirac relativistic equation [2]. The practical application of such a perturbative approach requires the knowledge about the *complete* Dirac spectrum of an atom (or ion), including not only bound– but also positive and negative energy continuum–states. In our study, this spectrum was represented by means of the Coulomb Green's function:

$$G_E(\boldsymbol{r},\boldsymbol{r}') = \sum_{\nu}\!\!\!\!\!\!\int \frac{\psi_\nu^\dagger(\boldsymbol{r})\,\psi_\nu(\boldsymbol{r}')}{E_\nu - E}\,, \qquad (1)$$

constructed from the eigensolutions $\psi_\nu(\boldsymbol{r}) \equiv \psi_{n_\nu j_\nu,\mu_\nu}(\boldsymbol{r})$ of the Dirac Hamiltonian. By using the analytical representation of $G_E(\boldsymbol{r},\boldsymbol{r}')$ in terms of the regular and irregular Whittaker functions [3] we were able to perform an accurate perturbative calculations of the angular as well as polarization properties of scattered Rayleigh photons.

With the help of the relativistic Green's function approach we investigated, in particular, the elastic scattering of completely linearly polarized x–rays on hydrogen–like ions in their ground state. For example, Fig. 1 displays the angular distribution (left panel) and the degree of linear polarization (right panel) of scattered photons for the case of xenon Xe^{53+} target and three different energies $\hbar\omega$

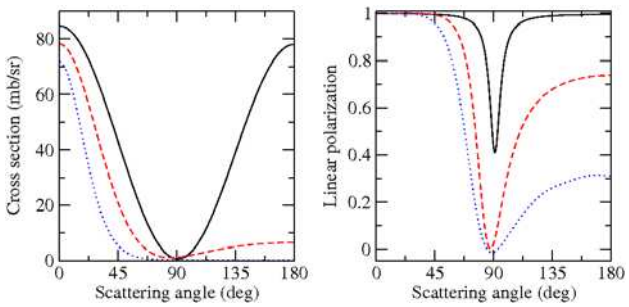

Figure 1: The angle–differential cross section (left panel) and the degree of linear polarization (right panel) of elastically scattered x–rays on hydrogen–like xenon Xe^{53+} ions in their ground state. Relativistic calculations were performed for the completely linearly polarized incident light with energies $\hbar\omega$ = 1.1 I_{1s} (solid line), 5 I_{1s} (dashed line) and 10 I_{1s}, where $I_{1s} \cong 41$ keV refers to the $1s$ ionization threshold. Data from Ref. [2].

of the incident light. As seen from the figure, both (angular and polarization) properties appear to be very sensitive to the photon energy. In particular, if $\hbar\omega \cong 45$ keV, which is just 10 % above the $1s$ ionization threshold, the Rayleigh photons are strongly polarized over the entire angular range, except for $\theta \approx 80$–100°, and their emission pattern is almost dipole–like, $W(\theta) \sim \cos^2\theta$. In contrast, the increase of the energy leads to (i) a strongly enhanced forward emission and to (ii) a significant *reduction* of the polarization of outgoing radiation. This reduction is largest for the backward scattering but may also reach 20–30 % for the emission angles in the range $30^\circ \lesssim \theta \lesssim 60^\circ$, where the photon yield is high. Based on our theoretical analysis, we argue that such a "depolarization" of light in the course of elastic scattering is caused mainly by the higher, non–dipole components of the electromagnetic field. The measurements of the depolarization effects, which is feasible today with the help of available solid–state detectors, can reveal, therefore, useful information about the details of photon–matter interactions in the extreme relativistic regime; the topic which attracts currently much attention both in intense–laser and heavy–ion physics.

References

[1] R. Pratt, Rad. Phys. Chem. **74**, 411 (2005).

[2] A. Surzhykov *et al.*, Phys. Rev. A **88**, 062515 (2013).

[3] P. Koval and S. Fritzsche, Comp. Phys. Commun. **152**, 191 (2003).

* Work supported by Helmholtz Association under the project VH–NG–421 and by the BMBF under the project No. 05K13VHA.

† a.surzhykov@gsi.de

 doi:10.15120/GR-2014-1-PNI-AP-17

Development of the HITRAP experimental facility

Z. Andelkovic[1], *S. Fedotova*[1], *F. Herfurth*[1], *N. Kotovskiy*[1], *B. Maaß*[2], *J. Steinmann*[3], *and G. Vorobjev*[1]

[1]GSI Helmholtzzentrum für Schwerionenforschung, Darmstadt; [2]TU Darmstadt; [3]Hochschule Darmstadt

Heavy few-electron ions are relatively simple systems in terms of electron structure which offer unique opportunities to conduct experiments under extremely large electromagnetic fields that exist around their cores. This makes them perfectly suited for various experiments including, but not limited to, tests of quantum electrodynamics at the strong field limit, multiple electron transfer or interaction of highly charged ions (HCI) with surfaces. In the recent decades the theory has advanced enough to be able to calculate quantities such as the g-factor of bound electrons or electron energy levels with high precision. Thus, the major challenge for such kind of experiments has remained the preparation of such highly charged ions.

As an extension of the existing GSI accelerator facility, the heavy ion trap (HITRAP) facility was conceived as the final deceleration stage for HCI. It is designed to provide cold bunches of up to 10^5 ions with charge states as high as bare uranium. The HITRAP decelerator consists of several stages designed to bring the energy of HCI from the initial 4 MeV per nucleon stepwise down into the sub-eV range. After the successful offline tests of the modified radio-frequency quadrupole (RFQ) - the second deceleration stage - it was installed back into the main beamline and equipped with diaphragms at the ion input and output. They will ensure ion beam injection on axis of the 4-rod structure, which was found to be crucial for the deceleration efficiency during the offline tests.

The final deceleration stage - the cooling trap - has seen some modifications for better high voltage stability and suppression of unwanted electron emission processes. After successful trapping of HCI from the EBIT in the year before, the ongoing work at the moment is to prepare the trap for the ions at 6 keV/u decelerated from the RFQ. A detailed simulation study of the resistive cooling process is carried out at the same time [1]. Together with electron cooling, this method will reduce the ion energy to the sub-eV level and prepare a cold bunch of heavy HCI for distribution to different experiments.

The HITRAP facility on the experimental platform included so far a Dresden EBIT and a transfer beamline connecting it to the cooling trap. In 2013 the branch connecting the EBIT and the HITRAP decelerator with various experiments has been completed, thus extending the low-energy beamline by some 15 m, as shown in the figure below. The new section includes nine quadrupole doublets, two 90° deflectors, four diagnostics chambers and an appropriate number of UHV pumps for reaching a residual gas pressure of 10^{-10} mbar. Ion bunches, including highly charged O, Xe and Ar ions have been successfully transported along the full beamline length. This result enables the planned laser spectroscopy experiments in the SpecTrap Penning trap [2], and also paves the way for other experiments associated with HITRAP, like the measurements of the bound-electron *g*-factor [3] and study of multiple electron transfer in cold atom-HCI collisions [4].

As an addition to the Dresden EBIT, plans and preparations were made for an installation of the high-energy S-EBIT [5]. Consigned to GSI as a loan from the Helmholtz Institut Jena, it currently being installed on the HITRAP experimental platform and connected with the existing infrastructure. This accelerator-independent source of heavy, highly charged ions will help bridge the shutdown time of the GSI accelerator complex during the preparation for FAIR and supply heavy HCI to the experimental stations.

References

[1] J. Steinmann, J. Groß, F. Herfurth, G. Zwicknagel, GSI Scientific Report 2013

[2] T. Murböck, et al. GSI Scientific Report 2013

[3] D. von Lindenfels, et al.: Phys. Rev. A **87**, 023412 (2013)

[4] S. Götz, et al.: Rev. Sci. Instrum. **83**, 073112 (2012)

[5] S. Trotsenko, et al. GSI Scientific Report 2013

SPARC at Storage Rings of FAIR*

Yu. A. Litvinov† [1,2], *Th. Stöhlker*‡ [1,3,4], *and the SPARC Collaboration*[5]

[1]GSI Helmholtzzentrum für Schwerionenforschung; [2]Ruprecht-Karls-Universität Heidelberg; [3]Helmholtz Institut Jena; [4]Friedrich-Schiller-Universtät Jena; [5]http://www.gsi.de/sparc

The FAIR project will be realized in stages as determined by the Modularized Start Version (MSV) [1]. Since the New Experimental Storage Ring (NESR), which is the main instrument for SPARC experiments in FAIR [3], is not within the first stage of the MSV, its realization will inevitably be delayed. Therefore, the MSV has triggered substantial efforts to investigate alternatives enabling unique experiments in the realm of atomic physics using stored and cooled ion-beams already within the MSV. Apart from the MSV program at a dedicated fix-target experimental hall, APPA-Cave, and laser-cooling experiments in SIS-100, these plans include the installation of the CRYRING at the presently operating ESR [2] and the realization of an experimental program with relativistic ions beams in the High-Energy Storage Ring (HESR) [4].

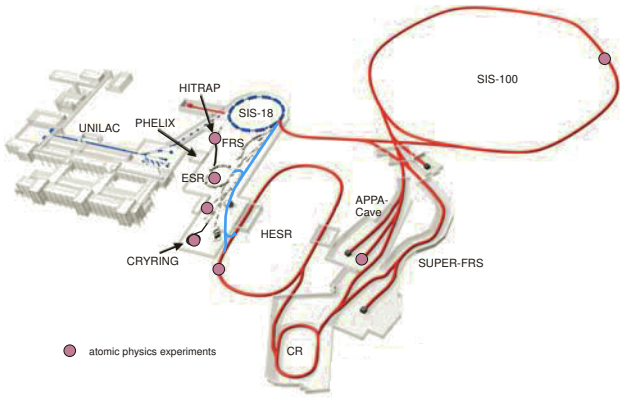

Figure 1: Schematic view of the presently operational accelerator facility at GSI (gray) and the initial phase of the future FAIR facility (red). The main locations of SPARC experiments are indicated, including the HITRAP, which is being commissioned at the ESR, and CRYRING, which is presently under construction. Possible beam lines for transport of protons and ions from SIS-18 directly to the HESR and of antiprotons and ions from HESR to the ESR are shown with light-blue color. These beam lines are currently subject of detailed investigations.

The latter was described in a dedicated feasibility study [5]. Since then the conditions for SPARC experiments were further investigated in a close collaboration with researchers from FZ Jülich. Stochastic and electron cooling of heavy ions has been studied in very detail. It was shown that – by using the available system [6] – stochastic cooling of ion beams will be possible at the injection energy of 740 MeV/u [7] as well as at the highest energies of a few GeV/u [8]. Furthermore, adding an available barrier bucket voltage will allow for a sufficient cooling of the ions also with dense internal targets [9]. The simulation of the full cycle SIS-100 → CR → HESR including bunching, cooling and acceleration has been performed [10]. These studies have shown that the SPARC experiments even with highest target densities can be performed in the HESR without any additional modifications of the HESR stochastic cooling and RF systems.

To facilitate the commissioning of the various machines of the FAIR facility, a direct beam line connecting SIS-18 and HESR could be imagined [11]. This would allow for an easier commissioning of the HESR on the one side. On the other side, since the HESR is capable to efficiently accelerate the stored beams, this would enable the exciting SPARC physics program [12] at a very early stage of FAIR, even before the commissioning of the complex accelerator chain SIS18-SIS100-CR-HESR is completed. A possible location of such a beam line is indicated in Figure 1.

With CRYRING@ESR two fully commissioned storage rings will be available, and, by installing an anti-proton transfer line, the physics program of the FLAIR collaboration could be realized at a very early stage. A possible beam line could connect the HESR with the ESR as, e.g., indicated in Figure 1. In such a case the cooled and slowed-down antiprotons would be extracted from the HESR at 9.5 Tm towards the ESR, where they would further be cooled and slowed-down to about 1.4 Tm, the injection rigidity of the CRYRING, and transferred to CRYRING.

Fruitful collaboration with T. Katayama, E. Mahner, R. Maier, D. Prasuhn, R. Stassen, M. Steck, H. Stockhorst on the SPARC@HESR issues is greatly acknowledged.

References

[1] FAIR Green Paper: The Modularized Start Version (2009).
[2] M. Lestinsky *et al.*: CRYRING@ESR: A Study Group Rep.
[3] R. Schuch *et al.*: SPARC Technical Proposal (2005)
[4] R. Maier *et al*: HESR Technical Design Report (2008)
[5] T. Stöhlker *et al*: SPARC Exp. at HESR: A Feasibility Study
[6] R. Stassen *et al.*, Proc. IPAC2013, Shanghai, China.
[7] H. Stockhorst *et al.*, Proc. IPAC2013, Shanghai, China.
[8] H. Stockhorst *et al.*, Proc. IPAC2012, New Orleans, USA.
[9] T. Katayama *et al.*, Proc. IPAC2013, Shanghai, China.
[10] T. Katajama and H. Stockhorst, in preparation (2014).
[11] T. Stöhlker *et al.*: Hyperfine Interactions, in press (2014).
[12] T. Stöhlker *et al.*: Phys. Scripta T **156**, 014085 (2013).

*Work supported by Helmholtz Institute Jena, Helmholtzzentrum Jülich, and the Helmholtz-CAS Joint Research Group HCJRG-108

† Y. Litvinov@gsi.de
‡ T.Stoehlker@gsi.de

 doi:10.15120/GR-2014-1-PNI-AP-19

Swift heavy ion induced radiation damage in $EuPO_4$ * †

A. Romanenko[1,2], *C. Trautmann*[1,2], *F. Fujara*[2], *and M. Lang*[3]

[1]GSI, Darmstadt, Germany; [2]TU Darmstadt, Germany; [3]The University of Tennessee, Knoxville, TN, U.S.A.

Europium phosphate ($EuPO_4$) is the synthetic analogue to the natural mineral monazite and is considered as a promising material for long term storage of radioactive waste because of its structural flexibility incorporate uranium and thorium without significant structure degradation due to self-irradiation. Earlier irradiation experiments with 800keV- Kr ions revealed a high radiation hardness of monazite-structure orthophosphates and low critical temperature, above which the material can no longer be amorphized [1]. In contrast to displacive radiation effects there is no information available about the response of $EuPO_4$ to the irradiation with swift heavy ions (SHI) where electronic energy loss processes dominate.

Single crystals of $EuPO_4$ were irradiated at the UNILAC facility using 2.0-GeV Au ions (energy loss 39 keV/nm). The experiments were performed at room temperature using a flux of 3×10^8 ions/cm^{2}s and fluences between 5×10^{11} and 1×10^{13} ions/cm^2.

For damage analysis, the irradiated samples were investigated by Raman spectroscopy using a Horiba Jobin Yvon LabRam HR800 system with a laser of λ = 473.1 nm.

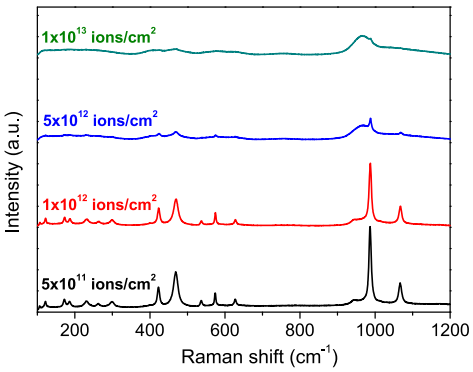

Figure 1: Raman spectra of $EuPO_4$ crystals exposed to 2.0 GeV Au ions of different fluences (spectra are stacked for better visualization). All spectra were recorded on spontaneously cleaved crystal planes normal to the irradiated surface at 10 μm depth.

Due to irradiation-induced stress accumulation, the crystals broke perpendicular to the irradiated surface. This created a flat normal-to-surface plane and allowed us to record Raman spectra along the full range of the ions.

Raman spectra of virgin lanthanide phosphates LnPO4 have previously been reported, assigning the most intense peak at 987 cm^{-1} in the $EuPO_4$ spectrum to the symmetric stretching mode of the $(PO_4)^{3-}$ group [2]. After applying a fluence of 5×10^{11} ions/cm^2, no significant change in the Raman spectrum was observed, while further irradiations result in an overall increase of the background and a strong broadening of all Raman bands (Fig. 1). At high fluences, a broad peak develops at around 960 cm^{-1}. Given by the similarity of Raman spectra of fully amorphized phosphates and amorphous phosphate glasses, we ascribe this band to the vibrations of the $(PO_4)^{3-}$ tetrahedron in the amorphous matrix. At a fluence of 1×10^{13} ions/cm^2, almost all bands from the original crystalline phase disappeared. The damage cross section was estimated by analyzing the band area of the $(PO_4)^{3-}$ symmetric stretching mode from the crystalline (987 cm^{-1}) and the amorphous (960 cm^{-1}) state as a function of fluence. Based on the single-impact model [3], the damage accumulation increases in the initial stage linearly with increasing fluence and saturates for track overlapping. Applying the Poisson law allows us to determine the track radius R.

$$\frac{A_c}{A_c + A_a} = \exp(-\pi R^2 \Phi) \qquad (1)$$

where Φ denotes the fluence, and A_c and A_a represent the respective band area of the crystalline (987 cm^{-1}) and amorphous (960 cm^{-1}) Raman peak. Fitting the data (Fig. 2) by Eq. 1 yields a track radius of R = 3.4 $\pm$ 0.2 nm which is consistent with track radii in other minerals.

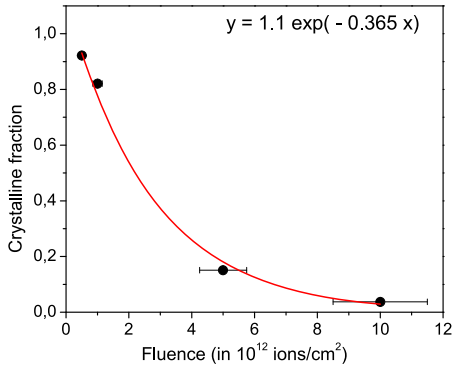

Figure 2: Crystalline sample fraction as a function of fluence. From the exponential decrease, the track radius for 2.0-GeV Au ions in $EuPO_4$ is deduced. The solid line corresponds to the fit equation given as inset.

References

[1] A.Meldrum, L.A.Boatner, R.C.Ewing, Phys. Rev. B, 56 (1997) 13805.

[2] G. M. Begun, G. W. Beall, L. A. Boatner, and W. J. Gregor, J. Raman Spectrosc. 11, 273 (1981).

[3] W.J. Weber, Nucl. Instr. Methods Phys. Res. B,166 (2000) 98.

* Supported by GSI-TUD cooperation and HGS-HIRe graduate school

† an.romanenko@gsi.de

New approach to investigate irradiated calcite crystals – UV Raman and Photoluminiscence with UV excitation *

S. Dedera †[1], *N. Schöppner*[1], *U. A. Glasmacher*[1], *M. Burchard*[1], *and C. Trautmann*[2,3]

[1]Institute of Earth Sciences, University Heidelberg; [2]GSI Darmstadt; [3]Technical University Darmstadt

In the past, calcite ($CaCO_3$) turned out as a sensitive natural detector for ion defects. Additional experiments shall now reveal, if there are more useful properties of this very common mineral.

During a test experiment at the SIS, a trigonal calcite crystal of $6\times6.5\times4$ mm^3 in size was irradiated with 192 MeV/u ^{238}U ions of fluence 1×10^{11} cm^{-2} (subsequently denoted as SIS-calcite). We observed a pronounced ionoluminescence and unexpected long phosphorescence for about 20 min, which was not reported so far.

Crystals from the calcite family are known to luminescent under UV excitation [1]. We thus exposed the SIS-calcite offline with UV light of wavelengths λ_L =366 nm ("long UV") and λ_S=254 nm ("short UV") to investigate whether the increase of defect concentration through ion irradiation changed the properties of the SIS-calcite.

No luminescence was detected for the "long UV"-excitation, whereas under the "short UV" excitation the SIS-calcite showed a thin line of greenish to yellowish luminescence localized around to the range where the electronic energy loss of the ions is maximum. The rest of the crystal did not contribute to luminescence.

Trigonal calcite crystals irradiated at the UNILAC with 11.1 MeV/u ^{197}Au-ions showed the same greenish to yellowish luminescence when stimulated with "short UV". The luminescence starts to become visible at a fluence of 1×10^9 ions/cm^2. Subsequently, experiments with UV-stimulated Raman spectroscopy and photoluminescence (PL) were performed to test the luminescence response to UV stimulation. The work is motivated by the expectation that a UV-stimulated change in the luminescence pattern may be a suitable non-destructive analytical technique to quantify defect concentrations in calcite crystals produced by bombardment with heavy ions in the low fluence regime ($< 1\times10^9$ Au-ions/cm^2).

The experiments were performed with the UV-Raman and photoluminescence spectrometer (UV-laser: 244 nm) of Jobin Yvon Horiba. Calcite irradiated with 1×10^6 Au-ions/cm^2 (11.1 MeV/u) show distinct photoluminescence with bands at about 520 and 545 nm (Fig. 1), which matches the greenish, yellowish color of the luminescence light whereas unirradiated calcite crystals show only a minor peak at 545 nm. When increasing the fluence to 1×10^8 Au-ions/cm^2, the amplitude of both peaks increases (Fig. 1). All spectra are taken with the following parameters: grate 300, objective 40×, accumulation 2×, hole 50.

Excitation (UV-laser: 244 nm) of the SIS-calcite also indicated the already known two bands with high amplitude (Fig. 2). In addition, a new peak at about 575 nm is observed.

Summarizing the first results, UV-excitation combined with photoluminescence spectroscopy is sensitive enough to detect crystal defects created by heavy ions (11.1 MeV/u ^{197}Au) at a fluence as low as 1×10^6 ions/cm^2.

So far Raman spectroscopy and detection with the UV-excitation (Laser: 244 nm) did not lead to any fluence-related change of the Raman bands.

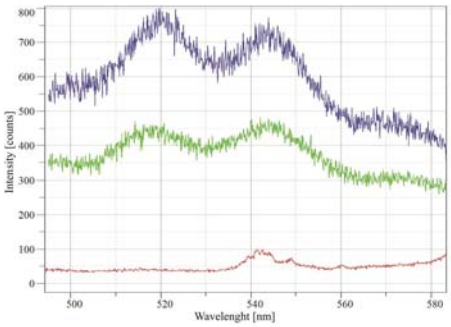

Figure 1: PL-Spectra of calcite crystals irradiated with 1×10^6 and 1×10^8 Au-ions/cm^2 (11.1 MeV/u). Spectra are not shifted, (detection time 20 s irradiated, 1 s non-irradiated).

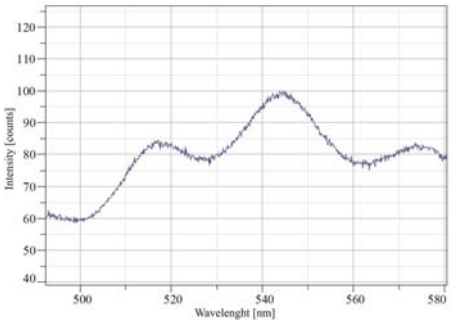

Figure 2: PL-Spectra of SIS-calcite crystal irradiated with 1×10^{11} U-ions/cm^2 (192 MeV/u). Strong luminescence due to good noise/signal ratio (detection time 5 s).

References

[1] M. Gaft, L. Nagli, G. Panczer, G. Waychunas and N. Porat. "The Nature of Unusual Luminescence in Natural Calcite $CaCO_3$." American Mineralogist 93, no. 1 (2008): 158-167.

* Work supported by BMBF Verbundprojekt 05K10VH1

† Sebastian.Dedera@geow.uni-heidelberg.de

 doi:10.15120/GR-2014-1-PNI-MF-02

Spectroscopic study on ion irradiated calcites and gypsum *

N. Schöppner † [1], S. Dedera[1], U.A. Glasmacher[1], M. Burchard[1], M. Zdorovets[2,3], and Christina Trautmann[4]

[1]Institute of Earth Sciences, University of Heidelberg, Germany; [2]Institute of Nuclear Physics, Almaty, Kazakhstan; [3]Gumilyov Eurasian National University, Astana, Kazakhstan; [4]TU Darmstadt and GSI Helmholtzzentrum Darmstadt, Germany

Within geosciences, the use of fission tracks in various minerals as a thermochronological analytical technique is of high importance. The visualization of spontaneous and induced fission tracks uses the well established etching technique. Carbonate minerals have been tested in the past with differentiated results. The latest research clearly indicates that fission tracks develop in carbonate minerals and that they can be revealed by specific etching conditions [1], [2]. As carbonate minerals are excellent minerals for spectroscopic analytical techniques, the application of those techniques to non-destructively deduce information on fission tracks was tested.

Various carbonate minerals were irradiated within two different ion energy ranges. Ions of GeV kinetic energy were available at the GSI, while irradiations at lower energy were performed at the RGP Institute Yadernoi Fiziki, Astana, Kazakhstan. Mono crystalline samples of carbonate used in these experiments are trigonal calcite ($CaCO_3$), rhomboedric aragonite ($CaCO_3$), monocline malachite ($Cu_2[(OH)_2/CO_3]$), trigonal rhodochrosite ($MnCO_3$), trigonal dolomite ($MgCO_3$), and monocline gypsum ($CaSO_4$*$2H_2O$). At GSI, the carbonate minerals were irradiated at the UNILAC accelerator with 11.1 MeV/u ^{197}Au and ^{209}Bi ions, applying fluences of 1×10^6, 5×10^6, 1×10^7, 5×10^7, 1×10^8, 1×10^{11}, and 1×10^{12} ions/cm^2. At the RGP Institute, the samples were irradiated at the Astana accelerator with 1.7 MeV/u ^{84}Kr ions applying fluences between 1×10^{10} and 1×10^12 ions/cm^2. The lower mass and energy of these Kr ions is closer to the conditions given by natural fission fragments from ^{238}U.

All crystals were analyzed by Raman spectroscopy using the LabRam HR800 UV spectrometer equipped with an OLYMPUS BXFM-ILHS optical microscope, a grating with 1800 grooves per millimeter and a Peltier-cooled CCD detector. During the spectroscopic measurements an objective of 50x magnification was used. The spectra were excited by laser light of wavelength 473.03 nm. The lateral resolution was $\sim$2 μm, the wave number accuracy 0.5 cm^{-1} and the spectral resolution was 1 cm^{-1}. First results are provided for irradiated calcite and gypsum (Figs. 1, 2). The revealed Raman spectra are similar up to a fluences of 5×10^{11} ^{84}Kr-ions/cm^2. Above those fluences a new Raman band appears at about $\sim$430 cm^{-1}. In addition, at 5×10^{11} ^{84}Kr-ions/cm^2 a shoulder appears at the left side of the main Raman band at about 1100 cm^{-1}.

Significant changes in the Raman spectra of gypsum appear above a fluence of 1×10^{10} ^{84}Kr-ions/cm^2. With increasing fluences the peak intensities decrease and the full width at half maximum of the bands (FWHM) become larger. This applies especially to the Raman band at 3404 cm^{-1}, which characterizes the H_2O band (Fig. 1). The amplitude decrease is an indication of irradiation-induced release of water. Similar effects were observed for irradiation of gypsum with neutrons [1, 2].

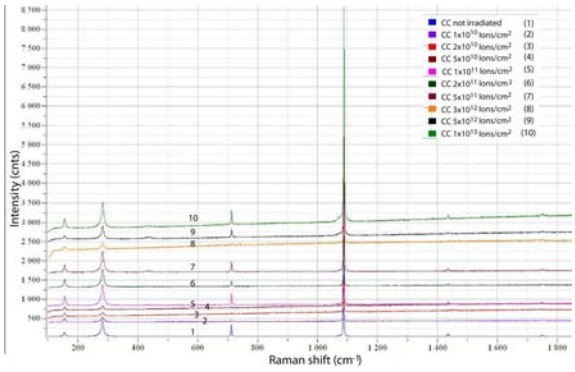

Figure 1: Spectra of calcites irradiated with fluences between 1×10^{10} and 1x10^{13} ^{84}Kr-ions/cm^2 and a spectrum of a non-irradiated calcite crystal.

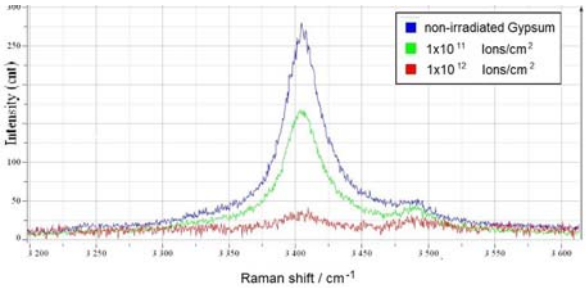

Figure 2: Raman spectra of gypsum before and after irradiation with ^{84}Kr -ions.

References

[1] http://www.patent-de.com/20060406/DE102004052158A1.html (2006). (Stand: 14.02.2014)

[2] A. R. Patel, K. S. Raju (1970): Radiation damage in gypsum. J. Phys. Chem. Solids, 31, 331-335.

* Work supported by GSI(UNILAC), Work supported by GSI-HD cooperation contract and HGS-HIRe graduate school

† nicole.schoeppner@geow.uni-heidelberg.de

High Aspect Ratio Nanotubes fabricated by Ion-Track Technology and Atomic Layer Deposition *

A. Spende[1,2], I. Alber[1], N. Sobel[3], C. Hess[3], M. Lukas[4], B. Stühn[4], R. Zierold[5], J. M Montero Moreno[5], K. Nielsch[5], C. Trautmann[1,2], and M.E. Toimil Molares † [1]

[1]GSI, Darmstadt, Germany; [2]Materials Research, Technische Universität Darmstadt, Germany; [3]Eduard-Zintl-Institut für Anorganische Chemie und Physikalische Chemie, Technische Universität Darmstadt, Germany; [4]Experimental condensed matter physics, Technische Universität Darmstadt, Germany; [5]Institute of Applied Physics, Universität Hamburg, Germany

Nanotubes and nanochannels embedded in solid state membranes are of high relevance in many different fields including nanofluidics, catalysis, health care, or solar energy harvesting. On the way to novel industrial applications, systematic basic studies on these nanostructures as well as development of suitable fabrication techniques to precisely tailor their dimensions and surface properties are required. For synthesis of cylindrical nanochannels anodic alumina and polymer membranes are frequently used.

In this study, we fabricated nanotubes of alumina (Al_2O_3), titania (TiO_2) and silicon dioxide (SiO_2) by combining the ion-track technology and atomic layer deposition (ALD). As template we used 30-μm thick polycarbonate foils, which were irradiated at the UNILAC with 2 GeV heavy ions and a fluence of 10^9 ions/cm^2. Subsequent chemical etching transforms each ion track into a cylindrical nanochannel [1]. Depending on the etching time, cylindrical nanochannels with a diameter between 55 and 400 nm and respective aspect ratios between 545 and 75 were fabricated. The etched membranes were coated by ALD with Al_2O_3, TiO_2 and SiO_2.

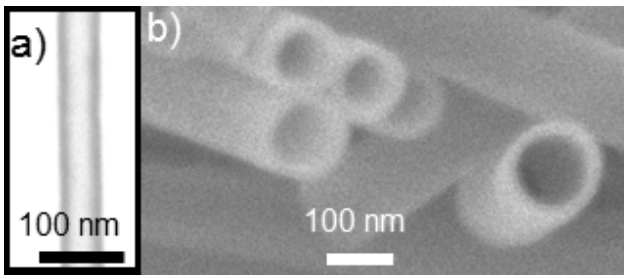

Figure 1: a) STEM image of a single SiO_2 nanotube with an aspect ratio of 545 and a wall thickness of 10 nm. b) SEM image of TiO_2 nanotubes with an aspect ratio of 207 and a wall thickness of 15 nm.

To study the successful coating along the complete length of the nanochannels the polycarbonate template is dissolved by wet-chemical methods. The resulting nanotubes are visualised by scanning electron microscopy (SEM) and scanning transmission electron microscopy (STEM) in SEM. Figure 1 displays representative images of SiO_2 (a) and TiO_2 (b) nanotubes.

Coated and uncoated samples were further investigated by small angle X-ray scattering (SAXS). Deduced nanochannel radii as a function of etching time are displayed in Figure 2. As expected the channel radii increase linearly with increasing etching time. The values of the coated channels are shifted by 10 nm to smaller radii, in complete agreement with the nominal coating thickness of the ALD process. The SAXS scattering pattern of the coated membranes show the same high-quality ondulations indicating highly conformal ALD coating.

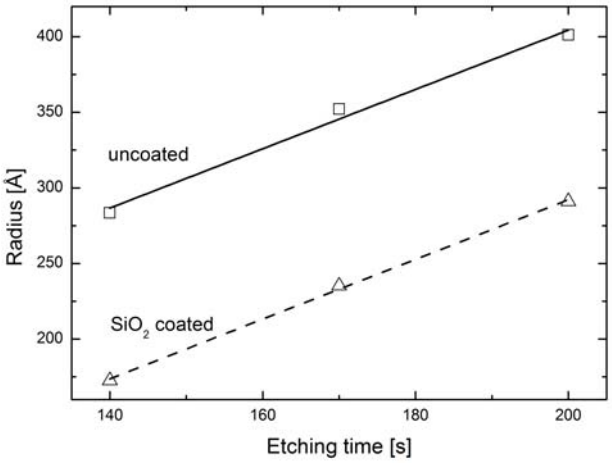

Figure 2: Nanochannel radius deduced from SAXS before (□) and after (△) ALD deposition of 10-nm SiO_2. Uncertainties are smaller than symbols.

In conclusion, these first results show the fabrication of inorganic nanotubes in ion-track etched polycarbonate membranes with aspect ratios above 500. The successful surface modification process creates new opportunities in the precise reduction of pore sizes for filtration or purification applications.

References

[1] M. E. Toimil-Molares, Beilstein J. Nanotechnol. 3 (2012) 860

* Work supported by DFG-FOR1583 and HGS-HIRe

† M.E.ToimilMolares@gsi.de

 doi:10.15120/GR-2014-1-PNI-MF-04

Generation of Physical Conditions Similar to Interior of Superearth Extrasolar Planets by Imploding Solid Iron in LAPLAS Experiments at FAIR *

N.A. Tahir[1], *A. Shutov*[2], *A.R. Piriz*[3], *and Th. Stöhlker*[1,4]

[1]GSI, Darmstadt, Germany; [2]IPCP, Chernogolovka, Russia; [3]UCLM, Ciudad Real, Spain; [4]IOQ Friedrich-Schiller Universität and Helmholtz Institute, Jena, Germany

Due to the discovery of a huge number of Extrasolar planets of different types (gas giants, frozen water rich and earth like rocky planets) over the past two decades, the subject of planetary science has entered into a new very exciting era. This contribution presents numerical calculations using the LAPLAS experimental scheme [1-3] to implode solid Fe to physical conditions that are predicted to exist in the interior of Extrasolar rocky planets named "Superearths" or "Exoearths". The target consists of a solid Fe cylinder having L = 4 mm and r = 0.2 mm that is enclosed in a W cylinder having an outer radius of 3 mm.

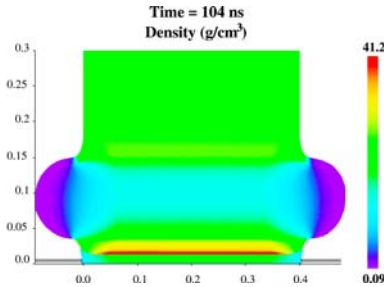

Figure 1: T vs time (Density distribution at the time of maximum compression 5×10^{11} ions.

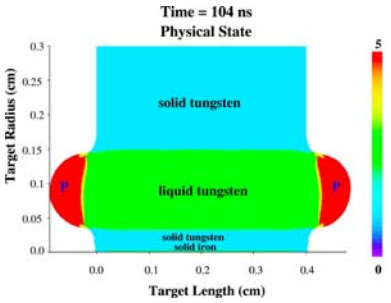

Figure 2: Phase state of the target corresponding to Fig. 1.

A hollow beam of 1 GeV/u U ions (that will be available at FAIR) that has an annular focal spot is used to implode the target. The beam intensity is considered to be 5×10^{11} ions per bunch where the bunch length is 50 ns. Numerical simulations have been done using the 2D hydrodynamic code, BIG2.

In Fig. 1 we present the target density at the time of maximum compression. It is seen that a shell of tungsten tamper with a density of about 40 g/cm^2 has been generated around uniformly compressed Fe. Fig. 2 shows the material phase corresponding to conditions presented in Fig. 1. It is seen that the compressed Fe and the compressed tungsten tamper are in solid phase whereas the tungsten region directly heated by the target is in liquid state.

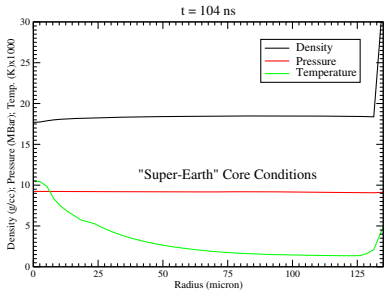

Figure 3: ρ, T and P vs r in Fe region using 5×10^{11} ions.

In Fig. 3 we plot the density, temperature and pressure vs radius in the iron region at L = 2 mm (target middle). It is seen that Fe has been compressed to twice the solid density where as the pressure is around 10 Mbar. These are conditions that are expected to exist in the interiors of huge earthlike Exoplanets.

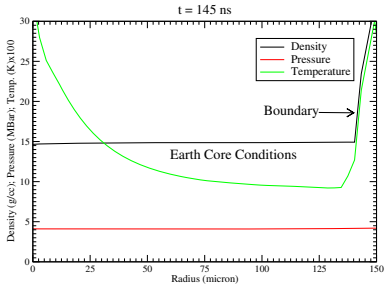

Figure 4: ρ, T and P vs r in Fe region using 2×10^{11} ions.

In Fig. 4 we plot the same parameters as in Fig. 3, but using a lower beam intensity of 2×10^{11} per bunch. In this case one achieves conditions similar to that in the earth core. LAPLAS experiment is a very efficient scheme to study planetary physics at FAIR.

References

[1] N.A. Tahir et al., PRE 63 (2001) 016402.

[2] N.A. Tahir et al., High Energy Density Phys. 2 (2006) 21.

[3] N.A. Tahir et al., New J. Phys. 12 (2010) 073022.

* Work supported by the BMBF

Operation and Improvements of PHELIX*

S. Götte[1], *C. Brabetz*[2], *U. Eisenbarth*[1], *S. Kunzer*[1], *M. Kreutz*[1], *D. Reemts*[1], *T. Stöhlker*[1,3], *L. Tymura*[1], *F. Wagner*[4], *B. Zielbauer*[1,3], *and V. Bagnoud*[† 1,3]

[1]GSI, Darmstadt, Germany; [2]Johann Wolfgang Goethe University Frankfurt, Germany; [3]Helmholtz Institute Jena, Germany; [4]Technical University Darmstadt, Germany

General overview

PHELIX, the workhorse of the plasma physics program at GSI has performed in line with prediction in 2013. In the wake of the decision to reduce the beam time offer for users at GSI, PHELIX reduced the time dedicated to external users by 30%. Nevertheless, even under these circumstances PHELIX has shown proper performance in its fifth year of operation: 10 experiments were realized which were served in 12 beam times for external users. Three of these were performed at the Z6 area (but without ions from the UNILAC), the rest in-house in the PHELIX laser hall (PLH). Altogether, 156 shifts were delivered by the PHELIX operating team. The average duration of the preparation of an experiment at PHELIX was about 4 days, the average duration of an external beam time 6 to 7 days.

Furthermore, upgrades and improvements have been commissioned in 7 internal beam times. The longest has been the commissioning of the new target chamber (37 days) at the PLH. This and other developments are illustrated in the following.

Operation of the laser facility

In 2013, GSI has focused its activity mainly on the preparation of FAIR and, as a consequence, the accelerator was shut down. For PHELIX, which should remain in operation throughout the building phase of FAIR, this means a shift from the combined laser-ion experiments at Z6 to more stand-alone experiments. To enable this, the target area in the PHELIX building was upgraded. This, together with the decision of GSI to reduce user beam time at PHELIX by 30% had a visible impact on the beam time offer, which was set for 2013 to 170 shifts. As can be seen in fig. 1, an appreciable part of the time has been used for external beam time (29%) and the preparation (17%) of these experiments. This is - as expected - less than in 2012 where nearly 50% of the available time was spent for experiments: 2012 was, however, an unusual year, as many experiments had to be scheduled to anticipate the accelerator shut down of 2013, a necessary step in the preparation of FAIR. In addition, some maintenance tasks were delayed and took place in 2013. In 2013 also the relation between preparation and beam time changed in favor of the preparation time: PHELIX was able to offer more of this which was of advantage to set up complex experiments. Development beam time (28%) and maintenance periods (17%) also increased compared to 2012 where this portion was 22% altogether. The time of shut down (9%) did not change noteworthy due to the high operational readiness of the small operating team.

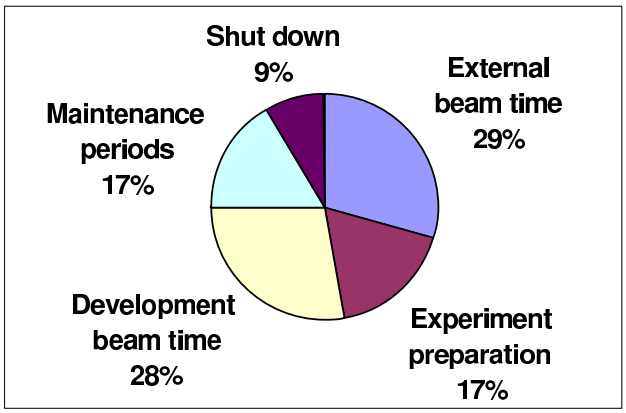

Figure 1: PHELIX usage in 2013

But the operation is not ensured by this team only: GSI supports by the help of several infrastructure departments. The PHELIX operation team is working together with these colleagues in close collaboration: To give an example, the radiation protection department is involved in nearly every beam time.

Shots are documented in the PHELIX shot database as described in the 2012 report. For 2013, 1655 shots were recorded totally in this data base. Since this includes all test shots and also the so-called snap shots (these data are taken to store actual settings of the system), the number of shots delivered for experiments is of more interest: these were 463 in 2013.

The database allows for an evaluation of failed shots: 40 of the experimental shots (8.6%) ended up with an error. One has to face the fact that this information is of less significance: On the one hand, no "failed shot" is recorded if the laser system shows an error which forbids to shoot, on the other hand a shot can be delivered mostly shortly after the failed shot occurred. Thus, there is no severe loss of time for the experiment. But it is of interest to classify the failed shots for their reasons; it turned out that the most failures are caused by hardware (37%) as well as by the PHELIX control system (*PCS*: 45%). The increase of the last (in 2012, less than 10% of failed shots were caused by the *PCS*) is due to necessary changes made to the system which will be described in the following. These prob-

*The acronym stands for **P**etawatt **H**igh **E**nergy **L**aser for heavy **I**on **Ex**periments

† v.bagnoud@gsi.de

 doi:10.15120/GR-2014-1-PNI-PP-02

lems have been solved in the meantime. Only 10% of the failed shots are caused by the operators (in 2012, the majority - 52% - happened due to this reason). This shows the high experience of those who operate the complex laser system, and also the increase of programmatically implemented help at the *PCS* in order to avoid operating errors. The last portion of 8% were caused by external reasons.

Anyhow, 423 successful experimental shots delivered in 2013 attest PHELIX to be a reliable scientific facility. It can be compared with others without any shame. The experimentalists appreciate the fact that nearly always the first shot is delivered in the early morning of the first day of the beam time - if the experimental setup is ready for operation.

Internal developments

In 2013, some modifications enabling full user service during the construction phase of FAIR have been completed with the upgrade of the high-energy target area in the PLH. By that, the experimental options have been improved while the handling of the experiments has been eased and the radiation protection was optimized. For details refer to [1].

Another goal during the ongoing preparation phase of FAIR is the development of innovative technical solutions, like the operation of high-energy lasers at higher repetition rates. A test bed has been set up in the past 18 months to tackle this issue with the particular task to upgrade the preamplifier of PHELIX to higher repetition rates and to develop the relevant diagnostics. This test bed is equipped with a separate pulsed power system. Upgrade activities in this field are described in more detail in [2].

The work on the improvement of the temporal characteristics of PHELIX has continued. First the uOPA stage (ultrafast optical parametric amplifier) in the short pulse frontend was made available to users and is rightfully documented [3]. The system is meanwhile fully integrated into the laser setup, has been used several times for experiments and is close to be operated in a daily routine. Secondly, the search and elimination of the sources of pre-pulses in the frontend and throughout the system was carried on, such that the quality of the temporal profile of PHELIX has been greatly improved. And last, a test beam time was conducted to measure the plasma expansion of the target before the main shot in order to quantify the effect of high-temporal-contrast pulses on laser-matter interactions [4].

An important component of the *PCS* has been changed during the year: the Beckhoff control bus systems have been equipped with Ethernet bus couplers. This piece of hardware connects several devices (for example nearly everything related to the pulsed power system) with the *PCS*. This change became necessary since the linear optical bus couplers used before can not easily be operated with the available hard- and software when changing the operating system of the computers from XP to WINDOWS 7. The migration of the operating system of the *PCS*-PCs was started afterwards at the end of the year.

All these improvements have been tested in several internal beam times.

Contribution to the scientific program and outreach

In 2013, seven peer-reviewed articles [5 - 11] were published on data collected at PHELIX. As seen in the past, these articles report on results often obtained during beam times which occurred longer before, since the analysis of data takes some time.

As a side effect, PHELIX was used to acquire data for the test of a new type of dosimeter which was developed by the GSI radiation protection department. Details can be found in [12].

Concerning the laser activities at FAIR, several meetings were held to understand the requirements of the different research fields. These have been written down in a project report in order to derive the parameters of a future laser facility. Finally, working on a draft of a design of such a facility has been started while in parallel resulting necessary change requests for the FAIR site management are in preparation.

Outlook for 2014

User beam time is granted at PHELIX by the scientific director of GSI after recommendation of an expert panel, the PPAC. In January 2013, the PPAC met at GSI and reviewed experiment proposals that amounted for more than 300% of the available yearly beam time.

References

[1] B. Zielbauer et al., this report

[2] U. Eisenbarth et al., Annual Report of the Helmholtz Institute Jena

[3] F. Wagner et al., Appl. Phys. B, online first DOI 10.1007/s00340-013-5714-9 (2013)

[4] F. Wagner et al., this report

[5] A. Frank et al., Phys. Rev. Lett. **110** 11 (2013)

[6] A. Tauschwitz et al., High Energy Density Physics **9** (11) 158-166 (2013)

[7] W. Cayzac et al., Rev. Sci. Instrum. **84** 043301 (2013)

[8] G. A. Vergunova et al., Plasma Physics Reports **39** (9) 755-762 (2013)

[9] S. Busold et al., Phys. Rev. Lett. Special Topics - Accelerators and Beams **16** (10) 101302 (2013)

[10] S. Busold et al., Nucl. Instrum. Methods A http://dx.doi.org/10.1016/j.nima.2013.10.025 (2013)

[11] D. Kraus et al., Phys. Rev. Lett. **111** 255501 (2013)

[12] F. Horst et al., this report

Upgrade of the PHELIX Target Area*

B. Zielbauer[†1,2], *C. Brabetz*[3], *G. Fehrenbacher*[1], *S. Götte*[1], *P. Kewes*[1], *S. Kunzer*[1], *D. Reemts*[1], *T. Stöhlker*[1,2], *L. Tymura*[1], *F. Wagner*[4], *and V. Bagnoud*[1,2]

[1]GSI, Darmstadt, Germany; [2]Helmholtz Institute Jena, Germany; [3]Johann Wolfgang Goethe University Frankfurt, Germany; [4]Technical University Darmstadt, Germany

In 2013, the upgrade of the PHELIX high-energy target area, dedicated to laser-only experiments in the PHELIX Laser Hall (PLH), has been completed. Due to this effort, the experimental possibilities could be broadened, experiment setup became simpler and radiation protection has been optimized. In April, the new chamber was commissioned by an internal beam-time testing the radiation shielding. Since then, eight experimental beam-times have been realized [1].

Experimental aspects

The most important improvement compared to the previous target chamber is that now, the full-aperture (25 cm) PHELIX beam can be transported into the target chamber which in itself allows for a doubling of the available energy. Together with the new, 22.5° incidence angle off-axis focusing parabolic mirror with an effective focal length of 400 mm, intensities of up to $1.1 \cdot 10^{22}$ W/cm^2 are attainable. However, due to aberrations caused by the beam transport and the parabolic mirror, low-energy measurements give an estimate of $2 \cdot 10^{21}$ W/cm^2 while diagnostics data taken during the shots show additional aberrations resulting in more realistic intensities of about $5 \cdot 10^{20}$ W/cm^2. These issues are to be addressed in the coming year with adaptive optics and the acquisition of a new glass paraboic mirror.

Furthermore, two idendical beam entrances through which the laser coming from the PW compressor can enter the chamber allow for a high degree of flexibility with multiple beams on multiple targets. Especially, the last turning mirror before the chamber lets through a leakage about 1% of the full beam energy which offers a versatile beam for pump/probe, shadowgraphy or interferometry setups with a temporal resolution of a few picoseconds [2].

From the practical point of view, the new chamber can now be accessed from three sides via specially developed sliding doors, allowing users to operate the target chamber without the use of a heavy-duty crane. The target manipulator system can be easily reconfigured for all allowed target positions. This year's experiments have shown that the electrical shielding of the manipulator stages is sufficient, however, additional shielding measures for the motor controllers and control PCs in the target area were necessary. The vacuum system has also been upgraded with a 450 m^3/h screw pump as well as an overall turbo pumping speed of 2800 l/s, allowing for a pump-down time of about 30 min from air pressure to $5 \cdot 10^{-5}$ mbar which is the upper limit for the operation of the optical compressor.

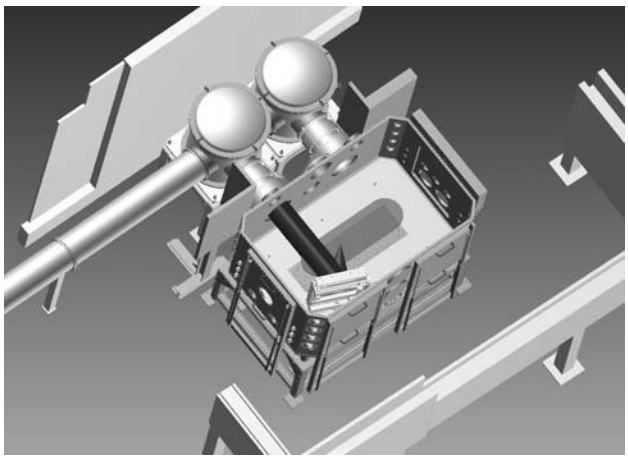

Figure 1: View of the experimental area in the PHELIX laserbay with the additional shielding around the target chamber; red: laser beam path via new parabola; green: permitted target position area

Radiation protection

Before the upgrade, the necessary radiation shielding was assured by means of metal bricks which had to be piled around the target in the vacuum chamber. This seriously limited the use of diagnostics and it was also labor intensive as the shielding material had to be removed after nearly every shot to exchange targets or read out diagnostics. Now, metal shielding panels were installed outside the new target chamber. The design reflects the building wall shape and material in order to minimize the amount of additional shielding material. Important parts are hidden behind the clean-room wall, others directly mounted at or close to the chamber as can be seen in fig. 1. If the target is mounted within a volume of $\pm$ 17.5x59x1 cm, the laser can irradiate the target from any direction without further shielding. The relevant documents like the radiation protection directive of PHELIX have been updated. Finally, the responsible authority has allowed GSI to operate PHELIX with laser intensities of up to $7 \cdot 10^{22}$ W/cm^2.

References

[1] S. Götte et al., this report

[2] F. Wagner et al., this report

*This work at the **P**etawatt **H**igh **E**nergy **L**aser for heavy-**I**on **Ex**periments has been supported by the BMBF contract 05E12CD2

†b.zielbauer@gsi.de

 doi:10.15120/GR-2014-1-PNI-PP-03

Preplasma characterization at PHELIX

F. Wagner[1], *S. Bedacht*[1], *A. Ortner*[1], *B. Zielbauer*[2,3], *M. Roth*[1], *and V. Bagnoud*[2,3]

[1]Technische Universität Darmstadt, Institut für Kernphysik, Darmstadt, Germany; [2]Helmholtz-Institut Jena, Jena, Germany; [3]GSI, Darmstadt, Germany

Introduction

The temporal contrast of high-power laser systems like PHELIX is a critical parameter for laser plasma experiments. The generation and amplification of short pulses using the chirped pulse amplification (CPA) scheme thereby entails a contrast degradation leading to an uncontrolled target pre-ionization. A preplasma is generated which strongly influences the interaction with the main pulse. To ensure well-defined initial parameters for laser plasma experiments as well as computer simulations a detailed knowledge about the preplasma expansion is required.

Temporal contrast at PHELIX

The temporal contrast of the PHELIX short-pulse system has been significantly increased within the last years. An optical parametric amplifier with a pump pulse duration of 1 ps has been developed and implemented at PHELIX. Using this device, we are able to tune the level of ASE between 10^{-6}, which is a typical value for a CPA system, and 10^{-11}. Moreover, all the compressed prepulses have been successfully removed ensuring an undisturbed target before the impact of the main pulse at the lowest ASE level. For more detailed information about the temporal contrast control at PHELIX see Ref. [1, 2].

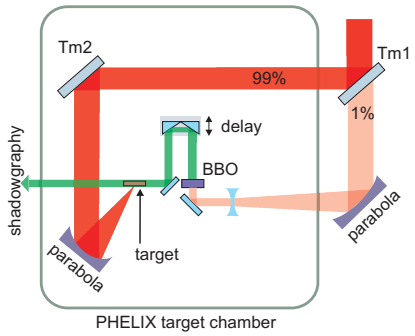

Figure 1: Setup of the preplasma diagnostics

Preplasma shadowgraphy

To evaluate the influence of different ASE levels on the preplasma, defining the initial conditions for laser-plasma experiments, we have developed a new preplasma diagnostics for the PHELIX target chamber which is depicted in figure 1. The main part of the beam is reflected by two turning mirrors (Tm1 and Tm2) and then focused onto the target to achieve an intensity of 10^{20} W/cm^2 while the transmission of 1 % through Tm1 is used as a probe beam. After being down collimated and frequency doubled this probe beam backlights the target and the target plane is imaged to a camera located outside the chamber. The temporal separation between the main pulse and the probe beam can be varied in the range of ± 200 ps allowing for the evaluation of the plasma expansion at different times before and after the impact of the main pulse.

Using this setup we took shadow images from flat copper targets with thicknesses around 5 μm for three different contrast levels. In figure 2 the size of the preplasma shadow is shown for different times. Time 0 ps corresponds to the impact of the main pulse. For an ASE level of $2 \cdot 10^{-7}$ we could identify a preplasma shadow which is nearly constant between -230 ps and 0 ps. The size of this shadow decreases by a factor on the order of two when the ASE contrast is increased by two orders of magnitude. At an ASE level of 10^{-10} no preplasma shadow was detected.

This measurement confirms that our maximum contrast level is high enough to prevent any major preplasma expansion. In a next step the measured data will be compared to simulations to link the shadow sizes to an actual plasma density.

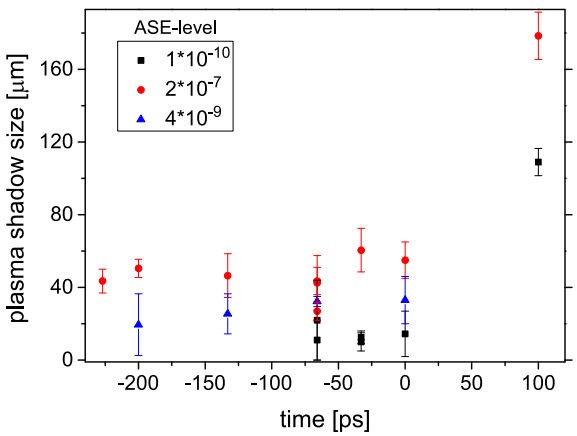

Figure 2: Size of the preplasma shadow for different times and three different ASE-levels

References

[1] F. Wagner et al, "Temporal contrast control at the PHELIX petawatt laser facility by means of tunable sub-picosecond optical parametric amplification", Appl. Phys. B. DOI 10.1007/s00340-013-5714-9 (2013)

[2] F. Wagner and V. Bagnoud, "Prepulse removement at the PHELIX short-pulse beam", GSI Scientific Report 2012 (2013)

Energy loss measurements of heavy ions in dense weakly coupled plasma generated by volumetric heating with hohlraum generated x-rays

A. Ortner[*1], *A. Blazevic*[2], *M. Basko*[7], *S. Bedacht*[1], *W. Cayzac*[2], *A. Frank*[5], *S. Faik*[6], *D. Kraus*[3], *T. Rienecker*[6], *G. Schaumann*[1], *D. Schumacher*[2], *An. Tauschwitz*[6,8], *F. Wagner*[1], *and M. Roth*[1]

[1]Technical University Darmstadt, Germany ; [2]GSI, Darmstadt, Germany; [3]UC Berkeley, USA ; [6]University Frankfurt, Germany ; [7]KIAM Moscow, Russia ; [8]HIC for FAIR, Germany

In two experimental campaigns in 2012 precise measurements of the energy loss of Ca ions in dense, partly ionized carbon plasma have been carried out. An unexpected hight increase of the stopping power in this weakly coupled plasma ($\Gamma \approx 0.5$) has been measured. This was the first time, that ion stopping in such a plasma was measured.

A 1 ns long, frequency doubled ($\lambda = 527$ nm) laser pulse with a total energy of 150 J is converted in a spherical cavity into X-rays with a radiation temperature of $T_r \approx 100$ eV. This Plackian radiation heats up a secondary cylindrical hohlraum to a radiation temperature of $T_r \approx 30$ eV. These soft X-rays are then used to heat volumetrically two thin carbon foils into a dense plasma state. A weakly coupled carbon plasma with an electron temperature of 5 eV to 15 eV and electron density of up to $5 \cdot 10^{21}$ cm^{-3} and an ionization degree of 2^+ to 4^+ is generated. The properties of the primary as well as of the secondary hohlraum have been extensively studied by RALEF2D hydro-simulations [2, 3] and characterized in several experimental campaigns [4]. It has been shown, that no gold from the walls of the cylindrical hohlraum flows into the ion path for about 5 ns, which allows us to study the interaction of an ion beam in a pure carbon plasma.

Fig. 1 shows the experimental setup used at the Z6 target area at GSI. The radiation temperature is measured with an X-ray streak spectrometer [4] and the electron density of the carbon plasma is characterized with a multi-frame interferometry. The ion energy loss is determined by a time of flight measurement of the delayed ion bunches. Details about the experimental setup and the double hohlraum targets can be found in [5].

* a.ortner@gsi.de

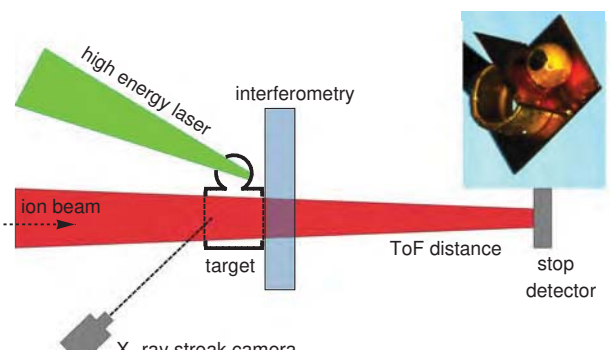

Figure 1: setup of the ion energy loss experiment

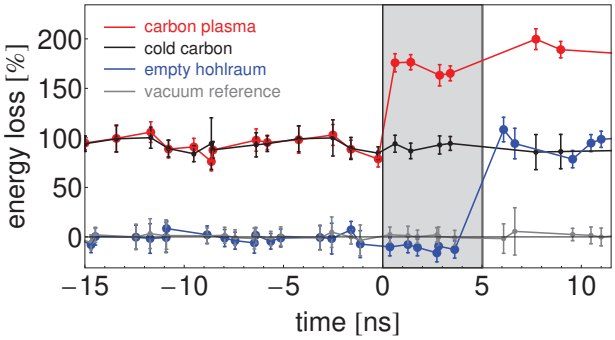

Figure 2: Energy loss results compared with an empty hohlraum, cold carbon and vacuum measurements. $t = 0$ ns indicates the beginning of the laser pulse. The gray area the 5 ns time probing window.

The experimental results are shown in Fig. 2 and compared to measurements of the ion bunch delay in cold carbon of the same areal density as well as to vacuum and to a empty hohlraum shot. The scale of the y-coordinate is normalized to the energy loss in cold carbon. As it can be seen on the "empty hohlraum" - measurement, the gold plasma coming from the wall, at earliest affects the ion bunches after 5 ns. In plasma an increase of the energy loss of +70 % is observed. Presently, our theoretical model basing on the CaSP code for the stopping-power calculation and on a newly developed Monte-Carlo code for the charge-state determination, cannot explain such a strong increase [6]. A crucial point to validate this theoretical approach is to compare the calculated charge state distribution with experimental data. For this reason, we will carry out a beam time in september 2014 where we will focus on the measurement of the charge state distribution of the outcoming ion beam after interacting with the plasma column.

References

[1] A. Ortner et al., GSI Report 2013-1, 374 p. (2013)
[2] M. M. Basko et al., GSI Report 2011-03 (2011)
[3] S. Faik et al., somewhere in this annual report
[4] D. Schumacher, PhD-Thesis, TU Darmstadt, (2012)
[5] A. Ortner et al., IFSA 2013 conference proceedings (2014)
[6] A. Ortner et al., somewhere in this annual report

 doi:10.15120/GR-2014-1-PNI-PP-05

Theoretical investigation of the charge transfer processes of heavy ions at intermediate energies interacting with a plasma

A. Ortner[*1], *A. Frank*[3], *A. Blazevic*[2], *and M. Roth*[1]

[1]Technische Universität Darmstadt, Germany; [2]GSI Darmstadt, Germany; [3]Helmholtz-Institut Jena, Germany

The influence of the plasma properties, like plasma density, temperature and ionization degree, on the development of the charge state distribution of a heavy ion beam interacting with this plasma was investigated theoretically by a Monte-Carlo code.

The charge transfer processes in plasma are quite different compared to those in cold matter due to the presence of free electrons and ionized atoms. In cold matter, the dynamic balance of the projectile charge state is mainly governed by impact ionization of the projectile and recombination with bound target electrons (non-radiative electron capture, NREC).

In plasma, the ionization processes are the same, but the rates increase significantly due to a reduced screening of the target nucleus potential. As in a plasma, the number of bound electrons is reduced, which consequently suppresses NREC, the recombination processes with free electrons, like radiative electron capture (REC), dielectronic recombination (DR) and three-body recombination (3BR), become more dominant. However, due to the much smaller cross sections for free electron capture processes, the recombination rates in plasma are typically dropping with higher ionization degrees. In addition, the plasma density is changing the mean free path length of the projectile ions which leads to higher collision rates and in consequence to increasing ionization rates with raising density.

The charge state of the projectile ion is determined by the ionization and recombination rates which are balancing each other out. After a certain interaction time in the plasma the charge state distribution reaches an equilibrium and a mean charge state can be determined. For our study we used an Ar^{16+} ion as projectile with an energy of 4 MeV/u interacting with a plasma column of 200 g/cm^{-2}. As shown in Fig. 1, the plasma parameter space varies from electron temperatures from 10 eV to 200 eV and ion densities of 10^{18} cm^{-3} to 10^{23} cm^{-3}.

* a.ortner@gsi.de

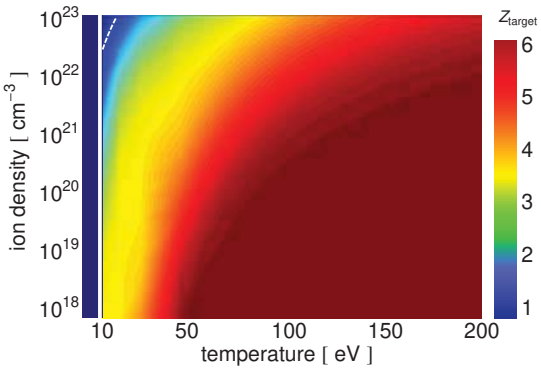

Figure 1: The plasma parameter space investigated in our study. The ionization degree of the carbon plasma is calculated by solving the saha equation.

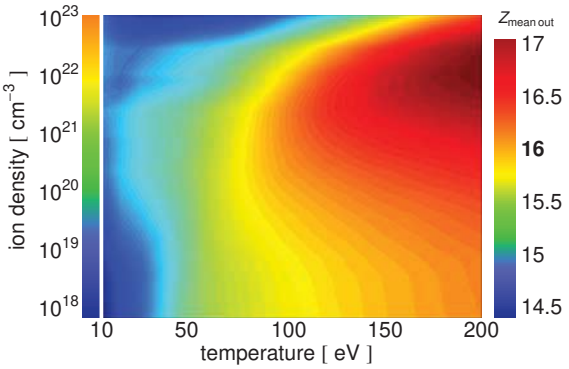

Figure 2: Mean charge state of an Ar^{16+} ion beam after interacting with 200 μg/cm^2 carbon plasma.

The calculated mean charge state in plasma compared to cold gas of the same density (color bar on the left side) is shown in Fig. 2. At hight temperatures one can clearly see the "density effect" where the charge state increases with higher densities. At low densities the temperature dependency, the so called "plasma effect" shows the reduction of the charge state to lower temperatures. As expected, in a hot plasma, the projectile mean charge state increases compared to the equilibrium charge state in cold matter of the same density. However, at low plasma temperatures, where a partly ionized plasma is predominant, both effects are compensating each other and even a decrease of the mean charge state in plasma compared to cold matter can be observed (e.g. $\rho = 5*10^{20}$ cm^{-3}, $T = 10$ eV to 50 eV). At detailed description of the code can be found in [1]. The code was benchmarked with experimental results [2]. This work was supported by the Helmholtz International Center for Fair and HGS-Hire.

References

[1] A. Frank, PhD-Thesis, TU-Darmstadt, (2012)

[2] A. Frank, A. Blazevic, W.Cayzac, A.Ortner, M.Roth et al., *Phys. Rev. Lett.* **110** 11 115001 (2013)

Radiation-hydrodynamic simulations of foils heated by hohlraum radiation*

S. Faik[1], *An. Tauschwitz*[1,4], *J. A. Maruhn*[1,2], *M. M. Basko*[2,3], *A. Ortner*[6], *A. Blažević*[5], *M. Roth*[6], *V. G. Novikov*[3], *and A. S. Grushin*[3]

[1]Goethe University, Frankfurt am Main, Germany; [2]EMMI, GSI, Darmstadt, Germany; [3]KIAM, Moscow, Russia; [4]HIC for FAIR, Frankfurt, Germany; [5]GSI, Darmstadt, Germany; [6]TU Darmstadt, Germany

An attractive way to generate a uniform plasma state for measurements of the ion stopping power is to heat a sample indirectly with the radiation of a millimeter-scale hohlraum. Recently, simulations of such a hohlraum target with an attached carbon foam [1] have been carried out with the newly developed code RALEF-2D. Now, new simulations are in progress to support another experimental approach at GSI. The target consists of two hohlraums, a primary spherical one irradiated by the PHELIX laser for the indirect X-ray heating of a secondary cylindrical hohlraum with two attached carbon foils. Simulations of the primary hohlraum [2] have shown to stay in good accordance with the experiment. Here we want to present the preliminary results of a series of simulations of the secondary hohlraum with the goal to find the optimum target configuration and to verify the ion stopping measurements [3].

The RALEF-2D code solves the one-fluid one-temperature hydrodynamic equations in two spatial dimensions and incorporates thermal conduction as well as radiation transport. The applied EOS, thermal conductivity, and spectral opacities were provided by the THERMOS code. Figure 1 shows the lateral cut of the simulated Cartesian (x, y) configuration which extends to infinity along the z-axis. Each carbon foil has an initial thickness $l_f = 1$ μm and areal density $<\rho_f l_f> = 0.1$ mg cm^{-2}. The supposedly empty parts of the simulated domain were filled with gases at density $\rho = 10^{-5}$ g cm^{-3}. The incoming X-rays of the primary hohlraum were set up in accordance with experimental measurements with a peak Planckian temperature of 93 eV. The X-ray heating ends at $t = 5$ ns. In the presented preliminary simulation the spectral energy transport by thermal radiation was treated with one frequency group. The final simulation will be done with 24 discrete groups $h\nu_i$ which implies a much longer computational time. The angular dependence of the radiation intensity was calculated with the S_{30} method, which offers 960 discrete ray directions over the entire 4π solid angle.

Figure 2 shows the free electron density and the LTE ionization degree at $t = 5.3$ ns when the expanding carbon plasma clouds collide. At this time the ablated gold plasma is close to get into the way of the ion beam. Before the collision the carbon free electron densities are of the order $n_e \approx 1 - 4 \times 10^{20}$ cm^{-3} with an ionization degree of $Z \approx 3.2 - 3.8$ at plasma temperatures $T \approx 10 - 16$ eV. Hence a time window of nearly 6 ns exists with appropriate plasma conditions for the ion stopping measurements.

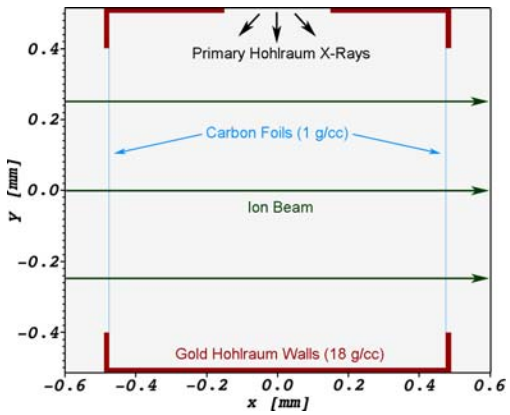

Figure 1: 2D lateral cut of the simulated configuration.

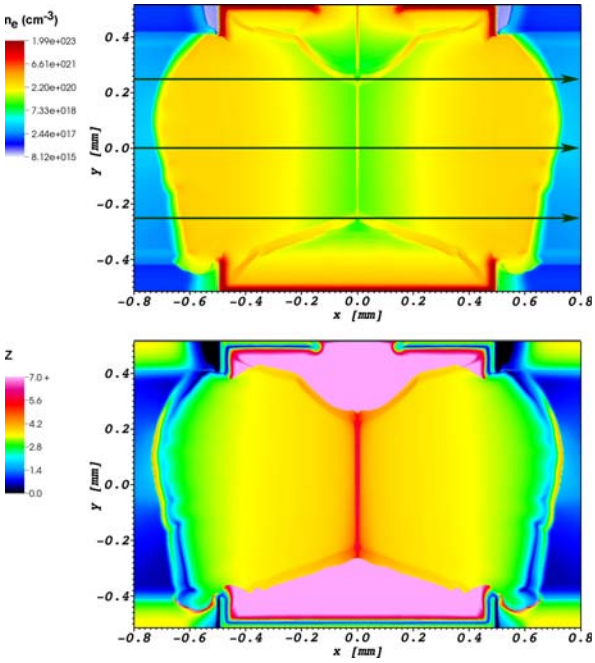

Figure 2: Color contour plots of the free electron density n_e and the LTE ionization degree Z at t = 5.3 ns, when the carbon plasma clouds collide at the hohlraum center.

References

[1] S. Faik et al., HEDP 10 (2014) 47.

[2] M. M. Basko et al., GSI Report 2011-03.

[3] A. Ortner et al., GSI Report 2013-1.

* supported by BMBF (Project 05P12RFFTR), HIC for FAIR, EMMI

 doi:10.15120/GR-2014-1-PNI-PP-07

Ion energy loss at maximum stopping power in a laser-generated plasma

W. Cayzac[1], V. Bagnoud[1,2], M.M. Basko[3], S. Bedacht[4], A. Blažević[1,2], O. Deppert[4], A. Frank[2], D.O. Gericke[5], L. Hallo[6], A. Knetsch[4], D. Kraus[7], G. Malka[8], A. Ortner[4], K. Pépitone[6], G. Schaumann[4], T. Schlegel[2], D. Schumacher[1], An. Tauschwitz[9,10], J. Vorberger[11], F. Wagner[4], and M. Roth[4]

[1]GSI; [2]Helmholtz institute Jena; [3]KIAM Moscow; [4]Technical University of Darmstadt; [5]University of Warwick; [6]CEA/CESTA; [7]University of California; [8]Univ. Bordeaux-CEA-CNRS CELIA UMR 5107; [9]University of Frankfurt; [10]HIC for FAIR; [11]MPI for physics of complex systems

Ion stopping in plasma is relatively well-understood for projectile velocities much higher than the thermal velocity of plasma electrons ($v_{ion}/v_{th} >> 1$), but large uncertainties remain around the stopping-power maximum, for $v_{ion}/v_{th} \approx 1$. This parameter region is of crucial importance for ICF and especially for the alpha-particle heating of the DT fuel. Yet, its theoretical description is difficult [1] and no experimental data are available in order to benchmark the existing theories and numerical codes. Within this collaboration, first measurements of this kind have been performed and compared with theoretical predictions.

The plasma was generated by the use of 100 μg/cm^2 carbon foils irradiated from both sides by the second harmonic frequency of the PHELIX and nhelix laser systems, where random phase plates were employed to reach a 1-mm-diameter top-hat uniform illumination [2]. This configuration resulted in a spatially quasi-homogeneous and fully ionized plasma slab after a few ns, which has been well-characterized by the joint use of multi-frame interferometry [3] and hydrodynamic simulations with the RALEF2D code [4]. The projectile energy was 0,5 MeV/u, and carbon ions were employed on the basis of Monte-Carlo calculations showing that they become completely stripped in the fully ionized plasma. In this way, the whole set of beam-plasma parameters is known, which enables reliable comparisons of ion energy-loss data with the theory for the first time. The energy loss was predicted theoretically by combining the results of the RALEF2D simulations and of the Monte-Carlo code, according to (i) perturbative stopping-power approaches basing on the first Born approximation: asymptotic Bethe and Bethe-Bloch formulas, standard stopping model (SSM), dielectric theory based on a linearized Vlasov equation, Li-Petrasso model, and (ii) a nonperturbative stopping description using a T-Matrix scheme [5].

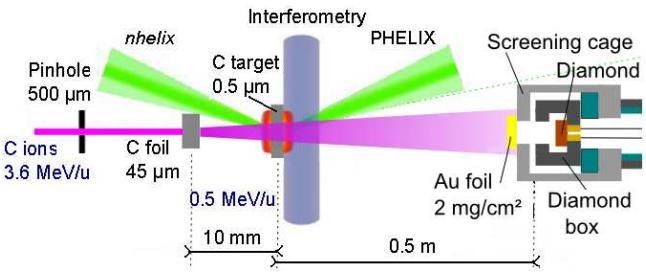

Figure 1: Schematics of the experimental setup.

The experimental setup is shown in Fig.1. The ions were decelerated to 0,5 MeV/u by using a carbon foil of 45 μm thickness. The time-of-flight distance was 50 cm, allowing a 100 keV energy resolution for an optimal test of the theories. The ions were detected on a specifically developed polycrystalline chemical-vapour-deposition (CVD)-diamond detector able to register 20 % of the beam and shielded against any plasma radiation [6].

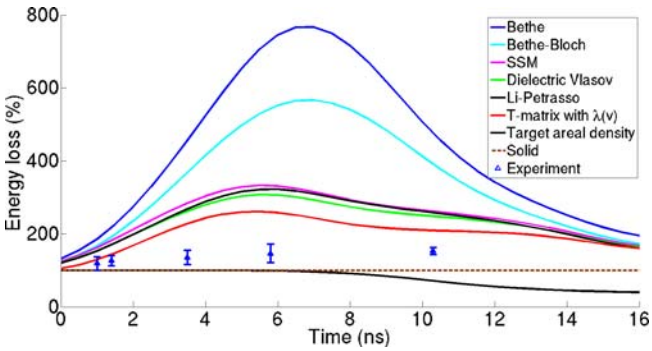

Figure 2: Energy loss as a function of time. 100 % corresponds to the energy loss in the solid foil. The experimental points are compared with the theoretical curves.

A first experimental campaign was conducted, and preliminary results are compared with the theoretical predictions in Fig.2. A maximum increase in energy loss in plasma of 53 % in relation to the cold target is observed. In the time frame where the plasma is hot and highly ionized and hence $v_{ion}/v_{th} \approx 1$, the obtained experimental values are thus significantly smaller than predicted by any theory. The precise interpretation of these discrepancies is in progress and further simulations as well as measurements are planned.

This project has been supported by CEA/CESTA and the Région Aquitaine as well as by BMBF and HIC4FAIR.

References

[1] D.O. Gericke et al., Phys. Rev. E **60**, 904 (1999)

[2] A. Frank et al., Phys. Rev. Lett. **110**, 115001 (2013)

[3] M. Boerner et al., Rev. Sci. Instrum. **83**, 043501 (2012)

[4] An. Tauschwitz et al., High Energy Density Phys. **9**, 158 (2013)

[5] D.O. Gericke et al., Laser Part. Beams, **20**, 471 (2002)

[6] W. Cayzac et al., submitted to J. of Physics, Conf. Ser. (2014)

A laser-driven proton beamline at GSI*

S. Busold[1], *D. Schumacher*[4], *O. Deppert*[1], *C. Brabetz*[2], *F. Kroll*[3], *A. Blazevic*[4,5], *V. Bagnoud*[4,5], *I. Hofmann*[4], *and M. Roth*[1]

[1]TU Darmstadt, IKP, Germany; [2]JWG Universität Frankfurt, IAP, Germany; [3]Helmholtz - Zentrum Dresden-Rossendorf, Germany; [4]GSI, Darmstadt, Germany; [5]Helmholtz Institut Jena, Germany

The LIGHT beamline. Laser-based ion acceleration became an extensively investigated field of research during the last 15 years. Within several micrometers particles are accelerated to MeV energies. The main drawback for many applications is their continuous exponential energy spectrum and large divergence angle from source. The exploration of proper beam shaping and transport is the major goal of the LIGHT collaboration [1], for which an experimental test beamline has been built at GSI. This *LIGHT beamline* at GSI is located at the Z6 area within the experimental hall. The PHELIX 100 TW laser beamline is currently capable of delivering up to 15 J of laser energy in a 650 fs short pulse on target, focused to intensities exceeding 10^{19} W/cm^2 within the Z6 target chamber. Protons could be accelerated via the TNSA mechanism to maximum energies of 28.4 MeV and propagated through a pulsed high-field solenoid with a field strength up to 9 T, which is used to select a specific energy interval from the continuous initial spectrum via chromatic focusing. A large capture efficiency of 34% of the initial protons within a selected energy interval (ΔE=(10$\pm$0.5) MeV) was measured [2].

The protons are weakly focused to a 15$\times$15 mm^2 spot at 3 m distance to the source, containing particle numbers $>10^9$ in a single 8 ns short bunch. The energy spread of the bunch is (18$\pm$3)% and the central part of the bunch can be described by a Gaussian-like distribution:

$$\frac{dN}{dE} = \frac{N_0}{E} exp\left(-\frac{(E-E_0)^2}{2\sigma^2}\right) \qquad (1)$$

Figure 1 (upper graph) shows the experimental results (E$_0$=9.6 MeV, σ=(0.7$\pm$0.06) MeV) compared to simulations.

First experiments on phase rotation. The cavity is a three gap spiral resonator, inserted to the beamline between 2 and 2.55 m distance to the laser target and connected to the UNILAC rf system. Injection at -90 deg synchronous phase and 100 kW input power leads to energy compression of the bunch. The energy spread at FWHM (ΔE/E$_0$=2.35σ/E$_0$) could be reduced to (2.7$\pm$1.7)% at a central proton energy of E$_0$=9.7 MeV (see lower graph in figure 1) and particle numbers of 1.2×10^9 ($\pm$15%) within the FWHM were measured. A detailed description has been published in [3].

Furthermore, the experimental setup allows for phase focusing. Simulations predict shortest possible bunch durations down to the sub nanosecond regime. Highest single bunch intensities of 10^{10} protons/ns are accessible. An experimental campaign is planned for 2014.

Thanks to the compact laser-driven source the whole beamline is only 3 m long in total and represents a currently unique combination of novel laser and conventional accelerator technology to generate highest single bunch intensities in the multi-MeV region.

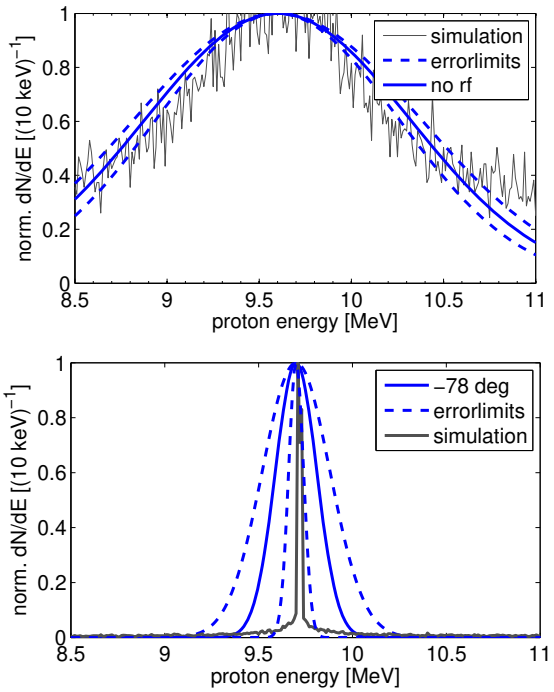

Figure 1: Simulated and measured proton spectra at a distance of 3 m to the source for solenoid focusing only (upper) and additional energy compression (lower figure) for a central bunch energy of E$_0$=(9.6$\pm$0.1) MeV.

References

[1] S. Busold *et al.*, *Shaping laser accelerated ion for future applications - the LIGHT collaboration*, NIMA **740**, 94-98 (2014)

[2] S. Busold *et al.*, *Focusing and transport of high-intensity multi-MeV proton bunches from a compact laser-driven source*, PRSTAB **16**, 101302 (2013)

[3] S. Busold *et al.*, *Commissioning of a compact laser-based proton beamline for high intensity bunches around 10 MeV*, PRSTAB **17**, 031302 (2014)

*This work is supported by the Helmholtz Institute Jena and HIC for FAIR.

 doi:10.15120/GR-2014-1-PNI-PP-09

Laser-driven ion acceleration with a hollow beam at PHELIX*

C. Brabetz[1], *S. Busold*[2], *O. Deppert*[2], *D. Schumacher*[3], *B. Zielbauer*[3,4], *and V. Bagnoud*[3,4]

[1]Johann Wolfgang Goethe-Universität, Frankfurt am Main, Germany; [2]Technische Universität Darmstadt, Darmstadt, Germany; [3]GSI Helmholtzzentrum für Schwerionenforschung, Darmstadt, Germany; [4]Helmholtz-Institut Jena, Jena, Germany

In the framework of the Laser Ion Generation Handling and Transport (LIGHT) research project at GSI, the reduction of the divergence of the laser accelerated ions is a central issue. One solution relies on engineering the electron sheath used in laser-driven proton acceleration (target normal sheath acceleration, TNSA) for reducing the initial divergence of the ion beam. In the experimental campaign conducted in 2013 a hollow laser focal spot has been used to drive proton acceleration. This focal spot is created via a spatial phase shaping element in the laser beam path. A qualitative effect of the focal spot shape on the ion beam divergence was observed as expected, and the energy cut-off in the proton spectrum was higher with the hollow focus.

Report on the 2013 beam time

During the beam time, we have continued our investigations on laser-driven ion acceleration with engineered beams. In total, we had 26 successful high-energy experiment shots on gold foils with different thicknesses with and without the hollow beam during that beam time. We have focused particularly on avoiding strong on-shot wave front distortion in the laser amplifier (astigmatism) because we saw how crucial this is for that kind of experiment. Therefore a newly developed bending mechanism was installed to the main folding mirror in the laser chain, addressing the on-shot astigmatism aberration. These efforts resulted in a significant improvement of the laser beam transport through the PHELIX system, as we could verify from the boost of the maximum proton energy measured by radiochromic film imaging spectroscopy [1].

The dependency of the achieved maximum proton energy and the envelope divergence on the used flat gold foil target thickness was experimentally shown. In contradiction to the widely accepted intensity scaling law of TNSA (the maximum proton energy scales with the square root of the laser intensity), higher proton energies were achieved in presence of the hollow focus. The focal spot size of the hollow focus is roughly two times larger compared to the Gaussian one. This results in an laser intensity drop by a factor of 4 and therefore a two times lower maximum proton energy was expected for the hollow laser beam. In shots with the hollow focus (with a 2π total step height of the phase shaping element) the dependency of the maximum proton energy on the target thickness could be observed (figure 1). With a larger hollow beam (4π) this effect is shifted to thicker targets. For a Gaussian focal spot no scaling was observable. With the optimum target thicknesses it was demonstrated that the half envelope divergence could be decreased by $\approx 3°$ (figure 2) in case of the hollow focus in comparison to the standard Gaussian focal spot.

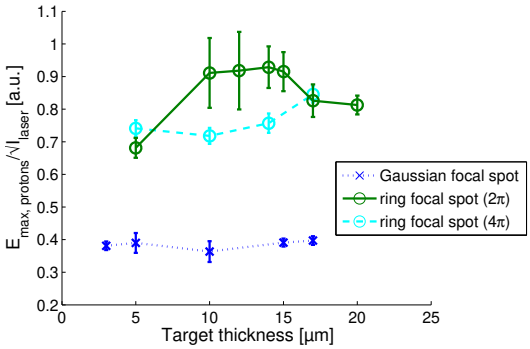

Figure 1: Scaling of the maximum proton energy with different target thicknesses. A connection of the maximum proton energy and the target thickness can be observed as well as a systematically higher scaled proton energy. Shots with the 2π hollow focus are drawn as solid, the 4π hollow focus as dashed, and the Gaussian focus as a dotted line.

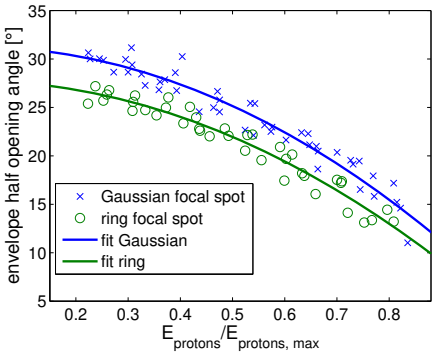

Figure 2: Comparison of different focal spot geometries and their effect on the envelope divergence angle. Each data point represents a RCF layer and the therein measured proton imprint size, scaled by the maximum proton energy of the corresponding shot for comparison. The tendency to achieve a smaller envelope divergence with the hollow beam can be observed, given by the two average lines.

References

[1] F. Nürnberg et al., Rev. Sci. Instrum. 80, 033301, 2009

* Work supported by GSI(PHELIX) / HGShire/ HIC for FAIR

Laser-driven Ion Acceleration with Cryogenic Hydrogen Targets*

S. Bedacht† [1], *O. Deppert*[1], *S. Geschwind*[1], *R. Jaeger*[1], *A. Kleinschmidt*[1], *F. Mertins*[1], *A. Ortner*[1], *V. Schanz*[1], *G. Schaumann*[1], *A. Tebartz*[1], *F. Wagner*[1], *B. Zielbauer*[2,3], *V. Bagnoud*[2,3], *M. Roth*[1], *and D.H.H. Hoffmann*[1]

[1]Technische Universität Darmstadt, Germany; [2]GSI, Darmstadt, Germany; [3]Helmholtz-Institut Jena, Germany

Abstract

We successfully demonstrated laser-driven ion acceleration with cryogenic hydrogen targets at *PHELIX*. By using short pulses with 200 J in 500 fs and the *uOPA* high contrast option [1] an intensity on target of around $5 \cdot 10^{20}$ W/cm^2 was obtained. This enabled the acceleration of ions from cryogenic hydrogen targets and plastic targets with energies up to 65 MeV/nucleon for protons, setting a new record for laser-driven ion acceleration at *PHELIX*.

Introduction

For laser-driven ion acceleration the mechanism of *Target Normal Sheath Acceleration* (*TNSA*) has been dominant for the last ten years. Typical experiments at *PHELIX* involving metal targets made from aluminum, copper, and gold with thicknesses in the range of 5 μm to 50 μm yielded proton energies of up to 40 MeV/nucleon. In order to achieve higher particle energies new mechanisms of laser-driven ion acceleration need to be exploited such as the *Laser Breakout Afterburner* (*BOA*) [2] scheme. This scheme relies on a phase of relativistic transparency of the target during the interaction with the laser, thus making high demands on both the driving laser pulse in terms of energy and temporal contrast as well on the target in terms of composition and thickness.

Setup

The experimental campaign *P060* was carried out in two runs of 10 and 20 shifts of *PHELIX* beam time in April and August of 2013, respectively. The experiment was set up inside the new target chamber in the *PHELIX* laser bay. It made use of the *uOPA* high contrast option [1] of the short pulse frontend and an off-axis parabolic mirror with an f/1.6 opening. With pulses delivering 200 J in 500 fs the peak intensity on target was on the order of $5 \cdot 10^{20}$ W/cm^2. For the production of hydrogen targets a custom made cryogenic target mount cooled by a cold head down to temperatures as low as 8 K was used. [3] The cryogenic hydrogen targets were produced just prior to the actual laser shot at the laser interaction point with a thickness of few μm to 100 μm. Additionally, thin plastic targets made from polymethylpentene with thicknesses in the range of 200 nm up to 1100 nm were used.

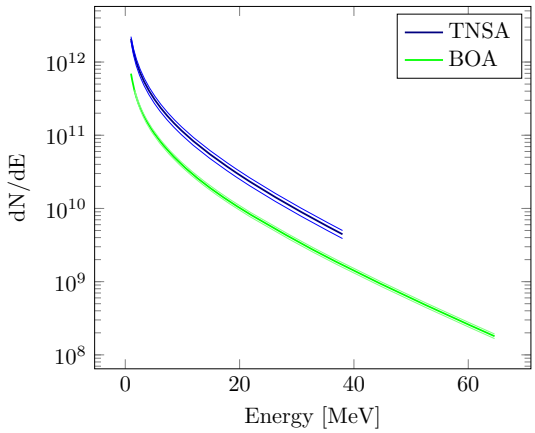

Figure 1: Particle distribution function dN/dE of laser-driven protons obtained from a 700 nm thick plastic target at *PHELIX* using radiochromic film. The blue and the green lines correspond to protons accelerated via the *TNSA* and *BOA* acceleration schemes, respectively.

Results

For the very first time pure cryogenic hydrogen targets and combinations of plastic substrates with layers of cryogenic hydrogen were employed for laser-driven ion acceleration. The pure cryogenic hydrogen targets yielded energies of up to 41 MeV/nucleon. Adding cryogenic hydrogen layers to 200 nm plastic substrates significantly improved the smoothness of the spatial profile of the accelerated ions and yielded higher ion energies of up to 57 MeV/nucleon. The shots at pure plastic targets yielded ion energies of up to 65 MeV/nucleon for a target thickness of 700 nm.

By tilting the target with respect to the laser propagation axis by an angle of about 10° two spatially separated ion beam profiles could be obtained. The ion beam along the target normal direction can be attributed to *TNSA* while the beam profile along the laser propagation axis corresponds to an acceleration via *BOA* [2]. The particle distribution function dN/dE of these two beams is shown in figure 1.

References

[1] F. Wagner et al., *Applied Physics B*, DOI 10.1007/s00340-013-5714-9 (2013)

[2] L. Yin et al., *Laser and Particle Beams*, DOI 10.1017/S0263034606060459 (2006)

[3] S. Bedacht et al., *GSI Scientific Report 2011*, PNI-PP-25, page 458 (2012)

* Work supported by TU Darmstadt, GSI(PHELIX), BMBF, HiPER

† s.bedacht@gsi.de

 doi:10.15120/GR-2014-1-PNI-PP-11

Coloration quenching of radiochromic films irradiated with proton energies close to maximum energy loss *

O. Deppert[1], *C. Brabetz*[2], *S. Busold*[1], *A. Schreiber*[1], *D. Schumacher*[3], *A. Blaževic*[3], *and M. Roth*[1]

[1]Technische Universität Darmstadt, Darmstadt, Germany; [2]Johann Wolfgang Goethe-Universität, Frankfurt am Main, Germany; [3]Helmholtzzentrum für Schwerionenforschung, GSI, Darmstadt, Germany

Radio**C**hromic **F**ilms (RCF) are widely used as beam diagnostics in the context of laser driven proton acceleration, where typically angular divergent beams (up to 25° half opening angle) with broad exponential energy spectra are generated. RCFs provide a precise measurement of the spatial beam profile and allow to determine the angular distribution. Moreover, used in a so called "stacked" configuration, where several RCFs are staggered behind each other, enables to fully reconstruct the spectral properties of the proton beam. This can be combined with special structured laser-targets to additionally reconstruct important beam parameters like proton source size and transverse and longitudinal beam emittance. The methods to fully characterize laser-accelerated proton beams were earlier published by our group as the so called **R**adiochromic film **I**maging **S**pectroscopy (RIS) [1].

In the scope of the ongoing research to further optimize the RIS, we have focused the attention to the response function of the active layer of different RCF types. Therefore, we have carried out precise dose calibrations with 10 MeV protons from the TANDEM accelerator at the Helmholtz-Zentrum Dresden-Rossendorf to reduce the uncertainty in deposited dose to be less than 5%. Besides this, we have implemented a multi-color-channel calibration [2] which handles each digitized RGB-channel independently. A dynamic range weighting allows to choose the optimum ratio of each calibration to calculate a weighted mean dose from the three color-values. This method extends the dose range of the RCF by a factor of four while at the same time increases the calibration precision over the whole dose range. Furthermore, we have investigated in detail the dose-response function if irradiated by proton energies close to their maximum energy deposition inside the active layer. The maximum energy deposition integrated over the thickness of the active layer material gets reached, if a proton with certain energy gets fully stopped at the end of the active layer material. Therefore, we carried out measurements to scan the proton energy around its maximum energy deposition and investigated its influence on the response function of the RCF. We used complementary scanning methods to vary the proton energy in front of the active layer, either by reducing the proton energy of the accelerator (direct scan) or by using stacked RCFs with aluminum foils of different thicknesses in front. The direct scan was additionally carried out for two different beam currents. To model our experiment we have used the GEANT4 toolkit [3] to simulate the energy deposition inside the active layer material of HD-V2 RCFs. We numerically investigated a parameter study for different proton input energies used in the experiment. It was found that the coloration of films irradiated close to the maximum energy loss is significantly reduced, resulting in a lower dose estimation from our calibration compared to the simulated deposited dose of GEANT4. The relative effectiveness η_{eff} (ratio of measured to simulated dose) of the response function is shown in figure 1. It can be clearly seen that the effectiveness follows a Bragg-curve like slope with its minimum of $(60.5 \pm 0.3)\%$ for input energies of (487 ± 22) keV which corresponds to the input energy of maximum integrated energy loss in the active layer. To fit the data-set (light-blue, 2σ confidence black-dashed) a parameterized Bragg-model was applied.

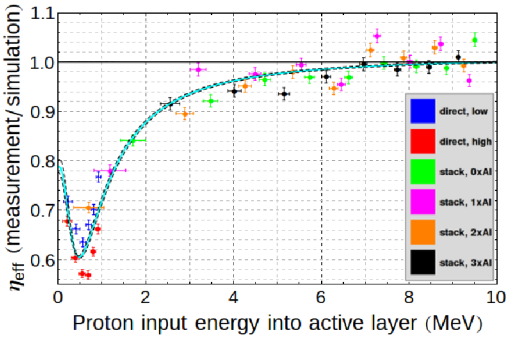

Figure 1: Relative effectiveness of RCF response function for different proton energies into active layer of HD-V2.

In order to deconvolve our results from the layer thickness we have developed a proton tracking routine based on the SRIM tables. It was embedded inside a least-square fitting routine. The model to deconvolve from layer thickness is derived from the derivative of the parameterized Bragg-model (self-similar ansatz) used before and optimized during the tracking. With this approach we were able to construct a relative differential effectiveness $d\eta_{\mathrm{eff}}/dx$ which can be applied to any MonteCarlo or tracking routine to calculate the response function of RCFs from the differential energy loss including the quenching correction.

Applied to laser-accelerated proton beams, the undervalue in calculated particle numbers will be approx. 20% if the effectiveness of the RCF is not taken into account.

References

[1] F. Nürnberg et al., Rev. Sci. Instrum. **80**, 033301, 2009

[2] O. Hupe et al., Med. Phys. **33**, 4085, 2006

[3] S. Agostinelli et al., Nuc. Instrum. Meth., **506.3**, 250-303, 2003

* This work is supported by **HIC4FAIR**.

Electron beam based space charge measurement of intense ion beams*

S. El Moussati†[1], *D.H.H Hoffmann*[1], *O. Meusel*[3], *U. Ratzinger*[3], *S. Udrea*[1], *D. Varentsov*[2], *and K. Weyrich*[2]

[1]TU Darmstadt, Germany; [2]GSI, Darmstadt, Germany; [3]Uni- Frankfurt, Germany

In order to determine the transverse profile of an intense, strongly focused ion beam, like those at the HHT experimental area at GSI or at the future facility FAIR, a non-invasive methode has been successfully developed and tested. This methode is based on the electrons which pass perpendicular through the ion beam and get deflected because of its the electromagnetic field and was designed as a possible alternative to gas scintillation [1].

Theoretical Model

The relationship between the charge in the ion beam and the deflection angle of an electron is given by the equations below [2]:

$$\frac{d}{dy}\theta(y) = -\left(\frac{e}{2\epsilon_0 E_e}\right)\cdot q(y)$$

$$|\theta_{max}| = \frac{e}{4\epsilon_0}\cdot\frac{\lambda}{E_e}$$

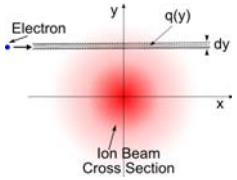

Inside the ion beam the charge $q(y) = \int \rho(x,y)\,dx$ is proportional to the first derivative of the deflection angle.

Outside the ion beam the deflection angle of the electrons stays constant and depends only on the line charge density (λ) of the ion beam and the electron energy (E_e).

Numerical Calculations

In order to test the theoretical model and to show that one can distinguish between different ion beam distributions several numerical calculations have been performed.

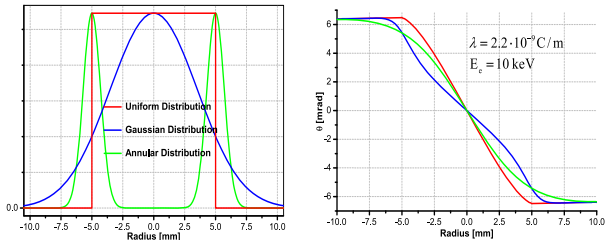

Figure 1: On the left: Uniform, Gaussian and annular transversal charge distributions of an ion beam as function of radius. On the right: The deflection angle of electrons, which pass perpendicular through the ion beam.

An ion beam with a radius of 5 mm and a line charge density $\lambda = 2.2\cdot 10^{-9}$ C/m has been considered. The electron beam had an energy of 10 keV and a slit shaped transversal cross-section which was tilted by 45^o with respect to the ion beam [3].

* Work supported by BMBF and the Helmholtz Russia Joint Research Group.

† s.elmoussati@gsi.de

Experimental Setup

At the FRANZ-Accelerator facility at the University of Frankfurt an electron beam system to measure the transverse profile of a cw Helium ($^4He^+$) beam was setup.

Figure 2: On the left is the electron beam system and on the right the detection system (Camera is out of image).

Experimental Results

The ion beam had an energy of 13.5 keV/ion and a line charge density of about $1.25\cdot 10^{-9}$ C/m. The electron beam had an energy of 2.3 keV and a slit shaped transversal cross-section which was tilted by 45^o with respect to the ion beam.

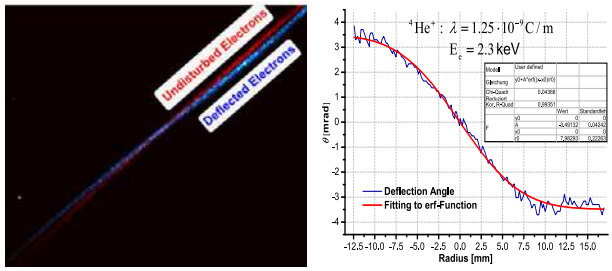

Figure 3: The left image shows one experimental result, the right image the analysis of this result.

Conclusion

An electron beam diagnostic device for the measurement of the transverse charge distribution of an intense ion beam was successfully developed and tested. The numerical simulations show a very good agreement to the theoretical model and the experiments were in good qualitative agreement with the theoretical predictions. Further investigations are needed to improve the precision of the method.

References

[1] D. Varentsov et al, Contributions to Plasma Physics **48**, pp. 586-594 (2008)

[2] Prabir K. Roy et al, Review of Scientific Instruments **76**, 023301 (2005)

[3] W. Blokland et al, Proceedings of 2011 Particle Accelerator Conference, New York, NY, USA, 1438 (2011)

 doi:10.15120/GR-2014-1-PNI-PP-13

Target development for Warm Dense Matter research

J. Helfrich[*1], *G. Schaumann*[1], *An. Tauschwitz*[2], *M. Basko*[3], *B. Lommel*[4], *B. Kindler*[4], *and M. Roth*[1]
[1]TU Darmstadt, Germany; [2]Uni Frankfurt, Germany; [3]KIAM, Moscow, Russia; [4]GSI, Darmstadt, Germany

Introduction

Carbon is one of the most abundant elements on earth. It's behavior in the Warm Dense Matter regime at very high pressures in the Mbar area and several thousand degrees Celsius is part of current research. A better understanding of carbon under these conditions is important for the understanding of planetary cores, beam dumps for accelerators or as a component of plastic in inertial confinement fusion targets and for Equation of State systems to improve and benchmark this equation [1]. These exotic states can be achieved in the laboratory by a shock wave which is driven by a laser. The final state depends on the laser intensity and the initial carbon structure and density. In previous experiments it was possible to generate liquid carbon and to prove it with X-ray scattering. This was made possible by the method of X-ray Thomson scattering, which is planned as a key diagnostic for the plasma physics research program at FAIR [2]. In the next step, the solid-liquid phase transition region should be determined more accurately. This will be intend with a new target geometry and a VISAR (Velocity Interferometer System for Any Reflector) detector.

Target design and Simulations

A novel idea is to reduce the laser intensity for the shock generation so far that there is no phase transition to the liquid state and then initiate the solid liquid phase transition using a further shock. This should be achieved by the reflection of a part of the initial shock wave from a fixed wall by a conical geometry (see figure 1).

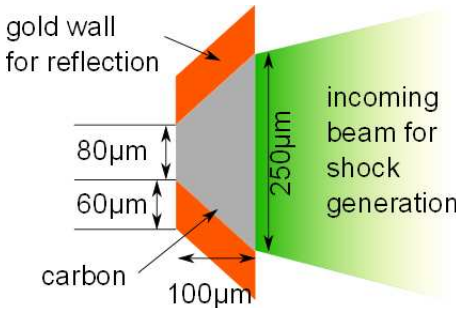

Figure 1: sketch of the cone target

The shock wave is reflected on both sides and converges at the center. Figure 2 shows a RALEF2D simulation of the target geometry [3]. In simulations it is clearly seen how the shock-wave is reflected from the gold wall resulting in an increase of the density and temperature of the shocked carbon.

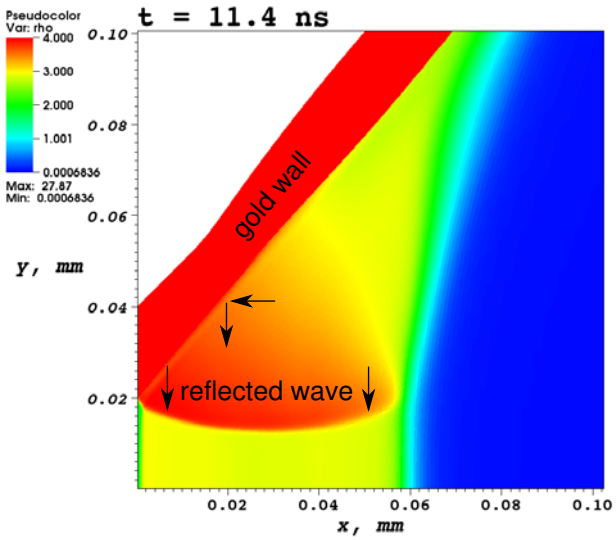

Figure 2: density increased by the reflected shock wave simulated with the RALEF2D code

The best reflective material has a high sound velocity and a high density such as osmium or uranium, but the processing, handling and safety aspects of these materials are not acceptable. The best compromise for the reflective wall is gold.

Target production

Target production is challenging due to the sub millimeter size of the samples. Cones were made from a carbon rod which was processed with a CNC precision lathe at the target laboratory of the TU Darmstadt. In the next step, the carbon was coated with gold. The gold coating was done by DC sputtering under argon in the target laboratory of GSI. For the shock wave reflection a good connection between the gold and carbon is require which is ensured by this method. This work was supported by BMBF project 05P12RDFA1.

References

[1] S. H. Glenzer, R. Redmer, Rev. Mod. Phys. 81, 1625 (2009)
[2] FAIR Baseline Technical Report (2006)
[3] M. M. Basko, J. Maruhn and An. Tauschwitz, GSI Scientific Report 2009: GSI Report 2010-1, p. 410.

*j.helfrich@gsi.de

Simulations of a conical target for Warm Dense Matter-experiments*

An. Tauschwitz[1,2], *M. M. Basko*[3,4], *J. A. Maruhn*[1], *J. Helfrich*[5], *and M. Roth*[5]

[1]Goethe University, Frankfurt, Germany; [2]HIC for FAIR, Frankfurt, Germany; [3]EMMI, GSI, Darmstadt, Germany; [4]KIAM, Moscow, Russia; [5]TU Darmstadt, Germany

In recent experiments at GSI liquid carbon was investigated using spectrally resolved x-ray scattering from laser-irradiated shocked carbon samples [1]. The goal of the upcoming experimental campaign is a more accurate determination of the solid-liquid phase transition of carbon. For these experiments it was proposed to used a conical target configuration which allows to increase the compression and the temperature in the laser-driven shock compared to irradiation of a plane foil [2]. The target consists of a tapered tube made of gold filled with graphite of $\rho_0 = 1.9\,\mathrm{g/cm^3}$ initial density. The wide side of the cone is irradiated with a laser. The length of the cone, $L = 140\,\mu$m and the radius of the narrow end, $r_1 = 20\,\mu$m were fixed by demand of the scattering diagnostics. The radius of wide side, $r_0 = 90\,\mu$m was adapted numerically to the nhelix laser parameters.

Simulations were done using the RALEF-2D code [3] which solves the one-fluid one-temperature hydrodynamic equations in two spatial dimensions by a second-order Godunov-type numerical scheme using the ALE approach. Thermal conduction, radiation transport, and laser energy deposition by means of inverse bremsstrahlung absorption are coupled using a symmetric semi-implicit approach with respect to time discretization. Here we present the results for a $\lambda = 532\,$nm laser pulse of 30 J over a focal spot of radius $r_f = 125\,\mu$m; the 11-ns long pulse was ramped with 3-ns linear rise and fall intervals. The spectral opacities and the equation of state data were generated with the THERMOS code [4].

For the planar carbon foil the simulation shows a density of $\rho = 3.3\,\mathrm{g/cm^3}$ and a temperature of $T = 0.25\,$eV. The calculated density distribution in the conical target is displayed in Fig. 1. A shock wave induced by the laser in the graphite propagates to the narrow end of the cone and becomes stronger due to reflection at the interface to the gold shell, as shown in Fig. 1a. An increase of density to $\rho = 3.4\,\mathrm{g/cm^3}$ due to reflection of the shock wave on the gold interface can be seen from the density distribution at $t = 9\,$ns. The reflection at the axis of symmetry corresponds to $t = 13.5\,$ns (Fig. 1b). Because of the converging axial symmetry, at this time the shock wave is amplified in a small region near the axis ($\rho = 4.75\,\mathrm{g/cm^3}$). A planar shock develops at the end of the cone with a density of $\rho = 3.75\,\mathrm{g/cm^3}$ and a temperature of $T = 0.7\,$eV resulting from the propagation of the laser launched shock at $t = 16\,$ns (Fig. 1c).

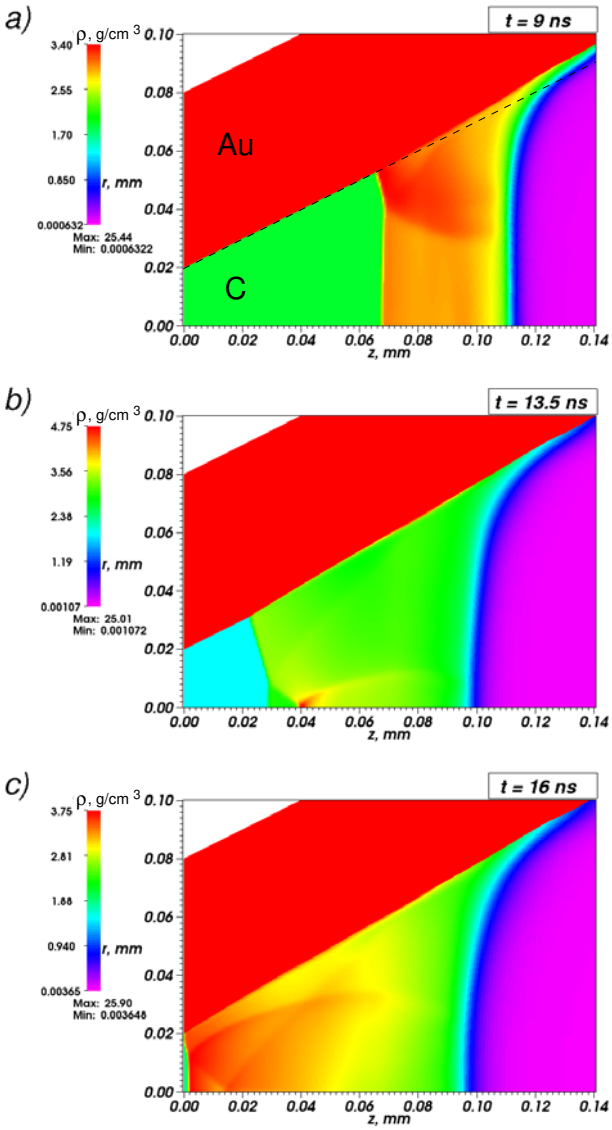

Figure 1: Color contour plots of density ρ in a conical target at different times. The laser beam comes from the right.

References

[1] D. Kraus et al., Phys. Rev. Lett. **111** (2013) 255501.

[2] J. Helfrich et al., "Target development for Warm Dense Matter research", this report.

[3] M. Basko, J. Maruhn, An. Tauschwitz, GSI Report 2011-03.

[4] A.F. Nikiforov, V.G. Novikov, V.B. Uvarov, *Quantum-statistical models of hot dense matter: methods for computation of opacity and equation of state*, Birkhäuser, 2005.

* supported by BMBF (Project 05P12RFFTR), HIC for FAIR, EMMI

 doi:10.15120/GR-2014-1-PNI-PP-15

Experimental Studies and Theoretical Interpretation of Hydrodynamic Tunneling of SPS Protons in Solid Targets *

R. Schmidt[1], *J. Blanco Sancho*[1], *F. Burkart*[1], *D. Wollmann*[1], *N.A Tahir*[2], *A. Shutov*[3], *and A.R. Piriz*[4]
[1]CERN, Geneva, Switzerland; [2]GSI, Darmstadt, Germany; [3]IPCP, Chernogolovka, Russia; [4]UCLM, Ciudad Real, Spain

The phenomenon of hydrodynamic tunneling has been experimentally studied at the CERN HiRadMat facility using the SPS beam [1]. The beam parameters include, proton energy = 440 GeV, bunch intensity = 1.5×10^{11}, bunch length = 0.5 ns, bunch separation = 50 ns and σ of the transverse intensity distribution = 0.2 mm. In two experiments, 108 and 144 proton bunches, respectively, were used and the protons were delivered in sets of 36 bunches each while a separation of 250 ns was considered between the bunch packets.

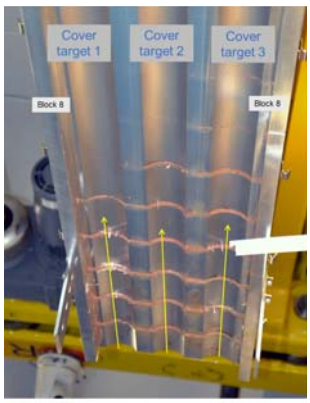

Figure 1: Photograph of the Al target cover

The target was composed of 15 identical solid copper cylinders, each 10 cm long having a radius of 4 cm, placed in a row. For diagnostic purposes, a gap of 1 cm was left between two neighboring cylinders. The beam is irradiated transversely at the face of the first cylinder.

The results of the experimental measurements are presented in Fig. 1 which is a photograph of the Al cover that was placed on the top of the target. It is seen that in the case of the experiment using 108 bunches, the material is deposited up to the gap between cylinder 7 and cylinder 8 whereas in the experiment with 144 bunches, the deposition of the melted/gaseous material is up to the gap between cylinders 8 and 9. To understand these results, detailed numerical simulations have been carried out running the FLUKA and BIG2 codes iteratively. For simplicity, we considered a single solid copper cylinder 150 cm long with a radius of 4 cm. This is a good approximation to the target used in the experiments.

In Fig. 2 are plotted ρ and T vs target axis at t =5800 ns when 108 bunches have been delivered. It is seen that the

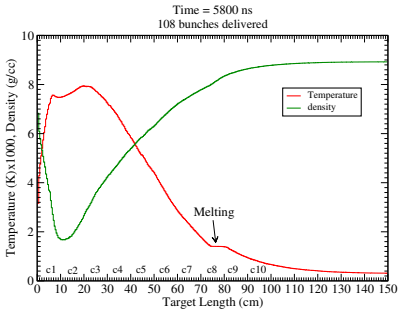

Figure 2: ρ and T vs target axis at t = 5800 ns [108 bunches]

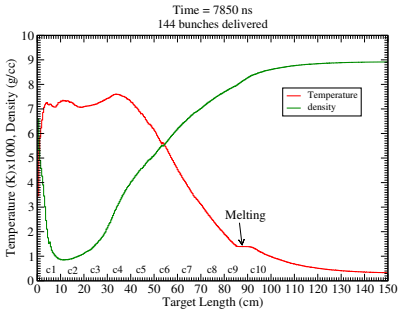

Figure 3: ρ and T vs target axis at t = 7850 ns [144 bunches]

flat part of the temperature curve that represents melting, lies within the second half (RHS part) of the eighth cylinder. This means that the material in the LHS half of the cylinder has been melted. The melted material escapes from the left face of cylinder number 8 and collides with the melted/gaseous material ejected from the right face of cylinder number 7 and is deposited on the target cover. This is in full agreement with the experimental observations.

Fig. 3 shows same variables as Fig. 2, but at t = 7850 ns when 144 bunches have been delivered. The melting region now lies in the RHS half of cylinder 9 while the left half part has been melted. The simulations thus predict material deposition at the target cover in the region between cylinder 8 and 9, in full agreement with the experimental measurements. These experiments therefore fully confirm the existence of the hydrodynamic tunneling.

References

[1] R. Schmidt et al., Proceedings of IPAC13, Shanghai, China, 2013.

* Work supported by the BMBF and EuCARD2

Numerical Simulations of Hydrodynamic Tunneling Experiments Performed at HiRadMat Facility Using SPS Proton Beam *

N.A Tahir[1], *F. Burkart*[2], *A. Shutov*[3], *R. Schmidt*[2], *D. Wollmann*[2], *J. Blanco Sancho*[2], *and A.R. Piriz*[4]
[1]GSI, Darmstadt, Germany; [2]CERN, Geneva, Switzerland; [3]IPCP, Chernogolovka, Russia; [4]UCLM, Ciudad Real, Spain

Extensive simulations carried out over the past 10 years to study the full impact of the LHC beam on solid targets has revealed substantial hydrodynamic tunneling of protons and their shower [1-3]. This effect has very important implications on the LHC machine protection design. In order to confirm the validity of these simulations, experiments have been carried out at the HiRadMat facility using 440 GeV protons impacting on solid targets. Detailed numerical simulations have been done to interpret the experiments. The experimental results together with a comparison with the simulations has been reported elsewhere [4,5]. In the present contribution we present the details about the simulations.

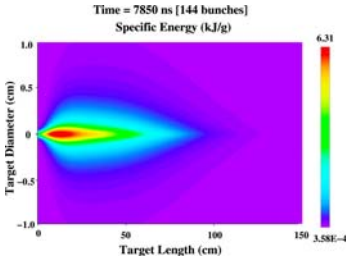

Figure 1: Energy distribution after 144 bunches.

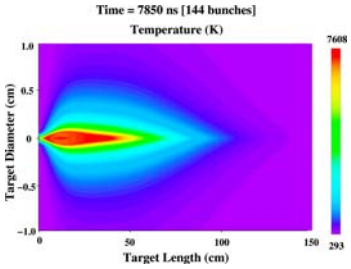

Figure 2: Temperature distribution after 144 bunches.

The simulations have been carried out running an energy deposition code FLUKA and a 2D hydrodynamic code BIG2 iteratively using an iteration interval of 700 ns. The beam parameters include, proton energy = 440 GeV, bunch intensity = 1.5x10^{11}, bunch length = 0.5 ns, bunch separation = 50 ns and σ of the transverse intensity distribution = 0.2 mm. In two experiments, 108 and 144 proton bunches, respectively, were used and the protons were delivered in sets of 36 bunches each while a separation of 250 ns was considered between the bunch packets. The target is considered to be a solid copper cylinder 150 cm long having a radius of 4 cm, which is a good approximation to the target used in the experiments [4,5].

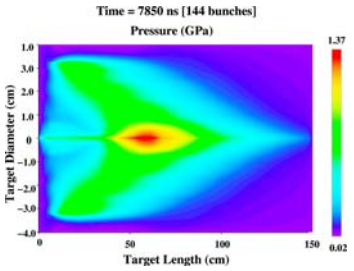

Figure 3: Pressure distribution after 144 bunches.

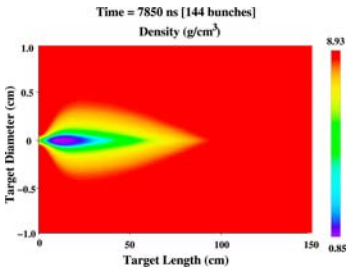

Figure 4: Density state after 144 bunches.

In Fig. 1, is plotted the specific energy deposition after 144 bunches have been delivered. It is seen that a maximum specific energy deposition of 6.3 kJ/g is achieved at the target center. Fig. 2 shows a corresponding maximum temperature of 7600 K. This high temperature generates a high pressure that leads to hydrodynamic motion in the target material (see Fig. 3). The hydrodynamic motion leads to substantial density depletion in the beam heated region which is the cause of hydrodynamic tunneling. The simulations show very good agreement with the experimental results [5].

References

[1] N.A. Tahir et al., JAP 97 (2005) 083532.
[2] N.A. Tahir et al., PRE 79 (2009) 046410.
[3] N.A. Tahir et al., PRSTAB 15 (2012) 051003
[4] R. Schmidt et al., Proc. of IPAC13, Shanghai, China, 2013.
[5] R. Schmidt et al., This year's annual report.

* Work supported by the BMBF and EuCARD2

 doi:10.15120/GR-2014-1-PNI-PP-17

Laser acceleration of small projectiles for hypervelocity impact experiments

E. S. Kjartansson[*2], *A. Ortner*[†2], *S. Sander*[2], *J. Helfrich*[2], *B. Cihodariu-Ionita*[1], *G. Schaumann*[2], *A. Blazevic*[1,3], *V. Bagnoud*[1,3], *and M. Roth*[2]

[1]GSI, Darmstadt, Germany; [2]Technical University Darmstadt, Germany; [3]Helmholtz Institute Jena, Germany

A new experimental concept is being developed to measure the enhanced momentum transfer during hypervelocity impacts of small solid projectiles on solid targets.

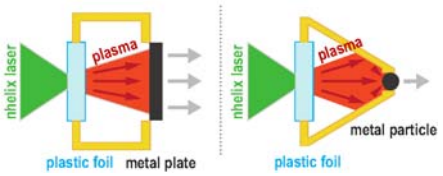

Figure 1: Proposed hohlraum target concepts for accelerating metal plates (left) and later small particles (right) to hypervelocities with the nhelix laser.

The magnitude of the *enhanced momentum transfer* caused by the ejection of material when a crater is formed on the target during hypervelocity ($v_{rel} \approx 10-15$ km/s) impacts is not well known for the materials and scales we are interested in, but it is believed to be at least tenfold [1, 2] compared to elastic collisions. We aim to measure the momentum transfer of dust-size metal particles colliding on larger metal targets with velocities in the aforementioned region. The collection of this data is critical e.g. to determine the feasibility of ideas proposed by G. Ganguli et. al.[3] for the active removal of space debris in the lower earth orbit. The experimental challenges of this project are both the acceleration of such small projectiles to hypervelocities and the accurate measurement of their velocities.

We will use a laser pulse from the nhelix laser system ($\sim$ 30 J energy over $\sim$ 7 ns @ 532 nm) to drive a plasma expansion from a plastic foil mounted at the front of a hohlraum target. The rapidly expanding plasma will be used to accelerate a secondary projectile target to hypervelocities without melting it. At first we aim at accelerating small metal plates as depicted on the left side in Fig. 1 and to measure their velocity and momentum transfer onto a ballistic pendulum. Ultimately, the goal will be to accelerate spherical dust-size metal particles to hypervelocities and to gather extensive data on the momentum transfer for different materials and parameters. The targets will be fabricated in our own target laboratory at the Technical University of Darmstadt.

To accurately measure the velocity of the projectiles, we have set up a VISAR (*Velocity Interferometer System for any Reflector*) at the Z6 experimental area. The VISAR can measure velocities in the hypervelocity regime time-resolved on a sub-nanosecond scale with 1% accuracy. The VISAR requires a laser with high temporal coherence for its measurements. For this purpose we have comissioned a custom Nd:YLF laser by Continuum and modified it to better suit our needs. Dichroic mirrors were installed into the cavity to subdue the dominating 1047 nm lasing line in favour of the more exotic 1320 nm line and a 1320 nm diode laser which acts as an injection seed for the main resonator was incorporated into the system to provide the required temporal coherence.

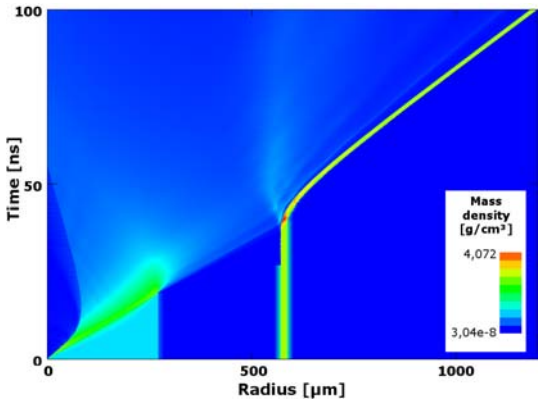

Figure 2: A simulation showing the temporal evolution (y-axis) of the mass density of a target consisting of a 270 μm plastic foil and a 16,5 μm aluminum metal plate, positioned 300 μm behind the plastic. The laser hits the plastic foil from the left edge at $t = 0$.

Simulations with the HELIOS 1D hydrodynamic code have been carried out (see Fig. 2) and are ongoing to help choose the initial values for important experimental parameters such as laser energy, plastic foil thickness and the distance between plastic foil and metal plate. Preliminary results indicate that plastic foils of thickness 50 - 100 μm combined with a distance of 300 - 600μm between plastic foil and metal plate is the optimal setup to reach velocities in the 10 - 20 km/s range without melting the metal plate.

References

[1] J. D. Walker and S. Chocron, Int. Journal of Impact Engineering 38, A1-A7, 2011

[2] W. M. Alexander and J. A. M. McDonnel, Adv. Space Rev. Vol.2, No.12, pp. 185-187, 1983

[3] G. Ganguli et al., Aerospace Conf., 2012 IEEE, pp. 1-9, March 2012

[*] e.s.kjartansson@gsi.de
[†] a.ortner@gsi.de

Radiation protection related x-ray spectrometry at PHELIX

F. Horst[1,2], *G. Fehrenbacher*[1], *T. Radon*[1], *E. Kozlova*[1], *K. Zink*[2], *and J. Breckow*[2]
[1]GSI, Darmstadt, Germany; [2]Technische Hochschule Mittelhessen, Gießen, Germany

Introduction

In the context of a bachelor thesis [1], a thermoluminescence dosimetry (TLD) based method has been developed for the measurement of photon spectra in ultrashort-pulsed radiation fields as generated e.g. during operation of the PHELIX-laser at GSI [2]. The method is a further development of a work from Behrens et al. [3] and has been validated at a clinical electron-linac (Elekta Synergy: 6 and 18 MeV) by comparing spectra measured by the developed method with spectra obtained by detailed Monte Carlo simulations of the linac. It has been first applied at PHELIX during a beamtime in December 2013. The following article presents the principle of the method of measurement and first results from the measurements at PHELIX.

Method of measurement

As a result of the sub-picosecond time scale of the laser pulses at PHELIX, an active measurement is quite difficult to implement. For that reason, TLD's are used. 10 TLD-cards (*Harshaw TLD-700H*) are placed into a stack of absorbers, made of various materials and thicknesses, surrounded by a shielding stepped from lower to higher Z materials. The prototype is shown on Figure 1.

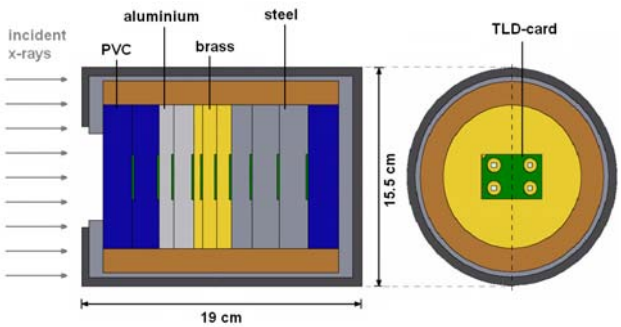

Figure 1: Schematic view of the TLD-spectrometer

The response functions of the 10 TLD's to monoenergetic photon- and electron-radiation were simulated by the use of the Monte Carlo code FLUKA [4]. The different gradients and thresholds of these response-functions (Figure 2) allow the reconstruction (unfolding) of photon spectra from the readings of the 10 TLD's. An algorithm for the purpose of unfolding bremsstrahlung spectra in the range of 30 keV to 100 MeV, resolved in 10 different energy bins, was developed (written in SCILAB [5]).

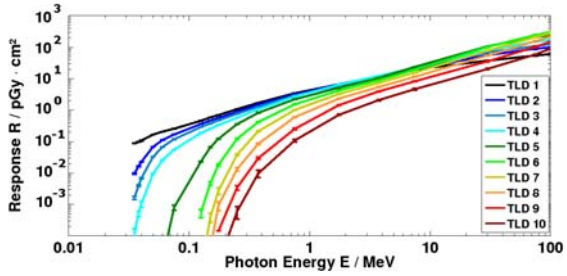

Figure 2: Simulated response-functions of the 10 TLD's to monochromatic photon radiation

First results

Figure 3 shows an x-ray spectrum, measured by this prototype at the PHELIX petawatt target area from the outside of the target chamber behind a 2 cm steel window during experiments in December 2013. The laser intensity deposited on the Ti-foil target was about 10^{19} W/cm^2. The distance between the target and the spectrometer was 80 cm. The presented x-ray spectrum is equivalent to an ambient dose of 80 ± 20 μSv/shot.

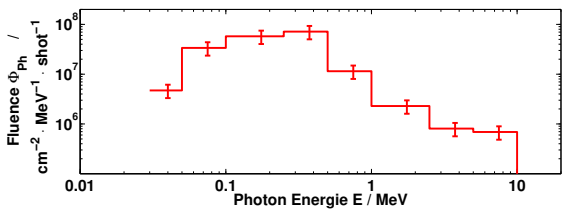

Figure 3: X-ray spectrum: measured at PHELIX

Repeated measurements with a variation of the window materials and thicknesses provided evidence, that the wall of the target chamber is the main x-ray source.

References

[1] F. Horst, "Röntgenspektrometrie am Petawattlaser PHELIX", bachelor thesis, Technische Hochschule Mittelhessen, 2014

[2] S. Götte et al., this report

[3] R. Behrens et al., "A thermoluminescence detector-based few-channel spectrometer for simultaneous detection of electrons and photons from relativistic laser-produced plasmas", Review of Scientific Instruments Vol. 74, 961, Feb 2003

[4] http://www.fluka.org/

[5] http://www.scilab.org/

 doi:10.15120/GR-2014-1-PNI-PP-19

Report of the biophysics department

M. Durante

[1]GSI, Darmstadt, Germany

The Scientific Activity of the Biophysics activity in 2013 led to tremendous breakthroughs in the field of medical physics and space radiation protection. The achievements are essential for the future FAIR activities, where the high-energy beams will open new possibilities for both medical and space research. It has been a very successful year also for the technological transfer, patents, and awards received by group members.

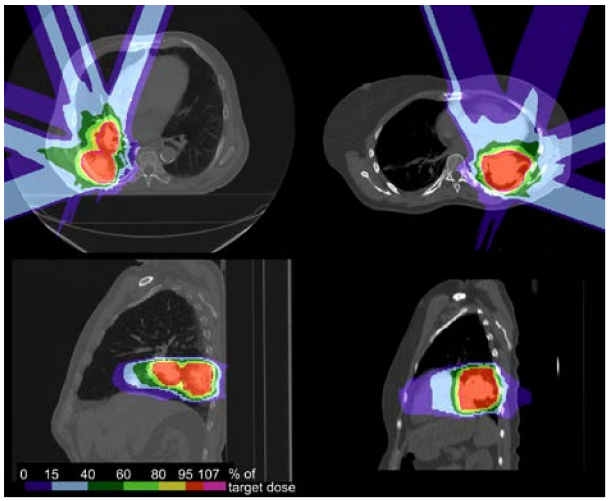

Figure 1: 4D-treatment plans of two lung cancer patients treated with C-ions. The distorted entry channel dose is a result of the differential motion between the target and other organs, such as the chest wall, during the breathing cycle. The sagittal cuts (bottom) illustrate the high conformity also in the SI main motion direction. From ref. [2]

Medical Physics

The Local Effect Model (LEM), developed by Dr. Michael Scholz, already used in treatment planning with heavy ions at HIT (Heidelberg) and CNAO (Italy), has been now extended to protons with a surprising result [3]. In fact, the relative biological effectiveness of protons is assumed to be 1.1, but our simulations show that it is much bigger than 1 at the end of the range, and this lead to a shift in the effective range of the protons (Figure 2). Taking into account the range shift is likely to lead to great improvements in proton therapy, where the market is much broader than in C-ion therapy (44 proton therapy centers are currently in operation worldwide).

In preparation for the PRIOR facility, to be installed in FAIR, we produced the first-ever high-energy proton image of an animal target with high-energy protons (800 MeV) at ITEP in Moscow, Russia and then at the Los Alamos National Laboratory in USA (Figure 3). The PANTERA experiment is an APPA project developed in strong collaboration between the Plasma Physics and Biophysics Department at GSI.

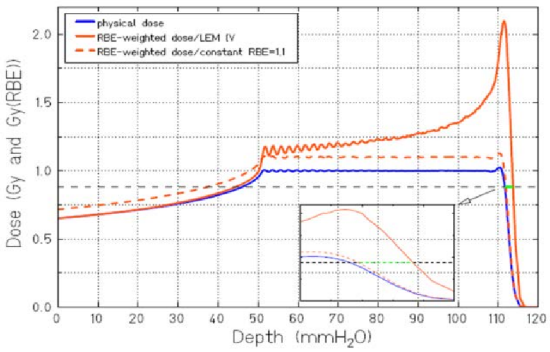

Figure 2: Predictions of the LEM model on the biologically effective dose (solid orange line) along a proton SOBP used for therapy. The increased effectiveness of the slow protons results in a range shift of 2-3 mm, which could hit an organ at risk below the tumor.

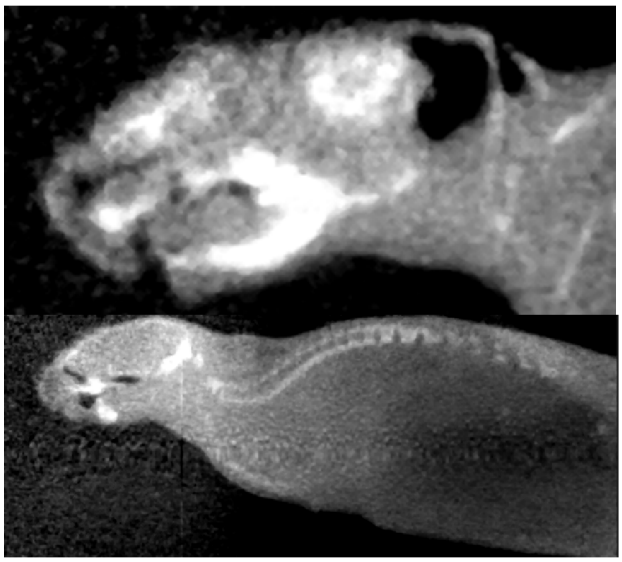

Figure 3: Proton radiography of a mouse obtained in 2013 at the Los Alamos National Laboratory using 800 MeV proton and a setup similar to that under construction at FAIR (PRIOR facility). The upper image is a zoom of the skull. The theoretical resolution at FAIR with 4.5 GeV protons will be 10 μm. From ref. [4].

doi:10.15120/GR-2014-1-BIOPHYSICS-01

Space Radiation

GSI is the European facility selected by ESA for ground-based cosmic ray simulations. During 2013, we ran the ESA-sponsored IBER (radiobiology) and ROSSINI (shielding) projects. Within IBER, we tested the possibility of using human tissue slices as an alternative to animal studies [9]. Shielding experiments using Mars and Moon soil are ongoing, within the project supported by ESA and led by the space company Thales-Alenia Space (Figure 4). Results are important to estimate the depth of the caves/tunnels to be selected by future Moon/Mars explorers to build underground planetary bases without breaking ground for excavation.

Figure 4: Martian soil under preparation for a shielding experiment in Cave A at GSI. The test is performed using 1 GeV/n 56Fe-ions, whose attenuation properties have been shown to simulate reasonably well the attenuation of cosmic rays. A better simulation will be possible at FAIR using 10 GeV/n ions. The research is supported by ESA (ROSSINI contract).

A recent research report at GSI [6] addressed an old question in space travel – the origin of light flashes, observed by astronauts during spaceflight (first reported by the crew of the Apollo 11 lunar mission). Heavy charged particles in the cosmic rays are responsible of the light flash (phosphene) experienced by the astronauts, but the target area in the head remained unclear: some authors proposed the eye, while others contended that the target could be the optical nerve or specific areas in the brain. A careful analysis of the treatment plans used at GSI to treat patients with head-and-neck tumors show a clear correlation between the dose in the retina and the perception of light flashes, as measured by the patient using a pushbutton (Figure 6). We conclude that the phosphenes are caused by direct heavy ion traversals through the retina.

Technological transfer

RaySearch Laboratories AB (a leading Swedish company in treatment planning software) has entered into a license agreement with GSI regarding techniques for calculating radiobiological effective dose in ion beam treatments. RaySearch acquired the rights to integrate algorithms and know-how from GSI related to the LEM in RaySearch's RayStation® treatment planning system. The LEM and RaySearch's algorithms for dose calculation will be built into the system's module for carbon treatment plan optimization. The first application of the system will be at the MedAustron facility under construction in Wiener Neustadt (Austria).

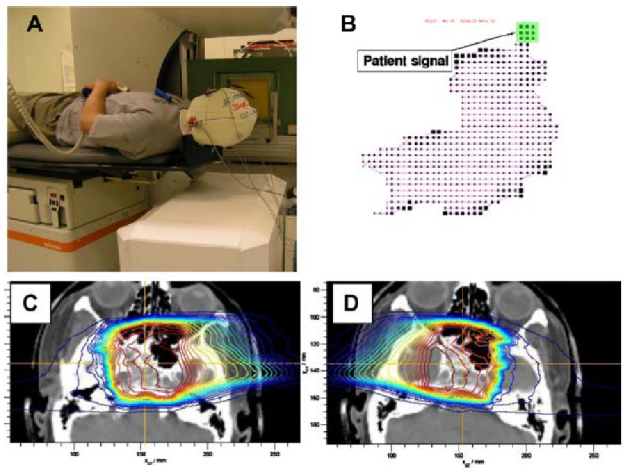

Figure 5: Example of the correlation between carbon beam-spot position in the head and phosphene reception in a patient. (A) Patient during the treatment with the fixation mask and holding the pushbutton. In this figure the beam is hitting the right side of the patients' head. (B) Beam scanning path (beam's eye view) for one slice of carbon ion irradiation. The area marked in green is correlated with phosphene stimulation, based on pushbutton time analysis. (C) Planned physical dose distributions for a two-field treatment in the same patient. The beam enters from the right side. The color scale indicates the fraction of the dose to the tumor. The patient reported phoisphenes when the field was in the eye (green area in B).(D) Same as in C, but beam from the left side. No dose deposition in the eye, and no light flashes reported by the patient. Note that the optical nerves are in the field in both right and left irradiation. Figures from ref. [6].

The 4D treatment plan concept has been patented by C. Graeff and C. Bert: Erstellung eines Bestrahlungsplans bei bewegtem Zielvolumen ohne Bewegungskompensation", Nr. 10 2011 056 339. The PANTERA idea for theranostics using high-energy protons was patented by H. Stöcker and M. Durante: COMBINED ION IRRADIATION AND RADIOGRAPHY DEVICE - PCT/EP2012/071567

 doi:10.15120/GR-2014-1-BIOPHYSICS-01

Awards

Marco Durante received the 2013 IBA Prize for Applied Nuclear Science and Nuclear Methods in Medicine from the European Physical Society (EPS) and the 2013 Bacq & Alexander award from the European Radiation Research Society (ERRS)

Daniela Kraft received the 2013 LH Gray Young Investigator award for the European Radiation Research Annual Meeting and the 2013 Christoph Schmelzer Award of the Verein zur Förderung der Tumortherapie mit schweren Ionen.

Lisa Herr won the Philipp Siedler Award 2013 of the Physikalischer Verein Frankfurt.

Thomas Friedrich got the GBS Award for Young Scientists 2013, awarded by the German Society for Biological Radiation Research.

Matthias Prall got the award for the best poster presented at the Workshop on "Particle Radiosurgery: A new Frontier in Physics in Medicine" in Obergurgl, Austria

References

[1] P. Steidl, T. Haberer, M. Durante and C. Bert, Gating delays for two respiratory motion sensors in scanned particle radiation therapy. Phys. Med. Biol. 58 (2013) N295-302.

[2] C. Graeff, R. Lüchtenborg, J.G. Eley, M. Durante and C. Bert, A 4D-optimization concept for scanned ion beam therapy. Radiother. Oncol. 109 (2013) 419-424.

[3] R. Grün, T. Friedrich, M. Krämer, K. Zink, M. Durante, R. Engenhart-Cabillic and M.Scholz, Physical and biological factors determining the effective proton range. Med. Phys. 40 (2013) 111716.

[4] B. Alpat, E. Pilicer, S.Blasko, D.Caraffini, F.Di Capua, V.Postolache, G.Saltanocchi, M.Menichelli, L.Desorgher, M.Durante, R.Pleskac and C.La Tessa, Total and partial fragmentation cross-section of 500 MeV/nucleon carbon ions on different target materials. IEEE Trans. Nucl. Sci. 60 (2013) 4673-4682.

[5] F. Merz, F. Gaunitz, F. Dehghani, C. Renner, J. Meixensberger, K. Schopow, C. Hellwig, M. Schäfer, M. Bauer, G. Taucher-Scholz, M. Durante and I. Bechmann, Organotypic slice culture of human glioblastoma reveals tumor-susceptibility to heavy ion therapy. Neuro-oncology 15 (2013) 670-681.

[6] D. Schardt, O. Kavatsyuk, M. Krämer and M. Durante, Light flashes in cancer patients treated with heavy ions. Brain Stimul. 6 (2013) 416-417.C.

Species conserved response at heterochromatic DNA damage *

I. Müller[1], *B. Merk*[1], *K.-O. Voss*[1], *N. B. Averbeck*[1], *B. Jakob*[1], *A. L. Leifke*[1], *G. Becker*[1], *M. Durante*[1,2], *and G. Taucher-Scholz*[1,3]

[1]GSI Helmholtzzentrum für Schwerionenforschung GmbH, Darmstadt, Germany; [2]TUD, Institut für Festkörperphysik, Darmstadt, Germany; [3]TUD, Fachbereich Biologie, Darmstadt, Germany

DNA double strand break (DSB) repair comprises several steps; besides different repair proteins also chromatin modifications are necessary and local as well as global chromatin decondensation takes place. Furthermore, recent findings in *Drosophila*, mouse, and baker's yeast show that DSBs within repetitive regions relocate to less repetitive chromatin [1-3]. Thus, relocation of DSBs might be a mechanism to prevent homology driven misrepair of repetitive sequences. Here we provide evidence that in the facultative heterochromatin of the human inactive X chromosome (Xi) decondensation occurs at DNA damage (Fig. 1 A and B) and DSBs are relocated to more open chromatin (Fig. 1 C, DSB marker 53BP1) [4]. Thus, DSB relocation is not limited to repetitive sequences but is a general process within repair of heterochromatic regions. Our results obtained in human cells indicate that decondensation at heterochromatic DSBs and their relocation is conserved from flies to mice and humans. In contrast to earlier findings [1-3], however, the DSB dependent chromatin modification of H2AX phosphorylation (γH2AX) shows not only relocation but additional H2AX phosphorylation takes place almost in the entire Xi area (Fig. 1 C, γH2AX signal). This increased γH2AX spreading is clearly LET (linear energy transfer) dependent as it is not seen upon carbon ion (not shown) but after calcium, titanium (not shown), or lead ion (Fig. 1 C) irradiation. The mechanism and functional relevance of this Xi wide γH2AX spreading will be analyzed in future studies.

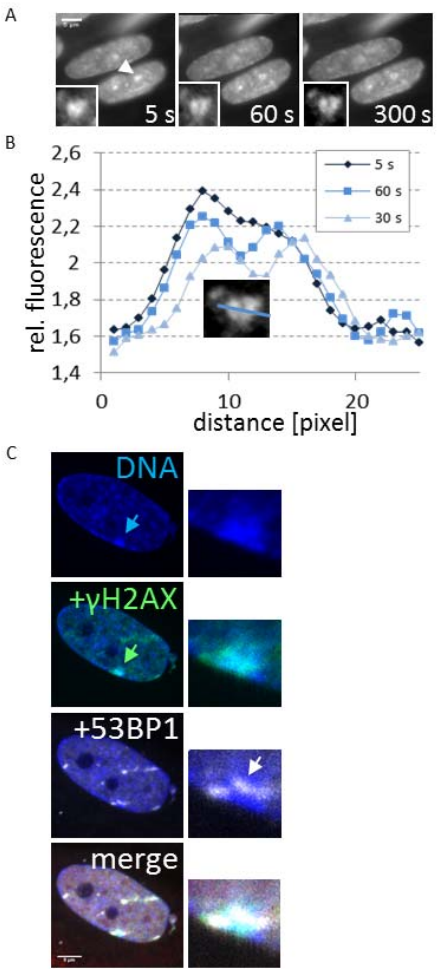

Figure 1: **(A)** Chromatin decondensation in the Xi chromosome of human cells. Real time DNA decondensation within Xi territories (arrow) identified by Hoechst 33342 DNA staining after irradiation with one gold ion at the GSI microprobe. Selected images of indicated time points are shown. The appearance of a darker area within the Xi (magnification in white box) represents the Xi decondensation at the ion hit. **(B)** The depletion of DNA staining intensities (i. e. occurrence of a darker area) over time at the site of an ion hit is exemplarily shown for intensity profiles along the line within the depicted Xi. **(C)** Relocation of heterochromatic DSBs is indicated by bending of 53BP1 (DSB marker) tracks around Xi 1 h after low angle lead ion (LET 13,500 keV/μm) irradiation (DNA signal: arrow indicates Xi; 53BP1 signal: arrow indicates bent 53BP1 track). Phosphorylation of H2AX occurs all over the ion hit Xi (arrow in γH2AX signal). Scale bars: 5 μm.

References

[1] J. Torres-Rosell *et al*. Nat Cell Biol, 9 (2007) p. 923 ff

[2] I. Chiolo *et al*. Cell, 144 (2011) p. 732 ff

[3] B. Jakob *et al*. Nucleic Acids Res, 39 (2011) p. 6489 ff

[4] I. Muller *et al*. Mutat Res, 756 (2013) p. 30 ff

* This work was part of HGS-HIRe and partially funded by the BMBF grant 02NUK001A.

 doi:10.15120/GR-2014-1-BIOPHYSICS-02

Visualization of DNA double-strand breaks induced by high LET particles and X-rays in murine bones and soft tissues*

M. Steinlage[1], *J. Mirsch*[1], *S. Conrad*[1], *C. Fournier*[2], *G. Taucher-Scholz*[2], *and M. Löbrich*[1]
[1]Darmstadt University of Technology, Germany; [2]GSI, Darmstadt, Germany (GREWIS)

DNA double strand breaks (DSBs) are the most lethal and cytotoxic type of DNA damage. DSBs can be induced by exogenous agents, such as ionizing radiation (IR), or by normal cellular processes, such as V(D)J recombination. DSBs generated by high LET radiation are more complex than low LET DSBs and generally more difficult to repair [1].

As part of the GREWIS project, this study is aimed at the biodosimetric measurement of inhaled radon gas in different murine tissues. Radon (Rn-222) is a radioactive noble gas; during its radioactive decay three biologically relevant α-particles are emitted. The goal of this project is to detect α-particle induced DSB tracks in murine tissues to reveal the diffusion patterns of radon gas inside the body and any potential accumulation in specific organs.

Radon gas is used for its therapeutic effects in radon therapy caves in Bad Gastein and Bad Kreuznach [2]. The main indications for therapeutic radon treatment include chronic inflammatory diseases and degenerative joint diseases, such as rheumatoid arthritis. Due to its long-lasting effects, radon therapy provides an alternative treatment option that often allows patients to stop taking other pain medications [3].

Prior to *in vivo* radon experiments, wild type C57BL/6 mice were irradiated with low fluence carbon ions at the GSI particle accelerator. This experiment was used to evaluate the staining efficacy of heavy ion induced DSBs in different murine tissues. Using paraffin embedded tissue sections, 53BP1 foci tracks after carbon ion irradiation were successfully visualized and quantified in murine lung, heart, liver, intestine, kidney, spleen, and brain tissues (Fig. 1 A). As radon therapy is predominantly prescribed for chronic inflammatory diseases of the musculoskeletal system, the visualization of radon induced DNA damage in bone tissue is central to this project. Therefore, efforts were focused on establishing a protocol for immunofluorescence staining in bone tissue. After formaldehyde fixation, bone tissue (*in vivo* irradiation with 10 mGy X-rays) was decalcified for 24 hours using an EDTA solution. The samples were subsequently embedded in paraffin and cut into 4μm sections using a microtome. Using γH2AX and 53BP1 antibodies, DNA damage was visualized in the compact bone, periosteum and bone marrow (Fig. 1 B).

Two animal experiments (radon concentrations: 440 kBq/m^3, 40 kBq/m^3) were recently conducted. C57BL/6 mice were exposed to radon for one hour and organs were subsequently harvested after 15 minutes, 24 hours and 7 days. Hence, future efforts will focus on the analysis of *in vivo* radon experiments.

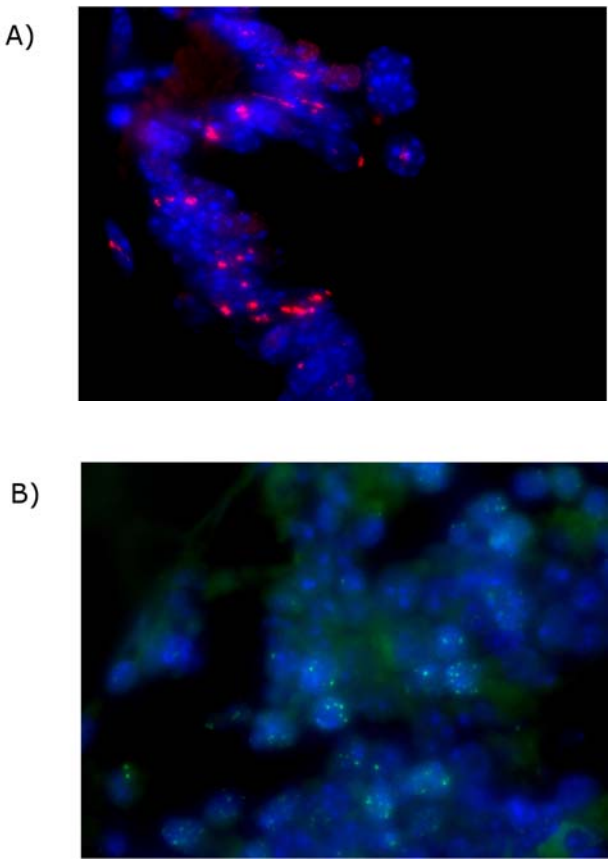

Figure 1: Visualization of DNA DSBs: (A) 53BP1 foci in murine lung tissue cells after carbon ion irradiation. (B) γH2AX foci in murine bone marrow after X-ray irradiation.

References

[1] R. Okayasu. Int. J. Cancer: 130 (2012) 991-1000

[2] K. Becker. Int. J. Low Radiation Vol. 1 (2004) 334-356

[3] B. Erickson. Dose-Response (2007) 5:48-62

*Funded by German federal ministry of research and education (BMBF/ 02NUK017E).

Formation of 5hmC following exposure to Ionizing Radiation *

M. Herrlitz[1,2], *F. Natale*[1,2], *A.L. Leifke*[1], *M. Durante*[1,2,3], *and G. Taucher-Scholz*[1,3]

[1]GSI, Darmstadt, Germany; [2]FIAS, Frankfurt Institute for Advanced Studies, Germany; [3]TUD, Darmstadt, Germany

Eukaryotic DNA methylation (DNAm), which is the addition of a methyl group on cytosine bases (C), is an epigenetic mechanism involved in several biological processes, including replication, transcription, and carcinogenesis. Besides methylcytosine (5mC), hydroxymethylcytosine (5hmC) is another modified C moiety. 5hmC is formed by the enzymatic activity of TET (ten eleven translocation) enzymes oxidizing 5mC to 5hmC and further to formyl- and carboxyl-cytosine, the latter being finally replaced by C via base excision repair [1]. Conversion of 5mC to 5hmC could change the DNA binding affinity of several proteins and thus influence regulation of gene transcription [2]. Previous works reported that ionizing radiation (IR) and DNA double strand break (DSB) repair processes are able to induce changes of DNAm levels [3, 4, 5]. However, these studies were performed several population doublings after IR exposure and could not rule out replication-dependent DNAm changes. Whether the latter may take place also at short times after exposure to IR remains controversial. Increased DNA methylase levels at later times ($\geq$ 24 hours) after IR exposure have been recently reported [6]. These findings suggest that increased DNAm levels would not occur until DNA repair is accomplished. Based on such observation, we hypothesize that IR may rather reduce DNAm levels at earlier times by triggering enzymatic activities regulating such process, e.g. TET enzymes. Therefore, we examined DNAm changes within one replication cycle time frame after IR ($\leq$ 24 hours), focusing on DNA demethylation. Namely, we investigated 5hmC formation as an intermediate of DNA demethylation and whether this modification was involved in the DSB repair. We investigated human fibroblasts 30 minutes after irradiation with carbon ions and observed 5hmC formation along the ion trajectory. Both fluorescence microscopy images and intensity profiles indicate that 5hmC signal colocalizes with γH2AX (DSBs marker) (Fig. 1). Similar results were obtained upon irradiation with X-rays (Fig. 2A). Colocalization was statistically verified using intensity correlation analysis (ICA) [7]. Briefly, PDM (Product of the Differences from the Mean) values were calculated for each pixel in both channels. If the signals were positively correlated, this would result in a positive PDM value and, thus, in a positive correlation. Our results show that most PDM values are positive, displaying a moderate positive correlation between 5hmC and γH2AX at DSBs ($R_{Pearson}$ = 0.425, Fig. 2B).

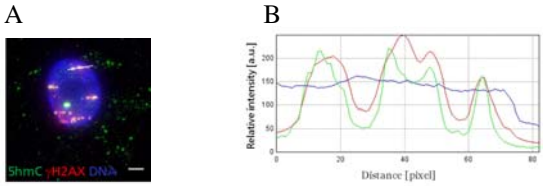

Figure 1: AG1522D cells were irradiated with carbon ions (LET: 170 keV/μm; fluence: 3x10^6 p/cm^2) under low angle, fixed after 30 minutes and stained against 5hmC (green) and γH2AX (red). DNA was stained with DAPI (blue). A) Micrograph showing 5hmC (green) formation at DSBs sites indicated by γH2AX (red). White line: ion trajectory; scale bar = 5 μm. B) Fluorescence intensity profiles showing colocalization of 5hmC (green) and γH2AX (red). DNA is illustrated by the blue line.

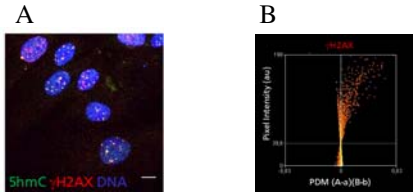

Figure 2: AG1522D human fibroblasts were irradiated with 0.5 Gy X-rays, fixed after 30 minutes and stained as in Fig. 1. A) 5hmC (green) accumulates at DSBs, indicated by γH2AX staining (red). Scale bar = 10 μm. B) ICA graph of γH2AX signal. The horizontal line indicates mean PFI values. With increasing PFI, PDM values increase.

Our results indicate that 5hmC is formed at DSB sites colocalizing with γH2AX, after both heavy ions and X-rays irradiation. Such observation suggests a possible involvement of 5hmC in the DSB repair. We are currently investigating the colocalization of 5hmC and γH2AX over time, during DNA repair, performing kinetics of foci formation in a time frame of $\leq$ 24 hours after irradiation.

References

[1] Ito et al. (2011) Science, 333, p. 1300 ff

[2] Spruijt et al. (2013) Cell, 152, p. 1146 ff

[3] Goetz et al. (2011) Radiation Research, 175, p. 575 ff

[4] Cuozzo et al. (2007) PLoSGenet, 3, p. 1144 ff

[5] O'Hagan et al. (2008) PLoSGenet, 4, e1000155

[6] Chaudhry et al. (2012) DNA Cell Biol, 31, p. 908 ff

[7] Li et al. (2004) J Neurosci, 24, p. 4070 ff

*Supported by Beilstein Stiftung (NanoL project). Work is part of HGS HIRe and partially funded by BMBF grant 02NUK001A.

 doi:10.15120/GR-2014-1-BIOPHYSICS-04

A discontinuous detection of phospho-histone H2AX in endothelial cells following low-dose irradiation is mediated by reactive oxygen species (ROS)*

S. Reichert[1], *M. Large*[1], *C. Fournier*[2], *C. Rödel*[1], *and F. Rödel*[1]
[1]Goethe-University Frankfurt am Main, Germany; [2]GSI, Darmstadt, Germany

Introduction

Since decades an anti-inflammatory efficacy of radiation therapy with single doses < 1 Gy is clinically well established in the treatment of benign and chronic degenerative diseases [1]. In line with that, recent experimental data indicate an involvement of a variety of cellular and molecular immune-modulatory mechanisms in these effects. Among them, an impact of low-dose irradiation on endothelial cells (EC) and mononuclear/polymorphnuclear leukocyte activity has been proven to comprise key elements in the modulation of inflammatory cascades [2]. Moreover, a non-linear dose response relationship, shared with non (DNA)-targeted properties of ionizing radiation [3], is a major characteristic of the mechanisms explored so far [4]. Recently, a putative interrelationship between DNA damage repair, induction of reactive oxygen species (ROS) and factors implicated in the regulation of antioxidant response pathways have been proposed to contribute to these discontinuous responses [5].

Material and Methods

HUVEC derived immortalized EA.hy926 cells were stimulated in a pro-inflammatory manner by tumor necrosis factor-α (20 ng/ml) 4 hours before irradiation with doses ranging from 0.3 to 1 Gy. To analyse DNA repair capacity, γ-H2AX foci were assayed at 1 hour, 4 hours and 24 hours after irradiation by immunofluorescence. ROS production and superoxide dismutase (SOD) activity were analysed by fluorometric 2',7'-dichlorodihydrofluorescein-diacetate (H2DCFDA) and colorimetric assays, respectively.

Results and Conclusion

Irrespective of stimulation by TNF-α, we observed in EA.hy926 EC a linear dose-response characteristic of γ-H2AX foci detection at early times (1 hours and 4 hours) after irradiation. On the contrary, at 24 hours the number of residual γ-H2AX foci was significantly ($p \leq 0.05$) elevated after a 0.5 Gy exposure (Figure 1a). To further analyse molecular mechanisms implicated in the biphasic induction of γ-H2AX foci the impact of ROS expression and enzymatic activity of SOD, reported to be involved in anti-oxidant defence [6] were investigated. As a result, a biphasic induction of ROS became evident at 24 hours after irradiation concomitant with a significant decrease in SOD activity, most pronounced at a dose of 0.5 Gy (Figure 1b).

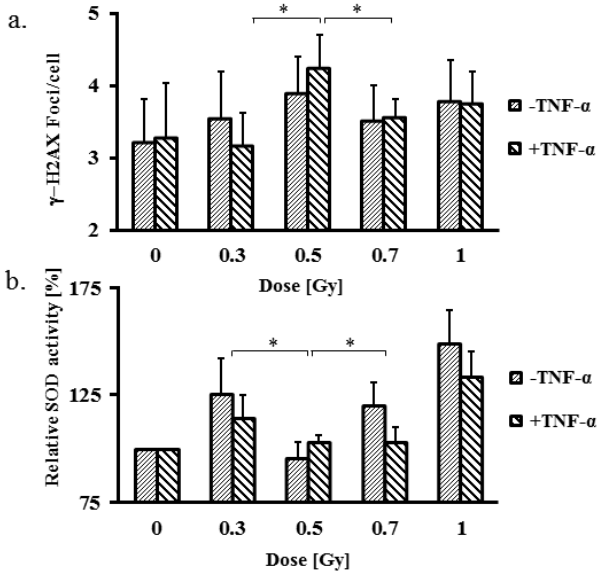

Figure 1: Dose kinetics of γ-H2AX foci detection (a) and relative SOD enzymatic activity (b) as measured by a colorimetric assay in stimulated (TNF-α, 20 ng/ml) EA.hy926 EC at 24 h following irradiation with the doses indicated. Data represent means $\pm$ SD from at least three independent experiments. Asterisks indicate significant differences ($p < 0.05$) vs. 0.3 Gy and 0.7 Gy irradiated ECs.

In conclusion, these data implicate a non-linear regulation of SOD activity and ROS production in EA.hy926 EC following irradiation with doses < 1 Gy that contributes to a discontinuous dose response relationship of γ-H2AX detection.

References

[1] Seegenschmiedt *et al.* Int J Radiat Oncol Biol Phys 2000;47:195–202.

[2] Rödel *et al.* Front Oncol 2012;2:120.

[3] Mothersill. Health Phys 2011;100:302.

[4] Rödel *et al.* Curr Med Chem 2012;19:1741–1750.

[5] Beels *et al.* Int J Radiat Biol 2010;86:760–768.

[6] Fukai. Antioxid Redox Signal 2011;15:1583–1606.

*This research was funded by BMBF (GREWIS, 02NUK017F) and EU (DoReMi, FP7-249689)

X-rays advance osteoblast differentiation probably involving the cholinergic system *in vitro*[*]

G. Thangaraj[1], *C. Fournier*[2], *and P. G. Layer*[1]
[1]Technische Universität Darmstadt, Germany; [2]GSI, Darmstadt, Germany

Introduction

Rheumatoid Arthritis (RA) is an autoimmune disorder and treatment with Radon is believed to suppress the severity of the disease. Thereby, associated with excess pain, cartilage undergoes severe destruction and synovial fluids accumulate in the joints. One of the mechanisms supposedly involved in RA is the *cholinergic anti-inflammatory pathway* (CAIP). Although a number of studies have shown that CAIP is involved in suppressing the inflammation through Vagus nerve stimulation, there are no studies existing that show the relationship between radiation therapy of RA and CAIP. In AP6 of the GREWIS project, we analyse the effects of radiation (X-rays, radon) on the expression of cholinergic components (ACh receptors, particularly the α7-nAChRs, a main player of CAIP, and AChE, ChAT), both *in vivo* and *in vitro* and their roles during radiation therapy.

Material and Methods

11/11.5 day-old embryos from pregnant C57BLC wild type mice were collected. Mesenchymal cells were isolated from limb buds, plated as high density micro-mass cultures and incubated for 2 weeks at 37°C. The micromass cultures were exposed to 0.5, 2 and 4 Gy X-rays initially after 24 hours of culturing and were fixed on 3, 5 and 7 days. Also, human primary osteoblast cells were cultured until passage 4, exposed to above mentioned X-ray doses and collected for mRNA isolation. Alcian blue staining marks cartilage development, while Alizarin red and alkaline phosphatase stainings indicates differentiation of osteoblasts. Cholinesterase enzyme activity was visualized by Karnovsky-Roots staining. cDNA was synthesized and used for PCR analysis.

Results

We previously showed that human osteoblast cells expressed an entire set of cholinergic components. These cells over-expressed acetylcholinesterase (AChE) when exposed to X-rays, which indicates that the cholinergic system might be involved in differentiation and osteogen-esis.

Cultures that were exposed to 2Gy X-rays showed earlier nodule formation and increased enzymatic activity for AChE and alkaline phosphatase suggesting that X-rays might induce an earlier differentiation by involving the cholinergic system.

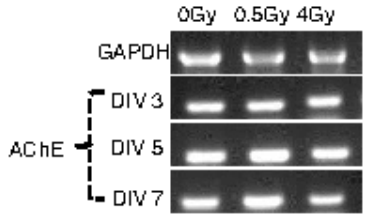

Figure 1: RT-PCR analysis of human osteoblasts. Note an over expression of AChE mRNA, particularly after 0.5Gy X-ray treatment com-pared to that of control (0Gy).

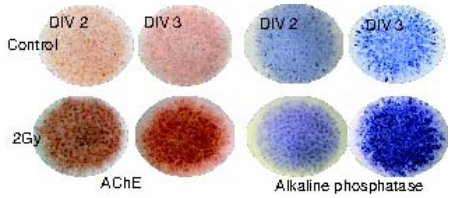

Figure 2: Histological stainings by Karnovsky Roots for AChE (4 on left) and alkaline phosphatase (4 on right) show increased enzyme activity and advanced nodule formation in 2Gy treated cultures.

Since we have focused on the importance of cholinergic system in diseases and treatment, we provide a direct evidence of the involvement of cholinergic system during cartilage differentiation in mouse micromass cultures.

Figure 3: Histological stainings by Karnovsky Roots for AChE (4 on left) and alkaline phosphatase (4 on right) show increased enzyme activity and advanced nodule formation in 2Gy treated cultures.

In future work, the effect of X-rays and radon on TNF-alpha transgenic mice will be investigated and the role of CAIP will be studied.

[*] Funded by BMBF (02NUK017A)

 doi:10.15120/GR-2014-1-BIOPHYSICS-06

The radiation-induced G2 cell cycle delay is comparable in human hematopoietic stem- and progenitor cells and mature lymphocytes*

E. Metzler[1], D. Kraft[1], A. Groo[1], M. Durante[1,4], G. Taucher-Scholz[1], H. Bönig[2], M. Volcic[3], M. Rall[3], D. Salles[3], C. Fournier[1], and L. Wiesmüller[3]

[1]GSI, Darmstadt, Germany; [2]Institute for Transfusion Medicine, Frankfurt University, Germany; [3]Gynecological Oncology, Ulm University, Germany; [4]Technische Universität Darmstadt, Germany

Introduction

Hematopoietic stem and progenitor cells (HSPC) constantly renew all mature blood cells e.g. peripheral blood lymphocytes (PBLs). Ionizing radiation generates DNA double-strand breaks (DSBs). Error-prone DSB repair activities can lead to chromosomal rearrangements which are considered to contribute to leukemogenesis [2]. Thus, the quality of DNA repair is essential. Because several mechanisms exist to repair DNA damage, we first measured the usage of distinct repair pathways after the induction of DSBs [3] and found differences in DNA repair pathway usage between HSPC and PBLs [4]. The choice of DNA repair mechanism is dependent on several factors, e.g. the cell cycle phase. When damage is introduced the cell cycle can be arrested at specific cell cycle checkpoints for repair. In this process many sensor and effector molecules are involved. Thus, we investigated in both cell types the cell cycle distribution upon stimulation and X-irradiation and a protein involved in the induction of cell cycle arrests.

Materials and Methods

CD34+ HSPC and PBLs were isolated from peripheral blood of healthy donors as described in [5]. G0-phase cells were cultured for 72h in expansion media supplemented with cytokines (HSPC) or PHA (PBLs) [5] to allow cell cycle entry. Asynchronous cells were exposed to 2Gy of X-rays (16mA, 250kV). At defined time points post irradiation cell cycle distribution was determined by DAPI staining and flow cytometry and protein amounts were determined by Western Blot analysis. Immunodetection was performed using the polyclonal anti-phospho-Chk2 respectively anti-Chk2 (both Cell Signalling) and anti-GAPDH (Abcam) antibody (loading control).

Results and Discussion

Figure 1 shows the cell cycle entry of stimulated PBLs resulting in an asynchronous cell cycle distribution after 72h. This is similar to HSPC (not shown). After irradiation with 2Gy of X-rays, PBLs undergo a transient G2 cell cycle arrest again similar to HSPC (not shown). All cells entered the cell cycle again after 48h post irradiation.

As the cell cycle analysis revealed a G2/M cell cycle delay we investigated the G2/M checkpoint protein Chk2. Figure 2 shows that the phosphorylation of Chk2 detected

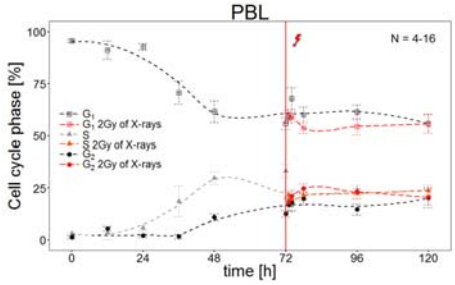

Figure 1: Cell cycle distribution in % for PBLs (n = 4–16) over a time period of 120h with stimulation for 72h before irradiation with 2Gy of X-rays (shown in red). Data are shown as mean ± SEM.

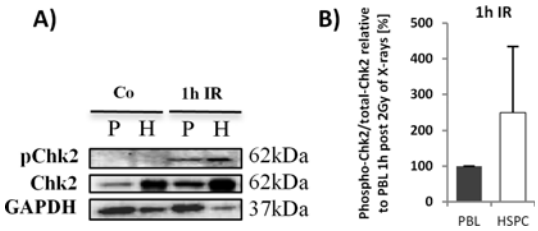

Figure 2: A) Immunodetection of phospho-Chk2, total Chk2 and GAPDH in PBLs and HSPC before (Co) and post irradiation (IR, 1h) with 2Gy X-rays. B) Phospho-Chk2 relative to total Chk2 normalised to PBL 1h post-IR (mean ± SD from 2 experiments)

1h after irradiation correlates with the observed G2 cell cycle delay for HSPC and PBLs (Fig.2, A). The relative phosphorylation of Chk2 to the total Chk2 amount revealed no significant difference in the phosphorylation activity in HSPC and PBLs (Fig.2, B).

Cell cycle distribution, radiation induced delay and Chk2 signalling are similar in PBLs and HSPC and thus cannot explain the observed differences in DNA repair pathway usage.

References

[1] Rithidech *et al.* (2007), Radiat Environ Biophys, 46(2):137–145

[2] Mohrin *et al.* (2010), Cell Stem Cell, 7(2):174–185

[3] Akyüz *et al.* (2002), Mol Cell Biol, 22(17):6306–17

[4] Kraft *et al.* (2011), GSI Report

[5] Becker *et al.* (2009), Int J Radiat Biol, 85(11):1051–1059

* Work financed by DLR/BMWi contract No. 50 WB 1225

Response of bone marrow progenitor cells to ionizing irradiation*

A.Groo[1], *D.Kraft*[1], *M.Hirschmann*[1], *L. Deloch*[3], *B. Frey*[3], *U.S. Gaipl*[3], *M.Durante*[1,2], *and C.Fournier*[1]

[1]Helmholtzzentrum für Schwerionenforschung GSI; [2]Technische Universität Darmstadt; [3]Universitätsklinikum Erlangen

Introduction

In the bone marrow, hematopoietic stem cells (HSC) and mesenchymal stem cells (MSCs) are responsible for the renewal of blood and skeletal structure of the body [1]. The bone metabolism is related to the tight balance between progenitor cells of MSCs and HSC- osteoblasts and osteoclasts (OCs), respectively. During chronic inflammatory diseases like rheumatoid arthritis (RA), the activity of bone resorbing OCs is enhanced and correlates with a high presence of inflammatory cells in the synovial fluid of RA patients [2]. An efficient treatment of RA is the exposure to low doses of ionizing irradiation, either photons or α-particles in radon galleries. Here we studied the impact of low dose X-irradiation on the differentiation and proliferation OCs and immune cells (Th17, Treg).

Material and Methods

OC and immune cells were generated from buffycoats of healthy donors (blood donor service Frankfurt). After X-irradiation, OC were generated from monocytes by adding RANKL and M-CSF. Treg/Th17 cells were differentiated from $CD4^+$ T cells in the presence of cytokines (IL-1β, IL-23, TGF-β) and stimulatory antibodies (CD3, CD8). Differentiated OC were identified by TRAP activity and F-actin ring formation, Th17 and Treg cells by immunophenotyping with anti-IL17 and anti-FOXP3 respectively.

Results and Discussion
Differentiation of OCs and immune cells (Th17, Treg) after Xray exposure

The measurement of the percentage of TRAP positive OCs 12 days following exposure to X rays (Fig. 1) showed that ionizing radiation has no influence on the differentiation of osteoclasts (osteoclastogenesis). The irradiated cells grew and fused to multinuclear OCs independent of the applied doses. The same applies for mouse osteoclastogenesis of C57BL/6 wild type and hTNF-alpha transgenic mice.

As IL-17 producing Th cells (Th17) are known to enhance osteoclastogenesis *in vitro*, we assessed the differentiation of Th17 and complementary Treg cells after irradiation. As shown in Fig. 2, after irradiation, the proportional distribution was shifted to a higher occurrence of Treg compared to inflammatory Th17 cells, which suggests an anti-inflammatory effect of low doses of X-irradiation.

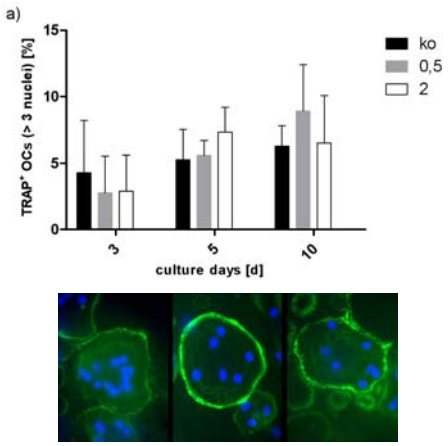

Figure 1: Frequencies of TRAP positive cells (OCs) within MNCs which were exposed to Xrays (0.5; 2 Gy) and stimulated for OCs differentiation. TRAP activity (a) and F-actin ring formation (b) were investigated. Only TRAP+ cells with >3 nuclei (DAPI) and intact F-actin ring were counted as OCs. (N=3,n=6).

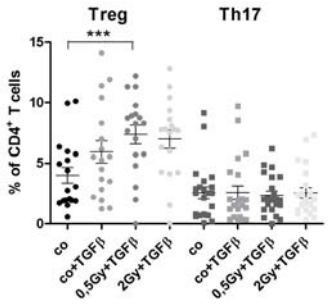

Figure 2: Human CD4+ T cells were irradiated with X-rays (0.5; 2Gy) and stimulated with CD3 and CD28 antibodies, in the presence of a cytokine cocktail (IL-1β, IL-23, and TGFβ) for 7 days. Distribution of Th17 and Treg cells were analysed by flow cytometry (N=4, n=8). Error bars represent SEM (***p<0.001).

References

[1] P. Bianco, 2011, Blood 117 (20) : 5281-5288

[2] Udagawa et al, 2002, Arthritis Res. 4: 281-289.

*This work was founded by the BMBF (GREWIS, 02NUK017A and 02NUK017G).

 doi:10.15120/GR-2014-1-BIOPHYSICS-08

Purified cultures of mouse embryonic stem cell-derived cardiomyocytes for electrophysiological studies with ionising radiation*

A. Helm[1], *S. Frank*[1,2], *J. Frieß*[3], *C. Thielemann*[3], *M. Durante*[1,2], *and S. Ritter*[†,1]

[1]GSI, Darmstadt, Germany; [2]Technische Universität Darmstadt, Germany; [3]University of Applied Sciences Aschaffenburg, Germany

High doses of ionising radiation to the heart are known to induce late-occurring ischemic heart disease [1] and epidemiological data suggest an increased risk of cardiovascular diseases also for an exposure to low doses [2]. To investigate putative adverse effects of ionising radiation on the electrophysiology of the heart, we recently set up a model system using mouse embryonic stem cell (mESC)-derived cardiomyocytes [3].

Briefly, this system is based on the differentiation of pluripotent stem cells through formation of embryoid bodies (EBs) [4]. EBs comprise a variety of different cell types, among them spontaneously contracting cardiomyocytes. For electrophysiological studies, EBs were seeded on the electrode array of a microelectrode array chip (MEA) and measurements were conducted. Data were analysed using the MATLAB based software *DrCell* developed at University of Applied Sciences Aschaffenburg [5]. Endpoints such as signal amplitude and shape, beat rate and conduction velocity were examined. This system, however, proved to be unstable. Large intra and inter-sample variations were observed most likely resulting from the progressive differentiation of cells in the embryoid bodies. Moreover, the small number and size of spontaneously contracting clusters (i.e. cardiomyocytes) renders this model system unsuitable for the detection of the anticipated small effects of IR on the electrophysiology of cardiomyocytes [3].

To overcome these drawbacks, we subsequently used a commercially available purified culture of mESC-derived cardiomyocytes (Cor.At, Axiogenesis, Fig. 1). Cor.At cells were seeded on the fibronectin coated electrode array of a MEA according to the manufacturer's protocol. Measurements were conducted at 24 h intervals and subsequently analysed with DrCell software.

Figures 2 and 3 exemplarily show data for two of the analysed endpoints, i.e. the number of active electrodes and the beat rate of control samples (n=35) of three different experiments. Regarding sample variations, purified Cor.At cardiomyocytes are more stable than contracting cardiomyocytes generated within an EB. Concerning the number of active electrodes (Fig. 2) larger variations are observed at day 1 and 2 in culture due to the recovery process after thawing and the time needed to build up a conducting network. At days 8 and 9 in culture, Cor.At cells start to detach from the MEA surface leading to higher variations in the number of active electrodes. However, from day 2 until day 7 the number of active electrodes is stable, reflected in small error bars. As shown in figure 3, from day 2 on the beat rate increases steadily with a considerably smaller inter-sample variations when compared to the number of active electrodes. Altogether our studies show that purified Cor.At cells are a suitable tool to investigate the effect of ionising radiation on the electrophysiological response of cardiomyocytes. Based on these data, x-ray experiments have been conducted and are currently analysed.

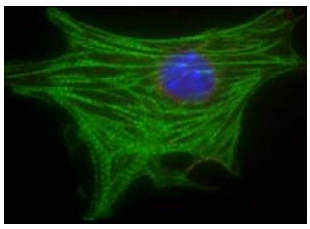

Figure 1: Representative immunofluorescence image of a Cor.At cardiomyocyte (red: connexin 43; green: cardiac-specific protein Troponin; blue: DNA).

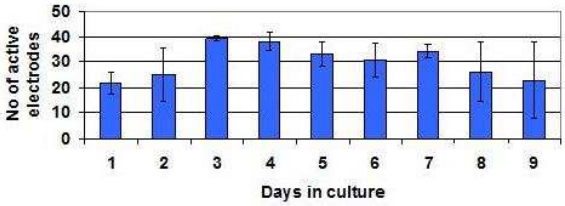

Figure 2: Number of active electrodes. Measurements were performed on control samples of three different experiments (total n=35, SEM).

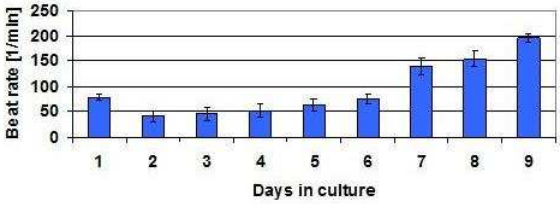

Figure 3: Beat rate. Measurements were performed on control samples of three different experiments (total n=35, SEM).

References

[1] Darby et al., N Engl J Med, 2013, 368(2)

[2] Little et al., Environ Health Perpect, 2012, 120(11)

[3] Materna et al., GSI Scientific Report 2012, 441

[4] Helm et al., GSI Scientific Report 2010, 455

[5] Nick et al., SPIJ, 2013, 7(2)

*The research leading to these results has received funding from the Euratom Seventh Framework Programm under grant agreement n° 295823 (PROCARDIO)

† s.ritter@gsi.de

Interaction of endothelial cells and lymphocytes after X-ray exposure*

N. Erbeldinger[1], *S. Meyer*[2], *J. Zimmermann*[1], *T. Dettmering*[1], *M. Durante*[1], *M. C. Cardoso*[2], *F. Rödel*[3], *and C. Fournier*[1]

[1]GSI, Darmstadt, Germany; [2]Technische Universität Darmstadt, Germany; [3]Universitätsklinikum Frankfurt, Germany

Introduction

Low-dose irradiation is an effective therapy for chronic inflammatory diseases [1,2]. We currently investigate radiation induced lowered adhesion of immune cells on the endothelial layer of the blood vessel walls as one possible modification of the in inflammatory processes. Beside alterations in the inflammatory pathways in irradiated cells, an increased frequency of apoptosis of exposed immune cells has been considered as responsible for a lowered adhesion [3].

Materials and Methods

X-ray irradiation (250 kV, 16 mA) was performed with isolated peripheral blood lymphocytes (PBL) or endothelial cells (EC). After exposure of either PBL or EC, the adhesion of unirradiated or irradiated PBL to TNF-α-stimulated (1 ng/ml) EC (primary HMVEC or Ea.hy.926 cells) was tested at 24h under static conditions. Cell death of PBL was quantified by flow cytometric analysis of annexin/propidium-iodide stained PBL. In irradiated EC, TNF-α induced NFκB signalling was analysed in parallel by quantification of the nuclear translocation of p65.

Results and Discussion

Fig. 1 shows that the adhesion of unirradiated PBLs to HMVEC is enhanced by TNF-α treatment (Fig. 1A), mimicking an inflammatory environment. Previously, we have shown for TNF-α treated HMVEC, which have been exposed to low dose irradiation, that the adhesion of PBL is decreased [4]. However, as shown in Fig. 1A, the adhesion of irradiated PBL to stimulated HMVEC displays also a discontinuity at low doses (minimum at 0.5 Gy). This is not reflected by the induction of apoptosis (Fig. 1B), indicating that cell death can only be a factor for the lowered adhesion at high doses, not at low doses.

Furthermore, TNF-α induced NFκB signalling was assessed after radiation exposure of EC (Ea.hy.926) as a putative molecular basis of the lowered adhesion of PBL to EC. In the presence of TNF-α, in 40% of unirradiated EC show nuclear translocation of p65, but irradiation did not modify this (Fig. 2), although adhesion was lowered (not shown). These results show that low dose exposure to PBL or EC reduce the adhesion of PBL to EC, but not based on radiation induced cell-death and modification of NFκB signaling.

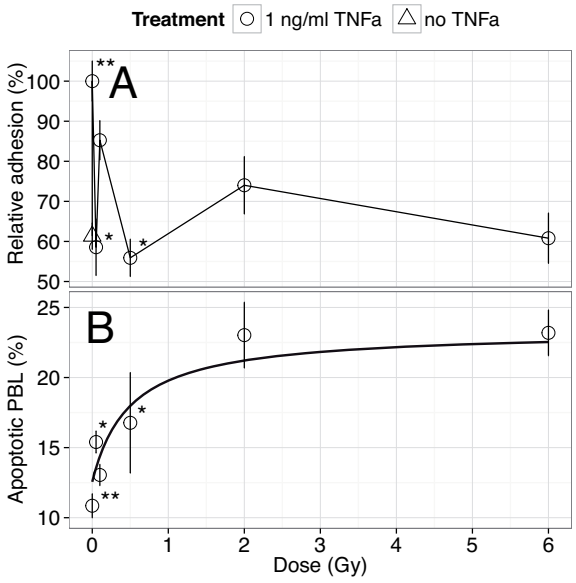

Figure 1: (A) Adhesion of irradiated PBL to stimulated and non-stimulated EC under static conditions. (B) Apoptotic frequencies of irradiated PBL under static conditions. N = 3 (triplicates); *N = 2; **N = 7

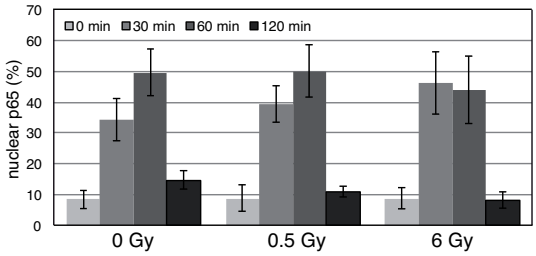

Figure 2: Ea.hy.926 cells expressing GFP-tagged p65(RelA). TNF-α treatment results in a 40% increased p65 transient activation. N = 2

References

[1] Rödel *et al.* (2007), Int J Radiat Biol 83(6): 357–366.

[2] Trott *et al.* (1999), Radiother Oncol 51(3): 197–203.

[3] Kern *et al.* (2000), Radiother Oncol 54(3): 273–282.

[4] Klinger *et al.* (2013), GSI Report 2013-1.

* Financially supported by GREWIS (02NUK017A and 02NUK017D) and FOI Bad Gastein

 doi:10.15120/GR-2014-1-BIOPHYSICS-10

Inflammatory cytokine release by vascular cells after X-irradiation*

T. Dettmering[1], *N. Erbeldinger*[1], *D. Lowe*[2], *M. Durante*[1], *R. Benotmane*[3], *S. Tapio*[4], *K. Raj*[2], *and C. Fournier*[1]

[1]GSI, Darmstadt, Germany; [2]Public Health England, Oxford, UK; [3]SCK-CEN, Belgium; [4]HelmholtzZentrum München, Germany

Introduction

Exposure to high radiation doses is considered to be responsible for the development of cardiovascular diseases (CVD), but also low doses are suspected to be a risk factor [1,2]. The development of CVD is mediated by changes in the cytokine release of endothelial and immune cells, whereas the role of smooth muscle cells is underinvestigated up to now [3]. We used a co-culture model of both cell types in order determine the cytokine release up to two weeks after irradiation, comparing low and high doses of X-rays. Here we present the results of Interleukin-6 (IL-6), a cytokine which can have both pro- and anti-inflammatory effects.

Materials and Methods

Human coronary artery endothelial cells (HCAEC) and human smooth muscle cells (SMC) were immortalized by hTERT overexpression. Cell types were either cultured separately or in co-culture for 3 d prior irradiation. After irradiation with 0.05, 0.1, 0.5 and 2 Gy X-rays, medium supernatants were collected after 4 h, 24 h, 1 week and 2 weeks and frozen at -80 °C. Medium was replaced 24 h before each time point. Concentrations of 21 inflammation-related cytokines in the supernatants of mono- and co-cultures were determined by bead-based protein arrays. Based on these results, IL-6 concentrations were quantified using ELISA (eBioscience) and data were analyzed using a custom pipeline written in the R language.

Results and Discussion

In Figure 1, the IL-6 release of unirradiated cells is shown over the time. While the IL-6 release rate of HCAEC remained almost unchanged, SMC and the coculture released initially high amounts of IL-6 that decreased rapidly during the following week. The IL-6 production of the co-culture after assembly exceedes the total amount of the two monocultures, pointing towards signaling processes occuring in the co-cultured cells.

There was no significant radiation-induced change of IL-6 release 4 h, 24 h or 2 weeks after radiation exposure (not shown). In contrast, 1 week after irradiation the IL-6 concentrations were $1.5\times$ (0.5 Gy) and $2\times$ (2 Gy) increased relative to control (Fig. 2). So far, this indicates no influence of very low doses ($\leq$ 0.1 Gy) on the release of this inflammatory mediator. Higher doses ($\geq$ 0.5 Gy), however, are able to increase the cytokine release in a vascular co-culture model, but mono-cultures remain unaffected by irradiation. Preliminary results from proteomics studies showed an induction of proteins that could be indicative of ongoing inflammation, thus supporting our results (not shown). Preliminary transcriptomic data of HCAEC show that genes involved in regulation of mitosis were strongly downregulated at 24 h post-IR, pointing towards a G2/M arrest (not shown). After 7 days, these genes are slightly but significantly upregulated after 2 Gy irradiation.

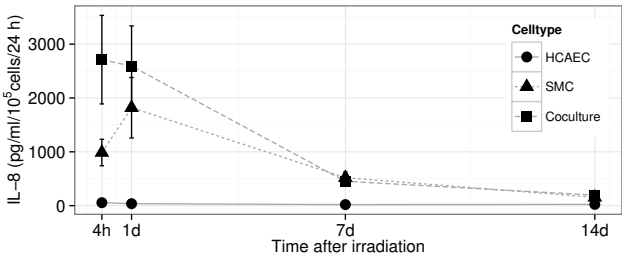

Figure 1: IL-6 cytokine release rate of unirradiated cells as a function of the time. Each sample was measured at least twice. Error bars show SEM. $N = 2, n = 6$

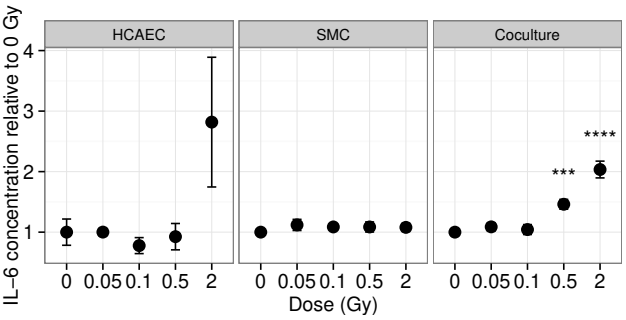

Figure 2: IL-6 cytokine release one week post irradiation. Concentrations have been normalized to 0 Gy sample. Error bars show SEM. *** $p < 0.001$; **** $p < 0.0001$. $N = 3, n \geq 9$

References

[1] Boerma and Hauer-Jensen. Cardiol Res Pract. 2010 Oct 4; 2011. pii: 858262.

[2] Adams *et al.* Semin Radiat Oncol. 2003 Jul; 13(3):346–56.

[3] Schultz-Hector *et al.* Int J Radiat Oncol Biol Phys 2007 Jan 1; 67(1):10–8.

*The research leading to these results has received funding from the Euratom Seventh Framework Programme under grant agreement no. 295823 ("PROCARDIO").

Inflammation-related response to irradiation in different human skin culture systems*

J. Wiedemann[1], *P. Simoniello*[1], *L. Madl*[1], *E. Thönnes*[1], *M. Durante*[1,2], *M. Podda*[3], *and C. Fournier*[1]
[1]GSI, Darmstadt, Germany; [2]Technische Universität Darmstadt, Germany; [3]Dept. of Dermatology, Darmstadt Hospital

Introduction

Chronic inflammatory skin diseases (eczema, psoriasis) can be treated with low doses of irradiation [1]. Exposure to UV, photons and radon can alleviate the symptoms suggesting an anti-inflammatory effect. Apoptosis can be related to this. The absence of an inflammatory response during apoptosis is not only due to lack of pro-inflammatory signals, but apoptotic cells can actively suppress an inflammation by the release of anti-inflammatory cytokines like TGF-β or IL-10 [2]. Changes induced by irradiation that are potentially related to inflammation in skin will be investigated.

Materials and Methods

Model systems with different complexity-levels have been used: monolayer cultures of human primary keratinocytes (NHEK; Lonza), co-cultures of primary keratinocytes and fibroblasts (NHDF; Lonza) and human full-thickness skin equivalents (EFT400; MatTek; Ashland). Samples were irradiated comparing low versus high X-ray and C-ion (186 keV/μm) doses or UV-B intensities, fixed and processed 12 hours, 24 hours and 3 days after irradiation for microscopic analysis and protein extraction. Hematoxylin & Eosin (H&E) staining and immunostaining against Caspase 3 and PARP have been performed. Cytokine release was quantified by ELISA.

Results and Discussion

No apoptosis was observed after X-ray and C-ion irradiation in all model systems [3]. Cleaved caspase 3 and cleaved PARP could only be detected in monolayer cultures of NHEK after UV-B intensities of 40 and 60 mJ/cm^2 (Fig. 1A); the same intensities could not induce apoptosis in the more complex systems (data not shown). These suggest that apoptosis is not a trigger for the release of anti-inflammatory cytokines. C-ion irradiation induced morphological changes after exposure to a high dose; but earlier compared to UV-B (not shown). 3 days after UV-B irradiation (100 mJ/cm^2), cobblestoned morphology of the basal layer and a reduced cohesion of the stratum corneum occur (Fig. 1B), indicating a radiation induced impairment of the differentiation process. The inflammatory response was assessed by detection of TGF-β and Il-1α release in monolayer- and co-cultures. In unirradiated co-cultures the release of TGF-β and Il-1α is suppressed by intercellular communication between NHEK and NHDF (data not shown) which is in agreement with the literature [4]. The enhancement of the pro-inflammatory cytokine IL1α in NHEK monocultures (data not shown) and co-cultures (fig.2) after exposure to moderate doses/intensities shows that the cytokine-balance is changed due to irradiation. Taken together, an induction of apoptosis was only observed for UV-B exposure, not for ionizing irradiation. Modifications of the keratinocyte differentiation and release of inflammatory factors was only observed for moderate and high doses of UV-B and ionizing radiation, but not for low doses. In future experiments the influence of immune cells on the radiation response will be considered.

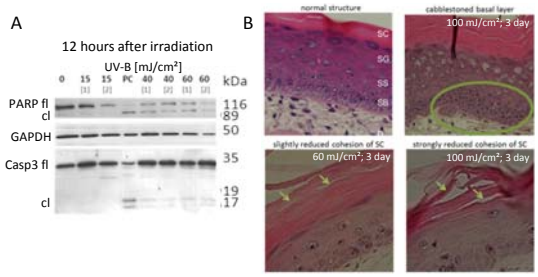

Figure 1: (A) Western Blot analysis of NHEK cells after UV-B irradiation. PC: positive control (HaCaT cells 5 days; 10 Gy X-ray); kDa: kilodalton; fl: full-length; cl: cleaved (B) H&E staining of tissue sections. circle: cobblestoned morphology in the stratum basale (sb); arrows: reduced cohesion of stratum corneum (sc)

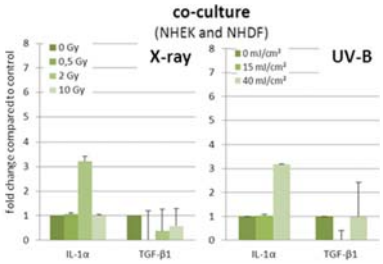

Figure 2: IL1α and TGF-β release of co-cultures after irradiation with x-ray and UV-B

References

[1] Rodel *et al.* (2002); Strahlenther Onkol 178:1–9
[2] Voll *et al.* (1997); Nature 390:350–351
[3] Simoniello *et al.* (2012). GSI Scientific Report. 432.
[4] Le Poole *et al.* (1999); Br J Dermatol 140:409–416

* Work supported by GREWIS No. 02NUK017A, DFG (GRK 1657) and HGS-HIRe.

 doi:10.15120/GR-2014-1-BIOPHYSICS-12

Immune system activation through Carbon ion irradiation (Ab-scopal effect)*

W. Tinganelli† [1,2], *T. Shimokawa*[3], *Y. Yamada*[3], *S. Koike*[3], *F. Natale*[4], *R. Okayasu*[2,3], *and Y. Furusawa*[2,3]

[1]GSI, Darmstadt, Germany; [2]IOL, NIRS-GSI, Chiba, Japan; [3]NIRS, Chiba, Japan; [4]TUD, Darmstadt, Germany

Metastasis and tumor recurrence are the main cancer poor prognosis cause. Carbon Ion radiation is one of the most innovative, powerful and for sure the less invasive methods for cancer treatment. Besides the well-known advantages derived from the better capacity to kill the tumor cells and to spare the healthy tissues around, tumor irradiation has been shown to produce in a statistical low number of cases not only the neoplastic malignant shrinking but also the shrink of metastasis located out of the irradiation field, a rare phenomenon known as ab-scopal effect. Despite the effect is extremely rare, its consequence on the cancer can be stunning, leading to the disappearance of malignant growths throughout the entire body also about the distal metastasis out of the irradiation field [1]. Study about how this happen is still on going, but is absolutely clear now that the immune system, and more specifically dendritic cells and T cells, is involved. Radiation would produce a complete rearrangement of the membrane cell antigens. This new "antigens set" would then be recognized by the dendritic cells as "not self" anymore and targeted by T cells [1]. The purpose of our project is to study the carbon irradiation effects on the immune-system.

C3H female mice were used for our experiments. Seven days before irradiation, 106 squamous carcinoma cells (SCCVII) were injected in both mice posterior limbs. Mice left tumor were irradiated at day zero with a 15 Gy SOBP of 6 cm at HIMAC-NIRS facility. PCR array (Qiagen immune and adaptive response pathway), blood PGE2 and HMGB1 ELISA and immuno-hystochemistry analysis at days 9, 16 and 25 of both tumor has been done (irradiated tumor and the abscopal tumor out of the irradiation field).

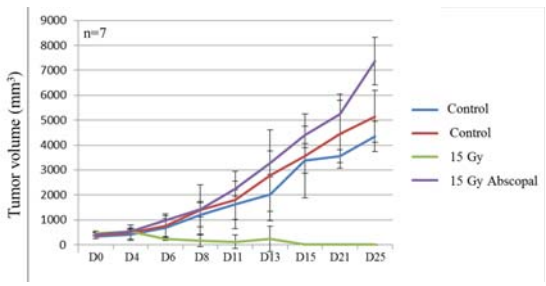

Figure 1: Twenty-five days tumor growth curve.

Twenty-five days after irradiation the ab-scopal tumor (out of the irradiation field) was bigger than the tumor control (Fig 3). This could be because of the increased PGE2 release after irradiation that could produce the Phoenix rising effect [2]. Furthermore PGE2 could be responsible for the T regulatory cells increase a well-known immune suppressor kind of cells [3]. ELISA blood analysis has been done (Fig 4). Nine days after irradiation the PGE2 was 3-4 times higher than the control. Sixteen and 25 days after irradiation the PGE2 level is not significant different from the control. Anyway PGE2 release level has not been normalized for the tumor mass. PCR array have been used for a gene expression array pathway. Clear immune-system activation has been found in the 15 Gy irradiated tumor while no activation has been found for the abscopal tumor.

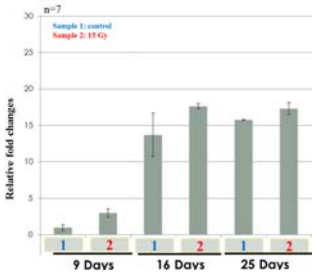

Figure 2: PGE2 ELISA relative fold changes for in vivo C3H female mice experiments after 9, 16 and 25 days. All the results have been normalized for the 9 days control.

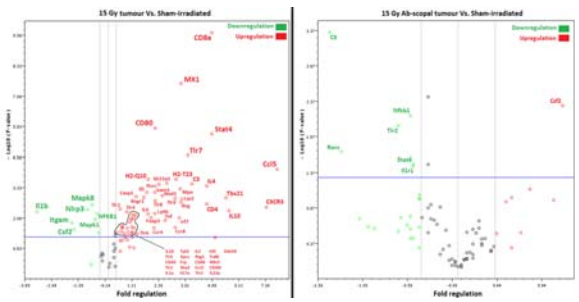

Figure 3: PCR array results of 15 Gy irradiated tumor (left) compared with the 15 Gy abscopal (right).

References

[1] Demaria S, Formenti SC, Front Oncol 3 (2013) 128

[2] Li F et al, Sci Signal 3 (2010) ra13

[3] Whiteside TL, Cancer Immunol Immunother 63 (2014) 67

* Work supported by IOL, International Open Laboratory.

† w.tinganelli@gsi.de

Image segmentation of alveolar macrophages reveals chronic inflammation in carbon ion irradiated rat lungs*

T. Dettmering[†1], *A. Krömmelbein*[2], *L. Naumann*[2], *H. Faber*[3], *M. Durante*[1], *P. van Luijk*[3], *R. P. Coppes*[3], *and C. Fournier*[1]

[1]GSI, Darmstadt, Germany; [2]Technische Universität Darmstadt, Germany; [3]Departments of Cell Biology and Radiation Oncology, University Medical Center Groningen, University of Groningen, The Netherlands

Introduction

Radiation-induced pneumonitis represents a severe side effect in lung tissue after radiotherapy. The chronic form of pneumonitis, which in some cases persists over many months after irradiation, is discussed to be an inducer of fibrosis, another severe side effect. One potential mechanism leading to fibrosis is the release of certain cytokines by invading immune cells (especially macrophages), which stimulate fibroblast proliferation and overproduction of extracellular matrix [1].

In view of the increased application of carbon ions in radiotherapy, we aimed to assess whether carbon ions are able to induce chronic inflammation in lung tissue. We quantified alveolar macrophages present in slices of rat lung tissue 42 weeks post irradiation. To achieve a better precision compared to the commonly used scoring of bright field images, we established immunofluorescence stainings of macrophages with subsequent image segmentation.

Materials and Methods

Adult male albino Wistar rats were housed as described [2]. Whole lungs were irradiated with carbon ions at the SIS facility (270 MeV/u, 13 keV/μm) at doses between 7.7–12.5 Gy. 42 weeks after irradiation, lungs were extracted and embedded in paraffin. 4 μm slices were cut and stained with a macrophage-specific antibody (ED1, AbD Serotec) followed by an Alexa Fluor 488-conjugated secondary antibody (Life Technologies) and counter-stained with DAPI. 40 images were recorded per slice with an epifluorescence microscope (Leica, 20$\times$ objective). Image segmentation was performed using the CellProfiler software [3]. Cells were segmented via the DAPI channel by OTSU thresholding. Cells were counted as ED1 positive if their median fluorescence intensity in the ED1 channel was ≥ 15 standard deviations higher than the median fluorescence intensity of the whole image. Data were analysed using a pipeline custom-written in the R language. Percentage of ED1 positive nuclei in relation to all nuclei was used to calculate per-slice values. Significance level was set to $\alpha = 0.01$.

Results and Discussion

The chronic inflammatory response did not yield a clear dose response (not shown). This is possibly due to the 42 week time span between irradiation and processing, during which dose responses might be obfuscated by ongoing physiological processes. For this reason we combined all doses and compared the results with unirradiated animals (Fig. 1). Unirradiated animals had a median of 10% macrophages in the lung tissue. This number increased to 15% in irradiated animals 42 weeks post irradiation. The irradiated animals demonstrated a significantly increased percentage of macrophages compared to unirradiated animals (WILCOXON test, $p = 0.0006$). We conclude that carbon ions are able to induce a chronic inflammatory response that persists at least 10 months post irradiation, which is in agreement with a study using X-rays [4].

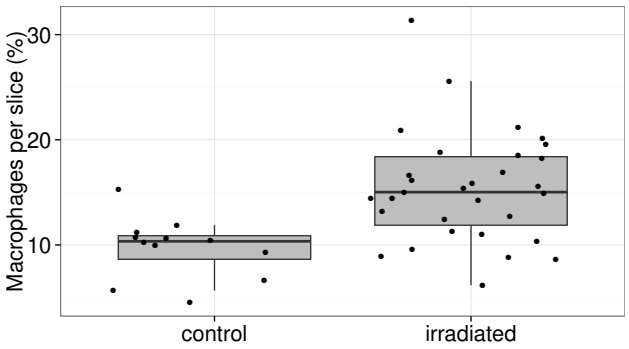

Figure 1: Percentage of macrophages per slice relative to whole cell count. Single dots represent single tissue slices of 4 control or 15 irradiated animals.

References

[1] Wilson and Wynn. Mucosal Immunol. 2009 Mar;2(2):103-21. doi:10.1038/mi.2008.85. Epub 2009 Jan 7.

[2] Coppes *et al.* Int J Radiat Oncol Biol Phys. 2011 Sep 1;81(1):62–9

[3] Carpenter *et al.* Genome Biol. 2006;7(10):R100. Epub 2006 Oct 31.

[4] Vujaskovic *et al.* Int J Radiat Oncol Biol Phys. 2001;50:851–5.

* Supported by HGS-HIRe and grant CBR-754842 from the University of Groningen

† t.dettmering@gsi.de

 doi:10.15120/GR-2014-1-BIOPHYSICS-14

Human embryonic stem cells: an ideal model for the risk assessment of ionizing radiation during early embryo development *

I. Schroeder[1], *S. Luft*[† 1], *P. Hessel*[1], *M. Durante*[1,2], *and S. Ritter*[‡ 1]
[1]GSI, Darmstadt, Germany; [2]Technische Universität Darmstadt, Germany

Diagnostic and/or therapeutic procedures that are based on ionizing radiation are being increasingly used. However, these procedures as well as the exposure to environmental radiation pose a threat to the early embryo possibly leading to prenatal death, growth retardation, organ malformation, mental retardation or childhood cancer [1]. Thus, a thorough risk assessment of radiation effects is mandatory in situations of inevitable or unintended exposure of the conceptus in utero. Data about the biological effects of a radiation exposure during the earliest stages of human development are scarce predominately stemming from atomic bomb survivors or observations made after fallouts (e.g. Chernobyl). However, human embryonic stem (hES) cells that are derived from the inner cell mass of the blastocyst during embryo development present a valuable tool to examine the radiation effects on early embryogenesis. Apart from their indefinite self-renewing capacity, hES cells are pluripotent thereby being able to differentiate *in vitro* into all cell types of the body deriving from the three germ layers endoderm, ectoderm and mesoderm (Fig.1). Therefore, the effect of radiation on pluripotent embryonic cells and their respective progeny can be easily analyzed on a molecular level. This is basis of the BMBF funded project "In vitro Untersuchungen zur Wirkung von dicht und dünn ionisierender Strahlung auf die frühe pränatale Entwicklung", which is performed in cooperation with the Universities of Applied Sciences Aschaffenburg and Albstadt-Sigmaringen.

In Germany, the work with hES cells requires ethical approval in accordance with the German Embryo Protection Act and the German Stem Cell Act and underlies certain restrictions regarding the choice of cell lines and the procedures used to study scientific questions. However, examining the effects of ionizing irradiation on early human development was regarded a top-ranking scientific goal and approval was granted to study the impact of ionizing irradiation. Yet, the initial GSI approval to use hES cells only comprised the analysis of cardiac differentiation with a limited number of hES cell lines. An amendment now allows us to use more sophisticated differentiation procedures, more suitable cell lines and not only cardiac differentiation protocols but also neuronal and endodermal ones to cover the entire developmental spectrum. Thus protocols for the generation of endoderm from human WA09 have been established (see GSI report S. Luft et al., 2013) as these cells later in development will give rise to lung, pancreas or liver. Likewise extra-embryonic endoderm differentiation is currently established as it provides signaling for cardiac differentiation, which has been shown to be impaired upon irradiation [2-3]. In summary, the hES cell based approach will provide insight into the impact of ionizing irradiation on human development and possibly cell regeneration.

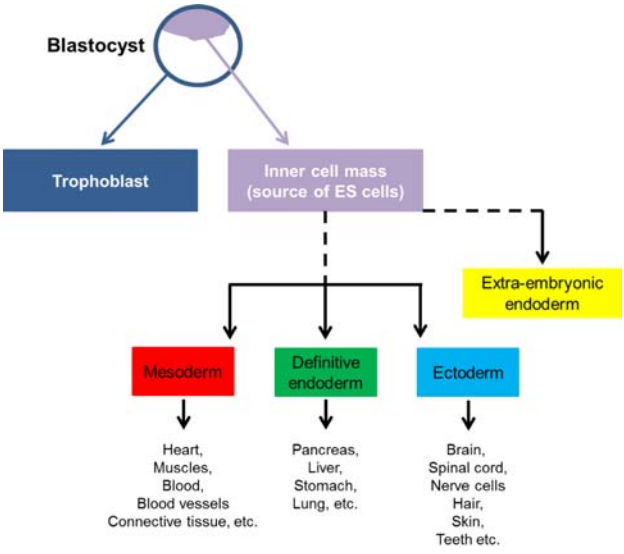

Figure 1: Human development can be mimicked by using human embryonic stem (hES) cells. hES cells can be differentiated *in vitro* into cells of the mesoderm, endoderm and ectoderm and their respective progeny. Likewise, they can form extra-embryonic tissue such as extra-embryonic endoderm, which gives rise to the yolk sac that provides early nourishment and serves as a circulatory system until the embryos internal circulation is established.

References

[1] McCollough CH et al., "Radiation exposure and pregnancy: When should we be concerned?", RadioGraphics 2007, 27: 909-918

[2] Helm A, "Influence of high- and low-LET radiation on the cardiac differentiation of mouse embryonic stem cells", Dissertation, 2013, Department of Biology, TU Darmstadt

[3] Luft S et al., "Fate of D3 mouse embryonic stem cells exposed to X-rays or carbon ions", Mutat Res. 2014, 760:56-63

* Work supported by BMBF grant 02NUK025A.
† S. Luft is supported by HGS-HIRe.
‡ s.ritter@gsi.de

Electrophysiological Effects of Ionising Radiation on Cortical Rat Neurons in vitro*

M. Mayer[1], *S. Ritter*[2], *and C. Thielemann*[1]

[1]University of Applied Sciences, BioMEMS lab, Aschaffenburg, Germany; [2]GSI, Biophysics division, Darmstadt, Germany

Motivation

Previous studies in mice and rats have shown that the developing central nervous system (CNS) is particularly sensitive against ionising radiation [3], yet there exists hardly any information if ionising radiation affects cellular communication of neuronal cells. Therefore we for the first time investigated the effects of X-ray on neuronal embryonic network using the method of microelectrode arrays (MEA). The cells, in this case primary cortex neurons from 18 to 19 days old rat embryos, were plated onto microelectrode arrays and reaggregated into an spontaneously, electrically active network. This network typically develops in three phases. First, electrical activity can be detected as random single spikes. Second, it starts to express a train-like spiking activity that further develops into burst-like activity. These bursts represent the mature signalling activity of the network [1]. With this method possible radiation induced effects can be extracellularly recorded.

Material and Methods

The experiments were performed with commercially available cortical rat neurons, isolated from 18 to 19 days old rat embryos. The cells were seeded onto the centre of the MEA chips and cultivated over a period of 4 weeks (Fig.1). This method can be used to assess the electrical activity of neuronal tissue and allows non-invasive, simultaneous recordings from 60 electrodes. In order to examine the effects of ionizing radiation on the neuronal network formation, the cells were irradiated after 16 days of cultivation with X-ray doses of 1 Gy and 2 Gy (90 kV, 33,7 mA) at the Technische Universität Darmstadt. Electrical signals could be recorded for about two weeks after irradiation and were analysed with regard to the number of spikes and bursts, the number of spikes per burst, the height of the amplitude, the duration of the bursts and other parameters.

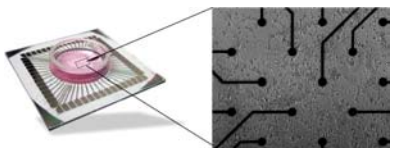

Figure 1: Cortical neurons from rat embryos on a MEA chip, cultured for 20 days in vitro.

* Funding for this project was provided by the Federal Ministry of Education and Research (02NUK025C).

Results

The first experiments showed that the neuronal network functionality is very robust and not affected significantly by the applied doses. None of the examined parameters provided clear evidence of radiation-induced changes in the electrophysiological response of the networks. As an example the number of network spikes per minute is shown in figure 2 as a function of dose. This parameter is very important since preceding studies have shown that the application of several drugs, such as carbamazepine (data not shown) and neurotoxins, such as methyl mercury chloride [2], leads to a reduction of the number of spikes within a defined period of time.

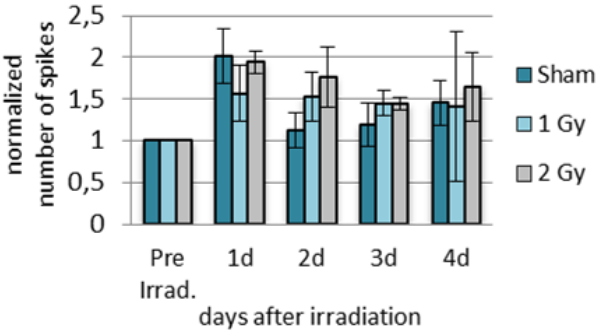

Figure 2: Number of spikes per minute of the neuronal network after X-ray exposure. The values are normalized to the measurement before irradiation (Pre Irrad.). Each bar represents at least three samples.

Conclusion

Our preliminary results suggest that the irradiation does affect neither the neuronal network nor the cell communication. It is planned to repeat this experiment applying higher doses. In addition, immunohistochemical techniques will be used to study radiation induced cell death.

References

[1] Heikkilä, T.J. et al. (2009) Human embryonic stem cell-derived neuronal cells form spontaneously active neuronal networks in vitro. Exp Neurol 218.1, 109-16

[2] Outinen, L.Y. et al. (2010) Human cell-based micro electrode array platform for studying neurotoxicity. Frontiers in Neuroengineering 3

[3] Schull, W.J. et al. (1990) Ionizing Radiation and the Developing Brain. Neurotoxicol Teratol 12, 249-260

 doi:10.15120/GR-2014-1-BIOPHYSICS-16

Effects of X-rays and titanium ions on cardiomyocyte cultures*

J. Frieß[1], *A. Heselich*[2], *S. Ritter*[3], *P. G. Layer*[2], *and C. Thielemann*[1]

[1]University of Applied Sciences Aschaffenburg, Germany; [2]Technische Universität Darmstadt, Germany; [3]GSI, Darmstadt, Germany

Motivation

For the pursuit of the planning of manned space missions to Mars [1; 2] as well as for the application of heavy ion irradiation in radio-therapy [3] an assessment of possible effects of high LET radiation on the cardiovascular system, especially heart muscle cells is needed. In order to approach this important field, we used for the first time microelectrode arrays (MEA). This method allows the recording and monitoring of electrophysiologic cardiac signals of primary cardiac cultures, seeded onto MEA-chips. Additionally, DNA damage and cell cycle progression were examined.

Material and Methods

Cardiac cells were isolated from chicken at developmental embryonic stage E8 and cultivated. Cells were seeded onto 60 electrode MEAs and 15 mm coverslips. The cultures were exposed to carbon (25 mm Bragg Peak, mean LET 75 keV/μm at sample position) or titanium ions (1 GeV/u) at the SIS-facility (GSI, Germany). X-ray exposure was conducted at the Technische Universität Darmstadt (135 kV; 19 mA / 90 kV; 33.7 mA). Electrophysiological properties of the cell cultures were measured before and after exposure. Signals of cardiac cells could be recorded for approximately one week and were analysed in terms of beat rate, conduction velocity, field action potential duration and general spike shape using the MATLAB software tool DrCell [4]. Cardiomyocytes cultured on coverslips were fixed at different time points after exposure and double strand break (DSB) accumulation and repair, proliferation and apoptosis were examined by immunohistochemistry.

Results

Experiments up to now indicate that heavy ion irradiation reduces the conduction velocity of cardiac signals [5]. Furthermore, cultures irradiated with titanium ions show a slight increase in the field action potential durations four hours after exposure compared to the sham irradiated controls (see figure 1). In contrast, cultures exposed to the same doses of X-rays exhibit a reduction in their field action potential duration in comparison to the non-irradiated controls. These results indicate different radiation qualities may have opposing effects on the electrophysiology of the exposed cells. This is also supported by other physiologic parameters such as the beat rate.

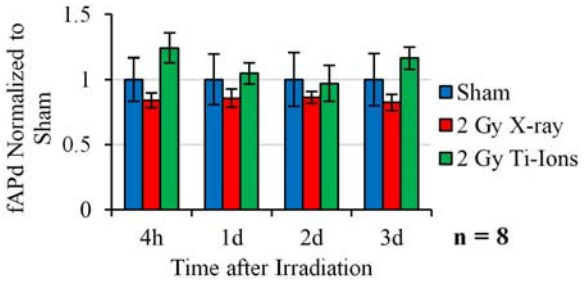

Figure 1: Field action potential durations (fAPd) are exemplarily plotted for cultures exposed to 2 Gy X-ray and titanium ions, respectively.

For both, X-ray and heavy ion radiation, we observed a late, but dose-dependent G1/S-checkpoint response analyzed by S-phase labeling. Irradiation with higher doses of heavy ions resulted in a stronger decrease of proliferation compared to similar doses of X-rays. We detected only small differences in G2/M-activation. We also observed a dose-dependent decrease in the number of mitotic figures 24 h after X-irradiation, whereas irradiation with heavy ions showed only slight decreases

Conclusion

X-ray and titanium ion exposure show opposing effects on some electrophysiologic characteristics at the same doses.

References

[1] Space Studies Board, National Research Council, "Radiation Hazards to Crews of Interplanetary Missions" National Academy Press, Washington DC, 1996

[2] R. J. White et al., "Humans in space", Nature, 2001, 409(6823), p. 1115

[3] M. P.Little et al., "Review and meta-analysis of epidemiological associations between low/moderate doses of ionising radiation and circulatory disease risks, and their possible mechanisms.", Radiat Environ Bio-phys, 2010 49(2), p. 139–53

[4] C Nick et al., "DrCell – A Software Tool for the Analysis of Cell Signals recorded with extracellular Microelectrodes", Signal Processing: An International Journal (SPIJ), 2013-2;7(2), p. 96-109

[5] J. Frieß et al, "Electrophysiological Effects of Heavy Ion Irradiation on Cardiomyocytes", GSI Report 2012 (2013) 480

*This work is supported by the DLR and ESA in the frame of the ESA IBER-10 program.

Effects of X-rays and carbon ions on pluripotency maintenance and differentiation capacity of mouse embryonic stem cells*

O. Arrizabalaga[†1,2], *A. Helm*[1], *S. Luft*[1,3], *P. Hessel*[1], *M. Durante*[1,3], *and S. Ritter*[‡1]

[1]GSI, Darmstadt, Germany; [2]IKERBASQUE Foundation for Research, Bilbao, Spain; [3]Technische Universität Darmstadt, Germany

Embryonic Stem (ES) cells have the ability to self-renew as well as to differentiate into cells of the three germ layers (ectoderm, endoderm and mesoderm) due to their pluripotency, giving rise to a variety of differentiated cells, such as cardiomyocytes [1]. They constitute an excellent model system to study the effects of ionizing radiation on early embryonic development that are still poorly understood [2]. The model system used for the present work is the mouse ES-D3 cell line, and the radiation effects on both the pluripotency maintenance and the ability to develop into cardiomyocytes was assessed.

The cells were exposed to X-rays (250 kV, 16 mA) or carbon ions (C-ions, 25-mm extended Bragg peak, energy range: 106-147 MeV/u with a mean LET of 75 keV/μm at sample position). Irradiated cells were grown under conditions that maintain pluripotency (i.e. cultured in the presence of leukaemia inhibitory factor, LIF) or directed to differentiate by embryoid body (EB) formation in the absence of LIF as previously described [3-4]. Ten days after differentiation initiation, beating clusters of cells can be observed by bright field microscopy. RNA from EBs on days 0, 4, 6 and 10 of differentiation was extracted and pluripotency markers' gene expression was measured by quantitative reverse transcriptase PCR (RT-PCR).

Pluripotency of the progeny of irradiated cells was examined by performing western blot (WB) analysis. Pluripotent cells express a complex combination of transcription factors and epigenetic regulators [5]. WB analysis of the transcription factors OCT3/4 and SOX2, two of the key players in ES cell pluripotency maintenance, showed that the protein amount of both was comparable to the non-irradiated control sample about 2 weeks after exposure to X-ray and C-ions (Figure 1).

To examine the differentiation potential of irradiated ES-D3 cells, they were differentiated via EB formation. Following C-ion exposure, the fraction of beating EBs was lower than in the control, while isodoses of X-rays exerted no effect (for more details see [4]).

The low fraction of beating EBs observed after C-ion exposure might result from a delayed differentiation of the cells. Exposed cells undergo a cell cycle delay [4]. Additionaly, cells are removed by apoptosis. This may impair EB formation and differentiation into cardiomyocytes, which depend on the initial cell number [4,6]. To investigate the pluripotency marker expression during the differentiation process, the expression of the genes coding for OCT3/4 (designated as POU5F1) and for SOX2 were assessed by quantitative RT-PCR. In the differentiating control cells POU5F1 gene expression decreased with time. The same effect was observed after X-ray irradiation, whereas this decrease was delayed in the C-ion exposed samples (Figure 2). Due to high inter-experimental variations in the gene expression of SOX2, it is difficult to draw firm conclusions (data not shown). Investigation of cardiac-specific gene expression is now underway.

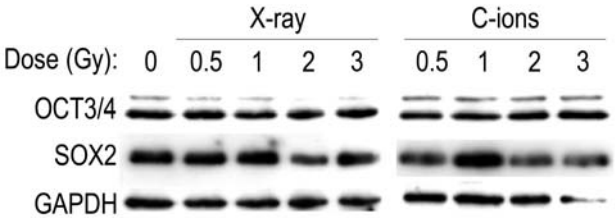

Figure 1: WB analysis of ES-D3 cells. They express pluripotency markers (OCT3/4 and SOX2) 10 and 17 days after exposure to X-rays or C-ions, respectively. GAPDH expression was used as loading control.

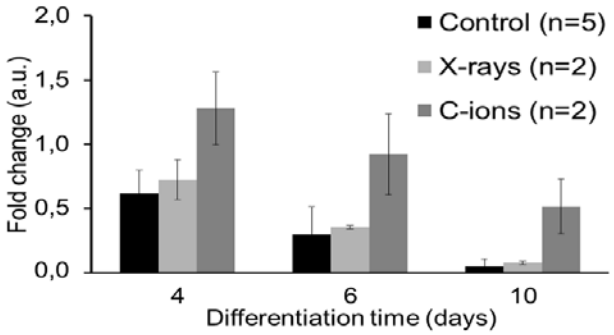

Figure 2: C-ion exposure delays pluripotency marker (POU5F1) expression in differentiating EBs compared to the day the differentiation started. RT-PCR quantification was normalized to the geometric mean of 18S rRNA and GAPDH. The average fold change is plotted, +/-SD.

References

[1] Itskovitz-Eldor, et al.,Mol. Med. 2000, 6, 88-95

[2] ICRP (2003) Biological Effects after Prenatal Irradiation (Embryo and Fetus), ICRP Publication 90

[3] Helm et al., GSI Scientific Report 2010, 455

[4] Luft et al., Mutat. Res., 2014, 760, 56–63.

[5] Thomson et al., Cell, 2011, 145, 875-889

[6] Preda et al., Tissue Cell, 2013, 45, 54-60

*Work supported by funding from the Euratom Seventh Framework Programme under grant agreement no 295823 (PROCARDIO).

† OA was funded by the Doctors specialization programme from the Basque Government.

‡ s.ritter@gsi.de

 doi:10.15120/GR-2014-1-BIOPHYSICS-18

Effect of hypoxia on the growth of glioma-initiating cells

C. Klein[1,2], *C. Hartel*[1], *I. Ahmed*[1,3], *S. Ritter*[1], *W.K. Weyrather*[1], *and M. Durante*[1,4]

[1]GSI, Darmstadt, Germany; [2]Chemistry Department, TU Darmstadt, Germany; [3]Biology Department, TU Darmstadt, Germany; [4]Condensed Matter Physics, TU Darmstadt, Germany

Introduction

Glioma-initiating cells (GICs) possess stem cell characteristics such as the ability for limitless growth, self-renewal and to differentiate into all kinds of cells found in the original tumour. GICs are held responsible for the strong radio- and chemoresistance of gliomas.

A solid tumour consists of an outer layer that is surrounded by a blood vasculature to provide both nutrition and oxygen. In the inner tumor layers, the oxygen concentration decreases with increasing distance from the blood vessels reaching numbers below 0.5 %. This hypoxic core is referred to as a stem cell niche. Studies concluded that hypoxia regulates glioblastoma stem cell properties and biomarker expression [1].

Materials and Methods

Three glioma cell lines (#10, #10-IR, and U87) were cultured as neurospheres in serum-free neurobasal A medium supplemented with B27, EGF and FGF. For the growth curves, 30.000 normoxic cells were seeded in T25 culture flasks and cultured under normoxia (21 % O_2) and hypoxia (1 % O_2). In the course of 2-3 weeks they were trypsinised and counted regularly. For the neurosphere formation assay 30.000 cells were seeded in T25 culture flasks then cultured under hypoxia and normoxia.

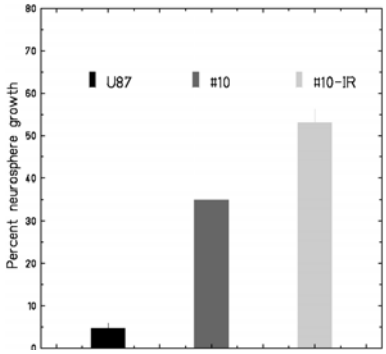

Figure 1: Percent neurosphere formation under hypoxia (1 % O_2), relative to neurosphere formation under normoxia. Error bars represent standard deviation, n=3.

Results and Discussion

The results from the neurosphere formation assay are displayed in figure1. The U87 cells showed a drastically reduced neurosphere formation ability under hypoxic conditions (less than 5 % relative to normoxia). For the cell lines #10 and #10-IR the neurosphere formation in hypoxia was 35 % and 53 %, respectively.

Cell growth curves were compiled for cell lines #10 and #10-IR and are displayed in figure 2. Due to the reduced growth of U87 cells in hypoxic conditions it was not possible to measure growth curves for this cell line. The doubling time (td) for #10 is 54 h in normoxic conditions and 107 h under hypoxic conditions. #10-IR cells have a td of 68 h under normoxia and 79 h under hypoxia.

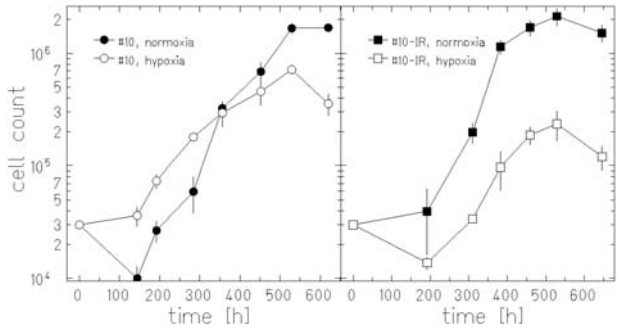

Figure 2: Growth curves of cell lines #10 (left panel) and #10-IR (right panel) under normoxic (closed symbols) and hypoxic (open symbols) culture conditions. Error bars represent standard deviation, n=3.

The cell lines # 10 and #10-IR were established as cell lines growing in serum-free self-renewal conditions [2] which promote the stem cell properties. The U87 cell line, in contrast, was established decades ago as a (bulk) glioblastoma cell line and is generally cultured in standard cell culture medium containing fetal calf serum. The ability of the cell lines # 10 and # 10-IR to grow well in a hypoxic environment, which is not shared by the U87 cells, could be a hint that the #10 and #10-IR cells are in a more stem-like state and can be used as a model for cancer stem-like cells while U87 cells are not an appropriate model for cancer stem-like cells.

References

[1] E.E. Bar et al. "Hypoxia increases the expression of stem-cell markers and promotes clonogenicity in glioblastoma neurospheres", Am J Pathol 177 (2010), p. 1491–1502.

[2] A. Barrantes-Freer et al. "Human glioma-initiating cells show a distinct immature phenotype resembling but not identical to NG2 glia"', J Neuropathol Exp Neurol 72(4) (2013) p.307

Cellular radiation response of mouse embryonic stem cell derived cardiomyocytes *

S. Frank[1,2], *A. Helm*[1], *M. Durante*[1,2], *and S. Ritter*[†,1]
[1]GSI, Darmstadt, Germany; [2]Technische Universität Darmstadt, Germany

To examine putative adverse effects of ionizing radiation on electrophysiological properties of cardiomyocytes, we recently performed a series of experiments with mouse embryonic stem cell derived cardiomyocytes (mESC-CM). For these studies mESC-CM were generated via embryoid body (EB) formation. Yet, this system proved to be unsuitable due to a low number of cardiomyocytes formed and pronounced inter- and intra-experimental variations [1]. To overcome these limitations pure mESC-CM (Cor.At cardiomyocytes, Axiogenesis) have been used in subsequent electrophysiological studies [2]. As a complement we also examined the cellular radiation response of Cor.At cells. For the experiments cells were seeded in chamber slides. Two days after seeding cells were irradiated with 0.5, 1 or 2 Gy X-rays (250 kV, 16 mA, 1.5 Gy/min). Radiation effects were examined at 1, 2, 3 and 4 days after exposure. Apoptosis, micronucleus formation and binucleation were analyzed by means of a DAPI nuclear staining; while the expression of connexin 43 (Cx 43) and troponin T was measured by immunocytochemistry (Figure 2 B, C). Our experiments show a dose- and time-dependent increase in the number of cells with micronuclei and in the number of apoptotic cells. Exemplarily, in figure 1 the apoptotic response of control and irradiated cultures (2 Gy X-rays) is plotted. In the control the spontaneous frequency of apoptotic cells was $\leq$8%. At 1 day after exposure to 2 Gy X-rays the number of apoptotic cells was as high as in the control samples, but it increased to 17% and 33% at day 2 and 4 after exposure. Interestingly, the number of binucleated cells, indicating maturation, rose in all samples with time and was not affected in the dose range examined (data not shown). Additionally, we analyzed the expression of Cx 43 (Figure 2 C), a main compound of cardiac gap junctions, in comparison to the expression of troponin T (Figure 2 B), a structural cardiac protein. An up-regulation of Cx 43 expression after an exposure to carbon ions has been observed for rabbit cardiomyocytes resulting in improved conductivity [3]. The analysis performed so far revealed pronounced sample variations, i.e. no consistent picture emerged. Altogether, our first experiments show that doses up to 2 Gy X-rays do not affect the maturation of Cor.At cardiomyocytes. However, a dose-dependent increase in the number of apoptotic cells and cells carrying micronuclei was detected. Due to the high sample variations, no firm conclusions on the impact of X-rays on the expression of Cx 43 and subsequently cellular communication can be drawn. In further studies refined technique will be used to study the expression of specific cardiac genes and first experiments with high LET radiation will be performed.

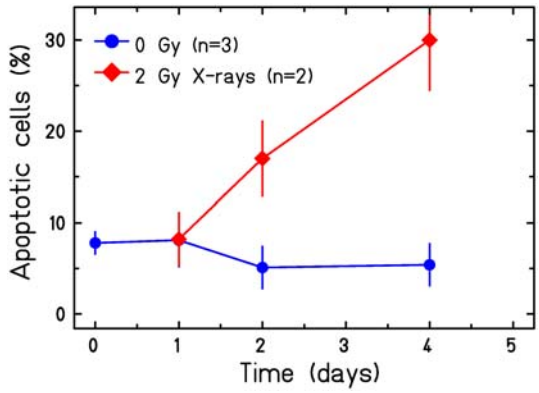

Figure 1: Percentage of apoptotic Cor.At cardiomyocytes in unirradiated or X-ray irradiated cultures. Cells were exposed at day 0.

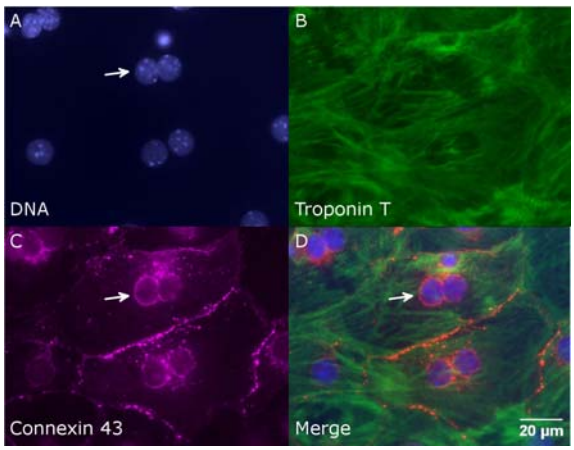

Figure 2: Immunofluorescence staining of Cor.At cells for connexin 43 (A) and troponin T (B), nuclei in (C) are stained with DAPI; merged images are shown in (D). Binucleated cells are indicated by an arrowhead in (C, D).

References

[1] Materna et al., GSI Scientific Report 2012, 441
[2] Helm et al., GSI Scientific Report 2013 (this issue)
[3] Amino et al., Cardiovasc Res, 2006, 72:412-421

*The research leading to these results has received funding from the Euratom Seventh Framework Programm under grant agreement n° 295823 (PROCARDIO)
† s.ritter@gsi.de

 doi:10.15120/GR-2014-1-BIOPHYSICS-20

Carbon ion induced vascular damage in the rat lung*

J. Zink[1], *T. Dettmering*[†1], *H. Faber*[2], *G. Ghobadi*[2], *P. Simoniello*[1], *M. Durante*[1], *P. van Luijk*[2], *R. P. Coppes*[2], *and C. Fournier*[1]

[1]GSI, Darmstadt, Germany; [2]Departments of Cell Biology and Radiation Oncology, University Medical Center Groningen, University of Groningen, The Netherlands

Introduction

Bronchial carcinomas are one of the most frequent causes of death in Germany. Radiotherapy is used in progressed stages of the cancer if the tumor cannot be removed surgically. The aim of radiotherapy is to control tumor growth by the administration of a high dose while the normal tissue surrounding the tumor is intended to be spared. Charged particles have the beneficial feature of an inverse depth dose distribution which means that the normal tissue can be spared while a high dose is absorbed by the tumor [1]. However, doses to the healthy tissue may be high enough to provoke side effects like pneumonitis or fibrosis. These effects are preceded by vascular damage, which is considered to be related to the pathogenesis of pneumonitis and fibrosis [2]. Here we investigated the impact of Carbon ions on blood vessel damage in the rat lung.

Materials and Methods

Lungs of adult male albino Wistar rats were irradiated with 270 MeV/u Carbon ions. Either 100% of lungs were irradiated (8.5 Gy or 12.5 Gy) or 50% (17.25 Gy) as described in [3]. After 8 weeks animals were sacrificed and lungs embedded in paraffin. Lung slices were stained with Verhoeff-van-Gieson staining, which allows distinguishing the different layers of a blood vessel. Vessel occlusion was determined by calculating the ratio of the thickness of the *Tunica media* to the diameter of the *Membrana elastica externa*. Only vessels with a maximum diameter of 50 μm and round shape were considered. Analysed vessels of 50% irradiated lungs were located exclusively in irradiated areas of the lungs.

Results and Discussion

A thickening of the vessel wall, mainly of the *Tunica media,* was observed after irradiation, which led to an occlusion of the blood vessel (Fig. 1). A higher dose induced a more pronounced occlusion of the blood vessels in comparison to a lower dose of Carbon ions (Fig. 2A). Interestingly, a higher irradiation volume had, despite the lower local dose, a stronger effect on the induced vessel occlusion than a smaller irradiation volume (Fig. 2B).

These results show for Carbon ions similar effects already reported for protons to blood vessels in the lung [4], which show that a low dose administered to a large volume is more efficient than a high dose to a small volume. The thickening of the vessel wall is probably due to an increased proliferation of smooth-muscle cells (SMC) that form the *Tunica media,* but potentially also due to an invasion of SMC into the *Tunica intima*. It was already shown that irradiated endothelial cells enhance the proliferation of SMC [5].

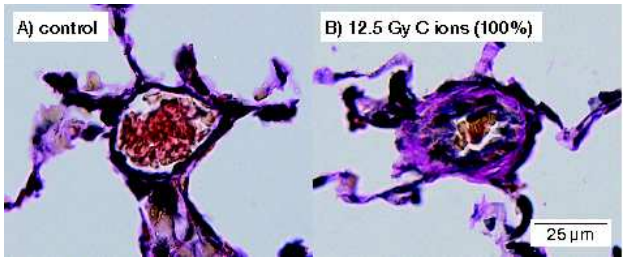

Figure 1: Representative example of a normal blood vessel (A) in comparison to an irradiated vessel 8 weeks after irradiation with Carbon ions (B).

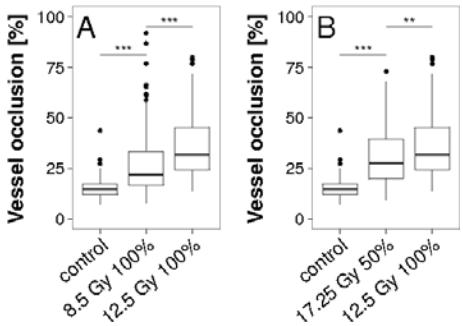

Figure 2: Vessel occlusion in the rat lung 8 weeks after irradiation with Carbon ions. Either the whole lung was irradiated (8.5 Gy and 12.5 Gy) or only 50% of the lung. Panel A shows the dose effect and panel B the volume effect.

References

[1] Kraft, G. (2000). Progr in Particle and Nuclear Phys.

[2] Coggle, J.E. *et al.* (1986). Environ Health Perspect.

[3] Coppes, R.P. *et al.* (2011). Int J Radiat Oncol Biol Phys.

[4] Ghobadi, G. *et al.* (2011). Thorax.

[5] Milliat *et al.* (2006). Am J Pathol.

* Supported by HGS-HIRe and grant CBR-754842 from the University of Groningen

† t.dettmering@gsi.de

Time course of radiation induced chromosome aberrations in mouse bone marrow cells*

N. Paz[1], *E. Nasonova*[1,3], *L. Deloch*[4], *B. Frey*[4], *US. Gaipl*[4], *M. Durante*[1,2], *and S. Ritter*[1]

[1]GSI, Darmstadt, Germany; [2]TU, Darmstadt, Germany; [3]JINR, Dubna, Russia; [4]Universitätsklinikum Erlangen, Germany

The analysis of chromosome aberrations (CA) in cells at the first post-irradiation mitosis is an established technique to estimate the absorbed dose and to assess the radiation risk. Within the GREWIS consortium we will use this method to examine the effects of either α-particles, Fe-ions or X-rays on murine bone marrow cells (BMC). Since BMC are an asynchronously growing cell population and the number and the types of primary aberrations depend on the cell cycle stage at exposure, CA have to be scored at multiple fixation times to obtain a reliable estimate of the damage produced within the initial cell population.

In preparatory experiments BMC were isolated from C57BL/6 wild type mice as described elsewhere [1] and cultured for 2 hours in medium containing EdU (0,1 μM) and colcemid (0,025 μg/ml). After 2 hours chromosome spreads were prepared. Analysis of the sample showed that 26% of the interphase cells incorporated EdU, i.e. are in S-phase; the mitotic index was 3%. Interestingly, one third of the metaphases was EdU-positive pointing to a subpopulation of BMC with a short G2-phase ($<$ 2h) (Fig. 1).

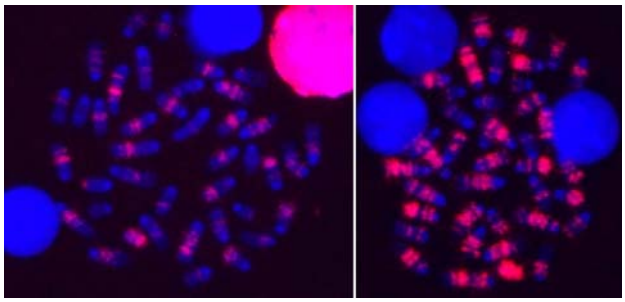

Figure 1: Chromosome spreads of BMC labelled for 2h with EdU. The labelling pattern shows that cells in late (left) or middle S-phase (right) reach mitosis within this time interval.

Subsequently, BMC were exposed *ex vivo* to 1 Gy X-rays (135kV, and 33,7mA). For chromosome analysis cells were harvested between 4h and 24h post-irradiation to cover the first post-irradiation cell cycle and stained with Giemsa. At 4h after exposure the mitotic index of BMC was too low for aberration scoring ($<$0.5%) indicating that radiation delays the progression of cells to mitosis. At the later times the mitotic index recovered and 100 metaphases were analysed per time-point. As shown in Fig. 2A a low yield of CA was found at 8h after exposure. The number of CA increased with time and reached a maximum between 16 and 20h. The aberration yield declined at 24h due to the dilution with undamaged or less damaged cells in second cycle metaphases (Fig. 2A). Chromatid-type aberrations dominated the aberration spectrum up to 20h post-exposure, while at 24h mainly chromosome-type aberrations were found (Fig. 2B). Altogether, the specific changes in the time-course of CA and the aberration spectrum demonstrate that most BMC reach the first mitosis after an exposure to 1 Gy X-rays within 24h. In subsequent studies we will examine, whether a later time-point is necessary for studies applying higher doses.

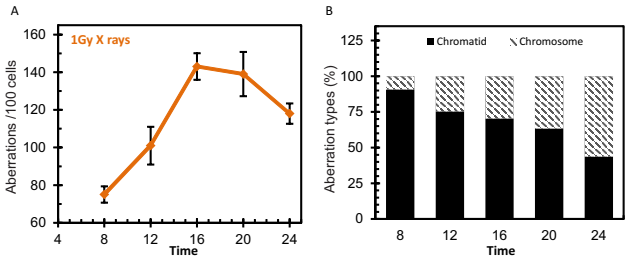

Figure 2: Aberration yield (A) and percentage of chromatid- and chromosome-type aberrations (B) measured in murine BMC at multiple harvesting times after exposure to 1Gy X-rays.

Recently we extended these studies to a human TNF-alpha transgenic mouse model [2]. The animals develop spontaneously arthritis and will be used within the consortium to study the health effects of radon in comparison to X-rays. As described above, BMC were isolated, exposed *ex vivo* to X-rays and CA were measured at several sampling times. The time course of CA in BMC of TNF-alpha mice was similar to that of wild type mice, with a maximum between 16 and 20h. Yet, the aberration yields were slightly higher in BMC from TNF-alpha mice. Currently, the experiments are repeated and mFISH analysis is performed to consolidate these results.

References

[1] N. Paz et al, GSI Scientific Report 2012 (2013)

[2] B. Frey et al, Autoimmunity, 42(4), May 2009, p. 346-8.

* Work supported by BMBF, grant 02NUK017A and 02NUK017G.

 doi:10.15120/GR-2014-1-BIOPHYSICS-22

Radioresistant subpopulation in a culture of glioma-initiating cells

C. Hartel[1], *Z. Yu*[1,2], *L. Babel*[1,3], *S. Ritter*[1], *W.K. Weyrather*[1], *E. Kim*[4], *A. Giese*[4], *and M. Durante*[1,5]

[1]GSI, Darmstadt, Germany; [2]Fudan University Shanghai Cancer Center, Shanghai, China; [3]Chemistry Department, TU Darmstadt, Germany; [4]Uniklinikum Mainz, Germany; [5]Condensed Matter Physics, TU Darmstadt, Germany

Introduction

According to the cancer stem cell hypothesis, a tumor comprises different cell types including tumor cells with stem cell properties. These cells, called cancer stem(-like) cells or tumor-initiating cells, are believed to be responsible for tumor initiation, progression and relapse. Moreover, it was found that these cells are more resistant to radiotherapy and chemotherapy than the bulk tumor cells. As heavy ion irradiation can effectively inactivate radioresistant cells, it was proposed that heavy ions could overcome the radioresistance of cancer stem-like cells [1]. Our irradiation experiments with glioma-initiating cells could indeed show that accelerated C- and Ti-ions reduced the neurosphere formation rate more effectively than X-rays [2]. A limiting factor in these experiments was the time-consuming counting of neurospheres, which had to be done manually using a phase-contrast microscope. In the last year, a software-based analysis system called CARL was developed at Hochschule Darmstadt (see Sonnemann et al., this report) and was now tested on glioma-initiating cells.

Materials and Methods

We used glioma-initiating cells kindly provided by Dr. E. Kim, Neurosurgery Department, University Hospital Mainz, Germany. The cells are a radioselected subpopulation of the cell line #10 described in a publication by Barrantes-Freer et al [3]. The cells were cultured as described previously [2] and irradiated with different doses of X-rays (0-12 Gy). To test the new software-based analysis-system CARL, the analysis was performed in parallel by eye under the phase-contrast microscope and with CARL.

Results and Discussion

Figure 1 shows the dose-effect curve for neurosphere formation after X-ray irradiation. The neurosphere formation rate was determined by eye under the microscope and by the CARL system. Both results are in good agreement. Similar tests were performed for other cell lines and showed good agreement between the automatic analysis and the scoring by eye (data not shown). A reference analysis by eye is of crucial importance for each cell line in order to adjust the software parameters. Once this is made, the software produces reliable results. Compared to the manual analysis, the CARL system is much faster (less than one compared to 15 minutes per sample), provides a size distribution of the neurospheres in addition to the number and the results are independent of the individual scorer.

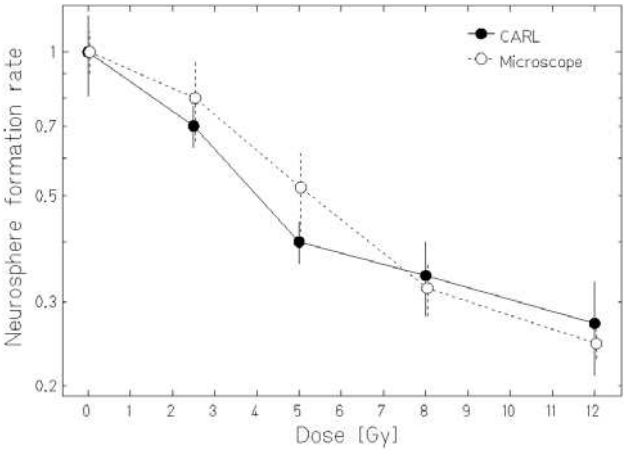

Figure 1: Neurosphere formation (normalized to unirradiated control) after different doses of X-rays. The neurosphere number was determined by eye under the microscope (open circles) or using the CARL system (closed circles). Error bars represent standard deviation of four flasks.

The curve progression in figure 1 shows the typical linear-quadratic behavior in the dose-range 0-5 Gy, but at higher doses the slope becomes shallower, indicating that the culture contains a subpopulation of radioresistant cells. This phenomenon was observed with a second line of glioma-initiating cells as well (data not shown), but not with U87-MG, an established line of glioblastoma cells (data not shown). Further experiments are necessary to characterize this radioresistant sub-group. According to the cancer stem cell hypothesis, these resistant cells could be a cell population in a more stem-like state. They could therefore be of special interest for the understanding of cancer stem-like cells, their mechanisms of radioresistance and how to successfully inactivate them.

References

[1] D. Pignalosa and M. Durante "Overcoming resistance of cancer stem cells" Lancet Oncol. 13, e187-e188 (2012)

[2] C. Hartel et. al. "First irradiation results unsing the neurosphere formation assay", GSI Scientific Report 2012 (2013) p. 443

[3] A. Barrantes-Freer et. al. "Human glioma-initiating cells show a distinct immature phenotype resembling but not identical to NG2 glia"', J Neuropathol Exp Neurol 72(4) (2013) p. 307

Preparatory experiments to investigate the radiosensitivity of human embryonic stem cells*

S. Luft[1], *I. Schroeder*[1], *P. Hessel*[1], *O. Arrizabalaga*[1,3], *P.G. Layer*[2], *M. Durante*[1,2], *and S. Ritter*[†1]

[1]GSI, Darmstadt, Germany; [2]Technical University, Darmstadt, Germany; [3]IKERBASQUE, Foundation for Research, Bilbao, Spain

Introduction

In humans the effect of ionizing radiation on the early embryonic development is not yet understood in detail. *In vivo* studies on mice have shown that lethality is the most frequent outcome after exposure in the pre-implantation stage [1].To estimate the risk of an *in utero* exposure, e.g. in case of accidental exposure or a medical treatment of an expectant mother [2] we chose H9 human embryonic stem cells (ESCs) as a model system. Differentiating ESCs *in vitro* resembles the early developmental stages of the embryo *in vivo*.

Cell culture system

Since human ESCs are very sensitive to spontaneous differentiation *in vitro*, an indispensable requirement for our studies is a cell culture that maintains a pluripotent and homogenous cell population. First experiments, where cells were enzymatically passaged resulted in a heterogeneous culture, containing pluripotent as well as a big proportion differentiated cells. Therefore, we set up the manual passaging of cells. This method is highly labour-intensive. However, it allows to select those colonies that most likely consist of cells being pluripotent (i.e. appear compact and homogenous) and reduce the fraction of those colonies that exhibit differentiated cells (heterogeneous colonies). In this weekly passaging, cells are cut in squares manually under the microscope under sterile conditions, transferred into a new petri dish on mouse embryonic feeder cells, and cultured for one week inlcuding daily mediumchanges. Seven days after seeding, colonies with compact and homogeneous morphology are passaged again.

Quality control of ESCs via immunocytochemistry

To verify the quality of the ESC culture, we established several immunocytochemisty methods to detect the presence of pluripotency markers. Since the network of proteins maintaining the pluripotency state in a cell is highly complex and interactive, we focused on several key proteins such as Nanog and Oct3/4. Figure 2 shows two manually passaged ESC colonies stained with antibodies against Nanog or Oct3/4, respectively. The fluorescence image reveals a clearly stained colony with a typical nuclear localisation of the pluripotency factors. In the lower panel, the colony growth is clearly visible, resulting in a more intense staining at the border of the colony due to higher cell density in this area. This method will also be used in future experiments to investigate differences between irradiated and non-irradiated ESCs.

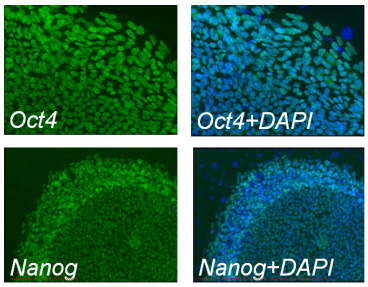

Figure 1: Immunocytochemical staining of pluripotency markers Oct4 (upper panel) and Nanog (lower panel) in human ESCs.

Differentiation capability into definitive endoderm

Another specific feature of ESCs is their differentiation capability. In general, pluripotent cells are able to differentiate into all three germ layers, namely endoderm, ectoderm and mesoderm that later give rise to a functional organism. Recently, we started investigating the differentiation capability of ESCs into definitive endoderm. We established a protocol based on studies of Baetge and colleagues [3, 4], in which ESCs are grown on matrigel for five days. Additionally, by adding specific supplements (like Activin A and Wnt3A) to the cell culture medium the differentiation into the endodermal lineage is triggered, while those cells that are not committed to endoderm undergo apoptosis. Following the differentiation protocol, the expression of genes specific for definitive endoderm like SOX17 and AFP will be measured by quantitative polymerase chain reaction.

In conclusion, the basis for an ESC-based *in vitro* assessment of irradiation effects on early human development has been established.

References

[1] W.U. Müller et al., Teratology, 42(6):643-650 (1990)

[2] M.W. Münter et al., Fertil Steril, 94(6):2329.e5-7 (2010)

[3] K.A. D'Amour et al., Nature Biotech, 24, 1392-1401 (2006)

[4] E. Kroon et al., Nature Biotech, 26, 443-452 (2008)

*Work supported by BMBF grant 02NUK025A and HGS-HIRe; OA was funded by the doctors specialization programme of the Basque Government.

† s.ritter@gsi.de

 doi:10.15120/GR-2014-1-BIOPHYSICS-24

Adaptive cell killing for ion beam treatment planning of hypoxic tumors *

E. Scifoni† [1], *M. Krämer*[1], *and M. Durante*[1,2,3]

[1]GSI, Darmstadt, Germany; [2]TUD, Darmstadt, Germany; [3]FIAS, Frankfurt am Main, Germany

Introduction

Recent *in vivo* molecular imaging techniques allow to provide informations on intra-tumor biological heterogeneity [1], i.e., to map qualitatively and quantitatively regions of different functional activity within a tumor tissue. Among these features, hypoxia, i.e., the condition of unsufficient cell oxygenation, has a great importance, since the increased radioresistance of the not fully oxygenated tissues, quantified by the oxygen enhancement ratio (OER) has a crucial impact on treatment prognosis.

Materials and methods

Several approaches for adapting a radiotherapeutical treatment of such heterogeneous tumors have been proposed, mainly based on a differential scaling of the dose (dose painting [1]) or redistribution of the linear energy transfer (LET painting [2]) across the target. Alternatively to these methods we suggested a "killing painting" approach, where the optimization drives the survival level to be uniform in the overall target. The GSI leading treatment planning system for particles TRiP98 [3] has beeen updated for this purpose. Beyond the multiple field optimization [4], the optimization task has been modified in order to adapt for an intratumour heterogeneity due to hypoxia, and then for a different oxygen content, varying from one voxel to another [5].

The gradients formulation which drives the optimization has been updated so that the oxygen distribution can be coupled with the dose averaged LET in each voxel, in each iteration step. Thus we achieve an optimal distribution of the latter, also adjusting the dose required to restore the prescribed cell killing effect.

Results

In figure 1 it is shown an example of a simulated water phantom where a tumor target has a smoothly varying oxygen distribution, logarithmically increasing with the distance from the target center. The optimization automatically drives the convergence of the irradiation parameters (fluences of the raster spots of each field) in order to produce the optimal plan, and one can clearly see how the LET is automatically adjusted, without any prescription, to match the hypoxic distribution. After evaluating the possible advantages of using different ions[6], we are going to extend this approach to the combination of different beam modalities in the optimization task.

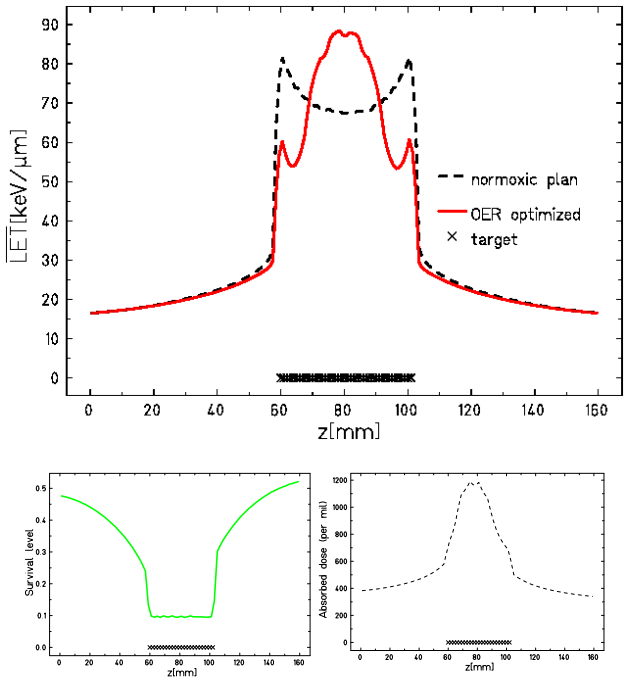

Figure 1: Upper panel: LET distribution in a conventional plan with two opposing ^{12}C ion fields compared with an OER-optimized plan for a tumor with an oxygenation smoothly decreasing towards its center. Lower panel: corresponding survival level (left hand side) and overall absorbed dose distribution (right hand side, in per mil of prescribed dose).

References

[1] S. M. Bentzen and V. Gregoire, Semin. Radiat. Oncol. 21(2011) 101.

[2] N. Bassler, J. Toftegaard, A. Lühr, B.S. Sørensen, E. Scifoni, M. Krämer, O. Jäkel, L.S. Mortensen, J. Overgaard and J.B. Petersen, Acta Oncol. 53 (2014) 25.

[3] M. Kramer and M. Durante, Eur. Phys. J. D 60 (2010) 195.

[4] A. Gemmel, B. Hasch, M. Ellerbrock, W.K. Weyrather and M. Kräemer, Phys. Med. Biol., 53 (2008) 6991.

[5] E. Scifoni, W. Tinganelli, W.K. Weyrather, M. Durante, A. Maier and M. Krämer, Phys. Med. Biol. 58 (2013) 3871.

[6] M. Krämer, E. Scifoni, F. Schmitz, O. Sokol and M. Durante,"Recent advances in treatment planning for ion beam radiotherapy", submitted to Eur. Phys. J. D.

* Work supported by EU, ULICE contract No.228436, and by Helmholtz-Portfolio, topic "Technology and Medicine".

† e.scifoni@gsi.de

An in silico Trial of X-rays vs Carbon Ions in Lung Cancer Radiosurgery

K. Anderle[1], J. Stroom[2], N. Pimentel[2], C. Greco[2], M. Durante[1], and C. Graeff[1]

[1]GSI, Darmstadt, Germany; [2]Fundação Champalimaud, Lisbon, Portugal

Introduction

Stereotactic body radiotherapy (SBRT) with photons to treat extra-cranial tumors in a single fraction has been shown to yield local control rates > 80 % with acceptable toxicity [1]. Scanned particle therapy (PT) has proven its efficacy for head and neck tumors, while treatment of mobile tumors of the lung is still challenging due to interplay and range changes. We performed an in silico case study comparing SBRT and PT (carbon ions) in lung cancer patients to investigate potential benefits of PT in radiosurgery.

Materials and methods

We used data of nine patients that were actually treated with SBRT at Fundação Champalimaud, Lisbon. The prescribed target dose is at least 24 Gy for 99 % of the target volume, with strict adherence to dose constraints for organs at risk (OAR). The actual SBRT treatment plans are compared to simulated treatment with PT using TRiP98 [2] on a 4D-CT. For SBRT, isotropic ITV-PTV margins of 3 mm were used. Due to range changes in PT we added margins 3 mm laterally and 1 mm in beam's eye view on CTV and then computed a range-considering ITV with 2 mm + 2 % range margins. Five times slice-by-slice rescanning was used to counter interplay.

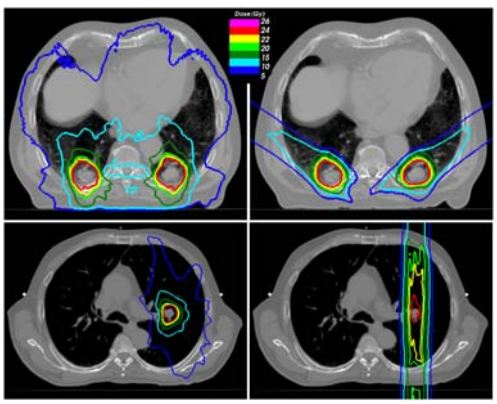

Figure 1: Dose cuts for SBRT (left) and PT (right) in two patients. The first patient (top) shows a favorable dose distribution of PT, while the second case (bottom) appears better suited for SBRT.

Results

Average peak to peak tumor motion was 5.6 mm (from 0.2 mm to 9.5 mm). Comparison of dose cuts between SBRT and PT is shown in Figure 1. Both therapies provided excellent target coverage and OAR doses within tolerances, except for three patients, where maximal allowed point dose in smaller airways was exceeded due to tumor proximity. Differences between SBRT and PT in dose deposition for 7 specific OAR are shown in Figure 2. On average all OAR receive less dose in PT, except for ipsilateral lung $D_{10\%}$. The most profound difference was in spinal cord and ipsilateral lung $D_{10\%}$, where the average dose difference was 4.2 Gy and -4.5 Gy, respectively.

Discussion

The results clearly indicate potential of PT in treating lung cancer. With smaller entry channel than SBRT, PT can deposit less dose in OAR, while maintaining same target coverage. This advantage varies with patient anatomy and lesion location, motion and size. The clinical relevance of possible further dose escalation or improved OAR sparing with scanned carbon ion therapy needs to be validated. This study will include a total of 20 patients, and also further investigate the robustness of PT.

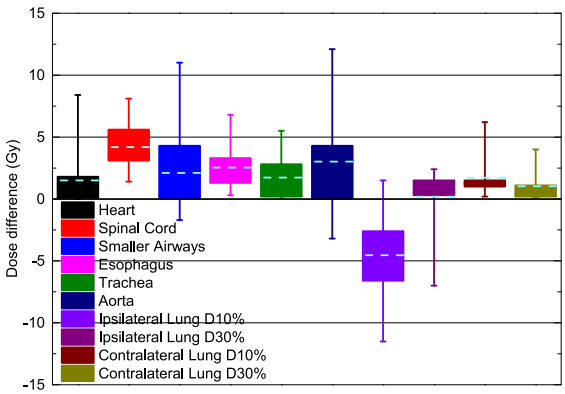

Figure 2: Box-and-whisker plot for dose difference between SBRT and PT for different OAR. Boxes contain data between 25 % and 75 %, dashed lines represent mean value and whiskers minimum and maximum values.

References

[1] Greco C, Zelefsky MJ, Lovelock M, et al. Predictors of local control after single-dose stereotactic image-guided intensity-modulated radiotherapy for extracranial metastases. Int J Radiat Oncol Biol Phys 2011; 79:1151-1157.

[2] Richter D, Schwarzkopf A, Trautmann J, et al. Upgrade and benchmarking of a 4D treatment planning system for scanned ion beam therapy. Med Phys 2013; 40:051722.

 doi:10.15120/GR-2014-1-BIOPHYSICS-26

Auger electrons emitted from metallic nanoparticles under proton irradiation*

C. Wälzlein† [1,2], *M. Krämer*[1], *E. Scifoni*[1], *and M. Durante*[1,2]
[1]GSI, Darmstadt, Germany; [2]FIAS, Frankfurt, Germany

The goal of radiation therapy is to deliver the maximum possible effective dose to the tumour while sparing the surrounding healthy tissue. Metallic nanoparticles (NPs) are of recent scientific interest as they might help to enhance the effective dose ration between tumour tissue and healthy tissue. Metallic NPs accumulate preferably in tumour tissue and high Z (Z: atomic number) materials provide a promising source for many low-energy electrons. For high Z materials, the emission of Auger electron cascades is a possible decay channel after irradiation. For one primary ionization event it is therefore likely that a large amount of electrons is emitted. Electrons with energies below 100 eV have short ranges and can lead to high localized damage, thus enhancing the effectiveness of the dose.

The GSI track structure Monte Carlo (MC) code TRAX [1, 2, 3, 4], whose main purpose is to properly describe creation and transport of low-energy electrons, has been further extended to allow the description of Auger electron cascades. Furthermore, cross sections have been assessed to properly describe electron creation and transport in metallic materials like gold, silver, platinum, gadolinium and iron. With these cross sections, including electron energies down to a few electron Volts, it is possible to calculate the paths of electrons on the nanometer scale. Electrons inside and outside metallic nanoparticles can be analyzed.

Calculations have been performed for 80 MeV proton projectiles and nanoparticles with a radius of 22 nm. It has been observed, that for NPs consisting of atomic Pt and Au, the number of emitted Auger electrons and cascades is much higher than for Gd. Spectra of emitted Auger electrons show, that a large number of Auger electrons with energies below 100 eV are emitted for Pt and Au. For Pt and Au, the absolute Auger electron yields are higher than for Gd and Auger electrons from different transitions can be observed. For Gd, almost all emitted Auger electrons have an energy of around 150 eV.

More details on these calculations and the resulting local dose in the surrounding tissue can be found in [4].

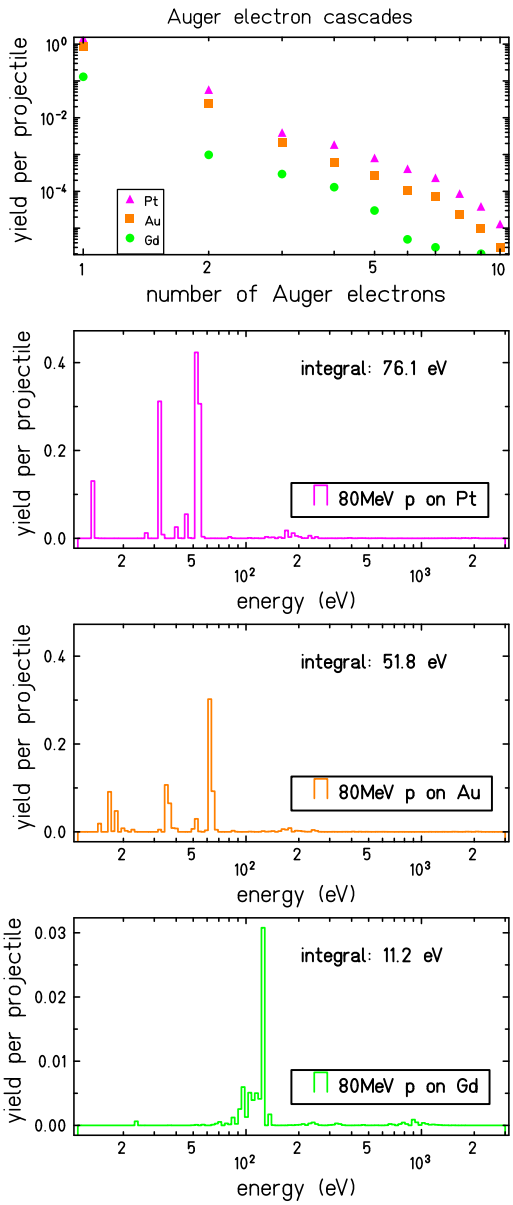

Figure 1: Comparison of Auger electron cascade distributions for Pt, Au and Gd (top panel) for 80 MeV protons incident on NPs with a radius of 22 nm. Below: spectra of Auger electrons created inside NPs made out of Pt, Au or Gd (from second to bottom panel).

References

[1] M. Krämer and M. Durante, Eur. Phys. J. D, 60 (2010) 195.

[2] C. Wälzlein et al., Appl. Radiat. Isotopes 83, (2013) 171.

[3] C. Wälzlein et al., Nucl. Instrum. Meth. B, 320, (2014) 75.

[4] C. Wälzlein et al., Phys. Med. Biol., accepted, (2014).

*Work supported by Beilstein Institute (NanoBiC project). Work is part of HGS-HIRe.

†c.waelzlein@gsi.de

Application of a LEM based DNA DSB kinetic rejoining model to the analysis of dose dependence after photon irradiation*

F. Tommasino[1], T. Friedrich[1], U. Scholz[1,2], G. Taucher-Scholz[1], M. Scholz[1], and M. Durante[1,2]
[1]GSI, Darmstadt, Germany; [2]Institut für Festkörperphysik, Technische Universität, Darmstadt, Germany

A DNA Double-Strand Break (DSB) kinetic rejoining model has been recently presented [1], which is based on the approach currently adopted in the Local Effect Model (LEM) for the description of radiation induced biological effects [2]. Shortly, the photon dose response data and an amorphous track structure model are combined together to calculate the initial pattern of DSB induced in the target (i. e. the cell nucleus). The chromatin contained inside the nucleus is considered to be organized in so-called Giant Loops, each one involving about 2 Mbp of genome [3]. The presence of such high-order chromatin structures allows defining two different classes of DSB, namely *isolated* (iDSB) and *clustered* ones (cDSB). An iDSB is defined as a single lesion inside a loop, while a cDSB is characterized by the simultaneous presence of more than one DSB. cDSB are expected to be more difficult for the cell to repair compared to iDSB, since they may result in the loss of the structural integrity of the chromatin loop, and possibly in the migration of DNA fragments from the DSB site. In order to describe the kinetics of DSB rejoining over time, the hypothesis is made, that iDSB are rejoined by the fast component while cDSB are processed by the slow component of rejoining which are often observed in the experiments. Thus, LEM calculations of induced DSB patterns are combined with a biphasic exponential decay function having a fast (τ_{fast}) and a slow (τ_{slow}) half-life, as described by the following equation:

$$U(t) = F_{fast} \cdot e^{-\frac{ln(2)}{\tau_{fast}}t} + F_{slow} \cdot e^{-\frac{ln(2)}{\tau_{slow}}t} \qquad (1)$$

where F_{fast} and F_{slow} correspond to the fraction of initial induced iDSB and cDSB, respectively. For a given data set involving a single cell line and different radiation qualities, Eq. 1 is used to simultaneously fit the experimental rejoining data. The initial fractions of iDSB and cDSB are fixed input parameters and characterize a specific dose and radiation quality, while the two half-life times are defined as global fit parameters. Further details can be found elsewhere [1,2].

The described model has been already applied to a large data set, where experiments performed using both low and high LET were included, obtaining an overall good agreement. The focus is now on the use of the model for the analysis of a specific biological end point. Specifically, we want to test the model ability to describe the delayed DSB rejoining observed after increasing doses of photon radiation [4]. In this case, the Poisson distribution is adopted for the calculation of initially induced DSB patterns. An example is shown in Fig. 1, where the effects of 20 and 200 Gy are compared. Both the experiments and the model clearly show a slowed-down rejoining at 200 Gy compared to the lower dose. Importantly, in the context of our model, this is only due to an increased fraction of induced cDSB, since the two half-lives are defined as global fit parameters and therefore are identical for all the considered doses. However, in contrast to what shown by Cucinotta et al [4], other works have been published where a dose dependence was not observed [5,6]. Thus, more data are needed to further support the results presented here.

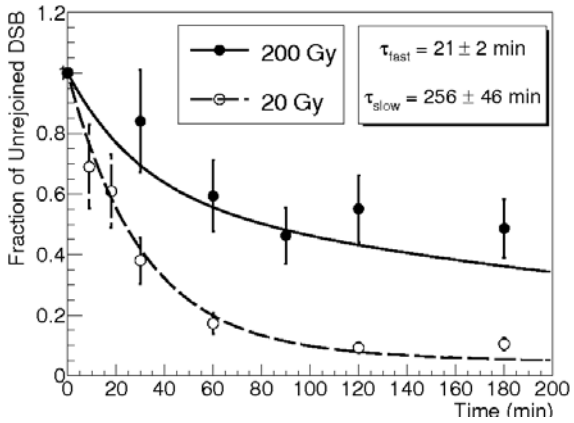

Figure 1: experimental data (symbols) and model predictions (lines) for the DSB rejoining over time after photon irradiation with 20 and 200 Gy. Experimental data were measured with filter elution techniques and are taken from Cucinotta et al [4].

A successful analysis of the end point presented here would further confirm the validity of the model. At the same time, it would be supportive for the relevance of the proposed DSB classes, and more in general of DSB clustering at the micrometer level, for the description of radiation induced biological effects not only at high but also at low LET.

References

[1] Tommasino et al., Radiat Res, 180 (2013), pp. 524-38.
[2] Friedrich et al., Int. J. Radiat. Biol., 88 (2012) pp. 103-7.
[3] Yokota et al., J. Cell Biol., 130 (1995) pp. 1239-49.
[4] Cucinotta et al., Int J Radiat Biol, 76 (2000), pp. 1463-74.
[5] Löbrich et al., PNAS, 92 (1995), pp. 12050-4.
[6] Kühne et al., Cancer Res, 64 (2004), pp. 500-8.

*This work was supported by a DFG-funded Graduiertenkolleg (GRK 1657). The work is part of HGS-HIRe.

 doi:10.15120/GR-2014-1-BIOPHYSICS-28

Comparison between different dose calculation algorithms available in TRiP98 and between the beam model of HIT and GSI

A. Eichhorn[1,2], *C. La Tessa*[1,3], *E. Scifoni*[1], *M. Krämer*[2], *K. Parodi*[5,4], *and M. Durante*[1,2]

[1]GSI, Darmstadt, Germany; [2]TU Darmstadt, Germany; [3]BNL, New York, USA; [4]Heidelberg University Hospital, Heidelberg, Germany; [5]LMU München, Germany

Last year the dose profiles behind thick bone-like targets and interfaces between bone-like material and water in the entrance channel were studied [1]. The experiment was performed at the 'Heidelberger Ion-Beam Therapy Center' (HIT) and the experimental results were compared with different simulations of the Treatment Planning System (TPS), TRiP98 [3]. The aim of the experiment was to validate TRiP98 for cases with thick inhomogeneous material in the beam entrance channel.

TRiP98 dose calculation algorithms

TRiP98 was developed at GSI for the radiotherapy pilot project and is constantly updated and used as a research prototype. The program performs physical and biological dose calculations and optimizations, amongst other tasks. The aim of the optimization process is to deliver the prescribed dose as homogeneously as possible in the tumor volume and, simultaneously, to reduce the dose in the healthy tissue and especially in the Organs At Risk (OAR).

The calculation of the physical dose distribution can be performed by three different implemented algorithms, which can be used for treatment planning. The classical one (CL) uses a fast interpolation technique between the 4 beam raster points neighbouring a CT voxel [2]. It offers very fast overview calculations but is less precise at the edges of the dose distribuition. A more advanced algorithm is all-points (AP). In contrast to the CL algorithm all points in the neighborhood are considered and the actual Gaussian shape of each beam spot is considered. AP is more precise than the CL algorithm, but also more time consuming. The latest and most precise one is multiple scattering (MS) [4]. For the MS algorithm the dose calculation is identical with the AP one, but the beam broadening with increasing depth is taken into account by adding a second Gaussian with a FWHM reflecting multiple coulomb scattering and nuclear angular distributions. AP and MS can be enhanced by accounting for the divergence of the beam as it exits the beam pipe (APDB and MSDB).

Results

The treatment plans for the experiment at HIT were optimized with the APDB algorithm, since base data for the more advanced MSDB algorithm was not available at this time. Hence small deviation between the measured data and the treatment planning were found. Recalculations with MSDB was performed with a HIT-specific pencil beam data base as soon as it became available [5]. Differences between the calculations with MSDB and APDB for the HIT-specific base data are shown in figure 1.

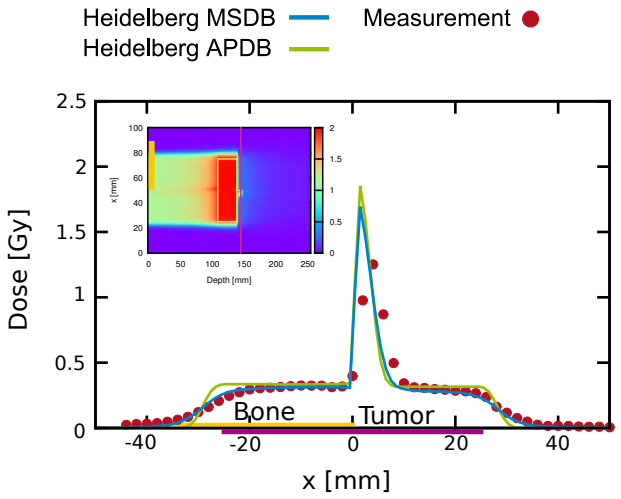

Figure 1: Comparision between the two different algorithms apdb and msdb of the HIT beam model and the measured data.

Therefore a precise recalculation of data measured at HIT is now possible with TRiP98.

In addition it is shown in [6], that the differences in the beam models of GSI and HIT are negligible and play no important role for recalculations.

References

[1] A.Eichhorn et al., '*Carbon beam dosimetry in bony tissue inhomogeneities: TRiP98 validation with experimental measurements*', GSI Scientific Report **2012** p. 460, (2013)

[2] M. Krämer et al., '*Treatment planning for heavy-ion radiotherapy:physical beam model and dose optimization*', Phys. Med. Biol., vol. **45(11)**, (2000)

[3] M. Krämer et al., '*Ion beam transport calculations and treatment plans in particle therapy*', Eur. Phys. J. D **60(95)**, (2010)

[4] G. Iancu et al., '*Analysis of the multiple scattering implementation in TRiP*', GSI Scientific Report **2006** p. 362, (2007)

[5] K. Parodi et al., '*Monte Carlo-based parametrization of the lateral dose spread for clinical treatment planning of scanned proton and carbon ions beams*', J. Radiat. Res. vol. **54**, (2013)

[6] A. Eichhorn, '*Investigation of dose profile inhomogeneities at the interface between water and bone-like materials following irradiaiton with therapeutic carbon ions*', Masterthesis, TU Darmstadt, Germany (2013)

Comparison of the beam mixing models proposed by Lam and Zaider & Rossi and a derived D_t extension for the Zaider & Rossi model *

O. Steinsträter[1], T. Friedrich[1], M. Krämer[1], M. Durante[1], and M. Scholz[1]
[1]GSI, Darmstadt, Germany

In the radiotherapy of cancer with heavy ions, treatment planning systems like TRiP [1] use externally calculated tables for the biological effect of monoenergetic ion beams and derive the effect of a therapeutic mixed beam from these data by means of a beam-mixing model. In TRiP, the effects of monoenergetic beams are predicted by the Local Effect Model (LEM) [2]. The full simulation approach of this model [3] predicts ion and energy dependent threshold values, D_t, for the transitions between linear-quadratic and pure linear part of dose-effect curves (Linear-Quadratic-Linear (LQL) model), but in the previously used version, the single particle approximation, such individual D_ts could not be estimated. Instead, as an approximation, an independence of the D_t value from the beam quality was assumed. This could be exploited by TRiP by using the very efficient beam-mixing model proposed by Zaider & Rossi [4]. In principle this model does not include a D_t and an extension is not straight-forward [5]. Nevertheless, for a constant D_t, the model could be extended by applying the D_t threshold after the actual beam-mixing ("constant-D_t extension"). As this approach could not be used for the varying D_ts of the full-simulation method, the much more flexible beam-mixing method proposed by Lam [6] has to be introduced. However, this model is conceptually different from the Zaider & Rossi approach and the predicted RBE-weighted doses (Relative Biological Effectiveness) deviate by a few percent. A theoretical understanding of the differences is therefore highly interesting, especially for the comparison with previous TRiP/LEM results.

In the LQ model (LQL without D_t threshold) dose-effect curves, $\epsilon(D)$, are described by $\epsilon = \alpha D + \beta D^2$. Formally, this could be separated in a linear effect $\epsilon_\alpha = \alpha D$ and a quadratic effect $\epsilon_\beta = \beta D^2$. As the Lam method can handle any dose-effect curve, the method could, formally, be applied to both effect-curves separately, resulting in $\overline{\epsilon_\alpha}$ and $\overline{\epsilon_\beta}$, and providing a new mixed effect $\overline{\epsilon} = \overline{\epsilon_\alpha} + \overline{\epsilon_\beta}$. This $\overline{\epsilon}$ is not the mixed-beam prediction of the original Lam model but, interestingly, it could be proven, that $\overline{\epsilon}$ is identically to the result predicted by the Zaider & Rossi model. In addition to a theoretical description of the model differences, this immediately leads to a D_t extension of the Zaider & Rossi method: For monoenergetic ϵ including a D_t, this threshold can be moved to the β part by using $\epsilon_\alpha = \alpha D$ and $\epsilon_\beta = \epsilon - \epsilon_\alpha$.

In this extension, individual ion and energy dependent D_t thresholds can be used, but for constant D_t this model does not exactly lead to the previously used constant-D_t method. This is shown in the figure, where relative differences between RBE-weighted doses calculated by TRiP/LEM for the new D_t extension and the constant-D_t method are plotted. Significant differences could mainly be found inside the SOBP (Spread-Out Bragg Peak) and only if the planned dose was above the photon D_t (blue/green curves in the figure: planned doses below/above $D_{t,\gamma}$).

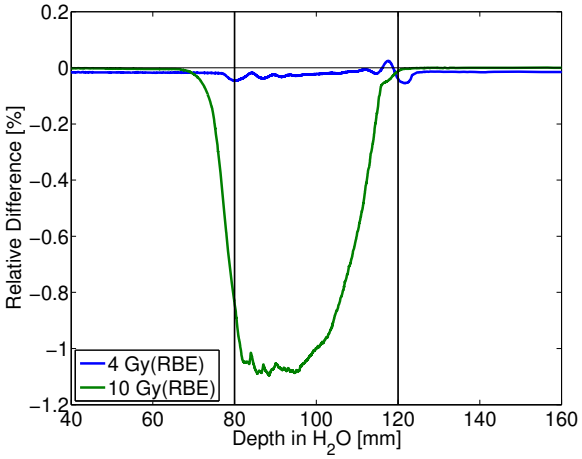

Figure: Relative differences of RBE-weighted doses between Zaider & Rossi D_t-extensions ((new−old)/old) predicted by TRiP/LEM (single particle approximation) for 4 Gy(RBE) (blue) and 10 Gy(RBE) (green) in the SOBP (marked). Carbon beam, $\alpha_\gamma = 0.313$ Gy^{-1}, $\beta_\gamma = 0.0615$ Gy^{-2}, $D_{t,\gamma} = 7.5$ Gy.

Conclusion: The beam-mixing models proposed by Zaider & Rossi and Lam could be expressed in the same mathematical framework which shows that the difference between both methods is completely related to the strict separation between linear and quadratic part of the dose-effect curves assumed by the Zaider & Rossi model. For instance, a high α value of a contributing monoenergetic beam can induce an increased mixed-beam β in the Lam model but not in the Zaider & Rossi model.

The derived D_t extension of the Zaider & Rossi model does not directly extend the constant-D_t extension used so far. However, differences are small (up to a few percent depending on the irradiated cell line), mostly seen in the SOBP, and generally negligible for RBE-weighted doses below the D_t of the reference photon irradiation.

References

[1] M. Krämer et al., Phys Med Biol, 45 (2000) 3319.
[2] T. Elsässer et al., Int J Radiat Oncol Biol Phys, 78 (2010) 1177.
[3] T. Friedrich et al., Int J Radiat Biol, 88 (2012) 103.
[4] Zaider & Rossi, Radiat Res, 83 (1980) 732.
[5] O. Steinsträter et al., GSI Sci Rep 2011 (2012) 524.
[6] G. K. Y. Lam, Radiat Res, 110 (1987) 232.

* Work supported by Siemens Healthcare.

 doi:10.15120/GR-2014-1-BIOPHYSICS-30

Fast 4D dose calculation with TRiP4D*

S. Hild[1,2,3], *A. Constantinescu*[1], *A. Eichhorn*[1], *K. Zink*[2], *M. Durante*[1,3], *C. Bert*[1,4], *and C. Graeff*†[1]
[1]GSI, Darmstadt, Germany; [2]TH Mittelhessen, Germany; [3]TU Darmstadt, Germany; [4]Universitaet Erlangen, Germany

Introduction

Treatment planning for scanned ion beams includes time intense calculation tasks (e.g. plan optimization and dose calculation) that take in the order of hours to complete. As reported in various publications treatment planning for moving tumors with a scanned ion beam has to account for the target motion via special 4D treatment techniques [1]. These techniques rely on a time resolved CT scan (4DCT) and an image registration map between all phases of this 4DCT. The additional dimension (time) elongates the calculation time for a 4D dose distribution. Rescanning, a motion mitigation technique that scans the target multiple times applying only a fraction of the total dose per scan, elongates the dose calculation proportional to the number of scans. This caused one single dose calculation of a rescanned treatment plan of a small cardiac volume to run longer than 45 hours. As these calculations are time critical for a planned experimental validation study which is planned for 2014, we worked on accelerating the 4D dose calculation of TRiP4D[2, 3] to be able to complete the treatment planning in a reasonable time frame.

Materials and Methods

The aim of reducing the dose calculation time from hours to minutes needed substantial improvement only possible with a combination of code optimization, reducing the overall workload and parallel execution.

The dose calculation routine of TRiP4D was profiled using the AIX profiler gprof. The profiler revealed the calculation of the water equivalent path length (WEPL) as the most time consuming function in a physical dose calculation as the WEPL of each voxel entering this calculation has to be calculated. We were able to reduce the number of interpolation steps carried out by this routine and thereby reduced the time spent for calculating the WEPL.

Additionally we restricted the dose calculation to a subset of voxels (see figure 1) and we added a new functionality to TRiP4D which determines the dose calculation window using the maximum lateral dimension of all fields. The treatment setup for treating atrial fibrillation will feature two lateral opposing fields so the dose calculation window in these cases has an optimal size (see figure 1). Finally the dose calculations have been carried out with an IBM Blade-Server PS701 (8 Cores, 4 hyper threads each) using the full amount of 32 parallel threads [4].

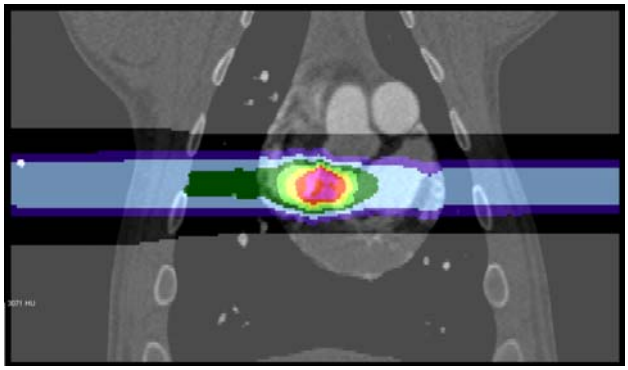

Figure 1: Coronal dose-cut from a treatment simulation for upcoming experiments. The dose is only calculated in the non shaded area around the two beam ports.

Results/Conclusion

The improvements reduced the time for 4D (rescanning) dose calculation to below 30 min (see table 1). Besides permitting the dose calculations for the planned experiments, fast 4D dose calculation also allows robustness studies with large parameter spaces in the future.

Table 1: Dose calculation time for all improvements made

$TRiP4D_{version}$	time of dose command
original	$> 45h$
+ changed WEPL routine	$29h$
+ dose window only	$5.5h$
+ 32 threads	$< 0.5h$

References

[1] C. Bert and M. Durante, "Motion in radiotherapy: particle therapy", Phys. Med. Biol. 56 (2011)R113-R144

[2] M. Kraemer et al. "Treatment planning for heavy ion radiotherapy: physical beam model and dose optimization", Phys. Med. Biol. 45 (2000) 3299-3317

[3] D. Richter et al. "Status of 4D Treatment Planning Implementations for TRiP98", GSI Scientific Report HEALTH37 (2010) 476

[4] J. Trautmann et al. "TRiP98: Parallelization of Dose Calculation", GSI Scientific Report HEALTH39 (2010) 478

* Work in part supported by HGS-HIRe
† c.graeff@gsi.de

Influence of the distal fall-off on the biological effective proton range

R. Grün *[1,2,3], *T. Friedrich*[1], *M. Krämer*[1], *K. Zink*[2,3], *M. Durante*[1,4], *R. Engenhart-Cabillic*[3], *and M. Scholz*[1]

[1]GSI, Darmstadt, Germany; [2]Institute of Medical Physics and Radiation Protection, TH-Mittelhessen, Gießen, Germany; [3]Medical Faculty of Philipps-University Marburg, Germany; [4]TU Darmstadt, Germany

Introduction: For the application of protons in radiotherapy a constant relative biological effectiveness (RBE) of 1.1 is considered in the treatment planning procedure. However, the results of in-vitro experiments [1, 2] show an increase of the RBE towards the distal end of a proton spread out Bragg peak (SOBP). RBE predictions of the local effect model (LEM IV; [3]) are consistent with these experimental data [5]. Due to the fact that the LET is further increasing in the declining edge of the SOBP the RBE is higher than the clinically used value of 1.1. As a consequence, this increased RBE leads to an extension of the biologically effective proton range. In the presented work we investigate the influence of the physical dose fall-off on the RBE and the biologically effective range of the proton beam.

Methods: Since the most distal proton Bragg peak that contributes to the proton SOBP determines the gradient of the dose fall-off, the treatment planning software TRiP98 [4] was used to calculate the physical and RBE-weighted depth dose distribution of monoenergetic proton Bragg peaks with energies ranging from 71 to 220 MeV. With increasing initial energy of the proton beam the distal dose fall-off gets broader, i.e. the gradient increases, due to range straggling in the absorber material. The corresponding RBE-weighted dose was calculated based on the RBE predictions of the LEM IV. The biological range extension and the RBE at maximum RBE-weighted dose were investigated for different dose-levels of 1-10 Gy absorbed dose and two different α/β-ratios of 2 Gy and 10 Gy, respectively. The biological range extension is defined as the difference of the RBE-weighted doses based on a constant RBE of 1.1 and the LEM IV based RBE at the 80 % isodose.

Results: Figure 1a illustrates the RBE at maximum RBE-weighted dose in the SOBP in dependence on the gradient of the 80-20 % dose fall-off. The RBE at maximum RBE-weighted dose is decreasing with increasing gradient of the distal dose fall-off. In contrast, the biological range difference is increasing with the flattening of the distal dose fall-off (fig. 1b). Further, the RBE and thus the biological range difference is larger for α/β-ratios of 2 Gy compared to 10 Gy and decreases with increasing dose [5]. The results show that the the gradient of the distal dose fall-off opposingly affects the RBE-weighted dose at the distal end of the SOBP and the biological range extension of the proton beam.

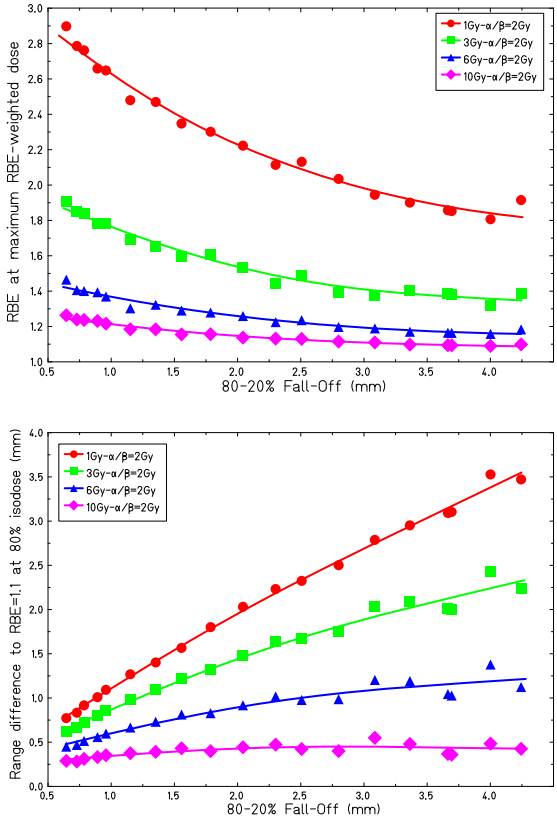

Figure 1: RBE at maximum RBE weighted dose (a) and biological range difference (b) in dependence on the distal penumbra for a α/β-ratios of 2 Gy and different physical dose levels of 1, 3, 6, and 10 Gy. The data points represent the distal fall-off for energies from 71 to 220 MeV.

Conclusion: The increasing RBE at the distal end and the biological range extension are influenced by both biological factors like the α/β-ratios of the cell or tissue type and physical factors like the gradient of the distal dose fall off. Hence, the initial beam energy and the depth modulation system used to create the SOBP mainly affect the balance between maximum RBE-weighted dose and biological range extension.

References:

[1] J. Tang et al., Brit J Cancer (1997) **76**:220.

[2] D. Bettega et al., Int J Radiat Biol (2000) **76**:1297.

[3] T. Elsässer et al., Int J Radiat Onc Biol Phys (2010) **78**:1177.

[4] M. Krämer and M. Scholz, Phys Med Biol, (2000) **45**:3319.

[5] R. Grün et al., Med Phys, (2013) **40**:111716.

* Work is part of HGS-HIRe

 doi:10.15120/GR-2014-1-BIOPHYSICS-32

Oxygen enhancement ratio of heavy ions in partial hypoxic conditions*

M. Durante† [1,2,3], *W. Tinganelli*[1,2], *E. Scifoni*[1], *R. Hirayama*[4], *M. Ozaki*[4], *Y. Kaneko*[4], *A. Maier*[1], *R. Hirayama*[4], *and Y. Furusawa*[2,4]

[1]GSI, Darmstadt, Germany; [2]IOL, NIRS-GSI, Chiba, Japan; [3]TUD, Darmstadt, Germany; [4]NIRS, Chiba, Japan

Hypoxia is a characteristic feature of locally advanced solid tumors resulting from an imbalance between oxygen (O_2) supply and consumption. As a tumor grows, it rapidly outgrows its blood supply, leaving portions of the tumor with regions where the oxygen concentration is significantly lower than in normal tissues. The possibility to scale the dose, but also to exploit in this connection the peculiar features of ion beams, namely the high linear energy transfer (LET) of part of their fields, for targeting specifically the hypoxic regions is highly promising, but requires the most accurate knowledge of the oxygen enhancement ratio (OER) in any voxel of the irradiated tissue, for any configuration of the irradiation parameters [1,2].

The main goal of our study was the verification, with a new set of experimental OER (Oxygen Enhancement Ratio) data points, of a semi-empirical model developed at GSI that is being used for the implementation of adaptive treatment planning in TRiP98 [1], for specifically targeting hypoxic tumors with particle beams. The latter model is based on an extension of the Alper Howard-Flanders formalism, for getting the two-dimensional dependence of the OER on LET of the irradiation mean and the oxygen concentration of the tissue.

Starting from a situation of five experimental points performed at GSI and HIT Heidelberg during the previous years [3] to verify our semi-empirical method other OER measurements were then necessary [4]. In the framework of the IOL, experimental points about the complete anoxic and different partially hypoxic conditions have been measured at NIRS. In the NIRS experiments most irradiations, with X-rays, carbon and silicon ions, were performed with glass petri dishes, seeded with CHO (Chinese Hamster Ovary) cells and gassed together with different mixtures of air, nitrogen and carbon dioxide in order to get the following different concentrations of O_2 (pO_2): 0%, 0.15%, 0.5%, 2%, 21%.

The results of the irradiations performed on the last year confirmed the initial data reported in [4] and are going to be published extensively as the first collection of OER measurements at intermediate range of LET and pO_2 [5]. The full ensemble of data showed a reasonable agreement with the prediction model and with the previous data from GSI, especially in the maximum slope region, where is the largest impact for treatment planning purposes. The higher OER values found for the very high LET are due to the large ions fragmentation, since we used the HIMAC-NIRS passive beam experimental room.

Finally one last experiment has been done to prove our semi-empirical model in an extended target (tumor phantom) irradiation with two opposed fields and for several oxygen concentrations (Fig.1). For the latter experiment the hypoxic chamber developed at GSI were used (left panel). Despite an occurred technical problem of absolute dosimetry, our experimental points, when all the differently oxygenated regions are recomputed with the physical dose scaled to match the oxic control, fit quite well with the calculated prediction data (right panel).

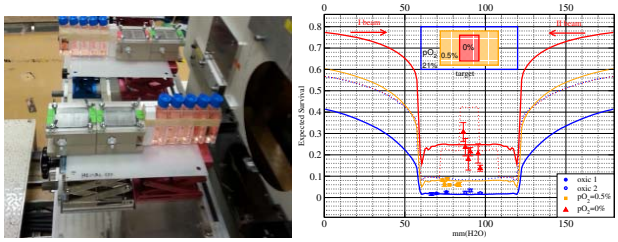

Figure 1: Multiple field irradiation of a complex tumor target with an anoxic core surrounded by hypoxic and then normoxic cells. Left panel: hypoxic chambers used for the irradiation phantom. Right panel: the experimental results are compared with the model prediction.

References

[1] E. Scifoni et al., Phys. Med. Biol. 58 (2013) 3871.

[2] E. Scifoni et al., this Report.

[3] W. Tinganelli et al., J. Radiat. Res. 54 (2013) i23

[4] M. Durante et al., GSI Scientific Report 2012 (2013) 468

[5] W. Tinganelli, M. Durante, R. Hirayama, Y. Furusawa, M. Krämer and E. Scifoni,"Oxygen enhancement ratio for intermediate values of oxygen concentration and LET: first in vitro measurements and impact on treatment planning for hypoxia", *in preparation*.

* Work supported by NIRS International Open Laboratory (IOL) grant to GSI.

† m.durante@gsi.de

Irradiation with α-particles causes rapid activation of K^+ channels in A549 cells*

B. Roth† [1], *C. Gibhardt*[1], *M. Durante*[1,2], *C. Fournier*[2], *and G. Thiel*[1]

[1]Membrane Biophysics, Technische Universität Darmstadt, Germany; [2]GSI, Darmstadt, Germany

Introduction

In previous experiments we found that radiation of the epithelial lung cancer cells A549 with photons and high-energy ions resulted in a rapid activation of K^+ channels and a concomitant hyperpolarization of these cells. We identified the human intermediate potassium channel hIK as the main irradiation responsive channels in these cells [1]. It is well established that this channel regulates in other types of cells the cell-cycle transition and cell migration via hyperpolarization of the plasma membrane [2]. In agreement with these data from the literature we also found that a block of hIK channels inhibited cell migration of A549 cells and we also observed that irradia-tion with photons stimulated migration [1]. To test if the activation of hIK channels is also induced by irradiation with α-particles we monitored the response of currents in A549 cells to irradiation with low doses of α-particles.

Material and Methods

We examined the conductance of ion channels in A549 cells by a planar patch-clamp technique before and after exposure to an α-particle source [3].

Results

The representative data in figure 1 show currents and the corresponding current voltage (I/V) relations of one A549 cell before and 3 min after exposure to 12.5 cGy α-particles; the later were emitted from an 241Am source. Comparison of the data collected before and after irradiation shows that this treatment causes an elevation of the instantaneous activating conductance and a small hyperpolarization of the free running membrane voltage in this representative cell. The irradiation induced conductance could be inhibited by adding 10 μM clotrimazole, a blocker of hIK type channels, to the external buffer; as a consequence of a block of hIK channels the cell depolarized. The response of cells to α-particles and the sensitivity of the irradiation-induced conductance to clotrimazole is equivalent to what was observed after irradiation with photons and high-energy ions [1]. The data hence foster the hypothesis that any type of ionizing irradiation and even single hits of a cell by an α-particle can stimulate the activation of hIK channels in A549 cells.

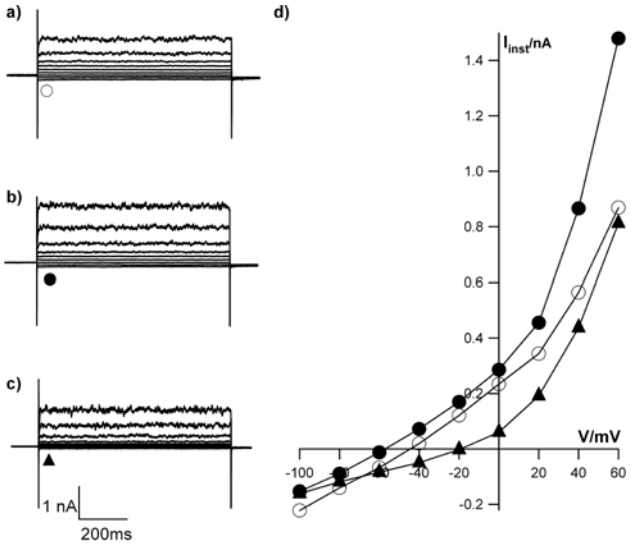

Figure 1: Current response of an A549 cell to a standard pulse-protocol before (a) and 3 min after irradiation with 12.5 cGy 241Am (3.66 MeV/u) (b). The I/V relation of the instantaneous activating current taken before (open circles) and after irradiation (closed circles) is shown in (d). The irradiation-augmented conductance can be inhibited by 10 μM Clotrimazole (c); the I/V relation after block with the specific hIK inhibitor Clotrimazole is shown as triangles in (d).

Conclusion

The present data show that the human intermediate conductance potassium channel hIK, a key player in the regulation of many cellular processes, is activated by low doses of α-particles. The results from these experiments suggest that an interpretation of positive and negative effects of α-particle irradiation in humans must consider the effect of this type of radiation on physiological processes under control of hIK channels.

References

[1] Roth B, Exposure to sparsely and densely ionizing irradiation results in an immediate activation of K^+ channels in A549 cells and in human peripheral blood lymphocytes PhD thesis TU Darmstadt (2014)

[2] Ouadid-Ahidouch (2008), The Journal of membrane biology, 221: 1–6

[3] Fertig N, Blick RH, Behrends JC (2002), 82: 3056–3062.

* Funded by BMBF 02NUK017B and HGS-HIRe

† roth@bio.tu-darmstadt.de

 doi:10.15120/GR-2014-1-BIOPHYSICS-34

A sensitivity analysis of the Giant LOop Binary LEsion model

L. Herr[*1,2], *T. Friedrich*[1], *M. Durante*[1,2], *and M. Scholz*[1]
[1]GSI, Darmstadt, Germany; [2]TU Darmstadt, Germany

The Giant LOop Binary LEsion model (GLOBLE) describes cell survival probabilities after photon irradiation in dependence of dose and dose rate. Its input parameters are closely linked to features of cellular repair of induced DNA double strand breaks (DSBs). Their values - derived e.g. from fits to experimental data - are considered to be cell line characteristic. Therefore, an investigation of the impact of the GLOBLE parameters on predicted cell survival probabilities helps to understand the extent in which certain repair features affect cell line specific radiosensitivities. In the following, it will be shown in how far a 10% increase in GLOBLE input parameters changes the model output.

Methods

In the GLOBLE, the effectiveness of radiation in cell killing depends on the spatio-temporal distribution of induced DSBs. The organization of the DNA in giant loops ($\approx$ 2 mega base pairs) whose ends are attached to the nuclear matrix suggests that a single DSB (isolated DSB, iDSB) in such a subunit is less harmful and faster to repair than multiple coexistent DSBs (clustered DSB, cDSB) since the latter allow for a loss of DNA fragments. In the model, iDSB or cDSB lead to lethal events with cell line specific probabilities ϵ_i or ϵ_c and the corresponding half-life times of repair are HLT_i and HLT_c. Depending e.g. on the dose, the dose rate, the linear energy transfer etc. the expected numbers of radiation induced iDSB and cDSB can be scored and with ϵ_i and ϵ_c the cell survival probability can be calculated. The model setup and examples for possible applications are presented in detail in [1,2].

In order to test the impact on cell survival the parameters of an hypothetical cell line $\epsilon_i = 0.0086$, $\epsilon_c = 0.32$, $HLT_i = 0.49h$ and $HLT_c = 5h$ were in turns increased by 10%. The relative change in the effect - the negative logarithm of the survival - was plotted over a range of doses and dose rates occurring in photon cell survival experiments.

Results and discussion

In figure 1 the relative change in the effect after a 10% increase of ϵ_i (A), ϵ_c (B) and HLT_i (C) is plotted over the dose and dose rate. Expectedly, higher probabilities for lethal events after DNA damage (A, B) increase the effectiveness of radiation in a dose and dose rate dependent manner. Panels A and B show that at low doses or dose rates, the lethality of iDSB (ϵ_i) has much more impact on cell survival probabilities than the one of cDSB (ϵ_c). In the transition to high doses and dose rates this overweight switches over-proportionally. This is due to the fact that the fraction of radiation induced iDSB is dominant at low doses and dose rates and that the fraction of cDSB grows over-proportionally when the dose and dose rate are increased.

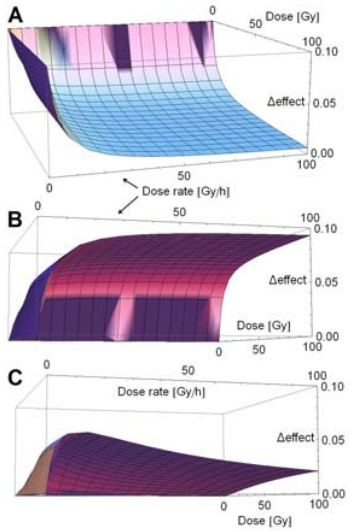

An increase of HLT_i generally raises the effectiveness of radiation since the probability to induce at least a second DSB in a giant loop - implying a more harmful cDSB - increases the longer an iDSB remains unrepaired. However, at low doses or dose rates the impact of HLT_i on cell survival is small due to the lack of cDSBs in this range. If the dose is increased, the parameter gains continuously in importance because of the growing fraction of cDSB. Due to the impossibility for a cell to repair some damage if high dose rates are applied, the impact of HLT_i initially grows with the fraction of cDSB if low dose rates are increased but decreases again after a maximal impact has been reached at dose rates around 10 Gy/h.

The impact of HLT_c on cell survival probabilities is negligible in comparison to the importance of the other three parameters and therefore not shown explicitly.

References

[1] Friedrich T, Durante M, Scholz M; Radiat Res 2012; 178: 385-394.

[2] Herr L, Friedrich T, Durante M, Scholz M; PLoS ONE 2014; 1(9).

*l.herr@gsi.de, supported by Studienstiftung des deutschen Volkes and HGS-Hire

Robust 4D-optimized treatment plans in scanned carbon ion beam therapy for intrafractionally moving lung cancer

C. Graeff[1] *and M. Durante*[1]
[1]GSI, Darmstadt, Germany

Introduction

The treatment of moving tumors with a scanned carbon ion beam is challenging due to interplay effects and range changes. This problem is even more acute for modern hypo- or single fractionated treatment, where averaging effects between fractions are diminished or missing. A technique for conformal treatment is tracking, where the ion beam is deflected to follow the target. This permits to compensate translatory motion components only and needs sophisticated hardware to cope with range changes online. Plans optimized on an entire 4DCT depicting the tumor motion over a breathing cycle inherently include the characteristic motion and also range information. Here, we present a modality that uses this 4DCT information to deliver homogeneous, conformal doses to each motion phase, and as such includes a form of rescanning.

Material and Methods

The treatment plans are generated separately for each motion phase, using the same set of beam energies, though not each plan necessarily has to use all energies. This is similar to single field uniform dose (SFUD) plans commonly generated for static tumors. In contrast to other motion mitigation techniques, a deformable registration between motion phases is not needed during optimization except to propagate the target contours. For delivery, the resulting independently optimized plans are then joined to a 4D plan, which can be irradiated using a 4D control system that was experimentally validated at GSI in 2012 [1]. Plans were computed for a lung cancer patient using 4 fields for a single fraction of 17.7 Gy(RBE). The patient had a complex tumor geometry with a motion amplitude of 12.7mm over the breathing cycle. The fields were both optimized separately (SFUD) and simultaneously (IMPT). DVH results were compared to a static (no motion) and interplay (no motion mitigation) plan on the same patient. We report dose coverage (V95) and the conformity number (CN). Interplay and 4D-optimized plans were calculated on the 4DCT and did not consider residual motion within the discrete motion phases.

Results

Exemplary dose cuts of the patient are shown in figure 1. For SFUD, the static case resulted in V95 of 98.5% and CN of 70.8%, which degraded to V95 of 72.5% and CN of 52.5% for interplay. 4D-optimization could restore V95 to 99.4% and CN to 75.6%. For IMPT, the results of the static case were V95 of 99.3% and CN 83.4% compared to V95 of 76.4% and CN of 56.4% for interplay. Again 4D-optimization maintained excellent coverage with V95 of 100.0% and CN of 82.1%. The IMPT plans indicate that the additional degrees of freedom from 4D-optimization on 10 motion phases as well as from the simultaneous optimization of fields leads to nominally better plan results.

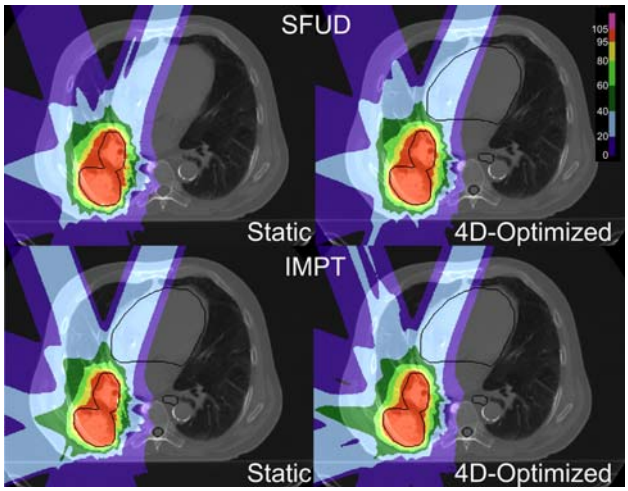

Figure 1: Axial dose cut of the sample patient for static (left panels) and 4D-optimized (right). The top row shows individually optimized fields, the bottom row simultaneous optimization. The static dose coverage could be completely restored.

Discussion

The presented 4D-optimizaton method leads to highly conformal irradiation of moving tumors, restoring or exceeding the results of an irradiation without motion. A major benefit of the proposed method with respect to robustness is the lack of dose gradients between motion phases. This is partially negated through the use of IMPT, which introduces gradient between fields, though not between motion phases. The results presented here will be experimentally tested in the GSI beam times of 2014.

References

[1] C. Graeff, R. Lüchtenborg, J.G. Eley, M. Durante, C. Bert, "A 4D-optimization concept for scanned ion beam therapy", Radiother Oncol. (2013) 109(3):419-24

 doi:10.15120/GR-2014-1-BIOPHYSICS-36

Studying inter- and intrafraction motion mitigation with sequential 4DCTs of NSCLC patients*

R. Brevet[†1], *D. Richter*[1,2], *C. Graeff*[1], *M. Durante*[1], *and C. Bert*[1,2]

[1]GSI, Darmstadt, Germany; [2]Universitätsklinikum, Medizinische Strahlenphysik, Erlangen, Germany

Introduction

The physical and biological properties of scanned carbon ion beam therapy potentially permit more conformal irradiation than photons. Range sensitivity and interplay renders treatment of moving tumors complex. Optimized treatment planning parameters, ITV-PTV margins and multiple field (using SFUD) were investigated to compensate for tumor motion and interfractional patient variability.

Material & methods

For 4 NSCLC lung tumor patients from the University of Texas MD Anderson Cancer Center (MDACC) [1], a total of 30 weekly 4DCT datasets were available. Reference phases of each subsequent CT were registered rigidly to mimic patient setup. Motion phases of each 4DCT were registered non-rigidly [2]. Single and multiple field gating plans were simulated using the GSI treatment planning system TRiP4D [3], including 4D-dose simulations. A range-considering ITV [4] was computed on the 4DCT of the first week for each field. Using one single field first, the impact of variations in focus size and length of the gating window (GW) was analyzed. Three beam foci (6, 10 and 15 mm full width at half maximum) and three GW (11.9, 30 and 50% of the amplitude) were studied. Using one single field again, the influence of range (3mm water-equivalent + 3%) and isotropic (3mm) ITV-PTV margins were investigated. Combination of both margins was also analyzed. Finally multiple fields (2 and 3 fields) simulations with and without ITV-PTV margins were performed. For each case, results were evaluated using the obtained V95 (dose coverage) and CN [5] (conformity number, see equation 1).

$$CN = \frac{V_{CTV,95\%}}{V_{CTV}} \times \frac{V_{CTV,95\%}}{V_{95\%}} \qquad (1)$$

Results & discussion

Table 1 shows that, using one field, the best V95 was obtained with the largest focus and the shortest GW. Combined with this best configuration, ITV-PTV margins permitted to increase V95 up to almost 98%, but a decreasing CN showed that more dose was delivered to the healthy tissue. Using multiple fields with ITV margins improved CN significantly but V95 only slightly compared to single field simulations. Finally, multiple fields combined with ITV-PTV margins yielded the best results in terms of V95, but CN, even though higher than for single field calculations, decreased compared to multiple fields calculations with ITV margins only.

Conclusion

It was shown here that using adapted parameters can improve dose delivery. However, the still unsatisfactory results can be further improved by using margins. Moreover, treatment with more fields is also a solution to increase target coverage and decrease regions of high dose in normal tissue. Using margins in addition allows to recover for positioning uncertainties.

Number of fields	Margins	Focus	GW	V95 (range)	CN (range)
1	ITV	6	50	**69.9** (42.8 to 94.5)	**0.39** (0.14 to 62)
		15	11.9	**88** (67.5 to 99.7)	**0.45** (0.17 to 0.66)
	ITV + isotopric 3mm	15	11.9	**93.7** (76.8 to 100)	**0.37** (0.18 to 0.52)
	ITV + range 3%+3mm	15	11.9	**95.9** (80.7 to 100)	**0.37** (0.2 to 0.53)
	ITV + isotropic 3mm + range 3%+3mm	15	11.9	**97.7** (81.8 to 100)	**0.32** (0.19 to 0.45)
2	ITV	15	11.9	**92.7** (75.8 to 100)	**0.51** (0.26 to 0.63)
	ITV + isotropic 3mm + range 3%+3mm	15	11.9	**99.1** (85.3 to 100)	**0.34** (0.22 to 0.46)
3	ITV	15	11.9	**92.9** (72.6 to 99.9)	**0.56** (0.31 to 0.58)
	ITV + isotropic 3mm + range 3%+3mm	15	11.9	**99.2** (83.7 to 100)	**0.37** (0.27 to 0.48)

Table 1: Impact of focus, gating window (GW), ITV-PTV margins and multiple fields on dose coverage (V95) and conformirty number (CN).

References

[1] Britton et al, 2007, Int. J. Radiat. Oncol. Biol. Phys. 68 (4) 1036-46

[2] Shackleford et al, 2010, Phys. Med. Biol. 55, 6329-6351

[3] Richter et al, 2013, Med. Phys. 40 (5) 051722

[4] Graeff et al, 2012, Med. Phys. 39, 6004-6014

[5] van't Riet et al, 1997, Int. J. Radiat. Oncol. Biol. Phys. 37 731–6

*RB is funded as an ESR within the EU-FP7 ENTERVISION framework, Grant Agreement no. 264552. Further funds received by DFG KFO 214.

[†] r.brevet@gsi.de

Towards helium ions for radiotherapy

F. Schmitz[1,2], *M. Krämer*[2], *and M. Durante*[2]
[1]Univ. Heidelberg; [2]GSI, Darmstadt, Germany

Rationale

The majority of ion beam radiotherapy sites uses protons, but an increasing number also applies heavier ions such as carbon. However, there might be room between these two, in particular for the helium isotopes. One of the major drawbacks of protons, for example, is the beam broadening due to multiple scattering. This is expected to be significantly reduced for helium beams, Fig.1.

Beam Modelling

Only few basic data are available to construct the pencil beam model for treatment planning with our inhouse TRiP98 system [1]. For ^{3}He previous work exists [2], based on GSI measurements. For ^{4}He, a literature search was performed to obtain basic cross section data and a semi-empirical model was established [3]. Fig.2 shows total nuclear reaction cross sections, one of the main ingredients to calculate depth dose distributions, since they determine the degradation of the ion beam as it passes tissue.

Results

Fig.3 shows typical depth dose distributions for various modalities applicable to tumour sites at approximately 15cm depth. Compared to protons, the helium Bragg peak is sharper, and compared to carbon ions, the fragmentation tail is significantly reduced. Only small differences are expected between the two helium isotopes.

Outlook

Since HIT is commissioning therapeutical ^{4}He beams, it would be attractive to perform further validation measurements. However, only comparative treatment planning studies involving multiple ions will allow proper assessment of potential benefits.

References

[1] M. Kraemer, E. Scifoni, C. Waelzlein, M. Durante, "Ion beams in radiotherapy - from tracks to treatment planning" J. Phys.: Conf. Ser., 373 (012017) : (2012)

[2] G. Kragl, "Tumortherapie mit schweren Ionen: Anpassung des Strahlmodells für ^{3}He", Diplomarbeit TU Wien, 2006; GSI Report Dipl. 2006-01

[3] F. Schmitz, "A semiempirical beam model for ^{4}He projectiles in ion beam radiotherapy", Master Thesis Univ. Heidelberg, 2013

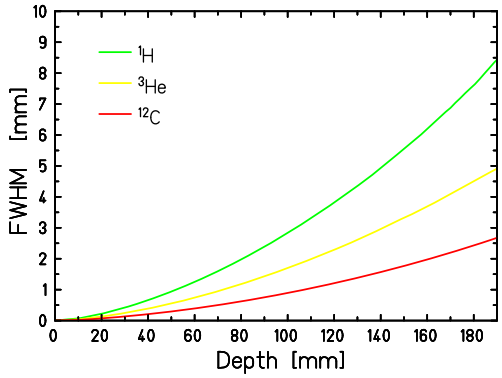

Figure 1: Beam broadening due to multiple scattering.

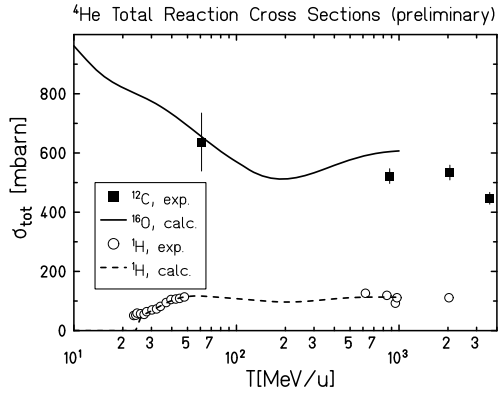

Figure 2: Total reaction cross sections.

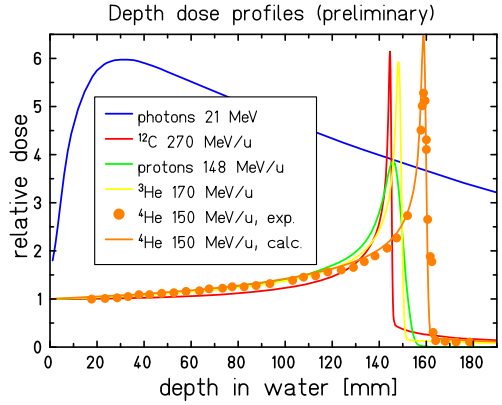

Figure 3: Depth dose distributions for various modalities.

 doi:10.15120/GR-2014-1-BIOPHYSICS-38

TLD Efficiency calculation for heavy ions: a new approach*

D. Boscolo[1,2], *E. Scifoni*[1], *M. Durante*[1], *V. Rosso*[4], *and M. Krämer*[1]
[1]GSI, Darmstadt, Germany; [2]University of Pisa, Italy

Thermoluminescence dosimeters (TLDs) are solid state detectors widely used in conventional radiation detection and dose verification. The development of ion beam cancer therapy and the research in radioprotection in space stimulated the use of the TLDs for heavy ions dosimetry. The main advantages of this kind of detector, compared, e.g., to ionization chambers, are the small dimensions, ease of handling, no interference on the radiation field and the usability in solid state phantoms. However the response of TLDs with dose is non-linear. It can be supralinear and saturation effects appear as well. The response of these detectors when irradiated with particle beams depends also strongly on the quality of the radiation. For this reason, in order to use TLDs with particle beams, and specifically, to get a prediction of their response in a treatment plan, a model that can reproduce the behavior of these detectors in different conditions is needed.

A new, simple and completely analytical, algorithm for the calculation of the efficiency depending on ion charge Z and energy E has been developed.
The approach investigated is based on the amorphous track structure model and on the knowledge of radial dose distribution for heavy ions D(r) and of the detector response to reference radiation, for this work X-ray, TL_γ. The response of the whole detector has been evaluated starting from the response to a single ion of the beam and considering the contributions of dose from the neighbouring tracks as adding up in a linear regime. This approach is realistic in a low dose approximation.

The relative efficiency R.E. has been derived according to

$$R.E = \left.\frac{S_{HI}}{S_\gamma}\right|_D \qquad (1)$$

using S_{HI} and S_γ the integral light sum of detector irradiated with heavy ions and X-ray, respectively.

Since X-ray's response curve is known and the dose deposition is uniform, the signal can be calculated directly from the total dose delivered by the ion. The thermoluminescence caused by ion is derived as

$$S_{HI} = 2\pi \int_0^{r_{max}} TL_\gamma(D(r))rdr \qquad (2)$$

where r_{max} is the maximum range of the secondary electrons.

In figure 1 it is shown the agreement of the present model with experimental data. Its main advantage, is that being fully analytical is computationally fast and can be then efficiently integrated in treatment planning verification tools. Furthermore, it is robust against modifications of the radial dose distribution of a single ion in the detector, as well as to different detector response models. A comparison with a statistical method based on Kellerer algorithm [2] has been also done, returning a good agreement.

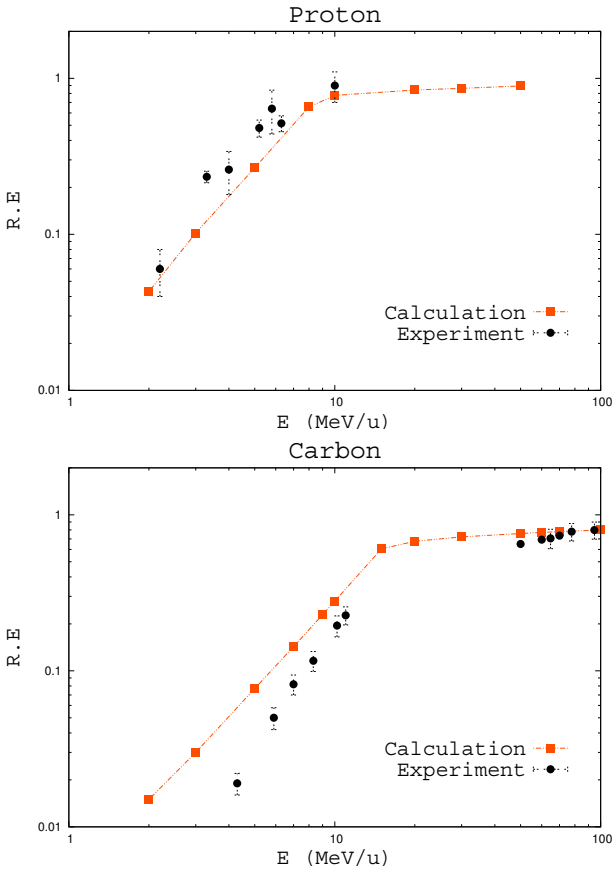

Figure 1: A comparison between experimental relative efficiency data [1] and calculation with the present approach for protons (up) and carbon ions (down).

References

[1] O. B. Geiß , M. Krämer, and G. Kraft. Efficiency of thermoluminescence detectors to heavy charged particles. NIM B, 142:592–598, 1998.

[2] S. Greilich et al., Efficient calculation of local dose distribution for response modelling in proton and ion beams (submitted), arXiv:1306.0185v1.

* Work supported by University of Pisa's Erasmus Placements project

Construction of a X-Ray Cabinet for Live Cell Experiments*

R. Khan[1], *A. Becker*[1], *G. Taucher-Scholz*[1,2], *M. Durante*[1,2], *G. Fehrenbacher*[1], *and B. Jakob*[1]
[1]GSI, Darmstadt, Germany; [2]TUD, Darmstadt, Germany

Introduction

Visualization of repair processes in living cells is of increasing importance to deduce molecular mechanisms in the cellular response to radiation. Observation of the dynamics of DNA repair factors directly at the beamline at ion induced damage sites provided insight into the regulation of the DNA damage response [1]. X-rays are frequently used as a reference in radiation biology. To compare our results of high LET to sparsely ionizing radiation, we constructed a x-ray cabinet for real time kinetic measurements of cellular radiation responses. Special emphasis was put on radiation safety aspects which were planed and conducted according to legal requirements by GSI radiation protection department.

Description

The new cabinet consists of an Isovolt 160M1/10-55 x-ray tube (GE Sensing + Inspection Technologies). The tube is operated by a voltage up to 35kV at a maximal current of 80 mA. Contribution of soft x-rays is minimized by an additional filtering of 0.5mm Al. At the target position of the microscope a dose rate of around 36 Gy/min can be achieved, which is sufficient for dynamic measurements which normally are performed at a dose below 2 Gy. The shielding of the housing was calculated in the radiation protection department according to these radiation parameters and safety requirements and manufactured in house. The front door of the cabinet is equipped with two independent interlock connectors with immediately power off the x-ray tube if opened accidentally. A blinking lamp on the wall signals operation. The cabinet was approved by the GSI radiation protection department, the TÜV and the radiation protection authority. For cell observation we use the same equipment as for beamline microscopy, which allows a direct comparison of results. The setup was described elsewhere [1]. Briefly it consists of an Olympus IX71 microscope (60x Planapo water NA1.2) with motorized stage and a piezo focussing system. Excitation light is provided using a fast switchable monochromator (Poly V, Till-Photonics). Image detection is done using a sensitive back illuminated EMCCD camera Andor ixon 888. The open cabinet equipped with the microscope and x-ray tube is shown in Fig. 1.

Figure 1: Open Cabinet

First experiments

First experiments were performed measuring the real time recruitment of GFP-tagged 53BP1 in human osteosarcoma cells (U2OS) after irradiation with 2 Gy. Figure 2 (left) shows the formation of radiation-induced foci at the time of 10min postirradiation. In Fig. 2 (right), the relative increase of the fluorescence at sites of double-strand breaks (DSBs) due to the accumulation of 53BP1 is shown.

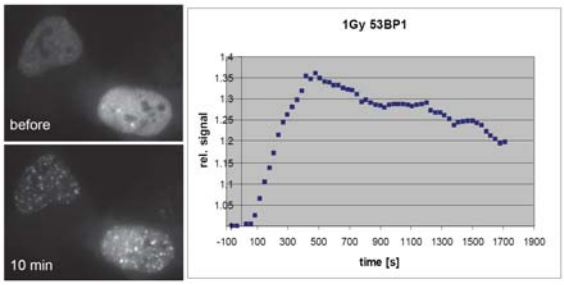

Figure 2: 53BP1 recruitment and corresponding kinetics

Outlook

In addition to conventional broadfiled x-irradiation, the setup will be equipped with micro-collimators made from stacks of GaAs with micro-channels (Microleman) in front of the cell samples to allow for a partial irradiation of cells. This setup tends to mimic the spatial dose distribution of charged particles and facilitates the analysis allowing a direct comparison of irradiated and non-irradiated areas.

References

[1] F. Tobias *et al.*, PLoS One. (2013);8(2):e57953

* Work supported by BMBF grant 02NUK001C; GRK1657 and HGS-HiRE

 doi:10.15120/GR-2014-1-BIOPHYSICS-40

Construction of an alpha-irradiation-setup for cells*

J. A. Adrian[1,2], C. Fournier[1], M. Durante[1,2], A. Maier[1], and G. Kraft† [1]

[1]GSI, Darmstadt, Germany; [2]TU Darmstadt, Darmstadt, Germany

Introduction

In the framework of the GREWIS project, the influence of Radon alpha particles is studied on biological objects. But for cell exposure the hit probability of individual cells is too small at therapeutic Radon concentrations and the non-hit cells will cover the affected cells. Therefore cells have to be exposed directly to low energy alpha particles from a radioactive source with higher doses. Consequently an alpha-irradiation-setup has been established using Americium-241 with a half life time of 432,2 years. Am-241 decays under the emission of alpha-particles with an energy of 5,486 MeV and gamma-radiation with 59,5 keV. Because of the low range of these high LET-particles a short distance between source and target is demanded [1]. In addition biocompatibility of all materials used has to be tested in experiments for cell growth, plating efficiency, X-ray cell killing and distribution of nucleus diameter.

Design

In the current design, a large area Am-241 source of 3,5 cm in diameter and an activity of 25 MBq is inserted in the basis of the irradiation chamber. Because of the high source activity only short but precise exposures are required. In order to guarantee a precise exposure, we interposed a fast mechanical shutter between the Am-241-source and the target. This shutter from the Sutter Instrument Company shields the alpha-particles entirely and is able to open within 12 ms. Thus we achieve to deposit nearly exactly the wanted dose. In figure 1 a crossection through the setup is given showing the Am-241 source, the shutter and a ring with mylar foil having a gap of only 2,7 mm between the source and the cells. Figure 2 shows the current version of the setup. To maintain this short distance, cells cannot grow under normal conditions in a petri dish or cell cultur flask but require to be seeded on a 2 μm thick foil. This mylar foil is attached to rings of stainless steel with an inner diameter of 35 mm.

Results

In order to confirm that the measured effects result from the alpha-irradiation and are not due to the special culturing conditions, several radiobiological experiments were performed. One of them is the comparison of cell survival after X-ray irradiation of CHO-K1 cells, cultivated in T25 cell cultur flask or on the mylar foil. From the results shown in figure 3 it can be derived that the clonogenic survival of CHO-K1 cells is not different comparing mylar foil and culture flasks.

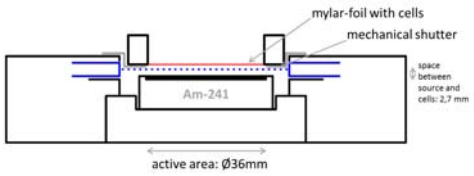

Figure 1: Crossection through the setup

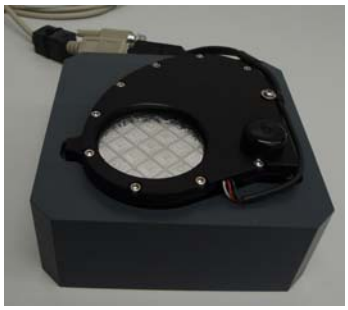

Figure 2: Picture of the Setup and the closed shutter

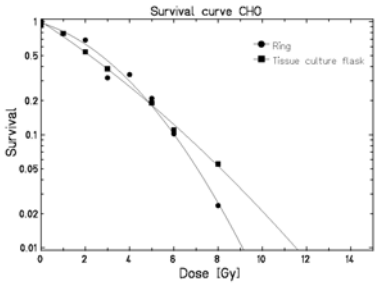

Figure 3: Survival of CHO cells after X-ray irradiation growing on mylar foil or culture flasks

References

[1] Lindsay A Beaton et. al., Development and characterization of an in vitro alpha radiation exposure system, Phys. Med. Biol. 56 (2011) 3645-3658

*Work supported by BMBF project funding reference number 02NUK017A

† g.kraft@gsi.de

A Detector setup for Heavy Ion Computed Tomography *

M. Takechi[1], *J. Kunkel*[1], *H. Risch*[1], *L. Magallanes*[2], *S.Brons*[2], *O. Jaekel*[2,3,4], *K. Parodi*[2,5], *I. Rinaldi*[2,5], *and B. Voss*[1]

[1]GSI, Darmstadt, Germany; [2]Heidelberg University Clinic, Heidelberg, Germany; [3]Heidelberg Ion Therapy Center, Heidelberg, Germany; [4]German Cancer Research Center, Heidelberg, Germany; [5]Ludwig Maximilians University Munich, Garching, Germany

Radiotherapy with ion beams is a method which allows the precise dose delivery to the tumor sparing the surrounding healthy tissue, thanks to the steep increase of the dose deposition at the end of the beam path (Bragg peak). The development of innovative imaging techniques is quite important for the precise treatment, improving the accuracy of the calculated ion ranges in tissue and avoiding range uncertainties.

A dedicated detector for range monitoring prior to or in-between treatment based on a stack of ionization chambers is being developed in GSI. The detector is designed to detect the depth of the Bragg peak of the ion beam penetrating the target. It consists of a stack of large-area parallel-plate ion chambers and passive or active absorbers (see Fig. 1(a)). A prototype based on the combination of 61 ICs (6mm gas gap, and 25μm thick aluminized Kapton foils for the signal electrodes) and absorber plates consisting of 3 mm thick slabs of PMMA has been developed at GSI. It was applied for the feasibility studies of the HICT method with ion beams at the Heidelberg Ion Therapy center (HIT)[1]. In order to achieve a higher resolution a new detector is currently set up at. Since the thickness of the absorbers gives the nominal resolution of the measured range, the new system with 1mm thick absorbers will have a 3 times higher granular structure than the prototype. A schematic drawing is shown in Fig. 1(b).

Along with the design, the response of the new detector has been simulated using GEANT4[2] and Garfield++[3]. The Bragg peak for a ^{12}C beam injected into the 128 parallel-plate ionization chambers interleaved with 1 mm PMMA absorbers has been simulated. The energy and angular straggling of the heavy-ion beam in the each absorber was calculated by GEANT4. The primary electrons from the beam and their drift tracks and induced currents in the ICs were calculated by Garfield++. The effect of the light fragments from the beam produced in the absorbers on the spectrum of Bragg peak is also studied. In Fig. 2 the simulated spectra for a 200 MeV/u ^{12}C beam and light fragments produced in the material traversed are shown. The production cross sections of light fragments are based on EPAX2[4]. In Fig. 2, a clear Bragg peak of ^{12}C can be seen. Aside from the assembly of a full scale detector system with 128 ICs further theoretical studies are in process.

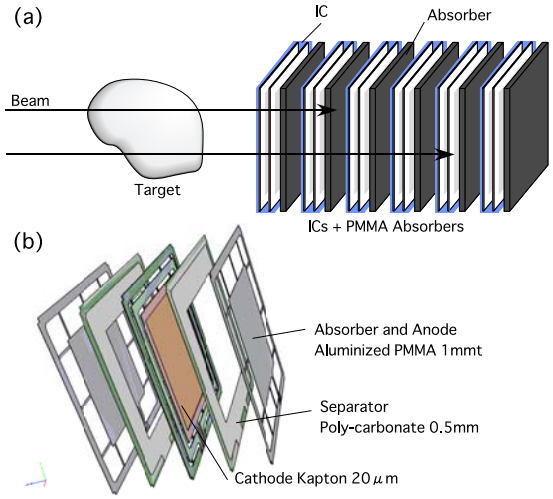

Figure 1: A schematic drawing of the principle of the range monitoring detector for cancer treatment (a), and designs of electrodes and absorbers for the detector (b).

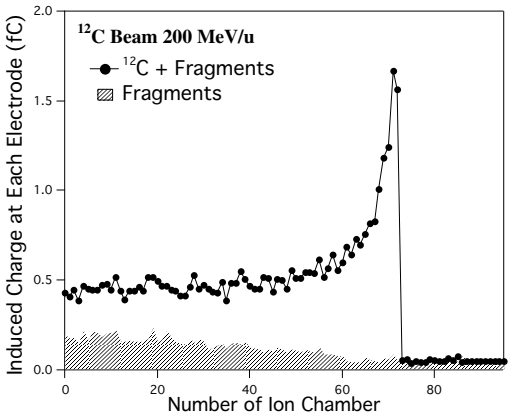

Figure 2: Spectra of ^{12}C beam and light fragments produced within the new detector, simulated using Garfield++ and GEANT4.

References

[1] I. Rinaldi et al., Phys. Med. Biol. 58 (2013) 413-427.

[2] S. Agostinelli et al., Nuclear Instruments and Methods in Physics Research A 506 (2003) 250.

[3] http://garfieldpp.web.cern.ch/garfieldpp/

[4] K. Summerer et al., Phys. Rev. C 61 (2000) 034607

* Work supported by GSI(RBDL), DFG (contract no.VO 1823/2-1)

 doi:10.15120/GR-2014-1-BIOPHYSICS-42

Development of an automatic counting system for cell spheroids in suspension

M.-P. Sonnemann[1], *C. Hartel*[2], *M. Scholz*[2], *M. Durante*[2,3], *and K. Sandau*[1]

[1]Hochschule Darmstadt, Optotechnik und Bildverarbeitung, Darmstadt, Germany; [2]GSI, Biophysik, Darmstadt, Germany; [3]TU Darmstadt, Inst. f. Festkörperphysik

Introduction

To understand the radiosensitivity of cancer stem(-like) cells or tumor initiating cells is of particular interest for applications in radiotherapy. However, in general it is challenging to determine radiosensitivity of these cells since they are often cultured in so-called self-renewal conditions in serum-free culture medium where they grow as spheroids. These cell spheroids do not attach to the culture flask and thus cannot be fixed and stained, so that manual counting of the spheroids gets extremely tedious. It is thus highly desirable to have an automated analysis system that is capable to detect unstained cell spheroids and to automatically scan complete culture vessels to determine the total number of spheroids.

Methods

The CARL (*Clonogenic Assay Recognition System*) system has been developed, implemented and tested using standardized commercially available components, like a 3840x2748 pixel CMOS camera (UI_1490SE from IDS), LED ring illumination (LDR-176LA-1 from CCS Inc.), and a motorized scanning stage (VT-80 2SM MLS from PImicos). The control software has been developed in Python language using the openCV image processing library on a Linux platform.

Analysis of a culture flask comprises the following steps:

- Image Acquisition: the required resolution of 10μm/pixel does not allow to cover the whole flask in a single field of view; thus, multiple images obtained by shift of the scanning stage have to be combined.
- Image Fusion: the special optical features of the culture vessels required combination of multiple images with different exposure settings and subsequent fusion to obtain a single image in HDR mode.
- Object recognition: a tophat filter is used for binarization and the watershed transformation for object separation.
- Object classification: several criteria like e.g. size and roundness are used to distinguish the cell spheroids from particles of artificial background.

A graphical user interface was implemented to control the general settings, the image acquisition and the analysis process. Figure 1 shows the setup of the automatic spheroid detection system.

Results

After extensive testing and calibration procedures the apparatus is now used in routine experiments. It could be demonstrated that the automatic counting is in good agreement with the results from manual counting; Figure 2 compares the results from manual scoring with the results obtained with the CARL system for U87 glioblastoma cells. Similar results have been obtained also for other cell lines (see e.g. Hartel et al., this report). An adapation of the system to facilitate also the analysis of cell colonies attached to the culture vessel seems feasible.

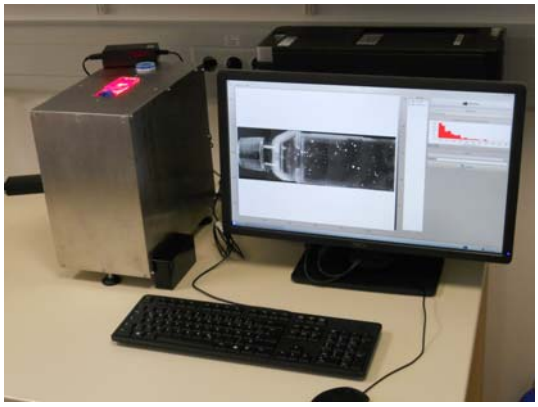

Figure 1: Setup of the CARL automatic cell spheroid detection system

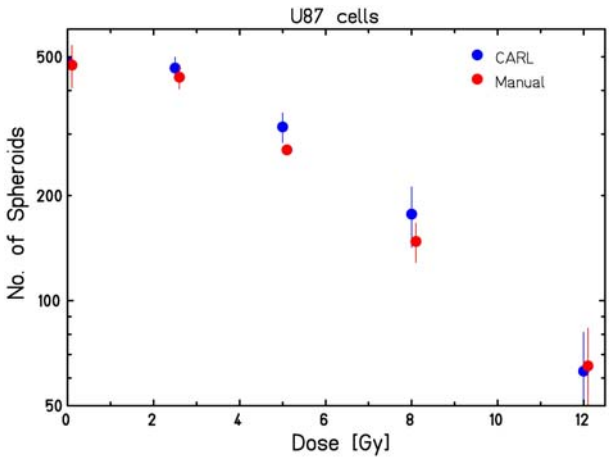

Figure 2: Comparison of manually counted and automatically analyzed spheroid numbers

Prototype of a rasterscan control system for BIOMAT@FAIR

W. Becher[1], H. Brandt[2], P. Skott[2], T. Friedrich[1], M. Durante[1,3], and M. Scholz[1]

[1]GSI/Biophysik, Darmstadt, Germany; [2]GSI/CSEE, Darmstadt, Germany; [3]TU Darmstadt, Institut für Festkörperphysik, Darmstadt, Germany

Introduction

The pencil beam scanning method (rasterscan) developed in the framework of ion beam therapy at GSI has proven to be extremely valuable not only in medical applications, but also for experimental applications in radiobiology and materials research. It allows to adapt the field size exactly to the needs of the individual experiments without collimating the beam and thus makes optimal use of the ions delivered by the accelerator. It is thus planned to use this method also in the future BIOMAT facility at FAIR. However, the currently used rasterscan control system in Cave A is based on technologies available in the 1990s and includes many features which are particularly relevant for patient safety, like e.g. redundancy and interlock systems. For many radiobiological experiments, though, less sophisticated techniques still allow to achieve a dose delivery with sufficient accuracy. The goal of the project described here was thus a redesign of the control system on a different hardware- and software platform, focusing on the core functions required in any scanning system.

Methods

At present the system is limited to 2D-scanning in x- and y-direction. The basic functions of the system comprise the automatic control of the scanning magnets, of the beam request and of the fast stop of extraction (Fig. 1). An ionization chamber signal is used to measure the beam intensity, which represents the input information required to control the scanning speed.

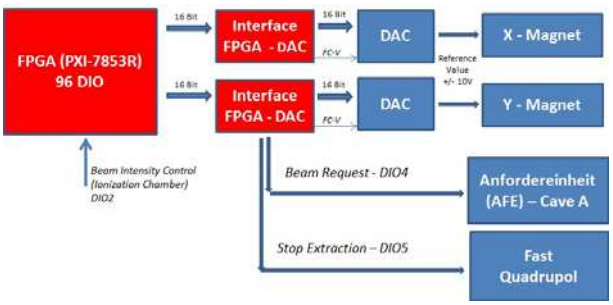

Figure 1: Block diagram of the rasterscan control system

The system is implemented on a real-time field-programmable gate array (FPGA) system (PXI-7853R from National Instruments) that is programmable in a LabView-FPGA environment.
The only in-house hardware developments that were required were the FPGA-DAC interface cards allowing to connect to the magnet power supplies, the beam request, the extraction control system and the signal input from the ionization chamber. The major advantages of such a system are:

- All functions that required dedicated hardware developments for the currently used system in Cave M and Cave A can now be implemented in software, which makes the system highly flexible.
- The flexibility makes the system future-proof, it can be easily adapted to the specific features of the accelerator control system that will be implemented within the FAIR project.
- All hardware components are commercially available components with widespread use, allowing to implement the system at comparably low costs and to facilitate the maintenance.

Results

After extensive testing of the system using a simulation environment first tests in Cave A have been performed. Dosimetric measurements as well as tests of the field homogeneity have been succesfully performed. Fig. 2 shows an example of a field irradiated with 2 Gy of 1 GeV/u Fe-ions. Further tests will be done within the beamtime in 2014, so that it is expected that the system is ready for routine applications at the end of 2014.

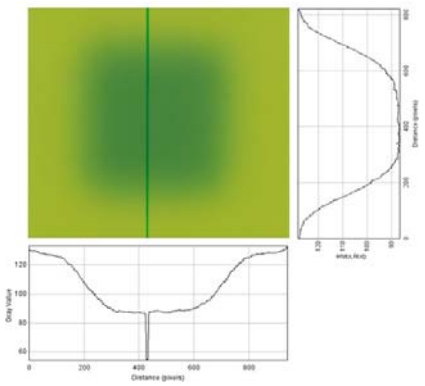

Figure 2: First test of the new rasterscan control system. A GafChromic film was irradiated with a dose of 2 Gy using 1 GeV/u Fe-ions (Field size: 40 mm x 40 mm). Histogramms show the density profiles along the x- and y-axis. The vertical line is an artificial line used as position reference.

 doi:10.15120/GR-2014-1-BIOPHYSICS-44

Radon exposure setup for cells and small animals *

A. Maier[1], *C. Fournier*[1], *M. Durante*[1,2], *M. M. Günther*[1,3], *and G. Kraft*[†1]
[1]GSI, Darmstadt, Germany; [2]TU Darmstadt, Germany; [3]Helmholtz-Institut Jena, Germany

Introduction

There is large interest in the understanding of the radiobiological response to radon exposure. This has several reasons: Radon is a main contributor for the natural exposure to radiation. For chronic exposure radon is probably the most important reason for lung tumor induction after smoking [1]. Radon exposure is also used in therapy of inflammatory diseases [2]. In the GREWIS project both, the genetic effects and anti- inflammatory action of radon and it's progenies (see Fig. 1) are studied in vitro and in vivo under precisely controlled conditions.

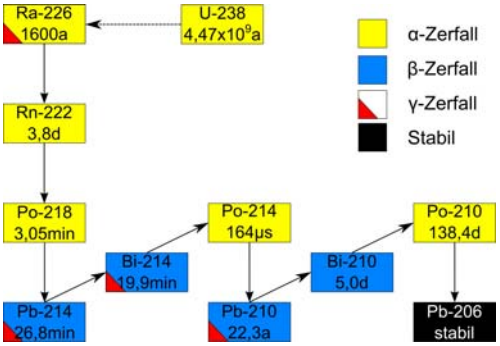

Figure 1: Decay chain

Requirement for measurement setup

For these experiments we constructed a radon exposure chamber (see Fig. 2) where measurements with cells and small animals can be performed. The following exposure parameters can be adjusted and monitored:

- Activity concentration of radon
- Temperature
- Humidity
- CO_2-concentration (only during cell experiments)

γ-Spectroscopy

A sample of 5g of activated coal was exposed to a radon activity of 620kBq/m^3 for 1h. A γ-spectrum was measured immediately after exposure using a HPGe-Detector. In the

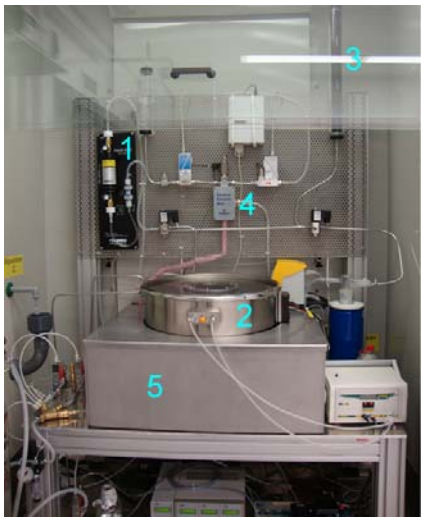

Figure 2: Radonchamber with (1) Radonsource, (2) Chamber, (3) Filter, (4) Air moistening system, (5) Waterbath

spectrum (Fig. 3) the energy lines with the highest emission probability are marked for the short-living decay products Pb-214 and Bi-214 which are clearly distinct from the background. With these measurement we could show the feasibility of this methode. Our next goal is to measure the distribution of the decay products in different materials like sections of animal tissue.

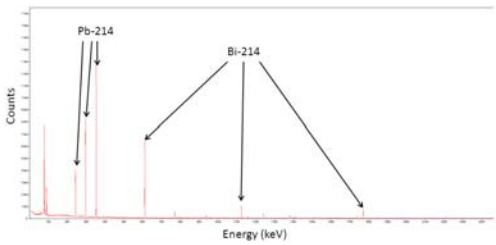

Figure 3: γ-spectrum of activated coal with energy lines of the decay products Pb-214 and Bi-214

References

[1] E. Radford, Potential Health Effects of Indoor Radon Exposure, Experimental Health Perspectives, Vol. 62, pp.281-287, 1985

[2] P. Deetjen et. al., Radon als Heilmittel: Therapeutische Wirkung biologischer Wirkungsmechanismus und vergleichende Risikobewertung, Verlag Dr. Kovac, 2005

*Work is supported by BMBF project funding reference number 02NUK017A

† g.kraft@gsi.de

The ROSSINI project at GSI*

C. Schuy† [1,2], *M. Rovituso*[1,2], *R. Pleskac*[1], *C. La Tessa*[1,3], *and M. Durante*[1,2]

[1]GSI, Darmstadt, Germany; [2]TU Darmstadt, Darmstadt, Germany; [3]BNL, New York, United States of America

Overview

The mitigation of health risks induced by the radiation environment in space, which consists of high energy protons from solar particle events (SPE), fast heavy ions coming from galactic cosmic rays (GCR) and trapped particles in the Earth magnetic field, is one of the most serious challenges in space exploration [1]. The radioprotection strategies applied nowadays include the preselection of astronauts, mission planning for low SPE probability, dietory factors, radioprotective agents and passive shielding [2]. The aim of the ROSSINI project (**R**adiati**O**n **S**hielding by **IS**RU and/or **IN**novative mater**I**als for EVA, Vehicle and Habitat) is to select innovative shielding materials and provide recommendations on space radioprotection for different mission scenarios. The project is a common effort of Thales Alenia Space, GSI, SpaceIT and ESA.

Experiments

The shielding effectivness of all candidate materials is characterized through dose reduction curves (setup similar to [3]) and for the most promising ones the mixed radiation field produced by heavy ions impinging on the target is investigated. Particle identification is performed using a dE/E-telescope and kinetic energy spectra are obtained using time-of-flight (setup similar to [4]). Numerous experiments where performed starting in 2012 at NSRL/Brookehaven National Lab (USA) and at Cave A/GSI using high energy heavy ion beams.

Status and outlook

Compared to prior experiments [5] major changes were introduced to the experimental setup as well as to the experimental side Cave A.

- The time-of-flight distance and therefore the energy resolution were improved by removing parts of the beamline.
- The data acquisition system was changed from CAMAC-based to VME to improve readout-rate and deadtime [6].
- Additional detectors added to complement the aquirred date, e.g. liquid scintillator.

An example plot obtained in a recent experiment performed at Cave A/GSI using 1 GeV/u ^{56}Fe impinging on Radel is shown in figure 1. Currently the measurred data is analyzed and the effects of the experimental optimization looks highly promising.

Additional experiments are planned for 2014 at GSI and BNL.

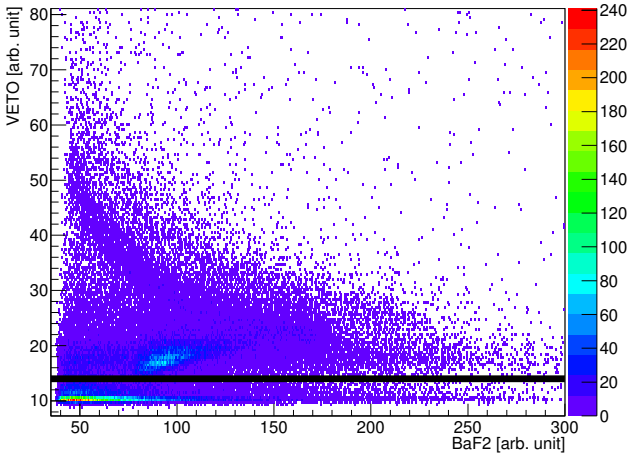

Figure 1: Recent measurement of 1 GeV/u ^{56}Fe impinging on 3.2 cm Radel at 30 degree. The corellation of the 9 mm VETO plastic scintillator signal and the signal of the BaF_2 scintillator can be used for particle identification. Uncharged fragments and photons are located below the black line, charged fragments, mainly hydrogen, are located above.

References

[1] Durante, M. & Cucinotta, F. A. (2011) Physical basis of radiation protection in space travel. Rev. Mod. Phys.

[2] Durante, M. (2008) Physical and biomedical countermeasures for space radiation risk. Z. Med. Phys.

[3] Schardt, D., Steidl, P., Kraemer, M., Weber, U., Parodi, K. & Brons, S. (2007) GSI Sci. Rep.

[4] Gunzert-Marx, K., Iwase, H., Schardt, D. & Simon, R. S. (2008) Secondary beam fragments produced by 200 MeV/u ^{12}C ions in water and their dose contributions in carbon ion radiotherapy. New J. Phys.

[5] Schuy, C., La Tessa, C., Rovituso, M., Piersanti, L., Tracino, E., Lobascio, C & Durante, M. (2012) Status of the ROSSINI project at GSI. GSI Sci. Rep.

[6] Piersanti, L., Schuy, C., La Tessa, C. & Durante, M. (2012) Development of a VME data acquisition system. GSI Sci. Rep.

* Work supported by ESA(RF:SGI-TASI-PRO-0226).

† Work is part of HGS-Hire

 doi:10.15120/GR-2014-1-BIOPHYSICS-46

Heart beat modelling in a water and anthropomorphic phantom

R. Kaderka[1], *A. Constantinescu*[1,2], *H.I. Lehmann*[3], *D. Packer*[3], *M. Durante*[1,2], *C. Graeff*[1], *and C. Bert*[1,4]

[1]GSI, Germany; [2]TU Darmstadt, Germany; [3]Mayo Clinic College of Medicine, USA; [4]Universitätsklinik Erlangen, Germany

Introduction

Atrial fibrillation represents the most common cardiac arrythmia. AV node ablation requiring an invasive procedure is the commonly used treatment choice at the moment. However, animal studies have shown that a similar result can be achieved non-invasively using ionising radiation. A method was described by Sharma et al [1] using photons to achieve AV node ablation.
As known from cancer patients using the Bragg peak characteristic of charged particles can lead to a more favorable dose deposition. In order to explore the potential of carbon ions for treatment of atrial fibrillation animal studies with swines are planned for 2014 at GSI. In this report a method for determining the dose deposition under influence of breathing and cardiac motion with the help of a phantom is described.

Figure 1: Picture of the Kuka robot holding the PMMA block with ionisation chambers inside the anthropomorphic breathing phantom.

Materials and methods

The main challenge when irradiating the AV node is the motion of the target. The target exhibits two interfering motion types: a slow motion (several seconds) with large amplitude due to breathing as well as a fast motion (around 120 beats per minute for swines) coming from the heart itself. The treatment procedure must incorporate means to mitigate the motion of the AV node.
Moving phantoms need to be used in order to experimentally study the dosimetric effects of breathing, heartbeat and motion mitigation techniques. For this purpose the target area is simulated by a PMMA block containing pinpoint ionisation chambers. The ion chamber block is mounted on an industrial robot Kuka KR5 sixx R850. The robot is capable of 6D motion and holds the target block either in water or an anthropomorphic breathing phantom. The latter phantom consists of a thorax and is actuated with a stepper motor to simulate the moving of the chest wall while breathing (Fig. 1).
The breathing functionality of the anthropomorphic phantom has been used for several years at GSI and is documented in [2]. The motion of the AV node has now been incorporated into the phantom motion mimicking patterns extracted from 4DCTs of four swines. The 4DCTs were taken by Mayo Clinic College of Medicine. The AV node displacement can be traced with sufficient accuracy (< 0.5 mm) by the robot. In order to study the effects of the different motion components, the robot control software can enable each movement type individually (Fig. 2).

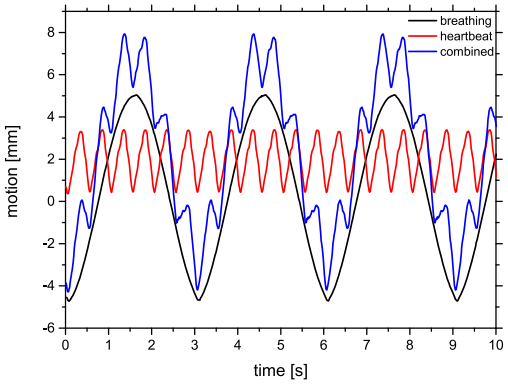

Figure 2: Motion trajectory of the target in superior-inferior direction showing breathing and heartbeat motion individually as well as the superposition.

Discussion

The robot is able to reliably reproduce a target trajectory coming from both breathing and cardiac motion in a phantom. The motion parameters can easily be manipulated in the control software to allow both quality assurance as well as research for a large variety of patients or animals.

References

[1] Sharma et al., HeartRhythm 7(6), 2010

[2] Steidl et al., Phys Med Biol 57(8), 2012

doi:10.15120/GR-2014-1-BIOPHYSICS-47

Heavy Ion Beam Irradiation of a Langendorff Heart

Matthias Prall[1], J. Bauer[2], A. Constantinescu[1], J. Debus[2], M. Durante[1], C. Graeff[1], T. Haberer[2], H. Hauswald[2], H. I. Lehmann[4], D. L. Packer[4], H. Prokesch[2], D. Richter[2], K. Sonnenberg[2], G. Szabó[2], R. Kaderka[1], S. Korkmaz[2], A. Weymann[2], and C. Bert[3]

[1]GSI, Darmstadt, Germany; [2]Universitätsklinikum Heidelberg, Germany; [3]Universitätsklinikum Erlangen, Germany; [4]Mayo Clinic College of Medicine, Rochester, MN, USA

The Biophysics group at GSI is currently starting experimental studies on radiosurgery of atrial fibrillation (AF) using ^{12}C beams. AF is one of the most common heart diseases. Its prevalence increases with age ($< 0.5\%$ in age group below 40, 0.7 % in the age group 55-59 and 17.8% in the age group above 85). In AF, disorganized electrical impulses usually originating in the pulmonary veins cause uncoordinated high frequent (300 - 600 min^{-1}) contractions of the atria (upper heart chambers). Symptoms are low blood pressure, shortness of breath, chest pain, irregular/racing heart beat or extreme fatigue. AF is responsible for 15-20 % of ischemic strokes. A common treatment is the interruption of electric pathways in the heart using catheter ablation. This surgical procedure is challenging, long (about 7 hours), only 52 % of patients can stop medication, 25% are treated at least twice and 6 % suffer from serious complications related to this intervention. A recent study has already demonstrated radiosurgery of the heart in live pigs using photons [1]. Our aim is to reproduce these results while improving target conformity and healthy tissue sparing using ^{12}C. Experiments with pigs and doses in the order of 30 Gy will be performed at GSI in 2014. Similarly to [1], the physiological effect is expected to evolve on the time scale of weeks to months.

The present report describes a pilot study in which we irradiated a small region in explanted pig hearts at HIT Heidelberg with very high doses (up to 160 Gy). The purpose was to gain knowledge about possible acute radiation effects (time scale of hours) resulting from ^{12}C-irradiation. These would be disadvantageous in our pig experiment. In our pilot study we applied dose to the atrioventricular (AV) node as here, a block of electrical conduction can accurately be identified in an ECG trace in real-time.

In each of our three experiments, a heart was extracted from a pig ($\approx$ 30 Kg) and kept in sinus rhythm in a so-called Langendorff setup (cf. Figs 1 and 2) for up to 7 h. The heart was perfused with Krebs-Henseleit (KH) solution via the coronary arteries (flow about 0.5 l/min). Using surgical wire it was fixed in a custom-built PMMA beaker (cf. Fig 2) in a bath of KH. The main circuit of our setup contained about 2 litres of KH. Carbogen gas (95% O_2, 5% CO_2) was used to aerate the solution. About every 30 min., 0.5 l of KH were exchanged to prevent acidfication. The temperature of the KH solution was kept at $T = 37°$C via heated water flowing through a heat exchanger in the oxygenator and the outer volume of the double-walled PMMA beaker. The heart beat induced motion of the myocardium was up to 1 cm. Prior to irradiation, the heart was scanned with 1 mm slice spacing in a PET/CT. The target (AV node) was delineated in the scans. A margin of 1 cm around the target volume (≈ 1.25 cm^3) was added to compensate motion. The initial alignment in the treatment room was performed using room lasers and fiducials attached to the beaker. Orthogonal x-ray images showing titanium clips attached to the heart were finally used to optimize the match with the CT images. Finally, dose was applied in fractions of 5 Gy and 10 Gy over a period of about 3 h. PET and CT scans were made after each experiment.

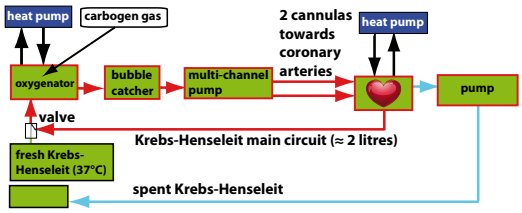

Figure 1: Sketch of the Langendorff setup. The main KH circuit is drawn in red.

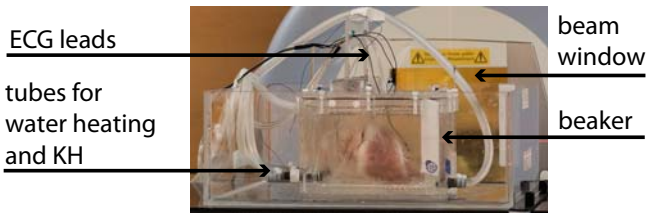

Figure 2: The heart in the double-walled PMMA beaker on the patient couch in the treatment room H1 at HIT. The heart is fixed to the bottom of the beaker with surgical wire.

In our three experiments, we applied a cumulative dose of 80, 90 and 160 Gy to the AV node. Whereas no acute radiation effects could be observed in the first two cases, a block of electrical conduction in the AV node could clearly be identified in the ECG after 160 Gy. On the one hand, this proves that it is possible to influence the electrical conduction system of the heart using ^{12}C beams. On the other hand our pilot study implies that no acute (adverse) radiation effects have to be expected while performing a pig experiment using doses in the order of 30 Gy.

References

[1] A. Sharma et al. Heart Rhythm. 2010 Jun;7(6):802-10

 doi:10.15120/GR-2014-1-BIOPHYSICS-48

Influence of cardiac motion on porcine AV node for the non-invasive treatment of atrial fibrillation with a scanned carbon ion beam*

A. Constantinescu[1,2], *H.I.Lehmann*[3], *C. Graeff*[1], *D.Packer*[3], *M. Durante*[1,2], *and C. Bert*[1,4]

[1]GSI, Darmstadt, Germany; [2]Technische Universität Darmstadt, Germany; [3]Mayo Clinic College of Medicine, Rochester, USA; [4]Universitätsklinik Erlangen, Germany

Introduction

Atrial fibrillation (AF) is the most common cardiac arrhythmia and occurs in ∼2 % of the western population older than eighty [1]. Since age is an important risk factor for this disease, the prevalence is estimated to double in the next fifty years. One treatment strategy for reducing the ventricular rate in AF patients is atrioventricular (AV) node ablation, requiring the implantation of a pacemaker. It has recently be shown in animal studies that a non-invasive ablation on this target site is feasible with photons [2]. Similar experiments with carbon ions are planned for 2014 at GSI, where the AV node of swines will be irradiated. In order to assess the target displacement due to heart beat motion volume histograms (MVHs) were analyzed.

Material and Methods

In order to study the displacement of the AV node during the cardiac cycle time resolved Computed Tomography (CT) scans of a swine, gated on heart beat were acquired. Treatment planning is usually based on native CT scans where the density information can be directly used as range information for the particle beam. As the heart muscle is a very dense structure a contrast enhanced CT scan of the swine was also acquired, enabling a comparison of the AV node motion based on the two different scans. In both cases the cardiac cycle was divided into twenty quasi-stationary sections (motion phases) (5% intervals of the cardiac cycle). Ablation lines for AV node were contoured (x≈2 mm, y≈5 mm, z≈3 mm). A non-rigid registration of the motion phases was carried out with the open source software Plastimatch. The MVHs were calculated with the in-house treatment planning software TRiP4D [3]. The motion of the AV node due to the influence of the heart beat was investigated by studying the displacement of the target in all nineteen motion phases compared to the reference phase (0%).

Results

In fig.1 the mean displacement and standard deviation of the AV node due to heart beat are shown for the different motion directions resulting from the native CT (in black) and the contrast enhanced CT (in red), respectively. While the native scan yields no significant displacement of the AV node, the contrast enhanced CT scan allows for a motion assessment.

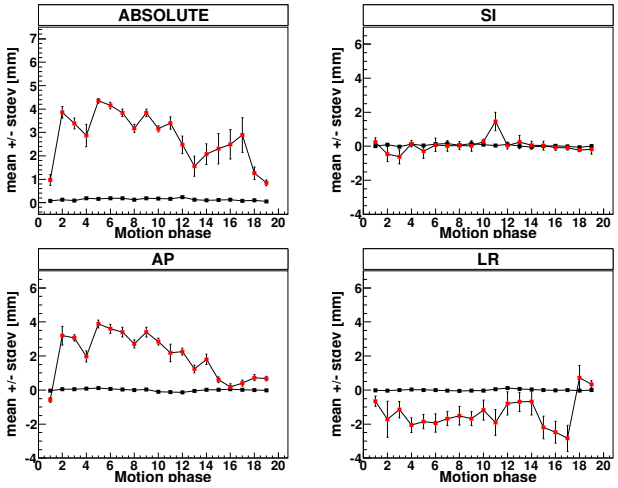

Figure 1: Displacement of AV node in superior-inferior (SI) direction, anterior-posterior (AP) direction and left-right (LR) direction. The absolute displacement is also plotted. Comparison between native CT data (black) and contrast enhanced CT (red) for one swine data set.

The mean absolute displacement of the AV node resulting from the contrast enhanced CT scans results to (2.78 ± 1.04) mm. It can be concluded that the motion is smallest in SI direction with a mean displacement of (0.04 ± 0.41) mm, while AP is the biggest motion direction with a mean displacement of (1.98 ± 1.30) mm.

Conclusion

Resulting from a contrast enhanced CT scan of a swine, the AV node seems to move significantly with an absolute displacement of up to 4 mm. The motion due to heart beat is hence not negligible when irradiating this cardiac target volume. This needs to be considered in the upcoming beam time at GSI where a non-invasive AV node ablation with scanned carbon ions will be carried out in swines.

References

[1] Zipes and Jalife, Cardiac Electrophysiology, 2009

[2] Sharma et al., HeartRhythm 7(6), 2010

[3] Richter D et al., Med Phys.40(5), 2013

* Work is part of HGS-HIRE

Online Bragg Peak monitoring for radiotherapy with ions using pixel sensors

M. Rovituso[*1], *C. La Tessa*[1,2], *C. Schuy*[1], *and M. Durante*[1,3]
[1]GSI, Darmstadt, Germany; [2]BNL, New York, USA; [3]TU, Darmstadt, Germany

Overview

The properties of the ^{12}C beam make this ion especially suitable for the treatment of deep seated and radioresistant tumors and tumors close to radiosensitive tissue. One of the main advantages of ions compared to photons is their inverse depth-dose profile (Bragg-Peak). However, the attenuation of the beam and the production of fragments when traversing body tissue, can significantly affect the actual position of the Bragg Peak in the patient. Thus, a method for real-time monitoring of the Bragg-Peak would be highly beneficial for online treatment verification. Tracking the secondary particles induced by the ion beam allows the reconstruction of the dose-depth relation.

Experiments

The MIMOSA-28 (CMOS) is a silicon pixel sensor with a 2 cm^2 sensitive area that showed excellent performances in charged particle tracking [1]. Starting from the detector setup for fragmentation measurements shown before [2], the CMOS can be placed at 60 or 90 degrees with respect to the primary beam direction or immediately after the target. The intersect of the measured tracks is a good estimate for the Bragg-Peak position [3].

Status

The CMOS were successfully tested at Brookhaven National Laboratory (USA) with 1 GeV/u Iron beam.

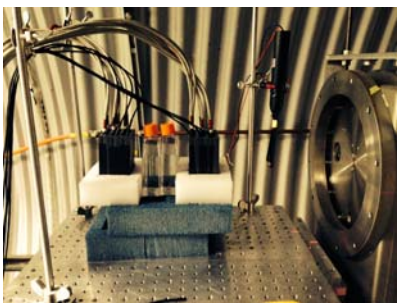

Figure 1: Example of the experimental setup used for 1GeV/u ^{56}Fe at BNL.

In Fig. 2 a map of the single hits on the sensor is shown which reproduce the beam profile.

Fig. 3 shows the different number of pixels fired by different kind of particle species. Some experiments showed a clear dependence of the release energy of the fragments and the pixels/cluster value that can be used to do particle identification.

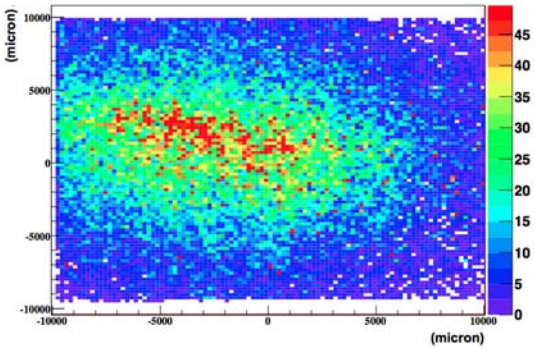

Figure 2: 2D map of the single hits on the CMOS sensor produced by 1GeV/u ^{56}Fe.

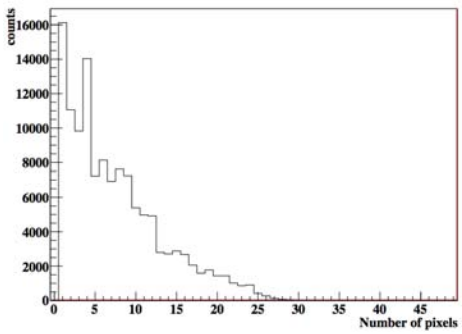

Figure 3: Cluster size distribution for 1 GeV/u ^{56}Fe.

Outlook

The method presented above was verified by experiments using PMMA targets and will be tested with an anthropomorphic phantom in March 2014 at GSI.

References

[1] J. Baudot et al., First test results of MIMOSA-26, a fast CMOS sensor with an integrated zero suppression and digitized output, IEEE Nucl. Sci. Symp. Conf. Rec. (2009) 1169

[2] M. Rovituso et al., Fragmentation of therapeutical carbon ions in bone-like materials, GSI Sci. Rep. 2012

[3] L. Piersanti et al., Measurement of charged particles yields from PMMA irradiated by a 220 MeV/u ^{12}C beam, accepted for publication in PMB 2014

* Work is part of HGS-Hire

 doi:10.15120/GR-2014-1-BIOPHYSICS-50

A phase-space representation of nucleon-nucleon potentials*

D. Weber[1,2], *H. Feldmeier*[1,2,3], *and T. Neff*[1,2]

[1]EMMI, Darmstadt, Germany; [2]GSI, Darmstadt, Germany; [3]FIAS, Frankfurt, Germany

Effective realistic nucleon-nucleon (NN) potentials that do not scatter to high momenta contain momentum dependent contributions. The Argonne potential [1] transformed by means of the Unitary Correlation Operator Method [2], for example, has a quadratic momentum dependence. Interactions arising from the Similarity Renormalization Group (SRG) method [3] show a more complicated momentum dependence, which is, however, not transparent as these potentials are constructed directly in matrix element representation.

To investigate the momentum dependence of NN potentials given by matrix elements, we use the phase-space representation introduced by Kirkwood [4]. In this representation the phase-space distribution $f_{ps}(\vec{r},\vec{p})$ for a density operator ρ and the representation $O_{ps}(\vec{r},\vec{p})$ of an operator $\mathcal{O}$ are given by

$$f_{ps}(\vec{r},\vec{p}) = (2\pi)^{3/2} \left\langle \vec{r}\right|\rho\left|\vec{p}\right\rangle\left\langle \vec{p}\right|\vec{r}\left\rangle \right. \quad (1a)$$

$$O_{ps}(\vec{r},\vec{p}) = (2\pi)^{3/2} \left\langle \vec{r}\right|\mathcal{O}\left|\vec{p}\right\rangle\left\langle \vec{p}\right|\vec{r}\left\rangle, \right. \quad (1b)$$

such that

$$\left\langle \mathcal{O} \right\rangle = \mathrm{Tr}\,(\rho\mathcal{O}) \int \mathrm{d}^3r\mathrm{d}^3p\, f^*_{ps}(\vec{r},\vec{p}) \cdot O_{ps}(\vec{r},\vec{p}). \quad (1c)$$

For a potential given in partial wave matrix elements $\left\langle kLM;S;T\right|\mathbf{V}\left|pLM;S;T\right\rangle$, with the momentum quantum numbers L and M and spin and isospin S and T, Eq. (1b) can be rewritten as

$$V_{ps}(\vec{r},\vec{p}) = 4\pi e^{-i\vec{r}\vec{p}} \sum_{L,M} i^L Y^L_M(\hat{\vec{r}}) {Y^L_M}^*(\hat{\vec{p}}) \times \int_0^\infty \mathrm{d}k k^2 \left\langle kLM;S;T\right|\mathbf{V}\left|pLM;S;T\right\rangle j_L(rk), \quad (2)$$

where Y^L_M is a spherical harmonic and j_L a spherical Bessel function. We describe the angular part of $V_{ps}(\vec{r},\vec{p})$ by an expansion in Legendre polynomials $P_\Lambda(\hat{\vec{r}}\cdot\hat{\vec{p}})$:

$$V_{ps}(\vec{r},\vec{p}) = \sum_\Lambda i^\Lambda V^\Lambda_{ps}(r,p) P_\Lambda(\hat{\vec{r}}\cdot\hat{\vec{p}}). \quad (3)$$

Fig. 1 shows the first terms of this expansion calculated by means of Eq. (2) from the matrix elements of different potentials, namely a local potential $V(\mathbf{r})$, a potential with quadratic momentum dependence, and a potential with quadratic angular momentum dependence. For the local potential, $V_{ps}(\vec{r},\vec{p})$ is just $V(r)$ and the phase-space representation does not depend explicitely on p and the angle between $\vec{r}$ and $\vec{p}$. For the quadratic momentum dependent potential $\mathbf{V} = \frac{1}{2}\left(\vec{\mathbf{p}}^{\,2}V(\mathbf{r}) + V(\mathbf{r})\vec{\mathbf{p}}^{\,2}\right)$ the phase-space representation shows a characteristic quadratic momentum dependence for $\Lambda = 0$ and a $\Lambda = 1$ contribution reflecting the fact that $\vec{\mathbf{r}}$ and $\vec{\mathbf{p}}$ do not commute. All higher Λ-contributions vanish. $V_{ps}(\vec{r},\vec{p})$ of the quadratic angular momentum potential contains terms up to $\Lambda = 2$. Potentials with more complicated momentum dependencies, for example from a SRG transformation, would create contributions also for higher Λ.

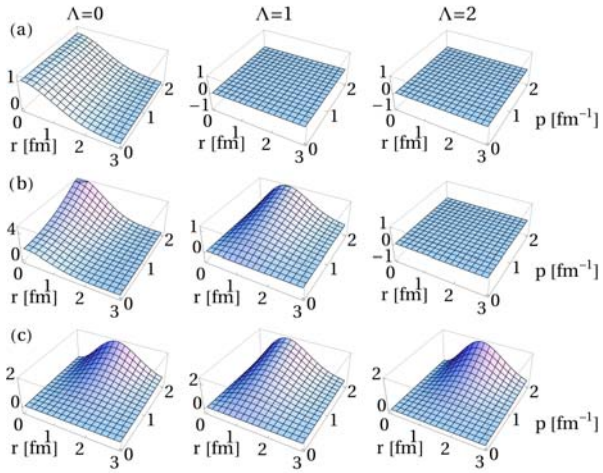

Figure 1: Phase-space representation $V^\Lambda_{ps}(r,p)$ in arbitrary units for (a) $\mathbf{V} = V(\mathbf{r})$, (b) $\mathbf{V} = \frac{1}{2}\left(\vec{\mathbf{p}}^{\,2}V(\mathbf{r}) + V(\mathbf{r})\vec{\mathbf{p}}^{\,2}\right)$, (c) $\mathbf{V} = V(\mathbf{r})\,\vec{\mathbf{L}}^2$. $V(r) = e^{-\frac{r^2}{2\,\mathrm{fm}^2}}$.

These results show that the phase-space representation is able to visualize the (non-) local structure of a potential. In further studies we plan to employ this method to investigate the momentum dependence of various realistic NN potentials given in matrix representation.

References

[1] R. B. Wiringa, V. G. J. Stoks and R. Schiavilla, Phys. Rev. C, 51, 38-51 (1995)

[2] R. Roth, T. Neff and H. Feldmeier, Prog. Part. Nucl. Phys., 65, 50 (2010)

[3] S. K. Bogner, R. J. Furnstahl and R. J. Perry, Phys. Rev. C, 75, 061001 (2007)

[4] J. G. Kirkwood, Phys. Rev., 44, 31 (1933)

* Supported by the Helmholtz Alliance EMMI

The ^{12}C continuum in a microscopic coupled channel calculation*

T. Neff[1,2] *and H. Feldmeier*[1,2,3]

[1]GSI, Darmstadt, Germany; [2]EMMI, Darmstadt, Germany; [3]FIAS, Frankfurt, Germany

For the description of scattering processes and resonances a proper treatment of the continuum is necessary. To achieve such a description in a microscopic many-body approach one has to connect compact configurations that describe the internal part of the wave function with external cluster configurations representing the open channels.

We have developed such an approach within fermionic molecular dynamics (FMD). FMD uses a wave-packet basis that allows to describe the internal parts of the wave function and the external cluster channels on equal footing. The matching to the asymptotic behavior as given by two point-like clusters interacting only via Coulomb is performed in the microscopic R-matrix formalism.

As a first example we discuss the continuum states in ^{12}C. We previously studied ^{12}C in bound state approximation [1]. The focus was on the properties of the Hoyle state, which lies just above the ^{8}Be-^{4}He threshold. Whereas the bound state approximation is expected to work well for a very narrow resonance like the Hoyle state this is no longer true for other resonances like the second 2^+ state. The resonance position and width for this state could only be determined very recently by direct excitation with photons [2]. The existence and the nature of other states in the continuum is still hotly debated.

To address these questions we extend our calculations with a proper treatment of the continuum. Before doing the full FMD calculation a study within the microscopic α-cluster model has been performed. The microscopic cluster model with full antisymmetrization and employing a phenomenological two-body interaction proved to be successful in describing many properties of ^{12}C. In the internal region the Hilbert space is built from three-α configurations on a triangular grid. In the external region ^{8}Be-^{4}He configurations are added. The ^{8}Be eigenstates are obtained in bound state approximation by diagonalizating configurations up to 9 fm distance. Our results will have to be checked for convergence with respect to increasing the number of included ^{8}Be (pseudo-) states. Technically the challenge is related to the restoration of rotational symmetry. First the intrinsic wave functions for ^{8}Be have to be projected on good angular momentum. In a second step the ^{8}Be-^{4}He configurations (with different orientations of the ^{8}Be spin) have to be projected on total angular momentum. For solving the Schrödinger equation with the microscopic R-matrix method, Hamiltonian and norm kernels for the different channels have to be calculated.

In Fig. 1 the calculated phase shifts (from the diagonal matrix elements of the coupled-channel S-matrix) in the 0^+ and 2^+ channels are shown. We included here the ^{8}Be ground state and the first 2^+ state at 3 MeV. In the ^{12}C 0^+ channel the extremely narrow Hoyle state resonance at 300 keV is not resolved when scanning over the energy. Its resonance properties can be calculated by employing Gamow boundary conditions. A second 0^+ resonance at 4 MeV is related to the opening of the ^{8}Be(2^+) channel. As can be seen in the inelasticities (the magnitudes of the diagonal S-matrix elements) there is a strong coupling between the ^{8}Be(0^+) and ^{8}Be(2^+) channels. When adding additional ^{8}Be channels we observe additional resonances in the region above 4 MeV. This might explain the experimental observation of a very broad resonance at 10.3 MeV. In the ^{12}C 2^+ channel a resonance of ^{8}Be(0^+)-^{4}He nature at 1.5 MeV is found. In a next step we will calculate the $B(E2)$ transition strength distribution to compare with the experimental result [2]. Additional resonances again appear after crossing the ^{8}Be(2^+)-^{4}He threshold.

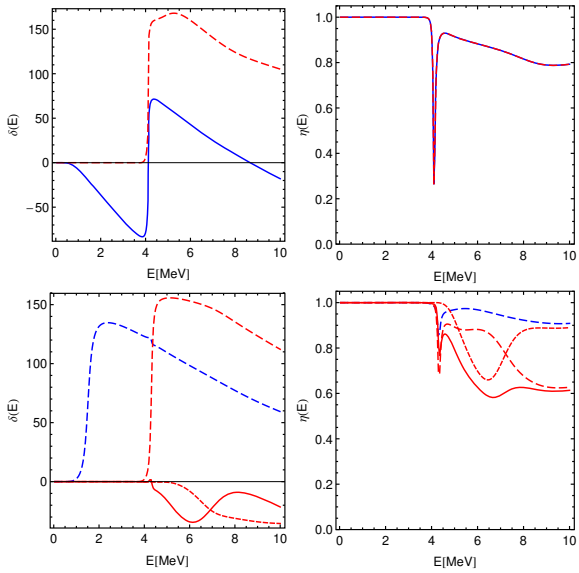

Figure 1: Phase shifts and inelasticity parameters for ^{8}Be-^{4}He scattering in 0^+ (top) and 2^+ channels (bottom). ^{8}Be(0^+) (blue lines) and ^{8}Be(2^+) (red lines) configurations are included.

References

[1] M. Chernykh *et al.*, Phys. Rev. Lett. **98**, 032501 (2007).

[2] W. R. Zimmermann *et al.*, Phys. Rev. Lett. **110**, 152502 (2013).

* Work supported in part by EMMI.

 doi:10.15120/GR-2014-1-THEORY-02

Theory of Nuclear Excitation and their Astrophysical Relevance *

N. Tsoneva[1,2] *and H. Lenske*[1,3]

[1]Institut für Theoretische Physik, Universität Gießen; [2]INRNE, 1784 Sofia, Bulgaria; [3]GSI Darmstadt

New modes of excitation in neutron-rich nuclei are described by an advanced Hartree-Fock-Bogoljubov (HFB) plus multiphonon approach.

Here, we report on recent spectroscopic studies in N=50 isotones based on the Quasiparticle-Phonon Model (QPM). The systematic calculations of dipole strength functions in these nuclei indicate enhanced $E1$ strength in the energy range from 6 to 10 MeV in agreement with the experimental observations [1]. From quasiparticle-random-phase approximation (QRPA) calculations, the energy region below E*$\leq$9 MeV is related to the pygmy dipole resonance (PDR) which total strength smoothly decreases with increasing charge number Z closely correlated with the thickness of the neutron skin. We point out that the QRPA is unable to account for the detailed description of the dipole strength function. However, three-phonon QPM calculations can reproduce the fine stucture of the latter fairly well as it follows from the comparison with the experiment [1]. Such precise knowledge of nuclear response functions is very important for the determination of photonuclear reactions cross sections for the astrophysics.

The microscopic strength functions have been implemented successfully into statistical reaction codes to investigate n-capture cross sections of astrophysical importance [2]. Our recent result on the n-capture cross section of the reaction ^{85}Kr(n,γ)^{36}Kr [2] is shown in Fig. 1. As seen, the microscopic calculations are in a very good agreement with the experimental data on the one hand and the HFB+combinatorial results on the other hand [2]. This agreement is confirming the predictive power of involved many-body theoretical methods like the QPM for exploratory investigations of n-capture reaction rates in hitherto experimentally inaccessible mass regions.

Recently, the fine structure of the $M1$-Giant Resonance (GR) in the nuclide ^{90}Zr was investigated [3]. Measurements performed in the range 7-11 MeV reveal a $M1$ resonance structure with centroid energy of 9 MeV and a summed strength of 4.5(4) μ_N^2. These data are fully reproduced in three-phonon QPM calculations [3]. The theoretical investigations which are presented in Fig. 2 indicate a strong increase of the contribution of the orbital part of the magnetic moment due to coupling of multiphononon states. Of special interest is the behavior of the M1 strength at higher energies close to and above the neutron-separation energy where the experimental accessibility is strongly reduced. For these regions, the theory predicts the existence

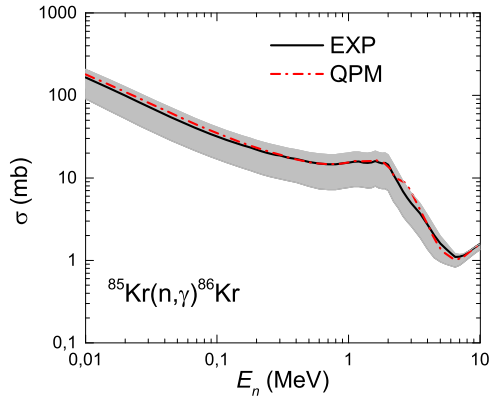

Figure 1: (color online) Cross section of $^{85}Kr^g(n,\gamma)^{86}$Kr calculated with TALYS using experimental dipole (in black) and QPM strength functions (in red) from Ref. [1]. The predicted uncertainties (shaded area) are derived from the experimental errors of the dipole strength function and from variations in the nuclear level density parameters.

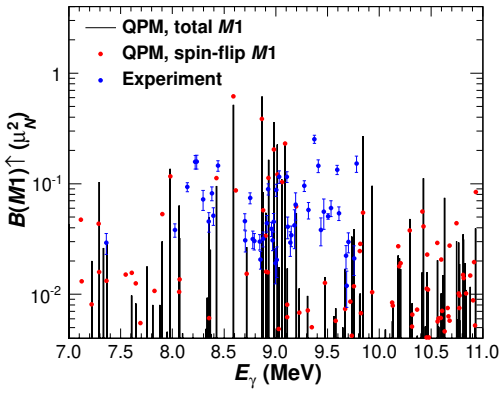

Figure 2: (color online) The measured M1 strength of discrete 1^+ levels in ^{90}Zr compared with three-phonon QPM predictions from Ref. [3].

of a strongly fragmented M1 strength with summed value of several μ_N^2. The latter is a very interesting finding which sheds light to the understanding of the long-standing problem with the quenching and dynamics of the M1 strength.

References

[1] R. Schwengner et al., Phys. Rev. **C 87**, 024306 (2013).

[2] R. Raut et al., Phys. Rev. Lett. **111**, 112501 (2013).

[3] G. Rusev et al., Phys. Rev. Lett. **110**, 022503 (2013).

* Work supported by the HIC for FAIR, GSI-JLU Giessen collaboration agreement, and BMBF Project No. 06GI9109.

Charged-current interactions for muon neutrinos in supernova*

A. Lohs[1,2], *G. Martínez-Pinedo*[1,2], *and T. Fischer*[3]

[1]Institut für Kernphysik (Theoriezentrum), Technische Universität Darmstadt, Darmstadt, Germany; [2]GSI-Helmholtzzentrum für Schwerionenforschung, Darmstadt, Germany; [3]Institute for Theoretical Physics, University of Wrocław, Wrocław, Poland

A core collapse supernova is emitting most of it's energy, up to 10^{53} erg in form of neutrinos of all flavours. The microphysics of neutrino transport is therefore an important ingredient to understand this astrophysical scenario. Present supernova simulations do not include charged current weak interaction for muon type neutrinos. These reactions are considered to be suppressed due to the large Q-value of the muon mass. As a consequence the spectra of muon and tau-type neutrinos is the same. Also the difference between ν_μ and $\bar{\nu}_\mu$ is minor. However, in the interior of a proto-neutron star chemical potentials and temperatures are large enough in the first seconds to allow for production of muons. Using conditions that were taken from 1D hydrodamical supernova simulations with full Boltzmann neutrino transport [1], we have derived and calculated the following reactions:

$$\nu_\mu + n \rightarrow p + \mu^- \qquad \nu_\mu + e^- \rightarrow \nu_e + \mu^-$$
$$\nu_\mu + \bar{\nu}_e + e^- \rightarrow \mu^- \qquad \bar{\nu}_e + e^- \rightarrow \bar{\nu}_\mu + \mu^-$$

The ν_μ-absorption on neutrons is calculated in analogy to absorption of electron-neutrinos [2, 3]. The three leptonic processes are derived similar to neutrino scattering on electrons [4, 5, 6]. We find that especially the absorption of ν_μ on neutrons and on electrons is a significant opacity source in the region where the neutrinos decouple energetically from the matter, at densities above 10^{13} g/cm^3.

We argue that charged current opacities for ν_μ will probably change the respective neutrino spectrum so it might differ significantly from the other heavy-neutrino flavours.

* Work supported GSI, HIC for FAIR, H-QM

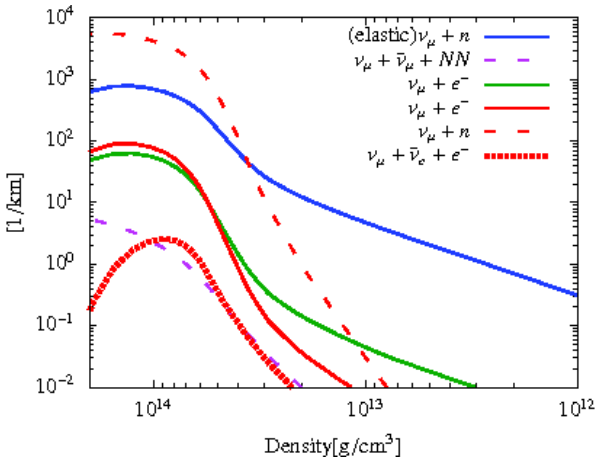

Figure 1: Spectraly averaged inverse mean free path of ν_μ

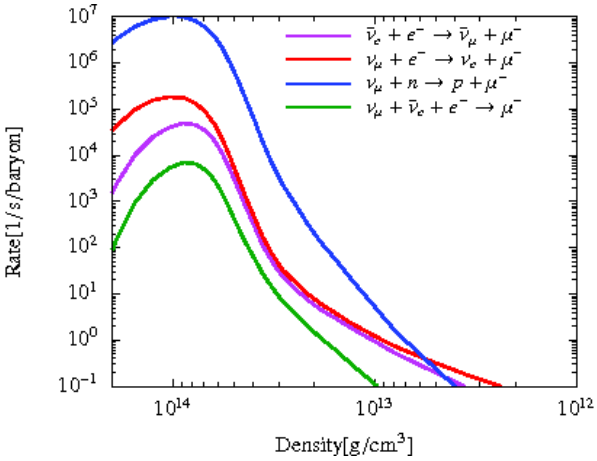

Figure 2: Rate of μ^--production per baryon per second

We also find that the production timescale of muons is comparably fast to the dynamical timescale. Muons will be in chemical equilibrium already at bounce. This should lead to the production of a positive net muon number in the core of the PNS. Also, once muons are present the charged current reactions contribute significantly to the equilibration of ν_μ of all energies. Eventually this might affect the deleptonization timescale of the PNS. The changes in the spectra could further be important for neutrino oscillations especially since the oscillations are sensitive to spectral differences. Finally we suggest that muonic charged current reactions should be implemented in future dynamical simulations of core collapse supernova to study their effects and to achieve an improved understanding of ν_μ spectra formation.

References

[1] T. Fischer, *et al.*, Astronomy and Astrophysics, **517** (2010), A80

[2] S. Reddy, M. Prakash, and J.M. Lattimer, Phys. Rev. D **58**, 013009 (1998)

[3] A.W. Steiner, M. Prakash, and J.M. Lattimer, Phys. Lett. B **509**, (2001), 10

[4] W.R. Yueh, J.R. Buchler, Astrophysics & Space Science, **41**, (1976), 221

[5] P.J. Schinder, S.L. Shapiro, ApJS, **50**, (1982), 23

[6] A. Mezzacappa, S.W. Bruenn, Astrophysical Journal, **410**, (1993), 740

 doi:10.15120/GR-2014-1-THEORY-04

Finite temperature pasta matter with the TDHF approximation *

B. Schuetrumpf[1], *M. A. Klatt*[2], *K. Iida*[3], *J. A. Maruhn*[1], *K. Mecke*[2], *and P.-G. Reinhard*[2]

[1]Institut für Theoretische Physik, Universität Frankfurt, D-60438 Frankfurt, Germany; [2]Institut für Theoretische Physik, Universität Erlangen-Nürnberg, D-91058 Erlangen, Germany; [3]Department of Natural Science, Kochi University, 2-5-1 Akebono-cho, Kochi 780-8520, Japan

Core-collapse supernova are relevant, e.g., for the synthesis of heavy nuclei and the formation of neutron stars. In such explosions, densities up to the nuclear saturation density as well as temperatures up to about $40\,\mathrm{MeV}$ are reached. If the mean nuclear density reaches about 10% of the nuclear saturation density, the matter forms rods to lower its surface energy. A further increase of density leads to slabs and even to inverted pasta, where the low density gas phase has the shape of the described pasta phases. Pasta shapes can be relevant e.g. for neutrino scattering which is important for the heat transport in a supernova or proto-neutron star.

The pasta matter is investigated here with the time-dependent Hartree-Fock approximation (TDHF) with the code explained in [1]. The wave functions on a 3d grid with periodic boundary conditions are evolved in time with finite time steps of $\Delta t = 0.1\,\mathrm{fm/c}$. For the present calculation a cubic box was taken with a lattice spacing of $1\,\mathrm{fm}$ and a box length of $16\,\mathrm{fm}$.

As initial conditions α-particles are distributed randomly in space keeping a minimal distance between them and in momentum space with a Maxwell-Boltzmann distribution. Free background neutrons are added as plane wave states with Fermi distribution of momenta. The setups are evolved in time until topological stability is reached. Then the temperature is roughly estimated with a Fermi gas approximation.

Fig. 1 exemplifies the emerging shapes, ordered by the mean density at which they appear. At low mean densities nearly spherical nuclei and "rods", infinitely long in one dimension, are found. "Rod(2)" and "rod(3)" are shapes where two or three rods are connected pointing in perpendicular directions. Note that for the slab shape which is doubly periodic and the rod(3) shape the gas and liquid phases are topologically identical. For higher volume fractions, the corresponding bubble shapes appear. All shapes can be uniquely classified by two simple scalar measures of the surface profile (Minkowski scalars), namely the integral mean curvature and the Euler number [2].

Figure 2 shows the map of the resulting pasta shapes. For the lowest temperature the shapes are well ordered. Pasta shapes exist for high temperatures at low densities. But the temperature for the transition to uniform matter decreases with increasing density.

*This work was supported by the BMBF under contract number 05P12RFFTG, DFG for the grant ME1361/11 and by Grants-in-Aid for Scientific Research on Innovative Areas through No. 24105008 provided by MEXT. The calculations have been performed on the cluster of the Center for Scientific Computing of the Goethe-Universität Frankfurt.

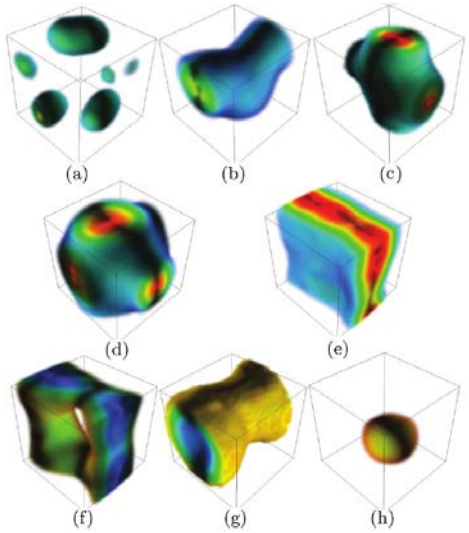

Figure 1: Shapes of pasta structures. Bubble shape illustrations show gas phase, indicated by the color-scale [from $0.03\,\mathrm{fm}$ (blue/light gray) to $0.12\,\mathrm{fm}$ (red/dark gray)]. (a) Sphere. (b) Rod. (c) Rod(2). (d) Rod(3). (e) Slab. (f) Rod(2) bubble. (g) Rod bubble. (h) Sphere bubble. This figure is taken from Ref. [2].

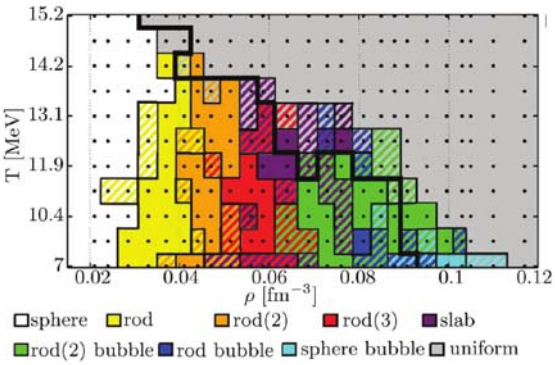

Figure 2: Map of pasta shapes for various temperatures and mean densities. Each dot represents two calculations. This figure is taken from Ref. [2].

References

[1] J. A. Maruhn, P.-G. Reinhard, P. D. Stevenson, and A. S. Umar, Comp. Phys. Comm. **to appear** (2014),arXiv:1310.5946

[2] B. Schuetrumpf, M. A. Klatt, K. Iida, J. A. Maruhn, K. Mecke, and P.-G. Reinhard, Phys. Rev. C **87**, 055805 (2013)

Symmetry energy of nuclear matter with liquid-gas phase transition and cluster formation*

S. Typel[1], *H.H. Wolter*[2], *G. Röpke*[3], *and D. Blaschke*[4,5]

[1]GSI Helmholtzzentrum für Schwerionenforschung, Darmstadt, Germany; [2]Ludwig-Maximilians-Universität München, Germany; [3]Institut für Physik, Universität Rostock, Germany; [4]Instytut Fizyki Teoretycznej, Uniwersytet Wrocławski, Poland; [5]Bogoliubov Laboratory for Theoretical Physics, JINR Dubna, Russia

The symmetry energy $E_{\rm sym}$ characterizes the energy change of strongly interacting matter when the isospin asymmetry δ is varied and all other independent quantities such as the baryon density n_B or temperature T are kept constant. The density dependence of $E_{\rm sym}$ is widely studied in experiment and theory since its precise form has a strong impact on the evolution of core-collapse supernovae and the structure and cooling of (proto) neutron stars.

For nuclear matter, the symmetry energy is usually calculated by assuming a uniform distribution of the constituent particles. However, dilute nuclear matter is not stable against density fluctuations and inhomogeneous matter on different length scales develops. E.g., at densities below saturation, clusters or macroscopic phases appear, which affect the actual density dependence of $E_{\rm sym}$. At finite temperatures, the symmetry free energy $F_{\rm sym}$ and the symmetry internal energy $U_{\rm sym}$ have to be distinguished. In addition, the results depend on the precise definition of the symmetry energy. These effects are studied in Ref. [1] using a relativistic density functional (RDF) approach with density dependent meson-nucleon couplings. The parameters of this phenomenological description are well constrained by fitting to properties of finite nuclei [2].

In nuclear matter at densities below saturation, the liquid-gas phase transition with coexisting low and high density phases was explicitly considered in the determination of the symmetry energy. As an example, the density dependence of $U_{\rm sym}$ for various temperatures is depicted in Figure 1 employing the finite difference formula, i.e. taking the difference of the energy per nucleon in pure neutron matter and in symmetric nuclear matter. This is equivalent to the standard definition using second derivatives with respect to the asymmetry δ only if the energy per nucleon is a quadratic function of δ. However, the former, finite difference definition gives more appropriate results for studying the variation of the energy with isospin. The liquid-gas phase transition leads to a substantial increase of the binding energy in symmetric nuclear matter due to the occurrence of a strongly bound high density phase. Hence a large finite symmetry energy is observed in particular at low temperatures even at very low densities.

In stellar matter, not only the strong interaction between the particles but also the electromagnetic interaction, which is artificially switched off in nuclear matter calculations, has to be considered. The charge neutrality condition is ensured by adding electrons and muons in proper amounts. The interplay between the surface tension and Coulomb repulsion leads to cluster formation on typical length scales with the size of nuclei. The RDF approach for nuclear matter has been extended to a generalized RDF with explicit cluster degrees of freedom [1, 2] including internal excitations of nuclei. Besides light (^{2}H, ^{3}H, ^{3}He, ^{4}He) and heavy nuclei ($A > 4$), nucleon-nucleon correlations in the continuum are included in an effective way [3]. They are necessary in order to reproduce the model-independent low-density benchmark, the virial equation of state. The formation and dissolution of cluster correlations are modeled by medium-dependent mass shifts, which are mainly driven by the action of the Pauli principle. With proper corrections for the effects of the Coulomb interaction, the symmetry energy in stellar matter exhibits similar features as in nuclear matter with liquid-gas phase transition.

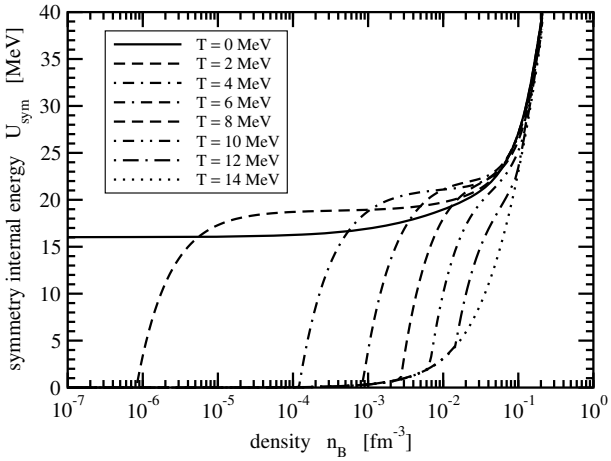

Figure 1: Density dependence of the symmetry internal energy of nuclear matter with liquid-gas phase transition for various temperatures.

References

[1] S. Typel, H.H. Wolter, G. Röpke and D. Blaschke, Eur. Phys. J. A 50 (2014) 17.

[2] S. Typel, G. Röpke, T. Klähn, D. Blaschke, and H.H. Wolter, Phys. Rev. C 81 (2010) 015803.

[3] M.D. Voskresenskaya and S. Typel, Nucl. Phys. A 887 (2012) 42.

*Work supported by the Helmholtz Association through the Nuclear Astrophysics Virtual Institute (VH-VI-417).

 doi:10.15120/GR-2014-1-THEORY-06

The chiral condensate in neutron matter *

T. Krüger[1,2], *I. Tews*[1,2], *B. Friman*[3], *K. Hebeler*[1,2], *and A. Schwenk*[2,1]

[1]IKP, Technische Universität Darmstadt, Darmstadt, Germany; [2]EMMI, GSI, Darmstadt, Germany; [3]GSI, Darmstadt, Germany

The chiral condensate is an order parameter for characterizing the chiral phase transition in dense and hot strongly interacting matter. Owing to the fermion sign problem, there are no first-principle QCD results for the phase diagram at low temperatures and high densities, the conditions probed in neutron stars. Recent observations of neutron stars with $2\,M_\odot$ masses provide general constraints on the equation of state (EOS) of cold strongly interacting matter, and put into question whether exotic phases that tend to soften the EOS are realized in neutron stars. At densities $n \lesssim n_0$, where $n_0 = 0.16\,\mathrm{fm}^{-3}$ denotes nuclear saturation density, the properties of nuclear systems have been studied systematically based on nuclear forces derived within chiral effective field theory and using renormalization group methods. In this work, we use chiral EFT interactions to study the chiral condensate as a function of density in neutron matter, based on perturbative calculations around the first-order Hartree-Fock energy.

The chiral condensate in neutron matter relative to the vacuum is given by [1]

$$\frac{\langle\bar{q}q\rangle_n}{\langle\bar{q}q\rangle_0} = 1 - \frac{n}{f_\pi^2}\frac{\sigma_{\pi N}}{m_\pi^2}\left(1 - \frac{3k_F^2}{10m_N^2} + \ldots\right) - \frac{n}{f_\pi^2}\frac{\partial}{\partial m_\pi^2}\frac{E_{\rm int}(m_\pi, k_F)}{N}\,. \quad (1)$$

The leading $\sigma_{\pi N}$ contribution to the chiral condensate in Eq. (1), which is due to the mass term in $E_{\rm free}/N$, is linear in density and is shown in Fig. 1 by the dashed line. For the density range shown in Fig. 1, where chiral EFT interactions can be applied with confidence, the kinetic energy contribution is only a 4% correction relative to the leading term, while relativistic corrections, indicated by the dots in Eq. (1), are negligible at these densities [1].

We calculate the explicit m_π dependence of nuclear forces by varying the value of the pion mass in the pion-exchange NN, 3N, and 4N interactions. At the NN level, we use the N^{3}LO potentials of Epelbaum, Glöckle, and Meißner [2] with cutoffs 450/500 and 450/700 MeV. With these NN interactions neutron matter is perturbative at the densities considered here [3, 4].

We find that nuclear interactions impede the restoration of chiral symmetry in neutron matter at zero temperature. The net effect of interactions remains below 10% for $n \lesssim 0.2\,\mathrm{fm}^{-3}$, but grows with increasing density. The dominant source of uncertainty is the $\sigma_{\pi N}$ term. We conclude that for moderate densities, say $n \lesssim 0.3\,\mathrm{fm}^{-3}$, a chiral phase transition in neutron-rich matter therefore seems unlikely, although we cannot exclude a strong first-order transition. For the densities considered here, we find a good convergence of the chiral condensate from N^{2}LO to N^{3}LO in chiral EFT. It would be very interesting to calculate the chiral condensate also for higher densities. While a systematic calculation in chiral EFT is difficult at densities much higher than $n = 0.2\,\mathrm{fm}^{-3}$, astrophysical observations provide valuable constraints.

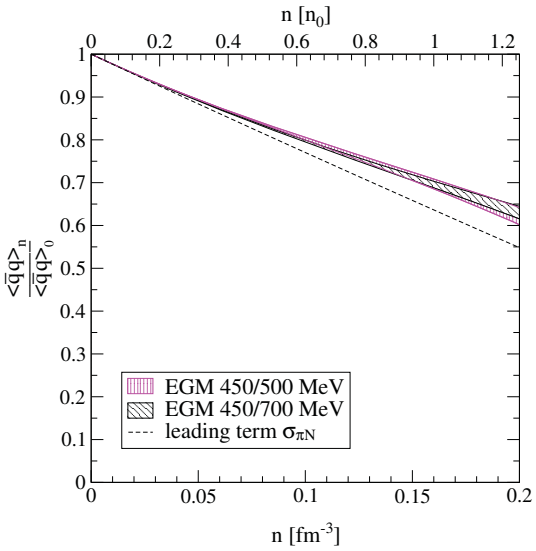

Figure 1: Chiral condensate $\langle\bar{q}q\rangle_n/\langle\bar{q}q\rangle_0$ as a function of density in neutron matter [1]. The dashed line is the leading pion-nucleon sigma-term contribution. The interaction contributions are obtained from the N^{3}LO neutron-matter calculation of Refs. [3, 4]. The bands for each NN potential include uncertainties of the many-body calculation, of the c_i couplings of 3N forces, and those resulting from the 3N/4N cutoff variation.

References

[1] T. Krüger, I. Tews, B. Friman, K. Hebeler, A. Schwenk, Phys. Lett. B276, 412 (2013).

[2] E. Epelbaum, W. Glöckle, and Ulf-G. Meißner, Eur. Phys. J. A 19, 401 (2004); Nucl. Phys. A 747, 362 (2005).

[3] I. Tews, T. Krüger, K. Hebeler, and A. Schwenk, Phys. Rev. Lett. **110**, 032504 (2013).

[4] T. Krüger, I. Tews, K. Hebeler, and A. Schwenk, Phys.Rev. C88, 025802 (2013).

* Work supported in part by EMMI, by the ERC Grant No. 307986 STRONGINT and by the DFG through SFB 634.

A low-energy effective model for quantum chromodynamics*

J. Berges[1] *and D. Gelfand*[1]
[1]University of Heidelberg, Heidelberg, Germany

In a low-energy effective model for quantum chromodynamics, we studied the real-time dynamics in a linear sigma model coupled to two light quark flavors. We found a dramatic amplification of quark production in the presence of highly occupied bosonic quanta for weak as well as strong effective couplings. For the mesonic sector we confirmed the existence of a turbulent scaling regime, known from previous studies of purely mesonic effective theories. Using for the first time real-time lattice field theory techniques with dynamical fermions in 3+1 dimensions, we demonstrated the failure of standard semiclassical descriptions based on the Dirac equation with a homogeneous background field to capture these phenomena [1].

To get a more detailed picture of quark dynamics and to test our approach we considered the range of validity of different methods: lattice simulations with male/female fermions, the mode functions approach and the quantum 2PI effective action with its associated kinetic theory. For strongly coupled quarks we found a rapid approach to a Fermi-Dirac distribution with time-dependent temperature and chemical potential parameters [2], while the mesons are still far from equilibrium.

We employed and improved the available real-time lattice techniques in order to investigate fermion–anti-fermion production in gauge theory, considering $1+1$ dimensional QED. In this non-perturbative approach the full quantum dynamics of fermions is included while the gauge field dynamics can be accurately represented by classical-statistical simulations for relevant field strengths. We computed the non-equilibrium time evolution of gauge invariant correlation functions implementing 'low-cost' Wilson fermions. Introducing a lattice generalization of the Dirac-Heisenberg-Wigner function, we recovered the Schwinger formula in $1+1$ dimensions in the limit of a static background field. We discuss the decay of the field due to the backreaction of the created fermion–anti-fermion pairs and apply the approach to strongly inhomogeneous gauge fields [3]. The latter allows us to discuss the striking phenomenon of a linear rising potential building up between produced fermion bunches after the initial electric pulse ceased and its decay, a phenomenon closely related to string-breaking in quantum chromodynamics.

Following these investigations we focused on the real-time dynamics of string breaking in quantum electrodynamics in one spatial dimension. A two-stage process with a clear separation of time and energy scales for the fermion–antifermion pair creation and subsequent charge separation leading to the screening of external charges was found [4]. Going away from the traditional setup of external static charges, we established the phenomenon of multiple string breaking by considering dynamical charges flying apart.

References

[1] J. Berges, D. Gelfand and J. Pruschke, Phys. Rev. Lett. **107** 061301 (2011)

[2] J. Berges, D. Gelfand and D. Sexty, Phys. Rev. D **89**, 025001 (2014)

[3] F. Hebenstreit, J. Berges and D. Gelfand, Phys. Rev. D **87**, 105006 (2013)

[4] F. Hebenstreit, J. Berges and D. Gelfand, Phys. Rev. Lett. **111** 201601 (2013)

* Work supported by HIC4FAIR/EMMI

 doi:10.15120/GR-2014-1-THEORY-08

Probing deconfinement with Polyakov loop susceptibilities *

Pok Man Lo[†1], *Bengt Friman*[1], *Olaf Kaczmarek*[2], *Krzysztof Redlich*[3], *and Chihiro Sasaki*[4]

[1]GSI, Darmstadt, Germany; [2]Universität Bielefeld, Bielefeld, Germany; [3]University of Wroclaw, Wrocław, Poland; [4]Frankfurt Institute for Advanced Studies, Frankfurt am Main, Germany

Deconfinement can be described by the spontaneous breaking of Z(3) center symmetry. The relevant quantities to study are the Polyakov loop and its susceptibilities. The Polyakov loop reflects the free energy of a static quark immersed in a hot gluonic medium. At low temperatures its thermal expectation value vanishes, signaling color confinement, while at high temperatures it is nonzero, resulting in a finite energy of a static quark and consequently the deconfinement of color. It is thus an order parameter for the deconfining phase transition.

The Polyakov loop susceptibility, on the other hand, represents fluctuations of the order parameter. It exhibits a peak at the transition temperature, and a width that signals the temperature window in which the phase transition takes place. While the basic thermodynamic functions of the SU(3) pure gauge theory, such as pressure and entropy, are well established within the lattice approach, the temperature dependence of the renormalized Polyakov loop and its susceptibilities are less clear. A careful study of these quantities will improve our understanding of the QCD phases.

In SU(3) gauge theory, the Polyakov loop is a complex-valued operator. One can therefore explore the fluctuations of the order parameter along the longitudinal (real) and transverse (imaginary) directions. However, the proper renormalization for these composite gluonic correlators remains ambiguous. One way to circumvent this problem is to consider the ratios of susceptibilities [1].

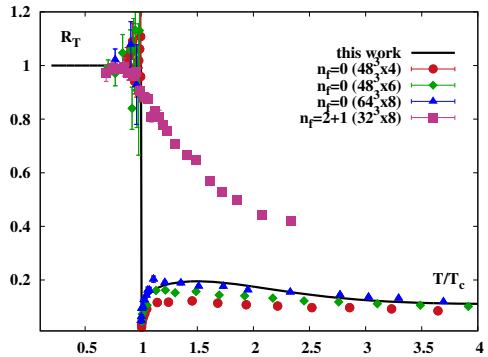

Figure 1: The ratio of Polyakov loop susceptibilities, $R_T = \chi_T/\chi_L$, in pure gauge system and in (2+1)-flavor QCD. The temperature is normalized to the (pseudo)critical value in each system. The lines show the results of the Polyakov loop model [2].

Fig. 1 shows the temperature dependence of the ratio of the transverse and longitudinal Polyakov loop susceptibilities, obtained in SU(3) gauge theory and in (2+1)-flavor QCD [2]. In the pure gauge limit ($N_f = 0$), the ratio R_T is discontinuous at T_c, and change only weakly with temperature on either side of the transition. This feature makes the ratio ideal for probing deconfinement. At high temperatures, the Z(3) symmetry is spontaneously broken. The pure gauge result indicates a small value for this ratio. In terms of an effective potential, this finding suggests that, around the global minimum associated with the symmetry-broken vacuum, the curvature in the transverse direction is much steeper than that in the longitudinal direction.

In the presence of light quarks, the Polyakov loop is no longer a true order parameter for deconfinement owing to the explicit breaking of the Z(3) symmetry. The ratio is smoothened and vary continuously across the pseudocritical temperature. One expects that the width of the crossover transition depends on the number of flavors and the values of quark masses. The value of R_T at high temperatures is found to deviate substantially from the pure gauge limit. An interpretation of this feature is still lacking.

We conclude that the ratio of Polyakov loop susceptibilities provides an excellent signal for the deconfinement phase transition. One immediate application of this work is to constrain the parameters used in effective models, thus providing a more realistic description of the QCD phase structure [2]. Further, more detailed lattice calculations are needed in order to obtain robust results for the gluonic correlation functions, as well as a better understanding of the systematic uncertainties.

References

[1] P. M. Lo, B. Friman, O. Kaczmarek, K. Redlich, and C. Sasaki, Phys. Rev. D **88** (2013) 014506.

[2] P. M. Lo, B. Friman, O. Kaczmarek, K. Redlich, and C. Sasaki, Phys. Rev. D **88** (2013) 074502.

* Work supported in part by FIAS and EMMI.

† pmlo@gsi.de

QCD phase structure and conserved charge fluctuations in a chiral effective model*

P. Rau[1], *J. Steinheimer*[1], *S. Schramm*[1], *and H. Stöcker*[2]
[2]GSI, Darmstadt, Germany; [1]FIAS, Goethe University, Frankfurt

Using the well-established chiral effective model for QCD matter, which includes all known hadrons up to $m = 2.6$ GeV and quarks, this study examines the phase structure of QCD matter and fluctuations of conserved charges focussing on the chiral and deconfinement phase transition. At small baryochemical potentials the effective model shows a smooth cross over in both order parameters and, at larger potentials, does not give indications for the existence of a first order phase transition and a critical end point. Compared to lattice QCD and thermal model fits of experimental data the chiral transition from the effective model is in line with recent data (Fig. 1).

At the phase transition conserved charges show large fluctuations which can be measured by susceptibility coefficients χ. Baryon number fluctuations are largely suppressed by the finite volume of hadrons and the suppressive particle interactions with vector fields (Fig. 2). It shows that in the hadronic phase below T_c coupling strengths are of the order of the nucleon couplings. However, in the quark sector above T_c, large fluctuations found in lattice QCD restrain quark vector couplings close to zero and particles at $T > T_c$ are almost acting like an ideal gas. With this model a realistic equation of state has been compiled which can be used for studying heavy ion collisions in dynamic models as well as neutron star properties.

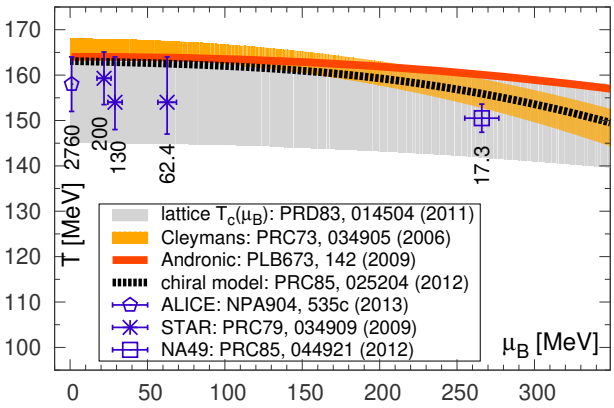

Figure 1: Chiral transition at small μ_B from lattice QCD (gray band) and from the chiral model (black line) contrasted to freeze-out curves from statistical and thermal model fits for SPS to LHC energies ($\sqrt{s_{\rm NN}}$ in GeV).

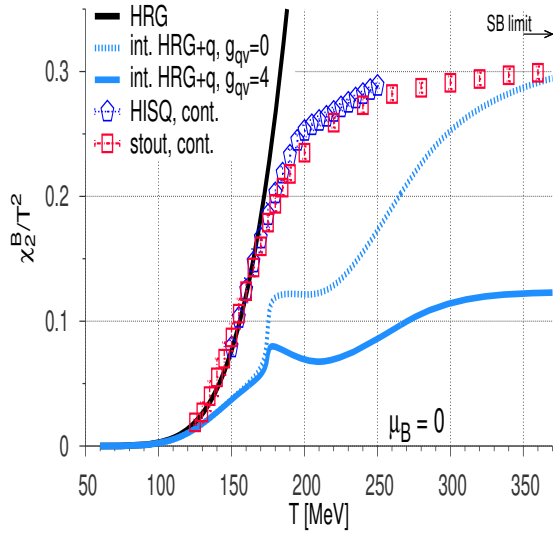

Figure 2: Second-order baryon number susceptibility of the hadron resonance gas (black line) and of the full model including hadrons and quarks (blue lines). Strong vector couplings suppress fluctuations and the Stefan-Boltzmann limit at high T may only be reached for vanishing quark vector couplings $g_{\rm qv}$ (dashed blue line).

Related publications in 2013:

1. P. Rau, J. Steinheimer, S. Schramm and H. Stöcker, *Chiral Hadronic Mean Field Model including Quark Degrees of Freedom*, J. Phys. G **40**, 085001 (2013).

2. P. Rau, J. Steinheimer, S. Schramm and H. Stöcker, *Conserved Charge Fluctuations in a Chiral Hadronic Model including Hadrons and Quarks*, arXiv:1308.4319 [hep-ph] (to be published in PLB).

* Work supported by HIC4FAIR

 doi:10.15120/GR-2014-1-THEORY-10

The role of fluctuations in the phase diagram of two color QCD*

N. Khan[1,2], *J. Pawlowski*[1,2], *F. Rennecke*[1,2], *and M. Scherer*[1,2]
[1]GSI, Darmstadt, Germany; [2]Universität Heidelberg, Germany

The investigation of the phase diagram of Quantum Chromodynamics (QCD) at finite temperature and density is an area of very active experimental and theoretical research [1] due to the existence of a variety of symmetry broken phases, the transitions between them and the presence of strong interactions. A straightforward application of lattice methods is inhibited by the property that for nonzero chemical potential the path integral measure of the QCD Lagrangian is complexAn instructive way to approach the full problem and to shed light on particular aspects is the investigation of deformations of QCD [2]. Generally, this can be achieved by changing e.g. mass parameters, symmetries or the field content. In this work, we will choose the latter two possibilities and study a theory similar to real QCD, however with two colors, $N_c = 2$, and two quark flavors $N_f = 2$. An appealing feature within this two-color two-flavor version of QCD is that, apart from the chirally broken mesonic phase of quark-antiquark pairs, it allows for the formation and (Bose-Einstein-) condensation of colorless diquarks, i.e. a bosonic baryon state. This results in a rich phase diagram with two dynamically competing order parameters.

In this work we employ a functional renormalization group (FRG) approach to an effective quark-meson-diquark model to study the phase diagram of two-color QCD. The FRG method is a suitable tool for the systematic study of (strongly) interacting field theories allowing for the formulation and computation of non-perturbative approximation schemes.The present work systematically extends the truncation scheme in Ref. [3] by taking into account the scale dependence of the wave function renormalizations as well as the renormalization of the Yukawa coupling between the quarks and the order parameter fields. Additional quantitative effects can be accessed systematically by extensions of the truncation scheme within the FRG. Here, we can monitor the quantitative corrections that are induced by the additional scale dependent quantities, namely the wave function renormalizations as well as the Yukawa interaction and study their impact on the phase diagram. Due to an alternative expansion scheme for the effective potential we gain direct access to the phenomenon of precondensation, a regime in the phase diagram where order occurs at intermediate scales but no order is found when all fluctuations are integrated out. In this way, we establish a refined picture of the FRG phase diagram for QC_2D, which is shown in Fig.1.

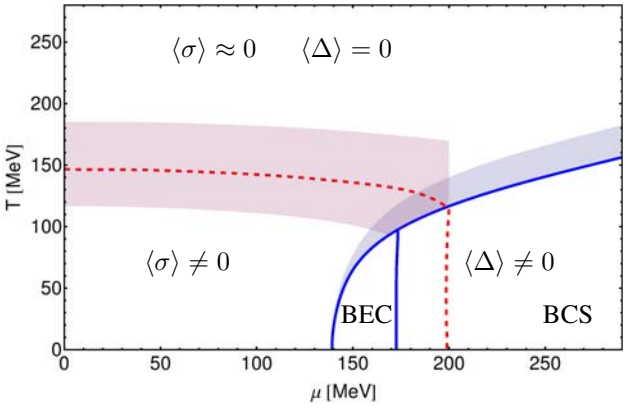

Figure 1: The phase daigram of QC_2D. μ is the baryon chemical potential in this plot.

The condensates are determined by the minimum of an order parameter potential, which is truncated to a one dimensional Taylor expansion up to six-point interaction terms. In addition, we have added a linear term in the chiral condensate σ, which causes chiral symmetry always to be broken, this is rooted in the fact that quarks have a small but finite current mass. At small temperatures and chemical potentials chiral symmetry is broken and quarks have a constituent mass of about 300 MeV. With increasing temperature the system undergoes a smooth crossover where chiral symmetry is nearly restored. The line and the shaded area in the left part of the figure mark the crossover and its width. At higher μ the system undergoes a second order phase transition at the onset of the diquark condensate Δ. At first the system is in BEC like state while at the limit of high chemical potentials the system spproaches a BCS like state. The line where the quark mass drops below the chemical potential indicates the region of the BEC-BSC crossover. The shaded area in the right part indicates the precondensation phase.

For the future this result is to be compared to lattice simulations, in order to evaluate our methods and truncation schemes.

References

[1] P. Braun-Munziger and J. Wambach, Rev. Mod. Phys. 81, 1031 (2009)

[2] L. von Smekal, Nucl. Phys. Proc. Suppl. 228, 179 (2012)

[3] N. Strodhoff, B.-J. Schaefer and L. von Smekal Phys. Rev. D85. 074007 (2012)

* Work supported by Helmholtz Alliance HA216/EMMI and by ERC-AdG-290623.

Higher order quark-mesonic scattering processes and the phase structure of QCD*

J. M. Pawlowski[1,2] *and F. Rennecke*[1,2]
[1]Universität Heidelberg, Germany; [2]GSI, Darmstadt, Germany

We study the chiral phase transition of two-flavor quantum chromodynamics (QCD) at finite temperature T and quark chemical potential μ [1]. At not too large chemical potential, the chiral dynamics in the vicinity of the phase boundary are driven by the lightest hadronic states, the pions and the sigma meson. Thus, in order to arrive at a quantitative picture of the matter sector of QCD, these mesonic degrees of freedom need to be taken into account accurately. We therefore employ a linear quark-meson model which captures spontaneous chiral symmetry breaking $SU(N_f)_L \otimes SU(N_f)_R \to SU(N_f)_V$. Quantum fluctuations are included by means of the functional renormalization group. The scale dependent effective action reads [2]:

$$\Gamma_k = \int_x \Big\{ iZ_{\psi,k}\bar{\psi}(\gamma_\mu\partial_\mu + \gamma_0\mu)\psi + \frac{1}{2}Z_{\phi,k}(\partial_\mu\phi)^2 + V_k(\rho) - c\sigma + h_k(\rho)\bar{\psi}(\gamma_5\vec{\tau}\vec{\pi} + i\sigma)\psi \Big\}, \quad (1)$$

where $\rho = \phi^2/2 = \vec{\pi}^2 + \sigma^2$. We systematically study the effect of higher order multi-meson as well as quark-antiquark multi-meson scattering processes on the chiral phase structure of QCD by expanding the effective potential $V_k(\rho)$ and the field-dependent Yukawa coupling $h_k(\rho)$ in powers of ρ. This corresponds to an expansion of the effective action Γ_k in terms of n-point functions. We observe that these higher order operators play a quantitatively important role for the chiral phase transition. Furthermore, the expansions of both, the effective potential and the Yukawa coupling, converge rapidly. This implies that we have good control over the quantitative precision of our results. For the effect of different parts of the truncation (1) on the phase boundary, see Fig. 1.

As a result of the explicit chiral symmetry breaking $-c\sigma$, which is directly related to finite current quark masses, we observe a crossover phase transition. The transition temperature/chemical potential in this case is not uniquely defined and we therefore compare different definitions of the phase boundary. Fig. 2 shows the resulting phase diagram. We find a crossover transition for $\mu < 291$ MeV. The large deviations in the transition temperatures between different definitions of the phase boundary indicate a very broad crossover. We note that the same is true for the curvature of the phase boundary at vanishing density. The crossover transition gets steeper towards the critical endpoint which we find at $(T_c, \mu_c) = (50, 291)$ MeV.

* Work supported by Helmholtz Alliance HA216/EMMI and by ERC-AdG-290623

For the future this analysis can be used as a starting point for studies aiming towards full QCD, including baryonic degrees of freedom as well as the gauge sector of QCD.

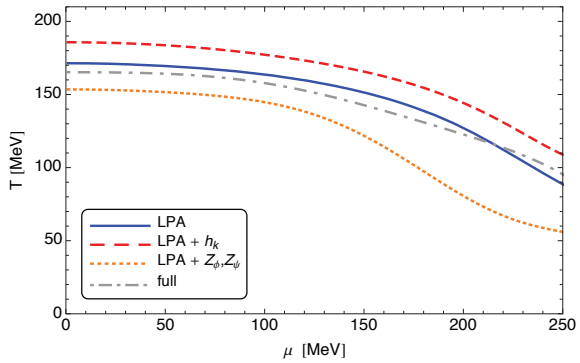

Figure 1: The crossover phase boundary for different truncations. LPA denotes the quark-meson model with only a running effective potential. The dot-dashed curve shows the full result of (1).

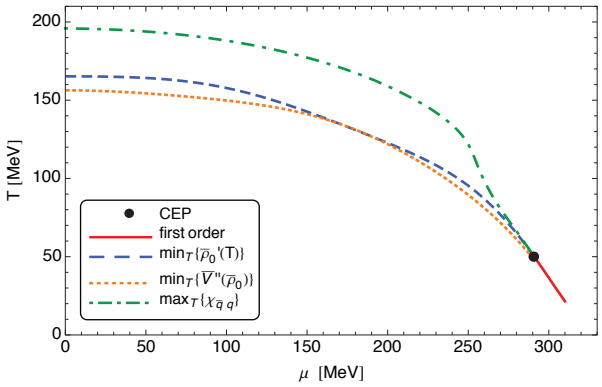

Figure 2: The phase diagram of the chiral transition of QCD. The crossover transition was extracted from three different quantities: the minimum of the effective potential (dashed), the quartic meson coupling (dotted) and the chiral susceptibility (dot-dashed).

References

[1] P. Braun-Munzinger and J. Wambach, "Colloquium: Phase diagram of strongly interacting matter", Rev. Mod. Phys. 81, p. 1031 (2009)

[2] J. M. Pawlowski and F. Rennecke, "Higher order quark-mesonic scattering processes and the phase structure of QCD", `hep-ph/1403.1179` (2014)

 doi:10.15120/GR-2014-1-THEORY-12

Inhomogeneous condensation in nuclear matter*

Achim Heinz, Francesco Giacosa, and Dirk H. Rischke
ITP, Frankfurt am Main, Germany

Introduction

Spontaneous breaking of chiral symmetry is a nonperturbative phenomenon in the QCD vacuum as well as at low temperature and densities. Hadronic theories of the low energy regime have to take this into account [1]. Chiral symmetry breaking appears in the hadron spectrum as a mass splitting of so-called chiral partners.

A re-occurring topic in the literature is the possibility that the order parameter for the chiral transition is a function of spatial coordinate [2]. A fruitful Ansatz to describe inhomogeneous condensation is the chiral-density wave (CDW).

We re-investigate the question of inhomogeneous condensation at nonzero density in the extended Linear Sigma Model (eLSM) where the baryons are introduced as parity doublets [3, 4]. The eLSM successfully describes hadron vacuum phenomenology both in the meson and baryon sector, it is therefore a natural choice for non-zero density studies including the CDW [5].

Non-zero density study

In the two-flavor case, $N_f = 2$, the scalar and pseudoscalar mesons are described by the matrix

$$\Phi = (\sigma + \imath\eta_N)t_0 + (\vec{a}_0 + \imath\vec{\pi}) \cdot \vec{t}\,,$$

and the vector and axial-vector mesons by

$$V^\mu = \omega^\mu t_0 + \vec{\rho}^\mu \cdot \vec{t}\,, \;\; A^\mu = f_1^\mu t_0 + \vec{a}_1^\mu \cdot \vec{t}\,,$$

where $\vec{t} = \vec{\tau}/2$, with the vector of Pauli matrices $\vec{\tau}$, and $t_0 = \mathbf{1}_2/2$. The model is invariant under the chiral group $SU(2)_R \times SU(2)_L$. The chiral condensate $\phi = \langle\sigma\rangle = Z f_\pi$ emerges upon spontaneous chiral symmetry breaking in the mesonic sector, where $f_\pi \simeq 92.4$ MeV is the pion decay constant and $Z \simeq 1.67$ is the wave-function renormalization constant of the pseudoscalar fields.

We now make the following Ansatz for the condensates, which is of the form of a chiral-density wave:

$$\langle\sigma\rangle = \phi\cos(2fx)\,, \langle\pi\rangle = \phi\sin(2fx)\,, \qquad (1)$$

In the limit $f \to 0$ we obtain the usual homogeneous condensation.

The baryons are introduced as two parity doublets Ψ_1 and Ψ_2, which transform according to the mirror assignment:

$$\Psi_{1,R} \to U_R\,\Psi_{1,R}\,, \qquad \Psi_{1,L} \to U_L\,\Psi_{1,L}\,, \qquad (2)$$

$$\Psi_{2,R} \to U_L\,\Psi_{2,R}\,, \qquad \Psi_{2,L} \to U_R\,\Psi_{2,L}\,. \qquad (3)$$

The mirror assignment allows for an additional chirally invariant mass term [6]:

$$m_0\left(\bar{\Psi}_{1,L}\Psi_{2,R} - \bar{\Psi}_{1,R}\Psi_{2,L} - \bar{\Psi}_{2,L}\Psi_{1,R} + \bar{\Psi}_{2,R}\Psi_{1,L}\right)\,. \qquad (4)$$

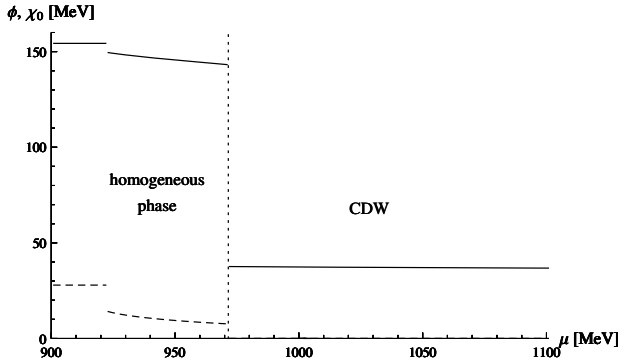

Figure 1: The condensates ϕ and $\bar{\chi}$ are shown as functions of μ.

In Fig. 1 the condensates ϕ and $\bar{\chi}$ are shown as functions of μ. For $\mu = 923$ MeV a first-order phase transition to the nuclear matter ground state takes place and at $\mu = 973$ MeV a transition to the CDW phase occurs. In terms of density, the onset of inhomogeneous condensation is at $2.4\rho_0$. Then, a mixed phase is realized between $2.4\rho_0$ to $10.4\rho_0$. However somewhere in the mixed phase the deconfinement phase transition should occur.

Outlook

Further studies of the model at zero and non-zero densities should be performed to test for general forms of inhomogeneous condensation. The eLSM should be extended to $N_f = 3$ in the baryon sector.

References

[1] S. Gasiorowicz et al. Rev. Mod. Phys. **41**, 531 (1969).

[2] A. B. Migdal, Rev. Mod. Phys. **50**, 107 (1978).

[3] D. Parganlija et al. Phys. Rev. D **82**, 054024 (2010);

[4] S. Gallas et al. Phys. Rev. D **82**, 014004 (2010).

[5] A. Heinz et al. arXiv:1312.3244 [nucl-th].

[6] C. DeTar et al. Phys. Rev. D **39**, 2805 (1989).

* Work supported by HGS-HIRe and HIC4FAIR.

Pions in a strong magnetic background *

G. Colucci† [1], *E. S. Fraga*[2], *and A. Sedrakian*[1]

[1]Institute for Theoretical Physics, J. W. Goethe-University, D-60438 Frankfurt am Main, Germany; [2]Instituto de Física, Universidade Federal do Rio de Janeiro, Caixa Postal 68528, Rio de Janeiro, RJ 21945-970, Brazil

We investigate the modification of the pion self-energy at finite temperature due to its interaction with a low-density, isospin-symmetric nuclear medium embedded in a constant magnetic background.

Nuclear matter in strong magnetic fields

The study of nuclear matter under strong magnetic fields has acquired a lot of attention during the last years in the contexts of heavy ion collision physics and lattice QCD [1]. In Ref. [2] we investigate some properties of isospin-symmetric nuclear matter in the limit of low density and temperature, embedded in a strong magnetic background. In particular, we compute the in-medium pion effective mass in the presence of a constant magnetic field to one loop. For this purpose, we consider fully relativistic chiral perturbation theory as a framework for our computation. This is needed to define consistently the fermion propagators in a magnetic background.

Pion self-energy in strong magnetic fields

The leading order interaction Lagrangian, which describe the low-energy phenomenology of nuclear matter, $\mathcal{L}^{(1)}_{\pi N}$, reads [3]

$$\mathcal{L}^{(1)}_{\pi N} = -\bar{\Psi}\left[\frac{g_A}{2f_\pi}\gamma^\mu\gamma_5\tau\cdot\partial_\mu\pi + \frac{1}{4f_\pi^2}\gamma^\mu\tau\cdot(\pi\times\partial_\mu\pi)\right]\Psi. \quad (1)$$

Here τ is the vector of Pauli matrices in isospin space, π is the isotriplet of pions, f_π the pion decay constant and g_A is the axial-vector coupling.

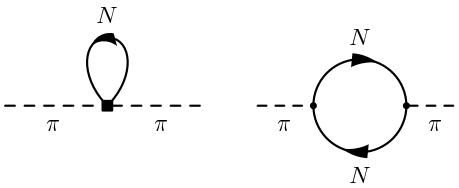

Figure 1: Diagrams contributing to the lowest-order in-medium pion self-energy.

The diagrams contributing to the pion self-energy from the Lagrangian (1) are shown in Fig. 1.

The effective pion mass is defined as:

$$m_\pi^{*\,2} = m_\pi^2 - \mathrm{Re}\,\Pi(m_\pi^{*\,2}, \mathbf{q}=0; \mathbf{B}) + (2n+1)|eB|\,, \quad (2)$$

where $\Pi(q)$ is the pion self-energy, $\mathbf{B}$ is the magnetic field and n is the index of the Landau level. The following results are computed within the lowest-Landau-level (LLL) approximation, which is valid for very intense magnetic fields.

Results

Fig. 2 displays our results for the pion effective mass, $\overline{m}_\pi$, as a function of the magnetic field, normalized to the trivial $|eB|$ shift in Eq. (2).

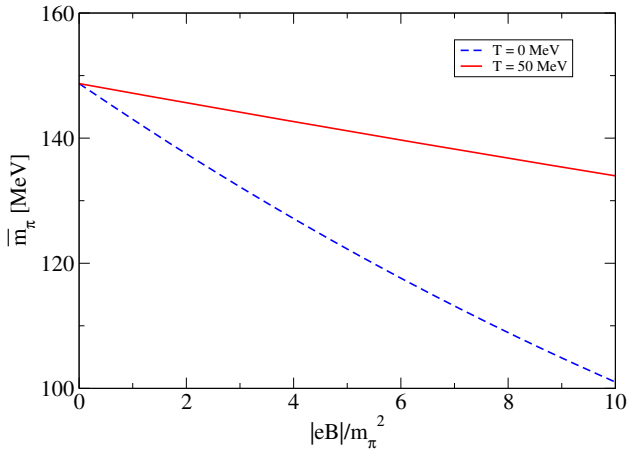

Figure 2: (Color online) Effective pion mass as a function of the magnetic field.

We find that the effective mass of the negatively charged pion drops by $\sim 10\%$ for a magnetic field $|eB| \sim m_\pi^2$, which favors pion condensation at high density and low temperatures.

References

[1] Dmitri Kharzeev, Karl Landsteiner, Andreas Schmitt, and Ho-Ung Yee. Strongly Interacting Matter in Magnetic Fields. *Lect.Notes Phys.*, 871:1–624, 2013.

[2] G. Colucci, E. S. Fraga and A. Sedrakian, Phys. Lett. B **728** (2014) 19

[3] R. Machleidt and D. R. Entem. Chiral effective field theory and nuclear forces. *Physics Report*, 503:1–75, June 2011.

* The work of GC was supported by the HGS-HIRe graduate program at Frankfurt University. The work of ESF was financially supported by the Helmholtz International Center for FAIR within the framework of the LOEWE program (Landesoffensive zur Entwicklung Wissenschaftlich-Ökonomischer Exzellenz) launched by the State of Hesse.

† colucci@th.physik.uni-frankfurt.de

 doi:10.15120/GR-2014-1-THEORY-14

Investigating the Transition Between Hydrodynamics and Transport *

D. Oliinychenko[1,3], *P. Huovinen*[2], *and H. Petersen*[1,2]

[1]Frankfurt Institute for Advanced Studies, Frankfurt am Main, Germany; [2]Institut für Theoretische Physik, Goethe Universität Frankfurt, Frankfurt am Main, Germany; [3]Bogolyubov Institute for Theoretical Physics, Kiev, Ukraine

Hybrid (hydrodynamics+transport) models are well suited to describe the dynamics of heavy ion collisions. However, there are common technical issues within such models that remain unsolved. In particular the established procedure of transforming hydrodynamics to transport by sampling particles according to the positive contributions of the Cooper-Frye equation [1] results in violating conservation laws. Typically, the hope is that small negative contributions will not influence the final results too much. The goal of our study is to explore the applicability range of this approach. We systematically investigate the behavior of Cooper-Frye negative contributions, in particular their dependence on hadron sort, collision energy (we consider the energy range of $\sqrt{s_{NN}} = 2-20$ GeV) and the criterion for the transition.

The negative contributions are calculated in two different ways: (I) hydro-based, assuming local thermal equilibrium and (II) particle-based, out of equilibrium. For this purpose many UrQMD events are generated and obtained particle trajectories are used to calculate the energy-momentum tensor $T^{\mu\nu}(t,x,y,z)$ on a space grid. In each grid cell the energy momentum tensor is transformed to the Landau rest frame (LRF) and a surface of constant LRF energy density is generated: $T^{00}_{LRF}(t,x,y,z) = \epsilon_0$, where ϵ_0 is an arbitrary parameter varied in the range 0.3 - 0.6 GeV/fm^3. Such surface mimics a typical transition surface that is used in hybrid models. Temperature and chemical potentials on the surface are obtained from a hadron gas equation of state. The negative contributions on this surface are calculated (I) from Cooper-Frye formula and (II) explicitly counting underlying particles.

The main results are as follows. The ratio of negative to positive contributions $x = [dN^-/dy]/[dN^+/dy]$ decreases with particle mass. It also decreases with collision energy as illustrated by Fig.1. In Fig. 1 one can also see that the value of x at midrapidity is 12 % at $E = 10$ AGeV while at $E = 160$ AGeV it is already around 3 % . It was found that x slightly grows with ϵ_0 and considerably increases at forward and backward rapidity if smooth transition surface is perturbed. This may be important for event-by-event calculations. Finally, x tends to be smaller for out of equilibrium "by particle" calculation than for Cooper-Frye calculation.

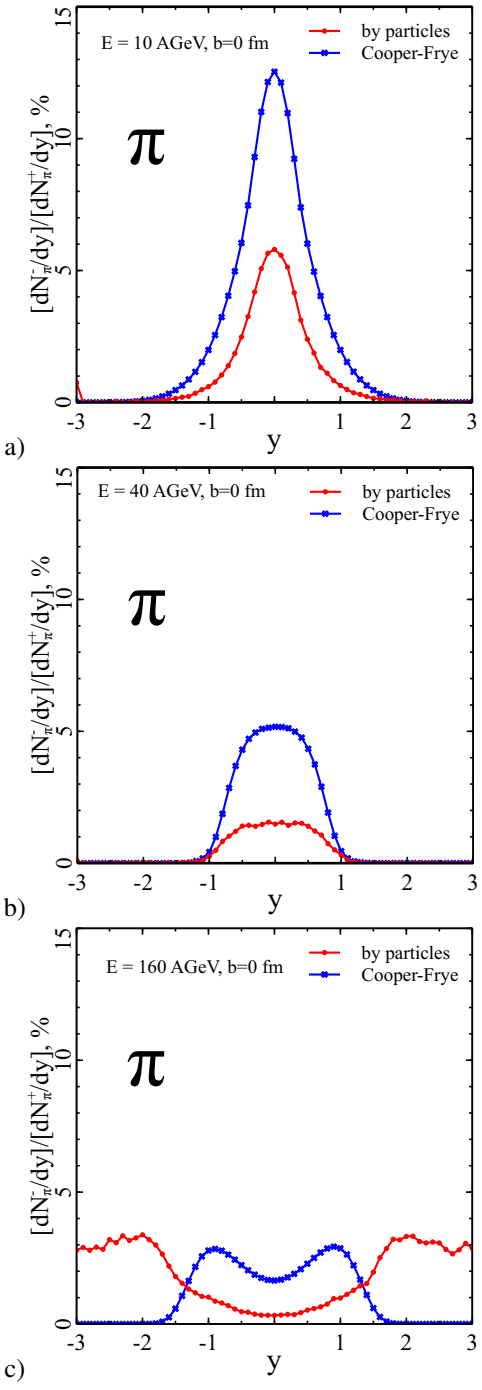

Figure 1: Negative contributions rapidity distribution for pions in central Au+Au collisions. $\epsilon_0 = 0.3$ GeV/fm^3. Crosses denote Cooper-Frye calculation while circles are "by-particle" calculation. Collision energy is a): $E = 10$ AGeV, b): $E = 40$ AGeV, c): $E = 160$ AGeV

References

[1] F. Cooper, G. Frye, Phys. Rev. D 10, 186, 1974

* Work supported by HIC for FAIR and Helmholtz-Nachwuchsgruppe VH-NG-822.

Collision Energy Evolution of Elliptic and Triangular Flow in a Hybrid Model*

J. Auvinen[1] *and H. Petersen*[1,2]

[1]Frankfurt Institute for Advanced Studies, Frankfurt am Main, Germany; [2]Institut für Theoretische Physik, Goethe Universität Frankfurt, Frankfurt am Main, Germany

We have studied the collision energy dependence of elliptic flow v_2 and triangular flow v_3 in Au+Au collisions within the energy range $\sqrt{s_{NN}} = 5 - 200$ GeV, utilizing a transport + hydrodynamics hybrid model [1,2]. The transport part is described by the Ultrarelativistic Quantum Molecular Dynamics (UrQMD), combined with an intermediate (3+1)-dimensional ideal hydrodynamical evolution phase using a chiral model equation of state. This approach provides a consistent framework for investigating both high-energy heavy ion collisions with negligible net-baryon density and a large hydrodynamically evolving medium, and the collisions at smaller energies with finite net-baryon density, where the hydrodynamics phase is very short-lived or does not exist at all.

The hybrid model reproduces the qualitative behavior of the experimentally measured elliptic flow (see Fig. 1(a)). While v_2 produced by hydrodynamics is considerably diminished at lower collision energies, this decrease is partially compensated by the transport dynamics, as shown in Fig. 1(b). The pre-hydrodynamics transport phase is of particular importance for understanding the collision energy evolution, while the hadronic rescatterings after the hydrodynamical phase contribute more systematically $\sim 10\%$ to the total flow at all energies. However, the viscous matter described by transport dynamics is unable to produce triangular flow, which consequently shows a significantly larger relative decrease in midcentral collisions with decreasing $\sqrt{s_{NN}}$ (Fig. 1(c)). Our conclusion is that the triangular flow provides the clearer signal for the formation of low-viscous fluid in heavy ion collisions.

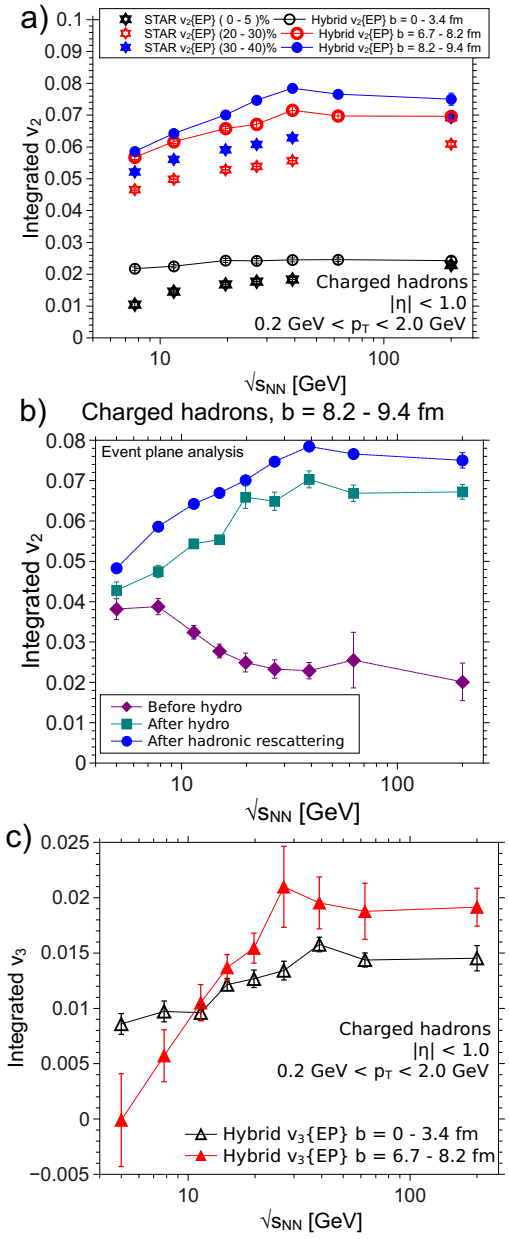

Figure 1: a): Integrated elliptic flow $v_2\{\mathrm{EP}\}$ for charged hadrons with $0.2 < p_T < 2.0$ at midrapidity $|\eta| < 1.0$ in Au+Au -collisions, for collision energies $\sqrt{s_{NN}} = 7.7 - 200$ GeV and three different impact parameter ranges, compared with the STAR data [3, 4]. b): Magnitude of $v_2\{\mathrm{EP}\}$ in midcentral collisions ($b = 8.2 - 9.4$ fm) at the beginning of hydrodynamical evolution (diamonds), immediately after the end of hydrodynamics phase (squares) and after the full simulation (circles). c): Integrated $v_3\{\mathrm{EP}\}$ in central collisions ($b = 0 - 3.4$ fm, open triangles) and midcentral collisions ($b = 6.7 - 8.2$ fm, solid triangles).

References

[1] J. Auvinen and H. Petersen, "Collision Energy Evolution of Elliptic and Triangular Flow in a Hybrid Model", PoS CPOD 2013 (2013) 034

[2] J. Auvinen and H. Petersen, "Evolution of elliptic and triangular flow as a function of collision energy in a hybrid model", Phys. Rev. C 88 (2013) 064908

[3] L. Adamczyk *et al.* [STAR Collaboration], "Inclusive charged hadron elliptic flow in Au + Au collisions at $\sqrt{s_{NN}}$ = 7.7 - 39 GeV", Phys. Rev. C 86 (2012) 054908

[4] J. Adams *et al.* [STAR Collaboration], "Azimuthal anisotropy in Au+Au collisions at $\sqrt{s_{NN}}$ = 200-GeV", Phys. Rev. C 72 (2012) 014904

* Work supported by HIC for FAIR and Helmholtz-Nachwuchsgruppe VH-NG-822. Computational resources have been provided by the Center for Scientific Computing (CSC) at Goethe Universität Frankfurt.

 doi:10.15120/GR-2014-1-THEORY-16

Initial conditions, hadronization and transport coefficients in heavy-ion collisions*

R. Marty[1], *E. Bratkovskaya*[1], *W. Cassing*[2], *and J. Aichelin*[3]
[1]FIAS, Frankfurt, Germany; [2]ITP, Giessen, Germany; [3]Subatech, Nantes, France

Introduction

The study of the properties of the Quark-Gluon Plasma (QGP) – formed in heavy-ion collisons – requires to understand how the initial quark and gluon distributions affect the final observables through the expansion and hadronization phases.

Initial conditions

The issue of initial conditions in relativistic heavy-ion collisions is a subject of intensive debate. Especially the assumption of thermal equilibrium after ∼1 fm/c is currently not supported by microscopic transport approaches. In our study we compare the Parton-Hadron-String Dynamics (PHSD) with the novel transport approach RSP (Relativistic quantum molecular dynamics for Strongly interacting matter with Phase transition or crossover) – based on the Nambu–Jona-Lasinio (NJL) model [1] – employing the same initial conditions from PHSD, which have a 'lumpy' energy density profile (see Fig. 1).

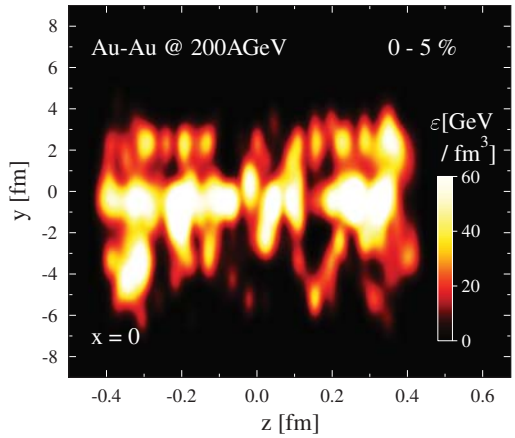

Figure 1: Initial energy density for cells in the local rest frame in the $y - z$ plane.

Comparison

Although we have the same initial energy density profile, the transport properties of bulk partonic matter in RSP and in PHSD are not the same [2]. The main difference between both approaches is that RSP uses light quarks which convert into hadrons using NJL cross sections, and that PHSD uses heavy partons (quarks and gluons) which combine into heavy hadrons with broad spectral functions which then decay into light hadrons.

The comparison of final hadronic observables (Fig. 2) shows that the initial parton distribution must be out of equilibrium in both approches (PHSD/RSP) in order to reproduce the multiplicity spectra dN/dp_T and $dN/d\eta$ and the elliptic flow v_2 for Au+Au at RHIC energies.

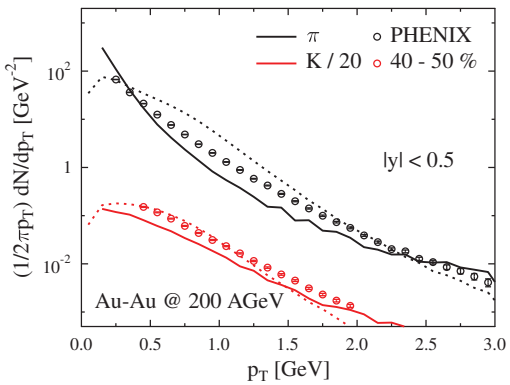

Figure 2: Transverse momentum distribution dN/dp_T of final charged pions and kaons in RSP (full lines) and PHSD (dashed lines).

Out of equilibrium

The conversion of fluid cells from one model to another – both out of equilibrium – keeps the interesting properties of the initial state: the anisotropy in momentum in p_T/p_z, the chemical mixture of species, and the particle density shift (for a given energy density in a cell, the equation of state gives a particle density which is not the one we really have in this cell in the out of equilibrium calculations).

Conclusion

This study shows the importance of non-equilibrium dynamics for the microscopic description of the quark-gluon-plasma created in heavy-ion collisions.

References

[1] R. Marty, J. Aichelin, Phys. Rev. C 87, 034912 (2013)

[2] R. Marty, E. Bratkovskaya, W. Cassing, J. Aichelin and H. Berrehrah, Phys. Rev. C 88, 045204 (2013)

* Work supported by the HIC for FAIR framework of the LOEWE program and the LOEWE-CSC for computational resources.

On- and off-shell heavy quark transport properties in the quark-gluon plasma*

H. Berrehrah[1], *E. Bratkovskaya*[1], *W. Cassing*[2], *P.B. Gossiaux*[3], *and J. Aichelin*[3]

[1]Frankfurt Institute for Advanced Studies; [2]Institut für Theoretische Physik, Giessen; [3]Subatech, Nantes, France

Within the aim of a dynamical study of on- and off-shell heavy quarks Q in the quark gluon plasma (QGP) - as produced in relativistic nucleus-nucleus collisions - we study the heavy quark collisional scattering on partons of the QGP and the underlying transport properties.

The collisional scattering cross sections σ^Q_{elas} are evaluated for perturbative partons (massless on-shell particles) and for dynamical quasi-particles (massive off-shell particles as described by the dynamical quasi-particles model "DQPM") using the leading order Born diagrams [1]. Figure 1 shows the elastic cross section of charm quark on a "u" quark as a function of $\sqrt{s}$, the energy in the c.m.s. of the collision for different temperatures. Comparing the DpQCD (Dressed pQCD) and IEHTL (Infrared Enhanced HTL) models where the partons have the DQPM pole masses in the first and are off-shell quasi-particles dressed by DQPM spectral functions in the second, we demonstrate that the finite width of the quasi-particles in the DQPM has little influence on σ^Q_{elas} except close to thresholds. The size of σ^Q_{elas} is dominated by the infrared regulator which in the finite temperature medium is determined by a dynamical gluon mass.

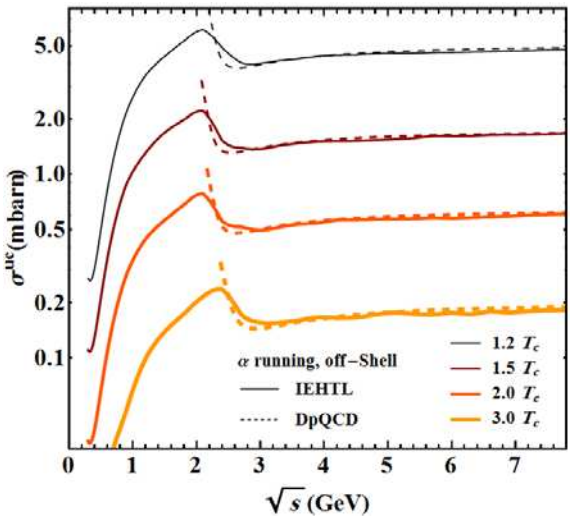

Figure 1: Elastic cross section of $uc \rightarrow uc$ for off-shell (solid lines) and on-shell partons (dashed lines) as a function of $\sqrt{s}$ for different temperatures.

Based on σ^Q_{elas} in a finite temperature medium [1], the on- and off-shell heavy quark dynamical collisional energy loss and transport coefficients are computed [2,3]. As an example, the charm drag coefficient is shown in figure 2 where both the on- and off-shell partons are employed. The Q momentum dependence of the drag is small in the non-perturbative models DpQCD/IEHTL compared to a pQCD calculations (HTL-GA with α constant or running). Our comprehensive comparison between perturbative and non-perturbative QCD based models shows out significant differences for the different Q transport characteristics. Nevertheless, our conclusion is that an explicit transport calculations in comparison to experimental data are needed to pin down the appropriate scenario, since the microscopic ingredients and the QGP background description are coupled and are specific to each model. The Q scattering cross sections and transport properties [1-3] will form the basis of a consistent study of the heavy quark dynamics in heavy-ion collisions at SPS, RHIC and LHC energies by implementing the partonic processes into the PHSD transport approach.

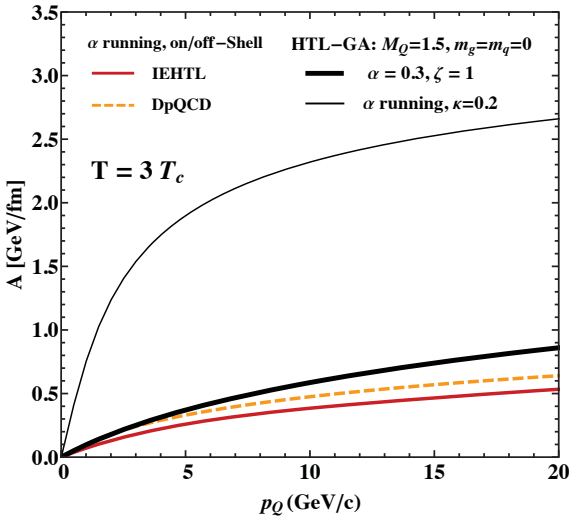

Figure 2: c-quark drag coefficient A from non-perturbative approaches DpQCD/IEHTL and the perturbative model HTL-GA as a function of the c-quark momentum.

References

[1] H. Berrehrah, E. Bratkovskaya, W. Cassing, P.B. Gossiaux, J. Aichelin and M. Bleicher, *arXiv:1308.5148 [hep-ph].*

[2] H. Berrehrah, E. Bratkovskaya, W. Cassing, P.B. Gossiaux, J. Aichelin, *arXiv:1311.0736 [hep-ph].*

[3] H. Berrehrah, E. Bratkovskaya, W. Cassing, P.B. Gossiaux, J. Aichelin., "Dynamical collisional energy loss and transport properties of on-shell and off-shell heavy quarks in vacuum and in the Quark-Gluon Plasma, *To be published.*

* Work supported by the HIC for FAIR framework of the LOEWE program and the LOEWE-CSC for computational resources.

 doi:10.15120/GR-2014-1-THEORY-18

Studies of jet quenching within a partonic transport model*

F. Senzel[1], *O. Fochler*[1], *J. Uphoff*[1], *Z. Xu*[2], *and C. Greiner*[1]

[1]Institut für Theoretische Physik, Johann Wolfgang Goethe-Universität, Max-von-Laue-Str. 1, D-60438 Frankfurt am Main, Germany; [2]Department of Physics, Tsinghua University, Beijing 100084, China

Jet quenching is one of the most promising phenomena for investigating hot and dense matter created in ultra-relativistic heavy-ion collisions at RHIC and LHC. Among the observables for characterizing the energy loss of a high-p_t parton are the suppression of particle spectra defined in terms of the nuclear modification factor R_{AA} [1] and the momentum imbalance A_J [2] of reconstructed di-jets. Both observables show a significant modification within heavy-ion collisions in comparison with p+p collisions [1, 2].

Within this report we show our progress in understanding jet quenching within the partonic transport model BAMPS [3], which numerically solves the 3+1D relativistic Boltzmann equation for quarks and gluons. While employing a running coupling $\alpha_s(t)$ evaluated at the momentum transfer of the respective, microscopic collision, BAMPS uses screened leading-order pQCD cross sections for the elastic $2 \to 2$ collisions and matrix elements calculated in a recently developed, improved Gunion-Bertsch approximation [4] for the inelastic $2 \leftrightarrow 3$ processes

$$\left|\overline{\mathcal{M}}_{X\to Y+g}\right|^2 = \left|\overline{\mathcal{M}}_{X\to Y}\right|^2 48\pi\alpha_s(k_\perp^2)\,(1-\bar{x})^2 \left[\frac{\mathbf{k}_\perp}{k_\perp^2} + \frac{\mathbf{q}_\perp - \mathbf{k}_\perp}{(\mathbf{q}_\perp - \mathbf{k}_\perp)^2 + m_D^2\,(\alpha_s(k_\perp^2))}\right]^2, \quad (1)$$

in which problems of the original GB matrix element [5] at non-zero rapidity of the emitted gluon are cured [4]. Since BAMPS is a classical transport model, the quantum Landau-Pomeranchuk-Migdal (LPM) effect is effectively implemented by a theta function $\theta(\lambda - X_{LPM}\,\tau_f)$ in the radiative matrix elements, where λ is the mean free path of the radiating parton and τ_f the gluon formation time.

After fixing the LPM parameter $X_{LPM} = 0.3$ by comparing to RHIC data, Fig. 1 shows the nuclear modification factor within BAMPS for gluons and quarks at LHC [6]. Additionally, the R_{AA} of charged hadrons obtained via a folding with AKK fragmentation functions is shown. The same X_{LPM} value for LHC simulations does not only describe the suppression of inclusive particle spectra, both at RHIC and LHC, nicely but also explains the momentum imbalance of reconstructed di-jets as shown in Fig. 2 [7].

Since BAMPS provides the full 3+1D microscopic information of all particles also studies of bulk observables like e.g. the elliptic flow v_2 are possible. Recently, these studies have shown that the *same* microscopic pQCD interactions as used in the jet quenching investigations lead to a sizable elliptic flow within the bulk medium [6].

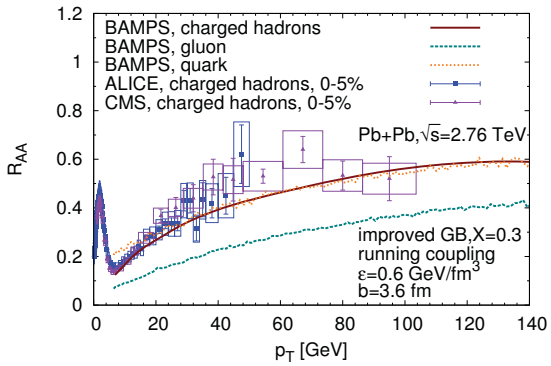

Figure 1: Nuclear modification factor R_{AA} of gluons, light quarks, and charged hadrons at LHC for PYTHIA initial conditions, a running coupling and LPM parameter $X_{LPM} = 0.3$ together with data of charged hadrons [1].

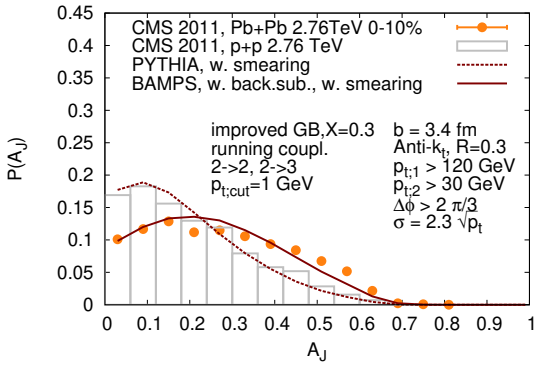

Figure 2: Momentum imbalance A_J of reconstructed jets in central Pb + Pb collisions at LHC for PYTHIA initial conditions, a running coupling and LPM parameter $X_{LPM} = 0.3$ together with data [2].

References

[1] ALICE Collaboration, Phys.Lett. **B720**, 52 (2013).

[2] CMS Collaboration, Phys. Lett. B **712** (2012) 176

[3] Z. Xu and C. Greiner, Phys.Rev. **C71**, 064901 (2005).

[4] O. Fochler et al., Phys.Rev. **D88**, 014018 (2013).

[5] J. Gunion and G. Bertsch, Phys.Rev. **D25**, 746 (1982).

[6] J. Uphoff et al., (2014), arXiv:1401.1364.

[7] F. Senzel et al., (2013), arXiv:1309.1657.

* Work supported by F&E Frankfurt/GSI, H-QM and HGS-HIRe.

Strange and heavy mesons in hot and dense nuclear matter: hadronic models and transport simulations for a road to FAIR*

D. Cabrera[1,2], *A. Ilner*[1,2], *J. M. Torres-Rincon*[3], *L. Tolos*[1,3], *J. Aichelin*[4], *E. Bratkovskaya*[1,2], *and W. Cassing*[5]

[1]FIAS, Frankfurt, Germany; [2]ITP, Frankfurt, Germany; [3]ICE (IEEC/CSIC), Bellaterra, Spain; [4]Subatech, Nantes, France; [5]ITP, Giessen, Germany

Introduction

Strage and heavy mesons probe interesting aspects of the strong interaction at extreme conditions, the different regions of the phase diagram being explored by experiments such as production reactions in nuclei, heavy-ion collisions (HICs) and the observation of macroscopic properties of neutron stars. Particularly, understanding their dynamics in the hadronic world is a crucial point to correctly analyse experimental information from HICs and perform realistic transport simulations. We study the properties of strange and heavy-flavoured mesons in a hot and dense nuclear medium within a selfconsistent coupled-channel approach based on the chiral Lagrangian.

Strange mesons in hot/dense matter

In the strangeness sector, we have completed a new determination of the in-medium scattering amplitudes and cross sections (such as $\bar{K}N \to \pi\Sigma$) in addition to the (off-shell) K and $\bar{K}$ spectral functions and quasi-particle properties, both at finite nuclear densities and temperatures, mimicking the expected scenario at FAIR experiments (c.f. Fig. 1). Our next step in this project is to implement our results in the IQMD and PHSD models, exploiting the successful collaboration between the transport groups of Nantes and FIAS-Frankfurt.

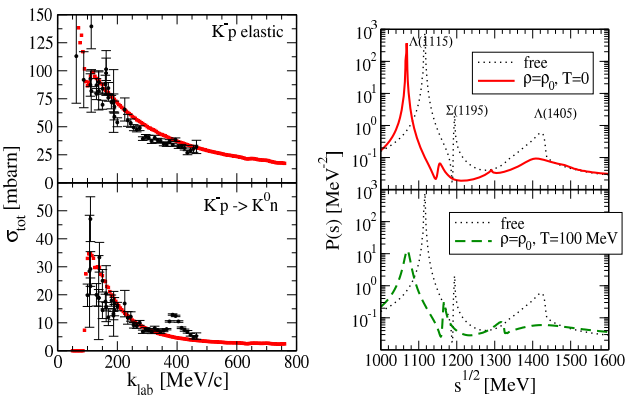

Figure 1: Left: K^-p elastic and $K^-p \to \bar{K}^0 n$ total cross sections (red squares: model). Right: Transition probability ($P \propto |T|^2$) for the K^-p elastic reaction at finite nuclear density (up) and temperature (down).

* Work supported by the HIC for FAIR framework of the LOEWE program and the BMBF project no. 05P12RFFCQ.

Heavy meson relaxation

In the heavy-flavour sector, our approach imposes partial-wave unitarity on the relevant scattering amplitudes (e.g. $D\pi$, $B\pi$), an essential requirement in order to extend the applicability of the low-energy theory (heavy-meson ChPT) to high temperatures $T \simeq m_\pi$. With a minimal set of parameters the unitarized theory dynamically generates the low lying heavy-light meson s-wave resonances ($D_{0,1}$, $B_{0,1}$) in good agreement with the available experimental data both in the charm and bottom sectors. Since a resonant interaction is bound to produce shorter thermalization times, accounting for this feature is important to produce a realistic estimation of the transport coefficients of heavy mesons in the hadronic phase of a heavy-ion collision (cf. Fig. 2).

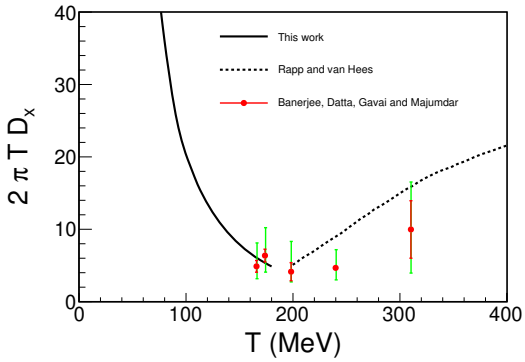

Figure 2: D-meson spacial diffusion coefficient around the crossover at $\mu_B = 0$.

References

[1] L. M. Abreu, D. Cabrera and J. M. Torres-Rincon, Phys. Rev. D **87** (2013) 3, 034019 [arXiv:1211.1331 [hep-ph]].

[2] L. Tolos, D. Cabrera, C. Garcia-Recio *et al.*, Nucl. Phys. A **914** (2013) 461 [arXiv:1211.7286 [nucl-th]].

[3] L. Tolos and J. M. Torres-Rincon, Phys. Rev. D **88** (2013) 074019 [arXiv:1306.5426 [hep-ph]].

[4] J. M. Torres-Rincon, L. M. Abreu, D. Cabrera *et al.*, to appear in Journal of Physics: Conference Series, arXiv:1312.3536 [hep-ph].

[5] D. Cabrera, L. M. Abreu, E. Bratkovskaya *et al.*, to appear in Journal of Physics: Conference Series, arXiv:1312.4343 [hep-ph].

[6] A. Ilner, D. Cabrera, P. Srisawad and E. Bratkovskaya, submitted to Nucl. Phys. A, arXiv:1312.5215 [hep-ph].

 doi:10.15120/GR-2014-1-THEORY-20

Heavy Quarks in Strongly Coupled Plasmas with Chemical Potential*

A. Samberg† [1,2] *and C. Ewerz*[1,2]

[1]Institut für Theoretische Physik, Universität Heidelberg, Philosophenweg 16, D-69120 Heidelberg, Germany;
[2]ExtreMe Matter Institute EMMI, GSI, Planckstraße 1, D-64291 Darmstadt, Germany

Introduction

In heavy ion collisions at RHIC and LHC, it is found that the produced quark–gluon plasma (QGP) is strongly coupled. We apply gauge/gravity duality [1] to study heavy quarks in strongly coupled non-Abelian plasmas. To approximate a dual description of QCD, we study non-conformal gauge theories by explicitly breaking the conformal invariance of the prototype AdS/CFT correspondence. As there is freedom in the way this breaking can be introduced, we study large classes of asymptotically AdS spacetimes, and try to uncover possible universal behavior common to all dual theories. Furthermore, to learn about the phase structure of strongly coupled gauge theories, and ultimately about parts of the QCD phase diagram, we include a chemical potential into our studies. Experimentally, this will be addressed *e. g.* in future FAIR experiments.

Specifically, we have computed the screening distance, the free energy, and a derived running coupling of heavy $Q\bar{Q}$ pairs moving in the strongly coupled plasmas described above. The methods used and results from studies in conformal theories are reviewed *e. g.* in [2].

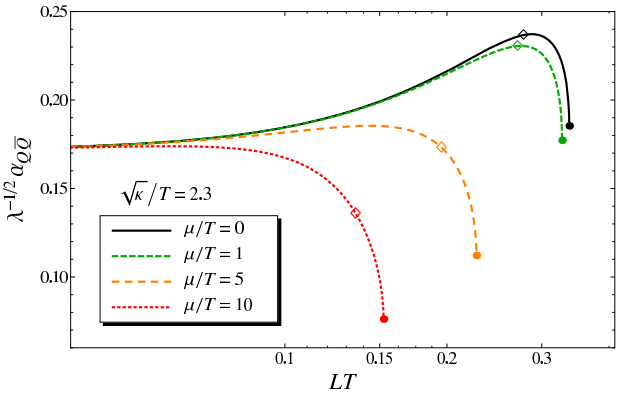

Figure 1: Running coupling $\alpha_{Q\bar{Q}}(L)$ in a non-conformal plasma at temperature T for varying values of the chemical potential μ. $\sqrt{\lambda}$ is a constant. At the endpoints of the curves, screening of the $Q\bar{Q}$ interaction due to the plasma takes over.

Free Energy and Running Coupling

We compute the free energy $F(L)$ of a bound $Q\bar{Q}$ pair with interquark distance L immersed in the medium. To get a handle on the effect of non-conformality on the interaction in more detail, we study the running coupling defined via the derivative of the free energy,

$$\alpha_{Q\bar{Q}}(L) \equiv \frac{3}{4} L^2 \frac{\mathrm{d}F(L)}{\mathrm{d}L} \,.$$

It is shown in Fig. 1. For small distances L, conformality is restored with $\alpha_{Q\bar{Q}}$ becoming constant, while for larger distances, both non-conformality and thermal effects lead to deviations of $\alpha_{Q\bar{Q}}$ from being constant. We have found a universal increase in $\alpha_{Q\bar{Q}}$ above the UV value due to non-conformality, both at vanishing and non-zero chemical potential μ. At still larger distances, thermal effects decrease $\alpha_{Q\bar{Q}}$. This pattern is also seen in QCD lattice data [3].

We have investigated the dependence of characteristic scales on temperature and chemical potential (*i. a.* the thermal drop-off scale L_{th} and the scale L_{max} where $\alpha_{Q\bar{Q}}$ assumes its maximum). At vanishing chemical potential, we have found that to leading order in our models with strong deformation away from conformality, $L_{\mathrm{max}} \sim \frac{c}{T^2}$, where c is the deformation parameter. This appears to be only weakly altered for $\mu > 0$. Generally, we have found that the effect of the chemical potential is relatively weak: also L_{th} varies more strongly under changes in T than in μ.

Comparing the free energy for non-zero μ to lattice data [4] where these are available, *i. e.* for $\mu/T \ll 1$, we find qualitative differences in the effect of the chemical potential that require further analysis. For our further studies, a very interesting outlook is to refine the comparison to lattice data to better characterize the commonalities and differences of holographic models for strongly coupled plasma and the QGP and to learn more about the nature of chemical potentials in holography.

Parts of these results were presented in [5], a more detailed account will be published elsewhere.

References

[1] J.M. Maldacena, Adv.Theor.Math.Phys. **2**, 231 (1998); S.S. Gubser, I.R. Klebanov, A.M. Polyakov, Phys. Lett. **B428**, 105 (1998); E. Witten, Adv.Theor.Math.Phys. **2**, 253 (1998).

[2] J. Casalderrey-Solana, H. Liu, D. Mateos, K. Rajagopal, U.A. Wiedemann, `arXiv:1101.0618`.

[3] O. Kaczmarek, F. Karsch, F. Zantow, P. Petreczky, Phys.Rev. **D70**, 074505 (2004).

[4] M. Döring, S. Ejiri, O. Kaczmarek, F. Karsch, E. Laermann, Eur.Phys.J **C46**, 179 (2006).

[5] C. Ewerz, A. Samberg, Proceedings of the Karl Schwarzschild Meeting 2013, Frankfurt, `arXiv:1312.5999`.

*Work supported by the Scientific Cooperation Agreement GSI–Heidelberg University.

† a.samberg@thphys.uni-heidelberg.de

Off-equilibrium photon production in heavy-ion collisions*

F. Michler[1], *H. van Hees*[1,2], *D. D. Dietrich*[1], *S. Leupold*[3], *and C. Greiner*[1]

[1]Goethe University Frankfurt, Max-von-Laue-Strasse 1, D-60438 Frankfurt, Germany; [2]FIAS, Ruth-Moufang-Strasse 1, D-60438 Frankfurt, Germany; [3]Institutionen för fysik och astronomi, Uppsala Universitet, Box 516, 75120 Uppsala, Sweden

As penetrating probes direct photons and dileptons provide insight into the hot and dense interior of matter created in heavy-ion collisions during its entire evolution. They are directly related with the electromagnetic-current correlation function in the strongly interacting medium. In this connection the most interesting signals are the p_t spectra of photons and dileptons and the invariant-mass spectra of dileptons from a thermalized medium to study the impact of the chiral phase transition in the QCD phase diagram to this current-correlation function.

However, to analyze experimental data on electromagnetic probes in heavy-ion collisions also a detailed understanding of all other "non-thermal" sources is important. In this study we investigate the contribution to the photon emission from the very early off-equilibrium state of the fireball created in heavy-ion collisions which are claimed to outshine the thermal emission from a QGP at high p_t in since here already contributions at order $\mathcal{O}(\alpha_{\mathrm{em}})$ of the electromagnetic coupling constant, which are forbidden in thermal equilibrium due to energy-momentum conservation, occur[1, 2, 3]. However, in this approach the photon rates are plagued by spurious vacuum-to-vacuum transition contributions which can not be renormalized in a proper way [4]. As shown in [5] this problem is related to "switching on and off" the electromagnetic interaction at finite times.

Motivated by these findings we investigate a toy model with quarks and antiquarks coupled to a classical time-dependent scalar field to mimick a time-dependent quark mass to investigate the pertinent emission of photons due to a possible chiral quark-mass shift in strongly interacting matter [6]. The advantage of this model is that it is compatible with current conservation and gauge invariance.

After analytically solving the Dirac equation for the quark-field operator coupled to a classical time-dependent scalar, we calculated the one-loop photon polarization tensor in 1^{st} order perturbation theory, employing the appropriate adiabatic switching of the electromagnetic interaction a la Gell-Mann and Low. We could explicitly show that this framework eliminates the spurious vacuum-to-vacuum transition contributions and allows to write the corresponding photon-emission rate as an absolute square, ensuring the positive definiteness of the photon-number density. For the realistic case of a smooth time dependence of the external field, mimicking a dropping quark-mass scenario by effectively switching the quark mass from its constituent value of $m_{\mathrm{c}} \simeq 0.35$ GeV to its bare value m_{b} for a duration of the off-equilibrium phase of $\tau = 1$ fm/c, the resulting time-integrated photon-momentum spectrum decays exponentially for large momenta and thus is UV integrable, leading to a finite photon yield from the underlying off-equilibrium process. Is has also been demonstrated that, e.g., using the adiabatic switch only for $t \to -\infty$ but not for $t \to \infty$ leads to an artificial enhancement of the photon-production rate by many orders of magnitudes due to spurious vacuum-to-vacuum transition contributions that cannot be properly interpreted as observable photon numbers.

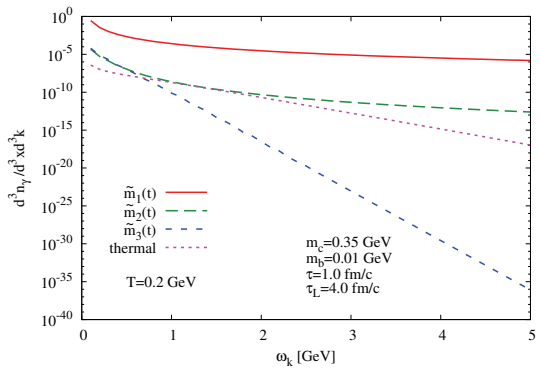

Figure 1: Comparison of the integrated off-equilibrium photon number for different mass-switching scenarios (instantaneous switch (solid line) and switching by a only 1st-order differentiable function (long-dashed line), leading implying the excitation of spurious modes and a UV divergent photon number, and a smooth switching function (short-dashed line) leading to a exponentially decreasing momentum spectrum and thus UV-finite photon-number densities with a photon spectrum from a thermalized QGP (lifetime 4 fm/c) at a temperature of 200 MeV.

References

[1] S.-Y. Wang and D. Boyanovsky, Phys. Rev. D **63**, 051702 (2001).

[2] D. Boyanovsky and H. de Vega, Phys. Rev. D **68**, 065018 (2003).

[3] D. Boyanovsky and H. J. de Vega, Nucl. Phys. A **747**, 564 (2005).

[4] E. Fraga, F. Gelis, and D. Schiff, Phys. Rev. D **71**, 085015 (2005).

[5] F. Arleo et al. (2004), `arXiv:hep-ph/0311131`.

[6] F. Michler, H. van Hees, D. D. Dietrich, S. Leupold, and C. Greiner, Annals Phys. **336**, 331 (2013).

* Work supported by HIC4FAIR/HGS-HIRe/HQM.

 doi:10.15120/GR-2014-1-THEORY-22

On finite volume effects in the chiral extrapolation of baryon masses

M.F.M. Lutz[1], K. Schwarz[1] and R. Bavontaweepanya[2], C. Kobdaj[2]

[1]GSI, Darmstadt, Germany; [2]Suranaree University of Technology, Nakhon Ratchasima, Thailand

We report on a comprehensive analysis of the available three flavour QCD lattice simulations of six different groups on the baryon octet and decuplet masses [1]. We obtained an accurate 12 parameter description of altogether more than 220 lattice data points, where we kept all data with pion masses smaller than 600 MeV. Our study extends previous works [4, 5, 6] and is based on the relativistic three-flavour chiral Lagrangian with baryon octet and decuplet degrees of freedom. The baryon self energies were computed in a finite box at N^{3}LO, where the physical masses are kept inside all loop integrals [1, 2]. The low-energy parameters were constrained by using large-N_c sum rules [3].

Accurate predictions for all relevant low-energy parameters were obtained. In particular we extracted a pion-nucleon sigma term of (39 ± 1) MeV and a strangeness sigma term of the nucleon of $\sigma_{sN} \simeq (4 \pm 1)$ MeV. The flavour SU(3) chiral limit of the baryon octet and decuplet masses was determined with (802 ± 4) MeV and (1103 ± 6) MeV. In our fits we used the empirical masses of the baryon octet and decuplet states as a constraint. That allowed us to perform independent scale settings for the various lattice data. We obtained results for the lattice scales that are compatible with previous estimates, but appear to be much more accurate. Detailed predictions for the baryon masses as currently evaluated by the ETM lattice QCD group are made.

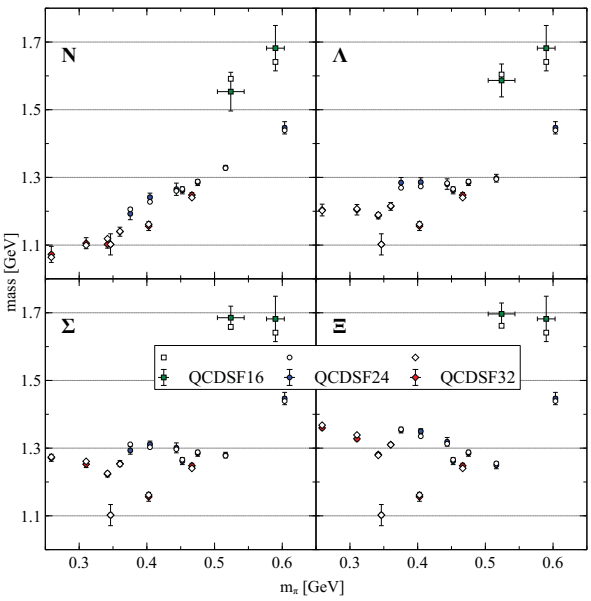

Figure 1: Baryon masses as a function of the pion mass as explained in the text. The open symbols are the result of our EFT analysis.

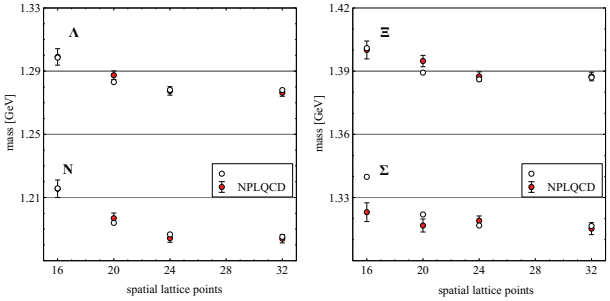

Figure 2: Baryon masses as a function of the pion mass as explained in the text. The open symbols are the result of our EFT analysis.

The 12 relevant low-energy parameter were determined by a global fit to all available lattice data with a $\chi^2/N \simeq 1.25$, which was shown to be dominated by a few outliers. It was emphasized that a stable fit with all parameters relevant at N^{3}LO is only possible upon the consideration of the lattice data at all available lattice volumes. In Fig. 1 we show a sample of our results where a comparison with QCD lattice simulations of the QCDSF-UKQCD group is provided. The description of the octet masses is excellent for all three different lattice sizes $16^3, 24^3$ and 32^3. In Fig. 2 the volume dependence of the baryon octet masses as studied by the NPLQCD group is scrutinized. Here our chi-square value is dominated by one outlier, the Σ mass on the smallest 16^3 lattice.

Our analysis points to some tension in the lattice data set on the baryon decuplet masses, in particular for the Δ mass of LHPC as compared to the predictions of HSC and PACS-CS.

References

[1] M. F. M. Lutz, R. Bavontaweepanya, C. Kobdaj, K. Schwarz, On finite volume effects in the chiral extrapolation of baryon masses, arXiv:1401.7805.

[2] A. Semke, M. F. M. Lutz, Baryon self energies in the chiral loop expansion, Nucl. Phys. A778 (2006) 153.

[3] M.F.M. Lutz, A. Semke, Large-N_c operator analysis of 2-body meson-baryon counterterms in the chiral Lagrangian, Phys. Rev. D83 (2011) 034008.

[4] A. Semke, M. F. M. Lutz, Quark-mass dependence of the baryon ground-state masses, Phys. Rev. D85 (2012) 034001.

[5] A. Semke, M. F. M. Lutz, Strangeness in the baryon ground states, Phys. Lett. B717 (2012) 242.

[6] M. F. M. Lutz, A. Semke, On the consistency of recent QCD lattice data of the baryon ground-state masses, Phys. Rev. D86 (2012) 091502.

The salar-isovector sector in the extended Linear Sigma Model*

T. Wolkanowski[1], *F. Giacosa*[1], *and D. H. Rischke*[1]

[1]Institut für Theoretische Physik, Goethe-Universität Frankfurt am Main, Max-von-Laue-Str. 1, 60438 Frankfurt am Main, Germany

We study basic properties of scalar hadronic resonances within the so-called extended Linear Sigma Model (eLSM), which is an effective model of QCD based on chiral symmetry and dilatation invariance. In particular, we focus on the mass and decay width of the scalar-isovector state $a_0(1450)$ and perform a numerical study of the propagator pole(s) on the unphysical Riemann sheets.

It is nowadays recognized that the scalar sector of hadronic particles is not well described by the ordinary $q\bar{q}$ picture based on a simple representation of $SU(3)$ flavour symmetry. One very simple reason is the mere fact that the number of physical resonances is much larger than the number of states that can be constructed within a $q\bar{q}$ picture. For instance, in the scalar-isovector sector it is possible to build up only one such state, though two isotriplets are definitely established, the resonances $a_0(980)$ and $a_0(1450)$ [1].

The extended Linear Sigma Model includes (pseudo)scalar as well as (axial-)vector states [2,3]. In this model, the scalar-isovector state is identified with the resonance $a_0(1450)$. In this report, we use the parameters of Ref. [3] in order to calculate the propagator of $a_0(1450)$: in this way we can test the effect of loops on this broad scalar state. Then, we focus on the region below the $K\bar{K}$ threshold and try to find out whether $a_0(980)$ emerges as a companion pole in the propagator.

For our purpose it is sufficient to give only the relevant interaction part of the Lagrangian for the neutral state a_0^0:

$$\mathcal{L}_{\text{int}} = Aa_0^0\eta\pi^0 + Ba_0^0\eta'\pi^0 + Ca_0^0(K^0\bar{K}^0 - K^-K^+) \,, \quad (1)$$

where π^0, η, η', K are the pseudoscalar mesons, and the constants A, B, C are combinations of the coupling constants and masses taken from Ref. [3]. They are constructed in such a way that the decay amplitude for each channel, $-i\mathcal{M}_{ij}$, is momentum independent. The optical theorem for Feynman diagrams can then be applied to compute the imaginary part of the corresponding self-energy loop $\Pi_{ij}(s)$, regularized by a Gaussian 3d-cutoff function with cutoff scale $\Lambda = 0.85$ GeV:

$$\int \mathrm{d}\Gamma \, |-i\mathcal{M}_{ij}|^2 = \sqrt{s}\, \Gamma_{ij}^{\text{tree}}(s) = -\,\mathrm{Im}\,\Pi_{ij}(s) \,, \quad (2)$$

where $\Gamma_{ij}^{\text{tree}}$ is the tree-level width coming from the model and $\mathbf{k}$ is the three-momentum of one of the emitted particles in the decay of the a_0^0 in its rest frame. The real part is obtained by the dispersion relation

$$\mathrm{Re}\,\Pi_{ij}(s) = \frac{1}{\pi} \fint \mathrm{d}s' \, \frac{\mathrm{Im}\,\Pi_{ij}(s')}{s - s'} \,. \quad (3)$$

After that, the self-energy is analytically continued to complex values, $s \to z$, while the continuation into the appropriate unphysical Riemann sheet(s) can be done by adding the discontinuities for each channel,

$$\Pi_{ij}^c(z) = \Pi_{ij}(z) + \text{Disc}\,\Pi_{ij}(z) \,, \quad (4)$$

where $\text{Disc}\,\Pi_{ij}(s) = 2i \lim_{\epsilon \to 0^+} \mathrm{Im}\,\Pi_{ij}(s + i\epsilon)$ and the superscript c indicates the continued function on the next sheet. Note that the appropriate sheet is taken to be the one closest to the physical region.

The complex propagator pole on the sheet nearest to the physical region has coordinates $\sqrt{s} = (1.412 - i0.141)$ GeV, hence a decay width of $\Gamma = 282$ MeV (in good agreement with both the tree-level result from our model and the experiment) and a mass of 1.412 GeV. While the (bare) mass $M_0 = 1.363$ GeV coming from the eLSM differs from the experimental value by at least ~ 50 MeV, the pole mass (as the real part of the propagator pole) lies within the experimental error. Thus, the inclusion of loops represents an improvement of the tree-level results. However, all in all, the loop contributions have just a minor influence on the tree-level values: this is important because it confirms that the fit of Ref. [3] is robust. One should perform this check for all other broad states entering in the eLSM.

Another interesting observation is the fact that we do *not* find a companion pole of $a_0(1450)$: the resonance $a_0(980)$ does not emerge for the values of the parameters determined in Ref. [3]. This result is robust upon variations of the parameters. As a possible outlook for future work one should try to include the $a_0(980)$ as a tetraquark state into the eLSM and/or perform a full scattering analysis so as to investigate the emergence of this resonance in more detail.

References

[1] J. Beringer *et al.* (Particle Data Group), *Phys. Rev.* **D86**, 010001 (2012)

[2] S. Janowski, D. Parganlija, F. Giacosa and D. H. Rischke, *Phys. Rev.* **D84**, 054007 (2011) [http://arxiv.org/abs/arXiv:1103.3238]

[3] D. Parganlija, P. Kovacs, G. Wolf, F. Giacosa and D. H. Rischke, *Phys. Rev.* **D87**, 014011 (2012) [http://arxiv.org/abs/arXiv:1208.0585]

*Work supported by HIC for FAIR, F&E Frankfurt and HGS-HIRe. Presented at the Workshop "Excited QCD 2014", Bjelašnica Mountain, Sarajevo, Bosnia–Herzogovina, February 2–8, 2014. Full version to be published in *Acta Phys. Polon. B Proceed. Suppl.* **7** in 2014.

 doi:10.15120/GR-2014-1-THEORY-24

In-Medium strangeness dynamics at $\overline{\text{P}}$ANDA*

T. Gaitanos[1] *and H. Lenske*[1,2]

[1]Inst. für Theor. Physik, Universität Giessen, Germany; [2]GSI Darmstadt, Germany

Hypernuclear physics opens a unique opportunity to explore the hyperon-nucleon (YN) and the hyperon-hyperon (YY) in-medium interactions at terrestrial laboratories. Such studies are important for a better understanding of the in-medium interactions with strangeness degree of freedom, which is still uncertain, but of relevance for nuclear astrophysics [1]. The experimental knowledge on multi-strangeness hypernuclei has been so far scarce. However, recent experiments at GSI are very promising. In the HypHI [2] experiment precise production rates of single-Λ ($S = -1$) hypernuclei were measured. An abundant production of double-Λ ($S = -2$) clusters is also expected in the $\overline{\text{P}}$ANDAexperiment [3] at FAIR.

We investigate theoretically the multi-strangeness dynamics within the Giessen-BUU (GiBUU) approach [4]. In particular, we have studied antiproton-induced reactions allowing for reactions of the secondary Ξ-beam on a second target. The formation of double-Λ hypernuclei occurs in the Ξ-interaction with the second target [5]. Two issues are of importance for the production of double-strangeness hypermatter, see Fig. 1. At first, the absorption of the Ξ-beam inside the target matter decreases with increasing energy. This is due to the strong decrease of the elementary $\Xi N \rightarrow \Lambda\Lambda$ channel [5]. Secondly, the abundance of bound Λ-hyperons also strongly decreases with rising incident Ξ-energy. This is mainly due to the repulsive vector field which becomes more pronounced as the particle energy increases. These effects lead to a rather strong energy dependent rise of the double-Λ hypernuclear production cross section. Thus low-energetic cascade beams should be used at $\overline{\text{P}}$ANDAin order to obtain high production rates of double-strangeness hyperfragments [5].

So far bare interactions for elementary YN, YY-channels have been used in transport approaches. However, at $\overline{\text{P}}$ANDAthe strangeness dynamics takes place at densities closely up to saturation. We have studied in-medium effects on various YN-processes by solving the Lippmann-Schwinger equation with a Pauli-exclusion operator for intermediate states as the leading-order in-medium effect [6, 7]. The elementary YN cross sections are indeed influenced by in-medium effects, in particular, at low energies, as shown in Fig. 2 (similar effects occur for quasi-elastic channels with strangeness exchange).

In the S=-2 sector the situation is still very controversial theoretically [8]. Presently we are investigating the influence of various calculations on S=-2-channels [9] on the strangeness production in $\bar{p}$-induced reactions and extending our studies to the S=-3 sector by accounting for the formation of Ω-baryons [10]. The preliminary results are very promising concerning a possible formation of multi-strangeness bound systems at $\overline{\text{P}}$ANDA. We emphasize the relevance of our theoretical results for the future activities at FAIR.

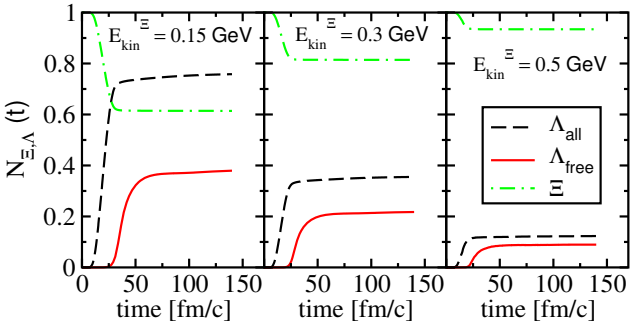

Figure 1: GiBUU results for the time dependence of all and free Λs and of Ξs for central Ξ-induced reactions on Cu-target at beam energies as indicated [5].

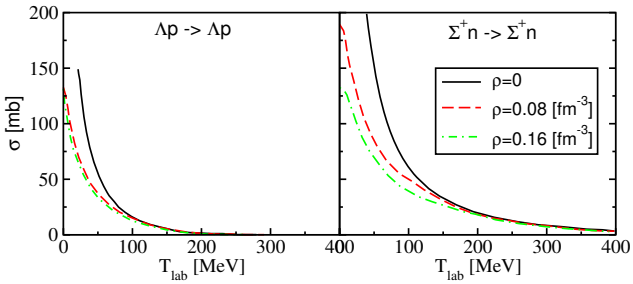

Figure 2: . Energy dependence of elastic in-medium cross sections for ΛN and ΣN scattering at various densities as indicated [7].

References

[1] J. Schaffner, I. Mishustin, Phys. Rev. C53 (1996) 1416.

[2] C. Rappold, *et al.*, Nucl. Phys. A622 (2010) 231.

[3] A.S. Lorente, *et al.*, Phys. Lett. B 697 (2011) 222.

[4] O. Buss, *et al.*, Phys. Rep. 512 (2012) 1.

[5] T. Gaitanos, *et al.*, Nucl. Phys. A881 (2012) 240.

[6] T. Gaitanos, *et al.*, Nucl. Phys. A914 (2013) 405.

[7] A. Obermann, Masters Thesis, 2011, Univ. Giessen, unpublished.

[8] J.K. Ahn, *et al.*, Phys. Lett. B 633 (2006) 214.

[9] T.A. Rijken, Y. Yamamoto, nucl-th/0608074; Y. Fujiwara, *et al.*, Phys. Rev. C64 (2001) 054001.

[10] T. Gaitanos, *et al.*, in preparation.

*Work supported by BMBF, DFG, HIC for FAIR, and GSI-JLU Giessen collaboration agreement

Charmonium production in $\bar{p}$A reactions at threshold*

Alexei Larionov[1,2], Marcus Bleicher[1,3], Albrecht Gillitzer[4], and Mark Strikman[5]

[1]Frankfurt Institute for Advanced Studies (FIAS), D-60438 Frankfurt am Main, Germany; [2]National Research Centre "Kurchatov Institute", 123182 Moscow, Russia; [3]Institut für Theoretische Physik, J.W. Goethe-Universität, D-60438 Frankfurt am Main, Germany; [4]Institut für Kernphysik, Forschungszentrum Jülich, D-52425 Jülich, Germany; [5]Pennsylvania State University, University Park, PA 16802, USA

Charmonium formation reactions on a proton at rest, $\bar{p}p \to R$ ($R = J/\Psi,\ \Psi',\ \chi_c$ etc.), proceed at the beam momentum $p_{\rm lab} = 4 - 6$ GeV/c. Replacing the proton by a nuclear target one gets a good possibility to explore the interactions of the charmonium with nucleons [1, 2]. The preference of the antiproton- to other hadron- and photon-induced charmonium production reactions on nuclei is in the slowness of the produced charmonium. Thus, its formation length is small [2]. On the other hand, nuclear Fermi motion reduces the cross section strongly, $\sigma_{\bar{p}A\to R(A-1)^*} \sim (10^{-4}-10^{-3})Z\sigma_{\bar{p}p\to R}$ at the on-shell peak [2], and broadens the beam momentum region by $\sim \pm p_{\rm lab}p_F/m$, where $p_F \simeq 0.3$ GeV/c is the Fermi momentum and $m = 0.938$ GeV is the nucleon mass.

The eikonal approximation is well suited to study the $\bar{p}A \to R(A-1)^*$ reactions by two reasons: (i) close to the on-shell peak the $\bar{p}p \to R$ formation cross section is large and dominates over other charmonium production channels, and (ii) typical transverse momentum transfers in the formation reaction ($\sim p_F$) and in the charmonium rescattering processes ($\sim 1/\sqrt{B_{RN}} \simeq 0.6$ GeV/c) are much smaller than $p_{\rm lab}$. Within the Glauber model the charmonium production cross section on a nucleus can be calculated as

$$\sigma_{\bar{p}A\to R(A-1)^*} = \int d^2b\, v_{\bar{p}}^{-1} \int_{-\infty}^{\infty} dz \mathrm{e}^{-\int_{-\infty}^{z} dz'\rho(z',b)\sigma^{\rm inel}_{\bar{p}N}} \times \Gamma_{\bar{p}\to R}(z,b)\mathrm{e}^{-\int_{z}^{\infty} dz'\rho(z',b)\sigma_{RN}(z'-z)}, \quad (1)$$

where

$$\Gamma_{\bar{p}\to R}(z,b) = \int \frac{2d^3p}{(2\pi)^3} v_{\bar{p}p}\sigma_{\bar{p}p\to R} f_p(z,b,\mathbf{p}) \quad (2)$$

is the in-medium antiproton width with respect to charmonium R production. $v_{\bar{p}p} = (s(s-4m_N^2))^{1/2}/2E_{\bar{p}}E_p$ is the antiproton-proton relative velocity. $v_{\bar{p}} = p_{\rm lab}/E_{\bar{p}}$ is the antiproton velocity in the target nucleus rest frame. $f_p(z,b,\mathbf{p}) \simeq \Theta(p_{F,p}-p)$ is the proton phase space density with $p_{F,p} = (3\pi^2\rho_p(z,b))^{1/3}$ being the local proton Fermi momentum. Exponential factors in (1) take into account the absorption of incoming antiproton by its inelastic collisions (annihilations mostly) and the absorption of the outgoing charmonium due to its dissociation on the target nucleon ($J/\Psi N \to \Lambda_c\bar{D}$). The corresponding cross sections are $\sigma^{\rm inel}_{\bar{p}N}$ and $\sigma_{RN}(z'-z)$. In the latter case we have checked that taking into account the formation length according to the color diffusion model [2] ($l_{J/\Psi} \simeq 0.4$ fm at $p_{\rm lab} = 4$ GeV/c) has practically no effect on the numerical results. In Fig. 1, the curves have been calculated with

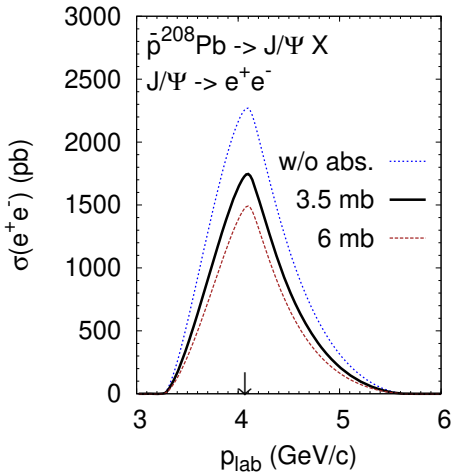

Figure 1: Beam momentum dependence of J/Ψ production cross section on ^{208}Pb. Vertical arrow: $p_{\rm lab} = 4.07$ GeV/c for on-shell J/Ψ production on proton target.

the three values of the $J/\Psi N$ dissociation cross section: $\sigma_{J/\Psi N} = 0,\ 3.5$ and 6 mb. The last two values represent the major uncertainty known from different analyses of J/Ψ production in photon-, hadron- and nucleus- induced reactions on nuclei. The J/Ψ production cross sections are sensitive to the selected values of $\sigma_{J/\Psi N}$ on the level of $\sim 20\%$. For lighter nuclei the sensitivity to $\sigma_{J/\Psi N}$ is reduced. Hence, the transparency ratio analysis can be done for different nuclei to determine the $J/\Psi N$ dissociation cross section (see [3] for details). This analysis can be performed in the future PANDA experiment.

References

[1] S.J. Brodsky and A.H. Mueller, Phys. Lett. B **206**, 685 (1988).

[2] G.R. Farrar, L.L. Frankfurt, M.I. Strikman, H. Liu, Nucl. Phys. B **345**, 125 (1990).

[3] A.B. Larionov, M. Bleicher, A. Gillitzer, M. Strikman, Phys. Rev. C **87**, 054608 (2013).

* Work supported by HIC for FAIR.

 doi:10.15120/GR-2014-1-THEORY-26

Lustre in WAN Environment and Development

T. Stibor, B. Alborea, S. Haller, C. Huhn, D. Klein, B. Neuburger, M. Pausch, V. Penso, C. Preuß, T. Roth, W. Schön, and J. Trautmann
GSI, Darmstadt, Germany

Lustre in WAN Environment

Recently, Lustre has been started to be employed in wide area networks (WAN) to enable efficient data access beyond local HPC and cluster environments [2]. In WAN environments challenging problems such as reliable tera-link connections and security related issues such as authentication and data privacy/integrity [1] need to be addressed. For addressing the first issue a 120 GBit/s high-speed connection between GSI and the LoeweCSC based on LNET routers was implemented (see Fig. 1). This is the first step for the general tera scale project in the context of FAIR enabling partnered research institutes Lustre access for processing data.

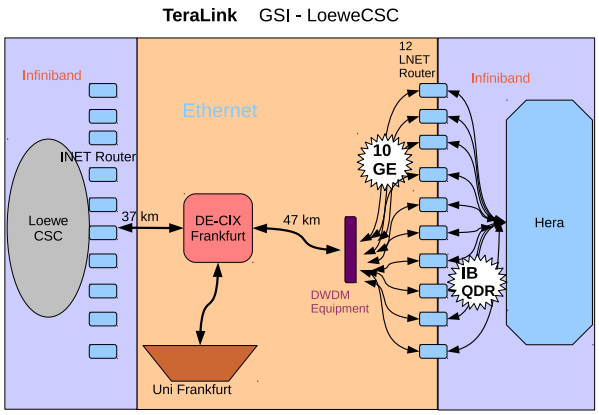

Figure 1: The high-speed connection is realized by bundling 12 machines equipped with 10 GBit/s ethernet cards acting as LNET routers. For seamless connecting both sides efficiently, Infiniband over IP is employed and network bandwidth saturation in experiments is achieved.

In the subsequent Section we briefly summarize the HPC development of a lightweight access control mechanism for addressing security related problems of Lustre in WAN environments.

A Lightweight Access Control Mechanism for Lustre in WAN Domains

For controlling access to Lustre of clients outside the GSI domain, a Linux kernel module based on Linux UID/GID and Lustre network identifier is developed. It allows to control *read* and *write* access on Lustre mount points comparable to Lustre's root squash functionality, however, for arbitrary specified UID's/GID's and Lustre network identifier ranges such as UID:$[1001 \ldots 2500]$,GID:$[2001 \ldots 3500]$, etc. In the context of wide area Lustre deployment the proposed mechanism enables a straightforward and lightweight access control of Lustre clients located in different wide area domains. The access control mechanism is implemented as a separate Linux kernel module and exports an access-granting function which is hooked into MDT system calls such `mdt_reint_open(...)` or `mdt_md_create(...)` to grant or deny access. For defining and removing rules, the Linux procfs is employed (see examples below).

Load kernel module & set rules:

```
>insmod ./lugac.ko
GSI Lustre UID/GID access control module v0.3 loaded
>echo "192.168.[67-70].[1-16]@tcp0 [500-600] 1012" > /proc/lugac
>echo "10.10.1.1@tcp5 [100-200] [100-200]" > /proc/lugac
```

Enforce rules:

```
user1@10.10.1.1:uid:5:gid:5>ls /lustre
ls:  cannot access /lustre:  Permission denied
user2@10.10.1.1:uid:105:gid:105>ls /lustre
data.raw
```

For more details and for studying the kernel module code see http://www.stibor.net/lugac.

Contributing Code to Lustre

The HPC group is now an active member of contributing and reviewing code for the Lustre file system, especially in the area of Kerberos and GSS. This encompass patches for latest Linux kernels as well as fixes for Kerberos and GSS (see http://git.whamcloud.com).

Outlook

The next project steps will encompass implementing a *kerberized* Lustre for $3.X$ Linux kernels to enable strong user authentication and data encryption/integrity. In addition, preliminary explorations and efficiency experiments on ZFS as a backbone file system for Lustre are performed.

References

[1] Josephine Palencia, Robert Budden, and Kevin Sullivan. Kerberized lustre 2.0 over the wan. In *Proceedings of the 2010 TeraGrid Conference*, pages 1–5. ACM Press, 2010.

[2] Stephen C. Simms, Gregory G. Pike, and Doug Balog. Wide area filesystem performance using lustre on the teragrid. In *Proceedings of the TeraGrid 2007 Conference*, 2007.

doi:10.15120/GR-2014-1-IT-01

Improving the logging infrastructure of HPC and Linux services

M. Dessalvi
GSI, Darmstadt, Germany

Introduction

Logging system events, especially for big IT infrastructures, is essential. Whenever a problem arise System Administrators turn their looks towards log files but as IT infrastructures grows in size and complexity the volume of the available logs will increase dramatically as well the resources needed to analyze them.

Overview

The GSI HPC group have already implemented multiple solutions, based on open source software, to analyze different kind of logs and events. A brief list of those software inlcude: Nagios, Netdisco, Collectd, MRTG graphs and Torrus.

Analyzing text logs files, produced by hundreds of hosts, is a daunting task. Traditionally, looking into such a massive amount of informations requires the use of specific utilities for searching, parsing, manipulating and extracting useful data. On UNIX/Linux systems these tools are usually available directly from the shell: cat, tail, grep, sed, awk , sort and many others. Unfortunately, these tools are not enough to spot trends and make correlations with different events scattered on multiple files.

To overcome this problem a solution was implemented, based on Logstash[1], Redis[2] and Elasticsearch[3], plus Kibana[4] as a web interface.

Logstash

Logstash is a tool for managing events and logs. It can be used to collect logs, parse them, and store them for later use.

The main idea behind this tool rely on the concept of plugins. A combination of different plugins let the admins create their own log pipeline and extract informations coming from different sources and store the results with different storage solutions.

A short list of the available plugins:

- Input: TCP/UDP, text files, Syslog, MS Windows Event logs, STDIN, etc.
- Filters: alter, collate, geoip, key value, metrics, multiline, XML, Zeromq, etc.
- Output: CSV, email , Graphite, StatsD, Elasticsearch, Nagios, XMPP, etc.

Different Logstash agents may be deployed to deal with logs from different sources and structures. The parsed results, in JSON format, is then pushed to Redis which acts as a broker between multiple Logstash agents and the Elasticsearch server.

Elasticsearch

Elasticsearch is basically a text indexing engine. It is based on Apache Lucene[5], a full-featured text search engine library written entirely in Java. Elasticsearch most interesting characteristic is its fast search responses, based on the concept of *inverted index*: instead of searching text strings directly, it creates an index from incoming text and performs searches on the index rather than the content. The Kibana web interface add an extremely flexible web interface for visualizing the collected data in real time.

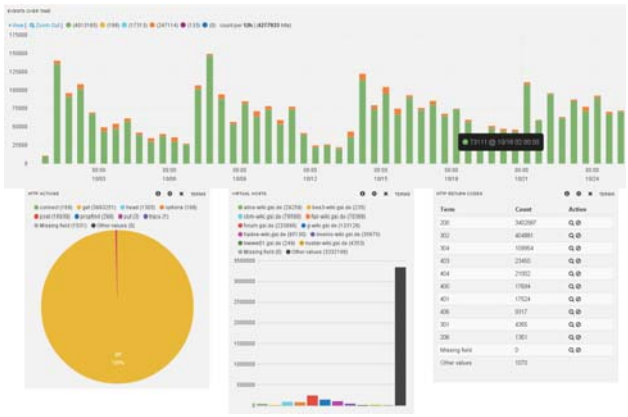

Figure 1: An example of the Kibana web interface for the Apache logs.

Outlook

Future developments of this solution will include a migration to the new 1.0 stable branch of Elasticsearch and extract even more informations from the logs through the combined use of Graphite[6] and Statsd[7].

References

[1] http://www.logstash.net
[2] http://www.redis.io
[3] http://www.elasticsearch.org/overview/elasticsearch/
[4] http://www.elasticsearch.org/overview/kibana/
[5] http://lucene.apache.org/core/
[6] http://graphite.wikidot.com/
[7] https://github.com/etsy/statsd/

 doi:10.15120/GR-2014-1-IT-02

Status of the FairRoot framework

M. Al-Turany[1], D. Bertini[1], R. Karabowicz[1], D. Klein[1], D. Kresan[1], A. Lebedev[1], A. Manafov[1], A. Rybalchenko[1], T. Stockmanns[2], F. Uhlig[1], and N. Winckler[1]

[1]GSI, Darmstadt, Germany; [2]FZJ, Juelich, Germany

Introduction

Using FairRoot one can create simulated data and/or perform analysis within the same framework. The framework delivers base classes which enable the users to construct their detectors and/or analysis tasks in a simple way [1, 2]. The user analysis is organized in tasks (FairTask). Tasks are executed sequentially in the order they are added to the run manager. One way to improve the performance of FairRoot on multi-core processors is to run the independent tasks in parallel. Which can be done by running each task in a separate thread or as separate process. However, by multi-threading an error in one thread can bring down all the threads in the process where in multi-process the different processes are insulated from each other by the OS or even the network, i.e: An error in one process cannot bring down directly another one. On the other hand, the inter-thread communication is faster than interprocess one. Trying to find the correct balance between reliability and performance we decided to use the multi-process concept with message queues for data exchange, i.e: Each "Task" is a separate process, which can be also multithreaded, and the data exchange between the different tasks is done via messages. This concept allow us to create different topologies of tasks that can be adapted to the problem itself, and the hardware capabilities. Some of the advantages of such a system are:

- Flexibility: Different data paths can be modeled by simply changing the topology of Tasks.
- Scalability: Spread the work over several processes and machines on the fly.
- Adaptive: Sub-systems are continuously under development and improvement and can be exchanged individually.

FairMQ: Base for data transport layer in FairRoot

Extending FairRoot to support multi-processes needs a solid and stable communication layer that should handle the whole communication in a transparent and stable way. Fortunately, such a layer exists already and is called ZeroMQ [3]. ZeroMQ is a very lightweight messaging system, specially designed for high throughput and low latency scenarios. It is open source, embeddable socket library that redefines the term socket as a general transport endpoint for atomic messages. ZeroMQ sockets provide efficient transport options for inter-thread, inter-process and inter-node communication (see Figure 1). Moreover it provides a Pragmatic General Multicast pattern (PGM), which is a reliable multicast protocol [3].

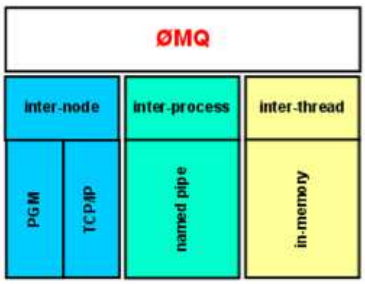

Figure 1: Message transport options in ZeroMQ. **Named Pipe**: Piece of random access memory (RAM) managed by the operating system and exposed to programs through a file descriptor and a named mount point in the file system. It behaves as a first in first out (FIFO) buffer

The zero in ZeroMQ refers to a culture of minimalism that permeates the project. They want to add power by removing complexity rather than exposing new functionality [4]. The library provides a built-in routing strategies for one-to-many or many-to-one communication scenarios. Each socket potentially comes with a sending and a receiving queue of configurable sizes.

The FairMQ package is described in more details by A. Rybalchenk in this report [5]

Outlook and future plans

We need to design and develop a dynamic deployment system (DDS) that can utilize any resource management system (e.g: Slurm, GridEngine, ...etc.). A monitoring and logging system is also under development (See report by Anar Manafov [6]).

References

[1] M. Al-Turany et al. The FairRoot framework *J. Phys.: Conf. Ser. 396 022001, 2012.*

[2] FairRoot: http://fairroot.gsi.de.

[3] http://www.zeromq.org/

[4] P. Hintjens, http://zguide.zeromq.org/page:all

[5] A. Rybalchenk and M. Al-Turany, Streaming data processing with FairMQ

[6] Anar Manfov, DDS: A New Dynamic Deployment System, this report

ALFA: A new Framework for ALICE and FAIR experiments

M. Al-Turany[1], P. Buncic [3], P. Hristov[3], T. Kollegger [1,2], V. Lindenstruth[1,2], and P. Vande Vyvre[3]
[1]GSI, Darmstadt, Germany; [2]FIAS, Frankfurt, Germany; [3]CERN, Geneva, Switzerland

Introduction

The FairRoot framework [1] started in 2003/2004 as a framework for CBM collaboration. Meanwhile it is used by 7 experiments as a base for their simulation and analysis: CBM, PANDA, R3B, ASYEOS and the GEM subgroup of FOPI at GSI/FAIR. The MPD experiment at JINR in Dubna and the EIC collaboration are also using the FairRoot framework as a base for their own software. The commonalities between ALICE and the FAIR experiments and their computing requirements lead to the expectation that large parts of the software framework can be written in an experiment independent way. The FairRoot project has already shown the feasibility of the approach of developing a common framework for several experiments. We therefore propose to develop the new common framework which will be called ALFA.

Technology background

The efficient use of a concurrent computing system requires the correct sequencing of the interactions or communications between different computational executions, as well as coordinating access to resources that are shared among executions. A number of different methods can be used to implement concurrent programs, such as implementing each computational execution as an operating system process, or implementing the computational processes as a set of threads within a single operating system process. The future framework has to support a heterogeneous and distributed computing system.

A message-based approach will allow us to run our software on all hardware platforms (from a laptop to an entire system with many thousands of cores and specialized hardware accelerators). An Open-source system such as ZeroMQ [2] and/or nanomsg [3] will be used as a lightweight messaging layer. What is today a single threaded application will be transformed into many small components running concurrently as independent processes (executing on the same node or distributed over the network) with some of them utilizing capabilities of specialized hardware (where available) and communicating by asynchronous messaging.

Proposed architecture

The proposed architecture will rely on a data-flow based model. It will contain a common transport layer. Common configuration, management and monitoring tools will be developed. The framework will provide unified access to configuration parameters and databases. It will include support for a heterogeneous and distributed computing system. The proposed architecture will also incorporate common data processing components.

Expected benefits from the common project

This common development will benefit to all experiments involved; it will shorten the time to deliver production quality code and will reduce the cost to develop it. The work in common will also allow a better coverage and testing of the code. Moreover, the extended user community will provide high quality documentation, training and examples.

A common framework will be beneficial for the FAIR experiments since it will be tested with real data and existing detectors before the start of the FAIR facility. For example, concepts for online calibrations and alignment can be tested in a real environment, similar to that of the planned FAIR experiments.

ALICE will benefit from the work already performed by the FairRoot team concerning features (e.g. the continuous read-out), which are part of the ongoing FairRoot development.

Outlook

A proof of concept for the design and the technology has been successfully implemented [4]. Work on different prototypes is just starting; for ALICE and CBM the prototypes are planned for the end of this year. Both prototypes should show the ability of the ALFA framework to transport huge amount of data and distribute it on a large cluster of compute nodes. For PANDA experiment a prototype is also planned for this year which will concentrate on using heterogeneous architecture (CPU and GPU) for the online event reconstruction. Implementing these prototypes simultaneously will help us identifying more common issues and will enhance the synergy between the deferent experiments. Naturally all common packages will be implemented in the ALFA framework.

References

[1] M. Al-Turany et al. The FairRoot framework *J. Phys.: Conf. Ser. 396 022001, 2012.*

[2] http://www.zeromq.org/

[3] http://nanomsg.org

[4] M. Al-Turany et al. Extending the FairRoot framework to allow for simulation and reconstruction of free streaming data . Accepted for publication by, Journal of Physics: Conference Series (2013)

 doi:10.15120/GR-2014-1-IT-04

Streaming data processing with FairMQ

A. Rybalchenko[1] *and M. Al-Turany*[1]
[1]GSI, Darmstadt, Germany

The FairRoot framework [1] is a framework for simulation, reconstruction and data analysis of particle experiments. Currently the framework is being extended to provide support for simulation, reconstruction and analysis of free streaming data. A number of components were introduced to the framework, under the common name of FairMQ, which allow flexible construction of topologies to distribute and process free streaming data. FairMQ is based on a prototype framework [3], developed in 2012/2013 at GSI, which relies on the ZeroMQ library for the transport and organization of data between system processes and/or network nodes. An example topology is presented in Figure 1. It includes two separate nodes (blue), each containing a number of processes (green and grey). Arrows indicate the data flow.

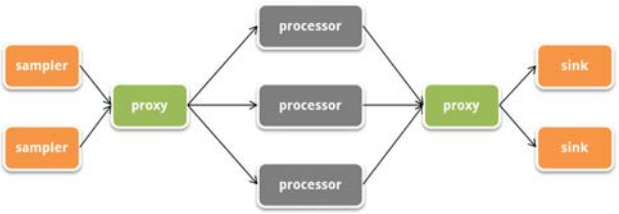

Figure 1: FairMQ example topology.

An example is implemented in FairRoot tutorials, which shows the workflow within the new scheme [7]. The example workflow demonstrates how to configure and run a topology, including components to read, process, distribute, collect and write data. The topology can be configured to run on a single node or on any number of nodes, allowing the user to monitor the system load more granularly and to add additional workers dynamically when necessary. A performance comparison with the traditional workflow was presented in [2], demonstrating significant performance benefits. On a 2 x 2.4 GHz Intel Xeon quad core node, the traditional execution setup with 8 parallel tasks reached a throughput of 2660 events/s. With the same data, FairMQ streaming system reached 7320 events/s, utilizing 9 system processes - 3 for task execution, 4 for I/O and 2 for data distribution.

Among the improvements which were introduced to FairMQ is a new component called the proxy. The proxy replaces splitter and merger components, which were used for merging/splitting of the data stream. The Proxy is more flexible than splitter/merger, because new nodes/processes can be added to it dynamically, without changing the configuration or even stopping the process. Using the proxy also simplifies the configuration, since it only occupies one network port for input and one for output, while splitter/merger would occupy a port for every new connecting node.

Moreover, FairMQ has a new layer that abstracts the specific transport implementation. By keeping framework and transport code independent, the framework can be easily adapted to emerging technologies in the future.

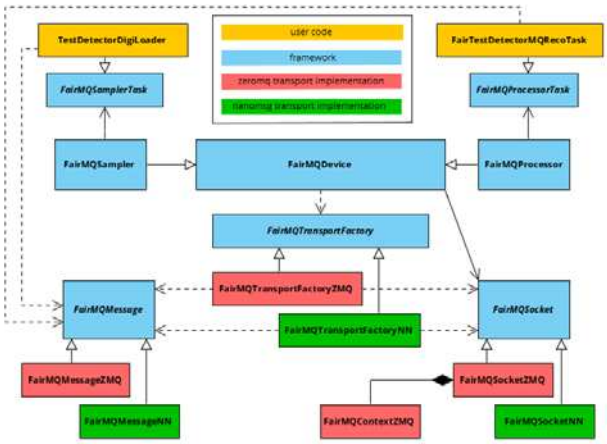

Figure 2: Transport layer abstraction.

At the moment two transport implementations can be used: ZeroMQ [4] and nanomsg [5]. Nanomsg is an emerging communication library, developed by the authors of ZeroMQ. While still in an early alpha stage, nanomsg aims to offer a number of advantages in comparison to ZeroMQ [6], which could to be useful for FairRoot. Most notable among these are better Zero-copy support (with shmem and RDMA) and a formal API for adding new transports such as Infiniband and Websocket.

References

[1] FairRoot: http://fairroot.gsi.de.

[2] M. Al-Turany, D. Klein, A. Manafov, A. Rybalchenko, F. Uhlig: Extending the FairRoot framework to allow for simulation and reconstruction of free streaming data. accepted for publication by, Journal of Physics: Conference Series (2013).

[3] D. Klein: Flexible data transport for the online analysis in a particle physics experiment. Bachelor thesis, Hochschule Darmstadt (2013).

[4] ZeroMQ: http://zeromq.org/.

[5] nanomsg: http://nanomsg.org/

[6] Differences between nanomsg and ZeroMQ: http://nanomsg.org/documentation-zeromq.html

[7] FairRoot Tutorial 3: https://github.com/FairRootGroup/FairRoot/tree/master/example/Tutorial3

DDS: A new Dynamic Distribution System

A. Manafov[1], *A. Lebedev*[1], *and M. Al-Turany*[1]
[1]GSI, Darmstadt, Germany

Dynamic Distribution System (DDS) is a tool-set that automates and dramatically simplifies the process of distribution of user defined processes with their dependencies on any resource management system using a given topology.

DDS is a successor of PoD [1][2]. Unlike PoD, which automates PROOF [3] deployment, DDS will handle any kind of user processes with complex dependencies between processes. The system is designed and being implemented within the new ALFA framework [4].

Concept

During 2013 a conceptual design of the system has been developed.

A key point of this design is the so called ẗopology languageï.e.: DDS is a user oriented system the definition of the topology by the user has to be simple and powerful at the same time. The basic building block of the system is a task. Namely, a task is a user defined executable or a shell script, which will be deployed and executed by DDS on a Resource Management System. To describe dependencies between tasks in a topology we use properties. For example, if one task wants to communicate with another task they can have the same property of a type TCP/IP port. In this case DDS will notice that, will find out a free port number on a destination system and set this number to configuration files of both user processes. Moreover, there will be different types of properties, for example, tasks can be dependent on each other via a file or a named pipe.

Tasks can be grouped into DDS collections and DDS groups. The difference between collections and groups is that collections are a signal to DDS topology parser that tasks of given collections will be executed on the same physical machine. This is useful if tasks have a lot of communication or they want to access the same shared memory. A set of tasks and task collections can be also grouped into task groups.

DDS utilizes a plug-in system in order to use different job submission front-ends. The first and the main plug-in of the system will be an SSH plug-in, which can be used to dynamically turn a bunch of machines to user worker nodes. The SSH plug-in is a perfect tool for a Cloud based solutions.

Outlook

The DDS system is in the initial development phase. We expect a lot of new features in the upcoming year.

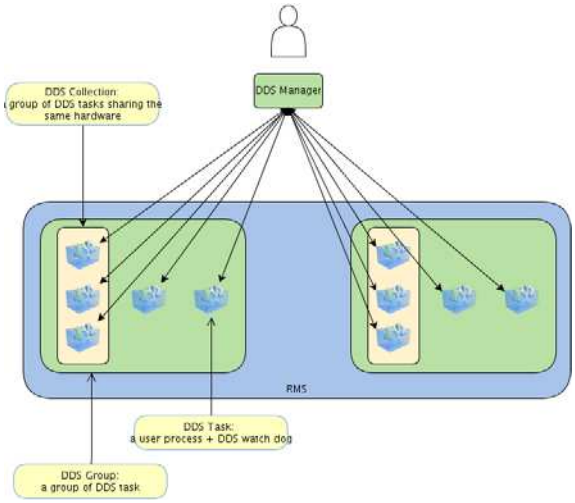

Figure 1: Illustration of the DDS concept.

1. Operational prototype of DDS with the ability to parse typologies such as examples of FairROOT tasks.
2. The operational prototype will be able to deploy single dependency tasks like a PROOF cluster or FairROOT analysis tasks. The deployment will be steered using the SSH plug-in on the Cloud and local computers.
3. Extend the plug-in machinery to cover the following Resource Management Systems: SLURM, LSF, Torque (PBS), Grid Engine, Condor, PanDA.
4. Extend the submission machinery to be able to deploy multi-dependency tasks.
5. Extend the complexity of the topology language to support custom types of task properties.

References

[1] A. Manafov et al, “PROOF on Demand”, IT-07, GSI Scientific Report 2012.

[2] PROOFonDemand(PoD),http://pod.gsi.de

[3] TheParallelROOTFacility(PROOF), http://root.cern.ch/drupal/content/proof

[4] M. Al-Turany et al., Status of the FairRoot framework, this report.

 doi:10.15120/GR-2014-1-IT-06

Event building in FairRoot

R. Karabowicz[1], *M. Al-Turany*[1], *D. Bertini*[1], *D. Klein*[1], *D. Kresan*[1], *A. Lebedev*[1], *A. Manafov*[1], *A. Rybalchenko*[1], *T. Stockmanns*[2], *F. Uhlig*[1], *and N. Winckler*[1]

[1]GSI, Darmstadt, Germany; [2]FZJ, Juelich, Germany

Introduction

This report presents first effort of constructing a common structure of event building in the FairRoot [1] computing framework. Set of classes has been implemented allowing management and development of event builders working on different data streams. A working example of event reconstruction using data from one of the PANDA detectors, the GEM Tracker, has been provided. The achievement of the full event reconstruction depends on the implementation of other event builders working on different data sets. We anticipate that the provided structure will also be aplicable to other experiments facing similar challenges.

Event building

In general, the event building requires information from most of experimental subsystems. Some will provide good event start time, others are designed to reconstruct particle trajectories, and yet another serve for particle identification. The complexity of the task suggests usage of different event builders for separate subsystems and then combining the information in an event builder manager to get a global picture of the event.

It should also be noted, that the event builders might have radically different functionalities. It is easy to imagine, that some of the subsystems will be able to provide crucial event characteristics and thus will be used for event reconstruction. However some will only be able to assign data to already identified events and thus will merely build up events. Trivially many will serve both goals.

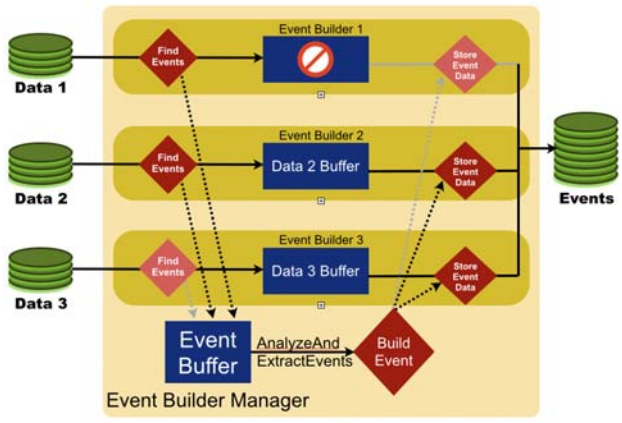

Figure 1: Schematic view of event building.

Figure 1 schematically presents a prototype design of the event building scenario. The reconstruction is handled by the Event Builder Manager, which contains 3 (in this example) independent event builders, that are getting time-sliced data from different sources. Event builders process input data in *FindEvents* functions, which may store the data in internal Data Buffers and/or send found events information to the Event Builder Manager.

The task of combining the information from different subsystems is performed by the *AnalyzeAndExtractEvents* function of the manager, which, in turn, triggers storing of the data for each identified event. This is performed by the *StoreEventData* function of the event builders, where the data in buffers have to be assigned to events.

Example implementation

GEM Tracker event builder was the first implementation of the presented scenario. The input for the event builder are the time slices with reconstructed particle trajectories in the GEM Tracker [2]. For each track an estimated track creation time is calculated using GEM timing information. Event builder looks for tracks with similar (closer than 5ns) creation time and calculates event time by taking center-of-gravity average. Even single trajectories are taken to mark reconstructed events due to the small detector average occupancy of around 3 tracks per event.

Around 80% of the realistic antiproton-proton collisions have reconstructable trajectories in the GEM Tracker. Out of them more than 90% have been properly reconstructed using the presented analysis scenario. About 2% of the events in the output have no matching simulated event.

Summary

This report addresses the question of the event building in the future experiments at FAIR. It proposes a common structure for such tasks within the FairRoot framework. Data from the different subsystems would be analyzed by different event builders and the whole effort would be coordinated by the experiment-specific Event Builder Manager. A preliminary example of the event builder operating on the data from only one of the PANDA detectors shows promising results. The future work should focus on the development and improvement of the event builders for different experimental subsystems as well as on the Event Builder Managers, that are foreseen to orchestrate the various event builders and take the final decision in the process of the event reconstruction.

References

[1] M. Al-Turany *et al*, "Status of the FairRoot framework", GSI Scientific Report 2013

[2] R. Karabowicz, "Time-based reconstruction in the GEM Tracker", GSI Scientific Report 2013

doi:10.15120/GR-2014-1-IT-07

New software for the R^{3}B calorimeter CALIFA within FairRoot*

Y. González[1,2] *and D. Kresan*[1]
[1]GSI, Darmstadt, Germany; [2]USC, Santiago de Compostela, Spain

Introduction

R^{3}B is a next generation experimental setup for studies of Reactions with Relativistic Radioactive Beams. Its aim is to provide a versatile reaction setup for kinematically complete measurements of reactions with high-energy radioactive beams [1]. CALIFA, the R^{3}B CALorimeter for In-Flight emitted pArticles detection, is one of the key detectors for the setup of R^{3}B.

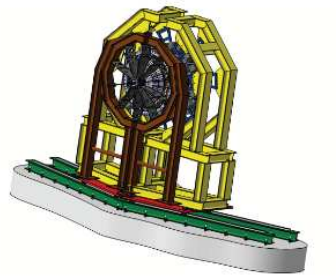

Figure 1: CALIFA calorimeter in last year report [2].

As CALIFA is included in the R^{3}B experiment, the software requirements will be handled by the FairRoot framework.

CALIFARoot

The framework FairRoot provides base classes which enable the users to construct their detectors and tasks in a straight-forward way [3]. Two important parts of the software for CALIFA have been developed for the framework: the unpacker and the raw-data publisher. Both of them will be fully explained in the next sections.

CALIFA unpacker

The unpacker is the element that allows us to extract the information obtained via the data aquisition system and save it in ROOT format. In order to create the unpacker for CALIFA we need three essential elements: a representation of a hit in one of the crystals, the unpack code to fully read the information obtained and to extract it, and a macro that provides information regarding how the unpacker will be handled and creates the ROOT file with the resulting data and histograms.

CALIFA raw-data publisher

The raw publisher, fully based on a javascript code called JSRootIO [4], is an useful feature for experiments that involve different institutes, as it allows them to start live analysis while the experiment is still running.

In order to do this, a webpage is generated and has to be uploaded to a server, along the ROOT file where the data shown is taken from. Two elements are necessary: the generator of the web file and code to add the histograms to the ROOT file that can be read with the javascript code. The webpage is currently able to use the javascript code both via an external link and with a local deployment, downloading the required files in the server.

Conclusion

Basic tools for CALIFA have been developed during the year 2013. Extended software, like database infrastructure, is expected to be developed during the year 2014.

References

[1] R^{3}B collaboration, `http://www.gsi.de/R3B`

[2] R^{3}B collaboration, "Status of the CALIFA/R^{3}B calorimeter", GSI Scientific Report 2012 (2013) 198

[3] FairRoot, `http://fairroot.gsi.de/`

[4] JSRootIO, `http://root.cern.ch/js/`

* Work supported by Ministerio de Economía y Competitividad(Spain) contract No. EIC-FAIR-2011-0061

 doi:10.15120/GR-2014-1-IT-08

Remote Event Client Implementation in FairRoot Framework

D. Kresan, F. Uhlig, and the FairRoot Group
GSI, Darmstadt, Germany

Introduction

FairRoot is a framework, which is used by future FAIR experiments for an implementation of the simulation, reconstruction and data analysis algorithms [1]. Requirement of both, the basic framework features and the user-defined tasks developments, is the usage of the same code for online and offline event reconstruction. In this report we will present an extensions to several base classes, which was done to provide the possibility for communication with a Data Acquisition (DAQ) server.

Online Data Processing

The possibility of online event reconstruction is an essential point for most of the experiments at FAIR, which are aiming to perform high-intensity measurements without a hardware trigger. Therefore, we implemented an additional functionality to the framework, which is sketched in figure 1. In order to avoid overloading of the main DAQ

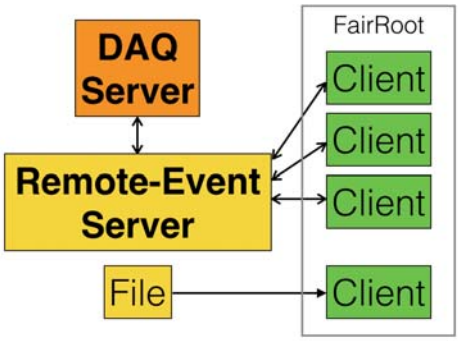

Figure 1: Illustration of the communication flow between a DAQ server and the FairRoot framework.

server with connections from multiple clients, an intermediate stage called "Remote-Event Server" [2] was introduced. There is also a possibility to connect a client directly to a file on disk, in order to support also the offline analysis. The class design allows supporting multiple data formats from a server or from a saved file. In the next subsection we shortly describe the Multi Branch System (MBS) [3] format used in many DAQ server implementations at GSI.

MBS Format

The data coming from the DAQ contains response from multiple detectors and is formed in sequences of events, each containing several sub-events. Each sub-event corresponds to one detector. A detector can be then identified via TYPE and SUB_TYPE values in the sub-event header. This header in a sub-event is then followed by the data.
A support for other data formats is provided, as was already requested by the CBM collaboration.

Server Side

The Remote-Event Server is to be started on a separate computer node. It connects directly to the specified DAQ server, and transmits the data using ROOT sockets to a specified network port. The name of the node, where this server is started, has to be used in a client configuration, described in the next section. For the testing purpose, one can send events with random numbers without connecting to a DAQ server.

Client Side

The Remote-Event Client is part of FairRoot. The steering class *FairRunOnline* implements an event-loop, and user-specified tasks execution. It gets the data from an object of the concrete implementation of the abstract base class *FairSource*. Detector-specific "unpacker" classes then process the received raw data events. The unpackers fill the data as arrays of ROOT objects, which are taken as input for the hardware calibration and further analysis.
This dedicated class design allows a user to easily switch in his analysis between online-streaming and stored data by changing just one line in the steering macro.
Further developments will focus on a class *FairRootSource*, which will be inherited from *FairSource* and will read simulated data from a ROOT file. This will allow to combine two steering classes *FairRunAna* (currently used for the analysis of Monte Carlo simulations) and *FairRunOnline* into a single implementation.

Summary

We presented in this report an extension to the FairRoot framework for communication with a Remote-Event Server. The implementation will be used in the detector tests for the future R^3B experiment. These experimental tests provide unique possibility for validation and verification of the dedicated detector-specific reconstruction algorithms.

References

[1] http://fairroot.gsi.de
[2] H. Göringer, http://www-aix.gsi.de/∼goeri/mbsnew/online.html
[3] H.G. Essel, N. Kurz, http://web-docs.gsi.de/∼mbs/v51/manual/gm_mbs_c.pdf

doi:10.15120/GR-2014-1-IT-09

FairDB: The FairRoot Virtual Database

Denis Bertini[1]
[1]Scientific Computing ,GSI, Darmstadt, Germany

Introduction

Since the setup of a typical heavy ion experiment at FAIR [1] is varying depending on the physic case to study, the FairRoot framework for simulation and analysis [2] should be able to handle a large amount of different parameters and their variation in time. Currently the FairRoot framework uses the Hades Runtime Database Library [3] as third-party code to initialize parameter from ascii or ROOT [4] input files. This report describes the new FairDB Virtual Database Library which extends the FairRoot framework initialization scheme to any SQL-Databases systems.

Database Interface

FairDB provides the user with a well-defined and uniform API for database manipulation. Using internally the ROOT `TSQLServer` class [4], the same user code can be executed independently on Oracle, MySQL, PostGresSQL and even SQLite SQL database engines (Fig. [1]).

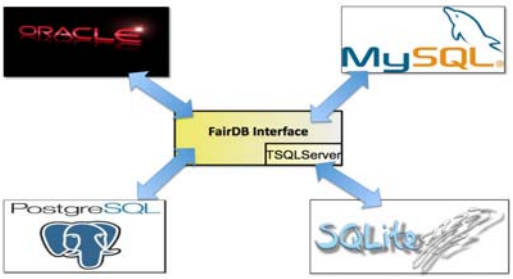

Figure 1: FairDB supported SQL-Database engines.

Design

FairDB separates the connectivity to the DBMS into a *front-end* and a *back-end* (Fig [2]). The *front-end* delivers the relational data model and implementation (tables, query algorithm, versioning etc ...) together with the database connectivity layer. The *back-end* defines the communication layer to specific DBMS using the appropriate client library. Recently the PostGresSQL lower level driver `TPgSQLServer.cxx` has been corrected and partially rewritten. The patch has been accepted and is part of the ROOT release 5-34-15.

Initialization

The SQL-Database input can be added to the FairRoot initialization scheme (Fig [3]) using the services of the general parameter input `FairRunTimeDB`. For accessing the data more than one database connection can be used according to a given user-defined URLs list.

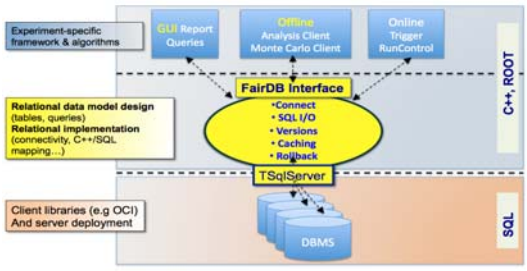

Figure 2: FairDB Design

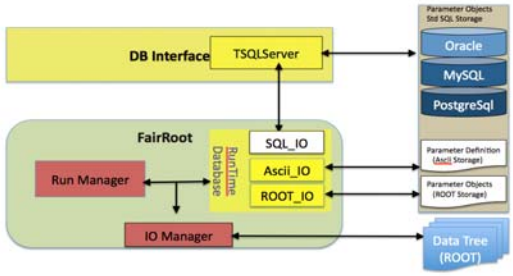

Figure 3: FairRoot initialization scheme including SQL Database input.

User Manual

In order to smooth the learning curve for the FairDB usage, a complete User Manual in PDF format has been written. It covers the general concept, database installation and all the FairDB interface features with tutorials [5].

References

[1] http://www.gsi.de/fair/

[2] The FAIR simulation and analysis framework 2008 J. Phys.: Conf. Ser. 119 032011

[3] http://web-docs.gsi.de/ ilse/initialization.htm

[4] R. Brun, F. Rademakers, P. Canal, I.Antcheva , D. Buskulic, O. Couet, A. and M. Gheata *ROOT User Guide* CERN, Geneva 2005.

[5] FairRoot Virtual Database (User Manual). `https://panda-wiki.gsi.de/foswiki/pub/Computing/PandaRoot/FairRootVirtualDatabase.pdf`

 doi:10.15120/GR-2014-1-IT-10

Time Based Version Management with FairDB

Denis Bertini[1]
[1]Scientific Computing ,GSI, Darmstadt, Germany

Introduction

Because of unprecedented interaction rate (10^7/s) and data rates from 100Gb/s up to 1Tb/s, experiments at Fair [1][2] employ self-triggered front-end electronics featuring a continuously sampling system where the detector subsystems are synchronized by a precision time stamp distribution system. In this context of free data streaming, time or more precisely time interval is the natural detector buffer identifier.
For this reason, FairDB [3] implements internally a version management for the parameter fully based on time.

Temporal Database

Conceptually in a relational database data is organized in two-dimensional space (attribute, tuple). FairDB implements a time-based version management by adding the time as a third dimension leading to a three dimensional model (attribute, tuple, time) as shown in Figure [1].

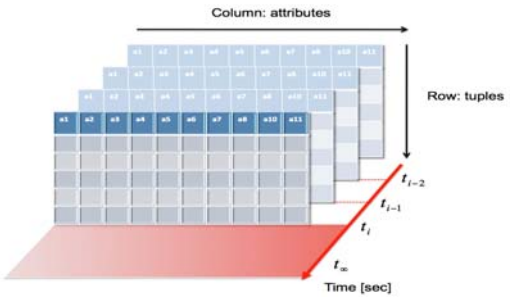

Figure 1: FairDB timed based versioning uses time as additional dimension to the relational data model.

Relational Model

FairDB separates the metadata table (logical data) from the payload data table (physical data). It uses a two-level hierarchy to store the physical data which is illustrated in Figure [2]. This two-level hierarchy data access corresponds to a two-table structure for each type of parameter data in the FairDB relational model. The two table are connected via a unique identifier primary key used as a sequence number.

Validity Range

Ultimately, any of the data retrieved could depend on the run or the time interval defining the event being processed. Detector relevant parameters, such as calibration constants,

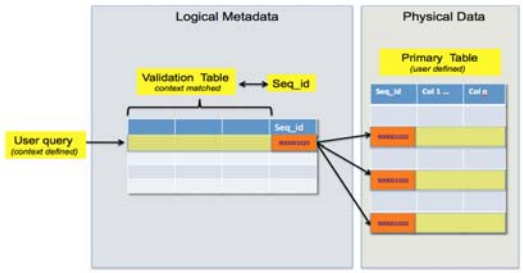

Figure 2: Data Table location Hierarchy

will change with time and the interface has to retrieve the correct ones for the current event time-slice. For this reason, all requests for data through the interface must supply information about:

- The date and time interval of event (in UTC)
- The type of data: real or Monte Carlo
- The type of Detector.

In FairDB this information is called a Context. In the database all information is tagged by a Context i.e by a validation range which identifies the type of data and detector and the ranges of date times for which it is valid.

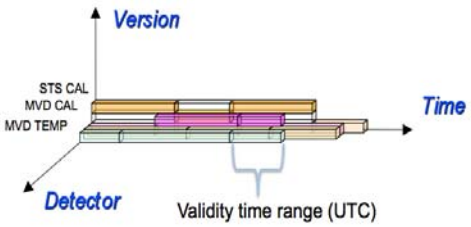

Figure 3: FairDB Multidimensional version management. Only the Validity Time Range is mandatory for parameter retrieval.

References

[1] The Data Acquisition and Trigger System of Panda, 2008 IEEE N57-1

[2] Simulation and reconstruction of free-streaming data in CBM, 2011 J. Phys.: Conf. Ser. 331 032008

[3] FairRoot Virtual Database (User Manual). `https://panda-wiki.gsi.de/foswiki/pub/Computing/PandaRoot/FairRootVirtualDatabase.pdf`

doi:10.15120/GR-2014-1-IT-11

FairDB SQL Persistency Scheme

Denis Bertini[1]
[1]Scientific Computing ,GSI, Darmstadt, Germany

Introduction

Conceptually FairDB [1] handles data as table i.e in a two-dimensional data structure with cells organized in rows and columns.
This is the reponsability of the FairDB framework to deliver an automatic parameter object to relational table mapping and a uniform API to access these object regardless of the internal relational representation.

Object to Table Mapping

FairDB eases the transition parameter object to the relational data model by implementing an automatic mapping procedure according to the following rules:

- **Class** definition corresponds to table definition
- **Columns** are the physical equivalent of the attributes
- **Rows** are the physical equivalent of objects instances

Additionnaly each record (rows or unit block of rows) on a table is uniquely identified. The purpose of the unique identifier is to act as the *primary key* on the table where it is defined and to be referenced as the *foreign key* by other related tables.
Figure [1] shows an example of object to table mapping in the case where the target parameter class is a simple class or is related through inheritance.

Figure 1: One-to-One Parameter object to relational table mapping.

SQL I/O scheme

FairDB provides a programmatic and uniform template based API to write and access parameter object. Like the Java SQL interface system (JDBC)[2], each data retrieval produces a pointer giving read access to a results table which corresponds to a subset of the underlying database table (Figure [2]). Each Row of the results table corresponds to a object, the type of which is user defined and table-specific.

Minimizing I/O with Level2 Cache

Another important point is to minimise I/O. Some requests, particularly for detector relevant parameters, can pull in large amounts of data but users must not load it once at the start of the job and then use it repeatedly since it may not be valid for all the data they process. Also multiple users may want access to the same data and it would be inefficient for each to have their own copy.
To deal with both of the above problems, the interface uses the concept of handle or proxy . When accessing a particular table, a table-specific pointer object is created. the corresponding object is usually very small is suitable to be stack based and passed by value, thus reducing considerably the risk of a memory leak.
During construction of the pointer, a request for data is passed down through the interface and the results table, which could be large, is created on the heap. The interface places the table in its cache and the user's pointer is attached to the table, but the table is owned by the interface, not the user.

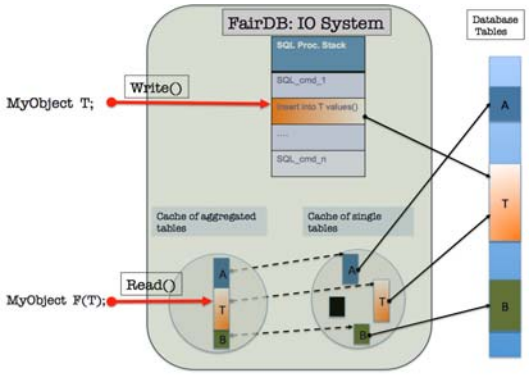

Figure 2: FairDB SQL I/O persistency scheme. Different level of Caches are used to store recently accessed table in on disk.

References

[1] FairRoot Virtual Database (User Manual). `https://panda-wiki.gsi.de/foswiki/pub/Computing/PandaRoot/FairRootVirtualDatabase.pdf`
[2] http://docs.oracle.com/javase/tutorial/jdbc/

 doi:10.15120/GR-2014-1-IT-12

E-Science Activities at GSI

K. Schwarz for the e-science group/Scientific Computing[1]
[1]GSI, Darmstadt, Germany

This article describes the work of the GSI e-science Group with the aim to operate an ALICE tier2 centre within the global environment of the LHC Computing Grid and to prototype a distributed computing environment for FAIR.

ALICE tier2 centre at GSI and ALICE Grid in Germany

The ALICE tier2 centre and the National Analysis Facility at GSI provide a computing infrastructure for ALICE Grid and for the local usage of the German ALICE groups. New data-sets are being transferred to GSI continuously and are processed on the local batch farm via daily running analysis trains. Disk space is provided via the Cluster File System Lustre. The storage resources pledged to the global ALICE community (550 TB) are provided via a Grid Storage Element which consists of an xrootd daemon running on top of the Lustre file system. Data stored on the Grid Storage Element can also be read from local ALICE jobs. The remaining Lustre capacity (4.7 PB) is used for local storage but has to be shared with other experiment groups of GSI/FAIR. Throughout the year GSI participates in centrally managed ALICE Grid productions and data analysis activities, but also analysis jobs of individual users are running on the ALICE tier2 centre. Since recently the routing problem between the GSI batch farm and the local ALICE Storage Element has been solved the average job efficiency of Grid jobs running at the ALICE tier2 centre is close to that of other high level tier 2 centres. The overall job share in 2013 contributed by GSI tier2 and Forschungszentrum Karlsruhe (ALICE tier1 centre) as well as the HHLR compute cluster at Goethe University in Frankfurt has been 11% of all ALICE Grid jobs worldwide. This corresponds well with the pledged CPU resources for 2013: 7000 HEP-SPEC06 for GSI tier2 (4% of the global T2 requirements) and 30000 HEP-SPEC06 for FZK (30% of the global T1 requirements)

CRISP and LSDMA

The Cluster of Research Infrastructures for Synergies in Physics (CRISP) project is a collaboration between different institutions and facilities related to physics research. GSI participated in Work Package 16 and contributed in developing a pan-European system for unique identification. As a prototype solution Umbrella has been presented. The work of this group concentrated on bridging solutions between the Umbrella system and X509 certificates as used in Grid communities as well as between Umbrella and EduGAIN.

The work of the Data Life Cycle Lab "Structure of Matter/FAIR" within the portfolio project "Large Scale Data Management and Analysis (LSDMA)" is being defined in close collaboration with the FAIR experiments. Main work topics are parallel and distributed computing as well as global data federations.

KOSI

Within the context of the KOSI program (Kooperativer Studiengang Informatik) from Hochschule Darmstadt there is a computing project in close collaboration with the GSI theory group. It explores the synergetic use of different software packages like Mathematica and MathCode from Wolfram with Geneva from Gemfony Scientific and with Lapack, ScaLapack and GSL on the GSI computer clusters. A first application on the chiral extrapolation of baryon masses has been worked out [1].

Preparation for FAIR

In order to be able to prepare a distributed computing concept for FAIR experience is being accumulated starting with currently existing computing environments. Currently the focus lies on the AliEn middleware since know-how is available due to the ALICE tier2 centre at GSI. Based on a gap analysis it will be decided if the FAIR computing requirements can be mapped on further developed current systems or if major components if not all have to be replaced. Well-grounded decisions can be done by evaluating the performance of test beds. Therefore PANDA-Grid came into existence and is now in successful operation since 2004. It has been extended to currently 15 sites in Asia, Europe, and North America. Among these 3 sites are running via WLCG infrastructure. The most recent site which joined is Orsay in France and also the GSI Icarus cluster has been interfaced to PandaGrid. The good collaboration between ALICE Offline and the PandaGrid project is being continued, so recently a common workshop in Torino took place. The central PandaGrid services as well as the central Grid data base (MySQL) are running at GSI while the central MonaLisa monitoring repository and a backup database are maintained in Torino.

References

[1] M.F.M. Lutz, K. Schwarz, R. Bavontaweepanya, and C. Kobdaj, "On finite volume effects in the chiral extrapolation of baryon masses", this report.

doi:10.15120/GR-2014-1-IT-13

High-Level Data Flow Description of FPGA Firmware Components for Online Data Preprocessing*

H. Engel[1], *F. Grüll*[1], *and U. Kebschull*[1]

[1]IRI, Institut für Informatik, Johann Wolfgang Goethe-Universität Frankfurt, Frankfurt, Germany

FPGA firmware for detector read-out is commonly described with VHDL or Verilog. Data processing on the algorithmic level is a complex task in these languages and creates code that is hard to maintain. There are high level description frameworks available that simplify the implementation of processing algorithms. A sample implementation of an existing algorithm and the comparison with its VHDL equivalent show promising results for future online preprocessing systems.

Field Programmable Gate Arrays (FPGAs) are widely used in high energy physics detector read-out chains due to their flexibility. The protocols and interfaces are usually implemented with hardware description languages like VHDL or Verilog. With FPGAs getting bigger and faster they become more and more suitable for performing complex data processing tasks. This can reduce the data volume and significantly ease demands on later software based processing steps. The drawback of the commonly used hardware description languages is that they are mostly working on the Register Transfer Level. This is perfect for high performance protocol and low level interface implementations. However, using these languages to implement data processing on an algorithmic level requires experienced developers and usually involves customized IP cores and latency matching of components. This creates a rather complex and static design. There are several high level hardware description frameworks available that provide their own languages to describe data processing steps on an algorithmic or data flow level. Some of them also come with an own framework including building blocks for PCIe or DRAM interfaces. This significantly speeds up the development compared to a description in plain VHDL or Verilog.

The underlying framework of this work is made by Maxeler Technologies. The platform generates a pipelined version of the algorithm after its data flow graph has been described in a Java-like programming language [1]. The compiler manages the scheduling of the design, inserts latencies in the generated pipelines wherever needed to keep the data in sync, and instantiates interfaces to PCIe or DRAM if required. A software environment with a device driver and C API provides easy to use stream interfaces to the hardware. The compiler translates the data flow description into VHDL code which is then run through the vendor tools.

The algorithm described in this way is the FastClusterFinder that was used as a VHDL core in the readout of the ALICE Time Projection Chamber during LHC run period 1 [2]. A simplified overview of the algorithm is shown in Fig. 1. The incoming raw data is decoded into a data stream with time and location information. The center of gravity and the deviation of peaks are calculated in time direction. In a second step neighboring cluster candidates are merged to get the center of gravity and the deviation of the full cluster in pad direction. The last step is a floating point division. The VHDL implementation is a rather complex design due to its data flow control structures and the number of fixed point and floating point arithmetics.

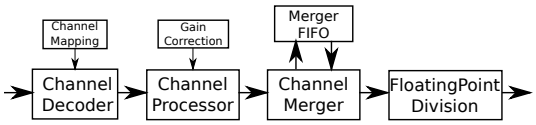

Figure 1: Schematic picture of the ALICE TPC FastClusterFinder algorithm.

A functionally identical version of the FastClusterFinder algorithm has been described with the Maxeler data flow description language. The behavior of this implementation has been verified in simulation using recorded detector data from ALICE TPC. The output of the data flow simulation is directly compared to the output of a Modelsim simulation of the original VHDL code. In comparison to the VHDL implementation the number of lines of code is significantly reduced for the data flow description. Especially the computing intensive parts of the design are very easy to understand and to maintain. The resource usage of the generated design in its current state is slightly different in details but overall in the same order of magnitude as the VHDL implementation.

This implementation shows that there are tools available to describe processing algorithms on an algorithmic or data flow level that are able to generate hardware with comparable resource usage but significantly reduced code volume. This greatly improves maintainability of the code. A next step will be to implement and test the code in actual hardware. Furthermore, the generation of VHDL code out of the data flow description allows the processing elements to be extracted from the vendor framework and integrated as IP core into an own firmware environment.

References

[1] Maxeler Technologies, *Programming MPC Systems*, White Paper, June 2013

[2] T. Alt and V. Lindenstruth, *Status of the HLT-RORC and the Fast Cluster Finder*, GSI Scientific Report 2009

* Work supported by HGS-HIRe, HIC4FAIR

 doi:10.15120/GR-2014-1-IT-14

gStore – the GSI Archive Storage for Experiment Data

H. Göringer, M. Feyerabend, M. Imhof, and S. Sedykh
GSI, Darmstadt, Germany

Overview

gStore is a client/server middleware developed at GSI and tailored according to the requirements of the GSI experiments. gStore provides high performance access 24 hours a day and 7 days a week. For running experiments, highly parallel online writing to dedicated gStore write cache is enabled, including online data copy to lustre for online experiment monitoring and analysis. Due to the design principles:

- reliable long term archive storage,
- full scalability in data capacity and I/O bandwidth,
- high performance access due to intrinsic parallelism,

gStore is well prepared for the challenges of the future FAIR T0 centre. Design principles and functionality are described in detail in GSI reports, talks, and two papers.[1]

Hardware Status

Experiment data are archived in two automatic tape libraries (ATLs), which are also used for backup of user data. The larger ATL has a storage capacity of 8.8 PByte and an I/O bandwidth of 2 GByte/s currently. The smaller ATL (1.3 PByte) is located in the remote BG2 building and contains copies of experiment (raw) and user backup data. This concept prevents from loss of valuable data in case of media damage and enables data recovery even in case of a disaster in the computing centre.

Data are accessed via data movers with read and write disk cache of 220 TByte overall. This large disk buffer hides the tape storage from the users to a big extent. The lustre file system /hera, a cluster file system with ˜ 3 PByte storage capacity, is the online storage for data analysis on Prometheus. The I/O bandwidth between gStore and /hera amounts to 2.5 GByte/s currently.

gStore Enhancements

Data copy to lustre. To utilize the available bandwidth, for retrieve processes from tape to lustre automatical parallelization by gStore has been implemented. The input data are sorted twice, according to their location on tape media and to the storage order on the media. Then files on different tape media are copied in parallel by different processes running on different data movers, and all files are read in optimal order from the corresponding media. Obviously the number of parallel processes is limited by the number of available tape drives, which is up to eight currently. It should be noted that this parallelization cannot be done by the users themselves, because they intentionally need not care about file location on tape and therefore do not have the corresponding information. Due to the high performance connection between gStore and lustre - matching the tape speed of 250 MByte/s - tape files are copied directly to lustre, skipping the otherwise mandatory staging step to gStore read cache. This additionally reduces the copy time considerably.

The parallelization concept works only efficiently if a large number of files is copied with one single (gstore) command, the more files are involved, the better. To specify many files, wildcard characters, a file list, recursive file operations, or any combination of them can be used. Thereby users need not keep track of files already archived in gStore or already staged or retrieved from gStore, respectively, because files already existing are never overwritten, except if explicitly specified otherwise. If some of the specified gStore files are not on tape, but already staged in read cache or still residing on write cache, additional copy processes on each data mover involved are started. Therefore a few tens of copy processes may initiated by one single user command

Removal of limitations in file number. To support as many files as possible in single commands, some limitations in file number have been identified and removed. Up to now with one single command more than 100,000 files have been processed successfully by users.

As an example, in a recursive user archive command 127,473 matching files have been found in lustre. 26,635 files have been rejected, mainly because they were already existing in gStore, or because they were empty or had invalid file names. The remaining 100,838 files, with file sizes from some 10 bytes to ˜ 1 GByte and ˜ 6.5 TByte size in total, have been archived successfully to the write cache of a data mover. With all latencies included, the average data rate amounted to 152 MByte/s.

Outlook

It is planned to implement automatic parallelization also for processes copying from lustre to gStore. Using up to 10 data movers in parallel, the overall copy time would be decreased by an order of magnitude.

Newer lustre versions soon available at GSI enable to implement and test the lustre HSM (Hierarchical Storage Manager) functionality with tape backend in gStore.

According to the road maps of big tape manufacturers, data capacity (now 4 TByte/tape) and I/O speed (now 250 MByte/s) will be doubled in the next years. With additional frames for tape media and tape drives, our ATL data capacity could be enhanced then to ˜ 100 PByte, which is already the order of magnitude needed for FAIR.

References

[1] see `http://www.gsi.de/informationen/wti/it/exp_daten/daten_speicherung_e.html` as starting point for more info

doi:10.15120/GR-2014-1-IT-15

 doi:10.15120/GR-2014-1-IT-15

FAIR@GSI progress in 2013

O. Kester[1]

[1]GSI, Darmstadt, Germany

In April 2012 the GSI advisory board requested GSI to establish a line management structure that focuses on the in-kind contributions of GSI to the FAIR project. The result is FAIR@GSI, which was established in August 2012. FAIR@GSI is responsible for the technical supervision of all FAIR accelerators, for the upgrade and operation of the existing GSI accelerator facility and for the procurement of the equipment GSI will provide in-kind to the FAIR accelerators and experiments. In 2013 FAIR@GSI is running with its seven divisions, which cover the accelerator sections and the according experiments as well as project coordination and the cross functional machine tasks. The focus on the project is the scientific and technical work on the work packages defined by the work breakdown structure (WBS). This comprises the technical supervision of all FAIR accelerators, the design and the construction of the systems and components GSI delivers in-kind and the upgrade and development of the GSI accelerator facility. FAIR@GSI delivers the project management for the sub project accelerator. The project coordination organizes the project planning, financial and procurement control, quality assurance, interfaces to the other sub-projects and the documentation and the data handling of project relevant information. In 2013 a solid resource loaded schedule of the project has been established.

In 2013 the collaborations with our partner institutes did progress. MoUs have been established with Budker institute concerning the design and technical supervision on the collector ring (CR) which will be shared in the future. As a start of the collaboration on the CR machine two GSI - BINP workshops have already been held this year, the first one in April and the second one in June 2013. During these workshops, many experts from BINP have visited GSI and discussed together with GSI experts the technical aspects of the CR magnets, the vacuum system design and the power supplies. CEA Saclay is already working on the proton sources and LEBT of the p-linac and will take over the technical supervision of the Super-FRS dipoles. The test infrastructure for the Super-FRS magnets at CERN is progressing due to the substantial support of CERN. The collaboration with Dubna on the SIS100 quadrupole modules and the testing of the quadrupole units is detailed out and contracts are in preparation or have been signed. Finally the collaboration with KVI in Groningen is another strong pillar, supporting the construction of the Super-FRS.

The superconduction (S.C.) magnets for the FAIR synchotron SIS100

In June the Babcock-Noell GmbH (BNG) delivered the First Of Series (FOS) superconducting (S.C.) dipole magnet for the FAIR synchrotron SIS100. The delivery of the dipole was the first step in the production phase of the heavy ion synchrotron SIS100, the primary beam driver accelerator of the FAIR project. According to the schedule, more than 112 dipole magnets will be produced and delivered to GSI in the next three years. The factory acceptance test (FAT) was successful and therefore the magnet has been prepared for site acceptance test (SAT) at GSI. However about 95 points have been identified in the FAT, which need to be adjusted for the series magnets. The magnet has to undergo a significant number of tests including cols tests. End of 2013 the magnet was tested for the first time at cryogenic temperatures (4 K) under pulse operation conditions. The magnet did exceed its designed performance and quench training went very well.

The ion optical lattice of SIS100 comprises 108 dipole modules and 83 quadrupole modules arranged in the 1086 m long SIS100 accelerator. The 83 quadrupole modules are split into 13 different configurations of arrangements of internal sub-devices. One configuration, appearing in the arc sections of SIS100, was selected to be designed up to a level ready for production. Based on the need of increasing operation safety of the SIS100 machine to a maximum, a consequent reduction of internal interfaces is required. Hence the concept of an integrated quadrupole doublet module was developed at GSI. Within one module two s.c. quadrupole magnets are integrated into a common cold mass, together with further corrector magnets, collimators, bus bar and current lead systems the cold mass is covered in a quadrupole doublet cryostat.

Magnet test facilities

The tests of the several hundred S.C. magnets cannot be done in a single facility. Therefore the different magnets will be tested in three different locations. Prototype magnets and all dipole magnets of SIS100 will be tested at GSI. Significant upgrades to the GSI test facility were needed in order to be ready to test the FOS superconducting dipole. The power converter had to be upgraded to double its maximum current (now up to 20 kA) adjusting its output voltage to the particular SIS100 and SIS300 magnets. High temperature super conductor (HTS) current leads were needed due to the limited cooling capacity of the cryogenic infrastructure at the prototype test facility of GSI. The power converter was optimized and commissioned with a test load. The security off-switch has already been integrated in the power converter. The current leads were delivered to GSI on the 10th of October and then mounted into the feed boxes. The preparation of the series test facility including procurement of the 2 kW cryo plant and the construction of the building for the

cryo plant has been significantly pushed forward in 2013.

The S.C. quadrupole units of the SIS100, will be produced at JINR/Dubna. The quadrupole units are combinations of a main quadrupole with a BPM, a sextupole or a steerer. To guarantee conformity of each of the 175 quadrupole units to the technical specifications they have to be subjected to detailed cold tests and measurements that certify the required performance. The according test infrastructure will be developed, manufactured and commissioned at JINR/Dubna. The units of the SIS100 superconducting quadrupole doublet modules (QDM) will be cold tested. This test facility will be available for testing superconducting magnets of the NICA accelerators as well and demonstrates the synergy of the common effort.

The huge Super-FRS magnets, dipoles and multiplets, will be tested at CERN in a collaboration of GSI, CERN and CEA Saclay. CERN will install a test facility with all infrastructure serving three test benches in hall 180. First cleaning and installation work on the infrastructure in this hall has been performed by CERN.

Preparation for the FAIR rf-systems

The rf-systems of SIS100 comprises (in the start version) 14 acceleration cavities, 9 bunch compressor cavities and one cavity for barrier bucket operation. For all cavity types, procurement has been started in 2013. A new rf-cavity was developed and realized in the framework of the SIS18-upgrade program in order to increase possible beam intensities for FAIR. The so-called „h=2-system“ was developed for the high current operation of SIS18 to flatten the ion density distribution in the bunch and therewith reducing the space charge forces acting on the particles in the bunch. It is essential for the later booster operation for the SIS100 with its high repetition and ramp rate. The “h=2”-cavity has been installed in the shutdown period of 2013 including all infrastructure installations required for the cavity operation. Based on the limited space in the synchrotron tunnel it was necessary to place the high-power-rf-amplifiers (weighting 1 ton) directly on top of the cavity. Due to that the height of the ring tunnel has been enlarged at the location of the cavities. Originally the new rf-system was installed and operated (without beam) in the testing-hall. This required serious efforts, because the supply devices, like the electrical supply from the common net, the oil cooling installation for one unit and the cooling water supply for the other unit, have been installed there additionally.

Beam cooling in the storage rings

The collector ring (CR) serves the fast stochastic cooling of antiproton and rare isotope beams. The FAIR Council has allocated the CR stochastic cooling system to GSI as an in-kind contribution. Intensive engineering, manufacturing and procurement activities on various system components have been done in 2013 at GSI. One of the main technical challenges is the cryogenic movable (plunging) pick-up electrodes. After extensive engineering design work, two novel water-cooled linear motor drive units have been assembled in the mechanical workshop and the existing prototype pick-up tank has been modified to accommodate them. These units are easier to maintain and made from aluminium, which is lighter than the previously used stainless steel. Their maximum range of plunging is now 70 mm.

In order to enhance the signal to noise ratio, which is the main challenge for the stochastic cooling of antiproton beams, the movable pick-up electrode modules are thermally coupled to flexible sheets, which are cooled by 2 helium cryoheads to about 30 K. The cryoheads also cool an intermediate cryoshield at 80 K.

Reconstruction started in cave-B for the CRYRING installation

In July 2013, the Transport & Installation department (CSTI) has successfully removed the FOPI superconducting magnet from cave-B. The removal of this magnet was an important step for the remodelling of cave-B as a future home of CRYRING@ESR, a Swedish in-kind contribution to FAIR. CRYRING@ESR is a heavy-ion storage ring and will be served with ion beams from ESR or from an independent ion injector. It will first deploy several key technologies for FAIR and serve as an experiment facility on low-energy highly-charged ions. After the move of the magnet the complete reconstruction of cave-B has already started.

Digital mock-up (DMU) of the FAIR machines

A very important task is the work in the digital model of the whole accelerator facility, which allows the check for interfaces, collisions with the building infrastructure and the proper alignment of the beam lines to the ion optical lay-out (IOL). This digital mock-up (DMU) is an essential part of the configuration management of FAIR@GSI and is a very successful example for excellent project work at GSI. A 3D-model for the IOL prepared with the beam optic program “Mirko” serves as the backbone for the representation of the beam lines. One of the main jobs of the DMU-team of the mechanical integration (ENMI) department is the visualization of results which have been developed by differenz scientific and technical departments. Many data types have to be transferred into the format of Catia.

As an example the normal conducting (N.C.) magnets are delivered by the magnet and alignment department (ENMA) as 3D-models which will be included in the DMU of the beam lines. After this, the vacuum chambers and diagnostic boxes will be chosen and positioned and collisions will be checked. Defining interfaces for components of different suppliers is one of the major tasks in the developmental stage. Cables, tubes and their ducts and trays towards the components, alignment concept, references, installation space, accessibility, fixation and many more things have to be cleared before the specifications can be released.

 doi:10.15120/GR-2014-1-FG-GENERAL-01

UNILAC Status Report

L. Groening[*1], *P. Gerhard*[1], *M. Maier*[1], *S. Mickat*[1], *A. Orzhekhovskaya*[1], *H. Vormann*[1], *and S. Yaramyshev*[1]

[1]GSI, Darmstadt, Germany

Maintenance Activities

In 2013 no beam has been provided by the UNILAC; the full year was dedicated to maintenance instead. This chapter summerizes the major works while the second one lists the ongoing upgrade design activies.

Media systems

The water distribution circuit providing cooling for the fourth Alvarez cavity and the IH cavity of the High Charge Injector (HLI) has been split into two independent circuits. The measure enhances the temperature stability of the two cavities which in the past suffered repeatedly from difficult incoupling of rf-power. General maintenance was done at the water pumps of the other circuits. The cooling water conduit of the Alverez section and of the transfer channel was renewed, including provision of de-ionized water for the drift tubes, couplers, and tuners. Many pumps underwent maintenance of the ball bearing and the exchange of oil. The ventilation systems of the High Current Injector (HSI) and the Alvarez section were completely revised.

Cavities

The UHV seals of some Alvarez cavities have been replaced by new ones produced on-site. The repair of UHV leakages at the junction between cavity A2a and the subsequent cavity BB5 required much more resources w.r.t. time and personell as expected. Repeated leakage occured after remounting the spokewheels. The same type of work was done at one single gap resonator. The cause of increased reflection of incoming rf-power at the HLI RFQ was identified as mechanical vibrations of the rods, being resonantly amplified at specific time structures of the rf-pulses [1]. The rf-power line to the RFQ of the HSI has been systematically checked in order to identify the origin of rf-reflection; the line proved not to be the cause, we rather assume sparking in the RFQ cavity.

Miscellaneous

The misalignment of the transfer channel beamline due to ground water settlement was quantified. Systematic beam loss surveillance was extended to the areas "transfer channel" and "experimental hall"; several steerers have been equipped with new bipolar power converters.

Upgrade Activities

Compact LEBT

The FAIR requirements on beam intensity of uranium and on the handling of the related infrastructure indicate the installation of a dedicated uranium source terminal together with the subsequent beam transport system. It shall be located between the existing terminals which feed the HSI. As a consequence the latter will not provide uranium in the future. This new branch (Compact LEBT) is under design, aiming at simplified beam optics, i.e. omission of bending magnets and shortening of the line. The expected gain in beam quality will be benchmarked to the todays performance. Details are summarized in dedicated reports [2, 3]. The activities include also studies on improved beam transport through the existing HSI as well as extensive measurements of the beam parameters provided by the existing high intensity uranium source.

Replacement of Alvarez DTL

The existing Alvarez-type DTL, providing acceleration from 1.4 to 11.4 MeV/u, is in operation for several decades. To ensure reliable operation for FAIR it ought to be replaced by a new DTL. The design activities of this new so-called HE-Linac have been started in close collaboration with the Goethe University of Frankfurt. Several options w.r.t. the cavity type are under investigation to ensure that the best choice is made for FAIR w.r.t. beam quality and cost efficiency. For details we refer to [4].

EmTEx

An Emittance Transfer Experiment (EmTEx) aims at demonstration of tailoring the 4d-phase-space distribution of the beam from the UNILAC such that its properties better match to the requirements of the synchrotron SIS18. The proof-of-principle with deuteron beams is foreseen in summer 2014. Last year saw the installation of the set-up in the transfer channel [5, 6].

References

[1] P. Gerhard et al., this report.

[2] H. Vormann et al., this report.

[3] S. Yaramyshev et al., this report.

[4] S. Mickat et al., this report.

[5] C. Xiao et al., PRST-AB **16** 044201 (2013).

[6] M. Maier et al., this report.

[*] la.groening@gsi.de

Status of the Compact LEBT Project

H. Vormann, S. Yaramyshev, A. Adonin, W. Barth, R. Berezov, L. Dahl, P. Gerhard, L. Groening, R. Hollinger, M. S. Kaiser, M. Maier, S. Mickat, K. Ochs, A. Orzhekovskaya, and C. Xiao
GSI, Darmstadt, Germany

To fulfil the intensity requirements for FAIR, a dedicated high current uranium ion source and Low Energy Beam Transport line will be built at the High Current Injector HSI [1]. This new injection line (Compact-LEBT) will be integrated into the existing complex with two branches, designed as a straight injection line without bending magnet (fig. 1). The joint use of the existing matching line (from switching magnet to RFQ) is foreseen.

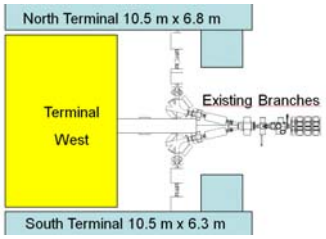

Figure 1: Scheme of the Compact-LEBT.

Design of the new Beam Branch

Preparing the design of the new branch, measurements directly behind the ion source had been available with different ions (e. g. argon, tantalum), but not with uranium beams. Now, such direct uranium measurements have been performed at the existing north terminal with the VARIS ion source [2]. The GSI standard mobile emittance device (horizontal and vertical) was used for emittance measurements behind the first triplet of the beam line. To measure the large beam directly behind the terminal, the emittance device from HOSTI was used (large grid size). Also tantalum beam was measured, to allow a comparison of the measurement results from HOSTI and from North Terminal. The good performance of the ion source was confirmed.

Simulations with the DYNAMION code, based on the measurement data, were used to optimize the designed beam line. For the recent design the use of a new quadrupole triplet in the crotch between the existing beam lines, and an already existing quadrupole quartet for focusing behind the terminal is proposed (fig. 2) [2].

Ion Sources

Measurements with different ion beams as tantalum and argon have been performed at the high current test injector (HOSTI), to investigate beam intensity and emittance for different extraction- and post acceleration geometries, long run tests of insulator materials, and the suitability of a solenoid magnet for high current operation [3].

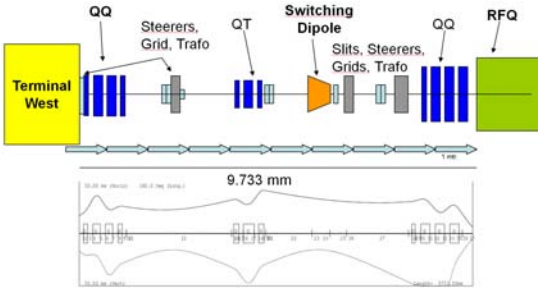

Figure 2: Recent layout of the Compact-LEBT.

A layout for the new uranium terminal (Terminal West) has been designed (fig. 3). The terminal contains a closed under-pressure system, it houses all sections like a high voltage area with power supplies, transformers and a working platform (closed electrical working area), and a service area with glove box (radiation protection controlled area).

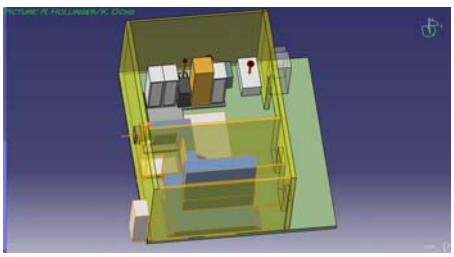

Figure 3: Principle layout of the Terminal West.

Components and Commissioning

While beam diagnostics components with larger apertures in the existing LEBT are already in operation since 2012, a new quadrupole quartet magnet with enlarged aperture (150 mm diam.) is not yet installed. It was delivered in late 2012, since then precise field mapping has been made. Tendering for the power supply is starting. A new switching magnet and steerers with larger aperture are under design, a new quadrupole triplet can be designed similar to existing triplets. Completion and commissioning are foreseen for 2017.

References

[1] L. Dahl, proc. LINAC 2006
[2] S. Yaramyshev et al., this report
[3] A. Adonin et al., this report

 doi:10.15120/GR-2014-1-FG-UNILAC-02

Investigation of the Compact LEBT Design Prerequisites

S. Yaramyshev, H. Vormann, A. Adonin, W. Barth, R. Berezov, L. Dahl, P. Gerhard, L. Groening, R. Hollinger, M. Maier, S. Mickat, A. Orzhekhovskaya, C. Xiao

GSI, Darmstadt, Germany

A new injection line [1,2,3] is proposed as a part of the upgrade and further development of the high current heavy ion linac UNILAC for the FAIR requirements. The final design of this straight line should be based on precise and complete information about beam current and emittance coming from ion source. An intense experimental campaign was carried out in June-November 2013 at the North Terminal of the UNILAC. Full and self-consistent data for uranium beam including detailed knoweledge about the beam current phase density in the transverse phase space has been obtained [4].

As the new LEBT (Low Energy Beam Transport) has no separation by bending magnets, the full spectra of different uranium charge states (2+, 3+, 4+, 5+, ...) will be transported through the line. Then the beam emittance of only design ions U4+ should be matched to the HSI-RFQ acceptance. Although the neighboring charge states could be partly separated at the LEBT, a significant portion of mainly U3+ ions will be also injected into the RFQ. This leads to an increased space charge effects and makes a strong influence on particle motion. Therefore an information about ratio U4+ / U3+ is important for proper beam transport and matching. Measurements of beam parameters have been performed at existing UNILAC beam line, directly behind North ion source terminal. Obviously a beam current and beam emittance could be measured only for all charge states together. The standard diagnostics is not able to distinguish ions with different charge states. To solve this problem, a set of measurements behind the first quadrupole triplet (UL4QT1) of the North LEBT was insistently proposed. As it is shown on Fig.1 (left), a different focusing efficiency for the different charge states leads to a complicate shape of a composite beam emittance.

To distinguish between different charge states a dedicated algorithm was proposed, developed and realized. A macroparticle distribution was generated from the raw data of measured (with slit-grid device) emittance. The density of macroparticles is proportional to the measured intensity in each bin. Beam dynamics simulations with DYNAMION code have been firstly done backward (upstream beam direction) through the measured magnetic field of the triplet. Two identical distributions, but with different charge state of macroparticles (U3+ and U4+) have been transported separately. In assumption that the beam parameters behind an ion source terminal are the same for every charge state, only a phase space overlapping of resulted particle distributions has been treated as an emittance formed by the complete beam. The obtained "realistic" particle ensemble has been simulated forward (downstream a beam), again separately as U3+ and as U4+. The transported particles at the position of measurements form separately beam emittances for different charge states which perfectly cover the originally measured phase space distribution (Fig. 1, right).

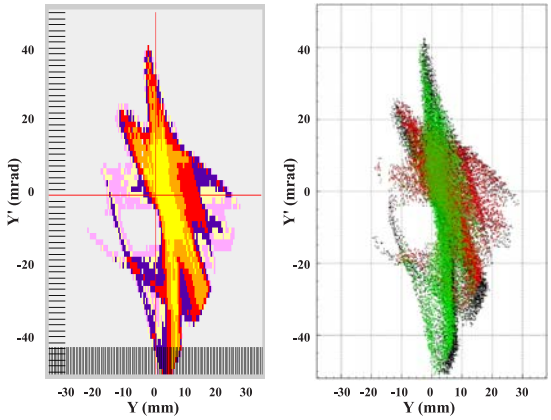

Figure 1: Measured beam emittance (left) and macroparticle distributions (right): generated from measurements (black), reconstructed U4+ fraction (green), reconstructed U3+ fraction (red)

Additionally a dedicated algorithm, based on least squares calculations, provides for an estimated U4+ intensity inside the measured one for all charge states together. With use of this algorithm one can extract from the recent measurements for the mixed beam (U3+ and U4+ mainly) the beam parameters for the design ion U4+ only. The beam current and emittance obtained with different settings of the ion source terminal are in the range of 20-35 mA inside 300-450 mm*mrad respectively. For comparison, the HSI-RFQ high current acceptance with these beam parameters is in the frame of 250-300 mm*mrad.

Generally the proposed coupling of detailed measurements and precise simulations acts as a virtual charge state separator. Being implemented simultaneously for both transverse phase planes, it provides for a better beam transport, refined matching with an RFQ acceptance, as well as for an improved UNILAC performance.

References

[1] L. Dahl et al, Proceedings LINAC 2002

[2] S. Yaramyshev et al, GSI internal Report 2009

[3] H. Vormann et al, these Proceedings

[4] S. Yaramyshev et al, GSI internal Report 2013

Investigation of beam brilliance of high current Ta-beam on HOSTI in the frame of compact-LEBT project

A. Adonin, R. Berezov, and R. Hollinger
GSI, Darmstadt, Germany

With the coming FAIR project the requirements for beam brilliance will be significantly higher compare to the values provided by existing high current injector. Therefore it is planned to build up a separate injector (Terminal West and Compact LEBT) designed specially for production of high current uranium beams [1]. Also it is necessary to improve and optimize the setup of high current uranium ion sources including extraction and DC post-acceleration systems. These improvements can be performed and demonstrated on high current test injector HOSTI [2].

In 2011 at HOSTI injector the setup has been modified. A new post acceleration system designed for maximum 150 kV voltage was installed. It is much more compact compare to the old one with reduced drift to the first focusing beamline element by 0.8 m. As a result ion beam losses are reduced as well (Fig.1).

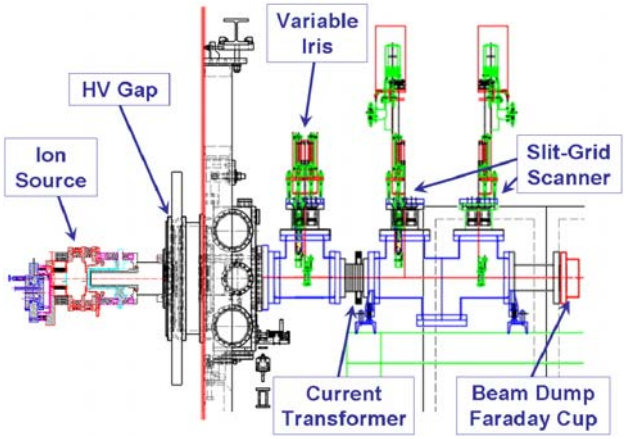

Figure 1: Scheme of the HOSTI setup with a new post acceleration system.

Several sets of measurements have been performed at HOSTI using high current non-radioactive ion beams (Ta, Ti and Ar) [3]. Different aspects related to improvement of performance of high currents ion sources were studied: mainly the investigation of beam brilliance of high current Ta-beam provided by vacuum arc ion source VARIS as function of beam aperture. The aperture of the ion beam was controlled with a variable iris installed directly behind the post-acceleration system (Fig.1). The measurements are shortly summarized in Fig.2. It is shown that there is an optimum beam aperture size with highest brilliance between 45 and 60 mm (iris aperture).

Measurements with various apertures of HV-electrodes in the post-acceleration gap have shown a strong influence of electrostatic beam compression in the gap on the beam emittance (Fig.3). Therefore the optimization of electrodes geometry in the post-acceleration system is one of the promising ways to increase the beam brilliance.

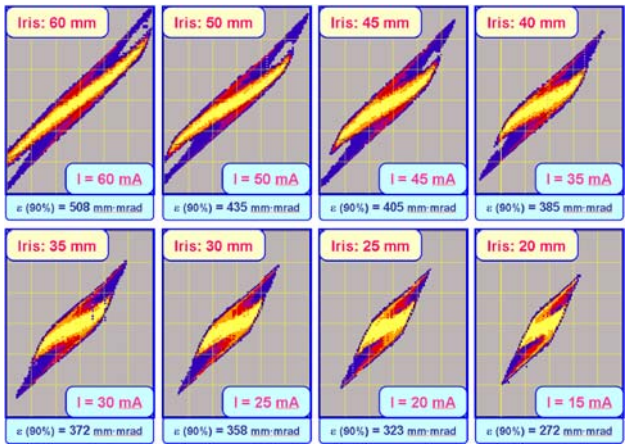

Figure 2: Emittance and current measurements of tantalum ion beam for various iris apertures with fixed ion source settings.

Various extraction systems have been tested and compared in order to achieve a more brilliant ion beam core: single hole, 7-holes and 13-holes (standard). It was proved that 13-holes extraction system is optimal for ion beam apertures $\geqslant$50 mm. While for small beam apertures ($\leqslant$40 mm) 7-holes system is advantageous. A single hole extraction system is not suitable for production of high current beams, however it provides the most brilliant beam core.

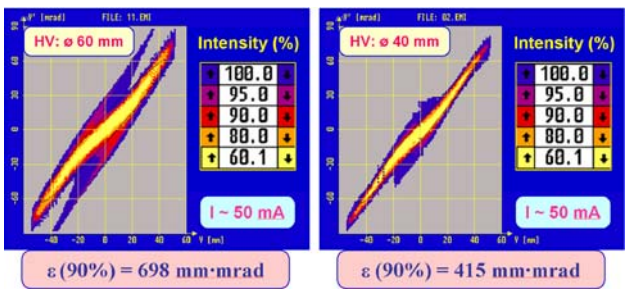

Figure 3: Emittance of Ta-beam with ø60 mm HV electrode (left) and with ø40 mm HV electrode (right).

References

[1] H. Vormann et al., this report

[2] A. Adonin, R. Hollinger, and P. Spädtke, Rev. Sci. Instrum. 81, 02B707 (2010)

[3] A. Adonin and R. Hollinger, Rev. Sci. Instrum. 85, 02A727 (2014)

 doi:10.15120/GR-2014-1-FG-UNILAC-04

Collimation and decoupling of ECR source beams for brilliance optimization*

C. Xiao† [1], *L. Groening*[1], *and O.K. Kester*[1,2]
[1]GSI, Darmstadt, Germany; [2]Goethe-Universität, Frankfurt am Main, Germany

Abstract

The four-dimensional transport of the transverse phase space of the extracted beam was calculated for the CAPRICE electron cyclotron resonance (ECR) ion source at GSI. The axial magnetic field adds an angular momentum to the extracted beam, resulting in a strongly x-y coupled beam. The report presents multi-particle tracking simulations, and the results illustrate that the beam brilliance can be improved by combination of multi-stage collimation with skew quadrupole decoupling.

Quadrupole Collimation Channel

The quadrupole collimation channel is placed behind the analyzing magnet in order to improve the beam brightness. An uncorrelated beam with desired Twiss parameters is assumed at the entrance of the quadrupole collimation channel being the periodic matched solution of the channel. Only particles in a defined phase space volume are transmitted through the entire channel, all other particles are stopped at the apertures along the channel. The magnetic quadrupole collimation channel has three cells including three identical magnetic quadrupole doublets and four four-jaw slits. For efficient and flexible collimation, each cell is set to cause a phase space rotation of 45 degree and multiple cells with overall phase advance rotation larger than 90 degree (145 degree in this channel). Four successive four-jaw slits are used for multi-stage collimation with the phase space rotation in between [1].

Skew quadrupole decoupling section

After charge-to-mass selection, two normal quadrupole doublets are used to match the analyzed beam into the quadrupole collimation channel. The quadrupole collimation channel, which consists of three normal quadrupole doublets with the same gradient but alternating sign are used to carry out the multiple-stage phase space rotation. The decoupling section comprises two normal quadrupole doublets and one skew quadrupole triplet, and their gradients are optimized by a numerical routine to remove the inter-plane correlations, thus minimizing the product of the horizontal and vertical rms emittances [2].

Collimation and decoupling simulation

In general, an ECR ion source beam possesses a large beam size and divergence. Therefore, higher order effects (aberrations) can not be avoided inside the solenoid. If the particle deviates from the center of the solenoid, it feels a non-linear force and the non-linear force causes the rms emittances and eigen-emittances to grow. Once the beam enters the analyzing magnet the horizontal rms emittance starts to increase gradually, but the vertical rms emittance is not changed. After charge selection, if the collimators are not adopted to cut particles, the rms emittances and eigen-emittances are almost constant until the first skew quadrupole. If the collimators are adopted, utilization of collimators stepwise decreases the rms emittances and eigen-emittances in the matching section. Inside of the skew quadrupole triplet, rms emittances are made equal to the separated eigen-emittances.

The behaviors of dimensionless brilliances and the transmission efficiencies along beam line with (horizontal half slit width h=2 cm and vertical half slit width v=2 cm) and without collimators are shown in Fig. 1.

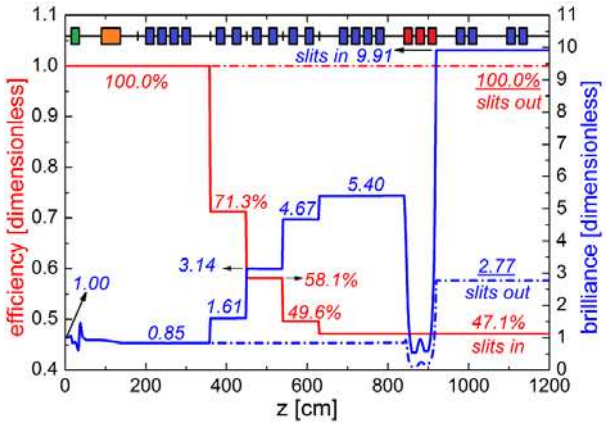

Figure 1: Dimensionless brilliance and transmission efficiency evolutions along the beam line with (solid lines) and without (dash lines) four successive slit collimators.

References

[1] C. Xiao, L. Groening and O.K. Kester, NIM-A, 2014, **738**: p. 167-176.

[2] C. Xiao, L. Groening and O.K. Kester, Phys. Rev. ST Accel. Beams **16**, 044201 (2013).

* Work supported by the Helmholtz International Center for FAIR and the Bundesministerium für Bildung und Forschung.
† c.xiao@gsi.de

Research and Development on ECR Ion Sources

K. Tinschert[1], R. Lang[1], J. Mäder[1], F. Maimone[1], J. Roßbach[1], and P. Spädtke[1]
[1]GSI, Darmstadt, Germany

Upgrade of the HLI microwave system

In the last years several experiments using the technique of frequency tuning were carried out at the ECR injector test setup (EIS) of GSI in order to investigate the influence on the performance of the CAPRICE-type ECR Ion Source (ECRIS) in terms of enhanced ion currents of high charge states [1] [2]. It was demonstrated that this technique allows increasing the ion current extracted from an ECRIS both for gaseous and for metallic elements [3].

In order to use this technique for the routine operation of the ECRIS installed at the high charge state injector (HLI) of GSI, the microwave injection system has been modified. Figure 1 shows a schematic view of the upgraded microwave system. A signal generator provides the microwave signal to be amplified by two traveling-wave tube amplifiers (TWTAs). Each of them provides up to 650 W in the frequency range 12.75-14.5 GHz. When the required power is higher than 650 W, i.e. for Ca or Ti beam production, the power of the two amplifiers is summed up through a WR62 waveguide power combiner. The system is integrated into the existing waveguide system with a WR62 mechanical switch. With this versatile setup the microwave input can be switched from the waveguide line connected to the klystron to the one where the upgraded system including the TWTAs is installed. Two directional couplers are inserted between the switch and the ion source. Microwave power probes are connected to each directional coupler to measure the forward power and the reflected power to and from the ECRIS. The knowledge of the reflection coefficient is beneficial to optimize the microwave coupling to the plasma which is a fundamental condition for a good performance and stable operation of the ECRIS [1].

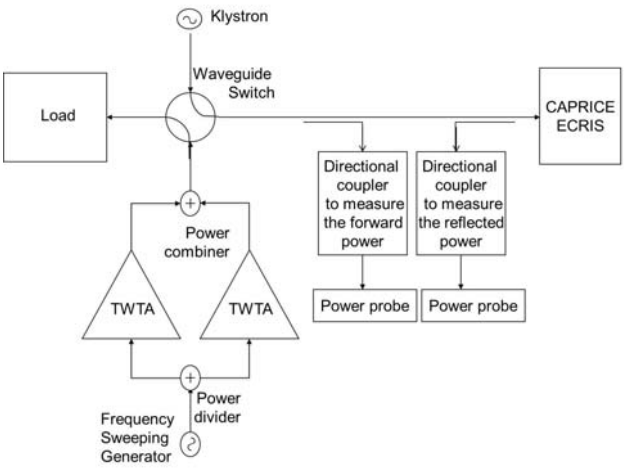

Figure 1: Block diagram of the upgraded microwave system of the HLI

X-ray spectroscopy

In the framework of the ENSAR-ARES collaboration (supported by the European Union Seventh Framework Programme FP7/2007-2013 under EU grant agreement n ° 262010) various experiments have been carried out on the investigation of X-ray emission from the CAPRICE ECRIS. The measurements were performed at the EIS test setup by using two different detectors. A Silicon drift detector (2-30 keV) has been mounted at the extraction electrode, and a high purity Ge detector (30-500 keV) has been placed behind the analyzing dipole magnet in 0 ° direction, respectively. The experiments were performed at different settings of the confining magnetic field and at different microwave frequencies to characterize the electron energy distribution and to investigate correlations with the charge state distribution (CSD) of the extracted ion beam. Results show that the tuning of the heating frequency considerably affects the plasma density. Details are reported in [4].

Beam profile measurements

Ion beams extracted from an ECRIS are in most cases characterized by an internal structure with inhomogeneous current density distribution. Viewing targets (VT) can be used to obtain a qualitative 2D image of the beam profile [5]. For quantitative measurement of spatially resolved 2D current density distributions a multiple Faraday cup array (FCA) is a versatile tool [6]. An in-situ comparison of VT and FCA performed at the EIS test setup in cooperation with L. Panitzsch (Institute for Experimental and Applied Physics, University of Kiel, Germany) could confirm good agreement. A detailed analysis of the data is in progress.

References

[1] F. Maimone et al., Rev. Sci. Instrum. 82, 123302 (2011)

[2] F. Maimone et al., Rev. Sci. Instrum. 83, 02A304 (2012).

[3] K. Tinschert, et al., Proc. of the 20th Workshop on ECR Ion Sources, Sydney, Australia, 25-28 Sept 2012.

[4] D. Mascali et al., Rev. Sci. Instrum. 85, 02A956 (2014).

[5] P. Spädtke et al., Rev. Sci. Instrum. 79, 02B716 (2008).

[6] L. Panitzsch et al., Rev. Sci. Instrum. 82, 033302 (2011).

 doi:10.15120/GR-2014-1-FG-UNILAC-06

Status of the EMittance Transfer EXperiment EMTEX * †

M. Maier[1] *and L. Groening,* [1]*O. Kester,* [1]*H. Leibrock,* [1]*C. Muehle,* [1]*I. Pschorn,* [1]*P. Rottländer,* [1]*C. Will,* [1]*C. Xiao*[1]

[1]GSI Helmholtzzentrum für Schwerionenforschung GmbH, Darmstadt Germany

In order to improve the injection efficiency of the round UNILAC heavy ion beam into the asymmetric acceptance of the SIS18 it would be of great advantage to reduce the horizontal emittance at the expense of increasing the vertical emittance by the so called emittance transfer [1]. As proof of principle a test set has been proposed with the ion optical layout described in [2]. The status of the proposed beam line at the transfer channel shown in Figure [1] is reported.

Experimental Setup

The EMTEX setup is situated in the existing TK beam line and consists of two quadrupole doublets, a split solenoid magnet with a foil stripper in the centre to prepare and magnetize the beam and three triplets including a skew triplet to administer the emittance transfer. The existing transfer channel beam line is not affected and may be used with the stored accelerator settings. While the two last triplets including the skew triplet are of old GSI possession and were refitted in our workshop, all other components had to be ordered newly.

Status of the subsystems

The two triplets including the skew triplet have been available in house and where overhauled by the magnet engineering division ENMA and the mechanic workshop CSTI of GSI. They are installed in the TK5 beam line [2], commissioned, and ready for use.

Figure 1: Setup for the emittance transfer experiment in the transfer channel TK (red), while the existing beam line (black) is not affected.

The solenoid magnet [3] has been designed by ENMA at GSI and manufactured at Danfysik. The vacuum chamber of the solenoid is a special design comprising a view port for on-line observation of the foil. For this reason the inside of the vacuum chamber had to be blackened to reduce reflections. Yet another special solution had to be developed by the GSI construction department for the connection box for the thick water cooled power cables. The solenoid with all components has been delivered, installed, and commissioned just in time.

Figure 2: The two existing, overhauled triplets installed in TK5. The first (left) triplet GTK5QT6 has been rotated by 45 degree to couple the x and y plane for the emittance transfer.

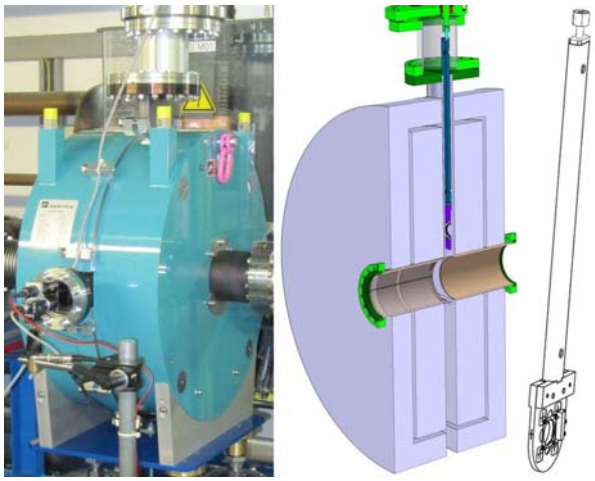

Figure 3: The solenoid installed in the beam line (left) and a schematic of the inner chamber and stripping foil arm (right).

Outlook

Unfortunately the delivery date for the quadrupoles has been delayed and they will be installed during the shutdown in May 2014. The first experimental run of EMTEX is scheduled for June 2014. In case of success it is foreseen to implement an emittance transfer setup in the HSI

References

[1] L. Groening, Phys. Rev. ST Accel. Beams 14, 064201 (2011)

[2] C.Xiao, L.Groening and O.Kester , Phys. Rev. ST Accel. Beams 16, 044201 (2013)

* Work supported by GSI(UNILAC) PSP code:2.14.11

† Work supported by Hic for Fair

Upgrade preparation for the 1.4 MeV/u gas stripper system for FAIR

E. Jäger[1], P. Scharrer[2], A. Yakushev[1], Ch. E. Düllmann[1,2,3], J. Khuyagbaatar[2], J. Krier[1], K.P. Horn[1], L. Groening[1], M. Bevcic[1], and W. Barth[1,2]

[1]GSI, Darmstadt, Germany; [2]HIM, Mainz, Germany; [3]Johannes Gutenberg-Universität Mainz, Germany

A key projectile for the FAIR facility will be ^{238}U. In routine operation of the GSI UNILAC, ^{238}U is generated by a MEVVA ion source that delivers ions with comparably low charge states (4^+), which are accelerated to 1.4 MeV/u in the high current injector (HSI). The 1.4 MeV/u beam passes a region of high gas density, in which the charge is increased to 28^+ by stripping of electrons. [1] Generally, higher intensities at charge states, preferably above 28^+, are desirable. This would allow to operate the accelerator more reliable and efficiently.

To optimize the stripping efficiency and potentially increase the achieved ion charge states a program to upgrade the gas stripper has started. The modified stripper setup is depicted in Fig. 1. As a first modification, switching from the continuously fed supersonic N_2-jet to a pulsed gas injection, synchronized with the beam timing structure, has been implemented. This allows to increase the gas pressure inside the stripper chamber during a beam pulse, while still reducing the total gas flow. The gas injection was positioned inside a T-fitting, which was installed in the main stripper chamber to match the beamline. In a first test the pressure in the main stripping section as function of the opening time of the valve and the pressure along the beamline adjacent to the gas stripper section were measured.

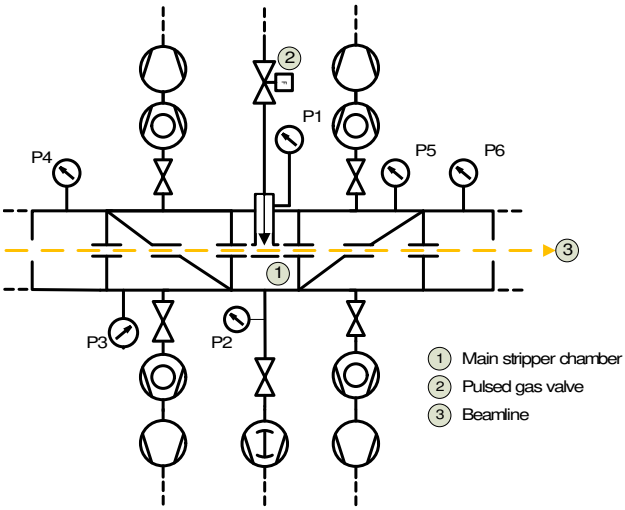

Figure 1: Schematic view of the modified 1.4 MeV/u gas stripper as to be used for first measurements with a pulsed gas valve in beam experiments in 2014.

The gas pressure on the valve was 3 MPa. The dependency of the pressure inside the stripper chamber and the pumping performance on the valve opening time was evaluated

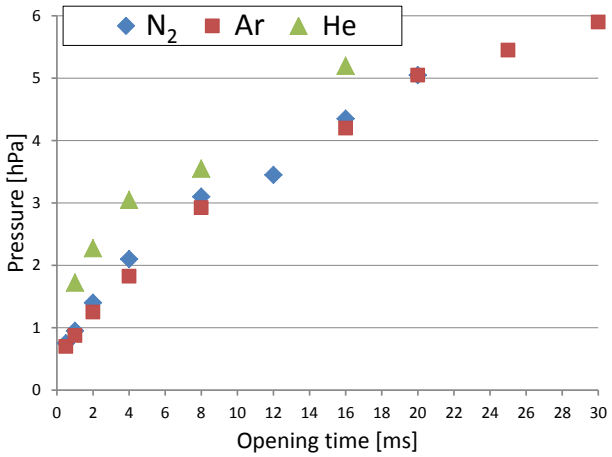

Figure 2: Pressure measurements at the gas stripper for different stripper gases as function of the opening time of the pulsed gas valve.

for three different gases (N_2, Ar and He). These gases are planned to be investigated as potential stripper gases in the future, together with Xe.

The results of the pressure measurements near the gas outlet in the main stripper chamber (diaphragm vacuum gauge at P1, Fig. 1) are shown in Fig. 2. As the pressure varried according to the pulsed gas flow regime, only the maximum pressure values during one pulse are shown. Note that the vacuum gauge was placed at an entry point on top of the main stripper chamber, so the shown pressures do not represent the real pressure in the beamline. The pressure increases with increasing opening time and starts to level off at longer opening times. N_2 and Ar are pumped at about the same rate whereas He is pumped less efficiently. Therefore, the pressure at the vacuum gauge is higher for He at the same opening times. The measured pressure increases to values above 5 hPa, independent of which gas was used. The pressure in the adjacent beamline was also measured (vacuum gauges P2-P6, Fig. 1).

The optimum conditions with respect to the pressure in the main stripping region and the adjacent beamline as well as the experimental charge state distribution will be evaluated in beam experiements in 2014.

References

[1] W. Barth, et. al., The new gas stripper and charge state separator of the GSI high current injector, Proccedings of LINAC, 2000.

 doi:10.15120/GR-2014-1-FG-UNILAC-08

Thermal Simulations of Thin Solid Carbon Foils for Charge Stripping of High Current Uranium Ion Beams at New GSI Heavy-Ion Linac*

N.A. Tahir[1], V. Kim[2], W. Barth[1], L. Groening[1], I.V. Lomonosov[2], A.R. Piriz[3], B. Schlitt[1], Th. Stöhlker[1,4], and H. Vormann[1]

[1]GSI, Darmstadt, Germany; [2]IPCP, Chernogolovka, Russia; [3]UCLM, Ciudad Real, Spain; [4]IOQ Friedrich-Schiller Universität and Helmholtz Institute, Jena, Germany

This paper presents an extensive numerical study of heating of thin solid carbon foils by 1.4 MeV/u uranium ion beams to explore the possibility of using such a target as a charge stripper at the proposed new GSI high energy heavy–ion linac. These simulations have been carried out using a sophisticated 3D computer code that accounts for physical phenomena that are important in this problem. The stripper is assumed to be a thin circular foil of solid graphite with density 2.28 g/cm^3 and radius, R_f = 1.5 cm while the uranium beam is incident perpendicular to its surface. Three different foil thicknesses including 20, 30 and 40 μg/cm^2, have been considered.

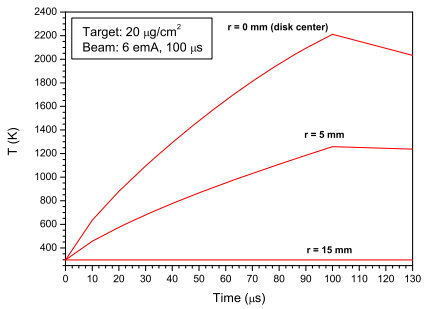

Figure 1: T vs time (during pulse length) at different points along foil radius, foil thickness = 20 μg/cm^2, current 6 emA and pulse length = 100 μs.

Two different current values, namely, 6 emA and 18 emA have been used where the latter is the FAIR design value. A pulse length of 100 μs is considered that leads to pulse intensities, N = 9.375 $\times$ 10^{11} and 2.8125 $\times$ 10^{12} for the beam current values of 6 emA and 18 emA, respectively. The transverse particle distribution in the focal spot is assumed to be Gaussian with σ = 3.67 mm, whereas the repetition rate of the ion beam pulses is 2 Hz.

The initial charge state is U^{4+} while the ion is stripped to a charge state of U^{39+} after passing through either 20 or 30 μg/cm^2 thick stripper foils. A slightly higher charged state of U^{40+} is achieved with a 40 μg/cm^2 thick foil. For simplicity, we assume in the calculations a uniform ion charge state along the foil thickness (39+ in case of 20 and 30 μg/cm^2 and 40+ in case of 40 μg/cm^2 thickness). In practice, however, there will be an exponential type charge distribution along the ion trajectory.

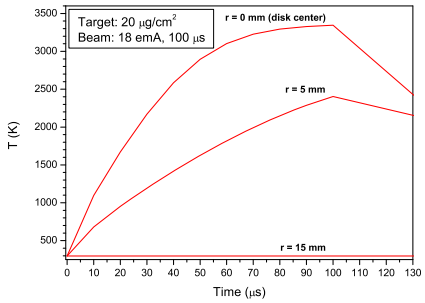

Figure 2: Same as in Fig. 1, but using beam current 18 emA

In Fig. 1 we plot the temperature for 6 emA current at three different points along the foil radius, namely, r = 0 (center), 5 mm and 15 mm (outer boundary), respectively. It is seen that a maximum temperature of around 2200 K is achieved at the target center at the end of the pulse (100 μs), whereas the maximum temperature at r = 5 mm is about 1250 K. The temperature at the foil boundary, on the other hand, does not change. It is to be noted that although the sublimation temperature of carbon in air is much higher (3925 K), the target could be damaged due to the induced thermal stresses [1,2]. The corresponding temeprature at the foil center in case of 30 and 40 μg/cm^2 is 2300 K and 2400 K, respectively. This is because diffusion of heat from the target center to the surface takes longer time that reduces the cooling rate.

In Fig. 2 we plote the same variables as in Fig. 1, but using 18 emA current. It is seen that the temperature at the foil center approaches the carbon sublimations temperature which means that it will not survive a single irradiation in this case. For 30 and 40 μg/cm^2 foil thickness, the maximum temperature is even higher. It is therefore concluded that use of a solid stripper foil is not feasible at the new high energy drift tube linac at GSI. Further details can be found in [3]

References

[1] N.A. Tahir et al., NIMB 276 (2012) 66.

[2] N.A. Tahir et al., NIMB 290 (2012) 43.

[3] N.A. Tahir et al., PRSTAB (2014) Submitted.

* Work supported by the BMBF

The Status of the High-Energy Linac Project at GSI *

S. Mickat[1], *W. Barth*[1], *G. Clemente*[1], *L. Groening*[1], *B. Schlitt*[1], *and U. Ratzinger*[2]
[1]GSI, Darmstadt, Germany; [2]Goethe University, Frankfurt, Germany

The High-Energy (HE) Linac is proposed to substitute the existing UNILAC post-stripper section. Mainly the post-stripper consists of the Alvarez Linac, which is in operation over four decades successfully. The main parameters of the HE Linac follow the design parameters of the existing post-stripper [1], e.g. the HE Linac reaches the same output energy of 11.4 MeV/u at about half of the lentgh. In comparison the beam pulse length and the pulse repetition rate is optimised to the FAIR requirements. The HE Linac will not provide with long duty cycle beams [2].

In the long term the substitution of the existing Alvarez is the only possibility to provide an adequate heavy ion injector for FAIR. The need for a future substitution is confirmed by a study recording the status of the existing post-stripper for investigating its future operating risk [3].

One important milestone for reducing the operating risk is the development of a new and modularised rf system, which is in progress [4]. The rf system can be applied to the existing Alvarez section as well as to the HE Linac in short pulse operation. Negotiations with commercial suppliers concerning the prototype of a high power amplifier are expected to be closed in spring 2014.

56 percent of the total costs are assigend to the rf systems (fig.1) according to the executive summary "Proposal for the HE Linac" [5], which was submitted in summer 2013 to the GSI supervisory board and the director's board.

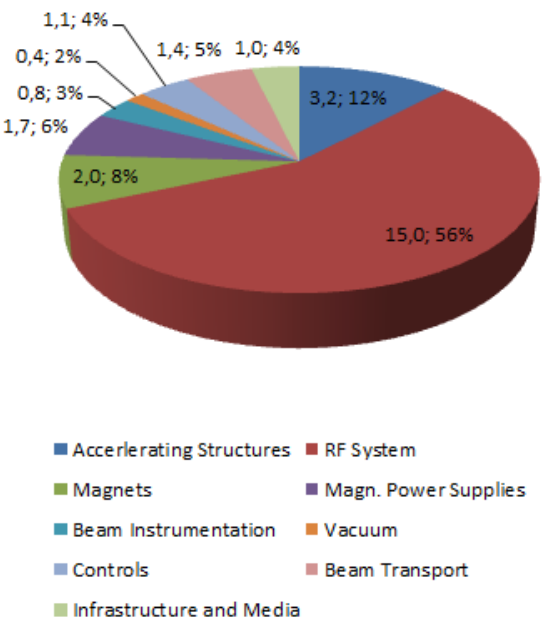

Figure 1: Investment cost of technical susbsystems in MEUR and percent. The total sum is 26.6 MEUR (based on prices of 2012)

Outlook

In November 2013 the GSI accelerator chain for Uranium beam was reviewed. The review comittee comprised five external and international recognised accelerator experts. As a result a window for the input beam parameters for the SIS18 is defined. For providing $2 \cdot 10^{11}$ U^{28+} particles a beam current of 15 mA at a pulse length of 80 μs within an emittance of 5 mm mrad is required for instance [6]. In addition a quasi Front-to-End simulation along the UNILAC shows, that by taking future upgrade options into account already, with the existing Alvarez section the Fair requirements are not reached [7]. Even by substituting the Alvarez section by the HE Linac the aim is not reached per se regarding the existing boundary conditions. Currently workpackages are defined together with the Institute of Applied Physics at Frankfurt University. Starting from the Ion sources to the SIS18 transfer channel every section is reinvestigated for improvements in beam quality and intensity.

References

[1] B. Schlitt et al., "Status of High Energy Linac Project at GSI", GSI Scientific Report 2012 (2013) 270

[2] S. Mickat et al., "Status of the sc cw LINAC at GSI", Exotic Nuclei, EXON-2012, Proceedings of the International Symposium (2013) 337

[3] S. Mickat, H. Vormann et al., "Die UNILAC Post-Stripper Sektion - Zustandsaufnahme und Betriebsrisiko", Internal Report (2013)

[4] M. Hoerr, B. Schlitt, G. Schreiber, W. Vinzenz, W. Barth, Internal Note (2013)

[5] B. Schlitt et al., "Proposal of a New Heavy Ion Post-Stripper Linac at GSI (HE-Linac) - Executive Summary" (2013)

[6] S. Appel, "SIS18 Injection: Parameters studies on MTI with space charge and longitudinal aspects" talk at the Rev. of FAIR Uranium Beam Parameters along the Accelerator Chain (2013)

[7] L. Groening, "HE-Linac: Layout and preliminary (quasi) Front-to-End Simulations" talk at the Review of FAIR Uranium Beam Parameters along the Accelerator Chain (2013)

* FAIR@GSI PSP code:6-6-7-06

 doi:10.15120/GR-2014-1-FG-UNILAC-10

CUPID: New System for Scintillating Screen based Diagnostics

B. Walasek-Höhne[1], *D. Acker*[1], *C. Andre*[1], *M. Bevcic*[1], *H. Bräuning*[1], *A. Bräuning-Demian*[1], *C. Dorn*[1], *R. Fischer*[1], *M. Glück*[1], *H. Graf*[1], *F. Hagenbuck*[1], *M. Hartung*[1], *R. Haseitl*[1], *T. Hoffmann*[1], *C. Kleffner*[1], *R. Lonsing*[1], *R. Mahr*[1], *T. Milosic*[1], *I. Pschorn*[1], *A. Reiter*[1], *H. Rödl*[1], *U. Scheeler*[1], *C. Schmidt*[1], *M. Schwickert*[1], *K. Steiner*[1], *C. Wetzel*[1], *J. Wiessmann*[1], *J. Wohlers*[1], *and R. Vincelli*[1]

[1]GSI, Darmstadt, Germany

Introduction

A new, fully FAIR-conformal system for standard scintillating screen based beam diagnostics was developed at GSI. To cover a wide range of foreseen applications, a new technical solution was required for diagnostics upgrade between the Experimental Storage Ring (ESR) and Cave A as a precursor to the upcoming FAIR High Energy Beam Transport lines. The newly developed system (Figure 1), including digital image acquisition, remote controllable optical system and mechanical design, was set up and commissioned without beam during the 2013 shut-down.

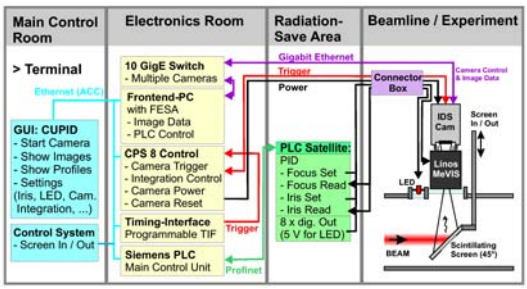

Figure 1: CUPID: overview of electronic devices and communication scheme.

CUPID System Layout

CUPID (Control Unit for Profile and Image Data) is based on the Front-End Software Architecture (FESA) [1] to control beam diagnostic devices. The FESA class for the digital GigE camera (IDS uEye UI-5240SE-M, radiation resistant CMOS type) acquires the images and preprocesses the optical data as required by the geometry of the setup (rotation, stretching). It calculates the projections and the intensity histogram and converts pixel number into a position in millimeters, which results in absolute beam position and width. The performance of the system reached more than 15 frames per second with one connected client. To avoid network overload, the front-end computer processing the camera images is equipped with two network cards: one for the standard accelerator network and one for the direct connection to the GigE cameras via a local 10 GBit network switch. If desired, the raw image data can be written to a file for offline analysis. Additionally, dedicated FESA classes access industrial Programmable Logic Controllers (PLCs) for a reliable slow control solution. A Siemens PLC (main unit and satellites) handles control of lens focus and iris motors (LINOS MeVis-Cm 16), read and set by a PID controller (FM355C). PLC digital outputs (SM322) switch the LED to illuminate the P43 target (ProxiVision) for calibration issues. Camera control, timing, as well as power supply and reset options for up to eight digital cameras are realized by the in-house developed Camera Power Supply controller CPS8.

Operating Features

The use of the FESA framework results in a clear separation between the data acquisition part and the graphical user interface (GUI) part. CUPID includes two parts: a) data acquisition and control using FESA and b) Java based analysis and display tools (see Figure 2). In the main control room, the user can select and start the camera in free-run or triggered mode, adjust the camera and iris settings as required for commissioning, alignment and transversal beam profile measurements. The GUI client displays the processed image, the horizontal and vertical intensity profiles as well as the intensity histogram. The display is automatically updated whenever the FESA class delivers new image data. If only profiles are needed, the image display can be disabled to reduce network load. CUPID is the first fully digital, FAIR control system compliant readout of scintillating screens for beam diagnostics.

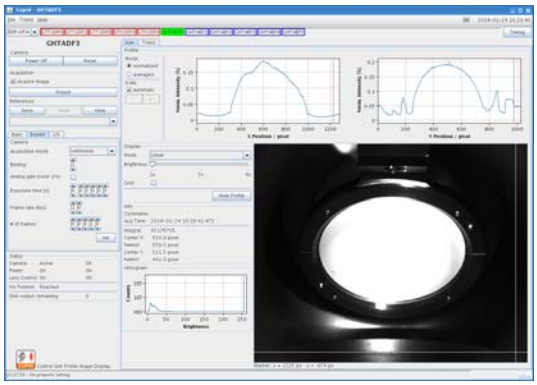

Figure 2: CUPID GUI with an image as well as horizontal and vertical profiles of a scintillating screen.

References

[1] R. Haseitl et al., "Development of FESA-based Data Acquisition and Control for FAIR", DIPAC 2010

REMBRANDT – The REMote Beam instRumentation And Network Diagnosis Tool

T. Hoffmann[1] *and H. Bräuning*[1]
[1]GSI, Darmstadt, Germany

Introduction

At FAIR, all beam instrumentation devices and associated data acquisition components will be distributed and installed over a large and partially inaccessible radiation exposed area. Besides operation of the device itself, like acquisition of data, it is mandatory to control also the supporting LAN based components like VME/μTCA crates, front-end controllers (FEC), middle ware servers and more, to reduce trouble-shooting efforts and reaction times on DAQ system failures. Fortunately, many commercial systems provide means for remote control and monitoring using a variety of standardized protocols. REMBRANDT is a Java framework, which allows the authorized user to monitor and control remote systems while hiding the underlying protocols and connection information such as IP addresses, user-ids and passwords.

Architecture

REMBRANDT is based on a client-server architecture, which is shown in Figure 1. The clients as well as the server are fully implemented in Java. Thus, the same application can be started in the main control room (Linux X-terminals) and/or on the office PC (typically Microsoft Windows) and can be distributed via Java webstart.

The REMBRANDT server periodically queries all devices within several separate monitor threads typically every 10 seconds. It also logs changes in the device states into a data base, send notifications by e-mail to maintainers, handles access control and provides a web server for read-only access to the device states and logs.

Several clients are available to the REMBRANDT user. Besides the main control and monitoring tool, clients for system information management, database and user administration are provided. All clients interact with the server exclusively by Remote Method Invocation (RMI), which is a proven standard mechanism within JAVA for procedure calls within a network. Thus, complex subscribe/publish procedures are avoided.

Currently, REMBRANDT supports the following protocols to control (switch on/off, regulate fan speed, etc.) and monitor different types of hardware: SNMP (Simple Network Management Protocol); iAMT (Intel Active Management Technology); IPMI (Intelligent Platform Management Interface); Ping; RDA (remote device access [1] for FESA [2] devices). REMBRANDT also provides direct terminal access to devices via telnet, ssh or iAMT SOL (Serial-Over-LAN). It hides the login information as well as the actual connection specifics, i.e. directly or via a terminal server. Besides obtaining a login shell this is mainly used to oberve the device boot process for diagnostic purposes.

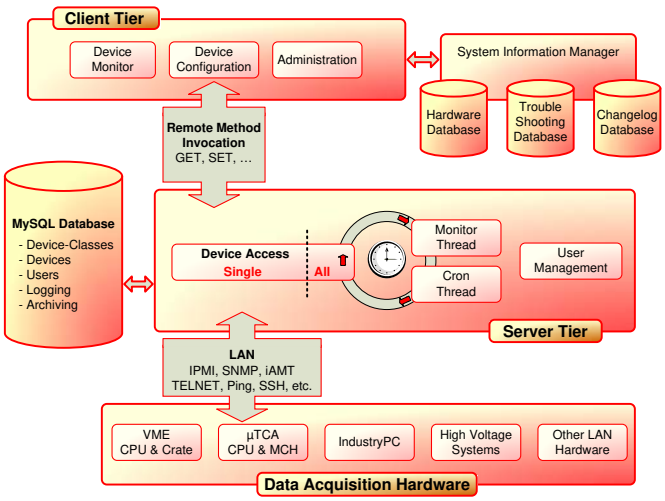

Figure 1: The REMBRANDT software architecture.

Outlook

REMBRANDT will significantly help to keep a status overview over the huge amount of expected BI DAQ and infrastructure systems at FAIR. It is currently in the test phase and already covers over 90% of the foreseen device types. Future development will focus on the scalability with a much larger number of devices and additional protocols like IPMI Serial-Over-LAN or evaluation of logfiles like syslog.

Furthermore, REMBRANDT should be considered as only one, albeit major, pillar in the global remote monitor and control concept for beam diagnostic devices. It is complemented by IP based KVM switches for VGA/USB equipped systems and PLC controlled power supply units of beam line installed DAQ components, such as digital cameras, to provide permanent access and full remote reset capability.

References

[1] N. Trofimov et al., "Remote Device Access in the New CERN Accelerator Controls Middleware", ICALEPCS'01, San Jose, California, USA, p. 496.

[2] T. Hoffmann, M. Schwickert, G. Jansa, "FESA at FAIR", PAC09, Vancouver, BC, Canada, p. 4794.

 doi:10.15120/GR-2014-1-FG-UNILAC-12

Retrofitting of a non-invasive Bunch Shape Monitor for GSI LINACs*

B. Zwicker[1,2], *C. Dorn*[1], *P. Forck*[1,2], *O. Kester*[1,2], *and P. Kowina*[1]
[1]GSI Helmholtzzentrum, Darmstadt, Germany; [2]Goethe Universität, Frankfurt

Introduction

Within the FAIR-Project a proton LINAC [1] is scheduled as a new injector for the SIS18. A non-invasive Bunch Shape Monitor (BSM) is foreseen to determine the longitudinal bunch structure with a phase resolution of 1°, with respect to the 325 MHz acceleration frequency. It is intended to ensure proper longitudinal matching of the accelerating structures. The presented device is based on the creation of secondary electrons by the ion beam passing a section of high local nitrogen pressure. The secondary electrons are accelerated by an external driving potential towards a time-resolved imaging system to obtain the bunch time structure [2].

Compensation of Beam Deflection

The applied driving potential has unwanted effects on the ion beam. For an 11.4 MeV/u beam with an applied voltage of -31 kV the beam deflection goes up to 0.7 mrad (for protons) according to CST based calculations. For the present monitor location at the transfer channel a significant fraction of the beam is lost [3]. To overcome this flaw, two additional electrodes have been designed and build to fit in the existing vacuum chamber. To design an appropriate electrode geometry a field simulation was performed, using CST finite element code.

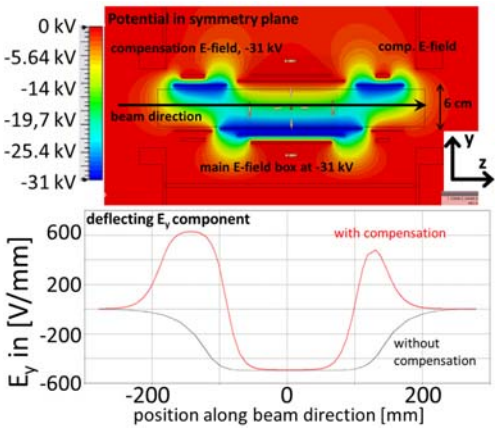

Figure 1: The upper image shows a CST simulation of the potential distribution at the symmetry plane along the beam axis. The lower image shows a calculation of the E-field along the beam axis.

The most advanced design for optimal compensation is an additional Field-Box with the same geometry split in the middle into two and to put one in front and one behind the original Field-Box. Due to the lack of available insertion space inside the BSM vacuum chamber, this solution is not an option. A more sophisticated design based on CST simulations was chosen, which stays as close as possible with the optimal layout (see Fig. 1). Finally the selected design is a compromise of two contrary objectives, namely achieving a sufficiently homogeneous high field strength with a fixed voltage of -31 kV and leaving enough space in a symmetry axis coaxial to the beam axis, at least 55 mm in diameter (iris size in front of the BSM). This does forbid two capacitor plates with a fixed distance. For sufficient compensation the distance between the capacitors plates is below 40 mm which allows a maximum field strength of 620 V / mm in comparison to the Field-Box with 420 V / mm. In addition the capacitor plates are bended in the middle to allow the beam free pass within a 60 mm diameter (see Fig. 2).
The achieved compensation at 5 mm around the beam axis is about 99 %, decreasing with distance to the axis. Within a 40 mm diameter the deflecting is still suppressed by 90 %, which corresponds to a remaining deflection angle of 0.07 mrad.

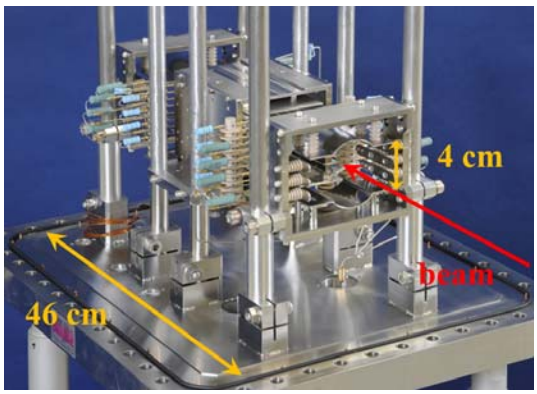

Figure 2: Two compensation electrodes installed in front and behind of the original Field-Box, the red arrow indicates the beam path.

References

[1] L. Groening et al., LINAC'12, Tel-Aviv, THPB034, p. 927
[2] P. Forck et al., DIPAC'05, Lyon, p. 48 ,
[3] B. Zwicker et al.,IBIC'13, Oxford, MOPC36

* Supported by EU-Project CRISP, WP3 T1 Non-intercepting Bunch Shape Monitors

Direct measurement of mechanical vibrations of the 4-rod RFQ at the HLI

P. Gerhard[1]
[1]GSI, Darmstadt, Germany

Introduction

The high charge state injector HLI at the UNILAC was equipped with a new 4-rod Radio Frequency Quadrupole RFQ in 2009. It has been in operation since 2010 [1]. At higher rf amplitudes, strong modulations of the rf matching with f_{mod} ≈500 Hz were observed, limiting the pulse length and rf amplitude achievable. They are attributed to mechanical oscillations of the rods, excited by the rf pulse. As these modulations could only be seen *during* the rf pulse, a direct, independent observation of the mechanical vibrations was needed.

Measurements

A laser vibrometer was used to investigate any movement of the rods independent of rf operation. The vibrometer uses the interference of a laser reflected from the surface of interest with the original light to determine the velocity of the surface. By pointing the laser through a vacuum window onto e. g. the back edge of a rod, we were able to measure the vibration of the rods in situ for different operational states [2].

Results

Fig. 1 shows the effect of the rf pulses on the rods, measured with the vibrometer continuously running, i. e. without synchronization to the rf pulses. Without rf power only some minor vibrations below 100 Hz are visible, excited by cooling water, pumps etc. With rf on, a strong line emerges at 500 Hz. For the inset, only data *between* the rf pulses were analysed. The spectrum shows the 500 Hz signal and a dominant feature at ≈350 Hz. We attribute these lines to different vibrational modes of the rod, with only the 500 Hz mode affecting the rf. Fig. 2 shows the amplitude of the vibration at 500 Hz for different pulse lengths at 50 Hz pulse repetition rate, according to standard operation. The periodic behaviour of the amplitude is consistent with operational experience, especially the minima indicate pulse lengths were operation of the RFQ is most stable. The periodicity of 2 ms matches the vibration frequency of 500 Hz. Together with the small linewidth corresponding to a decay time of 0.3 s (Fig. 1), this confirms the interference of sequentially excited vibrations, which cancel out during the rf pulse at certain pulse lengths [1].

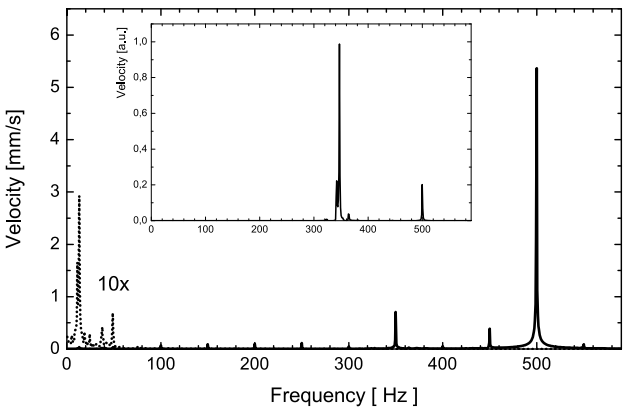

Figure 1: Frequency spectrum of the vibration velocity of the RFQ rod with rf off (dotted, 10 times magnified) and with rf pulses at 50 Hz pulse repetition rate (solid). Inset: Frequency spectrum of the free decay of the oscillations between the rf pulses at 1 Hz pulse repetition rate.

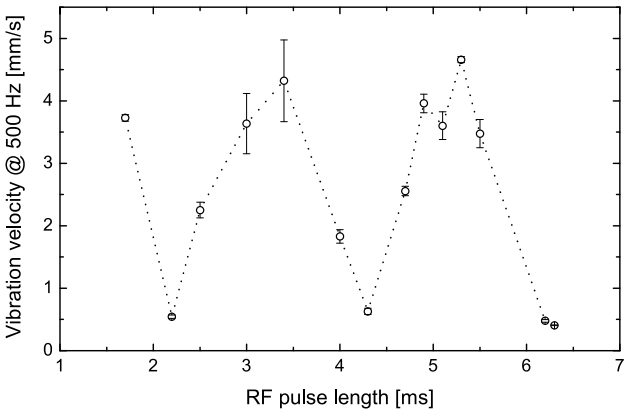

Figure 2: Velocity of the mechanical vibration as a function of the rf pulse length at 50 Hz pulse repetition rate.

Outlook

Mechanical and rf simulations of the present RFQ structure will be conducted to understand the vibration modes and their effect on the rf properties. Based on this, new electrodes will be designed to mitigate these effects.

References

[1] P. Gerhard *et al.*, "Experience with a 4–Rod CW RFQ", LINAC'12, Sept. 2012, Tel Aviv, THPB035

[2] We appreciate the extensive help and assistance of Kay–Obbe Voss, who also provided the laser vibrometer and other equipment.

 doi:10.15120/GR-2014-1-FG-UNILAC-14

Calculation of the quadrupole moment $\sigma_x^2 - \sigma_y^2$ for an asymmetrical Pick-up*

Joel Alain Tsemo Kamga[†1], *Wolfgang F.O. Müller*[1], *Thomas Weiland*[1], *Rahul Singh*[2], *Piotr Kowina*[2], *and Peter Forck*[2]

[1]Technische Universität Darmstadt, Institut für Theorie Elektromagnetischer Felder (TEMF), Schlossgartenstrasse 8, 64289 Darmstadt, Germany; [2]GSI, Planckstrasse 1, 64291 Darmstadt, Germany

Introduction

This report presents the simulation results for an asymmetric pick-up installed at GSI SIS-18. The pick-up is planned to be used as transverse beam size oscillations monitor at SIS-18, and possibly as a transverse emittance monitor [1] in future. The properties of the pick-up are studied in order to evaluate its usage as a quadrupole moment monitor. Further, a comparison of signal processing methods such as traditional difference over sum, log-ratio and modified log-ratio [2] with respect to the suppression of beam position contribution in the quadrupole moment $\sigma_x^2 - \sigma_y^2$ is presented.

Simulations and Results

Quadrupole signal for a centred beam

Assuming that the beam is long compared to the pick-up electrode, the pick-up properties are determined electrostatically with the simulation software CST EM Studio (Electrostatics solver). The quadrupolar signal Ξ for traditional diff-over-sum method is defined as $(R+L-T-B)/(R+L+T+B)$ where R, L, T and B are the voltages induced on the respective pick-up plates. It is calculated for a range of quadrupole moment such that transverse horizontal beam radius σ_x is varied from 7.5 mm to 50 mm while vertical beam radius σ_y is 7.5 mm.

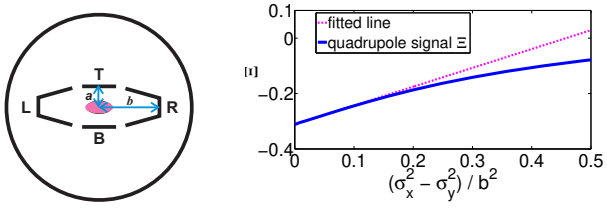

Figure 1: **Left**: front view of the pick-up design; **right**: quadrupole signal Ξ using the diff over sum method; σ_y/b = 0.075, $0.075 \leq \sigma_x/b \leq 0.5$, $\overline{x} = \overline{y} = 0$, b = 100.3 mm, a = 35.3 mm.

Figure 1 shows that the quadrupole signal is not linear in the whole range of the beam dimension used for the simulation. However, in the range covering typical SIS-18 beam dimensions, i.e. $0 \leq (\sigma_x^2 - \sigma_y^2)/b^2 \leq 0.05$, the curve fits well with a straight line (linear regression with the coefficient of determination R^2 = 0.9997), as shown by dotted line in Fig. 1. The slope m and the zero point $(\sigma_x^2 - \sigma_y^2)_0$ of the fitted line are 0.678 and 0.4593, respectively.

Effect of the beam position $(\overline{x}, \overline{y})$

Now, taking into account the beam position in the quadrupole signal, the beam dimension can be obtained simply by Eq. (1).

$$\frac{\sigma_x^2 - \sigma_y^2}{b^2} = \frac{\Xi}{m} + (\sigma_x^2 - \sigma_y^2)_0 - n\left(\frac{\overline{x}^2 - \overline{y}^2}{b^2}\right) \quad (1)$$

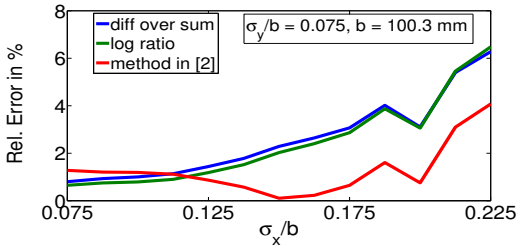

Figure 2: Relative error of the pick-up values of $(\sigma_x^2 - \sigma_y^2)/b^2$ at $\overline{x}/b$ = 0.075, $\overline{y}/b$ = 0.05; b = 100.3 mm

In Fig. 2, the relative errors in the calculated quadrupole moment for a variation of σ_x in the range of 7.5 mm to 22.5 mm with a constant σ_y = 7.5 mm and beam position ($\overline{x}$ = 7.5 mm, $\overline{y}$ = 5 mm) using different processing methods are shown.

Conclusions

In the beam size range of interest, the quadrupole signal calculated using the asymmetric pick-up is found to have a linear dependence on quadrupole moment for a centred beam. The dependence of quadrupole moment on beam position is studied by three signal processing methods. The modified log-ratio method shows the least influence of beam position on the quadrupole moment.

References

[1] R. H. MILLER, J. E. CLENDENIN, et al, "Nonintercepting Emittance Monitor", in *Proc. 12th International Conference on High Energy Accelerators* (Batavia, IL, 1983).

[2] Joel A. Tsemo Kamga, Wolfgang F.O. Müller and T. Weiland, "New method for reducing the contribution of the beam position in the quadrupole signal", GSI Scientific Report 2012.

* Work supported by GSI

† tsemo@temf.tu-darmstadt.de

Progress of the 325 MHz sc CH Cavity *

M. Busch†[1], *H. Podlech*[1], *U. Ratzinger*[1], *W. Barth*[2,3], *S. Mickat*[2,3], *and M. Amberg*[1,3]
[1]Institut für Angewandte Physik, Goethe Universität, Frankfurt; [2]GSI, Darmstadt; [3]HIM, Mainz

Abstract

At the Institute for Applied Physics (IAP), Frankfurt University, a superconducting 325 MHz CH-Cavity has been designed and built. The 7-cell cavity features a geometrical β of 0.16, corresponding to a beam energy of 11.4 AMeV. The design gradient is 5 MV/m. Main novel features of this resonator are a compact design, low peak fields, easy surface processing and power coupling. Furthermore a new tuning system based on bellow tuners inside the resonator will control the frequency during operation. The progress in processing the cavity as well as tuner drive measurements are presented.

Progess and Setbacks

After successful measurements [1] at Frankfurt the cavity was sent back to Research Instruments for final processing steps. Buffered Chemical Polishing and High Pressure Rinsing (s. fig. 1) have been performed.

Figure 1: Set-up for BCP (left), Mounting for HPR (right).

Afterwards a helium leak was found in the area of the pick-up pipe socket which led to a reaming of the pick-up pipe (s. fig.2). The subsequent reparation steps have been performed and the processing steps can be repeated.

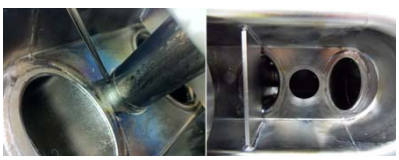

Figure 2: Helium leak at the pick-up pipe (left), Reamed pick-up pipe (right).

Tuner Measurements

The new dynamic frequency tuner for sc CH-Cavities consisting of a stepper motor and a fast piezo actuator provides slow and fast tuning by pushing/ pulling capacitive acting dynamic bellow tuners, which are welded on the girders inside the cavity. The slow tuner must be able to deflect the bellow tuner around +/- 1 mm, which corresponds to a tuning range of several hundred kHz to compensate frequency changes due to evacuation and cavity cool down. Additionaly, fast piezo actuators react on frequency variations in the range of several hundred Hz caused by dynamic effects like Lorentz-Force detuning or microphonics. A prototype of this frequency tuning system was built at the workshop of the IAP. First measurements at room-temperature have been performed.

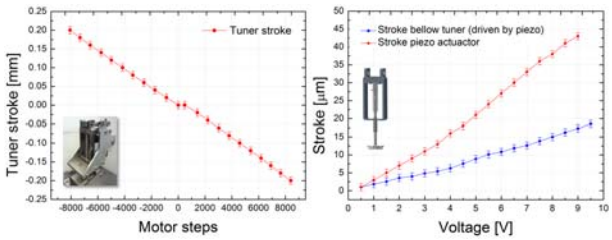

Figure 3: First tuner measurement results at room temperature.

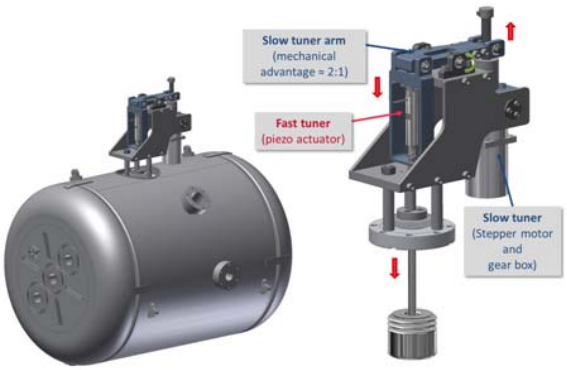

Figure 4: Mounting of the fast tuner system on the helium vessel (left). Main components of the tuner system (right).

References

[1] M. Busch, F. Dziuba, H. Podlech, U. Ratzinger, M.Amberg, "Cold Measurements on the 325 MHz CH Cavity", SRF 2013, Paris, France.

* Work supported by GSI, BMBF Contr. No. 06FY7102, FAIR@GSI PSP code:6-6-7-05
† busch@iap.uni-frankfurt.de

 doi:10.15120/GR-2014-1-FG-UNILAC-16

Controlled beam loss experiment at SIS18

L.Bozyk[1], *O.Kester*[1,2], *V.Lavrik*[*1,2], *and A.Reiter*[1]
[1]GSI, Darmstadt, Germany; [2]IAP University of Frankfurt, Frankfurt m Main, Germany

The FAIR beam loss monitoring (BLM) system is based on different types of particle detectors. Its main purpose is the minimisation of beam losses around the SIS100 synchrotron and protection of machine components from unnecessary activation. As a part of a BLM feasibility study an experiment with controlled losses on a scraper was performed at SIS18 section.

The aim of this study is the production of beam losses at a well defined position and the measurement of the shower intensity with BLM detectors. In the present setup two plastic scintillators of the existing BLM system were used. They are installed downstream of a scraper at a distance of 2 and 5 meters, respectively. The scraper was positioned close to the beam orbit. Uranium beams of different energies and intensities in the range of 100-900 MeV/u and 10^8-10^9 particles were utilized. The beam was injected into the SIS18 synchrotron, accelerated and then stored for several seconds. During that time the beam was excited and was slowly impinging on the scraper. The resulting count rates in the scintillators were monitored through the ABLASS data acquisition system[1] and further analysed with a ROOT code[2]. Figure 1 shows one BLM signal (blue curve) and the DC current transformer signal DCT (black curve) in arbitrary units. In the flattop region no significant BLM signal is detected. After 2 seconds the exciter was turned on and produced the shown BLM signal. It was carefully checked that no significant losses were produced at other locations around the sychrotron.

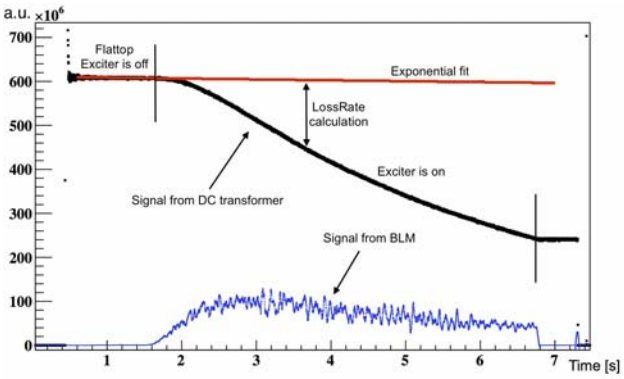

Figure 1: Measured signals of DCT and scintillator in a.u.

During the initial storage when the exciter is switched off only a small fraction of the beam is lost. In order to determine the beam life time (see red curve in figure 1) the beam current can be approximated by an exponential function. When the beam exciter is switched on, one can calculate the number of lost particles on the scraper for each time-bin by taking the difference between the extrapolated life time function and the actual number of particles measured by the DCT.

For each energy, the data were approximated by a linear fit and the ratio between BLM signal and loss rate was retrieved. One can interpret this ratio as a normalised shower intensity. This dependency between the ratio and the beam energy is shown in Figure 2. At low energies it seems to follow parabolic curve. Starting from 300 MeV/u the shower strength of the beam losses follows the expected linear trend which one expects from the results of Monte Carlo simulations. The experiment will be repeated with LHC type ionisation chambers[3] which will be installed during the next short shutdown in order to measure their response function and estimate their signal strength for possible SIS100 beam loss scenarios.

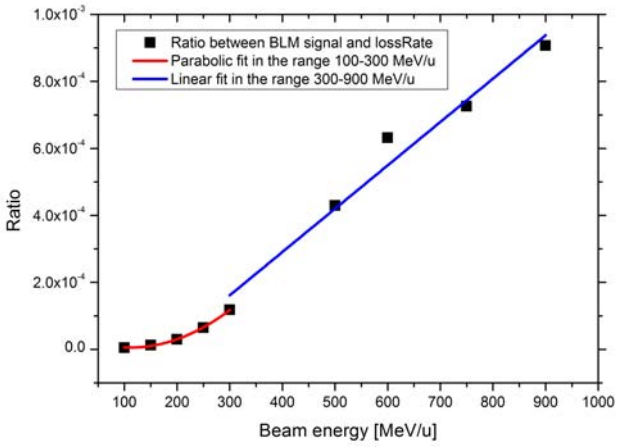

Figure 2: BLM signal to loss rate ratio in dependence on beam energy

References

[1] T. Hoffmann et al., "Experiences on Counter Applications and Beam Loss Measurement at the GSI Synchrotron", 11th Beam Instrumentation Workshop 2004 (BIW 04), Knoxville, Tennessee, USA, p.294

[2] R. Brun, F. Rademakers, "ROOT: An Object-Oriented Data Analysis Framework"; http://root.cern.ch

[3] M. Stockner, "Beam loss calibration studies for high energy proton accelerators", Ph.D. Thesis, Geneva, 2007.

* v.lavrik@gsi.de

Beam Phase Feedback for Dual-Harmonic Operation of RF Cavity Systems*

J. Grieser† [1], *U. Hartel*[1], *H. Klingbeil*[1,2], *U. Laier*[2], *D. Lens*[1], *K.-P. Ningel*[2], *S. Schäfer*[2], *and B. Zipfel*[2]
[1]Technische Universität Darmstadt, Darmstadt, Germany; [2]GSI, Darmstadt, Germany

Introduction

After completion of the FAIR Project, the SIS 18 will be used as pre-accelerator for the SIS 100/300 and its cavities will be run in dual-harmonic bunch lengthening mode (BLM). To damp longitudinal rigid dipole oscillations a phase feedback system is used [2] which was so far only tested for the single harmonic mode. The beam phase signal with respect to the group DDS (Direct Digital Syntheziser) signal driving the cavities is filtered by an FIR (Finite Impulse Respond) filter and fed back to the group DDS. On November 21st 2012 a beam experiment was carried out showing that dipole oscillations can be damped using an FIR filter also in the dual-harmonic mode. Some of the results were already presented in [1, 3].

Control Loop

An overview of the feedback loop is given in Fig. 1. Electrical (analog or digital) signals are indicated by a black arrow and optical signals by a dashed red arrow.

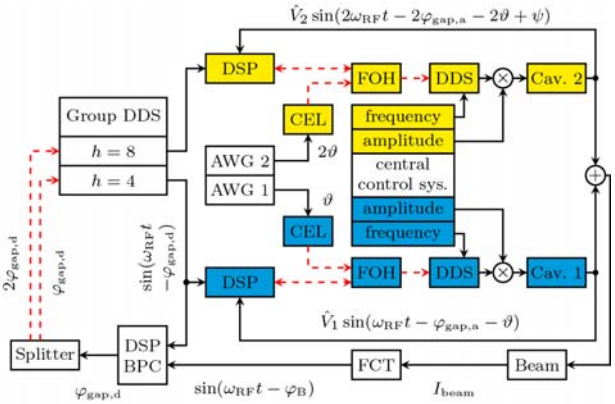

Figure 1: Beam phase feedback loop

To each gap voltage an additional phase shift ϑ (respectively 2ϑ) can be applied by means of an input voltage at the CEL (Calibration Electronics Modules) using an AWG (Arbitrary Waveform Generator). This is used to excite dipole oscillations on flattop while the basic frequency (and amplitude for acceleration) is supplied by the central control system. Both cavities synchronize with a group DDS signal whose phase can be changed by the splitter, doubling the desired phase shift $\varphi_{gap,d}$ at its input for the second harmonic ($h = 8$) cavity. Beam phase control is realized in the DSP (Digital Signal Processor) denoted as 'DSP BPC'. It consists of a phase detector, a digital filter, an integrator and a gain K as can be seen in Fig. 2. The beam current I_{beam} is measured with an FCT (Fast Current Transformer). The FOH (Fiber Optic Hub) transmits data between DSP, CEL and DDS of each cavity.

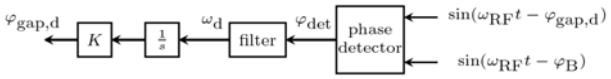

Figure 2: Block diagram of BPC DSP algorithm

The controller feeds back the phase difference $\varphi_{det} = \varphi_B - \varphi_{gap,d}$ (with φ_B: phase of bunch barycenter and $\varphi_{gap,d}$: desired cavity phase shift for $h = 4$), filtered by the FIR filter [2]

$$H_F(z) = -\frac{1}{4} + \frac{1}{2}z^{-1/(2T_s f_{pass})} - \frac{1}{4}z^{-1/T_s f_{pass}}, \quad (1)$$

where f_{pass} is the passband center frequency of the filter. The bunches were rigidly displaced by $\varphi_B(t_0) = 20°$ at a flattop energy of $E_{kin} = 120$ MeV/u, representing a test scenario in which a dipole oscillation with a defined amplitude is excited. Fig. 3 shows a dipole oscillation in closed and open loop. The additional damping is clearly visible.

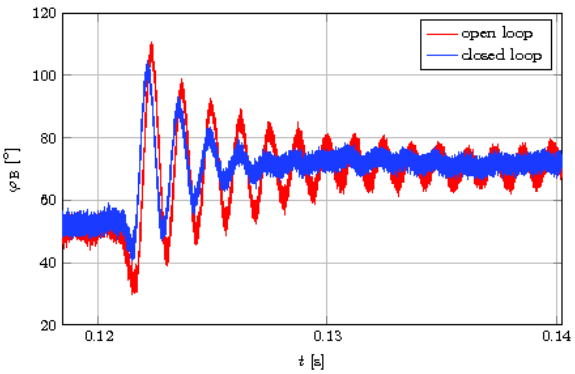

Figure 3: Measurement of dipole oscillation damping

Acknowledgment

The authors would like to thank W. Kaufmann, A. Klaus, H. G. König, D. Mondry, P. Moritz, H. Reeg, S. Reimann, G. Riehl, P. Schütt, P. Spiller, C. Thielmann, T. Winnefeld and others who have contributed to the success of the experiment but could not be listed here.

References

[1] J. Grieser et al., WEPME004, Proceedings of IPAC 2013
[2] H. Klingbeil et al., IEEE Trans. Nucl. Science, Vol. 54, No. 6, 2007
[3] H. Klingbeil and J. Grieser, GSI-Memo No. 07012013, 2013
[4] K.-P. Ningel et al., TUPEA037, Proceedings of IPAC 2010

* Work partly supported by GSI-TU Darmstadt cooperation contract
† jgrieser@rtr.tu-darmstadt.de, H.Klingbeil@gsi.de

 doi:10.15120/GR-2014-1-FG-SIS18-02

Measurement of the magnetic properties of the Ferroxcube 8C12m material*

K. Klopfer†[1], *W. Ackermann*[1], *H. Klingbeil*[1,2], *H.G. König*[2], *U. Niedermayer*[1], *and T. Weiland*[1]

[1]Technische Universität Darmstadt, Institut für Theorie Elektromagnetischer Felder (TEMF), Schlossgartenstraße 8, 64289 Darmstadt, Germany; [2]GSI, Darmstadt, Germany

Introduction

The accelerating cavities which are operated in the GSI SIS 18 synchrotron for the acceleration of heavy ions at harmonic number 4 are filled with Ferroxcube 8C12m ferrite material. The characteristics of such materials depend on a variety of parameters, notably the external bias magnetic field. This distinctive feature is used for tuning of the resonance frequency of the cavity according to the revolution frequency of the heavy ions. Evidently, for a better understanding of the tuning process, the knowledge of relevant material characteristics is inevitable. To this end, experiments were carried out at the GSI facility with the aim of determining the dependence of the complex permeability of the Ferroxcube 8C12m material both on the frequency and on the bias magnetic field strength.

Measurement setup

The basic measurement setup is as follows. Two ferrite ring cores equivalent to the ones actually installed in the SIS 18 cavity are mounted inside a copper cavity (cf. Fig. 1). The toroids can be biased via 105 crossed current windings with the help of the direct current I_{bias}. Moreover, the necessary alternating components are coupled to the device under test via one additional circuit, which consists of a centric wire and the cavity housing. This circuit is connected to a network analyzer (NWA) for the measurement of the input port voltage reflection coefficient, i.e. the S_{11}-parameter. For preparation of a defined remanence state, the bias current is driven to the maximum value for a short time.

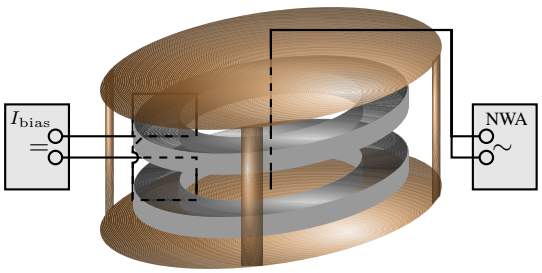

Figure 1: Schematic view of the measurement setup. Two ferrite ring cores with bias current windings are installed inside a cavity housing.

Data analysis

After the measurements, the real and imaginary part of the admittance of the device are available as a function of frequency for different bias currents. The values of the permeability are then extracted as follows. Firstly, it is assumed that the system can be described by an equivalent circuit, whose admittance is given by

$$Y = \frac{1}{R_0} + \mathrm{i}\omega C_{\mathrm{dist}} + \frac{1}{\mathrm{i}\omega L_{\mathrm{s}} + R_{\mathrm{s}}},$$

with the external resistance $R_0 = 50\,\Omega$, the distributed capacitance C_{dist} and the inductance and resistance of the toroids in series representation L_{s} and R_{s}, respectively. Whereas C_{dist} is obtained from a separate measurement, it is possible to formulate analytical expressions for L_{s} and R_{s}, which involve only geometric quantities and the complex permeability $\mu_{\mathrm{s}} = \mu'_{\mathrm{s}} - \mathrm{i}\,\mu''_{\mathrm{s}}$. Hence, by solving for the real and imaginary part of μ_{s}, one can finally evaluate the complex permeability for each frequency point. The obtained values for two different bias magnetic field strengths are shown in figure 2.

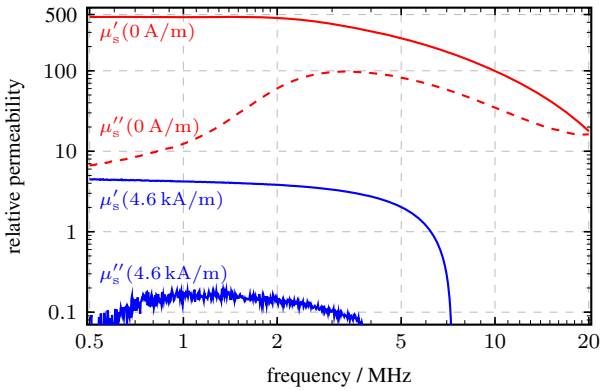

Figure 2: Real (μ'_{s}) and imaginary part (μ''_{s}) of the permeability as obtained from the data analysis for a bias magnetic field strength of $0\,\mathrm{A/m}$ and $4.6\,\mathrm{kA/m}$ (low RF-power values).

Summary and outlook

The complex permeability of the Ferroxcube 8C12m material was obtained from measurement as a function of both frequency and bias magnetic field strength. A more detailed data analysis together with a discussion of the obtained results will be published in the near future.

* Work supported by GSI
† klopfer@temf.tu-darmstadt.de

Status and Results of the TFS for SIS18/SIS100

M. Alhumaidi[2], U. Blell[1], J. Florenkowski[1], and V. Kornilov[1]
[1]GSI, Darmstadt, Germany; [2]TU Darmstadt, Darmstadt, Germany

In this short report, we show the current status of the project Transverse Feedback System (TFS) for the SIS 18, which can be commissioned later at the SIS 100 of FAIR project, upon its completion.

The TFS features and parameters are designed to have a large dynamic range such that it can be installed at the SIS 18 as well as the SIS 100. Testing the functionality of the System on a real beam at the SIS 18 is planned in the next few monthes.

A new concept for using multiple pickups in estimating the feedback correction signal in order to minimize noise power has been adressed. Furthermore, a distributed system design and synchronization scheme considering the current BPM Liberas of the existing SIS 18 facility has been developed.

System Design

We apply a new approach for mitigating noise at the PUs using more than two PUs at different positions to estimate the feedback correction signal for the Kicker position.

Data acquisition for the TFS takes place at distinct devices – namely, the Liberas. Therefore, the system has to be realized in a distributed manner. The main subsystems of the distributed TFS are the Libera devices for data acquisition, and the central unit for calculation, intensive operations and synchronization.

In order to achieve the synchronization between the TFS central unit and the distributed Liberas, time stamps are transfered in addition to the position data from the Liberas to the central unit. These time stamps are calculated in terms of shared reference wavefronts among all the TFS nodes. Specifically, we use the RF signal as a shared reference in our design. A time stamp is composed of wave front number, and time shift from this wavefront. In addition to the reference signal, a trigger signal is needed to indicate the start of counting the wave fronts. Figure 1 shows the form of the synchronization signals.

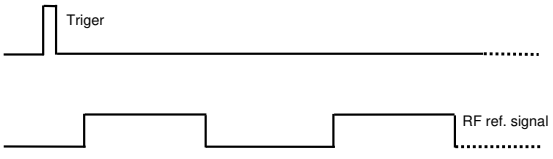

Figure 1: TFS synchronization signals.

In order to stabilize head-tail oscillations and higher order modes, which become dangerous for high beam intensities, many position measurements and kicks must be achieved for every bunch. Therefore, a bunch-by-bunch system would not be enough here, and we implement a wide-band feedback system.

Feedback parameters, e.g., revolution frequency and linear combination factors, are privided via the GSI interface cards FG 380.221. System configuration is done by an external computer via Ethernet connection.

Implementation

The TFS central unit electronics are shown in Figure 2. The System is implemented on a Virtex 6 FPGA ML605 kit from the company Xilinx. Several daughter cards has been deployed in order to connect this kit to the Kicker, the FG 380.221 cards, and the Liberas.

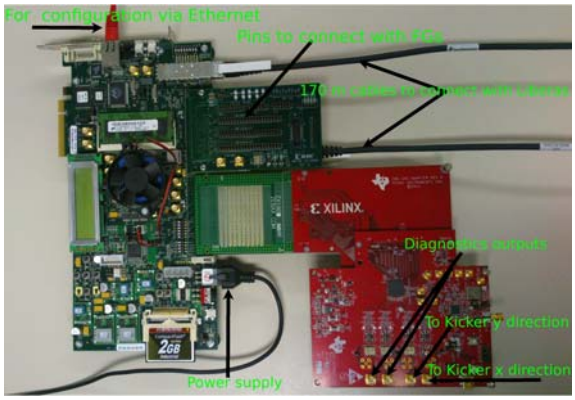

Figure 2: TFS board.

The beam position data from the PUs are sampled and preprocessed at the Libera kits from the company Intrumentation Technology. The data as well as the time stamps are then sent from the Liberas to the TFS central unit via two long fiber optical cables using Aurora multi-Gigabit communication. Clusters of Libers are considered to connect to multiple BPMs.

References

[1] M. Alhumaidi and A.M. Zoubir, “A TRANSVERSE FEEDBACK SYSTEM USING MULTIPLE PICKUPS FOR NOISE MINIMIZATION”, IPAC’11, September 2011, San Sebastin, Spain.

[2] M. Alhumaidi and A.M. Zoubir, “A ROBUST TRANSVERSE FEEDBACK SYSTEM”, IPAC’12, May 2012, New Orleans, USA.

[3] M. Alhumaidi and A.M. Zoubir ,“DETERMINATION OF OPTICS TRANSFER BETWEEN THE KICKER AND BPMs FOR TRANSVERSE FEEDBACK SYSTEM”, IPAC’13, May 2013, Shanghai, China.

 doi:10.15120/GR-2014-1-FG-SIS18-04

Observation and simulation of transverse BTFs of high energy bunched beams

P. Görgen[1] *and O. Boine-Frankenheim*[1]
[1]TEMF, TU-Darmstadt, Germany

Transverse Beam Transfer Functions (BTFs) are widely used in synchrotrons and storage rings to determine machine and beam properties (for example tune, tune spread, error resonances). In the projected SIS100, BTFs can potentially be used to measure the tune spread during proton operation. The transverse BTF $R(\omega)$ is the fraction of the complex beam response amplitude $A_{\text{resp}}(\omega)$ and the excitation amplitude $A_{\text{drive}}(\omega)$ at a excitation frequeny ω.

$$R(\omega) = \frac{A_{\text{resp}}(\omega)}{A_{\text{drive}}(\omega)} \tag{1}$$

In simple cases the BTF can be calculated analytically. For instance in the presence of tune spread caused by chromaticity, the imaginary part of the BTF is proportional to the transverse tune distribution in the corresponding plane [1].

The situation becomes more complex when the particle tune depends on the transverse amplitude of the particle as in the case of a nonlinear transverse element such as space charge or nonlinear fields. One example is a so-called electron lens, wherein an electron beam of the same profile as the ion beam is guided in parallel to the ion beam [2]. By adjusting the electron beam current and shape, a nonlinear lens can be set up which can be used to reduce transverse tune spread due to space charge (as could be envisioned for SIS100) or the beam-beam effect (for the Relativistic Heavy Ion Collider (RHIC)). We show how BTFs can be used to diagnose the proper operation of such a device.

Analytic calculation

In absence of SIS100 we focused on the case of an electron lens like one recently installed at RHIC. We make the assumption we are in the limit of coasting beams which we justify by the synchrotron frequency of the order of magnitude of the measurement time for a BTF sample. The conditions in SIS100 for high energy proton operation are similar in terms of synchrotron frequency. We calculate the BTF in the presence of a nonlinear lens analytically following [3] and obtain the result:

$$R_i(\omega) \propto \iint_0^\infty \frac{1}{\omega - \omega_i\,(J_x, J_y)} \frac{J_i \mathrm{d}\psi}{\mathrm{d}J_i} \mathrm{d}J_x \mathrm{d}J_y \tag{2}$$

With J_x, J_y the particle amplitude in action-angle variables, ω the frequency of the BTF, ω_i the amplitude dependent tune of the particles in the i direction ($i \in \{x, y\}$) and ψ the density of particles in J_x, J_y space. The presence of the derivative of the phase space density makes the BTF sensitive to fluctuations in the phase space density. The presence of J_i means the contribution of the particles increases with their amplitude. Particle-in-cell (PIC) simulations agree with eq. 2. Unfortunately unlike in the aforementioned case of chromaticity for typical ψ and ω_i we can only solve the integral in eq. 2 numerically. Thus, our best method for reconstruction of the tune distribution is fitting against eq. 2 for a known shape of ψ and ω_i.

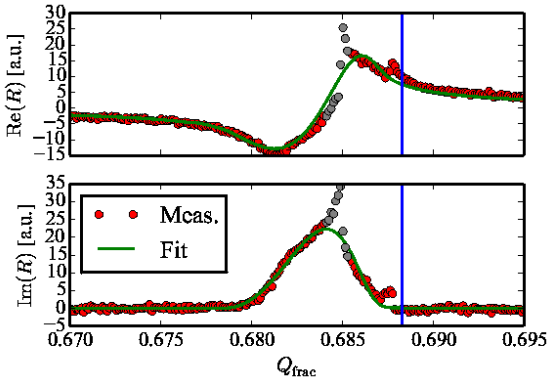

Figure 1: Exemplary BTF measurement of a beam undergoing a weak-strong beam-beam interaction as a substitute for an electron lens. Points are the measurement, the green line represents the fit. The fitting parameters are amplitude and the strength of the interaction ξ which is proportional to the tune spread.

After verifying the fit method in simulation [4] we validated the method in measurement with the beam-beam effect as a substitute for an electron lens in a machine experiment at RHIC. The interaction strenght recovered by the fit was in agreement with the expectation from measurements of the beam current and the emittance. The result of a BTF measurement is shown in Fig. 1 together with the fit.

The agreement between analytic results, simulations and measurement gives confidence that a similar method can be used to directly diagnose space charge tune spread of top energy protons in SIS100. The analytic equations follow the same approach. In application to SIS100 we plan to use our simulation model of the BTF that we successfully applied to RHIC to investigate electron lenses as a possible cure for space charge in SIS100.

References

[1] K. Y. Ng, *Physics of Intensity Dependent Beam Instabilities*, World Scientific, Singapore, 2006

[2] W. Fischer et al. *Construction Progress of the RHIC Electron Lenses*, Proceedings of IPAC 2012

[3] J. Berg, F. Ruggiero, CERN SL-AP-96-71

[4] P. Görgen et al, in, proceedings of 2013 ICFA mini workshop on beam-beam interactions.

 doi:10.15120/GR-2014-1-FG-SIS18-05

Ion source and 4-grid analyzer for the proton injector for FAIR

R. Berezov[1], *A. Adonin*[1], *N. Chauvin*[2], *J. Fils*[1], *V. Ivanova*[1], *and C. Ullmann*[3]
[1]GSI, Darmstadt, Germany; [2]CEA, Saclay, France; [3]IAP, Frankfurt am Main, Germany

The microwave ion source and the low energy beam transport section (LEBT) developed in a joint French-German collaboration (CEA/Saclay – GSI/Darmstadt) will serve as an injector for the compact proton LINAC for FAIR [1]. The microwave ion source is presented in Fig. 1. The ion source will be located on the platform with a potential of 100 kV inside the special cage (Faraday cage). This ion source operates in pulsed mode with a frequency of 2.45 GHz. RF power is provided by a magnetron (microwave generator) and injected into the plasma chamber. The plasma chamber has a length of 10 cm and the diameter of 9 cm.

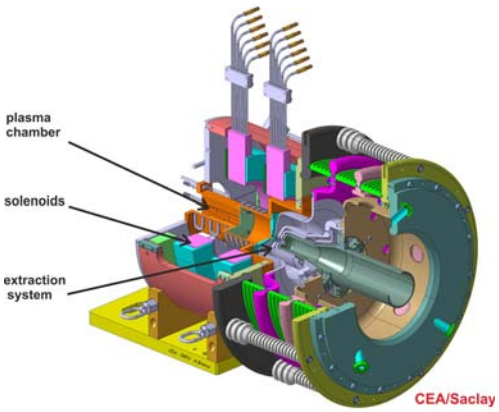

Figure 1: The microwave ion source for the p-LINAC.

The hydrogen gas is injected into the plasma chamber up to the pressure of $2.5{\cdot}10^{-3}$ Pa approximately. In order to increase the proton fraction the chamber is coated with two boron nitride discs. There are two coils with a magnetic field strength of 87.5 mT, which are used to confine the plasma. The "five electrodes" extraction system consists of a plasma electrode, puller electrode (50 kV), screening electrode (- 5 kV) and two ground electrodes [2]. The plasma electrode has an aperture of 8 mm. This extraction system allows the formation of high brightness ion beams with energies up to 100 keV and full beam currents of maximum 130 mA. The duty cycle of the ion source is 4 Hz with a flat top pulse length of 0.2 ms. The requirement for a rise and fall time is in the range of 100 - 200 μs. During the long time operation the ion source has shown its reliability with stable operation conditions and high performance, such as low noise level and small beam fluctuations < 5 % and pulse-to-pulse repetition < 2.5 % based on statistical inquiries. The low energy beam transport section consists of two solenoids and a diagnostic chamber in between. The solenoids have a length of 3 cm and maximum magnetic field strength of 500 mT [3]. There are two magnetic steerers, which are integrated into the solenoids for adjusting of the horizontal and vertical beam positions. The diagnostic chamber is equipped with a Wien filter, an iris, an Allison scanner, a SEM profile grid and a beam stopper. The total length of the compact LEBT from the plasma electrode up to the entrance flange of the RFQ is about 2.3 m. The commissioning of the proton injector at CEA/Saclay is planned for the beginning of 2015. During this time the measurements of the emittance, beam current, and determination of the beam fraction and stability of the ion source will be performed. For the measurement of the space charge compensation a modernized 4-grid analyzer will be used. The 4-grid analyzer mainly consists of 4 metal grids as shown in Fig. 2. The first grid on ground potential serves for preventing any disturbance within the probe and the plasma and also for reducing the plasma density. The second grid serves as an electron repelling grid to repel electrons from the plasma. The third grid slows the ions down to the point that only the ions with a higher kinetic energy can pass through the potential on the grid. The fourth grid is needed as a repeller for secondary electrons. For beam current measurements the Faraday cup will be used.

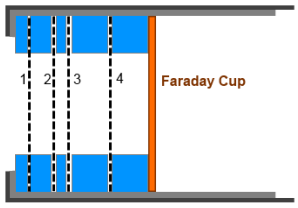

Figure 2: Schematic view of the 4-grid analyzer. 1: First grid on ground potential, 2: Electron repelling grid, 3: Retarding ion filtration grid, 4: Secondary electron suppression grid.

References

[1] R. Hollinger, W. Barth et al., "High current proton beam investigations at the SILHI-LEBT at CEA/Saclay", Linac06 (2006) 232.

[2] C. Ullmann, R. Berezov et. al., "The proton injector for the accelerator facility of antiproton and ion research (FAIR)", Rev. Sci. Instrum. 85, 02A952 (2014).

[3] R. Gobin et al., "Status of the Light Ion Source developments at CEA/Saclay", RSI, Vol.75, No. 5 (2004) 1414.

Mechanical Design for the p-LINAC BPMs Inter-tank Section

M. Almalki[1], P. Forck[1], J. Fils[1], W. Kaufmann[1], O. Kester[1], P. Kowina[1], C. Krüger[1], T. Sieber[1], and C. Simon[2]

[1]GSI, Darmstadt, Germany; [2]CEA-Saclay/DSM/Irfu, Gif-sur Yvette, France

Introduction

Four-fold button Beam Position Monitors (BPM) will be installed at 14 positions along the 30 m long FAIR p-LINAC [1,2,3]. At four locations, the BPM has to be integrated in the inter-tank section between the CCH and CH cavities within an evacuated housing. The mechanical design of these BPM-locations is most critical. The tight space allows 58 mm insertion length only between CH cavity and quadropole magnet walls. The mechanical design was adapted based on previous numerical simulations as well as the given inter-tank dimensions [4,5]. The device performance was optimized by simulations. Special attention is payed on reduction of the rf-noise at the BPM location as generated by cavity excitation.

BPM Mechanical Design

The BPM system has to cover a beam energy range from 3 MeV to 70 MeV. Moreover, different beam pipe apertures have to be considered (30 mm to 50 mm). A commercial 14 mm button pick-up produced by Kyocera [6] was chosen for this purpose. However, it has to be tested for a 50 Ω impedance matching, which can be influenced by the inner ceramics. The button sub-assembly unit composite a titanium electrode of 2 mm thickness connected to a SMA co-axial cable as shown in Fig. 1.

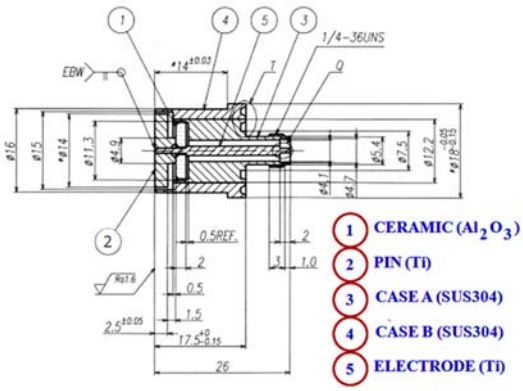

Figure 1: Scheme of commercial button from Kyocera.

The centre of the BPM inter-tank section is only 48 mm apart from the upstream drift tube boundary. The BPM mechanical design was optimized to control the rf field propagation into the tube reaching to the BPM's co-axial signal path [3,5]. The BPM (tube diameter of 30 mm) is connected to the CH entrance flange (20 mm) by a conical section with a length of 20 mm to reduce an rf pick-up signal to max. 5 mV [3]. This value is satisfactory compared to the signal voltage of ∼ 1V for nominal beam current of 35 mA. The assembly of the BPM consists of four buttons, a housing and a flange as shown in Figures 1 and 2, respectively. The buttons are recessed 0.5 mm from the inner radius of the tube to protect the electrode from stray beam impingement. Since the BPM is located near quadrupole magnet, a non-magnetic design is mandatory. Therefore, the housing and the flange will be fabricated from 316LN stainless steel. The buttons will be welded inside housing and both will be joined with the flange at the final assembly.

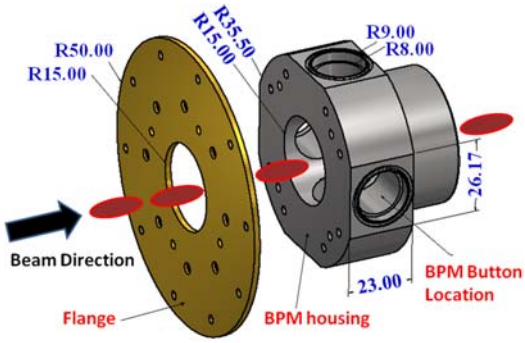

Figure 2: View of the BPM prototype parts.

Summary and Outlook

The first phase of CEA-GSI collaboration for the BPM system includes the design and fabrication of the first BPM prototype. Currently, a button-type BPM has been designed and is being fabricated. It will be used as a test device for the rf field propagation from the cavity to the BPM at GSI and for a dedicated test bench at CEA. The related results will be considered for the final design.

References

[1] L. Groening et al., "Status of the FAIR 70 MeV Proton LINAC", LINAC'12, Tel-Aviv, p. 927 (2012).

[2] P. Forck et al., "Design of the BPM System for the FAIR Proton-LINAC", GSI scientific report 2010.

[3] M. Almalki et al., "Layout of the BPM System for p-LINAC at FAIR and the Digital Methods for Beam Position and Phase Monitoring", IBIC'13, Oxford, p. 101 (2013).

[4] C. Simon et al., "Design Status of the Beam Position Monitors for the FAIR Proton LINAC", DIPAC'11, Hamburg, p. 356 (2011).

[5] W. Ackermann et al., "Unintentional Coupling of Accelerating Field to the BPM Pickups", GSI Annual Report 2011. p. 312 (2012).

[6] http://global.kyocera.com/

 doi:10.15120/GR-2014-1-FG-P-LINAC-02

FAIR HEBT System - Status Report

F. Hagenbuck, L. Bozyk, A. Krämer, B. Merk, C. Mühle, S. Ratschow, B.R. Schlei, P. Spiller, B. Walasek-Höhne, H. Welker, and C. Will
GSI, Darmstadt, Germany

Modifications in the HEBT System Layout

There were no changes in the ion optical layout since its last official transfer to the building planners in October 2012. However, currently a direct connection from SIS18 to the Collector Ring (CR) is considered without modifying the requirements for the building planning. For this the section TSN1 is modified in a way that the beam coming from SIS18 can be either injected straight into the end part of the Super-FRS ring branch (which is connected to the CR via the sections TFC1 and TCR1) or guided directly to the NESR as before (to avoid a collision with the Super-FRS cryo-supply this branch has to be lifted in this region by about 50cm-100cm compared to its original layout). Whereas the connection to the NESR is part of module 6 the currently discussed new connection to the CR via the Super-FRS would become part of module 0-3.
To fulfill the requirements for the beam halo at the CBM/HADES target, a halo collimation system has to be integrated in the compact beam line from SIS100 to the CBM cave. In a first step suitable positions from ion optical point of view with sufficient available installation space were determined in the sections T1C1 and T1C2. In the next step simulations taking into account the generation of secondary particles in the collimators will be performed.
The concept for the positions of safety beam plugs in the HEBT system was revised in coordination with the radiation protection department. Appropriate interlock magnets were identified and first simulations of the expected radiation level in building H0719A (main supply building north) were performed for beam deposition in the safety beam plug D20 located in section T1X2 in K0923A.
The concept to use the SIS100 machine setup beam dump in the HEBT system in K0619A for emergency dumping of light ions and protons from SIS100 was discarded. The new concept is described in [1].

Technical System Design

A first contract on the production of 51 dipole magnets including supports and vacuum chambers (batch 1) was closed between FAIR and Efremov Institute (St. Petersburg, Russia) in Aug 2013 and between FAIR and Budker Institute (Novosibirsk, Russia) in Jan 2013. The detailed specifications of batch 2 (17 dipole, 102 quadrupole, 80 steering magnets) were brought into the EDMS release process in Jan 2014. The detailed specifications of batch 3 (5 dipole, 71 quadrupole, 12 steering magnets) are currently under preparation and supposed to be available in spring 2014. The delivery of two pre-series magnets of batch 1 and their vacuum chambers is expected for the end of 2014. However, the production order for the series will follow the current partitioning HEBT A/B/C (defined by the project lead FAIR@GSI) which does not directly correspond to batch 1-3. Nevertheless, changes of the production order, e.g. due to changes in prioritization by the project lead or in civil construction, are possible.
In Oct 2013 the detailed specifications for 7 HEBT quadrupole power converter types were released. Currently a first contract between FAIR, the indian shareholder BOSE institute (Kolkata) and the provider ECIL (Electronics Corporation of India Limited) is under preparation. This contract will contain all quadrupole power converters needed for the 18Tm beamlines of module 0-3.
The major part of the detailed specifications required for the day zero beam diagnostics for the HEBT system was released (7/14) or is currently under approval (4/14). The indian shareholder BOSE institute started the tendering process of the HEBT beam diagnostics vacuum chambers in Jan 2014.
Major efforts were taken to deliver further required information for the building planning. E.g. 3D models of the SIS100 machine setup dump in K0619A, of the draft of the support structure including service platforms in building H0705A, of the course of Halfen rails for mounting HEBT300 at the tunnel ceiling as well as of free installation space for cable trays in G0702A were prepared. The HEBT supply areas in L0516A had to be rearranged significantly to provide mandatory escape routes, space for ascending traces and a smoke extraction shaft. Furthermore the review of the building plans of the 2. Vorabzug Rohbau took place, followed by 3D collisions checks (building with Hüllkontur) and coordination processes for cable routing.
A first draft concept for a transportation unit for assembly and disassembly on the injection and extraction ramp was worked out in an advanced design project between ENMI and the department of computer integrated design of the TU Darmstadt.
Furthermore much work was invested in project planning at the beginning of 2013. Twenty project plans including ressources (personnel, budget) and three different timelines for HEBT A/B/C were established by the WPLs as well as three major milestone plans for HEBT A/B/C by the MPL.

References

[1] C. Omet, “SIS100: Emergency dumping of protons and ions”, presentation at 10th MAC, November 2013

Interdisciplinary development of a support structure for components in building H0705A - A challenge for systematic requirements engineering

C. Will, M. Bevcic, Ch. Dorn, R. Fuchs, F. Hagenbuck, L. Heyl, A. Krämer, C. Mühle, I. Pschorn, H. Reich-Sprenger, B. Walasek-Höhne, and H. Welker*

GSI, Darmstadt, Germany

Building H0705A is a branching and crossing point for 8 beam lines in the planned FAIR facility. 2 beam lines are inclined. In addition several components of other beam lines have to be transported via this building to their final installation positions. One also has to take into account that the installation of support structures and components will take place according to project planning in two stages. Furthermore the consideration of the product life cycle takes a fundamental part of the definition of requirements for the support structure.

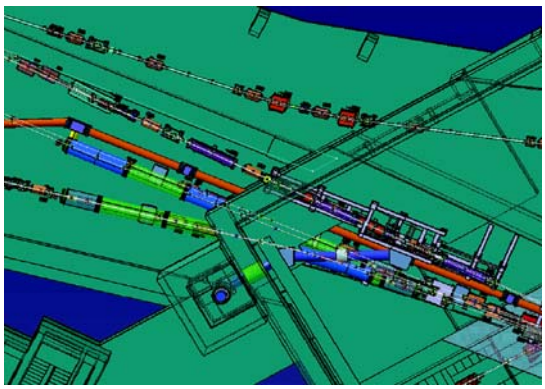

Figure 1: Top view of beam lines in building H0705A.

In a first step all involved departments, so called stakeholders, were identified. In a second step a team with members of magnet department, vacuum department, beam diagnostic department, assembly department, alignment department, power converter department, media supply department, digital mock-up (DMU) department and the responsible machine project leader (MPL) started with a global task analysis. The question had to be solved, what the task of the support structure is, and what this means in consideration of the two project stages and of the product life cycle of the components. The next step included the definition of parameters which influence the system. Not only technical aspects had to be taken into account but also already defined processes for installation and maintenance, as well as safety aspects like length of escape routes and earthquake safety are influencing items. This step was followed by a structural analysis. What areal, staff and organizational structures have to be considered? The analysis of given and demanded infrastructure of the building gives also boundary conditions for the development of the support structure. A main item in the requirement analysis was the definition of all tasks of the involved departments and the dependencies of and to other tasks. For supporting all functions an analysis of communication shows the flow of needed information [1].

After collection all items have to be classified:

- Functional requirements
- Technical requirements
- Requirements for use
- Quality requirements
- Requirements onto other components, e.g. infrastructure
- Contract and legal requirements [2]
- Requirements of the product life cycle

Due to this classification the specifications for the development, construction and installation of the support structure could be prepared. In addition a time schedule for installation tasks and a course of actions for maintenance purposes could be developed. The validation of results during the development process in reference to the defined and classified requirements helps to ensure that all demands of the stakeholders will be fulfilled at the end of the process.

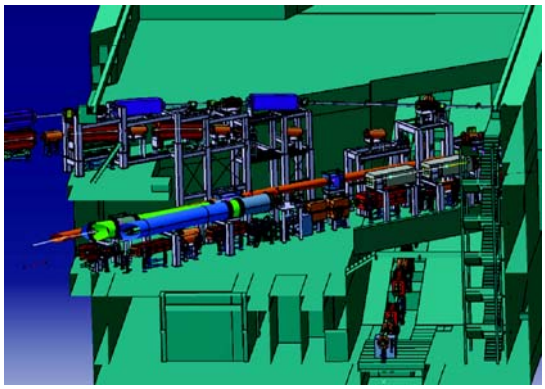

Figure 2: Beam lines with support structure in building H0705A.

References

[1] C. Ebert, Systematisches Requirements Engineering, Heidelberg: dpunkt.verlag, 2012.

[2] C. Rupp, Requirements- Engineering und Management, München, Wien: Carl Hanser Verlag, 2007.

* C.Will@gsi.de

 doi:10.15120/GR-2014-1-FG-HEBT-02

Status of the Superconducting Magnets for FAIR*

E. Fischer†, V. Bezkorovaynyy, A. Bleile, J. Ceballos, E. Floch, W. Freisleben, V. Maroussov, F. Marzouki, H. Müller, J. P. Meier, A. Mierau, H. Raach, P. Schnizer, F. Seifert, A. Stafiniak, K. Sugita, and P. Szwangruber

GSI, Darmstadt, Germany

Introduction

Within this paper we report shortly on all the many different activities of the group which now is mainly focused on procuring the magnets and associated systems for the FAIR project.

Superconducting Magnets

Rapidly cycling magnets for SIS100

Dipoles – production status and first tests The **F**irst **o**f **S**eries (FOS) dipole has been delivered [1, 2, 3] and its testing has been started. The magnetic field was measured during the first ramp up followed by a first training of the superconducting magnet with the second quench above nominal current and a current of 15.1 kA achieved.

In parallel the different findings and according actions have been discussed with the producer so that the SIS100 dipole magnet series can be produced swiftly as soon as the FOS SIS100 dipole has been qualified.

Quadrupole modules The quadrupole modules house all superconducting magnets of the SIS100 along with the beam vacuum chambers, beam position monitors and cryo-collimators.

The design of the quadrupole magnet and all corrector magnets in the quadrupole modules is finalised toward manufacturing. As the first of the SIS100 corrector magnets, the chromaticity sextupole magnet, has been constructed in collaboration with JINR. The iron yoke had been already prepared in the framework of the BMBF-JINR research contract. The coil will be wound and assembled into the iron yoke in the first half of 2014 at JINR. The test of the magnet will then follow.

In parallel the design of the first of series quadrupole module (type 2.5, see also Fig. 1) has been detailed intensively including all integrated components: the magnets, the support system up to the high temperature superconducting current leads. The suspension rods, connecting the cold mass with the cryostat, were designed to achieve a stability of the beam axis of $\pm$ 125 μm for the main quadrupoles and $\pm$ 175 μm for the associated correctors [4]. The design was further checked and approved to be a pressure vessel compliant with European standards.

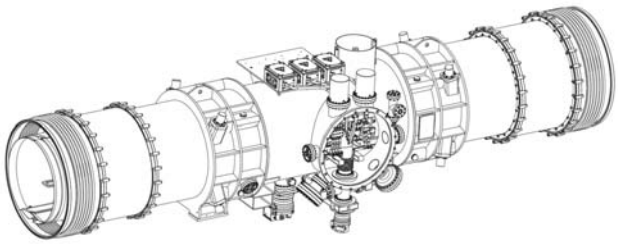

Figure 1: CAD Model of the fully integrated SIS100 quadrupole doublet module, type 2.5, including local current leads located in the central service port.

An order was placed with Babcock Noell for detailing all further quadrupole modules (five arc types, two arc termination types and two straight section types) along with the modules for injection and extraction, which shall be completed beginning of 2015.

Rapidly cycling magnets for SIS300

Magnets with fields up to 4.5 T are needed for SIS300. A first model magnet of the fast ramped $\cos\theta$, 4.5 T SIS300 magnets was developed and tested successfully in collaboration with INFN [5, 6]. It is now awaiting further tests and additional measurements at GSI. A second collared coil, with enhanced field quality and conductor performance [7] is under construction [8]. After successful manufacturing and testing of two prototype quadrupoles and a steering dipole for SIS300, the activities of IHEP (Protvino, Russia) concentrated on the development of wide aperture quadrupoles for FAIRs HEDgeHOB experiment.

Magnets of the Super-FRS

Dipoles A collaboration agreement was signed between GSI and CEA/Saclay concerning the procurement of the superconducting dipoles for the Super-FRS. Saclay will take over the design finalisation next to the technical follow up. FAIR will then tender these dipoles. A ready design is expected mid of 2014 together with a signed production contract in 2014.

Multipletts The specifications of the multiplets of the Super-FRS have been finished and the tendering process was started by GSI. Offers arrived in December. Negotiations with the companies are now under way; a contract should be signed within the first half of 2014. A general

* We acknowledge the support of the European Community-Research Infrastructure Activity under the FP7 program CRISP (Grant agreement no: 283745) Work Package 5. We acknowledge the support through the JINR–BMBF contract.

† e.fischer@gsi.de

overview over the superconducting magnets of Super-FRS can be found in [9].

Planning for Testing

Prototype test facility activities

The upgrade of the prototype test facility for testing the SIS100 magnets, which has been started in 2012, was finalised by the instalment of the new power converter able to deliver 20 kA at 22 or 66 V next to the HTS current leads. The power converter was brought into operation and tested successfully with a dummy load followed by testing and commissioning the HTS current leads up to 14 kA DC and 17 kA for slow ramps.

Series test facility activities

The procurement of the large scale systems has been started last year and finished with tendering the two power converters. Offers have been received with a tender to be awarded soon. In parallel the refurbishment of the building, the fabrication of the cryogenic infrastructure and the procurement of the current leads has been started.

SIS100 string test

A test string will be set up in the series test facility consisting of a dipole, quadrupole module and cryogenic supply components. Dedicated components are being specified with the assembly of the string foreseen in 2016. The string will provide information on the interplay of the components listed above next to training for the teams building and assembling the SIS100 machine.

Testing Super-FRS Magnets at CERN

The large scale Super-FRS magnets will be tested at CERN. The number of test benches (3), the area and layout of the test facility, have been defined and the measurement program has been evaluated. Based on these achievements the procurement of the infrastructure can start so that the test facility will be ready when the first of series magnets of the Super-FRS arrive.

Current Leads

Dedicated HTS current leads, required for testing the FOS dipole, were developed, procured and successfully tested. This successful test was a clear go for the series of current leads required for the series test facility and the SIS100 machine.

Additionally low current leads are required for the corrector magnets installed within the SIS100 quadrupole module which are based on a conduction cooled warm end and a HTS superconductor connecting them to the cold end. The design of these current leads was completed this year.

Electrical Systems and Magnet Protection

The existing quench detection setup was updated and tuned for testing and operating the HTS current leads and the SIS100 FOS dipole. Moreover the production of the new quench detection system for the dipole series test facility has started now. Further the protection schemes for the SIS100 dipole and quadrupole circuits have been optimised. A set of standard tests and alternative dry tests based on IEC 60851-5 were defined for testing the electrical insulation of superconducting wires.

Conclusion

The procurements of the different superconducting magnets required for FAIR along with the associated auxiliaries has been started. The telegraphic style of this paper reflects the many activities that are undertaken to realise the FAIR project within the given scope and schedule.

References

[1] W. Walter et al., “Manufacturing of the first of series SIS100 dipole magnet”, IPAC13 http://accelconf.web.cern.ch/AccelConf/IPAC2013/papers/moodb101.pdf

[2] E. Fischer et al. “Status of the SC Magnets for the SIS100 Synchrotron and the NICA Project”, IEEE T. Appl. Supercon. 2013 (23) 4100504

[3] P. Schnizer et al. “Design Optimization, Series Production, and Testing of the SIS100 Superconducting Magnets for FAIR”, IEEE T. Appl. Supercon. 2013 (23) 4101105

[4] J.P. Meier et al. “Cryo-technical Design Aspects of the Superconducting SIS100 Quadrupole Doublet Modules”, CEC 2013, to be published

[5] G. Volpini et al., “AC Losses Measurement of the DISCORAP Model Dipole Magnet for the SIS 300 Synchrotron at FAIR” , MT 23, 2013, to be published in IEEE Trans. Appl. Superconductivity.

[6] M. Sorbi et al., “Measurements and analysis of the SIS-300 dipole prototype during the functional test at LASA”, MT 23, 2013, to be published in IEEE Trans. Appl. Superconductivity.

[7] U. Gambardella et al., “An Experimental Study of Fine Filaments NmTi Strand for Fast Cycled Magnets”, MT 23, 2013, to be published in IEEE Trans. Appl. Superconductivity.

[8] H.Mueller et al., “Next Generation of Fast-Cycled Dipoles for SIS300 Synchrotron”, MT 23, 2013, to be published in IEEE Trans. Appl. Superconductivity.

[9] H. Müller et al., “Status of the Super-FRS Magnet Development for FAIR”, IPAC 2013, http://accelconf.web.cern.ch/AccelConf/IPAC2013/papers/thpme005.pdf

[10] K. Sugita et al. “String Test Preparation for the Superconducting SIS100 Accelerator of FAIR”, IEEE Journal Appl. Supercon. to be published. Available at http://dx.doi.org/10.1109/TASC.2013.2278842

 doi:10.15120/GR-2014-1-FG-SIS100-01

Cryogenics for SIS100 Accelerator*

B. Streicher[1], *T. Eisel*[1], *M. Kauschke*[1], *C. Schroeder*[1], *and H. Kollmus*[1]
[1]CSCY, GSI, Darmstadt, Germany

Introduction

The cryogenic system for the FAIR (Facility for Antiproton and Ion Research) superconducting (SC) SIS100 synchrotron (see Figure 1) can be divided into six sections. Each of these sections will be fed from a separate Feed Box (FB) which will supply liquid helium (LHe) for magnet, vacuum chamber and bus-bar cooling as well as gaseous helium (GHe) for thermal shield cooling. Each sixth of the ring consists of one cold arc and a straight warm section with normal conducting accelerating cavities. Yet the warm section still needs to include three SC quadrupole doublets. The design progress of the cryogenic system for the SIS100 is described in the following sections.

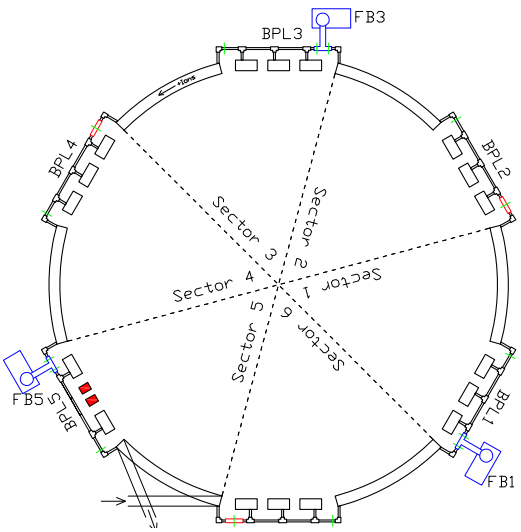

Figure 1: Schematic representation of SIS100 synchrotron showing six BPL sections.

Cryogenic System

By-pass Lines (BPLs) bypass each of the six straight warm sections of SIS100 to supply LHe and cold electrical connections to the SC quadrupole doublets within these sections. Each of the six by-pass sections is alternately equipped either with the FB or the End Box (EB) which intercepts the helium flow. The purpose of such an infrastructure is to be able to separate the ring into six sections which can be independently cooled down, warmed up and serviced. Detailed technical specification [1] concerning the BPL System was prepared and approved at GSI in 2013. Based on this, the in-kind contract was signed between FAIR and Wroclaw University of Technology (WUT). In conjunction with the cryogenic group CSCY, the WUT is currently preparing a complete technical solution of the proposed BPL System. Internal holding structure for both helium headers and bus-bars is being designed as well as new clamping solution to fix the bus-bar pairs. The most complicated components namely the connection boxes that interface BPL to quadrupole units and on both sides to the cold arcs are also being engineered. The WUT will manufacture all the components of the BPL sections according to specifications until the end of 2016.

During 2014 all technical specifications of all remaining cryogenic components for SIS100 namely the FBs, Current Lead Boxes (CLBs), Feed-in Lines (FILs) and Feed-in Boxes (FIBs) together with all the interfaces will be specified. These components will also be produced within the in-kind collaboration with WUT. First-of-series components delivered to GSI will be tested within the Serial Test Facility (STF) currently under construction. The test of the SIS100 "Mini String" (MS) will provide the opportunity to assemble and test a small scale model of SIS100 cryogenic infrastructure. It will be composed of two SC magnets representing the cold arc section joined with the small part of the BPL section. This MS will be fed from the FB joined together with the CLB to supply LHe and two pairs of cooled SC bus-bars for both magnets. The FB in question will be supplied using STF cold box manufactured by Linde Cryotechnik. The control system for the MS has to be also developed at GSI based on UNICOS platform.

Serial Test Facility for SC Magnets

In order to test the fast-ramped SC magnets for FAIR, a cryogenic test facility is designed and currently under construction at GSI. The overall capacity of the cryo plant is 1.5 kW @ 4.4 K equivalent and can be distributed to four test benches individually. In total 108 dipoles for the SIS100 will be tested at cold. The capacity of the cryogenic system is designed in a way, that one magnet can be cooled down and another magnet can be kept at cold for the measurements in the same time. The other two test benches serve for warming up and for magnet exchange, respectively. Beyond the dipoles, the high flexibility of the set-up allows also the testing of other FAIR magnets, like the SIS100 quadrupole modules or the operation of a string configuration.

References

[1] https://edms.cern.ch/document/1261140/8

*FAIR@GSI PSP code: 2.8.12 and 2.14.8.1.6

Cryogenic Tests of Ceramic Feedthroughs for SIS100 BPM

T. Reichert[1,2], *P. Burkhard*[1], *K. Gütlich*[1], *and P. Kowina*[1]

[1]GSI, Darmstadt, Germany; [2]Goethe Universität Frankfurt, Germany

Introduction

Due to the cryogenic environment in which the Beam Position Monitors (BPMs) will be used at SIS100 synchrotron special attention has to be turned to the BPMs' signal feed-throughs (FT) [1]. Present design considers titanium based, N-Type FTs isolated with Al_2O_3 ceramics and welded into CF-16 flange. In a temperature range between room temperature and 4.2 K the requirements for the FTs are threefold: *i*) high mechanical stability, *ii*) vacuum-tightness even after many cold-warm cycles, *iii*) good and stable electrical connectivity. These features were tested in 10 cold-warm cycles in the temperature range given above.

Methods and Results

Fig. 1 shows the test setup: Five N-type (FT) were mounted to a sixfold CF-16 crosspiece that was installed in a bath cryostat having a volume of 30 l. The free flange of the crosspiece was connected via a long stainless-steel pipe to a He leakage detector installed close to the cryostat. All M4 bolts (A4-80 stainless-steel) used at the flanges were fastened with a final torque of 2.6 Nm. One pair of spatially opposing FTs was electrically connected inside the crosspiece via a titanium rod equipped with spring contacts typically used in banana-connectors. This formed a 50 Ω transmission line with an intended impedance mismatch in the crosspiece center. The electrical connection between the two interconnected FTs and a Network Analyzer (NWA) was done by semiflex Tensolite coaxial cables. The quality of the electrical connectivity was measured using Time Domain Reflectometry (TDR) based on the analysis of the synthetic time domain signals measured by means of NWA [2]. Temperature monitoring was done

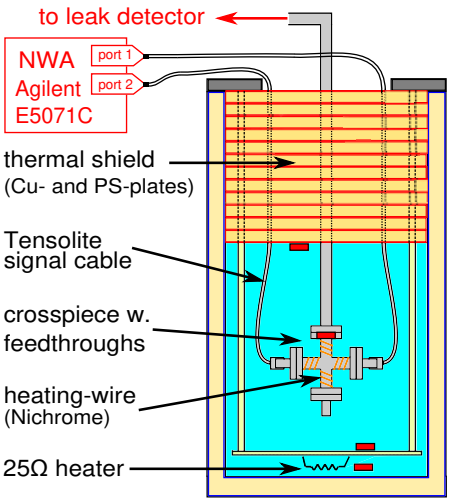

Figure 1: Cryogenic test setup

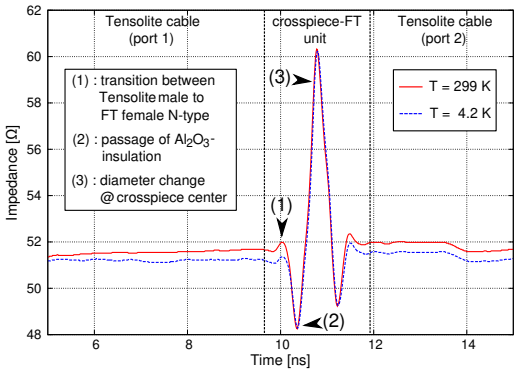

Figure 2: TDR signals at room and LHe temperature

by four resistive temperature sensors depicted in Fig. 1 by red boxes. The cryostat was equipped with a 25 Ω resistive heater for removing residual LN_2 left over from precooling. A Nichrome heating wire wound around the crosspiece was used to accelerate cold-warm cycling so that the average duration of a cycle could be reduced to less than 2 h. He leak rate monitoring was performed during the whole test. Since the crosspiece was immersed into LHe any leaks at the FT that could possibly occur should be immediately registered in the leakage detector. TDR measurements were done first at room temperature and have been repeated after LHe was filled into the cryostat to cool down the crosspiece to 4.2 K. Fig. 2 compares two TDR measurements made at 299 K and 4.2 K in one of the 10 cold-warm cycles. The characteristic points (1), (2) and (3) on the plot correspond to the electrical connections within the crosspiece-FT unit. In the crosspiece-FT region both TDR signals are highly congruent which proves that electrical connections between rod and FTs do not change with temperature. Moreover, this connection is even better if compared to the left and right part of the plot, where the cryogenic cables' passage between the outside and the inside of the cryostat is strongly effected by the temperature changes. Thus, it can be stated that the solution proposed here results in a stable and reproducible electrical connectivity under cryogenic conditions. Comparing Fig. 2 to the measurements made in the remnant cycles, the pointwise deviations of the impedance curves are below ± 0.05 Ω in the significant region of the crosspiece-FT unit. Furthermore, within ten cold-warm cycles, the crosspiece-FT unit did not exhibit any leaks maintaining a He leak rate in the order of 5×10^{-10} mbar · l/s. However, a slight loosening tendency of about 11 % of the initial torque was measured at the bolts used for flange mounting. The usage of foldable washers might be necessary.

References

[1] P. Kowina et al., *Proc. EPAC'06*, Edinbourgh, p.1022

[2] see e.g. www.home.agilent.com, Application Note 1287-12

 doi:10.15120/GR-2014-1-FG-SIS100-03

Design of a Mutual Inductance Based Quench Detector for the Corrector Magnets of the SIS100*

S. Ayet[†1], *E. Floch*[1], *W. Freisleben*[1], *K. Koch*[1], *and P. Szwangruber*[1]
[1]GSI, Darmstadt, Germany

The corrector magnets of the SIS100 employ a multi-strand superconducting wire known as Nuclotron [1] which is made out of up to 28 insulated strands rolled in parallel along a CuNi tube filled with liquid Helium. Due to this special construction of the Nuclotron cable, resistive bridge-based quench detectors will not be able to detect a symmetric quench (quench occurring at the same time in two or more strands) in these magnets. A novel quench detector based on the mutual inductance effect was developed in order to be able to detect all quench situations in the corrector magnets of SIS100.

Mutual Inductance Concept

The detectors based on this concept monitor two voltages: one is the voltage across the magnet and the other is the induced voltage in a secondary coil formed by one of the superconducting strands (see Figure 1).

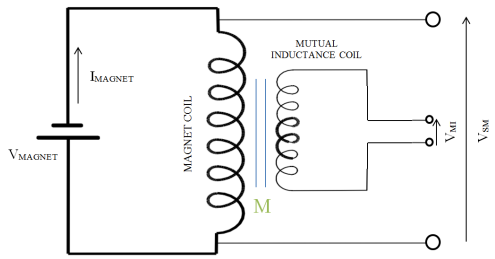

Figure 1: Diagram of the magnet and the acquired signals for the mutual inductance quench detection. V_{SM}: voltage across a single magnet coil, V_{MI}: voltage across the mutual inductance coil and M: Mutual inductance coefficient.

$$V_{SM} = L \cdot \frac{di(t)}{dt} + i(t) \cdot R_Q \tag{1}$$

$$V_{MI} = M \cdot \frac{di(t)}{dt} \tag{2}$$

In (1), the first term corresponds to the voltage across the coil of the magnet with inductance L. The second term corresponds to the quench voltage. In (2), the mutual inductance coefficient is proportional to the inductance L ($L = k \cdot M$). If we multiply (2) by k and we subtract it from (1), we obtain the quench voltage:

$$V_Q = V_{SM} - k \cdot V_{MI} = i(t) \cdot R_Q \tag{3}$$

If we define V_{TH} as the quench detection threshold, we can have two conditions:

- a) $V_Q \leq V_{TH}$: the coil is in superconducting state, $R_Q \approx 0\Omega$.
- b) $V_Q \geq V_{TH}$: the coil quenches, R_Q will rise and the quench protection system should be activated.

Mutual Inductance Quench Detector

A mutual inductance quench (MIQ) detector based on galvanic analog isolation barrier has been developed. This detector has been successfully tested in the lab with signal generators simulating the theoretical signals of the magnet during normal operating and quench conditions.

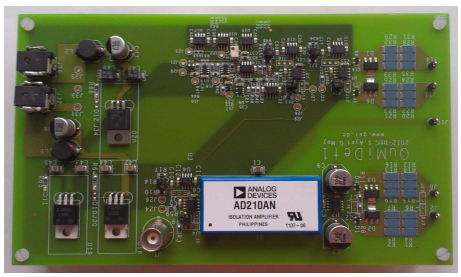

Figure 2: First version of the MIQ detector.

Outlook

After acquiring the signals (ramp up voltages, mutual inductance voltage...) of a real magnet (delivery expected on Q2-2014) and checking that the parameters (mutual inductance, impedances...) assumed during the development of this detector are correct, a second version of the detector with the following features is foreseen:

- Adjustment of quench detection parameters to the real SIS-100 magnets.
- Remote display of signals and voltages and remote control of all quench detector variables: signal processing parameters, thresholds, timing...
- Digital isolation based detector.

References

[1] Hamlet G. Khodzhibagiyan et al., "Design and Test of a Hollow Superconducting Cable Based on Keystoned NbTi Composite Wires", IEEE Transactions on Applied Superconductivity, Vol. 15, No. 2, June 2005

* *Quench Detection for SIS100:* PSP-Code 2.14.14.04

† s.ayet@gsi.de

Estimation of beam induced heat load in SIS100 kicker magnets

U. Niedermayer *[1] *and O. Boine-Frankenheim*[1,2]

[1]Institut für Theorie Elektromagnetischer Felder, TU-Darmstadt, Schlossgartenstr. 8 64289 Darmstadt; [2]GSI Helmholtzzentrum für Schwerionenforschung

Introduction

In the operation of synchrotrons with high intensity beams electromagnetic parasitic loss causes heating of components. Especially the recent incidences at the LHC [1] gave rise to investigate this phenomenon for SIS100. The components most susceptible to beam induced heat load in SIS100 are the kicker magnets. Their ferrite yokes are strongly lossy especially at higher frequencies.

Heat Load Computation

The total beam induced heat power can be calculated from the longitudinal coupling impedance (CI) and the beam power spectrum. Since the CI is broadband for those lossy components, the effects of different bunches are uncorrelated and therefore the total power is linear in the number of bunches. Nonetheless, the charge and the number of particles per bunch enters squared:

$$P = \frac{1}{2\pi} q^2 N_{ppb}^2 \omega_0^2 \sum_{k=-\infty}^{\infty} e^{-\sigma_t^2 k^2 \omega_0^2} Re\{\underline{Z}_{\parallel}(k\omega_0)\} \quad (1)$$

Here, $\omega_0/2\pi$ is the revolution frequency and σ_t is the RMS length of a Gaussian bunch. Subsequently, the scenario with the highest heat load in SIS100 is the high intensity (2e13) single proton bunch at top energy with $\sigma_t = 12.5$ns. The power in Eq. 1 is the instantaneous one. For the computation of temperature it has to be averaged over a SIS100 cycle. The crucial quantity in Eq. 1 is the CI. For structures like the kickers it can only be obtained numerically [2] or by bench measurements.

Impedance Computation

The heat load for a SIS100 (to SIS300) transfer kicker magnet has been investigated exemplary, since it might also be operated in a (Nitrogen-) cryogenic environment.

The CI is determined numerically by a code explained in [2]. A 2D approach is used, which means that a slice of the 3D model is taken and end-effects are neglected. Further the beam is assumed to be ultra-relativistic. The ferrite yoke consists of the material Ferroxcube 8C11 [3] which is a soft ferrite with dispersive complex permeability.

As visible in Fig. 1 the longitudinal CI has been investigated for two magnet gap configurations. The resulting power is 7kW for an open gap and 48W if it is filled by a copper sheet. Note that these values are worst case steady state, i.e. they have to be weighted by the SIS100 cycle. If the copper sheets are used, skew cutaways as in SIS18 kickers are not necessary.

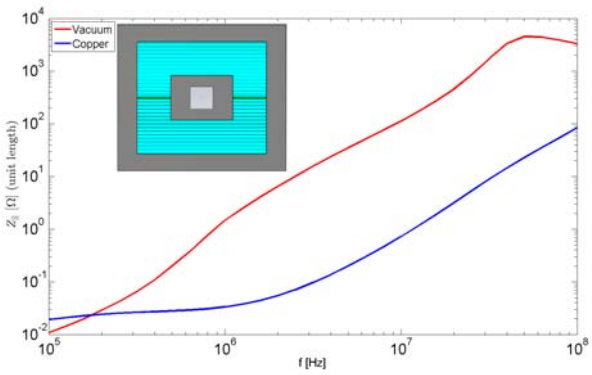

Figure 1: Longitudinal CI of a kicker magnet for vacuum or copper in the gaps (green). Each gap is 2.8mm wide.

Cooling and Temperature Equilibria

The heat conduction of Ferrite is quite good ($\lambda_{\mathrm{Ferrite}} \approx 4\ \mathrm{WK^{-1}m^{-1}}$) which allows to calculate a temperature of the ferrite independent of the position. Nonetheless, the thermal conduction off the ferrite is very poor since there is a small vacuum layer between the ferrite and its stand. Therefore the thermal interaction of the ferrite with its surrounding is dominated by radiation. From the Stefan-Boltzmann law one finds

$$T^4 = T_{rad}^4 + T_0^4 \approx \begin{cases} T_{rad}^4 & \text{if } T_{rad} \gg T_0 \\ T_0^4 & \text{if } T_{rad} \ll T_0 \end{cases} \quad (2)$$

$$T_{rad} = \sqrt[4]{\frac{P}{\sigma_{SB} C L K_\varepsilon}} \approx 200K \ \text{ for } \ \mathrm{P} = 50\mathrm{W}, \quad (3)$$

where the outer circumference is $C = 0.86$m, $L = 0.8$m and the average emissivity is assumed as $K_\varepsilon \approx 0.8$. Therefore cryogenic kickers are always at radiation temperature and warm kickers stay at room temperature for heat power below roughly 250W. This means that the impednace and heat load values for the improved design (with copper sheets) are acceptable.

References

[1] B. Salvant et al., Beam Induced Heating, LHC Beam Operation Workshop, Evian, 12-14 December 2011.

[2] U. Niedermayer and O. Boine-Frankenheim, proceedings of ICAP, Rostock, 2012

[3] Ferroxcube 8C11 Material Specification, 2002

* u.niedermayer@gsi.de

 doi:10.15120/GR-2014-1-FG-SIS100-05

Halo collimation of fully-stripped light and heavy ions in the SIS100 *

I.A. Prokhorov[1], *L. Bozyk*[2], *I. Strasik*[2], *and O. Boine-Frankenheim*[1,2]
[1]TEMF, TU-Darmstadt, Germany; [2]GSI, Darmstadt, Germany

Introduction

The FAIR synchrotron SIS100 will be operated with high-intensity proton and ion beams [1]. The collimation system should prevent beam loss induced degradation of the vacuum, activation of the accelerator structure and magnet quenches. A conventional two-stage betatron collimation system is considered for the operation with protons and fully-stripped ions [2]. We propose to use 1 mm thick tungsten foil as the first stage – primary collimator (scatterer) and two 400 mm blocks at as the second stage – secondary collimators (absorbers).

Interaction of heavy ions with collimators

For collimation studies we are interested in angular scattering, momentum losses and fragmentation of ions in the collimator material. A charged particle passing matter experiences multiple Coulomb scattering. According to Moliere theory, the angular distribution of scattered particles is roughly Gaussian with the r.m.s. angle θ_0 (Eq.1), $B\rho$ is the magnetic rigidity and x is the foil thickness.

$$\theta_0 = \frac{0.47}{\beta\,(B\rho)\,[Tm]}\sqrt{\frac{x}{X_0}}\left[1 + 0.038\ln\left(\frac{x}{X_0}\right)\right], \quad (1)$$

here X_0 is radiation length, tabular value for tungsten is $X_0 = 3.504mm$. Moliere theory predicts a Gaussian distribution in the range $10^{-3} < x/X_0 < 100$.

Momentum loss is described by (Eq. 2) with the corrections to standard Bethe-Bloch term L_0. The δL_{shell} correction represents the motion of electrons in the matter, δL_{Bark} is proportional to Z^3 and δL_{LS} takes into account the finite radii of heavy nuclei [3].

$$-\frac{\delta p}{p} = \frac{K}{\beta^4}\frac{Z_t}{A_t}x\left[L_0 + \delta L_{shell} + \delta L_{Bark} + \delta L_{LS}\right], \quad (2)$$

here $K = 3.07 \cdot 10^{-4} GeV g^{-1} cm^2$. According to [3], the momentum straggling has a Gaussian distribution for ions heavier than $^{40}Ar^{18+}$ at SIS100 injection energy.

Cross-sections and, hence, probabilities of the inelastic nuclear interaction for light and heavy ions passing through the tungsten foil were calculated using Tripathi formula [4]. The overall probability of fragmentation for $^{238}U^{92+}$ ions in our application is 6% and lower for lighter ions.

Simulation studies of cleaning efficiency

The simulation tool for cleaning efficiency studies uses an initial distribution of 10^5 halo particles and simulates their interaction with a collimator using implementation of models described above (Eqs. 1, 2). Then particles are tracked in the accelerator lattice with aperture limitations using MADX. After each consecutive turn, all particles are checked for impact on the primary collimator. In case of an impact, particle-material interaction is calculated.

A large portion of the halo particles is lost during the first pass through the collimation system (singlepass cleaning), however, high efficiency is gained after many turns (multipass cleaning), see Fig. .

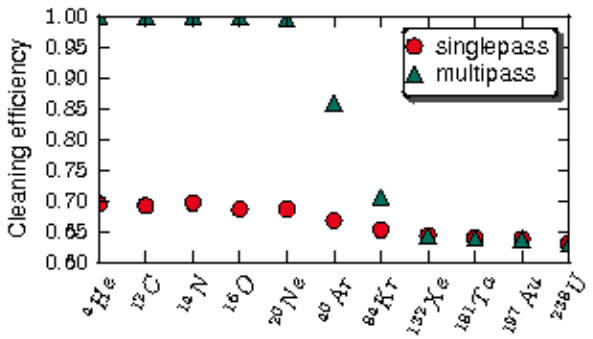

Figure 1: Cleaning efficiency at the injection energy for light and heavy ions.

The cleaning efficiency decreases with the mass number due to increasing momentum losses in the primary collimator. Strongly off-momentum heavy particles are unable to make one turn in the accelerator and are lost in the high-dispersion region of the lattice.

References

[1] P. Spiller et al., "Status of the SIS 100 heavy ion synchrotron project at FAIR", IPAC'13, Shanghai, May 2013, THPWO011

[2] J.B. Jeanneret, "Optics of a two-stage collimation system", Phys. Rev. ST-AB, vol. 1, 081001 (1998)

[3] A.H. Soerensen and J. Lindenhard. "Relativistic theory of stopping for heavy ions" Phys. Rev., A53:2443 (1996)

[4] GEANT4 Physics Reference Manual, Chapter 16

* Work is supported by German Federal Ministry of Education and Research (BMBF) contract no. 05P12RDRBM

Measurement of the behaviour of residual gas particles on cryogenic surfaces to improve the simulation of dynamic vacuum effects

F. Chill[1,2], L. Bozyk[2], O. Kester[1,2], and P. Spiller[2]
[1]Goethe-Universität, Frankfurt, Germany; [2]GSI, Darmstadt, Germany

Introduction

The dynamic vacuum refers to pressure rises occurring during beam operation in particle accelerators. It is caused by lost beam ions triggering stimulated desorption of gas particles from the walls which may cause even more beam loss. This has to be compensated by pumps as fast as possible to prevent a self-amplifying effect.
To achieve this, the cryogenic vacuum chambers of the SIS100 will act as surface pumps. They are able to pump gases according to their vapor pressure curves which are sufficiently low for stable beam operation for most gases. This is called *cryocondensation*. An important exception is hydrogen. Fortunately, it can be pumped to lower pressures by so called *cryosorption* if the surface coverage of the cold walls is sufficiently low [1]. This effect can be characterized by two parameters: The *sticking coefficient* describes the probability of a gas particle impacting on the surface to be bound. It is directly linked to the pumping speed provided by the cryogenic walls. The *mean sojourn time* describes how long a particle remains bound to a surface. Both parameters together determine the equilibrium pressure. Once known they will be used to improve the quality of simulation of the StrahlSim [2] code.

Measurement of the parameters

An UHV experiment (Figure 1) to determine these parameters is currently set up. The cold surface that will be tested is provided in the form of a small chamber which is cooled by a cold head. The target temperature range is 5 to 20 K. The measurement will be divided in two phases: At first, the pumping speed of the chamber is quantified at different temperatures and surface coverages to get the sticking coefficient. In the second phase, the corresponding equilibrium pressure is evaluated which yields the sojourn time.
To link the pressure values measured by the gauges to the desired parameters, the simulation code MolFlow+ [3] is used to perform a data inversion. An alternative method for interpretation of the data is the calculation of unknown vacuum properties like the pumping speed and the outgassing rate from known or measured properties like the pressures and the conductances. The VakDyn [4] equations, which are also the basis for the vacuum simulation in StrahlSim, provide a set of linear equations for this purpose. Simulations showed, that the warm part can be represented by two isobaric vacuum elements, but the cwt shows a continuous drop in pressure towards the cold chamber.

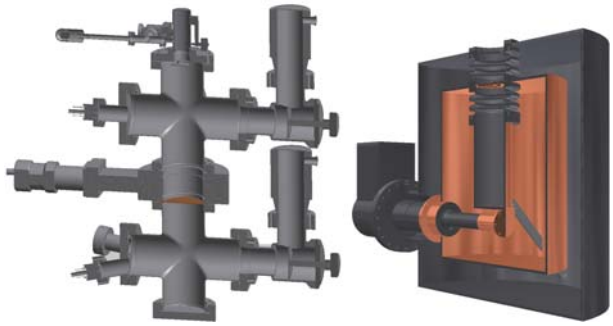

Figure 1: Draft of the planned experiment. Left side, top to bottom: Gas inlet with diffuser plate, first recipient with extractor gauge and turbo pump (closable with corner valve), gate valve to be closed for phase 2, defined conductance (copper bezel), second recipient with transition to the cold chamber, which is shown to the right. It consists of: A Cold-Warm-Transition (cwt) with a baffle, the inner chamber which is plated with copper for an equal temperature distribution, a copper radiation shield.

Current status and first measurements

The warm part is already in operation. The cold chamber is currently designed and built externally.
To calculate the integral outgassing in the warm part during pump down and after bake out, the corner valves are closed one at a time so the pumping speed for the valved off chamber is set to zero. The integral outgassing rate in this individual chamber is then equal to the gas flow through the bezel which can be calculated from the two measured pressure values.
Its value could be reduced by two orders of magnitude by baking the system at 200°C for 18 days. Thereby the most prominent residual gas species in the spectrum changed from water to hydrogen. The remaining water now originates mainly from the corner valves, which have been heated to only 100°C to protect the turbo pumps from excessive heat. Baking is continued to achieve lowest possible outgassing and thereby background for the experiments.

References

[1] E. Wallén, J. Vac. Sci. Technol., A 14, 1996, p. 2916
[2] P. Puppel, PhD Thesis, 2012
[3] R. Kersevan,`http://test-molflow.web.cern.ch`
[4] V. Ziemann, Vacuum 81, 2007, p. 866-870

 doi:10.15120/GR-2014-1-FG-SIS100-07

FPGA Based Tunable Digital Filtering for Closed Loop RF Control in Synchrotrons*

Konrad Möller† [1], *Martin Kumm*[1], *Peter Zipf*[1], *Kerstin Groß*[2], *Dieter Lens*[2], *and Harald Klingbeil* [2,3]
[1]Digital Technology Group, University of Kassel; [2]Accelerator Technology, Technische Universität Darmstadt; [3]GSI

Introduction

The longitudinal feedback system for the FAIR accelerator SIS100 will rely on digital filters for damping longitudinal bunch oscillations. Filters with a minimum time delay are needed, thus an implementation on a field programmable gate array (FPGA) is necessary. In addition, the filter implementation has to be flexible enough for a real-time adaptation of the filter coefficients during the acceleration ramp. This will enable the tuning of the longitudinal feedback with respect to the synchrotron frequency and other relevant parameters. The filter length will be considerably longer than the currently used three-tap filter of the beam phase feedback [1], offering more degrees of freedom.

Filter

In order to achieve a constant group delay an finite impulse response (FIR) filter was chosen. The fundamental operation of an N-tap FIR filter is the inner product of a vector containing N time shifted scalars of the filter input x with a vector c consisting of the filter coefficients. In a tunable filter design c has to be adapted to the current RF frequency. The adaption of the filter coefficients can be achieved by using a look-up table (LUT) based multiplication scheme on the FPGA. Here, a general purpose multiplier is replaced by a constant coefficient multiplier consisting of LUTs containing partial products followed by bit shifts and adders to calculate the final result. This concept, introduced in [2] was customized with reconfigurable LUTs (content can be changed during run-time) on recent FPGAs [3]. A reconfiguration can be performed in 16 clock cycles which corresponds to 160 ns in the current implementation. This is fast enough to tune the filter characteristics between the calculation of two filter outputs and thus leading to glitch-free switching.

The block diagram of the resulting dynamically reconfigurable FIR filtering is shown in Figure 1. Our implementation realizes a filter with up to $N = 64$ non-zero-taps. Between these taps a tunable number L of virtual zero-taps are inserted to tune the bandpass characteristics of the filter. In addition to this tuning possibility, a larger range of input samples is considered which allows filtering of lower frequency components as well.

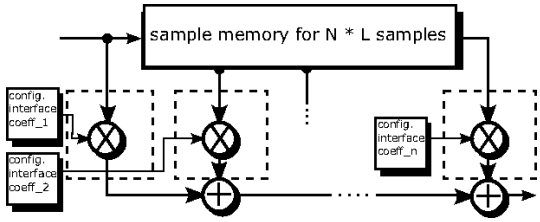

Figure 1: Dynamically reconfigurable FIR filter using reconfigurable LUT multiplication (in dashed lines)

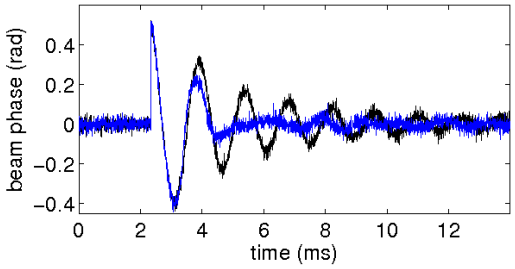

Figure 2: Simulation: open loop (black), closed loop (blue)

Simulation and Outlook

As an example, the closed-loop performance of an FIR filter used in a longitudinal beam phase feedback loop for SIS18 is shown in Fig. 2. In this nonlinear tracking simulation, Ar^{18+} with a kinetic energy of $11.4\,\mathrm{MeV/u}$ is assumed as ion species. At $t = 2.32\,\mathrm{ms}$, dipole oscillations are intentionally induced by an RF phase shift. The amplitude of the gap voltage is $1\,\mathrm{kV}$, resulting in a synchrotron frequency of $740\,\mathrm{Hz}$. In this case, the filter was designed as a highpass filter with $N = 15$ and $L = 30$.

In future several new filter designs will be possible due to the large number of taps. Further studies will also deal with the optimization of the filter design.

References

[1] H. Klingbeil, B. Zipfel, M. Kumm, and P. Moritz. A Digital Beam-Phase Control System for Heavy-Ion Synchrotrons. *IEEE Trans. Nucl. Sci.*, pages 2604–2610, 2007.

[2] K. D. Chapman. Fast integer multiplier fit in FPGA's. *EDN Access*, pages 79–80, 1994.

[3] M. Kumm, K. Moeller, and P. Zipf. Dynamically reconfigurable FIR filter architectures with fast reconfiguration. *Reconfigurable and Communication-Centric Systems-on-Chip (ReCoSoC), 8th International Workshop on*, 2013.

* Work supported by BMBF, contract No. 05P12RKRBE.
† konrad.moeller@uni-kassel.de

 doi:10.15120/GR-2014-1-FG-SIS100-08

Development of a tool for CBM STS module assembly *

D. Soyk[1], *J. Kunkel*[1], *C. Simons*[1], *C.J. Schmidt*[1], *and the FAIR@GSI RBDL*[1]
[1]GSI, Darmstadt, Germany

The assembly of a silicone strip sensor with microcable and the readout chip is called in the CBM STS collaboration a "module". To connect the double-sided CBM sensor with 1024 channels on each side via microcables to the CBM STS-XYTER chip the tab-bonding process was chosen. One microcable has 64 channels with a pitch of 116 μm and a lead width of 46 μm. The thickness of the aluminium lead is 14 μm and the thickness of the polyimide substrate is 10 μm. Consequently the microcable is easily floating, fragile and not easy to handle without tooling. For the assembly of the chip or of the sensor to the microcable, the microcable has to be moved in two translational and one rotational directions (see Fig. 1). Therefore

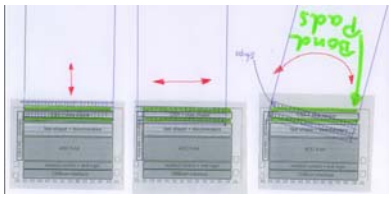

Figure 1: Degrees of freedom of the microcable.

the assembly tool needs at least two translational and one rotational degree of freedom to assure a correct alignment of the microcable to the sensor or chip. To realize these three degrees of freedom the microcable can be fixed and the sensor, respectively the chip, can be movable. Alternatively the microcable is movable and the sensor, respectively the chip, is fixed. Finally the microcable as well as the sensor respectively the chip are movable. For the first test version the decision was taken to move only the microcable and keep the sensor, respectively the chip, on a fixed position.

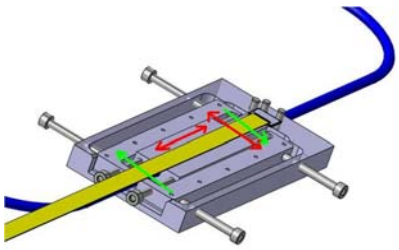

Figure 2: CAD model of assembly tool with chip and microcable (yellow). Red and green arrows indicates the different degrees of freedom.

To fixate the sensor respectively the chip and the microcable on the assembly tool it is a good choice to use vacuum, because the microcable would be deformed by mechanical clamping, and the clamping tools for sensor respectively chip will reduce the accessibility of the bond pads.

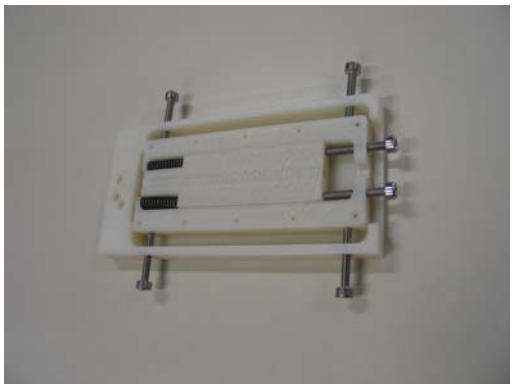

Figure 3: 3D model of the tool.

To speed-up the development the 3D CAD data (see Fig. 2) were printed using a 3D plotter and tested by the bond experts before the final tool was machined out of aluminium. Due to the printing process some fine structures on the tool were not perfectly shown (see Fig. 3), but it was precise enough to decide about the handling properties of the tool. In Fig. 4 the final tool in aluminium is shown.

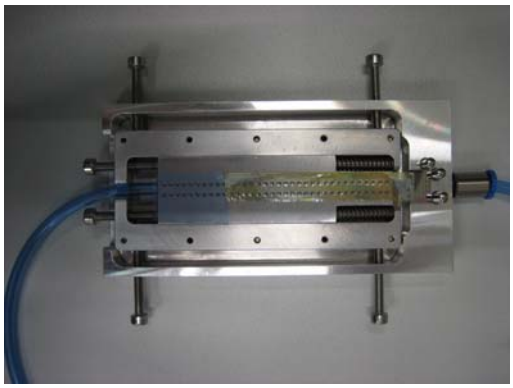

Figure 4: Final tool.

While using the final version of the tool it turned out that it works well and fulfills all requirements.

* Work supported by FAIR@GSI PSP code: 1.1.1.2.1.2.

Setup for adjustment of process parameters for CBM module production *

D.Soyk† [1], *C.Simons*[1], *C.J.Schmidt*[1], *I.Tymchuk*[2], *M.Protsenko*[2], *V.M.Borshchov*[2], *for the CBM collaboration*[1], *and the FAIR@GSI RBDL*[1]

[1]GSI, Darmstadt, Germany; [2]LTU, Kharkov, Ukraine

The sensor modules for the CBM STS comprise an STS microstrip sensor, 16 CBM STSxyter readout chips and 32 microcables of 64 leads each. The double-sided STS sensor has 1024 strips on each side. Consequently 2048 channels per module must be connected by means of 4096 bonds. It is obvious that the quality assurance of theses tab-bonds is a major ingredient to the yield of module production and reliability of the detector as a whole. Especially the huge number (around 1000) of needed modules for the entire CBM STS requires to have a detailed look at the tab-bond process and its parameters, as potentially required repair actions on defective modules will be time consuming and adds the risk of additional inadvertant damage to the module. Therefore it is the best solution to improve and bring the tab-bond process to perfection before starting the serial production of modules for the CBM STS.

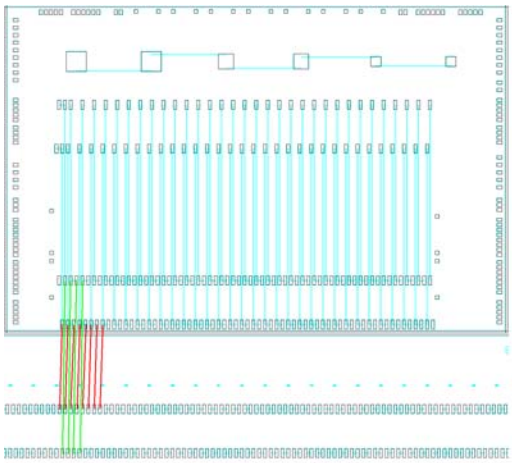

Figure 1: Dummy CBM STSxyter chip (up) and a partial plan of a CBM sensor dummy (down). The red lines are the connections via the microcable for the first row of bond pads. The green lines are the connections via a second microcable for the second row of the pads. In the upper part of the Dummy CBM STSxyter are the contact pads for the test equipment directly connected to the tab-bond pads in the lower part of the chip.

It is clear that for such process optimization no original full functional STS sensor and CBM STSxyter chip will be used or needed. The first reason is the costs of the original components and second reason is the missing of fast and easy ways to check the quality of the tab-bonds. For this reason, dedicated dummy-sensors as well as dummy-chips have been designed and manufactured. To check the quality of bonding two tests are necessary. One is the pull test to check mechanical adhesion of the aluminium lead of the microcable to the bond pad. The second is the electrical connectivity of the bond.

In order to make this test conclusive for the real module the microcable must the original, the surface and the material of the bond pads for dummy-sensors and -chips must be identical to the material on the original sensors and chips. Also, the Silicone wafer material and thickness should be identical. If these requirements to the microcables, dummy sensors and chips are fullfilled, it is possible to transfer the process data to the serial production process.

To improve the test routines for the electrical contacts, additional pads for test needles and connections between the pads were added to the dummy-sensors and -chips. (These additional features will for sure not be part of the layout of the final devices.) In figure 1 the scheme of electrical connections is shown with the layout of the dummy chip and sensor. On the dummy chip, each second pad of each row is electrically connected to a pad far away from the tab-bond area.(The first pad of a row is like the second also electrically connected to a shifted pad.) The non duplicated pad is electrically connected to its left neighbor. On the dummy sensor two neighboring pads of a row are electrically connected together.

The idea behind this set-up is to make an electrical connection between the pad of the test needle via the tab-bond on the chip, the microcable, the tab-bond on the sensor and back to the second test pad for each row. With this simple serial routing it is possible to check 4 tab-bond connections and two leads of the microcable with one single measurement. If the connection is good the first needle is kept on its starting position whereas the second needle is shifted to the next pad of the row. This daisy chaining now allows to check 8 tab-bonds and 4 leads of the microcable in one go. While continuing this daisy chaining it is possible to check numerous tab-bonds and microcable-leads. If a broken lead or damaged tab-bond is found the first needle of the test set-up must be moved to the unconnected pad and the second needle can step further.

With this test strategy we can reduce the number of single tests, because only broken leads or tab-bonds will cause a restart of the test procedure. Additionally the test procedure could be done automatically on a wafer prober.

At the moment the dummy chips and sensors have been delivered. We are now waiting for a sufficient number of sample microcables to start process optimization.

* Work supported by FAIR@GSI PSP code: 1.1.1.2.1.2.

† d.soyk@gsi.de

 doi:10.15120/GR-2014-1-FG-S-FRS-02

Silicon strip sensor layout for CBM STS *

D.Soyk[†1], *I.Tymchuk*[2], *J.Heuser*[1], *C.J.Schmidt*[1], *for the CBM collaboration*[1], *and the FAIR@GSI RBDL*[1]

[1]GSI, Darmstadt, Germany; [2]LTU, Kharkov, Ukraine

The CBM Silicon Tracking System will be equipped with double-sided Silicon micros-strip sensors, where the strips on the p-side are inclined by 7.5° with respect to the n-side strips as well as the sensor edge. The final and homogeneous layouts for the 3 different sensor lengths, namely 22mm, 42mm and 62mm, has been elaborated. Longer sensors may be realized as a daisy-chain of two 62mm sensors. The sensors will be produced by two vendors to avoid the stop of module production in case of problems with any one single vendor.

The stereo angle of 7,5° effects a correlation between the x and y coordinate of a bond pad on a strip. The x distance between to strips on the sensor is 58μm, equivalent to the pitch of the straight n-side strips. Therefore the second row of bond pads must have a y distance of at least once the multiple of 58μm/tan(7,5°). On the sensor a pad pattern with x distance of 58μm and y distance of ∼440,554μm is possible, but the minimum producible pitch for the long analog microcables is in x direction 116μm. In order to contact all strips, a double layered cable needs to be employed und thus a doubly staggered bond pattern is needed.

This leads to a checker-board-pattern where every second pattern-point is alternatingly reserved for a bond pad. The pitch of the bond pads is in x 116μm and in y ∼ 881.108μm (the center of the pads in the second row is shifted in x direction by 58μm relative to the center of the first row of pads). Figure 1 shows an exemple of the such pattern.

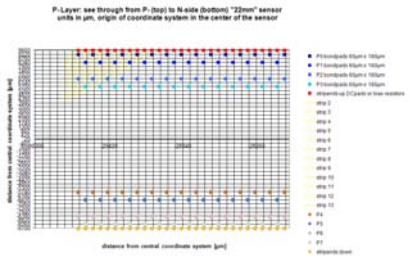

Figure 1: Schematic view on the bond pad and DC pad pattern.

As there are different lengths of sensors and as the pad rows should be located on the same x-position on the top edge as on the bottom edge it proved most adequate to allocate the origin of the coordinate system in the center of the sensor. Further, the distance from the coordinate center to the innermost pad row was fixed to be a multiple of the y-pitch of two staggered pad rows, namely 881.108μm . Consequently the distance from the outermost pad row to the edge of the sensor is a variable of the sensor length, as the pre-chosen lengths are none multiples of this pitch.

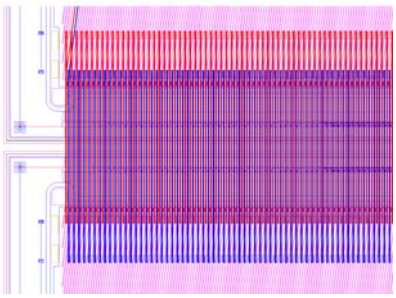

Figure 2: Schematic view of a sensor to sensor daisy chain. The red and blue lines are the leads of the short 58μm-pitch cable that serves to daisy chain two sensors.

These definitions together with the respective symmetry allow daisy-chaining of sensors of the same as well as different lengths to each other. Figure 2 shows two daisy-chained sensors with a microcable of a constant lead length.

Consequently, also one FEB-design may serve all sensor configurations as well as either sensor side. In figure 3 a scheme of a microcable connection between the foreseen CBM STSxyter chip and the STS sensor is shown.

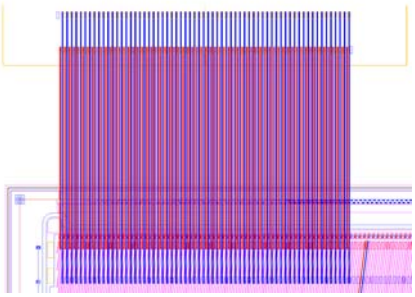

Figure 3: Schematic view of a sensor to chip connection. The red and blue lines are the leads of the microcable on two different layers with a pitch of 116μm.

All participating vendors will employ this layout of the bond pads even though they may vary the sensor design according to their proprietory design and production preferences.

* Work supported by FAIR@GSI PSP code: 1.1.1.2.1.1.

† d.soyk@gsi.de

A new Time-of-flight wall for R^{3}B *

M. Heil[1], A. Kelić-Heil[1], J. Gerbig[2], J. Frühauf[1], J. Hoffmann[1], K. Koch[1], N. Kurz[1], for the R^{3}B collaboration[1], and the FAIR@GSI RBRB[1]

[1]GSI, Darmstadt, Germany; [2]Goethe-Univerität, Frankfurt, Germany

Introduction and design goals

The beams provided by Super-FRS at FAIR will have higher energies and will be more intense than presently available. The goal of the new R^{3}B setup is to fully exploit the potential of FAIR beams. With the new super conducting magnet GLAD it will be possible to deflect fully-stripped ions up to the Pb region with energies up to 1 AGeV. Also the detectors of the R^{3}B setup should be able to scope with the new conditions.

One detector of the setup is the time-of-flight (ToF) wall made of plastic scintillators. The purpose of this detector is the measurement of the time-of-flight and the nuclear charge of the fragments after the reaction in the target. Together with the measured trajectory through a dipole field, the mass of the fragment can be identified. The charge is obtained by precise energy loss measurements of the fragments passing through the scintillators. With the Super-FRS at FAIR it will be possible to accelerate fully stripped beams up to the Pb region and consequently, the new ToF wall should be able to separate charge Z from Z-1 even for heavy fragments. For Pb fragments the energy loss measurements for Z and Z-1 are seperated by 2.4 % and a charge resolution of $\sigma_{\Delta_E}<1\%$ is needed in order to resolve them. Furthermore, since the unreacted beam also hits the fragment wall, the detector must be able to maintain the performance even at high beam rates up to 1 MHz. In order to match the momentum resolution of other parts of the setup the relative time-of-flight resolution should be around 0.1‰. Since the detector is placed typically between 12 and 20 m behind the target the shortest expected flight times are about 75 ns. This results in a required time resolution of $\sigma_t<17$ ps (see also contribution [1] in this annual report).

Although the current version of the ToF wall was successfully used in many experiments in the past, we plan to build a new ToF detector with superior time and energy resolution at beam rates up to 1 MHz. It is not planend to use a completely new detector concept but rather take advantage of the experience collected over the last years and advance the current design.

The detector will have four planes of scintillators and the active part will cover an area of 120x80cm^2. Each plane consists of 43 scintillators with the size 800x27 mm^2 and they are read out with photomultipliers on both far ends. The first two planes will have scintillators with a thickness of 3 mm and the last two planes a thickness of 5 mm, respectively. In this contribution we will focus on the performance of prototype detectors concerning the energy resolution and new readout-electronics at high rates.

* Work supported by FAIR@GSI PSP code: 1.2.5.1.2.1.

Prototype results and developments

In order to test the behaviour of the detector without beam, a test stand with a fast LED was developed (see master thesis of Julian Gerbig [2]). The LED emits light in the same wavelength region as the BC408 plastic scintillator, and the intensity as well as the pulse rate can be varied. In order to obtain realistic conditions, the LED was pulsed in random mode.

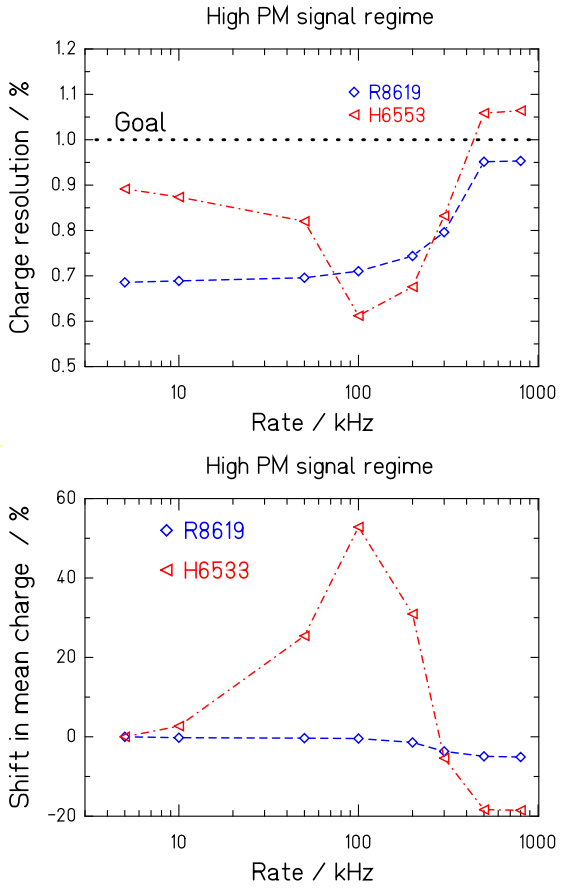

Figure 1: The plot on the top shows the relative charge resolution for each frequency for two differnet PMs. The bottom plot shows the shift in the charge measurments for different rates.

Two different PMs from Hamamatsu were tested, both with a diameter of 1 inch. Model H6533, a very fast PM (TTS: 0.25 ns) but without active voltage divider. This

 doi:10.15120/GR-2014-1-FG-S-FRS-04

model was used in the past experiments for the existing ToF wall (NTF). The second model R8619 is a cost effective PM with an active voltage divider (TTS: 1.2 ns).

At the beginning, the conditions of one of the last experiments were simulated. The intensity of the LED was set to simulate medium heavy nuclei, such as e.g. Ni and the voltages of the PMs were set in order to extract large charges as needed for the previously used read-out. The frequency was varied between 5 and 800 kHz. Although the energy resolution for both PMs was good for each individual rate, it was observed that the peak position shifted with frequency (see figure 1). In an experiment with varying beam rate during a spill this would lead to a bad resolution. Especially for the H6533 the shift is dramatic. For the R8619 the shift is much smaller but still visible and too large for resolving charges of heavy fragments.

The shift in the charge measurement stems from the PMs. Especially for large currents, the voltages at the last dynodes can not be kept constant and the gain of the PM is changing. The situation can be improved by taking active voltage dividers and by reducing the HV of the PMs and therefore also the anode current. But also the charge of the signal plays an important role. For small signal charges the R8619 is suited to measure the signals with a resolution (and shift) of less than 1% even for rates as high as 800 kHz as can be seen in figure 2.

It can also be seen that for too small charges, the relative resolution for charge measurements gets worse again. Therefore, for an excellent performance of the new ToF wall is is mandatory to use PMs with active voltage dividers and to reduce the signal amplitudes via the HV of the PMs to a region were the PMs work best with regard to rate stability and charge resolution. This also requires a change in the read-out electronics. So far, CAEN TDC were used and the signals of the PMs were split in a time and an energy branch. The analog signal for the energy branch was delayed by about 600 ns until the trigger decission was made. Especially this long delay caused a damping of the signals by a factor 10. The new read-out will convert the analog signals immediatelly in logic signals with a signal width which is either propotional to the time-over-threshold (ToT) or to the integrated charge (charge to time converter QTC). This signal is then recorded by a multi-event FPGA TDC such as the VFTX2 [3] developed at GSI. From the leading edge of the signal the timing can be obtained (see also contribution [4] in this annual report) and from the trailing edge the energy can be restored. In this way the signal is immediatelly digitized and no delays are needed. Since the VFTX2 is multi-hit cabable the hits can be read out much later.

Summary and outlookents

It is planned to build a new ToF wall for the R^{3}B setup at FAIR. As the existing one, it will consist of plasic scintillators but we aim for an improved energy ($\sigma_{\Delta E}$<1 %) and time resolution (σ_t<17 ps) even at higher beam rates.

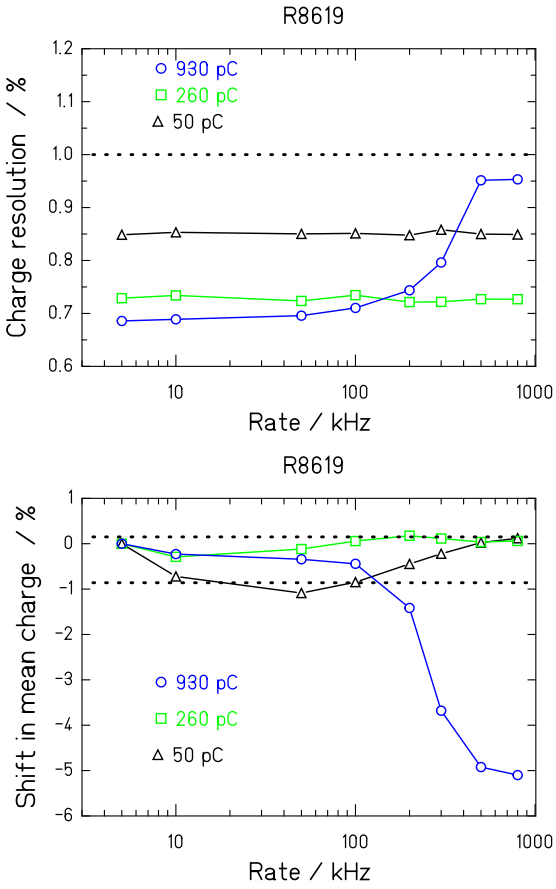

Figure 2: Shown are the charge resolution and the shift in mean energy for the PM R8619 for different loads of the PM. It can be seen that for medium charges (260 pC) a sufficiently good resolution can achieved, even at rates up to 800 kHz.

A test setup with a LED as light source has shown that this is possible with the use of PMs with active voltage dividers and with an adapted electronic read-out which allows to extract only small charges from the PMs. The electronics will be developped by the GSI EE department. We plan to prove the performance of a prototype in beam tests and detail the final layout of the new detector in a TDR.

References

[1] A. Kelić-Heil und M. Heil, “New time-of-flight system for the R^{3}B set-up”, contribution to this annual report.

[2] J. Gerbig, “Kalibrierung eines Szintillationsdetektors mit Hilfe von LEDs”, Masterarbeit 2013, Goethe-Universität Frankfurt

[3] J. Frühauf, J. Hoffmann, E. Bayer et al., “VFTX (VME-FPGA-TDC 10ps)”, Scientific Report 2012 GSI Report 2013-1, 300 p. (2013)

[4] R. Plag, M. Gilbert, M. Heil et al., “High precision multi-hit time-of-flight measurements at R^{3}B”, contribution to this annual report.

High precision multi-hit time-of-flight measurements at R^{3}B*

R. Plag[1], M. Gilbert[2], M. Heil[1], J. Frühauf[1], J. Hoffmann[1], K. Koch[1], N. Kurz[1], for the R^{3}B collaboration[1], and the FAIR@GSI RBRB[1]

[1]GSI, Darmstadt, Germany; [2]Goethe University Frankfurt, Germany

Introduction

The kinematically complete reaction measurements at the upcoming R^{3}B set-up require the identification and separation of heavy, relativistic reaction fragments. This requires a precise measurement of the time-of-flight in order to calculate the momentum of the particles with the necessary resolution of $\delta p/p = 10^{-3}$. Depending on the length of the flight path and the energy of the ions, this translates into a required time resolution of about 15 ps for ions with $A \gtrsim 150$ [1].

To reach this goal, two new detectors based on plastic scintillators have been developed for the time-of-flight measurement: An optimized start counter and a multi-layer time-of-flight wall [2] which will provide energy loss and position information as well.

The signals of the photomultipliers will be readout by a new multichannel front-end electronic card (TAMEX). This card has been designed by the GSI CSEE group for high-resolution time and charge measurements and is a combination of the existing LAND TACQUILA FEE and a FPGA TDC from the VFTX module.

Electronics

The VFTX module [3] provides a time resolution of less than 15 ps RMS over a long time range. This is achieved by a combination of a FPGA, a TDC and an external clock signal. The TDC measures the times of the rising and the falling edges of the detector signal with respect to the external 200 MHz clock signal, see Figure 1. The FPGA stores this TDC value together with the timestamp (cycle number) of the clock signal. This way, times can be measured with respect to the arbitrary origin of the clock.

In order to measure detector times with respect to a common start or trigger signal, the common start signal has to be connected to any free VFTX input channel as well. Since the external clock signal can be applied to multiple VFTX boards, the time reference for all VFTX channels is guarantied to remain synchronized over the whole period of the experiment.

In addition, the VFTX is able to record multiple hits per event (trigger) and channel which is not only useful for experiments with high beam intensities but also in cases where several secondary particles need to be detected, e.g. from the neutron shower in the Neuland detector [4] or if the incident particle breaks up in multiple fragments.

Measuring the times of both, rising and falling edge of the signal, provides the length of the signal which can - if properly shaped - be considered as a measure for the energy integral of the signal. For several detectors, a second electronics branch to measure the energy is therefore not necessary. For a precise charge measurement with the time-of-flight wall however, a more accurate energy measurement is necessary and will be available on the TAMEX card.

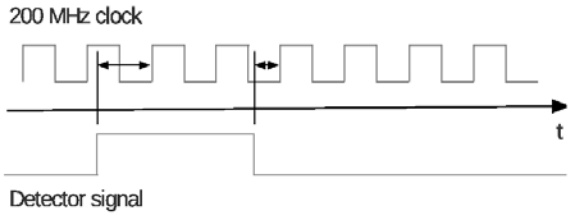

Figure 1: Measurement of rising and falling edge of a detector signal by the VFTX card.

While the TAMEX cards are not yet available, the circuit for the time measurement is already available in the VFTX modules and hence the time resolution of the whole chain detector / data acquisition / data analysis could already be tested.

Software

The current LAND/R^{3}B analysis software land02 has been adopted to analyse VFTX data. This required the handling of multiple times per event and channel, the introduction of calibration routines and the conversion of rising and falling time signals into an energy value.

While the external 200 MHz clock signal is assumed to be sufficiently stable, the TDCs need a bin-wise calibration in order to reach the designed time resolution. The calibration is performed by recording TDC times of random input signals. The resulting histogram of raw TDC times (without considering the clock cycle) should ideally resemble a perfect rectangle with 5ns width. The calibration routine calculates the width of each time bin such, that this goal is reached, see Figure 2.

* Work supported by FAIR@GSI PSP code:1.2.5.1.2.1.

 doi:10.15120/GR-2014-1-FG-S-FRS-05

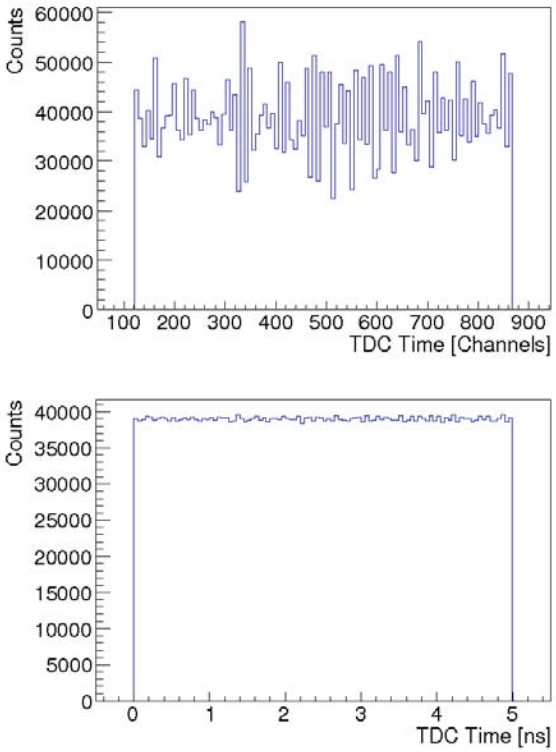

Figure 2: Top: Raw times (in channels) from random input signals. The variation of the bin contents reflects the non-linearity of the TDC. Bottom: The events are equally distributed after the calibration.

Test measurements

The new start counter consists of a square plastic scintillator of 5.5x5.5 cm^2 size and 0.5 mm thickness. The scintillator is read out on all four sides to improve the time resolution by averaging the four measurements. In order to reduce uncertainties from reflections of the scintillation light to an absolute minimum, the photomultipliers have been coupled to the scintillator material without any light guide.

The energy deposition of heavy ions was simulated by illuminating a small area (2mm diameter) with a Nitrogen UV laser (337 nm wave length). The time measurement was calibrated and analyzed using the updated land02 analysis software. The time resolution can be estimated by analysing the time difference of signals from opposite photomultipliers, see Figure 3. The resulting peak shows a width (σ) of 13 ps indicating a time resolution for an average of all four photomulipliers of well below 15 ps.

Summary

On the example of the optimized start detector it could be shown that time measurements with an uncertainty of less than 15 ps are feasible. The second time for the time-of-flight measurement will be measured by the multi-layer time-of-flight wall where up to 6 individual time measurements can be averaged. This will result in a similarily precise time information.

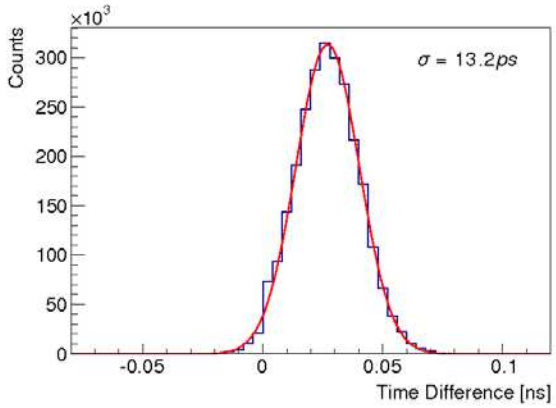

Figure 3: Time difference between left and right readout from a square 5.5x5.5cm ^{2} scintillator bar. The peak shows a width (σ) of 13 ps indicating a time resolution for the average of all four signals of well below 15 ps.

References

[1] A. Kelić-Heil et al., New time-of-flight system for the R^3B set-up, GSI Annual Report 2013

[2] M. Heil et al., A new Time-of-flight wall for R^3B, GSI Annual Report 2013

[3] J. Frühauf, N. Kurz, J. Hoffmann, E. Bayer, User-Manual VME - FPGA - TDC (VFTX2), Version 1.0, unpublished

[4] Technical Report for the Design, Construction and Commissioning of NeuLAND, oline at http://www.fair-center.eu/fileadmin/fair/publications_exp/NeuLAND-TDR-Web.pdf

New time-of-flight system for the R^{3}B set-up *

A. Kelić-Heil[1], *M. Heil*[1], *the R^{3}B collaboration*[1], *and the FAIR@GSI division*[1]
[1]GSI, Darmstadt, Germany

Introduction

The present LAND/R^{3}B experimental set-up can be used for identifying the reaction products up to the mass region $\sim$ 150. At the future R^{3}B set-up at FAIR, this problem will be overcome, and also the reaction products in the mass region 200 will be effectively separated and it will be possible to identify them. On the other hand, extending the experimental capabilities to this mass region would also imply improvements in the time-of-flight (TOF) resolution. Identification of the reaction residues in high-energy nuclear collisions is usually based on energy-loss measurements and charge-particle deflection in the magnetic field. The mass-over-charge ratio can be calculated as: $A/Z = e/(m_0c) \cdot (B\rho)/(\beta\gamma)$. Once the nuclear charge is obtained from the energy-loss measurements, relative uncertainty in the mass determination can be calculated as: $\Delta A/A \approx \Delta(B\rho)/(B\rho) + \gamma^2 \cdot \Delta TOF/TOF$. The challenge is to separate neighboring masses in the mass region 200, where relative difference in mass between two neighboring nuclei amounts to $\sim 5 \cdot 10^{-3}$. Thus, in order to be able to separate neighboring masses, the relative uncertainty in mass must be of the order $2 \cdot 10^{-3}$ assuming 3σ precision. The magnetic rigidity can be obtained via particle tracking with a relative uncertainty of the order of 10^{-3}. In order to fulfil the demand on the mass resolution in the mass region 200 at 1AGeV energy, the time-of-flight (TOF) has to be measured with a relative uncertainty better than $2.5 \cdot 10^{-4}$. Considering a flight path of $\sim$20m, this would mean that the ultimate TOF resolution should not exceed 20ps (sigma). While TOF is measured between two detectors giving start and stop signal, 20ps TOF resolution would mean that the time resolution Δt of each TOF detector should not exceed 15ps.

New TOF system

The new TOF system for the R^{3}B set-up will be based on the existing one but with improved capabilities. The start detector LOS will be made out of scintillator material, and will have dimensions of $55 \times 55 \times 0.5\,\mathrm{mm}^3$. The produced light will be collected directly, without any light guides, by 4 photomultipliers (PM). The PMs will be read out by a new multi-channel front-end card TAMEX developed by GSI CSEE group enabling high-resolution time measurements. The stop detector will be a multi-layer time-of-flight wall with high time and charge resolution and high-rate capabilities [1].

In the following, we will discuss different effects influencing Δt and search for the compromise between best performance and costs. We will use the statistical method [2] for calculating Δt of a scintillator detector.

Calculations of the time resolution

There are different statistical processes which are limiting the attainable Δt of scintillation detectors: Time spread in the energy transfer to the optical levels of the scintillation crystal, decay time of the excited states, fluctuations in the propagation time of photons through the scintillation crystal, creation of photo-electrons within a photo-multiplier, as well as the associated electronics. The first application of the statistical model for calculating achievable Δt has been done by Post and Schiff [2]. At this place, we will not discuss the method in details but refere the reader to the paper of Post and Schiff. The advantage of this model is that all above-mentioned contributions can be studied and optimized separately, which is not always easy when using Monte-carlo simulations.
One of the important ingredients of the statistical model is the shape of the measured light pulse. This shape is of course influenced by different processes mentioned above. The primary shape is given by the light-production mechanism, and in case of plastic scintillator it has been shown [3] that the best-suited shape is given by a convolution of an exponential and a Gaussian function, so-called ExpGaussian [4]. In case of small-size scintillation detectors the light-production mechanism has a dominant role. For timing properties of larger-size detectors light transport becomes very important, and to consider this effect we have followed the work of ref. [5]. Knowing the light-pulse shape seen by a PM, using the statistical model we can calculate the contribution of the scintillator σ_{sci}. The contribution from the PM is determined by its transient-time-spread (tts) and can be calculated as: $\sigma_{PM} = tts/(2.35 \cdot \sqrt{R_{tot}})$, where R_{tot} is total number of photo-electron pulses. The contribution of electronics σ_{el} has been measured to amount to 8ps per readout channel. Then, the total Δt for each detector Δt_{det} can be calculated as: $\Delta t_{det} = \sqrt{\sigma_{sci}^2 + \sigma_{PM}^2 + \sigma_{el}^2}$.

LOS detector

For the LOS detector we have performed two sets of calculations assuming 1 AGeV ^{208}Pb ions passing through the detector:
1. Expensive solution: Consisting of the scintillator mate-

* Work supported by FAIR@GSI PSP code: 1.2.5.1.2.1.

 doi:10.15120/GR-2014-1-FG-S-FRS-06

rial EJ232Q (rise time: 0.043ns, decay time: 0.608ns, light output: 19% of Anthracene) and a photomultiplier H6653 (tts: 0.16ns), see fig. 1.
2. Cost-effective solution: Consisting of the scintillator material EJ230 (rise time: 0.5ns, decay time: 1.5ns, light output: 64% of Anthracene) and a photomultiplier R9779 (tts: 0.25 ns), see fig. 2.
Fig. 1 shows that in case of the cost-expensive solution we can reach Δt of $\sim$4ps. In this case, Δt is determined only by the contribution from electronics. With the cost-effective solution, fig. 2, Δt is $\sim$8ps, but in this case Δt is given by the scintillator material. In both cases, the contribution of the photomultiplier, due to a large number of produced photoelectrons, is negligible. First tests with a

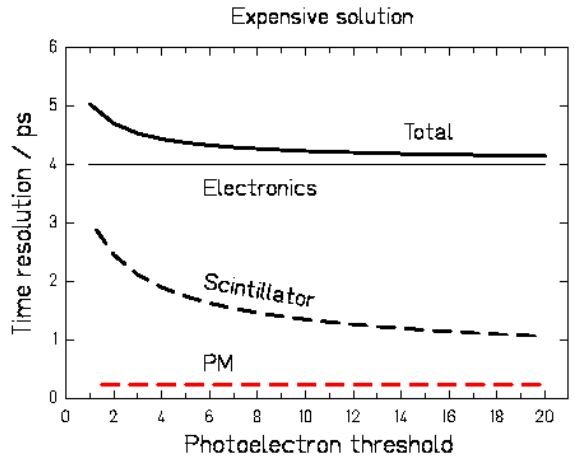

Figure 1: Contribution of different components to Δt of the LOS detector for the design option (1), see text.

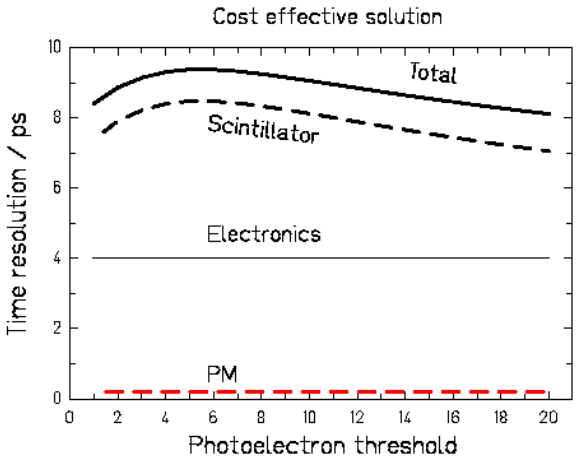

Figure 2: Contribution of different components to Δt of the LOS detector for the design option (2), see text.

Nitrogen UV laser have been performed, see [6].

New TOF wall detector

In the case of the new TOF wall we have assumed that the detector consists of 4 layers of EJ200 scintillator material (rise time: 0.9ns, decay time: 2.1ns, light output: 64% of Anthracene) and that the signals are read by R8619-20 photomultipliers (tts: 1.2ns). We have also assumed that 1 AGeV ^{208}Pb ions are passing through the detector. The results are shown in fig. 3. Also in case of the new TOF wall

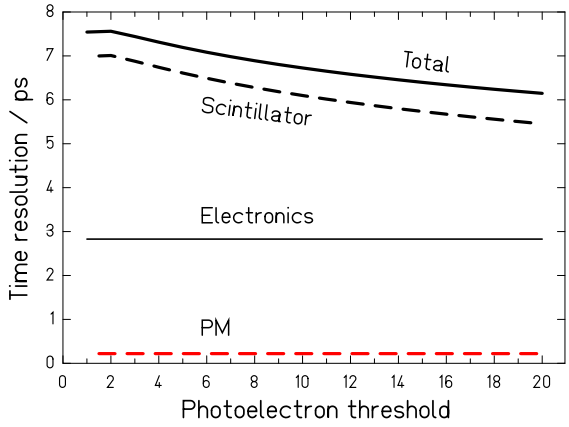

Figure 3: Contribution of different components to Δt of the new TOF wall detector.

the contribution of the PMs to the total Δt is negligible. Total Δt well below 15ps can be reached, and is mostly determined by the scintillator material. The use of more expensive PMs or scintillator materials is thus not needed.

Summary and outlook

Needed Δt of TOF start and stop detectors of 15ps can be reach. In case of the new TOF wall Δt is $\sim$8ps due to several-layers design. In case of the LOS detector, with a cost-effective solution Δt is $\sim$8ps, and thus well below 15ps. With the expensive solution, we could even reach Δt of 4ps. In 2014 prototypes of both detectors will be tested and results will be compared with present calculations.

References

[1] M. Heil, A. Kelić-Heil, J. Gerbig, "A new Time-of-flight wall for R^{3}B", contribution to this annual report.

[2] R.F. Post and L.I. Schiff, Phys. Rev. 80 (1950) 1113

[3] M. Moszynski and B. Bengtson, Nucl. Instr. Meth. 142 (1977) 417

[4] N.P. Hawkes and G.C Taylor, Nucl. Instr. Meth. A 729 (2013) 522

[5] P. Achenbach et al, Nucl. Instr. Meth. A578 (2007) 253

[6] R. Plag, M. Gilbert, M. Heil, "High precision multi-hit time-of-flight measurements at R^{3}B", contribution to this annual report.

Development of Heteroepitaxial DoI Plates for Diamond Detectors*

E. Berdermann[1], *S. Gsell*[2], *M. Fischer*[2], *M. Kiš*[†1], *M. Mayr*[2], *C.J. Schmidt*[2], *M. Schreck*[2], *C. Stehl*[2], *and M. Träger*[1]

[1]GSI, Darmstadt, Germany; [2]University of Augsburg, Germany

Typical size of the chemical vapor deposition (CVD) homoepitaxially grown diamond material (also known as the single crystal - SC) is limited to some 5 x 5 mm^2 due to the availability of growth substrates made from the high-pressure high-temperature (HPHT) diamond. Presently, the only material readily available for the production of diamond detectors with larger area ($\sim$10 cm^2) is polycrystalline (PC) film grown on silicon wafers with electronic characteristics far inferior in comparison to SC material.

In order to produce a large-surface high-quality material for diamond detectors different techniques for heteroepitaxial growing of diamond films are being investigated and developed at the University of Augsburg. By using yttrium-stabilized zirconium oxide (YSZ) buffer layer to produce iridium terminated substrate on silicon wafers [1] one can grow diamond films (also know as the diamond on iridium - DoI) that are far more homogeneous than PC, however, still burdened with defects. In last few years a remarkable improvement in lowering of the level of impurities and defects was achieved so that the presently produced samples - while still not comparable to SC material - are far superior to any PC material.

Most significant structural defect arising in heteroepitaxial growth are dislocations.In a recent study [2] in which the density of threading dislocations was determined by few methods over a large sample thickness, an inverse growth depth behaviour was found. While this at least in principle confirms that films with very low density of dislocations can be grown, presently procedure would not be economically effective therefore different growing techniques - *e.g.* epitaxial lateral overgrowth - are being developed.

In order to assess the quality *i.e.* electronic characteristics of new DoI samples a typical measurement of the charge collection efficiency (CCE) is performed by using the transient current technique (TCT). Alpha particles (^{241}Am) are used to test the sample with different polarizations and drift fields so that the properties for both types of charge carriers can be evaluated. In Fig. 1 the set of measurements with a recent DoI sample of 190 μm thickness at different drift fields is presented showing the saturation at values above 0.8 V/μm. While the overall triangular shape of wave forms indicate the presence of the charge recombination defects, additional flat-top slope is related to losses due to the charge carrier trapping within the sample. For this sample we have measured an average CCE of about 60% for holes, which is below the level of the best samples

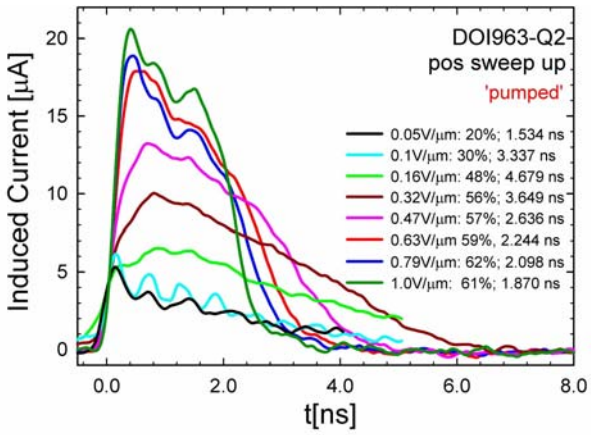

Figure 1: Pulse-shapes (waveforms) obtained for the drift of holes across the sample. The CCE is determined by waveform integration. Each waveform is an average from 1000 recorded events.

tested (>90%) [3]. On the other hand, the CCE for electrons (shown in Fig. 2) of about 40% is much better than previously measured ($\sim$10 %). In this case the saturation is observed at the higher drift field of 1.2 V/μm.

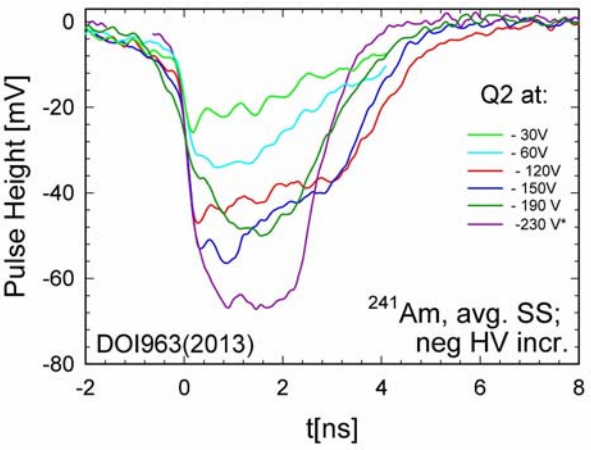

Figure 2: Pulse-shapes for the drift of electrons across the sample with 42 dB pre-amplification.

References

[1] S. Gsell *et al.*, Appl. Phys. Lett. 84, 4541 (2004)

[2] C. Stehl *et al.*, Appl. Phys. Lett. 103, 151905 (2013)

[3] E. Berdermann *et al.*, GSI Sci. Rep. 2011, 245

* This work was supported in part by HadronPhysics3 (grant agreement No 283286 under the EU FP7.)

† m.kis@gsi.de

doi:10.15120/GR-2014-1-FG-S-FRS-07

Laser Lithography for Production of Diamond Detectors

R. Visinka[1], *C. Simons*[1], *M. Träger*[1], *E. Berdermann*[1], *M. Kiš*[*1], *and C.J. Schmidt*[1]
[1]GSI, Darmstadt, Germany

Laser lithography system

Diamond detectors are usually produced from the electronic (detector) grade diamond material in a form of thin plate or film. In order to produce diamond detector, the plate has to be equipped with suitable (most often metallic) electrodes. Such metallic electrodes were - and still are - produced at GSI Target Laboratory by sputtering of one or more thin metal layers on the surface of the diamond. A particular electrode structure in that case is obtained by using stencil masks that are also a limiting factor since the minimal obtainable structure is of about 100 μm. To overcome this limitation the laser lithography system (shown in Fig. 1) was acquired and put into the operation in the GSI Detector Laboratory.

Figure 1: Lithography room in the clean room area of the Detector Laboratory. Working table with the spin coater and the hotplate (left in the photo), and the laser pattern generator with control computer (right).

The lithography system consists of *Ramgraber* M150 spin coater, *Ramgraber* M-HP150 hotplate, and the laser pattern generator *Heidelberg Instruments* μPG 101. The first two devices are suitable for processing of wafers up to $6''$ with wide variety of photoresist coatings. The μPG 101 is equipped with a solid state (diode) laser of 405 nm wavelength with maximum output power 100 mW. With present configuration the maximal writing area of 90 x 90 mm^2 can be processed with the minimal resolution of 1 μm. During 2013 the system was successfully commissioned and the first diamond detectors were produced and tested.

Diamond detector production

In contrast to common photo-lithography where photomasks are used to expose photoresist, in laser lithography the laser pattern generator is used to directly expose photoresist. In processing of diamond detectors two approaches are possible: in the lift-off process the photoresist coating is removed from the part of surface which needs to be metalized (*i.e.* occupied by the final electrode) and then after sputtering of the metallic layer over the whole diamond the remaining photoresist is "lifted-off" from the surface leaving the metallic electrode only in the previously photoresist-free area. In the other approach the metalization of the whole surface is made at first followed by photoresist coating and exposure. After developing and partial removal of the photoresist, the exposed (unprotected) metallic surface is etched until metallic layer is removed. After removal of remaining photo-resist the electrode is ready for further fabrication.

While the first approach is simpler in implementation since it does not require aggressive chemical treatment (etching), the latter is preferred in production of diamond detectors because it allows better diamond surface preparation for the metalization of electrodes.

An additional obstacle in processing of the diamond detectors is their shape and size; the typical surface of a single-crystal diamond is usually less than 5x5 mm^2 which presents challenge for spin-coating in cases where electrodes are up to the edge. As it can be seen from Fig. 2, during the spin coating of rectangular substrates the buildup of the photoresist beads in corners cannot be avoided. While such obstacle would be difficult to treat by the conventional photo-lithography, by recurrent exposure of the photoresist in corners we can produce desired electrode shape.

Figure 2: HADES diamond detectors prepared with the Cr+Au metalization, electrodes are processed with the laser lithography. Left: the corner of the diamond plate with the photoresist bead buildup, right: the electrode after etching and the photoresist removal. The feature size (gap between the electrodes) is 80 μm.

* m.kis@gsi.de

Optimizing the manufacturing method of detector parts *

J. Kunkel[1], *A. Ehret*[1,2], *S. Schwab*[1], *J. Weinert*[1], *B. Voss*[1], *for the PANDA collaboration , and the FAIR@GSI RBDL*[1]

[1]GSI, Darmstadt, Germany; [2]University of Applied Sciences, Darmstadt, Germany

For the Forward GEM-Tracker of the PANDA experiment at FAIR [1, 2], as part of structural elements of the so called GEM-Disc detectors, rings with high dimensional stability and optimized material budget need to be produced. The parts are up to 1.5 m in diameter, 8 mm width and only 0.5 mm thick. They need to withstand forces of up to 15 $N\,cm^{-1}$ in radial direction. Parts made from conductive material as well as highly isolating ones are required. Industrial products with the appropriate features are not available and thus the process was set up and optimized at GSI.

Finite Element Method (FEM) simulations (see figure 1) were done precedent to manufacturing sample parts. The results of these calculations show the necessity of uniform material properties in direction of the load. This can be achieved by compounds with specific material orientation. Composite materials of carbon fibre and resin have excellent properties in elastic modulus and tensile strength, and are electrically conductive. Compounds of glass fibre are non conductive but have a lower elastic modulus. Currently fibres made from basalt are under test which offer intermediate properties. They are non conductive, stiffer than glass fibres and commercially available at moderate prices.

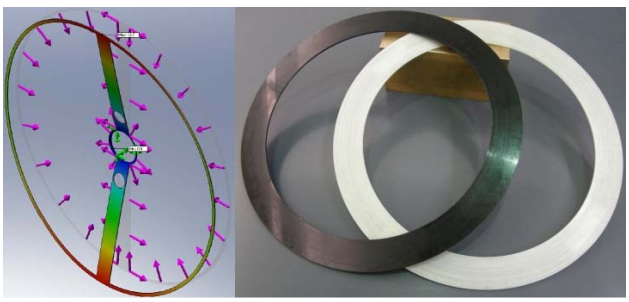

Figure 1: Left: FEM simulation is used to estimate the deformation of the part. Right: small test parts of basalt and glass fibres.

To achieve a uniform fibre orientation in the rings appropriate for the orientation of the radial loads they should withstand, a winding apparatus (see figure 2) has been build where the fibres are wound up to a spool. The winding motion is achieved by rotating the spool around its axis. A motor/gear/brake combination applies a constant tractive force on the roving (a bundle of fibres) which allows a controlled stacking of the fibres without larger flaws and with the desired high amount of fibre content (>60 %) in order to maximize the stability and minimize the material budget. Several types of resin have been used in the tests, the final choice will be made taking into account the need for ageing-free operation of the detectors. The winding is made up to a larger outer diameter of the ring than necessary. The excess material is later removed by milling. Also the connection to the centre bar and additional geometry (holes, chamfers, fillets etc.) are milled.

Figure 2: The devices to wind the rings with variable size, thickness and fibre content. The roving comes from the right, goes through a impregnating bath, and is kept on a constant force by a controlled brake before it is wound to the spool (shown on the left).

After producing parts of different material combination test for mechanical, chemical and physical properties will be performed together with the collaborating universities. Based on this tests both material and geometry will be optimized. By comparing the FEM results with the actual behaviour of the parts the simulation settings will be optimized. This will be very helpful for the simulation of other detector parts made of composite material.

References

[1] B. Voss, D. Auer, A. Ehret, C. Kaya, J. Kunkel, A. Neeb, A. Remers, J. Reuss, S. Schütz, Ed. Traut, El. Traut, E.T. Yamedji, The mechanical structures of the PANDA GEM-Tracker, GSI Scientific Report 2011, GSI Report 2012-1, 2012, p. 123

[2] B. Voss, J. Kunkel, R. Karabowicz, The GEM-Discs for the PANDA experiment, GSI Scientific Report 2010, GSI Report 2011-1, 2011, p. 338

* Work supported by FAIR@GSI PSP code: 1.4.1.

 doi:10.15120/GR-2014-1-FG-S-FRS-09

Characterizing the SOFIA/ANDES TwinMUSIC *

I. Kaufeld[1,2], M. Takechi[1], B. Voss[1], for the SOFIA/ANDES-collaboration , and the FAIR@GSI RBDL

[1]GSI, Darmstadt, Germany; [2]Hochschule RheinMain, University of Applied Sciences, Rüsselsheim, Germany

Preliminary values for the resolutions of various figures of merit have been deduced by the SOFIA TwinMUSIC [1] for the spectra of isotopes obtained from the fission of ^{238}U. The energy-loss resolution was measured to be $\sigma_{\frac{\Delta E}{E}} = 0.34\%$ with P25 gas (Fig. 1). This leads to a charge resolution of $\sigma_{Z_{1,2}} = 0.23 \pm 0.01$ for the measurements in $\frac{1}{2}$ of the TwinMUSIC and $\sigma_{Z_{1+2}} = 0.31 \pm 0.02$ for the sum of both. The steep falloff of $\Delta_{t,10-90\%} \approx 150ps$ of the drift times close to the cathode measured for single anodes yields a corresponding resolution of the straight-line fit to a track through the active volume of $\sigma_{dt,fit} = (268 \pm 40)ps$ (Fig. 2). For the electrical field settings applied the measured drift velocity is well reproduced by Magboltz simulations. After fine adjustment of the drift-times with the help of an adjacent MWPC, a position resolution for the single anode of $\sigma_{x,PB} = (28 \pm 11)\mu m$ and $\sigma_{x,FF} = (47 \pm 13)\mu m$ for the primary beam and fission fragments, respectively, can be deduced (Fig. 3). Consequently, the angular distribution of the fragments of $\approx 40mrad$ could be measured with a precision of $\sigma_{\Theta,FF} = (0.13 \pm 0.10)mrad$ by event-wise tracking.

The analysis of the data is still ongoing, further refinements on the achieved resolutions are to be expected. Isotopic mass yields have been be deduced and published elsewhere [2]. Changes in the design of the TwinMUSIC detector system are ongoing and will allow for an even better charge, position and angular resolution. We are aiming for a full 3D tracking operation with rates of $1 - 2\ MHz$ with a non-triggered DAQ. The potential of a low-pressure operation $(0.2 - 0.3atm)$ and the application of other, 'faster' gas mixtures will be tested too.

The next physics run is already scheduled 2014 at CaveC looking into more details of the isotopic mass distributions. In the far future, a more complete set of measurements will be performed in the context of R^{3}B (Reaction studies with Relativistic Radioactive Beams) at the FAIR (Facility for Antiproton and Ion Research) project at GSI/Darmstadt. Dedicated detector developments will be performed for those endeavors which foster similar developments e.g. for the instrumentation of the SuperFRS.

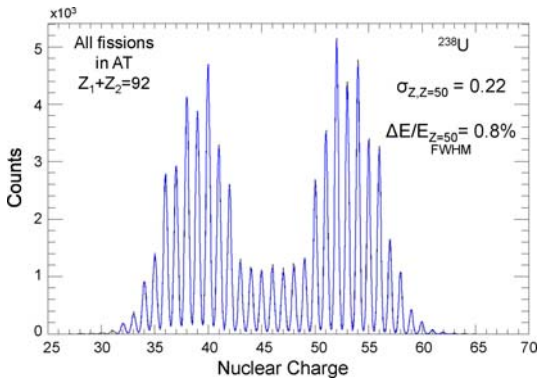

Figure 1: Nuclear charge distribution for electromagnetically exited fission inside the active target.

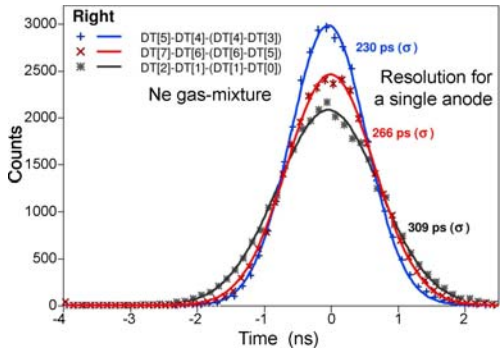

Figure 2: Distribution of the residuals for tracking of fragments inside the right compartment of the TwinMUSIC. The resolutions given are deduced for single anodes.

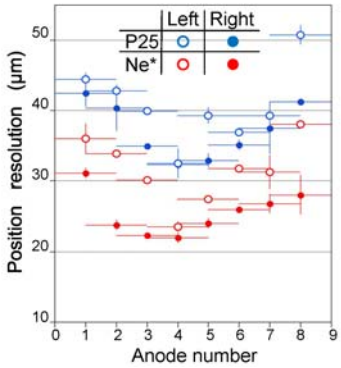

Figure 3: Position resolution obtained for the tracking of fragments inside the TwinMUSIC.

References

[1] B.Voss et al., "Results from the SOFIA/ANDES TwinMUSIC", GSI Report 2013-1, p.204 (2013)

[2] E. Pellereau et al., EPJ Web of Conferences 62, 06005 (2013)

* Work supported by FAIR@GSI PSP code: 2.4.

NeuLAND - from prototypes to double-planes*

K. Boretzky†[1], *B. Agrawal*[3], *G.D. Alkhazov*[11], *S. Altstadt*[9], *H. Alvarez Pol*[17], *V.A. Andreev*[11], *L. Atar*[2], *T. Aumann*[2,1], *V. Babić*[13], *P. Basu*[3], *D. Bemmerer*[4], *M. Bendel*[14], *D. Bertini*[1], *P. Bhattacharya*[3], *S. Bhattacharya*[3], *A. Blanco*[5], *J. Bonilla*[9], *C. Caesar*[2], *L. Cartegni*[7], *S. Chakraborty*[3], *A. Charpy*[13], *S. Chatterjee*[3], *M. Cherciu*[6], *L. Chulkov*[12], *M. Ciobanu*[6], *T. Cowan*[4,10], *U. Datta Pramanik*[3], *G. Dentinger*[2], *Z. Elekes*[18], *A.A. Fetisov*[11], *E. Fiori*[15], *P. Fonte*[5], *D. Galaviz*[7], *I. Gašparić*[19], *J. Gerbig*[9], *R. Gernhäuser*[14], *K. Göbel*[9], *V.L. Golotsov*[11], *M. Haiduc*[6], *T. Heftrich*[9], *J. Hehner*[1], *M. Heil*[1], *M. Heine*[2], *A. Heinz*[13], *A. Henriques*[7], *M. Holl*[2], *A. Ignatov*[2], *G. Ickert*[1], *J. Isaak*[15], *E.A. Ivanov*[11], *S. Jährling*[2], *J. Johansen*[2], *H. Johansson*[13], *J. Kahlbow*[2], *A. Kelić-Heil*[1], *O. Kiselev*[1], *R. Kissel*[2], *K. Kobayashi*[20], *D. Körper*[1], *D. Kresan*[2], *A.G. Krivshich*[11], *P. Kumar Das*[3], *T. LeBleis*[14], *C. Lederer*[9], *Y. Leifels*[1], *S. Lindberg*[13], *L. Lopes*[5], *B. Löher*[15], *J. Machado*[7], *J. Marganiec*[2], *L. Netterdon*[8], *T. Nilsson*[13], *V. Panin*[2], *J. Panja*[3], *S. Paschalis*[2], *A. Perea*[16], *S.G. Pickstone*[8], *B. Pietras*[17], *R. Plag*[1], *M. Pohl*[9], *M. Potlog*[6], *A. Rahaman*[3], *G. Rastrepina*[9], *A. Ray*[3], *R. Reifarth*[9], *T. Reinhardt*[10], *G. Ribeiro*[16], *M. Röder*[10], *D. Rossi*[1], *J. Sánchez del Rio*[16], *A. Sauerwein*[9], *D. Savran*[15], *H. Scheit*[2], *F. Schindler*[2], *S. Schmidt*[9], *P. Schrock*[2], *J. Silva*[15], *H. Simon*[1], *T. Sinha*[3], *M. Sobiella*[4], *K. Sonnabend*[9], *D. Stach*[4], *E. Stan*[6], *O. Tengblad*[16], *P. Teubig*[7], *R. Thies*[13], *L.N. Uvarov*[11], *P. Velho*[7], *V.V. Vikhrov*[11], *S.S. Volkov*[11], *V. Volkov*[2,12], *A. Wagner*[4], *F. Wamers*[2], *M. Weigand*[9], *M. Winkel*[14], *J. Wüstenfeld*[4], *D. Yakorev*[4], *A.A. Zhdanov*[11], *A. Zilges*[8], *K. Zuber*[10], *for the R³B collaboration , and the FAIR@GSI RBRB*[1]

[1]GSI, Darmstadt, Germany; [2]TU Darmstadt, Germany; [3]SINP Kolkata, India; [4]HZDR, Dresden-Rossendorf, Germany; [5]LIP, Coimbra, Portugal; [6]ISS, Bucharest, Romania; [7]Univ. Lisbon, Portugal; [8]Univ. of Cologne, Germany; [9]Univ. Frankfurt, Germany; [10]TU Dresden, Germany; [11]PNPI St. Petersburg, Russia; [12]Kurchatow Institute Moscow, Russia; [13]Chalmers Univ. of Technology, Göteborg, Sweden; [14]TU München, Germany; [15]EMMI, GSI Darmstadt, Germany; [16]CSIC Madrid, Spain; [17]U Santiago de Compostela, Spain; [18]MTA ATOMKI, Debrecen, Ungarn; [19]RBI, Zagreb, Croatia; [20]Rikkyo University, Tokyo, Japan

Overview

During 2013 the NeuLAND (new Large-Area Neutron Detector) project passed the important step from prototype tests to series production. Being one of the key instruments of the R^{3}B experiment [1] the NeuLAND demonstrator will be utilized in the 2014 beam times together with demonstrators of other major R^{3}B components.

NeuLAND is a highly granular detector composed of 3000 scintillator bars with a total volume of 250x250x300 cm^3. It enables the detection of fast neutrons with high efficiency, high time and spatial resolution and a high resolving power for multi-neutron events [2].

Despite the compact cubical arrangement of the NeuLAND components, the detector is built up from individual subgroups with an independent functionality, the so-called NeuLAND *double-planes*. This modular design facilitates maintenance and it allows upon experimental needs to split the detector in subdetectors being located at different positions with respect to the target area.

NeuLAND Double-Planes

During the previous year the first three double-planes of NeuLAND have been built. Here, we report about its different building blocks, the assembly into the double-plane structure and into the demonstrator frame. A double-plane is built up from 100 scintillator bars, 50 forming a vertical / horizontal oriented plane each. 200 photomultipliers (PMTs) serve to read out the scintillator bars from both far ends and consequently 200 channels of high voltage supply (HV) and read out electronics are required for each double-plane.

Scintillator Bars

The heart pieces of NeuLAND are the fully-active scintillator bars from BC408-equivalent with dimensions 250x5x5 cm^3 of rectangular shape. To avoid light losses at transitions between different materials, the bars are produced in one piece with its light guides at the two far ends. The light guides of conical shape are 10 cm long and connect the quadratical surface with a one-inch circular surface, thus leading to a total bar length of 270 cm. Within a frame contract concluded in 2013 the scintillator bars can be ordered in several fractions to fixed conditions over a period of four years. Within the first order 430 bars have been purchased allowing together with the prior existing

*Work supported by FAIR@GSI PSP code 1.2.5.1.2.5., by BMBF (06DA7047I, 06FY71051, 06KY71593,06DR134I, NupNET NEDENSAA 05P09CRFN5), by ENSAR, by GSI via the GSI-TU Darmstadt cooperation contract, by GSI F&E (DR-ZUBE) and by HIC for FAIR.

† k.boretzky@gsi.de

 doi:10.15120/GR-2014-1-FG-S-FRS-11

200 bars to built up six double-planes, thus a 20% NeuLAND demonstrator. The scintillator bars are delivered with reflective and with light-tight wrapping.

Prior to their assembly into double-planes the bars undergo a site acceptance test, controlling both the quality of the scintillator material itself and the surface finishing. The test procedure developed and carried out by the contributing NeuLAND collaborators comprises a measurement of the response to cosmic rays and a measurement of the light transport using a light emitting diode (LED) shining in at one far side of the scintillator bar and being detected at the opposite side. The resulting data are compared to the results for a quality-prooven reference bar. Figure 1 shows a typical QDC spectrum from such a combined cosmic and LED test.

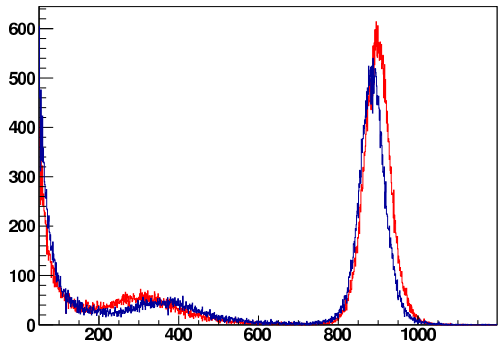

Figure 1: QDC spectra (counts vs. channel number) taken for the reference bar (red) and bar 29 (blue) of 2013 delivery. The prominent peak at about channel number 900 originates from the LED pulse, while the broad peak at channel number ≈300 stems from cosmic rays traversing the bar.

Photomultiplier

For the light read out from the scintillator bars one-inch PMTs are connected to the far ends of the scintillator bars. The selected NeuLAND PMT R8619-20 comprises high-quality performance with cost-effectivness; a fully active voltage divider has been developed for the use in NeuLAND in order to minimize the current demands. For the PMTs, as for the scintillator bars, a frame contract allows the fractional purchase at fixed conditions within the next four years. In the first order, PMTs to assemble the 20% demonstrator have been purchased.

The light-coupling between scintillator bar and PMT front face was subject to investigations taking into account not only the maximization of light read out, but also the long term sustainibility and the possibility to apply the coupling material to vertically and horizontally oriented PMTs. A coupling via silicon glue was selected after curing issues had been successfully minimized.

High Voltage Supply

The high voltage supply for the NeuLAND PMTs is supposed to be unitized in a manner, that each double plane is equipped with its own high voltage distribution system close by, thus enabling the modular operation of NeuLAND double planes. The final layout of the high voltage system is under investigation at the moment. During the 2014 beam times the NeuLAND demonstrator will be brought into operation using commercial high voltage supplies available from other GSI detector systems.

Read-Out Electronics

The current concept for the read-out electronics is based on a concept originally developed within the FOPI collaboration, the so-called Tacquila readout system. The system provides a fully integrated solution of both charge and time measurement behind a dedicated frontend-card which is used to condition and split the signals. Here, one part is directly connected to a QDC board, while the other is put through an discriminator and further provided to the time measurement using an ASIC based solution. A dedicated frontend has been developed and commissioned in the last years, using the LAND detector, providing an optimized signal treatment for photomultiplier signals. The frontend cards are controlled using the TRIPLEX card [3] which is also used to provide monitoring access to each channel in the electronics. Currently a new electronic readout system, based on the FEBEX readout architecture utilizing an FPGA TDC [4] called Tamex has been designed, and first prototypes are currently being built. The system makes use of the previously done developments, as it is compatible to the existing analog frontend, discriminator and controls environment, by reusing the already existing cards design. The digital backend does not rely any longer on the out phased ASIC and is furthermore multi-hit capable, as well it provides time-over-threshold information. All double planes as shown in figure 3 will such be equipped with their individual readout electronics for 200 channels, and can be operated in a self-sustained manner, making best use of a fully modular design.

NeuLAND frames

A dedicated frame structure was designed to assemble the scintillator bars and PMTs into double-planes. Fig. 2 shows from left to right an empty double-plane frame, a frame with half of the bars mounted and a fully equipped double-plane frame. Each bar is separately mounted to the frame using a block holding structure, which fits to the conical endings of the bars. In order to protect the horizontal bars from bending in the middle, each bar is supported twice using a metal band structure with individual segments for each bar (visible on the photograph in the middle of fig. 2).

The PMTs are mounted to the bars via guide tubes from stainless steel. A light-tight connection to the holding

Figure 2: The Photographs show (left to right) an empty double-plane frame, a frame after mounting of the vertically oriented bars and after installation of the support structure for the horizontally oriented bars and a frame after assembly of all scintillator bars prior to mounting of PMTs.

blocks is provided using O-rings. The far end of the guide tube is closed with an endcap containing a bajonet lock allowing an easy access to the PMT for maintenance. The signal and HV-cables are fed through an elastomer cap for light-tightness.

The signal and HV cable of the PMTs are connected to collector boards mounted along the read-out sides of the frame. Connections to these boards are provided via LEMO and CLIFF contacts, again allowing for an easy exchange of PMTs in case of maintenance. From the boards the cabling to HV distribution and to the readout electronic is provided via multipin connectors.

Assembly of NeuLAND substructures

A NeuLAND rack with two-fold purpose was built, see fig. 3. It serves for assembly of the NeuLAND double-planes and it allows to host up to six double-planes, thus the NeuLAND demonstrator.

The assembly, cabling and the commissioning of the NeuLAND double-planes is carried out by the funding collaborators.

Figure 3: Photograph of the NeuLAND mounting and demonstrator rack together with the first NeuLAND double-plane.

Results from the Experiment S406

In November 2012 150 scintillator bars in a special configuration with 15 layers of ten vertical bars each were exposed to monoenergetic fast neutrons stemming from deuteron breakup reactions in a CH_2 target, see last year's report for details [5]. Here we report about the status of the analysis of the collected neutron data and its implications on the NeuLAND simulation algorithms.

The calibration of the NeuLAND data taken in this experiment (S406) is completed. Apart from the usual calibration steps special care has been taken of the walk correction of the NeuLAND Tacquila channels. It improved the earlier reported value of time resolution for deuteron beam from $\sigma_t^D = 115$ ps to 96 ps. The data collected allow a detailed study of hit patterns of neutron-induced particle tracks. A top view of one event with a neutron interaction in the first plane is illustrated in fig. 4. One digit in the histogram corresponds to one bar. The neutron impinges from the left side. A high-energetic secondary particle is produced, which propagates through the detector (total depth of 0.75 m), indicated by the strict time order of the detected signals (z-axis).

The analysed neutron data in the NeuLAND test array is used to optimize the simulations. At this stage of the data analysis the neutrons are accepted as valid hits if a proper time correlation to the beam velocity is found. This might include besides reactions on the hydrogen also reactions on the carbon in the CH_2 target and breakup in the close-by start detector. As the next step the analysis of quasi-free scattered (QFS) protons in Crystal Ball and Silicon Strip Detectors is performed. The typical signa-

 doi:10.15120/GR-2014-1-FG-S-FRS-11

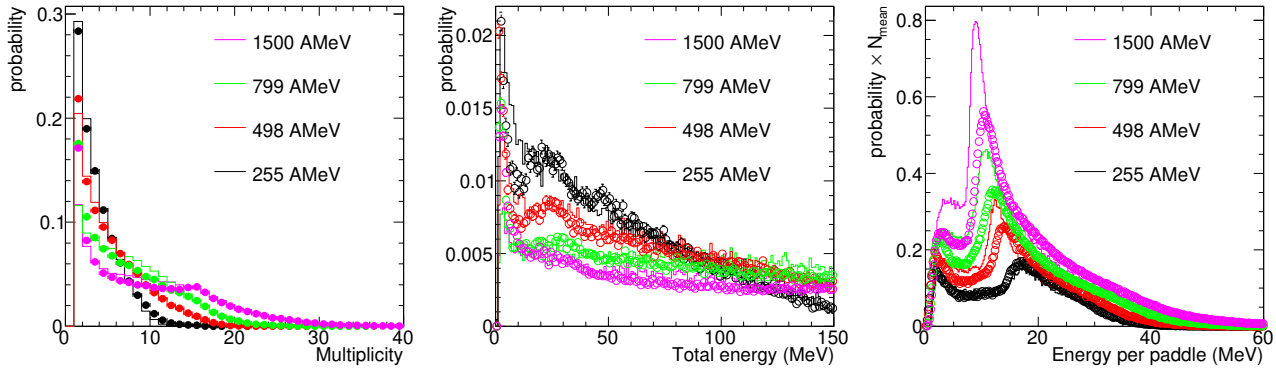

Figure 5: Probability distributions for neutrons of various energies from experimental data (symbols) and corresponding simulation (lines). Displayed in the left-hand panel is the hit multiplicity per incident neutron. The middle panel shows the total deposited energy in the NeuLAND test array per neutron and the right-hand panel the energy deposited per scintillator bar. For the latter the probability was multiplied with the average number of hits N_{mean} for each neutron energy.

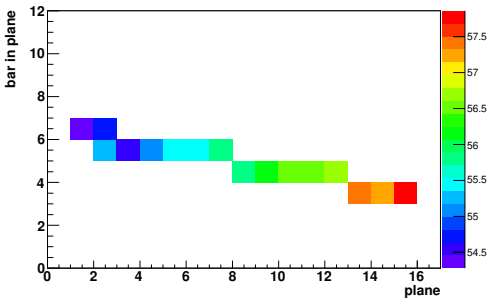

Figure 4: Display of one neutron-induced charged particle track traversing the NeuLAND test array. The time in ns is indicated on the z-axis.

tures for QFS events are observed in correlations of polar and azimuthal proton angles. The further analysis oriented to elimination of the background and the reconstruction of the neutron kinematics is underway.

In the NeuLAND simulation and reconstruction algorithm for experiment S406 neutrons, which are emitted from ppn reactions of deuteron with hydrogen in the target, are transported through the modelled experimental setup by calculating their interaction with scintillator bars using a step-wise Monte-Carlo simulation engine Geant3. During this step of simulation, the energy loss of induced charged particles is converted into light equivalent, also applying light quenching for protons. The output represents the so-called Monte Carlo Points, which describe the energy loss of one charged particle per one scintillator bar. Thus, a sophisticated hit producer (digitizer) algorithm is required, described below, in order to match with the real data from experiment.

On the single particle level, the light attenuation is taken into account according to the position of deposited energy in the detector and the time resolution is applied using a Gaussian smearing with $\sigma = 150$ ps. The general start time value for the charge integration is determined and the energy loss of all particles in each bar is integrated, applying position dependent time decay of the signal. As a next step the hits (digis) in the detector units are treated. The saturation of a single PMT is taken into account as well as the resolution of the QDC (smearing the calculated charge with a Gaussian of $\sigma = 3 - 4\%$) and the individual PMT thresholds using the values obtained from data analysis. The PMT saturation formula used here $QDC_{out} = QDC_{in} * 1./(1. + 0.012 * QDC_{in})$ is in agreement with laboratory tests of the NeuLAND PMT with LED light.

Various quantities are regarded to compare experimental results to simulations, see fig. 5. In the right hand panel the measured probability distribution of the hit multiplicity per incident neutron is compared to the simulated one for neutron energies ranging from 200 to 1500 MeV [1]. As expected the hit multiplicity increases with increasing neutron energy.

The probability distribution of the total deposited energy is displayed in the middle panel and the energy deposited per scintillator bar in the right-hand panel. It turned out, that two effects play a mayor role for the description of the data within the simulation. The individual realistic thresholds from the experiment are crucial for the comparison of multiplicity spectra and the low energy part of the energy spectra. The proper treatment of the PMT saturation is necessary for understanding higher energy deposition in a single bar and for the total energy deposition in the NeuLAND test array. The slight discrepancies at lower deposited energies may origin from differences in the PMT saturation due to different exposure to magnetic fields for the different beam energies and from background effects in the experiment not yet taken into account.

[1] The experimental data for 200 MeV are compared to simulation findings for 250 MeV, since the quasi free event generator was available for the slightly higher beam energy solely.

Overall a good agreement between data and simulation is found over this very large range of incident neutron energies with one consistent description of the physics processes in the R^3Broot simulation. This improvement in the description is a very valuable basis for the ongoing further development of algorithms for the final NeuLAND detector.

Perspectives

In spring and summer 2014 beam times take place at Cave C at GSI in order to commission demonstrators of various R^3B detectors. The first NeuLAND double-plane will be tested during the April beam time, for summer the commissioning of four to six double-planes (20% demonstrator) is scheduled. Due to the lack of beam time availability during 2015 at GSI, the further commissioning and use of several NeuLAND double-planes at RIKEN are planned.

References

[1] A next generation experimental setup for studies of Reactions with Relativistic Radioactive Beams, https://www.gsi.de/work/forschung/nustarenna/kernreaktionen/activities/r3b.htm

[2] NeuLAND@R3B: A Fully-Active Detector for Time-of-Flight and Calorimetry of Fast Neutrons, NeuLAND Technical Design Report, http://www.fair-center.de/fileadmin/fair/experiments/NUSTAR/Pdf/TDRs/NeuLAND-TDR-Web.pdf

[3] TRIPLEX, an Upgrade for the TACQUILA System, K. Koch et al, GSI Sci. Rep. 2010, PHN-IS-EE-07, p. 235.
Heading towards FAIR: upgrades on the R3B-Cave C electronics, C. Cäsar et al, GSI Sci. Rep. 2009, INSTRUMENTS-METHODS-30, p. 310.

[4] Field-Programmable-Gate-Array Based Signal Discrimination and Time Digitisation, C. Ugur et al., GSI Sci Rep 2012, PHN-SIS18-ACC-43 FAIR@GSI, p.299.
Design and implementation of a data transfer protocol via optical fibre, S. Minami et al., GSI SCIENTIFIC REPORT 2009, INSTRUMENTS-METHODS-51, p.331.

[5] K. Boretzky et al., Construction and Test of a Large NeuLAND Prototype Array, GSI Scientific Report 2012, http://repository.gsi.de/record/52093/files/PHN-ENNA-EXP-60.pdf

[6] D. Kresan et al., Recent Developments in NeuLAND, GSI Scientific Report 2012, http://repository.gsi.de/record/52097/files/PHN-ENNA-EXP-64.pdf

 doi:10.15120/GR-2014-1-FG-S-FRS-11

Simulations of the GEM-TPC response *

A. Prochazka[1], F. Garcia[2], R. Janik[3], V. Kleipa[1], J. Kunkel[1], C. Nociforo[1], M. Pikna[3], B. Sitar[3], P. Strmen[3], E. Tuominen[2], R. Turpeinen[2], B. Voss[1], and the FAIR@GSI Division[1]

[1]GSI, Darmstadt, Germany; [2]HIP, University of Helsinki, Finland; [3]FMFI, Comenius University Bratislava, Slovakia

The GEM-TPC detector response to 1GeV/u ^{197}**Au** projectile was simulated.

The GEM-TPC detector [1] is proposed to be a standard tracking detector for the Super-FRS [2]. The requirements for the GEM-TPC detectors are: a high rate capability(1MHz), a low amount of material in active volume and a large dynamic range(proton-Uranium). The GEM-TPC consists of the drift volume($20x8x7cm^3$) filled with a gas and uniform electric field, GEM foil stack located under the drift volume and the strip readout plane. A schematic view of the GEM-TPC is shown in Fig. 1(top).

For better understanding of the GEM-TPC design and its further improvements simulations were perfomed. The following simulation codes were used: Garfield++[3] to calculate drifts of the electrons through the drift volume, GEM stack and induction gap, ELMER software[4] to calculate electric field maps of the drift volume and the GEM foil using the finite element method(FEM).

In the first step the primary electrons from ^{197}Au beam at 1 GeV/u and their drift tracks inside the drift volume were calculated. The drift volume filled with P10 gas at normal pressure and temperature and $400V/cm$ electric field was assumed. The electrons position and time distributions at the top GEM foil were obtained.

In the second step a passing of the electrons through the GEM stack was simulated. The following parameters of the GEM foils were used: hole outer radius = $35\mu m$, hole middle radius = $15\mu m$, kapton thickness = $50\mu m$, hole pitch = $140\mu m$, copper thickness = $8.0\mu m$. The unit cell from which whole GEM foil was constructed is shown in Figure 1(bottom). The electric field between the GEM foils was set to 3kV/cm and the voltage over the GEM foil was set to 300V. The gain of the GEM stack and the position distribution after the stack was calculated.

In the third step the induced charge on the readout plane strips was calculated using the Shockley-Ramo theorem [3]. The weighting fields of the electrodes and electric field map were calculated using the FEM method. The electric field in the induction gap was set to 3kV/cm. The initial position of the electrons in the induction gap were taken according to the results from previous steps of the simulation. As an example the cluster size from ^{197}Au projectile and relative induced charges on the different strips (0.4mm wide, 0.5mm pitch, perpendicular to x axis) are shown in Figure 2. Other characteristics such as spatial and time resolution of the GEM-TPC will be studied with this method which can help in understanding the results of the test of the prototypes [1].

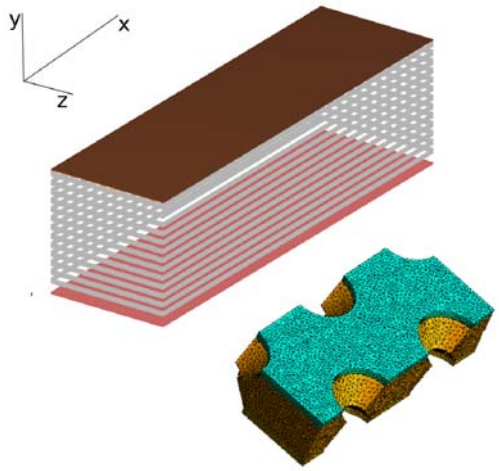

Figure 1: Top-left: Schematic view of the GEM-TPC drift volume showing the cathode (brown) and the field-cage strips (gray) forming an uniform electric field in y-direction. The beam is parallel to z axis. Bottom-right: the GEM cell unit used to construct the GEM foil showing hole positions, copper part(blue) and kapton part(orange).

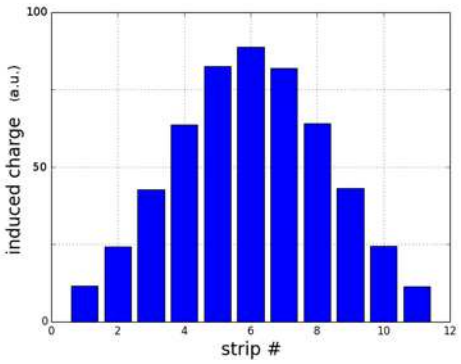

Figure 2: The cluster size and relative induced charge on the strips from ^{197}Au.

References

[1] F. Garcia et al., GSI Scientific report 2012(2013)173

[2] H. Geissel et al., Nucl. Instr. and Meth. B204(2003)71-85

[3] http://garfieldpp.web.cern.ch/garfieldpp/

[4] http://www.csc.fi/english/pages/elmer

* Work supported by FAIR@GSI PSP code: 2.4.6.1.3.

Threshold calibration of the n-XYTER readout ASIC *

I. Sorokin[1,2,3], *C.J. Schmidt*[1], *for the CBM collaboration , and the FAIR@GSI RBDL*

[1]GSI, Darmstadt, Germany; [2]Uni Frankfurt, Frankfurt am Main, Germany; [3]KINR, Kiev, Ukraine

The n-XYTER 1.0 front-end readout-chip [1] has been widely used in various projects at GSI, including the CBM experiment, the GEM-TPC and others. The calibration of its threshold scale has however never been reported.

A threshold calibration was performed on two n-XYTER chips, operated on Front-End Board rev. D. Since in most applications the n-XYTER is used without prior threshold trimming, the threshold was not trimmed before calibration in this case either (all trim registers were set to 16). The `Vbfb` register was set to 50, `VBiasS` adjusted such that the baselines are at around 2000 ADC units, and all other settings were kept at the `roclib` (rev. 4174) default values.

To determine the absolute value of the thresholds, pulses of the n-XYTER internal test pulser were injected in groups of 32 channels simultaneously. The number of the channels which the pulses were simultaneously injected to appeared to have no effect on the thresholds. A scan over pulse amplitudes (controlled through the `cal` register) was performed (Fig. 1). The threshold was considered to be equal to the pulse amplitude whenever the pulse detection efficiency was 50%. The corresponding amplitude, expressed in units of `cal`, was determined by fitting the scan data with an error function. Then a the calibration of the `cal` register gain was performed individually for each channel, at low thresholds: the pulse amplitude was measured in the n-XYTER slow lane, digitized with the on-board ADC and converted to the physical units using the calibration [2].

In Fig. 2 an example of the obtained threshold distributions for all channels of one chip, at three different `vth` register settings are shown. The mean thresholds as a function of `vth` for the two different chips are shown in Fig. 3 (the error bars are the variances). It can be seen that both the channel-to-channel as well as the chip-to-chip threshold variations are large (if no threshold trimming is done). In applications, where precise threshold setting is necessary, it is therefore recommended to perform the threshold trimming first, and then to redo the threshold calibration. The developed algorithms can be reused. For rough estimates the Fig. 3 can be used.

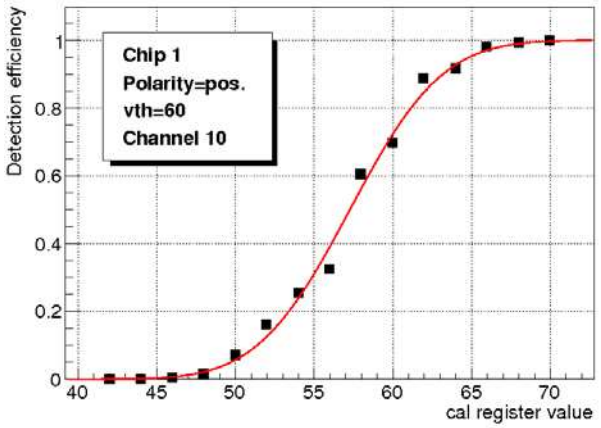

Figure 1: Example for the dependence of the detection efficiency vs. `cal` register setting.

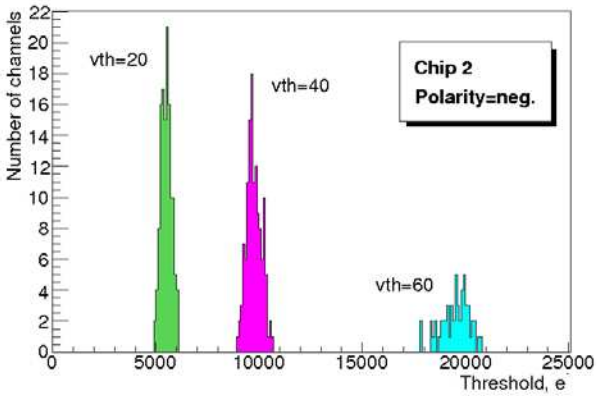

Figure 2: Example of the distributions of the thresholds of all channels in one chip at various `vth` settings.

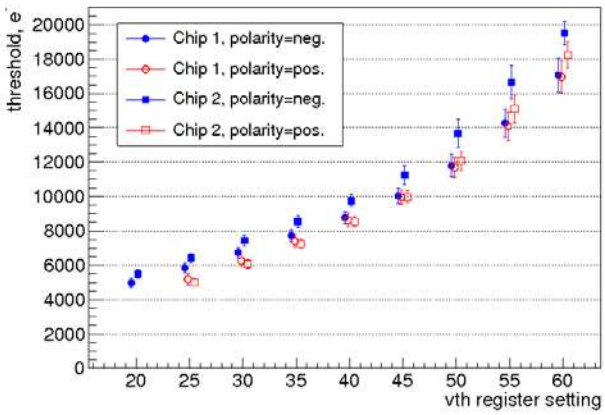

Figure 3: Threshold calibration plot. Points are shifted by $\pm$ 0.15, and $\pm$ 0.45 in x to improve visibility (initially they were at multiples of 5).

References

[1] A.S. Brogna et al., n-XYTER reference manual, unpublished. http://hipex.phys.pusan.ac.kr/drupal/sites/default/files/nXYTER.pdf

[2] I. Sorokin et al., Nucl. Instr. Meth. A 714 136-140 (2013). DOI:10.1016/j.nima.2013.02.013

* Work supported by HGS-HIRe, H-QM Helmholtz research school and FAIR@GSI PSP code: 1.1.1.2.1.2.

 doi:10.15120/GR-2014-1-FG-S-FRS-13

Time and trigger distribution for NUSTAR DAQ systems *

A. Charpy[1], J. Frühauf[2], A. Heinz[1], J. Hoffmann[2], H.T. Johansson[1], K. Koch[2], N. Kurz[2], S. Pietri[2], H. Simon[2], the EDAQ working group[2], and the FAIR@GSI division[2]

[1]Chalmers Univ. of Technology, Göteborg, Sweden; [2]GSI, Darmstadt, Germany

NUSTAR experiments will be based on a complex smorgasbord of devices and detectors of many different types with wildly varying speeds. Merging the data meaningfully together requires proper timing distribution and trigger interconnections. With detectors spread over different experimental areas, sometimes hundreds of meters apart, and often-changing experimental set-ups, a flexible integration approach is the key to success.

Time distribution

NUSTAR DAQ systems need distributed timing signals for two purposes:

- Time-of-flight measurements. The most demanding of these measurements ($<$ 10 ps at short distances) are driving the precision requirements.
- Inter-system event synchronisation. The event-wise data from different detectors, operated with common triggers but in separate dead-time domains, can be merged based on time. Requirement: a few 10 ns.

The FAIR infrastructure caters for these needs by two developments for the accelerator systems: BuTiS [1] and White Rabbit [2]. The Bunch Timing System distributes a stabilised frequency using optical fibres to distribution boxes that can be located in each experimental area. These reference signals can then be further sent to front-end boards that perform high-precision time measurements. The reference signal is effectively used to drive the front-end clock. Measurements have shown an precision better than 20 ps between systems separated by 2 km of optical fibre. For absolute timing, BuTiS-derived timing requires cooperation with an external reference to label the clock cycles, e.g. White Rabbit.

White Rabbit is a synchronous Ethernet protocol, i.e. the clocks of all switches and interface cards are synchronised to one device. It has demonstrated synchronisation better than 100 ps/km [3]; fully sufficient for all but the most demanding measurements. In addition to synchronising time, White Rabbit acts as 1 Gbps Ethernet connection.

For systems with lower timing requirements ($\sim$10 ns), which do not need a network connection, or when the overhead of aligning the local clock cycles with synchronous Ethernet is too constraining, a light-weight serial time distribution protocol is available [4]. Sender and receivers do not need to operate with the same clock frequency; the protocol is also uni-directional and medium independent.

Trigger distribution

Spatially distributed NUSTAR experiments require a very flexible scheme for connecting systems, and their triggers. The trigger logic of an experiment needs to communicate with participating detector systems, to

- receive trigger signals for coincidences.
- send master start and trigger decisions to front-end and read-out systems.
- receive dead-time information for use as veto signal.

These signals must be reasonably fast, with at most a few μs latency. (With analog delay lines this would have been a few 100 ns.) Thus, transport over any packet-switched network is not feasible, and hardware signals must be used. Manual changing of the hardware connections is very time consuming, especially so in the generally non-accessible SuperFRS tunnel. A staggering number of direct peer-to-peer connections would be needed with many detectors. Instead, remotely controlled FPGA-based switch-boxes are placed to allow the maximum flexibility. This approach works directly with trigger signals and dead-times, as those carry binary information.

For an MBS-compatible TRIVA-style trigger a few bits of information must be distributed (trigger number, event count, reset signal). For the systems to work correctly in sync, it is also necessary that the master listens to the dead-time of each involved slave. In order to avoid a dedicated electrical bus, connecting all systems in a hardwired dead-time domain, a uni-directional serial trigger protocol distributing triggers from the master module can be used, as demonstrated in a prototype environment [4].

Directing data-flow from arbitrary front-ends via event builders and time sorters to online analysis and storage is straight-forward using switched Ethernet connections.

References

[1] P. Moritz and B. Zipfel, GSI Scientific Report 2011, p. 478.

[2] J. Serrano *et al.*, "The White Rabbit Project", Int. Conf. on Accelerator and Large Experimental Physics Control System, Oct. 2009. Also http://www.ohwr.org/projects/white-rabbit.

[3] D. Beck, private communication.

[4] H.T. Johansson *et al*, "TRLO II – friendly FPGA trigger control", this report.

* Work supported by FAIR@GSI PSP codes: 1.2.2.4., 1.2.5.1.4. and 2.4.3.1.

TRLO II — friendly FPGA trigger control *

H.T. Johansson[1], *M. Heil*[2], *B. Löher*[3], *H. Simon*[2], *H. Törnqvist*[4], *the R³B collaboration , and the FAIR@GSI Divison*[1]

[1]Chalmers Univ. of Technology, Göteborg, Sweden; [2]GSI, Darmstadt, Germany; [3]EMMI, GSI Darmstadt, Germany; [4]TU Darmstadt, Germany

An easy-to-use command-line tool has been developed to simplify configuration of the TRLO II trigger logics. The system has also been enhanced with a serial trigger distribution protocol, to allow for greater flexibility in connecting multi-branch systems. The flexible FPGA trigger control TRLO II [1] for VULOM and TRIDI modules [2] has been used in over a dozen experiments with a number of different experimental setups. The system incorporates the functionality of most logic NIM modules. It also has features for advanced monitoring, e.g. recording of trigger alignment as well as plenty of general and specialised scalers and timer latches.

`trloctrl` — friendly setup utility

With around 60 types of 500+ setup registers, and 200 source and sink signals of comparably many variations, using the TRLO II could easily become a non-trivial task. The firmware now comes with a companion command-line interface for control, monitoring and read-out. This removes the need to set registers by compiled code. Complex configurations can be loaded from setup files, while one-off commands for testing can be issued quickly from a shell:

```
trloctrl "period(1)=2us" "ECL_OUT(3)=PULSER(1)"
trloctrl --print-config
```

Most functionality is provided via a library so that it can be used by other programs, e.g. in DAQ readout functions.

Serial time distribution revisited

A unidirectional serial time distribution protocol has already provided time-stamps for event synchronisation in a TITRIS-compatible manner [3] for a few experiments. The protocol has been redesigned to allow the transmitter and receivers to run at different nominal clock frequencies.

The precision is about 2 receiver clock cycles (20 ns in a VOLUM), and is thus suitable for event-synchronisation. The advantage compared to more precise solutions is the small resource usage and no need for special control of the FPGA clock. The sender and receiver require about 100 and 600 LUTs of general logic in a Virtex-4, respectively.

TRIMI — trigger distribution

To enable modules running the TRLO II to act as TRIVA replacements when operated with the MBS, a register-compatible mimic has been developed. This (TRIMI) component includes a serial protocol for trigger distribution and synchronisation between multi-crate systems. With the TRIMI essentially having its own register space, connections are controlled by a separate program: `trimictrl`. The peer-to-peer-like serial protocol makes it easy to configure inter-system connections via remote control.

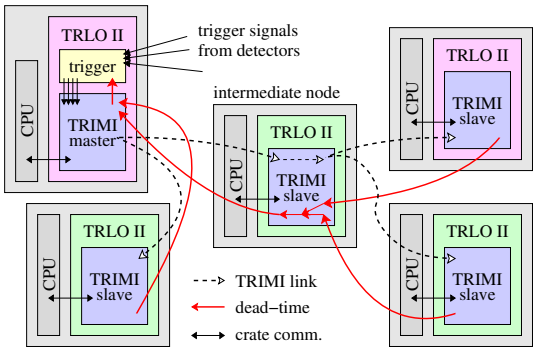

Figure 1: The TRIMI links and dead-time returns can be arranged in a tree structure with intermediate nodes doing fan-out/in and monitoring. The network topology for data flow is independent and can be treated as flat.

The master TRIMI transmits the trigger number and event count for each read-out trigger as a serial message, which is received by connected slave modules. In return, the slaves send their dead-time signals, which can be fanned-in on the way or collected individually by the master. In the latter case, the collecting module (master or intermediate, see Figure 1) also has the ability to record the duration of dead-time for individual slaves, allowing event-by-event performance investigations.

The FPGA footprint in a VULOM4 is about 1350 LUTs (7%), of which 1050 are related to the multi-system link capability. About half of those can be attributed to the full flexibility in which module in- and outputs are used.

After extensive synthetic tests, it is now being set up and verified for use in a detector test run in Cave C in 2014.

References

[1] H.T. Johansson *et al*, "TRLO II – flexible FPGA trigger control", GSI Scientific Report 2010 (2011) 231

[2] Developed at GSI-EE by J. Hoffmann *et al*. `https://www.gsi.de/fileadmin/EE/Module/VULOM/`

[3] J. Hoffmann and N. Kurz, "RISING Data-Acquisition with MBS Event Synchronization with Time Stamp Modules", GSI Scientific Report 2002 (2003), 224

* Work supported by FAIR@GSI PSP codes: 1.2.2.4., 1.2.5.1.4. and 2.4.3.1.

 doi:10.15120/GR-2014-1-FG-S-FRS-15

A 400 kA Pulsed Power Supply for Magnetic Horn at the pbar Separator

S. Mohite[1], *I. Petzenhauser*[1], *and K. Knie*[1]
[1]GSI, Darmstadt, Germany

In the planned FAIR pbar separator [1] scheme magnetic horn will be used as a focusing device for highly divergent antiproton beam as it is already in operation at CERN [2] successfully. To achieve the desired operational performance from the horn, it needs to be powered with a very high electrical current pulse of 400 kA peak amplitude with repetition rate up to 0.2 Hz. To limit the power consumption and associated thermal and mechanical stresses on the load-system the pulse duration should be as short as reasonably possible.

As shown in Fig. 1, a high-voltage, energy- storage capacitor bank will be charged by a dc supply to the rated voltage. This stored energy will be released on horn through switches and the discharge path, which includes a set of coaxial cables, adaption box and a radiation-hard stripline. An Adaptive Control Unit will provide communication interface between the accelerator control system and horn system. Possible technical realization of this system has

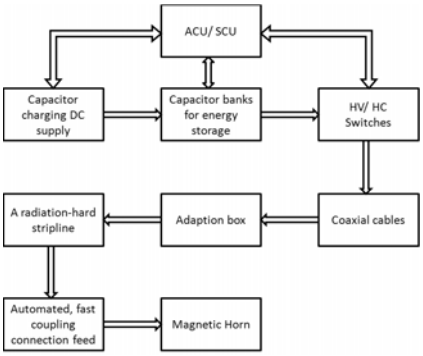

Figure 1: Schematic of the horn pulser system.

some key design aspects. Due to the building construction and radiation protection limitations, physical distance between the power supply and horn is $\approx$ 65 m. This means additional parasitic impedance. Therefore, resistance and inductance of the discharge path should be as small as reasonably possible. Another key element will be the necessary high voltage switches. A mini-workshop was organized on "Switches for FAIR-Magnetic Horn Pulser System". For the given the operating parameters, among the possible switch types are ignitrons and solid-state switches. As solid-state switches are not well-known in this power regime presently, the most likely solution seems to be the use of ignitrons. As an attempt for the systematic risk management, meeting has been organized with project control to address the safety concerns due to the mercury contents of the ignitrons. As a risk mitigation strategy, it has been decided to provide a shielding mechanism around the ignitrons in the form of metal containers for effective mercury containment.

Fig.2 shows the basic circuit to produce the required current pulse. A capacitor bank of $\approx$ 2 mF is charged to a voltage $\sim$ 15 kV and then discharged through switch S_D in a directly coupled damped circuit with $\approx$ 1.5 μH inductance and resistivity of $\approx$ $5m\Omega$. These values represent calculated total effective inductance and resistance, L_S and R_S respectively, of the system. The horn can be regarded as mainly an inductive load with small series resistance. The diode stack D is used to protect the capacitor from excessive reverse voltage during falling period of the horn current. Energy-damping resistor R_E is basically a protective device to dump the significant amount of magnetic energy and thus critically damp the horn current. The whole stored energy is dissipated during each operating cycle. In order to

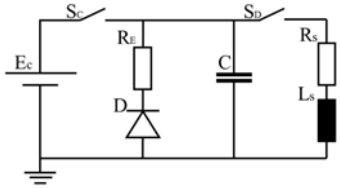

Figure 2: Simplified electrical equivalent circuit of pulser.

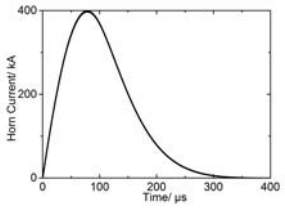

Figure 3: Critically-damped horn current waveform.

study the transient electrical behavior of the pulser circuit, an LTspice simulation [3] has been performed using calculated values of R, L, and C of major system components. A critically-damped horn current waveform, as shown in Fig.3, with 400 kA peak amplitude and duration of 125 μs FWHM has been calculated.

References

[1] A. Dolinskii et al., Nucl. Instr. Meth. A 629(2011)16.
[2] D.Boimond et al.,CERN/PS 94-02 (AR).
[3] LTspice simulation program from www.linear.com

 doi:10.15120/GR-2014-1-FG-P-BAR-01

Ion Optics of the High Energy Storage Ring for Operation With Heavy Ions*

O. Kovalenko[1,2], *A. Dolinskii*[1], *Yu.A. Litvinov*[1,2], *T. Stöhlker*[1,3,4], *and the SPARC Collaboration*[1]

[1]GSI Helmholtz Center; [2]Ruprecht-Karls University Heidelberg; [3]Helmholtz Institute Jena; [4]Friedrich-Schiller University Jena

Introduction

In this report we show the latest improvements of the optical properties of the High Energy Storage Ring (HESR) for the operation with heavy ions.

Modified ion optics of the HESR

The ion optical lattice with γ_{tr} = 6.2 [1], which is the standard optics for the PANDA experiment, was taken as a starting point. This lattice has low-beta insertions in the PANDA straight section. Apart from their main function (strongly focus the beam in the interaction region) it drives the amplitude functions to high values around the interaction point. In the case of the SPARC experimental program such amplitudes are not needed. Thus, by varying the strengths of the quadrupoles in the zero-dispersion straight sections a more relaxed behaviour of the beta-functions could be achieved. More precisely, the maximum beta amplitudes (β_x, β_y) = (222 m, 172 m) were decreased to (172 m, 153 m), respectively (see Fig. 1, around $s = 510$ m). This results in a smaller beam size and in an enhanced acceptance for operation with ions. Consequently, the calculations showed an increased dynamic aperture. A working point for the new optics is currently at (7.63, 7.60).

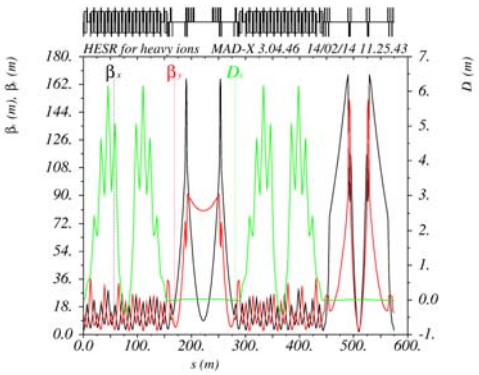

Figure 1: Optics for heavy ions

The beta function amplitudes at the waist of the beam at the PANDA target remained virtually unchanged. This means that the radius of the beam at the PANDA target location stays the same. An expected intensity of the heavy ions during the SPARC experiment is about 3 orders of magnitude less that the antiproton intensity in the PANDA experiment (10^8 vs. 10^{11}). Therefore, even for the bare uranium ions with charge 92+, the beam current for ions is roughly 10 times smaller than for antiprotons. Hence there are no harmful effects expected to the sensitive equipment of the PANDA detector due to intensive heavy ion beam and the SPARC experiments will not necessarily require the disassembling of the PANDA setup. Potential risks valid for both, the antiproton and ion, beams due to injection into the HESR still has to be studied.

Closed orbit bump at internal target location

In order to have the best possible beam-target overlap a feasibility of a closed orbit bump at the SPARC internal target location in the arc was investigated. With a present set of corrector magnets [2], only 3 correctors in the vicinity of the SPARC setup can be used for creating a bump. It allowed for varying the amplitude of the closed orbit at the given point. We proved that a $\pm$5 mm bump is possible (up to 8 mm if needed). In order to additionally vary the angle of the closed orbit, one extra corrector close to the SPARC target needs to be installed.

Closed orbit correction

A closed orbit correction was simulated. On the statistics of 500 seeds it was verified (see Fig. 2) that the maximum values of the closed orbit deviation are as high as 20 mm in a horizontal and 35 mm in a vertical planes. The closed orbit could be corrected down to 2 mm and 4 mm in the horizontal and the vertical planes, respectively.

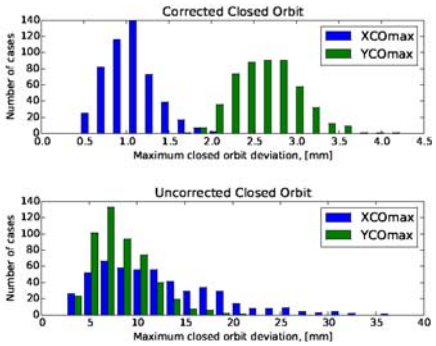

Figure 2: Both corrected (up) and uncorrected (bottom) in horizontal (blue) and vertical (green) planes

Fruitful discussions with colleagues from FZ Jülich and PANDA collaboration are greatly acknowledged.

References

[1] R. Maier. Proc. IPAC 2011, New York, USA (2011)

[2] B. Lorentz, Jülich, private communication

* Work supported in part by the Helmholtz-CAS Joint Research Group HCJRG-108 and Helmholtz Institute Jena

 doi:10.15120/GR-2014-1-FG-ESR-01

Progress report on the Collector Ring (CR)

A. Dolinskii[1], *U. Blell*[1], *O. Chorniy*[1], *C. Dimopoulou*[1], *O. Gorda*[1], *R. Heß*[1], *U. Laier*[1], *H. Leibrock*[1], *T. Mohite*[1], *S. Litvinov*[1], *J. Kurdal*[1], *I. Schurig*[1], *U. Weinrich*[1], *H. welker*[1], *and A. Kalimov*[2]

[1]GSI, Darmstadt, Germany; [2]St-Petersburg State Polytechnical University, Russia

To strengthen the Russian Contribution to the FAIR Project it was proposed to transfer a major part of the CR project responsibility from GSI to BINP (Novosibirsk). As a first step in this progress a Memorandum of Understanding (MoU) between FAIR, GSI and BINP has been signed. According to the MoU the BINP will take over the responsibility of design, construction, installation and commissioning of the CR system and major components. In order to secure a sound technical reference for this process the GSI CR project group updated the TDR of the

Collector Ring. BINP will provide an accelerator that fulfills the entire set of machine parameters described in this document. GSI remains responsible for the stochastic cooling, the RF system, the data supply, the control system and the experimental devices.

In 2013 three workshops between GSI and BINP took place, where the technical aspects of the CR magnets and vacuum system were discussed. At the end of the year a BINP project group for the collector ring was established. With the reception of the - by GSI produced - project documentation this project group started to investigate the system layout and to design and specify the dipole and vacuum units.

System design

3D CATIA model of the CR layout and building have been continued and completed for all ring and building sections. Modifications of the long straight sections of the CR were implemented. For the civil construction planning, major assumptions have been made for the crane and maintenance of the CR components. The CR building documents and drawings have been approved in the first iteration. Major collisions have been identified and removed in an interactive process between the engineering- and ion optical designers. Detailed requests for the supply room conditions were specified according to the component properties.

Ring layout

The distribution of wide and narrow quadrupoles in the ring and the overall lattice cell has been further optimized. The long straight sections of the CR have been modified to have more drift space for diagnostic devices and vacuum components. In this context seven wide quadrupoles are replaced by narrow ones. The number and position of the injection kicker magnets in the CR have been optimised taking into account 3D magnet field calculations of the whole kicker tank consisting of three modules.

Beam dynamics

Proposed straight section modification, where the several wide quadrupoles are replaced by narrow ones, breaks the CR super-periodicity from 2 to 1. Taking into account this aspect and new data about the magnetic field quality of all CR magnets the dynamic aperture has been calculated using the PTC tracking module implemented in the MAD-X code. In particular, the off-momentum dynamic aperture has been computed to determine the available dynamic momentum aperture for the different operation conditions as shown in figure 1.

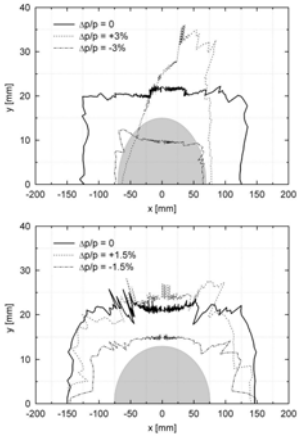

Figure 1: Dynamic aperture in the antiproton (left) and RIB (right) mode operation of the CR with the super-periodicity of 1.

The isochronous mode of the CR has been investigated further in detail. Different sort of nonlinear sources deteriorate the time resolution. It was shown that the influence of sextupole and octupole nonlinear effects can be completely compensated using sextupole and octupole corrections. The decapole effect is the most critical aspect. Without high order correction the required $\Delta T/T$ of 10^{-6} for mass resolution over the full CR momentum acceptance is not achievable. Simulations show that one family of a decapole corrector installed in the dispersive part of the CR is needed. To compensate the influence of the fringe field of quadrupoles on the ΔT the octupole correction is required. Using 4 octupole and 1 decapole families one can reach a resolution of $\Delta T/T = 3 \times 10^{-7}$, which corresponds to the mass resolution of $\Delta m/m = 10^{-6}$ [1].

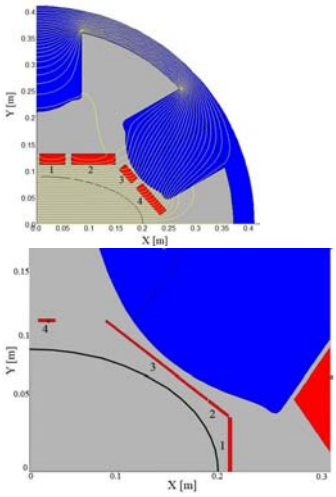

Figure 2: Cross section of sextupole (left) and quadrupole (right) with additional coils for vertical steering and octupole correction respectively.

Magnets

According to the 9th FAIR Machine Advisory Committee recommendations a fast ramping dipole magnet for the CR (1 T/s) must be designed. The time constant of the eddy current decay inside the yoke must be less than 5 ms that requires a yoke lamination thickness less than 2 mm. Requirements on integral field quality and magnet to magnet identity have been reconsidered in this context, too. The demand on the field quality of $\pm 10^{-4}$ has been fixed only for the maximum field level of 1.6 T. In the range below 1.6 T the relative magnet field deviation can be higher with a linear approximation up to $\pm 2.5 \times 10^{-4}$ at the field level of 0.8 T. The parameter "magnet to magnet identity" of the CR dipole magnet of 5×10^{-4} has been specified.

A new design of the wide sextupole magnet with a vertical corrector has been developed. The yoke length of the sextupole magnet is reduced by 10 cm. The four different coils must be embedded in the sextupole aperture over the vacuum chamber as shown in figure 2 (left). The design has been performed in such way in order to have only one power converter for all these coils.

In figure 2 (right) a preliminary design of the wide quadrupole magnets is shown with four additional coils, which produce the octupole field over the elliptical aperture with the axes of 400 mm and 180 mm. The field profile calculation has been performed using 2D and 3D OPERA codes. All these four coils together induce an additional quadrupole field component, which must be accounted by the main quadrupole magnet.

Injection/ Extraction

The CR requires full aperture kicker magnets with a total kick angle of 21 mrad. The kick flat-top must be at least 440 ns with a uniformity of 2%. The field uniformity of 2% is also requested inside the useful aperture. Due to the large kicker length compared to the available straight sections of the CR, it is necessary to split the kicker into nine modules. They are placed in three tanks, each containing three identical modules.

A 3D magnetic field of the kicker magnet consisting of 3 modules was calculated. In figure 4 the magnet field distribution in the middle plane of one kicker is shown. One can see that a strong field overlap between modules takes place. The particle tracking through this field shows that the effective deflection angle of one kicker tank is 7.1 mrad. The results of the 3D field analysis allowed to reduce the foreseen total amount of kicker modules from 12 to 9.

These kickers will be used both for injection and extraction of the beam in different optical modes within the rigidity range of 8 - 13 Tm. For these purposes a bipolar kicker system is required. One of the advantages of a bipolar kicker system is the possibility to determine the working mode of extraction or injection within a very short time (μs range).

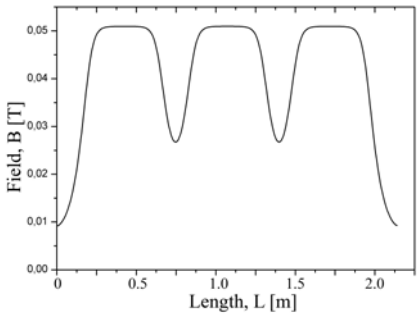

Figure 3: The vertical field distribution of one kicker magnet consisting of 3 modules. Here $(BL)_{eff}$=92 mTm, which gives kick angle x'=7.07 mrad.

Vacuum system

A bake-out of the vacuum system is not foreseen to be installed in the MSV of the FAIR project. However, the possibility of bake-ability in future has been considered. It was agreed that, if it is possible without extra cost and extra development efforts, all components should be designed in such way that they can be baked-out up to 300 °C after the MSV if necessary. In this case appropriate materials for bake-out have to be chosen and installation procedure must be foreseen. For all magnets the combination of magnet yoke aperture, actual vacuum chamber layout and estimated beam shape was analysed together in order to derive the available space for thermal insulation.

For the dipole vacuum chamber the shape and wall thickness must be designed considering dipole requirements to have the possibility of fast ramping of 1 T/m.

doi:10.15120/GR-2014-1-FG-CR-01

Stochastic cooling

The procurement procedure for the 1-2 GHz power amplifiers at the kickers was underway in 2013. The intermediate Cu cryoshield was assembled, successfully mounted into the prototype pick-up tank and finally gold plated. The notch filters have been finalized. Progress was made towards the design of the electrodes of the Palmer pick-up. More information one can find in ref. [2]. The new software development for Palmer cooling study has been performed [3].

References

[1] S. Litvinov, D. Toprek, H. Weick, et al., Nucl. Instr. and Meth. A **724** (2013) 20

[2] C. Dimopoulou et al., "Developments for the CR stochastic cooling system", this annual report

[3] M. Dolinska et.al., "Software development for stochastic cooling study in time domain", this annual report

Developments for the CR Stochastic Cooling System

C. Dimopoulou[1], D. Barker[1], R. Böhm[1], M. Dolinska[2], R. Hettrich[1], W. Maier[1], M. Kelnhofer[1], J. Krieg[1], R. Menges[1], C. Peschke[1], J. Rossbach[1], and L. Thorndahl[3]

[1]GSI, Darmstadt, Germany; [2]Frankfurt University; [3]CERN, Geneva, Switzerland

The large-acceptance Collector Ring (CR) is designed to provide fast stochastic cooling (SC) of antiproton and rare isotope beams. A detailed specification document [1] describing the complete CR SC system in the frequency bandwidth 1-2 GHz has been released. Intensive in-house engineering activities, preparation of the technical infrastructure taking into consideration electrical and mechanical safety issues as well as critical procurements of system components have taken place during 2013.

Electrodes and pick-up tanks, Simulations of the system performance

The layout and testing challenges of the prototype pick-up tank are explained in [1]. The new water-cooled linear motor drive units have been tested at room temperature with different acceleration profiles set by a control software. The linear motor drives fulfill the following specifications: (i) their maximum range of plunging is 70 mm following the shrinking beam size during stochastic cooling and (ii) at the end of the cycle, they move back out to their maximum aperture within 200 ms, before a new beam is injected. Their synchronous operation remains to be tested after re-assembly in the tank.

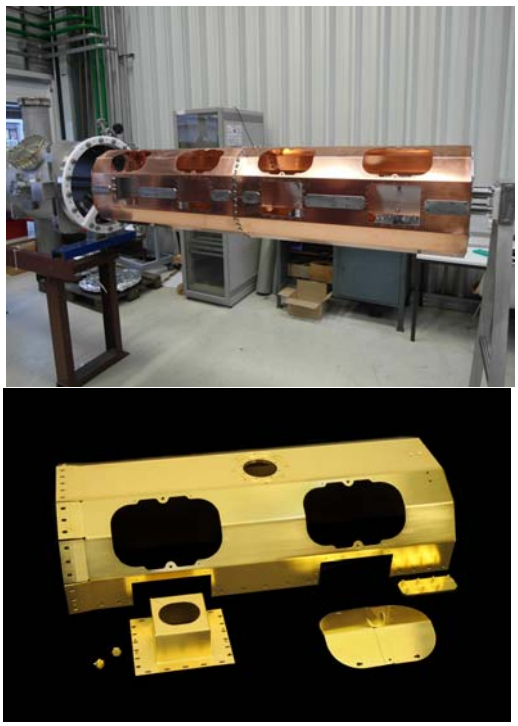

Figure 1: Up: Copper cryoshield before mounting in the prototype tank. Down: Cryoshield parts after gold plating.

The intermediate cryoshield, which will be held at 80 K inside the pick-up tank, was successfully inserted into the prototype tank at room temperature. It consists of 4 half-shells, each 1 m long, and bears holes for the motor drives and for assembling, it is made of oxygen-free copper (Fig. 1, up). Afterwards, its pieces were polished and galvanically gold plated (Fig. 1, down), so as to reach very low thermal emissivity. The preparation of the cryoshield was a complex interdisciplinary task completed at GSI.

Simulations with the HFSS code have converged to possible designs of the Faltin-type electrodes of the Palmer pick-up [2]. The Palmer cooling performance in the CR has been calculated using a Fokker-Planck approach, modified for this purpose, and implementing the properties of the suggested electrodes. With the confidence thus gained, engineering work on electrode prototypes could start.

In parallel, a numerical model for simulating the Palmer stochastic cooling of ions in the time domain has been written, cross-checked against analytical formulae, and subsequently applied to the CR case as well as to experimental data from ESR operation.

RF signal processing and operation codes

The RF block diagram of the complete SC system and its integration into the building has been refined [3] so as to save electrical length, since the flight time of the quasi-relativistic particles from pickup to kicker is very short.

After releasing the technical specification of the very demanding 1-2 GHz power amplifiers, the procurement procedure was launched. It has led to a first round of intensive technical negotiations with potential providers, aiming at awarding the contract beginning of 2014.

The design of the notch filters was optimized and their measured RF properties lie within the specifications. The mechanical assembly, including the thermally stabilized delay line, has been finalized.

Conformal to the defined standards of the FAIR control system, a new operation program covering all cooling branches of the ESR SC system has been developed and implemented to the existing RF hardware. This is a major step towards the preparation of such operation codes for the CR system.

References

[1] Doc F-DS-BC-01-SC-CR-v1.0.pdf, GSI EDMS Doc. 1316650/1; CR Technical Design Report 2014.

[2] D. Barker et al., JACoW Proc. COOL'13, WEPPO21.

[3] C. Peschke et al., JACoW Proc. COOL'13, WEPPO20.

 doi:10.15120/GR-2014-1-FG-CR-02

Software development for stochastic cooling study in the time domain

M. Dolinska[1] *and C. Dimopoulou*[2]
[1]Frankfurt University; [2]GSI, Darmstadt, Germany

The beam dynamics under the influence of the stochastic cooling forces can be studied by a particle by particle and turn by turn simulation in the time-domain. This treatment does not involve complicated, changing frequency spectra, which anyhow are likely to be incomplete by considering the Fokker-Planck Equation and its solution [1, 2]. To keep the computation times within reasonable limits, the scaling law that cooling times are proportional to the number of particles (for zero preamplifier noise and all other parameters remaining unchanged, except the gain) has been applied throughout. A special computer code has been developed to calculate beam cooling in the CR. Preliminary results for the Palmer method are presented. A typical simulation super-particle number is about $(1-10)\times 10^4$.

Time domain approach

The time domain algorithm is developed and applied to the Palmer cooling method. The possibility of using this method for simultaneous longitudinal and transverse cooling by a suitable choice of the pickup to kicker distance was described by Hereward [3]. According to this algorithm the coasting beam is generated in a 6D normalized phase space (X,X',Y,Y',Δp/p, ΔT). In the time coordinate (ΔT) this beam is split a certain number of samples. The time length t_s of samples depends on the choice of system bandwidth W: t_s=0.5/W. Having the particle time distribution of each sample the particle mixing is simulated by a simple particle migration from sample to sample, which means the flight time variation of each particle in the sample turn by turn is calculated at $t_i = t + \Delta t_i$, where

$$\Delta t_i = T_{loc}|\eta_{loc}|\frac{\Delta p}{p_i} \tag{1}$$

Depending on the way T_{loc} and η_{loc} equal T_{PK} or T_{KP} and η_{PK} or η_{KP} respectively. At Pick-Up (PU) each sample produces a signal $<X_n>$, which is proportional to momentum error and transverse error displacement of this sample. At the kicker (KK) the accessory of a particle to the certain sample s is defined and depending on the sample number s the single particle correction is calculated by

$$\frac{\Delta p}{p_i} = \frac{\Delta p}{p_i} - \frac{g}{D_{PU}}\cdot\langle X_n\rangle_s\cdot\alpha_p\cdot s(\Delta t), \tag{2}$$

$$X'_n = X'_n + g\cdot\langle X_n\rangle_s\cdot\alpha_t\cdot s(\Delta t), \tag{3}$$

where the g is a normalized gain, $\alpha_{p,t}$ is damping factor, which reduces the gain efficiency due to the noise. s(Δt) is a time profile of the signal. The Eqs. (2, 3) describe the cooling effect in the time domain approximation. One can see that for the Palmer method the momentum error of particles is corrected proportionally to the center gravity of sample, which characterized by average value of coordinate $<X_n>$. In the transverse plane the particle coordinates are rearranged and calculated by

$$\begin{pmatrix} X_{n,P,K} \\ X'_{n,P,K}\end{pmatrix} = \begin{bmatrix} C_{KP,PK} & S_{KP,PK} \\ -S_{KP,PK} & C_{KP,PK}\end{bmatrix}\begin{pmatrix} X_{n,P,K} \\ X'_{n,P,K}\end{pmatrix} \tag{4}$$

$C_{KP,PK}$ =cos(ΔμKP,PK); $C_{KP,PK}$ =sin(ΔμKP,PK);, Δμ is a phase advance from kicker to pick-up (KP) or from pick-up to kicker (PK). The gain damping factor $\alpha_{p,x}$ can be calculated by

$$\alpha_{p,x} = 1 - \frac{g}{2}(1+U_{p,x}) \tag{5}$$

Here, $U_{p,x}$ are the total noise-to-signal ratio. For Palmer cooling this value is taken from [3]

$$U_p = \frac{\epsilon^2_{rms}}{D^2_{PU}\delta^2_{rms}} + U_{N,S}; U_x = \frac{D^2_{PU}\delta^2_{rms}}{A^2_{rms}} + \frac{\epsilon^2_n}{A^2_{rms}} \tag{6}$$

Here, U_{NS} is the ratio of the thermal noise to the Schottky signal.

Numerical simulations

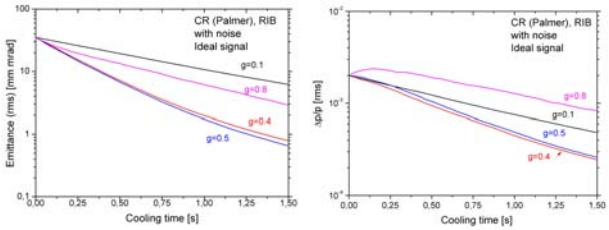

The calculated momentum spread and emittance evolution for different gain factors g are shown in Fig. 1. The Palmer cooling will be useful in the first stage of stochastic cooling of rare isotopes in the CR. After the rms Δp/p decreases below 0.1 %, it is possible to switch off the signals from the Palmer Pick up and turn to Notch filter cooling. From Fig.1 one can deduce that the rms Δp/p of 0.1 % becomes in 0.5 second for the U^{92+} beam if g=0.4.

References

[1] M. Dolinska et.al., Proc.of IPAC2011, p. 2298-2300.
[2] M. Dolinska et.al., Proc.of IPAC2013, p. 1028-1030.
[3] D. Möhl, Stochastic cooling , CERN/PS/DL 78-25.

Progress in development of resonant Schottky pickups with transverse sensitivity for the CR*

X. Chen[1], *M. S. Sanjari*[1,2], *J. Piotrowski*[3], *P. Hülsmann*[1], *Yu. A. Litvinov*[1,4], *F. Nolden*[1], *M. Steck*[1], *and Th. Stöhlker*[1,2,5]

[1]GSI, Darmstadt; [2]EMMI, Darmstadt; [3]AGH University, Kraków, Poland; [4]MPIK, Heidelberg; [5]HI-Jena, Jena

With its high-intensity and high-energy secondary beams, the FAIR facility will open a window to unexplored areas in atomic, nuclear, and particle physics. To take advantage of that, the ILIMA experimental program aims at high-precision mass and lifetime measurements of short-lived nuclides which will be accessible at the exit of the Super-FRS. The Collector Ring (CR) tuned into the isochronous ion-optical mode will be employed for this purpose. As a contribution to the ILIMA collaboration, our task is to develop an innovative resonant Schottky pickup with transverse sensitivity for the CR. The pickup will be used to measure the position of each stored ion, which in turn is essential for corrections of non-isochronous effects on a particle-by-particle basis.

Just like the previous Schottky pickup built for the ESR [1], we continue with a cavity-based design to achieve a high signal-to-noise ratio owing to its resonance nature. In general, three figures of merit are used to characterize such a cavity, i.e. *resonant frequency*, f, *quality factor*, Q, and *shunt impedance*, R.

Because of the boundary conditions in three dimensions, the EM waves in a cavity can only resonate at some discrete frequencies. The detection instrument will be tuned to one of these resonant frequencies in order to obtain the maximum induced signal. As a rule of thumb, it should not exceed the cut-off frequency of the ring to avoid any propagation outside the cavity. Due to the beam pipe considerations at the CR, we choose f to be about 400 MHz.

The quality factor describes how well a cavity stores electromagnetic energy at the resonant frequency. The less the EM power is dissipated away by heat conversion on the cavity wall, the higher the quality factor is. It is quantitated as: $Q = f/\Delta f_{3\mathrm{dB}}$, where $\Delta f_{3\mathrm{dB}}$ is the FWHM of the resonant peak in the frequency domain. For the sake of high sensitivity, we want the Q value to be as large as possible. Thus the material of the cavity should be a good electric conductor in order to reduce the energy loss due to heat.

Last but not least, the shunt impedance indicates the coupling strength between the cavity and the beam. Due to the same reason as for the quality factor, we want a high shunt impedance for the designed cavity. Additionally, we also require it to be distinct in respect of the transverse position, since the cavity has to identify the beam offsets. As a result, a mode geometry with a varying impedance vs. transverse position (such as the dipole mode) can be used.

Bearing these three important parameters in mind, we can obtain their values numerically by computer simulations. The simulation tool we are using is a commercial software CST STUDIO SUITE®. After the 3D model of the cavity is created and the boundary conditions are set properly, the *Eigenmode Solver* will calculate the EM field distribution at the resonant frequency. Then with the help of *Post Processing Templates*, we get the quality factor and the shunt impedance. We have studied several designs and accordingly simulated their features. Based on the simulation results, we have chosen an optimal design and have manufactured a model cavity.

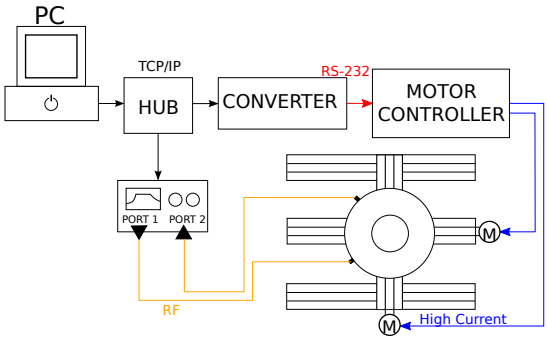

Figure 1: The schematic setup of the testing system for Schottky pickups. Taken from [2].

In parallel, we have also constructed an automatic computer-controlled testing system (Fig. 1) for the bench top measurements. Until now, we have performed the measurement of shunt impedances at different transverse positions in the beam pipe opening. We fixed the rod with two supports but moved the cavity instead. The cavity was placed on a motorized movement unit, which is controlled by a motor controller. It communicates with a PC over TCP/IP, via a converter to translate between Ethernet and RS-232. Also a Vector Network Analyzer (VNA) is connected to the PC by Ethernet cables. The automatic measurement is realized by a Java program, commanding the motor controller for cavity movements, the VNA for signal processing, and the PC for data acquisition. As a next step, we will perform the bead measurements to investigate the EM field distribution in the opening.

References

[1] F. Nolden, *et al., Nucl. Instrum. Meth. A*, **659** (2011) 69

[2] J. Piotrowski, BSc. Thesis, *AGH Univeristy*, (2013)

*This work is in part supported by the European Commission (PITN-GA-2011-289485), the Alliance Program of the Helmholtz Association (HA216/EMMI), and the Helmholtz-CAS Joint Research Group (HCJRG 108).

 doi:10.15120/GR-2014-1-FG-CR-04

The status of the CRYRING@ESR project*

F. Herfurth† [1], *M. Lestinsky*[1], *R. Bär*[1], *A. Bräuning-Demian*[1], *S. Litvinov*[1], *O. Dolinskii*[1], *W. Enders*[1], *M. Engström*[1], *B. Franzke*[1], *O. Gorda*[1], *A. Källberg*[2], *Y. Litvinov*[1], *I. Pschorn*[1], *A. Reiter*[1], *A. Simonsson*[2], *T. Sieber*[1], *J. Sjöholm*[2], *M. Steck*[1], *Th. Stöhlker*[1], *G. Vorobjev*[1], *and N. Winckler*[1]

[1]GSI, Darmstadt, Germany; [2]MSL, Stockholm University, Stockholm, Sweden

The low energy storage ring LSR [1] shall provide highly charged ions and antiprotons at low energy for two collaborations at FAIR, SPARC and FLAIR. Those collaborations intend to perform precision experiments pursuing atomic and nuclear physics questions. The LSR is a Swedish in-kind contribution to the FAIR facility in Darmstadt.

The LSR is the swedisch low energy storage ring CRYRING modernized and adapted to the additional needs for injection and ejection of antiprotons and highly charged ions at about 10 MeV/nucleon. CRYRING has been operated at the Manne Siegbahn Laboratory in Stockholm until 2010, was dismantled in 2012 and transported to GSI in the first months of 2013. At GSI it will be installed behind the ESR, as proposed and described in detail in 2012 by a swedish-german working group [2]. This proposal has been accepted end of 2012 by the relevant committees.

CRYRING can decelerate, cool and store heavy, highly charged ions and anti protons injected at about 10 MeV/nucleon down to a few 100 keV/nucleon. It provides a high performance electron cooler and a straight section for flexible experiment installations as for instance a gas jet target. It is equipped with it's own injector and ion source, to allow for standalone commissioning. The magnets are conceived for fast ramping, such that the whole deceleration (acceleration) can be as short as 150 ms.

After dismantling the ring in Stockholm under the supervision and with the help of the Transport and Installations department of GSI the components where transported to Darmstadt in spring 2013.

The concerned specialist departments of GSI for power converters, radio frequency supplies, magnets, survey and alignment, control system as well as beam diagnostics and electron cooling, scheduled the required work for getting the ring back into operation. This includes extended tests as well as modifications to meet the GSI and FAIR standards.

A detailed survey has been completed to prepare for the precise alignment of all components in the refurbished cave. The positions of the components have been marked on the floor to prepare for installation. Dipoles, quadrupoles and sextupoles, have been equipped with measurement points for the foreseen laser tracking alignment and the position of those references have been transferred to the beam axis for each devices.

Beam diagnostic devices like the in-ring transformer and the ionization profile monitors have been tested. The ionization profile monitor was installed under vacuum at the HITRAP experiment setup and tested with alpha particles from a local source.

Engineering models in 3D of the ring and the two injection lines, from the ESR and the local ion source, are basically completed. The cable planning is ongoing as well as the installation of the required infrastructure like lighting, cooling water and miscellaneous supplies.

Much time, effort and resources went into the preparation of the cave that should house CRYRING@ESR. The former experimental installation, FOPI, has been removed with the help of the FOPI collaboration and the cave has been reconstructed. Fig. 1 shows the recently completed cave. On the roof of the cave an area for power converters has been prepared and four containers for more fragile electronic equipment were installed.

Figure 1: The completed cave for the installation of CRYRING@ESR. The light spots on the floor indicate the position of the bending dipoles and straight sections. The future beam path is marked with the blue line.

For the upcoming year it is foreseen to install the still missing infrastructure, to assemble and commission all devices required to operate the ring, to install the ring and local injector hardware and to start commissioning with the local ion source.

References

[1] H. Danared, et al. (2011) "LSR - Low-energy Storage Ring, Technical design report", Manne-Siegbahn Laboratory, Stockholm University, version 1.3.

[2] M. Lestinsky, et al. (2012) "CRYRING@ESR: A study group report", Project study, GSI, Darmstadt,

* Work supported by GSI/HI Jena/FAIR@GSI PSP code:1.3.4.2./The SPARC collaboration/Uni Krakov/KVI Groningen

† F.Herfurth@gsi.de

 doi:10.15120/GR-2014-1-FG-CR-05

Beam Instrumentation for CRYRING@ESR

A. Reiter[1], C. Andre[1], H. Bräuning[1], C. Dorn[1], T. Hoffmann[1], W. Kaufmann[1], N. Kotovskiy[1], H. Reeg[1], T. Sieber[1], M. Schwickert[1], G. Vorobyev[1], B. Walasek-Höhne[1], and M. Witthaus[1]

[1]GSI, Darmstadt, Germany

Introduction

This report gives an overview of the beam instrumentation of the CRYRING@ESR experimental storage ring that is currently in the process of installation at GSI. CRYRING@ESR (see Fig. 1), together with ESR and HITRAP decelerator, will provide new opportunities for various research fields. An independent RFQ injector linac is available for commissioning of the new machine where FAIR standards will be applied for the first time. Three main concepts influence aspects of beam instrumentation:

- FESA: CERN Front-End Software Architecture, a development framework for data acquisition (DAQ) systems. Like any accelerator equipment, a DAQ system is required to provide a FESA control interface for seamless control system integration.
- GMT: General Machine Timing system, a new precision timing system with sub-ns precision based on the White Rabbit protocol. One programmable timing receiver board is installed in each DAQ system and controls execution of real-time actions and DAQ triggers.
- LSA: CERN LHC Software Architecture, the new data supply model for accelerator components. From LSA DAQ systems receive information on beam production, e.g. ion species, energy, charge state, that is needed for on-line calculations.

Linac Injector

The injector beam line will be equipped with dual detectors as used at HITRAP consisting of Faraday cup (FC) and viewing screen (SCR) on a common stepper motor drive. Two units, one before and one after the 90° spectrometer, match the ion source beam to the RFQ entrance. Two further units match the RFQ beam to the CRYRING injection. Longitudinal matching is adjusted by a new debuncher. For phase and energy measurements, three capacitive pickups have been added. The FC readout will be adopted from existing FESA systems. The SCR readout is described in [2].

CRYRING

After transport to GSI at the end of 2012, all detectors, front-end amplifiers and special low-noise electronics were carefully checked. Non-intercepting detectors are the eight beam position monitors (BPM), an integrating/parametric current transformer for bunched/coasting beam (ICT/PCT),

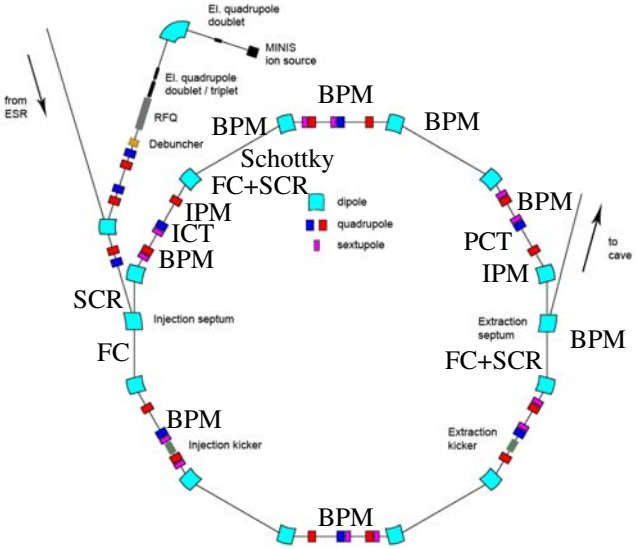

Figure 1: Layout and Diagnostics of CRYRING@ESR.

two ionisation profile monitors (IPM) and Schottky electrodes. Most equipment can be integrated in the new DAQ systems. Only new low-noise BPM amplifiers had to be designed with switchable 40/60 dB gain and bandwidth filter. The BPM DAQ is a new design based on μTCA components, a modern telecommunication standard with high throughput and reliability. The signals are acquired by 250 MSa/s ADCs of 16 bit resolution and position evaluation takes place directly on an FPGA. A prototype system is expected to be ready by the end of this year. For intensity measurements a VME scaler system combines signals of different detectors: Schottky and BPM sum signals, IPM count rates, ICT and PCT transformer signals. For profile measurements the IPMs are equipped with position-sensitive resistive anode encoders. The pre-amplifier signals are shaped in a spectroscopy amplifier and the output signals analysed by a peak-sensing ADC in a VME DAQ which calculates the histograms.
The existing 1st turn FC diagnostics will be upgraded by new FC and SCR detectors of FAIR standard. One special screen will be added at the end of the new injection section that has been upgraded for higher injection energies.

References

[1] M. Lestinsky et al., CRYRING@ESR Study Group Report, June 2012

[2] B. Walasek-Höhne, CUPID, this GSI report

 doi:10.15120/GR-2014-1-FG-CRYRING-01

STATUS OF THE SC CW-LINAC DEMONSTRATOR INSTALLATION

V. Gettmann[1], W. Barth[1,2], S. Mickat[1,2], M. Amberg[1], A. Orzhekhovskaya[2], H. Podlech[3], U. Ratzinger[3], F. Dziuba[3], and K. Aulenbacher[1,4]

[1]HIM, Mainz, Germany; [2]GSI, Darmstadt, Germany; [3]IAP, Frankfurt am Main, Germany; [4]IKP, Mainz, Germany

ABSTRACT

The kick-off for the cw Linac Demonstrator project at GSI was aimed at a "full performance" of a 217 MHz sc CH-Cavity at the GSI-High Charge Injector (HLI). Meanwhile the design of the key components like the 217 MHz CH-Cavity, two sc solenoids, and the cryostat itself is finalized and their fabrication has started.

The test environment at GSI is about to be completed, such that the commissioning of the sc cw Linac Demonstrator is planned in 2014, when the key components are expected to be delivered.

CW LINAC DEMONSTRATOR

The concept of a suspended support frame, which carries the cavity embedded by two sc solenoids, is followed [1]. The support frame as well as the accelerator components are suspended by eight tie rods each in a cross-like configuration (nuclotron suspension) balancing the mechanical stress during the cooling-down and warm up (Fig.1). This way the components will always stay within the tolerance limits related to the beam axis (longitudinal +/-2mm, transversal +/-0.2mm). The CH cavity is cooled with LHe directly using a He jacket out of titanium. The delivery is expected in 2014 [2]. The solenoids are connected to LHe pots inside the cryostat by copper tapes allowing dry cooling. The main coil out of NbSn and two compensation coils made from NbTi provides the maximum magnetic field of 9.3 T, and shields within 10 cm to acceptable 30 mT at the position of the neighboured cavity. The delivery is expected in 2014.

SETUP AT GSI HLI

Commissioning of the Demonstrator is planned in 2014 at the GSI HLI, which operates at 108 MHz. A new beam line in straightforward direction to the HLI, which transports the beam to the new radiation protection shelter locating the Demonstrator, was designed regarding beam dynamical simulations. The new beam line with focusing and steering magnets has been installed already as well as beam diagnostic components in front of and behind the Demonstrator. The beam line is equipped with profile grids, beam transformers, and an emittance measurement station. Phase probes are used for output energy measurements applying the time of flight (TOF) method.

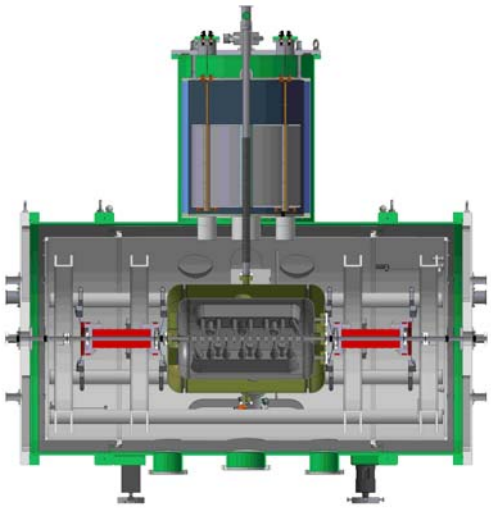

Figure 1: The cw Demonstrator comprising a CH cavity embedded by two solenoids on a support frame.

OUTLOOK AND FUTURE APPLICATIONS

The Demonstrator project is a proof of principle on the CH cavity. Successful full performance tests with beam of the sc CH cavity open a broad field of accelerator applications like the MYRRHA project [3] or the sc sw-LINAC at GSI [4]. Also the extension of the Demonstrator to a string of five CH cavities is proposed (advanced Demonstrator) [5].

References

[1] V. Gettmann et al., THE SC CW-LINAC DEMONSTRATOR – FIRST SECTION OF A SC CW-LINAC, Proceedings of SRF2011, Chicago, USA (2011)

[2] Dziuba et al. A Superconducting 217 MHz CH Cavity for the CW Demonstrator at GSI, these proceedings THP006, Paris, France (2013)

[3] D. Mäder et al., Consolidated Design of the 17 MeV Injector for MYRRHA, these proceedings MOP065, Paris, France (2013)

[4] S. Mickat et al., The status of the cw -LINAC at GSI, Proceedings of Exon2012, Vladivostok, Russia (2012)

[5] W. Barth et al., ADVANCED SUPER-CONDUCTING CW HEAVY ION LINAC R and D, Proceedings of IPAC2013 THPWO007, Shanghai, China (2013)

 doi:10.15120/GR-2014-1-FG-CW-LINAC-01

Accelerator Shutdown Report

S. Reimann[*1] *and U. Scheeler*[1]
[1]GSI, Darmstadt, Germany

This report describes the main service and upgrade measures of the GSI accelerator facility in 2013. The presented information is based on the work of the shutdown coordination and the corresponding MS-Project shutdown planning.

General Overview

At the beginning of 2013 the annual schedule for operation contained a long shutdown from January till August followed by a beam period of three month. At the end of 2013 there was a short second shutdown foreseen. In April due to budget constraints this beam period was shifted to 2014. Hence there was no accelerator operation in 2013 at all and the whole year was used for maintenance und upgrade work at the accelerators. For commissioning of the different components there were 6 dedicated working periods each lasting two weeks. These periods were used to switch on these components and to check their behaviour.

Work Packages

Table 1 shows the duration of the main work packages. Figure 1 displays the distribution of about 1000 shutdown schedule entries corresponding to the main topics. The extensive maintenance of the ALVAREZ II cavity, the RF-system, as well as the chemical cleaning of drift tubes were the major work packages at UNILAC. A water leak of the first drift tube of the High Current Injector IH1-cavity has been repaired. Also emittance measurements were perfomed at the beam line behind the MEVVA ion source. At the end of 2013, most parts of the EmTEx (emittance transfer experiment) have been assembled in the transfer channel.

Work package	Begin	End
Alvarez service	Dec 2012	Nov 2013
EmTEx	Apr 2013	Feb 2014**
H=2 cavity	Dec 2012	Feb 2014**
radiation resistant safes	Feb 2013	Dec 2013
SIS18 switching station	Jan 2013	Aug 2013
SIS18 beam diagnostics	May 2013	Dec 2013
ESR target section	Sep 2013	Jan 2014**
HTA beam line upgrade	Jun 2013	Jan 2014**

Table 1: Duration of different project tasks.

At the SIS18, the construction of the H=2-Cavity, the installation of a new ionisation profile monitor (IPM) and the NEG-coating of the triplet chamber at section 11 were

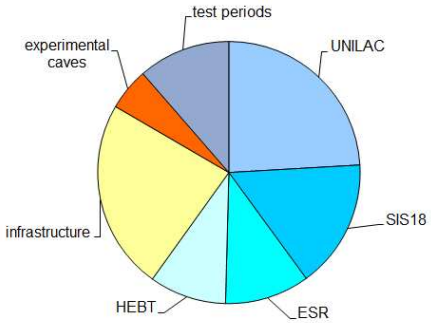

Figure 1: Work task distribution of the shutdown schedule.

dominating the shutdown work. Moreover, 11 radiation resistant safes have been installed on the ceiling of the SIS18-tunnel, to protect sensitive electronic components from radiation damage. Another major work package was the installation and commissioning of a new switching station for the SIS18-main power supply. The magnets, used for the horizontal orbit correction were equipped with new bipolar power supplies. At the ESR, the injection beam line and the target section has been redesigned and rebuild. The kicker module of the stochastically cooling device has been dismantled, repaired and reinstalled. At the HEBT, many water leaks of magnet coils have been found and repaired. Additional beam diagnostic components have been installed in the beam line from ESR to Cave A. The dismantlement of the components in Cave B, to gain space for the future installations of the CRYRING, has almost been completed. In addition all beam diagnostic systems, the vacuum system and all infrastructure installations have been checked and maintained.

Summary

Technical problems (unexpected need for repair of all crane tracks in TR-, TH- and ESR- hall, a cracked weld seam on the ESR-crane) as well as organisational problems (integration of all affected departments, delayed procurement and delivery of components) were the reasons for delays and forced a permanent adjustment of the shutdown schedule. Furthermore we have been faced with a shortage of manpower in all involved departments. About 4 % of the schedules tasks have to be shifted to the next shutdown. To improve the scheduling we will reorganize the structure of the project schedule to provide a better overview. The main work packages of the next break in operation have to be discussed and defined as soon as possible.

* s.reimann@gsi.de
** Expected completion date

Development of a FPGA based PCI-express to optical link interface card, KINPEX

*S. Minami**, *J. Hoffmann, N. Kurz, W. Ott, and S. Voltz*
GSI, Darmstadt, Germany

A new PCI-express (PCIe) to optical link interface card, KINPEX, has been designed and produced to replace a current PCIe card, PEXOR[1]. It provides high speed data transfer from front-end cards to standard personal computers (PC) to support experiments with high data rates at FAIR. Both cards are equipped with a high performance FPGA to control the whole system, a four-lane PCIe bus and four small form-factor pluggable (SFP) transceivers. For the KINPEX card, we have adapted Kintex-7 FPGA from Xilinx corp. for price-performance reason, while SCM40 FPGA from Lattice Semiconductor corp. was chosen for the PEXOR card at 2008. Detailed hardware specification is available from the reference [2].

Figure 1: KINPEX, a PCIe to optical link interface card.

The new FPGA firmware to operate the KINPEX card has been developed. It supports data exchange with a PC via PCIe bus, which is realized with the serial interconnect building block of the FPGA configured by an intellectual property (IP) core from the manufacturer. It is configured with a per lane data rate of 2.5 GT/s to be compatible with PEXOR. The IP core supports the physical, data link, and transaction layers of PCIe protocol and gives an example to process transaction layer packets (TLPs). The example was modified to perform 32-bit memory read/write access to control registers and four 256 KByte dual-port memories (DPMs) prepared for storage of data from SFPs. For the maximum data throughput, the DMA engine developed for PEXOR is utilized for KINPEX [1]. It provides maximum payload size of 128 bytes and performs two modes of data transfer. One transfer mode waits arrival of complete data to the DPMs from SFPs, before it sends data to the PC from each DPM in sequence. The other transfer mode is able to activate only one of the four SFPs, however it performs DMA data transfer via a FIFO memory as soon as stored data reaches payload size of 128 bytes.

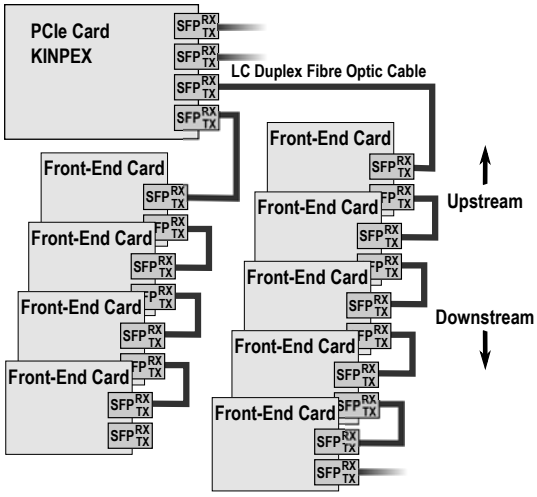

Figure 2: Connection of the PCIe card and the front-end cards.

The firmware supports communication with front-end cards via SFPs with GOSIP (gigabit optical serial interface protocol)[3]. It is a master and slave protocol with two modes of data transfer, address and block mode, and the main feature is that one SFP port of master is capable to control multiple slaves equipped with 2 SFPs. The front-end cards (slaves) can be chained in a way that one SFP of the front-end card upstream can be connected with the other SFP of the one downstream as shown in figure 2. Payload of data is kept as 1.6Gbps per SFP as PEXOR is.

The standard data acquisition (DAQ) system at GSI, Multi-Branch System (MBS) [4], has been upgraded to support the KINPEX cards and the system with the KINPEX card is working stable with expected performance.

References

[1] J. Hoffmann *et al.* GSI Scientific Report 2008, p275

[2] `https://www.gsi.de/fileadmin/EE/Module/Dokumente/kinpex1_pcb15.pdf`

[3] S. Minami *et al.* IEEE Trans. Nucl. Sci., vol. 58, no. 4, pp. 1816-1819, Aug. 2011

[4] H.G. Essel and N. Kurz, IEEE Trans. Nucl. Sci., vol. 47, no. 2, pp. 337-339, Apr. 2000

* s.minami@gsi.de

 doi:10.15120/GR-2014-1-FG-CS-02

Features of the new MBS Production Version 6.2

N.Kurz[1], *J.Adamczewski-Musch*[1], *and S.Linev*[1]
[1]CSEE, GSI, Darmstadt, Germany

Introduction

The general purpose data acquisition system MBS has been used in the past by a vast majority of GSI experiments. It will also be applied by many experiments at FAIR (e.g. NUSTAR) for data taking and for tests of future FAIR detector systems. A new production version 6.2 has been rolled out in 2013 to accommodate the requirements of experiments. Its new features and improvements, like support of new processor boards, PCI Express, Linux, and 10Gbit Ethernet will be described. For detailed information the MBS homepage (www.gsi.de → @work → Experiment-Elektronik → Datenerfassung → MBS) and release notes 6.2 therein can be consulted.

New Features

Linux for PCs: Currently the DEBIAN Linux versions with code names Lenny, Squeeze and Wheezy are fully supported as 32 bit machines. They have been set up to boot and run diskless as all MBS nodes.

10Gbit Ethernet: Due to ever increasing data rates, 10 Gigabit Ethernet has become inevitable and is now supported on PCs for all Linux flavours mentioned above. In a typical MBS setup a data throughput of 700 MB/s could be achieved without further software optimization.

Linux for RIO4 VME processor: Up to MBS version 5.0 LynxOS was the only supported real-time operating system available. Since the existence of LynxOS for future VME processor boards seems not be guaranteed, an effort has been undertaken to run MBS with Linux on the RIO4. A kernel module for the TRIVA VME trigger module has been developed. MBS is now fully supported. Single cycle VME A32D32 read accesses show a 10% higher speed with Linux compared to LynxOS. Network write speed is two times faster on Linux (80 MB/s). MBS template user readout functions are available.

IPV VME processor board: According to the supplier, the VME processor RIO4 will be purchasable for some years, but a follow up model seems not to be available at the time being with the performance characteristics required. In addition, the PPC processor chip utilized on the RIO4 will not be developed further. In a survey, alternative VME processor boards have been assessed.

The IPV 1102 from the company IOxOS has been identified as a candidate for the future. Its heart is a PowerPC P2020 from Freescale. Again a kernel module for the TRIVA trigger module has been developed and the IPC 1102 is now fully integrated into MBS. Simple template MBS user readout functions and VME mapping examples for more advanced VME block accesses are available.

PCI Express based MBS readout systems: Prior to MBS version 6.2, commodity PC hardware was used solely as MBS event-builders. New hardware developments made by CSEE department of GSI (www.gsi.de → @work → Experiment-Elektronik → Digitalelektronik → Module) required to extend the MBS PC capabilities as front end readout processors.

The PCI Express data concentrator board PEXOR and trigger module TRIXOR are the base of this new readout system. LynxOS drivers and Linux kernel modules for PEXOR and TRIXOR, and MBS user readout functions have been developed. They allow to control and readout frontend electronics (FEBEX, GEMEX) connected to PEXOR via optical links.

The TRIXOR has identical functionality as the VME trigger module TRIVA. It is possible to interconnect any number of TRIXOR and TRIVA modules on a common trigger system, to setup highly flexible MBS DAQ systems.

New sorting modes in MBS time sorter process m_to: The MBS time sorter and event-builder task is used to combine data from independent DAQ systems based on time stamp information. Up to now the TITRIS time stamp system developed by CSEE was used for this purpose.

Three new Foreign DAQ systems required to implement three new time stamp sorting algorithms: To combine the PANDA GEM-TPC system with FOPI an algorithm based on COMPASS (CERN) hardware was implemented. The EURICA experiment at RIKEN required an algorithm to combine BIGRIPS and MBS systems with the LUPO time stamper from RIKEN. Finally, AGATA and RISING MBS DAQ was combined using the AGAVA/GTS hardware provided from the AGATA community.

Currently supported MBS processor platforms

```
LynxOS 2.5:          CVC, E7, RIO2, PC
LynxOS 3.1:          RIO3
LynxOS 4.0:          RIO4, PC
Linux Debian   2.6: PC
Linux Debian   3.2: PC
Linux Sugarhat 2.6: RIO4
Linux DENX     3.3: IPV
```

FPGA Hit Finder and Energy Filter for the FEBEX Pipelining ADC

I. Rusanov[1], *J. Hoffmann*[1], *N. Kurz*[1], *S. Minami*[1], *C. Ugur*[1], *and S. Voltz*[1]
[1]GSI, Darmstadt, Germany

The FEBEX board was developed in CSEE Department of GSI. It features 16 differential analog inputs, 16 differential LVDS I/Os (max. 8 outputs) and a serial multi-gigabit connections to the backplane over a PCI Express [1]. The 16 differential analog signals go through 12-bit or 14-bit multi-channel pipeline ADCs with 50 MHz sampling rate.

The FEBEX boards are designed to work with globally triggered DAQ systems by accepting user defined trigger windows. The complete control and readout logic is implemented in a Lattice FPGA. Due to the FPGA's large memory size the trigger window can be set to a maximum of 8000 ADC's samples (20 ns per sample). The trigger window is divided to pre- (up to 2000 ADC's samples) and post- trigger windows, both of them are programmable. The length of the FEBEX data packed depends on the number of hits found and user defined settings. After the trigger's processing the data is moved out in block transfer mode with a rate of up to 2 Gbits per second over copper connections (back plane) and then via optical links to the PEXOR in the DAQ computer.

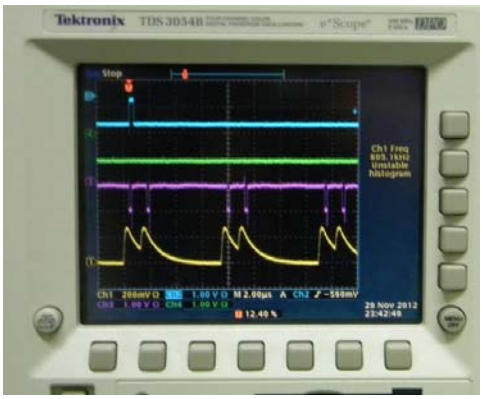

Figure 1: Self-triggering with double pulse detection.

For each channel in the core of the FPGA two methods for "self-triggering" are implemented: 3-steps comparator and Fast Trapezoidal Filter (FTF) for a leading edge selection and double pulse detection. The parameters of the FTF (both average windows and gap between them) are programmable (8 bit with maximal length of 255 ADC's samples). For both methods 12-bit thresholds are implemented for each channel individually. The generated "self-trigger" is sent out to the module for trigger selection and dead-time protection (EXPLODER [1]). This signal can be used as trigger system input.

The implemented FTF gives the system possibility to work in very "noisy" environment and to detect hits with very low amplitude.

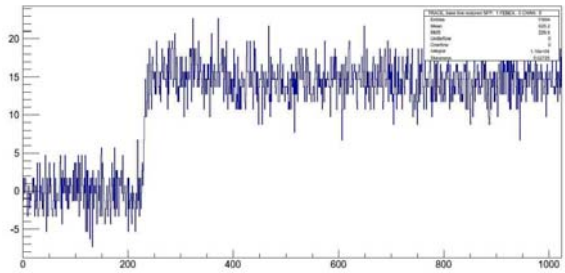

Figure 2: FEBEX signal trace with amplitude of 2 mV.

A new feature of the FEBEX board is the possibility to measure the energy of the differential input pulses. The FPGA's core includes a programmable Energy Trapezoidal Filter (ETF) for each channel (10 bit for each parameters of the ETF). The maximal length of the filter is 1023 ADC's samples.

Each FEBEX board can send out data packets in various formats: only ADCs traces with or without ETF data; summary data packets (measured energy and hit times) and ADCs traces with or without ETF data; only summary data packet and ADCs traces with or without ETF data, in case more than one hit was found in a single channel.

The FEBEX board can be programmed to operate with negative or positive input signals. Its core includes also slow control functionality over the optical link. The implemented SPI interface to the FPGA's flash memory gives the possibility to check and reload the FPGA programming file.

The interface, implemented in the FEBEX broad, is designed to work with Multi Branch System (MBS) data acquisition system [2]. Through the MBS system, via the optical interface, the user has full control over all components of FEBEX: configuration, testing, start/stop of data acquisition, data readout and data logging. The MBS runs under the operating system Linux and LynxOS and supports various hardware setups. Therefore, for each user defined hardware setup, the MBS data acquisition software requires user input data, describing the hardware setup and configuration parameters.

References

[1] www.gsi.de/fileadmin/EE/Module

[2] BS N.Kurz, The general purpose data acquisition system MBS, IEEE Trans. Nucl. Sci., vol. 47, no. 2, p. 336, Apr. 2000.

 doi:10.15120/GR-2014-1-FG-CS-04

Status of the software development for the FAIR accelerator control system

J. Fitzek[1], *S. Jülicher*[1], *and U. Krause*[1]
[1]GSI, Darmstadt, Germany

Introduction

The FAIR accelerator control system is currently being developed and the first prototype will be tested at CRYRING. The core parts are developed in close collaboration with CERN, Geneva, and the current focus lies on their enhancement in order to fully support the demanding requirements for FAIR. Significant progress could be achieved in the basic major frameworks: LSA for settings generation, CMW/RDA for communication and FESA for front-end software. Besides these activities, work started to support the upcoming commissioning of CRYRING. This report summarizes the developments during the year 2013.

FESA Framework

Software for the Front-End equipment control computer will be developed using the FESA (Front-End Software Architecture) framework [1], which was originally established by CERN. In a collaboration between CERN and GSI a complete redesign of the framework has started a couple of years ago. The new version, FESA-3, is now completed to be used in a productive environment. The classes for the test-operation of the proton linac ion source were developed with FESA-3 at GSI.

The new FESA-3 framework provides site-specific extensions to adapt and enhance the framework to the needs of the contributing institutes. As part of the adaptation, a set of GSI specific properties was defined and a preliminary connection to the future GSI timing system was integrated.

Not part of FESA, but tightly integrated, is the CERN network communication CMW/RDA (Common MiddleWare / Remote Device Access) framework. The framework, originally based on CORBA, is reworked using ZeroMQ for internal communication. GSI joined the development in 2013 to collaborate in all main parts. The new version is now stable and ready to be integrated in FESA-3.

LSA Framework

As basis for the settings management framework for the FAIR accelerator control system, the CERN LSA (LHC Software Architecture) framework [2] is used. Since 2007, a collaboration with CERN has been set up and the framework is being enhanced to support FAIR operations.

This year, the splitting of the framework components into generic functionality and institute specific parts was finalized in cooperation with CERN. A major refactoring of the framework took place during the long shutdown (LS1 at CERN) to achieve a clean and state of the art framework, following modern software architecture principles. Institute specific components were refactored according to these changes.

Concepts for enhancing the LSA framework to support flexible beam operations for FAIR have been worked out and first development started. This will enable the framework to support scheduling of parallel beams and the coherent calculation of machine settings throughout the facility.

To aid the machine modeling for CRYRING [3] and for future machines, tool development started to allow more efficient modification of the accelerator models present in LSA for new accelerators.

Other Activities

In addition to framework developments, first application development has started to support the upcoming commissioning of CRYRING in 2014. A new Device Control program is being developed as part of the new FAIR accelerator control system for device diagnosis and exploitation.

A small packaged version of the FAIR control system was developed that will be used at CEA Saclay for commissiong and test operation of the FAIR proton source. It includes FESA classes for controlling the equipment as well as an application to control and monitor the proton source. This application will be the basis for a general source control program for FAIR.

The names of the existing GSI devices were enhanced to achieve a common naming schema for GSI and FAIR devices. These changes were implemented in the present control system as a precondition for integration with the future FAIR control sytem.

Outlook

For 2014, the main focus of the control system software development will be the commissioning and operation of the CRYRING, which will be used as test bed for the new control system for FAIR.

References

[1] A. Guerrero et al., “CERN Front-End Software Architecture for Accelerator Controls”, ICALEPCS’03

[2] G. Kruk et al., “LHC Software Architecture LSA – Evolution Toward LHC Beam Commissioning”, ICALEPCS’07

[3] D. Ondreka et. al, “Project Status of the New Setting Generation System for GSI and FAIR”, this report

Project status of the new setting generation system for GSI and FAIR

D. Ondreka, I. Kraus, H. Liebermann, S. Reimann, and B. R. Schlei
GSI, Darmstadt, Germany

The progress made on the new setting generation system for FAIR and GSI regarding machine modeling and application development is reported. Developments of the LSA framework [1] are presented as part of the report on the development of the FAIR control system software [2].

Machine modeling

A major topic regarding machine modeling was the development of a generic model for longitudinal bunch manipulations in synchrotrons such as bunch merging and batch compression. These manipulations are implemented by operating the RF system at multiple harmonics, resulting in complex patterns of variation for frequency, amplitude, and phase of the individual cavities. An algorithm was implemented which allows the definition of any combination of merging and compression steps in any machine.

As an example, the proton stacking and compression scheme in SIS100 is described: The proton beam is accumulated by filling 4 out of 10 buckets with 4 injections from SIS18. After that, a combination of merging and compression steps is applied to gather the complete beam in a single bunch at harmonic number 5. The scheme uses two groups of RF cavities. Fig. 1 shows the temporal evolution of RF voltage and harmonic number h for one cavity of each group during this process.

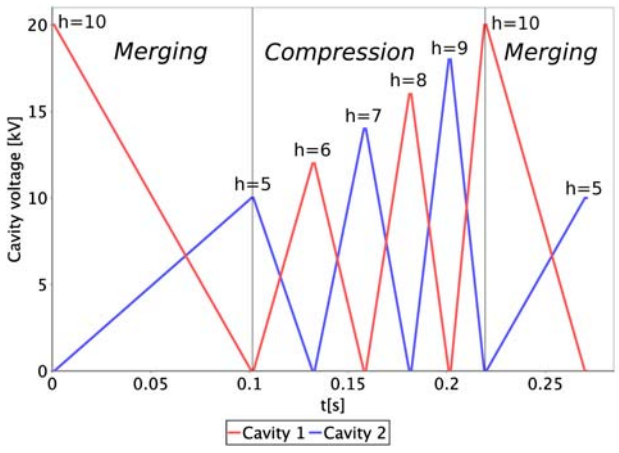

Figure 1: RF voltages for the creation of a single proton bunch in SIS100 at the injection level.

Another important topic concerned the implementation of a machine model for CRYRING, which will be controlled by a prototype of the new FAIR control system. In 2013 data on the ring hardware, such as power supply properties and magnet calibration data, and the ion optical layout, was imported into the LSA database and a hierarchy of relevant parameters created. Operational cycles were defined and corresponding set values calculated for all devices, starting from physics quantities like beam energy.

Fig. 2 displays the current in the main bending magnets for the acceleration of a proton beam from 300 keV to 30 MeV. In the second half the current is set back to the injection level again.

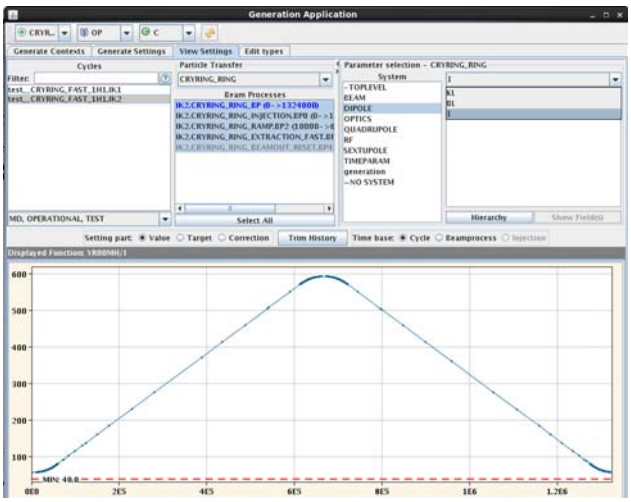

Figure 2: Control system application displaying the current in the main magnets for a CRYRING cycle.

Applications

The development of the Java version of MIRKO was continued. On the one hand, the functionality for its use as an online steering tool was implemented. On the other hand, significant effort was put into the further integration into the LSA development and build environment.

Another important activity concerned the adaptation of the application YASP from CERN for closed orbit correction in rings to the FAIR control system. This application is intended to become a standard tool in FAIR. This work will be continued in the coming year.

References

[1] G. Kruk et al., "LHC Software Architecture LSA – Evolution Toward LHC Beam Commissioning", ICALEPCS'07.

[2] J. Fitzek et al., "Status of the software development for the FAIR accelerator control system", this report.

 doi:10.15120/GR-2014-1-FG-CS-06

SCU system goes productive

M. Thieme[1], *W. Panschow*[1], *and S. Rauch*[1]
[1]GSI, Darmstadt, Germany

INTRODUCTION

The SCU (Scalable Control Unit), the future standard controller and timing receiver of the FAIR control system, is composed of a base board, equipped with a COM express CPU extension and a bus system for a variety of slave boards. A powerful FPGA (Field Programmable Gate Array) on the SCU base board and the module concept makes the platform highly flexible and scalable. A broad range of digital and analog IO functions will be provided by a set of slave boards. The SCU also implements the timing receiver for the GMT (General Machine Timing) in FAIR. The SCU is now used for the first time at CRYRING.

SCALABLE CONTROL UNIT (SCU)

The SCU (Figure 1) is mechanically a stack of up to three separated boards. There is the carrier board with an Arria II FPGA, two Small Form-factor Pluggable (SFP) slots, DDR3 RAM, parallel flash and a parallel bus (SCU bus) for controlling up to 12 slave devices. In addition the carrier board is equipped with White Rabbit [1] circuitry to realize the functionality required of the timing receiver for the GMT. A COM Express™ module with an Intel Atom CPU is mounted to the carrier board. It has Ethernet, USB and PCIe interfaces.

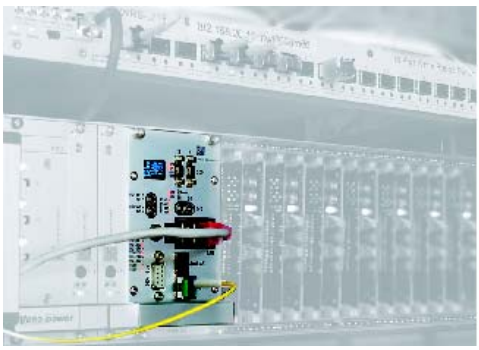

Figure 1: SCU with MIL-STD-1553 Extension

An optional extension board can be connected to the carrier board for dedicated hardware solutions especially for fast digital IO or for backwards compatibility that runs for example a MIL-STD-1553 based field bus interface. The SCU works as a front-end controller. On one side it is connected to the control system via Ethernet, on the other side it controls slave devices over the SCU bus.

THE SCU AS TIMING RECEIVER FOR THE GMT

As timing receiver it receives sub ns accurate timing information over a White Rabbit link, connected to an WR Switch. The White Rabbit receiver in the FPGA runs the Precision Time Protocol (PTP) in software on a LatticeMico32 (LM32) soft-core CPU. It is able, to do time stamping and generate pulses with a precision of 8 ns. With extra io hardware, a precision in the low ps range is possible.

SCU BUS SLAVES

The SCU communicates with devices via slave cards on SCU bus. On CRYRING different devices with variety of interfaces have to be served. For this reason a modular concept for slave cards were developed (Figure 2). This concept enables the provision of a wide range of cost-effective analog and digital interfaces. The required functionality is provided by a common base module with a powerful FPGA. The different physical interfaces are connected via interface modules. All interface modules use the same base module. A unique hardware identifier allows the auto-configuration of the firmware.

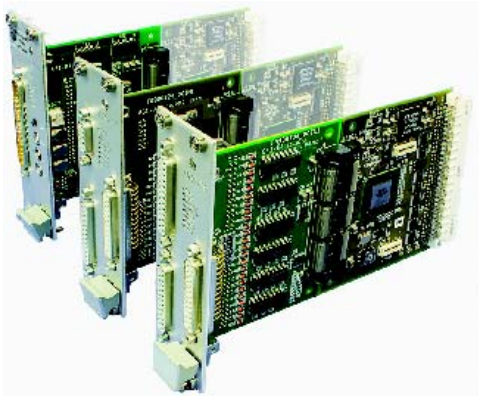

Figure 2: Modular concept for slave cards

References

[1] Moreira, P.; Serrano, J.; Wlostowski, T.; Loschmidt, P.; Gaderer, G.; , "White rabbit: Sub-nanosecond timing distribution over ethernet" Precision Clock Synchronization for Measurement, Control and Communication, 2009. ISPCS 2009. International Symposium on , vol., no., pp.1-5, 12-16 Oct. 2009

Paving the Way for the FAIR General Machine Timing System

D. Beck[1], J. Adamczewski-Musch[1], J. Bai[2], R. Bär[1], J. Frühauf[1], J. Hoffmann[1], M. Kreider[1], N. Kurz[1], C. Prados[1], S. Rauch[1], W. Terpstra[1], S. Voltz[1], and M. Zweig[1]

[1]GSI, Darmstadt, Germany; [2]Goethe Universität Frankfurt, Germany

Abstract

The task of the General Machine Timing system (GMT) is the hard real-time control of the GSI and FAIR accelerator complex with sub-ns precision. This is achieved by a distributed event generation system based on the notion of time in the facility. The prime features are time-synchronization of 2000 nodes using White Rabbit Precision-Time-Protocol (WR-PTP), distribution of International Atomic Time (TAI) time stamps, generation of trigger events for synchronization of equipment and providing infrastructure for common services of the accelerator control system. During the past two years, the foundations of the GMT have been specified, designed and implemented.

Introduction

The GMT is based on a common notion of time of all connected nodes, provided by WR-PTP [1]. A dedicated network based on Ethernet and dedicated WR switches distributes the commands broadcasted by a data master to all Timing Receivers (TR). Relevant commands are decoded and enqueued for timely execution. On time, none, one or more specific actions depending on the local configuration of the TR are executed. A central clock master serves as grand-master clock to which all nodes in the WR network synchronize their clock, phase and time. As the GMT is a time based system, the precision for synchronizing actions depends only on the quality of clock and phase synchronization via WR-PTP and not on the propagation time of commands distributed by the data master.

Hardware

More than 2000 TRs will be connected to the timing network. About 1200 Scalable Control Units (SCU) with integrated TR functionality will be the prime Front-End Computers (FEC) for equipment control and have been developed by the hardware group CSCOHW of the control system department [2]. About 500-1000 dedicated TRs of different form factors are required by beam instrumentation and Data AcQuisition (DAQ). So far, TRs in the three form factors PCIe, VME and stand-alone have been developed in a cooperation between the departments of Controls and Experiment-Electronics. As all TRs are derived from the embedded TR in the SCU, they are based on Field Programmable Gate Arrays (FPGA) from the Altera Arria® families and share many identical electronic components. The fundamental design principle is to maximize re-usability and similarity only adapting the host-bus bridge and I/O for each form factor.

Gateware

Code for FPGAs is called gateware. Although GSI's and CERN's TRs are based on FPGAs from different manufacturers, the gateware is manufacturer independent to a large extent. The concept is to separate functionality into different Intellectual Property (IP) cores which all have an interface to the System-on-Chip (SoC) Wishbone bus. All IP cores represent Wishbone devices that are interconnected via Wishbone crossbars. The crossbars do not only provide clock domain crossings but also allow to connect form factor specific Wishbone devices to a standard architecture common to all TRs. Each form factor needs to implement its own host-bus to Wishbone bus master bridge. The connection to the WR network providing a network interface and a WR link is always encapsulated in IP cores behind a dedicated Wishbone crossbar. All Wishbone devices provide Self-Describing Bus (SDB) records, that allow querying bus-addresses, vendor and product information. Every gateware includes at least one Lattice Micro 32 CPU (LM32) softcore [3] that allows to implement application specific firmware. Gateware and firmware is developed in collaboration with CERN in the framework of the Open Hardware Repository [5].

Driver

The main idea is to extend to SoC Wishbone bus outside the FPGA using the EtherBone protocol [4]. As EtherBone can run over any serial protocol, it only requires a form factor specific driver in the kernel implementing an interface to the Wishbone bus master interface on the TR's FPGA. This allows EtherBone to connect to the Wishbone devices of the TR over any host-bus to Wishbone bus master bridge and even network protocols such as UDP and TCP/IP.

Status

White Rabbit Network

15 production quality WR switches [6] have been obtained in 2013. All of them are in operation and work reliably with respect to their hardware. However, gateware and software are still missing some features. A clock master switch is already installed in the final position in the existing building BG at GSI. From here, already five locations

 doi:10.15120/GR-2014-1-FG-CS-08

at the existing facility are connected via optical fiber links. A part of the links will serve to connect equipment of the existing facility to the new timing system. Another part is used for testing equipment or to gain experience with long term operation of switches and equipment. Via appropriate patches, some dedicated links of up to five kilometer length have been set-up. Moreover, several kilometers of fiber have been exposed to environmental conditions on a building roof. Results of long term tests on WR clock and phase synchronization including multiple layers of switches are very promising and presented elsewhere [8].

Data Master

The data master schedules actions by broadcasting commands to the TRs via the WR network [9]. A first data master has been set-up based on a SCU and includes dedicated firmware in a LM32 softcore. The firmware generates the commands that are broadcasted to the nodes. It can be configured and controlled via a dedicated API which is used by a Front End System Architecture (FESA) class. Since May 2013 the data master is in operation successfully with very little downtime. This data master serves as a proof of principle and will be replaced by a parallel multicore version in 2014.

Timing Receivers

The focus of the past two years has been the development of the TRs in a joint effort of different groups. With respect to hardware, work has been carried out by CSCOHW (SCU) [2] and CSCOEE (VME, PCIe, standalone). CSCOTG has concentrated on gateware and software. The driver concept allows to access the TR from Linux user space via the EtherBone protocol in a transparent way independent of the host bus bridge - the same front-end software for equipment control can be used on different FECs independently of the form factor of the TR. As a proof-of-principle, functionality dedicated to the timing system has been integrated with FESA. This allows a FESA class subscribing to a so-called event-source within FESA and receiving a notification upon an event.

For the GMT, a main component of the gateware is the Event-Condition-Action (ECA) unit. It is a complex filter, comparing the *event* of a command received from the data master against *conditions* pre-configured by the TR's user. In case of a match, a pre-configured *action* will be scheduled for timely execution in a so-called action channel. On-time, the action channel triggers a receiving component. Here, the action such as IRQ generation, digital output or equipment action such as ramping a magnet is executed. The precision for triggering is 8 ns due to the 125 MHz system clock. If supported by the receiving component, an additional fine-delay feature allows more precise timing. All supported form factors allow fine-delay of 1 ns already in the FPGA. As a perspective, further refinement by PLL-phase-shifting (125 ps) or delay chains in transceivers of differential output pins (25 ps) might be possible inside the FPGA without the need of external fine-delay electronics.

Next to timely execution of actions, the ability for precise time stamping of triggers received by a TR is another key requirement to the GMT. As all TRs share a common notion of time, a timestamp latch unit is common to the gateware of all TRs. This feature has already been integrated by the Multi Branch DAQ System [7] and successfully tested with the form factors PCIe, VME and standalone over many weeks [8].

Conclusion and Outlook

Significant progress has been made on the hardware, gateware and software of the TRs. A timing network spanning the existing facility has been set up with about 15 WR switches. A first timing system has been set up in May 2013. Key components like the ECA unit, the Wishbone SoC architecture, the driver concept and the communication library EtherBone have been developed and implemented.

The next step is to set up the GMT for the recommissioning of CRYRING at GSI. Here, about 50 TRs are required for synchronization of equipment of the control system and beam instrumentation. At the beginning the GMT will only provide basic features. CRYRING serves as a test ground for the control system as a whole. This is important for validating the concepts, gaining experience of operation under on-line conditions and assures the quality of the components developed.

References

[1] J. Serrano, P. Alvarez, M. Cattin, E. G. Cota, P. M. J. H. Lewis, T. Włostowski et al., "The White Rabbit Project" Proceedings of ICALEPCS (2009) TUC004, Kobe, Japan.

[2] S. Rauch et al., "Performance Tests of the Standard FAIR Equipment Controller Prototype", Proceedings of ICALEPCS (2011) WEPMN018, Grenoble, France.

[3] W. W. Terpstra, "The Case For Soft-CPUs in Accelerator Control Systems", Proceedings of ICALEPCS (2011) THCHMUST05, Grenoble, France.

[4] M. Kreider et al., "EtherBone - A Network Layer for the Wishbone SoC Bus", Proceedings of ICALEPCS (2011) THCHMUST05, Grenoble, France.

[5] http://www.ohwr.org.

[6] http://www.ohwr.org/projects/white-rabbit/wiki/Switch.

[7] H. G. Essel et al., "The New Data Acquisition System at GSI", IEEE Trans. of Nucl. Science, Vol.43, No.1 (1996) 132 - 135.

[8] N. Kurz et. al, "White Rabbit Applications for FAIR Experiments", this report.

[9] M. Kreider et al., "The FAIR Timing Master: A Discussion of Performance Requirements and Architectures for a High-precision Timing System", Proceedings of ITA (2013), Wrexham, United Kingdom.

White Rabbit Applications for FAIR Experiments

N.Kurz[1], *J.Adamczewski-Musch*[1], *J.Frühauf*[1], *J.Hoffmann*[1], *D.Beck*[1], *M.Kreider*[1], *C.Prados*[1], *S.Rauch*[1], *W.Terpstra*[1], *and M.Zweig*[1]

[1]GSI, Darmstadt, Germany

Introduction

A White Rabbit (WR) based timing system will be used at FAIR as a field bus for accelerator controls. In addition WR Timing Receivers (WRTR) are required by FAIR experiments for the synchronizaton of independent detector sub-systems. For this purpose hardware latching of time stamps on WRTR has been implemented. A test bed has been set up to check this functionality. Furthermore it has been investigated if a WR synchronized 200 MHz clock can be used as reference for high precision time-of-flight measurements (TOF) with electronics resolution in the order of 10 ps RMS between independently operated and possibly far distant detector systems.

White Rabbit Timing Receivers (WRTR)

The development of the WRTR is a joint effort of the CSEE and CSCO departments of GSI. CSEE designed and produced the WRTR, CSCO developed and implemented the WR timing protocols on the FPGAs of the WRTR, including Linux kernel modules and libraries for user applications. Finally the adoption of the WRTR for the MBS data acquisition system and an additional VME driver development was made by CSEE.

Three types of WRTR boards have been investigated: The PCI Express based PEXARIA5, The VME board VETAR2 and the standalone module EXPLODER2. All boards can be accessed through Etherbone via USB and the WR network. In addition the PEXARIA5 can be accessed for high speed DAQ applications via PCI Express - and the VETAR2 via the VME protocol. It is important to note, that all WRTR types provide identical functionality.

All WRTR are connected to the WR network and their time base is syntonized and synchronized using the White Rabbit Precision Time Protocol (WR-PTP) implemented in the WRTR.

Global - versus Local Triggers

Basically two types of detector systems at FAIR have to be synchronized with the WRTR. The first and traditional type is readout at the occurrance of a single (global) trigger signal, producing a so called (sub)event. In the second type, often stated as triggerless, each channel is readout if a certain individually threshold is exceeded. Thus, these kind of systems produce a stream of data, whereas the entity of an event is a priori not present any more.

Synchronization of globally triggered, but independent sub-systems can be facilitated by latching time stamps in all sub-systems at the occurrance of the global triggers. By requiring time stamp differences to be inside an adjustable interval, data from different sub-systems can be connected in the data analysis. Synchronizing triggerless and/or globally triggered sub-systems works according the the same principle, but time stamp comparisons must be made for each individual channel or possibly groups of channels.

All these requirements can be provided with the WRTR. Synchronization of triggerless systems with WRTR is prepared and needs to be tested. It is not covered in this report.

Synchronizing Globally Triggered Systems

For this purpose a specified input channel on each WRTR is connected to a FIFO in its FPGA, where time stamps are stored and can be read out. Dead time protected and accepted global trigger signals are used to latch time stamps. The time stamps itself are 64 bit counters, currently with a granularity of 8 ns, referring to the 125 MHZ WR clock

A test system consisting of 4 independent MBS subsystems and all types of WRTR described above has been set up. Comparing time stamps differences of all 4 subsystems, a precicon of 5-8 ns (RMS) could be achieved in long term measurements over weeks.

High Precision TOF with WRTR

The WR-PTP protocol allows the adjustment of the 125 MHz WR clock of the WRTR in the sub nano second regime. Therefore it has been anticipated as reference clock for TOF measurements in the ps range. Since the VME TDC VFTX developed at CSEE requires a 200 MHz clock, a 200 MHz clock was derived from the native 125 MHZ in the FPGA of all types of WRTR and fed out. Another MBS test systems with up to 4 WRTR connected in various topologies to the WR network has been set up. The 200 MHz clock was fed into individual VFTX modules. A common reference signal was fed to all VFTX and their measured time differences estimated with a rate of 25 KHz. An intrinsic precision of 15-20 ps RMS between pairs of WRTR clocks have been observed. Long term tests revealed drifts in a band of 40-50 ps RMS for the differences of the reference signals. These results do not meet the requirements yet, but amongst others, possible improvements for the clock generation hardware have been identified.

 doi:10.15120/GR-2014-1-FG-CS-09

The credit-card sized, general purpose controls platform: HadCon2

P.Zumbruch[1]*, M.Traxler*[1]*, and M.Pligouroudis*[1]
[1]GSI, Darmstadt, Germany

Introduction

The HadCon2 (`http://wiki.gsi.de/EE/HadCon2`) is a low-cost, credit-card sized, general purpose I/O module for detector and experiment controls as well as for small data acquisition systems.

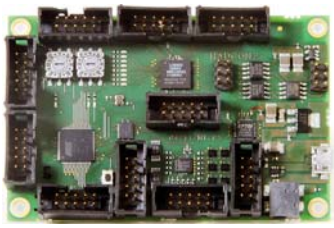

Figure 1: HadCon2

It is the successor of the discontinued first version HadCon a.k.a. HadShoPoMo.

The module has an ATMEL AT90CAN128 microcontroller providing a multitude of connectivity:

- I^2C (8-fold multiplexer, 4 internally used)
- 6 channel 1-wire master, slew-controlled 1-Wire Edges
- 8 channel 8bit DAC, galvanically isolated CAN-high speed transceiver
- 8 channel 10 bit SAR ADC, single ended, or up to 4 differential
- byte oriented SPI interface
- in total up to 53 programmable I/O lines

and

- a Lattice MachX02 FPGA for fast data processing tasks.

In contrast to its precursor HadCon, in favor of a more open access and long term maintenance, it doesn't have any CPU on board, but a USB connector to directly allow communication with any type and size of computer (e.g. standard PC, Raspberry Pi, DreamPlug, ...) having an USB port on one side and at the other end the microcontroller and the FGPA.

The communication is based on an ASCII based protocol API in view of easy implementation in detector control systems like e.g. EPICS[4] and LabVIEW[5] and easy control via the command line and scripts with human readable commands to communicate with all the interfaces available.

Use Cases

Originally developed for a power monitor board (HadShoPoMo) for HADES[1] the HadCon familiy serves/will serve many different applications and collaborations:

- **HADES MDC/RPC detector controls** - EPICS controlled 1-wire devices: temperature sensors, switches, ADCs.
- **HADES RPC dectector** - EPICS controlled CAN-based gas system
- **HADES RICH detector** - EPICS monitored ($10Hz$) current via internal ADC, in progress
- **PANDA APFEL ASIC[2]** - EPICS controlled, bit-banged interface to the SPI-like APFEL ASIC, in progress
- **NeuLand, R3B[3]** - Windows LabVIEW or EPICS controlled I^2C interface for TRIPLEX[6] front end control, in progress
- **FPGA projects**
  - **Waveform Generator** - FPGA based Waveform Generator, controlled by the HadCon2's API
  - **FPGA based 1-wire ADC** - 6 channel, max. 12bit ADC to be accessed by 1-Wire protocol, in progress.

References

[1] HadShoPoMo, `http://tinyurl.com/kvcbw5t`

[2] P. Wieczorek and H. Flemming, "Low Noise Preamplifier ASIC for the PANDA EMC", IEEE Nuclear Science Symposium 2010, Knoxville, USA, NSS-N47-74, Published in NSS/MIC, 2010 IEEE DOI: 10.1109/NSSMIC 2010.5873982 Page 1319 - 1322

[3] R3B collaboration, `http://www.gsi.de/r3b`

[4] Experimental Physics and Industrial Control System, `http://www.aps.anl.gov/epics`

[5] LabVIEW, National Instruments, `http://www.ni.com/labview/`

[6] "TRIPLEX, an Upgrade for the TACQUILA System", K. Koch et al, GSI Sci. Rep. 2010, PHN-IS-EE-07, p. 235.

The GSI Event Driven TDC ASIC GET4 V1.23

H. Flemming[1] *and H. Deppe*[1]
[1]GSI, Darmstadt, Germany

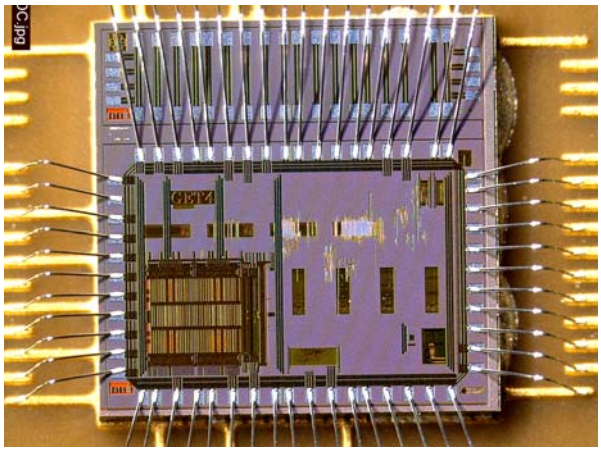

Figure 1: Die Picture of the GET4 ASIC.

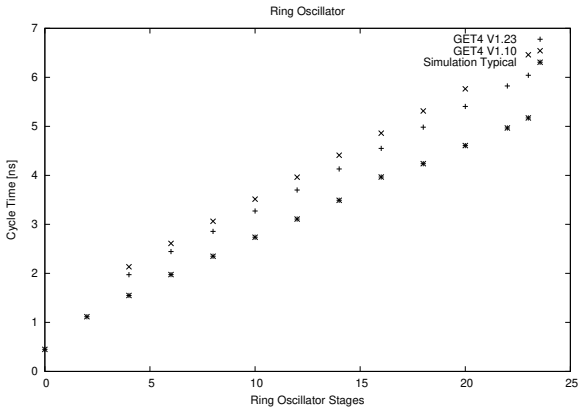

Figure 2: Measured and simulated cycle time of the internal ring oscillator.

Introduction

In the scientific report 2012[1] first results of the GET4 V1.10 ASIC the first fully equiped event driven TDC prototype taped out in 2012 (see figure 1) are reported. The excellent performance regarding timing precision was reported but also some minor bugs are mentioned.
To fix these bugs in 2013 a second iteration was taped out and tested. First results are presented in this report.

Logic Revision

Two faults of the read out logic have been found in GET4 V1.10[2]. A *sync*-flag in the epoch events was not set correctly and a setup and hold timing violation leads to data errors in the 24 bit read out mode with data rates below 160 MBit/s. To clear these faults the struture of the 24 bit serialiser was modified and the vhdl source code was corrected. Tests of GET4 V1.23 have shown that the *sync* flag now is set correctly and the 24 bit serialiser works correctly at all data rates.

Process Variations

The main problem of GET4 V1.10 was caused by process variation during the MPW run. The internal delays were significantly larger than in simulation and in previous ASICs. Figure 2 show the measurement results of a ring oscillator with configurable length which is integrated on the GET4 ASIC in comparison to simulation results in typical corner.

The measured cycle times of GET4 V1.10 as well as of GET4 V1.23 are significantly larger than the simulated times. The increment per stage of cycle times of V1.10 is about 6 % larger than that of V1.23. This unusual large delay of V1.10 caused several problems in getting the DLL into lock state as well as in data transfer from the TDC core to the read out logic. These problems are discussed in detail in [2]

To overcome the last mentioned problem a configurable delay element was integrated in the data transfer clock to adjust the clock phase for best fit with process speed. An increase of core voltage by 10 % as it was needed for operation of GET4 V1.10 is no longer required for GET4 V1.23.

Outlook

In the meantime also the TDC perfomance of GET4 V1.10 could be confirmed with GET4 V1.23. For detector tests with RPC timing detectors additional GET4 V1.23 ASICs will be bonded on PCBs to test the performance of the GET4 TDC in the 2014 GSI beam time as well as in long term cosmic tests.

References

[1] H. Flemming, H. Deppe, “The GSI Event driven TDC GET4 V1”, GSI Scientific Report 2012

[2] H. Flemming, “Results of GET4 Tests Known Bugs and Performance”, Talk given in the weekly CSEE meeting https://wiki.gsi.de/foswiki/pub/EE/EEMeetVortragArch/GET4V1.10Bugs.pdf

 doi:10.15120/GR-2014-1-FG-CS-11

Web interface in DABC

S.Linev[1]
[1]GSI, Darmstadt, Germany

User interface for DABC

DABC [1] is general-purpose DAQ framework, developed in GSI since 2007 and used in different applications. Because it cooperates with many other components (like slow control systems, other DAQ systems, online analysis), DABC requires a simple and flexible user interface for monitoring and control. Decision was taken to evaluate web protocols for implementing a user interface via normal web browser. As a starting point for development, JSRootIO project was considered.

The JSRootIO project

The JSRootIO [2] project is a new development of ROOT [3] team. Objects like histograms or graphs, stored in binary ROOT files, can be read and displayed with all modern web browsers. Usage of JavaScript allows to build interactive and very informative graphical elements.

Several important improvements were done to increase flexibility and usability of the JSRootIO graphics. A context menu was implemented, where convenient commands are provided: switch for lin/log axis, changing of draw options, toggle statistic box. Drawing and update of histogram statistic box was implemented - it is especially important for the case when histogram content is regularly updated. Also a significant performance improve (by factor 10) was achieved. At its present state JSRootIO allows to insert JavaScript-base ROOT graphics in arbitrary HTML page and provides look-and-feel of the original ROOT graphics.

A main disadvantage of JSRootIO is that it works only with ROOT files. This makes it difficult to use it for online tasks, where many objects should be frequently updated.

HTTP server in DABC

Instead of creating temporary files for online monitoring, one could provide specialized HTTP server delivering objects data directly to the browser. Mongoose [4] embeddable web server was chosen as basis for implementing http server in DABC. Mongoose implements basic web protocols and via callback functions provides possibility to construct user-defined response on the HTTP requests.

Specialized hierarchy of objects was introduced in DABC, where different kinds of data can be registered. Main aim of hierarchical organization - provide structural access to user-defined data. One could compare this hierarchy with file system - different sub-folders correspond to different parts of a big system, and files represent some parameters or objects. As response on HTTP requests, DABC server returns hierarchy descriptions (in XML files) or binary data from registered elements.

JavaScript code on the browser side interprets this hierarchy description and creates tree view, seen on the left side of Figure 1. On the right side of the web page selected items are displayed. On the example figure these are histograms, displayed using JSRootIO graphics. Also ratemeters and simple text output are supported. When monitoring is enabled, object content (histograms, ratemeters) will be updated regularly. It is possible to extend code for displaying of any user-defined kind of data.

As a result, HTTP server in very generic way provides direct access to the information from arbitrary DABC-based application. Such information can be explored, displayed and monitored in any modern web browser. No any intermediate files are necessary.

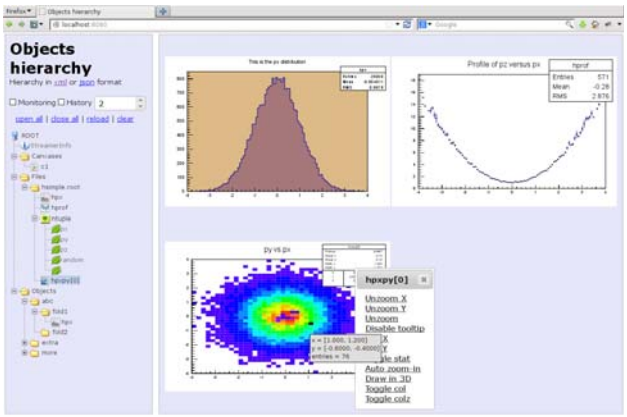

Figure 1: Web interface for ROOT application

FastCGI interface in DABC

FastCGI [5] is a protocol for interfacing interactive programs with standard web servers (like Apache or lighttpd or many others). Using FastCGI, one benefits from standard software and could integrate online applications into existing web infrastructure. FastCGI server was implemented for DABC and provides similar functionality as mongoose-based http server.

Monitoring of ROOT applications

The combination of DABC as web server and JavaScript code in web browser allows to implement live monitoring of arbitrary ROOT application. With a few function calls any ROOT-based application can start HTTP server and publish various objects like histograms or graphs. Figure 1 shows browser with several histograms, produced by running hsimple.C macro from ROOT tutorials.

In Go4 [6] production release 4.6.0, DABC-based HTTP server is also provided. Without modifications any existing go4-based analysis can start a web server, where all histograms, graphs, canvases and trees are available for display. One can also browse parameters and events objects members. Moreover, via a command interface one could suspend/resume analysis execution or clear histograms content by pressing button in the browser window.

Unified interface for many components

DABC provides flexible mechanisms to integrate different kinds of data into the framework - it could be raw data from front-ends, but also information from slow-control systems. For instance, plugin for MBS [7] can retrieve both raw lmd data and statistic information from arbitrary number of MBS nodes. Or FESA [8] plugin can acquire preselected subset of records from accelerator control system. Via unified HTTP interface all these kinds of information can be provided to the user.

With HTTP server one could also control DABC applications and all its components. The user can define commands, which are published via web interface in the browser. Typical use-cases: start/stop file writing, toggle logging mode, reset counters, and so on. Of course, all these commands can be protected from unauthorized use.

DABC allows to run many agents (slave applications), collecting information from different sources. HTTP server, running on the master node, will provides seamless access to data from all agents. This allows to build user interface for distributed (running on many nodes) and heterogeneous (acquiring different kinds of information) systems.

Conclusion

The web interface in DABC provides a unified view for data from many different frameworks like ROOT, Go4, MBS, FESA or DABC itself; support for EPICS and DIM is in development. Web interface could be used on many computing devices and typically does not require any additional software installations - just a normal web browser. The developed interface can be directly used with arbitrary Go4-based analysis; with minimal efforts it can be enabled for any ROOT-based application. Current DABC version 2.6 with the web interface was released in November 2013 and is available on the project home page [9].

References

[1] S. Linev, J. Adamczewski-Musch and P. Zumbruch, “Status of data acquisition software DABC”, GSI Scientific Report 2011 (2012) p. 64

[2] B.Bellenot, S.Linev, JSRootIO project, Journal of Physics: Conference Series, CHEP 2013 proceedings (submitted)

[3] ROOT project, http://root.cern.ch

[4] Mongoose embaddable web server, https://github.com/cesanta/mongoose

[5] FastCGI protocol, http://en.wikipedia.org/wiki/FastCGI

[6] Go4 project, http://go4.gsi.de

[7] MBS DAQ system, http://daq.gsi.de

[8] Front-End Software Architecture (FESA), https://www-acc.gsi.de/wiki/FESA

[9] DABC homepage, http://dabc.gsi.de

 doi:10.15120/GR-2014-1-FG-CS-12

POLAND - Low Current Profile Measurement Readout System

S. Löchner[*1], *J. Adamczewski-Musch*[1], *H. Bräuning*[2], *J. Frühauf*[1], *N. Kurz*[1], *S. Linev*[1], *S. Minami*[1], *and M. Witthaus*[2]

[1]GSI Darmstadt, Experiment Electronics (CSEE); [2]GSI Darmstadt, Beam Instrumentation (LOBI)

Abstract

The development of a 32 channel readout system for low-current profile measurements called POLAND (Profile Acquisition Digitiser) was done in collaboration between the Beam Instrumentation (LOBI) and the Experiment Electronics (CSEE) departments. This electronic system is capable to read out beam diagnostic devices like Secondary Electron Monitor (SEM)-profile grids, Multi-Wire Proportional Chambers (MWPC), Ionisation Chambers or similar devices of the future FAIR accelerator system. Transverse beam profiles with a time resolution down to the microsecond range can be measured with POLAND.

After intensive tests with a prototype version in recent years[1], the complete readout system, close to the final version, has been built in 2013. It contains the current-to-frequency converter units based on the QFW ASIC[2], the logic unit based on an FPGA and an optical readout for data transfer to a host PC, mounted all together in a 1U 19" rack crate. The system is designed to be read out via FESA or MBS, two standard data acquisition systems for FAIR. Together with different diagnostic systems, POLAND was tested in 2013 at different beam-tests at COSY and HIT.

The POLAND readout system

The developed hard- and software is described in [1] and in detail in [3]. The main changes from the previous version are: a compact but maintenance-friendly design, higher time resolution during the beam pulse measurement, and a daisy chain readout for easy expansion of the number of readout channels. A photography of a POLAND readout unit is shown in Fig. 1.

The system has been intensively tested in laboratories of CSEE and LOBI. During this time the FPGA software has been improved and further developed.

A first test under beam conditions was done in summer 2013 at COSY in Jülich. Here the new electronics was used for monitoring the 2 GeV proton beam. A significant improvement in beam analysis compared to existing systems was achieved. Also the time-resolved beam profile was measured to analyse the extraction structure of the COSY beam. A typical 3D measurement of a time-resolved beam profile is shown in Fig. 2.

Within a second beam test at HIT medical accelerator facility in Heidelberg both the software improvements of the readout system and the new detector components connected to POLAND could be tested.

Figure 1: Picture of a 32 channel readout system, including the four QFW units (left side) and the FPGA logic unit (middle). The complete system fits into a 1U 19" rack crate. All connectors are on the back side.

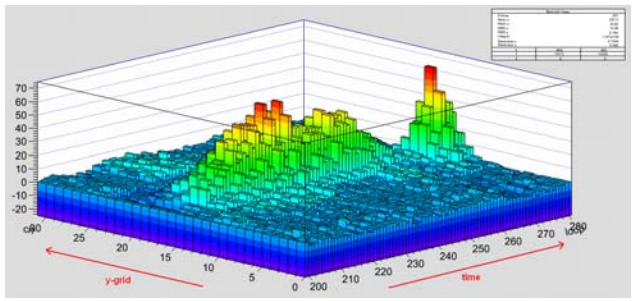

Figure 2: Time-resolved vertical beam profile measured at the 2013 COSY proton beam test. The beam extraction time was 7s with an "extra" short pulse at the end of the extraction.

Outlook

From February 2014, the system will be tested with various beam conditions at GSI experimental location UNILAC UX2 and HTP (after SIS 18) with different tasks. An important milestone will be the proton source acceptance test in summer at CEA/Saclay, France.

References

[1] M. Witthaus et al., Low Current Profile Measurements using a Current-to-Frequency-Converter (QFW), GSI Scientific Report, 2011

[2] H. Flemming and E. Badura, A high dynamic charge to frequency converter ASIC, GSI Scientific Report, 2004

[3] http://wiki.gsi.de/cgi-bin/view/EE/POLAND

* s.loechner@gsi.de

Status of the Coating Activities at the Magnetron Sputtering Facility

M.C. Bellachioma, J. Cavaco, Ch. Kolligs, A.Krämer, and J.Kurdal
GSI, Darmstadt, Germany

Vacuum upgrade of the Heavy Ion Synchrotron SIS18

The production of thin film coatings by means of magnetron sputtering facilities has been started at GSI in 2005, in the context of the technical developments for the construction of the Facility for Antiproton and Ion Research (FAIR). In fact, to improve the beam lifetime and the beam intensity of the existing heavy ion synchrotron (SIS 18) an intensive programme for the vacuum upgrade was undertaken and among the different measures the installation of non-evaporable getter (NEG) coated pipes was considered. The production of the thin film getter was carried out in two cylindrical magnetron sputtering facilities described in details in Ref.[1], and the thin film characterization was performed by means of different techniques carried out at GSI, in CERN, and at the Magdeburg University [2, 1].
During the upgrade shutdowns from 2006 to 2009 24 dipole magnet chambers, 11 long collimator chambers and 5 straight vacuum chambers were replaced by NEG coated UHV chambers, which corresponds to app. 65% of the SIS18 circumference. The commissioning of the upgraded UHV system has been performed at the beginning of 2010 [3]: the acceleration and extraction of 2x10$^{10}U^{28+}$ ions, which represents an intensity increase by a factor 100, was realized. In addition the achievable U^{28+} beam lifetime (t) was strongly improved, from $t < 1s$ before the UHV upgrade, reaching about $t = 11s$ after. During the measurements no increase of pressure was observed [3].

Collaboration with International Institutes

The experience acquired in the last years in the field of thin film coatings allowed the vacuum laboratory to carry out coating also for other Institutes. Starting from 2011 in collaboration with the company *FRIATEC AG*, for example, 6 ceramic chambers, elliptically shaped, were sputtered with a thin titanium layer to produce a required resistivity for **NSLS-II** (BNL). The collaboration, which resulted to be successfully, will proceed until the end of the current year.
Additionally, collaboration with the University of Heidelberg, the University of Princeton, and Hamburg were established in the last year, beside the support on the thin film production provided to the GSI groups.

Thin film coatings for FAIR

In the frame of the FAIR accelerator complex, the use of non-evaporable getter film is still under study. One of the possible application is on the dipole magnet chambers of the High Energy Storage Ring (HESR). The HESR, which will be completely realized by the Forschungszentrum Jülich (FZJ) is dedicated to strong interaction studies with antiprotons in the momentum range between $1,5$ and $15\ GeV/c$ [4].
The HESR dipole chambers, made by stainless steel, are more than 4 meters long, have a circular cross section of 89mm, and are characterised by a $8,2^o$ bending angle. For an easier integration of the dipole chambers into the sputtering system, a horizontal configuration of the facility is foreseen, and a design modification of the existing magnetron sputtering system is already ongoing, as shwon in Figure 1.

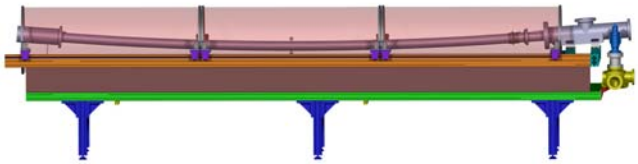

Figure 1: Drawing of the magnetron sputtering system, which will be used for the NEG coating of the HESR dipole chambers.

References

[1] M.C.Bellachioma et al., “Thin film getter coatings for the GSI heavy-ion synchrotron upgrade”, Vacuum 82, 2008, p.435

[2] M.Bender et al., “UHV-ERDA investigation of NEG coatings ”, Nucl. Instr.and Meth.B, Vol.268, 2010, p.1986 (2013) 56

[3] P.J.Spiller et al., “Acceleration of Intermediate Charge State Heavy Ions in SIS18”,IPAC 2010, Kyoto, Japan, p.669

[4] R.Toelle et al., “HESR at FAIR: status of technical planning”, PAC07, Albuquerque, New Mexico, USA

 doi:10.15120/GR-2014-1-FG-CS-14

Status of the SuperFRS Cryogenics*

Y. Xiang[1] *and H. Kollmus*[1]
[1]CSCY, GSI, Darmstadt, Germany

The Cooling of the SuperFRS

In March and April, 2013, two technical review meetings with R. Pengo, cryogenic expert from INFN, Italy and P. Lebrun, cryogenic expert from CERN have been organized by the cryogenic group CSCY at GSI on the issues mainly concerning the local cryogenics for Super-FRS. The challenge of cooldown the huge mass up to 1400 tons cold iron (cooldown enthalpy: about 112 GJ from 300 K to 4.5 K) has been addressed as one of the most important features of the Super-FRS local cryogenics. In order to reach a reasonable cooldown time of 3 to 4 weeks, it turned out during the cooldown calculation that a cooling power for Super-FRS cooldown will be of similar capacity as for the large ATLAS detector at CERN, the largest particle detector ever been built in the world (with the cooldown enthalpy about 121 GJ from 300 K to 4.5 K for its 680 tons aluminium alloy cold mass) [1]. Cryogenic engineering tells that the precooling with LN2 is necessary for especially large cold mass since approximately $\approx$ 80 % of the cool down load is from 300K to 80K. The capacity of a LN2 precooler for Super-FRS cooldown is specified at around 76 kW, which is about 25 % more than the maximum capacity for ATLAS cooldown at CERN. The comparison has been done in terms of the cooldown time predicted for the Super-FRS and needed for the ATLAS detector to reach 4.5 K operation states.

CERN Magnet Testing

In the five meetings in series since May, 2013 at CERN and at GSI with regards to the Super-FRS magnet testing, the cryogenic group CSCY has provided substantial supports in the planning of the cryogenic facility for the testing at CERN in terms of magnet cooldown / warmup limitations, LN2 precooler cooling power estimation, operation conditions, interface definition, and magnet cryostat protection against over-pressure (under different worst-case scenarios, i.e., quench and insulation vacuum loss to air), and corresponding safety device sizing and set pressure choice according to European Standards as well as the testing programme about cryogenic measurement. The operation modes have been integrated into the flow scheme design of the feedboxes for different magnet groups and discussed with the experts from RIKEN in the fifth workshop on next generation Fragment Separator in Dec. 2013 in Japan. The operation experiences of the cryogenic and magnet system in the Big-RIPS at RIKEN would help us to determine certain important operation parameters both in magnet testing and in the machine commissioning phases, such as maximum allowed cooldown /warmup rates between 300 K and 100 K temperature range. The operation experience of the SAMURAI superconducting dipole at RIKEN and the design experience of the Cyclotron Gas Stopper under construction at MSU would help us to make reasonable decision for the local cryogenics of the CBM dipole to choose proper cooling technology, by a number of small cryo-coolers or over cryogenic distribution from large plant.

Local Cryogenics and Cryo Plant 1

The combination of the cryogenic distribution for low energy branch and for the high energy cave into one branch should ease the radiation protection design for the High Energy Cave construction. The updated cryogenic distribution branching into four sections over the branch box makes potential staging of the Super-FRS construction possible. The concept for the 3D engineering design of the feedboxes for all groups of magnets have been unified both for the group of 3 long multiplets located in front of the target area and the group of 3 short ones behind, and for the rest multiplet groups as well. The 3D layout of the feedbox for dipole groups has been redone in order to fulfil the constraints at the bending sections of the tunnel. The space constraint due to the limited tunnel height in front of the target area has been eased with the updated installation concept of the safety valves on the multiplet. The DMU engineering check for the feedbox concept will be continuing under the new layouts in the target region and in the tunnel. The 3D layout of the cryogenic distribution transfer line in the Super-FRS tunnel and the buildings would be one of the next major tasks for 2014. In December 2013 a technical study was placed at two suppliers for refrigerators in order to get proposals for the best plant configuration in terms of shield cooliong, 4 K cooling including liquifaction for the current leads and cool down. For this study the heat loads of the magnets and the local cryogenics were carefully rechecked and adapted to the present configuration. The output of the study is expected for April 2014 and will be the basis for the spezification of the cryo plant 1.

References

[1] R. Pengo, et al., IEEE TRANSACTIONS ON APPLIED SUPERCONDUCTIVITY, VOL. 18, NO. 2, JUNE 2008, 379 - 382

*FAIR@GSI PSP code: 2.4.12 and 2.14.8.1.1

 doi:10.15120/GR-2014-1-FG-CS-15

JCR publications to the programme physics of hadrons and nuclei published in 2013

[1] E. Abbas, B. Abelev, J. Adam, , et al. Performance of the ALICE VZERO system. *Journal of Instrumentation*, 8(10):P10016 – P10016, 2013. doi: 10.1088/1748-0221/8/10/P10016.

[2] E. Abbas, B. Abelev, J. Adam, , et al. Charmonium and e^+e^- pair photoproduction at mid-rapidity in ultra-peripheral Pb–Pb collisions at $\sqrt{s_{NN}} = 2.76$ TeV. *The European physical journal / C*, 73(11): 2617, 2013. doi: 10.1140/epjc/s10052-013-2617-1.

[3] E. Abbas, B. Abelev, J. Adam, , et al. J/ψ elliptic flow in Pb-Pb collisions at $\sqrt{s_{NN}} = 2.76$ TeV. *Physical review letters*, 111(16):162301, 2013. doi: 10.1103/PhysRevLett.111.162301.

[4] E. Abbas, B. Abelev, J. Adam, et al. Mid-rapidity anti-baryon to baryon ratios in pp collisions at $\sqrt{s} = 0.9, 2.76$ and 7 TeV measured by ALICE. *The European physical journal / C*, 73(7):2496, 2013. doi: 10.1140/epjc/s10052-013-2496-5.

[5] B. Abelev, J. Adam, D. Adamová, , et al. D meson elliptic flow in non-central Pb-Pb Collisions at $\sqrt{s_{NN}} = 2.76$ TeV. *Physical review letters*, 111(10):102301, 2013. doi: 10.1103/PhysRevLett.111.102301.

[6] B. Abelev, J. Adam, D. Adamová, , et al. Multiplicity dependence of two-particle azimuthal correlations in pp collisions at the LHC. *Journal of high energy physics*, 2013(9):49, 2013. doi: 10.1007/JHEP09(2013)049.

[7] B. Abelev, J. Adam, D. Adamová, , et al. Centrality dependence of π, K, and p production in Pb-Pb collisions at $\sqrt{s_{NN}} = 2.76$ TeV. *Physical review / C*, 88(4):044910, 2013. doi: 10.1103/PhysRevC.88.044910.

[8] B. Abelev, J. Adam, D. Adamová, , et al. Centrality determination of Pb-Pb collisions at $\sqrt{s_{NN}} = 2.76$ TeV with ALICE. *Physical review / C*, 88(4):044909, 2013. doi: 10.1103/PhysRevC.88.044909.

[9] B. Abelev, J. Adam, D. Adamová, , et al. K^0_s and λ production in Pb-Pb collisions at $\sqrt{s_{NN}} = 2.76$ TeV. *Physical review letters*, 111(22):222301, 2013. doi: 10.1103/PhysRevLett.111.222301.

[10] B. Abelev, J. Adam, D. Adamová, , et al. Energy dependence of the transverse momentum distributions of charged particles in pp collisions measured by ALICE. *The European physical journal / C*, 73(12): 2662, 2013. doi: 10.1140/epjc/s10052-013-2662-9.

[11] B. Abelev, J. Adam, D. Adamová, , et al. Directed flow of charged particles at midrapidity relative to the spectator plane in Pb-Pb collisions at $\sqrt{s_{NN}} = 2.76$ TeV. *Physical review letters*, 111(23):232302, 2013. doi: 10.1103/PhysRevLett.111.232302.

[12] B. Abelev, J. Adam, D. Adamová, et al. Charge separation relative to the reaction plane in Pb-Pb collisions at $\sqrt{s_{NN}} = 2.76\ TeV$. *Physical review letters*, 110(1):012301, 2013. doi: 10.1103/PhysRevLett.110.012301.

[13] B. Abelev, J. Adam, D. Adamová, et al. Pseudorapidity Density of Charged Particles in p+Pb Collisions at $\sqrt{s_{NN}} = 5.02\ TeV$. *Physical review letters*, 110(3):032301, 2013. doi: 10.1103/PhysRevLett.110.032301.

[14] B. Abelev, J. Adam, D. Adamová, et al. Anisotropic flow of charged hadrons, pions and (anti-)protons measured at high transverse momentum in Pb–Pb collisions at $\sqrt{s} = 2.76TeV$. *Physics letters / B*, 719 (1-3):18 – 28, 2013. doi: 10.1016/j.physletb.2012.12.066.

[15] B. Abelev, J. Adam, D. Adamová, et al. Transverse Momentum Distribution and Nuclear Modification Factor of Charged Particles in p-Pb collisions at $\sqrt{s_{NN}} = 5.02TeV$. *Physical review letters*, 110(8): 082302, 2013. doi: 10.1103/PhysRevLett.110.082302.

[16] B. Abelev, J. Adam, D. Adamová, et al. Centrality dependence of charged particle production at large transverse momentum in Pb–Pb collisions at $\sqrt{s_{NN}} = 2.76$ TeV. *Physics letters / B*, 720(1-3):52 – 62, 2013. doi: 10.1016/j.physletb.2013.01.051.

[17] B. Abelev, J. Adam, D. Adamová, et al. Charged kaon femtoscopic correlations in pp collisions at $\sqrt{s} = 7TeV$. *Physical review / D*, 87(5):052016, 2013. doi: 10.1103/PhysRevD.87.052016.

[18] B. Abelev, J. Adam, D. Adamová, et al. Measurement of electrons from beauty hadron decays in pp collisions at $\sqrt{s} = 7$ TeV. *Physics letters / B*, 721(1-3):13 – 23, 2013. doi: 10.1016/j.physletb.2013.01.069.

[19] B. Abelev, J. Adam, D. Adamová, et al. Net-Charge Fluctuations in Pb-Pb Collisions at $\sqrt{s_{NN}} = 2.76$ TeV. *Physical review letters*, 110(15):152301, 2013. doi: 10.1103/PhysRevLett.110.152301.

[20] B. Abelev, J. Adam, D. Adamová, et al. Measurement of inelastic, single- and double-diffraction cross sections in proton–proton collisions at the LHC with ALICE. *The European physical journal / C*, 73 (6):2456, 2013. doi: 10.1140/epjc/s10052-013-2456-0.

[21] B. Abelev, J. Adam, D. Adamova, , et al. Centrality dependence of the pseudorapidity density distribution for charged particles in Pb–Pb collisions at $\sqrt{s_{NN}} = 2.76$ TeV. *Physics letters / B*, 726(4-5):610 – 622, 2013. doi: 10.1016/j.physletb.2013.09.022.

[22] B. Abelev, J. Adam, D. Adamova, , et al. Charge correlations using the balance function in Pb–Pb collisions at $\sqrt{s_{NN}} = 2.76$ TeV. *Physics letters / B*, 723(4-5):267 – 279, 2013. doi: 10.1016/j.physletb.2013.05.039.

[23] B. Abelev, J. Adam, D. Adamova, , et al. Measurement of the inclusive differential jet cross section in pp collisions at $\sqrt{s} = 2.76$ TeV. *Physics letters / B*, 722(4-5):262 – 272, 2013. doi: 10.1016/j.physletb.2013.04.026.

[24] B. Abelev, J. Adam, D. Adamova, , et al. Long-range angular correlations of π, K and p in p–Pb collisions at $\sqrt{s_{NN}} = 5.02TeV$. *Physics letters / B*, 726(1-3):164 – 177, 2013. doi: 10.1016/j.physletb.2013.08.024.

[25] B. Abelev, J. Adam, D. Adamova, et al. Long-range angular correlations on the near and away side in p–Pb collisions at $\sqrt{s_{NN}} = 5.02TeV$. *Physics letters / B*, 719(1-3):29 – 41, 2013. doi: 10.1016/j.physletb.2013.01.012.

[26] M. Ablikim, M. N. Achasov, X. C. Ai, et al. Observation of a Charged Charmoniumlike Structure in $e^+e^- \to \pi^+\pi^- J/\psi$ at $\sqrt{s} = 4.26$ GeV. *Physical review letters*, 110(25):252001, 2013. doi: 10.1103/PhysRevLett.110.252001.

[27] M. Ablikim, M. N. Achasov, O. Albayrak, et al. Search for η and η' $\to \pi^+ e^- \overline{\nu}_e$+c.c. decays in J/ψ → ϕη and ϕη'. *Physical review / D*, 87(3):032006, 2013. doi: 10.1103/PhysRevD.87.032006.

[28] M. Ablikim, M. N. Achasov, O. Albayrak, et al. Measurements of baryon pair decays of χ_{cJ} mesons. *Physical review / D*, 87(3):032007, 2013. doi: 10.1103/PhysRevD.87.032007.

[29] M. Ablikim, M. N. Achasov, O. Albayrak, et al. Evidence for $\eta_c(2S)$ in $\psi(3686) \to \gamma K_S^0 K^{\pm}\pi^{\mp}\pi^+\pi^-$. *Physical review / D*, 87(5):052005, 2013. doi: 10.1103/PhysRevD.87.052005.

[30] M. Ablikim, M. N. Achasov, O. Albayrak, et al. Study of the near-threshold ωϕ mass enhancement in doubly OZI-suppressed J/ψ → γωϕ decays. *Physical review / D*, 87(3):032008, 2013. doi: 10.1103/PhysRevD.87.032008.

[31] M. Ablikim, M. N. Achasov, O. Albayrak, et al. Search for η and $\eta^{'}$ invisible decays in J/ψ → ϕη and $\phi\eta^{'}$. *Physical review / D*, 87(1):012009, 2013. doi: 10.1103/PhysRevD.87.012009.

[32] M. Ablikim, M. N. Achasov, O. Albayrak, et al. Measurements of $\psi^{'} \to \overline{p}K^+\Sigma^0$ and $\chi_{cJ} \to \overline{p}K^+\Lambda$. *Physical review / D*, 87(1):012007, 2013. doi: 10.1103/PhysRevD.87.012007.

[33] M. Ablikim, M. N. Achasov, O. Albayrak, et al. Observation of η_c decay into $\Sigma^+\overline{\Sigma}^-$ and $\Xi^-\overline{\Xi}^+$ final states. *Physical review / D*, 87(1):012003, 2013. doi: 10.1103/PhysRevD.87.012003.

[34] M. Ablikim, M. N. Achasov, O. Albayrak, et al. Partial wave analysis of $J/\psi \to \gamma\eta\eta$. *Physical review / D*, 87(9):092009, 2013. doi: 10.1103/PhysRevD.87.092009.

[35] M. Ablikim, M. N. Achasov, O. Albayrak, et al. Precision measurements of $B[\psi(3686) \to \pi^+\pi^- J/\psi]$ and $B[J/\psi \to l^+l^-]$. *Physical review / D*, 88(3):032007, 2013. doi: 10.1103/PhysRevD.88.032007.

[36] M. Ablikim, M. N. Achasov, O. Albayrak, et al. Measurement of $\eta^{'} \to \pi^+\pi^- e^+e^-$ and $\eta^{'} \to \pi^+\pi^-\mu^+\mu^-$. *Physical review / D*, 87(9):092011, 2013. doi: 10.1103/PhysRevD.87.092011.

[37] M. Ablikim, M. N. Achasov, O. Albayrak, et al. Search for baryonic decays of ψ(3770) and ψ(4040). *Physical review / D*, 87(11):112011, 2013. doi: 10.1103/PhysRevD.87.112011.

[38] M. Ablikim, M. N. Achasov, O. Albayrak, et al. Partial wave analysis of $\psi(2S) \to p\overline{p}\eta$. *Physical review / D*, 88(3):032010, 2013. doi: 10.1103/PhysRevD.88.032010.

[39] M. Ablikim, M. N. Achasov, O. Albayrak, et al. Study of $\psi(3686) \to \omega K\overline{K}\pi$ decays. *Physical review / D*, 87(9):092006, 2013. doi: 10.1103/PhysRevD.87.092006.

[40] M. Ablikim, M. N. Achasov, O. Albayrak, et al. Study of $J/\psi \to \omega p\overline{p}$ at BESIII. *Physical review / D*, 87(11):112004, 2013. doi: 10.1103/PhysRevD.87.112004.

[41] M. Ablikim, M. N. Achasov, O. Albayrak, et al. Search for the lepton flavor violation process J/ψ → eμ at BESIII. *Physical review / D*, 87(11):112007, 2013. doi: 10.1103/PhysRevD.87.112007.

[42] M. Ablikim, M. N. Achasov, O. Albayrak, et al. Observation of a structure at 1.84 GeV/c^2 in the $3(\pi^+\pi^-)$ mass spectrum in $J/\psi \to \gamma 3(\pi^+\pi^-)$ decays. *Physical review / D*, 88(9):091502, 2013. doi: 10.1103/PhysRevD.88.091502.

[43] M. Ablikim, M. N. Achasov, D. J. Ambrose, et al. Evidence for $\eta_c \to \gamma\gamma$ and measurement of J/ψ → 3γ. *Physical review / D*, 87(3):032003, 2013. doi: 10.1103/PhysRevD.87.032003.

[44] M. Ablikim, M. N. Achasov, D. J. Ambrose, et al. Observation of Two New N^* Resonances in the Decay $\psi(3686) \to p\overline{p}\pi^0$. *Physical review letters*, 110(2):022001, 2013. doi: 10.1103/PhysRevLett.110.022001.

[45] M. Ablikim, M. N. Achasov, D. J. Ambrose, et al. Search for hadronic transition $\chi_{cJ} \to \eta_c\pi^+\pi^-$ and observation of $\chi_{cJ} \to K\overline{K}\pi\pi\pi$. *Physical review / D*, 87(1):012002, 2013. doi: 10.1103/PhysRevD.87.012002.

[46] M. Ablikim, M. N. Achasov, and O. Albayrak and. Measurements of the branching fractions for J/ψ and $\psi' \to \Lambda^0$ and Λ. *Physical review / D*, 87(5):052007, 2013. doi: 10.1103/PhysRevD.87.052007.

[47] A. Abuhoza*, H. R. Schmidt, S. Biswas*, U. Frankenfeld*, J. Hehner*, and C. J. Schmidt*. Setup optimization toward accurate ageing studies of gas filled detectors. *Nuclear instruments & methods in physics research / A*, 718:400 – 402, 2013. doi: 10.1016/j.nima.2012.08.045.

[48] P. Achenbach, M. Gómez Rodríguez, K. Tsukada, C. Ayerbe Gayoso, R. Böhm, O. Borodina*, D. Bosnar, V. Bozkurt*, P. Bydžovský, L. Debenjak, M. O. Distler, A. Esser, I. Friščić, Y. Fujii, T. Gogami, O. Hashimoto, S. Hirose, H. Kanda, M. Kaneta, E. Kim*, A. Margaryan, H. Merkel, U. Müller, S. Nagao, S. N. Nakamura, J. Pochodzalla, C. Rappold, J. Reinhold, T. Saito*, A. Sanchez Lorente, S. Sánchez Majos, B. S. Schlimme, M. Schoth, F. Schulz, C. Sfienti, S. Širca, L. Tang, and M. Thiel. Overview of the electromagnetic production of strange mesons at MAMI. *Nuclear physics / A*, 914:41 – 50, 2013. doi: 10.1016/j.nuclphysa.2013.01.019.

[49] L. Acosta, F. Amorini, R. Bassini, C. Boiano, G. Cardella, E. De Filippo, L. Grassi, C. Guazzoni, P. Guazzoni, M. Kiš, E. La Guidara, Y. Leifels*, I. Lombardo, T. Minniti, A. Pagano, M. Papa, S. Pirrone, G. Politi, F. Porto, F. Riccio, F. Rizzo, P. Russotto, S. Santoro, W. Trautmann*, A. Trifirò, G. Verde, P. Zambon, and L. Zetta. Probing the Merits of Different Event Parameters for the Identification of Light Charged Particles in CHIMERA CsI(Tl) Detectors With Digital Pulse Shape Analysis. *IEEE transactions on nuclear science*, 60(1):284 – 292, 2013. doi: 10.1109/TNS.2013.2237789.

[50] C. Adolph, M. Alekseev, V. Alexakhin, et al. Leading and next-to-leading order gluon polarization in the nucleon and longitudinal double spin asymmetries from open charm muoproduction. *Physical review / D*, 87(5):052018, 2013. doi: 10.1103/PhysRevD.87.052018.

[51] C. Adolph, M. G. Alekseev, V. Y. Alexakhin, et al. Measurement of the cross section for high-p_T hadron production in the scattering of 160-GeV/c muons off nucleons. *Physical review / D*, 88(9):091101, 2013. doi: 10.1103/PhysRevD.88.091101.

[52] C. Adolph, M. G. Alekseev, V. Y. Alexakhin, et al. Study of Σ(1385) and Ξ(1321) hyperon and antihyperon production in deep inelastic muon scattering. *The European physical journal / C*, 73(10):2581, 2013. doi: 10.1140/epjc/s10052-013-2581-9.

[53] C. Adolph, M. G. Alekseev, V. Y. Alexakhin, et al. Hadron transverse momentum distributions in muon deep inelastic scattering at 160 GeV/c. *The European physical journal / C*, 73(8):2531, 2013. doi: 10.1140/epjc/s10052-013-2531-6.

[54] C. Adolph, M. G. Alekseev, V. Yu. Alexakhin, et al. Leading order determination of the gluon polarisation from DIS events with high- hadron pairs. *Physics letters / B*, 718(3):922 – 930, 2013. doi: 10.1016/j.physletb.2012.11.056.

[55] G. Agakishiev, A. Balanda, R. Bassini, D. Belver, A. V. Belyaev, A. Blanco, M. Böhmer, J. L. Boyard, P. Cabanelas, E. Castro, S. Chernenko, T. Christ, M. Destefanis, J. Díaz, F. Dohrmann, A. Dybczak, T. Eberl, E. Epple, L. Fabbietti, O. V. Fateev, P. Finocchiaro, P. Fonte, J. Friese, I. Fröhlich, T. Galatyuk, J. A. Garzón, R. Gernhäuser, A. Gil, C. Gilardi, M. Golubeva, D. González-Díaz, F. Guber, M. Gumberidze, M. Heilmann, T. Heinz*, T. Hennino, R. Holzmann*, P. Huck, I. Iori, A. Ivashkin, M. Jurkovic, B. Kämpfer, K. Kanaki, T. Karavicheva, D. Kirschner, I. Koenig*, W. Koenig*, B. Kolb*, R. Kotte, F. Krizek, R. Krücken, W. Kühn, A. Kugler, A. Kurepin, S. Lang*, J. S. Lange, K. Lapidus, T. Liu, L. Lopes, M. Lorenz, L. Maier, A. Mangiarotti, J. Markert, V. Metag, B. Michalska, J. Michel, D. Mishra, E. Morinière, J. Mousa, C. Müntz, L. Naumann, J. Otwinowski*, Y. C. Pachmayer, M. Palka, Y. Parpottas, V. Pechenov*, O. Pechenova, T. Pérez Cavalcanti, J. Pietraszko*, W. Przygoda, B. Ramstein, A. Reshetin, M. Roy-Stephan, A. Rustamov, A. Sadovsky, B. Sailer, P. Salabura, A. Schmah,

E. Schwab*, J. Siebenson, Y. G. Sobolev, S. Spataro, B. Spruck, H. Ströbele, J. Stroth*, C. Sturm*, A. Tarantola, K. Teilab, P. Tlusty, M. Traxler*, R. Trebacz, H. Tsertos, V. Wagner, M. Weber, C. Wendisch, M. Wisniowski, T. Wojcik, J. Wüstenfeld, S. Yurevich, Y. V. Zanevsky, and P. Zumbruch*. Deep sub-threshold K*(892)^0 production in collisions of Ar + KCl at 1.76 A GeV. *The European physical journal / A*, 49(3):34, 2013. doi: 10.1140/epja/i2013-13034-7.

[56] G. Agakishiev, A. Balanda, D. Belver, A. Belyaev, J. C. Berger-Chen, A. Blanco, M. Böhmer, J. L. Boyard, P. Cabanelas, E. Castro, S. Chernenko, T. Christ, M. Destefanis, F. Dohrmann, A. Dybczak, E. Epple, L. Fabbietti, O. Fateev, P. Finocchiaro, P. Fonte, J. Friese, I. Fröhlich, T. Galatyuk*, J. A. Garzón, R. Gernhäuser, C. Gilardi, M. Golubeva, D. González-Díaz, F. Guber, M. Gumberidze, T. Heinz*, T. Hennino, R. Holzmann*, A. Ierusalimov, I. Iori, A. Ivashkin, M. Jurkovic, B. Kämpfer, K. Kanaki, T. Karavicheva, I. Koenig*, W. Koenig*, B. W. Kolb*, R. Kotte, A. Krása, F. Krizek, R. Krücken, H. Kuc, W. Kühn, A. Kugler, A. Kurepin, R. Lalik, S. Lang, J. S. Lange, K. Lapidus, T. Liu, L. Lopes, M. Lorenz, L. Maier, A. Mangiarotti, J. Markert, V. Metag, B. Michalska, J. Michel, E. Morinière, J. Mousa, C. Müntz, R. Münzer, L. Naumann, J. Otwinowski, Y. C. Pachmayer, M. Palka, Y. Parpottas, V. Pechenov*, O. Pechenova, J. Pietraszko, W. Przygoda, B. Ramstein, A. Reshetin, A. Rustamov, A. Sadovsky, P. Salabura, A. Schmah, E. Schwab*, J. Siebenson, Y. G. Sobolev, S. Spataro, B. Spruck, H. Ströbele, J. Stroth*, C. Sturm*, A. Tarantola, K. Teilab, P. Tlusty, M. Traxler*, R. Trebacz, H. Tsertos, V. Wagner, M. Weber, C. Wendisch, J. Wüstenfeld, S. Yurevich*, and Y. Zanevsky. Baryonic resonances close to the $\overline{K}N$ threshold: The case of $\Lambda(1405)$ in pp collisions. *Physical review / C*, 87(2):025201, 2013. doi: 10.1103/PhysRevC.87.025201.

[57] G. Agakishiev, A. Balanda, D. Belver, A. Belyaev, J. C. Berger-Chen, A. Blanco, M. Böhmer, J. L. Boyard, P. Cabanelas, S. Chernenko, A. Dybczak, E. Epple, L. Fabbietti, O. Fateev, P. Finocchiaro, P. Fonte, J. Friese, I. Fröhlich, T. Galatyuk*, J. A. Garzón, R. Gernhäuser, K. Göbel*, M. Golubeva, D. González-Díaz, F. Guber, M. Gumberidze*, T. Heinz, T. Hennino, R. Holzmann, A. Ierusalimov, I. Iori, A. Ivashkin, M. Jurkovic, B. Kämpfer, T. Karavicheva, I. Koenig*, W. Koenig*, B. W. Kolb, G. Kornakov, R. Kotte, A. Krása, F. Krizek, R. Krücken, H. Kuc, W. Kühn, A. Kugler, A. Kurepin, V. Ladygin, R. Lalik, S. Lang*, K. Lapidus, A. Lebedev, T. Liu, L. Lopes, M. Lorenz*, L. Maier, A. Mangiarotti, J. Markert*, V. Metag, B. Michalska, J. Michel*, C. Müntz, L. Naumann, Y. C. Pachmayer, M. Palka, Y. Parpottas, V. Pechenov*, O. Pechenova, J. Pietraszko*, W. Przygoda, B. Ramstein, A. Reshetin, A. Rustamov, A. Sadovsky, P. Salabura, A. Schmah, E. Schwab, J. Siebenson, Y. G. Sobolev, S. Spataro, B. Spruck, H. Ströbele, J. Stroth*, C. Sturm*, A. Tarantola, K. Teilab*, P. Tlusty, M. Traxler*, R. Trebacz, H. Tsertos, T. Vasiliev, V. Wagner, M. Weber, C. Wendisch, J. Wüstenfeld, S. Yurevich, and Y. Zanevsky. Inclusive pion and η production in p+Nb collisions at 3.5 GeV beam energy. *Physical review / C*, 88(2):024904, 2013. doi: 10.1103/PhysRevC.88.024904.

[58] G. Agakishiev, D. Belver, A. Blanco, M. Böhmer, J. L. Boyard, P. Cabanelas, E. Castro, S. Chernenko, M. Destefanis, F. Dohrmann, A. Dybczak, E. Epple, L. Fabbietti, O. Fateev, P. Finocchiaro, P. Fonte, J. Friese, I. Fröhlich, T. Galatyuk*, J. A. Garzón, R. Gernhäuser, C. Gilardi, M. Golubeva, D. González-Díaz, F. Guber, M. Gumberidze*, T. Heinz*, T. Hennino, R. Holzmann*, I. Iori, A. Ivashkin, M. Jurkovic, B. Kämpfer, T. Karavicheva, I. Koenig*, W. Koenig*, B. Kolb*, R. Kotte, A. Krása, F. Krizek, R. Krücken, H. Kuc, W. Kühn, A. Kugler, A. Kurepin, S. Lang*, J. S. Lange, K. Lapidus, T. Liu, L. Lopes, M. Lorenz*, L. Maier, A. Mangiarotti, J. Markert*, V. Metag, B. Michalska, J. Michel*, E. Morinière, J. Mousa, C. Müntz*, L. Naumann, Y. C. Pachmayer, M. Palka, V. Pechenov*, O. Pechenova, J. Pietraszko*, W. Przygoda, B. Ramstein, L. Rehnisch, A. Reshetin, A. Rustamov*, A. Sadovsky, P. Salabura, T. Scheib, A. Schmah, H. Schuldes, E. Schwab*, J. Siebenson, Y. G. Sobolev, S. Spataro, B. Spruck, H. Ströbele, J. Stroth*, C. Sturm*, A. Tarantola, K. Teilab*, P. Tlusty, M. Traxler*, R. Trebacz, H. Tsertos, V. Wagner, M. Weber, M. Wisniowski, C. Wendisch, J. Wüstenfeld, S. Yurevich, and Y. Zanevsky. An upper limit on hypertriton production in collisions of Ar(1.76 A GeV) + KCl. *The European physical journal / A*, 49(11):146, 2013. doi: 10.1140/epja/i2013-13146-0.

[59] M. M. Aggarwal, Z. Ahammed, A. L. S. Angelis, V. Antonenko, V. Arefiev, V. Astakhov, V. Avdeitchikov, T. C. Awes, P. V. K. S. Baba, S. K. Badyal, S. Bathe, B. Batiounia, C. Baumann, T. Bernier, K. B. Bhalla, V. S. Bhatia, C. Blume, D. Bucher, H. Büsching, L. Carlén, S. Chattopadhyay, M. P. Decowski, H. Delagrange, P. Donni, M. R. Dutta Majumdar, K. El Chenawi, A. K. Dubey, K. Enosawa, S. Fokin, V. Frolov, M. S. Ganti, S. Garpman, O. Gavrishchuk, F. J. M. Geurts, T. K. Ghosh, R. Glasow, B. Guskov, H. Å. Gustafsson, H. H. Gutbrod, I. Hrivnacova, M. Ippolitov, H. Kalechofsky, R. Kamermans, K. Karadjev, K. Karpio, B. Kolb*, I. Kosarev, I. Koutcheryaev, A. Kugler, P. Kulinich, M. Kurata, A. Lebedev, H. Löhner, L. Luquin, D. P. Mahapatra, V. Manko, M. Martin, G. Martínez, A. Maximov, Y. Miake, G. C. Mishra, B. Mohanty, M.-J. Mora, D. Morrison, T. Mukhanova, D. S. Mukhopadhyay, H. Naef, B. K. Nandi, S. K. Nayak, T. K. Nayak, A. Nianine, V. Nikitine, S. Nikolaev, P. Nilsson, S. Nishimura, P. Nomokonov, J. Nystrand, A. Oskarsson, I. Otterlund, S. Pavliouk, T. Peitzmann, D. Peressounko, V. Petracek, S. C. Phatak, W. Pinganaud, F. Plasil, M. L. Purschke, J. Rak, M. Rammler, R. Raniwala, S. Raniwala, N. K. Rao, F. Retiere, K. Reygers, G. Roland, L. Rosselet, I. Roufanov, C. Roy, J. M. Rubio, S. S. Sambyal, R. Santo, S. Sato, H. Schlagheck, H. R. Schmidt*, Y. Schutz, G. Shabratova, T. H. Shah, I. Sibiriak, T. Siemiarczuk, D. Silvermyr, B. C. Sinha, N. Slavine, K. Söderström, G. Sood, S. P. Sørensen, P. Stankus, G. Stefanek, P. Steinberg, E. Stenlund, M. Sumbera, T. Svensson, A. Tsvetkov, L. Tykarski, E. C. v. d. Pijll, N. v. Eijndhoven, G. J. v. Nieuwenhuizen, A. Vinogradov, Y. P. Viyogi, A. Vodopianov, S. Vörös, B. Wysłouch, and G. R. Young. Photon and η production in p+Pb and p+C collisions at $\sqrt{s_{NN}} = 17.4GeV$. *Nuclear physics / A*, 898:14 – 23, 2013. doi: 10.1016/j.nuclphysa.2012.11.010.

[60] Y. Aksyutina*, T. Aumann*, K. Boretzky*, M. Borge, C. Caesar*, A. Chatillon*, L. Chulkov*, D. Cortina-Gil, U. Datta Pramanik, H. Emling*, H. Fynbo, H. Geissel*, A. Heinz, G. Ickert*, H. Johansson*, B. Jonson, R. Kulessa, C. Langer*, T. LeBleis*, K. Mahata*, G. Münzenberg*, T. Nilsson, G. Nyman, R. Palit, S. Paschalis, W. Prokopowicz*, R. Reifarth*, D. Rossi*, A. Richter, K. Riisager, G. Schrieder, H. Simon*, K. Sümmerer*, O. Tengblad, R. Thies, H. Weick*, and M. Zhukov. Study of the ^{14}Be Continuum: Identification and Structure of its Second 2^+ State. *Physical review letters*, 111 (24):242501, 2013. doi: 10.1103/PhysRevLett.111.242501.

[61] Y. Aksyutina*, T. Aumann, K. Boretzky*, M. J. G. Borge, C. Caesar*, A. Chatillon*, L. Chulkov*, D. Cortina-Gil*, U. Datta Pramanik, H. Emling*, H. O. U. Fynbo, H. Geissel*, G. Ickert*, H. T. Johansson, B. Jonson, R. Kulessa, C. Langer*, T. LeBleis*, K. Mahata*, G. Münzenberg*, T. Nilsson, G. Nyman, R. Palit, S. Paschalis, W. Prokopowicz*, R. Reifarth*, D. Rossi*, A. Richter, K. Riisager, G. Schrieder, H. Simon*, K. Sümmerer*, O. Tengblad, H. Weick*, and M. V. Zhukov. Momentum profile analysis in one-neutron knockout from Borromean nuclei. *Physics letters / B*, 718(4-5):1309 – 1313, 2013. doi: 10.1016/j.physletb.2012.12.028.

[62] Y. Aksyutina, T. Aumann*, K. Boretzky*, M. J. G. Borge, C. Caesar*, A. Chatillon, L. V. Chulkov, D. Cortina-Gil, U. Datta Pramanik, H. Emling*, H. O. U. Fynbo, H. Geissel*, G. Ickert*, H. T. Johansson, B. Jonson, R. Kulessa, C. Langer*, T. LeBleis, K. Mahata, G. Münzenberg*, T. Nilsson, G. Nyman, R. Palit, S. Paschalis, W. Prokopowicz*, R. Reifarth*, D. Rossi*, A. Richter, K. Riisager, G. Schrieder, H. Simon*, K. Sümmerer*, O. Tengblad, H. Weick*, and M. V. Zhukov. Structure of the unbound nucleus ^{13}Be: One-neutron knockout reaction data from ^{14}Be analyzed in a holistic approach. *Physical review / C*, 87(6):064316, 2013. doi: 10.1103/PhysRevC.87.064316.

[63] ALICE. Multiplicity dependence of the average transverse momentum in pp, p–Pb, and Pb–Pb collisions at the LHC. *Physics letters / B*, 727(4-5):371 – 380, 2013. doi: 10.1016/j.physletb.2013.10.054.

[64] J. Alme, D. Fehlker, C. Lippmann*, M. Mager, A. U. Rehman, K. Røed, D. Röhrich, and K. Ullaland. Radiation tolerance studies using fault injection on the Readout Control FPGA design of the ALICE TPC detector. *Journal of Instrumentation*, 8(01):C01053 – C01053, 2013. doi: 10.1088/1748-0221/8/01/C01053.

[65] F. Amjad*, H. Weick*, J. Mattila, L. Orona, E. Kozlova*, M. Winkler*, K.-H. Behr*, and C. Karagiannis*. Survey on Remote Handling Logistics for Super-FRS. *International journal of advanced robotic systems*, 10:348, 2013. doi: 10.5772/56848.

[66] A. N. Andreyev, S. Antalic, D. Ackermann*, L. Bianco, S. Franchoo, S. Heinz*, F.-P. Hessberger*, S. Hofmann*, M. Huyse, Z. Kalaninová, I. Kojouharov*, B. Kindler*, B. Lommel*, R. Mann*, K. Nishio, R. D. Page, J. J. Ressler, B. Streicher, S. Saro, B. Sulignano*, and P. Van Duppen. β-delayed fission of $^{192,194}At$. *Physical review / C*, 87(1):014317, 2013. doi: 10.1103/PhysRevC.87.014317.

[67] A. N. Andreyev, M. Huyse, P. Van Duppen, C. Qi, R. J. Liotta, S. Antalic, D. Ackermann*, S. Franchoo, F. Heßberger*, S. Hofmann*, I. Kojouharov*, B. Kindler*, P. Kuusiniemi, S. R. Lesher, B. Lommel*, R. Mann*, K. Nishio, R. D. Page, B. Streicher, Š. Šáro, B. Sulignano*, D. Wiseman, and R. A. Wyss. Signatures of the Z=82 Shell Closure in α-Decay Process. *Physical review letters*, 110(24):242502, 2013. doi: 10.1103/PhysRevLett.110.242502.

[68] A. N. Andreyev, V. Liberati, S. Antalic, D. Ackermann*, A. Barzakh, N. Bree, T. E. Cocolios, J. Diriken, J. Elseviers, D. Fedorov, V. N. Fedosseev, D. Fink, S. Franchoo, S. Heinz*, F.-P. Hessberger*, S. Hofmann*, M. Huyse, O. Ivanov, J. Khuyagbaatar*, B. Kindler*, U. Köster, J. F. W. Lane, B. Lommel*, R. Mann*, B. Marsh, P. Molkanov, K. Nishio, R. D. Page, N. Patronis, D. Pauwels, D. Radulov, Š. Šáro, M. Seliverstov, M. Sjödin, I. Tsekhanovich, P. Van den Bergh, P. Van Duppen, M. Venhart, and M. Veselský. α-decay spectroscopy of the chain $^{179}Tl^{g} \rightarrow^{175} Au^{g} \rightarrow^{171} Ir^{g} \rightarrow^{167} Re^{m}$. *Physical review / C*, 87(5):054311, 2013. doi: 10.1103/PhysRevC.87.054311.

[69] A. Andronic*, P. Braun-Munzinger*, K. Redlich, and J. Stachel. The statistical model in Pb–Pb collisions at the LHC. volume 904-905, pages 535c – 538c. Quark Matter 2012, Washington D.C.(USA), North-Holland Publ. Co., 08/13/2012 - 08/18/2012 2013. doi: 10.1016/j.nuclphysa.2013.02.070.

[70] S. Antalic, F. Heßberger*, D. Ackermann*, M. Block*, S. Heinz*, S. Hofmann*, Z. Kalaninová, B. Kindler*, M. Leino, B. Lommel*, R. Mann*, K. Nishio, Š. Šáro, and B. Sulignano*. Nuclear Structure of Heavy N=153 Isotones. *Acta physica Polonica / B*, 44(3):387, 2013. doi: 10.5506/APhysPolB.44.387.

[71] T. Anticic, B. Baatar, D. Barna, J. Bartke, H. Beck, L. Betev, H. Białkowska, C. Blume, M. Bogusz, B. Boimska, J. Book, M. Botje, P. Bunčić, T. Cetner, P. Christakoglou, P. Chung, O. Chvála, J. G. Cramer, V. Eckardt, Z. Fodor, P. Foka*, V. Friese*, M. Gaździcki, K. Grebieszkow, C. Höhne*, K. Kadija, A. Karev, V. I. Kolesnikov, T. Kollegger, M. Kowalski, D. Kresan*, A. László, R. Lacey, M. van Leeuwen, M. Maćkowiak-Pawłowska, M. Makariev*, A. I. Malakhov, M. Mateev, G. L. Melkumov, M. Mitrovski, S. Mrówczyński, V. Nicolic, G. Pálla, A. D. Panagiotou, W. Peryt, J. Pluta, D. Prindle, F. Pühlhofer, R. Renfordt, C. Roland, G. Roland, M. Rybczyński, A. Rybicki, A. Sandoval*, N. Schmitz, T. Schuster, P. Seyboth, F. Siklér, E. Skrzypczak, M. Słodkowski, G. Stefanek, R. Stock, H. Ströbele, T. Susa, M. Szuba, M. Utvić, D. Varga, M. Vassiliou, G. I. Veres, G. Vesztergombi, D. Vranić*, Z. Włodarczyk, and A. Wojtaszek-Szwarc. System-size dependence of particle-ratio fluctuations in Pb + Pb collisions at 158A GeV. *Physical review / C*, 87(2):024902, 2013. doi: 10.1103/PhysRevC.87.024902.

[72] A. Arcones* and F.-K. Thielemann. Neutrino-driven wind simulations and nucleosynthesis of heavy elements. *Journal of physics / G*, 40(1):013201, 2013. doi: 10.1088/0954-3899/40/1/013201.

[73] I. C. Arsene*. J/ψ nuclear modification factor at mid-rapidity in Pb–Pb collisions at $\sqrt{s_{NN}} = 2.76TeV$. volume 904-905, pages 623c – 626c. Quark Matter 2012, Washington D.C.(USA), North-Holland Publ. Co., 08/13/2012 - 08/18/2012 2013. doi: 10.1016/j.nuclphysa.2013.02.093.

[74] T. Aumann*, C. Bertulani, and J. Ryckebusch. Quasifree (p,2p) and (p,pn) reactions with unstable nuclei. *Physical review / C*, 88(6):064610, 2013. doi: 10.1103/PhysRevC.88.064610.

[75] T. Aumann*, A. Zilges, and D. Savran*. Experimental studies of the Pygmy Dipole Resonance. *Progress in particle and nuclear physics*, 70:210 – 245, 2013. doi: 10.1016/j.ppnp.2013.02.003.

[76] R. Averbeck*. Heavy-flavor production in heavy-ion collisions and implications for the properties of hot QCD matter. *Progress in particle and nuclear physics*, 70:159 – 209, 2013. doi: 10.1016/j.ppnp.2013.01.001.

[77] A. M. Denis Bacelar, A. M. Bruce, Z. Podolyák, N. Al-Dahan, M. Górska*, S. Lalkovski, S. Pietri*, M. V. Ricciardi*, A. Algora, N. Alkhomashi, J. Benlliure, P. Boutachkov*, A. Bracco, E. Calore, E. Casarejos, I. J. Cullen, A. Y. Deo, P. Detistov, Z. Dombradi, C. Domingo-Pardo*, M. Doncel, F. Farinon*, G. F. Farrelly, H. Geissel*, W. Gelletly, J. Gerl*, N. Goel*, J. Gręboszˆ*, R. Hoischen*, I. Kojouharov*, N. Kurz*, S. Leoni, F. Molina, D. Montanari, A. I. Morales, A. Musumarra, D. R. Napoli, R. Nicolini, C. Nociforo*, A. Prochazka*, W. Prokopowicz*, P. H. Regan, B. Rubio, D. Rudolph, K.-H. Schmidt*, H. Schaffner*, S. J. Steer, K. Steiger, P. Strmen, T. P. D. Swan, I. Szarka, J. J. Valiente-Dobón, S. Verma, P. M. Walker, H. Weick*, and H. J. Wollersheim*. The population of metastable states as a probe of relativistic-energy fragmentation reactions. *Physics letters / B*, 723(4-5):302 – 306, 2013. doi: 10.1016/j.physletb.2013.05.033.

[78] J. Beller, N. Pietralla, J. Barea, M. Elvers, J. Endres, C. Fransen, J. Kotila, O. Möller, A. Richter, T. R. Rodríguez, C. Romig, D. Savran*, M. Scheck, L. Schnorrenberger, K. Sonnabend, V. Werner, A. Zilges, and M. Zweidinger. Constraint on 0νββ Matrix Elements from a Novel Decay Channel of the Scissors Mode: The Case of ^{154}Gd. *Physical review letters*, 111(17):172501, 2013. doi: 10.1103/PhysRevLett.111.172501.

[79] J. Berges* and S. Schlichting. The nonlinear glasma. *Physical review / D*, 87(1):014026, 2013. doi: 10.1103/PhysRevD.87.014026.

[80] C. A. Bertulani*, J. Fuqua, and M. S. Hussein. Big bang nucleosynthesis with a non-maxwellian distribution. *The astrophysical journal / 1*, 767(1):67, 2013. doi: 10.1088/0004-637X/767/1/67.

[81] A. Best, M. Beard*, J. Görres, M. Couder, R. deBoer, S. Falahat, R. T. Güray, A. Kontos, K.-L. Kratz, P. J. LeBlanc, Q. Li, S. O'Brien, N. Özkan, M. Pignatari, K. Sonnabend, R. Talwar, W. Tan, E. Uberseder, and M. Wiescher. Measurement of the reaction $^{17}O(\alpha, n)^{20}Ne$ and its impact on the s process in massive stars. *Physical review / C*, 87(4):045805, 2013. doi: 10.1103/PhysRevC.87.045805.

[82] A. Blanco, P. Fonte, J. A. Garzon, W. Koenig*, G. Kornakov, and L. Lopes. Performance of the HADES-TOF RPC wall in a Au + Au beam at 1.25 AGeV. *Journal of Instrumentation*, 8(01):P01004 – P01004, 2013. doi: 10.1088/1748-0221/8/01/P01004.

[83] M. Block*. Direct mass measurements of the heaviest elements with Penning traps. *International journal of mass spectrometry*, 349-350:94 – 101, 2013. doi: 10.1016/j.ijms.2013.02.013.

[84] I. Boettcher, S. Diehl, J. M. Pawlowski*, and C. Wetterich. Tan contact and universal high momentum behavior of the fermion propagator in the BCS-BEC crossover. *Physical review / A*, 87(2):023606, 2013. doi: 10.1103/PhysRevA.87.023606.

[85] A. Borschevsky*, M. Iliaš, V. A. Dzuba, V. V. Flambaum, and P. Schwerdtfeger. Relativistic study of nuclear-anapole-moment effects in diatomic molecules. *Physical review / A*, 88(2):022125, 2013. doi: 10.1103/PhysRevA.88.022125.

[86] A. Borschevsky, V. Pershina*, E. Eliav, and U. Kaldor. Ab initio predictions of atomic properties of element 120 and its lighter group-2 homologues. *Physical review / A*, 87(2):022502, 2013. doi: 10.1103/PhysRevA.87.022502.

[87] A. Borschevsky*, V. Pershina*, E. Eliav, and U. Kaldor. Ab initio studies of atomic properties and experimental behavior of element 119 and its lighter homologs. *The journal of chemical physics*, 138 (12):124302, 2013. doi: 10.1063/1.4795433.

[88] M. Bowry, Z. Podolyák, S. Pietri*, J. Kurcewicz*, M. Bunce, P. H. Regan, F. Farinon*, H. Geissel*, C. Nociforo*, A. Prochazka*, H. Weick*, N. Al-Dahan, N. Alkhomashi, P. R. P. Allegro, J. Benlliure, G. Benzoni, P. Boutachkov*, A. M. Bruce, A. M. Denis Bacelar, G. F. Farrelly, J. Gerl*, M. Górska*, A. Gottardo, J. Grębosz, N. Gregor, R. Janik, R. Knöbel*, I. Kojouharov*, T. Kubo, N. Kurz*, Y. A. Litvinov*, E. Merchan*, I. Mukha*, F. Naqvi, B. Pfeiffer*, M. Pfützner, W. Plaß, M. Pomorski, B. Riese*, M. V. Ricciardi*, K. Schmidt, H. Schaffner*, C. Scheidenberger*, E. C. Simpson, B. Sitar, P. Spiller*, J. Stadlmann*, P. Strmen, B. Sun*, I. Tanihata, S. Terashima, J. J. Valiente Dobón, J. S. Winfield*, H. Wollersheim*, and P. J. Woods. Population of high-spin isomeric states following fragmentation of ^{238}U. *Physical review / C*, 88(2):024611, 2013. doi: 10.1103/PhysRevC.88.024611.

[89] E. Bratkovskaya, W. Cassing, J. Aichelin, C. Hartnack, Y. Leifels*, H. Oeschler*, and L. Tolos. In-medium effects on strangeness production. *Nuclear physics / A*, 914:387 – 391, 2013. doi: 10.1016/j.nuclphysa.2013.01.012.

[90] J. Braun, J.-W. Chen, J. Deng, J. Drut, B. Friman*, C.-T. Ma, and Y.-D. Tsai. Imaginary Polarization as a Way to Surmount the Sign Problem in Ab Initio Calculations of Spin-Imbalanced Fermi Gases. *Physical review letters*, 110(13):130404, 2013. doi: 10.1103/PhysRevLett.110.130404.

[91] C. Caesar*, J. Simonis, T. Adachi, Y. Aksyutina, J. Alcantara, S. Altstadt*, H. Alvarez-Pol, N. Ashwood, T. Aumann*, V. Avdeichikov, M. Barr, S. Beceiro, D. Bemmerer, J. Benlliure, C. A. Bertulani, K. Boretzky*, M. J. G. Borge, G. Burgunder, M. Caamano, E. Casarejos, W. Catford, J. Cederkäll, S. Chakraborty, M. Chartier, L. Chulkov, D. Cortina-Gil, U. Datta Pramanik, P. Diaz Fernandez, I. Dillmann*, Z. Elekes, J. Enders, O. Ershova, A. Estrade*, F. Farinon*, L. M. Fraile, M. Freer, M. Freudenberger, H. O. U. Fynbo, D. Galaviz, H. Geissel*, R. Gernhäuser, P. Golubev, D. Gonzalez Diaz, J. Hagdahl, T. Heftrich, M. Heil*, M. Heine, A. Heinz, A. Henriques, M. Holl, J. D. Holt, G. Ickert*, A. Ignatov, B. Jakobsson, H. T. Johansson, B. Jonson, N. Kalantar-Nayestanaki, R. Kanungo, A. Kelic-Heil*, R. Knöbel*, T. Kröll, R. Krücken, J. Kurcewicz*, M. Labiche, C. Langer, T. Le Bleis, R. Lemmon, O. Lepyoshkina, S. Lindberg, J. Machado, J. Marganiec, V. Maroussov, J. Menéndez, M. Mostazo, A. Movsesyan, A. Najafi, T. Nilsson, C. Nociforo*, V. Panin, A. Perea, S. Pietri*, R. Plag, A. Prochazka*, A. Rahaman, G. Rastrepina*, R. Reifarth, G. Ribeiro, M. V. Ricciardi*, C. Rigollet, K. Riisager, M. Röder, D. Rossi*, J. Sanchez del Rio, D. Savran, H. Scheit, A. Schwenk, H. Simon*, O. Sorlin, V. Stoica, B. Streicher, J. Taylor, O. Tengblad, S. Terashima*, R. Thies, Y. Togano, E. Uberseder, J. Van de Walle, P. Velho, V. Volkov, A. Wagner, F. Wamers, H. Weick*, M. Weigand, C. Wheldon, G. Wilson, C. Wimmer, J. S. Winfield*, P. Woods, D. Yakorev, M. V. Zhukov, A. Zilges, M. Zoric*, and K. Zuber. Beyond the neutron drip line: The unbound oxygen isotopes ^{25}O and ^{26}O. *Physical review / C*, 88(3):034313, 2013. doi: 10.1103/PhysRevC.88.034313.

[92] L. V. Chulkov*, T. Aumann*, B. Jonson, T. Nilsson, and H. Simon*. Is there a low-lying 1^- state in ^{10}He? *Physics letters / B*, 720(4-5):344 – 346, 2013. doi: 10.1016/j.physletb.2013.02.037.

[93] V. F. Comas*, S. Heinz*, S. Hofmann, D. Ackermann*, J. A. Heredia*, F. Heßberger*, J. Khuyagbaatar*, B. Kindler*, B. Lommel*, and R. Mann*. Study of multi-nucleon transfer reactions in $^{58,64}Ni + ^{207}Pb$ collisions at the velocity filter SHIP. *The European physical journal / A*, 49(9):112, 2013. doi: 10.1140/epja/i2013-13112-x.

[94] J. M. Cornejo, A. Lorenzo, D. Renisch, M. Block*, C. E. Düllmann*, and D. Rodríguez. Status of the project TRAPSENSOR: Performance of the laser-desorption ion source. *Nuclear instruments & methods in physics research / B*, 317:522 – 527, 2013. doi: 10.1016/j.nimb.2013.05.060.

[95] M. D. Cozma, Y. Leifels*, W. Trautmann*, Q. Li, and P. Russotto. Toward a model-independent constraint of the high-density dependence of the symmetry energy. *Physical review / C*, 88(4):044912, 2013. doi: 10.1103/PhysRevC.88.044912.

[96] I. Danilkin*, M. Lutz*, S. Leupold, and C. Terschlüsen. Photon-fusion reactions from the chiral Lagrangian with dynamical light vector mesons. *The European physical journal / C*, 73(4):2358, 2013. doi: 10.1140/epjc/s10052-013-2358-1.

[97] V. Derya, J. Endres, M. Elvers, M. N. Harakeh, N. Pietralla, C. Romig, D. Savran*, M. Scheck, F. Siebenhühner, V. I. Stoica, H. J. Wörtche, and A. Zilges. Study of the pygmy dipole resonance in ^{94}Mo using the (α, α, γ) coincidence technique. *Nuclear physics / A*, 906:94 – 107, 2013. doi: 10.1016/j.nuclphysa.2013.02.018.

[98] B. Dönigus*. (Anti-)matter and hyper-matter production at the LHC with ALICE. *Nuclear physics / A*, 904-905:547c – 550c, 2013. doi: 10.1016/j.nuclphysa.2013.02.073.

[99] C. Droese, D. Ackermann*, L. Andersson, K. Blaum, M. Block*, M. Dworschak*, M. Eibach, S. Eliseev, U. Forsberg, E. Haettner*, F. Herfurth*, F. P. Heßberger*, S. Hofmann*, J. Ketelaer, G. Marx, E. Minaya Ramirez, D. Nesterenko, Y. N. Novikov, W. R. Plaß, D. Rodríguez, D. Rudolph, C. Scheidenberger*, L. Schweikhard, S. Stolze, P. G. Thirolf, and C. Weber. High-precision mass measurements of $^{203-207}Rn$ and ^{213}Ra with SHIPTRAP. *The European physical journal / A*, 49(1):13, 2013. doi: 10.1140/epja/i2013-13013-0.

[100] Z. Elekes, T. Aumann*, D. Bemmerer, K. Boretzky*, C. Caesar*, T. C. Cowan, J. Hehner*, M. Heil*, M. Kempe, D. Rossi*, M. Röder, H. Simon*, M. Sobiella, D. Stach, T. Reinhardt, A. Wagner, D. Yakorev, A. Zilges, and K. Zuber. Simulation and prototyping of 2m long resistive plate chambers for detection of fast neutrons and multi-neutron event identification. *Nuclear instruments $\&$ methods in physics research / A*, 701:86 – 92, 2013. doi: 10.1016/j.nima.2012.11.010.

[101] S. Eliseev, K. Blaum, M. Block*, C. Droese, M. Goncharov, E. Minaya Ramirez*, D. Nesterenko, Y. Novikov, and L. Schweikhard. Phase-Imaging Ion-Cyclotron-Resonance Measurements for Short-Lived Nuclides. *Physical review letters*, 110(8):082501, 2013. doi: 10.1103/PhysRevLett.110.082501.

[102] W. Erni, I. Keshelashvili, B. Krusche, et al. Technical design report for the $\overline{P}$ ANDA (AntiProton Annihilations at Darmstadt) Straw Tube Tracker. *The European physical journal / A*, 49(2):25, 2013. doi: 10.1140/epja/i2013-13025-8.

[103] C. Ewerz*, A. von Manteuffel, A. Schöning, and O. Nachtmann. The new measurement from HERA and the dipole model. *Physics letters / B*, 720(1-3):181 – 187, 2013. doi: 10.1016/j.physletb.2013.02.013.

[104] L. Fabbietti, G. Agakishiev, C. Behnke, D. Belver, A. Belyaev, J. C. Berger-Chen, A. Blanco, C. Blume*, M. Böhmer, P. Cabanelas, S. Chernenko, C. Dritsa, A. Dybczak, E. Epple, O. Fateev, P. Fonte, J. Friese, I. Fröhlich, T. Galatyuk, J. A. Garzón, K. Gill, M. Golubeva, D. González-Díaz, F. Guber, M. Gumberidze, S. Harabasz, T. Hennino, C. Höhne, R. Holzmann*, P. Huck, A. Ierusalimov, A. Ivashkin, M. Jurkovic, B. Kämpfer, T. Karavicheva, I. Koenig*, W. Koenig*, B. Kolb*, G. Korcyl, G. Kornakov, R. Kotte, A. Krása, E. Krebs, F. Krizek, H. Kuc, A. Kugler, A. Kurepin, A. Kurilkin, P. Kurilkin, V. Ladygin, R. Lalik, S. Lang*, K. Lapidus, A. Lebedev, L. Lopes, M. Lorenz, L. Maier, A. Mangiarotti, J. Markert, V. Metag, J. Michel, C. Müntz, R. Münzer, L. Naumann, M. Palka, Y. Parpottas, V. Pechenov*, O. Pechenova, J. Pietraszko*, W. Przygoda, B. Ramstein, L. Rehnisch, A. Reshetin, A. Rustamov, A. Sadovsky, P. Salabura, T. Scheib, H. Schuldes, J. Siebenson, Y. G. Sobolev, S. Spataro, H. Ströbele, J. Stroth*, P. Strzempek, C. Sturm*, O. Svoboda, A. Tarantola, K. Teilab, P. Tlusty, M. Traxler*, H. Tsertos, T. Vasiliev, V. Wagner, M. Weber, C. Wendisch, J. Wüstenfeld, S. Yurevich, and Y. Zanevsky. $pK^+\lambda$ final state: Towards the extraction of the ppK^- contribution. *Nuclear physics / A*, 914:60 – 68, 2013. doi: 10.1016/j.nuclphysa.2013.04.012.

[105] P. Fabbricatore, F. Alessandria, G. Bellomo, U. Gambardella, S. Farinon, R. Marabotto, H. Muller*, R. Musenich, M. Sorbi, and G. Volpini. The Curved Fast Ramped Superconducting Dipoles for FAIR SIS300 Synchrotron: From First Model to Future Developments. *IEEE transactions on applied superconductivity*, 23(3):4000505 – 4000505, 2013. doi: 10.1109/TASC.2012.2229332.

[106] T. Faestermann, M. Górska*, and H. Grawe*. The structure of ^{100}Sn and neighbouring nuclei. *Progress in particle and nuclear physics*, 69:85 – 130, 2013. doi: 10.1016/j.ppnp.2012.10.002.

[107] E. I. Fiks, Y. L. Pivovarov, O. V. Bogdanov, H. Geissel*, and C. Scheidenberger*. Influence of slowing down in the radiator on the Cherenkov radiation angular distributions from relativistic heavy ions at FAIR, SPS and LHC energies. *Nuclear instruments & methods in physics research / B*, 309:146 – 150, 2013. doi: 10.1016/j.nimb.2013.01.064.

[108] E. I. Fiks, Y. L. Pivovarov, O. V. Bogdanov, H. Geissel*, C. Scheidenberger*, and J. Ruzicka. Slowing-down of relativistic heavy ions and its influence on angular distributions of Vavilov–Cherenkov radiation. *Nuclear instruments & methods in physics research / B*, 314:51 – 54, 2013. doi: 10.1016/j.nimb.2013.05.033.

[109] C. S. Fischer* and J. Luecker. Propagators and phase structure of and QCD. *Physics letters / B*, 718(3): 1036 – 1043, 2013. doi: 10.1016/j.physletb.2012.11.054.

[110] E. Fischer*, H. Khodzhibagiyan, P. Schnizer*, and A. Bleile*. Status of the SC Magnets for the SIS100 Synchrotron and the NICA Project. *IEEE transactions on applied superconductivity*, 23(3):4100504 – 4100504, 2013. doi: 10.1109/TASC.2012.2232952.

[111] M. Fisichella, A. Musumarra, F. Farinon*, C. Nociforo*, A. Del Zoppo, P. Figuera, M. La Cognata, M. G. Pellegriti, V. Scuderi, D. Torresi, and E. Strano. Determination of the half-life of ^{213}Fr with high precision. *Physical review / C*, 88(1):011303, 2013. doi: 10.1103/PhysRevC.88.011303.

[112] L. Fister and J. M. Pawlowski*. Confinement from correlation functions. *Physical review / D*, 88(4): 045010, 2013. doi: 10.1103/PhysRevD.88.045010.

[113] A. Francis*, B. Jäger*, H. B. Meyer*, and H. Wittig*. New representation of the Adler function for lattice QCD. *Physical review / D*, 88(5):054502, 2013. doi: 10.1103/PhysRevD.88.054502.

[114] D. Garcia-Senz, R. M. Cabezon, A. Arcones*, A. Relano, and F. K. Thielemann. High-resolution simulations of the head-on collision of white dwarfs. *Monthly notices of the Royal Astronomical Society*, 436(4):3413 – 3429, 2013. doi: 10.1093/mnras/stt1821.

[115] M. Gascón, L. Schnorrenberger, B. Pietras, H. Álvarez Pol, D. Cortina-Gil, P. D. Fernández, I. Duran, J. Glorius, D. González, D. Perez-Loureiro, N. Pietralla, D. Savran*, and K. Sonnabend. Characterization of a CsI(Tl) array coupled to avalanche photodiodes for the Barrel of the CALIFA calorimeter at the NEPTUN tagged gamma beam facility. *Journal of Instrumentation*, 8(10):P10004 – P10004, 2013. doi: 10.1088/1748-0221/8/10/P10004.

[116] A. M. Gasparyan*, M. Lutz*, and E. Epelbaum. Two-nucleon scattering: Merging chiral effective field theory with dispersion relations. *The European physical journal / A*, 49(9):115, 2013. doi: 10.1140/epja/i2013-13115-7.

[117] R. Geithner, D. Heinert, R. Neubert, W. Vodel*, and P. Seidel. Low temperature permeability and current noise of ferromagnetic pickup coils. *Cryogenics*, 54:16 – 19, 2013. doi: 10.1016/j.cryogenics.2012.10.002.

[118] L. Giot*, J. A. Alcantara-Nunez, J. Benlliure, D. Perez-Loureiro, L. Audouin, A. Boudard, E. Casarejos, T. Enqvist*, J. E. Ducret, B. Fernandez-Dominguez, M. F. Ordonez, F. Farget, A. Heinz*, V. Henzl*, D. Henzlova*, A. Kelic-Heil*, A. Lafriaskh, S. Leray, P. Napolitani*, C. Paradela, J. Pereira, M. V. Ricciardi*, C. Stephan, K.-H. Schmidt*, C. Schmitt*, L. Tassan-Got, C. Villagrasa, C. Volant, and O. Yordanov*. Isotopic production cross sections of the residual nuclei in spallation reactions induced by Xe-136 projectiles on proton at 500 A MeV. *Nuclear physics / A*, 899:116–132, 2013. doi: 10.1016/inuclphysa.2012.12.119.

[119] L. Giot*, J. A. Alcántara-Núñez, J. Benlliure, D. Pérez-Loureiro, L. Audouin, A. Boudard, E. Casarejos, T. Enqvist*, J. E. Ducret, B. Fernández-Domínguez, M. Fernández Ordóñez, F. Farget, A. Heinz*, V. Henzl*, D. Henzlova*, A. Kelić-Heil*, A. Lafriaskh, S. Leray, P. Napolitani*, C. Paradela, J. Pereira, M. V. Ricciardi*, C. Stéphan, K.-H. Schmidt*, C. Schmitt*, L. Tassan-Got, C. Villagrasa, C. Volant, and O. Yordanov*. Isotopic production cross sections of the residual nuclei in spallation reactions induced by ^{136}Xe projectiles on proton at 500 A MeV. *Nuclear physics / A*, 899:116 – 132, 2013. doi: 10.1016/j.nuclphysa.2012.12.119.

[120] T. Goecke, C. Fischer, and R. Williams. Role of momentum dependent dressing functions and vector meson dominance in hadronic light-by-light contributions to the muon $g-2$. *Physical review / D*, 87 (3):034013, 2013. doi: 10.1103/PhysRevD.87.034013.

[121] N. Goel*, C. Domingo-Pardo, T. Habermann*, F. Ameil*, T. Engert*, J. Gerl*, I. Kojouharov*, J. Maruhn, N. Pietralla, and H. Schaffner*. Characterisation of a symmetric AGATA detector using the imaging scanning technique. *Nuclear instruments $\&$ methods in physics research / A*, 700:10 – 21, 2013. doi: 10.1016/j.nima.2012.10.028.

[122] P. Golubev, A. Wendt, L. Scruton, J. Taprogge, D. Rudolph, P. Reiter, M. A. Bentley, V. Avdeichikov, P. Boutachkov*, S. P. Fox, J. Gerl*, C. Görgen, R. Hoischen*, N. Kurz*, B. S. Nara Singh, G. Pascovici, S. Pietri*, H. Schaffner*, M. J. Taylor, S. Thiel, and H.-J. Wollersheim*. The Lund–York–Cologne Calorimeter (LYCCA): Concept, design and prototype developments for a FAIR-NUSTAR detector system to discriminate relativistic heavy-ion reaction productsf. *Nuclear instruments $\&$ methods in physics research / A*, 723:55 – 66, 2013. doi: 10.1016/j.nima.2013.04.058.

[123] A. Gottardo, J. J. Valiente-Dobón, G. Benzoni, A. Gadea, S. Lunardi, P. Boutachkov*, A. M. Bruce, M. Górska*, J. Grebosz, S. Pietri*, Z. Podolyák, M. Pfützner, P. H. Regan, H. Weick*, J. Alcántara Núñez, A. Algora, N. Al-Dahan, G. de Angelis, Y. Ayyad, N. Alkhomashi, P. R. P. Allegro, D. Bazzacco, J. Benlliure, M. Bowry, A. Bracco, M. Bunce, F. Camera, E. Casarejos, M. L. Cortes*, F. C. L. Crespi, A. Corsi, A. M. Denis Bacelar, A. Y. Deo, C. Domingo-Pardo, M. Doncel, Z. Dombradi, T. Engert*, K. Eppinger, G. F. Farrelly, F. Farinon*, E. Farnea, H. Geissel*, J. Gerl*, N. Goel*, E. Gregor*, T. Habermann*, R. Hoischen*, R. Janik, P. R. John, S. Klupp, I. Kojouharov, N. Kurz*, S. M. Lenzi, S. Leoni, S. Mandal, R. Menegazzo, D. Mengoni, B. Million, V. Modamio, A. I. Morales, D. R. Napoli, F. Naqvi*, R. Nicolini, C. Nociforo, A. Prochazka, W. Prokopowicz*, F. Recchia, R. V. Ribas, M. W. Reed, D. Rudolph, E. Sahin, H. Schaffner*, A. Sharma, B. Sitar, D. Siwal, K. Steiger, P. Strmen, T. P. D. Swan, I. Szarka, C. A. Ur, P. M. Walker, O. Wieland, and H.-J. Wollersheim*. New µs isomers in the neutron-rich ^{210}Hg nucleus. *Physics letters / B*, 725(4-5):292 – 296, 2013. doi: 10.1016/j.physletb.2013.07.053.

[124] G. Gürdal, E. A. Stefanova, P. Boutachkov, D. A. Torres, G. J. Kumbartzki, N. Benczer-Koller, Y. Y. Sharon, L. Zamick, S. J. Q. Robinson, T. Ahn, V. Anagnostatou, C. Bernards, M. Elvers, A. Heinz, G. Ilie, D. Radeck, D. Savran*, V. Werner, and E. Williams. Measurements of g($4_1^+, 2_2^+$) in ^{70,72,74,76}Ge: Systematics of low-lying structures in 30≤Z≤40 and 30≤N≤50 nuclei. *Physical review / C*, 88(1):014301, 2013. doi: 10.1103/PhysRevC.88.014301.

[125] L. V. Grigorenko, I. Mukha*, and M. V. Zhukov. Lifetime and Fragment Correlations for the Two-Neutron Decay of ^{26}O Ground State. *Physical review letters*, 111(4):042501, 2013. doi: 10.1103/PhysRevLett.111.042501.

[126] G. Guastalla, D. D. DiJulio, M. Górska*, J. Cederkäll, P. Boutachkov*, P. Golubev, S. Pietri*, H. Grawe*, F. Nowacki, K. Sieja, A. Algora, F. Ameil*, T. Arici*, A. Atac, M. A. Bentley, A. Blazhev, D. Bloor, S. Brambilla, N. Braun, F. Camera, Z. Dombrádi, C. Domingo Pardo, A. Estrade*, F. Farinon*, J. Gerl*, N. Goel*, J. Gręboszt, T. Habermann*, R. Hoischen, K. Jansson, J. Jolie, A. Jungclaus, I. Kojouharov*, R. Knoebel*, R. Kumar, J. Kurcewicz, N. Kurz*, N. Lalović*, E. Merchan*, K. Moschner, F. Naqvi*, B. S. Nara Singh, J. Nyberg, C. Nociforo*, A. Obertelli, M. Pfützner, N. Pietralla, Z. Podolyák, A. Prochazka*, D. Ralet*, P. Reiter, D. Rudolph, H. Schaffner*, F. Schirru, L. Scruton, D. Sohler, T. Swaleh, J. Taprogge, Z. Vajta, R. Wadsworth, N. Warr, H. Weick*, A. Wendt, O. Wieland, J. S. Winfield*, and H.-J. Wollersheim*. Coulomb Excitation of ^{104}Sn and the Strength of the ^{100}Sn Shell Closure. *Physical review letters*, 110(17):172501, 2013. doi: 10.1103/PhysRevLett.110.172501.

[127] L. M. Haas*, R. Stiele*, J. Braun*, J. M. Pawlowski*, and J. Schaffner-Bielich*. Improved Polyakov-loop potential for effective models from functional calculations. *Physical review / D*, 87(7):076004, 2013. doi: 10.1103/PhysRevD.87.076004.

[128] O. S. Haas*, O. Boine-Frankenheim*, and F. Petrov. Simulations of the electron cloud buildup and its influence on the microwave transmission measurement. *Nuclear instruments & methods in physics research / A*, 729:290 – 295, 2013. doi: 10.1016/j.nima.2013.07.051.

[129] K. Hadyńska-Klęk, P. J. Napiorkowski, A. Maj, F. Azaiez, M. Kicińska-Habior, J. J. Valiente-Dobón, T. Abraham, G. Anil Kumar, B.-Q. Arnés, D. Bazzacco, M. Bellato, D. Bortolato, P. Bednarczyk, G. Benzoni, L. Berti, B. Birkenbach, B. Bruyneel, S. Brambilla, F. Camera, J. Chavas, M. Ciemała, P. Cocconi, P. Coleman-Smith, A. Colombo, A. Corsi, F. C. L. Crespi, D. M. Cullen, A. Czermak, P. Désesquelles, B. Dulny, J. Eberth, E. Farnea, B. Fornal, S. Franchoo, A. Gadea, A. Giaz, A. Gottardo, X. Grave, J. Gręboszt, M. Gulmini, T. Habermann*, R. Isocrate, J. Iwanicki, G. Jaworski, A. Jungclaus, N. Karkour, M. Kmiecik, D. Karpiński, M. Kisieliński, N. Kondratyev, A. Korichi, M. Komorowska, M. Kowalczyk, W. Korten, M. Krzysiek, G. Lehaut, S. Leoni, A. Lopez-Martens, S. Lunardi, G. Maron, K. Mazurek, R. Menegazzo, D. Mengoni, E. Merchán*, W. Męczyński, C. Michelagnoli, J. Mierzejewski, B. Million, P. Molini, S. Myalski, D. R. Napoli, R. Nicolini, M. Niikura, A. Obertelli, S. F. Özmen, M. Palacz, A. Pullia, G. Rampazzo, F. Recchia, N. Redon, P. Reiter, D. Rosso, K. Rusek, E. Sahin, M.-D. Salsac, P.-A. Söderström, J. Srebrny, I. Stefan, O. Stézowski, J. Styczeń, C. Theisen, N. Toniolo, C. A. Ur, V. Vandone, R. Wadsworth, B. Wasilewska, A. Wiens, K. Wrzosek-Lipska, M. Zielińska, and M. Zięblíński. Towards the Determination of Superdeformation in ^{42}Ca. *Acta physica Polonica / B*, 44(3):617, 2013. doi: 10.5506/APhysPolB.44.617.

[130] J. H. Hamilton, S. Hofmann*, and Y. T. Oganessian. Search for Superheavy Nuclei. *Annual review of nuclear and particle science*, 63(1):383 – 405, 2013. doi: 10.1146/annurev-nucl-102912-144535.

[131] H.-W. Hammer, A. Nogga, and A. Schwenk*. Colloquium: Three-body forces: From cold atoms to nuclei. *Reviews of modern physics*, 85(1):197 – 217, 2013. doi: 10.1103/RevModPhys.85.197.

[132] C. Hartnack, H. Oeschler, Y. Leifels*, E. L. Bratkovskaya, and J. Aichelin. What heavy ion can teach us about strange particles and what strange particles can teach us about heavy ions? *Nuclear physics / A*, 914:392 – 395, 2013. doi: 10.1016/j.nuclphysa.2013.05.010.

[133] K. Hebeler*, J. M. Lattimer, C. J. Pethick, and A. Schwenk*. EQUATION OF STATE AND NEUTRON STAR PROPERTIES CONSTRAINED BY NUCLEAR PHYSICS AND OBSERVATION. *The astrophysical journal / 1*, 773(1):11, 2013. doi: 10.1088/0004-637X/773/1/11.

[134] F. Hebenstreit, J. Berges, and D. Gelfand. Simulating fermion production in 1+1 dimensional QED. *Physical review / D*, 87(10):105006, 2013. doi: 10.1103/PhysRevD.87.105006.

[135] F. Hebenstreit, J. Berges, and D. Gelfand. Real-Time Dynamics of String Breaking. *Physical review letters*, 111(20):201601, 2013. doi: 10.1103/PhysRevLett.111.201601.

[136] F. P. Heßberger*. Discovery of the Heaviest Elements. *ChemPhysChem*, 14(3):483 – 489, 2013. doi: 10.1002/cphc.201201011.

[137] T. K. Herbst, J. M. Pawlowski, and B.-J. Schaefer. Phase structure and thermodynamics of QCD. *Physical review / D*, 88(1):014007, 2013. doi: 10.1103/PhysRevD.88.014007.

[138] H. Hergert, S. K. Bogner, S. Binder, A. Calci, J. Langhammer, R. Roth, and A. Schwenk*. In-medium similarity renormalization group with chiral two- plus three-nucleon interactions. *Physical review / C*, 87(3):034307, 2013. doi: 10.1103/PhysRevC.87.034307.

[139] J. Heuser*. The Compressed Baryonic Matter Experiment at FAIR. *Nuclear physics / A*, 904-905:941c – 944c, 2013. doi: 10.1016/j.nuclphysa.2013.02.170.

[140] G. M. Hippel, B. Jäger*, T. D. Rae, and H. Wittig. The shape of covariantly smeared sources in lattice QCD. *Journal of high energy physics*, 2013(9):14, 2013. doi: 10.1007/JHEP09(2013)014.

[141] J. D. Holt and J. Engel. Effective double-β-decay operator for ^{76}Ge and ^{82}Se. *Physical review / C*, 87 (6):064315, 2013. doi: 10.1103/PhysRevC.87.064315.

[142] J. D. Holt, J. Menendez*, and A. Schwenk*. The role of three-nucleon forces and many-body processes in nuclear pairing. *Journal of physics / G*, 40(7):075105, 2013. doi: 10.1088/0954-3899/40/7/075105.

[143] J. D. Holt, J. Menéndez*, and A. Schwenk*. Three-Body Forces and Proton-Rich Nuclei. *Physical review letters*, 110(2):022502, 2013. doi: 10.1103/PhysRevLett.110.022502.

[144] J. D. Holt, J. Menéndez*, and A. Schwenk*. Chiral three-nucleon forces and bound excited states in neutron-rich oxygen isotopes. *The European physical journal / A*, 49(3):39, 2013. doi: 10.1140/epja/i2013-13039-2.

[145] W. Horiuchi, H. Feldmeier*, T. Neff*, and Y. Suzuki. Universality of Short-Range Nucleon-Nucleon Correlations in Nuclei. *Few-body systems*, 54(1-4):279 – 282, 2013. doi: 10.1007/s00601-012-0341-2.

[146] J. Isaak*, D. Savran*, M. Krtička, M. W. Ahmed, J. Beller, E. Fiori*, J. Glorius, J. H. Kelley, B. Löher*, N. Pietralla*, C. Romig, G. Rusev, M. Scheck, L. Schnorrenberger, J. Silva*, K. Sonnabend*, A. P. Tonchev, W. Tornow, H. R. Weller, and M. Zweidinger. Constraining nuclear photon strength functions by the decay properties of photo-excited states. *Physics letters / B*, 727(4-5):361 – 365, 2013. doi: 10.1016/j.physletb.2013.10.040.

[147] K. Itahashi, G. P. A. Berg, H. Fujioka, H. Geissel*, R. S. Hayano, S. Hirenzaki, N. Ikeno, N. Inabe, S. Itoh, D. Kameda, T. Kubo, H. Matsubara, S. Michimasa, K. Miki, H. Miya, M. Nakamura, T. Nishi, S. Noji, S. Ota, K. Suzuki, H. Takeda, K. Todoroki, K. Tsukada, T. Uesaka, H. Weick*, and K. Yoshida. First Precision Spectroscopy of Pionic Atoms at RI Beam Factory. *Few-body systems*, 54(7-10):1569 – 1572, 08/20/2012 - 08/25/2012 2013. doi: 10.1007/s00601-013-0669-2.

[148] M. Ivanov*. Identified charged hadron production measured with ALICE at the LHC. *Nuclear physics / A*, 904-905:162c – 169c, 2013. doi: 10.1016/j.nuclphysa.2013.01.058.

[149] Y. Iwata*, K. Iida, and N. Itagaki. Synthesis of thin, long heavy nuclei in ternary collisions. *Physical review / C*, 87(1):014609, 2013. doi: 10.1103/PhysRevC.87.014609.

[150] S. Jones, R. Hirschi, K. Nomoto, T. Fischer*, F. X. Timmes, F. Herwig, B. Paxton, H. Toki, T. Suzuki, G. Martínez-Pinedo*, Y. H. Lam, and M. G. Bertolli. ADVANCED BURNING STAGES AND FATE OF 8-10 M STARS. *The astrophysical journal / 1*, 772(2):150, 2013. doi: 10.1088/0004-637X/772/2/150.

[151] D. Jordan, A. Algora, J. Taín, B. Rubio, J. Agramunt, A. Perez-Cerdan, F. Molina, L. Caballero, E. Nácher, A. Krasznahorkay, M. Hunyadi, J. Gulyás, A. Vitéz, M. Csatlós, L. Csige, J. Äysto, H. Penttilä, I. Moore, T. Eronen, A. Jokinen, A. Nieminen, J. Hakala, P. Karvonen, A. Kankainen, A. Saastamoinen, J. Rissanen, T. Kessler, C. Weber, J. Ronkainen, S. Rahaman, V. Elomaa, U. Hager, S. Rinta-Antila, T. Sonoda, K. Burkard*, W. Hüller*, L. Batist, W. Gelletly, A. Nichols, T. Yoshida, A. Sonzogni, K. Peräjärvi, A. Petrovici, K. Schmid, and A. Faessler. Total absorption study of the β decay of $^{102,104,105}Tc$. *Physical review / C*, 87(4):044318, 2013. doi: 10.1103/PhysRevC.87.044318.

[152] Z. Kalaninová, A. N. Andreyev, S. Antalic, F. Heßberger*, D. Ackermann*, B. Andel, M. C. Drummond, S. Hofmann*, M. Huyse, B. Kindler*, J. F. W. Lane, V. Liberati, B. Lommel*, R. D. Page, E. Rapisarda, K. Sandhu, Š. Šáro, A. Thornthwaite, and P. Van Duppen. α decay of the very neutron-deficient isotopes $^{197-199}Fr$. *Physical review / C*, 87(4):044335, 2013. doi: 10.1103/PhysRevC.87.044335.

[153] K. Kamikado, N. Strodthoff, L. von Smekal, and J. Wambach*. Fluctuations in the quark-meson model for QCD with isospin chemical potential. *Physics letters / B*, 718(3):1044–1053, 2013. doi: 10.1016/j.physletb.2012.11.055.

[154] J. Khuyagbaatar, V. P. Shevelko, A. Borschevsky, C. E. Düllmann*, I. Y. Tolstikhina, and A. Yakushev*. Average charge states of heavy and superheavy ions passing through a rarified gas: Theory and experiment. *Physical review / A*, 88(4):042703, 2013. doi: 10.1103/PhysRevA.88.042703.

[155] N. Kobayashi, T. Nakamura, Y. Kondo, N. Aoi, H. Baba, S. Deguchi, N. Fukuda, G. S. Lee, H. S. Lee, N. Inabe, M. Ishihara, Y. Kawada, R. Kanungo, T. Kubo, M. A. Famiano, M. Matsushita, T. Motobayashi, T. Ohnishi, N. A. Orr, H. Otsu, R. Barthelemy, H. Sakurai, S. Kim, T. Sako, T. Sumikama, Y. Satou, K. Takahashi, H. Takeda, M. Takechi*, S. Takeuchi, K. N. Tanaka, N. Tanaka, R. Tanaka, Y. Togano, and K. Yoneda. Breakup Reactions of Drip-Line Nuclei Near N = 20, 28. *Few-body systems*, 54(7-10): 1441 – 1444, 08/20/2012 - 08/25/2012 2013. doi: 10.1007/s00601-013-0699-9.

[156] A. Krasznahorkay, M. Csatlós, L. Stuhl, A. Algora, J. Gulyás, J. Tímár, N. Paar, D. Vretenar, M. N. Harakeh, R3B Collaboration, and EXL Collaboration*. A New Method for Measuring Neutron-skin Thickness in Rare Isotope Beams. *Acta physica Polonica / B*, 44(3):559 – 562, 2013. doi: 10.5506/APhysPolB.44.559.

[157] A. Krasznahorkay, N. Paar, D. Vretenar, and M. N. Harakeh. Anti-analog giant dipole resonances and the neutron skin of nuclei. *Physics letters / B*, 720(4-5):428 – 432, 2013. doi: 10.1016/j.physletb.2013.02.043.

[158] J. V. Kratz*, M. Schädel*, and H. W. Gäggeler*. Reexamining the heavy-ion reactions $^{238}U + ^{238}U$ and $^{238}U + ^{248}Cm$ and actinide production close to the barrier. *Physical review / C*, 88(5):054615, 2013. doi: 10.1103/PhysRevC.88.054615.

[159] T. Krüger*, I. Tews*, B. Friman*, K. Hebeler*, and A. Schwenk*. The chiral condensate in neutron matter. *Physics letters / B*, 726(1-3):412 – 416, 2013. doi: 10.1016/j.physletb.2013.08.022.

[160] A. C. LaForge, R. Hubele, J. Goullon, X. Wang, K. Schneider*, V. L. B. de Jesus, B. Najjari, A. B. Voitkiv*, M. Grieser, M. Schulz, and D. Fischer. Initial-state selective study of ionization dynamics in ion-Li collisions. *Journal of physics / B*, 46(3):031001, 2013. doi: 10.1088/0953-4075/46/3/031001.

[161] S. Lalkovski, A. M. Bruce, A. M. Denis Bacelar, M. Górska*, S. Pietri*, Z. Podolyák, P. Bednarczyk*, L. Caceres, E. Casarejos, I. J. Cullen, P. Doornenbal*, G. F. Farrelly, A. B. Garnsworthy, H. Geissel*,

W. Gelletly, J. Gerl*, J. Grębosz*, C. Hinke, G. Ilie, D. Ivanova, G. Jaworski, S. Kisyov, I. Kojouharov*, N. Kurz*, N. Minkov, S. Myalski, M. Palacz, P. Petkov, W. Prokopowicz*, P. H. Regan, H. Schaffner*, S. Steer, S. Tashenov*, P. M. Walker, and H.-J. Wollersheim*. Submicrosecond isomer in $^{117}_{45}Rh_{72}$ and the role of triaxiality in its electromagnetic decay rate. *Physical review / C*, 88(2):024302, 2013. doi: 10.1103/PhysRevC.88.024302.

[162] S. Lalkovski, A. M. Bruce, A. Jungclaus, M. Górska, M. Pfützner, L. Cáceres*, F. Naqvi*, S. Pietri*, Z. Podolyák, G. S. Simpson, K. Andgren, P. Bednarczyk*, T. Beck*, J. Benlliure, G. Benzoni, E. Casarejos, B. Cederwall, F. C. L. Crespi, J. J. Cuenca-García*, I. J. Cullen, A. M. Denis Bacelar, P. Detistov, P. Doornenbal*, G. F. Farrelly, A. B. Garnsworthy, H. Geissel*, W. Gelletly, J. Gerl*, J. Grebosz*, B. Hadinia, M. Hellström, C. Hinke, R. Hoischen*, G. Ilie, G. Jaworski, J. Jolie, A. Khaplanov, S. Kisyov, M. Kmiecik, I. Kojouharov*, R. Kumar, N. Kurz*, A. Maj, S. Mandal, V. Modamio, F. Montes*, S. Myalski, M. Palacz, W. Prokopowicz*, P. Reiter, P. H. Regan, D. Rudolph, H. Schaffner*, D. Sohler, S. J. Steer, S. Tashenov*, J. Walker, P. M. Walker, H. Weick*, E. Werner-Malento, O. Wieland, H. J. Wollersheim*, and M. Zhekova. Core-coupled states and split proton-neutron quasiparticle multiplets in $^{122-126}Ag$. *Physical review / C*, 87(3):034308, 2013. doi: 10.1103/PhysRevC.87.034308.

[163] J. F. W. Lane, A. N. Andreyev, S. Antalic, D. Ackermann*, J. Gerl*, F.-P. Hessberger*, S. Hofmann*, M. Huyse, H. Kettunen, A. Kleinböhl*, B. Kindler*, I. Kojouharov*, M. Leino, B. Lommel*, G. Münzenberg*, K. Nishio, R. D. Page, Š. Šáro, H. Schaffner*, M. J. Taylor, and P. Van Duppen. β-delayed fission of $^{186,188}Bi$ isotopes. *Physical review / C*, 87(1):014318, 2013. doi: 10.1103/PhysRevC.87.014318.

[164] K. Langfeld and J. M. Pawlowski*. Two-color QCD with heavy quarks at finite densities. *Physical review / D*, 88(7):071502, 2013. doi: 10.1103/PhysRevD.88.071502.

[165] Z. Lécz*, O. Boine-Frankenheim*, and V. Kornilov*. Target normal sheath acceleration for arbitrary proton layer thickness. *Nuclear instruments & methods in physics research / A*, 727:51 – 58, 2013. doi: 10.1016/j.nima.2013.05.163.

[166] A. Lehmann, A. Britting, W. Eyrich, C. Schwarz*, J. Schwiening*, and F. Uhlig. Significantly improved lifetime of micro-channel plate PMTs. volume 718, pages 535 – 540. 12th Pisa Meeting on Advanced Detectors, La Biodola, Isola d'Elba(Italy), North-Holland Publ. Co., 05/20/2012 - 05/26/2012 2013. doi: 10.1016/j.nima.2012.11.109.

[167] D. Lens and H. Klingbeil*. Stability of longitudinal bunch length feedback for heavy-ion synchrotrons. *Physical review / Special topics / Accelerators and beams*, 16(3):032801, 2013. doi: 10.1103/PhysRevSTAB.16.032801.

[168] B. Löher, V. Derya, T. Aumann*, J. Beller, N. Cooper, M. Duchêne, J. Endres, E. Fiori, J. Isaak, J. Kelley, M. Knörzer, N. Pietralla, C. Romig, D. Savran, M. Scheck, H. Scheit, J. Silva, A. Tonchev, W. Tornow, H. Weller, V. Werner, and A. Zilges. The high-efficiency $\gamma - ray$ spectroscopy setup γ^3 at $HI\gamma S$. *Nuclear instruments & methods in physics research / A*, 723:136 – 142, 2013. doi: 10.1016/j.nima.2013.04.087.

[169] D. L. Lincoln, J. D. Holt*, G. Bollen, M. Brodeur, S. Bustabad, J. Engel, S. J. Novario, M. Redshaw, R. Ringle, and S. Schwarz. First Direct Double-β Decay Q-Value Measurement of ^{82}Se in Support of Understanding the Nature of the Neutrino. *Physical review letters*, 110(1):012501, 2013. doi: 10.1103/PhysRevLett.110.012501.

[170] S. Litvinov*, D. Toprek, H. Weick*, and A. Dolinskii*. Isochronicity correction in the CR storage ring. *Nuclear instruments & methods in physics research / A*, 724:20 – 26, 2013. doi: 10.1016/j.nima.2013.05.057.

[171] P. M. Lo*, B. Friman*, O. Kaczmarek, K. Redlich*, and C. Sasaki. Probing deconfinement with Polyakov loop susceptibilities. *Physical review / D*, 88(1):014506, 2013. doi: 10.1103/PhysRevD.88.014506.

[172] P. M. Lo*, B. Friman*, O. Kaczmarek, K. Redlich*, and C. Sasaki. Polyakov loop fluctuations in SU(3) lattice gauge theory and an effective gluon potential. *Physical review / D*, 88(7):074502, 2013. doi: 10.1103/PhysRevD.88.074502.

[173] V. Manea, D. Atanasov, D. Beck*, K. Blaum, C. Borgmann, R. B. Cakirli, T. Eronen, S. George, F. Herfurth*, A. Herlert, M. Kowalska, S. Kreim, Y. A. Litvinov*, D. Lunney, D. Neidherr*, M. Rosenbusch, L. Schweikhard, F. Wienholtz, R. N. Wolf, and K. Zuber. Collective degrees of freedom of neutron-rich A≈100 nuclei and the first mass measurement of the short-lived nuclide ^{100}Rb. *Physical review / C*, 88(5):054322, 2013. doi: 10.1103/PhysRevC.88.054322.

[174] S. Masciocchi*. Heavy-flavour production in ALICE at the LHC. *Nuclear physics / A*, 910-911:83 – 90, 2013. doi: 10.1016/j.nuclphysa.2012.12.059.

[175] R. Massarczyk, G. Schramm, A. Junghans, R. Schwengner, M. Anders, T. Belgya, R. Beyer, E. Birgersson, A. Ferrari, E. Grosse, R. Hannaske, Z. Kis, T. Kögler, K. Kosev, M. Marta*, L. Szentmiklósi, A. Wagner, and J. Weil. Electromagnetic dipole strength up to the neutron separation energy from $^{196}Pt(\gamma,\gamma')$ and $^{195}Pt(n,\gamma)$ reactions. *Physical review / C*, 87(4):044306, 2013. doi: 10.1103/PhysRevC.87.044306.

[176] E. A. McCutchan, C. J. Lister, T. Ahn, V. Anagnostatou, N. Cooper, M. Elvers, P. Goddard, A. Heinz, G. Ilie, D. Radeck, D. Savran*, and V. Werner. Shape coexistence and high-K states in ^{74}Se populated following the β decay of ^{74}Br. *Physical review / C*, 87(1):014307, 2013. doi: 10.1103/PhysRevC.87.014307.

[177] J. Michel, G. Korcyl, L. Maier, and M. Traxler*. In-beam experience with a highly granular DAQ and control network: TrbNet. *Journal of Instrumentation*, 8(02):C02034 – C02034, 2013. doi: 10.1088/1748-0221/8/02/C02034.

[178] L. Miguel*, H. Weick*, J. Mattila, F. Amjad*, E. Kozlova*, C. Karagiannis*, K.-H. Behr*, and M. Winkler*. Super-FRS Target Area Remote Handling: Scenario and Development. *International journal of advanced robotic systems*, 10:1 – 9, 2013. doi: 10.5772/57073.

[179] B. W. Mintz, R. Stiele, R. O. Ramos, and J. Schaffner-Bielich*. Phase diagram and surface tension in the three-flavor Polyakov-quark-meson model. *Physical review / D*, 87(3):036004, 2013. doi: 10.1103/PhysRevD.87.036004.

[180] D. Miskowiec*. ALICE Pb-Pb and p-Pb results. volume 44, pages 1553 – 1567. Epiphany conference on the physics after the first phase at the LHC, Cracow(Poland), Inst. of Physics, Jagellonian Univ., 01/07/2013 - 01/09/2014 2013. doi: 10.5506/APhysPolB.44.1553.

[181] D. Müller, M. Buballa, and J. Wambach. Dyson-Schwinger approach to color superconductivity at finite temperature and density. *The European physical journal / A*, 49(8):96, 2013. doi: 10.1140/epja/i2013-13096-5.

[182] D. Müller, M. Buballa, and J. Wambach*. Dyson–Schwinger study of chiral density waves in QCD. *Physics letters / B*, 727(1-3):240 – 243, 2013. doi: 10.1016/j.physletb.2013.10.050.

[183] G. Münzenberg*. Development of mass spectrometers from Thomson and Aston to present. *International journal of mass spectrometry*, 349-350:9 – 18, 2013. doi: 10.1016/j.ijms.2013.03.009.

[184] V. Modamio, J. J. Valiente-Dobón, S. Lunardi, S. M. Lenzi, A. Gadea, D. Mengoni, D. Bazzacco, A. Algora, P. Bednarczyk, G. Benzoni, B. Birkenbach, A. Bracco, B. Bruyneel, A. Bürger, J. Chavas, L. Corradi, F. C. L. Crespi, G. de Angelis, P. Désesquelles, G. de France, R. Depalo, A. Dewald, M. Doncel, M. N. Erduran, E. Farnea, E. Fioretto, C. Fransen, K. Geibel, A. Gottardo, A. Görgen, T. Habermann*, M. Hackstein, H. Hess, T. Hüyük, P. R. John, J. Jolie, D. Judson, A. Jungclaus, N. Karkour, R. Kempley, S. Leoni, B. Melon, R. Menegazzo, C. Michelagnoli, T. Mijatović, B. Million, O. Möller, G. Montagnoli, D. Montanari, A. Nannini, D. R. Napoli, Z. Podolyak, G. Pollarolo, A. Pullia, B. Quintana, F. Recchia, P. Reiter, D. Rosso, W. Rother, E. Sahin, M. D. Salsac, F. Scarlassara, K. Sieja, P. A. Söderström, A. M. Stefanini, O. Stezowski, S. Szilner, C. Theisen, B. Travers, and C. A. Ur. Lifetime measurements in neutron-rich $^{63,65}Co$ isotopes using the AGATA demonstrator. *Physical review / C*, 88(4):044326, 2013. doi: 10.1103/PhysRevC.88.044326.

[185] A. I. Morales, J. Benlliure, M. Górska*, H. Grawe*, S. Verma, P. H. Regan, Z. Podolyák, S. Pietri, R. Kumar, E. Casarejos, A. Algora, N. Alkhomashi, H. Álvarez Pol, G. Benzoni, A. Blazhev, P. Boutachkov*, A. M. Bruce, L. S. Cáceres*, I. J. Cullen, A. M. Denis Bacelar, P. Doornenbal*, M. E. Estévez-Aguado, G. Farrelly, Y. Fujita, A. B. Garnsworthy, W. Gelletly, J. Gerl*, J. Grebosz*, R. Hoischen, I. Kojouharov*, N. Kurz*, S. Lalkovski, Z. Liu, C. Mihai, F. Molina, D. Mücher, W. Prokopowicz*, B. Rubio, H. Schaffner*, S. J. Steer, A. Tamii, S. Tashenov*, J. J. Valiente-Dobón, P. M. Walker, H.-J. Wollersheim*, and P. J. Woods. β-delayed γ-ray spectroscopy of $^{203,204}Au$ and $^{200-202}Pt$. *Physical review / C*, 88(1):014319, 2013. doi: 10.1103/PhysRevC.88.014319.

[186] K. Morita*, B. Friman*, K. Redlich*, and V. Skokov. Net quark number probability distribution near the chiral crossover transition. *Physical review / C*, 88(3):034903, 2013. doi: 10.1103/PhysRevC.88.034903.

[187] N. Paar, H. Tutman, T. Marketin, and T. Fischer*. Large-scale calculations of supernova neutrino-induced reactions in Z=8–82 target nuclei. *Physical review / C*, 87(2):025801, 2013. doi: 10.1103/PhysRevC.87.025801.

[188] M. Palacz, J. Nyberg, H. Grawe*, K. Sieja, G. de Angelis, P. Bednarczyk, A. Blazhev*, D. Curien, Z. Dombradi, O. Dorvaux, J. Ekman, J. Gałkowski, M. Górska*, J. Iwanicki, G. Jaworski, J. Kownacki, J. Ljungvall, M. Moszyński, F. Nowacki, D. Rudolph, D. Sohler, D. Wolski, and M. Zięblíński. Odd-parity ^{100}Sn Core Excitations. *Acta physica Polonica / B*, 44(3):491, 08/27/2012 - 09/02/2012 2013. doi: 10.5506/APhysPolB.44.491.

[189] I. V. Panov, I. Y. Korneev, G. Martinez-Pinedo*, and F. Thielemann. Influence of spontaneous fission rates on the yields of superheavy elements in the r-process. *Astronomy letters*, 39(3):150 – 160, 2013. doi: 10.1134/S1063773713030043.

[190] C. Parascandolo, D. Pierroutsakou, C. Agodi, R. Alba, V. Baran, A. Boiano, M. Colonna, R. Coniglione, E. De Filippo, A. Del Zoppo, M. Di Toro, U. Emanuele, F. Farinon*, A. Guglielmetti, M. La Commara, C. Maiolino, B. Martin, M. Mazzocco, C. Mazzocchi, C. Rizzo, M. Romoli, D. Santonocito, C. Signorini, R. Silvestri, F. Soramel, E. Strano, D. Torresi, A. Trifirò, and M. Trimarchi. Dynamical Dipole Mode in the ^{192}Pb Mass Region. *Acta physica Polonica / B*, 44(3):605, 2013. doi: 10.5506/APhysPolB.44.605.

[191] V. Pershina-Naegele*. Predictions of redox potentials of Sg in acid solutions as a function of pH. *Radiochimica acta*, 101:749–752, 2013. doi: 10.1524/ract.2013.2121.

[192] V. Pershina-Naegele* and J. Anton. Theoretical predictions of properties and gas-phase chromatography behaviour of carbonyl complexes of group-6 elements Cr, Mo, W, and element 106, Sg. *The journal of chemical physics*, 138(17):174301, 2013. doi: 10.1063/1.4802765.

[193] B. Pietras, M. Gascón, H. Álvarez Pol, M. Bendel, T. Bloch, E. Casarejos, D. Cortina-Gil, I. Durán, E. Fiori*, R. Gernhäuser, D. González, T. Kröll, T. Le Bleis, N. Montes, E. Nácher, M. Robles, A. Perea, J. A. Vilán, and M. Winkel. CALIFA Barrel prototype detector characterisation. *Nuclear instruments & methods in physics research / A*, 729:77 – 84, 2013. doi: 10.1016/j.nima.2013.06.063.

[194] W. Plaß*, T. Dickel*, and C. Scheidenberger*. Multiple-reflection time-of-flight mass spectrometry. *International journal of mass spectrometry*, 349-350:134 – 144, 2013. doi: 10.1016/j.ijms.2013.06.005.

[195] E. Minaya Ramirez*, D. Ackermann*, K. Blaum, M. Block*, C. Droese, C. E. Düllmann*, M. Eibach, S. Eliseev, E. Haettner*, F. Herfurth*, F.-P. Hessberger*, S. Hofmann*, G. Marx, D. Nesterenko, Y. N. Novikov, W. Plaß*, D. Rodríguez, C. Scheidenberger*, L. Schweikhard, P. G. Thirolf, and C. Weber. Recent developments for high-precision mass measurements of the heaviest elements at SHIPTRAP. *Nuclear instruments & methods in physics research / B*, 317:501 – 505, 2013. doi: 10.1016/j.nimb.2013.07.055.

[196] C. Rappold*, E. Kim*, D. Nakajima*, T. Saito*, O. Bertini*, S. Bianchin*, V. Bozkurt*, M. Kavatsyuk, Y. Ma*, F. Maas*, S. Minami*, B. Özel Tashenov*, K. Yoshida*, P. Achenbach, S. Ajimura, T. Aumann*, C. Ayerbe Gayoso, H. C. Bhang, C. Caesar*, S. Erturk, T. Fukuda, B. Göküzüm*, E. Guliev, T. Hiraiwa, J. Hoffmann*, G. Ickert*, Z. S. Ketenci, D. Khaneft*, M. Kim, S. Kim, K. Koch*, N. Kurz*, A. Le Fèvre*, Y. Mizoi, M. Moritsu, T. Nagae, L. Nungesser, A. Okamura, W. Ott*, J. Pochodzalla, A. Sakaguchi, M. Sako, C. J. Schmidt*, M. Sekimoto, H. Simon*, H. Sugimura, T. Takahashi, G. J. Tambave, H. Tamura, W. Trautmann*, S. Voltz*, N. Yokota, and C. J. Yoon. Hypernuclear spectroscopy of products from ^{6}Li projectiles on a carbon target at 2A GeV. *Nuclear physics / A*, 913:170 – 184, 2013. doi: 10.1016/j.nuclphysa.2013.05.019.

[197] C. Rappold*, E. Kim*, T. Saito*, O. Bertini*, S. Bianchin*, V. Bozkurt*, M. Kavatsyuk, Y. Ma*, F. Maas*, S. Minami*, D. Nakajima*, B. Özel Tashenov*, K. Yoshida*, P. Achenbach, S. Ajimura, T. Aumann*, C. Ayerbe Gayoso, H. C. Bhang, C. Caesar*, S. Erturk, T. Fukuda, B. Göküzüm, E. Guliev, J. Hoffmann*, G. Ickert*, Z. S. Ketenci, D. Khaneft*, M. Kim, S. Kim, K. Koch*, N. Kurz*, A. Le Fèvre*, Y. Mizoi, L. Nungesser, W. Ott*, J. Pochodzalla, A. Sakaguchi, C. J. Schmidt*, M. Sekimoto, H. Simon*, T. Takahashi, G. J. Tambave, H. Tamura, W. Trautmann*, S. Voltz*, and C. J. Yoon. Search for evidence of ${}^{3}_{\Lambda}n$ by observing $d+\pi^-$ and $t+\pi^-$ final states in the reaction of $^{6}Li+^{12}C$ at 2A GeV. *Physical review / C*, 88(4):041001, 2013. doi: 10.1103/PhysRevC.88.041001.

[198] P. Rau, J. Steinheimer, S. Schramm, and H. Stöcker*. Chiral hadronic mean field model including quark degrees of freedom. *Journal of physics / G*, 40(8):085001, 2013. doi: 10.1088/0954-3899/40/8/085001.

[199] T. Rauscher, N. Dauphas, I. Dillmann*, C. Fröhlich, Z. Fülöp, and G. Gyürky. Constraining the astrophysical origin of the p-nuclei through nuclear physics and meteoritic data. *Reports on progress in physics*, 76(6):066201, 2013. doi: 10.1088/0034-4885/76/6/066201.

[200] T. R. Rodríguez* and G. Martínez-Pinedo*. Neutrinoless $\eta\eta$ decay nuclear matrix elements in an isotopic chain. *Physics letters / B*, 719(1-3):174–178, 2013. doi: 10.1016/j.physletb.2012.12.063.

[201] E. Roeckl* and I. Mukha*. Q values of radioactive decay: Examples from nuclear physics and related fields. *International journal of mass spectrometry*, 349-350:47 – 56, 2013. doi: 10.1016/j.ijms.2013.03.021.

[202] C. Romig, J. Beller, J. Glorius, J. Isaak*, J. H. Kelley, E. Kwan, N. Pietralla, V. Y. Ponomarev, A. Sauerwein, D. Savran*, M. Scheck, L. Schnorrenberger, K. Sonnabend, A. P. Tonchev, W. Tornow, H. R. Weller, A. Zilges, and M. Zweidinger. Low-lying dipole strength of the open-shell nucleus ^{94}Mo. *Physical review / C*, 88(4):044331, 2013. doi: 10.1103/PhysRevC.88.044331.

[203] D. M. Rossi*, P. Adrich*, H. Alvarez-Pol, T. Aumann*, J. Benlliure, M. Böhmer, K. Boretzky*, E. Casarejos, M. Chartier, A. Chatillon*, D. Cortina-Gil, U. Datta Pramanik, H. Emling*, O. Ershova, B. Fernandez-Dominguez, H. Geissel*, M. Gorska*, M. Heil*, H. Johansson*, A. Junghans, A. Kelic-Heil*, O. Kiselev*, A. Klimkiewicz*, J. V. Kratz, Krücken, N. Kurz*, M. Labiche, T. Le Bleis*, R. Lemmon, Y. Litvinov*, K. Mahata*, P. Maierbeck, A. Movsesyan, T. Nilsson, C. Nociforo*, R. Palit, S. Paschalis, R. Plag*, R. Reifarth*, D. Savran, H. Scheit, H. Simon*, K. Sümmerer*, A. Wagner, W. Walús, H. Weick*, and M. Winkler*. Measurement of the Dipole Polarizability of the Unstable Neutron-Rich Nucleus ^{68}Ni. *Physical review letters*, 111(11):242503, 2013. doi: 10.1103/PhysRevLett.111.242503.

[204] S. Rothe, A. N. Andreyev, S. Antalic, A. Borschevsky, L. Capponi, T. E. Cocolios, H. De Witte, E. Eliav, D. V. Fedorov, V. N. Fedosseev, D. A. Fink, S. Fritzsche*, L. Ghys, M. Huyse, N. Imai, U. Kaldor, Y. Kudryavtsev, U. Köster, J. F. W. Lane, J. Lassen, V. Liberati, K. M. Lynch, B. A. Marsh, K. Nishio, D. Pauwels, V. Perschina-Nägele*, L. Popescu, T. J. Procter, D. Radulov, S. Raeder, M. M. Rajabali, E. Rapisarda, R. E. Rossel, K. Sandhu, M. D. Seliverstov, A. M. Sjödin, P. Van den Bergh, P. Van Duppen, M. Venhart, Y. Wakabayashi, and K. D. A. Wendt. Measurement of the first ionization potential of astatine by laser ionization spectroscopy. *Nature Communications*, 4:1835, 2013. doi: 10.1038/ncomms2819.

[205] G. Röpke, N.-U. Bastian, D. Blaschke, T. Klähn, S. Typel*, and H. H. Wolter. Cluster-virial expansion for nuclear matter within a quasiparticle statistical approach. *Nuclear physics / A*, 897:70 – 92, 2013. doi: 10.1016/j.nuclphysa.2012.10.005.

[206] D. Rudolph, U. Forsberg, P. Golubev, L. G. Sarmiento, A. Yakushev*, L.-L. Andersson, A. Di Nitto, C. E. Düllmann*, J. M. Gates, K. E. Gregorich, C. J. Gross, F.-P. Hessberger*, R.-D. Herzberg, J. Khuyagbaatar, J. V. Kratz, K. Rykaczewski, M. Schädel*, S. Åberg, D. Ackermann*, M. Block*, H. Brand*, B. G. Carlsson, D. Cox, X. Derkx, K. Eberhardt, J. Even, C. Fahlander, J. Gerl*, E. Jäger*, B. Kindler*, J. Krier*, I. Kojouharov*, N. Kurz*, B. Lommel*, A. Mistry, C. Mokry, H. Nitsche, J. P. Omtvedt, P. Papadakis, I. Ragnarsson, J. Runke*, H. Schaffner*, B. Schausten*, P. Thörle-Pospiech, T. Torres*, T. Traut, N. Trautmann, A. Türler, A. Ward, D. E. Ward, and N. Wiehl. Spectroscopy of Element 115 Decay Chains. *Physical review letters*, 111(11):112502, 2013. doi: 10.1103/PhysRevLett.111.112502.

[207] T. Saito*, E. Kim*, D. Nakajima*, C. Rappold*, S. Bianchin*, O. Borodina*, V. Bozkurt*, M. Kavatsyuk, Y. Ma*, F. Maas*, S. Minami*, B. Özel Tashenov*, and K. Yoshida*. Latest Results From the HypHI Experiments at GSI: Hypernuclear Spectroscopy with Heavy Ion Induced Reactions. *Few-body systems*, 54(7-10):1211 – 1214, 2013. doi: 10.1007/s00601-013-0666-5.

[208] V. V. Sargsyan, A. S. Zubov, G. G. Adamian, N. V. Antonenko, and S. Heinz*. Production of exotic isotopes in complete fusion reactions with radioactive beams. *Physical review / C*, 88(5):054609, 2013. doi: 10.1103/PhysRevC.88.054609.

[209] M. Scheck, V. Y. Ponomarev, T. Aumann, J. Beller, M. Fritzsche, J. Isaak*, J. H. Kelley, E. Kwan, N. Pietralla, R. Raut, C. Romig, G. Rusev, D. Savran*, K. Sonnabend, A. P. Tonchev, W. Tornow, H. R. Weller, and M. Zweidinger. Decay pattern of the pygmy dipole resonance in ^{60}Ni. *Physical review / C*, 87(5):051304, 2013. doi: 10.1103/PhysRevC.87.051304.

[210] M. Scheck, V. Y. Ponomarev, M. Fritzsche, J. Joubert, T. Aumann, J. Beller, J. Isaak*, J. H. Kelley, E. Kwan, N. Pietralla, R. Raut, C. Romig, G. Rusev, D. Savran*, L. Schorrenberger, K. Sonnabend, A. P. Tonchev, W. Tornow, H. R. Weller, A. Zilges, and M. Zweidinger. Photoresponse of ^{60}Ni below 10-MeV excitation energy: Evolution of dipole resonances in fp-shell nuclei near N=Z. *Physical review / C*, 88(4):044304, 2013. doi: 10.1103/PhysRevC.88.044304.

[211] K. Schmidt, S. Akhmadaliev, M. Anders, D. Bemmerer, K. Boretzky*, A. Caciolli, D. Degering, M. Dietz, R. Dressler, Z. Elekes, Z. Fülöp, G. Gyürky, R. Hannaske, A. R. Junghans, M. Marta*, M.-L.

Menzel, F. Munnik, D. Schumann, R. Schwengner, T. Szücs, A. Wagner, D. Yakorev, and K. Zuber. Resonance triplet at $E_\alpha = 4.5\ MeV$ in the $^{40}Ca(\alpha,\gamma)^{44}Ti$ reaction. *Physical review / C*, 88(2):025803, 2013. doi: 10.1103/PhysRevC.88.025803.

[212] K.-H. Schmidt*, B. Jurado, R. Pleskač*, M. V. Ricciardi*, J. Benlliure, A. Boudard, E. Casarejos, T. Enqvist, F. Farget, A. Bacquias*, M. Fernandez, L. Giot, V. Henzl*, D. Henzlova*, A. Kelić-Heil*, T. Kurtukian, S. Leray, S. Lukić*, S. N. Ngoc*, P. Nadtochy, D. Perez, and C. Schmitt. High-precision measurement of total fission cross sections in spallation reactions of ^{208}Pb and ^{238}U. *Physical review / C*, 87(3):034601, 2013. doi: 10.1103/PhysRevC.87.034601.

[213] P. Schnizer*, E. Fischer*, K. Sugita*, J. P. Meier*, and A. Mierau*. Design Optimization, Series Production, and Testing of the SIS100 Superconducting Magnets for FAIR. *IEEE transactions on applied superconductivity*, 23(3):4101105 – 4101105, 2013. doi: 10.1109/TASC.2012.2236132.

[214] P.-A. Söderström, G. Lorusso, H. Watanabe, S. Nishimura, P. Doornenbal, G. Thiamova, F. Browne, G. Gey, H. S. Jung, T. Sumikama, J. Taprogge, Z. Vajta, J. Wu, Z. Y. Xu, H. Baba, G. Benzoni, K. Y. Chae, F. C. L. Crespi, N. Fukuda, R. Gernhäuser, N. Inabe, T. Isobe, A. Jungclaus, D. Kameda, G. D. Kim, Y.-K. Kim, I. Kojouharov*, F. G. Kondev, T. Kubo, N. Kurz*, Y. K. Kwon, G. J. Lane, Z. Li, A. Montaner-Pizá, K. Moschner, F. Naqvi, M. Niikura, H. Nishibata, A. Odahara, R. Orlandi, Z. Patel, Z. Podolyák, H. Sakurai, H. Schaffner*, G. S. Simpson, K. Steiger, H. Suzuki, H. Takeda, A. Wendt, A. Yagi, and K. Yoshinaga. Shape evolution in $^{116,118}Ru$: Triaxiality and transition between the O(6) and U(5) dynamical symmetries. *Physical review / C*, 88(2):024301, 2013. doi: 10.1103/PhysRevC.88.024301.

[215] S. Y. Shim*, S. Wilfert*, and C. Muehle*. Secondary magnetic field harmonics dependence on vacuum beam chamber geometry. *Physical review / Special topics / Accelerators and beams*, 16(8):082401, 2013. doi: 10.1103/PhysRevSTAB.16.082401.

[216] H. Simon*. Masses of unbound nuclear systems. *International journal of mass spectrometry*, 349-350: 172 – 180, 2013. doi: 10.1016/j.ijms.2013.05.013.

[217] H. Simon*. Halo Nuclei: Stepping Stones Across the Dripline. *Few-body systems*, 54(7-10):863 – 868, 2013. doi: 10.1007/s00601-013-0698-x.

[218] V. Skokov*, B. Friman*, and K. Redlich. Volume fluctuations and higher-order cumulants of the net baryon number. *Physical review / C*, 88(3):034911, 2013. doi: 10.1103/PhysRevC.88.034911.

[219] K. Sümmerer*. Erratum: Improved empirical parametrization of fragmentation cross sections [Phys. Rev. C 86, 014601 (2012)]. *Physical review / C*, 87(3):039903, 2013. doi: 10.1103/PhysRevC.87.039903.

[220] V. Somà*, C. Barbieri, and T. Duguet. Ab initio Gorkov-Green's function calculations of open-shell nuclei. *Physical review / C*, 87(1):011303, 2013. doi: 10.1103/PhysRevC.87.011303.

[221] C. Stahl, J. Leske, N. Pietralla, P. R. John, G. Rainovski, J. Gerl*, I. Kojouharov*, and H. Schaffner*. Identification of the proton $2p_{1/2} \rightarrow 2p_{3/2}$ M1 spin-flip transition in ^{87}Rb. *Physical review / C*, 87(3): 037302, 2013. doi: 10.1103/PhysRevC.87.037302.

[222] J. Stanja, C. Borgmann, J. Agramunt, A. Algora, D. Beck*, K. Blaum, C. Böhm, M. Breitenfeldt, T. E. Cocolios, L. M. Fraile, F. Herfurth*, A. Herlert, M. Kowalska, S. Kreim, D. Lunney, V. Manea, E. Minaya Ramirez*, S. Naimi, D. Neidherr*, M. Rosenbusch, L. Schweikhard, G. Simpson, F. Wienholtz, R. N. Wolf, and K. Zuber. Mass spectrometry and decay spectroscopy of isomers across the Z=82 shell closure. *Physical review / C*, 88(5):054304, 2013. doi: 10.1103/PhysRevC.88.054304.

[223] J. Struckmeier*. Generalized U(N) gauge transformations in the realm of the extended covariant Hamilton formalism of field theory. *Journal of physics / G*, 40:015007, 2013. doi: 10.1088/0954-3899/40/1/015007.

[224] Y. Suwa, T. Takiwaki, K. Kotake, T. Fischer*, M. Liebendörfer, and K. Sato. ON THE IMPORTANCE OF THE EQUATION OF STATE FOR THE NEUTRINO-DRIVEN SUPERNOVA EXPLOSION MECHANISM. *The astrophysical journal / 1*, 764(1):99, 2013. doi: 10.1088/0004-637X/764/1/99.

[225] P. Szwangruber*, E. Floch*, F. Toral, and T. Weiland. Three-Dimensional Quench Calculations for the FAIR Super-FRS Main Dipole. *IEEE transactions on applied superconductivity*, 23(3):4701704 – 4701704, 2013. doi: 10.1109/TASC.2013.2243198.

[226] G. Tagliente, P. M. Milazzo, K. Fujii, U. Abbondanno, G. Aerts, H. Álvarez, F. Alvarez-Velarde, S. Andriamonje, J. Andrzejewski, L. Audouin, G. Badurek, P. Baumann, F. Bečvář, F. Belloni, E. Berthoumieux, F. Calviño, M. Calviani, D. Cano-Ott, R. Capote, C. Carrapiço, P. Cennini, V. Chepel, E. Chiaveri, N. Colonna, G. Cortes, A. Couture, M. Dahlfors, S. David, I. Dillmann*, C. Domingo-Pardo*, W. Dridi, I. Duran, C. Eleftheriadis, M. Embid-Segura, A. Ferrari, R. Ferreira-Marques, W. Furman, I. Goncalves, E. Gonzalez-Romero, F. Gramegna, C. Guerrero, F. Gunsing, B. Haas, R. Haight, M. Heil*, A. Herrera-Martinez, E. Jericha, F. Käppeler, Y. Kadi, D. Karadimos, D. Karamanis, M. Kerveno, E. Kossionides, M. Krtička, C. Lamboudis, H. Leeb, A. Lindote, I. Lopes, S. Lukic, J. Marganiec*, S. Marrone, T. Martínez, C. Massimi, P. Mastinu, A. Mengoni, C. Moreau, M. Mosconi, F. Neves, H. Oberhummer, S. O'Brien, C. Papachristodoulou, C. Papadopoulos, C. Paradela, N. Patronis, A. Pavlik, P. Pavlopoulos, L. Perrot, M. T. Pigni, R. Plag*, A. Plompen, A. Plukis, A. Poch, J. Praena, C. Pretel, J. Quesada, R. Reifarth*, M. Rosetti, C. Rubbia, G. Rudolf, P. Rullhusen, J. Salgado, C. Santos, L. Sarchiapone, I. Savvidis, C. Stephan, J. L. Tain, L. Tassan-Got, L. Tavora, R. Terlizzi, G. Vannini, P. Vaz, A. Ventura, D. Villamarin, M. C. Vincente, V. Vlachoudis, R. Vlastou, F. Voss, S. Walter, M. Wiescher, and K. Wisshak. The $^{93}Zr(n,\gamma)$ reaction up to 8 keV neutron energy. *Physical review / C*, 87(1): 014622, 2013. doi: 10.1103/PhysRevC.87.014622.

[227] Y. K. Tanaka, S. Friedrich, H. Fujioka, H. Geissel*, R. S. Hayano, S. Hirenzaki, K. Itahashi, S. Itoh, D. Jido, V. Metag, H. Nagahiro, M. Nanova, T. Nishi, K. Okochi, H. Outa, K. Suzuki, T. Suzuki, and H. Weick*. Spectroscopy of η′ Mesic Nuclei with (p, d) Reaction. *Few-body systems*, 54(7-10):1263 – 1266, 08/20/2012 - 08/25/2012 2013. doi: 10.1007/s00601-012-0589-6.

[228] I. Tews, T. Krüger, K. Hebeler*, and A. Schwenk*. Neutron Matter at Next-to-Next-to-Next-to-Leading Order in Chiral Effective Field Theory. *Physical review letters*, 110(3):032504, 2013. doi: 10.1103/PhysRevLett.110.032504.

[229] Y. Togano*, Y. Yamada, N. Iwasa, K. Yamada, and T. Motobayashi. Hindered Proton Collectivity in the Proton-rich Nucleus ^{28}S: Possible Magic Number at Z=16. *Acta physica Polonica / B*, 44(3):475 – 478, 08/27/2012 - 09/02/2012 2013. doi: 10.5506/APhysPolB.44.475.

[230] A. Türler and V. Pershina-Naegele*. Advances in the Production and Chemistry of the Heaviest Elements. *Chemical reviews*, 113(2):1237 – 1312, 2013. doi: 10.1021/cr3002438.

[231] J. Łukasik, P. Pawłowski, A. Budzanowski, B. Czech, I. Skwirczyńska, J. Brzychczyk, M. Adamczyk, S. Kupny, P. Lasko, Z. Sosin, A. Wieloch, M. Kiš*, Y. Leifels*, and W. Trautmann*. KRATTA, a versatile triple telescope array for charged reaction products. *Nuclear instruments & methods in physics research / A*, 709:120 – 128, 2013. doi: 10.1016/j.nima.2013.01.029.

[232] A. Vascon, S. Santi, A. A. Isse, A. Kühnle, T. Reich, J. Drebert, C. Düllmann*, and K. Eberhardt. Smooth crack-free targets for nuclear applications produced by molecular plating. *Nuclear instruments & methods in physics research / A*, 714:163 – 175, 2013. doi: 10.1016/j.nima.2013.03.003.

[233] A. Vascon, N. Wiehl, T. Reich, J. Drebert, K. Eberhardt, and C. E. Düllmann*. The performance of thin layers produced by molecular plating as α-particle sources. *Nuclear instruments & methods in physics research / A*, 721:35 – 44, 2013. doi: 10.1016/j.nima.2013.04.050.

[234] G. Volpini, F. Alessandria, G. Bellomo, P. Fabbricatore, S. Farinon, U. Gambardella, G. Manfreda, R. Musenich, M. Quadrio, and M. Sorbi. AC Losses Measurement of the DISCORAP Model Dipole Magnet for the SIS 300 Synchrotron at FAIR. *IEEE transactions on applied superconductivity*, PP(89): 1 – 1, 2013. doi: 10.1109/TASC.2013.2280733.

[235] N. Warr, J. Walle, M. Albers, F. Ames, B. Bastin, C. Bauer, V. Bildstein, A. Blazhev, S. Bönig, N. Bree, B. Bruyneel, P. A. Butler, J. Cederkäll, E. Clément, T. E. Cocolios, T. Davinson, H. Witte, P. Delahaye, D. D. DiJulio, J. Diriken, J. Eberth, A. Ekström, J. Elseviers, S. Emhofer, D. V. Fedorov, V. N. Fedosseev, S. Franchoo, C. Fransen, L. P. Gaffney, J. Gerl*, G. Georgiev, R. Gernhäuser, T. Grahn, D. Habs, H. Hess, A. M. Hurst, M. Huyse, O. Ivanov, J. Iwanicki, D. G. Jenkins, J. Jolie, N. Kesteloot, O. Kester, U. Köster, M. Krauth, T. Kröll, R. Krücken, M. Lauer, J. Leske, K. P. Lieb, R. Lutter, L. Maier, B. A. Marsh, D. Mücher, M. Münch, O. Niedermaier, J. Pakarinen, M. Pantea, G. Pascovici, N. Patronis, D. Pauwels, A. Petts, N. Pietralla, R. Raabe, E. Rapisarda, P. Reiter, A. Richter, O. Schaile, M. Scheck, H. Scheit, G. Schrieder, D. Schwalm, M. Seidlitz, M. Seliverstov, T. Sieber, H. Simon, K. Speidel, C. Stahl, I. Stefanescu, P. G. Thirolf, H. Thomas, M. Thürauf, P. Duppen, D. Voulot, R. Wadsworth, G. Walter, D. Weißhaar, F. Wenander, A. Wiens, K. Wimmer, B. H. Wolf, P. J. Woods, K. Wrzosek-Lipska, and K. O. Zell. The Miniball spectrometer. *The European physical journal / A*, 49(3):40, 2013. doi: 10.1140/epja/i2013-13040-9.

[236] H. Watanabe, G. Lorusso, S. Nishimura, Z. Y. Xu, T. Sumikama, P.-A. Söderström, P. Doornenbal, F. Browne, G. Gey, H. S. Jung, J. Taprogge, Z. Vajta, J. Wu, A. Yagi, H. Baba, G. Benzoni, K. Y. Chae, F. C. L. Crespi, N. Fukuda, R. Gernhäuser, N. Inabe, T. Isobe, A. Jungclaus, D. Kameda, G. D. Kim, Y. K. Kim, I. Kojouharov*, F. G. Kondev, T. Kubo, N. Kurz*, Y. K. Kwon, G. J. Lane, Z. Li, C.-B. Moon, A. Montaner-Pizá, K. Moschner, F. Naqvi, M. Niikura, H. Nishibata, D. Nishimura, A. Odahara, R. Orlandi, Z. Patel, Z. Podolyák, H. Sakurai, H. Schaffner*, G. S. Simpson, K. Steiger, H. Suzuki, H. Takeda, A. Wendt, and K. Yoshinaga. Isomers in ^{128}Pd and ^{126}Pd: Evidence for a Robust Shell Closure at the Neutron Magic Number 82 in Exotic Palladium Isotopes. *Physical review letters*, 111 (15):152501, 2013. doi: 10.1103/PhysRevLett.111.152501.

[237] E. Wilson, Z. Podolyák, B. Fornal, R. V. F. Janssens, M. Bowry, M. Bunce, M. P. Carpenter, C. J. Chiara, N. Cieplicka, A. Y. Deo, G. D. Dracoulis, H. Grawe*, C. R. Hoffman, R. S. Kempley, F. G. Kondev, G. J. Lane, T. Lauritsen, M. W. Reed, P. H. Regan, C. Rodríguez Triguero, B. Szpak, P. M. Walker, and S. Zhu. Core Excitations Across the Neutron Shell Gap in ^{207}Tl. *Acta physica Polonica / B*, 44(3):381 – 385, 2013. doi: 10.5506/APhysPolB.44.381.

[238] J. S. Winfield*, H. Geissel*, J. Gerl*, G. Münzenberg*, C. Nociforo*, W. R. Plaß*, C. Scheidenberger*, H. Weick*, M. Winkler*, and M. I. Yavor. A versatile high-resolution magnetic spectrometer for energy compression, reaction studies and nuclear spectroscopy. *Nuclear instruments & methods in physics research / A*, 704:76 – 83, 2013. doi: 10.1016/j.nima.2012.11.186.

[239] R. Wirth*, E. Fiori*, B. Löher*, D. Savran*, J. Silva*, H. Álvarez Pol, D. Cortina Gil, B. Pietras, T. Bloch, T. Kröll, E. Nácher, Á. Perea, O. Tengblad, M. Bendel, M. Dierigl, R. Gernhäuser, T. Le Bleis, and M. Winkel. Particle identification using clustering algorithms. *Nuclear instruments & methods in physics research / A*, 717:77 – 82, 2013. doi: 10.1016/j.nima.2013.04.006.

[240] H. De Witte, S. Eeckhaudt, A. N. Andreyev, I. N. Borzov, J. Cederkäll, A. De Smet, D. V. Fedorov, V. N. Fedoseyev, S. Franchoo, M. Górska, H. Grawe*, G. Huber, M. Huyse, Z. Janas, U. Köster, W. Kurcewicz, J. Kurpeta, A. Płochocki, K. Van de Vel, P. Van Duppen, and L. Weissman. β^- decay of the neutron-rich isotope ^{215}Pb. *Physical review / C*, 87(6):067303, 2013. doi: 10.1103/PhysRevC.87.067303.

[241] R. N. Wolf, D. Beck*, K. Blaum, C. Böhm, C. Borgmann, M. Breitenfeldt, N. Chamel, S. Goriely, F. Herfurth*, M. Kowalska, S. Kreim, D. Lunney, V. Manea, E. Minaya Ramirez*, S. Naimi, D. Neidherr*, M. Rosenbusch, L. Schweikhard, J. Stanja, F. Wienholtz, and K. Zuber. Plumbing Neutron Stars to New Depths with the Binding Energy of the Exotic Nuclide ^{82}Zn. *Physical review letters*, 110(4):041101, 2013. doi: 10.1103/PhysRevLett.110.041101.

[242] C. Z. Xiang, N. Herrmann, I. Deppner, P. Loizeau, K. Wisniewski, Y. P. Zhang, D. C. Zhou, J. Frühauf*, S. Linev*, S. Manz*, and W. F. J. Müller*. The online data pre-processing for CBM-TOF. *Journal of Instrumentation*, 8(02):P02002 – P02002, 2013. doi: 10.1088/1748-0221/8/02/P02002.

[243] C. Xiao, O. Kester*, L. Groening*, H. Leibrock*, M. Maier*, and P. Rottländer*. Single-knob beam line for transverse emittance partitioning. *Physical review / Special topics / Accelerators and beams*, 16(4): 044201, 2013. doi: 10.1103/PhysRevSTAB.16.044201.

[244] Y. Xu, K. Takahashi*, S. Goriely, M. Arnould, M. Ohta, and H. Utsunomiya. NACRE II: an update of the NACRE compilation of charged-particle-induced thermonuclear reaction rates for nuclei with mass number $A\<16$. *Nuclear physics / A*, 918:61 – 169, 2013. doi: 10.1016/j.nuclphysa.2013.09.007.

[245] Q. Zhi*, E. Caurier, J. J. Cuenca-García*, K. Langanke*, G. Martínez-Pinedo*, and K. Sieja. Shell-model half-lives including first-forbidden contributions for r-process waiting-point nuclei. *Physical review / C*, 87(2):025803, 2013. doi: 10.1103/PhysRevC.87.025803.

Further publications to the programme physics of hadrons and nuclei published in 2013

[1] A. Andronic*. The charm of hot matter – charmonium and open charm measurements in Pb–Pb collisions with ALICE at the LHC. volume 455, page 012002. International on Discovery Physics at the LHC (Kruger 2012), Kruger(South Africa), IOP Publ., 12/03/2012 - 12/07/2012 2013. doi: 10.1088/1742-6596/455/1/012002.

[2] I. C. Arsene*. J /ψ Production in Pb-Pb collisions at $\sqrt{s_{NN}} = 2.76TeV$. volume 426, page 012023. FAIRNESS 2012, Hersonissos(Greece), IOP Publ., 09/03/2012 - 09/08/2012 2013. doi: 10.1088/1742-6596/426/1/012023.

[3] T. Aumann* and T. Nakamura*. The electric dipole response of exotic nuclei. *Physica scripta*, T152: 014012, 2013. doi: 10.1088/0031-8949/2013/T152/014012.

[4] P. Foka*. Overview of results from ALICE at the CERN LHC. volume 455, page 012004. 2nd International Workshop on Discovery Physics at the LH/C, (SOUTH AFRICA), IOP Publ., 12/03/2013 - 12/07/2013 2013. doi: 10.1088/1742-6596/455/1/012004.

[5] A. Gezerlis. Polarization in low-density neutrons. *Journal of physics / Conference Series*, 426:012011, 2013. doi: 10.1088/1742-6596/426/1/012011.

[6] M. Köhler*. Low-mass dielectron measurement in pp and Pb–Pb collisions in ALICE. volume 446, page 012049. Hot Quarks 2012, Copamarina(Puerto Rico), IOP Publ., 10/14/2012 - 10/20/2012 2013. doi: 10.1088/1742-6596/446/1/012049.

[7] K. Langanke* and H. Schatz. The role of radioactive ion beams in nuclear astrophysics. *Physica scripta*, T152:014011, 2013. doi: 10.1088/0031-8949/2013/T152/014011.

[8] Y. Leifels*. Strangeness production in heavy ion collisions -Constraining the KN – potential in medium. *Journal of physics / Conference Series*, 420:012019, 2013. doi: 10.1088/1742-6596/420/1/012019.

[9] G. Münzenberg* and H. Geissel*. NUSTAR – presence and prospects of nuclear structure research at GSI and FAIR. *Journal of physics / Conference Series*, 413:012006, 2013. doi: 10.1088/1742-6596/413/1/012006.

[10] M. Pfützner*. Particle radioactivity of exotic nuclei. *Physica scripta*, T152:014014, 2013. doi: 10.1088/0031-8949/2013/T152/014014.

[11] D. M. Rossi*, P. Adrich*, F. Aksouh*, H. Alvarez-Pol, T. Aumann*, J. Benlliure, M. Böhmer, K. Boretzky*, E. Casarejos, M. Chartier, A. Chatillon, D. Cortina-Gil, U. D. Pramanik, H. Emling*, O. Ershova, B. Fernandez-Dominguez, H. Geissel*, M. Gorska*, M. Heil*, H. Johansson*, A. Junghans, O. Kiselev*, A. Klimkiewicz*, J. V. Kratz, N. Kurz*, M. Labiche, T. L. Bleis*, R. Lemmon, Y. A. Litvinov*, K. Mahata*, P. Maierbeck, A. Movsesyan*, T. Nilsson, C. Nociforo*, R. Palit, S. Paschalis, R. Plag*, R. Reifarth*, H. Simon*, K. Sümmerer*, A. Wagner, W. Walus, H. Weick*, and M. Winkler*. Coulomb excitation of exotic nuclei at the $R^3B-LAND$ setup. *Journal of physics / Conference Series*, 420:012072, 2013. doi: 10.1088/1742-6596/420/1/012072.

[12] P. Russotto, M. Chartier, E. D. Filippo, A. Le Fevre*, S. Gannon, I. Gašparić, M. Kiš*, S. Kupny, Y. Leifels*, R. C. Lemmon, J. Łukasik, P. Marini, A. Pagano, P. Pawłowski, S. Santoro, W. Trautmann*,

M. Veselsky, L. Acosta, M. Adamczyk, A. Al-Ajlan, M. Al-Garawi, S. Al-Homaidhi, F. Amorini, L. Auditore, T. Aumann, Y. Ayyad, V. Baran, Z. Basrak, J. Benlliure, C. Boiano, M. Boisjoli, K. Boretzky*, J. Brzychczyk, A. Budzanowski, G. Cardella, P. Cammarata, Z. Chajecki, A. Chbihi, M. Colonna, D. Cozma, B. Czech, M. D. Toro, M. Famiano, E. Geraci, V. Greco, L. Grassi, C. Guazzoni, P. Guazzoni, M. Heil*, L. Heilborn, R. Introzzi, T. Isobe, K. Kezzar, A. Krasznahorkay, N. Kurz*, E. L. Guidara, G. Lanzalone, P. Lasko, Q. Li, I. Lombardo, W. G. Lynch, Z. Matthews, L. May, T. Minniti, M. Mostazo, M. Papa, S. Pirrone, G. Politi, F. Porto, R. Reifarth*, W. Reisdorf*, F. Riccio, F. Rizzo, E. Rosato, H. Simon*, I. Skwirczynska, Z. Sosin, L. Stuhl, A. Trifirò, M. Trimarchi, M. B. Tsang, G. Verde, M. Vigilante, A. Wieloch, P. Wigg, H. H. Wolter, P. Wu, S. Yennello, P. Zambon, L. Zetta, M. Zoric, and D. Rossi*. The ASY-EOS experiment at GSI: investigating the symmetry energy at supra-saturation densities. *Journal of physics / Conference Series*, 420:012092, 2013. doi: 10.1088/1742-6596/420/1/012092.

[13] H. Simon*. Halo nuclei, stepping stones across the drip-lines. *Physica scripta*, T152:014024, 2013. doi: 10.1088/0031-8949/2013/T152/014024.

[14] S. Typel*. Nuclei in Dense Matter and Equation of State. *Journal of physics / Conference Series*, 413: 012026, 2013. doi: 10.1088/1742-6596/413/1/012026.

JCR publications to the programme large-scale facilities for research with photons, neutrons and ions published in 2013

[1] B. Afra, M. D. Rodriguez, C. Trautmann*, O. H. Pakarinen, F. Djurabekova, K. Nordlund, T. Bierschenk, R. Giulian, M. C. Ridgway, G. Rizza, N. Kirby, M. Toulemonde, and P. Kluth. SAXS investigations of the morphology of swift heavy ion tracks in α-quartz. *Journal of physics / Condensed matter*, 25(4): 045006, 2013. doi: 10.1088/0953-8984/25/4/045006.

[2] M. Ali*, S. Nasir*, I. Ahmed, L. Fruk, and W. Ensinger. Tuning nanopore surface polarity and rectification properties through enzymatic hydrolysis inside nanoconfined geometries. *Chemical communications*, 49(78):8770, 2013. doi: 10.1039/c3cc45318a.

[3] M. Ali*, S. Nasir*, P. Ramirez, J. Cervera, S. Mafe, and W. Ensinger. Carbohydrate-Mediated Biomolecular Recognition and Gating of Synthetic Ion Channels. *The journal of physical chemistry / C*, 117(35):18234 – 18242, 2013. doi: 10.1021/jp4054555.

[4] Z. Andelkovic*, R. Cazan, W. Nörtershäuser*, S. Bharadia, D. M. Segal, R. C. Thompson, R. Jöhren, J. Vollbrecht, V. Hannen, and M. Vogel*. Laser cooling of externally produced Mg ions in a Penning trap for sympathetic cooling of highly charged ions. *Physical review / A*, 87(3):033423, 2013. doi: 10.1103/PhysRevA.87.033423.

[5] A. N. Artemyev*, V. M. Shabaev, I. I. Tupitsyn, G. Plunien, A. Surzhykov*, and S. Fritzsche*. Ab initio calculations of the $2p_{3/2} - 2p_{1/2}$ fine-structure splitting in boronlike ions. *Physical review / A*, 88(3): 032518, 2013. doi: 10.1103/PhysRevA.88.032518.

[6] B. Aurand*, B. Elkin, L.-O. Heim, B. Lommel*, B. Kindler*, M. Tomut*, C. Rödel*, S. Kuschel, O. Jäckel*, J. Barz, and T. Kuehl*. Preparation and characterization of nanometer-thin freestanding polymer foils for laser-ion acceleration. *Journal of polymer science / B*, 51(18):1355 – 1360, 2013. doi: 10.1002/polb.23340.

[7] B. Aurand*, S. Kuschel, O. Jäckel, C. Rödel, H. Y. Zhao, S. Herzer, A. E. Paz, J. Bierbach, J. Polz, B. Elkin, G. G. Paulus, A. Karmakar, P. Gibbon, T. Kühl*, and M. C. Kaluza. Radiation pressure-assisted acceleration of ions using multi-component foils in high-intensity laser–matter interactions. *New journal of physics*, 15(3):033031, 2013. doi: 10.1088/1367-2630/15/3/033031.

[8] K. Baker, G. Cantatore, S. A. Cetin, M. Davenport, K. Desch, B. Döbrich, H. Gies*, I. G. Irastorza, J. Jaeckel, A. Lindner, T. Papaevangelou, M. Pivovaroff, G. Raffelt, J. Redondo, A. Ringwald, Y. Semertzidis, A. Siemko, M. Sulc, A. Upadhye, and K. Zioutas. The quest for axions and other new light particles. *Annalen der Physik*, 525(6):A93 – A99, 2013. doi: 10.1002/andp.201300727.

[9] D. Banaś, A. Gumberidze*, S. Trotsenko*, A. V. Volotka, A. Surzhykov*, H. F. Beyer*, F. Bosch*, A. Bräuning-Demian*, S. Fritzsche*, S. Hagmann*, C. Kozhuharov*, A. Kumar, X. Ma, R. Mann*, P. H. Mokler*, D. Sierpowski, U. Spillmann*, S. Tashenov*, Z. Stachura, A. Warczak, and T. Stöhlker*. Two-photon energy distribution from the decay of the 2^1S_0 state in He-like uranium. *Physical review / A*, 87(6):062510, 2013. doi: 10.1103/PhysRevA.87.062510.

[10] D. Banaś, M. Pajek, A. Gumberidze*, A. Surzhykov, and T. Stöhlker*. Differential L-shell radiative recombination rate coefficients for bare uranium ions interacting with low-energy electrons. *European physical journal special topics*, 222(9):2317 – 2322, 2013. doi: 10.1140/epjst/e2013-02011-2.

[11] S. Banerjee, J. Koerner, M. Siebold, Q. Yang, K. Ertel, P. D. Mason, P. J. Phillips, M. Loeser, H. Zhang, S. Lu, J. Hein, U. Schramm, M. C. Kaluza*, and J. L. Collier. Temperature dependent emission and absorption cross section of Yb^{3+} doped yttrium lanthanum oxide (YLO) ceramic and its application in diode pumped amplifier. *Optics express*, 21(S4):A726, 2013. doi: 10.1364/OE.21.00A726.

[12] L. Belliard, T. W. Cornelius, B. Perrin, N. Kacemi, L. Becerra, O. Thomas, M. E. Toimil Molares*, and M. Cassinelli*. Vibrational response of free standing single copper nanowire through transient reflectivity microscopy. *Journal of applied physics*, 114(19):193509, 2013. doi: 10.1063/1.4831957.

[13] F. Bosch* and Y. Litvinov*. Mass and lifetime measurements at the experimental storage ring of GSI. *International journal of mass spectrometry*, 349-350:151 – 161, 2013. doi: 10.1016/j.ijms.2013.04.025.

[14] F. Bosch*, Y. A. Litvinov*, and T. Stöhlker*. Nuclear physics with unstable ions at storage rings. *Progress in particle and nuclear physics*, 73:84 – 140, 2013. doi: 10.1016/j.ppnp.2013.07.002.

[15] N. Brambilla, F. Karbstein*, and A. Vairo. Symmetries of the three-heavy-quark system and the color-singlet static energy at next-to-next-to-leading logarithmic order. *Physical review / D*, 87(7):074014, 2013. doi: 10.1103/PhysRevD.87.074014.

[16] S. Busold, D. Schumacher*, O. Deppert, C. Brabetz, S. Frydrych, F. Kroll, M. Joost, H. Al-Omari, A. Blažević*, B. Zielbauer*, I. Hofmann*, V. Bagnoud*, T. E. Cowan, and M. Roth. Focusing and transport of high-intensity multi-MeV proton bunches from a compact laser-driven source. *Physical review / Special topics / Accelerators and beams*, 16(10):101302, 2013. doi: 10.1103/PhysRevSTAB.16.101302.

[17] W. Cayzac, A. Frank, D. Schumacher, M. Roth, A. Blažević*, F. Wamers*, E. Berdermann*, M. Träger*, B. Voss*, and T. Hessling*. A spectrometer on chemical vapour deposition-diamond basis for the measurement of the charge-state distribution of heavy ions in a laser-generated plasma. *Review of scientific instruments*, 84(4):043301, 2013. doi: 10.1063/1.4798539.

[18] W. Chen*, G. Vorobyev*, D. Guo, P.-M. Hillenbrand*, F. Herfurth*, S. Hagmann*, U. Spillmann*, S. Trotsenko*, A. Gumberidze*, and T. Stöhlker*. Charge transfer of slow highly charged xenon ions in collisions with magnesium atoms. *Physical review / A*, 88(5):052703, 2013. doi: 10.1103/PhysRevA.88.052703.

[19] J. Colgan, J. Abdallah, A. Faenov, S. Pikuz, E. Wagenaars, N. Booth, O. Culfa, R. Dance, R. Evans, R. Gray, T. Kaempfer*, K. Lancaster, P. McKenna, A. Rossall, I. Skobelev, K. Schulze*, I. Uschmann*, A. Zhidkov, and N. Woolsey. Exotic Dense-Matter States Pumped by a Relativistic Laser Plasma in the Radiation-Dominated Regime. *Physical review letters*, 110(12):125001, 2013. doi: 10.1103/PhysRevLett.110.125001.

[20] A. Dauletbekova, K. Schwartz*, M. V. Sorokin, J. Maniks, A. Rusakova, M. Koloberdin, A. Akilbekov, and M. Zdorovets. LiF crystals irradiated with 150MeV Kr ions: Peculiarities of color center creation and thermal annealing. *Nuclear instruments & methods in physics research / B*, 295:89 – 93, 2013. doi: 10.1016/j.nimb.2012.11.004.

[21] B. Döbrich*, H. Gies*, N. Neitz, and F. Karbstein*. Magnetically amplified light-shining-through-walls via virtual minicharged particles. *Physical review / D*, 87(2):025022, 2013. doi: 10.1103/PhysRevD.87.025022.

[22] S. Demmler, J. Rothhardt*, S. Hädrich*, M. Krebs, A. Hage, J. Limpert*, and A. Tünnermann*. Generation of high-photon flux-coherent soft x-ray radiation with few-cycle pulses. *Optics letters*, 38(23):5051, 2013. doi: 10.1364/OL.38.005051.

[23] F. Dolde, I. Jakobi, B. Naydenov, N. Zhao, S. Pezzagna, C. Trautmann*, J. Meijer, P. Neumann, F. Jelezko, and J. Wrachtrup. Room-temperature entanglement between single defect spins in diamond. *Nature physics*, 9(3):139 – 143, 2013. doi: 10.1038/nphys2545.

[24] A. S. El-Said, R. A. Wilhelm, S. Facsko, and C. Trautmann*. Surface nanostructuring of $LiNbO_3$ by high-density electronic excitations. *Nuclear instruments & methods in physics research / B*, 315: 265 – 268, 2013. doi: 10.1016/j.nimb.2013.03.008.

[25] S. Fernandes, F. Pellemoine, M. Tomut*, M. Avilov, M. Bender*, M. Boulesteix, M. Krause, W. Mittig, M. Schein, D. Severin*, and C. Trautmann*. In-situ electric resistance measurements and annealing effects of graphite exposed to swift heavy ions. *Nuclear instruments & methods in physics research / B*, 314:125 – 129, 2013. doi: 10.1016/j.nimb.2013.04.060.

[26] A. Frank, A. Blažević*, V. Bagnoud*, M. Basko, M. Börner, W. Cayzac, D. Kraus, T. Heßling*, D. Hoffmann, A. Ortner, A. Otten, A. Pelka, D. Pepler, D. Schumacher, A. Tauschwitz, and M. Roth. Energy Loss and Charge Transfer of Argon in a Laser-Generated Carbon Plasma. *Physical review letters*, 110 (11):115001, 2013. doi: 10.1103/PhysRevLett.110.115001.

[27] S. Fuchs*, C. Rödel*, M. Krebs, S. Hädrich*, J. Bierbach*, A. E. Paz*, S. Kuschel*, M. Wünsche, V. Hilbert, U. Zastrau, E. Förster, J. Limpert*, and G. G. Paulus*. Sensitivity calibration of an imaging extreme ultraviolet spectrometer-detector system for determining the efficiency of broadband extreme ultraviolet sources. *Review of scientific instruments*, 84(2):023101, 2013. doi: 10.1063/1.4788732.

[28] S. A. Gardiner, H. Gies*, J. Jaeckel, and C. J. Wallace. Tunnelling of the 3rd kind: A test of the effective non-locality of quantum field theory. *epl*, 101(6):61001, 2013. doi: 10.1209/0295-5075/101/61001.

[29] H. Gies*, F. Karbstein*, and N. Seegert*. Quantum reflection as a new signature of quantum vacuum nonlinearity. *New journal of physics*, 15(8):083002, 2013. doi: 10.1088/1367-2630/15/8/083002.

[30] M. M. Günther, A. Britz, R. J. Clarke, K. Harres, G. Hoffmeister, F. Nürnberg, A. Otten, A. Pelka, M. Roth, and K. Vogt*. NAIS: Nuclear activation-based imaging spectroscopy. *Review of scientific instruments*, 84(7):073305, 2013. doi: 10.1063/1.4815826.

[31] A. Gopal*, S. Herzer*, A. Schmidt, P. Singh, A. Reinhard, W. Ziegler, D. Brömmel, A. Karmakar, P. Gibbon, U. Dillner, T. May, H.-G. Meyer, and G. G. Paulus*. Observation of Gigawatt-Class THz Pulses from a Compact Laser-Driven Particle Accelerator. *Physical review letters*, 111(7):074802, 2013. doi: 10.1103/PhysRevLett.111.074802.

[32] A. Gopal*, P. Singh, S. Herzer*, A. Reinhard, A. Schmidt, U. Dillner, T. May, H.-G. Meyer, W. Ziegler, and G. G. Paulus*. Characterization of 700 μJ T rays generated during high-power laser solid interaction. *Optics letters*, 38(22):4705, 2013. doi: 10.1364/OL.38.004705.

[33] C. Goyon, S. Depierreux, V. Yahia, G. Loisel, C. Baccou, C. Courvoisier, N. Borisenko, A. Orekhov, O. Rosmej*, and C. Labaune. Experimental Approach to Interaction Physics Challenges of the Shock Ignition Scheme Using Short Pulse Lasers. *Physical review letters*, 111(23):235006, 2013. doi: 10.1103/PhysRevLett.111.235006.

[34] M. Guerra, P. Amaro, C. I. Szabo, A. Gumberidze*, P. Indelicato, and J. P. Santos. Analysis of the charge state distribution in an ECRIS Ar plasma using high-resolution x-ray spectra. *Journal of physics / B*, 46 (6):065701, 2013. doi: 10.1088/0953-4075/46/6/065701.

[35] A. Gumberidze*, D. B. Thorn*, C. J. Fontes, B. Najjari, H. L. Zhang, A. Surzhykov*, A. Voitkiv, S. Fritzsche*, D. Banaś, H. Beyer*, W. Chen*, R. D. DuBois, S. Geyer*, R. E. Grisenti*, S. Hagmann*,

M. Hegewald*, S. Hess*, C. Kozhuharov*, R. Märtin*, I. Orban, N. Petridis*, R. Reuschl*, A. Simon, U. Spillmann, M. Trassinelli, S. Trotsenko*, G. Weber*, D. Winters*, N. Winters*, D. Yu*, and T. Stöhlker*. Electron- and Proton-Impact Excitation of Hydrogenlike Uranium in Relativistic Collisions. *Physical review letters*, 110(21):213201, 2013. doi: 10.1103/PhysRevLett.110.213201.

[36] J. Gunst, A. Surzhykov*, A. Artemyev*, S. Fritzsche*, S. Tashenov*, A. Maiorova, V. M. Shabaev, and T. Stöhlker*. Parity-nonconservation effects on the radiative recombination of heavy hydrogenlike ions. *Physical review / A*, 87(3):032714, 2013. doi: 10.1103/PhysRevA.87.032714.

[37] M. Hahn, A. Becker, D. Bernhardt, M. Grieser, C. Krantz, M. Lestinsky*, A. Müller, O. Novotný, R. Repnow, S. Schippers, K. Spruck, A. Wolf, and D. W. Savin. STORAGE RING CROSS SECTION MEASUREMENTS FOR ELECTRON IMPACT SINGLE AND DOUBLE IONIZATION OF Fe^{13+} AND SINGLE IONIZATION OF Fe^{16+} AND Fe^{17+}. *The astrophysical journal / 1*, 767(1):47, 2013. doi: 10.1088/0004-637X/767/1/47.

[38] A. G. Hayrapetyan, O. Matula*, A. Surzhykov*, and S. Fritzsche*. Bessel beams of two-level atoms driven by a linearly polarized laser field. *The European physical journal / D*, 67(8):167, 2013. doi: 10.1140/epjd/e2013-30191-x.

[39] S. Hädrich*, A. Klenke*, A. Hoffmann, T. Eidam*, T. Gottschall, J. Rothhardt*, J. Limpert*, and A. Tünnermann*. Nonlinear compression to sub-30-fs, 05 mJ pulses at 135 W of average power. *Optics letters*, 38(19):3866, 2013. doi: 10.1364/OL.38.003866.

[40] K. P. Heeg, H.-C. Wille, K. Schlage, T. Guryeva, D. Schumacher, I. Uschmann*, K. S. Schulze*, B. Marx*, T. Kämpfer*, G. G. Paulus*, R. Röhlsberger, and J. Evers. Vacuum-Assisted Generation and Control of Atomic Coherences at X-Ray Energies. *Physical review letters*, 111(7):073601, 2013. doi: 10.1103/PhysRevLett.111.073601.

[41] V. Hilbert, A. Blinne, S. Fuchs, T. Feigl, T. Kämpfer*, C. Rödel*, I. Uschmann, M. Wünsche*, G. G. Paulus, E. Förster*, and U. Zastrau. An extreme ultraviolet Michelson interferometer for experiments at free-electron lasers. *Review of scientific instruments*, 84(9):095111, 2013. doi: 10.1063/1.4821146.

[42] I. Hofmann*. Performance of solenoids versus quadrupoles in focusing and energy selection of laser accelerated protons. *Physical review / Special topics / Accelerators and beams*, 16(4):041302, 2013. doi: 10.1103/PhysRevSTAB.16.041302.

[43] M. Hornung*, S. Keppler, R. Bödefeld*, A. Kessler*, H. Liebetrau, J. Körner, M. Hellwing, F. Schorcht*, O. Jäckel*, A. Sävert, J. Polz, A. K. Arunachalam, J. Hein*, and M. C. Kaluza*. High-intensity, high-contrast laser pulses generated from the fully diode-pumped Yb:glass laser system POLARIS. *Optics letters*, 38(5):718, 2013. doi: 10.1364/OL.38.000718.

[44] F. Jansen, F. Stutzki, H.-J. Otto, C. Jauregui, J. Limpert*, and A. Tünnermann*. High-power thermally guiding index-antiguiding-core fibers. *Optics letters*, 38(4):510 – 512, 2013. doi: 10.1364/OL.38.000510.

[45] C. Jauregui, H.-J. Otto, F. Stutzki, F. Jansen, J. Limpert*, and A. Tünnermann*. Passive mitigation strategies for mode instabilities in high-power fiber laser systems. *Optics express*, 21(16):19375, 2013. doi: 10.1364/OE.21.019375.

[46] A. Jochmann, A. Irman, M. Bussmann, J. P. Couperus, T. E. Cowan, A. D. Debus, M. Kuntzsch, K. W. D. Ledigham, U. Lehnert, R. Sauerbrey, H. P. Schlenvoigt, D. Seipt, T. Stöhlker*, D. B. Thorn*, S. Trotsenko*, A. Wagner, and U. Schramm. High Resolution Energy-Angle Correlation Measurement of Hard X Rays from Laser-Thomson Backscattering. *Physical review letters*, 111(11):114803, 2013. doi: 10.1103/PhysRevLett.111.114803.

[47] S. Kahaly, S. Monchocé, H. Vincenti, T. Dzelzainis, B. Dromey, M. Zepf*, P. Martin, and F. Quéré. Direct Observation of Density-Gradient Effects in Harmonic Generation from Plasma Mirrors. *Physical review letters*, 110(17):175001, 2013. doi: 10.1103/PhysRevLett.110.175001.

[48] F. Karbstein*. Photon polarization tensor in a homogeneous magnetic or electric field. *Physical review / D*, 88(8):085033, 2013. doi: 10.1103/PhysRevD.88.085033.

[49] M. Kübel, N. G. Kling, K. J. Betsch, N. Camus, A. Kaldun, U. Kleineberg, I. Ben-Itzhak, R. R. Jones, G. G. Paulus*, T. Pfeifer, J. Ullrich, R. Moshammer, M. F. Kling, and B. Bergues. Nonsequential double ionization of N_2 in a near-single-cycle laser pulse. *Physical review / A*, 88(2):023418, 2013. doi: 10.1103/PhysRevA.88.023418.

[50] S. A. Khan, A. Tripathi, M. Toulemonde, C. Trautmann*, and W. Assmann. Sputtering yield of amorphous ^{13}C thin films under swift heavy-ion irradiation. *Nuclear instruments & methods in physics research / B*, 314:34 – 38, 2013. doi: 10.1016/j.nimb.2013.05.044.

[51] D. Kiefer, M. Yeung, T. Dzelzainis, P. S. Foster, S. G. Rykovanov, C. L. Lewis, R. S. Marjoribanks, H. Ruhl, D. Habs, J. Schreiber, M. Zepf*, and B. Dromey. Relativistic electron mirrors from nanoscale foils for coherent frequency upshift to the extreme ultraviolet. *Nature Communications*, 4:1763, 2013. doi: 10.1038/ncomms2775.

[52] T. Kiefer, T. Schlegel*, and M. C. Kaluza*. Plasma expansion into vacuum assuming a steplike electron energy distribution. *Physical review / E*, 87(4):043110, 2013. doi: 10.1103/PhysRevE.87.043110.

[53] M. Kienel*, A. Klenke*, T. Eidam*, M. Baumgartl, C. Jauregui, J. Limpert*, and A. Tünnermann*. Analysis of passively combined divided-pulse amplification as an energy-scaling concept. *Optics express*, 21(23):29031, 2013. doi: 10.1364/OE.21.029031.

[54] P. Kienle, F. Bosch*, P. Bühler, T. Faestermann, Y. Litvinov*, N. Winckler*, M. S. Sanjari*, D. Shubina*, D. Atanasov*, H. Geissel*, V. Ivanova*, X. L. Yan, D. Boutin*, C. Brandau*, I. Dillmann*, C. Dimopoulou*, R. Heß*, P.-M. Hillenbrand*, T. Izumikawa, R. Knöbel*, J. Kurcewicz*, N. Kuzminchuk, M. Lestinsky*, S. Litvinov*, X. W. Ma, L. Maier, M. Mazzocco*, I. Mukha*, C. Nociforo*, F. Nolden*, C. Scheidenberger*, U. Spillmann*, M. Steck*, T. Stöhlker*, B. H. Sun, F. Suzaki, S. Y. Torilov, M. Trassinelli, X. L. Tu, M. Wang, H. Weick*, D. Winters*, P. J. Woods, T. Yamaguchi, G. L. Zhang, and T. Ohtsubo. High-resolution measurement of the time-modulated orbital electron capture and of the decay of hydrogen-like $^{142}Pm^{60+}$ ions. *Physics letters / B*, 726(4-5):638 – 645, 2013. doi: 10.1016/j.physletb.2013.09.033.

[55] A. Klenke*, S. Breitkopf, M. Kienel*, T. Gottschall, T. Eidam*, S. Hädrich*, J. Rothhardt*, J. Limpert*, and A. Tünnermann*. 530 W, 13 mJ, four-channel coherently combined femtosecond fiber chirped-pulse amplification system. *Optics letters*, 38(13):2283, 2013. doi: 10.1364/OL.38.002283.

[56] A. Klenke*, M. Kienel*, T. Eidam*, S. Hädrich*, J. Limpert*, and A. Tünnermann*. Divided-pulse nonlinear compression. *Optics letters*, 38(22):4593–4596, 2013. doi: 10.1364/OL.38.004593.

[57] D. Kraus, J. Vorberger, D. Gericke, V. Bagnoud*, A. Blažević*, W. Cayzac, A. Frank*, G. Gregori, A. Ortner, A. Otten, F. Roth, G. Schaumann, D. Schumacher, K. Siegenthaler, F. Wagner, K. Wünsch, and M. Roth. Probing the Complex Ion Structure in Liquid Carbon at 100 GPa. *Physical review letters*, 111(25):255501, 2013. doi: 10.1103/PhysRevLett.111.255501.

[58] J. Krauser, H.-G. Gehrke, H. Hofsäss, C. Trautmann*, and A. Weidinger. Conductive tracks of 30-MeV C60 clusters in doped and undoped tetrahedral amorphous carbon. *Nuclear instruments & methods in physics research / B*, 307:265 – 268, 2013. doi: 10.1016/j.nimb.2012.12.081.

[59] M. Krebs, S. Hädrich*, S. Demmler, J. Rothhardt*, A. Zaïr, L. Chipperfield, J. Limpert*, and A. Tünnermann*. Towards isolated attosecond pulses at megahertz repetition rates. *Nature photonics*, 7(7):555 – 559, 2013. doi: 10.1038/nphoton.2013.131.

[60] S. Kreim, D. Atanasov, D. Beck*, K. Blaum, C. Böhm, C. Borgmann, M. Breitenfeldt, T. E. Cocolios, D. Fink, S. George, A. Herlert, A. Kellerbauer, U. Köster, M. Kowalska, D. Lunney, V. Manea, E. Minaya Ramirez*, S. Naimi, D. Neidherr*, T. Nicol, R. E. Rossel, M. Rosenbusch, L. Schweikhard, J. Stanja, F. Wienholtz, R. N. Wolf, and K. Zuber. Recent exploits of the ISOLTRAP mass spectrometer. *Nuclear instruments & methods in physics research / B*, 317:492 – 500, 2013. doi: 10.1016/j.nimb.2013.07.072.

[61] J. Körner, J. Hein*, H. Liebetrau, R. Seifert*, D. Klöpfel, M. Kahle, M. Loeser, M. Siebold, U. Schramm, and M. C. Kaluza*. Efficient burst mode amplifier for ultra-short pulses based on cryogenically cooled $Yb^3+:CaF_2$. *Optics express*, 21(23):29006, 2013. doi: 10.1364/OE.21.029006.

[62] S. Kuhn, A. Herrmann, J. Hein*, M. C. Kaluza*, and C. Rüssel. Sm^{3+}-doped La_2O_3–Al_2O_3–SiO_2-glasses: structure, fluorescence and thermal expansion. *Journal of materials science*, 48(22):8014 – 8022, 2013. doi: 10.1007/s10853-013-7613-1.

[63] W. Li, M. D. Rodriguez, P. Kluth, M. Lang, N. Medvedev, M. Sorokin, J. Zhang, B. Afra, M. Bender*, D. Severin*, C. Trautmann*, and R. C. Ewing. Effect of doping on the radiation response of conductive Nb–$SrTiO_3$. *Nuclear instruments & methods in physics research / B*, 302:40 – 47, 2013. doi: 10.1016/j.nimb.2013.03.010.

[64] D. Lindenfels*, M. Vogel, W. Quint*, G. Birkl, and M. Wiesel. Half-open Penning trap with efficient light collection for precision laser spectroscopy of highly charged ions. *Hyperfine interactions*, xx:1, 2013. doi: 10.1007/s10751-013-0961-z.

[65] P. Linusson, S. Fritzsche*, J. Eland, M. Mucke, and R. Feifel. Single-photon multiple ionization forming double vacancies in the $2p$ subshell of argon. *Physical review / A*, 87(4):043409, 2013. doi: 10.1103/PhysRevA.87.043409.

[66] Y. A. Litvinov*, S. Bishop, K. Blaum, F. Bosch*, C. Brandau, L. X. Chen, I. Dillmann*, P. Egelhof*, H. Geissel*, R. E. Grisenti*, S. Hagmann*, M. Heil*, A. Heinz*, N. Kalantar-Nayestanaki, R. Knöbel*, C. Kozhuharov*, M. Lestinsky*, X. W. Ma, T. Nilsson, F. Nolden*, A. Ozawa, R. Raabe, M. W. Reed, R. Reifarth*, M. S. Sanjari*, D. Schneider, H. Simon*, M. Steck*, T. Stöhlker*, B. H. Sun, X. L. Tu, T. Uesaka, P. M. Walker, M. Wakasugi, H. Weick*, N. Winckler*, P. J. Woods, H. S. Xu, T. Yamaguchi, Y. Yamaguchi, and Y. H. Zhang. Nuclear physics experiments with ion storage rings. *Nuclear instruments & methods in physics research / B*, 317:603 – 616, 2013. doi: 10.1016/j.nimb.2013.07.025.

[67] A. Lushchik, C. Lushchik, V. Nagirnyi, S. Pazylbek, O. Sidletskiy, K. Schwartz*, E. Shablonin, A. Shugai, and E. Vasil'chenko. On the mechanisms of radiation damage and prospects of their suppression in complex metal oxides. *Physica status solidi / B*, 250(2):261 – 270, 2013. doi: 10.1002/pssb.201200488.

[68] B. Marx, K. S. Schulze, I. Uschmann, T. Kämpfer*, R. Lötzsch, O. Wehrhan*, W. Wagner, C. Detlefs, T. Roth, J. Härtwig, E. Förster, T. Stöhlker*, and G. G. Paulus. High-Precision X-Ray Polarimetry. *Physical review letters*, 110(25):254801, 2013. doi: 10.1103/PhysRevLett.110.254801.

[69] E. Matei, I. Enculescu, M. E. Toimil Molares*, A. Leca, C. Ghica, and V. Kuncser. Magnetic configurations of Ni–Cu alloy nanowires obtained by the template method. *Journal of nanoparticle research*, 15(8):1863, 2013. doi: 10.1007/s11051-013-1863-3.

[70] O. Matula*, A. G. Hayrapetyan, V. G. Serbo, A. Surzhykov*, and S. Fritzsche*. Atomic ionization of hydrogen-like ions by twisted photons: angular distribution of emitted electrons. *Journal of physics / B*, 46(20):205002, 2013. doi: 10.1088/0953-4075/46/20/205002.

[71] N. A. Medvedev, K. Schwartz*, C. Trautmann*, and A. E. Volkov. Formation of the defect halo of swift heavy ion tracks in LiF due to spatial redistribution of valence holes. *Physica status solidi / B*, 250(4): 850 – 857, 2013. doi: 10.1002/pssb.201200720.

[72] N. A. Medvedev, A. E. Volkov, K. Schwartz*, and C. Trautmann*. Effect of spatial redistribution of valence holes on the formation of a defect halo of swift heavy-ion tracks in LiF. *Physical review / B*, 87 (10):104103, 2013. doi: 10.1103/PhysRevB.87.104103.

[73] A. Mooser*, H. Kracke*, K. Blaum, S. A. Bräuninger, K. Franke, C. Leiteritz, W. Quint*, C. C. Rodegheri, S. Ulmer, and J. Walz*. Resolution of Single Spin Flips of a Single Proton. *Physical review letters*, 110(14):140405, 2013. doi: 10.1103/PhysRevLett.110.140405.

[74] Y. Nakano, Y. Takano, T. Ikeda, Y. Kanai, S. Suda, T. Azuma, H. Bräuning*, A. Bräuning-Demian*, D. Dauvergne, T. Stöhlker*, and Y. Yamazaki. Resonant coherent excitation of the lithiumlike uranium ion: A scheme for heavy-ion spectroscopy. *Physical review / A*, 87(6):060501, 2013. doi: 10.1103/PhysRevA.87.060501.

[75] S. Nasir*, P. Ramirez, M. Ali*, I. Ahmed, L. Fruk, S. Mafe, and W. Ensinger. Nernst-Planck model of photo-triggered, pH–tunable ionic transport through nanopores functionalized with “caged” lysine chains. *The journal of chemical physics*, 138(3):034709, 2013. doi: 10.1063/1.4775811.

[76] R. Neumann*. Science and technology on the nanoscale with swift heavy ions in matter. *Nuclear instruments $\&$; methods in physics research / B*, 314:4 – 10, 2013. doi: 10.1016/j.nimb.2013.04.035.

[77] P. A. Ni, S. M. Lund, C. McGuffey, N. Alexander, B. Aurand*, J. J. Barnard, F. N. Beg, C. Bellei, F. M. Bieniosek, C. Brabetz*, R. H. Cohen, J. Kim, P. Neumayer*, M. Roth, and B. G. Logan. Initial experimental evidence of self-collimation of target-normal-sheath-accelerated proton beam in a stack of conducting foils. *Physics of plasmas*, 20(8):083111, 2013. doi: 10.1063/1.4818147.

[78] H.-J. Otto, F. Jansen, F. Stutzki, C. Jauregui, J. Limpert*, and A. Tunnermann*. Improved Modal Reconstruction for Spatially and Spectrally Resolved Imaging S^2. *Journal of lightwave technology*, 31 (8):1295 – 1299, 2013. doi: 10.1109/JLT.2013.2242430.

[79] H.-J. Otto, C. Jauregui, F. Stutzki, F. Jansen, J. Limpert*, and A. Tünnermann*. Controlling mode instabilities by dynamic mode excitation with an acousto-optic deflector. *Optics express*, 21(14):17285 – 17298, 2013. doi: 10.1364/OE.21.017285.

[80] J. Papuga, M. L. Bissell, K. Kreim, K. Blaum, B. A. Brown, M. De Rydt, R. F. Garcia Ruiz, H. Heylen, M. Kowalska, R. Neugart, G. Neyens, W. Nörtershäuser, T. Otsuka, M. M. Rajabali, R. Sánchez*, Y. Utsuno, and D. T. Yordanov. Spins and Magnetic Moments of ^{49}K and ^{51}K: Establishing the $1/2^+$ and $3/2^+$ Level Ordering Beyond N=28. *Physical review letters*, 110(17):172503, 2013. doi: 10.1103/PhysRevLett.110.172503.

[81] J.-F. Pietschmann, M.-T. Wolfram, M. Burger, C. Trautmann*, G. Nguyen, M. Pevarnik, V. Bayer*, and Z. Siwy. Rectification properties of conically shaped nanopores: consequences of miniaturization. *Physical chemistry, chemical physics*, 15(39):16917, 2013. doi: 10.1039/c3cp53105h.

[82] S. A. Pikuz, A. Y. Faenov, J. Colgan, R. J. Dance, J. Abdallah, E. Wagenaars, N. Booth, O. Culfa, R. G. Evans, R. J. Gray, T. Kaempfer*, K. L. Lancaster, P. McKenna, A. L. Rossall, I. Y. Skobelev, K. S. Schulze*, I. Uschmann*, A. G. Zhidkov, and N. C. Woolsey. Measurement and simulations of hollow atom X-ray spectra of solid-density relativistic plasma created by high-contrast PW optical laser pulses. *High energy density physics*, 9(3):560 – 567, 2013. doi: 10.1016/j.hedp.2013.05.008.

[83] A. R. Piriz and N. A. Tahir*. Physics of ablative Rayleigh–Taylor and Landau–Darrieus instabilities. *New journal of physics*, 15(1):015013, 2013. doi: 10.1088/1367-2630/15/1/015013.

[84] A. R. Piriz, S. A. Piriz, and N. A. Tahir*. High pressure generation by hot electrons driven ablation. *Physics of plasmas: devoted to original contributions to and reviews of the physics of plasmas, including magnetofluid mechanics, kinetic theory and statistical mechanics of fully and partially ionized gases*, 20:112704, 2013. doi: 10.1063/1.4833680.

[85] A. R. Piriz, Y. B. Sun, and N. A. Tahir*. Rayleigh-Taylor stability boundary at solid-liquid interfaces. *Physical review / E*, 88:023026, 2013. doi: 10.1103/PhysRevE.88.023026.

[86] M. E. Povarnitsyn, N. E. Andreev, P. R. Levashov, K. V. Khishchenko, D. A. Kim, V. G. Novikov, and O. Rosmej*. Laser irradiation of thin films: Effect of energy transformation. *Laser and particle beams*, 31(04):663 – 671, 2013. doi: 10.1017/S0263034613000700.

[87] G. Rodriguez Prieto, A. R. Piriz, J. J. Lopez Cela, and N. A. Tahir*. Dynamic stabilization of Rayleigh-Taylor instability: Experiments with Newtonian fluids as surrogates for ablation fronts. *Physics of plasmas*, 20(1):012706, 2013. doi: 10.1063/1.4789552.

[88] P. Ramirez, V. Gomez, M. Ali*, W. Ensinger, and S. Mafe. Net currents obtained from zero-average potentials in single amphoteric nanopores. *Electrochemistry communications*, 31:137 – 140, 2013. doi: 10.1016/j.elecom.2013.03.026.

[89] T. Rathje*, A. M. Sayler*, S. Zeng, P. Wustelt, H. Figger, B. D. Esry, and G. G. Paulus*. Coherent Control at Its Most Fundamental: Carrier-Envelope-Phase-Dependent Electron Localization in Photodissociation of a H_2^+ Molecular Ion Beam Target. *Physical review letters*, 111(9):093002, 2013. doi: 10.1103/PhysRevLett.111.093002.

[90] R. Riedel*, A. Al-Shemmary, M. Gensch, T. Golz, M. Harmand, N. Medvedev, M. Prandolini*, K. Sokolowski-Tinten, S. Toleikis, U. Wegner, B. Ziaja, N. Stojanovic, and F. Tavella*. Single-shot pulse duration monitor for extreme ultraviolet and X-ray free-electron lasers. *Nature Communications*, 4:1731, 2013. doi: 10.1038/ncomms2754.

[91] R. Riedel*, M. Schulz*, M. Prandolini*, A. Hage, H. Höppner, T. Gottschall, J. Limpert*, M. Drescher, and F. Tavella*. Long-term stabilization of high power optical parametric chirped-pulse amplifiers. *Optics express*, 21(23):28987 – 28999, 2013. doi: 10.1364/OE.21.028987.

[92] M. D. Rodriguez, B. Afra, C. Trautmann*, N. Kirby, and P. Kluth. The influence of swift heavy ion irradiation on the recrystallization of amorphous $Fe_{80}B_{20}$. *Microelectronic engineering*, 102:64 – 66, 2013. doi: 10.1016/j.mee.2012.05.030.

[93] V. A. Rodriguez, A. Bernhard, A. Keilmann, P. Peiffer, R. Rossmanith, C. Widmann, T. Baumbach, M. Nicolai, and M. C. Kaluza*. Development of a Superconducting Transverse-Gradient Undulator for Laser-Wakefield Accelerators. *IEEE transactions on applied superconductivity*, 23(3):4101505 – 4101505, 2013. doi: 10.1109/TASC.2013.2240151.

[94] J. Rothhardt*, S. Demmler, S. Hädrich*, T. Peschel, J. Limpert*, and A. Tünnermann*. Thermal effects in high average power optical parametric amplifiers. *Optics letters*, 38(5):763, 2013. doi: 10.1364/OL.38.000763.

[95] A. Russakova, M. V. Sorokin, K. Schwartz*, A. Dauletbekova, A. Akilbekov, M. Baizhumanov, M. Zdorovets, and M. Koloberdin. Color center accumulation in LiF crystals under irradiation with MeV ions: Optical spectroscopy and modeling. *Nuclear instruments $\&$; methods in physics research / B*, 313:21 – 25, 2013. doi: 10.1016/j.nimb.2013.08.007.

[96] S. Salem*, T. Stöhlker*, A. Bräuning-Demian*, S. Hagmann*, C. Kozhuharov*, D. Liesen*, and A. Gumberidze*. Angular distribution of photons for the simultaneous excitation and ionization of

He-like uranium ions in relativistic ion-atom collisions. *Physical review / A*, 88(1):012701, 2013. doi: 10.1103/PhysRevA.88.012701.

[97] D. Schauries, M. Lang*, O. H. Pakarinen, S. Botis, B. Afra, M. D. Rodriguez, F. Djurabekova, K. Nordlund, D. Severin*, M. Bender*, W. X. Li, C. Trautmann*, R. C. Ewing, N. Kirby, and P. Kluth. Temperature dependence of ion track formation in quartz and apatite. *Journal of applied crystallography*, 46 (6):1558 – 1563, 2013. doi: 10.1107/S0021889813022802.

[98] M. Schnell, A. Sävert*, I. Uschmann*, M. Reuter*, M. Nicolai, T. Kämpfer*, B. Landgraf*, O. Jäckel*, O. Jansen, A. Pukhov, M. C. Kaluza*, and C. Spielmann*. Optical control of hard X-ray polarization by electron injection in a laser wakefield accelerator. *Nature Communications*, 4:2421, 2013. doi: 10.1038/ncomms3421.

[99] M. B. Schwab, A. Sävert, O. Jäckel*, J. Polz, M. Schnell, T. Rinck, L. Veisz, M. Möller, P. Hansinger, G. G. Paulus*, and M. C. Kaluza*. Few-cycle optical probe-pulse for investigation of relativistic laser-plasma interactions. *Applied physics letters*, 103(19):191118, 2013. doi: 10.1063/1.4829489.

[100] Y.-L. Shi, C.-Z. Dong, X.-Y. Ma, Z.-W. Wu, L.-Y. Xie, and S. Fritzsche*. Polarization of M2 Line Emitted Following Electron-Impact Excitation of Beryllium-Like Ions. *Chinese physics letters*, 30(6): 063401, 2013. doi: 10.1088/0256-307X/30/6/063401.

[101] Y.-L. Shi, C.-Z. Dong, F. Stephan*, D.-H. Zhang, and L.-Y. Xie. Theory of X-Ray Anisotropy and Polarization Following the Dielectronic Recombination of Initially Hydrogen-Like Ions. *Chinese physics letters*, 30(2):023402, 2013. doi: 10.1088/0256-307X/30/2/023402.

[102] D. Shubina*, R. B. Cakirli, Y. A. Litvinov*, K. Blaum, C. Brandau*, F. Bosch*, J. J. Carroll, R. F. Casten, D. M. Cullen, I. J. Cullen, A. Y. Deo, B. Detwiler, C. Dimopoulou*, F. Farinon*, H. Geissel*, E. Haettner, M. Heil*, R. S. Kempley, C. Kozhuharov*, R. Knöbel*, J. Kurcewicz*, N. Kuzminchuk, S. A. Litvinov*, Z. Liu, R. Mao, C. Nociforo*, F. Nolden*, Z. Patyk, W. R. Plass, A. Prochazka*, M. W. Reed, M. S. Sanjari*, C. Scheidenberger*, M. Steck*, T. Stöhlker*, B. Sun, T. P. D. Swan, G. Trees, P. M. Walker, H. Weick*, N. Winckler*, M. Winkler*, P. J. Woods, T. Yamaguchi, and C. Zhou. Schottky mass measurements of heavy neutron-rich nuclides in the element range 70≤Z≤79 at the GSI Experimental Storage Ring. *Physical review / C*, 88(2):024310, 2013. doi: 10.1103/PhysRevC.88.024310.

[103] R. Singh*, O. Boine-Frankenheim*, O. Chorniy*, P. Forck*, R. Haseitl*, W. Kaufmann*, P. Kowina*, K. Lang*, and T. Weiland. Interpretation of transverse tune spectra in a heavy-ion synchrotron at high intensities. *Physical review / Special topics / Accelerators and beams*, 16(3):034201, 2013. doi: 10.1103/PhysRevSTAB.16.034201.

[104] N. Sirse, J. P. Booth, P. Chabert, A. Surzhykov*, and P. Indelicato. Chlorine atom densities in the $(3p^5)^2 p^o_{1/2}$ excited spin–orbit state measured by two-photon absorption laser-induced fluorescence in a chlorine inductively coupled plasma. *Journal of physics / D*, 46(29):295203, 2013. doi: 10.1088/0022-3727/46/29/295203.

[105] N. Stolterfoht, R. Hellhammer, B. Sulik, Z. Juhász, V. Bayer*, C. Trautmann*, E. Bodewits, G. Reitsma, and R. Hoekstra. Areal density effects on the blocking of 3-keV Ne^{7+} ions guided through nanocapillaries in polymers. *Physical review / A*, 88(3):032902, 2013. doi: 10.1103/PhysRevA.88.032902.

[106] S. Sturm, A. Wagner, M. Kretzschmar, W. Quint*, G. Werth, and K. Blaum. g-factor measurement of hydrogenlike $^{28}Si^{13+}$ as a challenge to QED calculations. *Physical review / A*, 87(3):030501, 2013. doi: 10.1103/PhysRevA.87.030501.

[107] F. Stutzki, F. Jansen, C. Jauregui, J. Limpert*, and A. Tünnermann*. 24 mJ, 33 W Q-switched Tm-doped fiber laser with near diffraction-limited beam quality. *Optics letters*, 38(2):97 – 99, 2013. doi: 10.1364/OL.38.000097.

[108] A. Surzhykov*, Y. Litvinov*, T. Stöhlker*, and S. Fritzsche. Hyperfine-induced effects on the linear polarization of $K\alpha_1$ emission from heliumlike ions. *Physical review / A*, 87(5):052507, 2013. doi: 10.1103/PhysRevA.87.052507.

[109] A. Surzhykov*, R. H. Pratt, and S. Fritzsche*. Two-photon decay of inner-shell vacancies in heavy atoms. *Physical review / A*, 88(4):042512, 2013. doi: 10.1103/PhysRevA.88.042512.

[110] A. Surzhykov*, V. A. Yerokhin, T. Jahrsetz*, P. Amaro, T. Stöhlker*, and S. Fritzsche*. Polarization correlations in the elastic Rayleigh scattering of photons by hydrogenlike ions. *Physical review / A*, 88 (6):062515, 2013. doi: 10.1103/PhysRevA.88.062515.

[111] M. N. Tahir, M. Ali*, R. Andre, W. E. G. Müller, H.-C. Schröder, W. Tremel, and W. Ensinger. Silicatein conjugation inside nanoconfined geometries through immobilized $NTA–Ni_{(ii)}$ chelates. *Chemical communications*, 49(22):2210, 2013. doi: 10.1039/c3cc38605h.

[112] N. A. Tahir*, J. Blanco Sancho, R. Schmidt, A. Shutov, and A. R. Piriz. Prospects of warm dense matter research at HiRadMat facility at CERN using 440 MeV SPS proton beam. *High energy density physics*, 9(2):269 – 276, 2013. doi: 10.1016/j.hedp.2012.12.010.

[113] N. A. Tahir*, A. Shutov, A. P. Zharkov, P. Spiller*, A. R. Piriz, G. Rodriguez Prietoc, C. Deutsch, and T. Stöhlker*. Ion Beam Driven High Energy Density Physics Studies at FAIR at Darmstadt: The HEDgeHOB Collaboration. *Contributions to plasma physics*, 53(4-5):292 – 299, 2013. doi: 10.1002/ctpp.201200112.

[114] S. Tashenov*, T. Bäck, R. Barday, B. Cederwall, J. Enders, A. Khaplanov, Y. Fritzsche, K.-U. Schässburger, A. Surzhykov*, V. A. Yerokhin*, and D. Jakubassa-Amundsen. Bremsstrahlung polarization correlations and their application for polarimetry of electron beams. *Physical review / A*, 87(2):022707, 2013. doi: 10.1103/PhysRevA.87.022707.

[115] A. Tauschwitz*, M. Basko*, A. Frank, V. Novikov, A. Grushin, A. Blazevic*, M. Roth, and J. A. Maruhn. 2D radiation-hydrodynamics modeling of laser-plasma targets for ion stopping measurements. *High energy density physics*, 9:158–166, 2013. doi: 10.1016/j.hedp.2012.12.004.

[116] L. Tkachenko, I. Bogdanov, S. Kozub, V. Sytnik, D. Varentsov*, S. Zinchenko, and V. Zubko. Development of Wide-Aperture Quadrupole Magnets for Plasma Experiments in the FAIR Project. *IEEE transactions on applied superconductivity*, 23(3):4000204 – 4000204, 2013. doi: 10.1109/TASC.2012.2229333.

[117] J. Tol, K. Dinse, H. Stork, F. Fujara, B. Schuster*, and K. Schwartz*. Anomalous Phases in Cavity-Free 240 GHz Pulsed ENDOR Spectra of 1.44 GeV Xe-Irradiated LiF. *Applied magnetic resonance*, 44(1-2): 117 – 132, 2013. doi: 10.1007/s00723-012-0407-9.

[118] M. Toulemonde, A. Benyagoub, C. Trautmann*, N. Khalfaoui, M. Boccanfuso, C. Dufour, F. Gourbilleau, J. Grob, J. Stoquert, J. Costantini, F. Haas, E. Jacquet, K.-O. Voss*, and A. Meftah. Reply to "Comment on 'Dense and nanometric electronic excitations induced by swift heavy ions in an ionic CaF_2 crystal: Evidence for two thresholds of damage creation' ". *Physical review / B*, 87(5):056102, 2013. doi: 10.1103/PhysRevB.87.056102.

[119] S. Ulmer, K. Blaum, H. Kracke, A. Mooser, W. Quint*, C. C. Rodegheri, and J. Walz. A cryogenic detection system at 28.9MHZ for the non-destructive observation of a single proton at low particle

energy. *Nuclear instruments & methods in physics research / A*, 705:55 – 60, 2013. doi: 10.1016/j.nima.2012.12.071.

[120] G. A. Vergunova, V. B. Rozanov, O. B. Denisov, N. Y. Orlov, and O. Rosmej*. Mathematical modeling of gas-dynamic and radiative processes in experiments with the use of laser and heavy-ion beams. *Plasma physics reports*, 39(9):755 – 762, 2013. doi: 10.1134/S1063780X13090080.

[121] M. Vogel and W. Quint*. Aspects of fundamental physics in precision spectroscopy of highly charged ions in Penning traps. *Annalen der Physik*, 525(7):505 – 513, 2013. doi: 10.1002/andp.201300032.

[122] M. Vogel*, G. Birkl, D. von Lindenfels*, W. Quint*, and M. Wiesel*. Switchable magnetic bottles and field gradients for particle traps. *Applied physics / B*, B(1-2):1, 2013. doi: 10.1007/s00340-013-5707-8.

[123] D. von Lindenfels*, M. Wiesel, D. A. Glazov, A. V. Volotka, M. M. Sokolov, V. M. Shabaev, G. Plunien, W. Quint*, G. Birkl, A. Martin, and M. Vogel. Experimental access to higher-order Zeeman effects by precision spectroscopy of highly charged ions in a Penning trap. *Physical review / A*, 87(2):023412, 2013. doi: 10.1103/PhysRevA.87.023412.

[124] A. Wagner, S. Sturm, F. Köhler, D. A. Glazov, A. V. Volotka, G. Plunien, W. Quint*, V. M. Shabaev, K. Blaum, and G. Werth. g Factor of Lithiumlike Silicon $^{28}Si^{11+}$. *Physical review letters*, 110(3): 033003, 2013. doi: 10.1103/PhysRevLett.110.033003.

[125] F. Wagner, C. P. João, J. Fils*, T. Gottschall, J. Hein, J. Körner, J. Limpert, M. Roth, T. Stöhlker*, and V. Bagnoud*. Temporal contrast control at the PHELIX petawatt laser facility by means of tunable sub-picosecond optical parametric amplification. *Applied physics / B*, 113(2):–, 2013. doi: 10.1007/s00340-013-5714-9.

[126] P. M. Walker, Y. Litvinov*, and H. Geissel*. The ILIMA project at FAIR. *International journal of mass spectrometry*, 349-350:247 – 254, 2013. doi: 10.1016/j.ijms.2013.04.007.

[127] W. Q. Wen*, M. Lochmann*, X. Ma, M. Bussmann, D. F. A. Winters*, W. Nörtershäuser*, B. Botermann, C. Geppert, N. Frömmgen, M. Hammen, V. Hannen, R. Jöhren, T. Kühl*, Y. Litvinov*, R. Sánchez*, T. Stöhlker*, J. Vollbrecht, C. Weinheimer, C. Dimopoulou*, F. Nolden*, and M. Steck*. Optical measurement of the longitudinal ion distribution of bunched ion beams in the ESR. *Nuclear instruments & methods in physics research / A*, 711:90 – 95, 2013. doi: 10.1016/j.nima.2013.01.058.

[128] A. N. Wenz, G. Zurn, S. Murmann, I. Brouzos, T. Lompe*, and S. Jochim*. From Few to Many: Observing the Formation of a Fermi Sea One Atom at a Time. *Science*, 342(6157):457 – 460, 2013. doi: 10.1126/science.1240516.

[129] F. Wienholtz, D. Beck*, K. Blaum, C. Borgmann, M. Breitenfeldt, R. B. Cakirli, S. George, F. Herfurth*, J. D. Holt, M. Kowalska, S. Kreim, D. Lunney, V. Manea, J. Menéndez, D. Neidherr*, M. Rosenbusch, L. Schweikhard, A. Schwenk, J. Simonis, J. Stanja, R. N. Wolf, and K. Zuber. Masses of exotic calcium isotopes pin down nuclear forces. *Nature*, 498(7454):346 – 349, 2013. doi: 10.1038/nature12226.

[130] R. N. Wolf, F. Wienholtz, D. Atanasov*, D. Beck*, K. Blaum, C. Borgmann, F. Herfurth*, M. Kowalska, S. Kreim, Y. Litvinov*, D. Lunney, V. Manea, D. Neidherr*, M. Rosenbusch, L. Schweikhard, J. Stanja, and K. Zuber. ISOLTRAP's multi-reflection time-of-flight mass separator/spectrometer. *International journal of mass spectrometry*, 349-350:123 – 133, 2013. doi: 10.1016/j.ijms.2013.03.020.

[131] T. Yamaki, N. Nuryanthi, H. Koshikawa, M. Asano, S. Sawada, T. Hakoda, Y. Maekawa, K.-O. Voss*, D. Severin*, T. Seidl*, C. Trautmann*, and R. Neumann*. Ion-track membranes of fluoropolymers: Toward controlling the pore size and shape. *Nuclear instruments & methods in physics research / B*, 314:77 – 81, 2013. doi: 10.1016/j.nimb.2013.05.028.

[132] X. L. Yan, H. S. Xu, Y. A. Litvinov*, Y. H. Zhang, H. Schatz, X. L. Tu, K. Blaum, X. H. Zhou, B. H. Sun, J. J. He, Y. Sun, M. Wang, Y. J. Yuan, J. W. Xia, J. C. Yang, G. Audi, G. B. Jia, Z. G. Hu, X. W. Ma, R. S. Mao, B. Mei, P. Shuai, Z. Y. Sun, S. T. Wang, G. Q. Xiao, X. XU, T. Yamaguchi, Y. Yamaguchi, Y. D. Zang, H. W. Zhao, T. C. Zhao, W. Zhang, and W. L. Zhan. Mass measurement of ^{45}Cr and its impact on the Ca-Sc cycle in y-ray bursts. *The astrophysical journal / 2*, 766(1):L8, 2013. doi: 10.1088/2041-8205/766/1/L8.

[133] M. Yeung, B. Dromey, D. Adams, S. Cousens, R. Hörlein, Y. Nomura, G. Tsakiris, and M. Zepf*. Beaming of High-Order Harmonics Generated from Laser-Plasma Interactions. *Physical review letters*, 110(16):165002, 2013. doi: 10.1103/PhysRevLett.110.165002.

[134] M. Yeung, B. Dromey, C. Rödel*, J. Bierbach*, M. Wünsche, G. Paulus*, T. Hahn, D. Hemmers, C. Stelzmann, G. Pretzler, and M. Zepf*. Near-monochromatic high-harmonic radiation from relativistic laser–plasma interactions with blazed grating surfaces. *New journal of physics*, 15(2):025042, 2013. doi: 10.1088/1367-2630/15/2/025042.

[135] D. T. Yordanov, D. L. Balabanski, J. Bieroń, M. L. Bissell, K. Blaum, I. Budinčević, S. Fritzsche*, N. Frömmgen, G. Georgiev, C. Geppert*, M. Hammen, M. Kowalska, K. Kreim, A. Krieger, R. Neugart, W. Nörtershäuser*, J. Papuga, and S. Schmidt*. Spins, Electromagnetic Moments, and Isomers of $^{107-129}Cd$. *Physical review letters*, 110(19):192501, 2013. doi: 10.1103/PhysRevLett.110.192501.

[136] U. Zastrau, A. Woldegeorgis, E. Förster*, R. Loetzsch*, H. Marschner, and I. Uschmann*. Characterization of strongly-bent HAPG crystals for von-Hámos x-ray spectrographs. *Journal of Instrumentation*, 8(10):P10006 – P10006, 2013. doi: 10.1088/1748-0221/8/10/P10006.

[137] M. Zürch, C. Kern, and C. Spielmann*. XUV coherent diffraction imaging in reflection geometry with low numerical aperture. *Optics express*, 21(18):21131, 2013. doi: 10.1364/OE.21.021131.

Further publications to the programme large-scale facilities for research with photons, neutrons and ions published in 2013

[1] P. Amaro, S. Schlesser, M. Guerra, E. Le Bigot, J. P. Santos, C. I. Szabo, A. Gumberidze*, and P. Indelicato. Absolute measurements and simulations of x-ray line energies of highly charged ions with a double-crystal spectrometer. *Physica scripta*, T156:014104, 2013. doi: 10.1088/0031-8949/2013/T156/014104.

[2] D. R. Atanasov, D. Balabanski, L. Batist, K. Blaum, F. Bosch*, D. Boutin*, C. Brandau*, C. Dimopoulou*, H. G. Essel*, T. Faestermann, H. Geissel*, S. Hagmann*, R. Heß*, P.-M. Hillenbrand*, P. Kienle, R. Knöbel*, C. Kozhuharov*, J. Kurcewicz*, M. Lestinsky*, S. A. Litvinov*, Y. A. Litvinov*, X. Ma, R. Märtin*, M. Mazzocco*, G. Münzenberg*, F. Nolden*, T. Ohtsubo, Z. Patyk, M. S. Sanjari*, C. Scheidenberger*, D. Shubina, U. Spillmann*, M. Steck*, T. Stöhlker*, B. Sun, T. Suzuki, S. Torilov, M. Trassinelli*, S. Trotsenko*, X. Tu, I. I. Tupitsyn, H. Weick*, N. Winckler*, M. Winkler*, D. F. A. Winters*, N. Winters*, H. Xu, T. Yamaguchi, X. Yan, Y. Yuan, and Y. Zhang. Half-life measurements of highly charged radionuclides. *Physica scripta*, T156:014026, 2013. doi: 10.1088/0031-8949/2013/T156/014026.

[3] D. Banaś, M. Pajek, A. Gumberidze*, A. Surzhykov, and T. Stöhlker*. K-shell differential radiative recombination rates for bare uranium ions interacting with low-energy electrons. *Physica scripta*, T156: 014045, 2013. doi: 10.1088/0031-8949/2013/T156/014045.

[4] K. Blaum, J. Dilling, and W. Nörtershäuser*. Precision atomic physics techniques for nuclear physics with radioactive beams. *Physica scripta*, T152:014017, 2013. doi: 10.1088/0031-8949/2013/T152/014017.

[5] K.-H. Blumenhagen*, E. Badura*, H. Bräuning*, J. Hoffmann*, K. Koch*, N. Kurz*, R. Märtin*, S. Minami*, W. Ott*, U. Spillmann*, T. Stöhlker*, G. Weber*, and M. Weber. Fully digital readout of segmented solid state detectors. *Physica scripta*, T156:014102, 2013. doi: 10.1088/0031-8949/2013/T156/014102.

[6] F. Bosch*, D. R. Atanasov, C. Brandau*, I. Dillmann*, C. Dimopoulou*, T. Faestermann, H. Geissel*, S. Hagmann*, P.-M. Hillenbrand*, P. Kienle, R. Knöbel*, C. Kozhuharov*, J. Kurcewicz*, M. Lestinsky*, S. A. Litvinov*, Y. A. Litvinov, X. Ma, F. Nolden*, T. Ohtsubo, Z. Patyk, R. Reuschl*, M. S. Sanjari*, C. Scheidenberger*, D. Shubina, U. Spillmann*, M. Steck*, T. Stöhlker*, B. Sun, M. Trassinelli*, S. Trotsenko*, X. L. Tu, H. Weick*, N. Winckler*, M. Winkler*, D. F. A. Winters*, T. Yamaguchi, and X. L. Yan. Beta decay of highly charged ions. *Physica scripta*, T156:014025, 2013. doi: 10.1088/0031-8949/2013/T156/014025.

[7] C. Brandau*, C. Kozhuharov*, A. Müller, D. Bernhardt, D. Banas, F. Bosch*, F. J. Currell, C. Dimopoulou*, A. Gumberidze*, S. Hagmann*, P.-M. Hillenbrand*, M. Heil*, M. Lestinsky*, Y. Litvinov*, R. Märtin*, F. Nolden*, R. Reuschl*, S. Sanjari*, S. Schippers, D. Schneider, D. Shubina*, H. Simon*, U. Spillmann*, Z. Stachura, M. Steck*, T. Stöhlker*, G. Weber*, M. Wiedeking, N. Winckler*, and D. F. A. Winters*. Probing nuclear properties by resonant atomic collisions between electrons and ions. *Physica scripta*, T156:014050, 2013. doi: 10.1088/0031-8949/2013/T156/014050.

[8] S. Fedotova*, E. Boulton*, N. P. M. Brantjes*, F. Herfurth*, N. Kotovskiy*, C. Krantz, D. Neidherr*, J. Steinmann*, and G. Vorobjev*. Cooling of highly charged ions — the HITRAP facility and Cooler trap. *Physica scripta*, T156:014095, 2013. doi: 10.1088/0031-8949/2013/T156/014095.

[9] S. Fritzsche*, T. Stöhlker*, and A. Surzhykov. 16th international conference on the physics of highly charged ions. *Physica scripta*, T156:010301, 2013. doi: 10.1088/0031-8949/2013/T156/010301.

[10] A. Gumberidze* and * SPARC Collaboration. Atomic physics at the future facility for antiproton and ion research: a status report. *Physica scripta*, T156:014084, 2013. doi: 10.1088/0031-8949/2013/T156/014084.

[11] S. Hagmann*, T. Stöhlker*, Y. Litvinov*, C. Kozhuharov*, P.-M. Hillenbrand*, U. Spillmann*, V. Shabaev*, K. Stiebing, M. Lestinsky*, A. Surzhykov, A. Voitkiv, B. Franzke*, D. Fischer, D. Schneider, D. Jakubassa, A. Artiomov, E. DeFilippo, X. Ma, R. Dörner, and H. Rothard. Few-body quantum dynamics of high- Z ions studied at the future relativistic high-energy storage ring. *Physica scripta*, T156:014086, 2013. doi: 10.1088/0031-8949/2013/T156/014086.

[12] A. G. Hayrapetyan and S. Fritzsche*. Bessel beams of laser-driven two-level atoms. *Physica scripta*, T156:014067, 2013. doi: 10.1088/0031-8949/2013/T156/014067.

[13] P.-M. Hillenbrand*, S. Hagmann*, T. Stöhlker*, Y. Litvinov*, C. Kozhuharov*, U. Spillmann*, V. Shabaev*, K. Stiebing, M. Lestinsky*, A. Surzhykov, A. Voitkiv, B. Franzke*, D. Fischer, C. Brandau*, S. Schippers, A. Mueller, D. Schneider, D. Jakubassa, A. Artiomov, E. DeFilippo, X. Ma, R. Dörner*, and H. Rothard. Future experiments using forward electron spectroscopy to study the quantum dynamics of high- Z ions at the ESR/CRYRING storage rings. *Physica scripta*, T156:014087, 2013. doi: 10.1088/0031-8949/2013/T156/014087.

[14] T. Jahrsetz* and A. Surzhykov*. Two-photon transitions in few-electron ions in the presence of static electric fields. *Physica scripta*, T156:014069, 2013. doi: 10.1088/0031-8949/2013/T156/014069.

[15] Y. S. Kozhedub, I. I. Tupitsyn, V. M. Shabaev, S. Hagmann*, G. Plunien, and T. Stöhlker*. Relativistic calculations of inner-shell atomic processes in low-energy ion–atom collisions. *Physica scripta*, T156:014053, 2013. doi: 10.1088/0031-8949/2013/T156/014053.

[16] A. V. Maiorova, A. Surzhykov*, S. Tashenov, V. M. Shabaev, and T. Stöhlker*. Production and diagnostics of spin-polarized heavy ions in the sequential two-electron radiative recombination. *Physica scripta*, T156:014046, 2013. doi: 10.1088/0031-8949/2013/T156/014046.

[17] I. A. Maltsev, G. B. Deyneka, I. I. Tupitsyn, V. M. Shabaev, Y. S. Kozhedub, G. Plunien, and T. Stöhlker*. Relativistic calculations of charge transfer probabilities in U^{92+}–$U^{91+}(1s)$ collisions using the basis set of cubic Hermite splines. *Physica scripta*, T156:014056, 2013. doi: 10.1088/0031-8949/2013/T156/014056.

[18] O. Matula*, S. Fritzsche*, and A. Surzhykov*. Polarization correlations between photons emitted in dielectronic recombination of high-Z ions. *Physica scripta*, T156:014051, 2013. doi: 10.1088/0031-8949/2013/T156/014051.

[19] S. McConnell*, A. Artemyev*, and A. Surzhykov*. Treatment of U^{92+}–U^{91+} collisions in spherical co-ordinates: going beyond the monopole approximation. *Physica scripta*, T156:014055, 2013. doi: 10.1088/0031-8949/2013/T156/014055.

[20] R. Märtin*, G. Weber*, R. Barday, Y. Fritzsche, J. Enders, U. Spillmann*, and T. Stöhlker*. Target-thickness effects in electron–atom bremsstrahlung. *Physica scripta*, T156:014070, 2013. doi: 10.1088/0031-8949/2013/T156/014070.

[21] T. Murböck, S. Albrecht, Z. Andelkovic*, R. Cazan*, V. Hannen, R. Jöhren, J. Vollbrecht, S. Schmidt*, D. Segal, R. Thompson, M. Vogel, C. Weinheimer, W. Nörtershäuser*, and G. Birkl. SpecTrap: precision spectroscopy of highly charged ions—status and prospects. *Physica scripta*, T156:014096, 2013. doi: 10.1088/0031-8949/2013/T156/014096.

[22] W. Nörtershäuser*, M. Lochmann*, R. Jöhren, C. Geppert*, Z. Andelkovic*, D. Anielski, B. Botermann, M. Bussmann, A. Dax, N. Frömmgen, M. Hammen, V. Hannen, T. Kühl*, Y. A. Litvinov*, J. Volbrecht, T. Stöhlker*, R. C. Thompson, C. Weinheimer, W. Wen, E. Will, D. Winters*, and R. M. Sánchez*. First observation of the ground-state hyperfine transition in $^{209}Bi^{80+}$. *Physica scripta*, T156:014016, 2013. doi: 10.1088/0031-8949/2013/T156/014016.

[23] R. Reuschl*, T. Gaßner*, U. Spillmann*, A. Bräuning-Demian*, A. Ananyeva*, H. Beyer*, K.-H. Blumenhagen*, W. Chen*, S. Hagmann, M. Hegewald, P. Indelicato, M. Schwemlein*, S. Toleikis, M. Trassinelli, S. Trotsenko*, D. Winters*, N. Winters*, and T. Stöhlker*. Lifetime measurement of the 2^3P_0 state in He-like uranium. *Physica scripta*, T156:014024, 2013. doi: 10.1088/0031-8949/2013/T156/014024.

[24] M. S. Sanjari*, P. Hülsmann*, F. Nolden*, A. Schempp, J. X. Wu, D. Atanasov, F. Bosch*, C. Kozhuharov*, Y. Litvinov*, P. Moritz*, C. Peschke*, P. Petri*, D. Shubina, M. Steck*, H. Weick*, N. Winckler, Y. D. Zang, and T. C. Zhao. A resonant Schottky pickup for the study of highly charged ions in storage rings. *Physica scripta*, T156:014088, 2013. doi: 10.1088/0031-8949/2013/T156/014088.

[25] A. Sobiczewski* and Y. A. Litvinov*. Quality of theoretical masses in various regions of the nuclear chart. *Physica scripta*, T154:014001, 2013. doi: 10.1088/0031-8949/2013/T154/014001.

[26] U. Spillmann*, K. H. Blumenhagen*, E. Badura*, M. Balzer, H. Bräuning*, J. Hoffmann*, K. Koch*, N. Kurz*, R. Märtin*, S. Minami*, W. Ott*, T. Stöhlker*, G. Weber*, and M. Weber. Employing digital pulse processing electronics for the readout of a Si(Li)—Compton—polarimeter for the SPARC collaboration. *Physica scripta*, T156:014103, 2013. doi: 10.1088/0031-8949/2013/T156/014103.

[27] T. Stöhlker*, Y. A. Litvinov*, V. Bagnoud*, U. Bechstedt, C. Dimopoulou*, A. Dolinskii*, C. Geppert*, S. Hagmann*, T. Katayama, T. Kühl*, R. Maier, W. Nörtershäuser*, D. Prasuhn, R. Schuch, M. Steck*, and H. Stockhorst. SPARC experiments at the high-energy storage ring. *Physica scripta*, T156:014085, 2013. doi: 10.1088/0031-8949/2013/T156/014085.

[28] A. Surzhykov*, A. V. Maiorova, V. M. Shabaev, T. Stöhlker*, and S. Fritzsche*. Parity violation in beryllium-like heavy ions. *Physica scripta*, T156:014027, 2013. doi: 10.1088/0031-8949/2013/T156/014027.

[29] C. I. Szabo, P. Amaro, M. Guerra, J. P. Santos, A. Gumberidze*, J. Attard, and P. Indelicato. Ion temperature and x-ray line width measurements of highly charged argon ions in an ECR ion source. *Physica scripta*, T156:014077, 2013. doi: 10.1088/0031-8949/2013/T156/014077.

[30] S. Tashenov, T. Bäck, R. Barday, B. Cederwall, J. Enders, A. Khaplanov, Y. Fritzsche, K.-U. Schässburger, A. Surzhykov*, and V. A. Yerokhin*. Observation of the spin–orbit interaction in bremsstrahlung. *Physica scripta*, T156:014071, 2013. doi: 10.1088/0031-8949/2013/T156/014071.

[31] W. Wen, X. Ma, D. Zhang, M. Bussmann, X. Zhu, D. Winters*, L. Meng, H. Liu, D. Zhao, Z. Wang, J. Li, R. Mao, T. Zhao, J. Wu, G. Li, X. Yang, Y. Liu, J. Yang, Y. Yuan, J. Xia, and H. Xu. Preparations for laser cooling of relativistic heavy-ion beams at the CSRe. *Physica scripta*, T156:014090, 2013. doi: 10.1088/0031-8949/2013/T156/014090.

[32] D. F. A. Winters*, V. Bagnoud*, B. Ecker*, U. Eisenbarth*, S. Götte*, T. Kühl*, P. Neumayer*, C. Spielmann, T. Stöhlker*, and B. Zielbauer*. A beamline for x-ray laser spectroscopy at the experimental storage ring at GSI. *Physica scripta*, T156:014089, 2013. doi: 10.1088/0031-8949/2013/T156/014089.

[33] V. A. Yerokhin*, A. Surzhykov*, R. Märtin*, S. Tashenov, and G. Weber*. Bremsstrahlung of polarized positrons scattered off atoms. *Physica scripta*, T156:014072, 2013. doi: 10.1088/0031-8949/2013/T156/014072.

[34] Y. H. Zhang, H. S. Xu, Y. A. Litvinov*, X. L. Tu, X. L. Yan, S. Typel*, K. Blaum, M. Wang, X. H. Zhou, Y. Sun, B. A. Brown, Y. J. Yuan, J. W. Xia, J. C. Yang, G. Audi, X. C. Chen, G. B. Jia, Z. G. Hu, X. W. Ma, R. S. Mao, B. Mei, P. Shuai, Z. Y. Sun, S. T. Wang, G. Q. Xiao, X. Xu, T. Yamaguchi, Y. Yamaguchi, Y. D. Zang, H. W. Zhao, T. C. Zhao, W. Zhang, and W. L. Zhan. Test of IMME in fp shell via direct mass measurements of $T_z = -3/2$ nuclides. *Journal of physics / Conference Series*, 420:012054, 2013. doi: 10.1088/1742-6596/420/1/012054.

JCR publications to the programme health published in 2013

[1] B. Alpat, E. Pilicer, S. Blasko, D. Caraffini, F. D. Capua, V. Postolache, G. Saltanocchi, M. Menichelli, L. Desorgher, M. Durante*, R. Pleskac*, and C. L. Tessa*. Total and Partial Fragmentation Cross-Section of 500 MeV/nucleon Carbon Ions on Different Target Materials. *IEEE transactions on nuclear science*, 60(6):4673 – 4682, 2013. doi: 10.1109/TNS.2013.2284855.

[2] G. Alphonse, M. Maalouf, P. Battiston-Montagne, D. Ardail, M. Beuve, R. Rousson, G. Taucher-Scholz*, C. Fournier*, and C. Rodriguez-Lafrasse. p53-independent early and late apoptosis is mediated by ceramide after exposure of tumor cells to photon or carbon ion irradiation. *BMC cancer*, 13(1):151, 2013. doi: 10.1186/1471-2407-13-151.

[3] S. Carozzo, D. Schardt*, L. Narici, S. E. Combs, J. Debus, and W. G. Sannita. Electrophysiological Monitoring in Patients With Tumors of the Skull Base Treated by Carbon-12 Radiation Therapy. *International journal of radiation oncology, biology, physics*, 85(4):978 – 983, 2013. doi: 10.1016/j.ijrobp.2012.08.010.

[4] S. E. Combs, M. Djosanjh, R. Potter, R. Orrechia, T. Haberer, M. Durante*, P. Fossati, K. Parodi, J. Balosso, U. Amaldi, M. Baumann, and J. Debus. Towards clinical evidence in particle therapy: ENLIGHT, PARTNER, ULICE and beyond. *Journal of radiation research*, 54(suppl 1):i6 – i12, 2013. doi: 10.1093/jrr/rrt039.

[5] M. Durante*, J. S. Bedford, D. J. Chen, S. Conrad, M. N. Cornforth, A. T. Natarajan, D. C. van Gent, and G. Obe. From DNA damage to chromosome aberrations: Joining the break. *Mutation research / Genetic toxicology and environmental mutagenesis*, 756(1-2):5 – 13, 2013. doi: 10.1016/j.mrgentox.2013.05.014.

[6] M. Durante*, N. Reppingen, and K. D. Held. Immunologically augmented cancer treatment using modern radiotherapy. *Trends in molecular medicine*, 19(9):565 – 582, 2013. doi: 10.1016/j.molmed.2013.05.007.

[7] T. Friedrich*, R. Grün*, U. Scholz*, T. Elsässer*, M. Durante*, and M. Scholz*. Sensitivity analysis of the relative biological effectiveness predicted by the local effect model. *Physics in medicine and biology*, 58(19):6827 – 6849, 2013. doi: 10.1088/0031-9155/58/19/6827.

[8] T. Friedrich*, U. Scholz*, T. Elsässer*, M. Durante*, and M. Scholz*. Systematic analysis of RBE and related quantities using a database of cell survival experiments with ion beam irradiation. *Journal of radiation research*, 54(3):494 – 514, 2013. doi: 10.1093/jrr/rrs114.

[9] C. Graeff*, R. Lüchtenborg*, J. G. Eley, M. Durante*, and C. Bert*. A 4D-optimization concept for scanned ion beam therapy. *Radiotherapy and oncology*, 109(3):419 – 424, 2013. doi: 10.1016/j.radonc.2013.09.018.

[10] R. Grün*, T. Friedrich*, M. Krämer*, K. Zink, M. Durante*, R. Engenhart-Cabillic, and M. Scholz*. Physical and biological factors determining the effective proton range. *Medical physics*, 40(11):111716, 2013. doi: 10.1118/1.4824321.

[11] E. Haettner*, H. Iwase*, M. Krämer*, G. Kraft*, and D. Schardt*. Experimental study of nuclear fragmentation of 200 and 400 MeV/ u 12 C ions in water for applications in particle therapy. *Physics in medicine and biology*, 58(23):8265 – 8279, 2013. doi: 10.1088/0031-9155/58/23/8265.

[12] S. Hild*, M. Durante*, and C. Bert*. Assessment of Uncertainties in Treatment Planning for Scanned Ion Beam Therapy of Moving Tumors. *International journal of radiation oncology, biology, physics*, 85(2): 528 – 535, 2013. doi: 10.1016/j.ijrobp.2012.04.011.

[13] C. P. Karger, P. Peschke, M. Scholz*, P. E. Huber, and J. Debus. Relative Biological Effectiveness of Carbon Ions in a Rat Prostate Carcinoma In Vivo: Comparison of 1, 2, and 6 Fractions. *International journal of radiation oncology, biology, physics*, 86(3):450 – 455, 2013. doi: 10.1016/j.ijrobp.2013.01.019.

[14] K. Laube, S. Menkel, C. Bert*, W. Enghardt, S. Helmbrecht, N. Saito*, and F. Fiedler. 4D particle therapy PET simulation for moving targets irradiated with scanned ion beams. *Physics in medicine and biology*, 58(3):513 – 533, 2013. doi: 10.1088/0031-9155/58/3/513.

[15] J. S. Loeffler and M. Durante*. Charged particle therapy—optimization, challenges and future directions. *Nature reviews / Clinical oncology*, 10(7):411 – 424, 2013. doi: 10.1038/nrclinonc.2013.79.

[16] B. D. Loucas, M. Durante*, S. M. Bailey, and M. N. Cornforth. Chromosome Damage in Human Cells by γ Rays, α Particles and Heavy Ions: Track Interactions in Basic Dose-Response Relationships. *Radiation research*, 179(1):9 – 20, 2013. doi: 10.1667/RR3089.1.

[17] N.-Y. Ma, W. Tinganelli*, A. Maier*, M. Durante*, and W. Kraft-Weyrather*. Influence of chronic hypoxia and radiation quality on cell survival. *Journal of radiation research*, 54(suppl 1):i13 – i22, 2013. doi: 10.1093/jrr/rrs135.

[18] B. Merk*, K.-O. Voss*, I. Müller*, B. Fischer*, B. Jakob*, G. Taucher-Scholz*, C. Trautmann*, and M. Durante*. Photobleaching setup for the biological end-station of the darmstadt heavy-ion microprobe. *Nuclear instruments & methods in physics research / B*, 306:81 – 84, 2013. doi: 10.1016/j.nimb.2012.11.043.

[19] F. Merz, F. Gaunitz, F. Dehghani, C. Renner, J. Meixensberger, A. Gutenberg, A. Giese, K. Schopow, C. Hellwig, M. Schafer, M. Bauer, H. Stöcker*, G. Taucher-Scholz*, M. Durante*, and I. Bechmann. Organotypic slice cultures of human glioblastoma reveal different susceptibilities to treatments. *Neuro-Oncology*, 15(6):670 – 681, 2013. doi: 10.1093/neuonc/not003.

[20] B. Meyer*, K.-O. Voss*, F. Tobias*, B. Jakob*, M. Durante*, and G. Taucher-Scholz*. Clustered DNA damage induces pan-nuclear H2AX phosphorylation mediated by ATM and DNA-PK. *Nucleic acids symposium series*, 41(12):6109 – 6118, 2013. doi: 10.1093/nar/gkt304.

[21] I. Müller*, B. Merk*, K.-O. Voss*, N. Averbeck*, B. Jakob*, M. Durante*, and G. Taucher-Scholz*. Species conserved DNA damage response at the inactive human X chromosome. *Mutation research / Genetic toxicology and environmental mutagenesis*, 756(1-2):30 – 36, 2013. doi: 10.1016/j.mrgentox.2013.04.006.

[22] G. Obe, S. Ritter*, and M. Durante*. Chromosome aberrations, DNA damage, and risk: Matrix reloaded. *Mutation research / Genetic toxicology and environmental mutagenesis*, 756(1-2):3 – 4, 2013. doi: 10.1016/j.mrgentox.2013.07.002.

[23] D. Pignalosa*, R. Lee, C. Hartel*, S. Sommer, A. Nikoghosyan, J. Debus, S. Ritter*, and M. Durante*. Chromosome inversions in lymphocytes of prostate cancer patients treated with X-rays and carbon ions. *Radiotherapy and oncology*, 109(2):256 – 261, 2013. doi: 10.1016/j.radonc.2013.09.021.

[24] D. Richter*, N. Saito*, N. Chaudhri, M. Haertig, S. Combs, D. Habermehl, K. Herfarth, O. Jaekel, M. Durante*, and C. Bert*. 4D Treatment Dose Reconstruction for Scanned Ion Beam Therapy. *International journal of radiation oncology, biology, physics*, 87(2):S183, 2013. doi: 10.1016/j.ijrobp.2013.06.472.

[25] D. Richter*, A. Schwarzkopf*, J. Trautmann*, M. Krämer*, M. Durante*, O. Jäkel, and C. Bert*. Upgrade and benchmarking of a 4D treatment planning system for scanned ion beam therapy. *Medical physics*, 40(5):051722, 2013. doi: 10.1118/1.4800802.

[26] I. Rinaldi, S. Brons, J. Gordon, R. Panse, B. Voss*, O. Jäkel, and K. Parodi. Experimental characterization of a prototype detector system for carbon ion radiography and tomography. *Physics in medicine and biology*, 58(3):413 – 427, 2013. doi: 10.1088/0031-9155/58/3/413.

[27] N. Saito*, N. Chaudhri*, A. Gemmel*, M. Durante*, E. Rietzel*, and C. Bert*. Prediction methods for synchronization of scanned ion beam tracking. *Physica medica*, 29(6):639 – 643, 2013. doi: 10.1016/j.ejmp.2012.08.003.

[28] D. Schardt, O. Kavatsyuk, M. Krämer*, and M. Durante*. Light Flashes in Cancer Patients Treated with Heavy Ions. *Brain stimulation*, 6(3):416 – 417, 2013. doi: 10.1016/j.brs.2012.08.003.

[29] E. Scifoni*, W. Tinganelli*, W. K. Weyrather*, M. Durante*, A. Maier*, and M. Krämer*. Including oxygen enhancement ratio in ion beam treatment planning: model implementation and experimental verification. *Physics in medicine and biology*, 58(11):3871 – 3895, 2013. doi: 10.1088/0031-9155/58/11/3871.

[30] M. Seregni, R. Kaderka*, G. Fattori, M. Riboldi, A. Pella, A. Constantinescu*, N. Saito*, M. Durante*, P. Cerveri, C. Bert*, and G. Baroni. Tumor tracking based on correlation models in scanned ion beam therapy: an experimental study. *Physics in medicine and biology*, 58(13):4659 – 4678, 2013. doi: 10.1088/0031-9155/58/13/4659.

[31] C. Stahler, J. Roth, N. Cordes, G. Taucher-Scholz*, and W. Mueller-Klieser. Impact of carbon ion irradiation on epidermal growth factor receptor signaling and glioma cell migration in comparison to conventional photon irradiation. *International journal of radiation biology*, 89(6):454 – 461, 2013. doi: 10.3109/09553002.2013.766769.

[32] P. Steidl*, T. Haberer, M. Durante*, and C. Bert*. Gating delays for two respiratory motion sensors in scanned particle radiation therapy. *Physics in medicine and biology*, 58(21):N295 – N302, 2013. doi: 10.1088/0031-9155/58/21/N295.

[33] O. Steinsträter*, C. Pantev, and C. Lappe. A Beamformer Analysis of MEG Data Reveals Frontal Generators of the Musically Elicited Mismatch Negativity. *PLoS one*, 8(4):e61296, 2013. doi: 10.1371/journal.pone.0061296.

[34] K. Stützer, C. Bert*, W. Enghardt, S. Helmbrecht, K. Parodi, M. Priegnitz, N. Saito*, and F. Fiedler. Experimental verification of a 4D MLEM reconstruction algorithm used for in-beam PET measurements in particle therapy. *Physics in medicine and biology*, 58(15):5085 – 5111, 2013. doi: 10.1088/0031-9155/58/15/5085.

[35] W. Tinganelli*, N. Ma*, C. Von Neubeck, A. Maier*, C. Schicker*, W. Kraft-Weyrather*, and M. Durante*. Influence of acute hypoxia and radiation quality on cell survival. *Journal of radiation research*, 54(suppl 1):i23 – i30, 2013. doi: 10.1093/jrr/rrt065.

[36] F. Tobias*, D. Löb, N. Lengert, M. Durante*, B. Drossel, G. Taucher-Scholz*, and B. Jakob*. Spatiotemporal Dynamics of Early DNA Damage Response Proteins on Complex DNA Lesions. *PLoS one*, 8(2):e57953, 2013. doi: 10.1371/journal.pone.0057953.

[37] F. Tommasino*, T. Friedrich*, U. Scholz*, G. Taucher-Scholz*, M. Durante*, and M. Scholz*. A DNA Double-Strand Break Kinetic Rejoining Model Based on the Local Effect Model. *Radiation research*, 180(5):524 – 538, 2013. doi: 10.1667/RR13389.1.

[38] D. Varentsov*, A. Bogdanov, V. S. Demidov, A. A. Golubev, A. Kantsyrev, P. M. Lang, D. N. Nikolaev, N. Markov, F. Natale*, L. Shestov, P. Simoniello*, G. N. Smirnov, and M. Durante*. First biological images with high-energy proton microscopy. *Physica medica*, 29(2):208 – 213, 2013. doi: 10.1016/j.ejmp.2012.03.002.

Further publications to the programme health published in 2013

[1] C. Agodi, Z. Abou-Haidar, M. A. G. Alvarez, T. Aumann*, F. Balestra, G. Battistoni, A. Bocci, T. T. Bohlen, M. Bondì, A. Boudard, A. Brunetti, M. Carpinelli, F. Cappuzzello, M. Cavallaro, D. Carbone, G. A. P. Cirrone, M. A. Cortes-Giraldo, G. Cuttone, M. D. Napoli, M. Durante*, J. P. Fernandez-Garcia, C. Finck, A. Foti, M. I. Gallardo, B. Golosio, E. Iarocci, F. Iazzi, G. Ickert*, R. Introzzi, D. Juliani, J. Krimmer, N. Kurz*, M. Labalme, A. Lavagno, Y. Leifels*, A. L. Fevre, S. Leray, F. Marchetto, V. Monaco, M. C. Morone, D. Nicolosi, P. Oliva, A. Paoloni, V. Patera, L. Piersanti*, R. Pleskac*, J. M. Quesada, N. Randazzo, F. Romano, D. Rossi, V. Rosso, M. Rousseau, R. Sacchi, P. Sala, A. Sarti, C. Scheidenberger*, C. Schuy*, A. Sciubba, C. Sfienti*, H. Simon*, V. Sipala, E. Spiriti, L. Stuttge, S. Tropea, and H. Younis. FIRST experiment: Fragmentation of Ions Relevant for Space and Therapy. *Journal of physics / Conference Series*, 420:012061, 2013. doi: 10.1088/1742-6596/420/1/012061.

[2] A. Ruciński, J. Bauer, P. Campbell, S. Brons, D. Unholtz, G. Habl, K. Herfarth, J. Debus, C. Bert*, K. Parodi, O. Jäkel, and T. Haberer. Preclinical investigations towards the first spacer gel application in prostate cancer treatment during particle therapy at HIT. *Radiation oncology*, 8(1):134, 2013. doi: 10.1186/1748-717X-8-134.

[3] S. K. Singh, A. Bencsik-Theilen, E. Mladenov, B. Jakob*, G. Taucher-Scholz*, and G. Iliakis. Reduced contribution of thermally labile sugar lesions to DNA double strand break formation after exposure to heavy ions. *Radiation oncology*, 8(1):77, 2013. doi: 10.1186/1748-717X-8-77.

Doctoral theses 2013 supported by GSI

Literatur

[1] B. Bathen. *Jet measurements and reconstruction biases in proton-proton and Pb-Pb collisions with ALICE at the LHC*. Dr., Westfälische Wilhelms-Universität Münster, 2013.

[2] O. Bertini. *Study of ${}^{3}_{\Lambda}H$ and ${}^{3}_{\Lambda}H$ in the reaction of ${}^{6}Li$ + ${}^{12}C$ at 2 A GeV*. Dr., Johannes Gutenberg Universität Mainz, 2013.

[3] W. Cayzac*. *Ion energy loss at maximum stopping power in a laser-generated plasma*. Dr., TU Darmstadt, 2013.

[4] V. Chetvertkova. *Verification of Monte Carlo transport codes by activation experiments*. Dr., Johann Wolfgang Goeth-Universität Frankfurt am Main, 2013.

[5] B.-F. Cihodariu-Ionita. *Interferometric Diagnosis of Warm Dense Matter*. Dr., Technische Universität Darmstadt, 2013.

[6] C. Cäsar. *Beyond the Neutron Drip-Line: Superheavy Oxygen Isotopes*. Dr., Technische Universität Darmstadt, 2013.

[7] I. Danilkin*. *Coupled-channel dynamics in mesonic systems*. Dr., Technische Universität Darmstadt, 2013.

[8] B. Dönigus*. *Investigation of baryons with strangeness and search for weakly decaying exotics with ALICE at the LHC*. Dr., TU Darmstadt, 2013.

[9] B. Ecker*. *Entwicklung kohärenter Lichtquellen im XUV-Regime*. Dr., Univ. Mainz, 2013.

[10] S. Fedotova*. *Experimental characterization of the HITRAP Cooler trap with highly charged ions*. Dr., Univ. Heidelberg, 2013.

[11] Frömmgen. *Kollineare Laserspektroskopie an radioaktiven Praseodymionen und Cadmiumatomen*. Dr., Univ. Mainz, 2013.

[12] T. Heftrich*. *Stellare Produktions- und Destruktionsraten des radioaktiven Isotops ${}^{60}Fe$*. Dr., Goethe Universität Frankfurt, 2013.

[13] P.-M. Hillenbrand*. *Elektronenspektroskopie im Fundamentalprozess der Elektron-Kern-Bremsstrahlung*. Dr., Univ. Gießen, 2013.

[14] R. Kliemt. *Simulations with the PANDA MVD*. Dr., Rheinische Friedrich-Wilhelms-Universität, Bonn (Germany), 2013.

[15] M. Lochmann*. *Laserspektroskopie der Grundzustands-Hyperfeinstruktur des lithiumähnlichen ${}^{209}Bi^{80+}$*. Dr., Univ. Mainz, 2013.

[16] A. Lymanets*. *Development of prototype components for the Silicon Tracking System of the CBM experiment at FAIR*. Dr., Johann Wolfgang Goethe-Univ. Frankfurt am Main, 2013.

[17] S. R. McConnell. *Two-centre problems in relativistic atomic physics*. Dr., Univ. Heidelberg, 2013.

[18] B. Merk*. *Aufbau eines Mikrobleichsystems an der GSI Schwerionen-Mikrosonde und dessen biologische Anwendungen*. Dr., Univ. Frankfurt, 2013.

 doi:10.15120/GR-2014-1-ANNEX-07

[19] A. Mierau*. *Numerische und experimentelle Untersuchungen gekoppelter elektromagnetischer und thermischer Felder in supraleitenden Beschleunigermagneten*. Dr., Technische Universität Darmstadt, 2013.

[20] A. Movsesyan*. *Quasi-free one-proton and one-neutron knockout reactions on ^{57}Ni*. Dr., TU Darmstadt, 2013.

[21] Q. H. Nguyen*. *(Bio)Molecular Transport and Recognition in Heavy Ion Track-Etched Polymeric Nanopores*. Dr., TU Darmstadt, 2013.

[22] M. S. Sanjari*. *Resonant pickups for non-destructive single-particle detection in heavy-ion storage rings and first experimental results*. Dr., Univ. Frankfurt/M, 2013.

[23] T. Seidl*. *Radiation hardness of superconducting magnet insulation materials for FAIR*. Dr., TU Darmstadt, 2013.

[24] N. Strodthoff. *Critical Phenomena in the Phase Diagrams of QCD-like Theories*. Dr., Technische Universität Darmstadt, 2013.

[25] A. Wendt. *Isospin symmetry in the sd shell: Coulomb excitation of ^{33}Ar at relativistic energies and the new 'Lund-York-Cologne-Calorimeter'*. Dr., Universität zu Köln, 2013.

[26] N. Winters*. *Der korrelierte Radiative Zwei-Elektroneneinfang untersucht in Ion-Atom-Stößen am ESR-Speicherring*. Dr., Univ. Heidelberg, 2013.

Organigramm

GSI Helmholtzzentrum für Schwerionenforschung GmbH

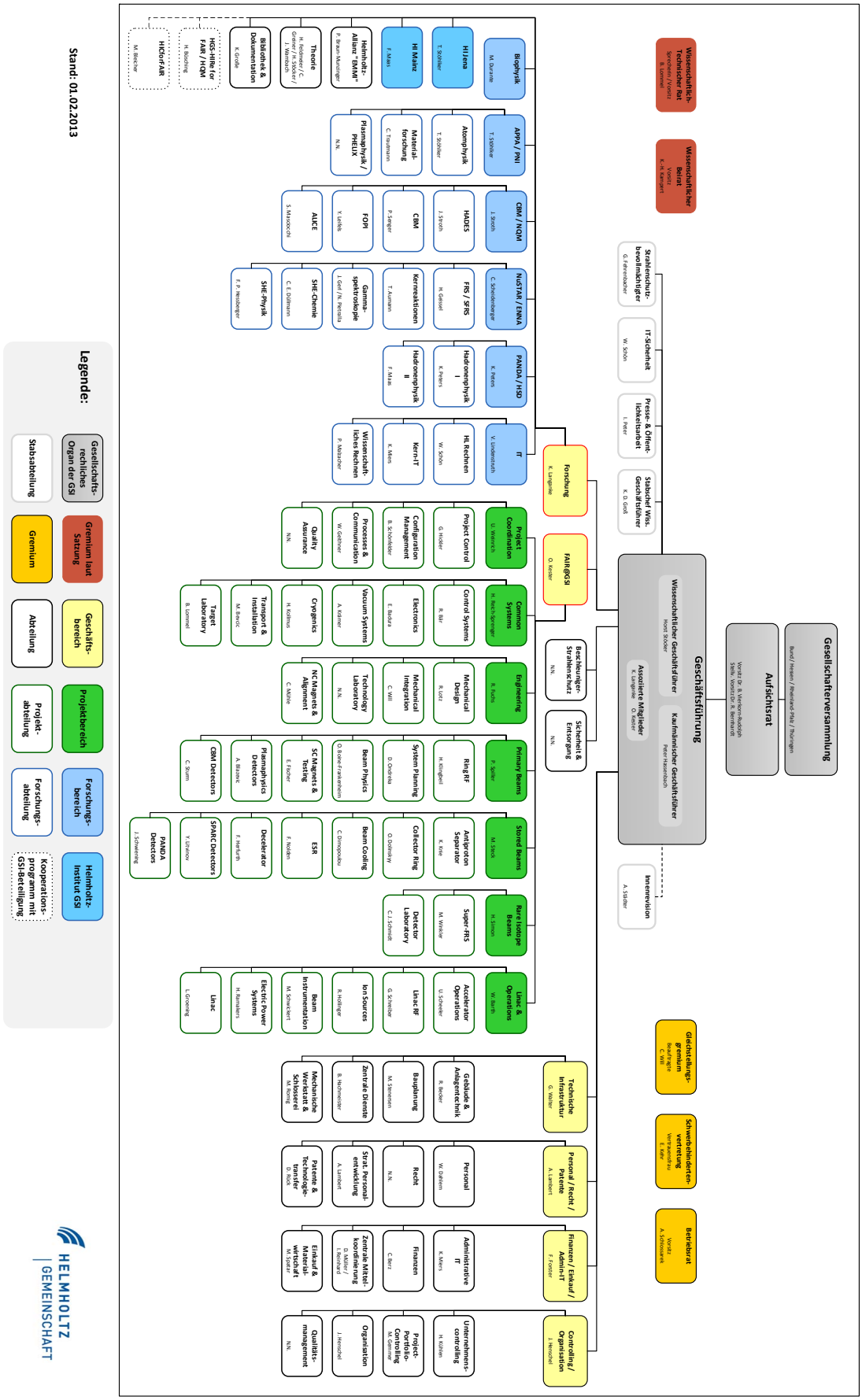

HELMHOLTZ GEMEINSCHAFT

doi:10.15120/GR-2014-1-ANNEX-08

List of Authors

Aberg, S. 126
Acker, D. 307
Ackermann, D. 125, 127, 128, 129, 130, 126
Ackermann, W. 315
Adak, R. P. 51
Adamczewski-Musch, J. 373, 378, 380, 385
Adamczewsky-Musch, J. 48
Adonin, A. 298, 299, 300, 319
Adrian, J. A. 243
Adrich, P. 135
Äystö, J. 98
Agramunt, J. 102, 109, 152
Agrawal, B. 346
Ahmad, N. 56
Ahmed, I. 221
Aichelin, J. 59, 269, 270, 272
Akber, A. 164
Aksouh, F. 135
Aksyutina, Y. 137
Alber, I. 180
Alborea, B. 279
Algora, A. 102
Alhumaidi, M. 316
Alkhazov, G. D. 346
Almalki, M. 320
Altstadt, S. 346
Al-Turany, M. 281, 282, 283, 284, 285
Alvarez Pol, H. 346
Alvarez-Pol, H. 135, 142, 143, 144, 153
Amberg, M. 312, 369
Ameil, F. 102, 117
Amend, W. 46
Amjad, F. 104
Andel, B. 128, 129
Andelkovic, Z. 171, 175
Anderle, K. 228
Andersson, L.-L. 125, 126
Andre, C. 307, 367
Andreev, V. A. 346
Andreyev, A. N. 128, 129
Andronic, A. 45, 66, 67, 70, 71
Angelis, G. De. 130
Anielski, J. 68
Antalic, S. 128, 129, 130
Aprodu, V. 42, 43, 48
Arend, A. 46
Arnold, O. 1
Arrizabalaga, O. 220, 226
Arsene, I. 70
Arsene, I. C. 71
Asai, M. 125
Atanasov, D. 161
Atar, L. 346
Audouin, L. 142, 143
Aulenbacher, K. 369
Aumann, T. 135, 136, 137, 138, 139, 144, 147, 346
Auvinen, J. 268
Avdeichikov, V. 144
Averbeck, N. B. 204
Averbeck, R. 69
Axiotis, M. 130
Ayet, S. 107, 104, 327
Ayyad, Y. 102, 142, 143, 153
Babel, L. 225
Babic, V. 346
Badura, E. 168
Bär, R. 365, 378
Bagnoud, V. 185, 189, 190, 191, 199, 182, 184, 192
Bai, J. 378
Balaceanu, A. 42, 43
Ball, M. 63, 64
Balog, T. 21, 25
Banas, D. 155, 157
Barker, D. 362
Barth, W. 298, 299, 304, 305, 306, 312, 369
Bartos, D. 42, 43, 48
Basko, M. 186, 195
Basko, M. M. 188, 189, 196
Basu, P. 346
Bathen, B. 68
Bauer, J. 250
Bavontaweepanya, R. 275
Bazzacco, D. 130
Beceiro-Novo, S. 139
Becher, W. 246
Beck, D. 378, 380
Becker, A. 242
Becker, G. 204
Bedacht, S. 185, 186, 189, 192
Bednarczyk, P. 117
Behnke, C. 8
Belier, G. 142, 143
Beliuskina, O. 131
Bellachioma, M. C. 386
Belogurov, S. 31
Bemmerer, D. 150, 346
Bendel, M. 144, 346
Benlliure, J. 102, 135, 142, 143, 144, 153
Benotmane, R. 213
Bercuci, A. 48
Berdermann, E. 342, 343
Berezov, R. 298, 299, 300, 319
Berger, M. 61, 62

Berger-Chen, J.-C. 2
Berges, J. 260
Bergmann, C. 45
Bergmann, J. 107, 108
Berrehrah, H. 270
Bert, C. 233, 239, 249, 251, 250
Bertini, D. 144, 281, 285, 288, 289, 290, 346
Bertini, O. 23, 25, 78
Bevcic, M. 304, 307, 322
Beyer, H. F. 155, 158
Bezbakh, A. 144
Bezkorovaynyy, V. 323
Bhattacharya, P. 346
Bhattacharya, S. 346
Bialas, N. 19
Bianco, L. 128, 129
Birkl, G. 171, 172
Blanco, A. 346
Blanco Sancho, J. 197, 198
Blaschke, D. 258
Blaum, K. 164, 165
Blazevic, A. 186, 187, 188, 189, 190, 193, 199
Bleicher, M. 278
Bleile, A. 323
Blell, U. 316, 359
Bloch, T. 144
Block, M. 125, 126
Bloemer, J. 64
Blog, T. 51
Blume, C. 46, 70, 71
Blumenhagen, K. H. 168
Blumenhagen, K.-H. 155, 157, 167
Böhm, R. 362
Böhmer, M. 135, 144
Bönig, H. 209
Boine-Frankenheim, O. 317, 330
Boll, R. A. 125
Bonilla, J. 346
Book, J. 70, 71
Boretzky, K. 135, 346
Borge, M. J. G. 144
Borschevsky, A. 132, 133
Borshchov, V. M. 26, 27, 36, 334
Bosch, F. 155, 161, 163, 164
Boscolo, D. 241
Boutin, D. 161
Boutoux, G. 142, 143
Bowry, M. 102
Bozyk, L. 313, 321, 330, 331
Brabetz, C. 182, 184, 190, 191, 193
Bräuning, H. 168, 307, 308, 367, 385
Bräuning-Demian, A. 307, 365
Brand, H. 125, 126
Brandau, C. 155, 157, 160, 164, 161
Brandt, H. 246
Bratkovskaya, E. 269, 270, 272
Braun-Munzinger, P. 70, 71
Breckow, J. 200
Brevet, R. 239
Brinkmann, K.-T. 80, 100
Britting, A. 79
Briz, J. A. 144
Brons, S. 244
Bruening, U. 53
Bühler, P. 161, 163
Buller, S. 154
Buncic, P. 282
Burchard, M. 178, 179
Burkart, F. 197, 198
Burkhard, P. 326
Busch, M. 312
Busold, S. 190, 191, 193
Caballero-Folch, R. 102, 109, 152
Cabanelas, P. 153, 144
Cabrera, D. 272
Caesar, C. 147, 346
Calvino, F. 102
Cano-Ott, D. 102
Caragheorgheopol, G. 42, 43, 48
Cardoso, M. C. 212
Carlsson, B. G. 126
Carmona Gallardo, M. 144
Carroll, J. J. 164
Cartegni, L. 346
Casarejos, E. 135, 142, 143, 144
Cassing, W. 269, 270, 272
Catanescu, V. 48
Cavaco, J. 386
Cayzac, W. 186, 189
Ceballos, J. 323
Cederkäll, J. 144
Chakraborty, S. 346
Charpy, A. 353, 346
Chartier, M. 135
Chatillon, A. 142, 135, 143
Chatterjee, S. 346
Chatterji, S. 23
Chattopadhyay, S. 51, 56
Chauvin, N. 319
Chen, W. 155, 157
Chen, X. 364
Cherciu, M. 346
Chernikova, N. F. 27
Chill, F. 331
Chorniy, O. 359
Chulkov, L. 136, 137, 144, 346
Cihodariu-Ionita, B. 199
Ciobanu, M. 40, 346
Clemente, G. 306
Colucci, G. 266
Conrad, S. 205
Constantin, F. 42, 43, 48

Constantinescu, A. 233, 249, 250, 251
Coppes, R. P. 216, 223
Corradi, L. 130
Cortes, G. 109, 102, 152
Cortes, M. L. 117
Cortina Gil, D. 139
Cortina-Gil, D. 135, 142, 144, 143
Cowan, T. 346
Cowan, T. E. 150
Cox, D. 126
Cox, D. M. 125
Cravo, E. 140
Crespo, R. 140
Cullen, D. M. 164
Cullen, I. J. 164
Czok, U. 111
Dahl, L. 298, 299
Das, S. 51
Dasgupta, M. 125
Datta Pramanik, U. 135, 346
Davinson, T. 102, 160
de Cuveland, J. 52
De Filippo, E. 157
Debus, J. 250
Dedera, S. 178, 179
Deloch, L. 210, 224
Deltuva, A. 140
Dendooven, P. 104
Dentinger, G. 346
Deo, A. Y. 164
Deppe, H. 40, 382
Deppert, O. 189, 190, 191, 192, 193
Deppner, I. 40, 42, 44
Derkx, X. 125, 126
Dessalvi, M. 280
Dettmering, T. 212, 213, 216, 223
Detwiler, B. 164
Deveaux, C. 38
Deveaux, M. 19
Di Julio, D. 144
Di Nitto, A. 126, 125
Dickel, T. 104, 105, 106, 107, 108
Dierigl, M. 144
Dietrich, D. D. 274
Dillenseger, P. 46
Dillmann, I. 109, 102, 152, 161
Dimopoulou, C. 155, 359, 362, 363, 161, 164
Diwisch, M. 108, 104
Dönigus, B. 73
Dörner, R. 157
Dolinska, M. 362, 363
Dolinskii, A. 357, 359
Dolinskii, O. 365
Domingo-Pardo, C. 102, 113
Dormenev, V. 84, 86
Dorn, C. 307, 309, 322, 367
Dracoulis, G. D. 164
Dubey, A. K. 51
Düllmann, C. E. 125, 126
Düllmann, C. E. D. 304
Dürr, M. 38
Duran, I. 144
Durante, M. 201, 204, 206, 209, 210, 211, 212, 213, 214, 216, 217, 220, 221, 222, 223, 224, 225, 226, 227, 228, 229, 230, 231, 232, 233, 234, 235, 236, 237, 238, 239, 240, 241, 242, 243, 245, 246, 247, 248, 249, 250, 251, 252
Duta, V. 42, 43
Dzhygadlo, R. 90, 91
Dziuba, F. 369
Eberhardt, K. 125, 126
Ebert, J. 104, 105, 107
Echler, A. 151
Eckstein, K. 64
Egelhof, P. 151
Egorova, I. 138
Ehret, A. 81, 344
Eichhorn, A. 231, 233
Eisel, T. 325
Eisenbarth, U. 182
Eissner, T. 86
El Moussati, S. 194
Elekes, Z. 346
Eliav, E. 133
Emling, H. 135
Emschermann, D. 45
Enders, W. 365
Engel, H. 292
Engenhart-Cabillic, R. 234
Engström, M. 365
Eom, J. 38
Epple, E. 3
Erbeldinger, N. 212, 213
Erhard, M. 109, 152
Ernst, B. 28
Ershova, O. 135
Eschke, J. 25, 29
Estrade, A. 102, 104
Evdokimov, A. 102
Even, J. 125, 126
Evers, M. 125
Ewerz, C. 273
Eyrich, W. 79
Fabbietti, L. 1, 2, 3, 6, 10, 61, 63, 64
Faber, H. 216, 223
Faestermann, T. 102, 161, 163
Fahlander, C. 125, 126
Faik, S. 186, 188

Farinon, F. 102, 104, 164
Farnea, E. 130
Fasel, M. 69
Fedotova, S. 175
Fehrenbacher, G. 184, 200, 242
Feldkamp, L. 68
Feldmeier, H. 253, 254
Ferber, N. 103
Fernandez-Dominguez, B. 35
Fetisov, A. A. 346
Feyerabend, M. 293
Fiks, E. 103
Fils, J. 319, 320
Fiori, E. 144, 346
Fischer, E. 323
Fischer, M. 342
Fischer, P. 50
Fischer, R. 307
Fischer, T. 256
Fitzek, J. 375
Flemming, H. 40, 382
Floch, E. 17, 18, 323, 327
Florenkowski, J. 316
Fochler, O. 271
Förster, E. 155
Fomichev, A. 144
Fonte, P. 346
Forck, P. 309, 311, 320
Forsberg, U. 126, 125
Fournier, C. 205, 207, 208, 209, 210, 212, 213, 214, 216, 223, 236, 243, 247
Fraga, E. S. 266
Fraile, L. M. 109, 152
Frank, A. 186, 187, 189
Frank, S. 211, 222
Frankefeld, U. 51
Frankenfeld, U. 23, 30
Franzke, B. 365
Freisleben, W. 323, 327
Frey, B. 210, 224
Friedrich, S. 100
Friedrich, T. 230, 232, 234, 237, 246
Frieß, J. 211, 219
Friese, V. 25, 33, 51
Friman, B. 259, 261
Fritzsche, S. 158, 174
Frühauf, J. 40, 44, 89, 336, 338, 353, 378, 380, 385
Fuchs, R. 322
Fujara, F. 177
Fujioka, H. 100
Furusawa, Y. 215, 235
Gadea, A. 130
Gaipl, U. S. 210, 224
Gaitanos, T. 277
Galatyuk, T. 7, 8, 11, 12, 13, 55
Galaviz, D. 102, 144, 346
Gales, K. 98
Gao, Y. 158
Garcia, C. 47
Garcia, F. 351
Garcia-Rios, A. 102
Gascon, M. 144
Gasik, P. 63, 64
Gaßner, T. 155
Gasparic, I. 346
Gassner, T. 167
Gates, J. M. 126, 125
Geissel, H. 98, 100, 101, 104, 105, 106, 107, 108, 102, 135, 161, 164
Gelfand, D. 260
Gelletly, W. 102
Gerbig, J. 336, 346
Gerhard, P. 297, 298, 299, 310
Gericke, D. O. 189
Gerl, J. 113, 115, 117, 121, 123, 126, 144
Gernhäuser, R. 102, 147, 144, 346
Geschwind, S. 192
Gettmann, V. 369
Gharibyan, N. 125
Ghobadi, G. 223
Ghosh, P. 25, 29, 51
Giacosa, F. 265, 276
Gibhardt, C. 236
Giese, A. 225
Giesen, U. 109, 152
Gilbert, M. 338
Gillitzer, A. 278
Glässel, S. 46
Glasmacher, U. A. 178, 179
Glorius, J. 160
Glück, M. 307
Göbel, K. 346
Görgen, P. 317
Göringer, H. 293
Götte, S. 182, 184
Götzen, K. 90, 91
Gohl, S. 150
Golotsov, V. L. 346
Golovkov, M. 144
Golubev, P. 115, 123, 126, 125, 144
Golubeva, M. 57
Gomez-Hornillos, M. B. 102
Gonzalez, D. 144
Gonzalez, Y. 286
Gorbinet, T. 142, 143
Gorda, O. 359, 365
Gorshkov, A. 144
Gorska, M. 135
Gossiaux, P. B. 270

Grabitz, P. 151
Graeff, C. 228, 233, 238, 239, 249, 250, 251
Graf, H. 307
Greco, C. 228
Gregorich, K. E. 126, 125
Greiner, C. 271, 274
Greiner, F. 105, 104
Grieser, J. 314
Grigorenko, L. 138
Grisenti, R. E. 158
Groening, L. 297, 298, 299, 301, 303, 304, 305, 306
Gromliuk, A. 82
Gronefeld, J. 66, 67
Groo, A. 209, 210
Groß, J. 173
Groß, K. 332
Groß, T. 167
Gross, C. J. 126
Grüll, F. 292
Grün, R. 234
Grushin, A. S. 188
Gsell, S. 342
Günther, M. M. 247
Guerrero, C. 102
Gütlich, K. 326
Gumberidze, A. 155, 157, 158, 160, 167
Gumberidze, M. 4, 5, 7, 8
Gunst, J. 169
Guo, D. L. 157
Guo, Z. Y. 165
Gutz, E. 100
H Hoffmann, D. H. 194
Haake, R. 68
Haberer, T. 250
Haettner, E. 104, 107, 164
Hagenbuck, F. 321, 322, 307
Hagmann, S. 157, 155, 158
Haiduc, M. 346
Haller, S. 279
Hallo, L. 189
Hamilton, J. H. 125
Hannen, V. 171
Harabasz, S. 7
Hartel, C. 221, 225, 245
Hartel, U. 314
Hartmann, W. 125
Hartnack, C. 59
Hartung, M. 307
Haseitl, R. 307
Hauswald, H. 250
Hayano, R. S. 100
Hebeler, K. 259
Heftrich, T. 346
Hehner, J. 346
Heide, M. 68
Heidel, K. 150
Heil, M. 102, 136, 138, 139, 117, 135, 147, 160, 336, 338, 340, 354, 144, 164, 346
Heine, M. 346
Heine, N. 45
Heinz, A. 142, 154, 265, 353, 143, 144, 346
Heinz, C. 131
Heinz, S. 131
Heinz, T. 25
Heiss, B. 144
Helfrich, J. 195, 196, 199
Helm, A. 211, 220, 222
Henner, J. 51
Henning, G. 121
Henning, W. 144
Henriques, A. 346
Herfurth, F. 173, 175, 365
Herr, L. 237
Herrlitz, M. 206
Herrmann, N. 40, 41, 42, 44, 59, 60
Herzberg, R.-D. 125, 126
Heß, R. 359, 155
Heßberger, F. P. 127, 129, 130, 125, 126
Heßberger, F.P. 128
Heselich, A. 219
Hess, C. 180
Hess, R. 161
Hessel, P. 217, 220, 226
Hettrich, R. 362
Heuchel, D. 64
Heuser, J. 21, 22, 23, 24, 25, 26, 33, 51, 335
Heuser, J. M. 27, 37
Heyl, L. 322
Higashi, Y. 100
Hild, S. 233
Hillebrand, P.-M. 161
Hillenbrand, P.-M. 157, 155, 158
Hinde, D. J. 125
Hinke, C. 102
Hirayama, R. 235, 235
Hirenzaki, S. 100
Hirschmann, M. 210
Höhne, C. 38, 39
Hoenle, A. 64
Hoffmann, D. H. H. 192
Hoffmann, J. 89, 125, 168, 336, 338, 353, 372, 374, 378, 380
Hoffmann, T. 308, 367, 307
Hofmann, I. 190
Hofmann, S. 128, 129
Hoischen, R. 123
Holl, M. 147, 346
Hollinger, R. 125, 298, 299, 300

Holzmann, R. 4, 5
Horn, K. P. 304
Hornung, C. 105, 107, 104
Horst, F. 200
Hristov, P. 282
Hu, Z. G. 165
Hübner, A. 125
Hülsmann, P. 364
Hug, F. 11
Huhn, C. 279
Huovinen, P. 267
Hutter, D. 52
Huyse, M. 128, 129
Ickert, G. 144, 346
Ignatov, A. 144, 346
Iida, K. 257
Ilias, M. 132
Ilner, A. 272
Imhof, M. 293
Indelicato, P. 155
Irfan, M. 56
Isaak, J. 346
Itahashi, K. 100
Itkis, M. G. 130
Ivanov, E. A. 346
Ivanova, V. 319, 161
Iwasaki, M. 100
Izumikawa, I. 161
Jäger, E. 125, 126, 304
Jaeger, R. 192
Jährling, S. 346
Jaekel, O. 244
Jagodzinski, P. 155
Jahan, H. 56
Jahrsetz, T. 174
Jain, V. 51
Jakob, B. 204, 242
Jakobsson, B. 144
Janik, R. 351
Jesch, C. 104, 105, 107
Jido, D. 100
Johansen, J. 346
Johansen, J. G. 147
Johansson, H. 346
Johansson, H. T. 135, 154, 353, 354, 144
Jonson, B. 136, 137
Jülicher, S. 375
Junghans, A. 135
Kaczmarek, O. 261
Kaderka, R. 249, 250
Kähler, P. 68
Källberg, A. 365
Kämpfer, T. 155
Kahlbow, J. 346
Kaiser, J. 11
Kaiser, M. S. 298
Kalaninov, Z. 128
Kalaninova, Z. 129
Kalantar-Nayestanaki, N. 104
Kaldor, U. 133
Kalicy, G. 90, 91
Kalimov, A. 359
Kalweit, A. 73
Kampert, K.-H. 38
Kaneko, K. 166
Kaneko, Y. 235
Karabowicz, R. 83, 281, 285
Kardan, B. 12, 13
Kaufeld, I. 345
Kaufmann, W. 320, 367
Kauschke, M. 325
Kebschull, U. 47, 292
Keitel, C. H. 169
Kelic-Heil, A. 117, 135, 142, 147, 336, 340, 143, 165, 346
Kelnhofer, M. 362
Kempley, R. S. 164
Kester, O. 295, 303, 309, 313, 320, 331
Kester, O. K. 301
Ketchieumen Tchitnga, A. M. 88
Kettunen, H. 151
Ketzer, B. 63, 64
Kewes, P. 184
Khan, N. 263
Khan, R. 242
Khomyakov, V. 25
Khuyagbaatar, J. 125, 126, 304
Kibedi, T. 164
Kienle, P. 161, 163
Kim, E. 225
Kim, V. 305
Kindler, B. 109, 128, 129, 125, 126, 152, 195
Kis, M. 40, 342, 343
Kiselev, O. 135, 147, 346
Kissel, R. 346
Kjartansson, E. S. 199
Klatt, M. A. 257
Kleffner, C. 307
Klein, C. 221
Klein, D. 279, 281, 285
Klein-Bösing, C. 68
Kleinschmidt, A. 192
Kleipa, V. 34, 351
Klett, J. 11
Klimkiewicz, A. 135
Klimova, L. V. 27
Klingbeil, H. 314, 315, 332
Klopfer, K. 315
Kmiecik, M. 144
Knetsch, A. 189
Kniajeva, G. N. 130
Knichel, M. L. 66, 67

Knie, K. 355
Knöbel, R. 108, 102
Knoebel, R. 104
Knöbel, R. 161, 164
Kobayashi, K. 346
Kobdaj, C. 275
Koch, K. 40, 117, 168, 327, 336, 338, 353
Kochenda, L. 38
Koczon, P. 28, 35
König, H. G. 315
König, K. 171
Koenig, W. 11
König, W. 12
Koenig, W. 13
Körper, D. 147, 346
Kohn, M. 68
Koike, S. 215
Kojouharov, I. 102, 117, 126
Kolb, B. 29
Kollegger, T. 282
Kolligs, C. 386
Kollmus, H. 325, 387
Kolosova, A. 31
Kopfer, J. 38
Korcyl, G. 12
Korkmaz, S. 250
Kornilov, V. 316
Kotovskiy, N. 175, 367
Kotula, J. 117
Kovalenko, O. 357
Kovtun, O. 157
Kowina, P. 309, 311, 320, 326
Kozhuharov, C. 131, 158, 160, 155, 157, 164
Koziel, M. 19
Kozlova, E. 200
Kozulin, E. M. 130
Krämer, A. 321, 322, 386
Krämer, M. 227, 229, 231, 232, 234, 240, 241
Kraft, D. 209, 210
Kraft, G. 243, 247
Kraft-Bermuth, S. 151
Kratz, J. V. 125, 126, 135
Kraus, D. 186, 189
Kraus, I. 376
Krause, U. 375
Kravtsov, P. 38
Krebs, E. 55
Krebs, M. 93
Kreider, M. 378, 380
Kresan, D. 41, 281, 285, 286, 287, 346
Kreutz, M. 182
Krieg, J. 362
Krieger, M. 49, 50
Krier, J. 125, 126, 304
Krivshich, A. G. 346
Kröll, T. 144
Krömmelbein, A. 216
Kroll, F. 190
Krücken, R. 135, 144
Krüger, C. 320
Krüger, T. 259
Krupko, S. 144
Krzewicki, M. 72
Kulik, D. 110
Kumar Das, P. 346
Kumawat, H. 90, 91
Kumm, M. 332
Kunkel, J. 31, 35, 82, 244, 333, 344, 351
Kunzer, S. 182, 184
Kurcewicz, J. 102, 104, 161, 164
Kurdal, J. 386, 359
Kurilkin, P. 17, 18
Kurz, F. 144
Kurz, N. 89, 100, 102, 125, 126, 135, 142, 168, 336, 338, 353, 372, 373, 374, 378, 380, 385, 143
Kushniruk, R. A. 27
Kuske, T. 84
Kuzminchuk, N. 161, 164
Kuzminchuk-Feuerstein, N. 104
La Tessa, C. 231, 248, 252
Laatiaoui, M. 125
Labiche, M. 135
Ladygin, V. 17
Lahiri, S. 125
Laier, U. 314, 359
Laitinen, M. 151
Lalik, R. 10
Lalovic, N. 123
Lane, G. J. 164
Lang, J. 107, 104
Lang, M. 177
Lang, R. 125, 302
Lapidus, K. 2, 6
Large, M. 207
Larionov, A. 278
Larionov, P. 23, 24, 25, 30
Laurent, B. 142, 143
Lavrik, V. 313
Layer, P. G. 208, 219, 226
Le Bleis, T. 135, 144
Le Fevre, A. 59
Lebedev, A. 281, 284, 285
Lebedev, S. 38
Lebedeva, E. 38, 39
LeBleis, T. 346
Lederer, C. 346
Lehmann, A. 79

Lehmann, H. I. 249, 250, 251
Leibrock, H. 303, 359
Leifels, Y. 59, 346
Leifke, A. L. 204, 206
Lemke, F. 53
Lemmon, R. 135
Lens, D. 314, 332
Lenske, H. 255, 277
Lestinsky, M. 365, 155, 157, 161
Lettmann, M. 119
Leupold, S. 274
Liebermann, H. 376
Liesen, D. 155
Lindberg, S. 154, 346
Lindenstruth, V. 52, 282
Linev, S. 12, 13, 48, 40, 373, 383, 385
Lippert, W. 107
Litvinov, S. 359, 365, 164
Litvinov, S. A. 161
Litvinov, Y. 102, 147, 365
Litvinov, Y. A. 135, 160, 161, 163, 164, 165, 166, 169, 176, 357, 364, 155, 157
Liu, Z. 164
Löbrich, M. 205
Löchner, S. 385
Löher, B. 354, 144, 346
Loetzsch, R. 155
Lohs, A. 256
Loizeau, P. 42
Loizeau, P.-A. 40, 41, 44
Lommel, B. 109, 125, 126, 128, 129, 152, 195
Lomonosov, I. V. 305
Lonsing, R. 307
Lopes, L. 346
Louchart-Henning, C. 121
Louis, P. 10
Lowe, D. 213
Lüttig, P. 66, 67
Luft, S. 217, 220, 226
Lukas, M. 180
Lutz, M. F. M. 275
Lymanets, A. 37
Ma, X. W. 161, 165
Maaß, B. 175
Machado, J. 346
Madl, L. 214
Mäder, J. 302
Märtin, R. 167, 168, 155
Magallanes, L. 244
Magnusson, J. 154
Mahata, K. 135
Mahmoud, T. 39, 38
Mahr, R. 307
Maier, A. 235, 243, 247
Maier, L. 10, 102, 161
Maier, M. 297, 299, 303, 298
Maier, W. 362
Maierbeck, P. 135
Maimone, F. 302
Maire, A. 70, 71
Maiti, M. 125
Maj, A. 144
Malakhow, A. 17
Malka, G. 189
Malygina, H. 29, 33
Man Lo, P. 261
Manafov, A. 281, 284, 285
Manil, B. 155
Mann, R. 128, 129
Manz, S. 40
Mao, R. 164
Mao, R. S. 165
Marganiec, J. 102, 136, 138, 139, 346
Marginean, N. 130
Margutti, J. 63, 64
Markert, J. 9, 55
Maroussov, V. 323
Marquard, M. 66
Marta, M. 109, 102, 152
Martin, A. 171, 172
Martin, J.-F. 142, 143
Martin, N. 73
Martinez, T. 102, 130
Martinez-Pinedo, G. 256
Marty, R. 269
Maruhn, J. A. 188, 196, 257
Marzouki, F. 323
Masciocchi, S. 69
Mathis, A. 63, 64
Mayer, M. 218
Mayr, M. 342
Mazzocco, M. 161
Mecke, K. 257
Mei, B. 165
Meier, J. P. 323
Meister, M. 160
Menegazzo, R. 130
Menges, R. 362
Merk, B. 204, 321
Mertins, F. 192
Metag, V. 100
Metzler, E. 209
Meusel, O. 194
Meyer, S. 212
Michel, J. 10, 13, 20
Michler, F. 274
Mickat, S. 297, 306, 312, 369, 298, 299
Mierau, A. 323
Miernik, K. 125
Mihaylov, D. 6

Milanovic, B. 19
Milosic, T. 307
Minami, S. 125, 168, 372, 374, 385
Mirsch, J. 205
Miskowiec, D. 65, 66
Mistry, A. 125, 126
Möller, K. 332
Mohite, S. 355
Mohite, T. 359
Mokry, C. 125, 126
Montagnoli, G. 130
Montero Moreno, J. M. 180
Montes, F. 102
Moore, I. 104
Movsesyan, A. 135, 147
Muehle, C. 303
Mühle, C. 321, 322
Mühlheim, D. 68
Müller, A. 160, 157
Müller, H. 323
Müller, I. 204
Müller, K. 151
Müller, W. F. O. 311
Münzer, R. 61
Mukha, I. 110, 102, 104, 161
Murböck, T. 171
Murin, Y. 26
Murin, Y. A. 27
Nacher, E. 144
Nagae, T. 100
Nagahiro, H. 100
Nam, Y. 38
Nanova, M. 100
Napoli, D. R. 102, 130
Nasonova, E. 224
Natale, F. 206, 215
Naumann, L. 216
Nazarenko, S. 108
Neff, T. 253, 254
Neiser, A. 12, 13
Netterdon, L. 346
Neuburger, B. 279
Niebur, W. 25, 29, 37, 51
Niedermayer, U. 315, 329
Nielsch, K. 180
Nilsson, T. 135, 154, 144, 346
Ningel, K.-P. 314
Nishi, T. 100
Nitsche, H. 125, 126
Nociforo, C. 98, 102, 104, 135, 351, 161, 164
Nörtershäuser, W. 171
Nolden, F. 364, 155, 161, 164
Nolte, R. 109, 152
Novikov, V. G. 188
Novotny, R. W. 84, 86
O. Boine-Frankenheim, 329
Ochs, K. 298
Oganessian, Y. T. 130
Okayasu, R. 215
Oliinychenko, D. 267
Omtvedt, J. P. 125, 126
Onderwaater, J. 72
Ondreka, D. 376
Orth, H. 88
Ortner, A. 185, 186, 187, 188, 192, 199, 189
Orzhekhovskaya, A. 297, 369, 299
Orzhekovskaya, A. 298
Ott, P. 12, 13
Ott, W. 168, 372
Otte, P. 12, 13
Otwinowski, J. 66, 67
Outa, H. 100
Ozaki, M. 235
Pachmayer, Y. 69
Packer, D. 249, 251
Packer, D. L. 250
Page, R. D. 128, 129
Palffy, A. 169
Palit, R. 135
Pang, G. K. 125
Panin, V. 346
Panja, J. 346
Panschow, W. 377
Papadakis, P. 125, 126
Paradela, C. 102, 142, 153, 143
Parodi, K. 231, 244
Paschalis, S. 135, 147, 346
Passfeld, A. 68
Patsyuk, M. 90, 91
Paulus, G. 170
Pauly, C. 25, 38
Pausch, M. 279
Pawlowski, J. 263
Pawlowski, J. M. 264
Paz, N. 224
Pechenov, V. 9
Pechenova, O. 9
Pellereau, E. 142, 143
Penso, V. 279
Pepitone, K. 189
Perea, A. 144, 346
Pershina, V. 132, 133
Peschke, C. 362
Petagna, P. 37
Peters, K. 77, 90, 91, 93
Petersen, H. 267, 268
Petri, M. 147
Petrick, M. 104
Petridis, N. 158, 155
Petris, M. 42, 43, 48
Petrovici, M. 43, 42, 48
Petukhov, O. 12

Petzenhauser, I. 355
Pfeffer, C. 144
Pfeiffer, B. 111
Pfutzner, M. 104
Pickstone, S. G. 346
Pietralla, N. 113, 115, 117, 119, 121, 144
Pietras, B. 142, 143, 144, 346
Pietraszko, J. 10, 11, 12
Pietri, S. 102, 104, 117, 353
Pikhtelev, A. R. 107
Pikna, M. 351
Pimentel, N. 228
Piotrowski, J. 364
Piriz, A. R. 181, 197, 198, 305
Plag, R. 136, 138, 135, 338, 147, 346
Plaß, W. R. 104, 105, 106, 107, 108
Plass, W. R. 164
Pleskac, R. 248
Pligouroudis, M. 381
Podda, M. 214
Podlech, H. 312, 369
Podolyak, Z. 102
Pohl, M. 346
Pomorski, M. 131
Poppenborg, H. 68
Potlog, M. 346
Prados, C. 378, 380
Prall, M. 250
Preuß, C. 279
Prochazka, A. 100, 102, 104, 142, 351, 143, 164
Prodan, L. 43, 42, 48
Prokesch, H. 250
Prokhorov, I. A. 330
Protsenko, M. 26, 36, 334
Protsenko, M. A. 27
Pschorn, I. 303, 322, 307, 365
Purushothaman, S. 104, 107
Quagli, T. 80
Quint, W. 170, 172
Raach, H. 323
Radon, T. 200
Radu, A. 43, 42, 48
Radulescu, L. 42, 43
Ragnarsson, I. 126
Rahaman, A. 346
Raj, K. 213
Rall, M. 209
Ramakers, H. 18
Ramos, D. 142, 143
Ramos, P. 12
Ranjan, M. 104
Rappold, C. 101
Rastrepina, G. 346
Rathsman, T. 154
Ratschow, S. 321
Ratzinger, U. 194, 306, 312, 369
Rau, P. 262
Rauch, S. 377, 378, 380
Ray, A. 346
Redlich, K. 261
Reed, M. W. 164
Reeg, H. 367
Reemts, D. 182, 184
Reese, M. 113, 115, 119
Reichert, S. 207
Reichert, T. 326
Reich-Sprenger, H. 322
Reifarth, R. 135, 160, 144, 165, 346
Reimann, S. 371, 376
Reinecke, S. 38
Reinhard, P.-G. 257
Reinhardt, T. 150, 346
Reisdorf, W. 59
Reiter, A. 313, 367, 307, 365
Reiter, M. P. 104, 106, 107
Renisch, D. 125
Rennecke, F. 263, 264
Riabov, Y. 38
Ribeiro, G. 346
Ricciardi, M. V. 165
Rice, S. 102
Richter, D. 239, 250
Riego, A. 102, 109, 152
Rienecker, T. 186
Rinaldi, I. 244
Rink, A-K. 104, 105
Rink, A.-K. 107
Rinta-Antila, S. 104
Risch, H. 244
Rischke, D. H. 265, 276
Ritter, S. 211, 217, 218, 219, 220, 221, 222, 224, 225, 226
Roberto, J. 125
Rodriguez-Sanchez, J. L 142, 143, 153
Rodriguez-Tajes, C. 142, 143
Rödel, C. 207
Rödel, F. 207, 212
Röder, M. 150, 346
Rödl, H. 307
Röpke, G. 258
Roether, F. 46
Röttger, S. 109, 152
Romanenko, A. 177
Roßbach, J. 302
Rossbach, J. 362
Rossi, D. 142, 143, 346
Rossi, D. M. 135
Rossi, M. 151
Rosso, V. 241
Rost, A. 11, 13, 12
Roth, B. 236

Roth, M. 185, 187, 188, 190, 193, 195, 196, 199, 186, 189, 192
Roth, T. 279
Rothard, H. 157
Rottländer, P. 303
Rovituso, M. 248, 252
Ruan, M. 130
Rubio, B. 102
Rudolph, D. 123, 126, 125
Runke, J. 125, 126
Rusanov, I. 374, 168
Rybalchenko, A. 281, 283, 285
Rykaczewski, K. 125, 126
Sagaidak, R. N. 130
Sahin, C. 88
Saini, J. 51
Saito, N. 81
Saito, T. R. 81, 101
Salabura, P. 7
Salles, D. 209
Samberg, A. 273
Sanchez, A. 88
Sanchez, J. 37
Sanchez del Rio, J. 144, 346
Sandau, K. 245
Sander, S. 199
Sanjari, M. S. 161, 163, 364, 155
Sanjari, S. 160
Sapple, P. 128, 129
Sarmiento, L. G. 126, 125
Sasaki, C. 261
Sauerwein, A. 346
Savran, D. 135, 144, 346
Scarlassara, F. 130
Schädel, M. 125, 126
Schäfer, S. 314
Schaffner, H. 102, 117, 126
Schanz, V. 192
Scharrer, P. 304
Schatral, S. 53
Schaumann, G. 186, 192, 195, 199, 189
Schausten, B. 125, 126
Scheeler, U. 371, 307
Scheidenberger, C. 95, 98, 101, 105, 106, 108, 111, 102, 104, 107, 161, 164
Scheit, H. 135, 147, 346
Schell, N. 167
Scherer, M. 263
Schindler, F. 346
Schippers, S. 157, 160
Schlegel, T. 189
Schlei, B. R. 321, 376
Schlitt, B. 305, 306
Schmidt, C. 36, 307
Schmidt, C. J. 22, 26, 27, 28, 34, 35, 333, 334, 335, 342, 343, 352
Schmidt, H. R. 37
Schmidt, K.-H. 165
Schmidt, R. 197, 198
Schmidt, S. 171, 346
Schmitt, T. 10
Schmitz, F. 240
Schnell, R. 80
Schnizer, P. 323
Schnorrenberger, L. 144
Schöffler, M. S. 157
Schön, W. 279
Schöppner, N. 178, 179
Scholl, S. 171
Scholz, M. 230, 232, 234, 237, 245, 246
Scholz, U. 230
Schramm, S. 262
Schreck, M. 342
Schreiber, A. 193
Schrock, P. 147, 346
Schroeder, C. 325
Schroeder, I. 217, 226
Schubert, R. 84, 86
Schuetrumpf, B. 257
Schulze, K. S. 155
Schumacher, D. 190, 191, 193, 186, 189
Schurig, I. 359
Schuy, C. 248, 252
Schwab, S. 344
Schwarz, C. 88, 90, 91, 93
Schwarz, K. 275, 291
Schweda, K. 66, 74
Schweitzer, T. 89
Schwemlein, M. 167, 155
Schwenk, A. 259
Schwickert, M. 367, 307
Schwiening, J. 90, 91, 93
Scifoni, E. 227, 229, 231, 235, 241
Seddiki, S. 57
Sedrakian, A. 266
Sedykh, S. 293
Segal, D. 171
Seifert, F. 323
Selyuzhenkov, I. 72
Semchenkov, A. 125
Senger, A. 54, 58
Senger, P. 15, 56
Senzel, F. 271
Shaughnessy, D. A. 125
Shimokawa, T. 215
Short, D. 105
Shuai, P. 165
Shubina, D. 163, 164
Shubina, D. B. 161
Shutov, A. 181, 197, 198

Sidorchuk, S. 144
Sieber, T. 320, 367, 365
Silva, J. 346
Simion, V. 42, 43, 48
Simionovici, A. 155
Simon, C. 34, 40, 44, 42, 320
Simon, H. 98, 136, 137, 135, 353, 354, 142, 143, 144, 147, 346
Simoniello, P. 214, 223
Simons, C. 36, 333, 334, 343
Simonsson, A. 365
Singh, R. 311
Singh, V. 130
Singla, M. 23, 25
Sinha, T. 346
Sitar, B. 351
Sjöholm, J. 365
Skott, P. 13, 246
Smith, K. 102
Sobel, N. 180
Sobiella, M. 346
Sokol, E. 102
Song, J. 38
Sonnabend, K. 346
Sonnemann, M.-P. 245
Sonnenberg, K. 250
Sorokin, I. 23, 24, 51, 25, 352
Soyk, D. 22, 26, 34, 35, 36, 333, 334, 335
Spädtke, P. 302
Spende, A. 180
Spiller, P. 321, 331
Spillmann, U. 167, 168, 155, 157, 158, 161
Stach, D. 150, 346
Stachel, J. 70, 71
Stafiniak, A. 323
Stahl, C. 119
Stan, E. 346
Steck, M. 364, 155, 161, 164, 365
Stefanini, A. M. 130
Stehl, C. 342
Steiger, K. 102
Steinegger, P. 125
Steiner, J. 125
Steiner, K. 307
Steinheimer, J. 262
Steinlage, M. 205
Steinmann, J. 173, 175
Steinsträter, O. 232
Stibor, T. 279
Stockmanns, T. 281, 285
Stöcker, H. 262
Stöhlker, T. 170, 174, 176, 181, 182, 184, 305, 357, 364, 155, 157, 158, 161, 164, 167, 168, 365
Stölker, T. 160
Strasik, I. 330
Streicher, B. 325
Strikman, M. 278
Strmen, P. 351
Stroom, J. 228
Stroth, J. 8, 19, 55
Stühn, B. 180
Sturm, C. 37, 25
Sümmerer, K. 139, 135
Sugita, K. 323
Sulek, Z. 117
Sun, B. 102, 164
Sun, B. H. 161
Sun, Y. 166
Sun, Z. Y. 165
Surzhykov, A. 158, 174
Suzaki, F. 161
Suzuki, K. 100
Suzuki, T. 100
Svoboda, O. 12
Swan, T. P. D. 164
Syndikus, I. 147
Szabo, C. I. 155
Szabo, G. 250
Szilner, S. 130
Szwangruber, P. 17, 18, 327, 323
Tahir, N. A. 181, 197, 198, 305
Taieb, J. 142, 143
Tain, J. L. 102, 109, 152
Takechi, M. 102, 104, 244, 345
Tanaka, Y. 104
Tanaka, Y. K. 100
Tanihata, I. 98
Tapio, S. 213
Tarasov, I. 86
Tarzila, M. 48
Tassan-Got, L. 142, 143
Taucher-Scholz, G. 204, 205, 206, 209, 230, 242
Tauschwitz, An. 188, 195, 196, 186, 189
Tebartz, A. 192
Tengblad, O. 144, 346
Tereshatov, E. E. 125
Terpstra, W. 380, 378
Testov, D. 102
Teubig, P. 144, 346
Tews, I. 259
Thäder, J. 75
Thangaraj, G. 208
Thiel, G. 236
Thielemann, C. 211, 218, 219
Thieme, M. 377
Thies, R. 154, 144, 346
Thönnes, E. 214
Thörle-Pospiech, P. 125, 126

Thomas, A. 12, 13
Thompson, R. 171
Thomson, J. 128, 129
Thorn, D. B. 158
Thorndahl, L. 362
Tinganelli, W. 215, 235
Tinschert, K. 125, 302
Tlusty, P. 12
Törnqvist, H. 354, 147
Toimil Molares, M. E. 180
Tolos, L. 272
Tommasino, F. 230
Toral, F. 17, 18
Torilov, S. Y. 161
Torres, T. 126
Torres De Heidenreich, T. 125
Torres-Rincon, J. M. 272
Träger, M. 11, 131, 342, 343
Trageser, C. 160
Trassinelli, M. 155, 161
Traut, T. 126
Trautmann, C. 177, 178, 179, 180
Trautmann, J. 279
Trautmann, N. 125, 126
Traxler, M. 10, 13, 12, 89, 381
Trees, G. 164
Trotsenko, S. 158, 167, 155, 157
Trzaska, W. H. 151
Tsemo Kamga, J. A. 311
Tsoneva, N. 255
Tu, X. L. 165, 166, 161
Türler, A. 125, 126
Tuominen, E. 351
Turpeinen, R. 351
Tymchuk, I. 22, 26, 36, 334, 335
Tymchuk, I. T. 27
Tymura, L. 182, 184
Typel, S. 139, 258
Udrea, S. 194
Ugur, C. 13, 89, 374
Uhlig, F. 41, 79, 25, 51, 281, 285, 287
Ullmann, C. 319
Uphoff, J. 271
Ur, C. 130
Uschmann, I. 155
Uusitalo, J. 125
Uvarov, L. N. 346
Van Cleve, S. M. 125
Van Duppen, P. 128, 129
van Hees, H. 274
van Luijk, P. 216, 223
Vande Vyvre, P. 282
Varentsov, D. 194
Vargas, J. 142, 143
Velho, P. 346
Venhart, M. 128, 129
Venkataramaniah, K. 111
Verhoeven, W. 45
Verlaat, B. 37
Vikhrov, V. V. 346
Vilan, J. A. 144
Vincelli, R. 307
Virtanen, A. 151
Visinka, R. 343
Vogel, M. 170, 171, 172
Volcic, M. 209
Volkov, S. S. 346
Volkov, V. 346
Vollbrecht, J. 171
Voltz, S. 372, 374, 378
von Lindenfels, D. 172
von Schmid, M. 144
Vorberger, J. 189
Vormann, H. 297, 298, 299, 305
Vorobjev, G. 175, 365
Vorobyev, G. 367
Voss, B. 81, 82, 103, 117, 244, 344, 345, 142, 143, 351
Voss, K.-O. 204
Wälzlein, C. 229
Wagner, A. 135, 150, 346
Wagner, F. 182, 184, 185, 186, 189, 192
Wagner, J. 69
Walasek-Höhne, B. 307, 321, 322, 367
Walker, P. M. 164
Walus, W. 135
Wamers, F. 136, 138, 144, 147, 346
Wang, M. 165, 166, 161
Ward, A. 126
Ward, D. E. 125, 126
Weber, D. 253
Weber, G. 167, 155, 158, 168
Weber, M. 168
Weber, S. 63, 70, 71
Wegrzecki, M. 125
Wehrhan, O. 155
Weick, H. 98, 108, 100, 102, 104, 135, 161, 164
Weigand, M. 346
Weiland, T. 311, 315
Weinberger, D. 150
Weinert, J. 344
Weinheimer, C. 171
Weinrich, U. 359
Welker, H. 321
welker, H. 359
Welker, H. 322
Wessels, J. P. 45, 68
Westerhoff, U. 68
Wetzel, C. 307
Weymann, A. 250
Weyrather, W. K. 221, 225

Weyrich, K. 194
Widmann, E. 100
Wiebusch, M. 20
Wiechula, J. 70, 71
Wiedemann, J. 214
Wiehl, N. 125, 126
Wiesel, M. 172
Wiesmüller, L. 209
Wiessmann, J. 307
Wilde, M. 68
Wilkinson, J. 74
Will, C. 303, 322, 321
Wilson, E. 102
Wimmer, C. 139
Winckler, N. 161, 163, 155, 157, 164, 281, 285, 365
Winfield, J. S. 102, 104
Winkel, M. 144, 346
Winkler, M. 98, 135, 164
Winkler, S. 144
Winn, M. 70, 71
Winters, D. 155
Winters, D. F. A. 161
Winters, N. 155, 161
Wirth, J. 10
Witthaus, M. 385, 367
Wohlers, J. 307
Wolf, A. 25
Wolkanowski, T. 276
Wollmann, D. 197, 198
Wolter, H. H. 258
Wood, R. 102
Woods, P. 102, 160
Woods, P. J. 161, 164
Wüstenfeld, J. 150, 346
Xia, J. W. 165
Xiang, C. 40, 44
Xiang, Y. 387
Xiao, C. 301, 303, 298, 299
Xiao, G. Q. 165
Xu, H. S. 165, 166
Xu, X. 165
Xu, Z. 271
Yakorev, D. 346
Yakushev, A. 125, 126, 304
Yakusheva, V. 125
Yamada, Y. 215
Yamaguchi, T. 161, 164
Yamakami, H. 100
Yan, X. L. 157, 161, 165
Yanez, P. 144
Yang, J. C. 165
Yaramyshev, S. 297, 298, 299
Yavor, M. I. 104, 107
Yeremin, A. 102
Yerokhin, V. A. 174
Yi, J. 38
Yoo, I.-K. 38
Yu, Z. 225
Yuan, Y. J. 165
Zang, Y. D. 165
Zaunick, H.-G. 80
Zdorovets, M. 179
Zhan, W. L. 165
Zhang, G. L. 161
Zhang, W. 165
Zhang, X. H. 165
Zhang, X. Y. 165
Zhang, Y. H. 165, 166
Zhdanov, A. A. 346
Zhou, X. H. 165
Zhu, X. L. 157
Zieblinski, M. 144
Ziegler, E. 155
Zielbauer, B. 182, 184, 185, 191, 192
Zierold, R. 180
Zilges, A. 346
Zimmermann, J. 212
Zink, J. 223
Zink, K. 200, 233, 234
Zinyuk, V. 60
Zipf, P. 332
Zipfel, B. 314
Zuber, K. 150, 346
Zühlsdorf, M. 90, 91
Zumbruch, P. 29, 25, 381
Zwalinski, L. 37
Zweig, M. 380, 378
Zwicker, B. 309
Zwicknagel, G. 173